Eurosensors XVII

The 17th European Conference on Solid-State Transducers
September 21-24, 2003 Guimarães, Portugal

Book of Abstracts

Edited by University of Minho

September 21-24, 2003
Guimarães, Portugal

Eurosensors XVII – Book of Abstracts

Published by:

University of Minho
Dept. of Industrial Electronics
Campus de Azurém
4800 – 058 Guimarães
Portugal
Tel.: +351 253510190
Fax: +351 253510189
http://www.dei.uminho.pt

ISBN: 972-98603-1-9

The Fundação Calouste Gulbenkian supported this book and the
conference proceedings of Eurosensors XVII.

Medida 3 do SIQE, Departamento da Educação Básica sponsored Eurosensors XVII.

Conference proceedings containing four-page papers
are available on CD-ROM published by University of Minho.

Welcome to Guimarães at Eurosensors XVII,

thanks to the authors, who sent us over 459 high-quality papers. Thanks to the members of the Executive Steering Committee, who came personally to Guimarães and, based on reviews made and arranged by the members of the Technical Programme Committee, composed the conference technical programme. We decided to accept 341 of contributed papers: 123 as oral and 218 as poster contribution. We believe that the result is a nicely balanced programme with excellent papers. As many as 41 countries are represented with papers. The technical programme continues with 3 oral parallel sessions and poster presentations. As in Prague, we decided to make the poster sessions plenary, not overlapping with oral sessions. Thanks for all the participants, exhibitors, sponsors and local organizers, who make this conference another successful event in the following series:

1987 Cambridge	1995 Stockholm
1988 Enschede	1996 Leuven
1989 Montreux	1997 Warsaw
1990 Karlsruhe	1998 Southampton
1991 Rome	1999 The Hague
1992 San Sebastian	2000 Copenhagen
1993 Budapest	2001 Munich
1994 Toulouse	2002 Prague

As started from The Hague, this book contains two-page abstracts. Four-page full papers are on CD-ROM proceedings and the authors are encouraged to submit extended paper to special volume of Sensors and Actuators. The annual Eurosensors Fellow award was established in 2000 to "acknowledge outstanding contributions to the field covered by the scope of the Eurosensors series of conferences". The 5000 Euro award was an idea of Eurosensors XIII chairman, R. Wolffenbuttel, and it is sponsored from the profit of the Eurosensors conferences. The typical profile of a prospective Eurosensors Fellow contains the following components: excellent recent work, getting established in the field, in the process of building up a research team within a European based affiliation. Prof. Udo Weimar was elected Eurosensors XVI Fellow. He will present his invited lecture during Eurosensors XVII. The name of the Eurosensors XVII Fellow will be disclosed and the award will be given during a special award ceremony at the Eurosensors XVII conference dinner. This year we will have at the beginning of the sessions on Tuesday afternoon (at 16:00) one keynote and two invited speakers.

Next Eurosensors conference will be organized by Universita di Roma “Tor Vergata”, Italy and it will be held in Rome.

Enjoy the conference and your time in Guimarães and in Portugal!

José Higino Correia
Eurosensors XVII General Chairman

Conference Organization

Eurosensors XVII Executive Committee

A. D'Amico	Chairman, Italy
J. H. Correia	Portugal
P. Ripka	Czech Republic
R. F. Wolffenbuttel	The Netherlands
F. O. Soares	Portugal

Local Organizing Committee

J. H. Correia (Chairman)	Dept. Industrial Electronics
J. G. Rocha	Dept. Industrial Electronics
G. Minas	Dept. Industrial Electronics
P. Mendes	Dept. Industrial Electronics
F. O. Soares	Dept. Industrial Electronics
N. F. Ramos	Dept. Industrial Electronics
P. Trabulo	Dept. Industrial Electronics
L. G. Gomes	Dept. Industrial Electronics
J. C. Ribeiro	Dept. Industrial Electronics
S. F. Ribeiro	Dept. Industrial Electronics
L. Gonçalves	Dept. Industrial Electronics
Dalila Durães	Dept. Industrial Electronics
S. Lanceros-Mendez	Dept. Physics
J. A. Mendes	Dept. Industrial Electronics
J. L. Afonso	Dept. Industrial Electronics
C. Couto	Dept. Industrial Electronics
J. Monteiro	Dept. Industrial Electronics

Eurosensors International Steering Committee

A. D'Amico (Chairman)	Italy
H. Baltes	Switzerland
G. Blasquez	France
S. Bouwstra	Dennmark
J. H. Correia	Portugal
J. Dziuban	Poland
J. Gardner	United Kingdom
F. J. Gutierrez Monreal	Spain
P. Hauptmann	Germany
B. Hök	Sweden
I . Iliev	Bulgaria
R. S. Jachowicz	Poland
B. E. Jones	United Kingdom
S. Leppavuori	Finland
I . Lundström	Sweden
H. Meixner	Germany
F. Menil	France
E. Obermeier	Germany
R. Puers	Belgium
M. Prudenziati	Italy
P. Ripka	Czech Republic
Ch. S. Roumenin	Bulgaria
Y. Vlasov	Russia
R. F. Wolffenbuttel	The Netherlands

Conference Organization

Eurosensors XVII International Program Committee

A. D'Amico
A. Bossche
A. van den Berg
Anderson Gert
Barry Jones
Bernard Michaux
Bob Puers
Z. Brzozka
Carsten Diehl
Chavdar Roumenin
Christophe Pijolat
Claude Martelet
Denise Wilson
Corrado Di Natale
Dimitris Tsoukalas
Dulce Geraldo
Ernest Obermeier
Fátima Bento
Filomena Soares
Francis Menil
G. A. Urban
Gerhard Wachutka
Gert F. Eriksen
Giorgio Sberveglieri
Hermann Sandmaier
Horia Chiriac
Ilia Iliev
J. R. Morante
B. Jakoby
Jan Dziuban
Jan G. Korvink
Jaume Esteve
Javier Gutierrez
Joao Pedro Conde
Jochen Kuhmann
Jose H. Correia
Juergen Brugger
Julian W. Gardner
Julio Martins
Karsten Dyrbye
Lina Sarro
Manuela Vieira
Maria Prudenziati
Maria Teresa Gomes
Marian Bartek
Matthias Müllenborn
Michael J. Schoening
Michiel Vellehoop
Milena Koudelka-Hep
W. Mokwa
Nico F. de Rooij
Nicole Jaffrezic
Oliver Paul
Paddy French
Paul Regtien
Paulo Freitas
Pavel Ripka
Pedro Silva Girao
Peter Hauptmann
Peter Payne
Philippe Renaud
Radivoje Popovic
Reinoud Wolffenbuttel
Rodrigo Martins
Roger de Reus
Rupert Chabicovsky
Ryszard Jachowicz
Sami Franssila
Seppo Leppavuori
Siebe Bouwstra
Simon Middelhoek
Tayfun Akin
Theo Doll
Thomas Gessner
Udo Weimar
Valentim Smyntyna
Wolfgang Benecke
Wouter Olthuis
Yuri Vlasov

Table of Contents

Nanorobotics

Ari Requicha

Professor of Computer Science and Electrical Engineering
Director, Laboratory for Molecular Robotics
University of Southern California, Los Angeles, CA 90080-0781
requicha@lipari.usc.edu
http://www-lmr.usc.edu/~requicha

Abstract:

Thie talk discusses nanorobotics and its connections with sensor/actuator networks. Nanorobotics encompasses: (i) design and fabrication of nanorobots with overal dimensions at or below the micrometer range and made of nanoscopic components; (ii) programming and coordination of large numbers of nanorobots; and (iii) programmable assembly of nanoscale components either by manipulation with SPMs (or other robotic devices), or by self-assembly.

Nanorobots are quintessential NEMS (nanoelectromechanical systems) and raise all the important issues that must be addressed in NEMS design: sensing, actuation, control, communications, power, and interfacing across spatial scales and between the organic/inorganic and biotic/abiotic realms. Nanorobots are expected to have revolutionary applications in such areas as environmental monitoring and health care, and to open new avenues of research and development in pervasive interaction with the physical word.

This talk begins by discussing nanorobot construction, which is still at an embryonic stage. The emphasis is on nanosensors and nanomachines, areas which have seen a spate of rapid progress over the last few years. The focus then changes to nanoassembly by manipulation with scanning probe microscopes (SPMs), which is a relatively well established process for prototyping nanosystems. Prototyping of nanodevices and systems is important for design validation, parameter optimization and sensitivity studies. Nanomanipulation also has applications in repair and modification of nanostructures built by other means. High-throughput SPM manipulation may be achieved by using multi-tip arrays. Experimental results show that interactive SPM manipulation can be used to accurately and reliably position molecular-sized components. These can then be linked to form subassemblies, which in turn can be further manipulated. Applications are presented.

From metal oxide gas sensors towards artificial olfaction and its application

U.Weimar

Institute of Physical and Theoretical Chemistry, University of Tübingen, Auf der Morgenstelle 15, 72076 Tübingen, Germany, email: upw@ipc.uni-tuebingen.de

***Summary**: The contributions presents the basics of the modelling approach for the metal oxide based gasc sensors established in the last years at the University of Tübingen. Also, a selection of applications succesfully solved in the frame of European projects is presented together with the input from or to the basic understanding of the gas sensing .*

***Keywords:** gas sensor microsystem and applications, modeling*
***Category:** 1 (General, theoretical and modeling), 5 (Chemical sensors), 10 (Applications)*

1 Introduction

This contribution presents on one side the modelling approach for metal oxide based gas sensors established in the last years at the University of Tübingen and on the other side some selected applications of this type of sensors. The applications were chosen either for their relevance or for highlighting the usefulness of the results of the modelling when one deals with practical problems.

2 Modelling

The Gas Sensor Group at the University of Tuebingen is involved in both basic research and application of, among others, metal oxide based gas sensors. The finding that a fractal knowledge is the result of research and development in this field was the reason for starting a modelling effort with the aim of putting together a research approach that results in a coherent picture integrating, both, basic understanding and sensor application aspects. The approach/research program was first time sketched in [1]. Its rationale is presented in what follows:

Assessment of the state of the art by literature survey and selection of an appropriate metal oxide system. The candidate used for this is SnO_2.

- SnO_2 is a wide band gap n-type semiconductor, its conduction type being related to the intrinsic oxygen vacancies. Gas sensors based upon this material are extensively used in the detection of toxic gases. Their advantages such as low costs and high sensitivities make them very attractive, whereas disadvantages such as lack of selectivity and strong interfering effect of water vapour still hinder their use as measuring devices.

Definition of objectives for the next steps:

- What are the relevant parameters to be focused at?
  - Identification of relevant problems, e.g. CO in presence of humidity
  - Typical 3S parameters (Stability, Sensitivity, Selectivity) as a basis for benchmarking.
- What are the experimental and boundary conditions?
  - Measure as much as possible in real world conditions and on real world samples. This was leading to measurements performed under gas atmospheres provided by gas mixing stations. Most of the measurements are electrical measurements and optical spectroscopy. For material characterization tasks also UHV techniques were used.
- Preparation of appropriate samples according to the following criteria:
  - "Simple" preparation of sensitive material, which avoids additives (where the additive role is not quite understood)
  - Very sensitive samples to get sufficient "effect" (good signal to noise ratio)
  - Optimised substrate (materials)
  - Solid experimental basis: High throughput reproducible preparation method, which ensures a high sample to sample reproducibility and consequently allows for testing of devices in totally different experimental rigs in different laboratories over a long period.
- Extensive testing for selection of appropriate combination of samples and relevant parameters. Anticipating a little bit, the main conclusions were:
  - The home-made SnO_2-based sensors live up to the standards of commercial SnO_2-based sensors. Especially the ones doped with 0.2% wt. Pd were showing excellent sensitivity for CO detection and a remarkable long-term stability and have been chosen for the following basic studies.
  - The CO detection is especially influenced by the presence of the humidity. Consequently, the water-CO combination was used as a model system.

- Selection of complementary experimental techniques appropriate to the a.m. aims
  - o DC resistance measurements are the "normal" way of sensor measurements and allow for a screening of large number of sensors.
  - o AC impedance spectroscopy as a technique which is applied in normal operation conditions. AC impedance spectroscopy provides knowledge on the different contributions (surface, bulk, contacts) to gas sensing.
  - o Work function change measurements by the Kelvin method are also performed in normal operation conditions. They additionally provide insight about surface reactions where free charge carriers are not involved.
  - o Catalytic conversion measurements in normal operation conditions give additional information about the gas sensing reaction paths.
  - o Infrared spectroscopy and especially DRIFT measurements are allowing (in principle) for the identification of surface species involved in the sensing process in normal operation conditions. It is one of the few spectroscopic techniques which can be applied in normal operation conditions.
- Development of necessary tools for the interpretation of the experimental findings ; the modelling should start from elementary steps governing those surface-molecule interactions which lead to charge transfer (adsorption, reaction, desorption, etc) and then show how these steps are linked with the macroscopic parameters describing the sensor response.
- Application of the interpretation tools to precisely planned experimental model systems.

Most of the experimental techniques were used in the past for studying gas sensors [2, 3, 4, 5, 6, 7, 8, 9, 10, 11, 12, 13]. However, they were never combined and applied to the same samples/sensors and their results never integrated in a complete modelling of gas sensing.

Partly, the experimental results and the modelling tools are already published [14, 15, 16, 17, 18] or submitted for publication[19, 20]. The general picture became clearer just recently [21].

The sensing of CO in the presence of water vapour seems to be described as follows:

1. CO sensing on tin oxide sensors is associated with combustion forming CO_2. The combustion is a linear phenomenon. The power law dependence of the resistance on the CO concentration is due to the transduction dominated by Schottky barriers.
2. Water adsorption results in the formation of:
   - hydroxyl groups bound to Sn atoms forming strong surface dipoles hence leading to changes in the electron affinity;
   - donors attributed to 'rooted' hydroxyl groups.
3. Oxygen adsorption results in temperature-dependent ionosorbed species (O_2^-, O^{2-} and O^-), with O^- dominating in the range of interest (250 to 400°C)
4. CO sensing occurs via two pathways:
   - reaction with ionosorbed oxygen and
   - reaction with hydroxyl groups, which changes the electron affinity and releases H atoms. The latter combines with associated water and provide donors (protonated water) i.e. free charge carriers.

   For lower concentrations and temperatures the reaction with OH groups dominate.
5. The resistance dependence -of the equivalent circuit resistors corresponding to the different elements in the sensing layer- on the CO concentration for dry and humid background air can be described by a power law ($R \sim p_{CO}^{-n}$) and resemble each other. The dependence of the exponent on the operation temperature can be related to two qualitatively different contributions to the layer resistance. These two contributions could be due to tin dioxide grains close to and further away from the catalytically active electrodes or due to the existence of depleted and undepleted grains.
6. The overall combustion of sensors is not the independent combination of the contributions of the different sensor parts. The presence of the substrate influences the combustion of the sensitive layer. The combustion of the sensor signal and the sensitive layer in contact with the Pt electrodes increase with increasing water vapour content of the gas.

The findings demonstrate that gas sensors based on metal oxides are complex devices and that it is not possible to understand them in the absence of a systematic approach. They also demonstrate that the proposed approach can be applied with a reasonable degree of success. The results obtained up to now are first steps in the understanding of the gas sensing with metal oxide sensors starting with the mechanistic level and continuing with the transducer function.

There are still a number of specific topics to be investigated and clarified; however, the already acquired knowledge allows for the next needed advancements especially towards the understanding of the role of dopants. The extension of the modelling to the study of the sensing of other target gases is envisaged; currently hydrocarbons' sensing is under investigation with the aim of understanding the role of electrodes in this process (see next paragraph).

2 Applications

From the point of view of applications it has to be stated clearly that the ones which are going in the

direction of large markets are from the industrial point of view the most appealing ones. Besides domestic applications e.g. as leak detectors in flats and buildings with combustion heating systems the automotive field is a large driver. Traditionally the combustion regulation and control with e.g. the lambda probe is a considerable field for the application of chemical gas sensors however the metal oxide sensors presented here are not really suitable for this field. This is mainly due to the high temperatures and the very hazardous environment in the exhaust manifold of a combustion engine. On the other hand comfort features for new cars are getting more in the focus of the automotive industry and consequently also applications where gas sensors are involved. Such a feature is the automated re-circulation flap which is closing upon "bad air quality" outside the car. A typical indicator for such a situation is carbon monoxide (CO) which is emitted by other cars and accumulated e.g. at large cross roads in an urban environment or in tunnels. Fig 1 is showing results of such a test drive where an electrochemical cell was used as a reference instrument for recording the actual CO concentration and an SnO_2 coated micromachined sensor was evaluated in parallel. The measurements were carried out in a joint European project called CIA (Chemical Imaging for Automotive applications, BRPR-CT96-0194).) to demonstrate the feasibility. The outcome of that is meanwhile picked up by the industry and commercialised.

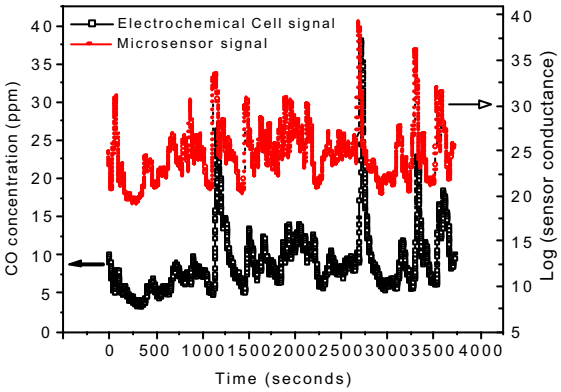

Fig. 3. SnO_2 based microsensor resistance and EC output time dependence during a test drive.

For the optimisation of the solving of this application, the knowledge acquired in the modelling is of big help; it provides the needed knowledge for designing a sensor with high CO sensitivity and low cross sensitivity to water.

In the frame of the CMOSSens project (IST-1999-10579) the main application was the residual oil monitoring in compressed air. It was necessary to devise a microsensor module which should allow a continuous monitoring of the proper functioning of the compressor line and provide an immediate alarm as soon as malfunctioning occurs. This applies to two environmental issues:

- First, the filters have no more to be changed on a time basis, but only in the moment their capacity is really exhausted as indicated by the sensor. This will help to save material and energy in the filter production.
- Second, as soon as malfunctioning occurs, not only the compressor, but also the whole production line behind the compressor is flooded with oil. This requires an extensive clean up and disposal of large quantities of hazardous waste. In addition, major components have to be completely replaced. The sensor will detect malfunctioning at an early stage, early enough to close the valves behind the compressor and protect the production line.

In order to fulfil this demand the most crucial step was the vaporisation of all residuals (e.g. oil and water aerosols). This was done using an expansion through capillaries. The main result is presented in Fig 2 showing the response of home made and commercial sensors to the exposure to an atmosphere containing 23.5 mg/m^3 of lubricant oil. The oil content was determined through independent gravimetric measurements. In the figure also the time dependency of the other parameters, which could influence the sensor resistance, is given

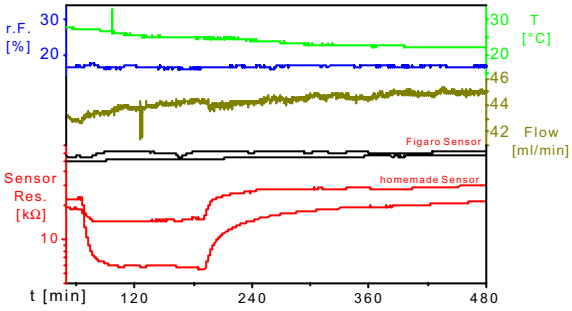

Fig. 2. Sensor resistance, humidity, flow and temperature time dependence during the exposure to a oil-containing atmosphere.

A very interesting finding of the presented work was the role played in the oil vapour detection by the combination between substrate and electrode materials. It was found that the best results were obtained by using a combination Al_2O_3 based substrate and Au electrodes. These facts are currently under investigation.

Another application area is the field of the so called "electronic noses". Even if the recognition of gaseous species by such a electronic sensor system and the biological olfaction are not directly comparable, the term "electronic nose" is meanwhile established in literature but will not be used in this description.

The information shown in Fig 3 is giving the correlation of independent test data for the artificial ageing of corn oil using UV irradiation. Here one can clearly see the necessity of a recalibration which determines the improvement in the prediction of the ageing time. Similar experiments can be also carried out with e.g. packaging material which was the topic

of a European project PARFUM (ESPRIT IT 20.848). Since the applications in this field needs a lot of assistance from the analytical chemistry field and real application know how, it turned out during the last decade that the "electronic nose" is much more a "application specific sensor system (a3s)" (following the statement of Andreas Hierlemann) and not a universal tool which can be applied always and everywhere. To reach this point of understanding it was also very useful to discuss these matters with all the experts which are grouped in the European projects NOSE (I and II). Since it is obviously getting now more application specific it makes also sense to develop more versatile, integrated, smart microsystems with appropriate data evaluation strategies which will be an important topic for FP6 in the European framework. The optimisation of the sensing components will have to be performed in a coherent manner like the one proposed in the previous section.

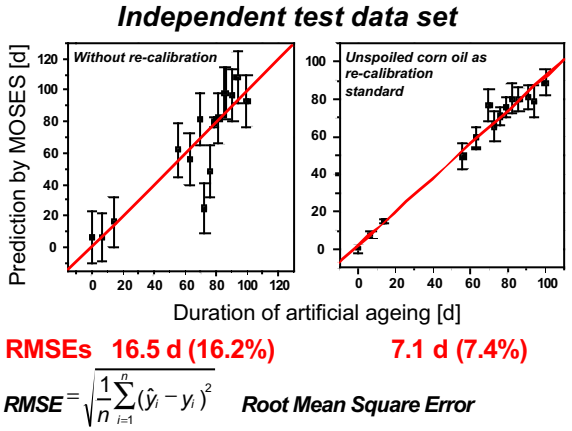

Fig. 3. Correlation between the prediction of the sensor system and the real ageing data.

The current research trend in this area is the building of flexible re-configurable sensor system by using microsystems technology with the aim of obtaining handheld instruments.

3 Conclusion

We think that by using the research approach presented above it is possible to expand this approach to other model systems including different metal oxides and target gas (mixtures) and in this way build-up the knowledge needed for the solving of relevant applications. It is important to remember that the identification of the research targets, the preparation of the needed samples and the use of the appropriate research methods are the crucial steps in any such attempt. The sensor science has to be elaborated by combining the interests and knowledge of sensor developers, sensor users and scientists aiming for the basic understanding; all these experts should talk to each other for mutual benefit. The users can clearly identify the relevant objectives, the developers can optimise the samples/sensors and the scientists will be able to build the knowledge needed for the further advancements. The latter will have to be validated by the development of better performing real world sensors able to be applied for solving relevant practical problems.

References

[1] N. Barsan, M. Schweizer-Berberich, and W. Göpel, Fresenius Journal of Analytical Chemistry (1999) 365, 287–304

[2] K.D. Schierbaum, U. Weimar, and W. Göpel, Sensors and Actuators B 2 (1990) 71.

[3] J. Mizsei and J. Harsanyi, Sensors and Actuators 3 (1983) 397.

[4] J. Mizsei and V. Lantto, Sensors and Actuators B 4 (1991) 163.

[5] H. Geistlinger, I. Eisele, B. Flietner, and R. Winter, Sensors and Actuators B 34 (1996) 499.

[6] S. Lenaerts, M. Honore, G. Huyberechts, J. Roggen, and G. Maes, Sensors and Actuators B 18-19 (1994) 478.

[7] J. Gutiérrez, M. Arés, M.C. Horrillo, I. Sayago, J. Agapito, and L. Lopez, Sensors and Actuators B 4 (1991) 359.

[8] F.J. Gutiérrez, L. Arés, J.I. Robla, M. Horrillo, I. Sayago, and J.A. de Agapito, Sensors and Actuators B 8 (1992) 231.

[9] L. Xingqin, C. Chunhua, X. Wendong, S. Yusheng, and M. Guangyao, Sensors and Actuators B 17 (1993) 1.

[10] Ovenston, D. Sprinceana, J.R. Walls, and M. Caldararu, Journal of Materials Science 29 (1994) 4946.

[11] U. Weimar and W. Göpel, Sensors and Actuators B 26-27 (1995) 13.

[12] G. Martinelli, M.C. Carotta, L. Passari, and L. Tracchi, Sensors and Actuators B 26-27 (1995) 53.

[13] M. Labeau, U. Schmatz, G. Delabouglise, J. Roman, M. Vallet-Regi, and A. Gaskov, Sensors and Actuators B 26-27 (1995

[14] N. Barsan and U. Weimar, Journal of Electroceramics, (2001) 7 (3): 143-167

[15] N. Barsan, A. Heilig, J. Kappler, U. Weimar, and W. Göpel, Conf. Proc. EUROSENSORS XIII, The Hague (The Netherlands), ISBN 90-76699-01-1 (9/1999) 183-184.

[16] J. Kappler, N. Barsan, U. Weimar and W. Göpel, Conf. Proc. EUROSENSORS XI, Warschau (P), ISBN 83-908335-0-6 (9/1997) 1177-1180.

[17] J. Kappler, N. Barsan, A. Tomescu, U Weimar, Thin Solid Films 391 2 (2001) 186-191

[18] S. Harbeck, N. Bârsan, U. Weimar, and V. Hoffmann, Thin Solid Films, 391,2001, 176-185

[19] S. Harbeck, A. Szatvanyi, N. Barsan, U. Weimar, V. Hoffmann, to be published in Thin Solid Films

[20] N. Bârsan, P. Siciliano, J. Kappler, M. Vantaggio, and U. Weimar, submitted to Sensors and Actuators B

[21] N. Barsan and U. Weimar, J. Phys.: Condens. Matter 15 (2003) R1-R27

Thin-Film Silicon Micromachined Resonators Processed at Low Temperatures for Sensor Applications

J. Gaspar[1,2], V. Chu[1] and J. P. Conde[1,2]

[1]INESC Microsistemas e Nanotecnologias, Rua Alves Redol, 9, 1000-029 Lisbon, Portugal
email: jgaspar@inesc-mn.pt http://www.inesc-mn.pt
[2]Materials Engineering Dept., Instituto Superior Técnico, Av. Rovisco Pais, 1049-001 Lisbon, Portugal

Summary: *This work reports on the fabrication and characterization of thin-film silicon micromachined bridges and cantilevers processed at low temperature (≤ 110 ºC) on glass and plastic substrates. The microelectromechanical structures are electrostatically actuated and the resulting deflection is optically monitored with subnanometric precision. Resonance frequencies of 30 MHz are detected and quality factors up to 3000 are observed in vacuum. The deflection of the structures, either at low-frequency or at resonance, is measured as a function of the actuating voltage, geometrical dimensions, structural materials and pressure. An electromechanical model is presented. A Young's modulus of 160 GPa is extracted for hydrogenated amorphous silicon and the elementary energy dissipation processes in thin-films are discussed.*

Keywords: *thin-films, low temperature, microelectromechanical structures, and amorphous silicon*
Category: *2 (Materials and technology)*

1 Introduction and motivation

Microelectromechanical systems (MEMS) use planar microelectronics fabrication techniques to produce 3D structures, which have both electronic and mechanical functionality. MEMS sensors and actuators can be based on a variety of different physical, chemical and biological principles [1].

Currently, most MEMS are made by bulk micromachining of crystalline silicon (c-Si) substrates or by surface micromachining of high-temperature poly-Si on a c-Si wafer substrate [1].

Thin-film MEMS aim to exploit the advantages of thin-film technology in the fabrication of MEMS on large area substrates such as glass and plastic. Because of the low temperature used in most thin-film processes [2], it is compatible with a wide variety of substrates. Thin-film technology is also CMOS compatible, allowing backend integration of MEMS with Si integrated circuits (IC's). Thin-film MEMS devices such as electrostatic actuators with integrated magnetic sensing and thermal actuators have been developed [3].

This paper reports on the fabrication and characterization of thin-film Si surface-micromachined electrostatic actuators processed at low temperatures on glass and plastic substrates. Electrostatic actuators play an important role in MEMS for applications such as optical switches, radio-frequency (RF) resonator filters or sensitive mass detectors [1]. The motivations for this work are (i) the possibility of obtaining high-performance resonators with this technology, and (ii) the structural and mechanical characterization of thin-film materials such as hydrogenated amorphous silicon (a-Si:H) and nanocrystalline Si (nc-Si:H).

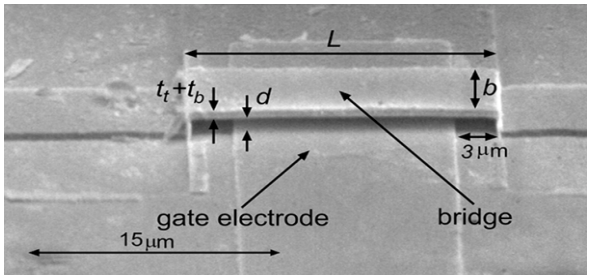

Fig. 1. SEM picture of a microbridge with gate electrode.

2 Experimental procedures

2.1 Sample preparation

Microbridges and cantilevers with an underlying gate electrode are fabricated on glass and plastic substrates using thin-film technology and surface micromachining. The maximum processing temperature used was 110 ºC. Fig. 1 shows a scanning electron micrograph (SEM) of a bridge structure.

The process starts with the deposition and patterning of a 100 nm-thick aluminum (Al) gate electrode. A 1 µm-thick photosensitive polymer is then spun and patterned by photolithography, forming the sacrificial layer. The structural material is then deposited and patterned into bridges and cantilevers. The structures consist of a-Si:H/Al and nc-Si:H/Al bilayers or doped a-Si:H or nc-Si:H single structural material. The sacrificial layer is then selectively removed, releasing the microstructures. Typical device dimensions are 1 µm for the air-gap (d), 4-100 µm for the length (L), 4-20µm for the width (b) and 100-500 nm for the thickness (t).

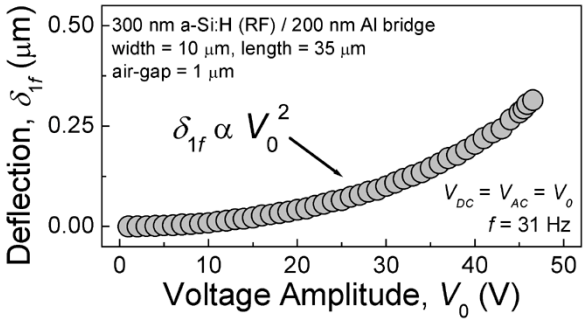

Fig. 2. Bridge deflection measured against V_G at 31 Hz.

2.2 Sample characterization

The microstructures are electrostatically actuated by applying a voltage, V_G, with DC and AC components, $V_G = V_{DC} + V_{AC}\sin(2\pi ft)$, between the gate and the structure. The resulting deflection is optically monitored by focusing a laser on top of the structure and measuring the reflected beam deviation with a quadrant photodetector. The deflection (at low frequencies f or at the resonance) is measured as a function of V_G, geometrical dimensions (L, b and t), type of structural material and pressure, P.

3 Results

3.1 Deflection dependence on gate voltage

Fig. 2 shows the deflection, δ_T, of an a-Si:H/Al bridge measured as a function of the applied gate voltage, V_G, at 31 Hz. δ_T is proportional to V_G^2 and amplitudes up to 300 nm are measured with a precision of 1 Å. It is possible to extract important materials elastic properties, such as the Young's modulus, E, from the δ_T dependence on V_G [4]. $E_{a\text{-}Si}$ ~ 160 GPa is thus estimated.

3.2 Resonance frequency and quality factor

The deflection of the microstructures is monitored as a function of the gate excitation frequency, f, and the resonance frequencies are typically in the MHz regime. Fig. 3 shows the resonance peak (f_{res} ~ 2.3 MHz) of a microbridge measured at 10^2 Torr and 10^{-6} Torr. As the pressure decreases, the resonance

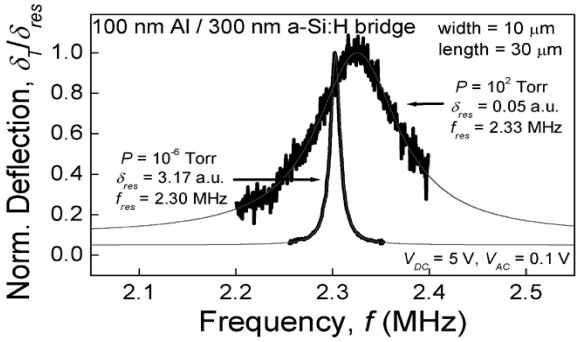

Fig. 3. Resonance deflection peaks of a microbridge at 10^2 Torr and 10^{-6} Torr.

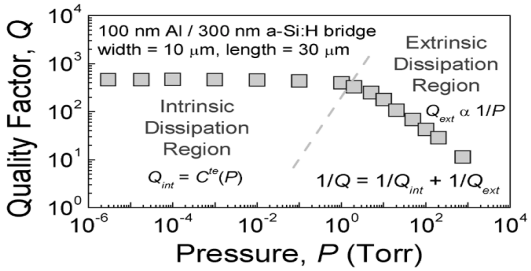

Fig. 4. Quality factor, Q, versus surrounding pressure, P.

amplitude, δ_{res}, increases by a factor of ~ 100 and the resonance peak narrows, i.e., the quality factor, Q, increases. Q^{-1} is proportional to the energy dissipation. The Q dependence on the pressure, P, is plotted in Fig. 4. For pressures above 1 Torr, Q decreases by a factor of ~ 100, and is limited by air damping [5], and for P < 1 Torr, Q is constant, and it is limited by intrinsic mechanisms.

In Fig. 5 (a), the intrinsic quality factor, Q_i, for n^+-a-Si:H bridges is plotted as a function of the length, L. Quality factors up to 3000 are obtained, which are comparable to those of c-Si and poly-Si resonators. The general trend of Fig. 5 (a) is that Q_i increases with L, suggesting that the main dissipation mechanism is thermoelastic dissipation [6]. Resonance frequencies, f_{res}, up to 30 MHz are detected (Fig. 5 (b)).

The thin-film resonators here described are promising for applications such as sensors/actuators arrays integrated with CMOS or biosensors arrays over glass and plastic substrates.

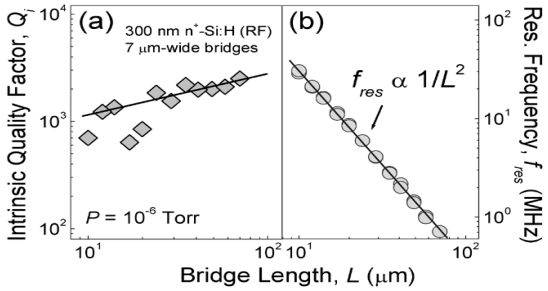

Fig. 5. (a) Intrinsic quality factor and (b) resonance frequency, measured as function of the length of n^+-a-Si:H bridges, at 10^{-6} Torr.

References

[1] M. Elwenspoeck, and R. Wiegerink, *Mechanical Microsensors*, Springer, 2001.

[2] R. A. Street, *Hydrogenated Amorphous Silicon*, Cambridge University Press, 1991.

[3] V. Chu, J. Gaspar, and J. P. Conde. *Mat. Res. Soc. Symp. Proc.* 715 (2002) A12.3.

[4] K. E. Petersen. *IEEE Trans. Elect. Dev.* ED-25 (1978) 1241-1250.

[5] W. E. Newell. *Science* 161 (1968) 1320-1326.

[6] R. Lifshitz, and M. L. Roukes. *Phys. Rev. B* 61 (2000) 5600-5609.

Metallic Triple Beam Resonator with Thick-film Printed Drive and Pickup

T. Yan[1], B. E. Jones[1], R. T. Rakowski[1], M. J. Tudor[2], S. P. Beeby[2] and N. M. White[2]

[1]The Brunel Centre for Manufacturing Metrology, Brunel University, Uxbridge, Middlesex UB8 3PH, UK
email: barry.jones@brunel.ac.uk http://www.brunel.ac.uk/research/bcmm/remise/
[2]Department of Electronics and Computer Science, University of Southampton, Highfield, Southampton, Hampshire, SO17 1BJ, UK

Summary: *A triple beam resonator fabricated in 430S17 stainless steel with thick-film piezoelectric elements to drive and detect the vibrations is presented. The resonator substrate was fabricated by a simultaneous, double-sided photochemical etching technique and the thick-film piezoelectric elements were deposited by a standard screen-printing process. The combination of these two batch-fabrication processes provides the opportunity for mass production of the device at low cost. The resonator, a dynamically balanced triple beam tuning fork (TBTF) structure 15.5mm long and 7mm wide, has a favoured mode at 6.2 kHz with a Q-factor of 3100 operating in air.*

Keywords: *thick-film, piezoelectric, metallic resonator, triple beam tuning fork*
Category: 4 *(Non-magnetic physical devices)*

1 Introduction

The thick film printing process has been successfully used to deposit piezoelectric materials onto silicon structures for fabrication of a silicon beam resonator and other silicon devices [1]. In this paper we describe the application of this process to the fabrication of a metallic triple beam resonator with screen-printed thick film lead zirconate titanate (PZT) drive and sense elements and present initial results from the device. This device, a metallic triple beam tuning fork structure with thick-film printed piezoelectric drive and pickup elements, is the first of its kind [2].

2 Resonator design and fabrication

The resonator consists of three beams (tines) aligned in parallel alongside each other and joined at a decoupling zone at each end which is in turn connected to the surrounding material. The central beam is twice the width of the two outer beams. The resonating element has a length of 15.5 mm, a thickness of 0.25 mm and beam widths of 2 mm and 1 mm. The distance between the beams is 0.5 mm. Finite element analysis (FEA) has been performed to predict the modal behaviour with stress distribution and eigenfrequencies of the resonator. Thick-film PZT elements were printed on separate regions at each end of the central beam, where maximum stresses exist as the resonator operates in its favoured mode of vibration. The PZT element at one end drives the vibrations, whilst the PZT element on the other end detects them. Positioning the PZT driving and sensing elements on the regions of maximum stresses maximises the degree of mechanical coupling between the active piezoelectric layer and the resonator for generation of both driving forces and sensing signals.

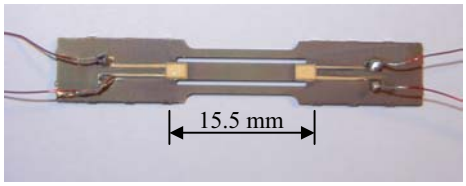

Fig. 1. Photograph of the metallic resonator.

The triple beam resonator has three different fundamental modes of vibration out of the plane of the wafer. In mode one, the three tines oscillate in phase. In mode two, the central tine does not oscillate while the outer tines vibrate at a phase of 180^{o} with respect to each other. In mode three, the central tine vibrates in anti-phase with the outer tines. This mode is the optimum for operating such a triple beam resonator, as both bending moments and shearing forces at the decoupling zone are cancelled out and very little vibration energy is coupled into the supporting frame at each end. This improves the Q factor of the device and therefore the performance of a resonant sensor employing such a device. The in-phase mode has the lowest resonant frequency, followed by the second and the third modes. There are also other higher-order modes of vibrations. A photograph of the metallic resonator is shown in Figure 1.

The substrate of the resonator was fabricated from a 0.5 mm thick 430S17 stainless steel thin wafer using a simultaneous double-sided photochemical etching technique, with a top pattern to define the layout of the resonator and a bottom pattern to etch in a standoff distance leaving the section of resonating element 0.25 mm thick. A dielectric layer was then deposited at the defined driving and sensing regions on the top surface of the resonator using a standard screen-printing process, and consecutively layers of bottom gold electrode, piezoelectric paste and top gold electrode, were deposited each with their own

screens. The dielectric layer was required to isolate the bottom electrode from the resonator substrate in order to polarise the piezoelectric layer in a later stage.

The fabricated resonators were sawn from the wafer and electrical connections were made by conventional wire bonding. The PZT elements were then connected in parallel and poled for one hour at 130°C with a voltage of 200 V across the electrodes. Given the measured PZT layer thickness of 50 μm, an electric field of strength 4 MV/m was generated during the polarising process. This aligns the dipoles within the PZT material enabling it to exhibit its piezoelectric properties.

3 Resonator operation and results

The resonator operating in air was first tested in an open-loop configuration in order to observe the vibration modes and confirm successful operation of the driving and sensing mechanisms. The PZT element at one end of the resonator was driven by an AC signal of 1V pk-pk from a Hewlett-Packard 89410A Vector Signal Analyser with the tracking generator scanning over a frequency range of 2-9 kHz. The PZT element on the other end of the resonator was connected to a Kistler 5011 Charge Amplifier and the output from the charge amplifier was fed back to the signal analyser for frequency response analysis of the resonator. Figure 2 shows the frequency response of the resonator with clear resonances at 2.2 kHz, 6.2 kHz and 6.8 kHz. These resonances correspond to the first, the third and the fourth vibration modes of the resonator respectively, according to the FEA predictions, with the third mode of vibration being far dominant due to the favourable dynamic structure balance associated with this mode. It is obvious that the peak corresponding to mode two is not visible, since in this mode the central beam, where the pick-up is located, is at rest.

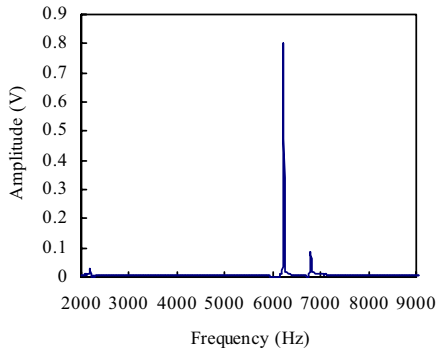

Fig. 2. Amplitude-frequency response of the resonator.

The Q factor of the resonator in air for mode three was measured to be 3100, which is excellent when compared to a Q-factor 70 of a silicon single beam resonator with PZT thick films operating in air [1] or a Q-factor 400 of a silicon triple beam resonator with thin films vibrating in air [3] or the Q-factors of other metallic resonators [4] in air.

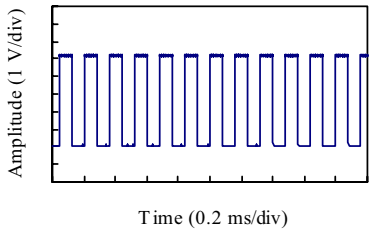

Fig. 3. Frequency output of the resonator in closed-loop.

Next, the resonator (in air) was tested in a feedback closed-loop configuration. The PZT sensing element was connected to a charge amplifier circuit, followed by a digital 90-degree phase shift circuit and a second stage amplification circuit all on one circuit board. The output from the second stage amplification was fed back to the other PZT element for driving. In such a way, the resonator was maintained at resonance in the required favourable mode of oscillation. Figure 3 shows the frequency output of the resonator in such a closed-loop operation.

4 Conclusions

This paper has reported for the first time a metallic triple beam resonator etched from stainless steel in which the vibrations are driven and detected by thick-film printed piezoelectric elements. The resonator has been characterised in an open-loop test which identified the modes of vibration and confirmed the successful operation of the device and of the driving and sensing mechanisms. The resonator has further successfully been operated in a closed-loop configuration with the designed associated electronics. The presented resonator has shown a good mode selectivity with a Q factor of 3100 operating in air, which compares very favourably with other reported resonators of similar structures operating in air.

Acknowledgements

The authors wish to acknowledge the support of EPSRC (Grant GR/R51773) and the industrial collaborators within the Intersect Intelligent Sensing Faraday Partnership Flagship Project (2002-2005) entitled "Resonant Microsensor Modules for Measurement of Physical Quantities (REMISE)".

References

[1] S. P. Beeby and N. M. White. Thick-film PZT – silicon micromachined resonator. *Electron. Lett.* 36 (2000) 1661-1662.

[2] B. E. Jones and N. W. White. Metallic resonators. Patent Application GB0302585·5.

[3] Th. Fabula, H. -J. Wagner and B. Schmidt. Triple-beam resonant force sensor based on piezoelectric thin films. *Sens. Actuators A* 41-42 (1994) 375-380.

[4] D. S. Randall, M. J. Rudkin, A. Cheshmehdoost and B.E. Jones. A pressure transducer using a metallic triple-beam tuning fork. *Sens. Actuators A* 60 (1997) 160-162.

A Novel Dynamic Thermoelastic Actuation Scheme for Microresonators

R. Mahameed and D. Elata

Faculty of Mechanical Engineering,
Technion - Israel Institute of Technology, Haifa 32000, Israel
Email: mrashed@tx.technion.ac.il

Summary: *A novel dynamic actuation scheme for deformable microstructures is presented. This actuation scheme makes use of the thermoelastic response of the structure material. In existing thermoelastic actuators, the driving forces are induced by a change in the structure temperature. In contrast, the novel thermoelastic actuation scheme exploits local gradients of the temperature to induce the driving forces. As a result, activation and termination of the driving forces in the novel scheme are far more rapid. The new scheme is employed to design a cantilever beam microresonator with high frequency and large deflection amplitudes.*

Keywords: *Thermal actuators, Modeling, Dynamic response*
Category: *1 (General, Theoretical and modeling)*

1 Introduction

Thermoelastic actuators offer a simple means of driving microsystems and they can be readily fabricated using standard materials and micromachining processes. Existing thermoelastic actuation schemes [1-3] (Fig. 1.) utilize the thermal expansion of deformable solids to achieve the required deflection. In these existing schemes, the driving forces are fully developed only when the thermoelastic elements have been heated to the required actuation temperature. Termination of the driving forces requires cooling of these elements (e.g., by conduction). Due to the thermal relaxation time, the response of these actuators is slow relative to other actuation methods (e.g., electrostatic actuation).

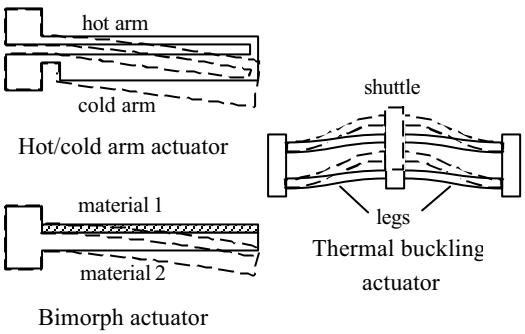

Fig. 1. Existing thermoelastic actuation schemes.

The novel thermoelastic actuation scheme presented in this work is characterized by a much shorter response time. In contrast to existing actuators, the driving forces in the novel actuation scheme are induced by local gradients of the temperature. These gradients fully develop within a time scale that is much shorter than the time required to heat or cool the entire thermoelastic elements.

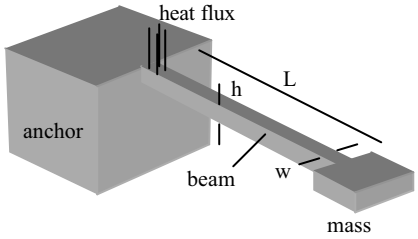

Fig. 2. Schematic view of a thermoelastic microresonator.

2 Principle of operation

The novel thermoelastic actuation scheme is demonstrated on a microresonator (Fig. 2). A resistive heater periodically supplies heat over a confined region of the upper surface of the deformable beam, in the vicinity of the anchor that also serves as a heat sink. The stable periodic temperature distribution that develops under the heater is schematically illustrated in Fig. 3, for a square waveform of supplied heat flux.

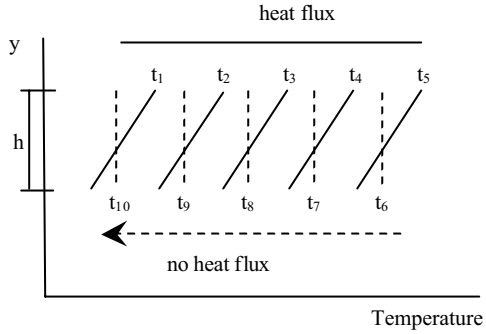

Fig. 3. Progression of the temperature distribution in the beam under the heater. Several time points t_i ($t_{i+1}>t_i$) during a single load cycle are considered.

The temperature gradient rapidly develops as heat is supplied, and maintains a constant amplitude whereas the temperature continuously increases. When heat supply is ceased, the temperature gradient rapidly vanishes whereas the temperature continuously decreases.

The temperature gradient under the heater induces a gradient in the thermal stress across the beam height. The gradient in thermal stress gives rise to an internal bending moment. This internal moment is proportional to the heat flux and is instantaneously activated and terminated. The periodic variations in this internal moment induce the steady vibrations of the beam.

By tuning the frequency of the heat flux wave-form to the natural frequency of the cantilevered beam, a resonance response is achieved.

The temperature gradient under the heater is proportional to the supplied heat flux. This gradient across the beam height h, is generated within a time scale of the order $\tau_h=h^2/\alpha$ where α is the thermal diffusivity of the structure material. In contrast, in the existing thermoelastic actuation schemes the thermoelastic elements have to be heated to the actuation temperature along their entire length L. This heating process occurs over a time scale of $\tau_L=L^2/\alpha$. Typically, the ratio between the height and length of thermoelastic actuator beams is $h/L\approx 1/100$. Therefore, using the temperature gradient across the beam height for actuation has the potential of reducing the thermal response time by four orders of magnitude relative to existing schemes ($\tau_h/\tau_L\approx 10^{-4}$).

3 Simulations

To demonstrate the novel actuation scheme and investigate its performance, the dynamic response of a microresonator beam was simulated. The results presented here relate to a thin Aluminum beam with the following dimensions (see Fig 2): L=800 [μm], h=10 [μm], w=100 [μm], m=2.7 10^{-9} [kg]. The microresonator was subjected to a periodic heat flux with maximal amplitude of q=6.4 10^8 [W/m^2].

The dynamic response was simulated with the ANSYS^{TM} finite element code using coupled-field harmonic analysis. The maximal deflection at the free edge of the beam was computed assuming a damping ratio of ζ=0.01 and neglecting convection.

The deflection amplitude as function of the frequency of the supplied heat flux is illustrated in Fig. 4. The resonance frequency of the system is 4.72 [kHz], and it is slightly larger than the free vibration frequency of the system because the beam is elongated due to the heating. The resonance amplitude is 22 [μm], and in the vicinity of the clamped edge of the beam the maximal von Mises stress is 78 [MPa] and the maximal temperature is 90 [^oC] over ambient temperature.

For this thermoelastic resonator, the thermal time scale across the beam height is τ_h=1 [μs], which suggests that it may be driven in frequencies of up to $f\approx 0.5$ [MHz].

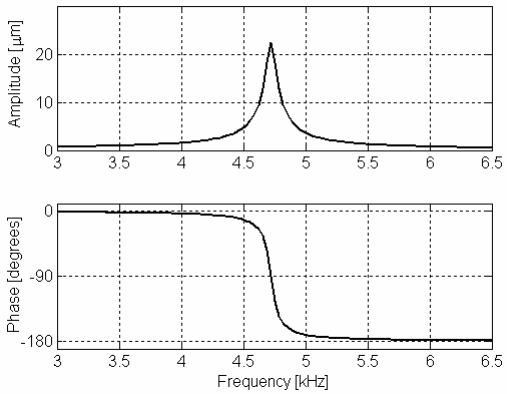

Fig. 4. Frequency response of the microresonator - free edge deflection and phase shift relative to the heat flux.

4 Discussion

The novel thermoelastic actuation scheme for microresonators presented in this work enables higher frequencies than can be achieved by using existing thermoelastic actuation schemes on structures of comparable dimensions.

Furthermore, the specific example analyzed here demonstrates that large deflection amplitudes may be achieved.

Thermoelastically actuated resonating structures of the proposed type may also have some advantages over common electrostatically actuated microresonators [4]. In electrostatic resonators a small gap must be designed between the driving electrodes to avoid the necessity of using high voltages. As a result of the small gap, kinematic constraints may be imposed on the deflection amplitude of the deformable element, and large damping forces may arise (unless the device is packaged in vacuum).

Furthermore, electrostatic forces are inherently non linear and therefore the dynamic response of electrostatic resonators may be non linear and may exhibit instabilities [5] that do not occur in thermoelastic actuators.

References

[1] R.S. Chen, et al., *JMM*, 12, 291-296, 2002.

[2] R. Hickey, et al., *JMM*, 13, 40-46, 2003.

[3] C.D. Lott et al., *Sensors and Actuators A*, 101, 239-250, 2002.

[4] C.T.-C. Nguyen et al., *Proc. IEEE*, 86(8), 1756-1768.

[5] S.D. Senturia, *Microsystem design*, Kluwer Academic Publishers, 2000.

Resonant MEMS microsensor for the measurement of fluid density and viscosity

O. Vancauwenberghe[1], A.R.H. Goodwin[2], E. Donzier[1], M. Manrique[2], and F. Marty[3]

[1]Schlumberger Doll Research, 36 Old Quarry Road, Ridgefield CT 06877, USA
email: vanco@slb.com
[2]Schlumberger Cambridge Research, High Cross Madingley Road, Cambridge CB3 0EL, UK
[3]Groupe ESIEE, SMM, Cité Descartes, BP 99, F-93162 Noisy-le-Grand, France

Summary: *A resonant MEMS microsensor was developed to measure fluid density and viscosity. It consists of a thin plate made of a SOI top layer vibrating at resonance in its first bending mode. Its working principle is based on the resonance frequency and quality factor affected by the surrounding fluid density and viscosity. Measurements have been done in a series of gases and liquids at different pressures and temperatures. The resonant MEMS is able to measure densities to ± 1% in the range of 1 to 1100 kg/m^3 and viscosities to ± 5% in the range of 10 to 10^5 µPa s.*

Keywords: *Density, viscosity, Resonant MEMS, vibrating plate, SOI*
Category: *4 (Non-magnetic physical devices)*

1 Introduction

In the petroleum industry, measurements of density and viscosity are required to determine the value of the produced fluid and production strategy. Density and viscosity measurements are also important in industrial process control, especially in chemical and food industries.

We took advantage of the fact that the vibration of a plate is affected by the surrounding fluid to design a resonant MEMS microsensor using SOI wafers and DRIE micromachining. In this paper, we will describe our sensor working principle and fabrication, and report the measurements obtained.

2 Principle of operation

The resonant MEMS microsensor, shown in Figure 1, consists of a thin vibrating plate made of the top silicon layer of a Fusion-Bonded SOI wafer. The use of SFB SOI wafers allows us to choose at will the thickness of the vibrating plate and simplifies the DRIE micro-machining steps by providing an etch stop with the buried oxide (BOX).

To drive into resonance the vibrating plate, magnetic forces are used as illustrated in Figure 2. The device is placed in a constant magnetic field B generated by an external electromagnet or a permanent magnet. With an alternating current I injected in a coil fabricated on the plate top surface, alternating Laplace forces F put the plate in forced oscillations. When the current is at the plate first natural frequency, the plate vibrates in resonance in its first bending or flexion mode with maximum amplitude. Piezoresistive gauges configured in Wheatstone bridges and placed close to the clamped edge are used to sense the varying strains in the plate as it oscillates. These bridges allows us to control and measure the resonance frequency f as well as the amplitude or equivalently the quality factor Q.

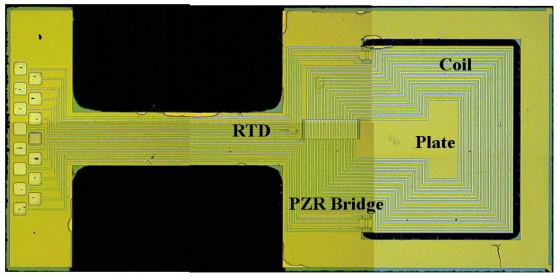

Fig. 1. Picture of the whole Si resonant MEMS microsensor with main components indicated.

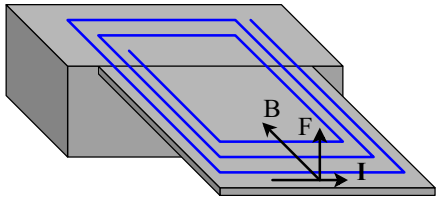

Fig. 2. Actuation principle by Laplace forces

When the MEMS sensor is placed in a given fluid, its resonance characteristics, f and Q, will be affected by the surrounding fluid as follows. The fluid in proximity to the oscillating plate is moved by the body's motion, adding effective mass or inertia to the intrinsic mass of the plate, hence decreasing f. The shearing associated with the fluid motion around the plate gives rise to viscous energy loss per cycle, and so makes $Q < Q_{vacuum}$. Thus, the density ρ and viscosity η of the fluid may be obtained by measuring f and Q of the vibrating plate in resonance.

3 MEMS fabrication

The starting wafer is a 4" SFB SOI wafer with a top Si layer 20 µm thick. A thermal oxide is first grown, then a 0.4 µm PolySi layer is deposited, implanted with boron and patterned to define an RTD for temperature in-situ measurement and the piezoresistive gauges for resonance control and f and Q measurements. After passivation and contact openings, a 1 µm thick aluminum layer is sputter deposited and patterned to define the coil and other interconnections.

DRIE is then used to etch from the front side the SOI layer around the plate and from the back side the Si substrate all underneath the plate. A final HF etch of the BOX layer releases the vibrating plate.

Figure 3 shows a completed resonant MEMS sensor in its package specifically designed to allow it to be dipped in various fluids, liquids or gases, at various pressures (up to 70 MPa or 10 kpsi) and temperatures (up to 150 °C).

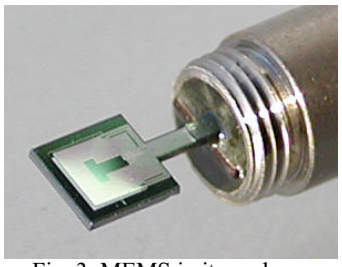

Fig. 3. MEMS in its package

4 Measurements

Table 1 shows f and Q measured in vacuum and in various fluids, namely inert gas (Ar), natural gas (CH_4), reservoir oil, formation water, and silicone oil. In vacuum and at 298 K, f_0 is 5.3 kHz, in good agreement with FEM simulations with ANSYS.

Fluid	ρ (kg/m^3)	η (mPa·s)	f (Hz)	Q
$P \to 0$			5326	4556
CH_4	7.23	0.011	4722	127
Ar	671	0.049	1429	60
Crude oil	774	1.02	1160	10
Brine	1060	0.99	1005	12
Si oil	1910	2200	527	2

Table 1. f and Q in vacuum and various fluids.

With some approximations, simple relations can be derived to describe the dependency of f and Q on the fluid density ρ and viscosity η:

$$\frac{f}{f_0} = \left(1 + \frac{\pi w}{4h}\frac{\rho}{\rho_{Si}}\right)^{-1/2} \quad \text{and} \quad Q\, f^{3/2}\sqrt{\eta\rho} = \text{CST}$$

where ρ_{si} is the Si density, w and h are the plate width and thickness and CST is a constant [1, 2, 3].

However, a more elaborate model [3] was necessary to account for the f and Q variations over the whole range of densities and viscosities for both gases and liquids.

To calibrate the microsensor, three parameters defined in the model need to be adjusted by fitting the measures taken with argon. After this rather simple calibration, densities in the range of 1 to 1100 kg/m^3 can be measured to ± 1%, and viscosities in the range of 10 to 10^5 µPa s to ± 5%. These accuracies on ρ and η were obtained by comparing measured values with either accepted literature or experimental values.

Figures 4 and 5 show the error on measured densities and viscosities for Ar, N_2, CH_4, heptane, crude oil, formation water and reference standards.

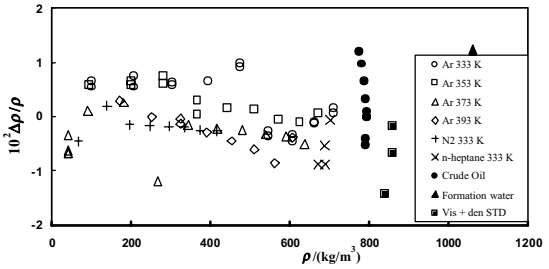

Fig. 4. Relative error on measured densities

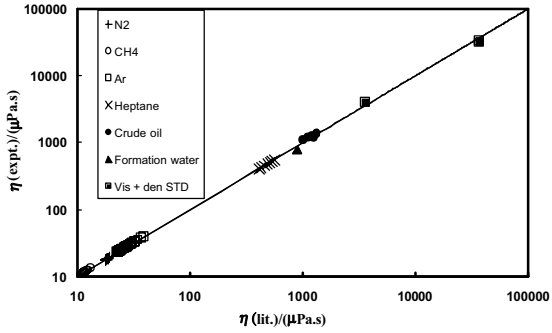

Fig. 5. Comparison between measured viscosities and referenced values

References

[1] J.E. Sader, "Frequency response of cantilever beams immersed in viscous fluids with applications to the atomic force microscope", *J. Applied Physics* 84 (1998) 64-76, and references therein.

[2] L.D. Landau, E.M. Lifshitz, Fluid mechanics, Pergamon (Oxford, 1989).

[3] A.R.H. Goodwin, E. Donzier, M. Manrique, O. Vancauwenberghe, to be published.

Surface Effects on Nanomechanics of Ultra-thin Silicon Resonators

Dong F. Wang[1,2], Takahito Ono[1] and Masayoshi Esashi[3]

[1]Graduate School of Engineering, Tohoku University, Sendai 980-8579, Japan
[2]Core Research for Evolution Science and Technology (CREST) – JST
[3]New Industry Creation Hatchery Center (NICHe), Tohoku University, Sendai 980-8579, Japan
Telephone: 81-22-217-6937, Fax: 81-22-217-6935, E-mail: dongfang@mems.mech.tohoku.ac.jp

Summary: *The downscaling of mechanical components is the simplest method to minimize the thermo-mechanical noise in various kinds of resonating sensors and Nano-electromechanical Systems (NEMSs). As the dimensions of a structure shrink, the surface effects tend to dominate the bulk properties in mechanical quality factors (Q-factors) and nonlinearity. This paper presents the findings on nanomechanical properties of ultra-thin single crystalline silicon resonators, with emphasis on their surface effects, such as atomic arrangements and surface resconstruction due to thermal treatment and gas adsorption. The surface loss mechanism in energy dissipation was also discussed with reference to support loss and thermoelastic loss. The results obtained in this study provide an insight into the understanding of surface effects on nanomechanics of resonating elements, and provide design guidelines for future's nanoengineered devices for ultimate sensing.*

Keywords: *surface effects, nanomechanics, ultra-thin silicon resonator, energy dissipation*
Category: *4 (Non-magnetic physical devices)*

1 Introduction

Ultra-thin single crystalline silicon cantilevers have versatile applications in various resonating sensors due to its excellent mechanical properties, low defect density, absence of grain boundaries and bending (stress free). However, the surface effects arising from the atomic arrangement and surface reconstruction on the energy dissipation are of paramount importance. This is not only because of downscaling but also due to easily oxidized fresh silicon surface. Unfortunately, relatively little is understood about this surface-related mechanism and its influence on energy dissipation in ultra-thin single crystalline silicon resonators during vibrating.

2 Experimental

Figure 1 shows a typical 50-nm-thick (100)-oriented Si cantilever array fabricated on a silicon-on-insulator (SOI) wafer using Si-based micro-machining. The array consists of rectangular-shape-cantilevers, and each cantilever is 3 μm wide by 50 μm in length. All measurements of resonant frequencies, Q-factors etc. were performed in an UHV system with a treatment and measurement chambers under a pressure lower than 1×10^{-7} Pa. The resonator was electrostatically actuated by applying a low actuation voltage between the resonator and a metal electrode. Laser beam of a Doppler vibrometer with a diameter of about 1.5 μm and a power of about 1 mW was focused onto the resonator surface to measure the vibration.

3 Results and discussions

Figure 2 shows both the resonant frequency and Q-factor of a (100)-oriented Si cantilever after treated by flash-heating at 1000°C for 30 s. The resonant frequency increased initially until about 150 min and gradually decreased thereafter. The balance of mass increase of molecule adsorption (mainly water molecules) and adsorption-induced surface stress may explain the observed behavior. In contrast, the Q-factor decreased and then gradually increased to a relatively stable value. After treated again by flash-heating, the Q-factor was further increased and was found to behave in a similar way as that after the first heating as shown in Figure 3. When the flash-heated cantilever was exposed to O_2 gas for 100 s (about 8 Langmuir), the resonant frequency increased and the Q-factor decreased drastically as shown in Figure 4. The exposure of O_2 gas breaks the Si-Si bonds and results in defect formation on the cantilever surface. When the O_2 supply was stopped at this stage, both the resonant frequency and Q-factor increased in the same way as shown in Figure 2. When the cantilever was exposed to O_2 gas again at 150 min after falsh-heating, no increase was observed for the resonant frequency, while the Q-factor decreased to some extent in comparison to the behavior shown in Figure 2. The formation of Si-O-Si bonds on the cantilever surface may be possibly related to the observed change in Q-factor as shown in Figure 4. The temperature dependence of Q-factor and nonlinear response of cantilever were also investigated as shown in Figures 5 and 6, respectively.

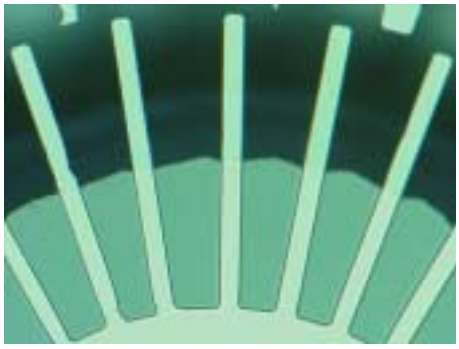

Figure 1. A typical view of 50-nm-thick (100)-oriented Si cantilever array. Each rectangular cantilever is 3 μm wide by 50 μm in length.

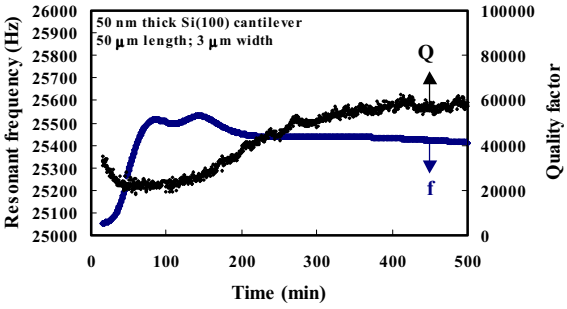

Figure 2. Time dependence of the resonant frequency and Q-factor of the 50-nm-thick (100)-oriented Si cantilever after surface treatment by flash-heating.

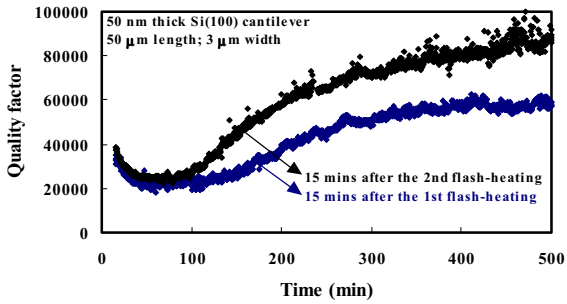

Figure 3. The comparison of time dependence of the Q-factors after the surface treatment by the first and the second flash-heating. Both curves decreased first and gradually increased thereafter.

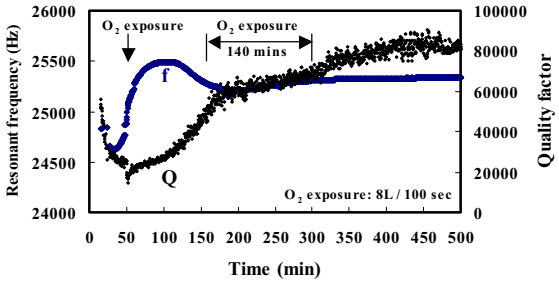

Figure 4. Effect of surface treatment by the exposure of O_2 gas on the resonant frequency and Q-factor of the flash-heated Si cantilever.

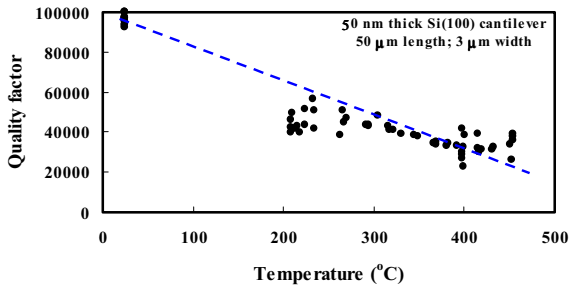

Figure 5. Temperature dependence of the Q-factor of the 50-nm-thick (100)-oriented Si cantilever. The Q-factor was plotted as a function of temperature as well.

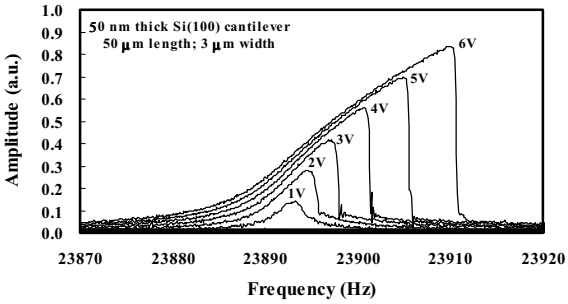

Figure 6. Typical nonlinear responses of the oscillating Si cantilever as a function of the actuation voltage.

References

[1] D. Rugar et al., Science **264** (1994) 1560.

[2] K.Y. Yasumura et al., J. Micro. Sys. **9** (2000) 117.

A Symmetrical and Decoupled Nickel Microgyroscope on Insulating Substrate

S. E. Alper and T. Akin

Middle East Technical University, Department of Electrical and Electronics Engineering, Ankara, Turkey
email: tayfun-akin@metu.edu.tr http://www.eee.metu.edu.tr/~tayfuna

Summary: *This paper presents a symmetrical and decoupled surface micromachined gyroscope fabricated by electroforming thick nickel on a glass substrate. The symmetric structure allows matched resonant frequencies for the drive and sense vibration modes for improved sensitivity, while the decoupled drive and sense oscillation modes prevents unstable operation due to mechanical coupling and achieving a low zero-rate output drift. The use of a glass substrate instead of a silicon substrate reduces noise due to the parasitic signal coupling by two orders of magnitude according to both simulated and measured results on fabricated devices. A capacitive interface circuit which is fabricated in a 0.8μm CMOS process is hybrid connected to the gyroscope, where the circuit has an input capacitance lower than 50fF and a sensitivity of 33mV/fF. Fabricated gyroscopes have close resonant frequencies for the drive and sense modes, as 37.2kHz and 38.3kHz, respectively. The fabricated gyroscope with 18μm-thick structural layer provides a Brownian noise floor of 7.3(deg/hr)/Hz$^{1/2}$ at vacuum. The overall rate sensitivity of the gyroscope is estimated to be 25deg/hr in 10Hz bandwidth.*

Keywords: *symmetric gyroscope, decoupled gyroscope, capacitive interface circuit, nickel electroforming*
Category: *4 (Non-magnetic physical devices)*

1 Introduction

Tactical-grade rate sensing applications require noise floor better than 0.01deg/sec and bias drift as low as 1deg/hr. These challenging requirements are difficult to achieve for MEMS-based Coriolis vibratory gyroscopes with current microfabrication technologies, unless dedicated mechanical designs and improved interface circuits are employed. In MEMS gyroscopes, it is essential to use matched resonance frequencies for the drive and sense mode vibrations for improving the sensitivity by the mechanical quality factor of the sense mode, which can be as high as a few thousand at vacuum [1]. This can be satisfied by designing symmetric suspensions for the drive and sense modes, in order to keep temperature-dependent drift small [2]. However, symmetric suspensions usually yield undesired mechanical coupling between drive and sense modes resulting in a high bias drift. Bias drift can be minimized if the gyroscope has decoupled vibration modes [3]; however, these gyroscopes usually have unsymmetrical suspensions and are subject to temperature-dependent drift. Some approaches aimed to achieve both symmetrical and decoupled gyroscope [4-6]. We have reported various symmetrical and decoupled gyroscopes (called SYMDEC) with different fabrication processes [5-6]. This paper reports development of an improved SYMDEC gyroscope with an 18μm-thick nickel structural layer on an insulating substrate, where the gyroscope is hybrid connected to a CMOS readout circuit with low input capacitance and high sensitivity.

2 Gyroscope Structure and Simulations

Figure 1 shows the 3D structure of the SYMDEC gyroscope. The drive mode (x-axis) of the gyroscope is electrostatically excited to oscillate at its resonance frequency. When an angular rate input is applied about the z-axis, the sense mode also starts vibrating due to the Coriolis coupling from the drive mode, and this vibration is sensed with a capacitive interface circuit. This structure has both symmetric suspensions and mechanically decoupled oscillation modes. The anchors of the structure are placed at the outermost corners and connected to the movable drive and sense electrodes with the help of suspension beams in such a way that the drive electrodes cannot vibrate along the oscillation direction of the sense electrodes and vice versa, therefore, the mechanical decoupling is achieved. In addition, the suspension beams supporting the proof mass are not attached to the anchors directly, rather the proof mass is supported by the beams attached to the movable drive and sense electrodes. This way, symmetry of the structure is preserved, while the drive and sense electrode motions are kept independent from each other. Figure 2 shows CoventorWare FEM simulations, where the drive and sense mode resonance frequencies of the two modes are matched at about 37kHz. Figure 3 presents the FEM simulation result showing that the drive mode coupling to the sense mode is less than 2%. Since the frequency of the coupling signal is twice that of the drive mode, it can be suppressed further with the readout electronics.

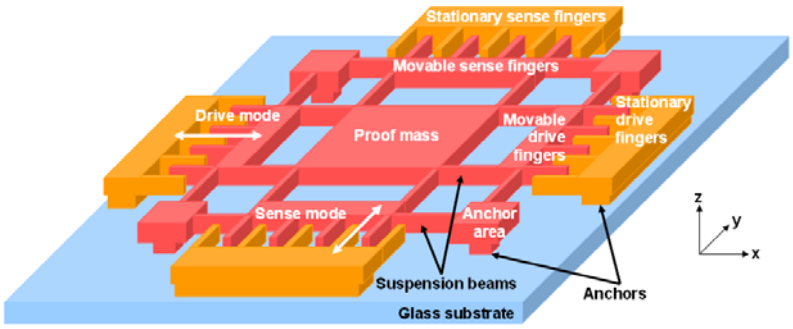

Fig. 1. 3D-structure of the SYMDEC gyroscope.

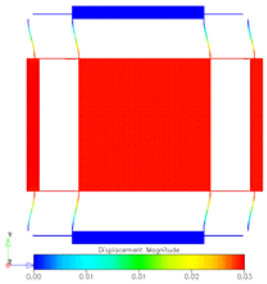

Fig. 3. The undesired coupling from drive to the sense mode is only 2% of the drive mode vibration amplitude.

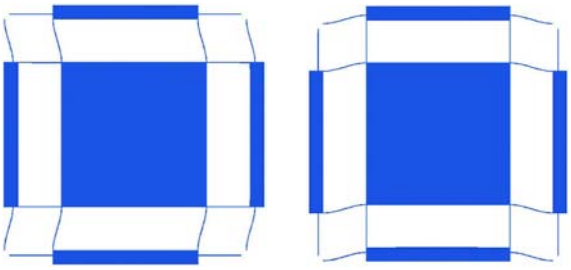

Fig. 2. CoventorWare modal simulations showing the mode shapes of the drive and sense modes, with resonance frequencies are matched at about 37kHz.

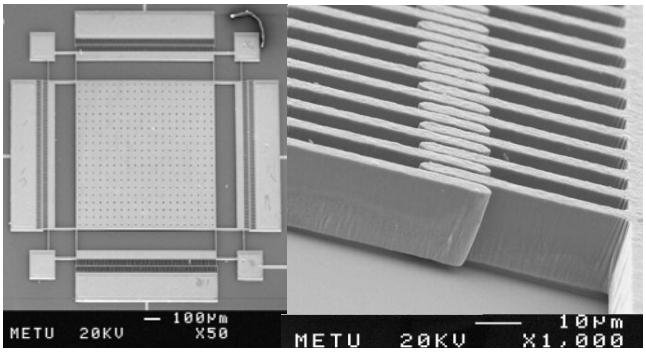

(a) (b)

Fig. 4. SEM pictures of the fabricated gyroscope. (a) Overall view and (b) close-up view of comb fingers.

3 Implementation and Test Results

The improved SYMDEC gyroscope is implemented by electroforming 18µm-thick nickel into a photoresist mold on top of a 4µm-thick copper sacrificial layer. Figure 4 shows the SEM pictures of the fabricated gyroscope. The capacitance from the drive mode to the sense mode is measured as 100fF by a precision impedance analyzer (HP4294A). When the expected capacitance of the comb fingers is extracted, the parasitic capacitance is determined as only 30fF, very small due to the insulating substrate. A capacitive interface circuit in a 0.8µm CMOS process is fabricated. Figure 5 shows the schematic of the interface circuit, which provides a measured input capacitance lower than 50fF and a measured sensitivity of 33mV/fF. This circuit is hybrid connected to the gyroscope. Figure 6 shows the measured resonance frequencies of the drive and sense modes of the gyroscope as 37.2kHz and 38.3kHz, respectively, by using the HP4395A network analyzer. The fabricated gyroscope provides a Brownian noise floor of 7.3(deg/hr)/Hz$^{1/2}$ at vacuum. The overall rate sensitivity of the gyroscope is estimated to be 25deg/hr in 10Hz bandwidth.

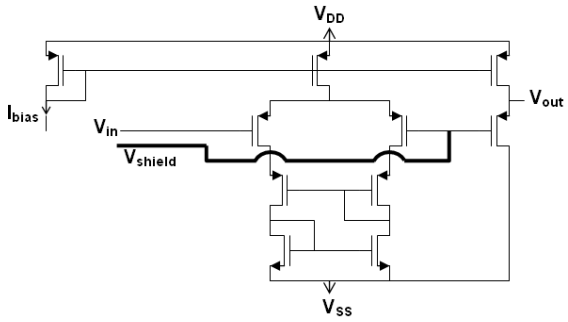

Fig. 5. Capacitive interface circuit with input capacitance lower than 50fF and sensitivity of 33mV/fF.

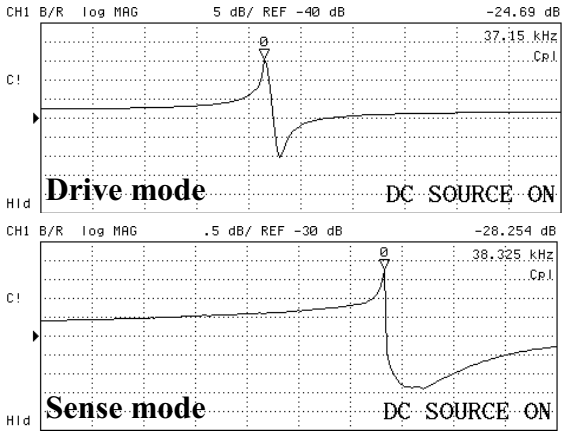

Fig. 6. Measured resonance frequencies of the drive mode and sense mode with a highly-sensitive capacitive interface circuit.

References

[1] N. Yazdi, F. Ayazi, and K. Najafi, *Proc. of the IEEE*, vol. 86, no. 8 (1998), pp.1640-1659.
[2] Y. Mochida, M. Tamura, and K. Ohwada, *MEMS'99,* pp.618-623.
[3] W. Geiger, J. Merz, T. Fischer, B. Folkmer, H. Sandmaier, and W. Lang, *Transducers'99*, pp. 1578-1581.
[4] M. S. Kranz and G. K. Fedder, *Symp. Gyro Tech. 1997*, pp. 3.0-3.8.
[5] S. E. Alper and T. Akin, *Sensors and Actuators A,* vol. 97-98C, April 2002, pp. 347-358.
[6] S. E. Alper and T. Akin, *Eurosensors'02*, pp. 814-817.

Acknowledgements

This research is sponsored by Research and Development Department of Ministry of National Defense (MSB ArGe) and Scientific and Technical Research Council of Turkey (TÜBİTAK).

A 16 Fabry-Perot Optical-Channels Array for Biological Fluids Analysis using White Light

G. Minas[1], J. C. Ribeiro[1], J. S. Martins[1], R. F. Wolffenbuttel[2] and J. H. Correia[1]
[1]University of Minho, Dept. of Industrial Electronics
Campus de Azurém, 4800-058 Guimarães, Portugal, gminas@dei.uminho.pt
[2]Delft University of Technology, Fac. ITS Dept. Microelectronics,
Mekelweg 4, 2628 CD Delft, The Netherlands

Summary: *This paper describes a biosystem (biological system) used to measure the concentration of biological substances in urine, serum, plasma or cerebrospinal fluid. Rather than just one channel, it comprises 16 optical-channels that enable the measurement of the concentration of 16 different biological substances. An array of 16 optical filters based on Fabry-Perot thin-films optical resonators has been designed. Each optical-channel is sensitive in a single wavelength with a Full-Width-Half-Maximum (FWHM) of 7 nm. The filter fabrication requires only 4 masks, used with different etch time. A commercially available band-pass optical filter with a band-pass wavelength in 450-650 nm is used. The biosystem requires only a white light source for illumination due the use of selective optical filters.*

Keywords: *biosystem, optical filter array, Fabry-Perot*
Category: *7 (Fluidic Devices)*

1 Introduction

Spectrophotometric analysis is one of the most commonly used analytical techniques for determining the concentration of a particular compound in biological fluids samples [1]. Usually, the samples need to be sent to a laboratory for spectrophotometric analysis, and the results become available after several hours or days. The need for rapid and on-line measurements led to the development of biosystems with the fluidic, detection and readout systems integrated in a single-chip [2]. The advantages associated with shrinking clinical analysis systems include improved efficiency with respect to sample size, integration, response times, costs, etc. Previously developed biosystems on-a-chip with absorbance detection require a wavelength dependent light or waveguides inserted into the biosystem for illumination [3, 4]. Illumination using only a white light source requires the use of selective optical filters.

2 Design of the 16 optical-channels array

A biosystem to measure the concentration of biological substances in biological fluids, by optical absorption, was previously implemented [4]. Its operation was successfully demonstrated in uric acid concentration detection. However, the measurements were carried out with a wavelength dependent light source (monochromatic light). An optical filter placed on the top of the biosystem allows the use of only a white light source. Rather than just one optical filter it has been developed a 16 optical filters array based on Fabry-Perot thin-films optical resonators. The device, schematically shown in Fig. 1 and Fig. 2, allows the measurement of the concentration of 16 biological substances in human's fluids (Table 1). The biosystem is composed by a glass die that contains the fluidic channels, including the optical filters, and a silicon die that contains the photodetectors and readout electronics. A commercially available band-pass optical filter on the top of the biosystem is used to avoid the non-visible spectrum.

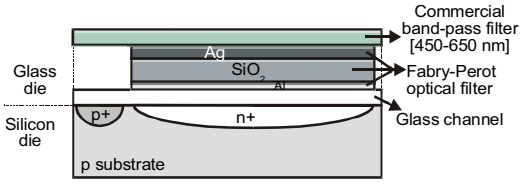

Fig. 1. Schematic structure of the biosystem for an individual optical-channel in cross-section.

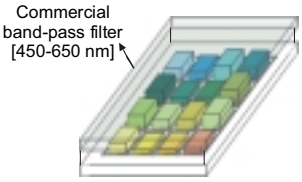

Fig. 2. The 16 optical filters (4x4 array) and the commercial band-pass filter. Each of the Fabry-Perot cavities is tuned to transmit in different spectral band.

The impinging spectrum is filtered by the optical filters to a single wavelength, and the intensity of the selected spectral component transmitted through the fluid is measured using an underlying photodetectors array. Thus, each optical-channel is composed by a Al/SiO_2/Ag layer stack functioning as the Fabry--Perot optical filter with an optical detector underneath (a CMOS standard photodiode). The 16 optical filters are tuned for a specific wavelength (third column of Table 1). The thickness of the SiO_2 layer determines the tuned wavelength. The optical

filters use metallic mirrors instead of high-performance dielectric mirrors due to the simplicity of their fabrication: only 3 layers are deposited and the wavelength selection is performed by changing only the thickness of the SiO_2 layer.

Table 1. The 16 biological substances that can be analyzed in the biosystem. U (Urine), S (Serum), P (Plasma) and CSF (cerebrospinal fluid) [1].

Biochemical Substance	Biological Fluid	Absorption spectra maximum peak (nm)
Uric Acid	U, CSF	495
Cholesterol	S	500
Glucose	S	505
Glutamic oxalacetic / pyruvic transaminase	S, P, CSF	510
Creatinine	U, S, P	515
Magnesium	S	520
Aldolase	S	525
Bile acids	S	530
Blood urea nitrogen	S, P	535
Salicylate	S	540
Hemoglobin	P	545
β Glucuronidase	S, U	550
Urea nitrogen	U, S, P	555
Bilirubin	S	560
Leucine aminopeptidase	U	565
Calcium	S	570

A thin-film optics software package (TFCalc 3.4) was used for the structural optimization of the optical filters. Simulation results show that a 20 nm Al / SiO_2 / 40 nm Ag layer stack is the best option for the optical filters in terms of optical characteristics and feasibility. The SiO_2 layer thickness changes between 637 nm and 742 nm with 7 nm steps. Each of the channels is sensitive to a single spectral band, with a FWHM = 7 nm (see Fig. 3).

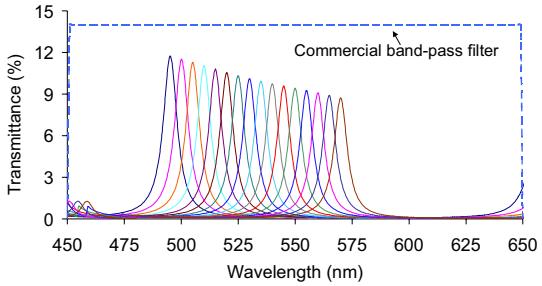

Fig. 3. Simulated transmittance vs. wavelength for the 16 optical filters array.

3 Fabrication of the 16 optical-channels array

The filter fabrication starts with the deposition of a 20 nm Al layer by evaporation. Then a 742 nm thick SiO_2 layer is deposited by chemical vapor deposition. In subsequent plasma etching steps (for which a mask is used, Fig. 4), the total thickness of the SiO_2 layer is decreased from 742 nm to 637 nm. The fabrication ends with the deposition of a 40 nm Ag layer. The 16-filter fabrication requires only 4 masks and 4 etching steps. The masks are used with different etch time (see Fig. 4). The filters can be easily tuned to different spectral bands by adjusting only the thickness of the SiO_2 layer without affecting the biosystem layout.

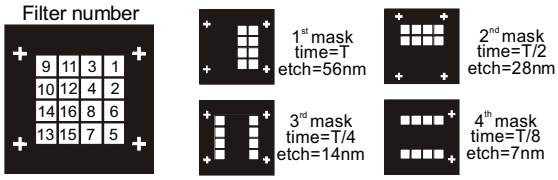

Fig. 4. The 4 masks used in the SiO_2 etching process. The filter number 1 ($\lambda = 495$ nm) is for uric acid; the filter number 2 ($\lambda = 500$ nm) is for cholesterol, and so one according to Table 1. The crosses are alignment marks.

4 Experimental Results

The 16 optical filters are now being fabricated. Meanwhile a single channel was previously fabricated and its operation demonstrated in the measurement of uric acid concentration ($\lambda = 495$ nm). A 200 W quartz tungsten halogen lamp was used as the white light source for biosystem illumination. The photodiode current was measured using a Keithley 487 picoammeter. The optical filter is composed of the 20 nm Al / 637 nm SiO_2 / 40 nm Ag layer stack. Optical spectra measurements on the biosystem show that the single channel is sensitive to its specific wavelength with a FWHM of 7 nm (Fig. 5).

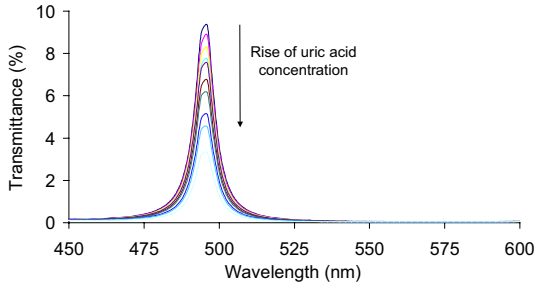

Fig. 5. Measured transmittance for a single channel for different uric acid concentrations ($\lambda = 495$ nm).

5 Conclusions

The reported biosystem offers a new approach for clinical analysis due to the measurements of the concentration of 16 different biological substances in human's fluids, with the same device. Moreover, the 16 optical-channels array allows the use of only a white light source for illumination. Therefore, the measurements can be performed in any place.

References

[1] "Biochemical and organic reagents" Sigma, 2002.
[2] S. C. Jakeway, A. J. de Mello, E. Russell, "Miniaturized total analysis systems for biological analysis," Fres. J. Anal. Chem, 366, 525-539, (2000).
[3] J. H. Hahn, K. W. Ro, B. C. Shim, K. Lim, US2003/0017079A1, Absorbance detection system for lab-on-a-chip, Jan. 23, 2003.
[4] G. Minas, et al. "Lab-on-a-chip for measuring uric acid in biological fluids," Proc. EurosensorsXVI, Czech Republic, 66-69, (2002).

Chemically driven switches for online detection of pH changes in microfuidic devices.

P. Mela[1], S. Onclin[1], M.H. Goedbloed[1], S.A.Levi[2], N.F. van Hulst[1], A. van den Berg[1]

[1]University of Twente and Mesa+ Research Institute, P.O. Box 217, 7500 AE Enschede, NL
[2]SusTech GmbH & Co. KG Darmstadt, Petersenstraße 20, 64287 Darmstadt
email: p.mela@el.utwente.nl http://www.mesaplus.utwente.nl

Summary: *The internal walls of microfabricated fluidic channels were functionalized with a self-assembled monolayer of Rhodamine B lactam. This molecule has the capability to interconvert between its open fluorescent amide form and the closed non-fluorescent lactam form upon changes of the pH conditions. The interconversion (switch) between the two reversible forms is achieved by addition of an acid or a base and is consistent with a reaction mechanism of the first order. This paper describes the online observation of such fluorescent switch covalently anchored to the channel and proposes this method as a possible sensor for the monitoring of pH changes in microreactors.*

Keywords: *Chemically driven switches, Rhodamine B, microfluidics, confocal microscopy*
Category: *7, 10 (Fluidic devices, chemical sensors)*

1 Introduction

Online detection of critical and sudden reactions occurring in microfluidic systems is an important issue in the developing field of microreactors.

A sudden and unexpected change in the pH conditions of a continuos-flow chemical process can lead to unexpected reaction pathways such as overheating, or in the worst scenario explosion. Chemical reactions in microfluidic devices occur on a faster timescale if compared to bulk reactions, therefore a fast online monitoring system is required to minimize risks [1].

2 Results and Discussion

The synthesis of RhB amide fluorescent core has been previously described at the single molecular level when incorporated in the core of metallodendrimers [2]. This molecule has the capability of reversibly switching between the lactam form **b** and the open amide form **a** upon changing the pH conditions (Figure 1). From the literature [3] it is known that rhodamine B derivatives containing primary amide groups at the 2'-position can easily be interconverted in the non-fluorescent spirolactam form under basic conditions [4]. Upon addition of a base, the RhB amide **a** reacts to its lactam form causing the loss of aromaticity in the pyrilium ring of the xanthene chromophore (Fig. 1).

A microfabricated glass channel (20 µm wide and 2 µm deep) was chemically modified by forming an NH_2 terminated monolayer on its surface. Subsequently the monolayer was reacted with a diluted solution of Rhodamine B oxalyl chloride. In this way it was possible to react Rhodamine B to the surface via amidation at the 2' position. The switching pH dependent function is now chemically linked to the surface. By using dilution of NH_2 groups on the surface (1/10 to 1/10000), it was possible to regulate the amount of dye reacting with

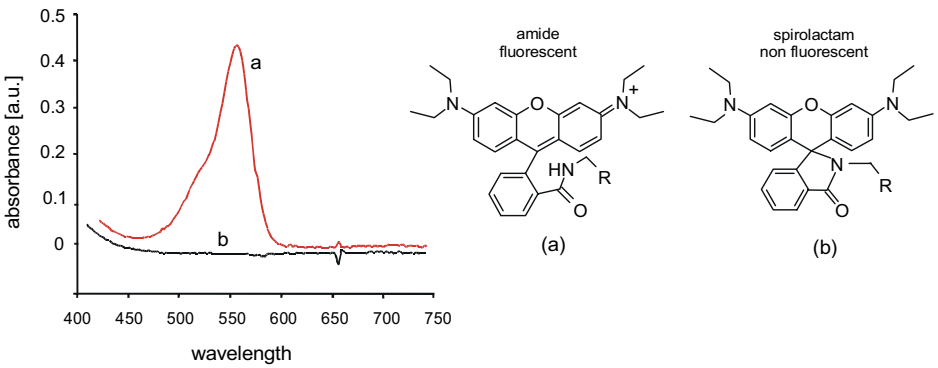

Fig. 1. UV-Vis spectrum of **a** and **b** and corresponding molecular structures.

the surface and therefore obtain an ideal concentration of function at the surface minimizing the possibility of interference between vicinal dye molecules because of steric hindering. The reaction is shown schematically in Figure 2.

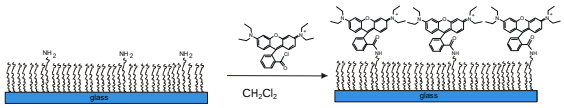

Fig. 2. Reaction scheme for the covalent bonding of RhB to glass.

After functionalization and subsequent extensive rinsing with several solvents, in order to remove physisorbed material, the microfluidic device was placed under a Laser Scanning Confocal Microscope (LSC) to detect the fluorescent signal emitted by the switches. A flow of dichloromethane (CH_2Cl_2) was pumped inside the channel by hydrodynamic pressure and an area of 40x40 µm was scanned. Subsequently the reservoir containing CH_2Cl_2 was emptied and filled with 20% triethylamine (NEt_3) in CH_2Cl_2 and the same area scanned again. A significant decrease in the overall intensity of fluorescence was observed. The channel was then rinsed with CH_2Cl_2 and filled with 20% Acetic acid (CH_3COOH) in CH_2Cl_2. In the subsequent scan a considerable increase of the fluorescence was seen (approximately 5-fold).
The rinsing procedure with CH_2Cl_2 was repeated and another off-on cycle (i.e. base-acid) performed. The fluorescence decreased again when the layer was addressed with the basic solution and a complete recovery of the fluorescence intensity was obtained upon release of the acid solution, ruling out the possibility that the previously observed low level of fluorescence could be due to desorption or damage to the monolayer. A control test in a microchannel without functionalized monolayer excluded the possibility of autofluorescence of the used solvents to cause the observed changes in fluorescence intensity. For each scan, the intensity distribution was determined (Fig.3).

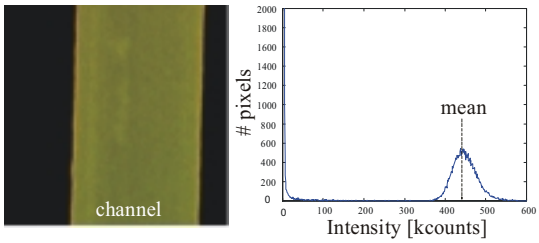

a) b)

Fig. 3. a) Example of confocal scanned image (40x40 µm area) and b) fluorescence intensity distribution obtained from the scan.

Fig. 4 shows the relative means of the distributions for two consecutive on-off cycles.

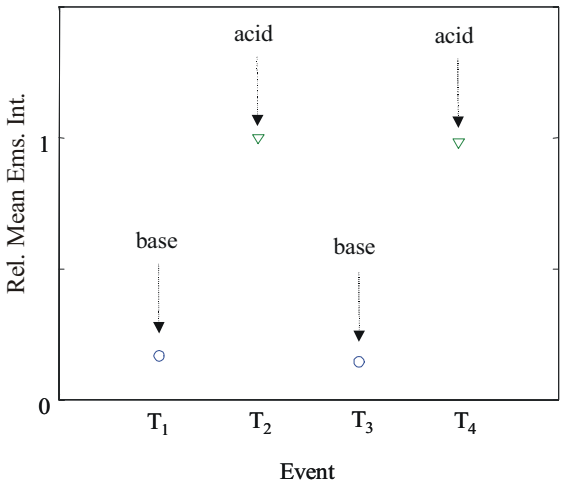

Fig. 4. Off-on switching of the molecules in the microfluidic channel. Relative mean fluorescence intensity after exposure to base (T_1, T_3) and to acid (T_2, T_4). Between events the system was flushed with CH_2Cl_2.

Conclusions

We have demonstrated the possibility to include a chemical sensor inside a microfluidic device by covalently binding it to the channels' walls. The molecular switch was able to sense two different pH conditions by responding to the external stimuli with a clear and reproducible change in the fluorescence behavior. Furthermore, by using high dilution of NH_2 groups on the surface, it is possible to minimize the number of switches in order to obtain a very diluted sample and allow single molecule studies [5]. The microfluidic network would then serve as a very effective tool to change the pH conditions in a controlled way.

References

[1] Manz, A., Becker, H., Eds. Microsystem Technology in Chemistry and Life Sciences. *Topics in Current Chemistr*y; Springer-Verlag: Berlin, Vol. 194.
[2] Levi, S. A.: *Supramolecular Chemistry at the Nanometer Level*, Ph.D. thesis Universiy of Twente, Enschede, The Netherlands, ISBN: 90-365-1671-4, 2001.
[3]Adamczyk, M.; Grote, J.: Efficient Synthesis of Rhodamine Conjugates Through the 2 '-Position; *Bioorg. Med. Chem. Lett.* 2000, *10*, 1539-1541.
[4]Adamczyk, M.; Grote, J.: Synthesis of Novel Spirolactams by Reaction of Fluorescein Methyl Ester With Amines; *Tetrahedron Lett.* 2000, *41*, 807-809.
[5] Levi, S.A.; Mela, P.; Van Veggel, F.C.J.M.; Reinhoudt, D.N.; van den Berg, A.; van Hulst, N.; *Microcontact switching of single molecules.* Proceedings of Micro Total Analysis Systems 2002.

Single Mask Integration of Micro-Fluidic and Micro-Optical Elements

A. R. Leeds[1], E. R. Van Keuren[1], T. W. Schneider[2], J. F. Currie[1], M. Paranjape[1]

[1]Department of Physics, Georgetown University, Washington DC, 20057
[2]Science Applications International Corporation (SAIC), McLean, VA 22102

Summary: We are presenting a novel design and process to integrating micro-fluidic and micro-optical elements. Light waveguides and fluidic microchannels have been constructed using single mask photolithography. This integration is performed with two devices: a hybrid with SU-8 waveguides and polydimethylsiloxane (PDMS) channels, and the other using only SU-8 for the waveguides and microchannel walls. Preliminary tests have demonstrated the ability of the waveguides to guide laser light to the microchannels exciting florescent dye present in the microchannels.

Keywords: micro-fluidic, micro-optic, SU-8, polydimethylsiloxane
Category: Fluidic devices

MEMS technologies have been used to fabricate microfluidic devices as well as planar lightwave circuits [1]. We have fabricated integrated microfluidic/optical-waveguide devices for use as optical chemical/biological sensors. The waveguides are made of SU-8, a photo-epoxy material commonly used for high aspect ratio molds or structural materials in MEMS fabrication, and more recently, as an optical material because of its low absorption and scattering [2]. Two devices are presented, one being a hybrid structure with polydimethylsiloxane (PDMS) microchannels and an embedded SU-8 waveguide, and the other with a structure made entirely of SU-8.

The devices were designed to detect fluorescence from samples in a microchannel, with light coupled into and out of the channels through SU-8 waveguides at either end.

PDMS / SU-8 hybrid design and fabrication

Figure 1 shows a schematic of the PDMS/SU-8 device. Fabrication of this hybrid device made use of a single-mask process in which SU-8 was patterned onto glass. PDMS was mixed and poured onto the SU-8. After curing, the PDMS with embedded SU-8 was removed from the glass using a Teflon release process

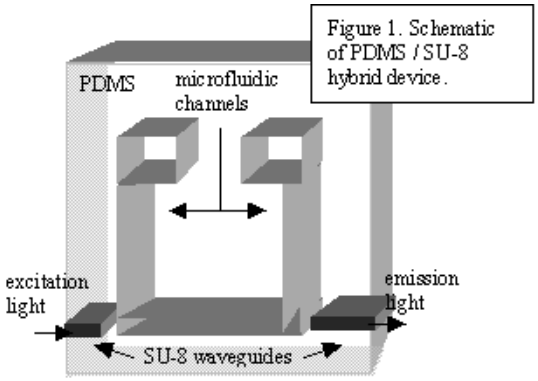

Figure 1. Schematic of PDMS / SU-8 hybrid device.

[3]. This allowed the single layer of SU-8 to serve as both mold for the PDMS and as the embedded waveguide. Sections of the SU-8 were removed from the PDMS to create open fluid channels, and 3000 Å of aluminum were deposited onto the channel walls to improve the light guiding capability to the output waveguide. The channels were sealed with another activated PDMS layer containing holes drilled for fluid interface. Fluid was injected and removed through luer fittings sealed into the holes of the top PDMS layer.

Figure 2a shows a picture of the device while figure 2b shows the SU-8 waveguide successfully directing light to the channels. In this case, a 10^{-4} M solution of the fluorescent dye Rhodamine B is being pumped through the channels and light from a HeNe laser

(wavelength 543 nm) is butt-coupled into the SU-8 waveguide on the left. The fluorescence emission from the dye can clearly be seen.

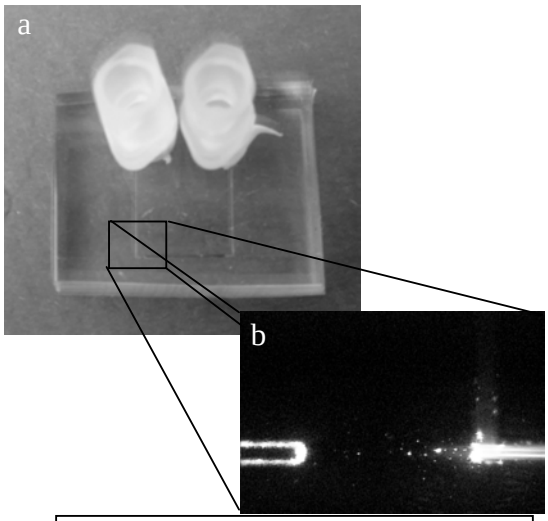

Figure 2. (a) Picture of SU-8 / PDMS hybrid device (b) Laser light enters through the SU-8 waveguide on the left and excites fluorescence in the fluidic microchannels

Adjustments

The use of two materials requires the space between the end of the SU-8 waveguide and the PDMS microchannels for structural integrity. This leads to considerable loss of the excitation and fluorescence emission due to scattering at the SU-8/PDMS and PDMS/fluid interfaces, as well as diffraction of the light between the waveguide end and the fluid channel. To reduce these problems, we have redesigned the device to be fabricated completely from SU-8, reducing the number of medium changes along the optical path.

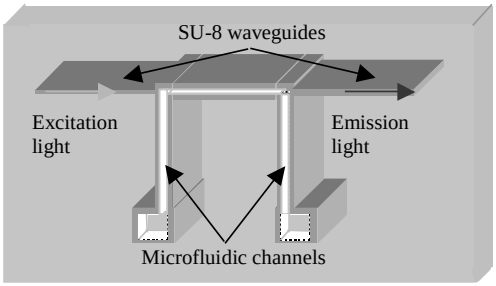

Figure 3. Schematic of the all SU-8 device on glass.

All SU-8 device design and fabrication

Figure 3 shows a schematic of the all SU-8 device, also fabricated with a single mask, in which the waveguiding regions couple directly into the microfluidic channel. The SU-8 is patterned onto glass, creating SU-8 walls and waveguides as shown in figure 4. The channels are then sealed with a glass slide using uncured SU-8 as the adhesive. Light from a laser is butt-coupled into the waveguide on the left. Imaging the output end shows light waveguiding through the entire device, from the input SU-8 waveguide, through the fluidic microchannel, and out through the second waveguide.

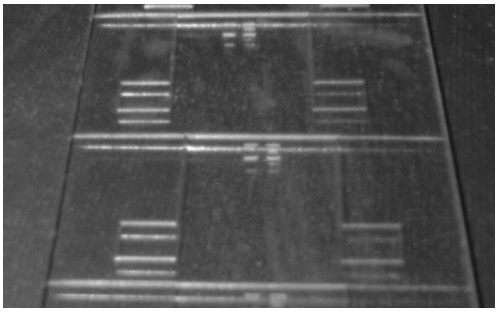

Figure 4. SU-8 patterned onto glass for the all SU-8 device. To achieve a clearer picture of the SU-8 design, the channels have not yet been sealed.

References

[1] K. Jinguji. Planar Lightwave Circuits. *NTT Review*. 70 (1995) 80-86.

[2] G. Lee, C. Lin and G. Chang. Microflow cytometers with buried SU-8/SOG optical waveguides. *Sensors and Actuators A*. 3559 (2003) 1-6.

[3] M. C. Cheng, A. J. Nijdam, J. A. Garra, A. P. Gadre, T. W. Schneider, R. C. White, M. Paranjape and J. F. Currie. Application of low surface energy layer in the package of microfluidic systems (in preparation).

Pressure Barrier of Capillary Stop Valves in Micro Sample Separators

Tzong-.Shyng (Jeremy) Leu and Pei-Yu Chang

National Cheng Kung University, Department of Aeronautics and Astranautics,
No. 1 Ta-Hsieh Road, Tainan 701, Taiwan
email: tsleu@mail.ncku.edu.tw http://www.iaa.ncku.edu.tw

Summary: *This paper presents a new method and an analytical model for characterizing pressure barrier of capillary stop valves inside micro sample separators based on active CD-like microfluidics platforms. The capillary stop valves and micro sample separator were fabricated on polycarbonate (PC) substrates by using hot embossing techniques. The passive valves stop the flow of a liquid inside the micro fluidic devices using a capillary pressure barrier when the channel geometry changes abruptly. Experiments are performed by rotating the micro sample separator on a platform. The liquid stopped inside the micro sample separator can be segmented using density gradient centrifugation. Various densities of samples required for an analysis can be separated by simply rotating at different speeds. Design parameters of the capillary valves used in the micro sample separator have been analyzed theoretically. It is shown the pressure barrier of the capillary valve design can be better predicted by using a modified 3D meniscus effect model.*

Keywords: *micro sample separator; capillary stop valve, LabCD*
Category: *7 (Fluidic devices)*

1 Introduction

Separation of various density samples is required in many biomedical devices. Current trends in lab-on-a-chip technology suggest a rapid growth in the need for high throughput as well as cost-effective diagnostic tools in biomedical applications. One of current technologies proven to be fast, disposable and cheap is so-called LabCD [1], a Lab-On-A-Chip based on CD-like technology and platform. Several fluidic functions on LabCD have been demonstrated for this purpose. Virtanen et. al. [2] have presented a on-chip technique to meter discrete nanoliter-sized liquid inside microchannel by using micropipette principle. Liquid flow inside micron-sized channels on LabCD platform can be controlled by manipulating the centrifugal force and the capillary force. A sudden expansion (or contraction) channel, called capillary stop valve, is usually used to stop the fluid by changing the channel geometry. When rotational speed increases, the centrifugal force becomes larger than the capillary force. Liquid starts to flow downstream. An angular velocity ω, called the burst frequency [3] is given if the centrifugal force is equal to the capillary force as

$$\omega=[\gamma\cos\theta/(\pi^2\rho\cdot\Delta R\cdot R\cdot d_H)^{1/2}$$

where ω is the angular velocity of the CD platform, γ is the surface tension, θ is the contact angle, ρ is the density of the liquid, ΔR is equal to R_2-R_1, the distance difference from the center of the CD to the capillary stop (R_2) and reservoir (R_1), R is equal to (R_2+R_1)/2 and d_H is hydrodynamic diameter of the channel.

When the angular velocity is smaller than the burst frequency, liquid will first stop at the capillary stops of the micropipettes. Therefore, liquid sample will first be metered inside a number of micropipettes and the excessive liquid overflows into a bypass chamber.

In this paper, we present several passive capillary stop valves that exploit a new method and an analytical model for characterizing pressure barrier inside these capillary stop valves using the measurement of the pressure barrier on LabCD platform. The capillary stop valves will be applied to a micro sample separator. The design and photography of the micro sample separator is shown in Figure 1.

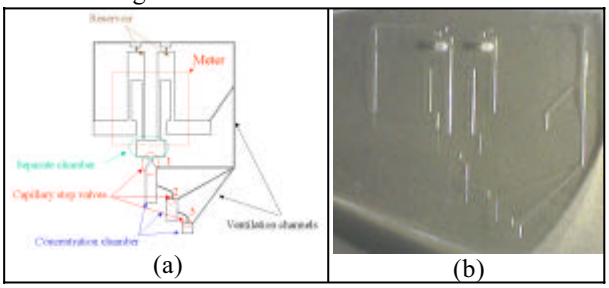

Fig. 1 (a) Sketch and (b) photograph of micro sample separator

In Figure 1, the micro sample separator consists of a separation chamber with two reservoirs on upstream end and a capillary stop valve on the downstream end, and three overflow concentration chambers with capillary stop valves. Experiments are performed by rotating the micro sample separator on a platform, as shown in Figure 2. The liquid will first stop inside the separation chamber. and segment using density gradient centrifugation As rotational speed increases, valve 1 opens and density-gradient fluid flow into concentration

chamber 1 and stops at valve 2. Various densities of samples required for an analysis can be separated by simply rotating at different speeds. For examples, lower density fluid will be flow into concentration chamber 2 when the rotational speed is further increased.

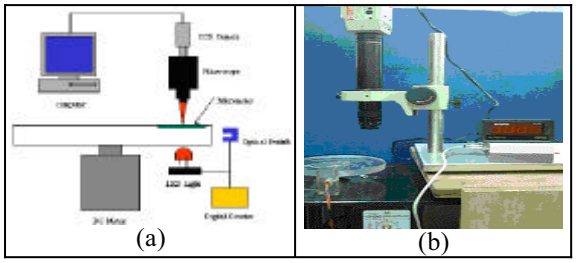

Fig. 2 (a)Sketch and (b)image of experimental setup

2 Results and Discussion

The micro sample separator was fabricated on polycarbonate (PC) substrates by using hot embossing techniques, as shown in Figure 1(b). The capillary stop valves used in the micro sample separator consist of a region of the microchannel with horizontal sudden expansion at different angle β, as shown in Figure 3.

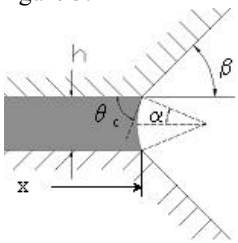

Fig. 3 Closeup of capillary stop valve region

Design parameter β of the capillary stop valves were analyzed theoretically. For a typical capillary stop valve inside the current devices, the width and height of the microchannels are 50 and 20 μm respectively. The aspect ratio of the microchannel is only 2.5. Three-dimensional meniscus effects have to take into consideration even the capillary junctions expand two-dimensionally. The results were shown in Figure 4. Two-dimensional surface energy analysis reported by P. F Man [4] is also performed for the comparison with current analytical and experimental results. In Figure 4, it is found that 2D analysis reported by P. F Man [4] did not well predict the experimental results. For better design of capillary stop valve, three-dimensional meniscus effects have to be considered in the current analysis. Therefore, a modified 3D meniscus effects analysis is proposed and found to better predict the experimental results. The pressure barriers predicted with modified 3D meniscus effect model match the experimental data until β is 50 degree. It is also noticed the prediction becomes overestimated when β is larger than 50 degree since the modified 3D meniscus effect analysis did not have good modeling for the meniscus shapes at corners of the capillary junction.

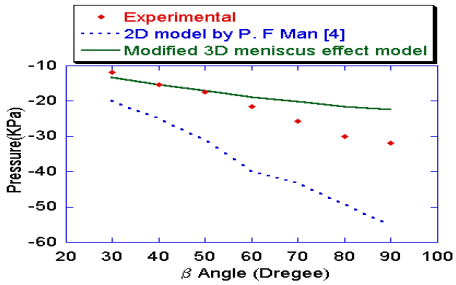

Fig. 4 Pressure barrier v.s. design parameter β angle of the capillary stop valve

Finally, the micro sample separator is tested while the rotational speeds increase from 0 to 1050 rpm. The designed burst frequency for capillary stop valves 1, 2, and 3, as shown in Figure 5(a), are ω_1=640, ω_2=870 and ω_3=1020 rpm respectively. At first, the liquid stopped ($\omega<\omega_1$) inside the separation chamber can be segmented using density gradient centrifugation. As rotational speeds increase to 640 rpm ($\omega_1\leq\omega<\omega_2$), 900 rpm ($\omega_2\leq\omega<\omega_3$) and 1050 rpm ($\omega_3\leq\omega$), valve 1, 2 and 3 open sequentially and separate fluid flow into concentration chamber 1, 2 and 3 based on the density gradient , as shown in Figure 5(b) and 5(c) and 5(d).

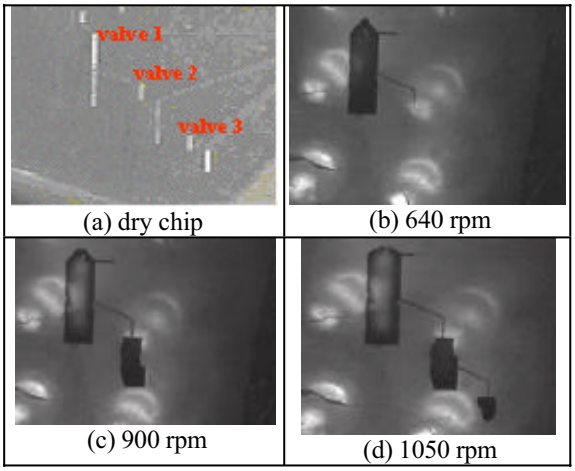

Figure 5 Micro sample separator is tested at different rotational speeds

References

[1] Marc J. Madou et. al., SPIE Proceedings. 3259, 80,San Jose, CA 1998

[2] Jorma Virtanen et. al. "Laboratory in a disk" United States Patent 6,030,581, February 29, 2000

[3] Marc J. Madou et. al. "Design and Fabrication of Polymer Microfluidic Platforms for Biomedical Applications" Antec 2001,p2534- p2538

[4] P.F. Man et. al., "Microfabricated Capillary-Driven Stop Valve and Sample Injector", MEMS Conference, Heidelberg, Germany, Jan. 25-29, 1998

A Ferrofluid Micropump for Lab-on-a-chip Applications

Christophe Yamahata[1], Mathieu Chastellain[2], Heinrich Hofmann[2], Martin A. M. Gijs[1]

(1) Institute of Microelectronics and Microsystems, Swiss Federal Institute of Technology Lausanne
EPFL, 1015 Lausanne, Switzerland, Christophe.Yamahata@epfl.ch
(2) Powder Technology Laboratory , Swiss Federal Institute of Technology Lausanne

Summary: *A disposable micropump is presented that uses the piston actuation principle and relies on the magnetic properties of a ferrofluid, a colloidal suspension of nanosize ferromagnetic particles. The cost effective micropump consists of 7 bonded layers of polymethylmetacrylate (PMMA) that are either micromachined or structured by powder blasting. Two silicone check-valves are also integrated in the microchip. External dimensions of our prototype are 36 mm x 22 mm x 5 mm. The magnetic liquid plug is externally actuated by a motorised permanent magnet. Water has been successfully pumped at a flow rate of 30 μL/min without backpressure; pumping is demonstrated up to a backpressure of 25 mbar.*

Keywords: *Micropump; Ferrofluid; Powder blasting; Check-valve; PMMA; Lab-on-a-chip.*

Category: *7 (Fluidic devices)*

1 Introduction

Advances in microfluidic MEMS technology and the interest of biochemical companies for integrated analytical systems have led to the Lab-on-a-chip (LOC) concept. The cost-effective transport of small quantities of biochemical fluidic samples, in the range of few microliters per minute, remains an important challenge for these devices.
The use of magnetic liquids is an innovative actuation method for fluid handling. Ferrofluid has shown its great potential in piston pumping [1]. Pérez-Castillejos [2,3] et al. reported different possibilities offered by using ferrofluids in microfluidics. Menz [4] and Wagner [5] et al. presented microfluidic systems containing ferrofluids displaced with integrated mobile magnets. Greiwell [6] realised an electromagnetically actuated ferrofluid micropipette. Hatch [7] and Kamholz [8] et al. realised a ferrofluid micropump where the ferrofluid plugs serves both for pumping and valving.
In this study, a miniaturized plastic pump using a ferrofluid pumping mechanism is fabricated using a simple and rapid prototyping technology. The prototype consists of two check-valves separated with a large channel that is filled with a ferrofluid plug. The external actuation avoids the integration of expensive elements, which is essential for implementation of a disposable cartridge.

2 Microfabrication of the micropump

Complex parts are realised with precision milling tools, while channels and other planar structures are realised using the powder blasting technique. This rapid prototyping method offers an efficient solution for the fabrication of fluidic devices, with minimum channel dimensions down to 100 micrometer.
In a first step, a metallic mask is realised by a CO_2 laser. Fluidic structures are realised in 250 micrometer thick polymethylmetacrylate (PMMA) sheets. The different layers are assembled into a monolithic three-dimensional microfluidic structure by an appropriate chemical binding step. The assembly step is realised in a hot press and only takes a few minutes. Silicone membranes also are integrated into the chip. The final prototype of our micropump is shown on Fig. 1.

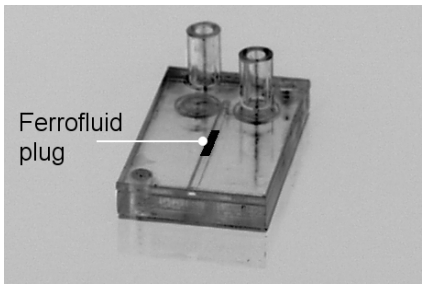

Fig. 1. Photography of the ferrofluid micropump. External dimensions: 36 mm x 22 mm x 5 mm.

3 Performance of the micropump

3.1 Check-valve characterization

A corrugated silicone membrane is taken from a commercially available check-valve. The performance of the integrated check-valve is tested on a dedicated chip before being integrated into the ferrofluid micropump.
As shown in Fig. 2., our assembled valve shows comparable characteristics with the original one and

has the characteristic of a fluidic diode with an opening pressure of about 10 mbar.

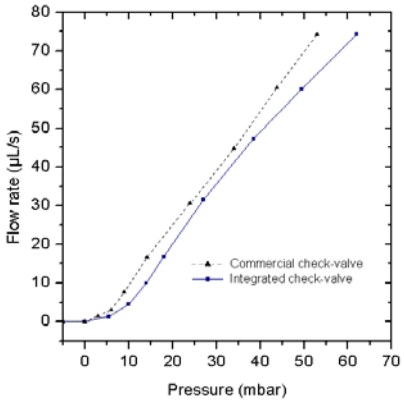

Fig. 2. Integrated check-valve characteristics compared to the commercial component.

3.2 Ferrofluid characterization

The water based ferrofluid used in the experiments is synthesized at the Powder Technology Laboratory of EPFL. A Quantum Design MPMS2 SQUID magnetometer is used for magnetic characterization of dried samples at 300 K. Measurements are reported in Fig. 3. The magnetic saturation of the ferrofluid is found to be 30 mT at this temperature, which will permit larger magnetic actuation forces than obtainable with most commercial ferrofluids.

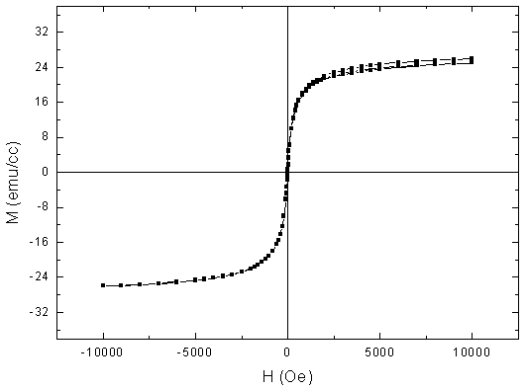

Fig. 3. Hysteresis loop of the sample when submitted to a magnetic field cycling between +10'000 and -10'000 Oe. The magnetisation is given per ml suspension.

3.2 Ferrofluid pump characterization

Water is pumped using a motorised rare-earth magnet that is displaced linearly at different speeds above the ferrofluid piston channel.
Measurements are done with a capillary placed at different heights in order to measure the effect of a backpressure. The pressure-flow characteristic is reported on Fig. 4. The maximum flow rate measured is about 30 microliters per minute, and a maximum backpressure close to 25 millibars is achieved with our ferrofluid.

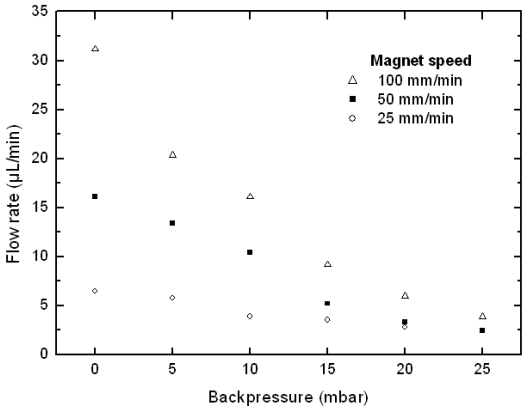

Fig. 4. Pressure-flow characteristics of water for different speeds of the rare-earth magnet.

4 Conclusion

A simple and low-cost prototyping method has been exploited to realise plastic microfluidic chips. A ferrofluid micropump has been realized showing its interesting potential for LOC applications.

Acknowledgement

The magnetic characterisation of the ferrofluid was carried out by Prof. K. V. Rao and A. Gupta, in the Department of Materials Science of the Royal Institute of Technology, Stockholm, Sweden.

References

[1] J. E. Leland, “Ferrofluid piston pump for use with heat pipes or the like”, US patent 5005639, 1991
[2] R. Pérez-Castillejos et al., “The use of ferrofluids in micromechanics”, *Sensors and Actuators A*, vol. 84, pp. 176-180, 2000
[3] R. Pérez-Castillejos et al., “Smart passive microfluidic systems based on ferrofluids for microTAS applications”, *Proc. Transducers 01*, Munich, Germany, 2001
[4] A. Menz et al., “Fluidic components based on ferrofluids”, *Proc. IEEE-EMBS conf. Microtechnologies in Medicine and Biology*, Lyon, France, 2000
[5] B. Wagner, M. Kreutzer, and W. Benecke, “Permanent magnet micromotors on silicon substrates”, *J. Microelectromech Syst.*, vol. 2, pp. 23-29, 1993
[6] N. Greivell, B. Hannaford, “The design of a ferrofluid magnetic pipette”, *IEEE Trans. Biomed. Eng.*, vol. 44, pp. 129-135, 1997
[7] A. Hatch, A. E. Kamholz, G. Holman, P. Yager, and K. F. Böhringer, “A ferrofluid Magnetic micropump”, *J. Microelectromech Syst.*, vol. 10, pp. 215-221, 2001
[8] A. Kamholz et al., “Magnetically actuated fluid handling devices for microfluidic applications”, US patent 6408884, 2002

Miniature taste sensing system based on dual SAW sensor device

G. Sehra, M. Cole and J. W. Gardner

University of Warwick, School of Engineering, Coventry, CV4 7AL, UK
email: G.S.Sehra@warwick.ac.uk http://www.eng.warwick.ac.uk/SRL/

Summary: *In this paper we report on a novel analytical sensing system, so-called electronic tongue, based upon a dual shear horizontal surface acoustic wave device, to discriminate between liquids with different basic tastes. 60 MHz IDT delay line sensors were micro-fabricated on 36° rotated Y-cut X-propagating $LiTaO_3$ and placed under a small PTFE housing containing the liquid under test. Synthetic samples were analyzed with the four basic tastes of sour, salt, bitter, and sweet. The electronic tongue device classified correctly all the different basic tastes. Finally, dultion tests have been performed in order to determine the detection limit of the taste sensor and hence its appliction potential.*

Keywords: *Smart tongue, SAW device, taste sensor*
Category: *6 (Biosensor)*

1 Introduction

The use of acoustic microsensors to detect the physical properties of liquids and gases, such as mass density and viscosity, offers the benefits of a real-time electronic read-out, small size, robustness, and low unit cost. By employing so-called chemical interfaces, the interaction of a chemical analyte with the sensor surface results in a change of propagating characteristics of the wave. In the food and beverage industries, environmental testing, and other areas, human sensory tests have mainly been performed, however, the results often depend on subjective judgment. Therefore the development of taste and odour sensors is very important. Surface acoustic wave (SAW) devices have the ability to directly respond to the mechanical and physical properties of materials in contact with the device surface. Here we propose a surface acoustic wave (SAW) electronic tongue sensor system that can be used to determine the different taste properties of liquid samples. The term "electronic tongue" was introduced at the Eurosensors X conference in 1996 [1] while the first concepts of taste sensors were published a few years earlier, in 1990 [2]. The reported devices were based on potentiometric principles utilising either ion selective lipid membranes or ion selective electrodes. Winquist et al. introduced a voltametric electronic tongue in 1997 [3]. Unlike electronic tongue devices reported so far, the devices described in this paper are miniature, low-cost, robust, durable, micropower devices based on physical rather than chemical principles. The main advantage of our proposed SH-SAW sensor is that it can detect various properties of an adjacent liquid without any coating films. The approach adopted is based on a generic fingerprint correlated to key physical parameters and so does not employ a bio-chemical selective layer. This in turn increases the lifetime and durability of the resultant devices, albeit with a loss of specificity.

2 Device design and operating principle

Two SH-SAW IDTs are designed using the software package L-Edit (Tanner Tools) and fabricated on 36° rotated Y-cut X-propagating $LiTaO_3$ (36YX.LT) substrate employed for simultaneous measurements of both mechanical (acoustic) properties, and electrical (electro-acoustic) parameters of the liquid under test. This is achieved through a dual delay line configuration, one shorted (metallized and electrically shielded) and the other left free (electrically active). This way, apart from mass loading and viscosity (shorted delay line), it is possible to monitor additionally the permittivity and conductivity (free delay line) of the liquid under test, parameters that can be related to taste properties, such as sweetness and saltiness. Figure 1 shows a picture of the fabricated SH-SAW device.

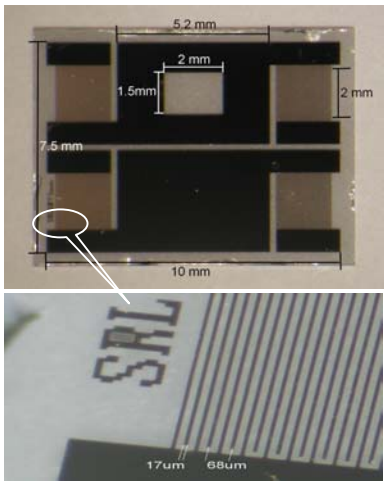

Figure 1. Photograph of fabricated SH-SAW device

The SH-SAW wave that propagates on the surface of $LiTaO_3$ substrate has an associated electric field that propagates several micrometers into a liquid. This electrical interaction (also known as the acousto-electric interaction) with the liquid affects the velocity and/or attenuation of SH-SAW propagation and it is utilised in sensing the dielectric properties of the liquids. When the surface is electrically shorted, the piezoelectric potential becomes zero and thus only horizontally polarised shear displacement waves interact with the fluid. In this case, mechanical properties including the viscosity and density will be detected. On the other hand, the piezoelectric potential at the free surface extends to the liquid and subsequently measures the complex dielectric properties such as relative permittivity and conductivity. Previous work on the analysis of different drinks [4] and fat content in milk [5] has been very encouraging.

3 Experimental method and results

In order to test the sample liquids the devices were mounted on a custom designed PCB below a PTFE cell that contains the liquid under test, see Figure 2. The experimental procedure for SH-SAW devices involves the measurement of both the phase velocity and attenuation of the SH-SAW signals propagating on the two delay lines of the sensor. The set-up includes a signal generator, the SH-SAW sensor and a vector voltmeter (HP 8505A). In this, an electrical signal is fed from the signal generator to the input IDTs; the amplitude ratio ΔV and phase difference $\Delta\phi$ between the input and output signals of each delay line were monitored by the vector voltmeter.

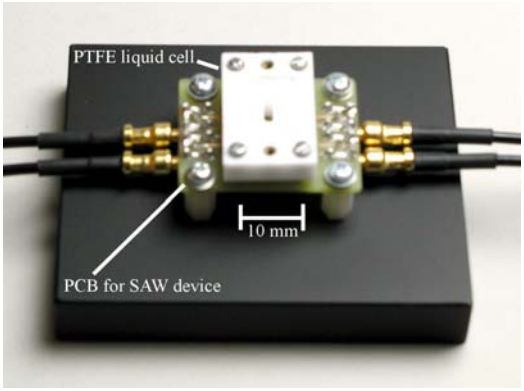

Figure 2. Total analysis taste system

The experiments were performed under controlled temperature conditions of 23 ± 0.1 °C using a commercial Dri-Bloc™ heater. Solutions used for the typical basic tastes were HCl (sour), NaCl (salt), quinine (bitter) and sucrose (sweet). Equal volumes of the mixtures (60 µl) where dispensed into the liquid cell using a micro-litre syringe and the device and cell cleaned and dried after each sample was tested using DI-water. The measurements were repeated randomly and 5 replicate measurements were conducted on each sample.

Figure 3 shows 3-D principal components analysis (PCA) of the attenuation and phase parameters for the different taste sample solutions. The concentrations used were 0.1 M for HCl, NaCl and sucrose and 1.3×10^{-4} M for quinine. The amplitude ratio and phase difference on each of the delay lines (electrical shorted and active) were used as the four parameters for the PCA.

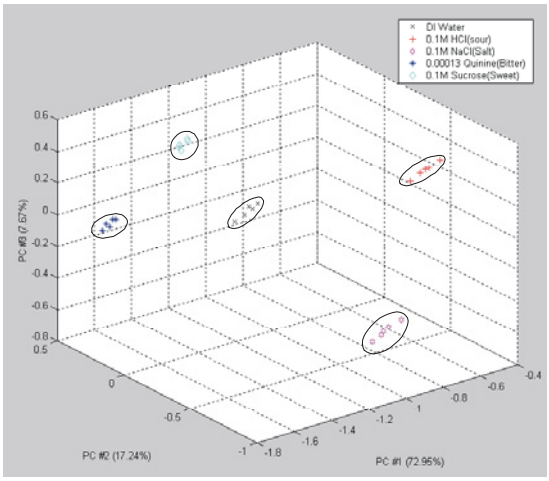

Figure 3. 3-D PCA plot for the different taste solutions showing 100 % separation

Further experiments were conducted to see the effect of diluting the different taste solutions using water and repeating the tests. The 0.1 M solutions were diluted in stages by a factor of 2^n where n varied from 1 to 5. Each time the volume of DI water was increased by a factor of 2^n and added to a fixed volume of the solutions. These results shown that the limit of detection is typically 0.1%.

4 Conclusion

A taste sensing system has been developed and is based upon a dual SAW sensor configuration. Preliminary results show that it is capable of discriminating between different basic tastes. A microsystem version is under design that will work at higher frequencies (433 and 869 MHz) and should improve sensitivity. It is believed that this system could be used as a simple, robust low-cost taste sensor.

References

[1] A. Legin, A. Rudinitskaya, Y. Vlasov, C. Di Natale, F. Davide, A. D'Amico, Technical digest of Eurosensors X, Leuven, Belgium, 1996, 427-430.

[2] K.Toko, K. Hayashi, M. Yamanaka, K. Yamafuji, Tech. Digest 9th Sens. Symp., Tokyo, Japan, (1990), 193-196.

[3] F. Winquist, P. Wide, I. Lundstrom, Analytica Chemica Acta, 357, (1997), 21-31.

[4] M. Cole, G.S. Sehra, J.W. Gardner and V.K. Varadan, Proceedings of the IEEE Sensor Conference, Florida 2002

[5] M. Cole, G. Sehra, J.W. Gardner, and V.K. Varadan, *IEEE Sensors Journal*, at press

Analysis and Optimisation of MEMS Electrostatic On-Chip Power Supply for Self-Powering of Slow-Moving Sensors

P. D. Mitcheson, P. Miao, B. H. Stark, A. S. Holmes, E. M. Yeatman, T. C. Green

Imperial College London, Dept. of Electrical & Electronic Engineering,
Exhibition Road, London SW7 2BT, United Kingdom
email: paul.mitcheson@imperial.ac.uk http://www.ee.imperial.ac.uk

Summary: *This paper presents the analysis and optimisation of an on-chip electromechanical power source specially adapted for self-powered sensors subjected to slow and irregular motion with amplitudes way in excess of device dimensions. Design architectures compatible with MEMS technology and initial experimental results of this parametric generator are presented. The main goals have been to maximise the energy generated in one motion cycle, and to minimise the acceleration necessary to initiate power generation. The analysis considers sinusoidal sensor motion for a range of energy extraction strategies resulting in interrupted motion of the moving plate. We conclude that carefully timed energy extraction and new suspension systems are necessary for slow-moving self-powered sensors.*

Keywords: *Micro-generator, self-powered sensors, motion-to-electric energy conversion*

Category: [1] *General, theoretical and modelling*

1 Introduction

Micro-generators have been reported [1-3] to generate enough power to supply a microelectronic circuit. They do, however, rely on rapid and regular vibration of several kHz. This motion stimulates a sprung mass into resonance, allowing its kinetic energy to be extracted. The extraction can be achieved using resonant electrostatic, electromagnetic or piezo-electric phenomena. Due to the restricted internal displacement of the mass, efficient generation only takes place below a certain amplitude of device motion.

Unfortunately, rapid and regular vibration restricted to minute amplitudes are clearly not available in many applications, and we are therefore developing new generator topologies in order to extract power from slow sweeping irregular motion more compatible with our human environment. A major challenge is to extract the maximum energy over a range of motion frequencies and amplitudes. In the case of our electrostatic generator, this requires adapting the timings of charging and energy extraction as well as the charge level, to the prevailing motion. Results from a detailed analysis of the adaptive (or parametric) energy extraction method and first measurements with the new geometry of the parametric generator are presented here.

2 Generator operation and topology

Energy conversion from irregular motion with amplitudes significantly greater than the dimensions of the generator requires special attention to the topology. Fig. 1 shows a cross-section of a suitable MEMS generator. The large mass of the moving plate is suspended in a silicon frame and charged via an auxiliary circuit. As the device is accelerated downwards, the plate travels upwards relative to the device and reduces the plate's capacitance to ground. The work against the attractive force between the capacitor plates results in the voltage on the plates rising and the gained energy can be extracted via a high-voltage low-current power electronic circuit.

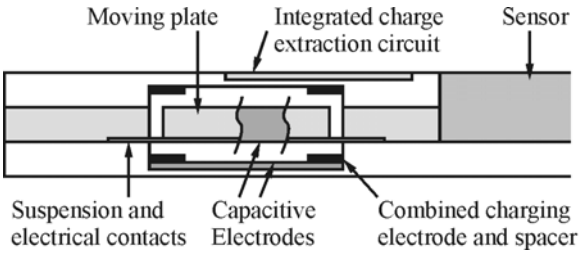

Fig. 1: Integrated micro-generator (cross-section).

Only a fraction of large amplitude device motion can be utilised due to the moving plate being constrained by typical MEMS dimensions. Therefore, in order to maximise the generated energy, the proof mass is controlled so as to move relative to the frame only at the peak of the acceleration.

The analysis was performed using a parametric generator model consisting of a mass within a frame attached to the moving source, with power extracted by a damper whose force is constant. The motion of the mass relative to the frame would normally be enhanced by resonance, but due to large irregular input motion we cannot take advantage this phenomenon. Fig. 2 summarises the results for three categories of generators. Normalised power generation is plotted from large amplitude motion ($Z_l/Y_0 \approx 0$) to low amplitude (vibration) ($Z_l/Y_0 > 1$), where Z_l and Y_o are the maximum internal displacement and the source motion amplitude respectively, for frequencies close to the resonant

device frequency (ω_c=1). The parametric case excels for low frequency motion and large amplitudes.

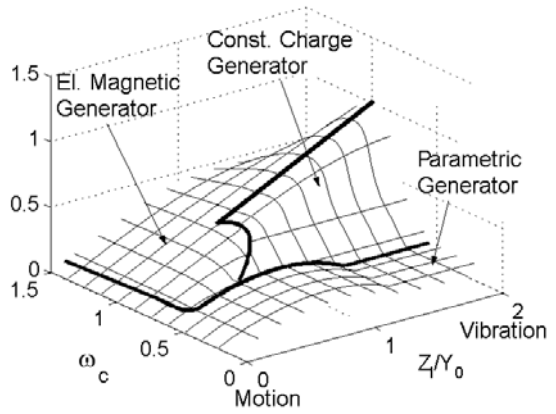

Fig. 2: Normalised power output for two resonant generator types and for the parametric electrostatic generator.

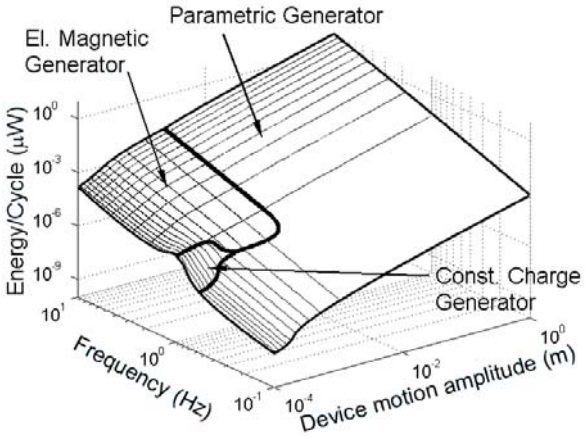

Fig. 3: Superior energy/cycle generation by parametric generator at low frequency and large motion amplitude (mass travel 0.5mm, moving mass 0.1g).

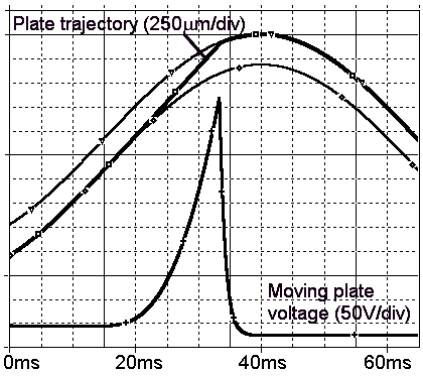

Fig. 4: Simulated flight path of the moving mass relative to the sinusoidal motion of the device. The initial charge on the plates is set to allow the mass only to break away once a certain acceleration is attained.

3 Experimental results

Fig. 5 shows a prototype generator with the wet-etched silicon frame and moving mass clamped between upper and lower acrylic plates. Spacers and contact electrodes are electroplated onto a quartz substrate. A highly flexible polyimide membrane forms the suspension.

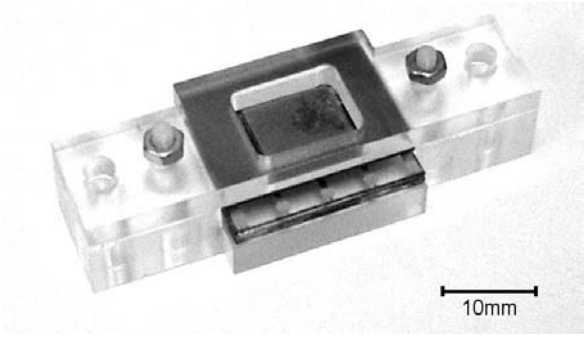

Fig. 5: Prototype generator inside acrylic clamp.

The measured waveforms in Fig. 6 show one half-cycle of the device with motion (Trace 1, 1mm/div), breakaway point (Trace 2) and discharge as the moving plate reaches the upper electrodes (Trace 3, 1kV/div).

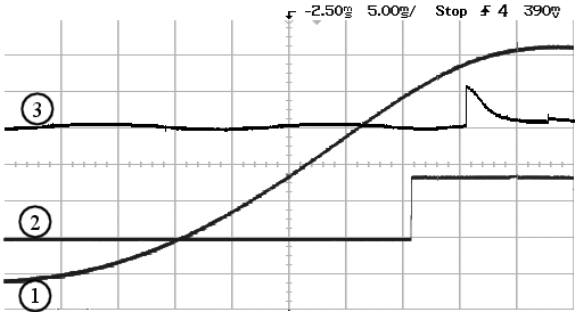

Fig. 6: Response of prototype generator on shaker table at 3.5mm amplitude and 10Hz. Motion (1), breakaway (2) and discharge (3).

4 Conclusions

An electrostatic generator has been designed based on a new, non-resonant operating principle which is shown to provide superior power output for low frequency, high amplitude motion. A meso-scale prototype has been fabricated and tested which illustrates the non-resonant motion and voltage amplification. Output power per cycle greatly exceeds previous examples operating at higher frequencies. Further work is needed to reduce the device dimensions, and to implement an efficient output circuit to obtain low voltage continuous power from the high voltage output pulses.

5 References

1. Meninger, S., Mur-Miranja, J.O., Amirtharajah, R., Chandrakasan, A.P. & Lang, J.H., *IEEE Trans VLSI* **9**, 2001, 64-67.

2. Amirtharajah, R. & Chandrakasan, A.P., *IEEE J. Solid State Circuits* **33**, 1998, 687-695.

3. Williams, C.B. & Yates, R.B., *Proc. Transducers '95,* Vol. 1, 1995, 369-372.

Modeling of Capacitive Coupling in Micromirror Arrays by means of Schwarz-Christoffel Conformal Mapping

A. Nannini[1], F. Pieri[1], G. Raffa[1,2]

[1]Dipartimento di Ingegneria dell'Informazione, Università di Pisa
Via Diotisalvi, 2 – 56126 Pisa (Italy)
[2]e-mail: giuseppe.raffa@iet.unipi.it

Summary: *Micromirrors for optical beam deflection can be fabricated as arrays of mirror sections, with advantages in terms of reliability and cost of the fabrication technology. In this work, we propose a fast method to extract capacitive couplings and electrostatic forces from a system of two-dimensional conductors, and we apply this method to the problem of interfering forces between adjacent sections of a micromachined, electrostatically actuated micromirror array. We compare the results with electrostatic FEM simulations obtained with a commercial package.*

Keywords: *Micromirrors, Schwarz-Christoffel transformation, capacitive couplings*
Category: *General, theoretical and modeling*

1 Introduction

Silicon micromachined micromirrors have been proposed as components for several different applications, among them optical communication switches. If the reflecting surface of such a mirror is parallel to the silicon substrate, a large distance between the moving mirror and the underlying substrate is necessary to obtain a reasonable maximum deflection angle with a mirror side of a few hundred μm (typical for deflection of a beam from an optical fiber). Such distances are not easily obtained with a surface micromachining technology. This problem is often overcome by adopting some kind of bulk technology and/or multi-wafer assembling [1, 2]. These solutions, however, pose obvious problems in terms of VLSI compatibility, reliability, and cost.

A different approach is possible if the mirror surface is sectioned in several slices, each suspended by torsional springs and independently actuated with electrodes under each mirror section, as sketched in Fig. 1. In this structure, every electrode exerts a force on the mirror section above it, but also a parasitic force on the adjacent mirror section. Considerable efforts have been made to model electromechanical behavior of single-section rotating mirrors (see, for example, [1]), but not for an array of mirrors as the one we propose. To model the parasitic force, we propose an approach based on the well-known Schwarz-Christoffel conformal mapping.

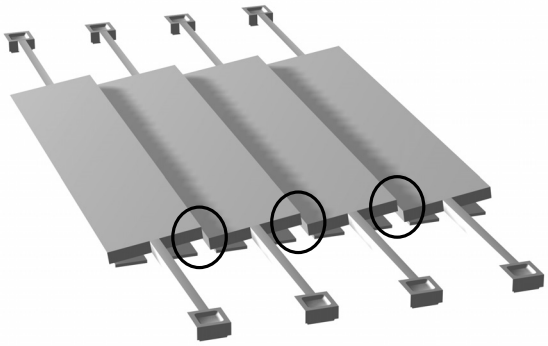

Fig. 1: Structure of the proposed micromirror array. Under every section the driving electrodes are shown. The circles mark the modeled zone(s).

2 The proposed approach

Schwarz-Christoffel transformation (SC) is applied in a large number of technical fields to evaluate several physical parameters in a closed form or numerically. In particular, this type of conformal mapping is a powerful tool to analyze two-dimensional electrostatic problems [3].

The SC transformation maps the inside part of a generic polygon into the upper half plane of a transformed domain [4]. A particular composition of two SC mappings, called simple combination, can be used to map a generic pair of two-dimensional conductors in a parallel-plate capacitance. This mapping combination can thus be used to calculate easily the capacitive coupling, by computing it in the final domain. This approach may be theoretically

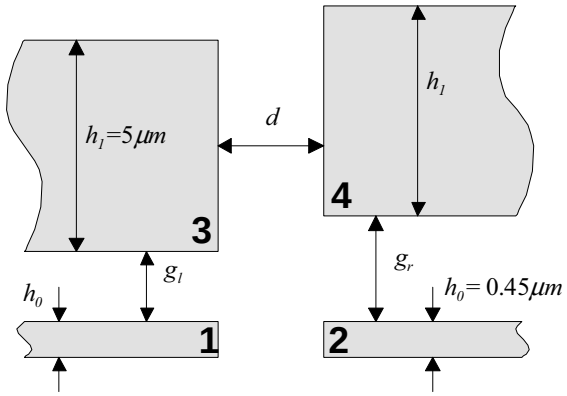

Fig. 2. Four-conductor system studied in this work.

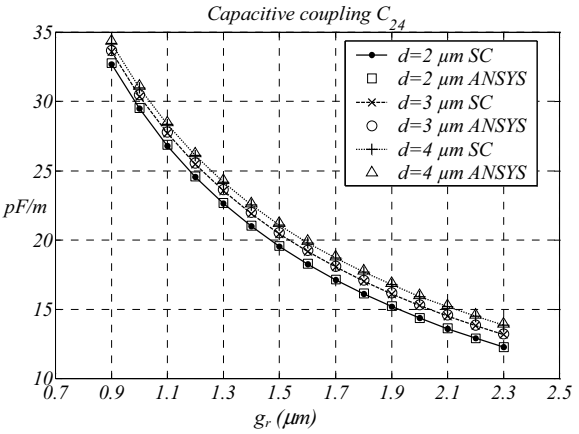

Fig. 3. Capacitance coefficient C_{24} for different values of d, and with $g_l = 1.6\mu m$.

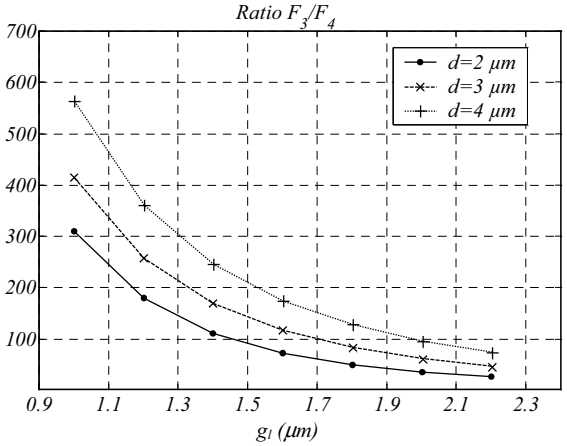

Fig. 4. Ratio between the forces acting on two adjacent sections when only the left mirror is driven.

extended to multi-conductor systems to extract the full capacitance matrix [5]. This is done by solving a certain number of equivalent problems with two conductors, which can be obtained by properly changing the potential distribution among the conductors.

The problem presented in the introduction can be modeled as a four-conductor problem. If we concentrate on the zones between two sections (marked by the circles in Fig. 1) and suppose small deflection angles, the geometry shown in Fig. 2 can be used, by noting that g_l and g_r are directly related to the deflection angles of the two sections.

SC transformations has been used to calculate capacitance matrices for three-conductor systems [6]. We developed a method based on analysis of regions limited by electric field lines [7] and extended it to the case of four conductors. Unfortunately, a closed solution for the problem of Fig. 2 cannot be obtained. Thus, to extend the aforementioned approach [7] we implemented a set of MATLAB™ scripts that perform calculations through the MATLAB™ SC toolbox developed by Driscoll [8].

Simulation results

The proposed method was first used to extract the capacitance matrix of the configuration shown in Fig. 2. The same capacitance coefficients were computed with the FEM package ANSYS™ for comparison. As an example, we report the absolute value of C_{24} as a function of g_r (i.e. when the right mirror is deflected and the left one is not) in Fig. 3. The relative error is below 0.6%.

We also evaluated the parasitic electrostatic force exerted by an array element on the adjacent one. This computation was performed by biasing electrode 1 of fig. 2, and with the other electrodes grounded. The forces were computed numerically as:

$$F_3 = \left(\frac{\partial U}{\partial g_l}\right)_{g_r} \quad , \quad F_4 = \left(\frac{\partial U}{\partial g_r}\right)_{g_l}$$

where U is the total electrostatic energy. The ratio F_3/F_4 is shown in fig. 4. It must be noted that these are the forces only at the mirror tips: this means that the total force on the left mirror is much greater than F_3, as also the part of the mirror not included in fig. 2 (and not modeled) is pulled down by the driving electrode. As the gap at rest for our target technology is about 1.6 μm, the forces were computed for g_r = 1.6 μm, thus supposing that the deflection of the right mirror is negligible. This hypothesis is confirmed *a posteriori* by the high value of F_3/F_4, which never descends below 20 for the geometries under test.

As the SC simulation times are several times lower than FEM solutions, this method can be effectively applied for rapid prototyping of electromechanical devices.

References

[1] O. Degani, Y. Nemirovsky, *J. Microelectromech. Syst.* 11 (2002) 20-26.

[2] J.T. Nee, R.A. Conant, R.S. Muller, K.Y. Lau, IEEE/LEOS International Conference on Optical MEMS, pp. 9-10, 2000.

[3] Ç.K. Koç and P.F. Ordung, *IEEE Trans. Computer-Aided Design* 8 (1989) 1025-1027.

[4] H. Kober, Dictionary of Conformal Representations. Dover Publications, New York, 1952.

[5] A. Hieke, *International Conference on Modeling and Simulation of Microsystems (MSM99)*, pp. 172-176, San Juan, Puerto Rico, USA, April 1999.

[6] G. Lorenz, R. Neul and S. Dickmann, *International Conference on Modeling and Simulation of Microsystems (MSM99)*, pp. 128-131, San Juan, Puerto Rico, USA, April 1999.

[7] G. Raffa, M.Sc. Thesis, University of Pisa, July 2001.

[8] T.A. Driscoll. SC Toolbox User's Guide: http://www.math.udel.edu/~driscoll/software/SC/.

Numerical simulation of an electrostatically-actuated micro-fluidic optical switch

A. Glière[1], M. Laporte[2] and E. Ollier[1]

[1]LETI – CEA Recherche Technologique, 17 rue des Martyrs, 38054 Grenoble Cedex 9, France
email: alain.gliere@cea.fr http://www.cea.fr
[2]OPSITECH, 15 rue des Martyrs, 38054 Grenoble Cedex 9, France

Summary: *A novel micro-fluidic switch for optical applications, is currently under development. Parallel to the development, a numerical model has been built to help design the micro-switches. The model takes into account the coupled physical phenomena involved in the process, namely the large deflection of a clamped circular diaphragm submitted to the spatially variable load due to the electrostatic pressure and the liquid damping. Numerical examples of the static and dynamic behavior of the micro-switches are presented, as well as a comparison of computed and measured values of the pull-in voltage.*

Keywords: *Modeling, MOEMS, Diaphragm, Electrostatic, Micro-fluidic*
Category: *1 (General, theoretical and modeling)*

1 Introduction

The device is based on the combination of planar lightwave technology and MEMS technology (Fig. 1). The principle of the switch relies on the motion of an index matching fluid in a trench etched on the propagation path of the optical wave guide. The motion of the fluid is controlled by the displacement of a mechanical diaphragm driven by an electrostatic actuator. Depending on the position of the index matching fluid in the trench, the propagation of light is modified, providing switching or attenuation functions.

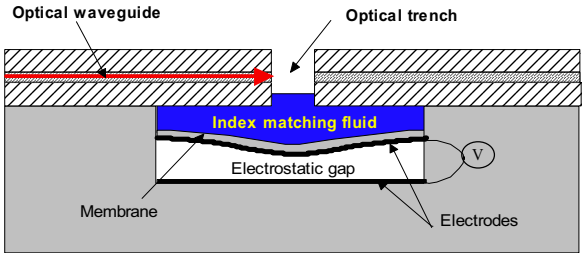

Fig. 1. Principle of the micro-fluidic optical switch.

The principle of the optical micro-switch is similar to that of other micro-devices based on the deflection of a diaphragm. A number of previous modeling publications, relevant to our work, have dealt with the numerical simulation of micro-pumps [1] and pressure sensors [2].

In a first part, this paper describes the actuator model and presents a comparison of computed pull-in voltage values with experimental data. In a second part, the damping effect due to the motion of the index liquid is taken into account in order to simulate the dynamic response of the optical micro-switch.

2 Electrostatic actuator modeling

The electrostatic actuation part of the optical micro-switch is composed of a clamped circular diaphragm and a rigid counter electrode, in a capacitor-like configuration. Applying a potential difference between the capacitor electrodes causes the diaphragm to bend and eventually, if the applied potential difference is greater than a pull-in voltage threshold, to go in contact of the counter electrode, because of the non linearity of the phenomenon.

The theory of large deflection of plates is applicable for deflections up to three times the diaphragm thickness [3]. As the electrostatic pressure is not spatially uniform, analytical solutions, such as that of Eaton [2], cannot be used in our case. Thus, the numerical approach of Voorthuysen [4], appropriate for large deflection, has been extended to the case of non uniform loads. The following set of partial differential equations is solved iteratively, for the displacement radial derivative f and the radial force per unit length N_r, by a finite difference method :

$$\frac{d^2f}{dr^2}+\frac{1}{r}\frac{df}{dr}-\frac{f}{r^2}=\frac{N_r f}{D}+\frac{1}{D.r}\int_0^r p.\rho.d\rho$$

$$r^2\frac{d^2N_r}{dr^2}+3r\frac{dN_r}{dr}=-\frac{hE}{2}f^2$$

with r the radial coordinate, p the position dependant electrostatic pressure, D the diaphragm flexural rigidity, h the diaphragm thickness and E the material Young modulus.

In this formulation, the built-in stress appears as a boundary condition on N_r. The electrostatic pressure is computed by the means of a straightforward plane multi-ring capacitor approximation. The displacement w is obtained by integrating f.

The contact of the diaphragm with the counter electrode is treated as a cancellation of the load in the contact zone. Under-relaxation is used to deal with this very strong non linearity.
As an example of computation, performed in Matlab, the variation of the pull-in voltage with the built-in stress and the electrostatic gap thickness is presented on Fig. 2.

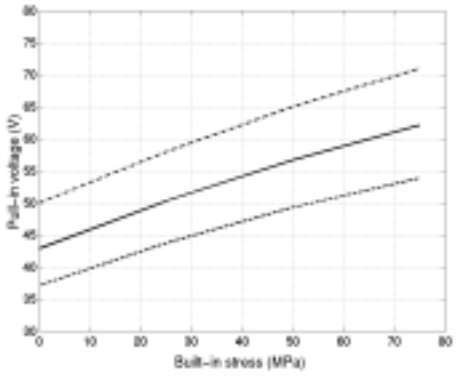

Fig. 2. Pull-in voltage versus built-in stress for several electrostatic gap thickness (1.0 µm, 1.1 µm and 1.2 µm from bottom to top).

A comparison between computed and measured values of the pull-in voltage has been performed. Using the experimental parameters (i.e. diaphragm radius: 110 µm, diaphragm thickness: 1.5 µm, electrostatic gap thickness: 1.1 µm), the computed pull-in voltage is 44 V. The average measured value is 59 V, with 8 V standard deviation. The probable causes of the discrepancy are the overestimation of the applied voltage due to resistive contact and the large uncertainty on the physical properties values, among which the built-in stress, whose influence on the pull-in voltage value is quite significant (Fig. 2.).
Additional experimental comparison with improved electrical contacts are currently under progress.

3 Dynamic behavior of the micro-switch

In order to model the dynamic behavior of the micro-switch, damping, due to the motion of the index matching fluid, must be taken into account.
Assuming that the pressure inside a micro-pump chamber is uniform and the pressure loss is mostly caused by inlets and outlets, some authors [1] based their fluid damping analysis on the Bernoulli equation. We chose instead to use the Reynolds equation for incompressible fluids, which is applicable in the lubrication or damping context [5] :

$$\nabla \cdot \left(\frac{(e-w)^3}{\eta} \nabla p \right) = 12 \frac{\partial w}{\partial t}$$

where η is the fluid dynamic viscosity, e the initial fluid tank thickness and w the diaphragm displacement. The Reynolds equation comes with its set of assumptions among which (i) the pressure is constant through the fluid thickness, (ii) the surface curvature is large compared with fluid thickness, (iii) the flow is laminar.
Assuming an axisymmetrical device geometry, the equation for the damping pressure is coupled to the diaphragm displacement set of equations. The dynamic behavior of the system is then calculated for a given voltage ramp.
The influence of geometrical or physical parameters can be studied. For instance, the dynamic of the displaced fluid volume is presented on Fig. 3 for several index liquid viscosities.

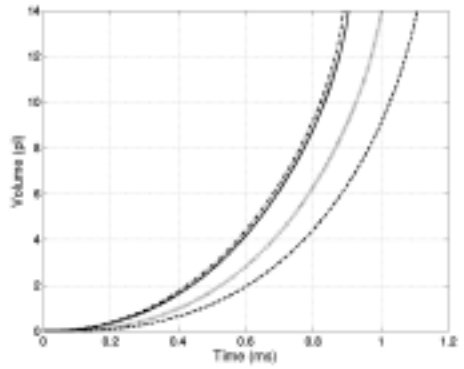

Fig. 3. Transient behavior of the displaced fluid volume for several fluid viscosities (resp. 0.5, 1, 5 and 10 times the water viscosity from top to bottom). The applied voltage ramp is 100 V/ms.

4 Conclusion

A model of electrostatically-actuated optical micro-switch has been developed. It takes into account the coupled physical phenomena involved in the process, namely the large deflection of a diaphragm submitted to built-in stress and a spatially variable load, due to the electrostatic pressure and the liquid damping pressure. Numerical examples are presented, which demonstrate the effectiveness of the present model.

References

[1] L. S. Pan, T. Y. Ng, G. R. Liu, K. Y. Lam, and T. Y. Jiang. Analytical solutions for the dynamic analysis of a valveless micro-pump - a fluid-membrane coupling study. *Sensors and Actuators* A 93 (2001) 173-181.
[2] W. P. Eaton, F. Bitsie, J. H. Smith, and D. W. Plummer. A new analytical solution for diaphragm deflection and its application to a surface micro-machined pressure sensor. In: *Modeling and Simulation of Micro-systems, Semiconductors, Sensors and Actuators*, San Juan, Puerto Rico, 1999.
[3] E. Suhir, *Structural analysis in micro-electronic and fiber-optic systems.*, vol. 1, Van Nostrand Reinhold, New York, 1991.
[4] J. A. Voorthuyzen and P. Bergveld. The influence of tensile forces on the deflection of circular diaphragms in pressure sensors. *Sensors and Actuators* 6 (1984) 201-213.
[5] A. Cameron, *Basic lubrication theory*, vol. Ellis Horwood Limited, Chichester, 1976.

Stability Limits Of Torque Gain In Angular Electrostatic Actuators

A. Pareek, M. R. Dokmeci, K. Heng, C. D. Fung, and C. H. Mastrangelo

Corning Intellisense, Wilmington, MA, USA 01887
email: pareekA@corning.com http://www.corning.com

Summary: *We present experimental and theoretical limits of stable voltage and torque gain as functions of DC bias and actuator dimensions for parallel-plate electrostatic actuators. This technique reduces the drive voltage by using a DC bias and non-linearity of torque with voltage. By optimizing the design of electrode length, gap, and bias, maximum stable range can be extended for a given DC bias. The pull in angle also depends on bias voltage. We show that for torque gain of 2-4, maximum angular range is maintained.*

Keywords: *torque gain, parallel-plate, electrostatic actuators*
Category: *1 (General, theoretical and modeling)*

Angular parallel-plate electrostatic actuators have received much attention recently as a means for implementing micro-mirror optical switches [1,2]. A pervasive problem with these devices is their high voltage requirement due to the large size and correspondingly large gaps. It is thus desirable to reduce the drive voltage to levels compatible with conventional electronics. The torque gain technique uses a DC bias V_B and the non-linearity of torque with voltage to reduce the drive requirement [3,4] (see Fig. 1). The resulting torque is magnified by gain $G\tau$. Large torque (and voltage) gains are achievable, but as the bias is increased, the actuator becomes unstable and pulls-in; therefore this method has been largely used for digital toggle applications, such as in TI's DMD.

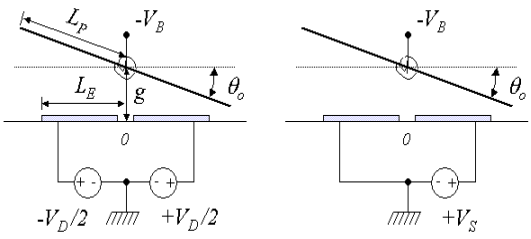

Fig.1. Schematic cross-section of typical angular electrostatic actuator showing biasing configurations. The device can be driven differentially or single ended. The significant parameter is the voltage span at the drive electrodes.

In this paper we present experimental and theoretical limits of stable voltage and torque gain as functions of DC bias and actuator dimensions. We show that through careful design, for a given bias and drive voltage the electrode length can be optimized for maximum stable range. We also demonstrate that pull-in behavior occurs at an angle that depends on V_B.

Figure 2 shows the cross-section of the bulk micromachined torsional mirror actuator used for

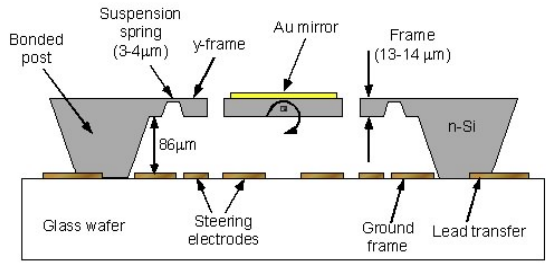

Fig. 2. Cross section of bulk micromachined mirror used for experiments. The entire structure is made of single crystal silicon.

the experiments. The device is constructed by anodically bonding a 7740 pyrex glass wafer with patterned metal electrodes to an SOI wafer with 100 μm-thick device layer. Prior to bonding, the silicon device layer is anisotropically etched to precisely define the thickness of both flexures and mirror support plate. Electrical lead transfers are

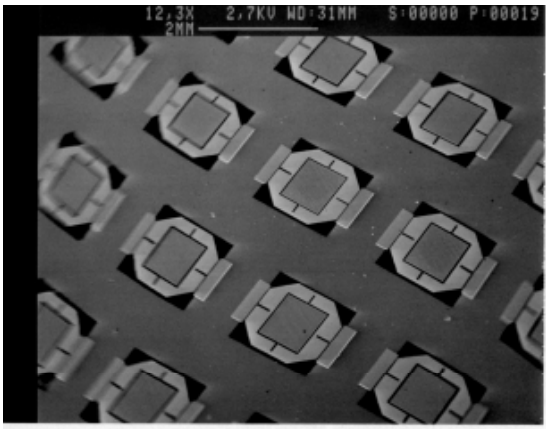

Fig. 3. SEM photograph of a MEMS mirror array.

made by overlapping the glass metal onto the silicon, and lead wires are routed to bonding pads

located at the edge of the chip through grooves etched on the silicon. The SOI carrier substrate is selectively etched and the buried oxide is removed. Next the Au mirrors are defined, and the gimbal structure is patterned using deep RIE. Figure 3 shows photographs of a device array. The electrode length is L_E = 195 µm.

A high torque is achieved when a DC bias $-V_B$ is applied to the movable plate, and a differential or single ended voltage V_D is applied to the drive electrodes. For an angular range θ_o, voltage and torque gains $G_V = V_o/V_D$ and $G\tau = (G_V)^2$, respectively, where V_o is the minimum voltage

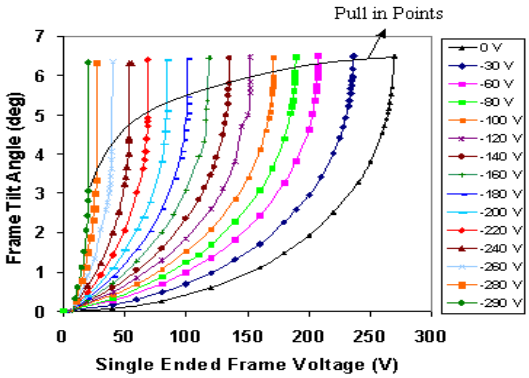

Fig. 4. Single-ended deflection of actuator for different DC biases (right scale).

necessary to stably deflect the actuator at θ_o with $V_B = 0$. Figure 4 shows deflection curves for outer frame versus DC bias voltage. The single ended drive voltage is reduced as the bias voltage is increased, but the stable angular range (at the onset of pull-in) is gradually reduced. Figure 5 shows the single ended voltage gain achieved as a function of

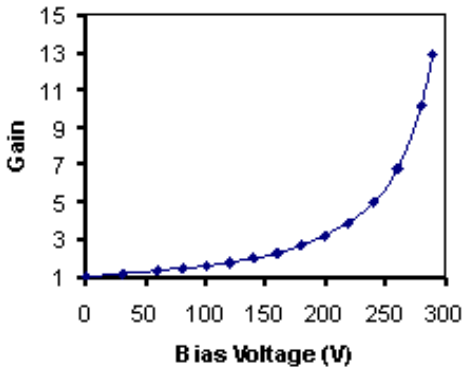

Fig. 5. Single-ended voltage gain for maximum angular range as a function of DC bias voltage.

the DC bias. Figure 6 shows the stable angular range that can be achieved for different gains. For

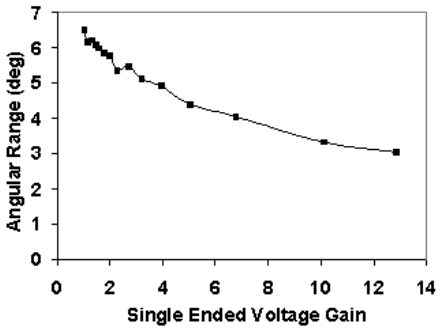

Fig. 6. Angular range versus (stable) voltage gain. There is little loss in the angular range for voltage gains 2-4.

voltage gains of 2-4 the angular range is minimally reduced. Figure 7 shows the corresponding full range single ended voltage for different biases. The curve is almost a straight line. The paper will discuss both theoretical and experimental results in detail.

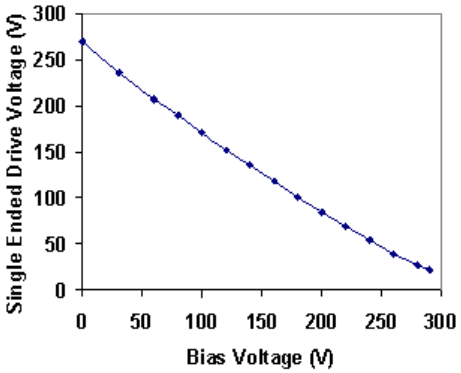

Fig. 7. Single-ended drive voltage required for maximum deflection for a given DC bias.

References

[1] S. H. Hinton, *An Introduction to Photonic Switching Fabrics*, Plenum, 1993

[2]. D. Bishop, "The Lucent Lambdarouter: MEMS technology of the future here today", *IEEE Communications Mag*., vol. 40(8), pp. 75-79

[3]. L. Hornbeck et al, "Spatial Light Modulator", US *Patent 5,061,049*, Oct. 29, 1991.

[4]. L. J. Hornbeck, "Deformable-mirror spatial light modulators", *Proc. Spatial Light Modulators and Applications III, SPIE* vol. 1150, pp. 86-10, 1998.

Finite Element Modeling and Simulation of Micro-Switch Pull-in Voltage and Contact Force

R.A. Coutu Jr.[1], L.A. Starman[2], J.R. Reid[2], and P.E. Kladitis[1]

[1]Air Force Institute of Technology, Electrical and Computer Engineering Dept., 2950 P. St., Wright-Patterson AFB, OH, USA
email: ronald.coutu@afit.edu http://en.afit.edu/eng/
[2]Air Force Research Laboratory, AFRL/SNHA, 80 Scott Dr., Hanscom AFB, MA, USA

Summary. *Metal-to-metal contact switches depend on having adequate contact force to achieve desired, low contact resistance [1, 2]. Electrostatically actuated micro-switches can only produce contact forces on the order of micro-Newtons (μN). In this study actuation voltages were applied to cantilevers until they buckled onto the bottom electrode. Overdriving devices in this manner resulted in somewhat higher contact forces. The difference between initial contact and buckling was defined as the useful range of contact force. Micro-switches, modeled and simulated using CoventorWare [3], were anyalyzed to determine useful force range. This was further investigated by varying the bottom electrode's dimensions.*

Keywords: MEMS, micro-switch, contact force, pull-in voltage, electric contact, FEM, CoventorWare
Category: 1 (General, theoretical, and modeling)

1 Introduction

Finite element modeling and simulation design tools are useful for evaluating microelectromechanical system (MEMS) cantilever switch designs prior to device fabrication. In this study, micro-switches were modeled and simulated, using the CoventorWare [3] finite element software package, to determine pull-in voltage and the maximum useful contact force.

2 Modeling

The micro-switch design was drawn using a 2D layout editor, converted to GDS format, and imported into CoventorWare [3]. The cantilever beam in Figure 1 was $75\mu m$-wide and $400\mu m$-long and the dimple or contact area was approximately $8\mu m$ in diameter. The precise contact area, determined by material hardness and surface roughness was not considered here.

Next, the foundry, modeled after the fabrication process developed by the Air Force Research Laboratory's Sensors Directorate (AFRL/SND), was defined. Table 1 summarizes the process and typical layer thicknesses. The elastic modulus and poisson's ratio for the structural layer were 80 GPa and .42, respectively [4]. Residual or stress gradients, due to fabrication, were assumed to be zero and the cantilevers flat after release.

The 3D model, generated from the 2D layout, the material properties, and the foundry process was meshed using finite volume elements. A careful mesh analysis was accomplished to ensure accurate, timely simulation results. This iterative analysis consisted of comparing relative mesh quality (i.e. the number of nodes) and the resulting beam buckling voltage. CoventorWare's free meshing option (tetrahedral-shaped elements) was used to the mesh the structural layer because it provided the best overall nodal coverage.

Beam buckling voltage was evaluated after each simulation run to determine if an increased mesh quality was needed. Figure 2 shows that structural layer

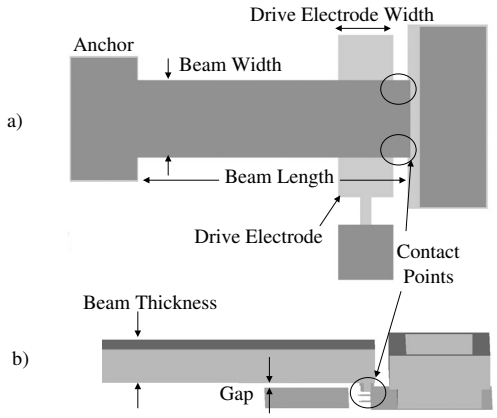

Fig. 1: Micro-Switch Layout (a) 2D layout, Top View (b) 3D Layout, Side View.

Table 1: Typical Layer Thicknesses using the AFRL/SND Micro-Switch Fabrication Process.

Layer	Material	Thickness
Beam/Structural	Plated Gold	$4.3\mu m$
Gap/Sacrificial	Polymethylglutarimide (PMGI)	$3.2\mu m$
Drive Electrode	Evaporated Gold	$.3\mu m$
Dimple/Contact	Gold	$1.2\mu m$

**The views expressed in this article are those of the authors and do not reflect the official policy or position of the United States Air Force, Department of Defense, or the U.S. Government.

meshes greater than about 650 nodes did not change the buckle voltage by more than one volt.

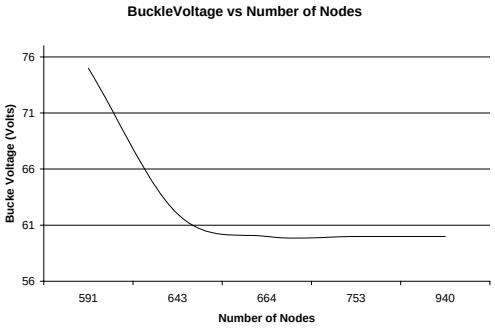

Fig. 2: Mesh Analysis Results using a Micro-Switch with a $200\mu m$-Wide Drive Electrode.

3 Simulation

The simulations were accomplished using CoventorWare's mechanical and combined solution solvers. The mechanical solver was used to fix all degrees of freedom at the anchor and define contact surfaces under the dimples [3]. The combined solution solver was used to generate electrostatic actuation force by applying DC voltage between the beam and bottom electrode. Note from Figure 3 that properly defined boundary conditions can greatly simply the device's 3D model.

A pull-in analysis with a voltage trajectory of zero to 75 volts with one volt increments was used. An "imaginary" dielectric layer was defined on top of the drive electrode to avoid crashing the simulation upon reaching the beam's buckle voltage.

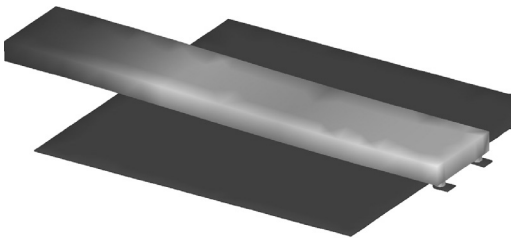

Fig. 3: Micro-Switch with Pull-in Voltage applied. The device has a $300\mu m$-Wide Drive Electrode.

From Table 2, we find that the pull-in voltage decreases as the drive electrode width increases. Maximum contact force, defined as the force one step prior to beam buckling, has a parabolic relationship with the drive electrode's width. For this switch geometry, a peak contact force of $35.5\mu N$ occurred while using a $150\mu m$-wide drive electrode. The corresponding pull-in voltage was approximately 21 volts. The values in Table 2 correlate well with both analytically derived models and experimentally collected results.

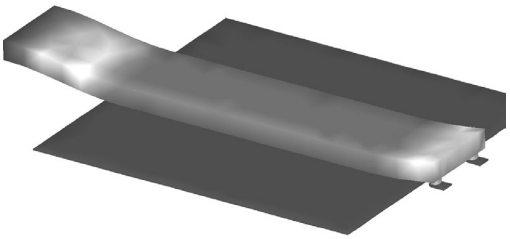

Fig. 4: Micro-Switch with Buckle Voltage applied. The device has a $300\mu m$-Wide Drive Electrode. Note the high stress areas near the anchor and contact regions.

Table 2: Micro-Switch Contact Force Ranges for Devices with Drive Electrodes from $50\mu m - 350\mu m$-Wide.

Width	Pull-in Voltage	Maximum Contact Force
$50\mu m$	32 volts	$11.0\mu N$
$100\mu m$	24 volts	$27.5\mu N$
$150\mu m$	21 volts	$35.5\mu N$
$200\mu m$	21 volts	$29.9\mu N$
$250\mu m$	21 volts	$29.8\mu N$
$300\mu m$	20 volts	$25.4\mu N$
$350\mu m$	20 volts	$25.1\mu N$

4 Conclusions

Using CoventorWare, micro-switches were simulated and approximate pull-in voltages and maximum contact forces and were predicted. Nominal pull-in voltages were approximately 21 volts and maximum contact force was approximately $35\mu N$. These simulations show that cantilever micro-switches with this geometry have very low contact force. In addition, the simulations show CoventorWare to be a useful tool for evaluating micro-switch designs, predicting contact force, and even selecting appropriate electric contact metallurgy prior to fabricating devices.

Acknowledgments: The authors gratefully acknowledge the efforts of AFRL/SND, Wright-Patterson AFB, OH, in developing the switch fabrication process.

References

[1] S. Majumder, N. McGruer, G. Adams, P. Zavracky, R. Morrsion, and J. Krim. "Study of contacts in an electrostactically actuated microswitch." *Sensors and Actuators A*, Vol. **93**, No. 1, August 25, 2001, pg. 19–26.

[2] D. Hyman and M. Mehregany, "Contact physics of gold microcontacts for MEMS microswitches." *IEEE Transactions on Componets and Packaging Technologly*, Vol. **22**, No. 3, Sept 1999.

[3] CoventorWare, Inc. "Analyzer Reference Guide, Rev A." www.coventor.com, 2001.

[4] G. Kovacs, "Micromachined Transducers Sourcebook." McGraw-Hill, New York, 1998.

Electro-Mechanical Compensation of the Temperature Coefficient of the Pull-In Voltage of Microstructures

L.A. Rocha, E. Cretu and R.F. Wolffenbuttel

Delft University of Technology, Faculty ITS,
Dept. for Micro-electronics, Mekelweg 4, 2628 CD, Delft, The Netherlands
Email: L.Rocha@its.tudelft.nl

Summary: *The pull-in voltage of a suspended microstructure can be used as on-chip voltage reference in a compatible MEMS-IC process. Pull-in is detected using capacitive displacement measurement. The stability is affected by an initial parasitic charge buildup and a temperature sensitivity of -149 μV/K. A burn-in procedure is required to minimize the first effect. The temperature coefficient is compensated for by applying additional temperature dependent electrostatic energy to the microstructure. Devices fabricated in an epi-poly process and designed for a nominal pull-in voltage at 5 V have a measured value at 4.7424 V. Drift becomes negligible after 50 hours of operation. The temperature reproducibility is within the resolution of the readout at 100 μV over a temperature range between 20 °C and 60 °C.*

Keywords: *Microelectromechanical systems, pull-in voltage, temperature compensation*
Category: *10 (Applications)*

1 Introduction

The long-term stability of a DC voltage reference based on the pull-in of a microstructure, is affected by two effects: parasitic charge build-up at the insulator layers on top of the actuation electrodes [1,2], and a temperature coefficient due to thermal expansion and thermal dependence of the Young's Modulus on the material used [2]. The work reported here, focuses on the second source of uncertainty and a simple and efficient way to reduce the temperature coefficient of the DC voltage reference is presented.
For stable operation as a DC reference, residual stress should not compromise long-term stability, therefore, a single-ended clamped beam or a structure with folded suspension should be used. The structure used was fabricated in an epi-poly process [3,4] and is an one degree of freedom structure with folded springs, with two sets of actuators: one periodically driven to pull-in and the other to compensate for temperature (Fig. 1).

2 Pull-In Analysis

The pull-in of such a 1DOF structure is expressed as:

$$V_{pi} = \sqrt{\frac{8}{27}} d \sqrt{\frac{k}{C_0}}\,, \qquad (1)$$

where d is the initial gap distance, C_0, the initial capacitance and $k = 4Eh\left(\frac{b}{L}\right)^3$ is the spring constant (E, h, b and L are the Young's Modulus, thickness, width and length respectively). The polysilicon structure has a thermal expansion coefficient $\alpha = -3\times10^{-6}/K$ and a Young's Modulus thermal coefficient $\beta = -67\times10^{-6}/K$ [5]. Disregarding the effect of thermal expansion on C_0, k remains as the temperature dependent part and can be expressed as $k(T) = k(1+(\alpha+\beta)T)$ (not considering quadratic terms). Introducing this temperature dependent spring on (1) and taking the derivative to temperature (T), we get:

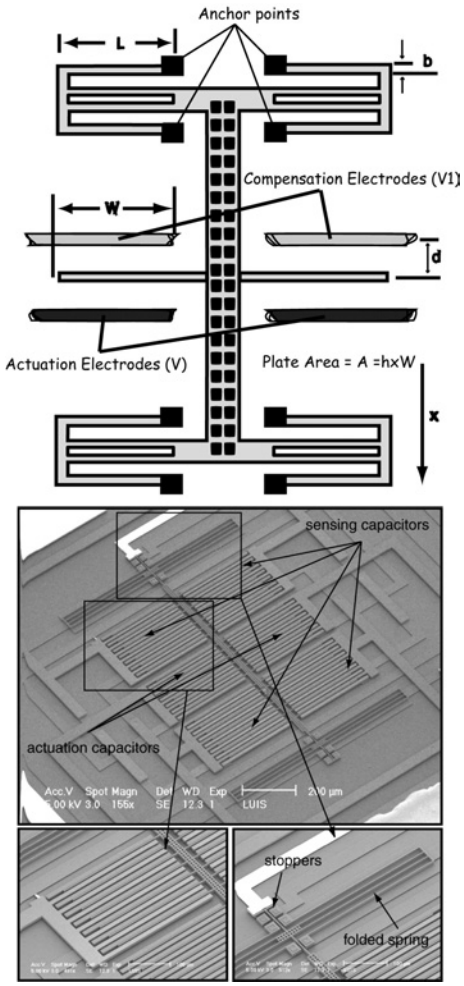

Fig. 1. Schematic and photograph of the microfabricated device used on the experiment.

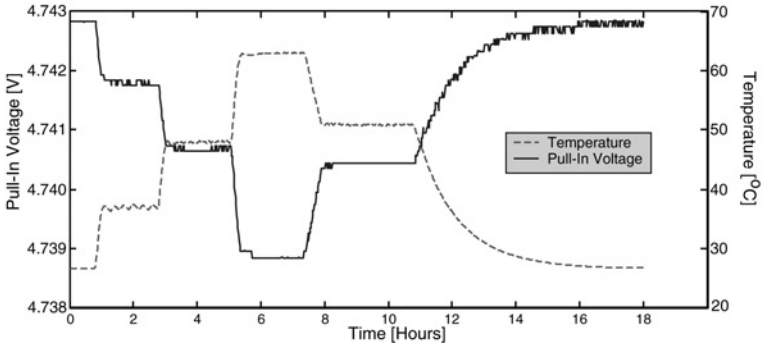

Fig. 2. Pull-In Voltage versus Temperature

$$\frac{\partial V_{pi}}{\partial T} = \sqrt{\frac{8}{27}} d \sqrt{\frac{k}{C_0}} \frac{(\alpha+\beta)}{2.\sqrt{(1+(\alpha+\beta)T)}} = V_{pi} \frac{(\alpha+\beta)}{2.\sqrt{(1+(\alpha+\beta)T)}} \quad (2)$$

From (2) it can be concluded that the pull-in thermal coefficient is not linear, and that it increases with temperature (note that $(\alpha+\beta)<0$). For the device presented, and considering a linear temperature coefficient (T=0°C in (2)), a TC of -149µV/K results. Measurements performed on a sample device (Fig. 2) are in agreement with this analysis, showing a TC of about -100µV/K, and increasing for high temperatures.

As V_{pi} is determined by the potential energy in the system ($\partial^2 U_p / \partial x^2 = 0$) and temperature decreases the mechanical energy ($\partial k / \partial T < 0$), a second set of electrodes can be used to add electrostatic energy. The second set of electrodes (V_1 in Fig.1), enables us to introduce a positive TC (applying a voltage proportional to the square root of the measured temperature) compensating for the negative TC introduced by the mechanical properties. Fig. 3 shows the computed and measured pull-in changes for increasing V_1 at constant temperature. From the graph we find a slope of 28.125mV/V_1^2. To achieve zero TC: $\frac{\partial V_{pi}}{\partial T} + \frac{\partial V_{pi}}{\partial V_1} = 0$, a value V_1^2=3.55mV/K is required.

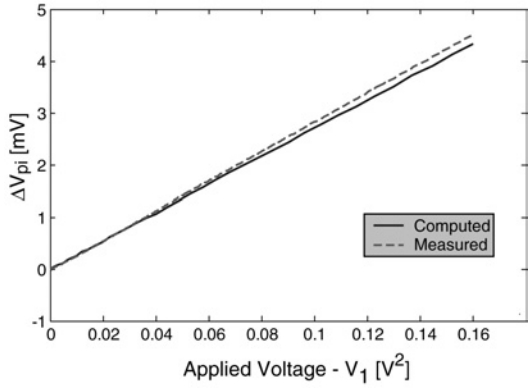

Fig. 3. Pull-In voltage changes at increasing V_1

3 Results and Conclusions

A feedback loop control for V_1 based on the measured temperature was implemented and the results are shown in Fig.4. For temperatures beyond 50°C, the non-linear effects are clearly visible, as the control was implemented on the assumption of a constant TC.

Therefore, this new electro-mechanical approach for compensating the temperature dependence of pull-in greatly reduces the TC. Present devices show a stable pull-in voltage within a 100µV range (equipment resolution limit) over a temperature range of 40K (273K to 313K).

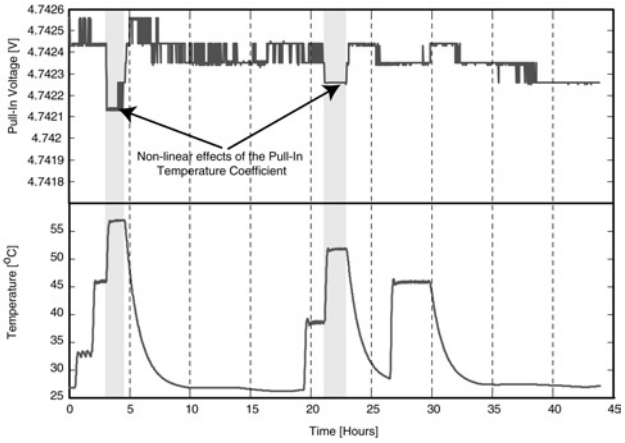

Fig. 4. Pull-in Voltage versus Temperature with compensation control.

References

[1] J. Kyynäräinen, A.S. Oja and H. Seppä, "Stability of micromechanical devices for electrical metrology", *IEEE Trans. Instrum. Meas.,* vol. 50, pp. 1499-1503, December 2001.

[2] L.A. Rocha, E. Cretu and R.F. Wollfenbuttel, "Stability of a micromechanical pull-in voltage reference", accepted for publication in *CPEM 2002 Special Issue of the IEEE Trans. Instrum. Meas.*

[3] http://www.vdivde-it.de/mst/imsto/Europractice/Bosch/default.html

[4] M. Offenberg, F. Lärmer, B. Elsner, H.Münzel and W.Riethmüller, "Novel process for an integrated accelerometer", *in Proc. Transducers95*, 1995, vol.1, pp. 589-593.

[5] Bosch, "Micromachining Foundry Design Rules", version 2.01, 2000.

A hydrocarbon sensor based on p-type strontium titanate-ferrate

K. Sahner, R. Moos

University of Bayreuth, Chair of Functional Materials, 95440 Bayreuth, Germany
email: Kathy.Sahner@Uni-Bayreuth.de http://www.lff.uni-bayreuth.de

Summary: *In this contribution, a resistive hydrocarbon sensor based on heavily iron doped strontium titanate, $Sr(Ti_{1-x},Fe_x)O_{3-\delta}$ is described. The sensor materials were screen-printed on aluminia substrates and exposed to different gas atmospheres. Experiments on temperature dependency and cross sensitivity of the sensor signal were conducted. It is shown that the sensitivity towards hydrocarbons is especially pronounced in the temperature range between 350 °C and 450 °C for samples with x=0.3..0.4.*

Keywords: *gas sensor, thick film, resistive oxygen sensor, titanates, strontium titanate-ferrate*
Category: *5 (Chemical sensors)*

1 Introduction

For many years, several research groups have focused on the semiconductor material $SrTiO_3$ as a material for resistive oxygen sensors [1-3]. Of late, heavily iron doped $SrTiO_3$ ($Sr(Ti_{1-x},Fe_x)O_{3-\delta}$ with $0 \le x \le 0.5$, STFx) was investigated [4]. Here, a major advantage is the temperature *in*dependency of this p-type ceramic conductor: in the temperature range between 700°C and 900°C, the sensor resistance of a specimen with a ferrate content x of about 35% does not vary with temperature but it depends strongly on the oxygen partial pressure. Defect chemical models were suggested to explain the relationship between the resistance of STF sensors and oxygen partial pressure [5].

However, material properties of STF at lower temperatures are less understood: in the temperature range below 450°C, the electrical resistance of STF films depends strongly on the concentration of reducing components in the ambient gas. Especially, this effect is highly sensitive to hydrocarbons. Inexpensive hydrocarbon sensors, which are very interesting for industrial and automotive applications, can be manufactured by screen-printing.

2 Experimental

2.1 Sample Preparation

The original STF powders with a particle size of approx. 1µm were synthesised by using a conventional mixed oxide route. A printable paste was prepared and screen-printed on aluminia substrates. A set of platinum electrodes underneath this porous ceramic layer served as electrical contacts. On the sensor backside, a platinum heater structure was screen-printed allowing to control the temperature of the STF thick film.

2.2 Measurement Methods

Sensor specimens were exposed to different gas atmospheres (10% O_2 in N_2). As representative hydrocarbon species, propane was added in different concentrations. The sensor resistance was measured using the four-wire technique.

3 Results and discussion

Fig. 1 shows a typical sensor response curve of a sensitivity measurement at two different sensor temperatures. As can be seen, the sensor signal is stable with a jump of about 1.5 % per 100 ppm propane and does not show saturation effects even at high hydrocarbon concentrations.

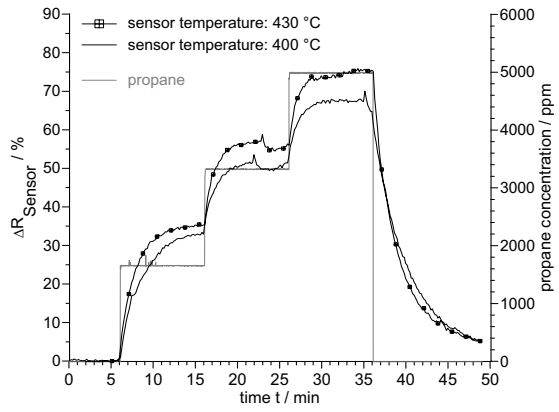

Fig. 1. Sensor response of a thick film STF sensor (x=0.4, R_0(400°C, 10% O_2) = 2.6 kΩ) to different propane concentrations.

A major drawback is the pronounced temperature dependency of the sensor signal, which suggests the underlying mechanism being a thermally activated adsorption process. For practical use, one has to solve these problems, e.g. by simultaneously measuring the actual sensor temperature in order to correct the resistance signal.

In Table 1, the different STFx-compositions are compared qualitatively. The sensor resistance R_0 at 400°C and 10% O_2 depends strongly on the iron content. Whereas undoped strontium titanate and STF10 have a high resistance and show only poor sensor properties, material compositions with x ≥ 0.2 have more promising sensor characteristics.

Table 1. Comparison of STF sensors at 400°C

material	resistance R_0 / kΩ
undoped ST	> 1000
STF10	500
STF20	100
STF30	50
STF40	10
STF50	5

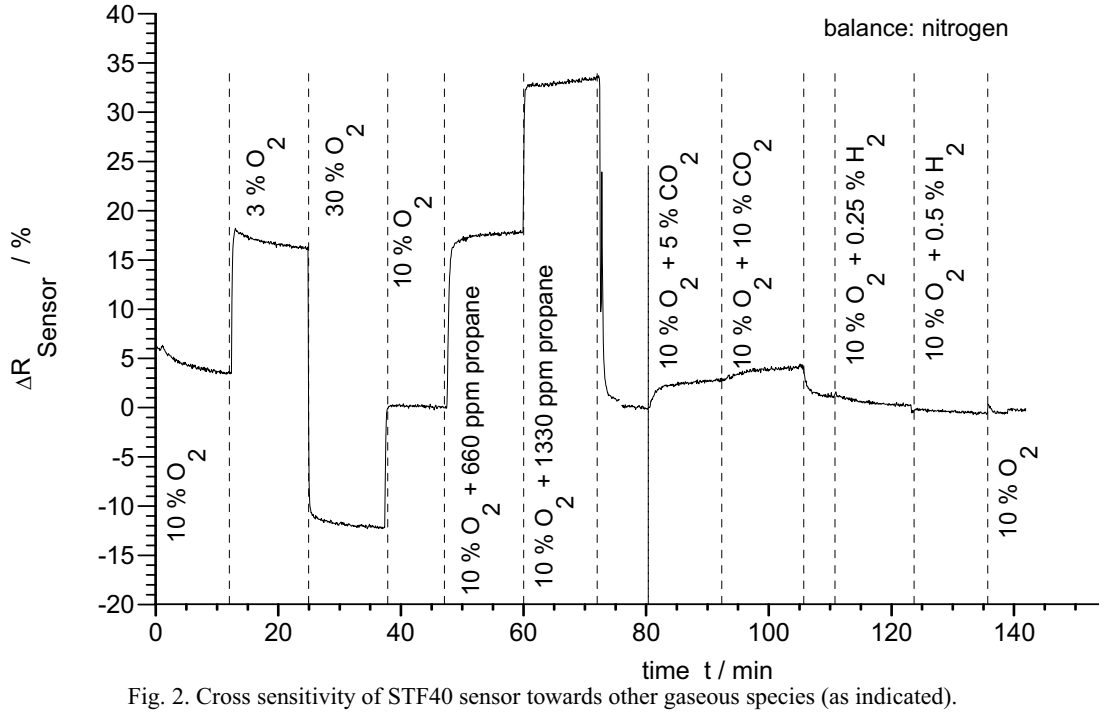

Fig. 2. Cross sensitivity of STF40 sensor towards other gaseous species (as indicated).

Cross sensitivity of the sensitive ceramic layer towards other gaseous species has been another research aspect. The influence of other exhaust components such as oxygen, hydrogen, and carbon dioxide, on the sensor resistance was investigated by exposing the sensor to different synthetic gas compositions. Fig. 2 shows an exemplary curve of a cross sensitivity measurement. Some gases such as oxygen have a notable impact on the sensor resistance whereas others, e.g. hydrogen, apparently do not have any influence. A possible explanation might be given by an adsorption model. Besides the very promising results, it should be mentioned that up to now, two main problems exist. There is a drift of the sensor resistance with time, and the quantitative reproducibility of the measurement deserves further investigation.

Future work is going to evaluate the sensor system quantitatively. Furthermore, aging processes of the material as well as the underlying sensor mechanism are going to be further investigated. It is anticipated that the sensor properties are mainly governed by grain boundary processes. Therefore, microstructural studies as well as impedance spectroscopical studies will be conducted.

References

[1] U. Schönauer, Response times of resistive thick film oxygen sensors, *Sensors and Actuators B* 4 (1991), 431-436.

[2] J. Gerblinger, H. Meixner, Electrical conductivity of sputtered films of strontium titanate, *J. Appl. Phys.* 67 (1990) 7453-7459

[3] H. Zhengh, O. T. Sørensen, Influence of CO_2 in dry and wet atmospheres on the response of Mg-doped $SrTiO_3$ ceramic oxygen sensors, *J. Eur. Ceram. Soc.* 19 (1999) 1987-1996.

[4] R. Moos et al., Materials for temperature independent resistive oxygen sensors for combustion exhaust gas control, *Sensors and Actuators B* 67 (2000) 178-183.

[5] W. Menesklou et al., High temperature oxygen sensors based on doped $SrTiO_3$, *Sensors and Actuators B* 59 (1999) 184-189.

A Novel Miniaturized Oxygen Sensor with a Solid-State Ceria-Zirconia Reference

N. Rajabbeigi[1], B. Elyassi[1], A. Khodadadi[1] and S.S. Mohajerzadeh[2]

[1]University of Tehran, Faculty of Eng., Dept. of Chem. Eng., Catalysis and Reaction Engineering Lab., Iran
email: khodadad@ut.ac.ir
[2]University of Tehran, Faculty of Eng., Dept. of Electrical Eng., Thin-film Lab., Iran

Summary: *A self-contained, miniature, electrochemical-type oxygen sensor is described which uses an oxygen ion conducting solid electrolyte (YSZ). Unlike conventional oxygen sensors, in which one side of the sensor needs to be directly exposed to the air reference, the oxygen sensor presented in this paper exploits a solid solution of 25% zirconia in ceria as the reference. This novel oxygen sensor exhibits an anomalous behavior in transition from rich-to-lean regimes where the polarity of the created voltage changes from a positive value of +300mV to a negative value of –80 mV at λ =1.04.*

Keywords: *oxygen sensor, solid-state reference, ceria-zirconia*
Category: *5 (Chemical sensors)*

1 Introduction

We report, for the first time, a novel oxygen sensor based on yttria stabilized zirconia (YSZ), in which air reference is replaced by a solid solution layer. Unlike conventional oxygen sensors, in which one side of the sensor needs to be directly exposed to the air reference, this new type oxygen sensor exploits a solid solution of 25% zirconia in ceria as the reference. This solid solution has thermal expansion coefficient near that of YSZ, high oxygen storage capacity (OSC), and high thermal stability in exhaust gas environment [1]. This oxygen sensor exhibits an anomalous behavior in transition from rich-to-lean regimes where the polarity of the created voltage changes from a positive value to a negative one. This sensor can be miniaturized, yielding a low cost sensor with a fast response, especially during cold start. Schematic diagram of the oxygen sensor with solid-reference is shown in Fig. 1.

2 Experimental

YSZ and ceria-zirconia powders, used in fabrication of the oxygen sensor, were prepared from their corresponding nitrates solutions, followed by drying and calcination. X-ray diffraction analyses of ceria-zirconia powder calcined at 500°C for 3hrs and YSZ powder sintered at 1100°C for 12hrs reveal the formation of crystalline oxide solutions, Figs. 2-3.

For sensor fabrication, fine calcined YSZ powder was pressed into a 2mm-thick pellet with 14mm diameter. A platinum layer was sandwiched between the solid-reference and YSZ pellet to make the inner contact. After sintering at 1100°C for 12hrs, second platinum layer (Herause OS3) was screen-printed on YSZ side of the prepared pellet and sintered at 920°C for 10mins [2]. Fig. 4 shows SEM views of surface and cross-section of the fabricated sensor.

The response of the sensor was investigated in presence of a simulated exhaust gas of (6.0%CO and 0.2%C_2H_6 in He) at different temperatures of 300, 325, 350, 400 and 450°C. The mixture was prepared by admixing a flow of simulated gas with air. The ratio of flow rates of the simulated gas and air was varied to prepare rich and lean regimes. λ is the ratio of the actual air-to-fuel ratio to that of stoichiometric ratio.

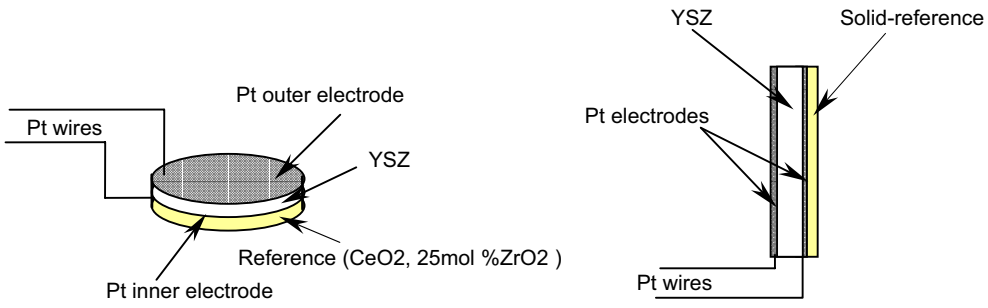

Fig. 1: Oxygen sensor prototype with the solid-state reference on one side

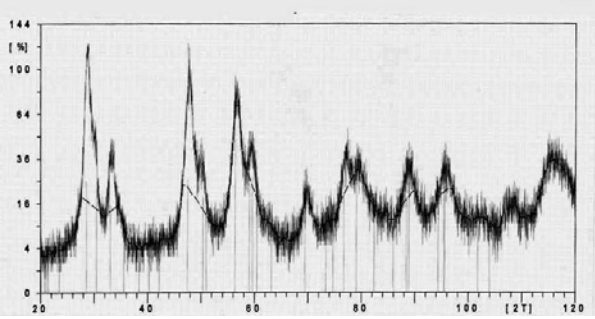

Fig. 2: XRD of YSZ powders sintered at 1100°C for 12hrs.

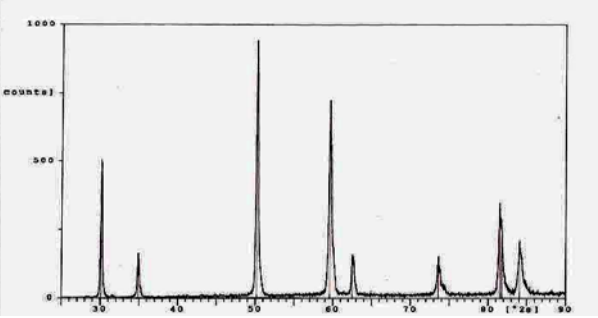

Fig. 3: XRD of solid-reference (CeO_2 75%, ZrO_2 25%) sintered at 1100°C for 12hrs.

3 Results and discussion

As displayed in Fig. 5, the sensor shows a sharp transition from +300mV to -80mV at λ=0.92 when exposed to the simulated exhaust gas, while for commercial oxygen sensors this transition occurs between 1000-100mV. We believe this phenomenon occurs because the content of exchangeable oxygen in solid-reference is less than that of exhaust gas in lean region and more than that in rich case. The occurrence of the voltage transition at λ<1 could be attributed to different diffusion coefficients of C_2H_6 and oxygen and also different adsorption rate constants of C_2H_6 and CO [3]. Sintering at higher temperatures could enhance sensor's performance [4]. As shown in Fig. 6 by using a mixture of 8.4%CO in He mixed with air, the transition occurs at λ =1.04. The sensor exhibits hysteresis at low temperatures of 300 and 325°C, Fig. 7, as observed in regular YSZ sensors [3].

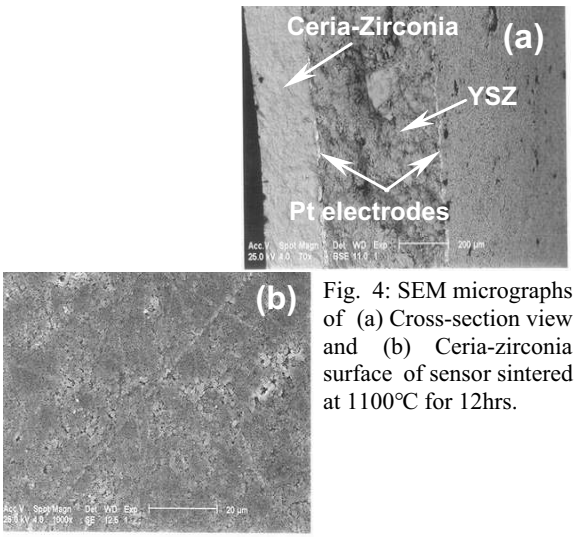

Fig. 4: SEM micrographs of (a) Cross-section view and (b) Ceria-zirconia surface of sensor sintered at 1100°C for 12hrs.

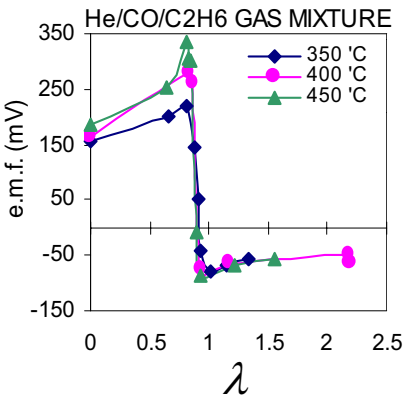

Fig. 5: Response of sensor in (He 93.8%, CO 6.0%, C_2H_6 0.2%) gas mixture at 350, 400 and 450°C.

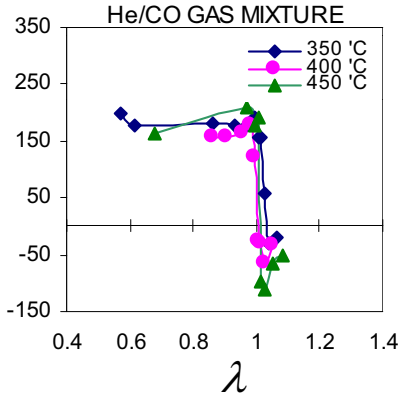

Fig. 6: Response of sensor in (He 91.6%, CO 8.4%) gas mixture at 350, 400 and 450°C.

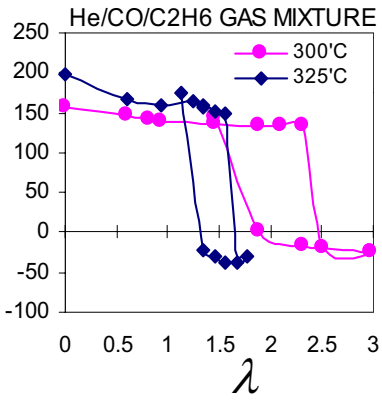

Fig. 7: Hystersis in sensor's response in (He 93.8%, CO 6.0%, C_2H_6 0.2%) gas mixture at 300 and 325°C.

4 Conclusion

In conclusion, we have successfully fabricated a novel solid-state reference oxygen sensor whose response to simulated exhaust gas shows an anomalous transition from positive to negative voltages. Preparation of miniaturized sensors on silicon-based membranes using thin film technology is underway.

References

[1] C.E. Hori, H. Permana, K.Y. Simon Ng, *Applied Catalysis B: Environmental*, **16** (1998) 105-117.
[2] Z. Peng, M. Liu, E. Balko, *Sensors and Actuators B*, **72** (2001) 35-40.
[3] A.D. Brailsford, E.M. Logothetis, *Sensors and Actuators B*, **52** (1998) 195-203.
[4] S.C. Singhal, *Solid State Ionics*, **135** (2000) 305-313.

Development of pH-ISFET sensors for the detection of bacteria

M.L. POURCIEL-GOUZY, W. SANT, I. HUMENYUK, L.MALAQUIN, X. DOLLAT, P. TEMPLE-BOYER

LAAS-CNRS, 7 avenue du colonel Roche, 31077 TOULOUSE Cedex 4, France
temple@laas.fr http://www.laas.fr

Summary: *Ion sensitive field effect transistor (ISFET) microsensors including a SiO_2/Si_3N_4 pH-sensitive gate structure and a titanium/gold pseudo-electrode have been used for the detection of the Lactobacillus Acidophilus bacteria. First results have shown that such applications require high bacterial concentrations and therefore small analysis volumes. Therefore, the pH-ISFET have been adapted by fabricating micro tanks from plexiglass or polydimethyl siloxane (PDMS). Thus, the bacteria detection has been possible in several minutes by monitoring the pH variations. These works will allow the development of ChemFET microsensors for biological applications and more precisely for medical analysis.*

Keywords: *ChemFET, pH, biological detection*
Category: *5 (Chemical sensors)*

1- Introduction

Many medical analysis are performed through the monitoring of pH variations during various biochemical reactions. However, the developed technique is very time-consuming. For example, in the case of bacteria, they must be grown on a specific medium. Once quantity is important enough, they are isolated, purified and put in touch with a medium containing a specific element. Metabolisation of this element by the bacteria will generate either their growth, either a pH variation, due to an oxidation or a fermentation, generally manifested by colour variation of indicator present in the medium for detection. In order to improve this detection technique, chemical microsensors must be adapted according to the medical analysis specifications.

This work deals with the use of pH-ISFET sensors for the detection of bacteria and more precisely for the monitoring of the glucose assimilation by *Lactobacillus Acidophilus*. In this case, pH variation is induced by production of lactic acid by the bacteria in contact with glucose.

2- Experiments

Ion-sensitive field effect transistor (ISFET) microsensors including a SiO_2/Si_3N_4 pH-sensitive gate structure and a gold pseudo-electrode have been fabricated using a standard P-well silicon technology [1]. They have been used for the detection of bacteria. First attempts were made in aqueous solution of glucose (20 $g.L^{-1}$). The minimum reaction volume needed due to the size of the sensor was about 2 mL. Thus, the necessary amount of bacteria was much important to see the hoped pH fall.

With this assessment, we then thought to reduce the reaction volume to increase bacterial concentration. Thus, the pH-ISFETs have been adapted to the detection of bacteria by reducing the analysis volume to a minimum size around one microliter. Thus, microtanks were made up with a straight through pierced plexiglass cube and were stuck with a silicon paste on the pH-ISFET sensors so that the hole comes exactly above the sensitive gate (figure 1).

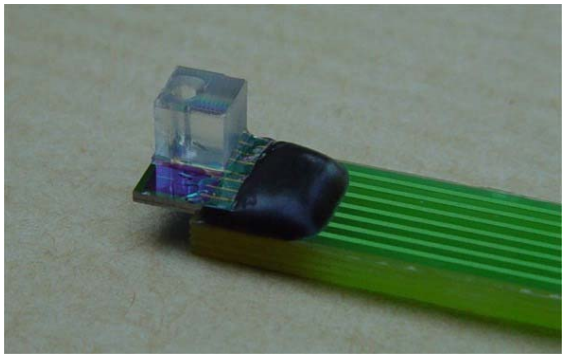

Fig. 1. Plexiglass micro-tank reported on ISFET chip

The gate-source voltage V_{GS} being applied to the solution either by the titanium/gold pseudo-electrode, pH-ISFET sensors were characterised by I-V measurements, the V_{GS} voltage variations being monitoring for a constant drain-source current I_{DS}.

PH measurements were studied using three standard buffer solutions (pH = 4.01, 7.00 and 10.01). Detection of *Lactobacillus Acidophilus* by monitoring the variation of pH in a glucose solution (20 $g.L^{-1}$).

3- Results

The first pH measurements evidence a a linear relation between the solution pH and the ISFET gate voltage V_G (figure 2). The sensitivity is around 43 mV/pH. It's far enough of the theoretical Nernst law value (59 mV/pH). This decrease should be related to the use of the titanium/gold pseudo-electrode [1].

The second step was to proceed to attempt with bacteria. The micro volume was filled with the glucose solution, and after a few minutes, bacteria were added directly from the petri box where they were grown.

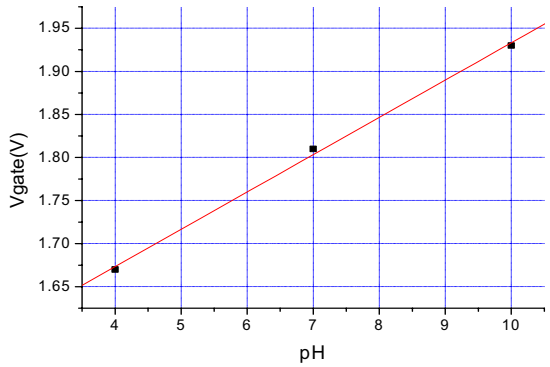

Fig. 2. Gate voltage as a function of pH for plexiglass tank.

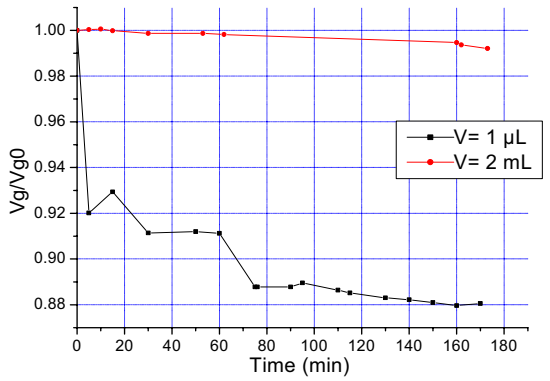

Fig. 3. Gate voltage vs time during metabolisation of glucose by *Lactobacillus.*

Typically, we had the kind of response presented on figure 3. The first drastic pH fall is the consequence of the bacteria insertion in the micro-tank. Indeed, bacteria growth medium is radically acid so the pH variation when micro-organisms are added in the relatively neutral glucose solution (pH=7.5). Then, a plateau is evidenced which should be interpreted as a latency period. Finally, the continuous pH decrease can traduce the production of lactic acid due to the presence of glucose in the solution. It is also important to compare these variations with those obtained in a 2 mL volume. In this case, pH decreases slowly and it takes finally several hours before that the detection of the *Lactobacillus* bacteria could be evidenced (figure 3).

4- Perspectives

Theses results have encouraged us to think to a more adjustable device and, above all a device compatible with micro electronic collective fabrication techniques. Therefore, we chose to fabricate micro-tank with polydimethyl siloxane (PDMS) (figure 4). PDMS naturally sticks on the silicon chip. Once the moulded PDMS tank is positioned, it's definitively fixed with non reticulated PDMS and we let the device dry for several hours.

Next attempts should allow to compare the microanalysis methods and to give us more information about the sensor behaviour and pH variations in presence of bacteria. This will be obtained through the detection of the *Lactobacillus* bacteria behaviour versus different sugars (fructose, lactose,...).

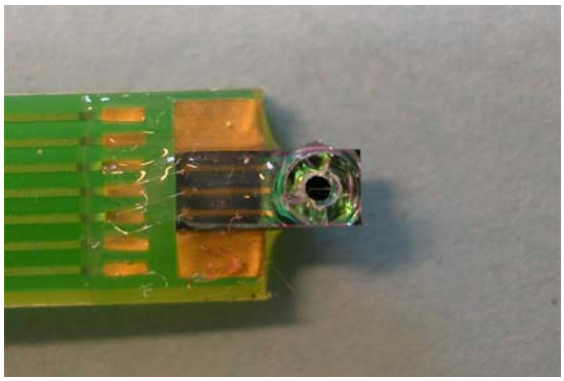

Fig. 4. Detail of the PDMS reported micro-tank

5- Conclusion

pH-ISFET sensors have been successfully adapted to the detection of bacteria by developing micro-tanks thanks to different fabrication techniques. These works will be continued by improving the micro tanks fabrication and by developing the pH-ISFET sensors for the detection of different bacteria.

References

[1] W. Sant, M.L. Pourciel, J. Launay, T. Do Conto, A. Martinez, P. Temple-Boyer: "Development of chemical field effect transistors for medical analysis", Proceedings of the 16th European Conference on Solid-State Transducers, EUROSENSORS XVI, September 15-18 2002, Prague, CZECH REPUBLIC, p.619-620

Amorphous Silicon as Semiconductor Material for High Resolution LAPS

Werner Moritz[1] , Tatsuo Yoshinobu[2], Friedhelm Finger[3], Steffi Krause[4], Michael J. Schöning[5]

[1]*Humboldt University Berlin, Brook-Taylor-Str. 2, 12489 Berlin, Germany, werner.moritz@rz.hu-berlin.de*
[2]*Institute of Scientific and Industrial Research, Osaka University, Osaka 567-0047, Japan*
[3]*Institute of Photovoltaics, Research Centre Jülich, 52425 Jülich, Germany*
[4]*Department of Chemistry, University of Sheffield, Sheffield S3 7HF, UK*
[5]*University of Applied Sciences Aachen, Div. Jülich, and Institute of Thin Films and Interfaces, Research Centre Jülich, 52425 Jülich, Germany*

Summary: *The lateral resolution of photocurrent techniques such as Light-addressable Potentiometric Sensors (LAPS) or Scanning Photo-induced Impedance Microscopy (SPIM) is limited by the properties of the semiconductor material used. For bulk silicon, the best results reported in the literature are in the range of 20 µm. Different semiconductor/insulator-structures were studied to improve the lateral resolution. The best results were obtained using thin layers of amorphous silicon. The resolution was better than 1 µm and was only limited by optical constraints. Structures of 400 nm dimensions were visualized by photocurrent measurements.*

Keywords: *LAPS, photocurrent, semiconductor, amorphous Si*
Category: *5 (Chemical sensors)*

1 Introduction

Since the introduction of the Light-addressable Potentiometric Sensor (LAPS) [1] in 1988 and Scanning Photo-induced Impedance Microscopy (SPIM) [2], several groups have been interested in improving the lateral resolution of these techniques [3-7]. A theoretical description of the photocurrent distribution in the semiconductor was given in [7]. It was shown that the lateral diffusion of the charge carriers out of the illuminated area of the semiconductor is the limiting factor for further improvement. The diffusion length is determined by the carrier concentration, the mobility and the recombination rate. In [6] the influence of the charge carrier concentration for bulk silicon was shown experimentally. The presence of charges in the insulator or at the interfaces can cause photocurrents several hundreds of micrometers away from the gate metallization [8]. The best values of lateral resolution reported for bulk silicon have been about 20 µm.

In this paper we report on the lateral resolution of photocurrent using amorphous silicon as the basis semiconductor material. A thin double-layer insulator was deposited on top of this amorphous silicon to achieve the required field-effect structure.

2 Experimental

Thin amorphous silicon (a-Si) films were prepared on corning 1737 glass substrates. First Al (500 nm)/ZnO (700 nm) was deposited as the ohmic contact. Afterwards, a-Si and SiO_2 (30 nm) and Si_3N_4 (50 nm) insulator layers were deposited by PECVD (plasma-enhanced chemical vapour deposition). The thickness of the a-Si was varied in the range of 0.3 to 1.5 µm. For the gate contact, a structure with different metal thickness, as shown in Fig. 1, was prepared to allow determination of the decay of the signal at a metal edge.

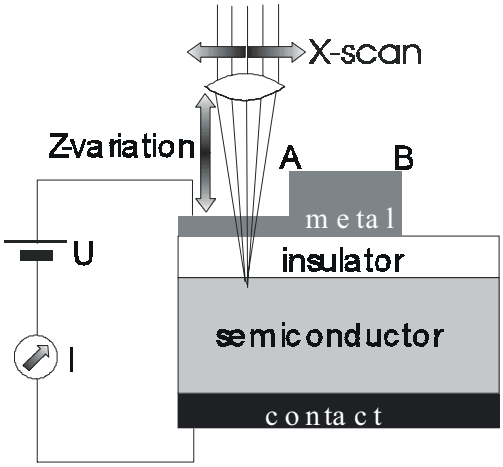

Fig. 1 Scheme of the semiconductor structure and the light scan

Scanning the laser light passing position A permits to adjust the focus by z-variation. During a scan from position B to areas without gate metallization the photocurrent decays to zero providing information about lateral resolution.

A diode laser with λ=640 nm and the optics of a DVD drive were used in combination with an xy-positioning system with a resolution of better than 50 nm.

3 Results and discussion

The Metal/Insulator/Semiconductor (MIS) structures described above showed good insulator quality and only samples with DC current smaller than 10 pA at ±2 V were investigated in more detail. A typical photocurrent/voltage curve is given in Fig. 2 demonstrating a sufficiently low concentration of charges in the insulator and at the interfaces as required for LAPS applications. The photocurrent increased with the thickness of the amorphous silicon layer.

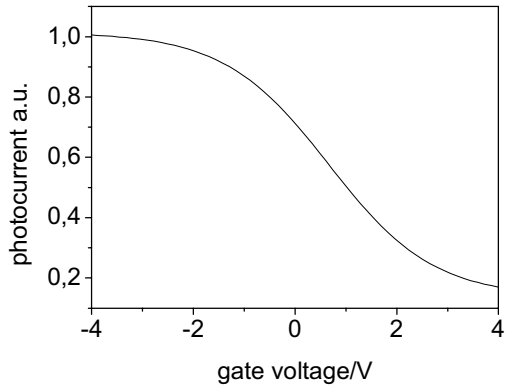

Fig. 2 Photocurrent/voltage curve of the MIS-structure

In Fig. 3, a 600 µm x 600 µm photocurrent scan is shown. The outer part had a gate metallization of 150 nm Au, and an area of 400 µm x 400 µm is free of metal. In contrast to other semiconductors investigated, no increase of the photocurrent at the metal edge was observed but the signal is immediately decreased. Furthermore, the resolution was much better than for other materials. A line scan is shown in Fig. 4. It can be seen that the decay of the signal occurs in a range smaller than 1 µm. For measurements with such a high resolution close to the wavelength of the light, the intensity distribution of the laser beam has to be considered. This means that the curve in Fig. 4 could be due to the laser spot profile, i.e. the resolution determined by the semiconductor properties could be even better. This is

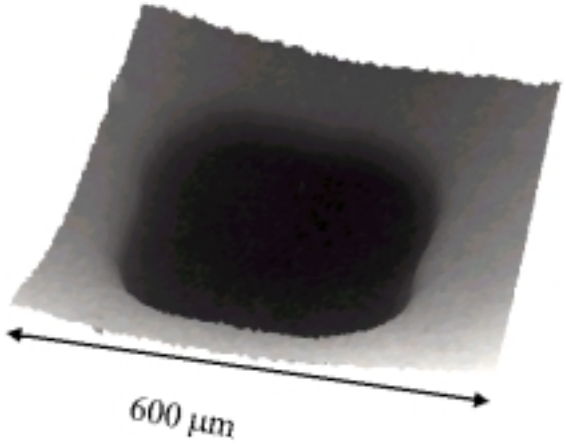

Fig. 3 600 µm x 600 µm scan around a hole of 400 µm x 400 µm etched into 150 nm Au gate

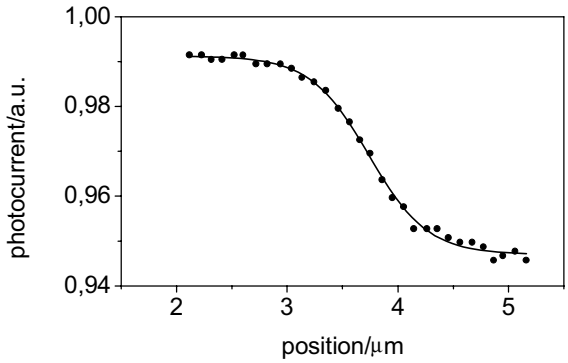

Fig. 4 Scan from metallized to non-metallized area

in accordance with the diffusion length in amorphous silicon, which is in the nm range.

Some influence of the ohmic contact geometry was observed and will be discussed.

The resolution was found to be independent of the thickness of the a-Si. As optical parameters are limiting our measurement, this was to be expected.

In conclusion, amorphous silicon can be used as a material for LAPS measurements with very high lateral resolution. Further improvements can be achieved by an optimised optical setup.

References

[1]Hafeman, D.G., Wallace, P., McConnell, H.M., Science 240 (1988) 1182
[2]Krause, S., Talabani, H., Xu, M., Moritz, W., Griffiths, J., Electrochimica Acta 47 (2002) 2143
[3]Nakao, M., Yoshinobu, T., Iwasaki, H., Jap. Journal. Appl. Physics, 33 (1994) L 394
[4]Ito, Y., Sensors and Actuators B, 52 (1998) 107
[5]Nakao, M., Inoue, S., Yoshinobu, T., Iwasaki, H., Sensors and Actuators B, 34 (1996) 234
[6]George, M., Parak, W.J., Gaub, H.E., Gerhardt, I., Moritz, W., Kaesen, F., Geiger, H., Eisele, I., Sensors and Actuators A, 86 (2000) 187
[7]Parak, W., Hofmann, U.G., Gaub, H.E., Owicki, J.C., Sensors and Actuators A,63 (1997) 47
[8]Filippni, D., Lundström, I., J. Appl. Phys., 91 (2002) 3896

Tuning of the resonant frequency by means of phase adjustment in SAW oscillators for gas detection

J. Fontecha[1], M.J. Fernández[1], I. Sayago[1], J.P. Santos[1], J. Gutiérrez[1], M.C. Horrillo[1], I. Gràcia[2], C. Cané[2], E. Figueras[2]

[1]Instituto de Física Aplicada (CSIC), Serrano 144, 28006 Madrid, Spain
email: carmenhorrillo@ifa.cetef.csic.es http://www.ifa.csic.es/
[2]Centro Nacional de Microelectrónica, (CSIC), Campus UAB, 08193 Bellaterra, Barcelona, Spain

Summary: *The purpose of this paper is to present a method for tuning the resonant frequency of a typical Delay Line SAW oscillator by means of a method simple and widely used in microwave circuits. It consists of a quadrature hybrid coupler in whose coupled arms are placed two identical terminations: a capacitor C and an inductor L in series. The output signal has the same amplitude than the input one and its phase is changed depending on the value of C and L. The oscillator designed in this way exhibits stable frequency response and operates with a wide range of coatings in measurements with volatile organic compounds.*

Keywords: *Oscillator, SAW sensor, polymer*
Category: *5 (Chemical sensors)*

1 Introduction

Surface Acoustic Wave (SAW) devices are well known to offer high surface-mass detection sensitivity for chemical sensing, [1]. Apart of the compact structures, the advantages of these devices are their small size, low cost, high sensitivity and fast responses. SAW devices are very sensitive to mass changes on their surfaces, then if a coating film is placed over the SAW propagation path it acts concentrating vapor molecules from the ambient gas at the device surface. The total mass of the film is increased due to the gas sorption and diffusion taking place a change in the propagation velocity of the acoustic wave. The velocity changes are performed indirectly with extremely good precision using the device as the resonating element in a delay line oscillator circuit, (figure 1).

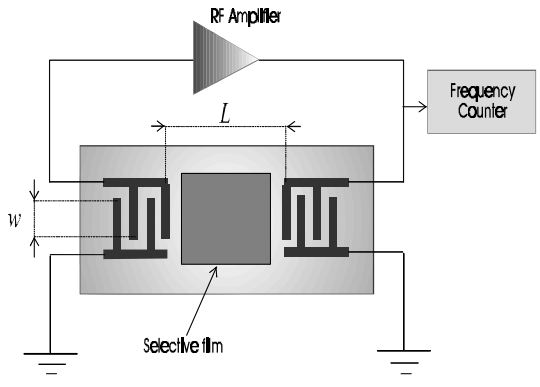

Figure 1.- Gas sensor SAW oscillator system

Oscillations occurs only when the amplifier gain is greater than the losses of the delay line. Then the oscillator for SAW sensor applications must be designed in the way that it must operate with a wide variety of SAW characteristics, [2]. Even though for a given design the device frequency will be approximately the same, the loss through the device will vary quite dramatically depending of the coating film chosen and the thickness deposited.

As it is well known, the polymer films are the best chemical interface to detect organic vapors because of their high sensitivity, fast vapor diffusion, reversible responses and good ability to work at room temperature. The polymer coating must be chosen to interact with an analyte as selectively as possible, then, both the choice of chemical film and the sensor design greatly influence in the frequency signal response, [3].

2 Experimental

The oscillator designed must have a large gain margin at the desired oscillation frequency in order to compensate any loss that occur in the feedback loop. The SAW sensor used in this work has been fabricated on ST-X quartz substrate at a frequency of 157 MHz. It has 100 finger pairs with a finger width and spacing of 5 μm and both the length L and aperture W (figure 1) are of 2 mm, being the dimensions 9 mm × 4 mm × 0.5 mm. The lowest insertion losses of the device are about 14 dB. Taking into account that the polymer film deposited will add 10 dB or more depending of the thickness and that the

sorbed gas molecules will also contribute to the total losses, taking a margin of 6 dB as recommended in the literature [2], the amplifier gain requirements will be at least 30 dB.

We use the feedback/loop method to design the amplifier circuit. We do not use simulation of the components but we measure the S parameters of the total open loop. The amplifier has two cascaded RFIC amplifiers and three attenuators in T configuration placed at the input, separating the two amplifiers and at the output. The value of the attenuators is fixed from the IC amplifier gain, the SAW device losses and the ones of the other components of the circuit: the directional coupler and the phase matching circuit. The S_{12} parameter in most of SAW delay lines fulfills the phase 0º condition for more than one frequency in the range where the whole loop amplitude gain is bigger than 1. So the oscillator can hop between several frequencies. In order to avoid this drawback we have implemented a phase adjust component consisting of a 90º hybrid coupler in whose two coupled arms are placed a capacitor and an inductor in series finished in an open circuit, (figure 2). With this

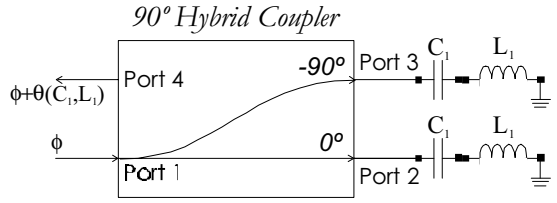

Figure 2.- Circuit for frequency adjustment of the delay line SAW oscillator.

arrangement the phase can be adjusted from –180º to 180º. Several phase shift at 157 MHz due to these components are shown in the Table 1.

Table 1. Values of the phase shift corresponding to several values of L_1 and C_1 for the circuit of figure 2

Inductance	*Capacity*	*Phase Shift*
33 nH	12 pF	87.8º
15 nH	68 pF	179.7º
22 nH	47 pF	-179.7º
56 nH	180 pF	-90.4º

Therefore the oscillation frequency can be adjusted to the required value, e.g. to the maximum of the amplitude of S_{12} of the whole open loop, very near the synchronous frequency of the SAW device, f_0. Although the amplifiers are working in a non linear point of their gain curves, the S_{12} phase variation is not so important as the amplitude variation, then the final phase is very close to 0º and hence the oscillation frequency is very near f_0.

To test the performance of our oscillator designs we chose as coating materials two well known polymers for SAW sensor applications: Polyepichlorohydrin (PECH) and Polyeteruretano (PEUT) and different concentrations of volatile organic compounds were measured. The films were sprayed with different thicknesses on the whole device surface, including IDTs, using an airbrush and controlling thickness and losses by means of a HP 8510B vector network analyzer. A typical sensor response of a PECH coated device to low concentrations of toluene in synthetic air is shown in figure 3. In this case the film introduced losses of 3 dB and a shift of the resonance frequency of 400 kHz equivalent to a thickness about

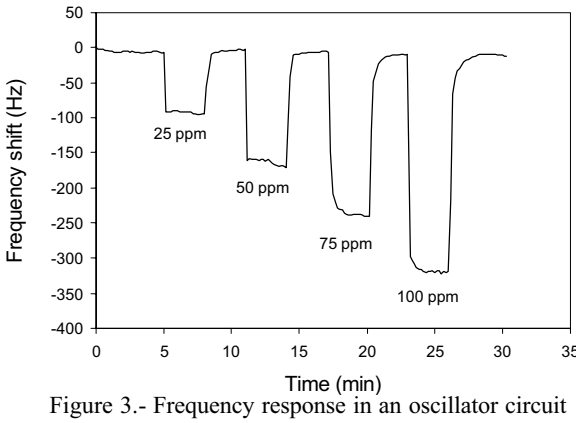

Figure 3.- Frequency response in an oscillator circuit of a SAW sensor coated with a film of PECH (90 nm) to toluene.

90 nm. Concentrations of the test gas vary from 25 to 100 ppm in steps of 25 ppm. The total gas flow rate was 200 ml/min. After each exposure, the device was purged with pure synthetic air to allow the sensor to return to the initial conditions. Each sorption and desorption cycle lasted 3 minutes.

The frequency measurement from the oscillator circuit shown in figure 3 exhibits excellent properties with respect to linearity and reversibility, negligible baseline drift, fast response, reversibility and good sensitivity.

References

[1] D.S. Ballantine, et al. Acoustic wave sensors: Theory, design and physico-chemical applications. *Academic Press,* (1997).

[2] R.F. Schmitt, J.W. Allen, R. Wright. Rapid design of SAW oscillator electronics for sensor applications. *Sensors and Actuators B* 76 (2001), 80-85.

[3] M.J. Fernández, J. Fontecha, M.C. Horrillo, I. Sayago, L. Otero, M. García, R. Gómez-Espinosa, J. Gutiérrez, C. Cané, I. Gràcia. Different designs of SAW sensors to detect organic vapors. *Proc. of the Eighth Int. Symp. on Olfaction and the Electronic Nose*, pp. 134-138, Washington, 2001.

Ceramic hot-plates for gas sensors

F. Rettig[1], R. Moos[1]

[1]University of Bayreuth, Chair of Functional Materials, Universitätsstr. 30, 95440 Bayreuth
email: Frank.Rettig@Uni-Bayreuth.de http://www.lff.uni-bayreuth.de

Summary: *A new type of gas sensor is presented that combines the advantages of micro machined silicon gas sensors and ceramic gas sensors. LTCC-technology which, is the cutting edge for manufacturing printed circuit boards for high frequency applications, is used to produce gas sensors. The sensor devices are shaped like already known hot-plate low-power micro machined silicon gas sensors. The low thermal conductivity (3W/mK) leads to a low power consumption (1W at 400°C) compared to classical ceramic gas sensors. The inexpensive manufacturing technology is a remarkable advantage for small series compared to the expensive silicon technology. This contribution presents first results for LTCC hot-plate gas sensors that include production, measurements, and simulation of such devices. Important thermal properties like power consumption and temperature distribution are measured and compared to FEM-simulations. The results of the simulations are used to improve the temperature distribution on the hot-plate.*

Keywords: *hot-plate, LTCC, low temperature cofired ceramics, gas sensor, FEM, SnO_2*
Category: *5 (Chemical Sensors)*

1 Introduction

Chemical gas sensors can be categorized by production technology into ceramic gas sensors and micro machined silicon gas sensors. Each of them has its own advantages. Ceramic gas sensors are high temperature stable and the manufacturing technology is inexpensive. On the other hand the low power consumption and the possibility of integration are the main advantages of micro machined silicon gas sensors [1]. Silicon gas sensors can be produced cheaply only in very large series. However, there is a need for a gas sensor system that shows high flexibility, low cost production technology, possibility of integration, low power consumption and high temperature stability. LTCC materials (low temperature cofired ceramics) meet these requirements. The materials show low thermal conductivity of about 3 W/mK and the manufacturing technology is inexpensive and flexible. The sensors are integrable into printed circuit boards. Nevertheless, only few authors use LTCC for gas sensors [2].

Here, a gas sensor is presented, which is integrable. The active area (hot-plate) can be heated to several hundreds °C. It is suspended by four beams. For micro machined silicon gas sensors hot-plates are state of the art due to their low power consumption.

2 Experimental

2.1 Sensor manufacturing

First, the metallisation (e.g. heaters) is applied onto the tapes by screen-printing. After punching the tapes are laminated uniaxially with a pressure of about 250bars. Then the laminate is cofired at about 850°C. Fig. 1 shows the typical design of a sensor.

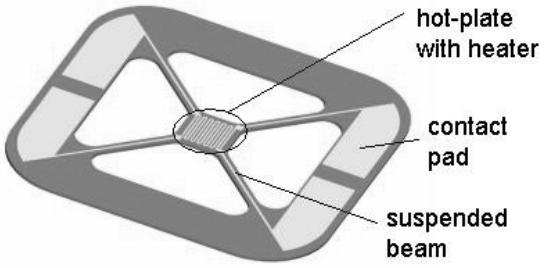

Fig. 1: Typical design of an LTCC-sensor

2.2 Sensor measurements

At first the power consumption of the gas sensors was determined. The temperature of the hot-plate was measured by an infrared pyrometer. The power consumption was calculated by the voltage and the current needed to heat the hot-plate to its operating temperature. Fig. 2 depicts the power consumption of sensors with different hot-plate sizes. One would have expected that the power consumption increased proportionally to the surface area. Since the heat convection coefficient at the vertical areas is much higher than on the horizontal areas, the power consumption does not increase proportionally to hot-plate surface.

The temperature distribution was measured by an infrared camera. Fig. 3 shows the temperature distribution picture of an initial device with a meander shaped heater (Fig. 1).

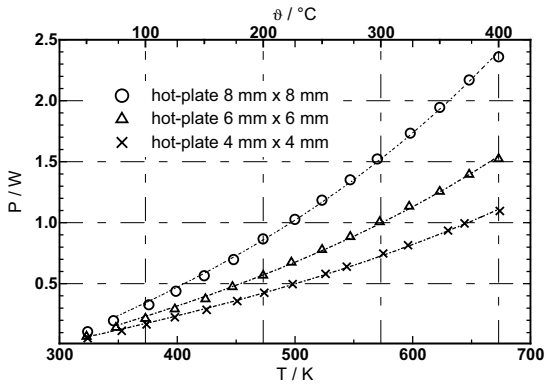

Fig. 2: Measured power consumption of sensors devices with different hot-plate sizes

It can be seen that in this case the temperature on the hot-plate varies very strongly in all directions.

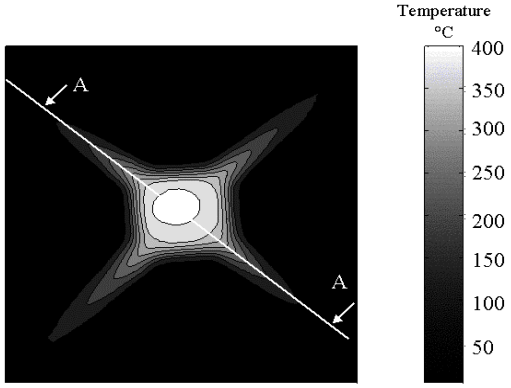

Fig. 3: Temperature distribution of a typical Sensor

However, a uniform temperature distribution on the hot-plate is desirable for a good gas sensor [3].

3 Simulation

FEM calculations were used to optimize the thermal properties of the sensors. The aim is to vary the geometry of the heater until the temperature distribution on the hot plate is uniform. First of all, the measured temperature distribution of the initial sensor devices was recalculated using a commercially available FEM program (ALGOR).

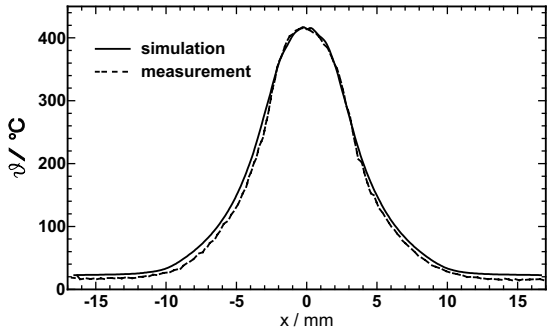

Fig. 4: Comparison of simulated and measured temperature profile (section AA in Fig. 3)

Fig. 4 compares the measured temperature profile (section AA in Fig. 3) with the simulated one of the same section. The simulated profile agrees very well with the measured profile.

In the next step, the geometry of the heater was varied to improve the temperature distribution of the hot-plate. Due to the uniform heat generation on the hot-plate the meander shaped heater shows a poor performance. In order to homogenize the temperature distribution the losses due to heat conduction in the beams should be compensated by increased heat generation. Therefore a double spiral heater performs better with respect to temperature distribution.

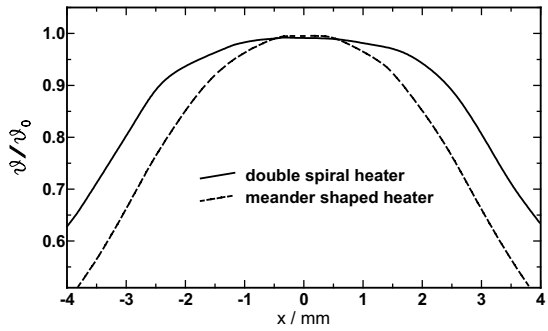

Fig. 5 Calculated temperature distribution of meander shaped heaters and double spiral heaters (section AA in Fig. 3)

Fig. 5 shows the improvement of the temperature distribution from the meander shaped heater to a double spiral heater.

4 Conclusion and Outlook

First LTCC gas sensors have been produced. The sensors show reduced power consumption compared to typical ceramic gas sensors [4]. It is possible to simulate the temperature distribution of such a sensor. First improvements in temperature distribution have been introduced.
As an outlook gas sensitive layers will be applied onto the sensors and first sensitivity measurements will be conducted.

References

[1] I. Simon et. al.: Micromachined metal oxide gas sensors: opportunities to improve sensor performance. *Sensors and Actuators* B 73 (2001) 1-26.
[2] H. Teterycz et. al.: New design of an SnO_2 gas sensor on low temperature cofiring ceramics. *Sensors and Actuators* B 47 (1998) 100 - 103.
[3] R. Bauer et. al.: Optimization of thermal distribution in ceramics an LTCC structures applied to sensor elements. *Microelectronics international 15* (1998) 34 - 38.
[4] H. Zheng et al.: Integrated oxygen sensors based on Mg-doped $SrTiO_3$ fabricated by screen-printing. *Sensors and Actuators* B 65 (2000) 299 - 301.

Kinetics of the Response to Gas in Metal Oxide Thin Film Sensors Doped with Catalytic Metals

A. Šetkus[1], C. Baratto[2], G. Faglia[2], A. Galdikas[1], Ž. Kancleris[1], G. Sberveglieri[2], D. Senulienė[1]

[1]Semiconductor Physics Institute, 11 A. Goštauto, LT-2600 Vilnius, Lithuania
email: setkus@uj.pfi.lt http://www.pfi.lt
[2]University of Brescia, 9 Via D. Valotti, 25133 Brescia, Italy

Summary: *The kinetics of the resistance response to a steep change in gas composition are experimentally and theoretically investigated in tin oxide thin film sensors surfaces of which were modified by catalytic metals. H_2 and CO gases were used in the tests. Based on the phenomenological model the stationary signal of the response is related to the density of the chemisorption centers for the gas and oxygen while the time constants are dependent only on the rate parameters of the surface reaction and are independent on the density of the centers. Influence of the density of impurities and the size of the cluster is discussed.*

Keywords: *gas sensors, impurities, kinetics*
Category: *5 (Chemical sensors)*

1 Introduction

The response time and the recovery time usually are used to describe the kinetic characteristics of metal oxide gas sensors in most studies. In general, these parameters are assumed equal to a time interval during which the major portion of the response signal is measured (e.g. [1]). In spite of lack of explicit theoretical understanding of the response kinetics it is desirable to develop the methods for improvement of the kinetic characteristics of metal oxide sensors with the aim to increase the speed of the analysis performed by an electronic nose.

In present paper an influence of catalytic metals on the kinetic characteristics of tin oxide sensors was experimentally and theoretically investigated. A phenomenological model was employed for the interpretation of the experimentally measured response to a steep change in gas composition of the atmosphere.

2 Phenomenological model

Based on phenomenological model [2] the kinetics of the resistance response was related to the surface reaction rates such as gas adsorption rate (Φ_B), desorption rate (β_B) and the rate for the bimolecular interaction (ν_B). The stationary signal and the resistance response to a steep change in gas composition were described by the phenomenological relationships. Phenomenological time constants τ were defined for quantitative characterization of the kinetics because these constants might be evaluated from the experimental transients by the standard methods based on multiexponential decays similar to

$$R(t) = a_0 + \sum_{i=1}^{N} a_i \exp(-t/\tau_i). \qquad (1)$$

Weighting coefficients a_0 and a_i might be related to the rate parameters of the surface chemical reaction. Some details are described in [2].

3 Experimental

Thin films of gas sensors were deposited by magnetron sputtering in pure Ar atmosphere with consequential oxidation in humid synthetic air. Similar initial films of pure Sn were used for four types of the sensors. Each type of the sensors was manufactured by the post-growth doping of the film surfaces with individual catalyst (no. 1 - Pt, 2 - Mo, 3 - W, 4 - Ag). The fifth type (no. 5) was manufactured of the oxidized films previously grown by a sequential deposition of pure Sn and Mo. The films were grown on the prototype structure with the contacts of pure Pt and the heater.

During the gas tests, the sensors were mounted in a test chamber through which synthetic air was flowing at the constant rate (typically 200 ml/minute). A steep change in the atmosphere composition was produced by switching of the chamber inlet connection from the clean air channel to the channel in which the air contaminated with fixed amount of CO or H_2 gas flowed.

DC-electrical resistance was measured for each of the sensors mounted in the same gas chamber. Time dependence of the resistance was obtained by sampling the signals with frequency of 1 Hz. the temperature of a sensor was set at individual values within the interval from about 450 K to 800 K long before the measurements.

4 Results and discussions

The transients were measured at various concentrations from about 10 ppm to 100 ppm of H_2 gas and from about 50 ppm to 1200 ppm of CO gas. Monotonous decrease of the resistance was typically observed for the sensor response to the gases. Recovery to clean air was not studied here.

The dependencies of the phenomenological time constants τ_i and the weighting coefficients a_i on gas concentration P_{gas} were evaluated from experimentally measured transients. In the interval of small gas concentrations ($\Phi_B \equiv \delta_B P_{gas} << \beta_B+\nu_B\Theta_{O2}$), the dependence of the time constant on concentration is described by $\tau_{iB} = (\delta_{iB}P_{gas} + \beta_{iB}+\nu_{iB}\Theta_{O2})^{-1}$ with Θ_{O2} as the initial coverage of the surfaces with the oxygen species. The parameters δ_{iB} and $\tau^*_{i0}= (\beta_{iB}+\nu_{iB}\Theta_{O2})^{-1}$ were evaluated

The pairs of related parameters a_{i0} and τ^*_{i0} are displayed as a set of the points in the two-dimensional plot. In this plot, the weighting coefficient a_{i0} (relative part of the response attributed to the corresponding component) defines the ordinate and the time constant τ^*_{i0} defines the abscissa of the individual point in the orthogonal graph. Such the spectrum of the kinetic parameters quantitatively describes the basic profile of the transient of the sensor response that is independent on the gas concentration. Typical spectrum for the sensor doped with Pt (no. 1) and exposed to H_2 gas at T_{sensor}= 575 K is presented in Fig. 1.

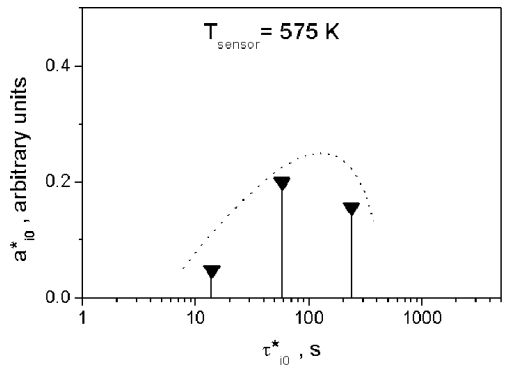

Fig. 1. The distribution of the relative part of the response to H_2 gas per component defined by the time constant τ^*_{i0} for tin oxide sensor with Pt.

The distributions of the weighting coefficient per set of the components were compared for all the sensors in the plot similar to Fig.1. Typical spectra corresponding to the response of the sensors to H_2 gas at T_{sensor}= 475 K are shown in Fig. 2. The transient of the sensor no. 3 is described by a set of nearly equal weighting coefficients a_i corresponding to the series of the time constants. In the kinetics of the sensors 1, 2 and 4, the longer time components are dominant. This result exhibits comparatively slow response to gas.

An influence of the gas concentration on the

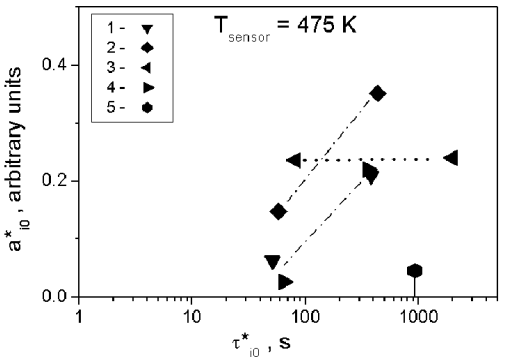

Fig. 2. The distribution of the weighting coefficients per component defined by the time constant τ^*_{i0} for various tin oxide sensors.

spectra $a^*_{i0}(\tau^*_{i0})$ was described by a distribution of the slope coefficient δ_{iB} per component.

Activation energies of the reaction rates were evaluated from dependencies of the phenomenological coefficients on temperature. It was demonstrated that desorption prevails over the bimolecular interaction at comparatively low temperatures. At higher temperatures, a change of the response mechanism was supposed.

Based on the phenomenological model, the experimental results might be explained by additional chemisorption centers for the target gas. These centers should be associated with the clusters of the catalytic metals. Assuming that the centers are located at the edges of the clusters and in the vicinity of the reaction sites then an increase in the center density will increase the response. In contrast to this the rate parameters of the bimolecular interaction will not be changed. This mechanism suggests the criteria for choosing of catalyst: it should be the impurity metal on the surfaces of which the gas binding energy is higher.

From the accepted model follows that the doping might modify the kinetics of the response if the most of the oxygen chemisorption centers are created by the catalyst point defects on the surfaces of the basic metal oxide. It seems reasonable to expect that the rate parameters of the reaction will be unique in these centers if compared to the centers on the surfaces of pure metal oxide.

References

[1] N. Butta, M. Melli and S. Pizzini. Influence of surface parameters and doping on the sensitivity and on the response times of tin oxide resistive sensors. *Sens. Actuators B: Chem.* 2 (1990) 151.

[2] A. Šetkus. Heterogeneous reaction rate based description of the response kinetics in metal oxide gas sensors. *Sens.Actuators, B, Chem.* 87 (2002) 346-357.

A hygrometric sensor with porous membrane coated on both sides with Au

Y. Miyoshi[1], K. Mitsubayashi[2], S. Iguchi[2], Y. Wakabayashi[2], T. Takeuchi[3]

[1]Faculty of Info-Sci., Hiroshima City Univ., 3-4-1 Ohtsukahigashi, Asaminami-ku, Hiroshima 731-3194, Japan
[2]Tokai University, Dept. of Human and Info. Science, 1117 Kitakaname, Hiratsuka, Kanagawa 259-1292, Japan
email: mitsu@keyaki.cc.u-tokai.ac.jp
[3]Graduate School of Sci-Tech, Kobe University, 1-1 Rokkodai-cho, Nada-ku, Kobe 657-8501, Japan

Summary: *A flexible sensor constructed in a sandwich configuration with a hydrophilic poly-tetrafluoroethylene membrane placed between two gold deposited layers was evaluated for use as a hygrometric sensor. The electric impedance of the device with desiccants ($CaCl_2$, NaCl, and Na2SO4) as hygroscopic material was measured at 100 Hz alternating frequency, and the device with calcium chloride was calibrated against moisture over range of 30 to 4000 ppm. The application of calcium chloride as desiccant was effective for detecting the low concentration of moisture in the gas phase.*

Keywords: *hygrometric sensor, moisture, LCR meter, porous membrane, Au deposited membrane*
Category: *5 (Chemical sensors)*

1 Introduction

The detection and quantification of gaseous substances, such as moisture, odors, toxic and combustible gases, with high sensitivity and selectivity ale required in many different areas [1]. The moisture analysis is required in the many fields, i.e. quality control of natural gas in the compressed-gas cylinder in order to prevent the hydration of the natural gas with moisture by decompressing to normal pressure.

On the other hand, we constructed and reported flexible conductimetric and glucose sensors (thickness: 80 μm) in a sandwich configuration with a hydrophilic poly-tetrafluoroethylene membrane placed between two gold deposited layers [2-4]. In this work, a hygrometric sensor was also developed using the fabrication techniques of the flexible device for analyzing a lower concentration of moisture in the gas phase.

2 Experimental

2.1 Construction of flexible hygrometric sensor

The structure of the flexible hygrometric sensor is shown in Figure 1.

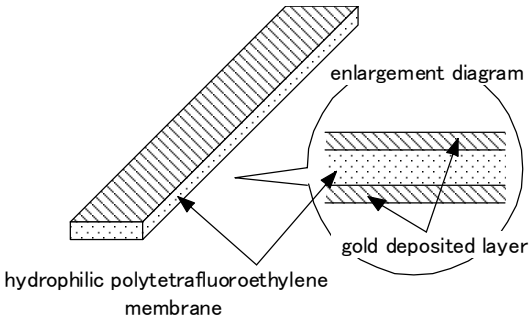

Fig. 1. Hygrometric sensor with porous membrane coated on both sides with Au-layers.

Gold electrodes were formed directly using vapor deposition onto both sides of a hydrophilic polytetrafluoroethylene (H-PTEF) membrane (JGWP14225, thickness: 80 μm, pore size: 0.2 μm, NIHON MILLIPORE KOGYO K.K., YONEZAWA, JAPAN); this membrane offers chemical stability, tear resistance, and flexibility.

The thickness of each gold electrode layer was 1000 Å. Electrodes on both sides were kept at equal intervals across the H-PTFE membrane. The membrane was shaped by knife into a 3 mm-wide strip. Deposited gold adhered to the membrane and could not be peeled off by mechanical stress such as bending. The gold deposited membranes retain their flexibility even after vacuum evaporation.

In order to improve the sensitivity of the device, desiccants as hygroscopic materials were contained into the porous PTFE-membrane, by dipping the hygrometric sensor into desiccant solution and drying.

After inspection of electrical shorts, the flexible hygrometric sensor was stored at room temperature except when in use for measurement.

2.2 Evaluation of flexible hygrometric sensor

Behavior of the sensor was calibrated using nitrogen gases with varying concentration of moisture, supplied from a moisture generator (101, Parametrics Japan Corp., Tokyo, Japan) (Figure 2).

The concentration of moisture in the gas phase was calculated from electrical impedance of the device measured by personal computer-controlled LCR meter (HP4263A, YUKOGAWA-HEWLETT-PACKARD, LTD., Tokyo, Japan) system using the four-probe method at 100 Hz alternating frequency. A commercial available

hygrometer was applied to the moisture measurement system for a sensor calibration.

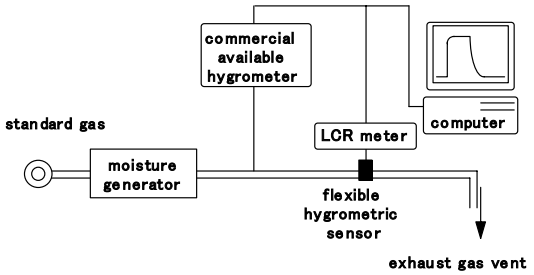

Fig. 2. Schematic diagram of moisture measurement system with flexible hygrometric sensor and commercial available hygrometer.

3 Results and Discussion

3.1 Hygrometric sensor with calcium chloride

Figure 3 illustrates the calibration behavior of the flexible hygrometric sensor with calcium chloride (1.0 mmol/l solution) as desiccant to varying concentration of moisture. The sensor output was presented as difference between the steady state impedance in the moisture gas and an asymptotic impedance value.

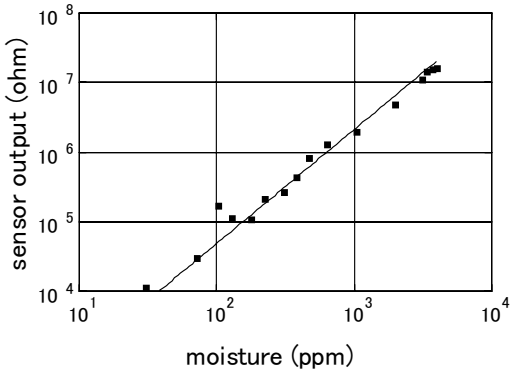

Fig. 3. Calibration behavior of the flexible hygrometric sensor.

The flexible hygrometric sensor was calibrated against the moisture in the gas phase over the range of 30 to 4000 ppm, with a correlation coefficient of 0.996 deduced by exponential regression analysis as shown by the following equation:

$$\text{sensor output (ohm)} = 26.1[\text{moisture (ppm)}]^{1.64}$$

The effect of the concentration of calcium chloride on the electric impedance of the flexible hygrometric sensor is shown in Figure 4. As the figure indicates, the behavior of sensor impedance to moisture concentration is dependent on the solution concentration for the $CaCl_2$ impregnation. The application of $CaCl_2$ desiccant (more than 1.0 mmol/l) to the porous membrane was effective for detecting the low concentration of moisture.

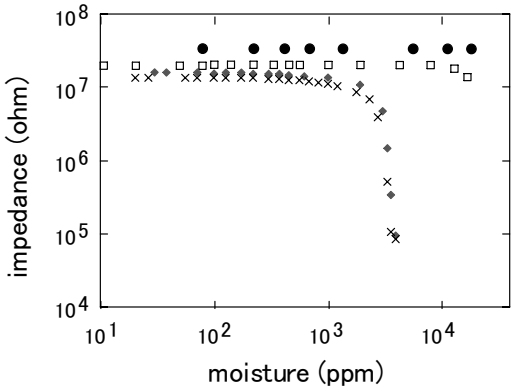

Fig. 4. Effect of $CaCl_2$ concentration on the impedance output of the flexible hygrometric sensor for moisture analysis. (● : w/o, □ : 0.01 , ♦ : 1.0, x : 2.0 mmol/l)

3.2 Effect of desiccants on sensor behavior

Figure 5 illustrates the effects of the desiccants on the electric impedance of the hygrometric device.

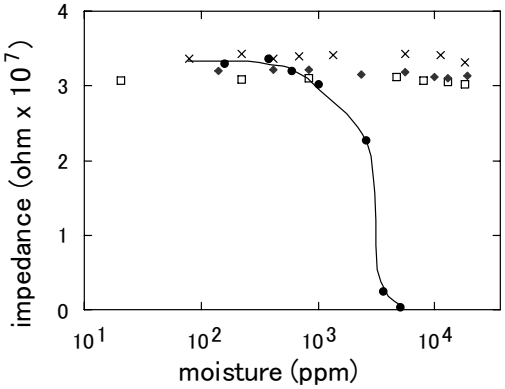

Fig. 5. Effect of desiccants as hygroscopic material on the impedance output of the flexible hygrometric sensor for moisture analysis. (0.1 mmol/l impregnation; ○ : $CaCl_2$, □ : NaCl , ♦ : Na_2SO_4, x : w/o desiccant)

As the Figure 5 indicates, the application of calcium chloride gave the widely change in the electric impedance of the flexible hygrometric sensor, thus allowing the effective measurement of moisture in the gas phase.

References

[1] T.J. Hwang, *Sensors and Actuators B*, **40**(1997), 187-195.
[2] K. Mitsubayashi, K. Yokoyama, T. Takeuchi, E. Tamiya, I. Karube, *Anal. Chem*., **65**(No.24) (1993), 3586-3590.
[3] K. Mitsubayashi, J.M. Dicks, K. Yokoyama, T. Takeuchi, E. Tamiya, I. Karube, *Electroanalysis*, 7(No.1) (1995), 83-87.
[4] K. Mitsubayashi, K. Ogasawara, K. Yokoyama, T. Takeuchi, T. Tsuru, I. Karube, *Tech. Health Care*, 3(1995), 117-121.

Polyimide Membrane: A new substrate for microsensors

Muhammad Aslam, C. Gregory and J.V. Hatfield

University of Manchester Institute of Science and Technology, EE & E Dept., Sackville Street, P. O. Box 88
Manchester M60 1QD UK
Email: j.hatfield@umist.ac.uk

Summary: *Presented here is a rugged polyimide membrane of thickness in the region of 1 – 10 μm. The area of the membrane is not limited by the fragility of the material. The elastic modulus of the material enables it to be used in any number of applications ranging from heated sensor support, to a fluid pump component capable of withstanding high hydrostatic forces. Membranes of one kind or another have been especially useful in a range of sensor types. These membranes are often made from silicon nitride on bulk etched silicon. This results in a fragile membrane of limited area. The application described here uses the thin rugged polyimide membrane to reduce the power consumption of a metal oxide gas sensor.*

Keywords: *polyimide membrane, bulk etching, and sensor array*
Category: *05(Chemical Sensors)*

1 Introduction

For the fabrication of low power, small size gas sensors, the substrate itself plays an important role. Typically, silicon, silicon dioxide or silicon nitride membranes supported on a silicon wafer have been used as a substrate [1]. We have adopted a new approach to develop such sensor systems on polyimide membranes and an effort is being made (to be reported) to develop thin-film, metal oxide sensor arrays. The most popular material for gas sensing is tin oxide (SnO_2). This material is heated to an elevated temperature of 200-300°C to activate its sensing characteristics.

The polyimide membrane exhibits good mechanical and thermal properties. Also, it is easy to control layer thickness (hence strength) as compared with oxide or nitride. The basic goal is to achieve a sensor with low power consumption, and controlled temperature distribution across the sensing layer on a polyimide membrane.

2 Experimental work

In the fabrication of polyimide membranes, the basic step is to etch back silicon <100> wafer. Instead of conventional etch stop techniques, another method, Gold/Silicon/TMAH galvanic etching is carried out [2, 3]. The process flow is as shown in fig.1. Essentially, the process involves coating both sides of an oxidized silicon wafer with a Au/Cr etch mask. Apertures, that will define the membranes, are etched in the Au/Cr, SiO_2 on the backside of the wafer. The silicon is then bulk etched in a 25% TMAH solution.

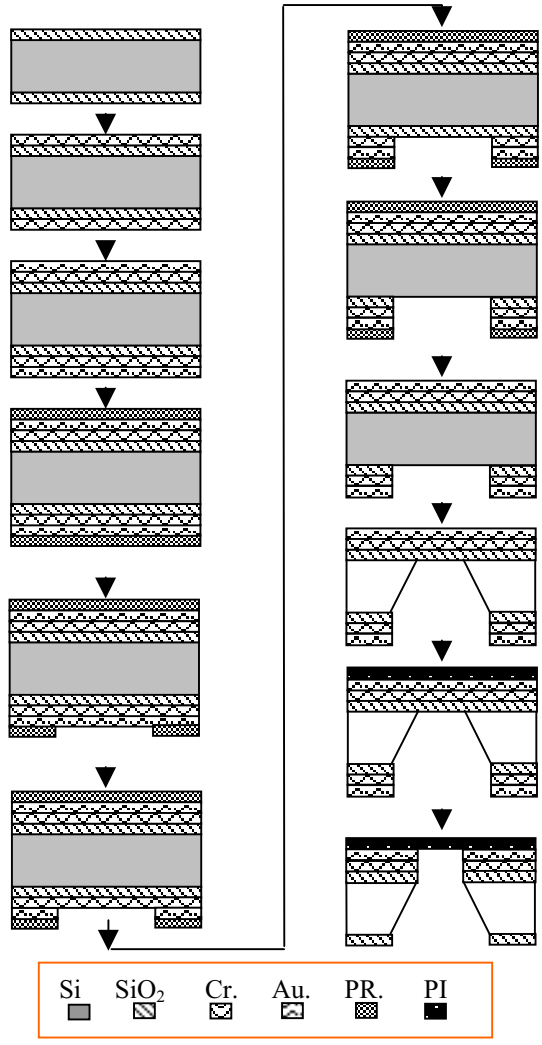

Fig. 1. Illustrating process flow.

The etch rate of this solution is about 1μm/minute at 90°C. The TMAH etchant is not toxic as compared with KOH and EDP and also it is more user friendly for MOS or CMOS post-processing in clean room conditions.

Once etching is complete through to the front-side SiO_2, the PI membrane is applied over the front-side gold by spin coating. The polyimide used was PI2575 from HD MicroSystems (DuPont). The thickness of membrane depends upon the spin coating speed and viscosity of the material. The curing temperature profile for the polyimide membrane is a critical parameter for proper cure. The polyimide is cured in a nitrogen atmosphere at an elevated temperature of 400°C for 30 minutes. The SiO_2 and Au/Cr is then etched away from the back of the membrane to release the PI.

An array of polyimide membranes is shown in fig. 2. The size of membrane is 3.5 x 3.5 mm and an array of four metal oxide gas sensors is developed on each membrane. The membranes so produced can also be used for developing different sensors, microwave antenna arrays, ultrasonic sensors and micro-speakers [4].

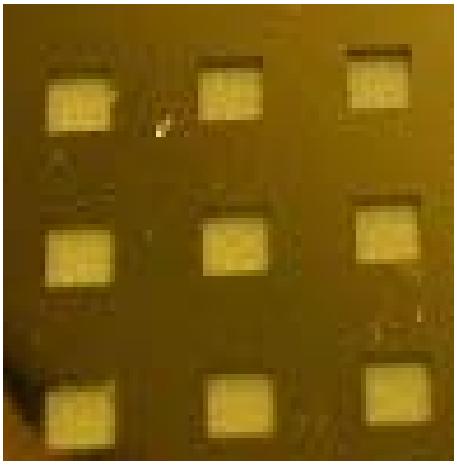

Fig. 2. Array of PI membranes on <100> Si frame

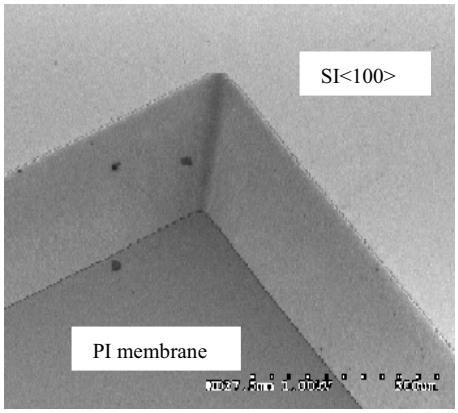

Fig. 3 SEM cross-section of bulk etched <100> silicon; x100 mag.

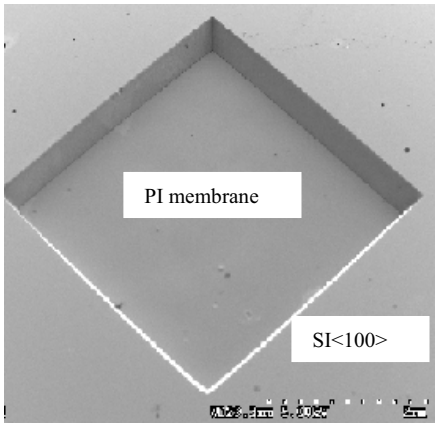

Fig. 4. SEM view of bulk etched Si<100> window 3.5x3.5mm^2, x25 mag

The SEM cross-sections in fig3 and fig.4 show the anisotropic etching of silicon wafer with the polyimide membrane in place.

In conclusion low power sensor fabrication on polyimide membrane is attractive because:

1. It is a thermally better insulator than oxide or nitride membranes.
2. Also, a relatively thick layer as compared to oxide or nitride can be achieved with this material.
3. It is robust and not fragile as oxide or nitride layers.
4. The surface of spin-on polyimide is smooth.
5. The deposition of platinum (for micro heaters) on polyimide is straightforward and there is no need for an adhesion layer as in the case of oxide or nitride membranes.

References:

[1] A. Dibbern," A Substrate for Thin Film Gas Sensors in Microelectronic Technology" Sensors and Actuators B 2 (1990) pp: 63-70.

[2] P.J. French, M. Nagao and M. Esashi, "Electrochemical etch-stop in TMAH without externally applied bias", Sensors and Actuators, A56, 279-280 (1996).

[3] C.M.A. Ashruf, P.J. French, P.M. Sarro, W.v.d.Vlist, E.L. Oemar, L.J. Breems, and J.J. Kelly, "Practical considerations of the galvanic etch-stop for device applications", Proc. Transducers'99, p..560, Sedai, Japan (1999).

[4] C. Shearwood, M. A. Harradine, T. S. Birch and J. C. Stevens," Applications of Polyimide Membranes to MEMS technology" Microelectronics Engineering 30 (1996) pp 547 – 550.

AES Study of Cu - Ion-selective Membranes Based on Chalcogenide Glasses

R. Tomova, G. Spasov, R. Stoycheva-Topalova, A. Buroff

Central Laboratory of Photoprocesses "Acad. J.Malinowski",
Bulgarian Academy of Sciences, Acad. G. Bonchev st., bl. 109, 1113 Sofia, Bulgaria
e-mail: reni@clf.bas.bg, http://clf.bas.bg

Summary: *Thin film sensors on the basis of evaporated layers of chalcogenide glasses for heavy metal ions are developed. In spite of the promising results and good electrochemical performance, the long-term stability of chalcogenide-based thin film sensors is still a problem. In this paper, AES study was made to clarify the problem with "the aging" of chalcogenide thin film membranes.*

Keywords: *sensors, chalcogenide glasses*
Category: *5 (chemical sensors)*

1 Introduction

Electrochemical sensors based upon selective vitreous membranes were extensively studied in the last years with an increasing interest for miniaturized devices. Chalcogenide glasses with their flexible structure, enormous variations of properties and almost unlimited ability for doping and alloying were proven to be very promising materials for chemical sensors for analysis of industrial aqueous solutions and the environment monitoring of pollutant gases [1].

We are developing ion-selective membranes on the basis thin evaporated layers of pure and doped chalcogenide glasses. The realized heavy metal sensors showed high sensitivity towards Ag^{+}, Cu^{2+} and Pb^{2+} ions, respectively down to the concentration range of 10^{-6} mol/L, short response time and good selectivity to interfering ions [2-4]. The sensor performance is comparable to those of conventional non-miniaturized bulk ISEs with the similar compositions. In this paper, "the aging" of As_2S_3/Ag/Cu thin film membranes was studied by AES analysis.

2 Experimental

Experimental samples were prepared by vacuum deposition of Cr layer on Si or $Si/SiO_2/Si_3N_4$ substrates, followed by thermal deposition of As_2S_3, Ag and thermal or e-beam deposition of Cu. The light exposure of the evaporated layers with metal-halogen lamp assures the homogeneous distribution of metals in the whole thickness of the layers. The content of samples in atomic % was determined by measuring the deposition rate with quartz microbalance technique. Riber's microprobe ASC 2000 and ion gun CI 40 modules from the surface analyses combine LAS 3000 were used to study the depth distribution of the dopants in chalcogenide membranes. A 3 keV Ar ion beam bombarding the sample at 20^0 of normal was used for sputter depth profiling. The primary e-beam energy was 3 keV and current - about 7.10^{-3} μA. Auger electron peaks at energies 152 eV, 272 eV, 510 eV, 529 eV, 920 eV, 1228 eV and the doublet 351-356 eV were chosen for the elements S, C, O, Cr, Cu, As and Ag respectively [5]. The peaks were scanned in the differentiated mode at a modulation voltage 4V peak-to-peak. A semi-quantitative procedure based on our own reference profiles and methods of pure element standard and elemental sensitivity are used to recalculate the Auger signal data in atomic percents.

3 Results and discussion

It is known that photodiffusion of Ag and Cu in As_2S_3 led to homogeneous amorphous compounds containing Ag up to 39 - 41 at.% [6] or Cu - 33-37 at. % [7]. Above this concentration the compounds became heterogeneous. It could be expected that membranes with concentration of Cu and Ag up to 38-41 at. % (30 % Cu + 11 % Ag) have amorphous structure, i.e. nearly all studied membranes.

The results presented in fig. 1a show that Cu diffuses in As_2S_3 layers during the deposition time independent on the sequence of evaporation - before or after As_2S_3. AES profile does not depend on the illumination of layers. At Cu+Ag concentration higher than the solubility maximum (41 %), Cu diffuses predominantly, replacing the Ag previously deposited. The excess Ag stay undissolved under or above As_2S_3 depending on the sequence of deposition (fig.1b). According the thermochemical model of photodoping [7] the chemical reaction between As_2S_3 and Ag is endothermic (is not beneficial energetically), while the reaction between As_2S_3 and Cu is exothermic and energetically favorable. That's why from thermodynamically point of view most probably, one can expect only the diffusion intermixing at

As_2S_3/Ag system while at As_2S_3/Cu fast exothermic exchange reaction should take place, producing Cu_2S and $Cu_{2-x}S$.

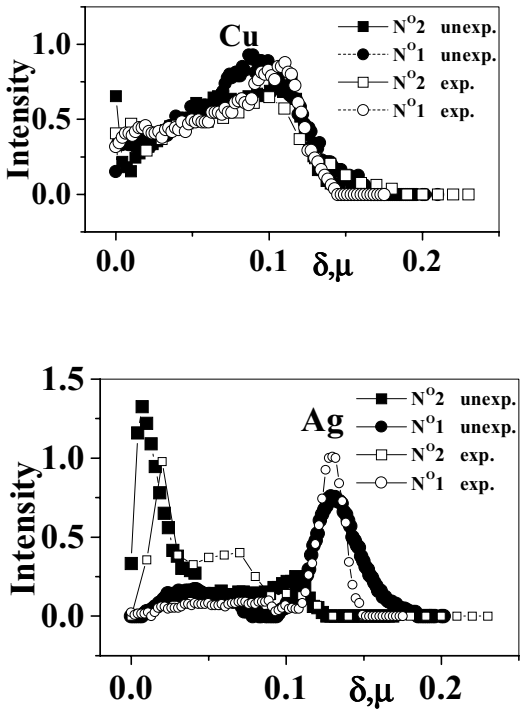

Fig. 1. AES depth profiles of Cu and Ag for samples with $Ag_{12}Cu_{31}$ content in different order of evaporation: on the top of As_2S_3 (N 2) and under As_2S_3 (N 1), before (solid symbols) and after (empty symbols) exposure.

The light exposure influences the distribution of Ag in As_2S_3 matrix - the concentration gradient of Ag moves up to As_2S_3. The sequence of evaporation has a significant importance on the metal distributions. The change of the profiles is stronger when Ag and Cu are evaporated after As_2S_3 (№ 2 in fig 1b).

Electrochemical treatment shifts Cu profile (fig.2a) towards the lower concentration, while Ag profile (fig.2b) - to the higher. Besides, the surface concentration of Cu decreases, while surface concentration of Ag is the same. It could be concluded that part of Cu moves away from the subsurface layer, decreasing its density. Probably this change in the structure could be the reason for further faster deterioration of the properties of the membranes, increasing its "response time".

4 Conclusion

It was established that the concentration of metals distributed in As_2S_3 matrix determines the electrochemical properties of the membranes. The metals distribution depends on the way of evaporation and the light exposure. Electrochemical treatment influences strongly the Cu concentration in the subsurface region. That's could be the reason for the increasing of response time with the aging of the membranes. The e-beam evaporation of Cu enhances the stability of ion-selective membranes due to the more stable metal distribution.

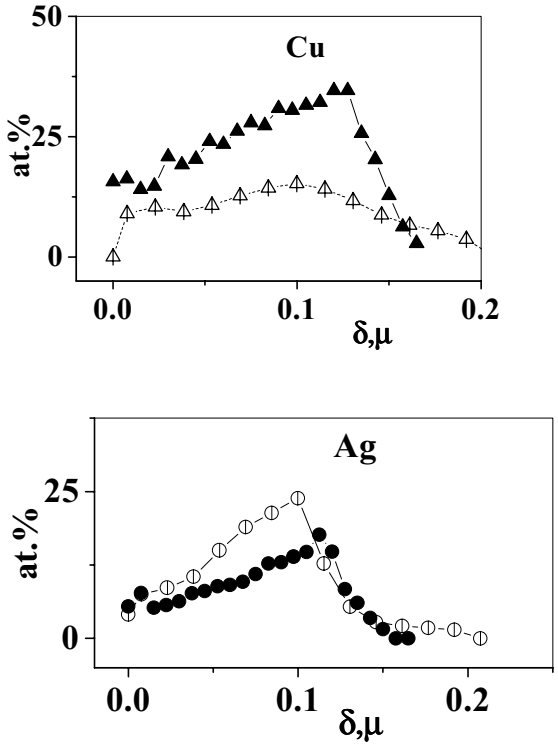

Fig.2. AES depth profiles of Cu (a) and Ag (b) before (solid symbols) and after (empty symbols) electrochemical treatment

It was established that the plasma polymer film (PHMDSO) deposited on the top of chalcogenide glass membrane improves the electrochemical characteristics - increases the sensitivity and long-term stability and keeps the response time [8]. The results obtained are promising for the development of low-cost, highly reliable sensors.

References

[1] Yu. Vlasov, Y. Ermolenko, A. Legin, Y. Murzina, *J.Aanl. Chem*., 54 (1999) 476

[2] R.Tomova, R.Stoycheva-Topalova, A. Buroff, Proc. ISCMP'98, ed. N.Kirov, J. Marshal, World. Sci. Publ., Singapore, p.501-504

[3] R.Tomova, J.Assa, R.Stoycheva, A.Buroff, J.Non-Cryst. Solids, 260 (1999) 195-198

[4] R.Tomova, G.Spassov, R.Stoycheva, A.Buroff, J.Non-Cryst. Solids, 266-269 (2000) 985-988

[5] Handbook of Auger Electron Spectroscopy, JEOL, Tokyo, 1982, ed: T. Sckine et al.

[6] A.Kolobov, S.Elliott, Advances in Physics, 40, (1991) 625-684

[7] M.Sopinsky, M.Kostyshin, J.of Optoelectronics and Advanced Materials, 3 (2001) 411-420

[8] R. Tomova, Nanoscience & Nanotech.'02, eds. E.Balabanova, Heron Press, Sofia 2002, p.115-117

Novel odor sensor utilizing surface plasmon resonance

Y. Kitade[1], S. Naka[1], Y. Sekikawa[1], Y. Takei[1] and H. Nanto[1]

[1]Advanced Materials Science R&D Center, Kanazawa Institute of Technology,
3-1 Yatsukaho, Mattou, Ishikawa 924-0838, JAPAN
e-mail: hnanto@neptune.kanazawa-it.ac.jp

Summary: *Odor sensor based on the surface plasmon resonance (SPR) is studied for detection of harmful gases such as ammonia and amine gases. It is found that the SPR sensor with acrylic acid thin film as molecular recognition membrane exhibited an excellent selectivity and high sensitivity for ammonia, and amine gases.*

Keywords: *surface plasmon resonance, odor sensor, molecular recognition membrane, ammonia*
Category: *5 (chemical sensors)*

1 Introduction

Surface plasmon resonance (SPR) is an optical phenomenon in which incident light excites a charge-density wave at the interface between a highly conductive metal and a dielectric material. The conditions for excitation are determined by the permittivities of the metal and dielectric material. The SPR transduction principle is widely used as an analytical tool for measuring small changes in the refractive index of a thin region adjacent to the metal surface. The optical excitation of surface plasmon on a thin metallic film has, therefore, been recognized as a promising technique for sensitive detection of chemical species [1]. Several methods have been employing to monitor the excitation of SPR by measuring the light reflected from the sensor interface. These include analysis of angle modulation [2], wavelength modulation [3], intensity modulation [4] and phase modulation [5].

In this paper, we show that harmful gases such as ammonia, trimethylamine and triethylamine gases can be detected by measuring the SPR using angle modulation.

2 Experimental

Optical SPR sensors are sensitive to change in the refractive index of a sample near sensor surface. The SPR was measured using the Kretschmann configuration (Toa DKK: PR-40), illustrated in Fig.1, with a prism and a thin highly conductive gold metal layer deposited on the prism base. The LED emitting 660 nm light was used as light source in order to excite the SPR. The SPR reflection spectrum (reflected light intensity versus angle of incidence with respect to the normal of the metal/dielectrics interface) is measured by coupling transverse magnetically polarized monochromatic light into the prism and measuring the reflected light intensity of the ray exciting the prism versus the angle of incidence.

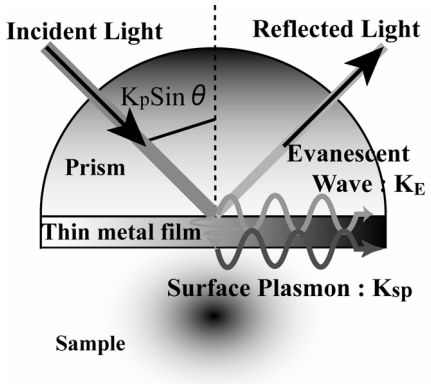

Fig. 1. Kretschmann configuration for generating the surface plasmon waves.

In order to utilize this system as a novel odor sensor, a very thin film of acrylic acid as a molecular recognition membrane was deposited on the gold metal thin film using plasma chemical vapor deposition (CVD) method. The acrylic acid thin film was deposited under the following conditions: The total pressure was 100 [Pa]. The pressure of acrylic acid monomer gas was about 20 [Pa]. The RF power supplied in the chamber was about 100 [W]. The Ar gas of about 80 [Pa] was used as carrier gas.

The reflected light was measured using CCD camera attached to a personal computer. The angle at which the minimum reflected intensity occurs, is the resonance angle at which coupling of energy occurs between the incident light and the surface plasmon waves. The schematic configuration of the SPR system is shown in Fig.2.

The harmful gases such as ammonia, acetaldehyde, propion-aldehyde, xylene, toluene, torimethylamine, triethylamine, dimethyamine, hormaldehyde, were used as testing gases.

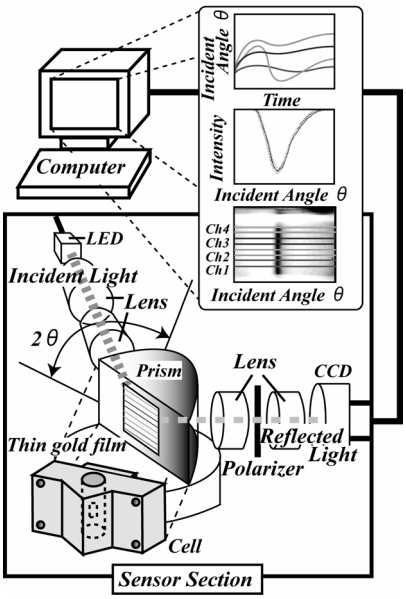

Fig. 2. Schematic diagram of SPR sensor system.

3 Results and Discussion

Figure 3 shows typical response of SPR sensor with acrylic acid thin film as a molecular recognition membrane for exposure to each testing gas. The concentration was 1000 [ppm] for each gas. It can be seen that the SPR sensor responded to only ammonia, trimethylamine and triethylamine gases. This result suggests that the SPR sensor coated with acrylic acid thin film exhibits good selectivity for ammonia and amine gases.

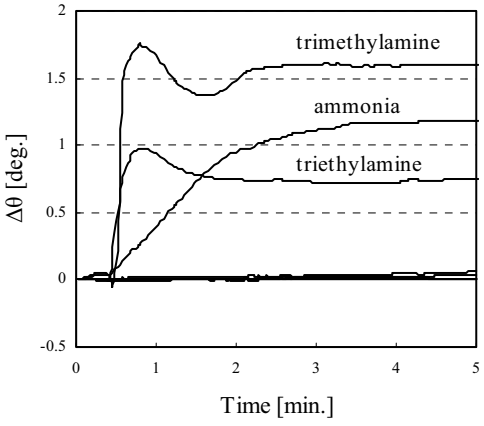

Fig. 3. Responces of SPR sensor coated with acrylic acid thin film for various gases, where $\Delta\ \theta$ is resonance angle change.

Figure 4 shows the dependence of the SPR sensor on the concentration of ammonia, which indicating that the output of the SPR sensor increases with increasing the ammonia concentration. At present, lowest sensitivity of the SPR sensor coated with acrylic acid thin film for ammonia and amine gases can be estimated to be about several ppm, because the accuracy of the SPR angle change is about 0.001 [degree].

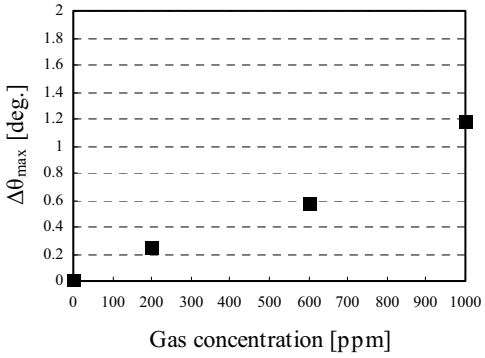

Fig. 4. Dependence of maximum resonance angle change $\Delta\ \theta_{max}$ on gas concentration of the responses of acrylic acid thin film exposure to ammonia gases of various concentration .

4 Conclusions

The odor sensor using SPR phenomenon was demonstrated in this work. The SPR sensor with acrylic acid thin film as molecular recognition membrane exhibited high sensitivity and excellent selectivity for ammonia, trimethylamine and triethylamine gases, which indicating that it is possible to use for the detection of freshness of fishes because the ammonia and amine gases are given out during the deterioration of fishes after death [6].

Acknowledgements

The authors wish to thank M. Komura and S. Sanada for their excellent assistance with the experiments. This work was partly supported by a Grant-in-Aid for Scientific Research and the foundation for High-Tech Research Center from the Ministry of Education, Science, Sports and Culture of Japan.

References

[1] B. Liedberg, C. Nylander and I. Lundstrom, *Sensors and Actuators*, 4 (1983) 299.

[2] E. Kretschmann, *Z. Phys.*, 241(1971)313.

[3] K. S. Johnston, S. R. Karlson, C. Jung and S. S. Yee, *Matr. Chem. Phys.*, 42(1995) 242.

[4] B. Chadwick and M. Gal, *Jpn. J. Appl. Phys.*, 32(1993) 2716.

[5] S. Nelson, K. S. Johnston and S. S. Yee, *Sensor and Actuators*, B35/36(199) 187.

[6] Y. Shimizu, Y. Takao and M. Egashira, *J. Electrochem. Soc.*, 135(1988) 2539.

Development of a micro chemical gas sensor with an inner-circulation diffuser pump

N.Yamaguchi[1], M.YANG

Tokyo Metropolitan University, 1-1, Minami-Osawa, Hachioji-shi, Tokyo,192-0397 Japan
[1] E-mail:yamaguti-noritomo@c.metro-u.ac.jp

Summary: *A micro Chlorine gas sensor with an inner-circulation diffuser pump was newly developed. The sensor based on electro-chemical principle, and only has the size of one-tenth in comparison with the conventional one. The sensor consists of an air-liquid separation membrane, a PZT-driven diffuser pump and micro electrodes, which were manufactured by micro machining. The inner-circulation is generated by driving the diffuser pump with a trapped air working as a buffer in order to preserve the condition of internal reagent. The properties of the sensor were evaluated by circulation rate of the pump, pressure-proof of the membrane and responsibility to Chlorine gas.*

Keywords: *chemical gas sensor, miniaturization , diffuser pump, inner-circulation,*
Category: *5 (chemical sensor)*

1 Introduction

Application of MEMS (Micro Mechanical Electro system) for mechanical sensors and actuators attracts attention. On the other hand, μTAS (Micro Total Analysis System) is expected as the new technique of performing analysis, such as the field of chemistry, medicine, and pharmacy. In such a field, as the reaction by liquid in many cases, the devices for carrying or/and mixing liquids are necessary. Development of micro pump[1] and micro mixer became vary important. In this Study, a micro Chlorine gas with internal reagent was developed. A micro diffuser pump with a function of circulating the internal reagent was developed and applied to the sensor.

2. Development of micro electro-chemical gas sensor

The electro-chemical gas sensor consists of two internal electrodes, WE (Working Electrode) and CE (Counter Electrode), and internal reagent is covered by air-liquid separation membrane. Bias voltage is impressed between two electrodes. While chorine gas reacts the internal reagent, and current flows as output of a sensor. While miniaturization of the sensor, leak or evaporation of internal reagent and decline in reaction rate due to dullness of the reagent could be issues to overcome.

In this study, we designed a micro sensor with a function of inner-circulation for filling and refreshing the internal reagent. The sensor has two-layer structure, which was made of Si and SiO_2 with thickness of 100μm and 1mm, respectively. The air-liquid separation membrane was manufactured by micro machining a slit on Si with several micron width by using anisotropic etching and coating water-repellent. The inner circulation diffuser pump consists of a diaphragm with PZT film bonded on its surface, a closed diffuser channel and an air-trapping valve. The developed pump and principle of inner-circulation are shown in Fig. 1. The diaphragm was connected to two diffusers with different shape on right and left. In this case, it is impossible to pumping the diaphragm in closed room filled with liquid due to incompressibility of liquid. Here, we trap air by using a value in the closed channel, and use the trapped air as the compressive buffer to circulate the flow while pumping the diaphragm. The generation of inner-circulation is as follows. By impressing a bias voltage on the PZT film, the diaphragm is bent downward so that the liquid under the diaphragm spitted out to the channel through the diffusers, and the trapped air is compressed. On the contrary, while the diaphragm stretched back, the liquid is drawn back from the channel through the diffusers and the trapped air is expanded. Due to the pressure difference between the left and right diffusers during pumping and drawing, the inner-circulation from right to left is then generated.

The prototype sensor with valves and electrodes is then developed, and shown in Fig.2

3. Evaluation of sensor properties

The following properties of the sensor were valuated in this study.

-Inner-circulation rate

-Water pressure proof of air-liquid separation membrane

-Response to leakage chlorine gas

Using the polystyrene bead with a diameter of 20 μm as a tracer, a flow is visualized, and analyzed. Fig. 3 shows the relation between the flow velocity and a drive waveform or frequency. While obtained volumetric flowrate by the sine wave was 14.lμL/min, the rectangle wave is 39.7μL/min. When the amount of trapped air was changed, the maximum volumetric flowrate was changed. As a result, it is considered that the compressed air is playing an auxiliary role of pumping.

Water pressure proof is measured using pressure sensor. Processed sensor with slit of 1μm×2mm has water pressure proof of 20kPa.

Experiment of response to leakage chlorine gas was performed using chlorine gas of 10ppm. The sensor responded with a signal of 20nA.

An inner circulation diffuser pump was developed using the mechanism trapping air. The sensor made as an experiment has air-liquid separation film with the water pressure-proof of 20kPa, and has the refreshment function of internal reagent. Developed sensor specification and function show Table.1. The response of the sensor to chlorine gas is under working. This sensor is applicable to other gas sensor changing reactive solution and electrodes.

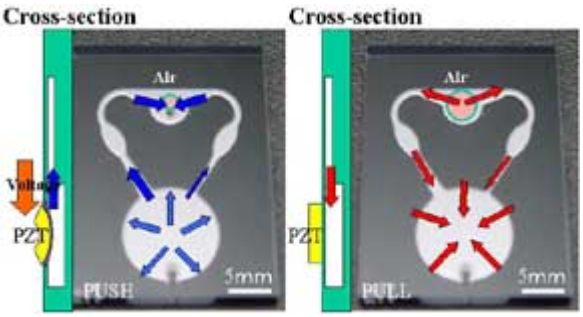

Fig 1. Principle of the circulation type of diffuser pump

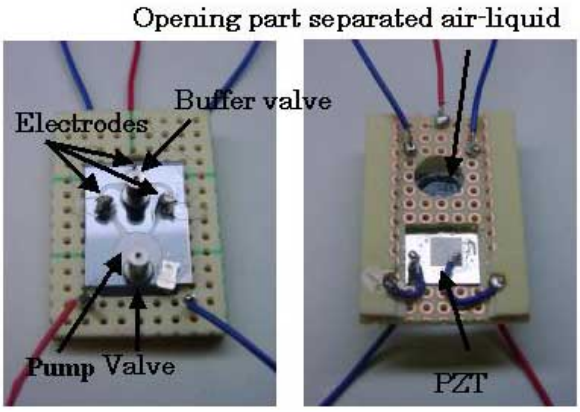

Fig.2 Prototype chlorine gas sensor

References

[1]A.K.S.Matsumoto, R. Maeda," Development of Bi-directional Valve-less Micropump for liquid"Proceedings MEMS'99,Florida

[2]K. Hosokawa, T. Fujii, and I. Endo ,"Droplet-based nano/picoliter mixer using hydrophobic macrocapillary vent," Proc.Micro Electro Mechanical System,(1999),388-393,Orland, USA

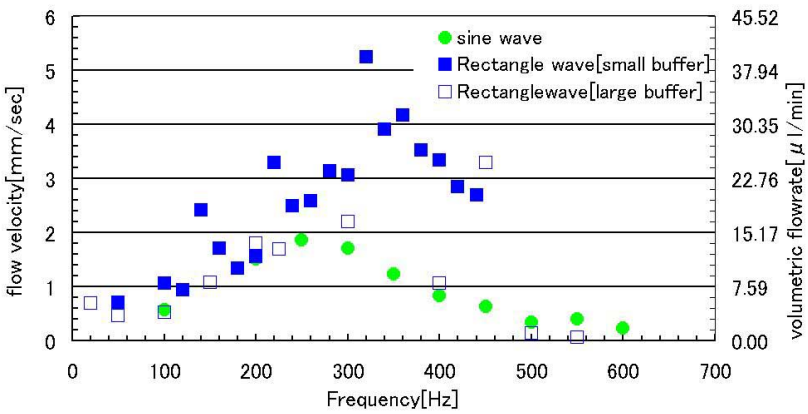

Fig. 3 shows the relation between the flow velocity and a drive waveform or frequency.

Table. 1 Specification and function of sensor

Specifications	
Size	15mm× 20mm× 1.1mm
Weight	3.8g
Piezoelectric element	Thickness 100μm
Material of body	Si,SiO_2
Material of Electrode	Pt φ 0.3, 0.8mm
Function	
Air-liquid separation function	
Opening size	2mm×1～2μm
Water pressure-proof	about 20kPa
Circulation function	
Rectangle wave	320Hz 39.7μl/min
sine wave	250Hz 14.9μl/min

Concentration discrimination of H_2S/NO_2 mixtures in different reference atmospheres

Omar HELLI[1], Maryam SIADAT[2] and Martine LUMBRERAS[3]

LICM – CLOES – SUPELEC – Université de Metz
2, Rue E. Belin, 57070 Metz - France

Phone : 33.3.87.37.85.61 Fax : 33.3.87.37.85.59
E-mail : [1]helli@ese-metz.fr, [2]siadat@ese-metz.fr, [3]lumbre@ese-metz.fr

Summary: *Lots of environmental problems due to the atmospheric pollution have increased the interest for the development of portable multisensors systems (electronic noses) for gas detection applications. In this way, we use a metal oxide sensor array dedicated to two industrial and environmental gases, alone or mixed. These gases have an antagonist influence on the sensor layers, reducing (H_2S) or oxidising (NO_2). So the sensor time responses present different behaviours, according to the (low or high) concentrations of the gases. In addition, humidity presents a notable reducing influence. We present in this work a new method to discriminate successfully the concentration of the atmosphere components.*

Keywords: *Gas-sensor, humidity effect, electronic-nose, environmental pollution, Discriminant Factorial Analysis.*

Category: *5 (Chemical sensor), 10 (Applications)*

1 Introduction

The use of the electronic noses is increasing these last years for application such as environmental pollution. In this field of interest, we develop a sensor array using metal oxide semiconductor gas sensors. These sensors are highly sensitive but present an undesirable cross-selectivity. The aim of our work is to study a sensor array dedicated to industrial environmental pollution gases, H_2S (1-11ppm) and NO_2 (1-5ppm), alone or mixed, in dry synthetic or wet synthetic air + CO_2. These gases have antagonist effect (reducing-oxidising) on the sensitive layer.

2 Experimental

The array is composed of six Tagushi Gas Sensors (TGS-800;813;822;825;832;2105) placed in a continuous flow controlled measurement system.

We have characterized our sensor array along this procedure: 50min reference atmosphere, 50min studied atmosphere, 50mn reference atmosphere to regenerate the sensors,…. We used two different reference atmospheres: dry synthetic air, and (30,50,68%RH) wet synthetic air + 500ppm CO_2. The H_2S time response has a reducing behaviour with notable increasing conductance, while the NO_2 time response presents a weak decreasing conductance, representing an oxidizing nature. Regarding the mixtures, the sensor time responses present different behaviours, according to the (low or high) concentrations of the gases, whatever the used atmosphere (figure 1 and 2). Comparing these figures, the humidity induces an enhancement of the conductance. So we have to take into account all these different behaviours.

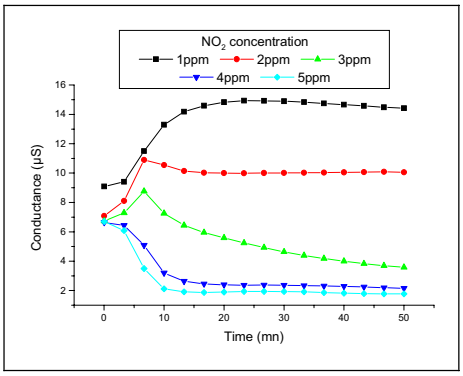

Fig. 1. Conductance time response for the TGS-825 sensor H_2S(1ppm)+NO_2(1-5ppm)

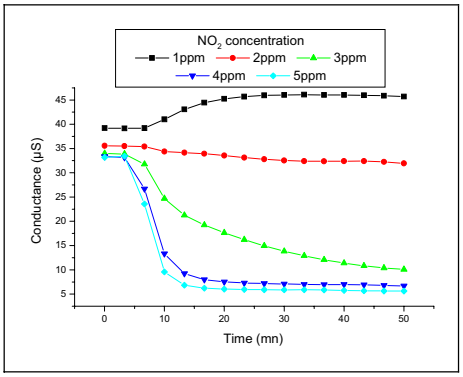

Fig. 2. Conductance time response for the TGS-825 sensor H_2S(1ppm)+NO_2(1-5ppm)+H_2O(50%)+CO_2(500ppm)

3 Results

From all the sensor time responses, we have deduced three non-redundant representative variables: the steady-state conductance, the conductance dynamic slope, the reference conductance (drift correction), grouped in a data-base and analyzed by Discriminant Factorial Analysis.

The concentration discrimination of the gases studied alone is satisfactory whatever the used reference atmosphere. Concerning the mixtures, the results are difficult to obtain specially for the NO_2 whatever the reference atmosphere (81.1% classification success in wet atmosphere and 86.0% in dry atmosphere). This fact can be explained in part because the sensors present a higher sensitivity to H_2S or humidity than to NO_2. To ameliorate these results we must first discriminate the entire data-base along with the atmosphere (dry or wet). Concerning the H_2S concentration discrimination, we must separate along with the reference atmosphere in four subsets (dry, 30, 50, 68%RH) and then discriminate the H_2S concentration in each subset (100% success) (figure 3). Concerning the NO_2 concentration discrimination, we must first separate in atmosphere subsets, secondly in H_2S subsets, and then we obtain a good discrimination of NO_2 (100% success) (figure 4). Unknown test samples where 100% identified.

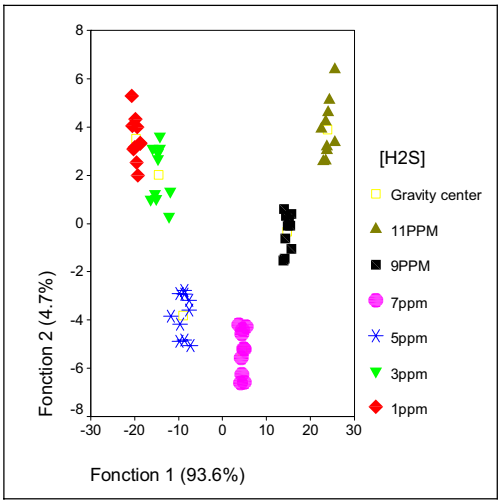

Fig. 3. H_2S concentration discrimination in the mixtures H_2S(1-11ppm)+NO_2(1-5ppm)+H_2O(68%)+CO_2(500ppm)

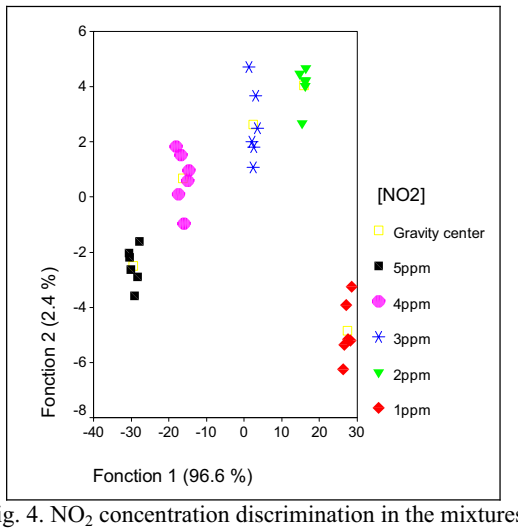

Fig. 4. NO_2 concentration discrimination in the mixtures H_2S(7ppm)+NO_2(1-5ppm)+H_2O(30-68%)+CO_2(500ppm)

4 Conclusion

From all these results, we show that the quality of the carrier atmosphere (dry or wet) and the nature of the gases (reducing or oxidising) must be taken into account to obtain a good identification of the atmosphere components, and then a successfully concentration discrimination.

Reference

[1] D. Gnani, V. Guidi, M. Ferroni, G. Faglia and G. Sberveglieri. High-precision neural pre-processing for signal analysis of a sensor array. *Sensors and Actuators B*, 47, 1998, 77-83.

[2] C. D. Natale, A. D'Amico, F. A. M. David, G. Faglia, P. Nelli and G. Sberveglieri. Performance evaluation of an SnO_2-based sensor array for the quantitative measurement of mixtures of H_2S and NO_2. *Sensors and Actuators B*, 20, 1994, 217-224.

[3] O. HELLI, M. SIADAT and M. LUMBRERAS. Metal oxide sensor array evaluation for the concentration determination of H_2S and NO_2 pollutant gases in atmosphere containing wet air + CO_2., , *conf. of Sensor2003,* 13-15 May 2003, Nuremberg, Germany.

Microstructure control of thermally stable TiO_2 obtained by hydrothermal process for gas sensors.

A. Ruiz[1], G. Sakai[2], A. Cornet[1], K. Shimanoe[2], J.R. Morante[1], N. Yamazoe[2]

[1]E.M.E., Electronics Dept., University of Barcelona, C/ Marti i Franques 1, 08028 Barcelona, Spain
email: ana@mm.kyushu-u.ac.jp http://www.el.ub.es
[2]Kyushu University, Materials Science Dept., Fac. of Engineering Sciences, Kasuga, Fukuoka 816-8580, Japan

Summary: *Mono-dispersed nanocrystalline titanium dioxide with enhanced thermal stability has been prepared by hydrothermal process. The hydrothermal treatment stabilizes the surface in a way that prevented thermally caused grain growth and allowed to maintain anatase type structure even after calcination at 800°C. Hydrothermally treated TiO_2 calcined at 600 °C consisted of small anatase nanospheres with average diameter of 13nm and improved gas sensitivity to diluted CO in air at high temperatures.*

Keywords: *TiO_2, anatase, hydrothermal, gas sensor*
Category: *5 (Chemical sensors)*

1 Introduction

Since the observation that the adsorption of gas molecules on the surface of a semiconductor produces a significant change in the electrical resistance, there has been a sustained effort to use this property for purposes of gas detection. To improve the performances of semiconductor gas sensors, important factors to be taken into consideration are grain size, size distribution, additives, crystallographic phase, microstructure and thickness, as well as the intrinsic semiconductor properties. Regarding structural forms of TiO_2, anatase and brookite metastable phases irreversibly convert to rutile phase at temperatures around 600 °C entailing an increase in grain size. Usually, to prevent such thermal effects, titania has been modified with additives [1]. However, it has been reported that hydrothermal treatments can produce thermally stable materials with enhanced gas sensitivity [2]. This works aims at describing the effects of the hydrothermal treatment in the TiO_2 structural and electrical properties. For that purpose, TiO_2 has been submitted to hydrothermal process and the influence of stabilisation processes on the crystallographic structure (i.e. crystallinity and grain size) as well as on the electrical behaviour has been studied.

2 Sample preparation and characterization.

Titanium alkoxide, 0.5M diluted in isopropanol, was added dropwise to an aqueous solution of HNO_3 and let to be peptized overnight. After peptization, the precipitate (titanic acid gel) was washed with pure water. Some part of the gel was suspended in 200ml of an aqueous HNO_3 solution at pH = 3 and subjected to a hydrothermal process at 150°C for 3 hours. The as-precipitated and the hydrothermally treated TiO_2 were dried and calcined at temperatures between 600°C and 900 °C for structural and electrical analysis.

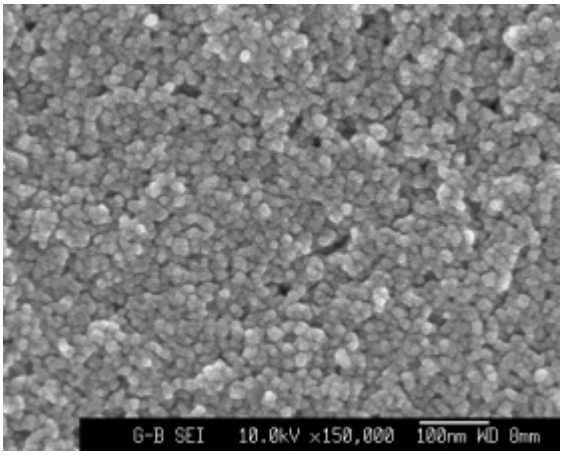

Fig. 1. SEM image of hydrothermally treated TiO_2 after calcination at 600°C.

Table 1. Crystallite size from XRD for the precipitated TiO_2 gel and the hydrothermally treated TiO_2 sol after calcination at different temperatures (D_a indicates anatase grain size, and D_r rutile grain size).

T (°C)	Precipitated Gel		Hydrothermally treated sol	
	D_a (nm)	D_r (nm)	D_a (nm)	D_r (nm)
120	5.48	-	6.20	-
600	29.32	41.42	13.15	-
700	33.93	48.11	22.01	-
800	-	56.03	33.94	-
900	-	> 65	42.10	> 65

The grain sizes of TiO_2 determined from XRD for the samples calcined at various temperatures are summarized in Table 1. After hydrothermal treatment, the diameter of the TiO_2 particles increased slightly, from 5.48nm to 6.20nm. However, it is clearly observed that after conventional annealing, the hydrothermally treated TiO_2 presented smaller grain sizes than the untreated one. As seen in Fig. 1, rather uniform distribution of spherical shape particles were synthesized at 600 °C, and the grain size observed by SEM was consistent with XRD results. Moreover, the phases identified by XRD revealed that the hydrothermal process was able to suppress the anatase-to-rutile transformation. The rutile content calculated from XRD spectra is shown in Fig.2. Even at temperatures as high as 800°C, the rutile percentage was only 5%.

In order to study the electrical behaviour of the hydrothermally treated TiO_2, thick films were fabricated and the resistance was monitored under concentrations of CO gas at various operating temperatures. In particular, sensing behaviour of the materials calcined at 600 °C and 800 °C is shown in Figs. 3, 4 and 5. It is observed that the 600°C calcined material (13nm), which consisted of smaller crystalllites that the 800°C one (34nm) gave larger sensor response to CO, which could be attributed to grain size refinement. Both materials exhibited a quick response and recovery after CO exposure, as illustrated by the response transients in Fig. 5.

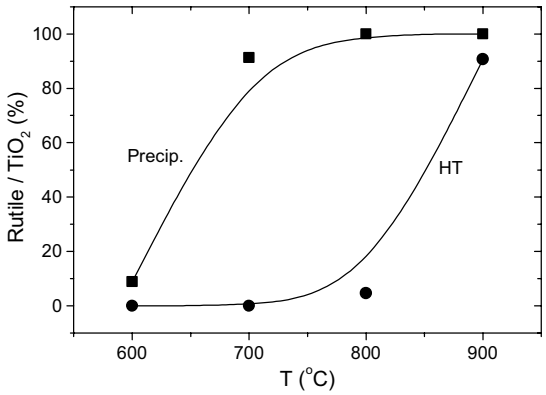

Fig. 2. Rutile percentage of as-precipitated gel (Precip.) and hydrothermally treated sol (HT) determined by XRD.

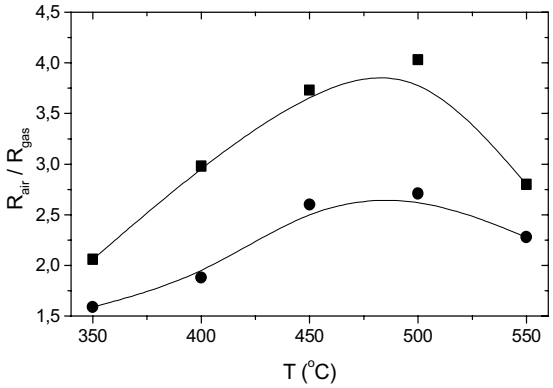

Fig. 3. Sensor response to 500 ppm CO for hydrothermally treated TiO_2 samples calcined at 600°C (■) and 800°C (●) as a function of operating temperature.

3 Conclusions

The hydrothermal treatment provides a method to prepare uniform, mono-dispersed nanocrystalline anatase with strong resistance to grain growth in later calcination processes. While the as-precipitated gel exhibited completely rutile phase at 800 °C, the hydrothermally treated sol preserved anatase phase stabilized up to 800 °C and the grain size was kept at 34 nm. At 600°C, the titania particles exhibited spherical shape with a grain size as small as 13 nm. This particular material showed a stable and enhanced sensitivity to CO at high working temperatures.

References

[1] A. Ruiz, G. Sakai, A. Cornet, K. Shimanoe, J. R. Morante, N. Yamazoe. *Cr-doped TiO_2 gas sensor for exhaust NO_2 monitoring.* Sens. Actuators B, in press.

[2] N.S. Baik, G. Sakai, K. Shimanoe, N. Miura, N. Yamazoe. Sens. Actuators B 65 (2000) 97-100.

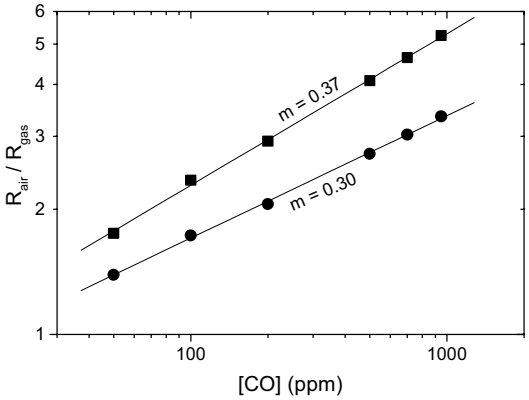

Fig. 4. Sensor response to different concentrations of CO at an operating temperature of 500°C for hydrothermally treated TiO_2 samples calcined at 600°C (■) and 800°C (●).

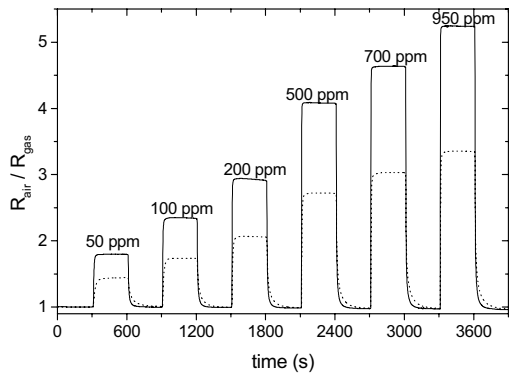

Fig. 5. Response transients to steps of CO at an operating temperature of 500 °C for hydrothermally treated TiO_2 samples calcined at 600°C (solid line) and 800°C (dot line).

Anomalous behaviour of α-Fe_2O_3-based thick film sensors studied by conductance and work function change measurements

A.Gurlo, M.Sahm, A.Oprea, N.Barsan, U.Weimar

Institute of Physical and Theoretical Chemistry, University of Tübingen, Auf der Morgenstelle 15, 72076 Tübingen, Germany, email: alexander.gurlo@ipc.uni-tuebingen.de

Summary: *Transition from p- to n- type response, induced by the change in the gas concentration and the operating temperature, was observed for α-Fe_2O_3-based semiconducting sensors. This phenomenon is due to the different contribution of surface electrons and holes in the overall conductivity, which leads for the predominating either p-type or n-type response.*

Keywords: *work function, indium oxide, iron oxide, carbon monoxide, ethanol, water*
Category: *5 (Chemical sensors)*

1 Introduction

Semiconductor oxides were classified according to the sign of the resistance change due to the exposure to reducing (H_2O, CO, EtOH) gases as *"n"*-type (resistance decreases, e.g. In_2O_3, ZnO, SnO_2) or *"p"*-type (resistance increases, e.g. Cr_2O_3, CuO) [1]. In some cases, the changing of the behaviour of the oxides, e.g. from *p*- to *n*- or the opposite were recorded for single (pure or differently doped) oxides [2-6] or for mixtures of *n*- and *p*- type oxides [7-9]. For the latter case the switching seems to be related to the dominating contribution of one of the material in the overall conductivity [7,9].

The explanation of the switching from one type to the other is a matter of debate; some authors attribute this phenomenon to different kind of surface reactions in different conditions (humidity, temperature, composition, etc..) [6,7,9], others to the change of surface type of conduction induced either by special ambient conditions (pure oxygen for long periods [3]) or additives (Rh clusters at the surface [5]).

In order to provide an explanation, in the present study simultaneous work function changes and conductance measurements were performed. We observed *p-n* switching for α-Fe_2O_3 based (alone or in combination with In_2O_3) thick film sensors, induced by changes in the gas concentration and the operating temperature. Choosing of In_2O_3 and α-Fe_2O_3 as sensing materials was basically determined by the fact, that for α-Fe_2O_3 contradicting results can be found in the literature concerning its conductivity, i.e. typically *n*-type conductivity for low temperatures and pure oxide and *p*-type for high temperatures and impure oxide are found [10]. In_2O_3 is a typical n-type oxide semiconductor.

2 Experimental

The thick film sensors based on the individual oxides (α-Fe_2O_3 and In_2O_3) and on the mixed oxides α-Fe_2O_3-In_2O_3 (Fe:In=1:9 and 9:1) prepared by screen printing of the corresponding oxide paste on alumina substrates were investigated by the conductivity measurements. Simultaneous conductivity (under constant voltage polarisation) and work function measurements were performed on the α-Fe_2O_3-In_2O_3, 9:1 sensor in a Kelvin probe (Mc Allister KP6500) set up. In the same ambient atmosphere the resistance of a Pd/SnO_2 sensor was measured as a reference.

3 Results and Discussion

3.1 Conductivity measurements

The main results can be summarized as follows:

- resistance in air increases in the order In_2O_3<α-Fe_2O_3-In_2O_3(1:9)< α-Fe_2O_3-In_2O_3(9:1)< α-Fe_2O_3;
- all the compositions show much higher response to EtOH and propanal than for CO;
- In_2O_3 and α-Fe_2O_3-In_2O_3(1:9) show typical *n*-type response both in dry and humid air in the temperature range 250-350°C; the resistance in the humid air is lower in comparison with the one in dry air,
- α-Fe_2O_3 and α-Fe_2O_3-In_2O_3(9:1) show transition from *p*- to *n*-type response depending on the operating temperature, humidity and gas concentration (Table 1, Fig. 1); the resistance in the humid air is higher in comparison with the one in dry air.

Table 1. Sign of the resistance change induced by the exposure of the ethanol vapour (*"+"* and "–" mean increase and decrease in the resistance of the sensor at 250°C.)

Sensor	R [MΩ]		EtOH			
			20 ppm		250 ppm	
RH, %	0	50	0	50	0	50
In_2O_3	2kΩ	1kΩ	–	–	–	–
α-Fe_2O_3-In_2O_3, 1:9	1	0.04	–	–	–	–
α-Fe_2O_3-In_2O_3, 9:1	25	45	+	–	–	–
α-Fe_2O_3	100	650	+	–	–	–

The obtained results clearly show, that for each analyte (ethanol, propanal, CO) one can find the conditions (e.g. operating temperature, humidity, concentration range, materials) in which the *p-n* switching is observed.

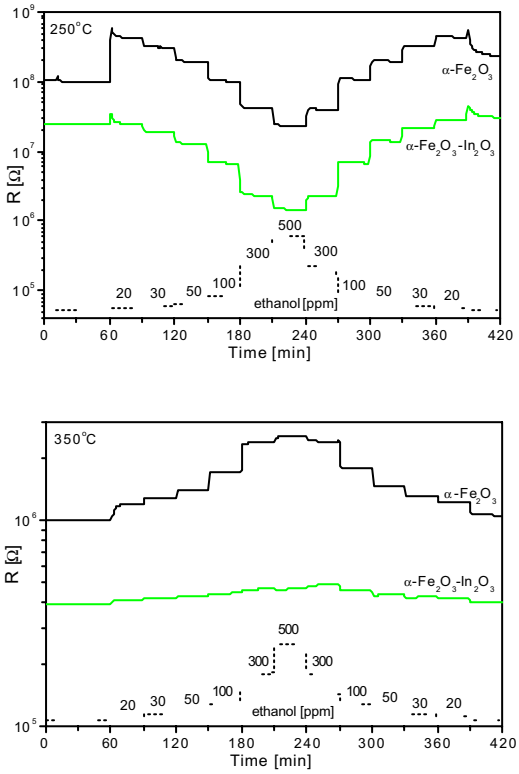

Fig. 1. Change of the sensor resistance under exposure to EtOH in dry air.

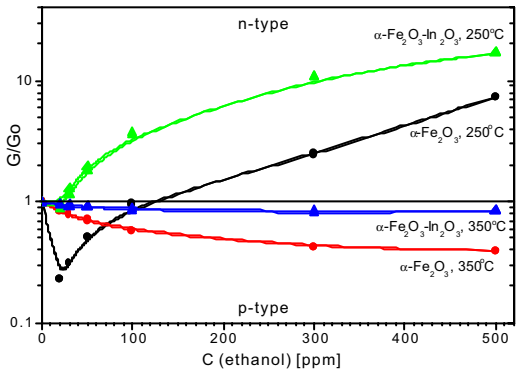

Fig. 2. Change of the relative sensor conductance as a function of EtOH concentration in dry air.

3.2 Simultaneous work function and conductivity measurements

In order to clarify the reasons for the *p*- to *n*-switch, work function measurements were also performed. At this moment the results obtained for the mixture α-Fe_2O_3-In_2O_3, 9:1, are available and presented in the abstract (Fig. 3). As one can see, exposure to two different reducing gases (CO and ethanol) are determining a decrease in the work function of the sensing material and this one increases with increasing gas concentration. With decreasing band bending the conductivity firstly decreases (region A to B), then reaches a minimum (point B) and afterwards increases (region B to C). Due to the fact that there is a monotonous decrease of the work function, one can state that there is no change in the gas reaction. Accordingly, the reason for the *p* to *n* type switch is electronic; in the absence of the reducing gases the surface band bending is such high that it determines a *p*-type conductivity at the surface of the iron oxide. During the exposure to reducing gases the band bending decreases and the same happens to the concentration of the dominant surface free charge carriers, namely the holes. Simultaneously the concentration of electrons increases and it determines a *n*-type conductivity. The situation is probably very similar to the ones described in [3, 10].

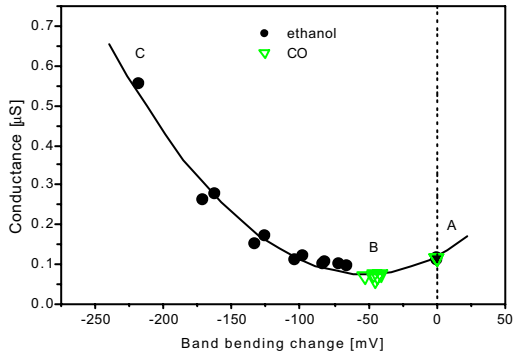

Fig. 3. The conductance of α-Fe_2O_3-In_2O_3(9:1) sensor as a function of the band bending change, determined by simultaneous work function and conductivity measurements at ≈300°C.

Conclusions

The obtained results indicate, that basically the same surface reaction with the gas is accompanied with different transducing of chemical change on the surface into bulk electrical signal. This allows the possibility to distinguish between these two contributions into overall sensor signal and describe the detection mechanism.

Acknowledgements

This work was supported in the frame of the GASMOH (ICA2-CT-2000-10041) project. The oxide powders were prepared in Istituto per la Microelettronica e i Microsistemi, IMM-CNR, Sezione di Lecce, Via Arnesano, 73100 Lecce, Italy.

References

[1] D.E.Williams. *Sensors and Actuators B* 57 (1999) 1-16.
[2] A.Bielanski, J.Deren, J.Haber. *Nature* 179 (1957) 668.
[3] N.Barsan, R.Grigorovici, R.Ionescu, M.Motronea, A.Vancu. *Thin Solid Films* 171 (1989) 53-63.
[4] A.A.Vasiliev, M.A.Polykarpov. *Sensors and Actuators B*7 (1992) 626-629.
[5] B.W.Licznerski, K.Nitsch, H.Teterycz, K.Wisniewski. *Sensors and Actuators B* 79 (2001) 157-162.
[6] G.Korotcenkov, V.Brinzari, A.Cerneavschi, V.Golovanov. *SGS'2002, Book of Abstracts,* 30.
[7] N.Savage, B.Chwieroth, A.Ginwalla, B.R.Patton, A.Akbar, P.K.Dutta. *Sensors and Actuators B* 79 (2001) 17-27.
[8] A.Gurlo, N.Barsan, U.Weimar, P.Siciliano, Y.Shimizu, M.Ivanovskaya, *E–MRS Spring Meeting*, 2003.
[9] V.Dusastre, D.E.Williams. *J.Mater.Chem.* 9 (1999) 965-971.
[10] R.F.G.Gardner, F.Sweet, D.W.Tanner. *J.Phys.Chem. Solids.* 24 (1963) 1175-1181.
[11] S.R.Morrison, *The Chemical Physics of Surfaces*, 2nd ed., Plenum Press, NY, 1990, p. 61-63.

A multisensor based on laser scanned silicon transducer (LSST): development and properties

Yu. Ermolenko[1], T. Yoshinobu[2], Yu. Mourzina[3], M.J. Schöning[3,4], Yu. Vlasov[1] and H. Iwasaki[2]

[1]Faculty of Chemistry, St. Petersburg State University, 199034, St. Petersburg
[2]Inst. of Scientific and Industrial Research, Osaka University, 8-1 Mihogaoka, Ibaraki, Osaka 567-0047, Japan
[3]Institute of Thin Films and Interfaces, Research Centre Jülich, 52425, Jülich, Germany
email: y.mourzina@fz-juelich.de http://www.fz-juelich.de
[4]University of Applied Sciences Aachen, Division Jülich, Ginsterweg 1, 52428, Jülich, Germany

Summary: *The multisensors with sectional membranes based on various lithium, calcium, and potassium ionophores with different selectivity have been developed based on laser scanned silicon transducer (LSST), where the response of the sensor can be scanned with a laser beam over the sensor surface. It has been demonstrated for the first time that by applying these multisensors (Li^+/K^+ and Ca^{2+}/K^+) as a multisensor system, the concentration zones for simultaneous determination of lithium, potassium, and calcium ions in complex solutions have been enlarged significantly. It has been shown that using such a multisensor system based on reversible ion-exchange processes and reproducible membrane potentials at the phase boundary membrane/solution, makes it possible to overcome the restricted selectivity in comparison with single sensors. The multisensor is suggested as a prototype of a new kind of a mutisensor system for chemical analysis.*

Keywords: *multi-sensor, laser scanned silicon transducer, multicomponent analysis*
Category: *5 (Chemical sensors) or 10 (Applications)*

1 Introduction

Multisensors that are capable of measuring concentrations of more than one chemical species are not only convenient, but are essential in (bio-)chemical analysis, environmental monitoring and medicine. Semiconductor transducers are advantageous for the construction of multisensor devices, since they offer the benefits of miniaturization by the microfabrication processes already at hand.

In this study, we elaborated the multi-sensors for simultaneous measurement of concentrations of various ions (Li^+/K^+ and Ca^{2+}/K^+) in multicomponent solutions. The multisensors developed are based on the laser scanned semiconductor transducer (LSST) [1,2] functionalized with polymeric membranes containing ionophores. For processing multidimentional data from multisensors, artificial neural network (ANN) was employed.

The first aim of the present investigation was to create a multisensor system (MSS) as a single multisensor based on membranes with reversibility with regard to the ionic exchange at the interface membrane/solution and on the equilibrium and stable electrode potentials of MSS in complex solutions. The second aim was to demonstrate the possibilities of the elaborated MSSs to overcome the selectivity restrictions, which exist for individual sensors.

2 Elaboration of a multisensor based on LSST

The cross-section of the multisensor system based on the LSST, and the measuring cell with the multisensor with a four-sectional membrane are schematically presented on Fig. 1.

For the sensor fabrication, $Si/SiO_2/Si_3N_4$ (SCHEM^{TM} sensors, Horiba) plates were used as substrates.

We found that the development of the hybrid multi-sensor required: 1) hydrophobization of the Si_3N_4 surface layer by means of chlorosilane, 2) decreasing the conventional ratio of PVC-plasticizer by 2 times for depressing the intrinsic pH sensitivity of the sensor, 3) introducing up to 3 to 5 wt. % of ionophores and about 50 mol. % (relative to ionophore) of lipophilic additives.

Specially elaborated ion-sensitive membrane compositions based on potassium ionophores valinomycin and bis(benzo-15-crown-5), lithium ionophores Li-III (N,N-Dicyclohexyl-N',N'-diisobutyl-cis-cyclohexane-1,2-dicarbamide) and Li-VI (6,6-Dibenzyl-14-crown-4), and calcium ionophore t-HDOPP-Ca were deposited on a silanized surface of a $Si/SiO_2/Si_3N_4$ transducer. The boundary frames (Fig. 1b) were prepared with a mixture of PVC-plastisizer (50:50 wt. %).

3 Characteristics of the individual sensor elements

The optimised sensors were characterised in the solutions of primary ions (K^+, Li^+, or Ca^{2+}), when

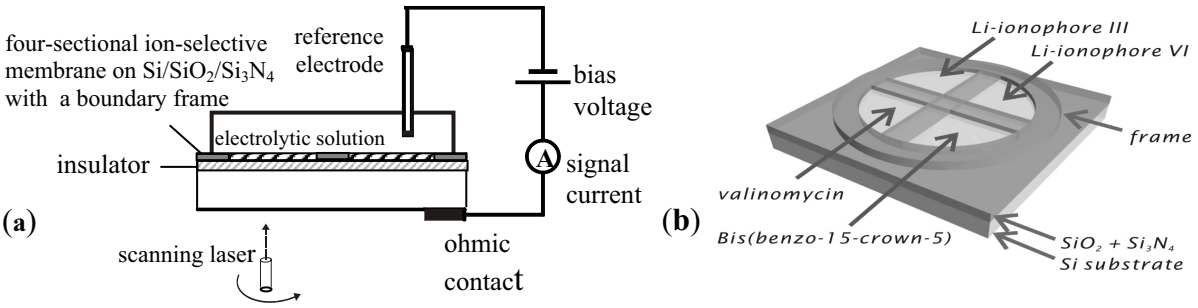

Fig. 1. Schematic representation of (a) - the cross-section of the multisensor system based on the laser-scanned semiconductor transducer (LSST); (b) - the measuring cell with the multisensor with the four-sectional membrane.

addressing the K^+-, Li^+-, or Ca^{2+} -sensitive membrane sections, respectively, with a laser beam. For example, for the K^+/Ca^{2+} double sensor, the sensitivity was found to be 57±1 mV/pK and 27±1 mV/pCa in the concentration ranges from 10^{-5} to 10^{-1} mol l^{-1}.

To define the regions of the concentration ratio of primary ions, where the determination of these ions by means of a single sensor is inaccurate or not possible because of the insufficient selectivity of the sensors, we paid special attention to the determination of the selectivity coefficients ($K_{K/Li}$, $K_{Li/K}$; and $K_{K/Ca}$, $K_{Ca/K}$) of each membrane section (each ionophore) in a wide range of concentrations of the interfering ion.

4 The concept of the multisensor system

More than one membrane can be integrated on the sensor surface of LSST. Fig. 1b shows an example of a four-in-one multisensor, in which four membranes are integrated on a 17x17 mm^2 surface of n-$Si/SiO_2/Si_3N_4$ transducer. The sections are sequentially illuminated with an infrared laser beam for measurements. This multisensor has been successfully applied for the analysis of multicomponent solutions. An ANN was employed to compensate for the influence of interfering ion.

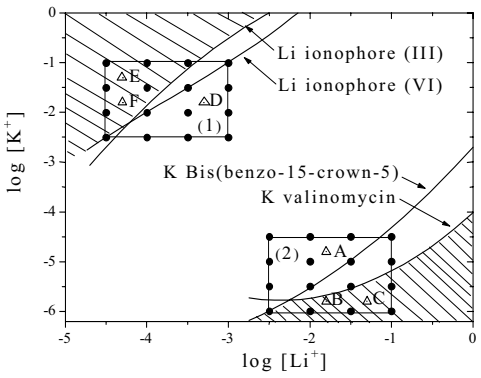

Fig. 2. The areas of using laser scanned MSS for the analysis of mixed Li-K solutions. The curves in figure show the Li-K concentration pairs, which equally influence the potential of each membrane section (the curves were built using the data on the selectivity of each membrane section).

Based on the selectivity data obtained, we selected concentration zones, e.g., areas 1 and 2 in Fig. 2, of the mixed (Li and K) solutions for testing the multisensor as a MSS. It should be emphasized that in the shaded zones, determination of the concentrations by means of each of the individual sensors is inaccurate or fails because of the restricted selectivity. The groups of points (•) mark the zones, where the MSS was used for the measurements in two-component solutions. The data of these measurements were used for training ANN and building a calibration model. Points (Δ) A - E mark the concentrations of the test solutions, which were analysed by means of the laser scanned MSS and the calibration model. The results of multicomponent analysis will be presented. The accuracy of the determination of the concentrations of Li^+ and K^+ with a Li^+/K^+ multisensor in solutions containing both ions in different concentration ratios (K-rich and Li-rich solutions) was found to be 10 to 20 %. The elaborated multi-sensor is proposed as a prototype of a new sort of multi-sensor system for chemical analysis. Using this new kind of multisensor based on LSST allows to enlarge the concentration ranges for simultaneous determination of ions in complex solutions.

Acknowledgement

The author gratefully acknowledge the support from Russian Fund for Basic Researches (no.02-03-32740), Postdoc Grant from Russian Ministry of Education and Administration of St. Petersburg (no. PD 02-1.3-461), Fund of the Ministry of Russian Federation on fundamental researches in the field of natural and exact sciences (no. E02-5.0-85), Ministry of Education, Culture, Sports, Science and Technology of Japan, Grant-in-Aid for Scientific Research (contract no. 14550791), and from the Foundation for Biomedical Research and Innovation, Kobe, Japan.

References

[1] D.G. Hafeman, J. W. Parce and H.M. McConnel. Light-addressable potentiometric sensor for biochemical systems. *Science* 240 (1988) 1182-1185.

[2] Yu. Ermolenko, T. Yoshinobu, Yu. Mourzina, K. Furuichi, M.J. Schöning, Yu. Vlasov and H. Iwasaki. The double K^+/Ca^{2+} sensor based on laser scanned silicon transducer (LSST) for multi-component analysis, *Talanta* 59 (2003) 785-795.

An impedance effect of an ion-sensitive membrane: Characterisation of an EMIS sensor by impedance spectroscopy, capacitance-voltage and constant-capacitance method

A. Poghossian[1], Th. Mai[2], Yu. Mourzina[1], M.J. Schöning[1,2]

[1]Institute of Thin Films and Interfaces, Research Centre Jülich, D-52425, Jülich, Germany
email: a.poghossian@fz-juelich.de
[2]University of Applied Sciences Aachen, Division Jülich, Ginsterweg 1, D-52428, Jülich, Germany

Summary: *An impedance effect of a membrane on the characteristics of a capacitive EMIS (electrolyte-membrane-insulator-semiconductor) sensor has been investigated using a K^+-sensitive EMIS sensor as a model system. The sensor utilises a valinomycin-containing PVC membrane with different contents of plasticizer. The developed EMIS sensor has been characterised by impedance spectroscopy, capacitance-voltage and constant-capacitance method. It is shown, that an improvement of the accuracy of the measurements can be achieved by means of correction of the capacitance-voltage curves using preliminary defined values of the membrane resistance and capacitance as well as by choosing an optimal working frequency range. The sensors' behaviour in terms of ion-sensitivity, stability, hysteresis, linear concentration range, detection limit and response time have been investigated.*

Keywords: *capacitive (bio-)chemical sensor, K^+-sensitive EMIS structure, impedance spectroscopy, capacitance-voltage, constant- capacitance mode*
Category: *5*

1 Introduction

(Bio-)chemical sensors based on the principle of the field-effect in semiconductor structures such as an ISFET (ion-sensitive field-effect transistor) or LAPS (light-addressable potentiometric sensor) have been extensively studied in recent years for both acidification and extracellular ion-concentration detection and cell potential measurement (see, e.g. recent reviews [1,2]). The third type of a semiconductor field-effect sensor – an EIS (electrolyte-insulator-semiconductor) capacitive sensor combines some advantages of the LAPS (a complete flatness, a simple layout, the easy and low cost fabrication) and the ISFET (the absence of a light source, the possibility of miniaturization), and thus, could also be very attractive for cellular applications, in particular, for the acidification and extracellular ion-concentration detection.

Being in its basic structure as a pH-sensitive sensor, the EIS sensors sensitive towards other ions or analytes are often constructed by deposition of an additional membrane containing subsequent chemical or biological recognition elements (so-called EMIS (electrolyte-membrane-insulator-semiconductor sensor)). An impedance effect of this additional membrane is not always negligible resulting to unusual capacitance/voltage curves and consequently, to inaccurate measurements.

In this work, the impedance effect of the membrane on the characteristics of the capacitive EMIS sensor has been investigated using a K^+-sensitive EMIS sensor with a valinomycin-containing PVC-based membrane as a model system. Therefore, the developed EMIS sensor has been characterised by impedance spectroscopy, capacitance-voltage (C/V) and constant capacitance (ConCap) method. An optimal working frequency range has been found for the correct C/V and ConCap measurements using preliminary evaluated values of the membrane resistance and capacitance. With the aim of future application for extracellular potassium-ion concentration measurements, the sensors' behaviour in terms of ion-sensitivity, stability, hysteresis, linear concentration range and detection limit have also been tested in a physiological buffer solution. The effect of PVC/plasticizer ratio in the membrane on the sensor behaviour is discussed, too.

2 Experimental

The K^+-sensitive EMIS sensors have been prepared by depositing of the valinomycin-containing PVC membranes (with a thickness of ~10 μm) onto the Si-SiO_2-Si_3N_4 structures (p-Si, ρ=5-10 Ωcm, 30 nm SiO_2, 50 nm LPCVD Si_3N_4). Two membrane compositions with PVC/plasticizer ratio of 1:2 (C1) and 1:1 (C2) have been tested. In order to improve the adhesion of the ion-sensitive membrane as well as to suppress the intrinsic pH sensitivity of the transducer surface, prior to the membrane deposition, the surface of the Si_3N_4 was silanised by means of treatment in 5% solution of chlortrimethylsilane in hexane. The sensors have been characterised in solutions with different

content of KCl from 10^{-5} M up to 10^{-1} M by impedance spectroscopy (in accumulation, depletion and inversion ranges), C/V and ConCap method in a frequency range of 0.1 Hz-1 MHz, 20 Hz-1 MHz and 100-180 Hz, respectively.

3 Results and discussion

Fig. 1(a) shows the impedance spectra in the accumulation range for the developed K^+-sensitive EMIS sensor with membrane composition C2 in a 10^{-3} M KCl solution. For comparison, the impedance spectra of the EIS sensor without the ion-sensitive membrane is presented, too. As it could be expected, the addition of the ion-sensitive membrane shifts the impedance curve to a low frequency range. For the EMIS sensor, a linear behaviour is observed at frequencies above 2-3 kHz, which bends over to a plateau of constant impedance at lower frequencies (<1 kHz). Such a behaviour of the impedance curve can be assigned to the bulk resistance (R_M) and capacitance (C_M) of the ion-sensitive membrane in parallel [3]. At very low frequencies (<10 Hz) the membrane impedance is lower, thus making the impedance of the Si_3N_4-SiO_2-Si structure more significant.

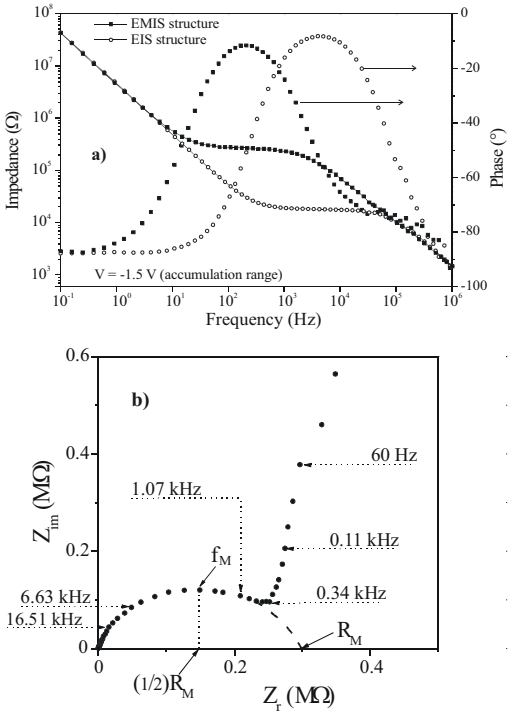

Fig. 1. Impedance spectra of the EMIS and EIS sensors (a) and Nyquist plot for EMIS sensor (b).

Fig. 1(b) shows a Nyquist plot for the same EMIS sensor, from which the characteristic frequency of the ion-sensitive membrane (f_M=2.1 kHz), the membrane resistance (R_M=300 kΩ), capacitance (C_M=0.25 nF) and thickness (~9 μm) have been evaluated.

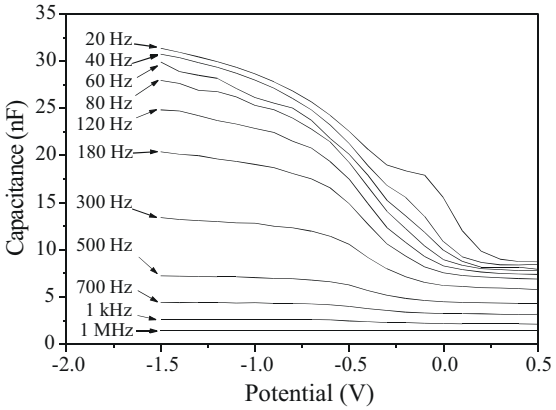

Fig. 2. Frequency dependance of the C/V curves for the EMIS sensor.

Fig. 2 shows the C/V curves of the EMIS sensor as a function of frequency. A typical C/V response only results when the frequency is lower than 500-600 Hz. This frequency range corresponds very well to the impedance response that lies in the rapidly rising vertical part of the Nyquist diagram (Fig. 1b). At high frequencies (>1 kHz) the curves are strongly deformed yielding to practically flat curves. Therefore, to avoid any correction in the measured results, consequently it is necessary to choose a sufficiently low frequency range for the C/V measurements. Nevertheless, at too low frequencies (<40-60 Hz) unusual C/V curves (a second plateau at 20 Hz) are observed again that can be probably attributed to slow surface states in the semiconductor. Thus, by given values of the membrane resitance and capacitance, the choice of an optimal working frequency range may be of critical importance when testing the EMIS sensors. Therefore, the further C/V and ConCap characterization of the developed EMIS sensors in terms of sensitivity, stability, hysteresis, linear concentration range, detection limit and life time have been performed at the chosen optimal frequency range of 100-180 Hz. The better working characteristics (sensitivity: 53±2 mV/pK; linear range: $2\cdot10^{-5}$-10^{-1} M; detection limit: $5\cdot10^{-6}$ M; hysteresis: 2 mV; response time: 5-12 s; lifetime: >6 months) have been obtained for the sensor with membrane composition C2. Details of experiments and results will be presented and discussed at the conference.

References

[1] M.J. Schöning and A. Poghossian. *Analyst* 127 (2002) 1137-1151.

[2] F. Hafner. *Biosens. Bioelectron.* 15 (2000) 149-158.

[3] A. Demoz, E.M.J. Verpoorte and D.J. Harrison. *J. Electroanal. Chem.* 389 (1995) 71-78.

New concepts of miniaturised reference electrodes in silicon technology for potentiometric sensor systems

Anette Simonis[1,2], Hans Lüth[2], Joseph Wang[3], Michael J. Schoening[1,2]

[1]University of Applied Sciences Aachen, Ginsterweg 1, 52428 Juelich, Germany, m.j.schoening@fz-juelich.de
[2]Institute of Thin Films and Interfaces, Research Centre Juelich GmbH, 52425 Juelich, Germany
[3]New Mexico State University, Las Cruces, NM 88003-8001, USA

Summary: *Two different types of reference electrodes have been realised by means of thick-film technique and thin-film technique (pulsed laser deposition (PLD), electron-beam evaporation/chlorination). For inner electrolyte, KCl-containing membranes have been deposited and different coatings have been used to protect the reference electrode from a fast leaching out of KCl. The reference electrodes realised by means of thick- and thin-film technique were stable during a period of more than two months. The averaged drift during a typical measurement time of 10 hours was less than 0.1 mV/h for the thick-film reference electrodes with cellulose nitrate (CN) as protective coating. The averaged drift rate of the thin-film reference electrodes was about 0.3 mV/h. The thick-film reference electrode was combined with a thin-film pH sensor together on one chip. The characteristics of the "one-chip" sensor were investigated in the capacitance/voltage (C/V) and constant capacitance (ConCap) mode.*

Keywords: *reference electrode, pH sensor, one-chip, thick-film technique, thin-film technique*
Category: *5 (Chemical sensors)*

1 Introduction

In the last years, a considerable interest has been taken place in the development of potentiometric sensors for a variety of chemical and biological analytes in aqueous solutions [1]. The use of semiconductor-compatible fabrication techniques offers features, like low-cost fabrication and miniaturisation, but up to now the missing integrated reference electrode formed an obstacle for an early commercialisation. A lot of appendages to realise reference electrodes in silicon planar technology have been published [2], but they suffer from the drawback of instability of the potential and a high cross-sensitivity towards anionic ions. Therefore, in this work two different types of reference electrodes have been fabricated and characterised with regard to the long-term stability and their not desired cross-sensitivity towards H^+- and Cl^--ions. The reference electrodes, fabricated by means of thick-film technique have shown the best features. Therefore, a thick-film reference electrode has been integrated together with a thin-film pH sensor on one chip.

Characterisation of miniaturised reference electrodes

A schematical view of the structure of the reference electrodes is given in Fig. 1.

To realise the miniaturised reference electrodes, in a first step the Ag/AgCl layer was brought up onto the silicon substrate. Three different deposition methods have been used:

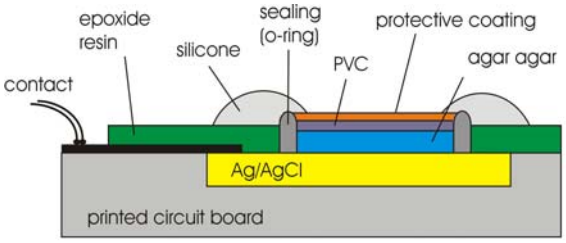

reference element (Ag/AgCl):
- evaporation/chlorination
- PLD (additional Ag_2S)
- thick-film technique

protective coating:
- nafion (N)
- cellulose nitrate (CN)

Ag/AgCl	membrane	protective coating
evaporation/chlorination	agar agar	PVC/CN
evaporation/chlorination	agar agar	PVC/N
PLD	agar agar	PVC/CN
PLD	agar agar	PVC/N
thick-film technique	agar agar	PVC/CN
thick-film technique	agar agar	PVC/N

Fig. 1: Cross section of the miniaturised reference electrode. The table gives an overview of the combinations of the Ag/AgCl, the membrane and the protective coating.

I) The Ag/AgCl ink was screen-printed onto the silicon substrate (thick-film technique).
II) A composition of 35% AgCl and 65% Ag_2S was deposited by means of PLD.
III) Ag was deposited by means of electron-beam evaporation and then, a part of Ag was chlorinated to AgCl.

In a second step, the KCl-containing agar agar membrane and a PVC/N or PVC/CN protective layer were fixed on the Ag/AgCl layer, respectively.

The reference electrodes were characterised with regard to the reproducibility of the start potential and the drift of the potential during a measurement time of 10 hours. The potential of the miniaturised reference electrode was recorded against a conventional reference electrode in Titrisol buffer, pH 7, without KCl. In Fig. 2, the drift of the potential of two thick-film reference electrodes with protective coating of PVC/CN is demonstrated over a measuring period of

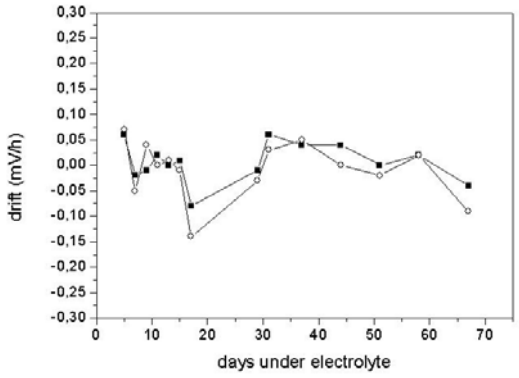

Fig. 2: Drift of the potential of two thick-film reference electrodes. Each measurement point corresponds to the average drift rate of the reference for 10 hours. CN was used as protective coating.

70 days. The averaged drift during a measurement period of more than two months was less than 0.1 mV/h. The maximum difference in the start potentials was found to be less than 4 mV. Thick-film reference electrodes with a protective coating or PVC/N had drift rates of 0.1 to 0.3 mV/h and the difference in the start potential was up to 17 mV. In general the drift rate and the maximum difference in the start potential of thin-film reference electrodes is larger than the results of thick-film electrodes. In contrast, for thin-film reference electrodes with Ag/AgCl, fabricated by means of evaporation/chlorination and a protective coating of PVC/CN, the drift rate was about 0.3 mV/h. To investigate the influence of the concentration of the chloride ions, the reference electrodes have been tested in KCl solutions in the concentration range from 10^{-4} mol/l to 10^{-1} mol/l. Independent of the fabrication method of the Ag/AgCl layer, using PVC/CN as protective coating, a potential maximum difference of about 4 mV was observed. Using PVC/N, the shift of the potential was about 20 mV.

Thin-film pH sensor and thick-film reference electrode on one chip

Since the most stable characteristics in terms of drift behaviour, cross-sensitivity and long-term stability have been found for the thick-film reference electrode, this type has been used in an integrated potentiometric sensor system. As result, an "one-chip" sensor has been fabricated that allows to miniaturise the reference electrode together with a pH sensor chip (see Fig. 3). To avoid an influence of a parasitic capacitance, the Ag/AgCl ink was deposited on the additional thick SiO_2 layer (1.35 µm), prepared by means of plasma-enhanced chemical vapour deposition.

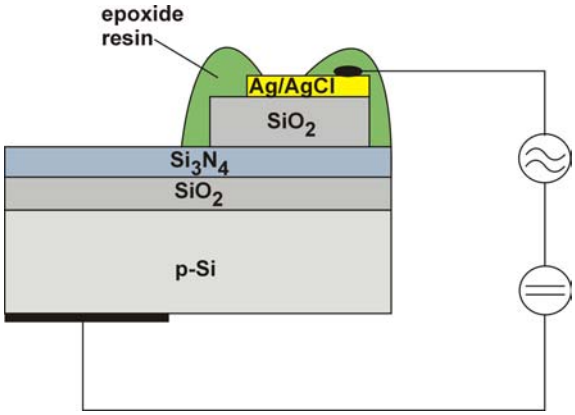

Fig. 3: Cross section of the "one-chip" sensor consisting of a thin-film pH sensor and a thick-film reference electrode.

The "one-chip" pH sensor has been characterised by C/V and ConCap methods in the pH range between pH 7 and pH 5 (Titrisol buffer). The C/V curves were comparable to those measured with a conventional reference electrode. The ConCap curves show a clearly dependence of the potential towards the pH values with a nearly Nernstian sensitivity. Details of the experiments and measurements will be presented at the conference.

Acknowledgements

The authors thank the State Ministry of Nordrhein-Westfalen (Germany) for financial support.

References

[1] K. Cammann, U. Lemke, A. Rohen, J. Sander, H. Wilken, and B. Winter. Chemo- und Biosensoren - Grundlagen und Anwendungen. *Angewandte Chemie.* 103 (1991) 519-541.

[2] H. Kaden, W. Vonau. Reference electrodes for electrochemical measurements. *Journal für praktische Chemie, Chemiker-Zeitung.* 340 (1998) 710-721.

One-electrode gas sensors on the base of In_2O_3-doped ceramics

G. Korotcenkov[1], I. Boris[1], V. Brinzari[1], Yu. Lychkovsky[2], G. Karkotsky[2], V. Golovanov[3], A.Cornet[4], E.Rossinyol[4]

[1]Lab. of Micro- and Optoelectronics, Technical University of Moldova,
Bld. Stefan cel Mare, 168, Chisinau, 2004, Moldova, E-mail: koro@ch.moldpac.md
[2]INNOVATSENSOR, Ltd, Minsk, Belarus,
[3]South-Ukrainian University, Odessa, Ukraine
[4]University of Barcelona, Barcelona, Spain

Summary: *Gas sensing characteristics of one-electrode sensors on the base of In_2O_3 doped ceramics are discussed in this report. In_2O_3-based ceramic with such doping elements as Cu, Zn, B, Al, Ga, P, Bi, Cr, Mn, Fe, Co, and Ni (1-10 weights %) was prepared by sol-gel technology. It was shown that doping by Cu, Ga, Zn increases gas response to CO and H_2. Addition of Cu, P and Mn improve selectivity of these sensors during detection of H_2 and CH_4.*

Keywords*: In_2O_3; one-electrode sensor; doping; gas response*
Category: *5 (Chemical sensors)*

1 Introduction

Among various single-metal oxides In_2O_3 appeared to be rather attractive in a view of sensitivity to carbon monoxide and methane. However, the utilizing of undoped In_2O_3 for the detection of CO, H_2, CH_4 in the presence of other gases is so far limited. It has been shown elsewhere that In_2O_3-based sensors fabricated as one-electrode sensors, where a platinum wire spiral is embedded inside a sintered In_2O_3 ceramic button featured by a low power consumption, fast response time and small deviation of initial parameters [1].

Aiming at improving a selectivity and sensitivity of the one-electrode semiconductor sensors, the In_2O_3 ceramic was modified by loading of different dopants, including oxides of III group elements and transient metals.

2 Experiment

Studied one-electrode In_2O_3-based gas sensors had structure shown in Fig.1. They were manufactured using technology described in [1].

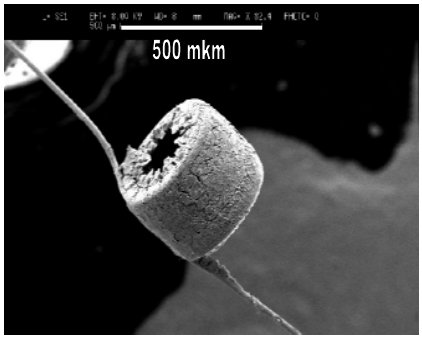

Fig. 1. The view of one- electrode gas sensor

In_2O_3-based ceramic was prepared by sol-gel technology. The concentration of an impurity input in solution for obtaining In_2O_3 powders estimated in recalculation on oxide was equaled 1-10 weight %. Such elements as Cu, Zn, B, Al, Ga, P, Bi, Cr, Mn, Fe, Co, and Ni were used as doping impurities.

Structure, morphology and the element composition of ceramics were controlled by a SEM method with a capability X-ray analysis. For these purposes we have used the scanning electronic microscopes Jeol JSM840 and Stereoscan JS360 Cambridge Instruments.

Gas sensing characteristics were measured in steady state mode using flow type reactor. CO (0.2 %), H_2 (0,1 %), CH_4 (0,5 %) relating to the reducing gases and ozone (~1ppm) were used as tested gases. The air humidity during measurements was supported at a level 35-40%RH or ~1-3%RH. During measurements such gas sensing parameters as absolute (Δ U) and relative ($\Delta U/U$) gas response, where ΔU- the change of voltage drop on the sensor at replacement of ambient atmosphere, were controlled. The electrical power dissipated by the sensor was used as a main parameter characterizing the operating temperature of one-electrode sensor.

The following measurements were conducted during these experiments:

- influencing of doping on conductivity and structure of In_2O_3-based ceramic;
- influencing of doping on gas response and speed of response;
- influencing of doping on selectivity of gas response;
- influencing of doping on sensitivity of gas sensing characteristics to air humidity.

3 Results and Discussions

The testing of In_2O_3-based GS in transient mode has shown that they have a good gas response. In most cases even at disseminated electrical power 60-70 mW, that corresponds to temperature in an active zone equaled 200-250°C, response time did not exceed 60 sec, and recovery time did not exceed 3 min. At the optimum operation conditions τ_{rec} and τ_{res} did not exceed 10-15 sec independently of a type of doping element in In_2O_3-based matrix.

The influencing of doping on gas response is shiwn in Fg.2. The improvement of gas response of In_2O_3-based ceramic containing second oxide at a level 2-4 weights% is observed only for elements I (Cu), II (Zn), and specially III (B, Ga) groups. Thus, the increase of concentration of a doping element is always accompanied by decrease of gas response.

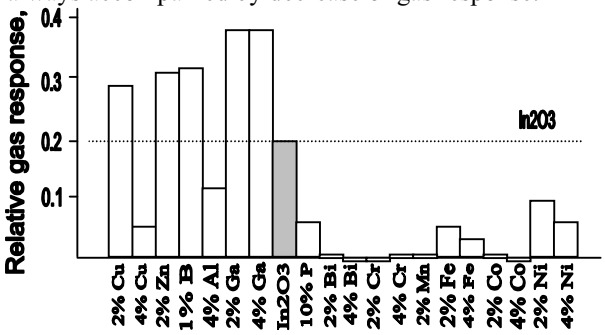

Fig.2. Influence of In_2O_3 doping on gas response to CO

The important point in our analysis is that the influence of doping elements on gas sensing properties of one-electrode In_2O_3-based gas sensor does not coincide with catalytic activity of these additives [2] (Fig.3). We believe that effect of gas sensitivity improvement is a result of structural optimization of studied In_2O_3-based ceramic.

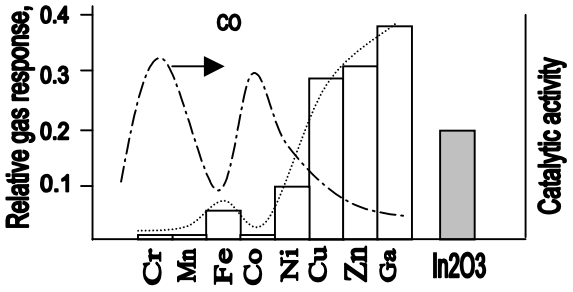

Fig. 3. Gas response of In_2O_3 doped GS to CO and catalytic activity of transition metals

The influence of doping on selectivity of gas response is shown in Fig.4. The gas selectivity was calculated as a ratio of maximum gas response to separated gases.

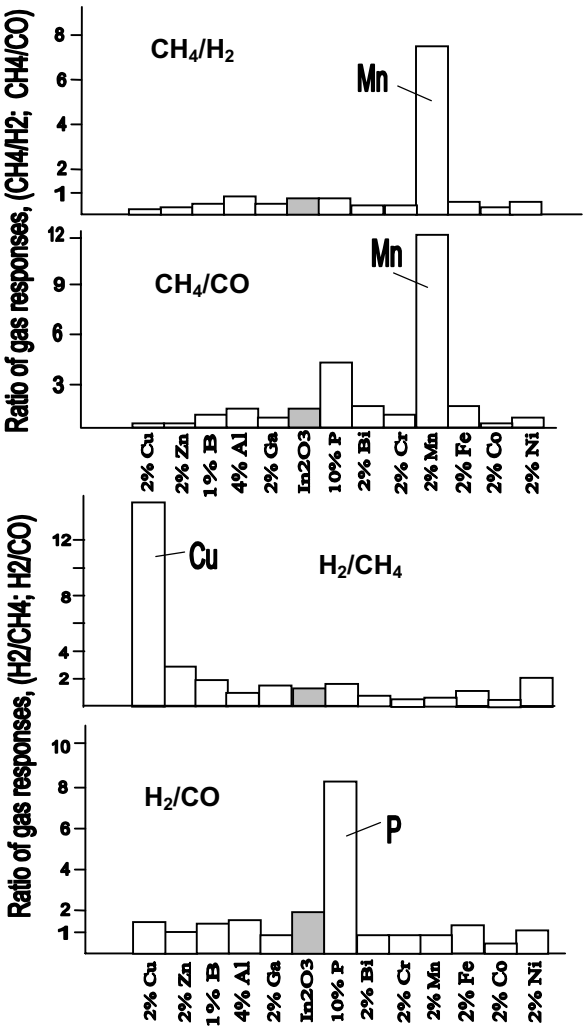

Fig.4 Influencing of In_2O_3 doping on selectivity of gas response to H_2 and CH_4

It was determined that the introducing of separate doping elements in In_2O_3-based matrix can essentially improve this parameter. For example at the doping by Cu In_2O_3 gas sensor starts showing good selectivity to H_2 detection in atmosphere containing CH_4. Doping by phosphor improves selective detection of both H_2 and CH_4 in atmosphere containing CO. Introducing in In_2O_3-based ceramic both Cu and P depresses sensitivity to ozone.

Addition of Zn and Ga in In_2O_3 ceramic provide maximum increase of gas response (Fig.2). However, this doping do not promote the selectivity improvement of In_2O_3-based gas sensor

References

[1]. S.N. Malchenko Y.N. Lychkovski and M.V. Baykov, *Sensors and Actuators* **B 7** (1992) 505.

[2]. O.V.Krilov, V.F.Kisilev, Adsorption and catalysis on transition metals and theirs oxides, Moscow, Chemistry, 1981, 288 pp. (in Russian)

Ozone poisonous effect and regeneration of pseudo Schottky Pd-InP gas based sensor

L. Mazet, C. Varenne, A. Pauly, J. Brunet, J.P. Germain

Université Blaise Pascal, Clermont-Ferrand II, 24 avenue des Landais 63177 Aubière Cedex, France
email: mazet@lasmea.univ-bpclermont.fr

Summary: *This article deals with Pseudo Schottky diode based gas sensor made with palladium metallization. Such layer permits catalytic dissociation on two powerful oxidizing gas, nitrogen dioxide and ozone, constituting main urban atmospheric pollution. After many O_3 submissions, degradation of gas sensor parameters appears, probably due to ozone poisonous effect on palladium. H_2 reduction and ultra high vacuum treatment of metallization layer allows us to find again initial response and recovery time and to increase sensor sensitivity. Such regeneration will permit to have reproducible measurements of low NO_2 and O_3 concentrations.*

Keywords: *gas sensor, Schottky diode, regeneration*
Category: *5 (Chemical sensors)*

1 Introduction

In industrialized countries, air quality monitoring has become a priority since atmospheric pollutants have been identified for their noxious effects on human health and vegetation. Among all the pollutants, it's now of great interest to measure two powerful oxidizing gases: nitrogen dioxide (NO_2) and ozone (O_3). As existing monitoring techniques need bulky and expensive apparatus, it's very difficult for air pollution monitoring society to achieve a dense mapping of pollution evolution. To extent the number of monitoring location, low costs reliable and selective solid state semi conductor gas sensor are necessary.

2 Experiments

In this paper, we present an original device grown on p type Indium Phosphide (InP-p) which have a Schottky structure with a thin semiconductor gas sensitive layer between the rectifying contact and the bulk substrate. Schottky contact metallization is realized with a noble metal (Pd). The devices are made by successive evaporations of metallic thin layers on InP-p bulk substrate with a contact scheme consisting in Pd/Ge/Pd/InP-p. Annealing process at 320°C make Ge to diffuse at the InP metal interface creating a thin n type InP layer sensitive to oxidizing gas. Using such monocristalline based structure allows to avoid, for a part, the reproducibility problems occurring with gas sensors made with polycrystalline or molecular materials.

Pseudo Schottky diode is mounted on a heating substrate. Measurements are done by recording current variation of the structure under a fixed bias voltage of 1Vdc. Then the sensor is submitted to different NO_2 and O_3 concentrations (20, 50, 80, 100 ppb diluted in purified air) with varying operating temperature (40, 60, 80, 100, 120°C) to determine the best working conditions. As sensitivity decreases and the response time becomes shorter when the operating temperature increases, an optimum temperature of 100°C have been chosen for other experiments. Table 1 lists the main parameters (response, response time and recovery time) for NO_2 and O_3 concentrations at a temperature of 100°C. Let us notice that the sensor give reproducible results when it's only submitted to NO_2 specie.

Table 1. Response ($\Delta I/I_0$), response time and recovery time (in hour) of Pseudo Schottky diode at 100°C for different NO_2 and O_3 concentrations (in ppb).

NO_2 (ppb)	20	50	80	100
Response	0.15	0.24	0.30	0.33
Response time (hour)	0.4	0.4	0.4	0.4
Recovery time (hour)	0.8	0.8	0.8	0.8
O_3 (ppb)	20	50	80	100
Response	0.16	0.19	0.20	0.21
Response time (hour)	0.37	0.37	0.37	0.35
Recovery time (hour)	1.42	1.42	1.44	1.45

The catalytic properties of palladium on NO_2 and O_3 have been investigated. Some studies based on HREELS and TPD spectra concerning NO_2 adsorption on palladium surfaces have shown that NO_2 is chemisorbed molecularly at 110K [1]. Decomposition into NO (a) and O (a) is observed upon heating to 180K and thus a competitive process occurs between decomposition and desorption of NO_2 specie.

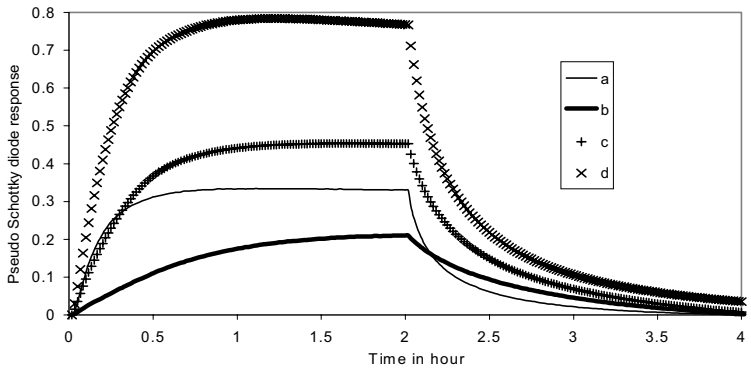

Fig. 1. sensor response with 100 ppb of NO_2 at 100°C (a) initial structure (b) after O_3 submission (c) after H_2 treatment (d) after ultra high vacuum treatment.

For O_3, which is a more reactive oxidant than NO_2 because of its very weak O-O bond, palladium demonstrates the highest conversion efficiency among many catalysts (Pt, Ni...) [2]. To explain the mechanism of O_3 and NO_2 decomposition, some reactions are suggested [3]:

For O_3: $O_3 + * \rightarrow O^* + O_2$

For NO_2: $NO_2 + 2^* \rightarrow O^* + NO^*$

And $2\ O^* \rightarrow O_2 + 2^*$

In the last reaction two oxygen atoms can produce oxygen molecule; * represents surface species and no assumption were made about the nature of active sites.

For our pseudo Schottky gas sensor, after many O_3 submissions we can see a degradation of gas sensor parameters: for NO_2 detection on figure 1, response and recovery time rise up and the sensitivity falls; for O_3, on figure 2, only the sensitivity is affected. Such degradations can be interpreted as ozone poisonous effect on palladium metallization. We assume O_3 decomposition induced strong Pd-O bond at the palladium surface which decrease the number of surface active sites.

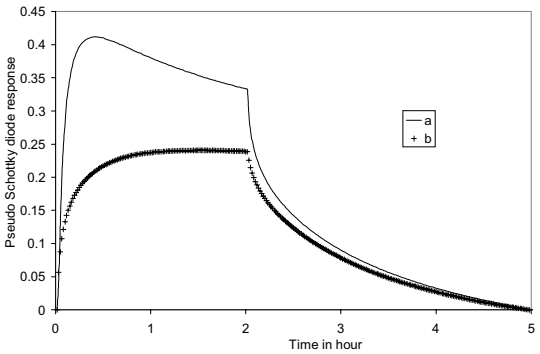

Fig. 2. sensor response with 100 ppb of O_3 at 100°C (a) initial structure (b) after O_3 submission.

To reduce this ozone poisonous effect, the sensor was submitted to H_2 at 180°C for 15 minutes. After this treatment, the sensor was tested with 100 ppb of NO_2. We can observe on figure 1 that the sensitivity rises up and an improvement of response time and recovery time. J Mizsei [4] and coworkers show that one thousand ppm of H_2 in air is enough for the reduction of a continuous surface Pd-O layer to isolated Pd particles with a proper heat treatment. This reduction is accompanied by a change in morphology layer: it's transformed to uniform Pd size grains, which increase the specific surface layer and thus sensor sensitivity.

To find again initial sensor characteristics, structure was placed in an ultra high vacuum chamber (10^{-7} mbar). Submitted to 100 ppb of NO_2, sensor shows, on figure 1, the same response and recovery time as initial structure and sensitivity is more important. We assume all species have desorbed and increase of sensitivity is due to higher specific surface layer.

3 Conclusion

These different treatments (oxidation, reduction and ultra high vacuum) of pseudo Schottky diode permit to have sensor regeneration cleaning the gas sensitive layer. We can then expect to have reproducible measurements with dynamic technique cleaning the gas sensitive layer before each O_3 concentrations measurements. The possibility of increasing sensor sensitivity is of great interest to measure more precisely O_3 and NO_2 low concentrations.

References

[1] D.T. Wickham, B.A. Banse and B.E. Koel. Adsorption of nitrogen dioxide and nitric oxide on Pd (111). *Surface Science.* 243 (1991) 83-95.

[2] M.C. Wu, N.A. Kelly. Clean air catalyst system for on road application. *Applied Catalysis B.* 18 (1998) 79-91.

[3] B. Dhandapani, S.T. Oyama. Gas phase ozone decomposition catalysts. *Applied Catalysis B.* 11 (1997) 129-166.

[4] J. Mizsei, J. Voutilainen, S. Saukko, V. Lantto. Structural transformations of ultra-thin sputtered Pd activator layers on glass and SnO_2 surfaces. *Thin Solid Films.* 391 (2001) 209-215.

Integrated optical refractometer based on rib-ARROW waveguide

R. Bernini[1], S. Campopiano[2], L.Zeni[2] and P.M. Sarro[3]

[1]National Research Council CNR-IREA, via Diocleziano 328, Napoli, Italy
email: bernini.r@irea.cnr.it http://www.irea.cnr.it
[2]Second University of Naples, Dep. Of Information Technology, Aversa, Italy
[3]DIMES-ECTM, TU-Delft NL-2600 GB Delft, The Netherlands

Summary: *The development of a new refractive index sensor using silicon-based integrated waveguide intended for sensing applications is presented. The device is based on rib ARROW (AntiResonant Reflecting Optical Waveguide) structure that, with a suitable design, shows a strong dependence of the attenuation on the analyte refractive index. Practically, the ARROW acts like a vertical interferometer that directly responds to an analyte refractive index variation with an intensity modulated signal, simplifying fabrication and avoiding ambiguities typical of the conventional interferometers. Experimental results obtained for this proposed sensor show a good sensitivity in the range of refractive index of 1.33-1.47.*

Keywords: *optical sensors, refractometers, integrated optics*
Category: *5 (Chemical sensor)*

1 Introduction

Over the years, integrated optical devices are increasingly being used in chemical and biochemical sensing applications [1-3]. The use of optical sensors is attractive because of the high sensitivity, immunity to electromagnetic interference, the robustness in aggressive environments offered. In this work, we present a new optical integrated refractometer sensor based on a rib antiresonant reflecting optical waveguide (ARROW). In the next we describe how the sensor works and the preliminary experimental results obtained.

2 Working principle of the sensor

The integrated refractometer sensor is based on an ARROW waveguide. Figure 1 shows a schematic representation of a typical ARROW structure based on silicon technology. The core and the second cladding regions are silicon dioxide layers (SiO_2) with the same low refractive index $n_c=n_2=1.470$ at a wavelength $\lambda=0.612\mu m$ and thickness, respectively, $d_c=4\mu m$ and d_2 whereas the first cladding is a silicon nitride layer (Si_3N_4) with a higher refractive index $n_1=2.010$ and thickness d_1.

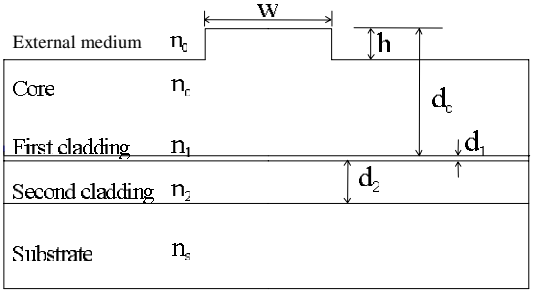

Fig. 1. Transverse section of the rib-ARROW waveguide.

The substrate is silicon (Si) with a complex refractive index $n_s=3.87-i0.02$. The lateral confinement is achieved by means of a rib structure with a width $W=6\mu m$ and an etching depth $h=1\mu m$. The refractive index of the outer material n_0 is supposed to vary.

Usually, in order to minimize the optical losses of the ARROW waveguide, the thicknesses of the two cladding layers are designed to be antiresonant ($\lambda/4$) at the operating wavelength [4-5]. This means that the cladding layers act as an high reflectivity Fabry-Perot mirror (R>99.9%).

However, if the thicknesses of the cladding layers are chosen to be near to the resonance ($\lambda/2$), the waveguide attenuation is strongly influenced by the external medium refractive index. This peculiar property of the ARROW waveguide can be used in order to realize a simple integrated refractometer, based on the ARROW waveguide itself acting as a vertical interferometer.

To clarify the sensing mechanism, figure 2 shows the modal profile of the TE ARROW fundamental mode for two different upper cladding refractive indexes, $n_0=1.46$ and $n_0=1$, respectively. As it can be seen, as far as the external medium refractive index decreases the mode profile is less confined inside the core (i.e. the peak in the second cladding is increased), resulting in an attenuation decrease.

The change in the attenuation implies a modulation of the light intensity. In the following, this intensity modulation mechanism is used as sensing principle for the proposed sensor: by monitoring the optical output power we can detect the refractive index variations of the external medium.

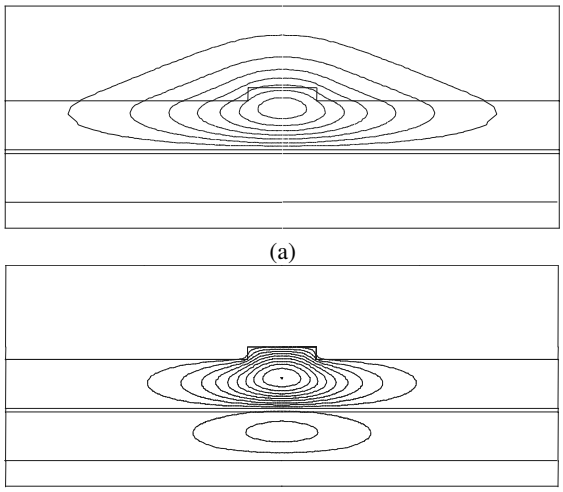

Fig. 2. Field distribution of the TE fundamental mode for: (a) n_0=1.46 and (b) n_0=1.

3 Fabrication and experimental results

The waveguide sensor is realized, starting from silicon substrate, as a multilayer structure composed by silicon dioxide (d_2=3.8μm), silicon nitride (d_1=0.450μm) and silicon dioxide (d_c=4.0μm) layers. This multilayer stack was deposited by Plasma Enhanced Chemical Vapor Deposition (PECVD) at a temperature of 400º C. The low deposition temperature and the conventional equipment used make this process fully compatible with bipolar or CMOS IC processes. Figure 3 shows the SEM picture of the realized rib-ARROW transverse section.

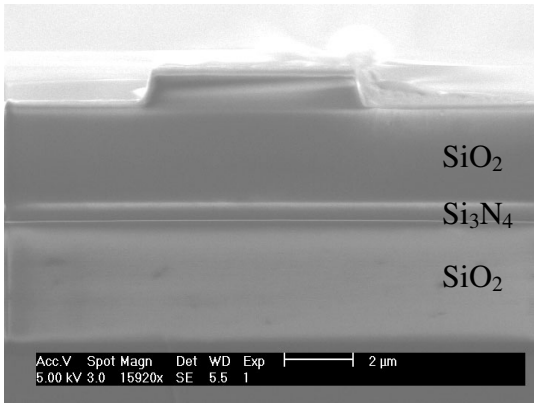

Fig. 3. SEM picture of the rib-ARROW structure.

In order to characterize the sensor, we have used a flow cell, with a channel length varing from 5.5mm to 8.5mm, clamped onto the sample. A syringe system is used to deliver the liquid to be analyzed. As light source we use a LED diode with a wavelength λ=0.612μm. The intensity modulated light of the diode was TE -polarized by a Glan-Thompson polarizer and than end-fire coupled into the device by microscope objective. The device output collected using an objective lens and focused onto a Si photodetector. Output from the detector was measured using lock-in amplifier.

Device characterization has been carried out by using seven liquids as external medium with different refractive index values ranging from 1.330 to 1.4746.

Preliminary measurements have been made on the equivalent planar sensor: in figure 4 it is shown the output power P_T versus the external medium refractive index n_0, for three sensing length L=5.5mm, 6.5mm, 8.5mm.

Assuming that a change in the normalized output power P_T equal to ΔP_{Tmin}=0.01 can be detected, with L=8.5mm and at a measured index of n_0=1.46, we find that the minimum refractive index variation appreciable is Δn=6e-4.

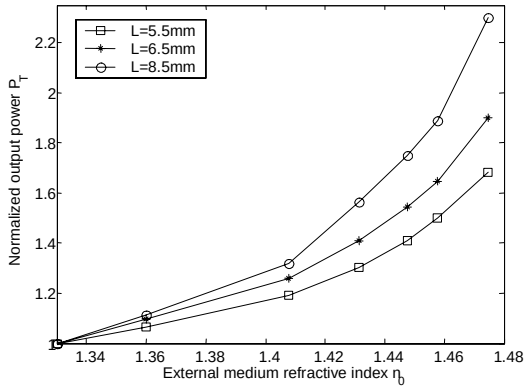

Fig. 4. Measured output power sensor P_T versus the external medium refractive index for different values of the sensing length L.

Work is now in progress on the characterization of the rib-ARROW structure.

References

[1] B. Maisenholder, H.P. Zappe, M. Moser, P.Riel, R.E. Kunz, and J. Edlinger, Electron. Lett. Vol.35, pp.986-988, 1997.

[2] G.J. Veldhuis, J.H. Berends, R.G. Heideman and P.V. Lambeck, Pure Appl. Opt., pp. L23-L26, 1998.

[3] G.J. Veldhuis, L.E.W. van der Veen and P.V. Lambeck, J. Lightwave Technol., Vol.17, pp.857-864, 1999.

[4] F. Prieto, A. Llobera, D. Jiménez, C. Doménguez, A. Calle, and L. M: Lechuga, J. Lightwave Technol., Vol.18, pp.966-972, 2000.

[5] J.M. Kubica, Opt. Letters, Vol.20, pp.40-42, 1995.

Influence of Catalytic Nanostructures Embedded in Mesoporous Filter on Gas Sensors Performances

A. Cabot, J. Arbiol, I. Jiménez, E. Rossinyol, and J.R. Morante

Enginyeria i Materials Electronics, Departament Electrònica, Universitat de Barcelona, c/Martí i Fraanquès 1, 08028 Barcelona, Catalonia, Spain
email: acabot@el.ub.es http://www.cemic.ub.es

Summary: *Mesoporous materials have received much attention as supporting catalytic elements in the field of catalysis. In this work we propose the use of these structures to eliminate interfering and poisoning gases from semiconductor gas sensor surfaces. Moreover, catalytic sieves are able to increase the response to specific gases by decomposition of the molecules surrounding the sensing layer, increasing overall selectivity of the device. In the present work SBA-15 silica structures are used as a support for Pd, Pt, Ru and Au as catalytic elements. This materials are deposited on the top of SnO_2 and WO_3 layers. Interesting influences of the filter layer on the sensor response are analysed.*

Keywords: *catalytic filter, gas sensor, WO_3, SnO_2*
Category: 5 *(Chemical Sensors)*

1 Introduction

While semiconductor gas sensors exhibit high sensitivity, their stability and selectivity are still unsatisfactry for many applications.

Recently, mesoporous materials have received much attention due to their excepcional characteristics. They present a very high specific surface area, around 1000 m^2/gr, and an ordered channel/pores distribution with size ranging between 2nm and up to 30nm [1]. These structures are also excellent candidates as supporting frames for metal and oxide compounds.

These unique properties has made these materials to attract much attention in the field of catalysis, due to its potentially high activity [2,3]. As the catalytic transformation of the reactants can be very selective, it also makes these materials promising candidates as gas sensor catalytic filters.

Furthermore, silica structures are effective electrical insulators, therefore changes on the catalytic active membrane have any or minor electrical influence on the base sensing material.

In this sense, these structures may be used to improve gas sensing device properties by preconditioning the gas mixtures arriving to the sensing layer. Influence of interfering and poisoning gases can be avoided by its transformation into innocuous species in the membrane layer. Alternatively, the catalytic layer could also decompose the target gas into more active compounds or activate limiting reaction steps near to the surface of the sensing layer, increasing in this way the sensitivity and also the overall selectivity of the device.

In this work, the influence of catalytic nanostructured embedded in SBA-15 mesoporous silicas is reported. Different catalytic elements such as Pd, Pt and Ru have been fixed by impregnation in the inner walls of the mesoporous structure channels. These materials are deposited on the top of tin oxide and tungsten oxide sensors. Measures of the sensor response to different gas mixtures are analysed.

2 Experimental

SBA-15 mesoporous silica was synthesized following the procedure reported by Zhao et al. using Pluronic P123 triblock copolymer ($EO_{20}PO_{70}EO_{20}$) [1]. Thus obtained materials were calcined in air at 600ºC for 4h. Catalytic additives were introduced by impregnation of the SBA-15 silica with aqueous solution of the corresponding chloride compound under primary vacuum, followed by slow evaporation of water.

For the electrical characterisation, sensors were fabricated by mixing the powders with an organic binder and then printing the obtained paste onto alumina substrates with Pt electrodes and heater. Similar procedure was used to obtain a SBA-15 silica paste, which was printed on the top of the SnO_2 or WO_3 layer.

Chemical composition of the catalytic elements was investigated by XPS. Moreover catalytic conversion of the gas species was analysed as a function of the material temperature in a gas reactor equipped with an IR detector.

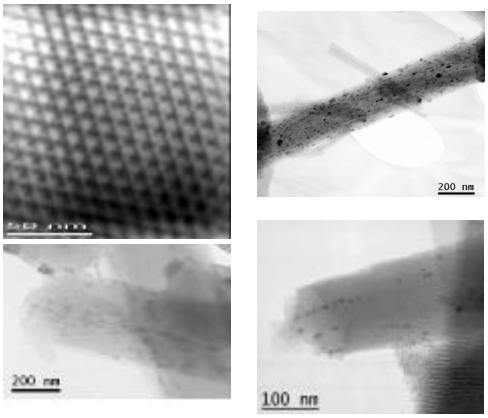

Fig. 1. From left to right and from top to bottom: SBA-15 silica structure; RuO_2 nanoparticles inside the mesoporous structure; Pd sticks inside the channels; and Pt nanostructures embedded in it.

3 Results and Discussion

SBA-15 structure has a hexagonal array of mesopores with a lattice constant of 9.18nm and a narrow pore size distribution. The mesopores are arranged in structures grouping a few hundred pores with length up to 2μm (figure 1).

Pd, Pt, Ru and Au were chosen as the catalytic active particles. These elements were fixed on the silica walls by means of impregnation of the chloride components under vacuum. Figure 1 shows different TEM images of the mesoporous silica containing metallic Pt and Pd nanostructures and nanoclusters of RuO_2. Gold was unable to enter inside the pore structure with the method used in this work, alternatively forming large metallic agglomerates, which are shown to be poorly catalytic active. The localisation of the catalytic element inside the pore walls is basic in order to take profit from the whole surface area of the structure and to physically limit, by encapsulation, the growth of the additive nanostructures, thus obtaining large distributions of catalytic elements. Gas molecules are considered to randomly flow through the whole pore structure owing to the small size of the gas molecules object of our study if compared with the 8 to 10nm of the channel diameters considered in this work [4].

Catalytically modified mesoporous materials were deposited over SnO_2 and WO_3 layers as typical sensing materials. Thick films sensors, with different active filter layers, were tested for different gas mixtures; mainly CH_4-CO and CO-NO_2 with different humidity and oxygen compositions. The experimental data corroborate that it is easy to separate CH_4 from CO and CO from NO_2 (figure 2), using appropriated catalytic nanoestructures and working temperatures.

In the example exposed on figure 2, the SiO_2:Pt filter is shown to eliminate the response to CO and NO_2 in the whole range of temperature. RuO_2 nanocomposites, on the other hand, are able to eliminate NO_2 response keeping that to CO invariable. Au introduction on the silica has little influence on the sensing device. Finally Pd eliminates the response to NO_2 and also that to CO in the high range of temperature of this last gas detection, but with the presence of water molecules in the low range of temperatures it greatly increases the response of the material to this gas, probably by reaction of the CO molecules with the hydroxyl groups producing H_2, which has a high influence on the base material electrical properties. More measurements are being carried out in this moment to elucidate this point.

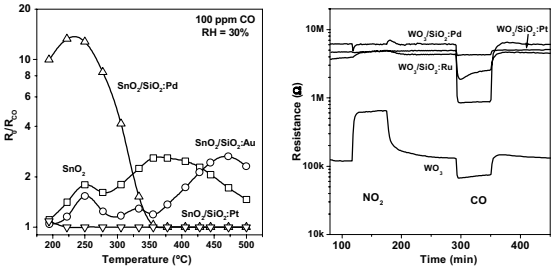

Fig. 2. Left: Response of tin oxide sensors recovered with different filter layers to 100ppm of CO in synthetic air with a 30% relative humidity. Right: Response to 1ppm NO_2 and 100 ppm CO of four WO_3 sensors recovered with different filter layers.

A complete morphologic, structural and functional characterisation of these active filters have been performed, while involved mechanisms are being analysed in order to explore the powerful of this kind of active filter in the field of gas sensor.

References

[1] D. Zhao, Q. Huo, J. Feng, B.F. Chmelka, G.D. Stucky, Nonionic Triblock and Star Diblock Copolymer and Oligomeric Surfactant Syntheses of Highly Ordered, Hydrothermally Stable, Mesoporous Silica Structures, *J. Am. Chem. Soc.*, 120 (1998) 6024-6036.

[2] D. Trong On, D. Desplantier-Giscard, C. Danumah and S. Kaliaguine, Perspectives in catalytic applications of mesostructured materials, *Appl. Catal. A*, 222 (2001) 299-357.

[3] S.H. Joo, S.J. Choi, I. Oh, J. Kwak, Z. Liu, O. Terasaki and R. Ryoo, Ordered nanoporous arrays of carbon supporting high dispersions of platinum nanoparticles, *Nature*, 412 (2001) 169-172.

[4] R.S.A. de Lange, K. Keizer and A.J. Burggraaf, Analysis and theory of gas transport in microporous sol-gel derived ceramic membranes, *J. Membrane Sci.*, 104 (1995) 81-100.

ISFET Operation in Pass-Transistor Mode without Readout Circuits

Arkadiy Morgenshtein[1], Uri Dinnar[1] and Yael Nemirovsky[2]

[1] Bio-Medical Engineering Department, Technion, Haifa, Israel
[2] Electrical Engineering Department, Technion, Haifa, Israel
E-mail: arkadiy@tx.technion.ac.il

Summary: *An operational concept was developed and tested for ISFET chemical sensor without readout circuitry, based on a phenomenon of threshold voltage drop, which is considered as parasitic event in most of the known applications in digital electronics, but appears to be extremely useful in ISFET-based applications. The operational concept is followed by measurements of the test-chip and the commercial ISFET sensor, and by applicability discussion.*

Keywords: *ISFET, sensor, readout, microsystem*
Category: 5 *(Chemical sensors)*

1 Introduction

Although numerous readout techniques were developed for ISFET during the years 0, one question remains open – is it possible to derive signals from ISFET without applying any readout circuitry?
The benefits of readout-less sensory are obvious: the area and power consumption are reduced, less limitations exist on bandwidth and stability of the sensor, the design complexity is minimized. Sensors without readout would be much more suitable for array-type monitoring in biotelemetry and miniaturized clinical applications.
The main reason for application of readout circuit attached to ISFET, is the fact that the fluctuations of pH influence the threshold voltage, which is the internal parameter of the FET and does not manifest itself as voltage signal at the output, but as a fluctuation of the transconductance. The transconductance is a passive parameter, and in order to derive a voltage or current signal from its fluctuations, the sensor has to be attached to conditioning and transmitting circuitry.
In this study an operational concept was developed and tested for ISFET sensor without readout circuitry. It is based on a phenomenon of threshold voltage drop, which is considered as parasitic event in most of the known applications in digital and mixed-signal electronics, but appears to be extremely useful in ISFET-based applications.
The operational concept is presented in this paper, followed by measurements of the test-chip and the commercial ISFET sensor. The applicability of the sensor is also discussed.

2 Pass-Transistor Logic

One of the fields of electronics that is "suffering" from threshold voltage drop is the Pass-Transistor Logic (PTL). This technique was initially developed in order to provide a low-power alternative to the classic CMOS logic design [2]. Although it triggered numerous research efforts in the world of digital design, it failed to capture a major role in real logic LSI's. The main reason for this is the voltage drop in the output [3], which is caused by and equal to the threshold voltage of the pass transistor.
Basic PTL is based on application of a control signal to the gate of n-type transistor. Additional input is applied to the diffusion of the MOSFET, and is transferred through the transistor according to the value of the control signal. PTL circuits are much simpler than standard CMOS implementations, but have an important drawback in means of logic signals. When the signal that is transmitted through the pass gate is high, a voltage drop occurs at the output and the value of the signal is lower than it was in the input. This drop is caused by the fact that in order to allow current conduction, the difference of the potentials between the gate and the source of the FET has to be higher then V_T. As soon as the output node is charged to high value, and the voltage across the FET equalizes to V_T, the current flow is stopped, and so does the output charging, leaving a V_T drop in the output. In case of the ISFET, such voltage drop becomes a valuable property, eliminating the need in conditioning and transmitting circuitry.

3 ISFET as Pass-Transistor

In order to perform the pH measurement in ISFET sensor without readout, it has to be operated in Pass-Transistor mode. The basic structure of ISFET as pass transistor is presented in Fig. 1. By applying square wave to the gate or to the drain, while keeping the second input high, we produce sampling of the pH fluctuations – each time when the pulse is high, a V_T drop occurs bringing up the changes caused by the pH. Note, that the application of a constant high voltage to gate and square pulse to drain is preferable, due to the requirement of constant potential at the reference electrode.

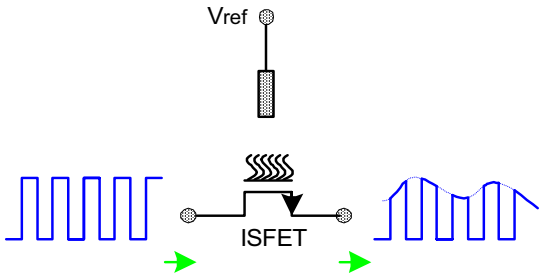

Fig. 1. *Basic structure of ISFET as Pass-Transistor*

The measurements of the test chip were performed using various forms and frequencies of the pH fluctuations. Fig. 2. shows the response to sinus signal that was measured simultaneously by n-type and p-type FETs. The operational concept of p-type Pass-Transistor is similar to n-type, but the drop occurs at low voltage (V_T appears instead of expected 0V).

In order to assure proper operation in real ISFET devices, measurements were performed using commercial ISFET sensors. During the experiment the ISFET sensor was placed in pH7, pH4 and pH9 solutions. Fig. 3. shows the results of one of the experiments in which ISFET was operated as pass-transistor, sampling a triangle signal at higher frequency.

If needed, the original VT fluctuations in it analog form can be easily derived from the set of samples by applying a Lop Pass Filter (LPF) to the output of the ISFET.

A simple and yet efficient operational concept of ISFET Pass-Transistor makes it an attractive platform for various applications and advanced features:

- The pulse amplitude modulation that is performed during ISFET pass transistor operation is identical to sampling operation in the input of Analog-to-Digital Converter. Thus, the ISFET pass transistor can be combined with the ADC, as part of the Sample & Hold structure.
- In case of Pass Transistor ISFET, the sampling is carried out at relatively high frequencies, which are above the practical frequency of pH fluctuations in clinical applications. Higher frequency results in more accurate response and in reduced 1/f noise [4].
- The modulation of ISFET can be performed using the digital data from the measurement system that have to be transmitted to the output, for example: synchronization series, location data, pixel counting, etc. In this way, the need in a separate data line is eliminated.
- Symmetric pulse biasing applied to the reference electrode was experimentally shown as effective for ISFET drift compensation [5].
- The Pass Transistor ISFET has a potential for implementation in array-type sensors, where the small size and simplified control of the sensor is of a great importance.

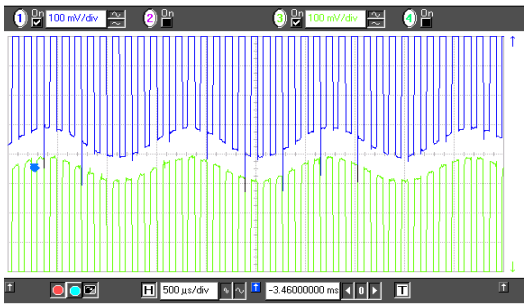

Fig. 2. *Simultaneous response to sinus signal in n-type and p-type ISFETs*

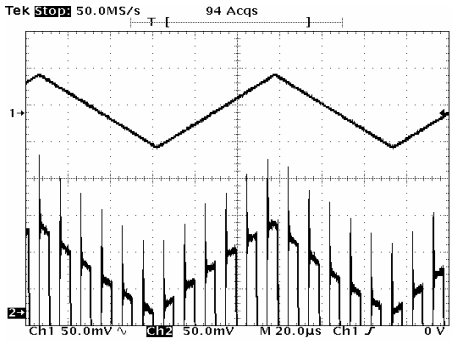

Fig. 3. *Commercial ISFET operating in Pass-Transistor mode.*

4 Conclusions

A simple but efficient operational concept of ISFET as Pass Transistor was presented based on the threshold voltage drop, which is known as problematic in logic design, but appears to be useful in pH sensing. The method was tested in test-chip measurements and experiments with commercial ISFET sensors, showing a response fully correlated with theoretical expectations.

The removal of readout interface at the sensor level proves to be an important benefit, which can contribute to simplified and efficient design and operation of pH sensors in biotelemetry and miniaturized clinical equipment.

References

[1] P. Bergveld, A. Sibbald: Analytical and Biomedical Applications of Ion-Selective Field Effect Transistors, *Comprehensive Analytical Chemistry*, vol. 12, 1988.

[2] N.H.E. Weste, K. Eshraghian: *Principles of CMOS VLSI Design*, pp.51-57, 1993.

[3] K. Yano, Y. Sasaki, K. Rikino and K. Seki: Top-down Pass-Transistor Logic Design, IEEE J. Solid-State Circuits, vol. 31, pp. 792-803, 1996.

[4] C.G. Jakobson, Y. Nemirovsky: 1/f Noise in Ion Sensitive Field Effect Transistors from Subthreshold to Saturation, *IEEE Trans. on Electron Devices*, vol. 46, pp. 259-261, 1999.

[5] P.A. Hammond, D. Ali, D.R.S. Cumming: A Single-Chip pH Sensor Fabricated by a Conventional CMOS Process, *Eurosensors XVI*, 2002.

Thin-Film a-Si LAPS: Preparation and pH Sensitivity

T. Yoshinobu[1], M. J. Schöning[2,3], F. Finger[4], W. Moritz[5] and H. Iwasaki[1]

[1]ISIR, Osaka University, 8-1 Mihogaoka, Ibaraki, Osaka 567-0047, Japan
e-mail: nov@sanken.osaka-u.ac.jp http://www.sanken.osaka-u.ac.jp/~nov/
[2]ISG-2, Research Centre Jülich, 52425 Jülich, Germany
[3]University of Applied Sciences Aachen, Division Jülich, Ginsterweg 1, 52428 Jülich, Germany
[4]IPV, Research Centre Jülich, 52425 Jülich, Germany
[5]Humboldt University Berlin, Brook-Taylor-Str. 2, 12489 Berlin, Germany

Summary: *To improve the spatial resolution of the light-addressable potentiometric sensor (LAPS), it is necessary to reduce the thickness of the semiconductor layer, which, however, causes a problem of the mechanical strength. In this study, a thin-film LAPS was fabricated with amorphous silicon (a-Si) deposited on a transparent glass substrate. The current-voltage characteristics and pH sensitivity of a-Si LAPS were investigated.*

Keywords: *LAPS, amorphous silicon, pH*
Category: *5 (Chemical Sensors)*

1 Introduction

The light-addressable potentiometric sensor (LAPS) [1,2] is a semiconductor-based chemical sensor with an electrolyte-insulator-semiconductor (EIS) structure as shown in Fig.1.

The principle of LAPS resembles that of the EIS capacitance sensor, in which the variation of the width of the depletion layer is detected. In the case of the EIS capacitance sensor, a small oscillating voltage is applied and the ac current is measured to determine the capacitance of the EIS structure. In this case, the measurement is averaged over the whole sensing surface in contact with the electrolytic solution. In the case of LAPS, as is suggested by its name, the measured area on the sensing surface is defined by illumination, which generates the ac photocurrent to be measured.

Because of this "light-addressability", LAPS can be used as a basis of an integrated multisensor [3], in which different regions on the sensing surface are individually accessed by the light. The LAPS is also the basis of the chemical imaging sensor [4], in which a focused laser beam scans the sensing area to visualize the two-dimensional distribution of the ion concentration.

In both cases, the spatial resolution of the LAPS is an important factor. It limits the density of measuring points on the multisensor and the smallest size of structures that can be visualized by the chemical imaging sensor.

It has been demonstrated both experimentally and theoretically [5,6] that the spatial resolution is determined by the beam size and the lateral diffusion of photocarriers in the semiconductor substrate. With focusing optics, the beam size can be reduced down to the scale of the wavelength of the light. The lateral diffusion is determined by the thickness of the semiconductor layer as well as by the material parameters such as the diffusion length of minority carries and the absorption coefficient of the light.

Several attempts have been made to improve the spatial resolution of the LAPS and the chemical imaging sensor by thinning the Si substrate [5], using a silicon-on-insulator (SOI) substrate [7] and using a GaAs substrate [8].

In this study, a thin-film LAPS was prepared with amorphous silicon (a-Si) deposited on a transparent glass substrate. The a-Si seems to be an ideal material for a high-resolution LAPS, for the feasibility of large-area thin films and availability of the mature technologies.

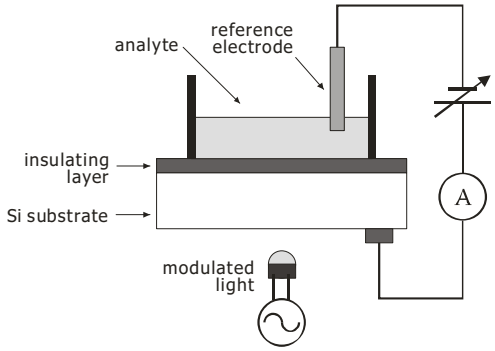

Fig.1 The schematic of the light-addressable potentiometric sensor (LAPS).

2 Preparation of a-Si LAPS

The a-Si thin films were prepared by the glow discharge method on Corning 1737 glass substrates with 500 nm of Al grids and 700 nm of ZnO as the contact. The substrate temperature, the flow rate of monosilane and the working pressure were 280ºC, 40 sccm and 700 mTorr, respectively. Phosphine

was used for n-type doping. The insulating layers of SiO_2 and Si_3N_4 were prepared by the plasma-enhanced chemical vapor deposition (PECVD) method.

Two different structures of a-Si LAPS were prepared:

glass/ZnO/n-type a-Si/undoped a-Si/SiO_2/Si_3N_4

and

glass/ZnO/undoped a-Si/SiO_2/Si_3N_4.

For each structure, three samples were prepared with different thickness of the undoped layer of 0.4, 0.7 and 1.2 μm, respectively.

3 Characteristics of a-Si LAPS

Figure 2 shows the current-voltage characteristics of a-Si LAPS with and without n-type a-Si layer for a pH7 buffer solution. Here, the bias voltage is defined as the voltage applied to the solution with respect to the substrate.

For a-Si LAPS with n-layer, the obtained curves are similar to those of LAPS with n-type semiconductor. For a-Si LAPS without n-layer, the polarity of the curve is opposite. As the a-Si layer becomes thicker, the photocurrent increases due to increased absorption of the incident light.

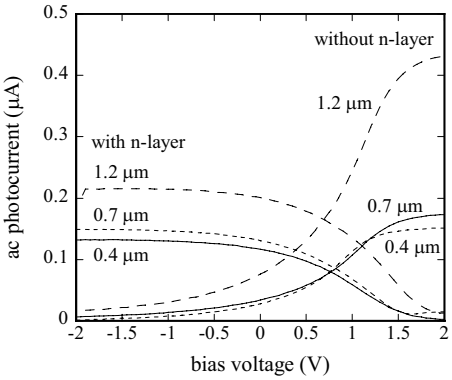

Fig.2 Current-voltage characteristics of a-Si LAPS.

Figure 3 shows the response of a-Si LAPS with 0.4 μm undoped layer to different pH values. The current-voltage curve shifts along the voltage axis depending on the pH value from 4 to 10.

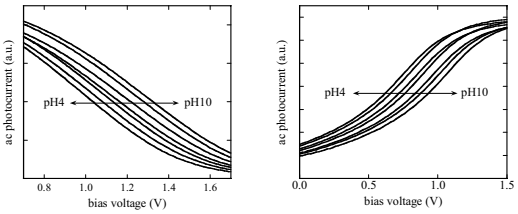

Fig.3 Current-voltage curves of a-Si LAPS with (left) and without (right) n-layer for different pH values.

Figure 4 shows the calibration plots, in which the bias voltage at the inflection point of each curve in Fig.3 is plotted versus pH. The pH sensitivity is calculated to be 51.9 and 53.6 mV/pH, respectively.

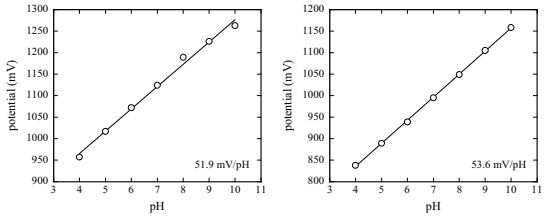

Fig.4 Calibration plots of a-Si LAPS with (left) and without (right) n-layer.

These results indicate the possibility of a-Si as a semiconductor material for fabrication of thin-film LAPS with a high spatial resolution.

Acknowledgments

This work was partially supported by the Ministry of Education, Culture, Sports, Science and Technology of Japan, Grant-in-Aid for Scientific Research (contract no. 14550791), the Foundation for Biomedical Research and Innovation, Kobe, Japan and the German State Ministry of Nordrhine-Westfalia.

References

[1] D. G. Hafeman, J. Wallace Parce and H. M. McConnell, Light-Addressable Potentiometric Sensor for Biochemical Systems. *Science* 240 (1988) 1182-1185.

[2] J. C. Owicki, L. J. Bousse, D. G. Hafeman, G. L. Kirk, J. D. Olson, H. Garret Wada and J. Wallace Parce, The Light-Addressable Potentiometric Sensor: Principles and Biological Applications. *Annu. Rev. Biophys. Biomol. Struct.* 23 (1994) 87-113.

[3] M. Shimizu, Y. Kanai, H. Uchida, T. Katsube, Integrated Biosensor Employing a Surface Photovoltage Technique. *Sensors and Actuators B* 20 (1994) 187–192.

[4] M. Nakao, T. Yoshinobu and H. Iwasaki, Scanning-Laser-Beam Semiconductor pH-Imaging Sensor. *Sensors and Actuators B* 20 (1994) 119-123.

[5] M. Nakao, T. Yoshinobu and H. Iwasaki, Improvement of Spatial Resolution of a Laser-Scanning pH-Imaging Sensor. *Jpn. J. Appl. Phys.* 33 (1994) L394-L397.

[6] M. George, W. J. Parak, I. Gerhardt, W. Moritz, F. Kaesen, H. Geiger, I. Eisele, H. E. Gaub, Investigation of the Spatial Resolution of the Light-Addressable Potentiometric Sensor. *Sensors and Actuators A* 86 (2000) 187–196.

[7] Y. Ito, High-Spatial Resolution LAPS, *Sensors and Actuators B* 52 (1998) 107-111.

[8] W. Moritz, I. Gerhardt, D. Roden. M. Xu and S. Krause, Photocurrent Measurements for Laterally Resolved Interface Characterization. *Fresenius J. Anal. Chem.* 367 (2000) 329-333.

Novel Ga_2O_3 based MRISiC Schottky Diodes for Hydrogen Gas Sensing

A. Trinchi[1,4], M.K. Ghantasala[2,4], S. Kaciulis[3], L. Pandolfi[3],
W. Wlodarski[1,4], Y.X. Li[1,4] and S.Viticoli[3]

[1]School of Electrical and Computer Eng., RMIT University, GPO Box 2476V,
Melbourne, Victoria 3001, AUSTRALIA
email: avt@ieee.org http://www.ece.rmit.edu.au
[2]IRIS, Swinburne University of Technology, Hawthorn, Victoria, AUSTRALIA
[3]Institute for the Study of Nanostructured Materials, ISMN-CNR,
Monterotondo (RM), ITALY
[4]CRC for Microtechnology, AUSTRALIA

Summary: *The hydrogen gas sensing performance of Pt/Ga_2O_3/SiC based Schottky diodes are presented in this paper. The metal oxide semiconducting Ga_2O_3 thin films were prepared by the sol-gel process and deposited onto the SiC by the spin coating technique. A Pt layer was deposited on the top of the Ga_2O_3 forming the Schottky diode. The diodes were biased at a constant current varying from 1 to 2 mA and their responses to H_2 in different ambients was measured. The sensors had a very stable baseline varying from its mean value by only 0.014%. Their responses were repeatable towards H_2 at operating temperatures between 300 and 600°C. When exposed to 5,000 ppm of hydrogen at an operating temperature of 600°C, a voltage shift of over 250 mV was observed.*

Keywords: *Gallium Oxide, Hydrogen, RBS, Schottky diode, XPS*
Category*: 5 (Chemical sensors)*

1 Introduction

Hydrogen is a major cause of corrosion, whereby it weakens metals internally. Due to its small size, hydrogen molecules can penetrate into metals and affect properties such as strength and durability, resulting in embrittlement. This form of corrosion greatly impacts on gas pipelines, the pressed steel industry and in aircraft applications, among many others. Other important applications for hydrogen sensors include: fire warning systems, leakage detection and monitoring of processes control systems, and for hydrogen driven vehicles.

In 1975 Lundstrom and coworkers [1] first reported the sensitivity of a Pd Metal-Oxide-Semiconductor (MOS) based field effect structure towards hydrogen gas. As a result, modifications to this device and research into other gas sensitive MOSFETS, MOS capacitors and Schottky diodes has increased dramatically. With the advent of silicon carbide technolgy [2], a new generation of field effect devices operating at high temperatures, and in harsh environments is being developed.

Such high temperature sensors can allow for the direct monitoring of combustion processes. Schottky diodes are advantageous because of the simple electrical circuitry required to operate these sensors. The simplest silicon carbide Schottky diode based gas sensor is one that consists of a catalytic metal deposited on silicon carbide. The hydrogen and hydrocarbon gases dissociate on the catalytic metal surface and diffuse through the metal/semiconductor. This results in a dipole layer that changes the Schottky diode's electrical properties in proportion to the concentration of gas [3].

The selectivity, sensitivity and stability of such diodes is increased with the addition of metal oxide layer between the SiC and catalytic metal. This layer is selected for its reactivity to the target gas [4]. Un-doped Ga_2O_3 has been reported for monitoring hydrocarbons and hydrogen employing conductometric sensors [5]. Coupled with SiC, which also has a strong affinity to hydrocarbons, these Metal/Reactive Insulator/ Silicon Carbide (MRISiC) devices are promising for high temperature gas sensing applications.

In this paper we present the hydrogen gas sensing performance of novel Pt/Ga_2O_3/SiC Schottky diode based gas sensors. Their response to various concentrations at different forward bias currents and at different operating temperatures is investigated.

2 Experimental and Results

The MRISiC based Schottky diode employs the n-type 6H polytype of SiC with a titanium layer as the ohmic contact. The metal layers were deposited by electron beam evaporation and DC magnetron sputtering. Gallium isopropoxide was used as a precursor solution for the sol-gel prepared Ga_2O_3 thin film and were deposited by the spin-coating technique. An alumina micro heater was placed beneath the structure to control the operating temperature of the device.

Rutherford Backscattering Spectrometry (RBS) and X-ray Photoelectron Spectroscopy (XPS) techniques were employed to completely reveal the chemical composition of the investigated films. The influence of the chemical composition on the gas-sensitive properties of the films was also investigated. Fig. 1 shows the measured and simulated RBS spectra of the Ga_2O_3 thin film annealed in air for 1hr at 700°C. The simulated RBS data reveals the films have a thickness of approximately 110 nm. It was also noted that as the annealing time increased, the oxide layer thickness increased, however was limited to around 130nm.

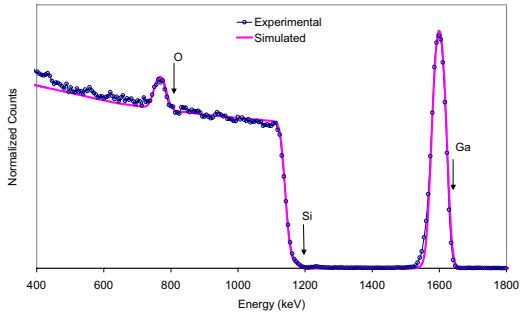

Fig. 1: Simulated and experimental RBS spectra of Ga_2O_3 on SiC annealed at 700ºC

For gas sensing measurements, the diodes were placed in a multi channel gas calibration system and exposed to different concentrations of hydrogen. This results in a change in the carrier concentration and in the Schottky barrier height, which results in a change in the bias voltage. Hence the response of the Schottky diodes to hydrogen gas was measured as the change in voltage when operated in constant current mode. The response was investigated at temperatures up to 600°C.

Two baseline gases were used, these being ultra high purity N_2 and 5% O_2 in N_2. Fig 2 below shows the response of the diode to 1% and 0.5% H_2 balanced in N_2 at an operating temperature of 300°C. The forward bias current was 1mA. At this temperature the response time is approximately 28 seconds whereas the recovery time is larger, approximately 4 minutes. When the ambient gas was changed to 5% O_2 in N_2, as seen in Fig. 3, the response time decreased to around 20 seconds and the recovery time also decreased. Additionally from these two graphs it is observed that with less oxygen content in the ambient gas, the response increases, ie from 145 to 195 mV for 0.5% H_2. Such results were consistent for all operating temperatures investigated.

The results presented suggest the increased oxygen content of the ambient gas mixture provides a higher hydrogen gas response due to the increased number of active oxygen sites. This is in agreement with Jacobsen et al. [6] who investigated $Pt/CeO_2/SiC$ Schottky diodes. According to them, the diffusion of oxygen into the metal oxide surface creates more sites for hydrogen atoms.

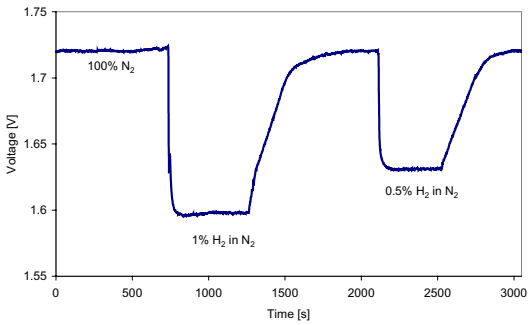

Fig 2. Response to H_2 gas in N_2 at operating temperature of 300°C with forward bias current of 1 mA.

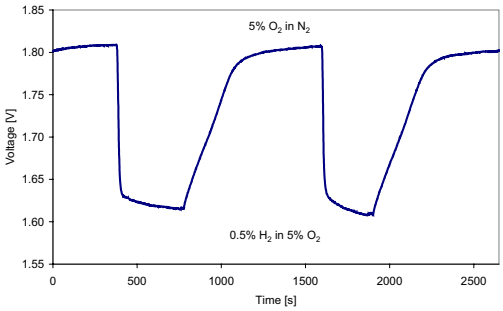

Fig 2. Response to H_2 gas in 5% O_2 in N_2 at operating temperature of 300°C with forward bias current of 1 mA.

In conclusions, we have successfully characterized and demonstrated the H_2 gas sensing performance of novel Ga_2O_3 MRISiC Schottky diodes. These diodes show responses of around 190mV at 300°C and over 250 mV at temperatures up to 600°C. They are promising for industrial H_2 gas sensing applications.

References

[1] I. Lundstrom, S. Shivaraman, C. Svensson, L. Lundkvist, "Hydrogen Sensitive MOS Field-Effect Transistor", *Appl. Phys. Lett.,* 26 (1975) 55-57

[2] J. B. Casady, R. W. Johnson, "Status of Silicon Carbide (SiC) as a Wide Bandgap Semiconductor for High Temperature Applications: A Review", *Solid-State Electronics*, 39 (1996) 1409-1422

[3] L. G. Ekedahl, M. Eriksson, "Hydrogen Sensing Mechanisms of Metal Insulator Interfaces", *Acc. Chem. Res.,* 31 (1998) 249-256

[4]<http://www.nasatech.com/Briefs/Jan99/LEW16544.html>.

[5] T. Weh, J. Frank, M. Fleischer, H. Meixner, "On the mechanism of hydrogen sensing with SiO_2 modificated high temperature Ga_2O_3 sensors", *Sensors and Actuators, B*, 78 (2001) 202-207

[6] S. Jacobsen, U. Helmersson, L. Ekedahl, I. Lundstrom, P. Martensson, A. Lloyd-Spetz, "Pt/CeO_2 SiC Schottky Diodes With High Response to Hydrogen and Hydrocarbons", Proceedings of the Transducers '01, (2001) 832-835.

Reducing of total number of ion-selective electrodes in sensor array for liquid analysis

Patrycja Ciosek, Wojciech Wróblewski, Zbigniew Brzózka

Warsaw University of Technology, Dept. of Analytical Chemistry, Noakowskiego 3, Warsaw, Poland
email: brzozka@ch.pw.edu.pl http://csrg.ch.pw.edu.pl

Summary: *An electronic tongue based on the sensor array of ion-selective electrodes combined with pattern recognition tools was applied to qualitative analysis of mineral waters and apple juices. The method of reducing total number of sensors in the array was described. It was found that before and after reducing the number of sensors, this device is capable of reliably discrimination between different brands of mineral waters and apple juices.*

Keywords: *electronic tongue, sensor array, ion-selective electrodes (ISEs), Principal Components Analysis (PCA), qualitative analysis of liquids*
Category: 5 *(Chemical sensors)*

1 Introduction

The use of multicomponent measurements together with pattern recognition tools for an extraction of information from sensor array responses is a new direction of qualitative analysis of complex liquid media. A few devices of this type, called "electronic tongue", have been presented: multichannel electrode with lipid-polymer membranes [1], array of non-selective potentiometric sensors based on chalcogenide glass membranes [2] and system based on voltammetry [3]. Various pattern recognition techniques, such as PCA [1-3], artificial neural networks [2] and other were used.

A method of reducing number of sensor in an array has not been discussed so far. After reducing sensor array should perform specific task with the same or better capability to discriminate between different classes of samples. Quantitative specification of discrimination capability of the array before and after reducing the number of sensors is indispensable to perform further classification procedures.

2 Experimental

The membranes contained ionophores (Table 1), 65 wt.% plasticizer, 33 wt.% high-molecular-weight PVC and 20-50 mol% versus ionophore lipophilic salt. The method of membrane preparation and electrode conditioning were the same as for standard ISEs. Two electrodes (IS 561, Philips) for each membrane composition were prepared. One standard pH electrode was also included, giving 17-sensors array. All measurements were carried out with cells of the following type: Ag, AgCl; KCl 1M / CH_3COOLi 1M / sample solution // membrane / internal filling solution; AgCl, Ag. All measurements of eight brands of mineral water, tap water, Oligocene water and eight brands of apple juices were performed as conventional direct potentiommetry, without any sample pretreatment. Sensor outputs were autoscaled to assure better performance of the following step, which was Principal Component Analysis.

Table 1. Ionophores used for membranes preparation

An electrode number	An electrode type	Ionophore
1, 2	Cl^-	1 wt.% TPPClMn
3, 4	F^-	1.5 wt.% ionophore VII
5, 6	NO_3^-	3,5 wt.% TDMAC
7, 8	HCO_3^-	1 wt.% ETH 6010
9, 10	K^+	1 wt.% valinomycin
11, 12	Na^+	1 wt.% ionophore X
13, 14	NH_4^+	2 wt.% nonactine
15, 16	Ca^{2+}	2 wt.% ETH 1001

3 Results and discussion

A sensor array generates data of high dimensionality, hard to handle and visualize. PCA is a linear feature-extraction technique, finding new direction in the pattern space, so that they explain the maximum amount of variance in the data set as possible. Usually the first two Principal Components (PC1, PC2) are sufficient to transfer the majority of the variation of the samples. Fig. 1 presents PCA plot discriminating different brands of waters (electrodes 1-16 and pH electrode were used). PC1 and PC2 together contain 60.6% of the variance of all data set (Table 2). A good separation between all kinds of samples is observed. To describe the ability of particular electrodes to distinguish between different classes of water, ratio of variances between classes and the sum of internal variance in all classes was calculated (factor F) [4]. Electrodes displaying the highest values of F were chosen to create reduced sensor array (electrodes 3, 4, 7-12 and pH electrode). Fig.

2 presents PCA plot for water samples of reduced, nine-electrode array. PC1 and PC2 together contain then 92.4% of the variance of all data set, which can be the result of reducing unsubstantial data and redundant information. Consequently the ability of PC1 and PC2 to discriminate between different brands of water is bigger. Factor F values before reducing was calculated as $8.8*10^2$ for PC1 and $1.4*10^3$ for PC2 compared to $2.5*10^3$ and $2.0*10^3$ respectively after reducing (Table 2). Analogous results were obtained also in the case of eight brands of apple juices.

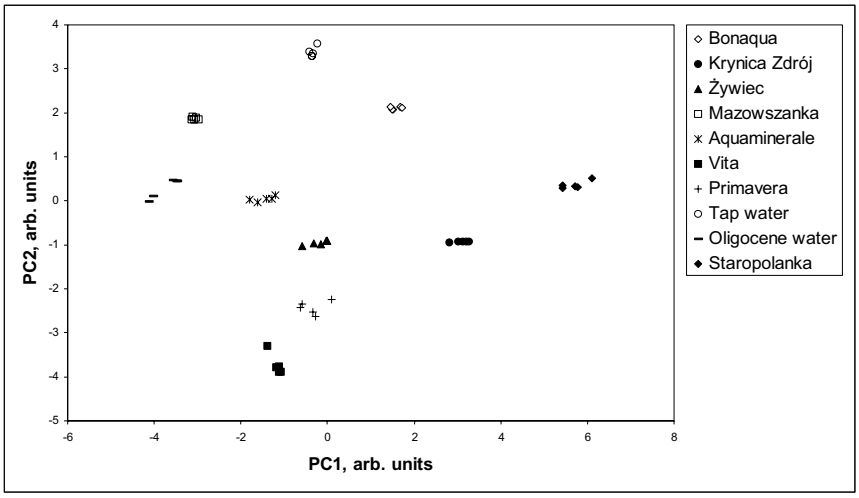

Fig. 1. PCA plot of different brands of mineral waters before reducing number of sensors in the sensor array.

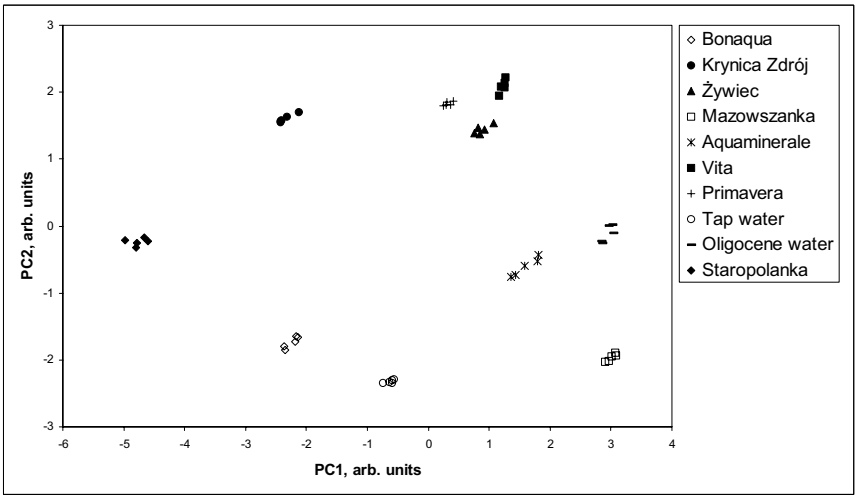

Fig. 2. PCA plot of different brands of mineral waters after reducing number of sensors in the sensor array.

Table 2. Parameters of the ISEs array before and after reducing of number of sensors

	% variance explained by PC1	F_{PC1}	% variance explained by PC2	F_{PC2}
before reducing	43.2	$8.8 * 10^2$	17.4	$1.4 * 10^3$
after reducing	63.9	$2.5 * 10^3$	28.5	$2.0 * 10^3$

Acknowledgments
This work was financed by grant of Warsaw University of Technology „Microsystems: constructions, design, technologies".

References

[1] K. Toko. Taste sensor with global selectivity. *Materials Science and Engineering C4* (1996) 69.

[2] Yu. G. Vlasov, A. V. Legin, A. M. Rudnitskaya, A. D'Amico, C. Di Natale. <<Electronic tongue>> - new analytical tool for liquid analysis on the basis of non-specific sensors and methods of pattern recognition. *Sensors & Actuators B* 65 (2000) 235.

[3] F. Winquist, P. Wide, I. Lundstrom. An electronic tongue based on voltammetry. *Analytica Chimica Acta* 357 (1997) 21-31.

[4] J. Mazerski. Fundamentals of chemometrics. Wydawnictwo Politechniki Gdańskiej (2002) 163.

Morphology implications on the performances of cavitand based chemical sensors

M.Suman[1], L. Cristofolini[2] and E. Dalcanale[1]

[1] Dipartimento di Chimica Organica ed Industriale, Università di Parma
[2] Dipartimento di Fisica, Università di Parma
Parco Area delle Scienze 17/A, 43100 Parma – Italy; phone: +39-0521905463, fax: +39-0521905472
e-mail: suman@nemo.unipr.it; web site group: http://www.unipr.it/~chimorg/dalcanale.htm;

Summary: *Cavitands work as satisfying sensitive organic layers in QCM by the modulation of weak interactions, generated into a pre-organized cavity. They have to be equipped with long hydrocarbon chains at the lower rim, to achieve a fast adsorption-desorption kinetic. On the contrary the absence of these chains increases the selectivity because of a larger number of active cavities. Morphological AFM and optical microscopy studies allow to explain these diverse performances and correlate them to a complete different surface morphology and layer porosity, giving information for the design of effective sensors, which exhibit the right compromise between permeability-reversibility and sensitivity proprieties.*

Keywords: *cavitand, QCM, surface morphology, AFM, optical microscopy, kinetic, sorption, recovery*
Category: *5 (Chemical sensors)*

1 Introduction

Chemical sensors require an optimization of strength and cooperation of the weak interactions involved. In this sense we have collected important evidences of the synergy obtainable by the introduction of multiple functional groups opportunely oriented with respect to a pre-organized resorcinarene cavity [1]. Furthermore, morphology and structure of their receptor layer has to be adapted to amplify the molecular recognition proprieties and maximize the reversibility: unfortunately this objective is often in contrast with the desired selectivity.

2 Abstract

In the course of Quartz Crystal Microbalance (QCM) measurements, the resulting mass changes (due to the temporary interaction with the analyte) and eventual changes in the viscoelastic proprieties of the organic layer, produce variations in the fundamental resonance frequency.
Application of the Sauerbrey equation in its linear range required the presence of a uniform and homogeneous layer across the entire active region of the resonator, but this assumption is reasonable only for nonpolar polymers [2] and has to be tested for any new kind of receptor.
In the case of cavitand based organic layers, there are strong evidences that a adequate sensor behavior can be reached only if they are equipped with long hydrocarbon chains at the lower rim. Figure 1 reports response traces to CH_3CN vapors obtained by a non-specific polymer (PECH) and two cavitands, which differs only for the presence (or absence) of these chains.

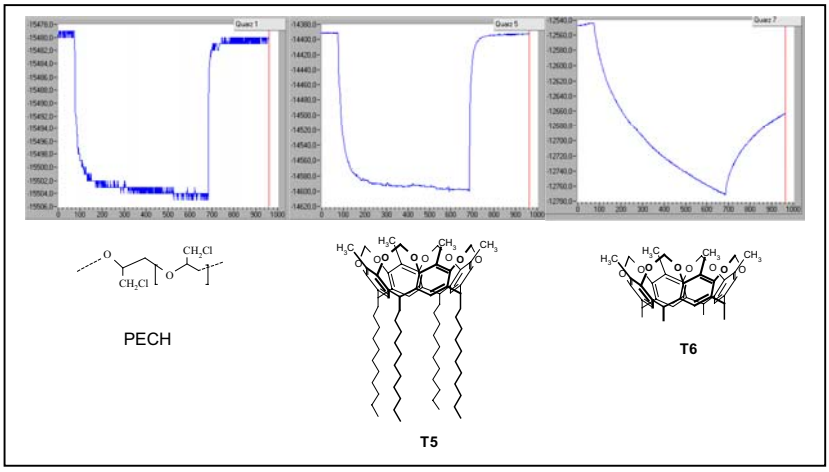

Fig. 1. Response traces of PECH, cavitand T5, cavitand T6 to CH_3CN (1500 ppm in the gas phase)

Their main specific interactions, responsible for selective complexation are hydrophobicity, CH-π and dipole-dipole interactions [3]: therefore both furnish significant responses with respect to PECH; T5 has a microporous structure which determine a fast sorption-desorption process, however its chains increase the number of unspecific dispersive interactions too.
The histogram reproduced in figure 2 expresses the normalized responses to CH_3CN vapors of T5 and T6 with respect to PECH: under the same conditions T6 is more selective than T5 because it benefits of a larger number of active cavities.

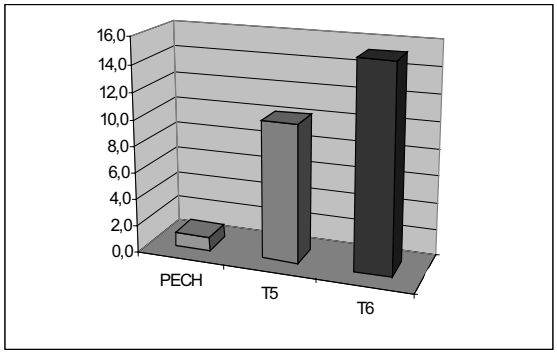

Fig. 2. Selectivity patterns normalized to PECH

On the other hand T6 present a too much slow kinetic of adsorption and recovery, unsuitable to applications in chemical sensors, where a right sensitivity has to be matched by a satisfying reversibility [4]. Microscopy studies allow to explain these diverse performances and correlate them to a complete different surface morphology and layer porosity. In particular, in this field the use of Atomic Force Microscopy (AFM) as a powerful technique of surface imaging is currently under investigations; optical microscopy has been initially considered because of its low cost and easy utilization. Above all it is useful to integrate optical images into digital measurements with dedicated software: en example is reported in figure 3. Cavitand morphology on QCM supports is assimilable to "droplets", since the lipophilic cohesion forces within its molecules are stronger than adhesion at the gold electrode surface: droplets dimension and distribution is completely different when T5 and T6 are compared together. Defined the choice of the best cavitand receptor, a second objective of these studies is to understand what happens to the active layer after the first hours of exposure to the vapors of the analyte. In fact the spray coating technique probably leaves little amounts of solvent (in general $CHCl_3$ or CH_2Cl_2) entrapped into the organic material, determining some morphological reassessment in the first period of life of the sensor device.

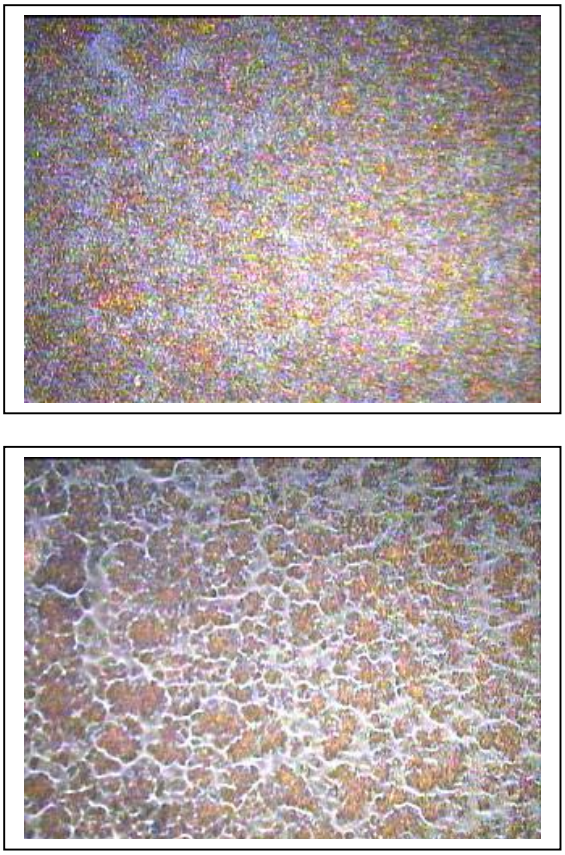

Fig. 3. Layer distribution on QCM surface - optical microscopy images 700x700 μm
3a (top): T6 ; 3b (down): T5

In conclusion, the comprehension of the correlation between QCM responses and the morphology of their active layers is extremely important to design an effective sensor which exhibit the right compromise between permeability-reversibility and sensitivity proprieties.

References

[1] M. Suman, F. Ugozzoli, E. Dalcanale, *Proc. 8th National Conference on Sensors and Microsystems*, pp. 25, Trento, Italy, 12–14 February 2003.

[2] K. Bodenhofer, A. Hierlemann, G. Noetzel, U. Weimar and W. Gopel, *Anal. Chem.* 68 (1996) 2210-2218.

[3] J. Hartmann, P. Hauptmann, S. Levi, E. Dalcanale, *Sensors & Actuators B* 35 (1996), 154-157

[4] M. Suman, N. Bouzouane, E. Barbieri, F. Ugozzoli, E. Dalcanale, *Journal of Supramolecular Chemistry* 2 (2002), in press

Development of a Sol-Gel Optical Sensor for Analysis of Zinc in Pharmaceuticals

Paula Jerónimo, Alberto N. Araújo and M. Conceição Montenegro

REQUIMTE/ Dept. of Physical-Chemistry, Faculty of Pharmacy (UP)
R. Aníbal Cunha 164, 4050-047 Porto, Portugal
email: anaraujo@ff.up.pt

Summary: *A Zn(II) optical sensor was developed by incorporating 4-(2-pyridylazo)resorcinol (PAR) in a sol-gel thin film. Acid- and base- catalyzed methods to prepare the sol-gel layers have been studied, as well as different types of precursors and different PAR concentrations. Sensors based on co-polymerization of TEOS with 3-APTES, basic catalysis, water:alkoxyde ratio of 4 and PAR concentration of 1 mg ml^{-1} showed optimum performance in the proposed working conditions. The sensor was coupled to a multicommutated flow system and applied to the direct determination of Zn(II) in pharmaceuticals. Optical transduction was based on the use of a dual-color LED and a photodiode. The sensor showed optimum response at pH 5.5 and its regeneration was accomplished with a solution of KSCN acidified to pH 3 with HCl.*

Keywords: *sol-gel films, Zn(II) optical sensor*
Category: *5 (Chemical sensors)*

The sol-gel chemistry [1] has been widely used in the development of chemical sensors due to its simplicity and versatility. By this process glass-like materials incorporating different dopants are prepared at room temperature, allowing final structures with mechanical and thermal stability as well as good optical characteristics. The sol-gel process comprises the hydrolysis of an alkoxyde precursor under acidic or basic conditions, followed by polycondensation of the hydroxylated monomers to form a porous gel network. Afterwards, gel aging and drying can be conducted under controlled conditions in order to obtain densified solid matrices. During these reaction stages organic and biological recognizing elements can be incorporated and become entrapped in the matrix, yet remaining sterically accessible to small analytes that diffuse into the pore network. The properties of the final network structure (thickness, pore size and pore distribution, etc.) can be manipulated by appropriate control of the process chemical variables. Although structures with different shapes and configurations may be obtained, thin films are usually preferred for optical sensing due to their short response time and good optical transparency.
The association between sensors and automated flow techniques offers many advantages, such as simpler manipulation of solutions, simplified manifolds, reagent economy and cleaner determination procedures. Additionally, there is an increase in sensitivity, stability and selectivity.

In this work Zn(II) optical sensors were prepared by incorporating 4-(2-pyridylazo)resorcinol (PAR) in sol-gel thin films. PAR is a heterocyclic azo dye that forms complexes with the vast majority of transition metals. In acetate medium (pH 3-6) PAR forms a red-orange 1:2 (metal:ligand) complex with zinc (ε = 8.3 X 10^4) which can be monitored spectrophotometrically [2, 3]. Considering the goals of high selectivity, reversibility, fast response and stability, several sol-gel cocktails (Table 1) were produced in order to obtain a sensor with optimized characteristics.

Table 1. Composition of sol-gel cocktails for preparation of sensor thin films (all values in mL).

	F1	F2	F3	F4
TEOS	4	3.6	-	3
MTES	-	0.4		-
3-APTES	-	-	4	1
Ethanol	16	16	16	16
HNO_3 10^{-1} M	2	2	-	-
TMAOH	-	-	2.176	2.176

PAR was previously dissolved in ethanol in increasing concentrations. All solutions were allowed to gelate at room temperature and all the films were obtained by spin-coating (3000 rpm, 15 seconds, 80 µl) on glass slides 18 x 18 mm. After coating, all films were dried at room temperature for several days. Different silicon alkoxydes were used as precursors; besides TEOS, MTES and 3-APTES were also included in this study in order to achieve more structurally stable structures in a short time. Acid and base catalyzed methods were tested and different concentrations of immobilized PAR were studied. The different sensor films obtained were characterized in terms of spectral characteristics, response time and extent of indicator leaching. Sensors F4, based on co-

polymerization of TEOS with 3-APTES, basic catalysis, water:alkoxyde ratio (R) of 4 and PAR concentration of 1 mg ml^{-1}, were found to be the most suitable to be used as Zn(II) sensors in the proposed working conditions. In fact, 3-APTES was observed to stabilize the structure and also seemed to improve the uptake of the dye into the sol-gel. The use of a basic catalyst was found to offer many advantages when producing optically transparent gels with high concentrations of 3-APTES [4]. Acid catalyst leads to immediate precipitation of 3-APTES resulting in cloudy and double-phased gels, unsuitable for optical applications. Basic catalysis is also favorable for the complexation mechanism of PAR. For the acid catalyzed films no reaction with zinc occurred, probably because of ionization of *para*-OH group in the PAR molecule, which occurs in acidic medium. Concentrations of PAR higher than 1 mg ml^{-1} disturbed the optical quality of the films and the homogeneous distribution of the dye. The R value of 4 was adopted following previous work conclusions [5]. Optimum complex formation for this film was obtained at pH 5.5, with maximal absorption at the wavelength of 500 nm (Fig. 1). The regeneration of the sensor was accomplished with a KSCN solution (1 mol l^{-1}) with pH adjusted to 3 by addition of HCl.

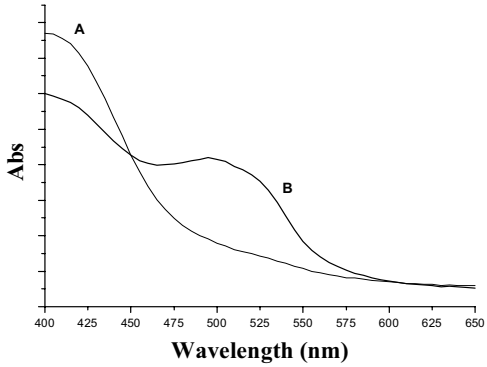

Fig. 1. Absorbance spectra of (A) PAR in sensor F4 and (B) PAR-Zn(II) complex in sensor F4 at pH 5.5.

In order to study the developed sensors in flow conditions, two coated slides were placed in a home-made flow cell (Fig. 2) and coupled to a multicommutated flow system (Fig. 3). Flow-rate was fixed at 0.8 mL min^{-1} and equal and reduced activation cycles of valves V1 and V2 were selected in order to provide appropriate injection of sample in the carrier (acetate buffer solution, pH 5.5). Valve V3 was responsible for the insertion of regeneration solution. Valve V4 was included to enable sample change.

The absorbance of the Zn(II)-immobilized PAR was monitored using a dual-colour (green/red) LED and a photodiode, in order to increase sensitivity and overcome Schlieren noise. The procedure enabled to determine Zn(II) in the concentration range between 9 and 22 µg l^{-1}.

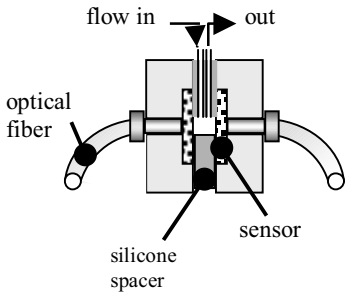

Fig. 2. Flow cell configuration, cross sectional view.

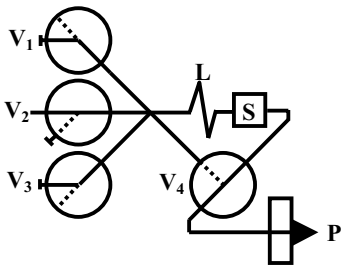

Fig. 3. Diagram of the flow manifold for Zn(II) determination. V_1, V_2, V_3 and V_4 - three-way solenoid valves: (---) corresponds to the activated position and (—) corresponds to the off position; L - mixing coil, 25 cm long; S - sensor; P - peristaltic pump.

Based on the high sensitivity achieved one can speculate that the developed sensor can be miniaturized in order to be coupled to microfluidic devices.

References

[1] C.J. Brinker, G.W. Scherer, *Sol-Gel Science*: *The Physics and Chemistry of Sol-Gel Processing*, Academic Press, New York, 1990.

[2] Z. Marckzenko, *Separation and Spectrophotometric Determination of Elements*, Ellis Horwood, Wiley, New York, 1986.

[3] M.F. Molina, J.M. Bosque-Sendra, M. Nechar, R. El-Bergmi, *Anal. Chim. Acta* 398 (1999) 281-290.

[4] D.A. Nivens, Y. Zhang, S. Michael Angel, *Anal. Chim. Acta* 376 (1998) 235-245.

[5] P.C.A. Jerónimo, A.N. Araújo, M.C.B.S.M. Montenegro, D. Satinský, P. Solich, *Anal. Chim. Acta*, submitted for publication.

Agnowledgement

Paula Jerónimo wishes to thank FCT and FSE (III QCA) for a PhD Grant (SFRH/BD/2876/2000).

Chemical Sensors of the Capacitive type Using Thin Silicon Membranes Covered With Chemical Selective layers – Fabrication And Evaluation

S.Chatzandroulis, E.Tegou, D.Goustouridis, S.Polymenakos, D.Tsoukalas

NCSR "Demokritos", Institute of Microelectronics, 15310, Agia Paraskevi, Athens, Greece
email: stavros@imel.demokritos.gr http://www.imel.demokritos.gr

Summary: *Capacitive type chemical sensing devices based on a silicon/polymer bimorph structure have been fabricated and evaluated. Upon exposure to analytes the polymer covering the thin silicon membrane swells inducing a deflection on the membrane which is measured as a capacitance change between membrane and substrate. Five different polymer layers were used. Exposure to water, methanol and ethanol vapors was used for evaluating performance. Sensitivities ranging from 4.5fF/%RH for PDMS up to 29fF/%RH for PHEMA covered devices, are reported. Devices covered with PHEMA, PVAc and PMMA also exhibit strong response upon exposure to methanol and ethanol atmospheres*

Keywords: *chemical sensor, bimorph, capacitive*
Category: *5(Chemical Sensors)*

1 Introduction

Chemical sensing devices have received great attention in recent years as new applications in environmental monitoring and food industry, are emerging. [1-3]. In these applications discrimination of simple and complex odors may be achieved by either highly selective sensors or by arrays of sensors combined with appropriate pattern recognition algorithms. In this paper a chemical sensor based on polymer/silicon bilayers in membrane configuration is reported. The device utilizes a capacitive pressure sensor covered by a chemical sensing layer, which forces the sensor membrane to deflect upon sorption of chemical substances from the environment. Five different chemical layers [poly-hydroxy-ethyl-methacrylate (PHEMA), poly-methyl-methacrylate (PMMA), poly-vinyl-acetate (PVAc), epoxy-novolac (EPN) and poly-dimethylsiloxane (PDMS)] are investigated. Sensitivities to relative humidity of 29fF/%RH for PHEMA covered devices to 4.5fF/%RH for PDMS are reported. Devices covered with PHEMA, PVAc and PMMA also exhibit strong response upon exposure to methanol and ethanol atmospheres. Differences in sensitivities between these layers may be exploited in constructing an effective chemical discriminating array. In order to characterize the devices, and evaluate the performance of each polymer layer, exposure to volatile organic compounds (methanol and ethanol) and humidity was used.

2 Experimental

Capacitive type silicon pressure sensors fabricated with an already presented technique [4] are used as the basic building module for the reported device. This type of sensor is characterized by the thin silicon diaphragm (typically less than 4um) and small diaphragm to substrate spacing (<1um). For reason of increasing device sensitivity the sensor membrane is designed to operate in a pre-deflected mode at close proximity to substrate, with a touchdown pressure of around 13kPa. Solutions of PHEMA (4% w/w), PMMA (5% w/w), PVAc (5% w/w), EPN (41% w/w) and PDMS (3% w/w) were subsequently applied over the sensor membrane using a micropipette and post-apply baked to insure solvent evaporation (figure 1).

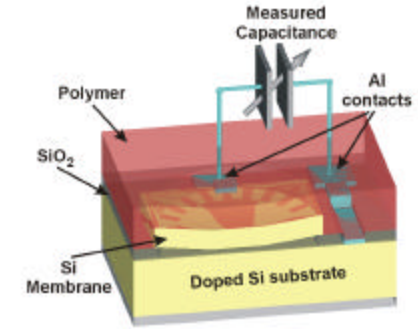

(a)

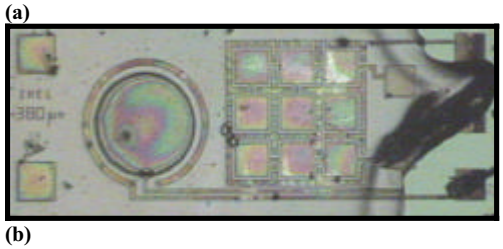

(b)

Figure 1.
(a) Sensor schematic view,
(b) Photographic view. The pressure sensor die is completely covered with polymer (in this case PHEMA).

A typical capacitance to pressure curve is shown in figure 2. On the same plot experimental data of the sensor covered with PHEMA as a function of relative humidity are plotted. The data suggest that polymer swelling for 1% RH rise corresponds to a pressure variation of 236Pa.

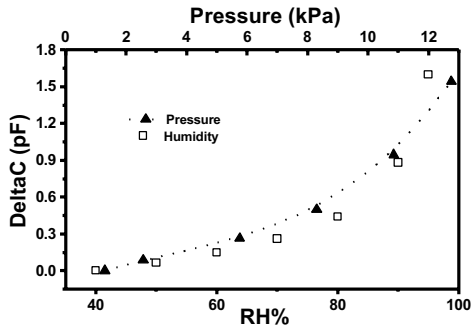

Figure 2 Capacitance change versus pressure curve and corresponding change as a function of relative humidity after the sensor has been covered with PHEMA.

Testing of the devices was performed in a chamber were relative humidity and temperature are controlled to within ?0.1% and ?0.1°C, respectively. The response versus relative humidity for the five polymer layers is depicted in figure 3. On the same plot the pressure necessary to obtain same response is also shown. For volatile compound testing, methanol and ethanol vapors are introduced in the test setup via a dry nitrogen flux going through a bubbler with the respective compound. The atmosphere is interchanged between dry nitrogen and the volatile compound mix. Figure 4 depicts the maximal capacitance change between the two states. In all cases the response to methanol is higher than for ethanol. This is attributed to the longer chain length of ethanol molecules. Among all layers, PHEMA presents the highest response to water vapors. This can be explained by the hydrogen bonding between the OH group of PHEMA molecule and water molecules. On the other hand, PDMS, being a hydrophobic polymer, presents the lowest response to humidity.

In another experiment dry nitrogen flow was split in two components: one carrier flow bubbling through ethanol at a variable rate, and one diluting component of 590ml/min. The two components were subsequently mixed so that controllable lower proportions may be achieved. For this test the sensor consists of four spin coated with PHEMA membranes which were connected in parallel. The samples are subjected into variable mixing ratios of ethanol vapors. In figure 5 the response of the sensor for three mixing ratios is depicted. In region A dry nitrogen is fed in chamber. Then ethanol is added at concentrations of 8700, 19275 and 29000 ppm before exposing the sensor to dry nitrgen again.

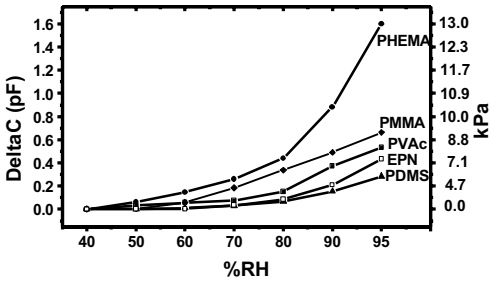

Figure 3 Capacitance change versus relative humidity response for the five polymers used. The right Y-axis shows the pressure necessary to obtain same response.

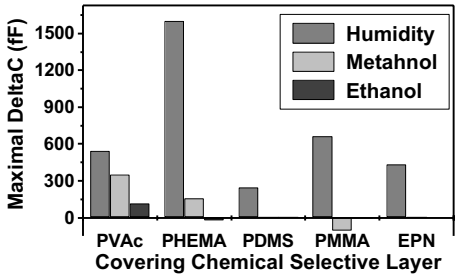

Figure 4 Maximal capacitance change for all chemically selective layers used, upon exposure to humidity, methanol and ethanol

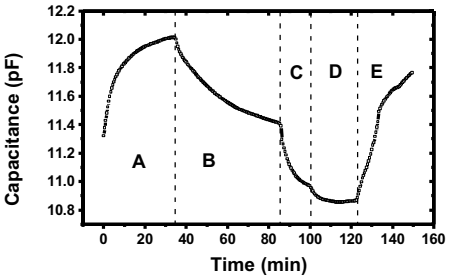

Figure 5 Response of a four membrane sensor covered with PHEMA.

References

[1] M.K.Baller *etal*, "A cantilever array-based artificial nose", Ultramicroscopy 82 (2000) p 1-9

[2] C.D.Natale *etal*, "An electronic nose for food analysis" Sensors & Actuators B 44 (1997) p 521-6

[3] A.Boisen *etal*, "Enviromental sensors based on micromachined cantilevers with integrated readout", Ultramicroscopy 82 (2000) p 11-16

[4] D.Goustouridis, S.Chatzandroulis, P.Normand, D.Tsoukalas "A miniature self-aligned pressure sensing element" J.Micromech. Microeng. 6 (1996), p.33-35

Sensor sensitivity study of the thin and thick WO_3 films.

S. Krutovertsev, O. Ivanova, M. Lee, E. Sudakov, A. Zabrodsky,
A. Nikolaev, O. Redina, A. Pislyakov

JSC "Practic-NC", Zelenograd, Moscow, 124460, Russia
email: pnc@orgland.ru http://www.pnc.ru

Summary: *In this paper comparison of technical characteristics of thin and thick WO_3 films obtained by two different methods – the thermal sputtering in vacuum and thick film technology are presented. Resistance-versus-temperature dependences of the films are studied within range 100-450°C. Behaviour of sensitive layer in different oxygen environments on various temperatures; sensor characteristics towards H_2O, microconcentrations NO_2, H_2S is discussed.*

Keywords: *tungsten oxide, gas sensor, thick film, thin film*
Category: *5 Chemical sensors*

1 Introduction

The oxides of transition metals are used as sensitive layers of sensors [1-3], owing to their high electrical and physical characteristics, i.e. good extrinsic ion conductivity, large forbidden gap, surface properties prevailing over those of bulk, widely variable stoichiometry. Comparative study of WO_3 thick film sensing features obtained by two different methods, thick film technology and by thermal sputtering in vacuum, is presented.

2 Experimental

The films were deposited on a sensor presented on fig. 1. The sensitive element consists of an alumina substrate measured 2x0.5x0.2 mm. One side of the substrate is covered with a gas sensitive film, the other side of the substrate platinum film heater is deposited. The film heater is, at the same time, a thermal resistor in the sensor. Platinum wires 20 mm in diameter connect the sensitive element with leads of a glass panel.

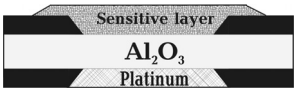

Fig. 1 Construction of semiconductor sensors

WO_3 powder with fine particles less than 0.5 μm was annealed for 1 hour at 600°C. The obtained film thickness was 15-25 μm.
The other method was used to obtain thin films of 0.2-0.5 μm on the UVN-71 P3 device at evaporation temperature of 500°C.

The properties of the sensors were examined by the method of dynamic gas blending utilizing the sample gas mixtures, the "Environics"-4000 gas mixture generator and test ampoules manufactured by "Dräger". The investigations were carried out under the sensor thermal stabilization conditions in the range 100 – 450°C. Sensor heating, conductivity and resistance measurements were maintained by two 16-channel measurement units (fig. 2) and IBM PC program which operates in real time. Up to 32 sensors can be to be placed in the measurement chamber. The device has function to maintain a stable sensor temperature in the range 30-500°C with accuracy 1°C. The developed measurement unit allows to conduct simultaneously measurements of resistance of gas-sensitive layers on 32 channels in the range 500 Ohm – 1,5 GOhm with accuracy 2,5%. Besides that, the measurement unit regulates and controls sensor heating processes during the measurements.

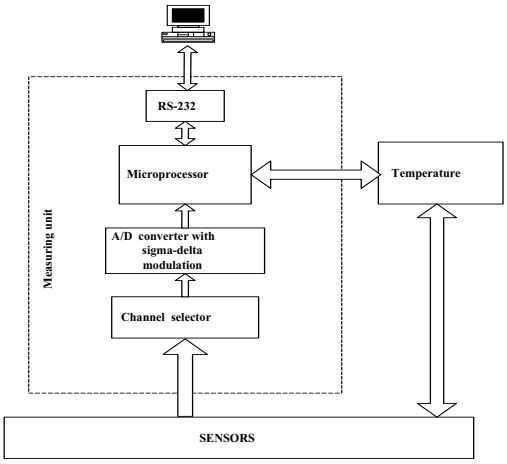

Fig.2 Sixteen-channel meter of gas sensors parameters.

The measurements show that resistance of the films obtained by vacuum thermal sputtering is much higher than that of the films received by thick film technology. This fact is bound with film thickness and, possibly, with higher macro- and bulk defects concentration of the latter films. However, both films demonstrated similar resistance-versus-temperature dependence. It may be explained by a fact that films of both types feature the same micro-structure. Fig.3 shows resistance-temperature curves.

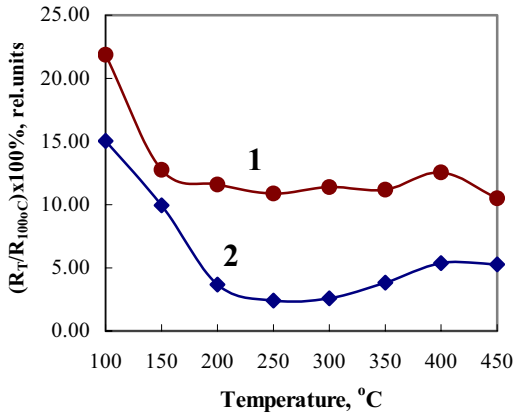

Fig.3 Typical curves of resistance versus film temperatures in the air:
a- thick film;
b- thin film;
R_T- Resistance at different temperatures;
R_{100oC}- Resistance at 100°C.

Film behaviour in air containing 15-28 vol.% of oxygen at temperatures 100-400°C was investigated. Fig.4 show that film obtained by different methods demonstrate the same behaviour type under equal conditions. Apparently, that the films possess the same stoichiometry.

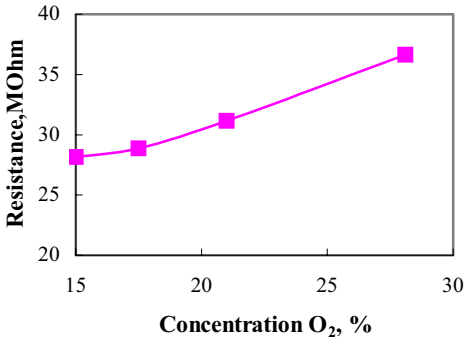

a) thin film

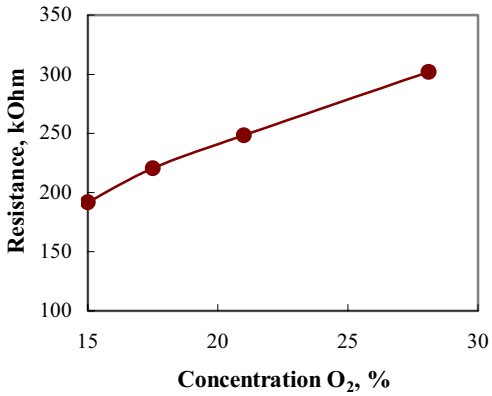

a) thick film

Fig.4 Typical sensor resistance dependence versus oxygen concentrations in air at 400°C.

Humidity influence on the WO_3 films resistance was studied. The measurement were taken on both type films in the 3-90% relative humidity at 100-400 °C. It is shown that at relative humidity less than 30% the films are more sensitive to humidity changes.

Maximal resistance changes occur at temperatures less than 200 °C and practically negligible at temperatures higher than 300 °C.

Preliminary investigation evidence that the WO_3 films feature maximal sensitivity to NO_2 at temperatures less than 300°C. Films sensitivity to NO_2 micro-concentrations at 150-200 °C was studied. All the films show maximal sensitivity at 150°C. Thick films demonstrate the highest sensitivity to 5 ppb of NO_2 at 150 °C and increase resistance by 5 times.

WO_3 films sensitivity to the H_2S micro-concentrations at 250-350°C was investigated. The maximal resistance change at 5 ppb of H_2S is observed at 300-350 °C. The resistance of the films obtained by the two methods drops its value by 3 times at 350 °C.

3. Conclusions

This paper presents comparative sensor temperature characteristics the WO_3 thin and thick films. It is shown that the films demonstrate similar temperature dependence. Varying of oxygen concentration reversibly change the films characteristics. The films curves are similar for the both types of films. All films are mostly sensitive to the relative humidity less than 30% at temperatures less than 200°C. The films show high sensitivity to 5 ppb of NO_2 at low temperatures. The WO_3 thick films display a higher sensitivity. The films obtained by these two methods demonstrate high sensitivity to 5ppb of H_2S at 300-350°C. The film sensor characteristics can be purposely changed by varying conditions of film formation (temperature, annealing time, sputtering velocity, activating dopes) and by varying temperature of films.

References.

1. M. Fleischer, H. Meixner, Selectivity in high-temperature operated semiconductor gas-sensors, Sensors and Actuators, B, 1998,v.52, pp.179-187.
2. J.L. Solis, V. Lantto, Gas-sensing properties of Sn_xWO_{3+x} mixed oxide thick films, Sensors and Actuators, B, 1998,v.48, pp.322-327.
3. K. Aguir, C. Lemire, D.B.B. Lollman, Electrical properties of reactively sputtered WO_3 thin films as ozone gas sensor, Sensors and Actuators, B, 2002, v.84, N 1, pp.1-5.

Desorption phenomena of a gas enrichment unit for using sensors below odor threshold

J. Nieß[1,2], T. Hamacher[1], P. Boeker[1] and E. Weber[2]

[1]University of Bonn, Dept. of Agricultural Eng., Nussallee 5, 53115 Bonn, Germany
email: j.niess@uni-bonn.de
[2]Freiberg Technical University, Dept. of Organic Chemistry, Leipziger Strasse 29, 09596 Freiberg (SA.), Germany

Summary. *A simple thermal desorption unit (TDU) can enhance the detection limits of chemical sensors below odor thresholds. However these simple designs can exhibit unwanted side effects that hamper effectiveness. Potential problems, methods for investigation and a solution are illustrated with an example.*

Keywords: Absorber, pre-concentration, odor
Category: 5 (Chemical sensors)

1 Introduction

Chemical sensors often do not have the sensitivity needed for detecting odors. Pre-concentration with a thermal desorption unit can solve this problem [1][2][3]. Most commercial TDU's are designed for use with gas chromatography and therefore retain not enough analyte for a chemical sensor. Development of a simple TDU for use with sensors is limited to a single stage design. Therefore effectiveness of the TDU can be limited and requires critical evaluation. This paper discusses potential problems. Methods for investigation are illustrated with an example.

2 Mass Balance of Absorption

Pre-concentration is based on diminishing the carrier gas volume of a given analyte mass. During the absorption phase (Index $_A$) a given analyte concentration (m_A/V_A) is absorbed for a long time (t_A) at a high flow rate ($\mathrm{d}V_A/\mathrm{d}t_A$). In the desorption phase (Index $_D$) a fast temperature increase is used to release the analyte. Desorption time (t_D) of the peak is a function of temperature profile, which mainly depends on heating power and absorber design. The goal of absorber design is to achieve a high analyte concentration during desorption (m_D/V_D). Dilution by carrier gas is minimized by reducing gas flow ($\mathrm{d}V_D/\mathrm{d}t_D$), but other phenomena can require choosing an optimal flow rate.

Enrichment to concentrations above vapor pressure of the pure analyte is restricted by condensation. Desorption can be slowed down by high analyte concentration in the gas phase. Due to a high gradient in concentration and long transport time diffusion can lead to peak broadening. Re-absorption onto improperly chosen surface materials is favored by long transport times. Finally the dead volume of the sensor dilutes narrow peaks. The experimental part of this article illustrates some of these effects. The mass balance of absorption can be written as:

$$t_A \frac{m_A}{V_A} \frac{\mathrm{d}V_A}{\mathrm{d}t_A} = t_D \frac{m_A}{V_D} \frac{\mathrm{d}V_D}{\mathrm{d}t_D}$$

The enrichment factor F is defined as $c_{D\max.}/c_A$ (Fig. 1). F is the maximum amplification obtainable with negligible sensor volume.

$$F = \frac{\frac{m_D}{V_{D\ \max.}}}{\frac{m_A}{V_A}} = \frac{t_D}{t_A} \frac{\frac{\mathrm{d}V_D}{\mathrm{d}t_D}}{\frac{\mathrm{d}V_A}{\mathrm{d}t_A}}$$

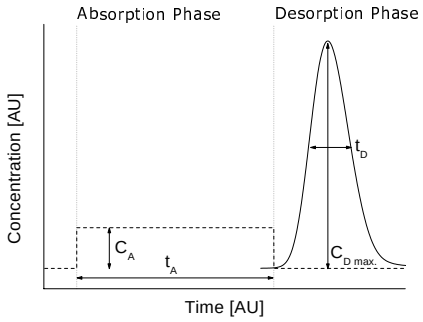

Fig. 1: Definition of enrichment factor and peak height

3 Experimental

The setup is described in [2]. 1-Butanol is absorbed for 300 s at 100 ppmv and 60 ml/min carrier gas flow rate onto 32 mg Tenax TA (Scientific Instrument Services, Ringoes NJ, USA) at room temperature (22 °C). This is close to the 10% breakthrough point as defined in [2]. Absorbed analyte mass (default: 300 s), temperature profile (4.7 V) and carrier gas flow (10 ml/min) are varied. The use of different heating voltages results in temperature profiles given in Fig. 2. After a 300 s cool down time the next cycle can start.

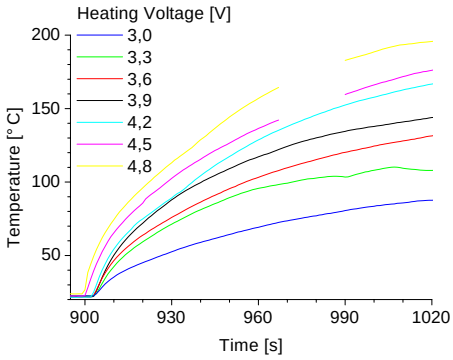

Fig. 2: Temperature profiles

4 Results and Discussion

For desorption peaks a Gaussian shape like in Fig. 1 is expected. The peaks of Fig. 3 are different. Above 120 s absorption time desorption peaks follow an envelope curve until the increased analyte mass has been desorbed. Variations of temperature profile and carrier gas flow are used to investigate the reason of this effect. Condensation can be excluded by comparing detector signal levels of input (without absorber) and signal at peak maximum.

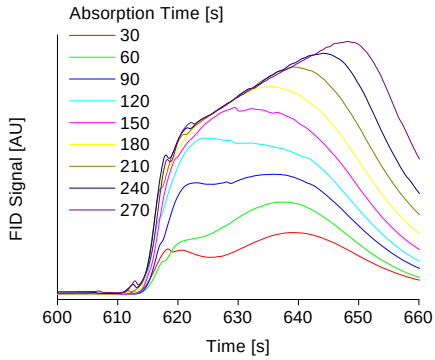

Fig. 3: Desorption peaks as function of absorption time

Increasing heating voltage does not have a significant effect on peak shape (Fig. 4). This can be explained by the low effect it has on the heating rate at low temperatures. However an increase of the slope of the linear part of the peak is visible. So the effect takes place in the absorber and is temperature dependant.

Increasing carrier gas flow gives shorter and higher peaks (Fig. 5). The overall peak shape remains.

From these experiments the unusual peak shape can be explained as a kinetic inhibition. Analyte concentration in the gas phase reaches a critical level and hinders diffusion of absorbed analyte. Accelerating kinetics by increasing temperature has no essential effect. Increased carrier gas flow improves the situation by diluting the analyte. This allows for faster desorption rates but does not cancel the inhibition.

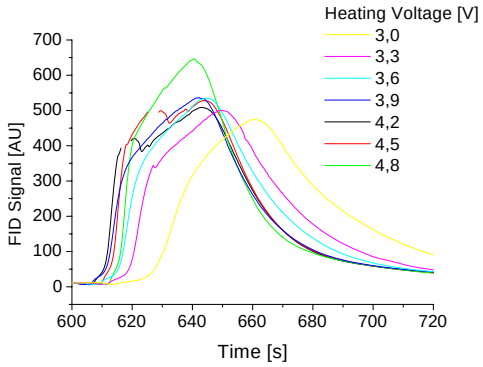

Fig. 4: Desorption peaks as function of temperature profile

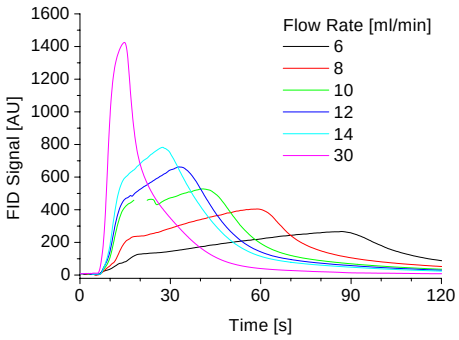

Fig. 5: Desorption peaks as function of flow rate during desorption

5 Acknowledgment

This work was supported by a research grant from the German Ministry of Science and Technology (Grant 16SV 1311).

References

[1] T. Hamacher, J. Nieß, P. Schulze Lammers, B. Diekmann and P. Boeker. Online odour measurement close to the odour threshold with a QMB sensor system with integrated preconcentration unit. In: J. Saneistr and P. Ripka, eds. *Proc. Eurosensors XVI*, pp. 15–16, Prague, Czech Republic, 15–18 September 2002. Czech Technical University.

[2] J. Nieß, T. Hamacher, P. Schulze Lammers, E. Weber and P. Boeker. A miniaturized thermal desorption unit for chemical sensing below odor threshold. In: J. Saneistr and P. Ripka, eds. *Proc. Eurosensors XVI*, pp. 581–582, Prague, Czech Republic, 15–18 September 2002. Czech Technical University.

[3] T. Nakamoto, Y. Isaja, T. Ishige and T. Moriizumi. Odor-sensing system using preconcentrator with variable temperature. *Sensors and Actuators B* **69** (2000) 58–62

A non-pixel image reader for continuous image detection based on tandem heterostructures

M. Vieira, M. Fernandes, P. Louro, A. Fantoni and I. Rodrigues
Electronics Telecommunications and Computer Dept, ISEL, Lisbon, Portugal, mv@isel.pt.

Summary: *Large area n-i-p-n-i-p a-SiC:H heterostructures are used as sensing element in a Double Color Laser Scanned Photodiode image sensor (D/CLSP).*
This work aims to clarify possible improvements, physical limits and performance of CLSP image sensor when used as non-pixel image reader. Here, the image capture device and the scanning reader are optimized and the effects of the sensor structure on the output characteristics discussed.
The role of the design of the sensing element, the doped layer composition and thickness, the read-out parameters (applied voltage and scanner frequency) on the image acquisition and the colour detection process are analysed.
A physical model is presented and supported by a numerical simulation of the output characteristics of the sensor.

Keywords: *Tandem pinpin heterostructures, image and colour detection, real time readout.*
Category: 4 (non-magnetic physical devices), 10 (Applications)

1 CLSP operation and image representation

1.1 Single p-i-n structure

Large area p-i-n a-SiC:H heterostructures are used as Colour Laser Scanned Photodiode image sensor, CLSP. The CLSP [1, 2] consists on one large single cell detector (4×4 cm^2) and the image is captured by sequentially detecting scene information at discrete XY coordinates. The design allows a continuous sensor without the need for pixel-level patterning takeing advantage of the amorphous silicon technology. Advantages to this approach are high resolution, uniformity of measurement along the sensor and the low cost/simplicity of the detector. It can also be integrated vertically, *i.e.* on top of a read-out electronic, which facilitates low cost large area detection systems where the signal processing can be performed by an ASIC chip underneath.
The CLSP operation and image representation are based on the analysis of the electrical field profile, induced across the capture device by a steady-state light pattern illumination. Low local electrical fields are ascribed to illuminated regions and high electrical fields to dark zones. In the dark regions the carriers generated by the scanner are separated by the electric field and collected, while those generated inside the illuminated regions mostly recombine inside the bulk. So, by mapping the ac component of the photocurrent, i_{ac}, during the scanning of the capture device it is possible to reconstruct the projected light pattern feature.
In this device the high resistive SiC doped layers confine the photogenerated carriers at the different generation regions and, driven by the scanner, extract information on the image colour and intensity. In short circuit mode, it can detect a black and white image with a spatial resolution of 20 µm. For reading out the RGB colour signals three forward appropriate voltages, close to the open circuit conditions, have to be successively applied in order to collect information to yield the reconstruction of a colour image.

1.2 Double n-i-p-n-i-p structure

When a single p-i-n heterojunction is used as sensing element, the generated carriers can diffuse away from the generated point and escape into the direction paralel to the junction. This effect leads to image smearing. Significant improvement can be achieved if the carriers generated by the light pattern and the emitted light from the scanner can be kept near the junction active region. This carrier and optical confinement can be implemented by using a tandem heterojunction. In the resulting stacked structure (Fig.1) the front a-Si:H i- layer is thick enough to absorb all the light incoming from the image; the rear one is thinner and based on a-SiC:H in order to enhance light transmission from the scanner.

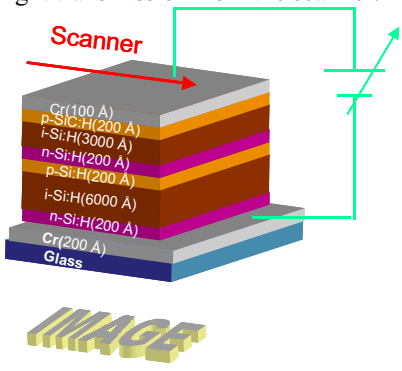

Fig.1 D/CLSP reader and the sensing element structure.

The first p-i-n photodiode, the photodetector, confines the carriers at the illuminated regions while the second one, the reader, driven by the optical scanner, gives information on their location (image shape), density

(image intensity) and absorbed wavelength (image colour).

1.3 Light to dark sensitivity

In fig. 2 the spectral sensitivity without optical bias (dark) and under green illumination (illuminated regions) is displayed.

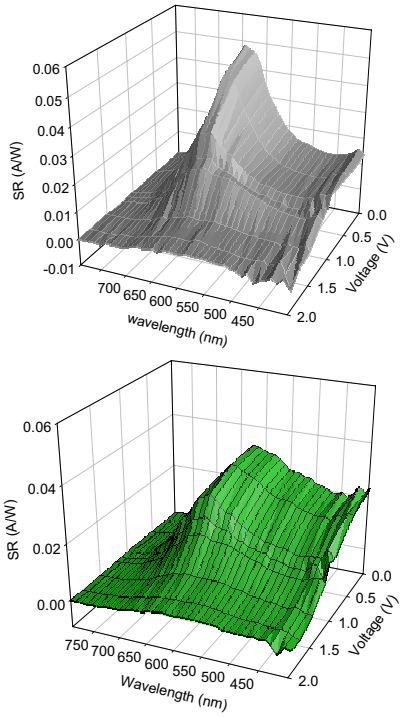

Fig. 2 Spectral response in a tandem structure under different applied bias without (a) and under green illumination (b).

The spectral response depends on the optical and electrical bias. At 650 nm (scanner wavelength) it is much higher in dark than under illumination confirming that this tandem structure can be used as an image sensor sensing element.

1.4 Electrical model

The proposed electrical model is presented in Fig.3. The current across both diodes is the same and the potential drop is shared by both diodes and depends on their photocurrents.

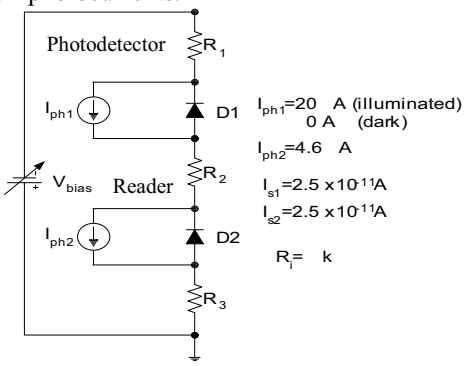

Fig. 3 Electrical model for the D/CLSP.

Circuit analysis simulation show that at low voltages (V<0.8 V) and under illumination the photodetector is self forward biased and the reader becomes reverse biased. The carriers generated at the photodetector (load, ON state) are injected into the reader (photodiode, OFF state) where they recombine, are trapped or collected, depending on its reverse current. A good fit between experimental and simulated data is obtained (see Fig.4).

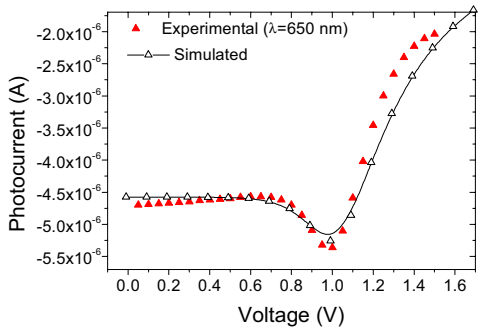

Fig. 4 Experimental and simulated photocurrent as a function of the electrical bias.

1.5 Acquired images

Fig. 5 compare the same image acquired using a single and a double structure showing an improved resolution. The readout frequency was also optimised leading to a value of 1kHz, showing that scan speeds of 1000 lines per second can be achieved without a significant degradation of the resolution.

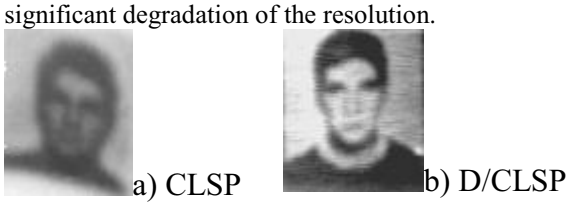

a) CLSP b) D/CLSP

Fig. 5 Same image acquired using (a) single n-i-p and (b) double n-i-p-n-i-p structure.

2 Conclusions

A new design based on a stacked n-i-p-n-i-p structure is proposed for the Color Laser Scanned Photodiode sensor, CLSP. Optical and carrier confinement was achieved. A B/W image was acquired under short circuit condition with improved resolution when compared with the single structure.

Readout of 1000 lines per second was achieved allowing continuous and fast image sensing without the need of pixel patterning.

1. M. Vieira, M. Fernandes, J. Martins, P. Louro, A. Maçarico, R. Schwarz, and M. Schubert, Mat. Res. Soc. Symp. Proc., 609 (2000) A14.2.
2. M. Vieira, M. Fernandes, J. Martins, P. Louro, A. Maçarico, R. Schwarz, and M. Schubert, IEEE Sensors Journal, Vol 1, No. 2 (2001) 158-167.

Perspectives on a CMOS quad-cell matrix for fast wavefront sensing at low-light levels

D. W. de Lima Monteiro and G. Vdovin

Electronic Instrumentation Lab. - ITS - Delft University of Technology
Mekelweg 4, 2628 CD Delft, The Netherlands
email: davies@titus.et.tudelft.nl http://guernsey.et.tudelft.nl

Summary: *Wavefront sensing techniques are used to estimate optical distortions. These aberrations can be present in single components - such as lenses and mirrors -, in optical systems –such as the human eye - and in light beams – such as one propagating through a turbulent atmosphere. In some applications, e.g. ophthalmology and astronomy, the light power available is limited and the need for a highly sensitive sensor is inevitable. In this paper we report on the feasibility to improve a fast Complementary Metal-Oxide-Semiconductor (CMOS) wavefront sensor, based on an array of quad cells, for low-light level applications.*

Keywords: *wavefront sensing, Hartmann method, quad cell, CMOS, low-light level*
Category: *4 (Physical sensors)*

1 Introduction

Dynamic detection of optical aberrations is necessary in fast changing systems, as in surface inspection of industrial parts, or in retinal imaging or also in astronomical observation through a turbulent atmosphere. In the latter two situations, not only real-time detection is needed but also a good detector sensitivity to low-light levels.

A suitable method for dynamic wavefront sensing is the Hartmann technique, in which a light beam, whose associated wavefront is imprinted with the distorted profile of the optical system, is sampled into a number of sub-beams; the angular deviations of the latter with respect to a reference direction enable the calculation of the wavefront profile, as indicated in Figure 1.

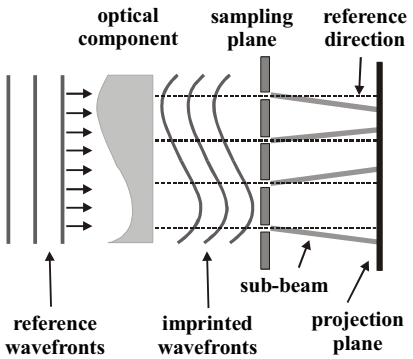

Fig. 1. Hartmann wavefront sensing technique.

The Hartmann sensor consists basically of two planes: the sampling plane and the projection plane. The sampling plane in this case is an opaque mask with a grid of sub-apertures. Conventionally a CCD camera is positioned at the projection plane, where we observe a grid of light spots; by computing the centroid position of each spot we are able to calculate the angle between the sampled beam and the reference direction. Therefore the respective wavefront tilt at each sub-aperture is known and an approximation to the wavefront profile can be directly obtained.

1.1 A custom CMOS chip x CCD camera

Although very sensitive for low-light levels, off-the-shelf CCD cameras feature limited frame rates, up to around 75Hz. Besides, the output of a camera is a bitmap that needs to be processed such that the spot positions are obtained. This is usually a lengthy process and altogether the repetition rate of the wavefront sensor is brought down to around 25Hz.

As regards operational frequency a custom CMOS chip with a matrix of addressable quad cells offers a much higher repetition rate and a simple combination of the quad-cell output signals is directly related to the spot position. We need for this approach one quad cell per sampled light spot. Standard CMOS, however, is not optimized for photodetection and a good spot-position accuracy at low-light levels (<10nW/spot) a number of issues have to be taken into account.

2 The CMOS wavefront sensor

We have fabricated a Hartmann sensor with a 64-sub-aperture mask and a standard CMOS chip with 256 pixels clustered four-by-four as discrete quad cells. Each pixel consists of a 300x300-μm^2 double-junction photodiode and is connected to an analog switch, in a passive-pixel architecture. An integrated demultiplexer selects all pixels from a

specific quad cell at a time, depending on the external digital address supplied. A detail of the implemented chip is shown in Figure 2.

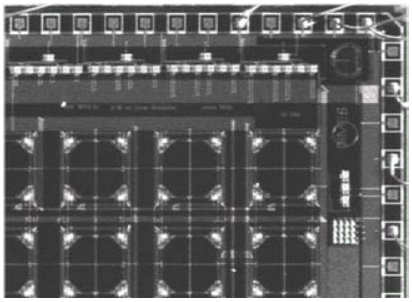

Fig. 2. Detail of the fabricated CMOS sensor.

We used a standard 1.6-μm n-well CMOS process to fabricate the chip. Photodetection, especially for longer wavelengths, and analog-signal swing are favored in this conservative process when compared to sub-micron processes. This is mainly because the depletion layers are wider, the junctions are deeper and the supply voltage is higher.

2.1 Sensor performance

This sensor can be readout at a repetition rate of about 3kHz, which is much faster than conventional wavefront sensors. The signals from the sensor are directly translated into spot positions and an algorithm approximates the wavefront profile based on a set of appropriate polynomials, namely Zernike terms. The software routines altogether do not take longer than 150 μs.

The wavefront accuracy depends on the optical power per spot (indirectly, via the spot-position resolution) and on the spatial-frequency spectrum of the wavefront. The higher the optical power and the lower the spatial frequencies, the better the wavefront-measurement accuracy. For instance, if the desired accuracy is λ/10 (λ=633nm) for spatial frequencies representing the most common aberrations in optical systems (9 Zernike polynomials), then with the current sensor we need a 10-μm position resolution for each quad cell, implying in 2.5-μW spots.

2.2 Sensor improvement for low-light levels

For applications in which low optical power levels are available, we should be able to decrease the amount of light per spot by at least three orders of magnitude and keep the signal-to-noise ratio high enough to guarantee a reasonable accuracy. To accomplish this a number of steps has to be taken in the direction of light collection improvement and noise reduction.

- **lenslet array** *versus* **perforated mask**

We fabricated inexpensive close-packed microlens arrays and when such an array replaces the perforated mask at the sensor sampling plane, the total light collected by the sensor improves by a factor 3.

- **anti-reflective coating**

The number of photons effectively penetrating in silicon is dramatically affected by any dielectric layer left on the top of the photosensitive structure. Simply removing all dielectric layers is not a practical solution both because the bare Si surface reflects nearly half of the light incoming at a normal incident angle – for wavelengths in the visible spectrum - and because thermal oxide inevitably grows there where the Si surface is exposed to air. The sensor features a 40% total quantum efficiency. This figure doubles when a single well-controlled oxide layer is applied to the top of the detector.

- **signal-transfer noise**

kTC noise source is associated with charging a capacitance through a resistance. It represents one of the chief noise contributions in our sensor, due to the huge pixel capacitance (50pF) coupled to the signal line through a select switch. This and amplification noise are significantly suppressed when an active-pixel architecture is used with a well matched amplification stage. Then the photodiode capacitance is isolated from the signal line by a buffer transistor, and the replacing noise contributions are those of the channel resistance of the buffer transistor, which is orders of magnitudes lower and the kTC noise associated with the reset transistor, which can be reduced by using low-capacitance photodiode junction (*n-well*/*p-epilayer*) and largely eliminated by double sampling.

- **dark current**

The dark current density of the chip is 1800pA/cm^2 @300K. This becomes detrimental to the signal-to-noise ratio when the previous noise sources are eliminated. It is known that dark current halves for every 8-^{o}C decrease in temperature. To diminish its contribution without altering a standard process, a Peltier element attached to the chip represents a way to bring it to levels compared to optimized CMOS processes (200pA/cm^2).

Conclusions

We presented the performance parameters of a custom CMOS chip for wavefront sensing based on a matrix of position-sensitive detectors. It operates at a much faster rate than conventional wavefront sensors but the wavefront-reconstruction accuracy is not yet sufficient for applications where the incoming optical power is scarce, e.g. ophthalmology or astronomy. To achieve a good accuracy at low-light levels, we discussed a number of improvements, both in light-collection efficiency and noise reduction, while still keeping the standard CMOS process unaltered. These upgrade steps encompass both off-chip changes (sampling-plane substitution and local cooling) and pixel/readout design issues.

Susceptibility of Cerium Oxide Thick Film Structures to γ- Radiation

K. Arshak and O. Korostynska

Electronic & Computer Engineering Dept., University of Limerick,
Plassey Technological Park, Limerick, Ireland
e-mail: khalil.arshak@ul.ie

Summary: *Investigations into gamma radiation-induced changes in the electrical properties of CeO_2 thick films of various structures were carried out. Carbon doping was used to control the resistivity of the films. Screen-printed capacitors, resistors and pn-junctions were exposed to a disc-type ^{137}Cs source with an activity of 370 kBq. All devices showed an increase in the values of current with the increase in radiation dose up to a certain level. It was found that devices with pn-junction structure exhibited the most sensitivity to γ-rays as their leakage current significantly increased with exposure dose.*

Keywords: *γ-radiation, thick films, CeO_2, pn-junction*
Category: *4 (Non-magnetic physical devices)*

1 Introduction

The measurement of radiation dose is of an ever increasing importance to the estimation of the risks and benefits inherent by the use of ionising radiation in biology, industry, medicine, military applications and research.

The aim of this paper is to document the use of Cerium oxide (CeO_2) thick films with various structures in γ- radiation dosimetry. Both pure and carbon-doped CeO_2 films were screen-printed in form of capacitors, resistors and pn-junctions. Undoped CeO_2 is an n-type material and its conductivity is directly related to oxygen diffusion [1]. CeO_2 has been used for fast-response gas sensors due to its high diffusion coefficient for oxygen [2]. Semiconductor nuclear detectors generally employ one of a number of device configurations (planar, sandwich, grid, etc.) [3]. The electrical properties of the films are highly dependent on both type and composition of the materials used [4]. This work investigates the effects of radiation-induced changes in the electrical properties of CeO_2 thick film structures for dosimetry application.

2 Experimental procedure

Polymer pastes were made of 92 wt.% of CeO_2 and 8 wt.% of $C_8H_{18}O_3$ with Ethylenglycolmonobutylether as a solvent. Devices having capacitor- and resistor-type structures and pn-junctions were manufactured using DEK RS 1202 automatic screen-printer. An impedance analyser (HP 4277A LCZ-meter) was used to measure the variations in both the capacitance and the conductance with frequency. Films of CeO_2 doped with 0.2 wt.% of C were printed on single side polished P⟨100⟩ silicon wafers to from a pn-junctions. A disc-type ^{137}Cs source with an activity of 370 kBq was used for exposing the samples to γ-radiation at room temperature.

3 Results and discussion

3.1 Capacitor-type structures

The variations of capacitance (Fig. 1) and conductance (Fig. 2) versus frequency at different radiation doses were measured for CeO_2 devices having capacitor configuration.

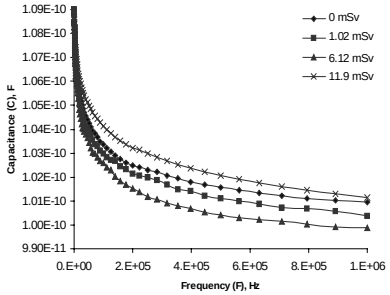

Fig. 1. Plots of capacitance C versus frequency F at different exposure doses for CeO_2 thick film capacitors.

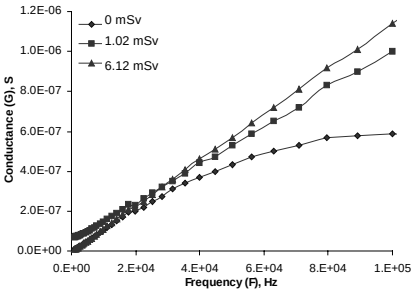

Fig. 2. Dependence of conductance G on frequency F at different radiation doses for CeO_2 thick film capacitors.

It was found that the capacitance decreased, while conductance increased with the increase in radiation dose up to 6.12 mSv. Exposure dose of ~12 mSv resulted in damage of these capacitors.

3.2 Resistor-type structures

Resistor-type devices were having Ag electrodes and were made with Carbon-doped CeO_2.

Fig. 3 and Fig. 4 show plots of I-V characteristics of CeO_2 thick film resistors doped with 0.2 wt.% and 0.5 wt.% of carbon respectively.

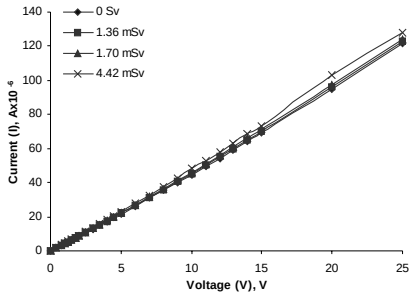

Fig. 3. Plots of I-V characteristics for CeO_2 thick film resistors doped with 0.2 wt.% of C.

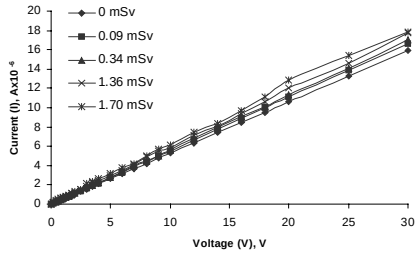

Fig. 4. Plots of I-V characteristics for CeO_2 thick film resistors doped with 0.5 wt.% of C.

Since these devices exhibited lower resistance compared to undoped CeO_2 films, radiation-induced changes in their electrical properties were more pronounced. Resistors doped with 0.2 wt.% of C showed gradual increase in the values of current with the increase in dose up to 4.42 mSv, whereas resistors with 0.5 wt.% of C sustained a lower dose of 1.7 mSv and were damaged on further exposure.

3.3 PN-junctions

Fig. 5 shows current-voltage plots of as-deposited and γ-irradiated CeO_2/Si samples that behaved like backward diodes. Backward diodes are widely used for very fast switching in HF applications as they show no appreciable charge-storage effects.

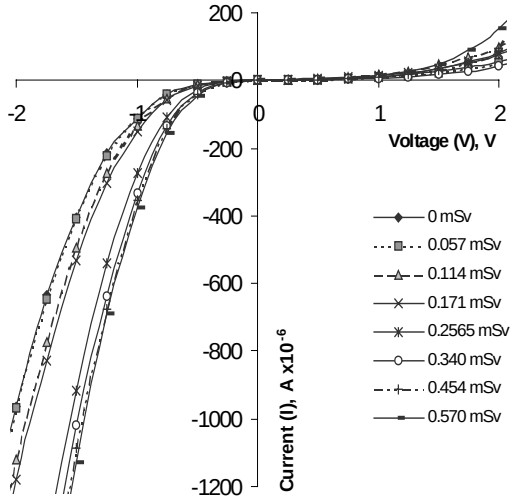

Fig. 5. Changes in I-V plots of CeO_2/Si backward diode with the increase in γ-radiation doses.

The value of leakage current under the reverse-biased conditions increased considerably with the increase in radiation dose up to a level of 570 μSv, while no consistent changes were observed in the values of current when the diode was forward-biased. Fig. 6 illustrates the dependence of normalized current $(I-I_0)/I_0$ with dose under the applied voltage of -1.5 V for CeO_2/Si backward diode.

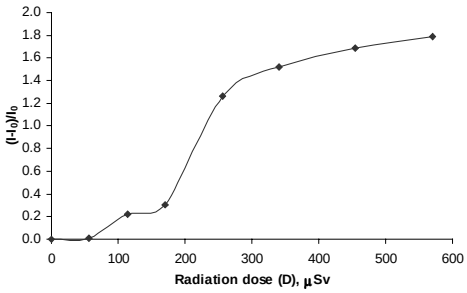

Fig. 6. Dependence of normalized current $(I-I_0)/I_0$ with radiation dose under the applied voltage of –1.5 V for CeO_2/Si backward diode.

Exposure to radiation resulted an increase in the leakage current, caused by the grain boundaries, which served as current paths. Another reason for the worsening of the electrical properties is that the films were damaged by the creation of radiation defects in the form of broken Ce-O bonds and partially due to lowering the barrier height at the Ag/CeO_2 interface.

4 Conclusion

Screen-printed CeO_2 thick films devices, such as capacitors, resistors and pn-junctions were explored in terms of their susceptibility to the exposure of γ-radiation. PN-junctions formed with CeO_2 doped with 0.2 wt.% of C were found to be more sensitive to γ-radiation, as they showed increase in the values of current with the increase in dose up to 570 μSv, and are suitable for low-dose dosimetry. Thick film capacitors with undoped CeO_2 have sustained radiation exposure with a dose of 6.12 mSv and could be recommended for high-dose applications.

Acknowledgments

This research was conducted with the assistance of AMT Ireland in the University of Limerick, as part of the RADSENAD project (ref. PRP00/AMT/06), which is sponsored by the Enterprise Ireland Development Funds.

References

[1] M. Kamiya et al. Oxygen diffusion in CeO_2. *J. Electrochem. Soc*. 147-3 (2000) 1222–1227.
[2] N. Izu et al. Numerical analysis resistive oxygen gas sensors. *Sensor. Actuat. B-Chem*. 87-1 (2002) 99-104.
[3] T.E. Schlesinger et al. CdZnTe as a nuclear radiation detector material. *Mat. Sci. Eng. R.* 32 (2001) 103-189.
[4] K. Arshak et al. Thin films of $(TeO_2)_{1-x}(In_2O_3)_x$ as γ-radiation sensors. *Sensor Review*. SR 23:1 (2003) 48-54.

Shear Stress Sensitive Piezo-FET Stress Sensors with Offset Reduction of Non-Mechanical Contributions

Michael Doelle, Patrick Ruther, and Oliver Paul
IMTEK - Microsystem Materials Laboratory (MML), University of Freiburg
Georges-Koehler-Allee 103, D-79110 Freiburg, Germany
e-mail: doelle@imtek.de phone: +49 761 203 7193 fax: +49 761 203 7192

Summary: *This paper reports novel Piezo-FET stress sensors sensitive to shear stress components with respect to the <110>-directions. The devices are based on the transverse pseudo-Hall effect. The stress sensitivity coefficients Π_{11} and Π_{12} for these devices are extracted from measurements. The experimental setup is characterized using three dimensional (3D) finite element (FE) simulations to analyze the stress state on the surface of the test chip. Non-mechanical offset contributions, e.g., magnetic share, to the signal of these devices are reduced by means of fourfold orthogonal switching.*

Keywords: *stress sensor, piezoresistance, offset reduction*

Category: *4 (Non-magnetic physical devices)*

1 Introduction

The small size of MOSFETs and the large number of electrical modes of operation motivate the use of these devices as stress sensors. Piezo-FETs with high sensitivity to normal stress components with respect to the <110>-directions have been reported in [1]. For a successful application of Piezo-FETs in CMOS-compatible high density stress sensor arrays shear stress sensitive devices are desirable. Therefore, such devices are evaluated in this paper.

Furthermore, a method to reduce the non-mechanical offset, e.g., magnetic contributions, of such devices is described.

2 Experimental

The MOSFETs used in this study were fabricated using the 0.6 µm CMOS process CUP of Austria*micro*systems. The test chip contains NMOS and PMOS devices with various channel lengths and widths. Figure 1 shows as an example a square NMOS-device with four source/drain contacts where two opposite contacts serve as pseudo Hall-contacts. They are integrated to measure changes of the potential distribution in the channel region under mechanical loads appearing as a transverse voltage V_{trans}. The mechanical loads are introduced to the test chip die which is attached to a silicon bar using epoxy resin, with a four point bending bridge as schematically shown in Fig. 2. In addition to the Piezo-FET devices, diffused resistor based Wheatstone bridges were integrated on the test chip to provide independent stress signals.

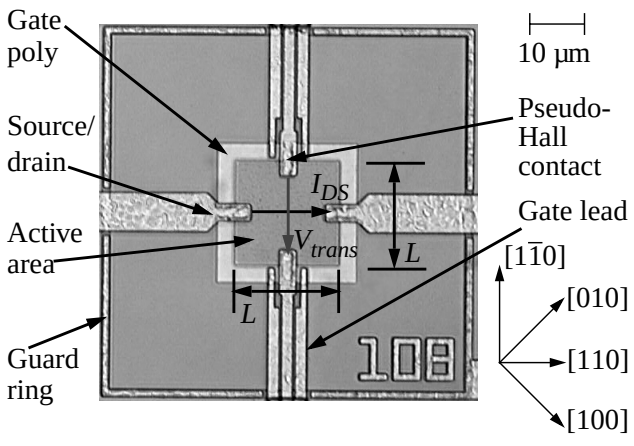

Fig. 1: Optical micrograph of a square NMOS test structure with active area length of L = 19.2 µm.

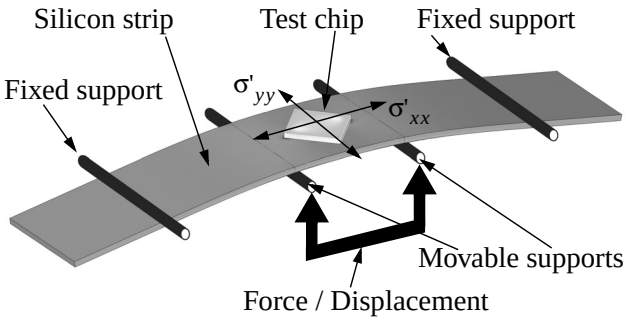

Fig. 2: Schematic view of the four-point bending setup. Black bars illustrate the supports to deflect the silicon strip.

The stress sensitivity of silicon-based MOSFET inversion layers is described by the three coefficients Π_{11}, Π_{12}, and Π_{44} corresponding to the piezoresistance coefficients π_{11}, π_{12}, and π_{44} of diffused resistors. In a coordinate system referring to the <110>-directions (see Fig. 1) the transverse voltage V_{trans} is

$$V_{trans} = (\Pi_{11} - \Pi_{12})\sigma_{xy} V_{DS} G/2 \,, \qquad (1)$$

with V_{DS} the drain-source voltage, σ_{xy} the mechanical shear stress component, and G the geometry factor close to 1. As in the four-point bending setup no shear stress components can be applied to the test chip, the chip is rotated by 45° with respect to the silicon strip and Eq. 1 is transformed to a new coordinate system. Accordingly, in a coordinate system referring to the <100>-directions V_{trans} is

$$V_{trans} = (\Pi_{11} - \Pi_{12})(\sigma'_{xx} - \sigma'_{yy}) V_{DS} G/2 \,. \qquad (2)$$

3 Results

3.1 Sensitivity Coefficients

A typical measurement of V_{trans} as a function of the gate voltage V_{GS} for increasing stress values $(\sigma'_{xx} - \sigma'_{yy})$ for two values of the drain-source voltage V_{DS} is given in Fig. 3. The stress sensitivity coefficients $(\Pi_{11,n} - \Pi_{12,n})$ and $(\Pi_{11,p} - \Pi_{12,p})$ for NMOS and PMOS devices with different side lengths L (4.8 µm, 9.6 µm, 19.2 µm) were extracted from these measurements. The stress values at the position of the devices were determined using the diffused resistor bridges and piezoresistance coefficients found in [2,3]. As an example for the 9.6 µm NMOS device a $(\Pi_{11,n} - \Pi_{12,n})$ of 0.55 10^{-9} Pa^{-1} was obtained. This result is in good agreement with measurements based on the longitudinal effect in Piezo-FETs [4].

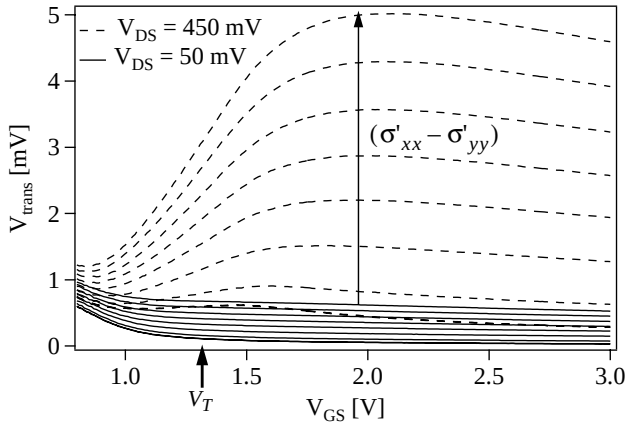

Fig. 3: Transverse voltage V_{trans} vs. V_{GS} for two values of V_{DS} for increasing stress $(\sigma'_{xx} - \sigma'_{yy})$ of a square NMOS. Active area side length is L = 9.6 µm.

3.2 Simulations

For a better understanding of the complex stress state on the test chip surface, 3D FE simulations were preformed using ANSYS 6.1. Figure 4 shows the distribution of the stress components $(\sigma'_{xx} - \sigma'_{yy})$ on the surface of the test chip rotated 45° with respect to the silicon strip.

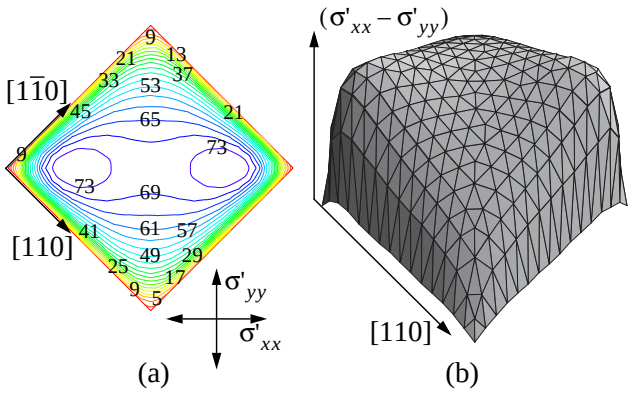

Fig. 4: Stress components $(\sigma'_{xx} - \sigma'_{yy})$ (a) on the surface of the chip calculated using 3D FE simulations with stress levels given in MPa and (b) 3D visualization of the stress distribution.

3.3 Offset Compensation

The voltage V_{trans} in the Piezo-FETs at σ = 0 MPa is two orders below V_{DS}, e.g., about 0.31% of V_{DS} (1.31 mV) for a 19.2 µm PMOS device at V_{DS} = 450 mV and V_{GS} = –3V. Non-mechanical contributions to V_{trans} can partially be determined using fourfold orthogonal switching, where the direction of the current and the measuring direction are changed as indicated in Fig. 5. The sum of V_{trans} for all four

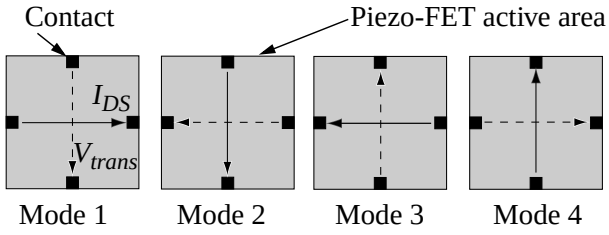

Fig. 5: Fourfold orthogonal switching of I_{DS} and the direction of V_{trans} measurement in a square MOSFET with four source/drain/pseudo-Hall contacts.

switching modes at σ ≠ 0 MPa, i.e., the residual offset is illustrated in Fig. 6 for different V_{GS} and V_{DS}. For compensation this residual offset is then subtracted from the actual measurement. By using this method the non-mechanical signal component in V_{trans}, e.g., caused by the earth magnetic field, is extracted for the above example to 45 µV per direction of I_{DS} at V_{GS} = –3 V and V_{DS} = 450 mV. The residual offset is smallest when the device is operated in the linear region.

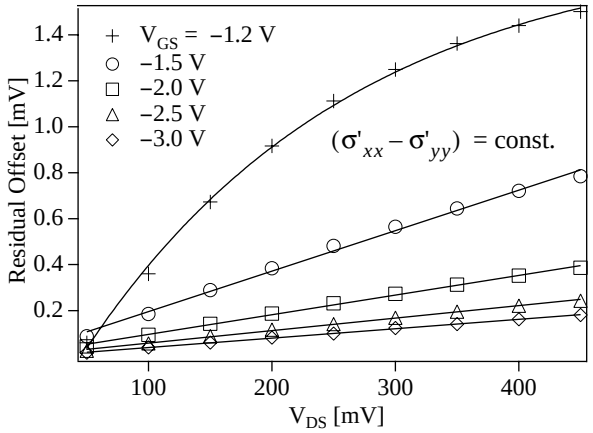

Fig. 6: Residual offset of a PMOS device remaining after fourfold orthogonal switching as a function of V_{DS} and V_{GS} (lines are exponential fit for V_{GS} = –1.2 V, and linear fits for all other V_{GS} values).

4 References

[1] M. Doelle, P. Ruther, O. Paul; Proc. IEEE MEMS'03, 2003, pp. 490-493.

[2] C.S. Smith; Phys. Rev., Vol. 94, 1954, pp. 42-49.

[3] O.N. Tufte, E.L. Stelzer; Phys. Rev., Vol. 133, No. 6a, 1964, pp. 1705-1716.

[4] A.T. Bradley, R.C. Jaeger, J.C. Suhling, K.J. O'Connor, IEEE Trans. Electron Devices, Vol. 48, No. 9, 2001, pp. 2009-2015.

A Novel Pressure Telemetry via RF Power Transmission

Jin Suk Jeong, Hyeun Joong Yoon and Sang Sik Yang

School of Electronics Engineering, Ajou University
San 5 Wonchun Dong, Paldal Gu, Suwon, 442-749, South of Korea
E-mail: ssyang@ajou.ac.kr http://www.ajou.ac.kr/~mems/

Summary: *This paper presents the fabrication and test of a telemetry pressure sensor which can be applied to the intracranial pressure measurement. The measuerment system consist of an LC resonance circuit, an external antenna and the power meter. A novel pressure measurement method via RF power transmission is proposed and various characteristic test results are presented.*

Keywords: *Telemetry pressure sensor, LC resonance, Power transmission*
Category: *4 (Non-magnetic physical devices)*

1 Introduction

Recently, a pressure sensor gets applied to the diagnosis and treatment of some diseases by detecting the variation of pressure in a human body such as an eyeball, vessel and skull, etc. Implantable telemetry pressure sensors have been fabricated by micromaching.[1] In the previous work, we detected the pressure variation by measuring the resonance frequency shift. [2]

We fabricated a telemetry pressure sensor and measured the transmitted power with the power meter. And the pressure sensor is tested to obtain the various charateristics of the sensor.

2 Structure and Fabrication

Figure 1 shows the structure of the telemetry pressure sensor. The sensor consists of a spiral inductor and a variable capacitor. The inductor is fabricated by electroplating on a Pyrex glass substrate. The capacitor consists of two Cr/Au electrodes. One electrode is on the Pyrex glass substrate and the other is on a *p*+ diaphragm of a silicon substrate. The sensor has a small size of 8.05 mm × 7.8 mm so that it can be easily implanted into a cerebral ventricle. The size of the *p*+ diaphragm is 3 mm × 3 mm × 1.5 μm.

Figure 2 shows the fabrication process of the sensor. The upper substrate is fabricated by several micromachining technologies such as doping, evaporation and silicon etching. The lower substrate is fabricated by evaporation and electroplating. The photographs of the sensor and the external antenna is shown in Figure 3. The antenna consists of a coil inductor and feed lines for impedance matching.

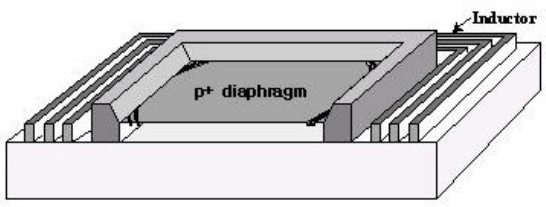

Fig. 1. The structure of the telemetry pressure sensor.

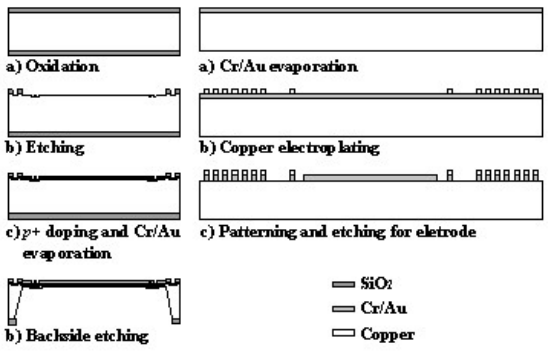

Fig. 2. The fabrication process of the pressure sensor.

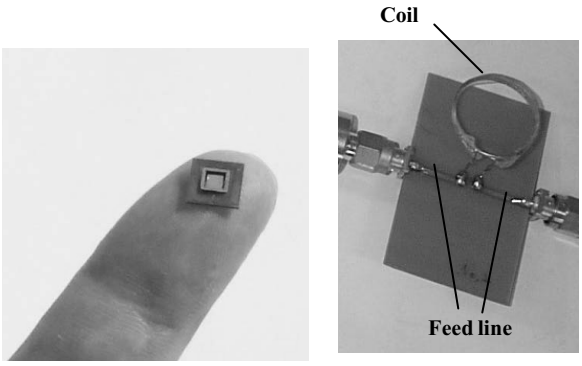

(a) Sensor (b) External antenna

Fig. 3. The photographs of the sensor and the external antenna.

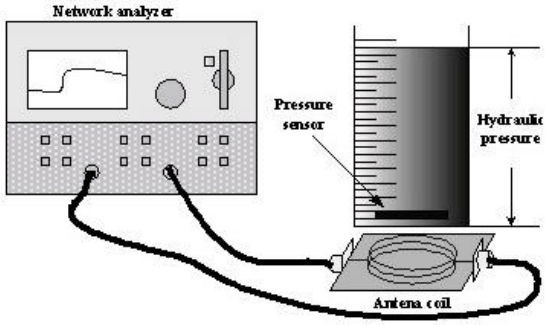

Fig. 4. The measurement setup with a network analyzer.

3 Test and Results

Figure 4 shows the measurement setup including the sensor and the antenna. The sensor is located on the bottom of a beaker and the antenna is placed beneath the beaker. Two feed lines are connected to the network analyzer. Figure 5 shows the phase of S_{21} obtained from the network analyzer. The measured resonance frequency is about 160 MHz. Figure 6 shows the phase of S_{21} for various pressures at the frequency of 159 MHz. As the pressure increases, the phase of S_{21} decreases linearly in the range of 10 to 110 mmH_2O. The sensitivity is -0.08 deg/mmH_2O.

Figure 7 shows the power transmission measurement setup similar to that of Figure 4 except that the signal generator and the power meter are used instead of the network analyzer. The frequency and magnitude of the input signal are 170 MHz and 10 dBm, respectively.

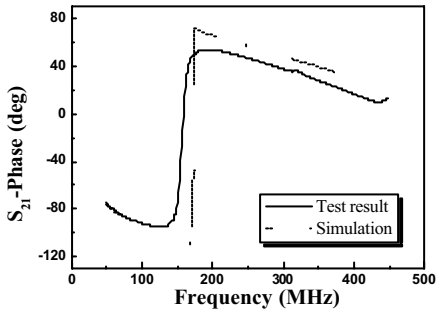

Fig. 5. The phase of S_{21} in a frequency domain.

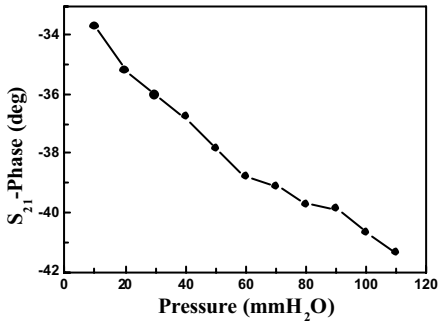

Fig. 6. The phase of S_{21} for various pressures.

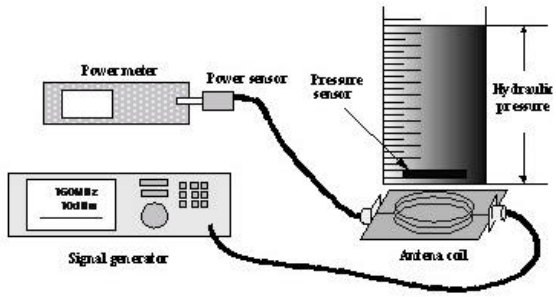

Fig. 7. The test setup with a powermeter.

Figure 8 shows the transmitted power measured with a power meter for various pressures with or without the pig skin between the sensor and the antenna. The result shows the sensitivity decreases a little. Figure 9 shows the transmitted power when the sensor is at the center of the antenna and when the sensor is 10 mm off the center. The sensitivity is not sensitive to the location of the sensor and is –0.005 dBm/ mmH_2O in the range between 10 to 100 mmH_2O. These results illustrate that the sensor is feasible to measure the intracranial pressure.

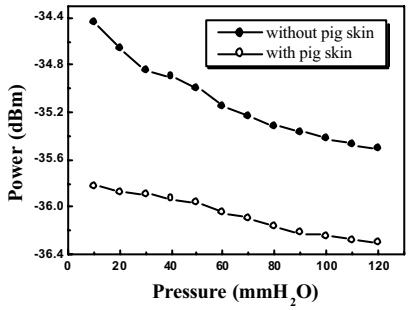

Fig. 8. The transmitted power with or without pig skin.

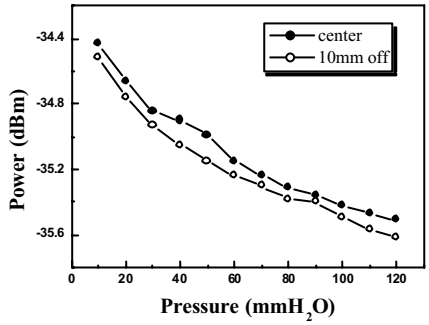

Fig.9. The transmitted power for two sensor position.

References

[1] Orhan Akar, Tayfun Akin, Khalil Najafi, "A wireless batch sealed absolute capacitive pressure sensor," Sensors and Actuators A95 (2001) 29-38.

[2] Soon Young Kim, Hak Jin Kim, Jin Sung Park, Sang Sik Yang, "A Telemetry Silicon Pressure Sensor of LC Resonance Type," Design, Test, Integration and Packaging of MEMS/MOEMS 2001, Cote d'Azur, France, 2001. 4.

Novel structure for large area image sensing

M. Fernandes[1], M. Vieira[1] and R. Martins[2]

[1] ISEL, Electronics and Communications Dept., R. Cons. Emídio Navarro, 1949-014 Lisboa, Portugal
email: mfernandes@isel.pt http://www.isel.pt
[2] FCTUNL, Materials Sc. Dept, Portugal

Summary: *This work presents preliminary results in the study of a novel structure for a Laser Scanned Photodiode (LSP) type of image sensor. In order to increase the signal output, a stacked n-i-p-n-i-p structure with an intermediate light blocking layer. The image and scanner are absorbed in separated junctions; the device photocurrent is dependent on the local illumination conditions on the image side junction. The results show that the structure can be successfully used as an image sensor even though some optimization is needed to enhance the performance of the device.*

Keywords: *large area, image, photodiode*
Category: *4 (Non-magnetic physical devices)*

1 Introduction

In recent works the suitability of a-SiC:H structures to be used as large area image sensors was proven [1,2]. The advantages of this approach are quite obvious like the feasibility of large area deposition and on different substrate materials (e.g. glass, polymer foil, etc.), the simplicity of the device and associated electronics. Nevertheless, and due to the physical process involved, charge collection modulation by the local illumination conditions, the device exhibits reduced signal amplitude forcing the use of lock-in amplification. In order to increase the signal level a different structure was investigated, which consists on two stacked n-i-p structures separated by a reflecting layer. The readout process is similar to the previous one [1] with the difference that in this structures the image and scanner are incident on opposite sides of the sensor.

2 Experimental

2.1 Sample preparation

The proposed structure was fabricated in a three chamber load-lock UHV-system by Plasma Enhanced Chemical Vapour Deposition (PE-CVD) at 13.56 MHz radio frequency on a glass substrate.
The structure is composed by two stacked n-i-p diodes separated by a Cr light screening layer (see Fig. 1). The p-doped layer in the second diode was fabricated introducing methane during the deposition process, in order to decrease the conductivity of the material, which is of crucial importance for device operation. The light screening layer is composed by 290x290 μm^2 Cr pixels with 40 µm spacing and was formed by thermal evaporation of a 90 nm Cr film, followed by photolithography and reactive ion etching. This layer prevents the light crossing one junction from getting to the other one. The patterning is performed to decrease the lateral conductivity which as a negative effect on the spatial resolution of the device. The electrical contacts are formed by two semitransparent Cr contacts on each side of the structure.

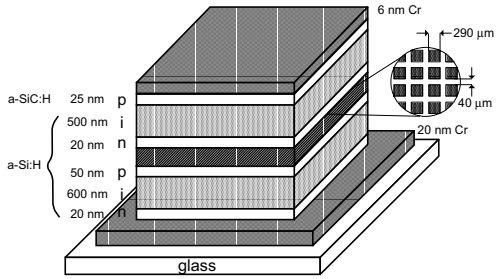

Fig. 1. Structure of the device

2.2 Readout

The image readout process relies on the same principle of the LSP sensor [1], with the difference that image and scanner are incident on opposite sides of the sample, as shown in Fig. 2. This approach simplifies the optical system since image and scanner have different optical paths. As scanner was used a 633 nm low power solid state laser. The beam deflection is controlled by a two axis deflection system capable of high speed scan.
The current from the device is amplified by a current to voltage converter with selectable gain and converted to digital format by a signal acquisition card installed on a computer. Two additional photodiodes provide the synchronization signals for scanner position information, necessary for the image restoration process.
The data is stored as a matrix of photocurrent values which provide information about local

illumination conditions on each position of the active area of the device. Further processing algorithms like fixed pattern noise suppression are performed by software.

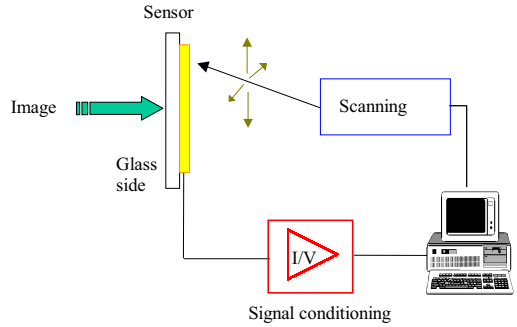

Fig. 2. Readout system

3 Results and discussion

Fig.3 shows the signal obtained in several fast line scans with different image intensities. In this experiment the central area of the sensor is illuminated while the outer region is kept in dark. The scan speed is 10000 lines per second and the sensor active area of ~ 1cm.

When the scan is performed with no image (dark) the photocurrent increases when the scanner enters the active area of the device with a rise time on the order of 10 µs and remains almost constant until the scanner exists the sensor, where the same transient is observed. The rise and fall time of the signal are limiting factors for the scan speed and are dependent on the impedance of the signal amplifier (10kΩ).

Under these conditions there is no current generation in the first junction (glass side), since the blocking layer prevents the scanner light from reaching it. The fact that the current is not completely constant can be ascribed to the variation in the Cr film thickness across the sensor.

When the sensor is illuminated with some light pattern the photocurrent remains the same in dark zones (for low image intensities) and increases (proportionally to the light intensity) in the illuminated zones.

In the last situation the charge generation occurs in both junctions at the same position so the charges are generated across the whole sensor, which justifies the increase in the photocurrent.

With the scanner out of the illuminated region, an increase in the photocurrent is still observed due to lateral currents in the doped layers in the first sensor. This problem can be avoided if the conductivity of the doped layers is decreased by the incorporation of carbon as in the second junction. The lateral currents are responsible by a smearing effect on the image, which increases with the light intensity due to the increase of these currents.

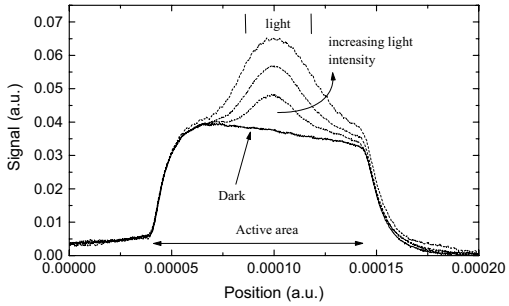

Fig. 3. Signal obtained on several line scans with different image intensities.

The image signal (Fig. 4) is obtained by the subtraction of the dark scan, which also eliminates the fixed pattern noise due to thickness or material properties variation in the different layers.

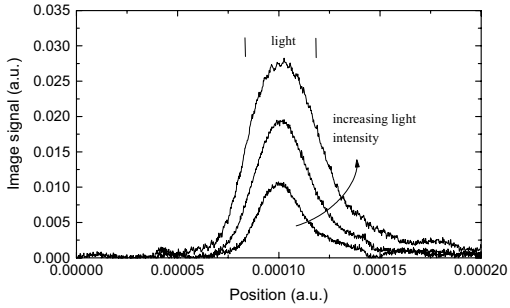

Fig. 4. Image signal, obtained by dark signal subtraction.

4 Conclusions

This work presents the first results obtained with a novel structure for an LSP type image sensor. The results show that a better signal to noise ratio can be achieved with this approach while the same functionality is maintained.

Additionally some enhancements in the structure are proposed to optimize the device performance.

Acknowledgements

The authors would like to thank Dr. Yuriy Vygranenko for the fabrication of the sensors used in this work.

References

[1] M. Vieira, M. Fernandes, J. Martins, P. Louro, A. Maçarico, R. Schwarz, and M. Schubert, IEEE Sensors Journal, Vol 1, No. 2 (2001) 158-167.

[2] M. Vieira, M. Fernandes, J. Martins, P. Louro, A. Maçarico, R. Schwarz, and M. Schubert, Mat. Res. Soc. Symp. Proc. S. Francisco, USA, April 2000

Using Phase Sensitive Techniques to Improve the Resolution of Optical Position Sensitive Detectors

M. Hendawy and P. Lee
Department of Electronics, University of Kent, Canterbury, Kent, CT2 7NT, UK.
Email: mfmh1@ukc.ac.uk

***Summary**: Optical Position Sensitive Detectors (PSDs) based on the lateral photo-effect are popular because they can detect the light spot position continuously without any dead region. This paper presents an alternative technique for measuring the position of a light-spot incident on 1-D sensor that uses phase sensitive detection instead of the commonly used ratio of output currents. Simulated results using an ideal and non-ideal system and an RC transmission line model for a 1-D PSD are presented and show that, at least 10 times improvement in the position resolution compared to the amplitude based position measurements.*

***Keywords**: Sensors, PSD, Opto-electronic sensors.*
***Category**: 4 (Non-magnetic Physical Devices)*

1 Introduction

The behaviour of the lateral photo-effect PSD has been analysed by several models [1-4]. When a PSD is non-uniformly illuminated by a sinusoidal light excitation, the different time delay experienced by the photo-generated currents in travelling different path lengths from the incident light spot position to the lateral contacts introduces a position-dependent phase different between the sinusoidal currents at that contacts. Detection of the phase difference between the output currents at the lateral contacts allows the determination of the position of the incident light beam.

2 Background

In this section, an RC transmission line model for a 1-D PSD is assumed and its equivalent circuit is shown in Fig.1. The circuit elements are defined as follows: R is the resistance per unit length, R_S is the junction leakage resistance per unit length, C is the junction capacitance per unit length, $I(X, t)$ is the generated photo-current at $X = X_1$, Z_L is the load impedance at $X = l$, and Z_S is the load impedance at $X = 0$.

When the load impedance is small compared to the sheet resistance of the resistive layer, the load impedance can be replaced by an electrical short circuit. In addition, the output of the PSD is normally connected to a current-to-voltage converter so that the load impedance seen by the PSD is very small. In this case: $Z_L = Z_S = 0$, and the expressions for the ac currents through the lateral contacts can be given in the following form:

$$I_L = \mathrm{Re}\left[\frac{Sinh[\gamma(L - x_1)]}{Sinh[\gamma L]} e^{jwt}\right] \qquad (1a)$$

$$I_R = \mathrm{Re}\left[\frac{Sinh[\gamma x_1]}{Sinh[\gamma L]} e^{jwt}\right] \qquad (1b)$$

The expressions for the currents given by (1) are applied to some commercial samples of a 1-D PSD [5].

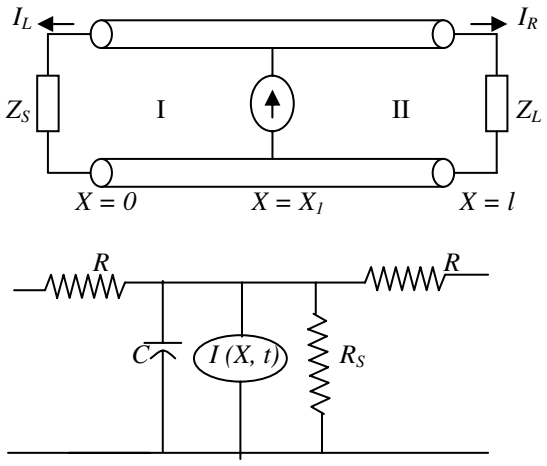

Fig. 1. The equivalent circuit model for the PSD.

3 Ideal Sinusoidal Incident Light Beam

A model of a 1-D PSD using an ideal sinusoidal light beam modulated at frequency 20 KHz, 100 KHz and 1 MHz is performed with MATLAB software. The input current I_S and the generated photo currents I_L and I_R, at frequency f = 1 MHz and at incident light spot position X =2.5 mm, are illustrated in Fig. 2.

The simulation results for different samples are listed in Table 1. The simulations show that the position average phase difference/mm has improved with a high-modulated frequency.

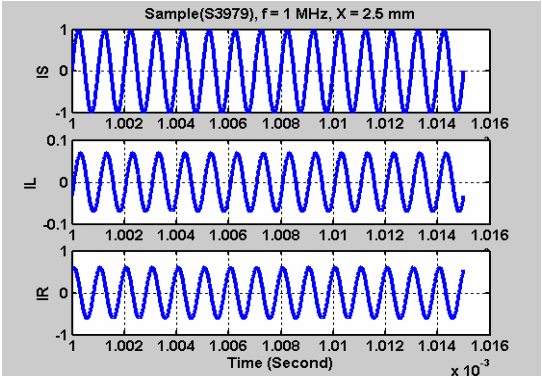

Fig. 2. The sinusoidal input and output currents.

Table 1. The RC transmission line parameters and average phase difference/mm for 1D-PSD.

Samples number		S3979	S3931	S3932	S3270
Active area(mm^2)		1*3	1*6	1*12	1*37
R (Ω / mm^2)		47K	8.3K	4.7K	0.4K
R_S (Ω / mm^2)		1M	1M	1M	1M
C (F / mm^2)		7pF	7pF	7pF	7pF
Average phase-diff. mm (°/mm)	F=20 kHz	2.18	0.79	0.86	0.09
	F=100 kHz	10.86	3.91	4.24	0.47
	F=1 MHz	84.09	32.70	28.19	4.16

4 Complete Correlation Based Position Detection System.

A non-ideal system set-up for position measurement of 1-D PSD using phase detection method is shown in Fig. 3. The RC transmission line model for the PSD, expressed by Equation 1, were used. A result for the measurement system has been obtained using MATLAB software.

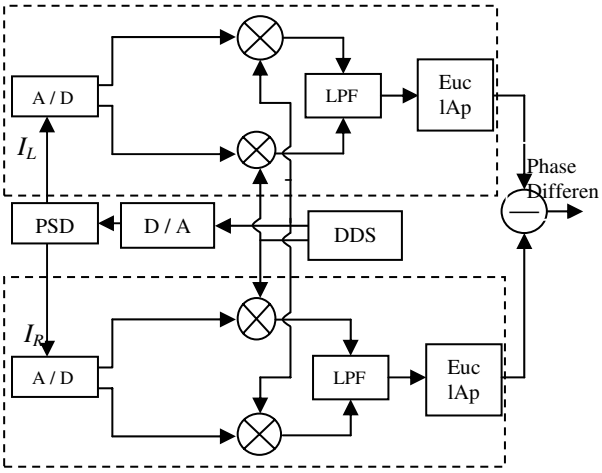

Fig. 3. Basic block diagram of the phase method of position detection.

Simulation results for the position resolution and the position sensitivity for the non-ideal system are listed in Table 2. In addition, the position resolution by an amplitude detection method for the same samples, are listed in same table. The simulations show that, when using phase sensitive methods, the position resolution is improved by over 100 times than those for the amplitude position detection method. It was assumed in these simulation that all the circuit elements and the laser diodes has linear characteristics. But even with non-linear elements, it is expected that around 10 times improvement in position resolution could be achievable by this technique.

Table 2. The Position sensitivity and the position resolution for a non-ideal 1D PSD.

Samples number		S3979	S3931	S3932
Position Sensitivity (°/mm)	F=100 kHz	0.13	0.07	0.08
Position Resolution (n m)		0.08	0.1	0.5
DC-Position Resolution. (μ m)		0.1	0.2	0.3

5 Conclusion

In this work, the generalised equations derived from the RC transmission line model for 1-D PSD is used for calculate the generated photocurrents at its lateral contacts. The phase detection method for an ideal sinusoidal incident beam on 1-D PSD is simulated using MATLAB software. The simulation results show that the average phase difference/mm has improved with a higher modulation frequency.

For a non-ideal phase-detector, simulations have shown that the achievable position resolution using phase sensitive methods is improved over 100 times than for the amplitude position detection method. However these simulations have yet to include the effects of non-linearities in the light source or noise in the PSD. But even with these effects it is expected that a 10 times improvement in position resolution could be achievable using this technique.

References

[1] G. Lucovsky, "Photoeffects in nonuniformly irradiated p-n junctions", *Journal of Applied Physics*, vol. 31, No. 6, pp. 1088-1095, June 1960.

[2] W. P. Connors, "Lateral photodetector operating in the fully reverse-biased mode", *IEEE Trans. Electron Devices*, vol. ED-18(8), pp. 591-596, 1971.

[3] A. K. Dutta and Y. Hatanaka, "A study of the transient response of position-sensitive detectors, *Solid-state Electronics*, vol. 32, pp. 485-492, 1988.

[4] C. Narayanan, A. B. Buckman, and I.Bush-Vishniac, "Position detection of multiple light beams using phase detection", *IEEE Trans. Instrumentation and Measurement*, vol. 43(6), pp. 830-836, 1994.

[5] Hamamatsu product literature, "One-dimensional PSD S3979, S3931, S3932, S3270".

A Novel Pull-in Accelerometer

H. Yang, L. S. Pakula and P. J. French

Delft University of Technology, Mekelweg 4, 2628CD, Delft, The Netherlands
email: h.yang@its.tudelft.nl

Summary: *Described in this paper is a novel accelerometer, which measures the pull-in time to obtain the acceleration. As the pull-in time is a semi digital signal, the output of the device can be measured with a full digital circuit. No analog readout circuit is needed. The sensitivity and nonlinearity are comparable with the differential capacitive sensing devices. The accelerometer has been fabricated by surface micromachining. Al was used as the mechanical layer while PSG was used as the sacrificial layer. The pull-in voltages have been measured. An extensive measurement is under way.*

Keywords: *accelerometer, pull-in, surface micromachining*
Category: *4 (Non-magnetic physical sensors)*

1 Introduction

The surface micromachined accelerometers usually have low pull-in voltage, which makes the capacitive sensing difficult [1]. W. C. Tang proposed a novel digital accelerometer in 1994 [2], which measured the pull-in voltage to obtain the acceleration since the pull-in voltage is the function of the acceleration.

It has been found by the authors that the pull-in time is also a function of the acceleration [3]. A novel accelerometer, which measures the pull-in time, has been designed.

The principle of the device is shown in Fig.1. Pulse voltages ϕ_1 and ϕ_2 are applied to the electrodes 1 and 2 alternately to make the mass be pull-in at the stoppers 1 and 2 alternately. The pull-in time from the stopper 1 to 2 is T_1, and from the stopper 2 to 1 is T_2. If there is no acceleration in the x direction, T_1=T_2=T_0. If there is an acceleration in the x direction, the differential pull-in time, ΔT=T_2-T_1, is proportional to the acceleration. ΔT is a pulse-width-modulated signal and can be measured with a digital circuit. The sensitivity and the non-linearity are similar to that of the differential capacitive sensing.

The accelerometer has been fabricated by the surface micromachining technology. As Al is used to make the structure, the pull-in time can be obtained by measuring the contact between the mass and the stopper.

2 Principle

When the mass moves from one stopper to the other, the movement is governed by the equation

$$m\ddot{x} + c\dot{x} + kx = \frac{\varepsilon\varepsilon_0 AV^2}{2(d_0 - x)^2} + ma \qquad (1)$$

To keep the device working in the pull-in mode, the driving voltage must be higher than the minimum pull-in voltage and the previous pulse voltage should be held long enough to make sure that the initial condition is $\dot{x} = 0$.

When the damping is zero, an analytical expression of the differential pull-in time can be found to be [3]

$$\Delta T = S\tilde{a} + N\tilde{a}^3 + o(\tilde{a}^3) \qquad (2)$$

where $\tilde{a} = ma/kd_0$, S and N are the constants determined by the resonant frequency, the driving voltage and the mass-stopper gap. It can be obtained from Eq.(2) that the differential pull-in time is proportional to the acceleration. As $\tilde{a}$ is always smaller than 1 in the full working scale, the nonlinearity is small.

When the damping is not zero and not very large, Eq.(1) cannot be solved analytically. Matlab was

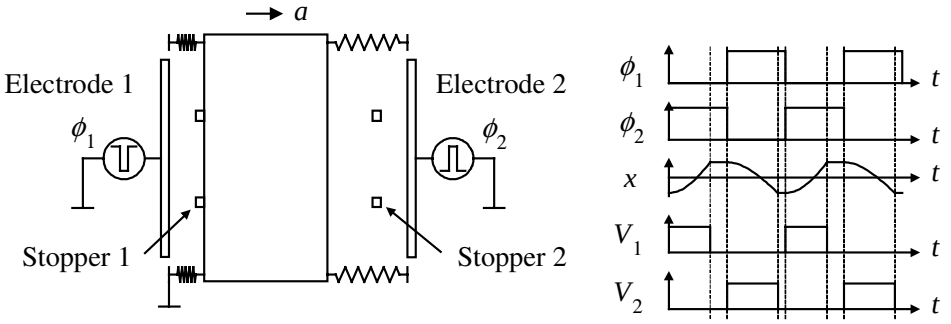

Fig.1 The principle of the pull-in operation

used to analyze the equation numerically. The analysis showed that the sensitivity and the nonlinearity are comparable to the differential capacitive accelerometers.

3 Design

A surface micromachined accelerometer has been design. The whole structure is made by 3μm Al. The mass is supported by four folded beams. The mass is 400μm×800μm. Each fold of the beam is 2.5μm×150μm. Interdigital electrodes are used to drive the mass. There are 62 fingers on each side of the mass. Each finger is 3μm×100μm. The finger-electrode gap is 2μm. The mass-stopper gap is 1μm. The mass-substrate gap is 1μm.

The electrical and mechanical properties have been calculated. The resonant frequency is calculated to be 4kHz. When the displacement is 0, the damping ratio is calculated to be 0.057. The pull-in voltage is calculated to be 4.86V. The pull-in voltage of fingers is higher than 10V when the mass is at the pull-in position.

The static and dynamic properties of the accelerometer in pull-in mode are analysed numerically with Matlab. When the driving voltage is 8V, the pull-in time is calculated to be 77μs. Fig. 2 shows the differential pull-in time with respect to the acceleration, which was obtained by simulation. The non-linearity is 0.87%FS.

As the structure is made by Al, the pull-in time can be obtained by measuring the contact between the mass and the stopper. The pull-in time can be measured with the normal TTL circuit.

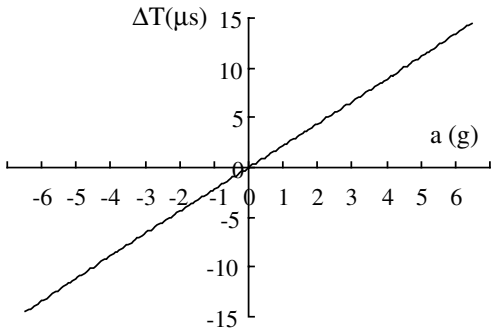

Fig. 2. The output under the 8V driving voltage

4 Fabrication and Measurement

The device has been fabricated by the surface micromachining technology. Al was chosen as the mechanical layer. PECVD PSG was used as the sacrificial layer. 73%HF was used to release the structure. Fig.3 shows the SEM photo of the device.

The capacitance-voltage measurement was performed before packaging. The result was shown in Fig.4. The pull-in voltages were measured to be 8.1V and 8.7V in the positive and the negative directions respectively. The pull-in voltages are higher than the theoretical values and slightly asymmetric because the structure is slightly bent according to the SEM photo in Fig.3. The asymmetry of the pull-in voltages can be compensated by the driving circuit. An extensive measurement is under way.

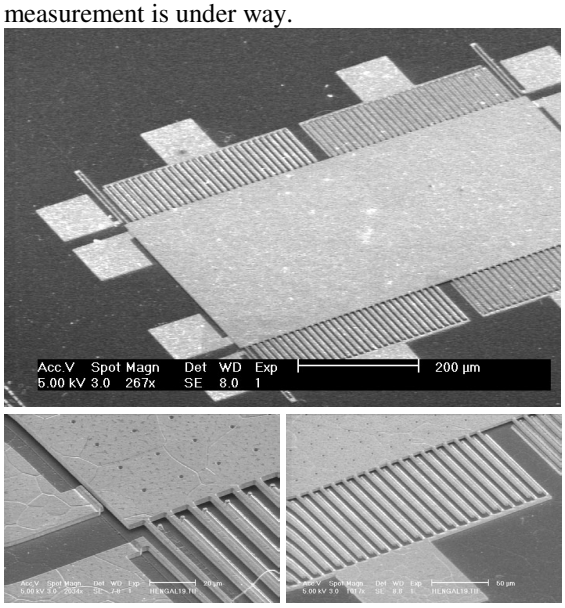

Fig. 3 The SEM photo of the pull-in accelerometer and the close-ups of the stopper and the fingers.

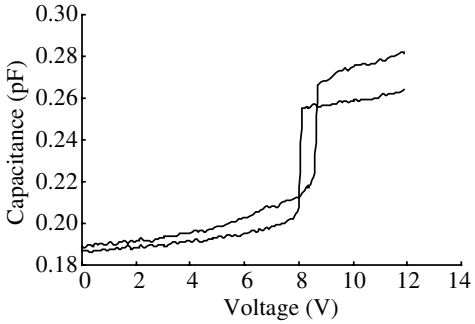

Fig.4 CV measurement

5 Summary

A pull-in accelerometer, which features a digital output, has been designed and fabricated by surface micromachining technology. The pull-in voltages have been measured. The pull-in voltages are a little bit higher than the theoretical results. An extensive measurement is under way. The results will be presented in the paper.

References

[1] M. Bao et al, Effects of electrostatic forces generated by the driving signal on capacitive sensing devices, Sensors and Actuators, A84, Issue 3, pp. 213-219.

[2] W. C. Tang, Digital Capacitive Accelero-meter, US Patent 5353641, Oct. 11, 1994.

[3] H. Yang et al. A novel operation mode for accelerometers, Pacific rim workshop on transducers and micro/nano technologies, July 22-24, 2002, Xiamen, China, pp.303-306.

CMOS X-Ray Imager for Dental Radiography

N. F. Ramos[1], J. G. Rocha[2], S. Lanceros-Mendez[3],
R. F. Wolffenbuttel[4] and J. H. Correia[2]

[1]University of Minho, Dept. Ind. Electronics, Campus de Azurem, 4800-058 Guimaraes, Portugal.
Tel: +351 253 510190 Fax: +351 253 510189 Email:Email: nramos@dei.uminho.pt http://www.dei.uminho.pt
[2]University of Minho, Dept. Ind. Electronics, Campus de Azurem, 4800-058 Guimaraes, Portugal.
[3]University of Minho, Dept. Physics, Campus de Gualtar, 4710-057 Braga, Portugal.
[4]Delft University of Technology, Lab. Electr. Instr., Delft, The Netherlands

Summary: *This paper describes a 64 pixels X-ray imager architecture and fabrication process. The imager is composed by a 8×8 photodiodes array, fabricated in CMOS process, and an array of wells £lled with scintillating crystals. A thick-£lm of aluminum is etched in order to achieve square wells with 500 μm depth. The wells are £lled with CsI:Tl scintillating crystals and placed above the photodiodes. The scintillating crystals convert the X-ray energy into visible light, which is guided into the photodiodes by the re¤ective aluminum walls, avoiding crosstalk between adjacent detectors. Usually, the spatial resolution of the scintillating x-rays detectors is identical to the scintillators thickness. By using the light guides, the scintillator thickness can be adjusted in order to achieve optimal absorption ef£ciency, since the spatial resolution is established by the pixel size (200 μm side).*

Keywords: X-ray, Digital Radiology, Scintillator, Etching
Category: 4 (Non-magnetic physical devices)

1 Introduction

During the last sixty years, the concept of medical imaging has been associated to X-ray imaging systems based on silver £lms, which perform image acquisition and provide physical support for image storage and display. These systems usually demand very strict exposure requirements, due to the narrow brightness depth of the traditional radiographic silver £lms. They also offer very few possibilities of image processing [1].

The advantages of digital radiographic systems may be divided into four classes:

- Reduction of the radiation dose,
- Less time from image acquisition to image display,
- Possibility of image manipulation using digital image processing techniques, and
- Remote storage and retrieval.

The £rst advantage of digital radiology is the possibility of dose reduction. In conventional radiology, the dose is determined by the sensitivity of the image receptor and the £lm brightness depth. In digital radiology, both these constrains can be relaxed. Dose reduction can be achieved by adjusting the dose to give the required signal to noise ratio in the image.

The second advantage is very important in medical emergency situations. The digital X-ray systems can provide images in a few seconds while developing a silver £lm takes several minutes.

The third advantage of digital radiology is the possibility of changing the characteristics of the image during the medical evaluation. The way of mapping the image in levels of brightness on a screen can be completely controlled by the user.

The fourth advantage of digital radiology is the possibility of image storing in a computer database and/or transmission of the images to long distances.

The X-ray imaging systems for dental medicine must £ll some particular requirements:

- It must be inexpensive, easy to use and easy to replace, since most of the dental medicine technicians do not have a good knowledge on radiology.
- Reduction of the radiation dose is very important since the energy and intensity required to cross a tooth and produce an image are signi£cantly high.
- The sensor active area can be small (about $15\ mm \times 20\ mm$), which allows the use of standard fabrication processes.

Due to the high number of dental medicine facilities, the development of X-ray imagers for dental radiography is very interesting for the market.

2 System design

In dental medicine imaging, the X-rays are produced with voltages from $50\ kV$ to $70\ kV$. These voltages produce an intensity peak ranging from $40\ keV$ to $60\ keV$, approximately. A standard silicon wafer

(525 μm thick) only absorbs about 3.38% [1] of the 60 keV X-rays energy, not being suitable for the making of X-rays sensors.

Therefore, a x-ray scintillation layer is necessary to convert X-rays into visible light, which is then converted to an electric signal by means of an array of photodiodes.

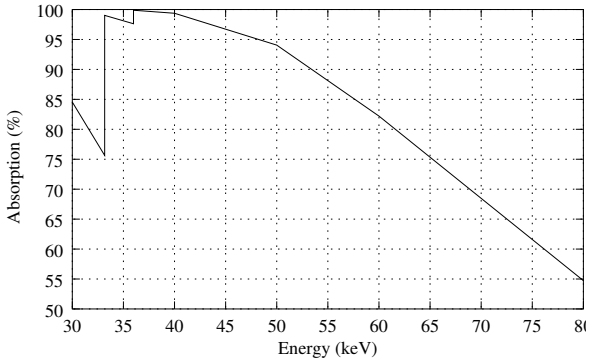

Fig. 1: Absorption of the 500 μm scintillator (CsI:Tl).

Figure 1 shows the percentage of X-rays absorbed by a $500\mu m$ thick CsI:Tl layer (simulated results). From 40 keV to 60 keV the scintillator absorbs more than 80% of the X-rays.

Each scintillator is isolated from its neighbors by aluminum, which allows multiple re¤ections and guides all produced light to the photodiode.

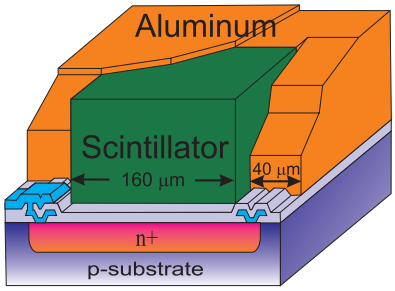

Fig. 2: Structure of each pixel.

Moreover, introducing a re¤ective layer above the scintillator (in the X-rays path) con£nes the light inside the scintillator for increasing the ef£ciency.

Therefore, the device consists of many micromachined aluminum cavities, where the scintillator is deposited. This structure is placed above the silicon die, which contains the photodetectors and readout electronics. Figure 2 shows the structure of one pixel.

3 Fabrication

The photodiodes are fabricated using a standard CMOS n-well 1.6 μm process (Fig. 3 (a)). The chosen photodiode structure was the n+ substrate due to its highest quantum ef£ciency and to its spectral response in the green region of the spectrum. This spectral response is appropriate because, the scintillating crystal used in this work yields green light.

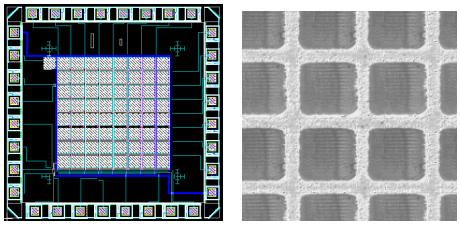

(a) (b)

Fig. 3: (a) CMOS photodiodes array. (b) Photo of the aluminum cavities £lled with the scintillator.

The cavities opened on the thick-£lm of aluminum were made using an excimer KrF laser MINex (Lambda Physik) working in pulsed rating at 248 nm with pulse energy of 30 mJ and peak power of 2 mW, optical mirror and lenses for focusing of the laser beam, translation table with the sample and controlling system. The translation table has an absolute accuracy of 3.6 μm and repeatability of 0.9 μm [1].

The LASER was focused on the surface of the aluminum thick-£lm, using a plano-convex lens with a focal distance of 250 mm. With this setup, the diameter of the LASER cannot be smaller than 71 μm, due to the scattering of the LASER photons. However, this is acceptable for making 160 $\mu m \times 160$ μm cavities.

The cavities are £lled with the scintillator by a clamping pressure machine, in a low-temperature vacuum chamber. Figure 3(b) shows the aluminum cavities £lled with the CsI:Tl scintillator.

4 Conclusions

This approach, scintillators encapsulated in aluminum plus CMOS photodiodes, reveals to be suitable to dental radiography imagers. The aluminum encapsulation allows to increase the scintillator thickness with low cross-talk and good spatial resolution. The re¤ectivity of the aluminum inner-walls of the cavities are poorly affected by the LAT etching. CMOS technology allows to implement x-ray detectors which reveals advantages relatively to the CCD technology. As a future work the size of the cavities will be reduced, in order to increase spatial resolution.

References

[1] J. G. Rocha, N. F. Ramos, et. al., “X-rays Microdetectors Based on an Array of Scintillators: A Maskless Process Using LASER Ablation,” Proc. of IEEE Sensors Conference, 10-12 June 2002, Orlando, Florida, USA.

Responsivities of multiple junction photodiodes and a photoMOSFET

Anssi Mäkynen, Riku Venetjoki, Pasi Palojärvi and Juha Kostamovaara

University of Oulu, Department of Electrical and Information Engineering,
FIN-90014 University of Oulu, Finland
email: anssi.makynen@ee.oulu.fi

Summary: *Responsivities of CMOS/BiCMOS-compatible multiple stacked junction photodiodes and a photoMOSFET has been measured. Multiple junction photodiodes can be used to resolve wavelength of a narrowband illumination source such as LED or laser beacon in a wavelength division multiplexed sensors based on position-sensitive detectors (PSDs), for example. The photoMOSFET provides responsivity in excess of 100 A/W and could be used as the basic building block of an array type PSD.*

Keywords: *CMOS photodiode, photoMOS, Position-sensitive detector*
Category: *4 (Non-magnetic physical devices)*

1 Introduction

Photodetector structures implemented using standard BiCMOS process have been characterized. The test chip included pn-photodiodes with one, two and three stacked junctions, and two PMOS-phototransistors. The idea of using multiple overlapping junctions was that the different spectral responses of the junctions could be used to detect the ”colour” of narrow band light. The idea with the photoMOSFET transistor was to obtaining much higher responsivity than with the pn-photodiodes. Multiple junction photodiode structure will be used to resolve wavelength of a narrowband illumination source such as an LED or laser beacon in a wavelength division multiplexed position-sensitive detector (PSD). Multiple junctions are inherently available in a pinched well CMOS lateral effect PSD [1]. The photoMOSFET will be used as the basic building block of a new PSD in which an area array of small photoMOSFETs are used as photdetectors. The high responsivity of the photoMOSFET is expected to provide high sensitivity similarly to the phototransistor PSD proposed in Ref. [1].

2 Multiple junction photodiodes

The absorpton of light in silicon generates electron-hole pairs. The generation rate depends on the wavelength of the light and on the depth from the silicon surface. The generation rate is

$$G(x,\lambda) = \Phi_0 \alpha(\lambda) e^{-\alpha(\lambda)x}, \qquad (1)$$

where $\alpha(\lambda)$ is the absorption coefficient and Φ_0 the flux of the incident light. For a given depth x_d by changing the wavelength of the light, the carrier generation rate varies. It has the maximum at λ_p corresponding to $\alpha(\lambda_p) = 1/x_d$. If a buried pn junction is formed at a depth of x_d and under reverse bias conditions, photogenerated carriers in the depletion region will be separated by the electric field, thus leading to a drift current. In the neutral regions photo-generated carriers moving to the depletion region edges contribute to diffusion current. These photo-current components are directly related to the carrier generation rate. Thus the spectral response of the buried junction gives a single peak curve which reaches its maximum near wavelength λ_p. As the junction depth increases the peak wavelength increases. By implementing three junctions in stacked form, there will be three photocurrents passing through the three junctions. The spectral responses of each junction has a peak at a characteristic wavelength depending on the junction depth. Short wavelength light is absorbed near the Si surface, while longer wavelength light is absorbed deeper in the material [2,3].

The simple pn-diode utilises a junction between p-substrate and n-well as a photosensitive region (Fig. 1). In the douple-junction photodiode first junction (I) is between p-diffusion and n-well and the second one (II) between n-well and p-substrate. In the triple-junction photodiode the first junction (I) is between n-polysilicon and p-diffusion, second junction (II) between p-diffusion and n-well, and the third (III) between n-well and p-substrate. Responsivities of the different junctions of the photodetectors at 630 nm and 850 nm are presented in Table 1.

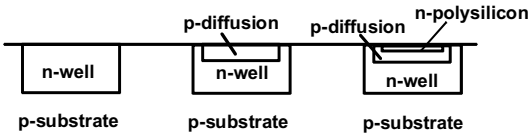

Fig. 1. Constructions of the single-, douple- and triple-junction BiCMOS photodiodes.

Table 1. Responsivity of the single-, douple- and triple-junction photodetectors.

Wave-length [nm]	Single [A/W]	Double [A/W]		Triple [A/W]		
	I	I	II	I	II	III
630	0.3	0.04	0.09	0.035	0.065	0.13
850	0.26	0.005	0.10	0.031	0.038	0.15

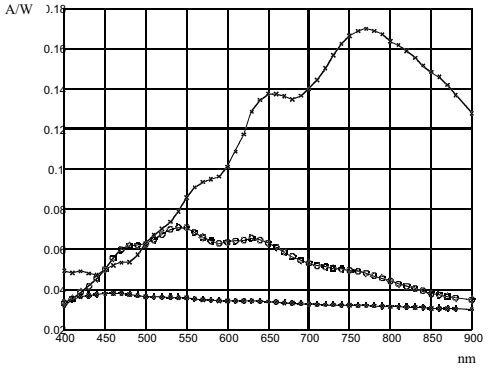

Fig. 2. Responsivities of the triple-junction photodiode: * denoted first junction, ° second junction and x the third junction.

Responsivities of the triple-junction photodiode between 400 nm and 900 nm are presented in Fig. 2. First junction at the surface has lowest responsivity and peaks at the "blue" while the third junction, whose distance from the chip surface is largest provides highest average responsivity of all, and peaks at "red"/near infrared region. The behaviour of the second junction falls between the first and the third. The differences in responsivities in case of multiple junction detectors makes narrow band light detection possible since the ratio of the photocurrents decreases monotonously. Thus it should be possible, for example, to identify illumination sources such as LED or laser beacons in a position sensing system composing of a CMOS PSD with at least two stacked junctions. Possible implementation in case of CMOS PSD is depicted in Figure 3.

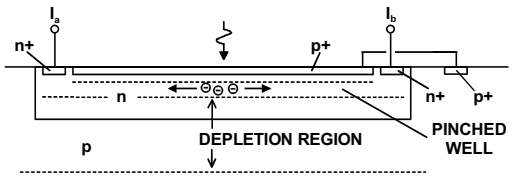

Fig. 3. Multiple junctions are inherently available in a pinched well CMOS lateral effect PSD [1].

3 PhotoMOSFET

The photoMOSFET is a PMOS transistor with a floating n-well body. The photons absorbed near the n-well/p-substrate junction change the potential of the n-well, which then through the back-gate transconductance (body effect) modulate the drain current. The implemented photoMOSFETs measured 200 µm x 200 µm and 16 µm x 16 µm. In both cases the gate dimensions were 10 µm x 0.8 µm. The biasing arrangement of the photoMOSFETs is presented in Fig. 4. The responsivity of the photo-MOS is heavily dependent on biasing as presented in Table 2. The result shows that higher than 100 A/W responsivity is possible.

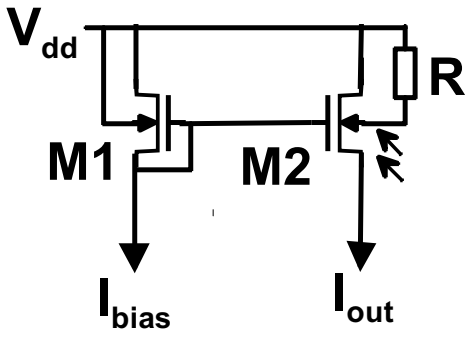

Fig. 4. PhotoMOSFET biasing ($W/L_{M1} = W/L_{M2}$).

Table 2. Responsivity of the photoMOSFET.

I_{bias} [µA]	Responsivity [A/W] (R in MΩ)	
	1	10
1	30	1.5
10	75	5
100	160	11

References

[1] A. Mäkynen, T. Ruotsalainen, T. Rahkonen and J. Kostamovaara. CMOS-compatible position-sensitive devices (PSDs) based on photodetector arrays. Provisionally accepted for *Sensors and Actuators A* (2003).

[2] M. B. Chouikha, G. N. Lu, M. Sedjil and G. Sou. Colour detection using buried triple pn junction structure implemented in BiCMOS process. *Electronics Letters* 34 (1998) 120–121.

[3] M. L. Simpson, M. N. Ericson G. E. Jellison, W. B. Dress, A. L. Wintenberg and M. Bobrek. Application specific spectral response with CMOS compatible photodiodes. *IEEE Trans. Electron Dev.* 46 (1999) 907–913.

The Development and Application of a Fiber Bragg Sensor Interrogation System Using a Commercial CCD Spectrometer

J. Alves[1], C. Félix[2], A. Carvalho[3] and A. Lage[4]

[1,2]Instituto Superior Engenharia Porto, 431 Dr. A. Bernardino de Almeida Street, 4200-072 Porto, Portugal
[1]Dep. Física, email: jaa@isep.ipp.pt [2]Dep. Civil, email: cfelix@fe.up.pt
[3,4]Faculdade Engenharia Univ. Porto, Dep. Electrotecnia, Dr. Roberto Frias Street, 4200-465 Porto, Portugal
[3]email: asc@fe.up.pt [4]email: alage@fe.up.pt

Summary: *Although the advantages of the optical fiber sensors are already established and well known, some issues related to appropriate application and characteristics to be developed still remain as study object. Namely object of discussion is the method to improve the sensibility of the measurement system through using a transducer capable of increasing the measure range In the paper, the performance obtained with a Strain Measurement System based on Fiber Bragg Gratings and a Spectrometer with CCD technology is shown. On a development stage, they are shown some results, obtained during the laboratory tests of a civil structure, specifically on a step of the benches of the new Futebol Clube do Porto Stadium, with a comparison face to conventional methods.*

Keywords: *Optical Sensors, Fiber Bragg Sensors, Strain Measurement and Displacement Transducer*
Category: *Physical Sensors and Applications*

1 Introduction

The use of Fiber Bragg Gratings (FBGs) has come to be spread as sensing elements on structural monitoring. Characteristics as multi point operation, achieved by spatial, time or wavelength division multiplexing (WDM) techniques, immunity to electromagnetic interference and good measurement accuracy, have impulsed this optical method to be improved..

The analysis of FBGs based systems has been performed through a spectral frequency analyzer designed as optical laboratory equipment.

The usage in field measurements becomes a hard task as well as it is a very expensive and rigid solution.
So for this project the main challenge is to develop an interrogation system, which can be compact, versatile and a low cost measurement instrument, regarding to solutions implemented nowadays. Usage of technology based on CCD allows at integrating the FBGs method and at getting such system.
The work related to was carried out in an experimental infrastructure allowing effective comparison with conventional methods.

2 Interrogation System

Looking for Fig. 1, it can be seen that the major alteration comparing to the conventional experimental setup is the change of the OSA (Optical Spectrum Analyzer) by a CCD Spectrometer. As a fundamental difference between the two instruments, it can be pointed out the reached resolution. The OSA has a considerably better resolution, having the CCD spectrometer the economical factor on his side.
Other considerations can be done about acquisition rate. If the number of FBGs is reduced to just one, and considering the acquisition time and peak detection method, the two instruments become very similar ones. If the number of FBGs is increased, we can take profit of the CCD spectrometer and the developed peak detection method, reducing the time per acquisition.

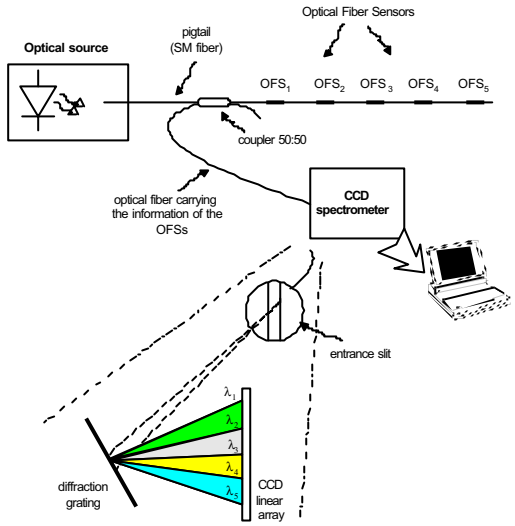

Fig. 1: Model of the developed interrogation unit

3 Strain Measurement Transducer

For the measurement of displacements on concrete Civil structures it was developed a transducer that converts the displacement into a strain, on a spring plate. They were constructed two similar prototypes: one using a full Wheatstone-bridge with

four active Strain Gauges and the other using a single OFS (Optical Fiber Sensor).
Using a displacement table (with a position resolution of 1 μm), the laboratorial validation and calibration of these two transducers are performed. The results of the calibration are shown on the next two figures. It can be seen the agreement between the results of Fig. 2 and Fig. 3, confirming the expected linearity of the response.

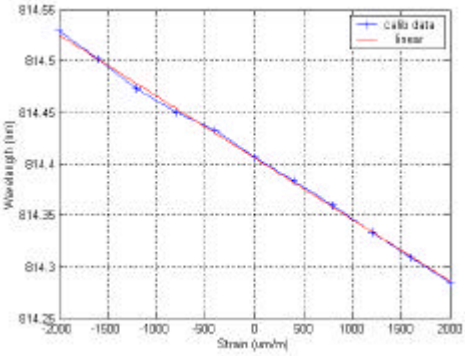

Fig. 2: Optical Transducer Calibration result

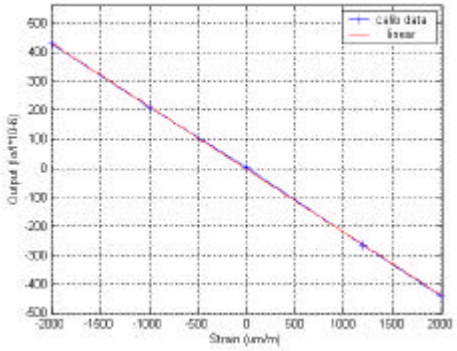

Fig. 3: Electrical Transducer Calibration result

4 Laboratorial Application

With the objective of studying the behavior of the benches of the new FCP stadium, a set of laboratorial tests on a pair of steps was conducted (Fig. 4). One of these tests was the load/unload test. Both transducers were installed on the lower face of the middle span section, as a mean to obtain comparable results.

Fig. 4: Picture of the simple support bench structure

It should be noticed that the conventional transducer is a commercial one, naturally producing a well-conditioned signal at output. However the FBG interrogation system output signal is shown just without any conditioning besides conversion strain input into electrical output.
Fig. 5 shows the results of the test, presenting *Strain* as output. The results confirm the expectances resulting from performed theoretical analysis.

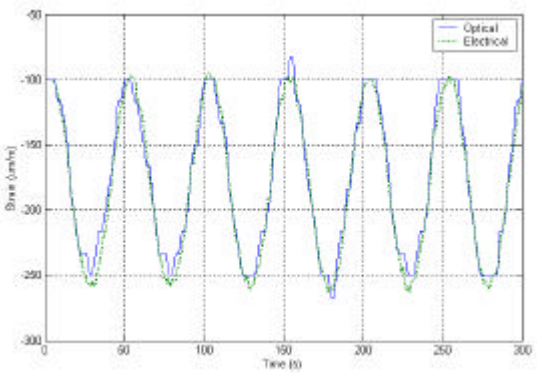

Fig. 5: Graphical results with both Transducers

5. Final Considerations

The results obtained with these tests reveal a good response of the Optical Transducer. Nevertheless, significant facts and future developments must be pointed out:

- All these results were obtained under controlled temperature conditions;
- The apparent great accuracy obtained with the transducers illustrates the good performance of the optical sensor in terms of sensibility;
- Further developments will include the temperature compensation and the sensor sensibility amplification and resolution.

The results carried out encourage to keep on this researching line. In fact, since guaranteed good measurement characteristics, the proposed system seems to solve some of the difficult issues on instrumentation of this kind of applications. Namely it should be remarked those ones related to grounding, electromagnetic interference, physical deterioration of the sensor element, what prejudices lifetime of the equipments and repeatability of the measurements.

References

[1] Alves J., Carvalho A., Lage A., "Desenvolvimento e Aplicação de um Sistema de Interrogação de Redes de Bragg", *VII Congresso de Mecânica Aplicada e Computacional*, April 2003

[2] Kashyap, Raman, "Fiber Bragg Gratings", Academic Press, 1999

[3] Measures, Raymond M., "Structural monitoring with fiber optic technology", Academic Press, 2001

Quartz-based sensors for both microgravimetric and optical detection

J. Zhang, S. O'Shea, X. D. Su*

Institute of Materials Research and Engineering, Research Link 3, Singapore 117602
*Corresponding Email: j-zhang@imre.a-star.edu.sg

This paper describes the technique to monitor biomolecular adsorption with a quartz based microchip. The microchip made from quartz crystal is demonstrated which can be used as a common platform for both quartz crystal microbalance (QCM), and optical detection. It can provide a multi-parameter bio-detection sensor.

The microchip consists of a transparent piezoelectric substrate (quartz, lithium niobate) with either one or both of the electrodes made from a transparent, conductive thin film. Transparent, conductive thin films with high electrical conductivity and suitable optical properties (i.e. high transmission rate and low optical loss) include transparent semiconductor metal oxides (e.g. Indium tin oxide, Zinc tin oxide) or conductive polymers. The advantage of this microchip is that complimentary signals (optical film thickness from SPR, acoustic film thickness from QCM, characteristic optical spectra for specific bio-molecules, fluorescent images for tagged biological markers, etc) can be obtained simultaneously, thereby giving additional information on the molecular binding at the sensor surface. Furthermore, the principles and concepts listed here are also suitable for multiple arrays of such sensors fabricated on the same substrate. Such arrays are potential devices in realistic applications for multiple biomedical assay and microchip.

In this paper, the quartz based sensor were begun from the transparent conductive semiconductor oxide, Indium tin oxide, which was prepared by the rf-sputtering technique. The conventional photolithography technology was employed to form the electrodes on the double sides of quartz crystals. The conventional oscillation circuit and the impedance/network analyzer were employed to measure the frequency response. And the UV-vis photospectrometer, with the wavelength ranging from 400 to 1100nm, was used to measure the optical properties.

Some combined microgravimetric and optical florescent detection experiments were also undertaken and demonstrated. First, one of the ITO surfaces was primed with the silane HDMS or made biologically active by coating with an aminosilane (APTES). Then, the devices were exposed to antibody targets (Ab) labeled with FITC fluorescence probes.

The corresponding frequency shift of the chip as the microgravimetric sensor had been observed, as shown in Figure 1. The frequency shift before and after the affinity reaction is ~1000Hz, demonstrating that the chip can act as a microbalance. The optical detection in the transmission mode in Figure 2 had shown that this chip also can be measured by the UV-vis spectrophotometer. Figure 3 showed the visual results obtained by the fluorescent microscopy.

These results demonstrate that with the ITO electrode transparent electrodes, a microchip that can simultaneously measure microgravimetric and optical responses can be realised.

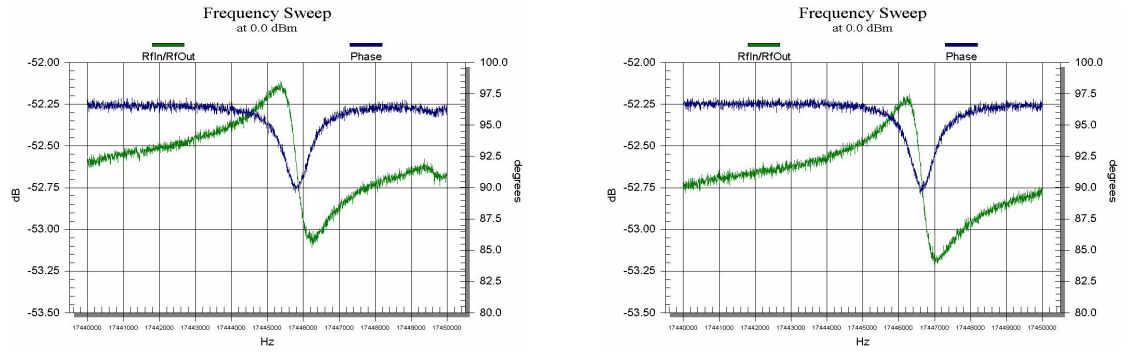

(a) (b)

Figure 1. Frequency response of Microchip #2 before and after mass loading with antibody. (a) Before the mass loading, the resonant frequency is f_0 ~17,447,000Hz; (b) after the mass loading, the resonant frequency is about f_0'~17,446,000Hz, i.e. a frequency shift of ~1000Hz occurs on adsorption of the antibody.

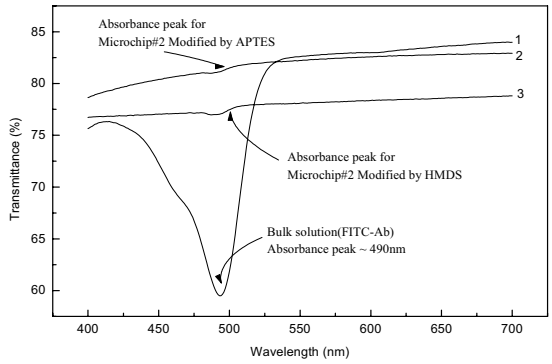

Figure 2. Transmittance spectra for Microchip under different conditions: (1) Exposed to a bulk solution of FITC-Ab, (2) After FITC-Ab adsorption onto an ITO surface modified with aminosilane APTES, (3) After FITC-Ab adsorption onto an ITO surface modified with silane HDMS.

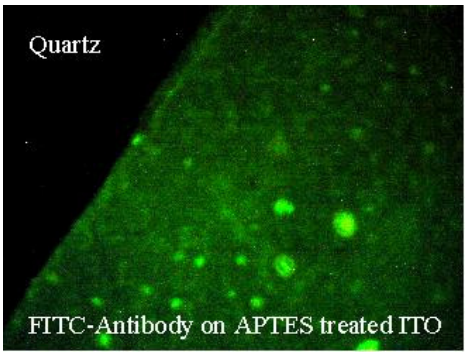

Figure 3. Photo of Microchip under the fluorescent microscope. The excitation UV-light is projected from the backside and the observation is proceeded from the front-side. Fluorescently tagged antibody can be observed adsorbed onto the ITO surface.

Reference:

J Zhang, S O'Shea, Singapore patent Application Number: 200207922-6.

An optical biosensor for on line detection of organotin compounds with a bioluminescent bacteria

G. Thouand[1], H. Horry[1,4], MJ. Durand[1], Ph. Daniel[2], P. Picart[3] and L. Bendriaa[2,3]

[1]Université de Nantes, IUT de la Roche-sur-Yon, département Génie Biologique, Laboratoire CBAC/BSCA, 18 Bd G. Defferre, 85035 La Roche-sur-Yon, France. email: gerald.thouand@laroche.univ-nantes.fr
[2]LPEC, UMR CNRS 6087, Avenue Olivier Messiaen, 72085 Le Mans Cedex 9, France.
[3]École Nationale Supérieure d'Ingénieurs du Mans, rue Aristote, 72085 Le Mans Cedex 9, France, LAUM, UMR CNRS 6613, Avenue Olivier Messiaen, 72085 Le Mans Cedex 9, France.
[4]Biolumine S.A., Plate-forme Vendée Recherche, Parc d'Activités de la Croix Verte, 85600 Boufféré, France.

Summary: *The paper presents the development of a bacterial bioluminescent biosensor (LUMISENS I). The system is composed of a bioreactor surrounding by autonomous devices that allow the real-time control and monitoring of the bioluminescence and bacterial response factors: growth rate, cell density, temperature, pH, dissolved oxygen. This survey present the experiments that were conducted to chose the optical transducer, the features of the biosensor and the application of LUMISENS I to the on line and continuous detection of TBT during a 7 days experiment.*

Keywords : *LUMISENS I, optical biosensor, tributyltin*
Category : *6 (Biosensors)*

Introduction

The measurement of compounds constitutes a major tool for regulatory agencies as well as for the control and the monitoring of processes in industrial areas. Thus, the development of new detection methods like biosensors becomes desirable since they are fast, reliable, sensitive and easy to use. Biosensors couple a biological element (enzyme, antibody, cells, nucleic acid) to a physical partner (transducer) that can transform a biological signal (redox potential variation, pH variation, light production,…) in an easy detectable electric signal [1].

LUMISENS I was developed for the detection of organotin compounds such as tributyltin (TBT). These biocides have been extensively used in antifouling paints and are currently present in marine and terrestrial environments [2]. Because of its high toxicity, TBT has been well monitored and it is currently on the list of the 20 prioritary substances from the European Parliament since 2002 [3].

LUMISENS I is an optical biosensor since the sensitive part of the device is a highly sensitive bioluminescent bacteria. We present below the bioelement, the device itself and the current results

Biosensing element

The bioelement is a recombinant bioluminescent bacteria namely *Escherichia coli* TBT3 (EC::*lux*AB TBT3) obtained after random insertions of the *lux*AB genes of *Vibrio harveyi* in the *Escherichia coli* DH1 chromosome [4]. The strain specifically detects TBT or DBT with a detection limit of 26 $\mu g.L^{-1}$ TBT and 0.03 $\mu g.L^{-1}$ DBT (Fig.1) [5].

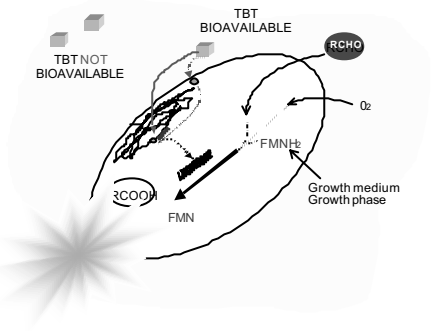

Fig. 1 Induction of bioluminescence of the EC::*lux*AB TBT3 strain with TBT. TBT induces the production of the enzyme luciferase that catalyses the oxidation of a reduced flavine mononucleotide co-factor and a long chain aldehyde (RCHO) leading to an oxidized flavine mononucleotide, a fatty acid (RCOOH) and light.

Optical transducer

The optical transducer of LUMISENS I was developed in order to measure the bioluminescence of EC::*lux*AB TBT3 and other strains with a photomultiplier tube (PMT) due to its high sensitivity. Nevertheless, the choice of the optical equipments, like lenses, optical fibers and PMT depends on the spectral characteristics of the emitter (i.e. the bioluminescent strains in our case). Hence, those equipments should be the same whatever the strains, and their growth conditions. Thus, *in vivo* bioluminescence spectra of several bioluminescent strains were recorded with a highly sensitive spectrometer initially devoted to Raman scattering. When spectra were compared between all the studied bacteria, no difference was observed between all the

strains tested and whatever the growth conditions (Fig.2). Hence, the transducer developed here can be used in all circumstances [6]

Biosensor LUMISENS I

The biosensor features (i) the mini-bioreactor that allows a stable and reproducible environment for the bacteria as well as an *in situ* contact with the toxic compound, (ii) the transducer and the analytical light device permits the real-time monitoring and analysis of the bioluminescence (Fig. 3). The bioreactor is hermetically closed by a screw-down stainless-steel lid. The lid allows the fixation of micro-probes (oxygen, temperature, pH), the injection of liquid by a dedicated hole, the inlet and outlet of the culture medium and TBT.

The data are monitored with the Acquisition/Regulation Device controller which manages the signals from probes. The bioluminescence is recorded with the PMT Device. Light emitted from bacteria in the bioreactor is focussed via a convex lens at the entrance of a glass bundle fibre optic fixed at the intake of a pipe screwed to the lid of the bioreactor. The other part of the optic cable was connected to the PMT. Data are transferred to a dedicated LabView interface.

First results reported that a synthetic glucose medium gave a better detection limit than LB medium. A high growth rate (0.9 h^{-1}) provided maximum bioluminescence and a simple air bubbling was enough to provide oxygen for the growth and the light emission. Basically, because of the single *lux*AB insertion, decanal must be added for the bioluminescence reaction leading to a difficulty to use the strain as the bioelement. We overcame this with a continuous addition of decanal that was not toxic up to 300 µM throughout a 7 days experiment (Fig.4).

Although the optimisation of the performances of the biosensor is under development, thanks to its original design, LUMISENS I already appear as a warning system for the on-line monitoring of TBT [7].

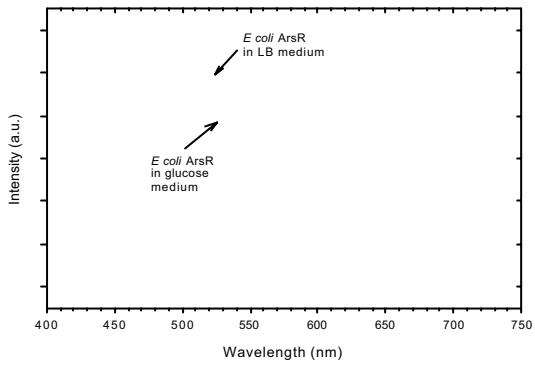

Fig. 2. Spectral emission of the bioluminescente EC::*lux*AB ArsR in two different culture conditions. (Results are similar for EC::*lux*AB TBT3).

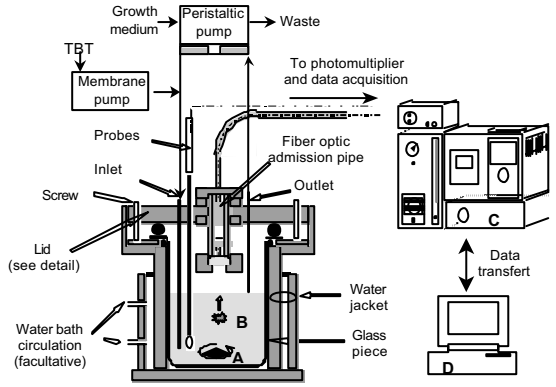

Fig. 3. Schematic representation of LUMISENS I. A: Agitation, B: Bioluminescent bacteria, C : Photomultiplier and Acquisition/Regulation Devices, D : Graphical interface

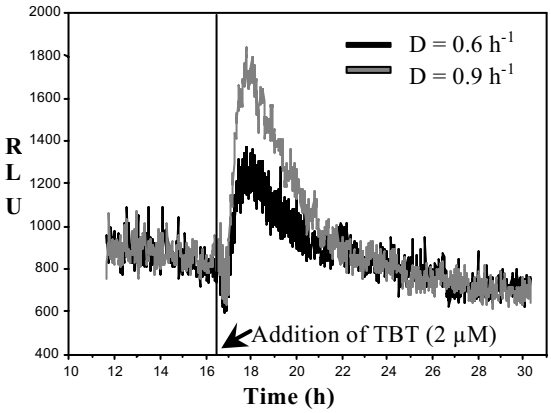

Fig. 4. Application of LUMISENS I to the detection of TBT (RLU : relative light unit)

References

[1] E. Kress-Rogers. Biosensors and electronic noses for practical applications. In: E. Kress-Rogers (ed). *Handbook of biosensors and electronic noses, medicine, food and the environment*. CRC Press, New York, (1997) 3-39.

[2] J.S. White, J.M. Tobin and J.J. Cooney. Organotin compounds and their interations with microorganisms. *Can. J. Microbiol.* 45 (1999) 541-554.

[3] EEC N°2455/2001/EC, decision of the european parliament and of the Council of 20 November establishing the list of prioritary substances in the field of water policy and amending Directive 2000/60/EC, Official Journal, L331, 44, 15 december 2001.

[4] A. Guzzo, M.S. DuBow. Construction of a stable, single copy luciferase gene fusions in *Escherichia coli*. *Arch. Microbiol.* 156 (1991) 444-448.

[5] M.J. Durand, G. Thouand, T. Ivanova, P. Vachon and M.S. DuBow. Specific detection of organo-tin compounds with a recombinant luminescent bacteria, *Chemosphere* (2003) (in press).

[6] G.Thouand, Ph. Daniel, H. Horry, P. Picart, M.J. Durand, K. Killham, O.G.G. Knox, M.S. DuBow and M. Rousseau. Comparison of the spectral emission of *lux* recombinant and bioluminescent marine bacteria, *Luminescence* (2003) (in press).

[7] G. Thouand, H. Horry, M.J. Durand, P. Picart, L. Bendriaa, Ph. Daniel and M.S. DuBow, Development of a biosensor for on line detection of tributyltin with a recombinant bioluminescent *Escherichia coli* strain, *Appl. Microbiol. Biotechnol.* (2003) (in press).

A Triple Electrode System for Cell Growth Detection as Basic Unit for High Throughput Screening

E. Spiller[1], T. Frömmichen[1], A. Zimmermann[2], A.E. Sippel[2] and G.A. Urban[1]

[1]University of Freiburg, Inst. f. Mikrosystemtechnik, Georges-Köhler-Allee 103, 79110 Freiburg, Germany
email: spiller@imtek.de http://www.imtek.uni-freiburg.de
[2]University of Freiburg, Institut für Biologie III, Schaenzlestrasse 1, 79104 Freiburg, Germany

Summary: *Functionalized nuclear receptors of yeast cells (e.g. ordinary brewers yeast) can be used to detect and determine a great variety of substances very specifically. If a certain substance binds to the nearly arbitrarily modified receptor it induces cell division under specific conditions and therefore increases cell mass. This increase can be determined by non-invasive conductometric measurements very rapidly. Possible applications are hormone-monitoring, doping control, the development of an artificial nose and HTS (High Throughput Screening).*

Keywords: *BioMEMS, HT screening, cell based biosensor, biomass monitoring*
Category: *6 Biosensors*

1 Introduction

Sensor system based on receptors residing directly on the surface of a substrate suffer from the disadvantage of ambiguity. The receptor usually binds a class of substances (growth factors, cytokines, hormones). Optical, gravimetrical and electrochemical measurement methods determine the amount of the bound class of substances. In cooperation with the Institute of Biology (University of Freiburg) it is now possible to circumvent these disadvantages by a new sensor concept. The basis of this system are yeast cultures (Saccharomyces cerevisiae), which contain specifically adapted nuclear receptors (or members of other receptor classes, e.g. RTK, GPCR) [1]. These genetically modified receptors (according to the substance to be observed) lead in the case of ligand-binding to a signal transduction, which then induces cell division. The resulting increase of biomass is a measure for analyte concentration. Cell concentration in suspensions can be determined by conductometric measurements. In this paper we present the measurement setup and design concept.

2 Theoretical Aspects

The interior of biological cells is effectively shielded by the capacitive behavior of the cell membrane at frequencies substantially below the so-called characteristic frequency f_c (approximately 1MHz for yeast suspensions). Therefore the current path through the suspension is restricted depending on the amount of viable cells [2].

The Maxwell-Fricke equation [3] relates the volume fraction of cells in suspension H to the ratio of the conductivities of the electrolyte σ_{el} and the suspension σ_{susp} where F is a form factor (= 2 for spherical cells).

$$\frac{\sigma_{susp}}{\sigma_{el}} = \frac{1-\frac{H}{F}}{1+\frac{H}{F}}$$

The measured resistance R_m depends on medium conductivity and cell constant, which is determined by the geometrical arrangement.

$$R_m = K_i / \sigma_i \quad ; \quad (i = E, S)$$

$$\Leftrightarrow K_i = \frac{\Phi}{A_i \nabla \Phi}$$ A: electrode area; Φ: potential

It is intended to measure resistance changes in the range of 0.1-1Ω over a period of 5h. The measurement set up includes three electrodes in a ring structure, which are covered by a membrane layer establishing a configuration with two different cell constants K_i [4], [5].

Yeast cells are hindered to penetrate the membrane whereas the conductivity of the membrane layer is mainly influenced by the electrolyte itself. The planar arrangement could be transformed by conformal transformation into a plane parallel configuration. Because of the ring configuration the surface areas have to be taken into account in the calculations. In the transformed space the electrode for current injection CI is opposite to the electrodes for measurement of the electrolyte conductivity CE and for suspension conductivity CS, respectively. The transformation allows estimation of cell constants and optimisation of electrode geometry and membrane height so that the resulting currents are mainly flowing through the membrane layer I_{CE} and through the suspension I_{CS}, respectively (see section Experimental).

The initial number of cells is 10^4/µl, the expected maximum number of cells that could be cultivated is

approximately 10^5/µl (=3 cell divisions). The decrease of conductivity is therefore 3mS/cm.

3 Experimental

One realisation prerequisite was miniaturization to µl-scale to allow for HT-Screening applications. We decided to use 1536 well (12µl) microtiter plates (Greiner Labortechnik), which were supplied without bottom foil. The conductometric sensor elements were processed on a glass wafer in thin-film technology. Electrode material is Pt/Pt-black on a Ti layer. In order to reduce polarization impedance, the electrodes are galvanically platinized which results in a double-layer capacitance of approximately 4mF/cm².

The dimension of the outer ring CI and CE, respectively, is 150µm width at an electrode distance of 100µm. The radius of the inner electrode CS was calculated to 320µm at distance to CE of 50µm. Membrane height is 150µm. Fig. 1 shows the resulting field distribution computed by finite element analysis.

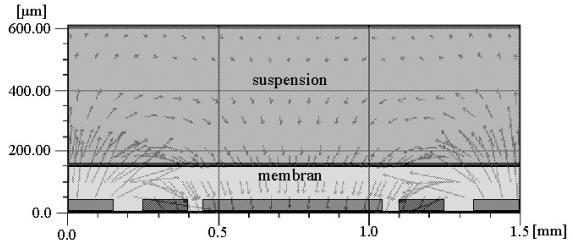

Fig. 1. Field distribution in section of measurement chamber according to electrode dimensions described in the text.

The measurement frequency was chosen as 150kHz to reduce the influence of the electrode polarisation but still to provide blocking of the yeast cells. To avoid non-linearities the signal amplitude is 10mV. A Frequency Response Analyzer Solartron 1260 in combination with a preamplifier was used for current injection and recording of the currents flowing through the electrolyte (membrane) and the suspension, respectively.

First results have been obtained with genetically engineered yeast strains containing mammalian nuclear receptors fusion proteins. Fig. 2 shows the response of the yeast culture within the measurement time of 4,5h, which corresponds to 3-4 cell division processes. Up to 1200 seconds the swelling of the membrane is dominant. Estrogen receptor strains where used to detect physiological concentrations of the estrogenic ligand molecules. 1 nM estrogen can easily be detected with this very sensitive and selective measuring system.

To measure the cell growth individually in the different well plates a passive switching matrix is under development which can read out the conductivity sequentially without the need of integrating active elements. It is expected that with this device an electronic microtiter-plate can be realized to speed up biological relevant HT screening and facilitate parallel screening for different types of receptors.

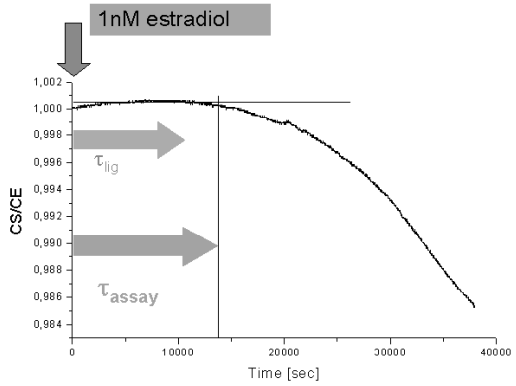

Fig. 2. Measurement signal

References

[1] Kinoshita et al., "The identification of two novel ligands of the FGF receptor by a yeast screening method and their activity in Xenopus development", *Cell* ***83*** (1995) 621–630

[2] H.P. Schwan, „Electrical Properties of tissue and cell suspensions", In: J.H. Lawrence, C.A. Tobias (Eds.). *Advances in Biological and Medical Physics.* **5** (1957) 147-209.

[3] H. Fricke, "A mathematical treatment of the electric conductivity and capacity of disperse systems", *Physical Review.* **24** (1924) 575-587.

[4] A. Varlan, P. Jacobs and W. Sansen, "New design technique for planar conductometric haematocrit sensors", *Sensors and Actuators B.* **34** (1996) 258-264.

[5] P. Jacobs, A. Varlan and W. Sansen, "Design optimisation of planar electrolytic conductivity sensors", *Medical & Biological Engineering & Computing*. **33** (1995) 802-810.

Simultaneous Detection of Two Polycyclic Aromatic Hydrocarbons at Sub-ppb Levels Using SPR Immunosensor

K. V. Gobi and N. Miura
Advanced Science and Technology Center for Cooperative Research, Kyushu University, Kasuga-shi, Fukuoka 816-8580, Japan. E-mail: gobi@astec.kyushu-u.ac.jp

Summary: *A novel surface plasmon resonance (SPR)-based flow immunosensor is fabricated for simultaneous detection of benzo(a)pyrene (BaP), a potential endocrine disrupter, and 2-hydroxybiphenyl (HBP), a carcinogen. The SPR immunosensor working with indirect competitive immunoreaction method is demonstrated to detect the low-molecular-weight antigens simultaneously at sub-ppb levels. Monoclonal antibodies against HBP and BaP are subjected to undergo competitive immunoreaction with HBP and BaP and the antigen-protein conjugates immobilized on the SPR sensor chip. The SPR responses of the immunoreaction are followed to determine the concentration of HBP and BaP in a mixed analyte solution. The SPR immunosensor is demonstrated to detect HBP and BaP at the same time in the concentration range of 0.1 – 1000 ppb with a response time of approximately 20 min. The SPR immunosensor shows negligible cross-sensitivity to the two analytes and for several other polycyclic aromatic hydrocarbons.*

Keywords: *Endocrine disrupting chemicals, Simultaneous detection, 2-Hydroxybiphenyl, Benzo(a)pyrene, SPR sensor, Immunoassay*
Category: *6 (Biosensors)*

1. Introduction

Remarkable research and development activities aimed at the realization of biosensors for the measurement of chemical and biological quantities have been witnessed in the last two decades. SPR sensors are much desired for detection and identification of environmental toxic pollutants and food-borne pathogens because of short analysis time, real-time measurement, portable for field analysis, cost-effective, etc. Detection of several antigens at the same time is important in the fields of pollution monitoring, health diagnosis and so on. Benzo(a)pyrene and 2-hydroxybiphenyl are known to either affect the endocrine system or cause tumors in animals and human. We have already reported the quantitative analysis of small molecules such as morphine, methamphetamine and BaP by using SPR-based immunosensors [1-4]. We report here highly sensitive and selective, simultaneous detection of sub-ppb levels of BaP and HBP using an SPR-based flow immunosensor. The cross-sensitivity of the immunosensor to the two analytes and the other endocrine disrupting chemicals will be discussed.

2. Experimental

HBP-bovine serum albumin conjugate (HBP-BSA), BaP-BSA and monoclonal antibodies against HBP and BaP (abbreviated as HBP-mAb and BaP-mAb, respectively) were gifts from Kyoto Electronics Manufacturing. HBP-BSA and BaP-BSA were synthesized by covalently binding the antigens with BSA using a short aliphatic chain spacer (-$(CH_2)_3$-CO- for HBP; -CO-$(CH_2)_2$-CO- for BaP). The sensor assembly was composed of an SPR angle analyzer (DKK, SPR-20, Japan), a flow cell and a microtube peristaltic pump. The schematic diagram of the SPR-sensor setup is shown in Fig. 1. A thin gold-layer sputtered microscopic glass-slide (18 x 18 x 0.2 mm) with a thin chromium-film as an adhesion layer was used as base for sensor chip. The thickness of the gold film was ca. 50 nm. The sensor chip was equipped with a flow-cell module consisting two channels (1 x 10 mm) in parallel. Test solutions were let to flow at a rate of 0.25 cm^3/min and the running buffer was phosphate buffered saline (PBS; pH 7.2). Solutions of antibodies, antigens and conjugates were prepared with PBS. All measurements were carried out at room temperature of 25 ± 1 ℃.

3. Results and Discussion

The detection principle of the SPR immunosensor is based on an indirect inhibition method, which has been first introduced to the biosensor technique for the detection of drug molecules by us in 1992 [5] for the then otherwise impossible detection small molecules and has been described elsewhere [3]. HBP-BSA and BaP-BSA were immobilized on

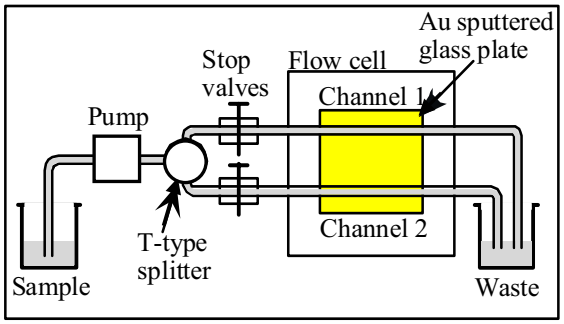

Fig. 1. Schematic diagram of the SPR sensor setup for simultaneous detection of BaP and HBP. Dimensions of flow cell: width = 1 mm, depth = 0.2 mm.

the sensor chip by simple physisorption. HBP-BSA was immobilized on one site of the sensor chip by the flow of 75 ppm HBP-BSA in one of the two channels, and BaP-BSA was immobilized on the other site by the flow of 75 ppm BaP-BSA in the other channel. The SPR angle of the two sites of the sensor chip increased independently due to the adsorption of HBP-BSA and BaP-BSA on the sensor chip. Then, 1000 ppm BSA solution was let to flow three times into both channels to block any non-specific adsorption sites available on the sensor chip. The SPR angles of the sensor chip did not change further either by the flow of 20 ppm BSA or PBS solution.

The HBP-BSA and BaP-BSA immobilized SPR chip thus prepared is employed in simultaneous detection of HBP and BaP in a mixed solution. A mixture of 20 ppm HBP-mAb and 10 ppm BaP-mAb was let to flow into both the channels in the presence and absence of different concentrations of a mixture of HBP and BaP. Typical SPR angle transients observed to the flow of a mixture of the two antibodies in the presence and absence of a mixture HBP and BaP are shown in Fig. 2. When the flow of a mixture of the two antibodies was started, the SPR angles of the HBP-BSA and BaP-BSA immobilized chip increase due to the immunoreaction with HBP-mAb and BaP-mAb, respectively; the SPR angle shifts are 0.439 deg. and 0.192 deg., respectively. In the presence of HBP and BaP, a part of the antibodies will become inactive due to the inhibitive immunoreaction between the antibodies and the antigens, HBP and BaP. Thus, the SPR angle shift for a particular concentration of the antibody will decrease by the presence of the corresponding antigen. In the presence of HBP and BaP of 1 ppb each, the SPR angle shifts of the HBP-BSA and BaP-BSA immobilized sensor chip decrease and are 0.343 deg. and 0.144 deg., respectively. SPR angle shifts for analyte solutions containing both HBP

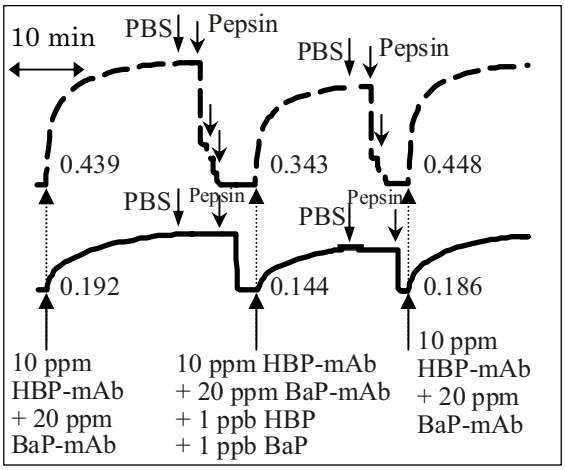

Fig. 2. Time transients of SPR angle of the HBP-BSA and BaP-BSA immobilized sensor chip to the flow of HBP-mAb and BaP-mAb together in the presence and absence of a mixture of 1 ppb HBP and 1 ppb BaP.

and BaP at different concentrations (0.01 – 1000 ppb) were determined. From the dependence of the SPR angle shift on the concentration of HBP and BaP, the concentration of HBP and BaP is demonstrated to be determined simultaneously in the range of 0.1 – 1000 ppb. The regeneration process for multiple-use of the sensor chip on treatment with a pepsin solution has been established. The sensor chip was found to detect each HBP and BaP selectively and was found to show negligible cross-sensitivity against other endocrine disrupting chemicals, benz(a)anthracene and 2,4-dichlorophenoxyacetic acid, and the details will be discussed in our presentation.

4. Acknowledgements

We gratefully acknowledge Ms. C. Kataoka, Kyoto Electronics Manufacturing for helpful comments and Prof. Y. Shoyama and Dr. H. Tanaka, Kyushu University for MALDI-TOF MS analysis. This work has been partially supported by grants from Ministry of Economy, Trade and Industry (METI), Japan and Japan Society for the Promotion of Science (JSPS), Japan.

(References)

[1] N. Miura, H. Higobashi, G. Sakai, A. Takeyasu, T. Uda and N. Yamazoe, *Sens. Actuator B* 13 (1993) 188–191.

[2] G. Sakai, S. Nakata, T. Uda, N. Miura and N. Yamazoe, *Electrochim. Acta* 44 (1999) 3849–3854.

[3] N. Miura, M. Sasaki, G. Sakai and K.V. Gobi, *Chem. Lett.* (2002) 342–343.

[4] K. V. Gobi, M. Sasaki, Y. Shoyama and N. Miura, *Sens. Actuator B* 89 (2003) 137–143.

[5] N. Miura, H. Higobashi, G. Sakai, A. Takeyasu, T. Uda and N. Yamazoe, Tech. Digest of 4-IMCS, (1992) 228–231.

Optimized CMOS Photodetector Structures for the Detection of Biological Reporters

R.A. Yotter, M.R. Warren, J.R. Greegor, and D.M. Wilson

University of Washington, Dept. of Electrical Engineering, PO Box 352500, Seattle, WA 98195-2500 USA
email: raytrace@u.washington.edu http://www.ee.washington.edu/

Summary: *A novel CMOS photodiode structure optimized for detection of biological fluorescent reporters is presented. The devices, realized in 1.5µm CMOS technology, have a 40% increased signal-to-noise response for green light compared to blue-enhanced CMOS photodiode structures. The photodiode geometry uses a lightly-doped striped cathode geometry to maximize the depletion region in areas of highest light absorbance, increasing the sensitivity to green light. The light doping of the interdigitated fingers and the Gaussian doping profile further increases the sensitivity. The devices are designed to be integrated in total analysis systems which rely on the detection of fluorecent or phosphorescent reporters, and which are compact, low-power, and low-cost.*

Keywords: *photodetector, photodiode, stripe-shaped photodiode, CMOS, fluorescence detection.*
Category: *6 (Biosensors)*

INTRODUCTION

A CMOS photodetector optimized for detecting biological reporters is presented. The photodiode structure uses interdigitated n-well fingers to increase the depletion region in areas of maximal absorption of green light. For a silicon device, photons at shorter wavelengths are absorbed near the surface (corresponding to blue or ultraviolet light), and photons at longer wavelengths are absorbed deeper within the substrate (corresponding to red light). Green light is absorbed both near the surface and deeper within the substrate, and an interdigitated n-well structure places the depletion region within the maximum absorption area for green light. Furthermore, an n-well structure is advantageous because the doping is light, which increases the depletion region width. The sensitivity is further enhanced from the Gaussian doping profile of the n-well, which creates a near-intrinsic region within the junction (analogous to a *pin* junction). The CMOS photodetector can be integrated in a total analysis system that is compact, low-power, and low-cost, while the superior reporter detection capabilities of this photodiode will enable higher sensitivity for the system. This detector is ideal for use in biological life-on-a-chip applications that rely on detection of green fluorescent or phosphorescent reporters.

EXPERIMENTAL RESULTS

The signal-to-noise ratio (SNR) for a photodetector is a metric that can be used to determine whether a biological reporter can be detected. Experimental results demonstrate that the new photodiode structure increases the SNR by 40% for green light compared to other CMOS photodiode structures.

Four photodiode structures were fabricated using the AMI 1.5µm CMOS process. To determine the best geometry, the photodiode structures had different finger width *W* and finger spacing *D* (Figure 1). Two structures were green-enhanced photodiodes with interdigitated n-wells. The geometries were (W=6.4µm, D=4.8µm) and (W=8µm, D=6.4µm). The two other structures were blue-enhanced photodiodes fabricated as described in [1], except with a geometry designed for operation at 5V reverse bias. The geometries for the blue-enhanced photodiodes were (W=3.2µm, D=3.2µm) and (W=2.4µm, D=3.2µm). Both blue-enhanced structures included a planar n-well/p-substrate photodiode deep within the substrate, which increased their sensitivity to light at longer wavelengths. This geometry was the best possible blue-enhanced structure for maximizing sensitivity. All photodiode structures had the same lateral area, and three structures had approximately the same active area. The active area of the blue-enhanced (W=2.4µm, D=3.2µm) structure was larger due to layout constraints.

The photodiode structures were simulated using the LUMINOUS package in ATLAS (Figure 2). The simulation results indicated that the SNR for the green-enhanced (W=8µm, D=6.4µm) structure increased by up to 20% (λ=500nm) compared to other optimized photodetector structures. The simulated and experimental results differed due to three effects: (1) the nonlinear absorption spectrum of the silicon nitride passivation layer was not simulated; (2) the metal connections to fingers did not reduce the active area in the simulations; and (3) the 10nm or greater wavelength window for the experimental results increased optical intensity and SNR.

Of the four devices fabricated, the 4.8µm-spaced interdigitated n-well device showed a 40% improvement in the sensitivity to green light (center wavelength at 500nm) compared to the blue-enhanced structure. Figure 3 shows the SNR for all four devices as a function of optical wavelength.

The detection of fluorescence from a biological reporter was also measured. The photodetectors measured the fluorescence from 1µM fluorescein, and the signal was integrated using an integrating circuit was similar to the gated integrator used by

Simpson et al. to measure bioluminescence [2]. The results (shown in Table 1) demonstrated that the green-enhanced structures could generate a signal that is 4.5 times larger than other photodetector structures.

REFERENCES

[1] A. Pauchard, P.-A. Besse, R.S. Popovic, "A silicon blue/UV selective stripe-shaped photodiode," *Sensor Actuat. A–Phys.,* **A76**(1-3), 172-177 (1999).

[2] M.L. Simpson, G.S. Sayler, et al., "An integrated CMOS microluminometer for low-level luminescence sensing in the bioluminescence bioreporter integrated circuit," *Sensor Actuat. B–Chem.*, **72**(2), 134-140 (2001).

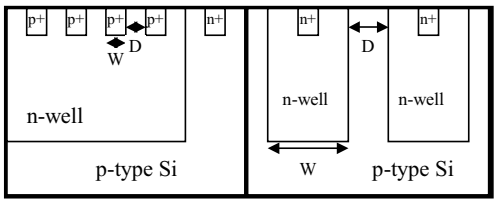

Figure 1. Photodiode doping profiles. This figure shows the cross-sectional geometry of the blue-enhanced structure (left) and the geometry of the green-enhanced structure (right). The blue-enhanced structure uses interdigitated p+-diffusion fingers to increase the depletion region area near the surface of the detector, while the green-enhanced structure uses n-well fingers to increase the depletion region slightly deeper within the substrate.

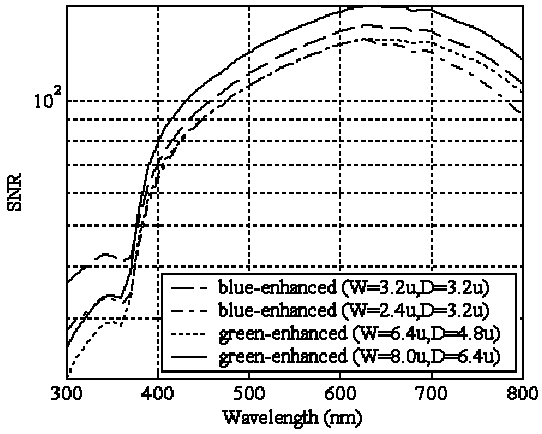

Figure 2. Photodiode simulation results. All devices were simulated using the LUMINOUS package in ATLAS. The optical intensity was 1mW/cm^2, and the noise current was extracted from the I-V curves under no-light conditions.

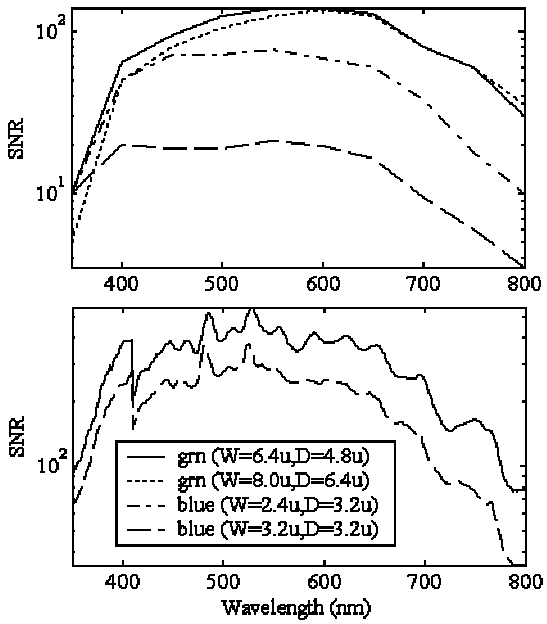

Figure 3. Photodiode Experimental Results. In the top figure, the the response is measured every 50nm with a 10nm optical excitation slit. The active area of the blue-enhanced (W=2.4μm,D=3.2μm) structure is larger than other photodetectors, increasing its SNR. In the bottom figure, the response is measured for two devices with similar active areas every 10nm with a 20nm optical excitation slit. The larger slit increases the SNR, and the two devices are the green-enhanced (W=6.4μm, D=4.8μm) and blue-enhanced (W=3.2μm, D=3.2μm) structures. The nonlinear absorption spectrum of silicon nitride is apparent in this figure.

CMOS PHOTODIODE	I_F (pA)	*SNR*
Green (W=6.4μm,D=4.8μm)	0.225	1.10
Green (W=8μm,D=6.4μm)	0.175	1.07
Blue (W=3.2μm,D=3.2μm)	0.075	1.05
Blue (W=2.4μm,D=3.2μm)	0.05	1.02

Table 1. Photodiode response to 1μM fluorescein. The response was measured using an integrating circuit as described in [2]. The signal I_F was determined by taking the difference between the response in the presence and absence of the fluorescent signal. The optical train included excitation and emission filters for the biological reporter. Because the optical signal intensity is low, the SNR is near threshold for the detectors.

Development of a micro device for Evaluation of Dioxin Toxicity by Immunoassay method

Kazumi Uchiyama, Ming YANG*, Tsuyoshi SAWAZAKI**, Hiroya Shimizu**, Satoru Itoh***
*Graduate School of Engineering, Tokyo Metropolitan Univ., Tokyo 192-0397, JAPAN
**TOADKK Co., Saitama 350-1388, JAPAN

Summary: *The Ah-Immunoassay method in a Bio-MEMS was applied for evaluation of dioxin toxicity in this study. The aim of the research is to develop a real time sensing system by using a micro instrument with novel function, which combines the biological field and micro instrumentation, for the analysis of Dioxins generated at the air flue. The micro instrument was made of Si and glass by photolithograph fabrication. We established prototype model for the system. Micro beads coated with Avidine was used as a reaction medium. Reaction chamber was filled with the micro beads and then the receptor immunoassay was carried out in the micro chamber. Poly-aromatic hydrocarbon with highly flat structure was used as a test sample. The reactivity was evaluated with fluorometry. The fluorescence was detected by fluorescent microscopy.*

Keywords: *Bio-MEMS, Immunoassay, Dioxin*
Category: *6 (Biosensors)*

1. Introduction

Evaluation of Dioxins usually needs individual measurements of several isomers followed by the calculation of toxicity factor. The method needs very expensive instrumentation and takes much time to obtain final result. In order to solve these problems, we examined immunochemical measurement. Among several kinds of assays, we found the use of receptor immunochemical assay was the most suitable one. The Ah-Immunoassay method which is one of the bio-assays using the toxic discovery mechanism by using the reagent Ah receptor which is participating in toxic discovery directly. Although the lab analysis kit for the Ah-Immunoassay is marketed, it may take about several hours using 96 hole plate for the analysis. In this study, we developed a micro device for the Ah-Immunoassay. By combining the biological field and micro instrumentation, we aim to realize a real time sensing system for evaluation of dioxin toxicity.

2. Development of Micro Bio-Chip for Ah-Immunoassay

A micro bio-chip was designed and fabricated for the Ah-Immunoassay. The chip was made of Si and pyrex-glass by micro machining. The developed micro bio-chip is shown in Fig.1. Reaction chamber with a depth of 60 micrometers was filled with the micro beads and then the receptor immunoassay was carried out in the micro chamber. Micro beads coated with Avidine was used as a reaction medium in order to increase reaction surface area. In the reaction chamber, a dam with slits was made by ICP process to stop the beads, but not reagent flow out of chamber. Width of slits was 10 micrometers and diameter of the beads is larger than 18 micrometers.

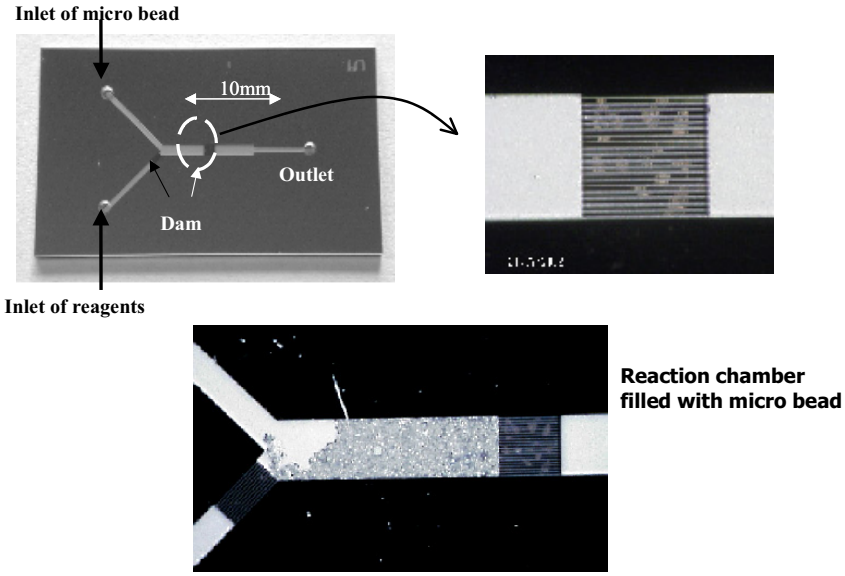

Fig.1 Micro Bio-chip for Ah-Immunoassay measurement

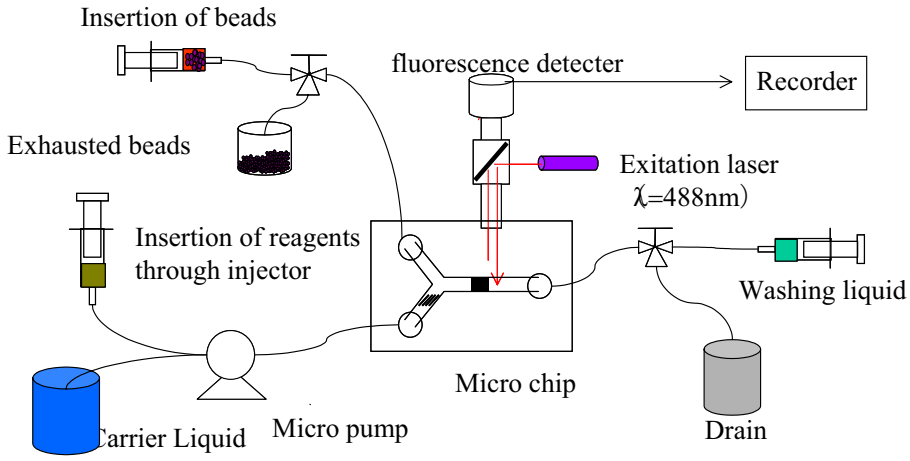

Fig.2 Configuration of Ah-Immunoassay measurement system

The configuration of the Ah-Immunoassay measurement system is shown in Fig. 2. The reagents and the samples are transported into the micro chamber with carrier liquid by using a syringe pump sequentially. The reactivity is evaluated with fluorometry. The fluorescence was detected by fluorescent microscopy.

3. Evaluation of Dioxin Toxicity

Since the rate-determining step for most of the immunochemical reaction is diffusion of the antibody and antigen, it takes several hours to complete the reaction. Application of the reaction to micro scale reaction chamber (such as 100 micrometers cubic) would anticipate the great reduction of the reaction time.

First, the Ah-Immunoassay measurement was carried out for evaluation of Toxicity of alternate material, α-napht-flavone. The experiment was performed by steps shown as follows.

-filling up micro reaction chamber with the micro beads

-supplying the sample and the reagent according to the procedure of the Ah-Immunoassay method.

-the sample and the reagent flow through the micro beads. The complex of Biotinylated DNA, hydrocarbon receptor and α-napht-flavone is bonded to the surface of the beads.

-After washing the excessive chemicals and sample without toxicity in the chamber, fluorescence reagent (FDP:Fluorescein diphosphate) is Supplied to label the complex.

-the labeled FDPs are detected by irradiating fluorescence excitation laser at the micro chamber. Figure 3 shows the resultant relation between detected intensity of fluorescence and concentration of napht-flavone. By the macroscopic observation, reaction was so efficient that it takes only 2 – 3 minutes to observe the coloring reaction showing the size effect of micro chamber and micro beads. The amount of chemicals used for the micro chamber is thousand times smaller than those by usual plate. While the reaction time in the commercial kit of the Ah-Immunoassay was 1 - 2 hours, total detection was checked by reaction time for 10 - 30 minutes. The detection limit at this time was an equivalent for dioxin 1pg. Moreover, it was reducible in 1/40 of a conventional quantity also about the reagent. This result showed that this system was useful to continuation detection of dioxin. Micro instrumentation concluded to be essential. This instrumentation is suggested to have a very good responsibility and cost performance.

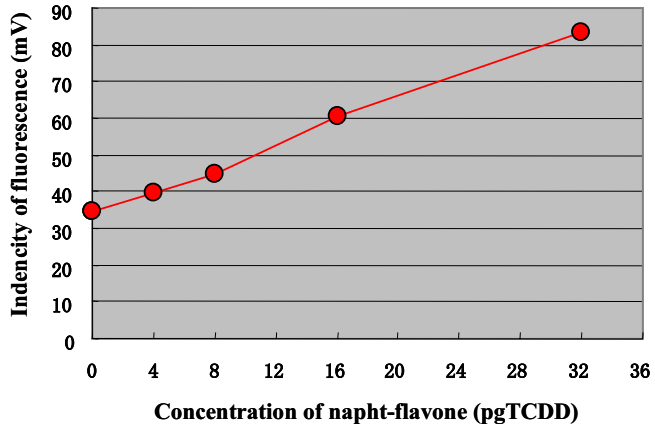

Fig.3 Resultant relationship between detection strength and concentration of α-napht-flavone by Ah-Immunoassay measurement in the micro chamber

QCR – Response to Separated Molecule Clusters

Ralf Lucklum, Benedikt Schlatt, Peter Hauptmann

Otto-von-Guericke-University, Institute for Micro- and Sensor Systems (IMOS),
POB 4120, 39016 Magdeburg, Germany, email: ralf.lucklum@et.uni-magdeburg.de

Summary: *The Acoustic Load Concept is a powerful tool to describe the transduction mechanism of Quartz Crystal Microbalance sensors. It especially draws a much more complete picture than the well known Sauerbrey equation. In the first part major conclusions of this concept are summarized, which are relevant especially for chemical sensor applications. For large biomolecules and molecule clusters the validity of the model assumptions must be called into question. In the second part signatures of an extended model are presented, which consider separated molecules and molecule clusters, and compared with experimental results. This step allows a better insight of signal generation in biosystems.*

Keywords: QCM, viscoelastic materials, biomolecules, molecule clusters
Subject category: 6 Biosensors

1 Introduction

Since Sauerbrey has shown the high sensitivity of Quartz Crystal Resonators (QCR) to mass loading the QCM-principle has entered different application fields as physical, chemical and biochemical sensor. Many recently published experimental results prove the capability of this and other acoustic principles to determine far more than a pure mass change. Most known is the viscosity of a liquid as analyzed by Kanazawa. The sensitivity of acoustic-wave based sensors to viscoelastic properties of thin films is one of the best analyzed features of those sensors. In the so-called non-gravimetric regime the QCR responds to both mass accumulation AND to material properties of an attached film or the adjacent medium.

The transmission line model (TLM), either in its complete physical notation or as Acoustic Load Concept (ALC) or as lumped element BVD approximation, allow a very exact prediction of the sensor behavior. They are especially sufficient for almost all chemical acoustic sensor applications.

Recent experimental findings, mostly in biosystems, have been published, which cannot be explained by the simple microbalance understanding. Even viscoelastic contributions of a tightly bonded biofilm hardly cover the reported data. One idea to overcome this discrepancy but keeping the advantages of the ALC is the generalization of the acoustic load, the central value within the electromechanical models. This contribution considers biomolecules and molecule clusters as single units interacting with the acoustic device. The molecules of interest are presented by model substances much larger than the molecules of the surrounding fluid (usually an aqueous buffer) but much smaller than the wavelength of the probing acoustic wave. Molecule clusters (e.g. liposomes) have a size larger than the penetration depth of the acoustic wave in the fluid.

2 The Acoustic Load Concept

The transmission line model is an electromechanical model of acoustic wave generation and one-dimensional wave propagation in a multilayer arrangement of a piezoelectric disc and non-piezoelectric layers on top [1]. The matrix concept often used to solve the set of wave equations furthermore requires continuity of particle displacement (velocity) and stress at each interface between the acoustic device and the films [2]. Whereas the TLM is the most accurate model in all regimes, the acoustic load concept is an assumption sufficiently exact for almost all chemical and biochemical applications of quartz crystal sensors. The advantage of this concept is a direct link between the experimentally easily accessible values resonant frequency shift and equivalent resistance (also quality factor, dissipation factor e.t.c.) and the real and imaginary component of the acoustic load acting at the interface to the acoustic device [3]. It therefore avoids the elaborate way the quartz crystal transfer function. The ALC easily recovers the mass sensitivity of QCRs as well as the sensitivity to density and viscosity of a contacting liquid. It allows the estimation of viscoelastic contributions to the frequency shift if non-rigid films are deposited onto a QCR surface [4].

The BVD model is another specific result of the TLM model, valid near resonance of the quartz crystal. This model summarizes the physical parameters of both the quartz crystal and the acoustic load in lumped elements of an electrical circuit and provides easy access to simulation programs.

Whereas the acoustic signal transmission from the acoustic load to the electrical response is sufficiently well covered by the TLM or its approximations, the origin of the acoustic load is only well described in the case of a uniform and homogeneous film or an arrangement of those films.

3 Single Element Approach

The challenging task is now the development of a method to relate properties of biomolecules or molecule clusters to the acoustic load effective for the acoustic sensor. One cannot assume a priori that biolayers generally fulfill the ALC requirements. Signatures of non-uniformities, incomplete surface coverage and interfacial sub-layers have been calculated with generalized film parameters within the generalized acoustic load concept (GALC) [5]. Fig. 1 shows a GALC analysis of an interfacial water-like layer between the driving quartz crystal and a uniform layer of biomolecules. It depicts the importance of the coupling point density, if the biomolecules do not completely displace the buffer. Generalized film parameters describe acoustically effective film properties different from the intrinsic material properties or geometric values of the film. They have the potential to incorporate effects not present in a one-dimensional approximation. The original physical meaning is replaced by (complex) values which must be determined with other models. For example, the imaginary part of the shear modulus accounts for energy dissipation during wave propagation through a viscoelastic material and is therefore called loss modulus. Other mechanisms dissipating acoustic energy act similarly and give rise to an apparently increased dissipation value although the material parameter has not been changed. This concept keeps the simplicity of the one-dimensional TLM nonetheless the effective load may be calculated from a two- or three-dimensional model.

We will present a QCR study of model systems both theoretically and experimentally. We are interested in different states, from separated "particles" to the formation of a complete film. We primarily analyze the frequency shift and the change of the equivalent resistance, however, most of the experiments have been performed at fundamental mode and several overtones using a network analyzer. From these values the effective load generated in the different states can be calculated and compared with model predictions. The sensor surfaces have been modified with standard techniques like self assembled monolayers and LB-films to vary hydrophobicity/ hydrophilicity, to realize specific and non-specific binding, or to change bonding strength. Furthermore liposomes of different size have been employed to modify bonding density and the distribution of liposomes and buffer molecules near the interface to the acoustic device. Special care must be taken in the experimental design to guarantee a high sensor-to-sensor reproducibility to be able to determine the small differences in absolute values, which is necessary to compare the experiments with theoretical predictions.

References

[1] R. Lucklum, C. Behling, R.W. Cernosek, S.J. Martin: Determination of complex shear modulus with thickness shear mode resonators, *J. Phys. D: Appl. Phys.* 30 (1997), 346-356.

[2] R. Lucklum, G. McHale: Treatment of Slip in a Generalized Acoustic Load Concept, 2000 IEEE/EIA International Frequency Control Symposium, Proceedings, 40-46; G. McHale, R. Lucklum, M.I. Newton, J.A. Cowen, P. Hauptmann: Influence of Viscoelasticity and Interfacial Slip on Acoustic Wave Sensors, J. Appl. Phys. 88 (2000), 7304-7312.

[3] C. Behling, R. Lucklum, P. Hauptmann: The non-gravimetric quartz crystal resonator response and its application for polymer shear moduli determination, *Meas. Sci. Technol.* 9 (1998), 1886-1893.

[4] R. Lucklum, C. Behling, P. Hauptmann: Role of Mass Accumulation and Viscoelastic Film Properties for the Response of Acoustic-Wave-Based Chemical Sensors, *Anal. Chem.* 71 (1999), 2488-2496.

[5] R. Lucklum, P. Hauptmann: The Generalized Acoustic Load Concept for QCM – Mass Sensitivity, Viscoelasticity, and Other Phenomena, The 16th European Conference on Solid-State Transducers, Proceedings CD pp. 41-44.

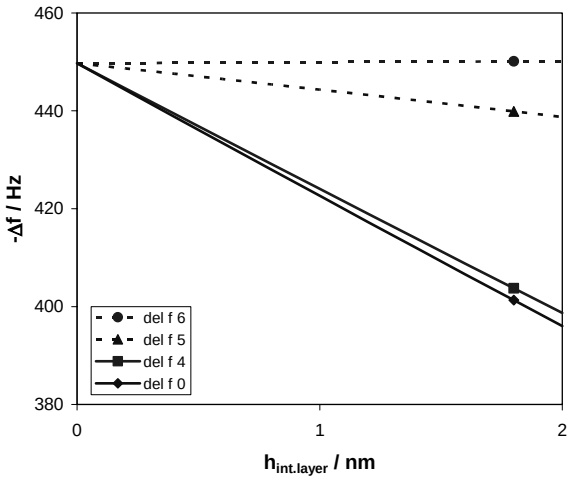

Fig. 1: Frequency shift generated from a 20 nm rigid film (G'=1 GPa, G"=100 MPa), "bonded" to the acoustic device via an interfacial layer, which varies from a viscoelastic liquid (full lines) to a viscoelastic solid (dotted line). The number in the legend is the exponent of the shear storage modulus (unit: Pa) of the interfacial layer, the viscosity of the interfacial layer is 1 cP.

New type of biosensors based on detection of superparamagnetic nanoparticles

P.I. Nikitin, P.M. Vetoshko, M.V. Valeiko

General Physics Institute, Academy of Sciences of Russia,
38 Vavilov St, Moscow, 119991, Russia e-mail: nikitin@kapella.gpi.ru

Summary: *A new low noise magnetic detection method is developed and used for design of a new type of biosensors based on detection of nano-sized superparamagnetic particles, which serve as labels for reactions between different biological agents. Registration of concentration less than 1 ng/ml of different biological agents has been demonstrated. The developed method can be used for medical diagnostics, point of care, for water analysis and food industry monitoring.*

Keywords: *Biosensors, superparamagnetic nanoparticles, low-noise magnetic measurements*
Category: *6 (Biosensors)*

1 Introduction

Existing biosensing techniques use labeling of biologically active molecules by radioactive, fluorescent, or enzyme markers, which enable detecting specific binding of a labeled molecule to an analyte. The use of radioactive isotopes leads to an environmentally undesirable situation, while fluorescent or enzyme labels are unstable, require relatively complicated and time-consumable techniques for the ultimate detection of the labels.

The bioanalysis approach based on labeling molecules with magnetic particles is free from the mentioned above drawbacks. Besides, magnetic micro-spheres have been successfully used in life science for magnetic separation of biological components (antigens, antibodies, DNA, etc.) for about two decades. The magnetization process in such particles is now under extensive study with the interest stemming from different applications.

We have developed a new principle of very sensitive measuring of magnetic susceptibility (at the level of relative change of 10^{-8}) and magnetic nanoparticles counting. The method is compatible with different immunoassay formats such as mini-columns, chromatographic strips, flow system for continuous multi-agent detection, etc.

2 Results

In our experiments, we used mainly nano-sized Fe_3O_4 particles with diameters of 20 – 200 nm. Such particles are more appropriate for bio-analyses than micron-sized ones because they provide much more flexibility in labeling and suitability for a much wider class of bio-reagents and do not aggregate in solutions. The particles covered by different shells, for example, a polystyrene shell with COOH-modified surface or streptavidin, were used for direct immobilization of different monoclonal antibodies.

Magnetic beads (MB) are advantageous while using as labels in comparison with other labels, because they are:

- stable (like radioactive labels),
- environment friendly,
- highly detectable with the developed method,
- widely used for bio-components separation,
- affordable,
- usable in non transparent liquids and suspensions,
- can be covered by different shells.

The readout device has its own digital processor and a liquid crystal display for indication of output signals. Besides, its digital output signal can be sent directly to a network or a notebook. The measuring time is about 1-5 seconds. So the developed method can be used for monitoring of bio-chemical reactions in real time, for study kinetics of different reactions and measurements of affinity constants between biological agents in real time.

One of a biosensor prototype is shown in Fig. 1. Its calibration curve shown in Fig. 2 was obtained as follows: the known weight of 100 nm particles of Fe_3O_4 was diluted in 0.5 ml of distilled water and poured in test tube #24. Then the solution was diluted twice, etc. The result shows that the device has linear dynamic range of 4-5 orders of magnitude. It can detect at least 10^4 of used particles (tube #9).

The developed method opens a number of possibilities for automation of biological analyses, for example, monitoring of various dangerous biological agents and biological weapons in a flow through system.

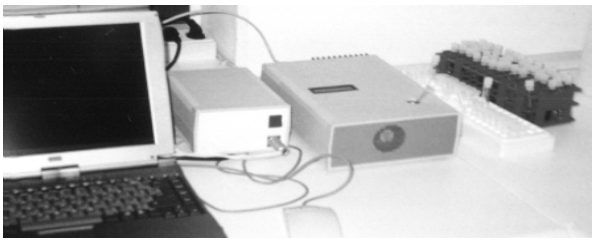

Fig. 1. Desktop biosensor

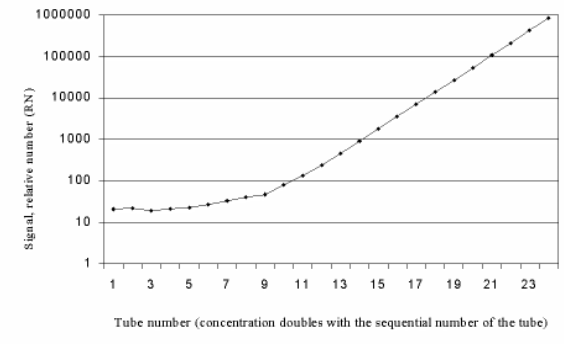

Fig. 2. Calibration curve

A modification of the prototype shown in Fig. 3 was assembled to readout immunochromatographic strips based on MB.

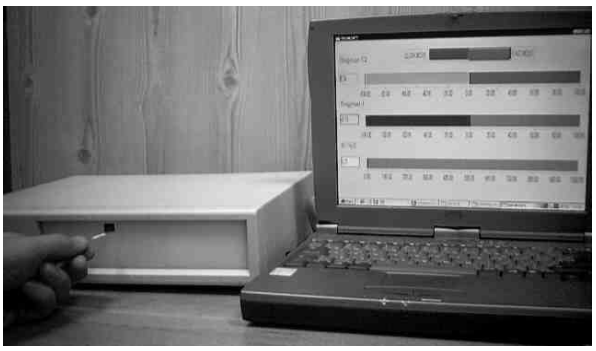

Fig. 3. Strip reader

The hand-held magnetometric immunosensor systems for detection of various dangerous biological agents and biological weapons (BW) are shown in Fig. 4 together with a glass capillary tube with the receptor zone (a USA quarter is shown for scale comparison).

The developed method opens a number of possibilities for automation of biological analyses, for example, monitoring of various dangerous biological agents and biological weapons in a flow through system.

Fig. 4. Handheld version of the biosensor

Development of multi-agent detection option is now in progress as two different sensor designs. In the first one, shown in Fig. 5,: several receptors are immobilized in different zones that are sequentially spread along the sensor surface and separated from each other. In the second design, several parallel sensor surfaces with different receptors on each surface are surrounded by different coils, connected to a single micro processor unit.

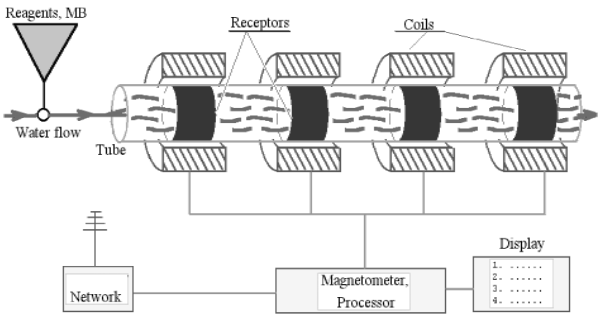

Fig. 5. Multi-analyte automated biosensing system

Registration of concentration less than 1 ng/ml of different biological agents has been demonstrated. This corresponds to medical diagnostic standards and can be further improved. Besides, the developed technology has large linear dynamic range (5 orders) and a number of additional important advantages such as possibility to analyse opaque liquids or suspensions, to be incorporated in an automatic set-up for continuous monitoring of dangerous biological agents, etc.

Label Free Spectral Correlation Biosensors

P.I. Nikitin, B.G. Gorshkov, M.V. Valeiko and T.I. Ksenevich

General Physics Institute, Academy of Sciences of Russia,
38 Vavilov St, Moscow, 119991, Russia e-mail: nikitin@kapella.gpi.ru

Summary: *A new label-free Spectral Correlation biosensing method is developed. It is based on measurements of correlation signal of two interferometers in an original optical scheme. In the first scanned Fabry-Perot interferometer the distance between two mirrors is periodically changed by a peizoelectric driver. The second interferometer is a simple microscope cover glass plate (biochip) with different recognition spots or flow channels. Two- and 96-channel biosensors are designed to register bio- and chemical components in real time. The sensogram drifts for these devices expressed in terms of layer thickness were 20 pm/hour and 40 pm/hour, respectively.*

Keywords: *Biosensors, array, optics, interference, phase measurements.*
Category: *6 (Biosensors)*

1 Introduction

Label-free optical methods for detecting biological and chemical interactions have a number of advantages such as possibility to monitor reactions in real time and good reliability of results obtained by fewer operations. Among such methods, one can mention those based on the surface plasmon resonance SPR [1].

In papers [2,3] we proposed and successfully tested a simple and robust method of direct optical detection of reactions on a surface, which used a simplest microscope cover glass as a sensor chip. The method provides an information signal that is independent of the refractive index of the solution and has wide dynamic range. In this paper, we further develop the method and extend it for a new multi-channel biosensor variant. Such approach can be used for design of "optoelectronical tongue" for multi-analyte monitoring of liquids.

2 Results

The developed spectral correlation scheme of the biosensor is shown in Fig. 1. Radiation from a superluminescent laser diode *1* passes through a scanned Fabry-Perot interferometer *2*, then through a semi-transparent mirror *3* and is incident onto a sensor glass plate *4*. A piezoelectric actuator scans the interferometer base (the distance between mirrors). The radiation reflected from the plate is directed by the semi-transparent mirror to a photodetector *6* through projection optics *5*.

We have designed two options of the device. The first device is designated for two-channel detection of biochemical reactions in a flow mode. It has one additional reference channel, so we used three separate photodiodes as the photodetector *6* to record intensity of the light reflected from each flow channel formed on a glass plate. The second option of the device is intended for detection of parallel reactions in 96 separate cells in a standard ELISA plate format. The bottom of this ELISA frame was the glass *4* plate 50 μm thick. A CCD camera was used as the photodetector *6* to record images of 96 separate cells. The image from the camera was processed by a computer, which also controlled the Fabry-Perot interferometer.

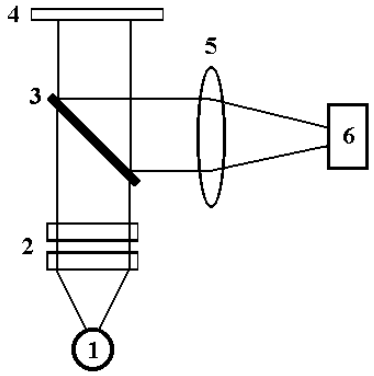

Fig. 1. Scheme of Spectral Correlation biosensor

In our experiments, a microscope cover glass with a biomolecular layer immobilized on its surface was used as a sensitive layer. A reaction of this layer with a chosen component of the solution was the object of investigation. We used interference between two beams: the first beam was reflected from the bottom surface of the glass slide, and the second one reflected from the upper surface with the biological

agent layer [2]. The result of the interference depends on the phase thickness of the sensitive layer. During the reaction under study, some components of the solution adhere to the surface of the biomolecular layer, whereas the other ones detach from it. This leads to a change of the phase difference between the interfering waves.

While scanning the base Fabry-Perot interferometer the signal recorded by the photodetector periodically changes. A change of phase of this correlation signal was used for calculation of the change of thickness of the biological layer on the glass surface.

A photograph of the two-channel biosensing device in flow mode is shown in Fig. 2

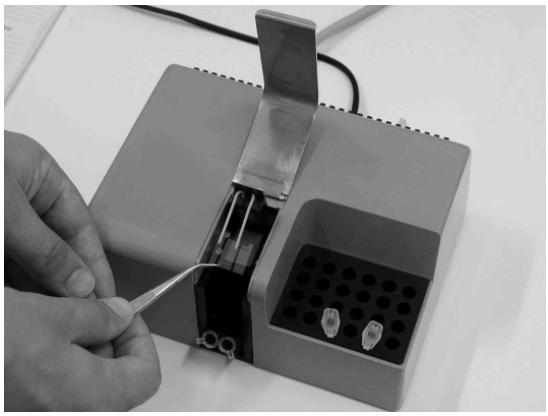

Fig. 2. Photo of two-channel biosensor

Before performing biochemical experiments, the glass plate surface was subjected to repeated chemical cleaning and then aminated and biotinylated as described in [2,3]. The biotinylated glass slide was inserted into the sensor system. Then the solution of streptavidin was circulated through the sensor cell. After rinsing the surface with the PBS buffer, the solution of biotinylated goat antibodies specific to human hIgG passed through the cell. Such sensor chip was used to detect IgG in buffer at concentrations of 100, 300 and 500 ng/ml (sensograms a, b, c in Fig. 3, respectively). The hIgG solution was injected in the flow cell at the moment indicated by arrow *1*. This was accompanied by an increase in the adsorbed layer thickness due to the specific binding reaction between hIgG and antibodies. The thickness of the adsorbed layer did not decrease after subsequent circulation of the buffer solution through the cell (arrows *2*). The arrows *3* correspond to circulation of the acid buffer solution at pH 2.2. In this case, desorption of hIgG molecules was observed. The regenerated chip was used to detect higher concentration of hIgG.

The experiments showed that non-specific binding of BSA was negligibly small. The drift of the two-channel device expressed in layer thickness

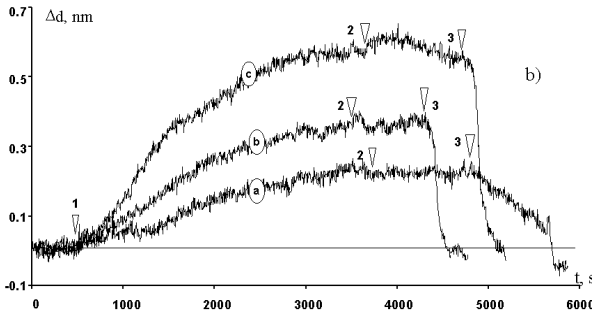

Fig. 3. Sensogram of biochemical reacton

terms was 20 pm/hour. Similar experiments with the 96–cell reader showed detectability of 1 μg/ml of hIgG, and the long-term drift was equal to 40 pm/hour.

This method can be easily extended to detect reactions in either a big array format such as the 1536-well ELISA format or a small micro-array with the reaction spot of 1-10 microns. The major hardware and data processing techniques are the same, and it is only necessary to adjust proper optic elements to obtain array images.

3 Conclusions

Thus, a new label-free biosensing method has been developed for real time detection and investigation of surface biochemical reactions, which uses a simplest microscope cover glass as the sensor chip and has high sensitivity at pm range of biological layer thickness change (or ≈ 1 pg/mm^2). Besides, the method provides an information signal that is independent of the refractive index of the solution, has wide dynamic range and is well compatible with multi-channel biosensing systems. The method can be successfully applied in medicine and ecology, e.g. for high-throughput screening, epitope mapping, testing samples for presence of toxic or infection agents, detection of the DNA hybridisation, testing of pharmaceuticals, etc.

References

[1] B. Liedberg, C. Nylander, I. Lundström, *Biosensors and Bioelectronics* 10 **(**1995) pp.i-ix.

[2] P.I. Nikitin, B.G. Gorshkov, M.V. Valeiko, S.I. Rogov, *Quantum electronics* 30 (2000) 1099-1104.

[3] P.I. Nikitin, B.G. Gorshkov, M.V. Valeiko, S.I. Nikitin, *SPIE Proceedings* 4578 (2001) pp. 126-135.

Optoelectronic detection of DNA molecules on thin-film DNA microarrays using an amorphous silicon photodetector

F. Fixe[1,2], D.M.F. Prazeres[2], V. Chu[1] and J.P. Conde[1,3]

[1]INESC Microsistemas e Nanotecnologias, Lisbon, Portugal, Rua Alves Redol, 9, 1000-029 Lisbon, Portugal.
email: ffixe@inesc-mn.pt http://www.inesc-mn.pt
[2]Biological Engineering Research Group, Instituto Superior Técnico, 1049-001 Lisbon, Portugal
[3]Department of Materials Engineering, Instituto Superior Técnico, 1049-001 Lisbon, Portugal

Summary: *The objective of this work is to demonstrate the use of an amorphous silicon (a-Si:H) photodetector to measure the density of covalently-bound, fluorescent-tagged, DNA molecules. This device is based on the photoconductivity of a-Si:H in a coplanar electrode configuration. Excitation of a fluorescently tagged biomolecule with UV light results in the emission of visible light which is then converted into an electrical signal in the photodetector, thus detecting the presence of tagged DNA molecules. The design, fabrication and characterization of this integrated a-Si:H bio-detector is described. An array of such detectors can be used for optoelectronic data acquisition in DNA chip applications.*

Keywords: *a-Si:H photodetector, DNA microarrays, thin-films*
Category: *6 (Biosensors)*

1 Introduction

Current DNA-chip operation is based on the optical acquisition of the photoluminescence emission from the fluorescent-tagged DNA target molecules that hybridize with immobilized DNA probe molecules in the array. Although these optical systems show high sensitivity, it would be advantageous to avoid the need for the complex image acquisition system, and to be able to collect the hybridization pattern on the DNA-chip electronically. This would be particularly important for applications such as clinical point of care diagnostics. In this paper a detection approach in which the presence of fluorescent-tagged DNA molecules is optoelectronically detected by an integrated thin-film a-Si:H photodetector thin-film is described.

2 Methods and materials

2.1 Device concept

The device is based on the photoconductivity of a-Si:H in a coplanar electrode configuration (Fig. 1). The spectral response of this device has a broad peak between 550-600 nm (Fig. 2, circles). The dye 1-(3-(succinimidyloxycarbonyl)benzyl)-4-(5-(4-methoxyphenyl)oxazol-2-yl) pyridinium bromide (PyMPO, SE) was chosen as the fluorescent tag due to its large Stoke's shift ($\lambda_{excitation}$=400 nm; $\lambda_{emission}$=560 nm) and because it can be chemically attached to the amine termination of the DNA molecule. Measurement of the spectral response curve of the detector in the presence of PyMPO shows an increase in the detector signal in the 400-450 nm range when PyMPO is present. This occurs because the PyMPO, when excited at this wavelength, emits in the visible. This emission is then absorbed by the a-Si:H and converted into a photocurrent signal. To improve the signal to noise ratio of the device, it is crucial that the photoresponse of the sensor be as low as possible in the UV excitation range.

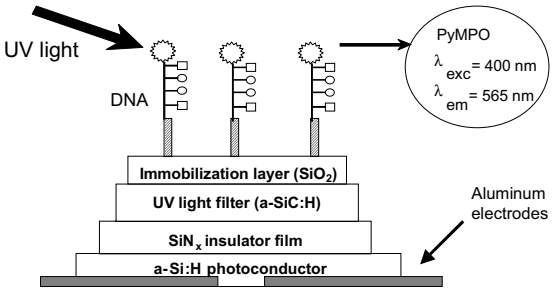

Fig. 1. Schematic diagram of the integrated bio-detector with immobilized tagged DNA molecules: a-Si:H (photoconductor), SiN_x (insulator film), a-SiC:H (UV light filter) and SiO_2 (functional layer for the DNA immobilization and hybridization).

2.2 Methods

The device (Fig. 1) is fabricated on a glass substrate. The length of the bottom aluminum parallel metal contacts ranges between 30 μm and 3 mm and their separation between 5 μm and 500 μm. The a-Si:H, silicon nitride (SiN_x), amorphous silicon-carbon (a-SiC:H) and silicon dioxide (SiO_2) thin-films are deposited by RF-PECVD. The single strands DNA is marked with PyMPO on the 3´-end and purified by gel filtration. To immobilize the DNA, the SiO_2 is chemically treated by oxidation, silanization and cross-linking [1].

3 Results

3.1 Incorporation of barrier and filter layers

Since the a-Si:H layer has a significant photosensitivity in the UV, to improve the sensitivity of the device a-SiC:H UV filters were deposited above the a-Si:H photoconductor to lower its absorption of light at the excitation energy (figure 2). A thin SiN_x layer was used to protect the a-Si:H from carrier spill-over from the a-SiC:H.

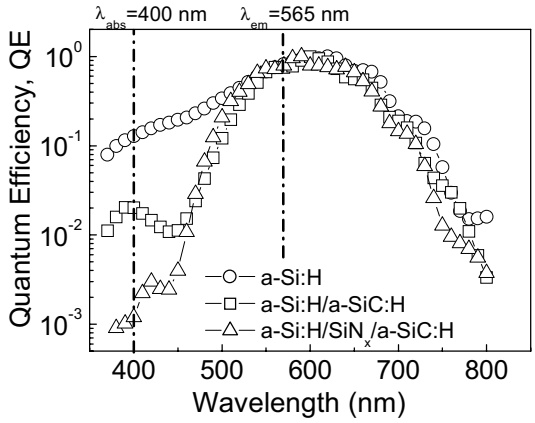

Fig. 2. Improvement of the sensitivity of the device at 400 nm, by adding the two thin films: SiN_x (barrier layer) and aSiC:H (filter layer).

3.2 Optoelectronic DNA calibration curve

Different concentrations of DNA marked with PyMPO were detected and the detection limit of the present device structure shown in Fig. 3 was of the order of 100 pmol/cm^2. From the literature [2,3], the typical density of DNA immobilized and hybridized on a functionalized surface is in the range of 1-200 pmol/cm^2. Improvements of device sensitivity and the DNA calibration curve will be presented.

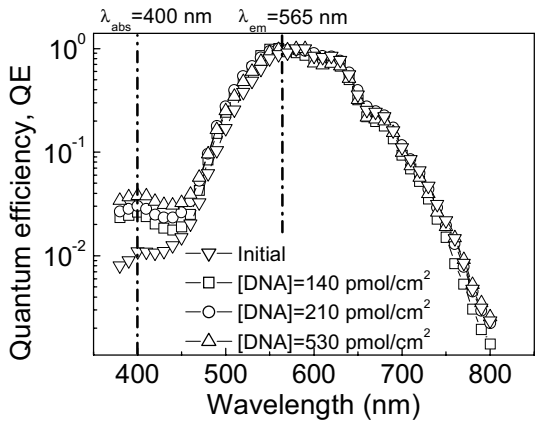

Fig. 3. Different DNA concentrations (tagged with PyMPO) detected with the aSi:H bio-detector.

3.3 Improvement of Device Sensitivity

To lower the UV sensitivity of the device at 400 nm, an interference filter composed of a high-refractive-index quarter wave layer, followed by a multilayer of 15 bilayers of (λ/4) of SiO_x (n=1.57) / SiN_x (n=1.89) was fabricated. This filter reflects 95% of the light at this wavelength (figure 4).

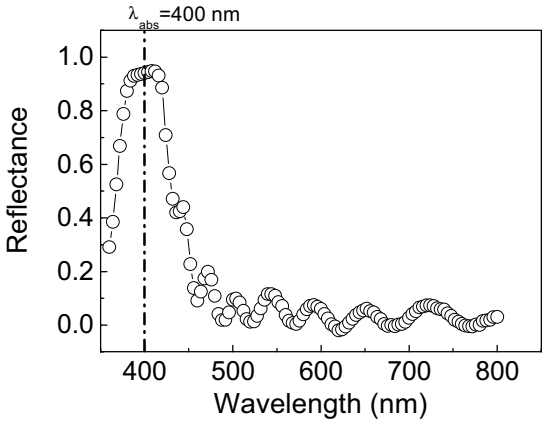

Fig. 4. Reflectance spectrum of an interference filter on glass with 15 bilayers of SiO_x and SiN_x .

The use of this type of filter above the detector/barrier/filter stack decreases the device signal at the wavelength where PyMPO absorbs and increases the detector sensitivity.

The detection system described above is suitable for rapid, reliable and inexpensive detection of nucleic acids in a wide variety of applications [4,5] of DNA microarrays.

References

[1] F. Fixe A. Faber D. Gonçalves D.M.F. Prazeres R. Cabeça V. Chu G. Ferreira and J.P. Conde *Mat. Res. Soc. Symp. Proc.* 723 (2002) O2.3.1.
[2] Rogers, Y.H. Jiang-Baucom P. Huang Z. Bogdanov V. Anderson S. and Boyce-Jacino M.T. *Anal. Biochem.50*, 266 (1999) 23-30.
[3] Beier, M. and Hoheisel, J. *Nuc. Ac. Res.* 27 (1999) 1970-1977.
[4] Wang, J. *Nucl. Acids Res.* 28 (2000) 3011-3016.
[5] Ramsay G. *Nature Biotechnol.* 16 (1998) 40-44.

Investigation of electrochemical properties of redox enzymes in organic solvents.

A.Konash, E. Magner

University of Limerick, CES Department, Plassey Technological Park, Limerick, Ireland
e-mail: **anastassija.konash@ul.ie** , http:// www.ul.ie

Summary: *Galactose oxidase was used as a model enzyme study the effect of nonaqueous media on the rate of electron transfer between redox enzyme active centers and mediators using cyclic voltammetry. All experiments were conducted in carbonate buffer, 1,1'-dimethylformamide, 1,1'-dimethylsulfoxide, 1,1'-dimethylacetamide. Different enzyme immobilization procedures are compared.*

Keywords: *Galactose oxidase, immobilized, mediated bioelectrocatalysis, solvent effect.*
Category: *6 (Biosensors)*

1. Introduction

Biocatalysis and biosensing via enzymes in organic solvents have recently received considerable attention because of the possibility to control the enzyme catalytic properties by changing the physical and chemical properties of the reaction medium. Although work has been conducted toward the application of enzymes in organic solvents not much information is available about the properties of redox enzymes in nonaqueous medium. Knowledge of the influence of the solvent/reaction medium on the electron transfer process would be very useful for designing biosensors and/or biofuel cells [1].
One of the useful techniques to study electron transfer process in enzymes is cyclic voltammetry. In this work some results concerning the electrochemical behavior of galactose oxidase in organic solvents are presented.

2. Experimental

A conventional three-electrode cell was utilized for cyclic voltammetry experiments. Glassy carbon, platinum wire and silver/ silver chloride electrodes were used as working, counter and reference electrodes, respectively.
To construct the enzyme electrode galactose oxidase (Sigma) was cross-linked with glutaraldehyde (Riedel-de Haen) on the surface of glassy carbon electrode in the presence of Nafion® (Sigma) and bovine serum albumin (Sigma). The electrodes were allowed to dry and stored in the carbonate buffer in the fridge while not in use. Tetrabutylammonium perchloride (Sigma) was utilized as the electrolyte for organic solvent experiments. 3-methoxybenzyl alcohol (Sigma) was used as the substrate for galactose oxidase. Ferrocene methanol was used as a mediator throughout the experiments.

3. Results and discussion

Initially, immobilization of the enzyme was achieved by cross-linking with glutaraldehyde on the electrode surface. [2] However, the response of such electrodes was not stable and the enzyme film was readily lost from the electrode surface. In order to retain the enzyme Nafion® solution was added to the immobilization mixture. This substantially improved the stability of the enzyme electrode.
Nevertheless, a reproducible response for the electrode was still not achieved. To increase the reproducibility of the catalytic current bovine serum albumin was added to the immobilization mixture; this stabilized the electrode response as observed by repeated scanning (see figure 1).

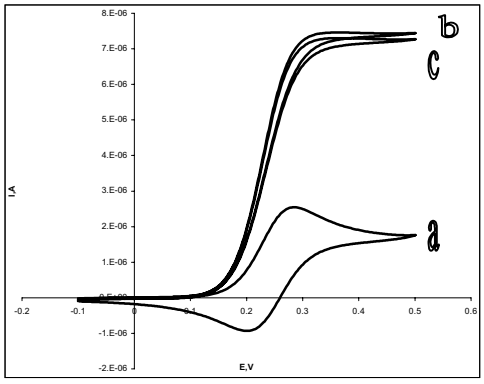

Figure1. Cyclic voltammograms of the enzyme electrode, containing Nafion and BSA, in carbonate buffer (50 mM, pH=10.8) (a); in presence of 54mM of 3-methoxybenzyl alcohol, first scan (b); fourth scan (c). The scan rate was 5 mV/s and the concentration of ferrocene methanol 0.5 mM.

The pH dependence of mediated bioelectrocatalysis is present in figure 2. From the graph it can clearly be seen that the optimal pH for the immobilized enzyme/mediator system is about 10.8. Thus, a buffer pH of 10.8 was used throughout the experimental work. [3]

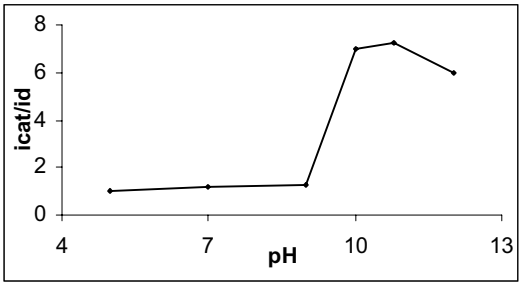

Figure 2. pH dependence of icat/id of the enzyme electrode in the presence and absence of 54 mM 3-methoxybenzyl alcohol. ([mediator] = 0.5 mM).

The response of the enzyme electrode was checked in dimethylacetamide, dimethylformamide, and dimethylsulfoxide. [4] An example of the cyclic voltammetry in DMSO is presented in Figure 3.

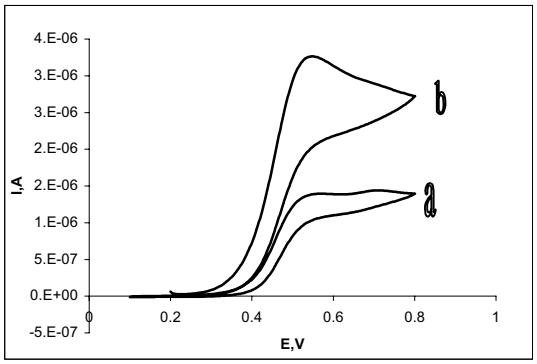

Figure 3. Cyclic voltammograms of the enzyme electrode in DMSO (a); in the presence of 54 mM 3-methoxybenzyl alcohol (b). Concentration of ferrocene methanol 0.5mM ; potential sweep rate 5mV/s.

Similar voltammetric responses were obtained in all solvents tested. Some electrochemical characteristics and catalytic current obtained are present in table 1. The ratio I_{cat}/I_d in all three solvent was less then that obtained in buffer. The reasons for such decrease are currently under investigation.

Table 1. Cyclic voltammetric parameters of 0.5 mM ferrocene methanol on a glassy carbon electrode (area 0.071 cm^2) modified with 114 U cm^{-2} galactose oxidase in the presence and absence of 54 mM 3-methoxybenzyl alcohol. Scan rate was 5mV/s.

Solvent	E_p mV	$i_{cat}*10^{-6}$ A	i_{cat}/i_d
Carbonate buffer	256	10.0	3.22
1,1'dimethylsulfoxide	545	3.26	2.36
1,1'dimethylacetamide	607	1.25	1.25
1,1'dimethylformamide	520	3.50	2.92

4. Conclusion

The mediated electrochemistry of galactose oxidase immobilized on the glassy carbon electrode was studied in organic solvents. The dependence of the enzyme electrode's behavior on the enzyme immobilization procedure and the pH of the solution were studied. Some electrochemical characteristics of the mediated bioelectrocatalytic system in organic solvents were obtained.

References

[1] K. Kano, T. Ikeda. *Anal. Sci.*, 16 (2000) 1013-1021
[2] E.I. Iwuoha, M.R. Smyth, M.E.G. Lyons. *J. Electroanal.Chem.* 390 (1995) 35-45
[3] A. Petersen, E. Steckhan. *Bioorg. Med. Chem*. 7 (1990) 2203-2208.
[4] K. Yokoyama, M. Kawada, E. Tamiya. *J. Electroanal. Chem.,*434 (1997) 217-224.

Thin film conductometric urea sensor

A. Steinschaden[1], G. Urban[2], R. Chabicovsky[1]

[1] Vienna University of Technology, Institute of Industrial Electronics and Material Science, Gusshausstrasse 27-29, A-1040 Vienna, Austria homepage: http://www.iemwt.tuwien.ac.at
email: Andreas.Steinschaden@aon.at rupert.chabicovsky@tuwien.ac.at
[2] Albert-Ludwigs-Universität, Institute für Mikrosystemtechnik, Georges Köhler Allee 103, D-79110 Freiburg
email: urban@informatik.uni-freiburg.de

Summary: *Conductometric measurements are of interest in analytical chemistry. Selectivity can be achieved with enzyme membranes. In this paper we present a miniaturized urea sensor formed by means of photolithography, thin film and plasma technologies. The 4-electrode measurement method increases the sensitivity at high background conductivity. The electrodes are coated with a poly-HEMA membrane wherein urease is immobilised.*

Keywords: *urea sensor, conductometric sensor*
Kategory: *6 (Biosensors)*

1. Introduction

A huge amount of physiological parameters can be measured, and most of them are still analysed in clinical chemical analysers. To support the physicians with facts more quickly, work is being focused on miniaturized sensors. One of the highly interesting parameters is the concentration of urea. Many basic physical and chemical effects to realize urea sensors are already known [1-4]. In our work we use the principle of impedance measurement. One difficulty arising with this measuring method is the faraday resistance of the electrode-solution interface. The only way to eliminate this systematic interference on the results is to apply four-electrode measurements [2]. The conductometric transducer is coated with an urease-containing poly-HEMA membrane, wherein urea is decomposed according equation (1).

$$NH_2-CO-NH_2+H_2O \xrightarrow{Urease} 2NH_3+CO_2 \quad (1)$$

Additional ions are produced proportional to the urea concentration due to the dissolution of the ammonium and the carbon dioxide as shown by the equation (2) and (3).

$$2NH_3+2H_2O \rightarrow 2NH_4^+ + 2OH^- \quad (2)$$

$$CO_2+H_2O \rightarrow H_2CO_3 \rightarrow HCO_3^- + H^+ \leftrightharpoons 2H^+ + CO_3^{2-} \quad (3)$$

2. Sensor fabrication

The thin film electrodes were deposited on a 0.3 mm thick glass substrate. Patterning was done by photolithography and lift-off technique. The electrodes consist of a 60 nm platinum layer and a 60 nm titanium film as an adhesion layer. Both films were deposited by electron beam evaporation.

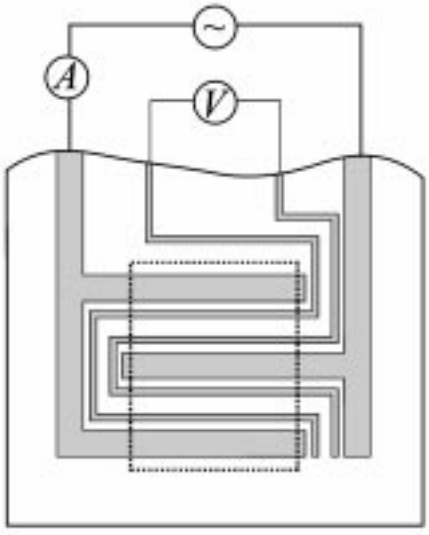

Figure 1: Schematic drawing of the electrodes for 4-electrode measurements. The dashed lines indicate the position of the enzyme membrane.

The shape of the total electrode system is shown in figure 1. There are 66 electrode-fingers present with 5µm width and spacing between electrodes. The outer part of the electrode system is insulated by a 0.2 µm thick SiN_x coating. This layer is deposited by a PECVD process and patterned by a plasma etching process. The non-insulated part of the electrode system is coated with a poly-HEMA membrane where the enzyme urease was immobilised (figure 2) [2]. The membrane was spun on and exposed to UV-light through a mask. Afterwards the membrane was developed in 1:1 ethyleneglycol:H_2O and dried for 1 day at room temperature. Crosslinking of the enzyme was done for 3 hours in 1 % glutaraldehyde solution to enhance the stability of the sensor.

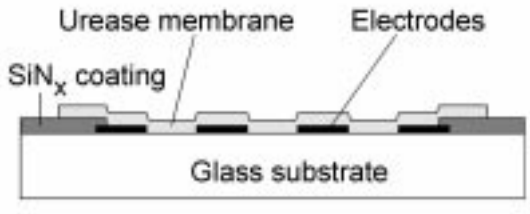

Figure 2: Schematic cross sectional view of the electrode system and the membrane.

3. Measurements and results

3.1. Experimental set up

Experiments were carried out with an automated flow system (figure 3).

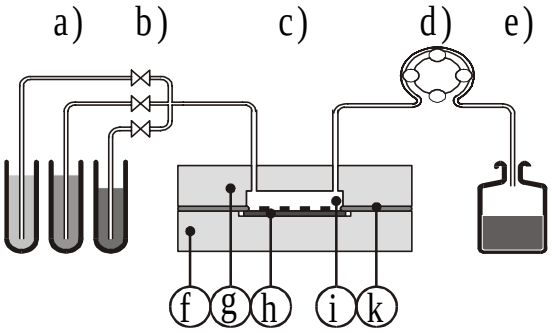

Figure 3: Scheme of the flow system: a) urea solution container, b) electrically controlled fluid valves, c) flow cell, d) peristaltic pump, e) waste, f), g) flow cell, upper and lower shell, h) sensor, i) flow channel, k) sealing

The urea concentration was altered within the physiological range of 100µmol/l up to 30mmol/l. A physiological 150mmol/l NaCl solution is used to generate the background conductivity. The applied measurement voltage is sinusoid with 10mV$_{eff}$ and a frequency of 10kHz. The time period between two subsequent concentration steps was 300 seconds. Measurements were taken every 15 seconds.

3.2. Results

The results of measurements without background conductivity are shown in curve a), figure 4. The results fit to the regression $y = 0.0011 + 0.0097 * x$.

The result for a measurement with the background conductivity of a physiological 150mmol/l NaCl solution and a concentration of 1mmol/l urea up to 10mmol/l urea is printed in figure 4, plot b). The results fit to the regression line $y = 0.0068 + 0.0127 * x$.

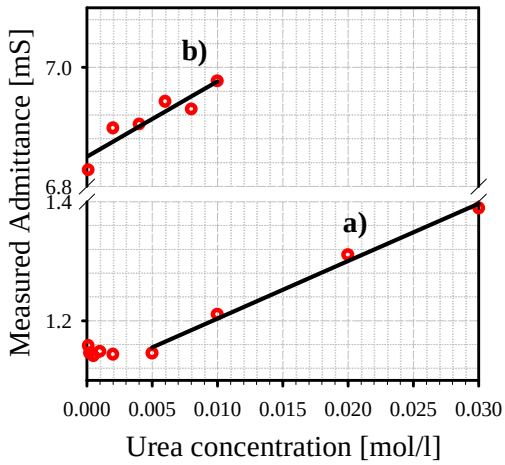

Figure 4: Measurement result: a) without background conductivity and b) with the conductivity of a 150 mmol/l NaCl solution.

4. Conclusions

The results show the feasibility of a conductometric urea sensor with miniaturized sensor structures. Applying four-electrode measurement technique gives a linear measurement result independent of the background conductivity. The measurement range covers the physiological range of urea concentration and background conductivity.

References

[1] Kenji Yoneyama, Yusuke Fujino, Tetsuya Osaka, Ikuo Satoh, Amperometric sensing system for the detection of urea by a combination of the pH-stat method and flow injection analysis, *Sensors and Actuators* B 76 (2001) 152-157.

[2] A. Steinschaden, D. Adamovic, G. Jobst, R. Glatz, G. Urban, Miniaturized thin film conductometric biosensors with high dynamic range and high sensitivity, Sensors and Actuators B 44 (1997) 365-369.

[3] Fang Zeng, Shuizhu Wu, Zaiwu Sun, Hongyuan Xi, Ruifeng Li, Zhilin Hou, Urea sensing materials via solidified crystalline colloidal arrays, *Sensors and Actuators* B 81 (2002) 273-276.

[4] Kenji Yoneyama, Yusuke Fujino, Tetsuya Osaka, Ikuo Satoh, Amperometric sensing system for the detection of urea by a combination of the pH-stat method and flow injection analysis, *Sensors and Actuators* B 76 (2001) 152-157.

[5] Andrei B. Kharitonov, Maya Zayats, Amir Lichtenstein, Eugenii Katz, Itamar Willner, Enzyme monolayer-functionalized field-effect transistors for biosensor applications, *Sensors and Actuators* B 70 (2000) 222-231.

A Sweating Thermal Environment Meter

J. C. A. F. Mendes[1] and M. C. G. Silva[2]
[1]Departamento de Engenharia Mecânica, Instituto Superior de Engenharia de Coimbra, Instituto Politécnico de Coimbra, R. Pedro Nunes, 3030-199 Coimbra, Portugal, +351 239 790200
email: jfmendes@isec.pt, http:// www.isec.pt
[2]Departamento de Engenharia Mecânica, Faculdade de Ciências e Tecnologia
Universidade de Coimbra -Pólo II, 3030 Coimbra, Portugal, +351 239 790729
email: manuel.gameiro@dem.uc.pt, http:// www.dem.uc.pt

Summary: *An innovative thermal environment meter, capable of simulating dry and evaporative heat losses of the human body was developed. It has an ellipsoid shape and is made of porous ceramic material. Its inner volume is fulfilled with water heated to a temperature similar to the deep-body temperature of a person. Evaluation of a given environment is derived after measured values of electrical power required to keep the water temperature constant and lost of weight due to water evaporation on the external surface of the sensor.*
Sensor was calibrated, in terms of the Standard Effective Temperature index, which becomes it a very useful tool for the characterization of thermal environments, especially those where the human thermal regulation system needs to use sweating mechanism.

Keywords: *thermal comfort, seating, SET*
Category: *6 (Biosensors*)

1 Introduction

Growing comfort demands of people and collective conscience about need for efficient management of energetic resources explain the importance nowadays given to the evaluation of thermal environments.
A practical way to perform this type of evaluation is to use a measuring device with a sensor that is simultaneously sensitive to the influence of most of physical parameters characterizing thermal environment and capable of summarizing the conjugated effect of all them in only one value.
Madsen [1] developed a thermal comfort meter with an ellipsoid shape sensor that simulates human body sensible heat losses. It determines PMV and PPD comfort indices, accordingly to the ISO 7730 Standard and the equivalent and operative temperatures. Its working principle is based upon the human thermal regulation model, derived by Fanger [2], where the relationships between the comfort sensation felt by a person and his skin temperature and heat losses are established. Madsen's meter simulates only dry heat losses of the human body. However, there are many environmental situations, where time evolution of the relative humidity and its effect on the human sweating deserve a detailed following, which justifies the need for sensors capable of simulating not only dry, but also evaporative latent heat losses.

2 Sensor and Measuring Chain

An ellipsoid shape sensor was made of ceramic porous material. The porosity of its wall was set, in the manufacturing process, in such a way that, for the environmental conditions foreseen for its future use, an uniform continuous humid layer could be formed on the external surface, but without water dropping. This is a condition that rarely occurs for the human body, where, only for very particular cases, such a skin humidification rate is reached.
It should be stated that this sensor, in spite of being sensitive to the same environmental variables as a human person, has a different thermal regulation mode. It behaves like somebody who would adjust his metabolic rate to the varying environmental conditions to keep a fixed deep body temperature
The inner of the sensor was filled with normal water and a small glass bulb lamp (12 V and maximum power 35 W) of the type commonly mounted in lights of cars was used as heater. It was supplied through an industrial temperature controller Omron E5 CS, which received the input signal from a Pt100 thermal resistance, dived in the water inside the sensor. The temperature was set to 36.5±0.5 ºC, a value close to the typical human deep body temperature.
Two output variables about the sensor were collected - the electric power supplied to the heating lamp and the loss of water by evaporation in its surface. To measure the loss of water, along the time, the sensor was weighted by a precision balance A&D 3000, with a resolution of 0.01 g. The balance values were digitally sent to a computer through RS232 serial port. A data acquisition application was written in the software language Testpoint to automate the tests. The environmental parameters characterizing the thermal conditions inside the test chamber were also acquired and

monitored along the tests. A PC computer, through a plug-in interface board Keithley DAS 800, acquired the analogue signals of all transducers.

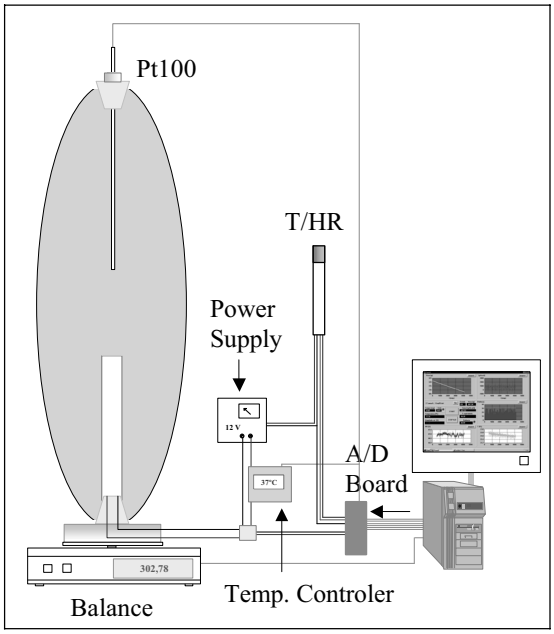

Fig. 2. Measuring chain.

3 Preliminary tests

In figure 3 the time evolution of the sweating rate, defined as the mass decay per time unit and per surface unit [g/(h. m^2)], during a test done under non-uniform environmental conditions, is presented. Relative humidity was varied and the other environmental parameters (air temperature, radiant temperature and air velocity were kept constant). Analyzing the response to the humidity variations, a good sensitivity of the sensor is verified. Also a good repeatability of the response of the sensor is checked, e.g. when the zones A and B, where a repetition of the environmental conditions occurred, are compared.

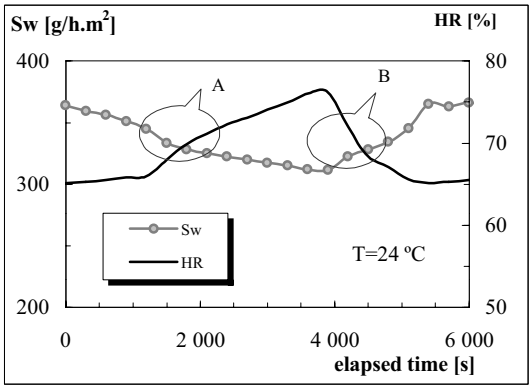

Fig. 4. Time evolution of sweating rate in non-constant environmental conditions.

4 Calibration for SET measurement

Calibration of the sensor was done, for different environmental conditions defined by various combinations of air temperature, air velocity and relative humidity, inside a small climatic chamber developed for this purpose It consisted in building an analytical model that establishes relationships between an environmental evaluation index and values measured by the sensor (required thermal power (Q_T) and sweating rate (S_w)).

Standard Effective Temperature (SET) [3] was selected as the most appropriate index for this sensor, because it considers the combined effects of air temperature, radiant temperature, air velocity, humidity and clothing wearied by people inside the space under evaluation. It is defined as the uniform temperature of an imaginary enclosure, with null air velocity and a relative humidity of 50 %, where an occupant would lose the same heat amount as in the actual environment.

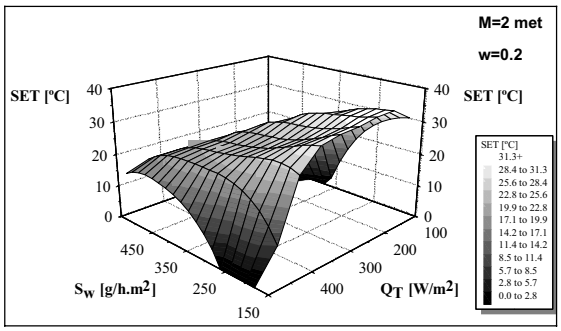

Fig . 7. Response of the sensor in terms of SET

To build the calibration model, the sensor was subjected to different environmental conditions, corresponding to different SET values, and its output values (Q_T and S_w) were collected. A two-variable fourth order polynomial function was used to fit the experimental points of SET values expressed as a function of Q_T and S_w. The 15 numeric coefficients of the polynomial were obtained through a regression process, by the least squares method.

References

[1] T. L. Madsen. A new instrument for measuring thermal comfort. *Proc. 5th International Congress for Heating Ventilating and Air-Conditioning*, Copenhagen, 1971.

[2] P. O. Fanger. Thermal comfort. *McGraw-Hill Book Company.* New York (1993) 244 p.

[3] A. P. Gagge *et al.*. The role of clothing in meeting FEA Energy Conservation Guidelines. *ASHRAE Trans.* 82 (1977) 234–2473.

Enhancement of BG spore capture on an Immunosensor, using a flow-through Ultrasonic Standing Wave system

S.P. Martin[1], L. Kuznetsova[1], M. McDonnell[2], J.J. Hawkes[3] & W.T. Coakley[1]

[1] Cardiff University, School of Biosciences, PO Box 915, Cardiff, CF10 3TL, UK, email. Martinsp@cf.ac.uk

[2] DSTL Porton Down, Salisbury, Wiltshire, SP4 0JQ, UK

[3] Dept. of Instrumentation & Analytical Science, UMIST, PO Box 88, Manchester, M60 1QD, UK

Summary: The development and characterisation of an immunosensor for *Bacillus subtilis var. niger* (BG spores) is described. The glass reflector of an ultrasonic standing wave chamber of acoustic pathlength of the order of ¼ wavelength was coated with immobilised anti-BG spore antibodies. The spores were driven by radiation force towards a pressure node at the glass surface. Significant ultrasound enhancement of spore capture was detected by a fluorescence microscopy technique at concentrations of 10^5 per ml.
Keywords: Ultrasonic standing wave, immunosensor, BG spore
Category: 6

1. Introduction

Procedures that enhance molecular [1] or bacterial approach towards and interaction with a defined immobilised matrix on solid surfaces are of particular relevance in optimising biosensor performance. An approach has recently been described in which a quarter wavelength ultrasonic standing wave chamber has been employed to deposit spores from flow onto a solid surface [2]. A 200 fold increase in capture was obtained at 6.6 x 10^6 spores/ml. In the present work spore capture has been examined as a function of acoustic pressure amplitude and flow rate through the chamber. The consequences for spore capture are reported.

2. Methods

2.1 Ultrasonic technique. The frequency at which the voltage across the transducer was a maximum, was employed in the spore capture experiment. The chamber was connected to the amplifier output, which was controlled by a PC.

2.2 Preparation of slides. The slides were cleaned, the surfaces were modified using APTS in acetone, then glutaraldehyde, and Protein A in that order, before the immobilisation of the anti-BG spore Ab. The slides were stored in a dry state at 4 °C, until use. The immobilised antibody remained active for at least 3 days.

2.3 Assay method. The slide was installed into the chamber. A BG spore solution was pumped through the chamber at a constant flow rate, while an ultrasonic standing wave was produced at the predetermined frequency. The spore suspension was exposed for the periods described, allowing the capture of the spores by the immobilised antibody on the reflector surface. The chamber was then emptied. A solution of the fluorescent dye, Auramine O at 2 % (in PBS) was added for 2 min. The chamber was then washed for 2 min with distilled water at a flow rate of 6 ml/min. Images (area = 0.148 mm^2) of the fluorescently labelled captured spores were taken *in situ* using an Olympus BX41M microscope with a F-view camera, and analysed using Analysis® software (Soft Imaging System, Münster, Germany).

3. Results & Discussion

3.1 Optimisation of flow rate through the chamber. A range of flow rates from 0 to 0.4 ml/min was used, with the BG spores concentration at 1 x10^7 /ml,and an exposure time of 5 min. At this concentration of spores, the maximum capture was at 0.2 ml/min (see fig. 1), where 7460 spores were observed per mm^2. The capture was 1900 spores per mm^2 at the lower flow rate of 0.1 ml/min. The difference is even more

significant in the absence of flow through the chamber, where only 223 spores per mm^2 were captured. The observation that a low flow rate will lead to lower capture is attributed to the lower number of spores passing through the chamber in a given time. The spores also tended to form clumps at the lower flow rate. At flow rates above the optimal, the residence time in the field is reduced and the yield falls. In all further experiments, the flow rate of 0.2 ml/min was used.

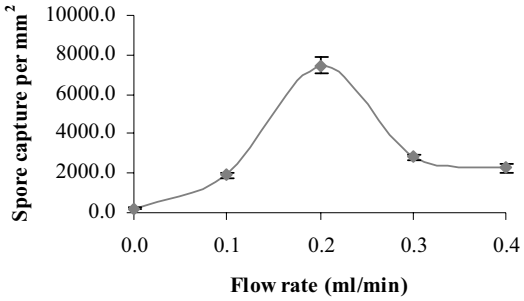

Fig 1. The effect of flow rate through the chamber upon the capture of BG spore (at 1 $x10^7$ spores/ml) at the reflector surface.

3.2 Optimisation of the acoustic pressure. The acoustic pressure amplitude in the standing wave is linearly proportional to the driving voltage applied to the chamber and can be controlled by varying that voltage. The radiation force driving the spores to the node is proportional to the pressure amplitude squared. If the pressure is too low, then the BG spores will not reach the node before they are carried away by the flow through the chamber. If the pressure is too high, the spores will form aggregates or clumps, which reduce the possibility of spore capture at the reflector surface. In our experiments, we found that the optimal pressure was 470 kPa (950 spores captured). At pressures below the maximum (304 kPa 27 spores captured) many spores were not reaching the reflector and at greater pressures (e.g. 630 kPa 201 spores captured), the spores were forming clumps (see fig 2). In all further experiments, an acoustic pressure of 470 kPa was used.

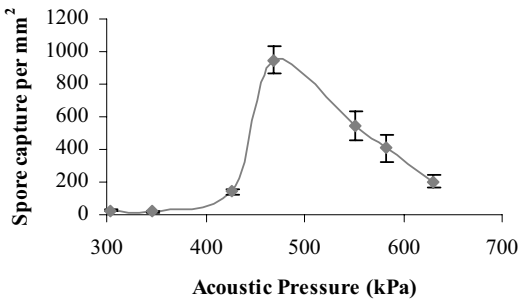

Fig 2. The influence of acoustic pressure upon the capture of BG spores (at 1 x 10^6 /ml and an exposure time of 1 min) at the reflector surface.

3.3 Capture of BG spores at different concentrations. The concentrations studied ranged from 1 x 10^6 to 1 x 10^4 spores/ml. At all concentrations, BG spores were captured at the reflector surface (see fig 3). The capture of BG spores between the concentration of 1 x 10^6 (2024 spores per mm^2) and 1 x 10^5 (496 spores per mm^2) was significantly greater than the background (approx. 105 spores/mm^2 at both concentrations). At lower concentrations (less than 1 x 10^5 spores/ml), it was observed that the spores tended to clump together, and move in a stream to another clump at a diagonal to the flow direction. The clumps formed at a distance of approximately 40 μm below the reflector. This clumping may explain the poor capture levels at these concentrations.

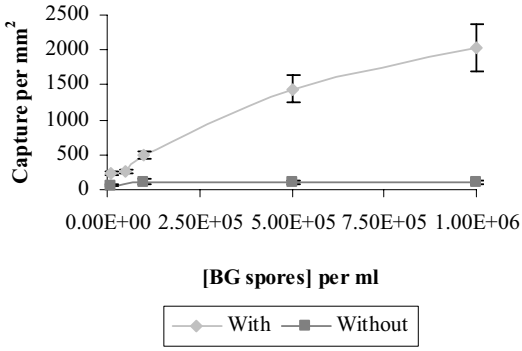

Fig 3. The capture of BG spores over the range of 1 x 10^6 to 1 x 10^4 /ml (1 min exposure time), using the optimised flow rate and acoustic pressure.

4. Conclusions

In the present work, the flow rate through the chamber and the acoustic pressure were optimised at 0.2 ml/min and 470 kPa, respectively, to maximise capture. Ultrasound enhanced the capture of BG spores between the concentrations of 1 x 10^6 and 1 x 10^5 spores /ml, ranging from a 20 and 4.5 fold increase respectively, using the present method. It is expected that resolution of the problem of clump formation away from the surface will lead to further significant improvement in the lower detection limit.

References

[1] M. Nisnevitch, M. Kolog-Gulcho, D. Trombka, B.S. Green, & M.A. Firer. Journal of Chromatography B 738 (2000) 217-223

[2] Hawkes, J.J., Long, M.J., Coakley, W.T., McDonnell, M. In preparation (2003)

SPM & LK are supported by the BBSRC (Research grant No. 72/E17416)

Development of a Portable Acoustometric Immunosensor and Its Application for Pesticides Detection

O.D. Hendrickson[1], A. Priev[2,3], O. Garbuzenko[2], A.V. Zherdev[1] and B.B. Dzantiev[1]

[1]Institute of Biochemistry Russian Acad. Sci., 33 Leninsky prospect, 119071 Moscow, Russia
email: bdzan@online.ru http://webcenter.ru/~bdzan/Index.htm
[2]Department of Biochemistry, The Hebrew University – Hadassah Medical School, Jerusalem, 91120, Israel
[3]NDT Instruments Ltd., Jerusalem, Israel

Summary: *A portable immunosensor based on the measurement of ultrasonic velocity and absorption has been developed. 14 enzymes were tested as labels for acoustometric immunoassays. High-sensitive detection of polymeric substrates hydrolysis was demonstrated; amylases and proteases can be revealed in nanogram range. Bacillary α-amylase was used as the label for enzyme-modulated immunoassay of the pesticide atrazine. The reached assay sensitivity, 0.1 ng/ml, is acceptable for ecological monitoring. Acoustic measurements were combined also with a liposomal immunoassay based on the detection of sedimentation after the formation of immune complexes and their aggregation by water-soluble polyelectrolytes.*

Keywords: *portable immunosensor, ultrasonics, pesticides, enzyme immunoassay*
Category: *6 (Biosensors)*

1 Introduction

Acoustic detection of biomolecules and their rearrangements in solution, based on precise measurements of ultrasound absorption and velocity, is a very effective analytical approach. However, application of the acoustic approach is limited nowadays by the absence of portable measuring devices.

The important field of potential use of such devices is control of pollutants in the environment and food. Widespread monitoring of pollution should be based on suitable analytical techniques that can be used for on-site measurements.

Basing on the given above reasons, in the current work new acoustometer has been proposed and tested in the immunodetection of pesticides.

2 Design of the acoustometer

The created device is based on employing of cylindrical standing acoustical waves, in contrast to conventional devices using plane acoustic waves. The measuring cell is just a metal tube (10 mm long) excited at natural frequencies of radial oscillations of the liquid column filling the tube. The frequency of this resonator is proportional to ultrasound velocity, and the width of the resonance peak is proportional to ultrasound absorption.

This approach enables one to make rapid analyses in little volumes of samples (0.05-0.2 ml). About 30 sec are required for quantitative characterization of acoustic changes in solution.

The device (Fig. 1) is realized as a differential two-channel block with programmed control of temperature in the range 10-90°C and possibility of measurements at fixed or scanning temperature. Sensitivity of the acoustometer to changes of ultrasound velocity is 10^{-4}%, and to changes of ultrasound absorption – 0.1%. Dynamic range of the acoustometer for ultrasound velocity is 900-1700 m/sec, and for ultrasound absorption – 10-150 dB/m. Reproducibility of baseline – $\pm 10^{-3}$%.

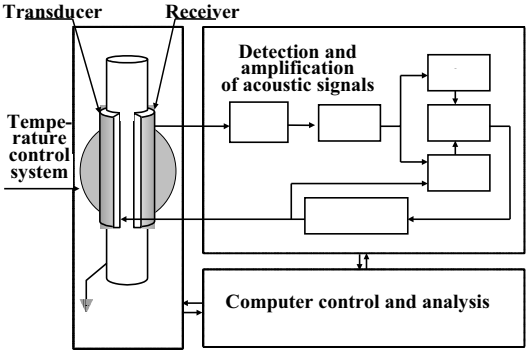

Fig. 1. Principal block scheme of the acoustometer.

The presented approach is far superior over known techniques of ultrasonic measurements in respect to high precision, possibility to analyze small volume samples and simple handling.

3 Screening of enzyme labels

Catalytic activities of 14 enzymes including α-amylase, β-amylase, glucoamylase, β-galactosidase, alkaline protease, alkaline phosphatase, peroxidase, ribonuclease and urease were characterized by the

created acoustometer. All calibration curves have extremely wide range of quantitative concentration measurements (3-4 orders). The obtained results for sensitivities of some enzymes revealing are presented in Table 1.

Table 1. Acoustic determination of enzyme activities (duration – 15 min).

Enzyme	Turnover number	Limit of detection, ng/ml
α-Amylase	60,000	0.4
Urease	9,000,000	4
Alkaline protease	2,100	5
α-Chymotrypsin	1,500	10
Creatine kinase	25,000	15

Sensitivity of acoustic detection of enzymatic reactions is determined by their rate and acoustic effect. In the case of low-molecular weight substrates the acoustic effect is mainly determined by changes of hydration. For high-molecular weight substrates one more effect influences a change in intrinsic compressibility: the loss of a compact structure of biopolymers results in an increase of the acoustic effect by several orders of magnitude. This effect occurs to a great degree in the hydrolysis of starch, globular proteins (casein, ovalbumin), and lipids (egg phosphatidylcholine liposomes), when intraglobular interactions are replaced for hydrational ones.

4 Enzyme-modulated immunoassay

According to the data obtained, bacillary α-amylase was proposed as the label for acoustometric enzyme-modulated immunotechnique (EMIT) of pesticides detection. This assay is based on activity modulation of an amylase-pesticide conjugate as a result of conformational changes in the catalytic site caused by interaction with anti-pesticide antibodies. The enzymatic activity is restored after adding the sample to be tested if it contains pesticide molecules.

Conjugates of α-amylase with two widely used triazine herbicides, namely atrazine and simazine, were synthesized. For both systems the assay conditions were optimized, including duration of the stages, concentrations of the reactants, and protocol of acoustic measurements. Relationship between acoustic signal and enzymatic activity of the conjugates was studied. Antibody influence on the activity confirmed the possibility of the competitive assay.

Calibration curves for atrazine were obtained; working range of its quantitative detection was 0.1-10 ng/ml (Fig. 2). The named characteristics satisfy modern requirements of ecological monitoring and allow recommending the proposed system as a prospective analytical method.

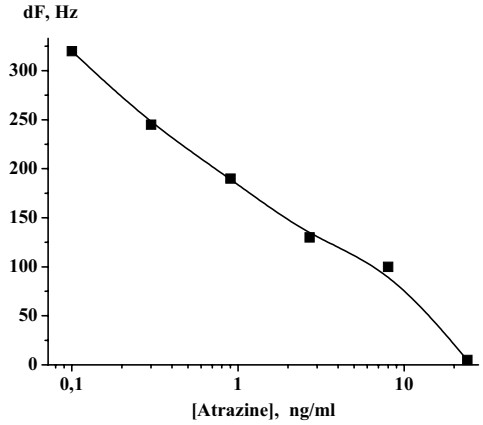

Fig. 2. Calibration curve of atrazine detection by enzyme-modulated immunoassay.

5 Liposomal immunoassay

The proposed acoustic sensor was combined also with a liposomal immunoassay using polyelectrolyte carriers. The assay includes three steps: (1) interactions in solution of pesticide-containing sample, pesticide-liposome conjugate, anti-pesticide antibodies, and polyanion-protein A conjugate, (2) binding of the formed polyanion-containing complexes with polycation and (3) acoustical measurement of the liposomes sedimentation caused by the interpolymeric reaction. Unilamellar 100 nm liposomes were formed from lipid-atrazine conjugate and native lipid. During the assay anti-pesticide antibodies interact competitively with the liposomal antigen and antigen molecules in the sample to be tested. Polyanion polymethacrylate and polycation poly(N-ethyl-4-vinylpyridinium) were used as the separation system. The liposomes were stabilized by the insertion of polyethylene glycol covalently attached to lipid compound to prevent their non-specific interactions.

The described approach was applied for atrazine detection. Due to exclusion of the enzymatic stage the assay duration is reduced from 30-40 min to 15 min with the same sensitivity.

At whole, the proposed approach can be used for different analytical tasks. Hydrolytic enzymes were found to be effective enhancers of the detected signals in this kind of the sensoric systems. The developed immunoassay protocols have perspective of application for detection of different practically important compounds.

This work was made possible by Award 99-1461 of the INTAS Foundation.

Oxidoreductase-based biosensors as analytical tools for use in bioremediation monitoring

D. Cotella[1], P. Micheletta, G. Caputo, C. Santoro[2] and G. Berta[1]

University of Eastern Piedmont "A.Avogadro",
[1]Dept. of Advanced Sciences and Technologies, c.so Borsalino 54 - 15100 Alessandria, Italy,
email: cotelladiego@hotmail.com
[2]Dept. of Medical Sciences, via Solaroli 17 - 28100 Novara, Italy

Summary: *In-situ bioremediation processes should be accompanied with suitable analytical tools for a fast, reliable and especially economic real-time monitoring of bioremediation efficiency. Here we present a panel of enzyme-based biosensor for monitoring the biodegradation performances of oxidoreductases, a class of enzymes whose importance as bioremediation tools has been described [1]. Using the enzyme Toluene/o-xylene monooxygenase as experimental model, we developed a number of different biosensors for the detection of the main substrates/intermediates/products of the enzyme.*

Keywords: *oxidoreductase, bioremediation, BTEX, catechol, phenol*
Category:*6 (Biosensors)*

1 Introduction

Oxidoreductases belong to a large class of enzymes that catalyze biological oxidation/reduction reactions. Since many chemical and biochemical transformations involve oxidation/reduction processes, the potential biocatalytic applications of such enzymes are very attractive. These applications span from the synthesis of commercial value compounds (pharmaceuticals in particular) to the oxidative degradation of pollutants and the construction of biosensors for a variety of analytical and clinical applications [1].
Biodegradation of toxic chemicals such as aromatic compounds (BTEX, PCBs, PAHs and others) is an important priority in technologically advanced societies. Several bioremediation strategies are based on the improvement of degradative properties of soil bacteria, both native and genetically engineered [2]. Novel approaches use fungi as bioremediation tools, preferably in conjunction with a host plant [3-4].
The enzyme Toluene/o-xylene monooxygenase (ToMO) from *Pseudomonas stutzery* OX1 [5] is active on a broad spectrum of substrates and is able to hydroxylate aromatic rings at different positions through two consecutive monooxygenation reactions (Fig. 1). ToMO oxidizes toluene, benzene, ethylbenzene, xylenes, phenols, cresols, naphtalene, styrene and probably other aromatic and non-aromatic pollutants. The potential application of ToMO in bioremediation strategies has been suggested [6]. Here we present a panel of biosensors for the detection of the main substrates/ intermediates/products of ToMO activity.

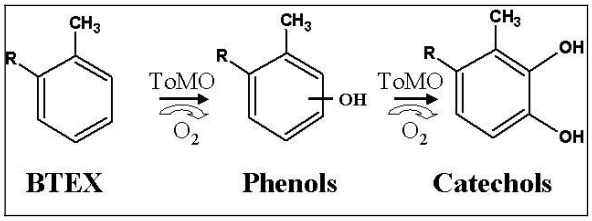

Fig.1. Biochemical pathway of the enzyme Toluene/o-xylene monooxygenase from *P.stutzery* OX1

2 Experimental

The following oxidoreductase-based biosensors have been developed:
- a whole-cell sensor for BTEX, based on a recombinant *Escherichia coli* strain expressing the ToMO enzyme; the detection is carried out by the electrochemical oxidation of the catechols at +600 mV;
- an enzyme electrode for phenols, based on the enzyme tyrosinase (polyphenol oxidase, PPO) immobilized on a nylon membrane; the detection is carried out by electrochemical reduction of quinones at –200 mV;
- a colorimetric test for catechols based on the purified enzyme catechol 2,3-dioxygenase (C23O). The enzyme converts the substrate (catechols) into a intensely coloured product (hydroxymuconic semialdehyde). The detection is also possible through the electrochemical monitoring of oxygen consumed by the C23O.

The analytical performances of biosensor were tested. In particular, the detection limit and linearity range

for each class of pollutants were estimated (Fig. 2,3 and 4) .

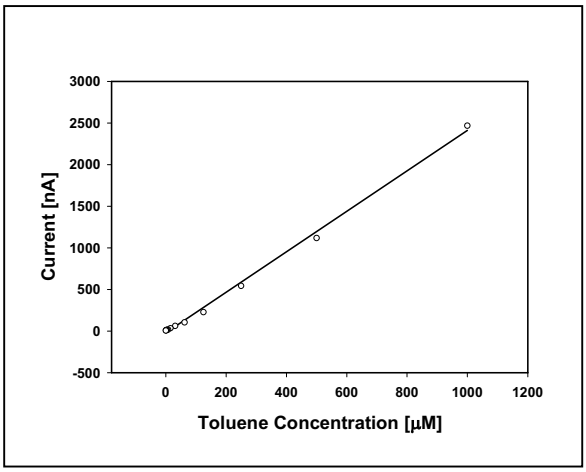

Fig. 2. Calibration curve for Toluene.

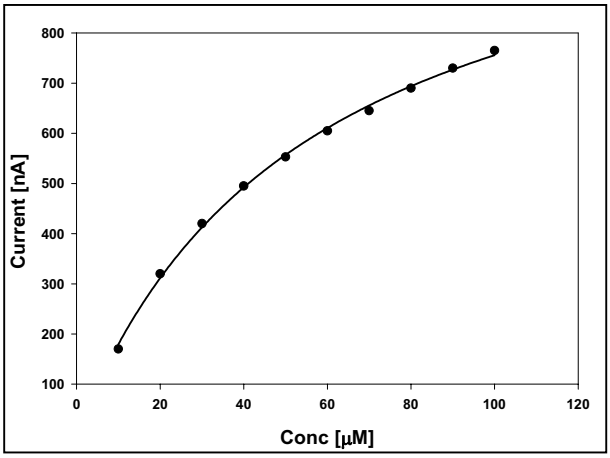

Fig.3. Calibration curve for phenol

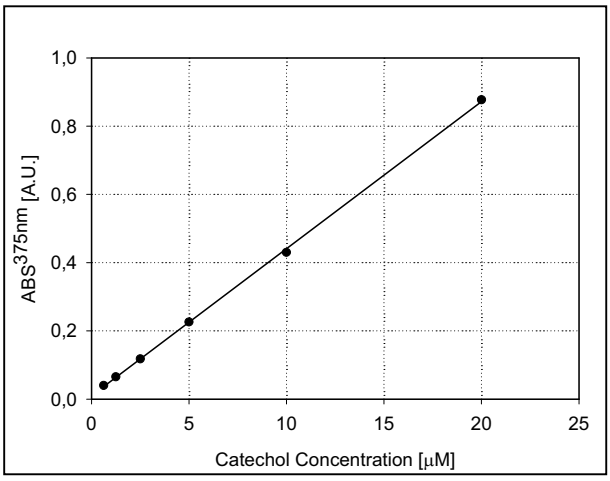

Fig. 4. Calibration curve for catechol

3 Conclusions and discussion

Our results show the possibility to evaluate the ToMO performances by monitoring both substrates than products of the enzyme. Using a strategy based on oxidoreductase enzymes it would be possible to build miniaturized, portable biosensors based on *screen printed electrodes* (SPE) technology for in-field applications.

Abbreviations

BTEX: Benzene, Toluene, Ethylbenzene, Xylene;
C23O: Catechol 2,3-dioxygenase;
PAHs: Polyaromatic hydrocarbons;
PCBs: Polychlorobiphenyls;
PPO: Polyphenol oxidase;
ToMO: Toluene/o-xylene monooxygenase

Acknowledgement

This work is supported by the EU project GENOMYCA (QLK5-CT-2000-01319)

References

[1] S.W. May, *et al*. The potential of oxidoreductase enzymes in biotechnology. *Nat. Biotechnol.* 1 (1983) 677-686.
[2] M. Romantschuk, *et al.* Means to improve the effect of *in situ* bioremediation of contaminated soil: an overview of novel approaches. *Environ. Pollut.*107 (2000) 179-185.
[3] C. Novotny, *et al.* Removal of PCBs by various white root fungi in liquid cultures. *Folia microbiol.* 42 (1997) 136-140.
[4]http://www.inra.fr/Internet/Centres/Dijon/bbceipm/genomyca/
[5] G. Bertoni, *et al.* Cloning of the genes for and characterization of the early stages of toluene catabolism in *Pseudomonas stutzery* OX1. *Appl. Environ. Microbiol.* 62, (1996) 3704-3711.
[6] D.Ryoo *et al.* Aerobic degradation of tetrachloroethylene by toluene/o-xylene monooxygenase of *Pseudomonas stutzery* OX1. *Nature Biotechnol.* 18 (2000) 775-778.

Development of Micro Catalytic Combustor for MEMS Power Generation

Tzong-.Shyng (Jeremy) Leu, Shun-Yi Li and Ren-Re Liao

National Cheng Kung University, Department of Aeronautics and Astranautics,
No. 1 Ta-Hsieh Road, Tainan 701, Taiwan
email: tsleu@mail.ncku.edu.tw http://www.iaa.ncku.edu.tw

Summary: *With the growing trend in miniaturization of microsystems, high energy density (small size, low weight) power generators are required. In this paper, MEMS-based micro catalytic combustors were fabricated to study the feasibility and performance of microscale combustion. The micro catalytic combustion chamber, 1mm wide with 1mm deep, 20mm long and coated with platinum (Pt) catalyst and micro temperature sensors on the wall, were fabricated by using MEMS technology. Experimental results show the wall temperature increases substantially indicating that a large amount of energy is released during catalytic hydrogen oxidation. Gas phase combustion occurs even the diameter of the micro combustor is less then the quench diameter of gas-phase hydrogen-air combustion. Temperatures above 1000°K are achieved in the current micro catalytic combustor.*

Keywords: *micro catalytic combustor; power MEMS*
Category: *7 (Fluidic devices)*

1 Introduction

The development of MEMS technology has spurred the needs for the high energy density (small size, low weight) power generators [1]. Microsystems such as micro air vehicles and micro robots are limited by the weight of the available power system. Currently, most of the power systems used in microsystems are battery. Top battery available (Lithium) has an energy density about 1.2 MJ/kg. However, typical liquid hydrocarbon fuels have an energy density about 45 MJ/kg. It means a micro combustor with a only 3% system efficiency can compete with top batteries [2]. Therefore, the primary incentive in this research is to use combustion of hydrogen/air for MEMS power generation. Micro catalytic combustors were designed, fabricated and studied experimentally to examine the feasibility and performance of microscale combustion.

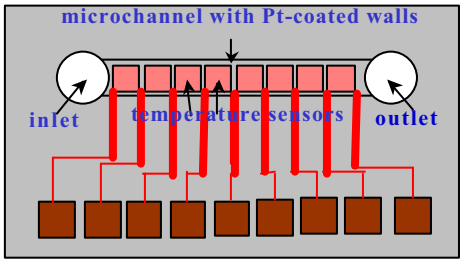

Fig. 1. Sketch of the micro catalytic combustor design

2 Combustor design and fabrication

Figure 1 shows the design of the micro catalytic combustor. The micro catalytic combustion chambers, 1mm wide with 1mm deep, 20mm long and integrated with platinum (Pt) catalytic walls and micro temperature sensors, were fabricated by using MEMS technology. There are total 8 temperature sensors located from the inlet to the outlet of the micro catalytic combustor. The 1.0 mm height H of the micro catalytic combustion chambers was chosen because this size is smaller than the quenching diameter of gas-phase hydrogen-air combustion [3] and because it is comparable to sizes proposed in many microscale combustor designs. Figure 2 shows the size of the micro catalytic combustor compared with a coin.

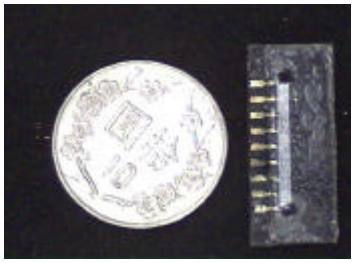

Fig. 2. Photograph of MEMS-fabricated micro catalytic combustor

3 Experimental results

During testing, the catalyst wall temperature is preheated to either 176°C or 260°C, while the inlet composition and mass flow rates of H_2 and air were kept constant. Equivalence ratios vary from fuel lean to fuel rich were investigated in the micro catalytic combustor. Microscale reaction was studied as function of preheated wall temperature, total mass flow rate (resident time) and inlet compositions in the micro catalytic combustor. Figure 3 shows the wall temperature distributions as the wall temperature T_o is preheated at 176°C and 260°C, while the inlet composition and mass flow rate of H_2 and air were kept at. 75 SCCM and 188 SCCM (stoichiometric) conditions. The wall temperature increases indicating that a huge amount

of heat is generated during catalytic reaction. The maximum wall temperature can reaches above 1000°K. Figure 4 shows the luminescent micro catalytic combustor when wall temperature is fixed at 260°C and the mass of flow rates of H_2/Air are 75/188 SCCM (stoichiometric condition).

Micro catalytic combustion was further investigated as a function of the mass flow rates, while the preheated wall temperature, and inlet compositions in the micro catalytic combustor are kept constant. Figure 5 shows the wall temperature distributions as the total mass flow rates (sum of the mass flow rate of H_2 and Air) are increased from 105 SCCM to 263 SCCM, while the preheated wall temperature and inlet air/H_2 equivalence ratio are fixed at 260°C and 2.5 respectively. As the total mass flow rate increased (resident time decreased), the average wall temperature distributions of micro catalytic combustor increase, indicating that the reaction time is much shorter than the resident time of the current experimental conditions. The reactants react and generate energy in a very short time (<resident time ~ 4.8msec at total mass flow rate 263 SCCM).

Figure 6 shows the wall temperature distributions as the H_2 mass flow rates are increased from 37.6 SCCM to 94 SCCM, while the preheated wall temperature and mass flow rate of air are fixed at 260°C and 188 SCCM respectively. In Figure 6, the wall temperature distributions make no difference between fuel rich (H_2 mass flow rate 94 SCCM) and stoichiometric (H_2 mass flow rate 75 SCCM) conditions, but decreases at fuel lean (H_2 mass flow rate 37.6 SCCM) situation. It is suspected that a fixed or total amount of hydrogen fuel completes the reaction and release the same amount of energy disregarding fuel rich or stoichiometric conditions. In the current experimental results, a larger fraction of heat loss relative to heat generation resulting in the decrease of wall temperature from the inlet to the outlet within the micro catalytic combustor is also noticed. The heat loss problems become significant as micro combustors are scaled down [3]. Therefore, combustion in microscale is possible only if optimal thermal and chemical managements are achieved.

References

[1] Kaoru Maruta and Koichi Takeda, Lars Sitzki, Kevin Borer and Paul D. Ronney, Steffen Wussow, Olaf Deutschmann, "Catalytic Combustion in Microchannel for MEMS Power Generation", The Third Asia-Pacific Conference on Combustion, June 24-27, 2001, Seoul, Korea.

[2] A. Carlos Fernandez-Pello, "Micro-Power Generation Using Combustion: Issues and Approaches", the 29th International Symposium on Combustion, July 21-26, 2002, Sapporo, Japan

[3] Kaoru Maruta, Koichi Takeda, Jeongmin Ahn, Kevin Borer, Lars Sitzki, Paul Ronney, Olaf Deutschmann,"Extinction Limits of Catalytic Combustion in Microchannels", Webpage at http://carambola.usc.edu/Research/MicroFIRE/ISC29MarutaCatCombModel.pdf

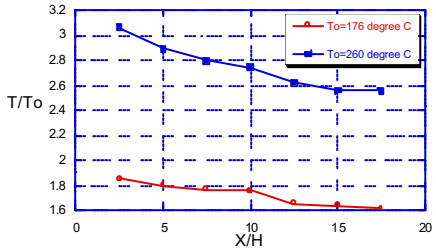

Fig. 3 Wall temperature distribution at wall temperatures T_o = 176°C and 260°C, while the inlet composition of H_2 and air were kept at. 75 SCCM and 188 SCCM (stoichiometric) conditions. (H=1.0 mm)

Fig. 4 Photograph shows Pt-catalyzed H_2 oxidation reaction generates huge amounts of energy and illumines the micro catalytic combustor.

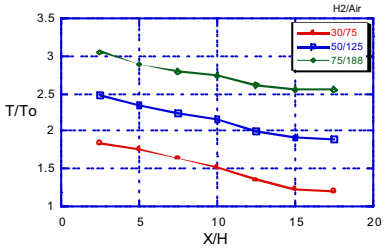

Fig. 5 Wall temperature distributions as the total mass flow rates are increased from 105 to 263 SCCM, while the preheated wall temperature and inlet air/H_2 equivalence ratio are fixed at 260°C and 2.5 respectively. (T_o = 260°C, H=1.0 mm)

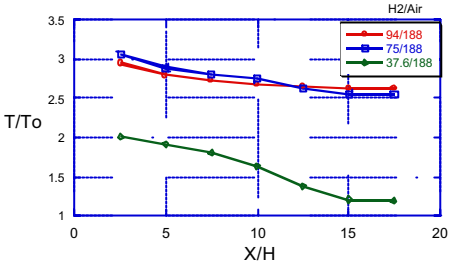

Fig 6 Wall temperature distributions as the H_2 mass flow rate is increased from 37.6 to 94 SCCM, while the preheated wall temperature and air mass flow rate are fixed at 260°C and 188 SCCM. (T_o = 260°C , H=1.0 mm)

New Deep Glass Etching Technology for Fabrication of a Micro Peristaltic Pump

M. Bu[1], T. Melvin[1], G. Ensell[1], J. S. Wilkinson[2] and A. G. R. Evans[1]

[1]Department of Electronics and Computer Science, University of Southampton, Highfield, Southampton, UK, SO17 1BJ
Email: mb00r@ecs.soton.ac.uk http://www.micro.ecs.soton.ac.uk/mems/index.html
[2]Optoelectronics Research Center, University of Southampton, Highfield, Southampton, UK, SO17 1BJ

Summary: *We report on a new masking method that uses multilayered metals combined with thick SPRT200 photoresist, for wet etching glass up to 300 μm deep. This was successfully utilized in the process for fabricating the components of a micro peristaltic pump. Various mask materials, which can be patterned by standard photolithography and metal etching processes, were investigated to eliminate pinholes when an etching depth of 300 μm in the Pyrex wafer was required for fabrication of the micro pump. The fabrication process of the micro peristaltic pump is briefly described.*

Keywords: *deep glass etching, masking technology, micro peristaltic pump*
Category: *7 (Fluidic devices)*

1 Introduction

Wet etching of glass in concentrated hydrofluoric acid (HF) is widely used because of its fast etching rate. But the formation of pinholes during wet etching in HF is a notorious problem, especially when Cr/Au is used as the etching mask and deep etching is required. Other masks such as polysilicon [1], amorphous silicon [1], SU-8 [1-2] and anodically bonded silicon [3] have been used to solve the problem. However, most of them require special facilities, which are not feasible in most standard micro fabrication laboratories.

A novel mask, which can be patterned by standard photolithography and a metal etching process, was investigated in this work to eliminate pinholes formed in the glass during wet etching in HF.

2 Investigation of Masking Methods for Deep Glass Etching

To eliminate the pinholes when an etch depth of 300 μm on a 500 μm thick Pyrex wafer is required, 4 types of mask with different thickness were investigated. These are Cr/Au (60/500nm) covered with Shipley S1818 photoresist (2.2μm), Cr/Au/Cr/Au (60/400/60/400nm) covered by S1818 (2.2μm), and Cr/Au/Cr/Au (60/400/60/400nm) covered by Shipley SPRT220 photoresist (10μm and 20μm). The etching results in Fig. 1 (a, b and c) show that pinholes of various densities and diameters appeared in the Pyrex, when the first three kinds of mask were used. Only the mask with Cr/Au/Cr/Au (60/400/60/400nm) and 20 μm thick SPRT220 were used successfully to etch the Pyrex up to 300 μm deep without pinholes appearing.

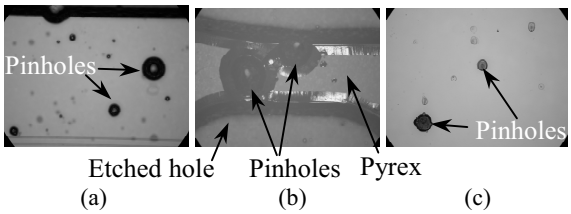

Fig. 1: Pinholes with various densities and diameters were formed in the Pyrex after 38 minutes of etching in 48% HF when different masks were used. (a) With a mask of Cr/Au (60nm/500nm) covered with Shipley S1818 (2.2μm). (b) With a mask of Cr/Au/Cr/Au (60/400/60/400nm) covered with S1818 (2.2μm). (c) With a mask of Cr/Au/Cr/Au (60/400/60/400nm) covered by SPRT220 (10μm).

Fig. 2 shows an etched Pyrex chip using a mask of Cr/Au/Cr/Au (60/400/60/400nm) with 20 μm thick SPRT220 for a micro pump PCR chip [4]. The pump membrane is larger than 6 cm^2 and 200 μm thick and there are no pinholes visible under the microscope. The results indicate that this new masking technology for deep etching of glass is able to prevent pinholes forming using standard photolithography processes.

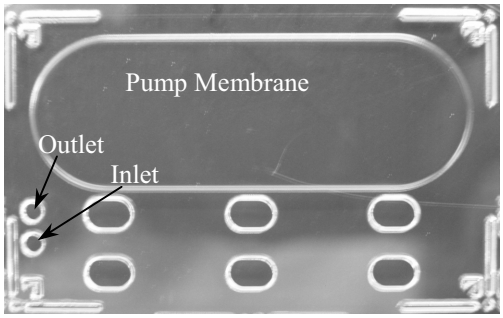

Fig. 2. A Pyrex chip etched in 48% HF for a micro peristaltic pump using a mask of Cr/Au/Cr/Au (60/400/60/400nm) with 20 μm thick SPRT220. The etch depth is 300 μm.

3 Fabrication Process for the Micro Pump

The fabrication process for the micro peristaltic pump includes two parts: the process on the Pyrex wafer and the process on the silicon wafer. Then the two wafers were bonded together by anodic bonding technology.

The fabrication process on a 500 μm thick Pyrex wafer is illustrated in Fig. 3. The process starts with the etching of alignment marks (1 μm deep) in 7:1 buffered hydrofluoric acid (BHF), on both sides at the same time, using 2.2 μm thick S1818 photoresist as the mask (a). After stripping off the S1818, a multi-layer of Cr/Au/Cr/Au (60/400/60/400nm) was evaporated on both sides (b). Then 20 μm thick SPRT220 was spun and patterned on the upper side of the Pyrex to define the pump membrane and inlet/outlet holes (c). The SPRT220 was hard baked at 115°C for 10 minutes. Another SPRT220 layer of 20 μm thickness was spun and patterned on the bottom of the Pyrex to allow etching from both sides (d). Another hard bake at 115°C was done for 50 minutes. After that, the Cr/Au/Cr/Au multi-layer was etched sequentially in Au and Cr etchants (e). Finally, the wafer was immersed in 48% HF for 38 minutes to achieve an etch depth of 300 μm and a 200 μm thick pump membrane (f). When the etching was complete, the SPRT220 was stripped off (g). The Cr/Au/Cr/Au multi-layer was stripped off sequentially by Au and Cr etchants. Finally, another layer of Cr (20 nm) was evaporated on the bottom of the Pyrex wafer and then patterned by photolithography and wet etching in Cr etchant (h).

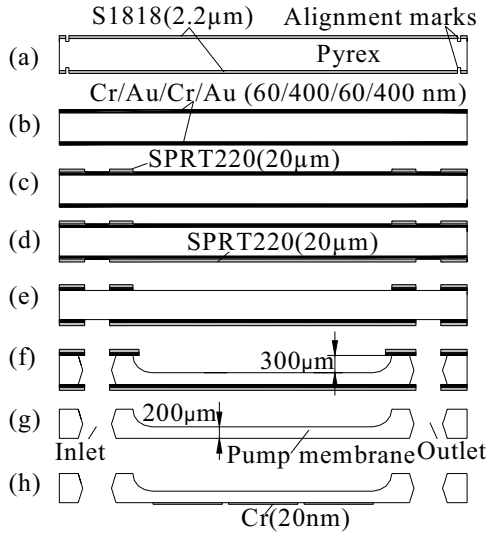

Fig. 3. Fabrication process on the Pyrex wafer

The fabrication process on a 500 μm thick silicon wafer begins by growing a layer of silicon dioxide (100 nm) and depositing a layer of LPCVD silicon nitride (160 nm) on the silicon substrate. SPR510 photoresist was patterned on the wafer, and then the Si_3N_4/SiO_2 layers were etched by reactive ion etching (RIE). The photoresist was stripped off before anisotropic etching of silicon was carried out in 30% KOH solution at 70°C to fabricate 250 μm deep connection channels. The process on the silicon ended with the stripping of Si_3N_4 and SiO_2.

Anodic bonding was carried out when the silicon wafer and the Pyrex wafer were put together on top of a hotplate at a temperature of 400 °C. A voltage of 400 Volts was applied to the Pyrex and silicon via anodic and cathodic electrodes connected to the silicon and Pyrex, respectively. The bonding was prevented in the areas where there was Cr patterned on the bottom of the Pyrex. The Newton rings shown in Fig. 4 indicate that three pump chambers were formed. Three PZT discs were glued on the top of these three pump membranes by conductive glue (not shown in Fig. 4).

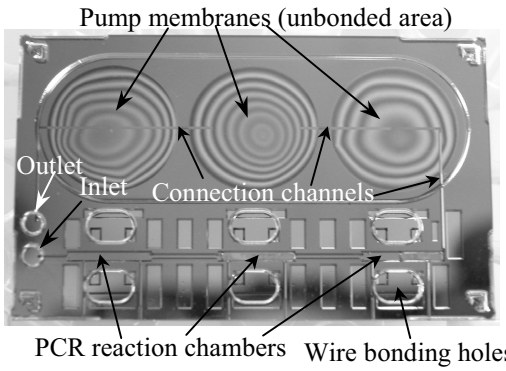

Fig. 4. A micro machined peristaltic pump (before gluing the PZT discs on the pump membranes).

4 Conclusion

A novel masking technology for deep etching of glass employing standard photolithography and metal etching processes was investigated to prevent the formation of pinholes in the glass. This technology was successfully used to fabricate the components of a micro peristaltic pump using Pyrex substrates.

References

[1] D. C. S. Bien, P. V. Rainey, S. J. N. Mitchell and H. S. Gamble, Characterisation of Masking Materials for Deep Glass Micromachining, *Proceedings of Micromechanics Europe 2002*, pp. 103-106, Sinaia, Romania, 2002.

[2] J. Zhang, K. L. Tan, G. D. Hong, L. J. Yang and H. Q. Gong, Polymerization optimization of SU-8 photoresist and its applications in microfluidic systems and MEMS, *J. of Micromechanics and Micromachining,* 11 (2001) 20-26

[3] T. Corman, P. Enoksson and G. Stemme, Deep Wet Etching of Borosilicate Glass Using an Anodically Bonded Silicon Substrate as Mask, *J. of Micromechanics and Micromachining,* 8 (1998) 84-87

[4] M. Bu, T. Melvin, A. G. R. Evans, J. Wilkinson, Design and Simulation of a Micro Pump PCR Chip, *Proceedings of Micromechanics Europe 2002*, pp. 145-148, Sinaia, Romania, 2002.

Influence of Wall Wettability on Bio-Fluid for Bio-MEMS Chip

K. Kanda[1] and M. Yang

Tokyo Metropolitan University, Department of Mechanical Engineering,
1-1, Minami-ohsawa, Hachioji-shi, Tokyo 192-0397, Japan
Email[1]: kanda@comp.metro-u.ac.jp

Summary: *Micro Bio-assay chips consisted of Si and Pyrex glass are on developing. To understand bio-fluid characteristics in a micro-chip, we investigated relationships between pressure drop and volumetric flowrate in surface treated micro-tubes to hydrophilic and hydrophobic. Results for hydrophilic tubes with scales over 20μm for diameter show the relationships agree with fluid dynamics theory accurately. On the other hand, results for hydrophobic tubes show volumetric flowrates are larger than theoretical value and increase ratio of volumetric flowrates of bio-fluid is less than that of pure water .The effects of interaction between bio-molecules and wall surface are indispensable to design of μTAS or Bio-MEMS chips.*

Keywords: *Micro-Fluidics, Bio-Fluid, Wettability*
Category: *7 (Fluidic devices)*

1 Introduction

In Bio-MEMS or μTAS chips attracting attention in late years, reagents or samples are generally driven and controlled as fluid. Thus researches and developments of micro fluidic devices (e.g. micro pump, micro valve, micro mixer and so on) have been carried out [1]. Though correct understanding on influences of size effects, wall properties and fluidic characteristics on flow is important issues in fluidic device design, much of those remain unknown. Also, it becomes crucial issues in micro scales that bio-molecules are agglutinated to the wall or clustered.

Bio-Assay chips which consist of Si and Pyrex glass for detection of dioxin and have thin slits for damming micro-sphere coated by reaction reagent have already developed by the authors (shown in Figure 1). Actually, when we handle these bio-chips including bio-fluid, above issues lead to blockages or damages of channels. In this study, we aim to evaluate influences of size effects and wall wettability on bio-fluid flow. These evaluations lead to establishment of design logic for micro-fluidic devices, μTAS chips and Bio-MEMS chips.

2 Experimental apparatus and condition

To investigate influences of wall wettability on flow, relationships between pressure drop and volumetric flowrate of bio-fluid in micro-tubes were evaluated. Pressure drop and volumetric flow were measured by apparatus shown in Figure 2. The volumetric flow rates are controlled simultaneously by a Harvard Apparatus PHD2000 syringe pump. Flowrates produced by this syringe pump are slightly unsteady. Root-mean-square pressure fluctuations of 6.2% were observed in a micro-tube at Reynold's number of 0.75. Fluid driven by syringe pump is branched right before micro-tube, static pressure of fluid at there is measured by resonated pressure sensor. Pressure at micro-tube outlet is atmosphere pressure. Thus, output of pressure sensor is pressure drop.

Silica tubes were used as micro-tubes. Silica tubes were surface-treated to hydrophilic by 5%NaOH aqueous solution or hydrophobic by PTFE series coating agent. Approximately 2.5μm thickness hydrophobic layer was produced in silica tubes with 100μm and 150μm diameter.

BSA(bovine serum albumin) aqueous solution was used as bio-fluid because BSA is most essential in bio-application.

3 Results and Discussion

Experimental volumetric flowrates ratio for theoretical value of pure water and BSA aqueous solution in hydrophilic and hydrophobic silica tubes plotted by pressure drop is shown in Figure 3. In hydrophilic silica tubes, the relationships between pressure drop and volumetric flowrate agree with Poiseuille equation for both pure water and BSA aqueous solution over 20μm diameter. In hydrophobic tubes, results show increasing ratio of volumetric flowrates become larger than theoretical value with diameter decreasing. Furthermore, increasing ratio of volumetric flowrates for BSA aqueous solution in hydrophobic tube was smaller than those for pure water.

Increasing of volumetric flowrates for theoretical value may be caused by flow slip at hydrophobic boundary. Results show that flow slip over hydrophobic boundary occurs with bio-fluid, too.

That increasing ratio of volumetric flowrates for BSA aqueous solution was smaller than those for pure water may indicates hydrophobic effect was weakened by agglutination of bio-molecles to the wall. These results support hypothesis that cause of flow slip is existence of air on hydrophobic wall. By applying flow slip on hydrophobic surface to mTAS or Bio-MEMS chips, drag reduction or resolution of blockage are expected.

4 Conclusion

In this study, influences of wall wettability and size effects on bio-fluid were evaluated as essential evaluations for Bio-MEMS applications. Results show fluid slip of bio-fluid over hydrophobic wall is smaller than that of pure water. Applying these results, surface treated Bio-chips to resolve issues such as blockages or damages of channels are on developing.

References

[1] R. H. Liu et al., J. MEMS, Vol. 9 No. 2, June (2000) 190-197.

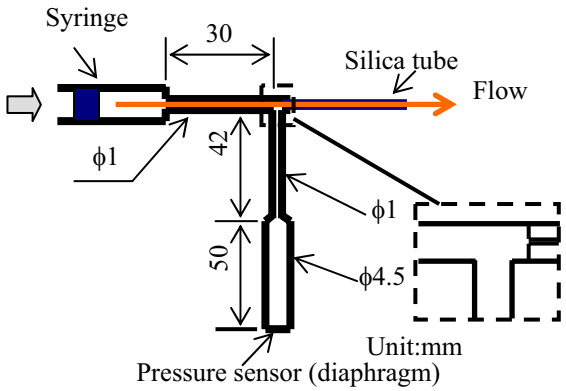

Fig.2 Diagragm and dimensions of experimental apparatus

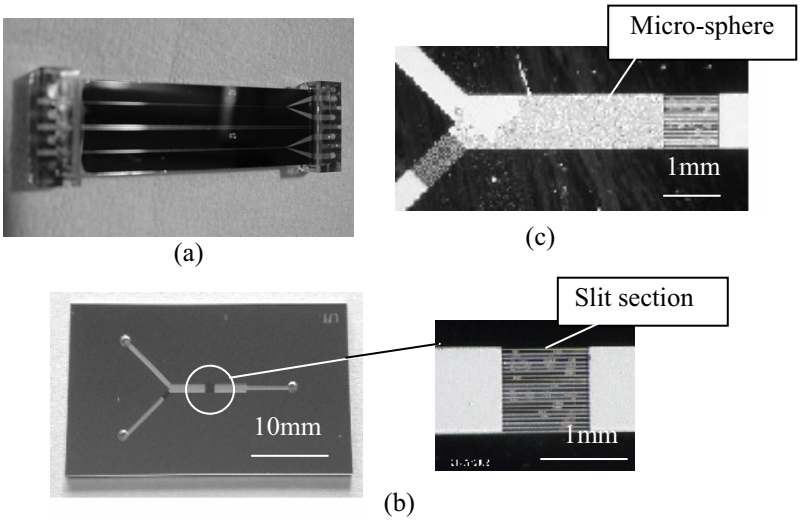

Fig.1 Micro-channel chip with a straight reaction chamber (a), with a slit in a straight micro-channel and enlarged photo of chamber (b) which can dam micro-sphere fixed the reaction reagent on its surface for bio-assay application (c)

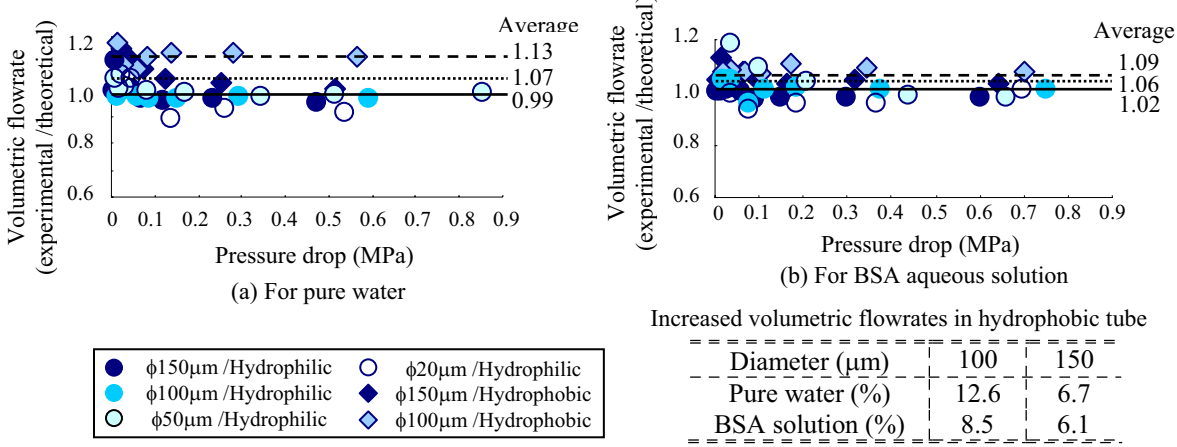

Increased volumetric flowrates in hydrophobic tube

Diameter (μm)	100	150
Pure water (%)	12.6	6.7
BSA solution (%)	8.5	6.1

Fig.3 Increasing ratio of volumetric flowrate for pure water and BSA aqueous solution in surface treated silica tube

A bidirectional valveless peristaltic micropump with chemical resistance and a very simple design

Dae-Sik Lee[1], Jong Soo Ko, Haesik Yang, and Youn Tae Kim

[1]Bio-MEMS Team, Electronics and Telecommunications Research Institute (ETRI), Yuseng-gu, Daejeon, 305-350, Korea
email: dslee@etri.re.kr http://www.etri.re.kr

Summary: *A planar bi-directional valve-less peristaltic micropump for controlling bio samples fluids was designed with a very simple structure and fabricated employing MEMS technologies, including DRIE process in silicon, chemomechanical polishing, and silicon-glass anodic bonding techniques. The proposed micropump was able to control bi-directionally the flow rate of test water at ~ 12 ㎕/min (20 nℓ/stroke) and test air at ~ 60 ㎕/min (100 nℓ/stroke) based on a frequency of 10 Hz at a voltage of 120 V_{pp}. Actuation modeling of the PZT-glass actuator was performed using the CoventorWare, and the simulation results agreed well with the experimental measurements.*

Keywords: *Micropump, bi-directional pumping, valveless, biocompatible, piezoelectric*
Category: *7 (Fluidic devices)*

1 Introduction

Recently, there has been an increased interest in research on microfluidic systems, like micro total analysis systems (μ-TAS) and microdosage systems, which use MEMS technologies to create certain advantages, such as, a smaller dead volume, reduction in samples and reagents, high throughput, and rapid response [1-3]. One of the main components in a microfluidic system is a micropump. Due to the increasing need in the biochemical and biomedical industries, various efforts to manipulate down to nanoliter or picoliter samples have already been attempted [1,4]. However, for these applications, a micropump is needed that can reliably control liquids with a simple structure in a micro liter range. Accordingly, the current study designed and fabricated a bi-directional valveless silicon-glass peristaltic micropump for the transportation of biological samples in a micro total analysis systems with a water flow rate of 0.1 ~ 10 ㎕/min, with the merits of bio-compatibility, absolute reduction in the conventional fabrication steps, and simplification of the assembling procedures.

2 Experiments

The proposed micropump consists of an inlet, three pump chambers, three PZT actuators, flow microchannels, and an outlet, as shown in Fig. 1. A three-dimensional model was employed to perform a mechanical simulation for the micro-actuation of the proposed micropump. As regards the fabrication process, the pump chambers were formed using DRIE or KOH wet etching on the front side of a polished silicon wafer, with a depth of 10-20 ㎛. A 200 ㎛-thick flat glass plate (Pyrex 7740) was used as the upper cover plate. The liquid inlet and outlet holes were made with a sand blaster (20 ㎛ sand particles). The fabrication process of the proposed micropump is summarized in Fig. 2. The fabrication of the proposed pump only involved two masks with a simple structure. The implemented micropump is shown in Fig. 1(b). Deionized (DI) water and air were used as the test fluids. The pump performance was measured as a function of the signal voltage and operation frequency received by the three PZT disks generated from the function generator and the overlapping duty was set as one third.

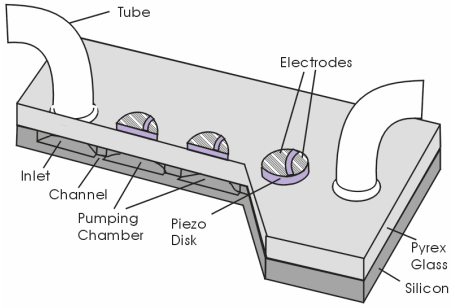

(a)

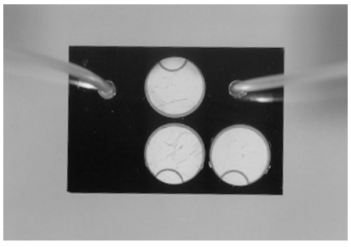

(b)

Fig. 1. Schematic diagram (a) and the photograph (b) of the proposed peristaltic piezo micropump.

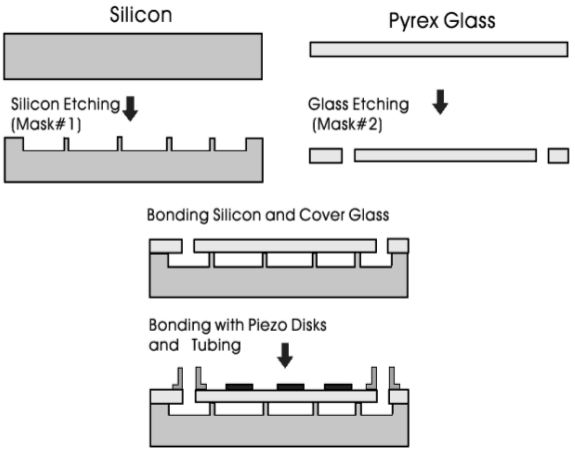

Fig. 2. Process chart of the proposed micropump.

3 Results and Discussions

The maximum deflection at the center of the pumping membrane with two kinds of fluids, i.e. water and air(density (kg/m^3) of air and water is 12 and 998, and coefficient of viscosity (kg/(m·s) is 1E-5 and 1.8E-3, respectively, at 1 atm. and 20 ℃), in the pump chamber at the applying frequency of 10 Hz as a function of an applying voltage, is shown in Fig. 3 as the result when using both the laser displacement meter and the CoventorWare simulator. Micro-actuation in both simulation and measurement values results were similar with only a slight variation within a range of 80 ~ 120 V_{pp}. The deflection of membrane with air mass in pump chamber was larger than that with water mass in the chamber. It is caused by that air has smaller density and viscosity than water.

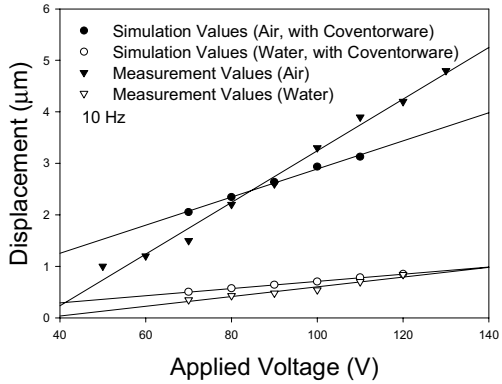

Fig. 3. Maximum membrane deflection result as a function of the membrane thickness for both water and air at the frequency of 10 Hz.

The measured air flow rates of the micropump at an applied frequency of 10 Hz with a voltage range of 60 ~ 120 V_{pp} are shown in Fig. 4. The pumping rate of the micropump with an operating voltage of 120 V_{pp} exhibited about 60 ㎕/min. From Fig. 4, a stroke volume within an applying voltage range of 60 ~ 120 V_{pp} and at an applying frequency of 10 Hz, was 30 ~ 100 nℓ, with a stroke of 1.2 ~ 4.2 ㎛.

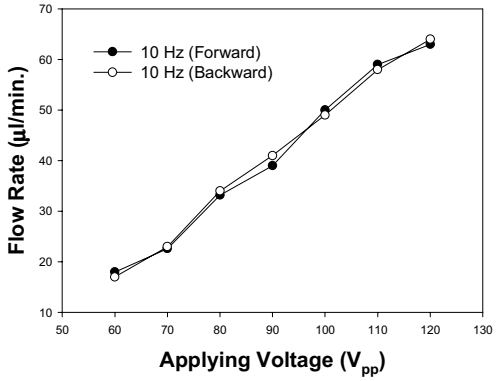

Fig. 4. Measured air flow rate as a function of the applying voltage.

The measured water flow rates of the micropump at an applied frequency range of 1~10 Hz with a voltage range of 80 ~ 120 V_{pp} are shown in Fig. 5. The water pumping rate of the micropump at 10 Hz with an operating voltage of 120 V_{pp} was about 12 ㎕/min. From Fig. 5, a stroke volume within an applying voltage range of 80 ~ 120 V_{pp}, and at an applying frequency of 10 Hz was 10 ~ 20 nℓ, with a stroke in the range of 0.4~0.8 ㎛. As for both water and air, we could see the pumping bi-directionally in the nearly same flow rates, and it would be caused by that the three chambers were arranged in symmetric position on a chip.

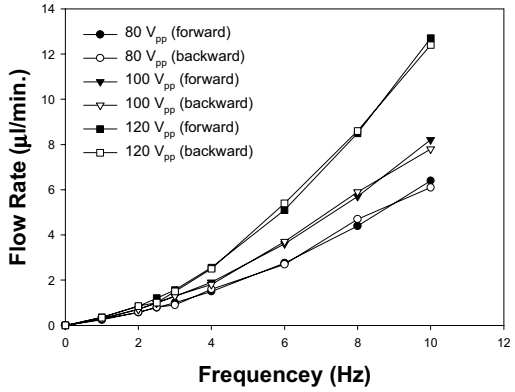

Fig. 5. Measured water flow rate as a function of the applying frequency.

References

[1] H. G. Craighead, Nanoelectronmechanical Systems, *Science* 290 (2000) 1532-1535.

[2] P. Dario, M. C. Carrozza, A. Benvenuto, A. Menciassi, Microsystems in Biomedical Applications, *J. Micromech. Microeng.* 10 (2000) 235-244.

[3] A. Olsson, P. Enoksson, G. Stemme, and E. Stemme, *Journal of microelectromechanical systems*, 6 (1997) 161-166.

[4] M. A. Burns, B. N. Johnson, et al. *Science* 282 (1998) 484-487.

Very low flow rate behavior of micromachined hot-plate anemometers

G. Barillaro[1], P. Bruschi[1], D. Navarrini[1], M. Piotto[2]

[1]University of Pisa, Information Department, Via Diotisalvi, 2, 56122 Pisa - Italy
email: p.bruschi@iet.unipi.it
[2] CNR, IEIIT, Via Diotisalvi, 2, 56122 Pisa - Italy.

Summary: *The increase of microfluidic applications has led to a growing request for more accurate miniaturized flow sensors suitable for operating in gas velocity as low as few cm/s or less. In this work a micromachined anemometer, consisting of a suspended membrane equipped with a polysilicon heater and a poly-p/poly-n thermopile as the temperature sensor, has been analytically and experimentally characterized in very low nitrogen flow rate. Our scope was to investigate the sensor operating limits in terms of sensitivity and dynamical range and to propose some solutions in order to improve the sensors performances.*

Keywords: *hot-plate, anemometer, free convection*
Category: *7 (Fluidic devices)*

1 Introduction

In many fields of application, including household appliances, biomedical and aerospace systems, the sensor operating range must include very low flow regimes, involving gas velocities of the order of few cm/s and below. In these operating conditions, in order to provide a good accuracy, very expensive and cumbersome devices, which often suffer from reduced operating range and relatively long response time, are typically employed. Integrated thermal sensors seem to be the best candidates in order to override these problems. Moreover, monolithic sensors benefit of the typical advantages resulting from the integration, low cost and small size, high reliability and, finally, the possibility of integrating electronic circuits for signal conditioning and amplification.
However, though thermal sensors have been widely studied in the past, very few papers [1] have been devoted to study and model their behaviour at very low gas velocities.
In this work we analyse the response of a silicon micromachined anemometer in the nitrogen flow rate range [0-150] SCCM. The role of parasitic thermal conducting paths and free convection terms in determining the lowest detectable gas velocity is investigated thoroughly by means of both purposely devised experiments and detailed calculations.

2 Sensor description and analysis

The flow sensor presented in this work is a classic micromachined hot wire anemometer, consisting in a suspended membrane equipped with a polysilicon resistive heater and a poly-*n*/poly-*p* thermopile as the temperature sensor. The device, visible in figure 1, has been fabricated by means of front side bulk micromachining applied as a post-processing step to a standard CMOS silicon chip. Further details on the sensors description can be found in ref. [2].
In regime of forced convection, the hot wire anemometer response is usually well described in terms of the King's law [3].

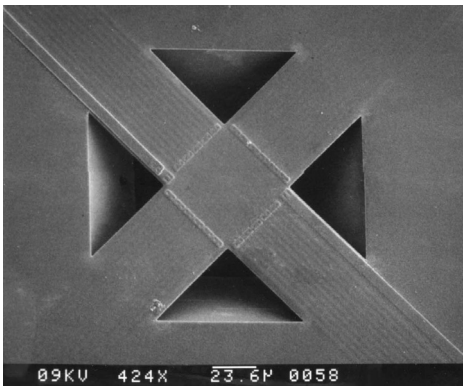

Fig. 1. SEM micrograph of the hot-plate.

Instead, in the range of our interest, while the radiation effect can still be neglected, the free convection thermal conductance become more and more important with respect to forced convection one as the gas velocity is reduced. In addition thermal conducting paths (the suspending arms and the air gap under the membrane) contributes to the output signal adding a constant offset term, far greater then the flow-dependent signal (due to forced convection).
In figure 2.a, the various conductance terms which determine the sensor response are indicated. Briefly, the term G_{MF} is representative of both free and forced convection from the membrane to the gas, G_A and G_{SA} correspond to the thermal conduction through the air gap and the suspending arms, respectively. T_M, T_G and T_S are the membrane, the gas and the substrate temperatures, respectively. Analytical calculations of these conductances by means of dimensional analysis techniques [4] show that a transition between

forced and free convection regimes occurs for a threshold flow rate Φ^* given by the following equation:

$$\phi^* = 2.645 \cdot \frac{d}{\sqrt{L}} Pr^{\frac{1}{6}} \cdot S \cdot (g \cdot \beta)^{\frac{1}{2}} \cdot (T_M - T_G)^{\frac{1}{2}}$$

where L is the square membrane linear dimension, d is the distance between the membrane and the chip edge, g is the gravity acceleration, Pr and β are the nitrogen Prandtl number and compressibility, respectively, while S is section of the pipe utilised for the tests (see next section).
As a result, the sensor response, analysed by means of the lumped element model reported in figure 2.b shows a flow rate behaviour which does not follow the classical dependence on the velocity square root, but it is marked by a sensitivity threshold in correspondence of Φ^*.
Substituting in the equation written above the corresponding values, we found a threshold flow rate Φ^* included in the range of our interest.

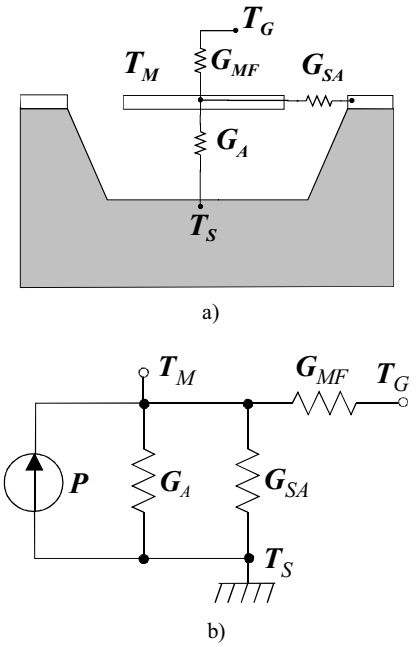

Fig. 2: In the vertical section of the sensor (a) the thermal conductance terms involved in the equivalent electrical network (b) are indicated.

3 Preliminary results and discussion

Flow measurement tests have been carried out on the sensor using ultra-pure (99%) nitrogen gas at room temperature. The chips were exposed to a gas stream in the range (0-150) SCCM, flowing out from a stainless steel pipe of 0.75 mm diameter. The chip has been placed inside a properly designed sample holder, at 5 mm from the gas outlet orifice. The sample holder was fabricated in such a way that the gas flow incidence angle α with respect to the membrane surface could be manually varied. The anemometer output signal, consisting in the thermopile output voltage measured in constant heating power configuration, is reported in figure 3 as a function of the flow rate.

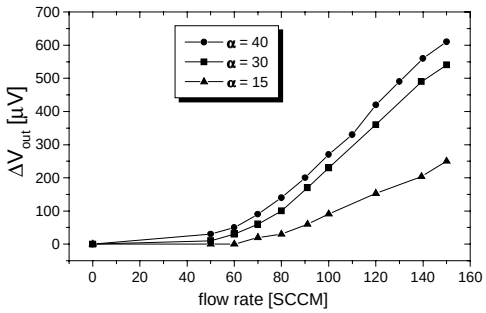

Fig. 3: Sensor output signal as a function of the flow measured for different gas incidence angles.

As predicted by our analysis, a sensitivity threshold is clearly visible in the sensor response around a gas flow rate of 50 SCCM, corresponding to a gas velocity of about 1.8 m/s; for higher values, the output signal shows a nearly linear behaviour as a function of the flow rate, differing from the square root behaviour, typical of the forced convection region. Figure 3 also shows the dependence of the sensor output signal on the gas incidence angle α. In particular, higher values of α result in a sensitivity increase and in a slight shift of the threshold flow rate Φ^* towards lower values.
This feature could be exploited in order to enhance the sensor performances, in terms of sensitivity and dynamical range. Anothe possible way to reduce the Φ^* value consists in increasing the membrane size L: however, to obtain a significant advantage, the membrane size must be increased a lot, because of the square root dependence of Φ^* on the parameter L. This solution is then not compatible with the fabrication process, which imposes a maximum etching time in order to prevent the aluminum pads damaging during the post processing step [2].
As a conclusion, a physical limit for the application of thermal integrated anemometers to very low gas flow sensing has been individuated. This limit, intrinsically related to the microstructure lenght scale, can be, however, overridden by means of differential structure, which, in principle, are less sensible to free convection effects.

References

[1] A. Giani, F. Mailly, R. Bonnot, F. Pascal-Delannoy, A. Foucan, A. Boyer, *Microelectronics Journal*, 33(2002), 619-625.
[2] P. Bruschi, P. Mesuraca, M. Piotto, *Sensors and Microsystems*, pp. 335-339, World Scientific Publisher, 2000.
[3] L. V. King:, *Proc. R.. Soc. London*, 90 (1914), pp. 563-570.
[4] F. Kreith, *Principles of Heat Transfer*, Intext Educational Publisher, New York (1973).

Performance Comparison of Dielectrophoretic Particle Sorters based on a Novel Analysis Method

J.H. Nieuwenhuis and M.J. Vellekoop

Institute of IEMW, Vienna University of Technology, Gusshausstrasse 27-29, A-1040 Vienna, Austria
email: nieuwenhuis@tuwien.ac.at http://www.iemw.tuwien.ac.at

Summary: *In this paper three particle sorters based on negative dielectrophoresis are compared using a novel analysis method. By equating the formulas for dielectrophoresis, drag and buoyancy, the velocity vectors for the particles with respect to the liquid can be obtained. When this information is combined with the liquid velocity vectors 3-dimensional particle trajectories can be calculated. The maximum allowed flow speed for which the sorters still work is the performance criterion applied here. The configuration with electrodes on both sides of the channel proved to have the best performance.*

Keywords: *dielectrophoresis, particle sorter, simulation*
Category: *7 (Fluidic devices), 1 (General, theoretical and modelling)*

1 Introduction

In this paper flow-through particle sorters with negative dielectrophoresis actuation are analysed. By calculating 3-dimensional particle trajectories the performance of three different electrode configurations is compared. The sorters consist of a gradually sloped dielectrophoretic actuator that is used to divert the particle from its straight trajectory to one side of the flow-channel so that it can be sorted out with a simple y-junction configuration (see figure 1). The sorters studied here are designed to be used in combination with a sheath flow that assures that the particles will enter the sorting area in the middle of the channel.

Currently the biosensor field is rapidly growing in importance and numerous lab-on-a-chip based systems are emerging. Many of them are equipped with some kind of integrated sensors. The functionality of such systems can be greatly extended by adding a flow sorter to sort out rare bio-particles (e.g. cells) based on the readings of the sensors. The sorter configurations studied here are to be applied in an integrated cytometer equipped with a near-field optical particle shape sensor [1].

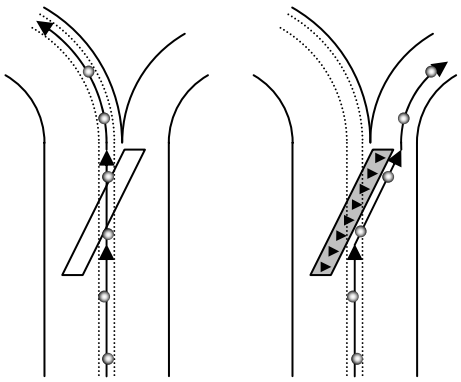

Fig. 1, without actuation the particle ends up in the left branch of the sorter (left) and when the sorter is actuated it is forced into the right branch of the channel

2 Theory

Dielectrophoresis is the phenomenon that when a particle is placed in an inhomogeneous electrical field it will experience a force when its permittivity differs from the surrounding medium. Frequently the formula for dielectrophoresis [2] is combined with that of the buoyancy force for static analyses such as the levitation height of a particle. However, here we also add the formula for the drag force to obtain the equation for the motion of a particle in an inhomogeneous electric field. When the forces are constant a steady state will be reached (after an initial transient period) where the settling speed of the particle with respect to the liquid is given by:

$$v_{settle} = \frac{\varepsilon_l r^2 K_{CM} \nabla E_0^2}{3\eta} + \frac{2r^2(\rho_l - \rho_p)g}{9\eta} \quad (1)$$

where ε_l is the permittivity of the liquid, r is the radius of the particle, K_{CM} is the Clausius-Mossotti function, η is the viscosity of the liquid, ρ_l and ρ_p are the densities of the liquid and the particle respectively and g is the gravitational constant. The first part of this equation is caused by dielectrophoresis and the second part is determined by buoyancy. The time constant for this process is:

$$\tau = \frac{2\rho_p r^2}{9\eta} \quad (2)$$

For the situation studied here: polystyrene particles with a radius of 10 μm in purified water, the time constant is only 22.4 μs. Because of this short time-constant the particles can be considered to travel at settling-speed constantly, as long a there are no sudden changes in the electric field. With a gradually sloping sorter configuration as analysed here this seems justified.

What is not considered here is the influence of Joule heating, which could slightly reduce the force. However in [3] it is demonstrated that this effect is only of importance in well conductive

media (> 1 S/m) or at very low flow-speeds. Since distilled water is considered and the flow speed is significant, Joule heating can be neglected.

3 Comparing electrode configurations

Three different electrode configurations were analysed. A configuration (I) with two equally sized electrodes on the bottom of the channel, a similar configuration (II) but now with the left electrode extending up to the channel wall and a third configuration (III) with one electrode on the bottom of the channel and one at the top (see figure 2).

Using finite element simulations the electric field distribution for each electrode configuration was calculated in a 2D plane (see figure 2 left). By applying formula 1 the velocity vectors for a particle with respect to the liquid can be calculated. The streamlines for this velocity-vector field are plotted in the right part of figure 2 for a polystyrene particle with a radius of 10 µm in water and with AC-voltages of ± 3V. When combined with the velocity distribution of the liquid itself (also obtained using finite element simulation) the 3-dimensional vectors are obtained that describe the complete particle motion. By repeating the procedure with a slight horizontal off-set for the electric field, the 3D particle velocity vector field for the sloped sorter layout is obtained. This can be used to calculate particle trajectories (see figure 3).

The maximum (average) flow-speed of the liquid for which the particle trajectories could follow the sorter was determined for each electrode configuration. The situation depicted in figure 3 shows a particle sorter operated just over the maximum flow-speed: one of the particle

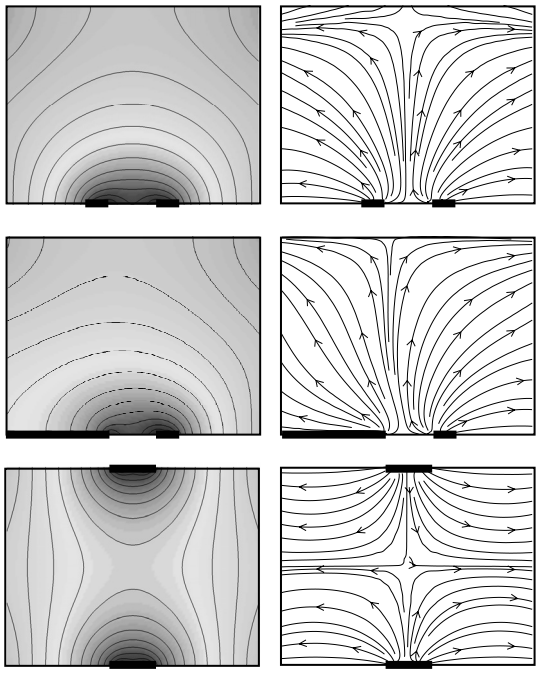

Fig. 2, the distributions of the electric field (left) and the stream-lines for v_{settle} (right) in a cross-section of the channel for the three electrode configurations analysed

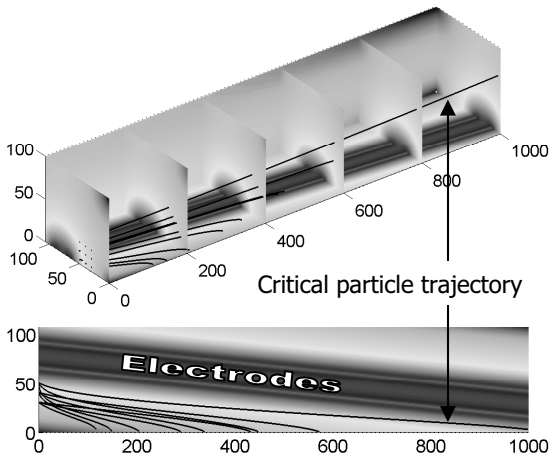

Fig. 3, 3D particle trajectories (black lines) in 3D-view (top) and top-view (bottom) for sorter configuration I

trajectories can no longer follow the slope of the electrodes. The slope of the sorter was 1:20 in this simulation and the particle trajectories start in an area of 30 µm x 30 µm on the bottom of the channel, located 15 µm right of the sorter (see figure 3). Under these conditions maximum allowed flow-speeds were obtained of 0.9, 2.6 and 6.8 mm/s for configurations I, II and III respectively.

The results can be explained as follows. Besides pushing the particle sideways, configurations I and II also lift the particle up into a region where their field intensities are much weaker and therefore the maximum force is reduced. Configuration III in contrast hardly causes any lift of the particles and on top of that its electrical field extends over the full height of the channel. Configuration II performs better than I, because it has a larger gradient in the electric field due to its asymmetry.

4 Conclusions

In this paper the performance of dielectrophoretic particle sorters was studied using a novel analysis method. The configuration with electrodes on both sides of the channel (III) performed best. If electrodes on only one side of the channel are allowed than the asymmetrical configuration (II) has the better performance.

References

[1] J.H. Nieuwenhuis, J. Bastemeijer, A. Bossche, M.J. Vellekoop, Dynamic Particle-Shape Measurements Using a Near-Field Optical Sensor, Proc. of 1st IEEE Sensors Conference, June 12-14, 2002, Orlando, Florida, USA

[2] T.B. Jones, Electromechanics of Particles, Cambridge University Press, Cambridge, USA, 1995, p. 36

[3] T. Schnelle, T. Müller, G. Gradl, S.G. Shirley, G. Fuhr, Paired microelectrode system: dielectrophoretic particle sorting and force calibration, Journal of Electrostatics 47 (1999) pp. 121-132

Micromachined flow sensor on silicon membrane

V. Guarnieri[1], M. Decarli[2], A. Bagolini[1], A.A. Vasiliev[3], M. Zen[1] and G. Soncini[2]

[1]ITC-irst, via Sommarive, 18, 38050 Povo (TN)
email: guarni@itc.it http://www.itc.it
[2]Dept. Of Information and Communication Technologies, via Sommarive, 14, 38050 Povo (TN)
[3]RRC Kurchatov Institute, Institute of Molecular Physics, 123182, Moscow, Russia

Summary: *Design, realisation and testing results of an integrated air flow sensor based on micromachined technology are reported. The mass airflow sensor architecture is based on a dedicated microelectronic thermal (hot-wire) anemometer design. Two different layouts for the two different splittings projected one for a polysilicon resistor and the other one for a gold resistor has been implemented. This device has a very small sensor size, with a low power consumption, a good accuracy, a very low signal to-noise ratio, an excellent frequency response, a simultaneous fluid temperature measurement and a low fabrication cost.*
We realised a micro air flow sensor prototype, fabricated with MEMS technologies. Electro-mechanical tests have been carried out thus demonstrating the high performance of the device.

Keywords: *air flow, MEMS*
Category: *07 (Fluidic devices)*

1 Introduction

Fluid flow measurement plays an important role in many industrial processes. Flow sensors are used to measure the mass, average velocity, differential pressure, temperature, or volumetric flow of a gas or liquid [1]. The working mode of the system is very simple: when there is no flow, the temperature profile around a hot resistor on the membrane is symmetrical. When gas flows, the symmetry is perturbed and we can measure this by controlling the difference in the resistance of the heaters. A flow rate can then be correlated to this differential change in temperature.
Silicon micromachining tools, semiconductor and MEMS fabrication technologies are used to fabricate the hot-wire system with polysilicon or gold resistors easily integrated onto a silicon substrate. Integrated silicon flow sensors offer advantages in terms of fast response times, lower cost (batch fabrication), and integration with on-chip signal conditioning CMOS circuitry to enhance the performance.

2 Layout

All the devices are designed with the L-Edit Tanner tool software. We designed 4 resistors for every die, 2 on the membrane acting as the heating elements and other 2 on the silicon rim. In the process run we splitted the fabrication of the resistors. The first process develops 4 polysilicon resistors with high resistance, the second one had 4 resistors fabricated with gold metal. The silicon die dimensions are 2,2 x 2,7 mm^2. The hot square area of the 2 central heaters is 250 x 250 μm^2. The membrane has a rectangular shape of 1,0 x 1,5 mm^2. The dimension of the back opening correspond to of 1744 x 2244 μm^2.

3 Fabrication process

The starting material is a 4-inch, 500 µm thick, 16-24 Ωcm, p-type, (100) oriented double side polished silicon wafer. After an initial cleaning, we grew a field oxide of 250 nm at 975°C for 1 hour. Onto this oxide we deposited 200 nm of Silicon Nitride with a LPCVD deposition at 795 °C. On the backside we deposited a low thermal oxide used as a masking layer, the thickness is 300 nm of LPCVD undoped LTO at 430 °C [2]. The following deposition is an LPCVD undoped polysilicon of 450 nm with a temperature of 620 °C; four different implantations are performed in order to obtain 4 different resistivities. All wafers are implanted with BF_2 with energy of 80 KeV. A Boron drive-in was carried on at 975 °C for 30 minutes. A multilayer doped oxide LPCVD BPSG deposition 400 nm (reflow process at 925 °C) was performed in order to obtain a surface uniformity. After the contact openings we deposited a multilayer metal to contact the polysilicon resistors. Four metal layers are required in order to avoid the possible interdiffusion between the gold and the polysilicon layers. A first Titanium (30 nm) sputter deposition is used as an adhesion layer, then 200 nm of Titanium Nitride used as a diffusion barrier with the Cr/Au metal evaporated by ULVAC, with 20/150 nm respectively. The last 2 lithographic masks were used to define the 2 different layout splittings, the first one for the Poly metal define sequence and the second one for the Gold sequence. Silicon is then anisotropically removed from the backside by

TMAH etching in order to obtain a multilayer dielectric membrane [3].

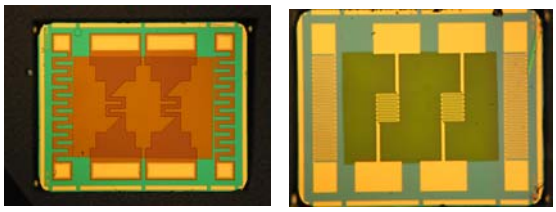

Fig. 1. Microscope photos of the poly and gold devices.

The packaging of the Silicon die is a very important step to reach an optimised set up system. We designed a prototype of the package in which the silicon die is glued on a plastic SMD. The package is placed inside a dedicated pipe so that the fluid flows on the surface of the sensor. The encapsulation and protection of microelectronic device is made with a two component resin with a low viscosity.

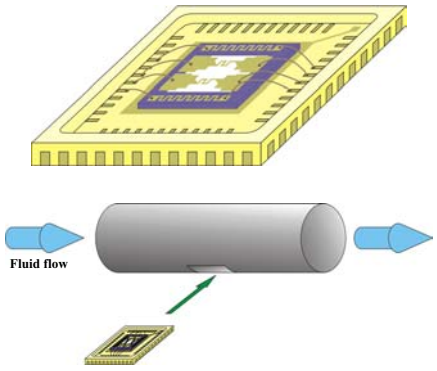

Fig. 2. Device SMD package and fluid flow scheme.

4 Experimental results

Preliminary tests were performed in order to electrically and thermally characterize the device. The I-V characteristic response and TCR (temperature coefficient resistance) of both poly and gold air flow sensors were carried on obtaining a value of 316 ppm/°C for the poly resistors and 293 ppm/°C for the gold.
We preliminary tested our packaged samples with a dedicated set up system; as a fluid we used standard air controlled by a MKS mass flow controller operating in a range from 0 to 250 SCCM. In table 1 the measured flow rates as well as the Reynolds number are reported. The test were conducted in a laminar flow by using a 6 mm tube diameter. The graph in Fig. 3 shows the response of our sensor to different air flows.

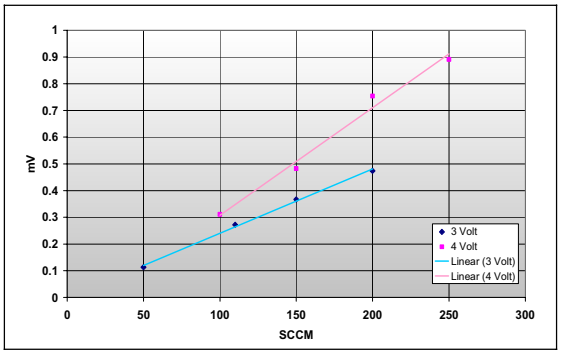

Fig. 3. Sensitivity of the air flow sensor versus different flow rates for 2 different bridge bias voltages.

Table 1. Flow rates and Reynolds number for different SCCM in a tube with 4 cm diameter

Flow [SCCM]	Flow Rate [m/s]	Reynolds Number
10	5.90E-03	2.35
50	2.95E-02	11.73
100	5.90E-02	23.46
150	8.85E-02	35.19
200	1.18E-01	46.92
250	1.47E-01	58.65

5 Conclusion

We designed, fabricated, packaged and preliminary tested a silicon integrated flow sensor based on the hot wire anemometer basic principle. We managed to obtain a small size MEMS device with a robust dielectric membrane, with a very high frequency response and high sensitivity to low fluid flows. Further work will be required to obtain a more stable packaging in order to avoid the losses and turbulences due to this prototype device configuration.

References

[1] B.W. van Oudheusden, Silicon flow sensor, *IEE Proceedings*, Vol. 135, Pt.D, No.5, September 1988
[2] Rossi, P. Temple-Boyer, D. Esteve, "Realization and performance of thin SiO_2/Si_3N_4 membrane
for microheater applications", *Sensors and Actuators A*, vol. 64, pp. 241-245, 1998
[3] C.Rossi, E.Scheid, D.Esteve, "Theoretical and experimental study of silicon micromachined microheater with dielectric stacked membranes", *Sensors and Actuators A*, vol. 63, pp. 183-189, 19

SU-8-Based Fluidic Devices

P.Svasek[1], E.Svasek[1], M.Vellekoop[2], B.Lendl[3]

[1]Ludwig Boltzmann Institute of Biomedical Microtechnology, Gusshausstrasse 27-29, A-1040 Vienna, Austria
email: peter.svasek@tuwien.ac.at
[2]Institute of Industrial Electronics and Material Science, Vienna University of Technology
[3]Institute of Chemical Technologies and Analytics, Vienna University of Technology

Summary: *The epoxy-based photoresist SU-8 is, due to its superior mechanical and chemical properties, a very convenient material for the fabrication of miniaturised fluidic devices. In this paper we present a technology for the batch-fabrication of fluidic devices that combines polymer and metal layers. Together with a novel polymer-based wafer bonding technique it is possible to build "2 ½ dimensional" fluidic devices. Devices that have been realized are a micromixer for time resolved FTIR-spectroscopy and a flow-through-cell for the combination of capillary-electrophoresis with IR-spectroscopy.*

Keywords: *SU-8, micromixer, IR-spectroscopy, fluidic devices, wafer bonding*
Category: *7 (Fluidic devices)*

1 Introduction

During the last years SU-8 has become a widely used material for MEMS and miniaturized fluidic devices. It can be deposited by spin- or spray coating in a wide range of layer thickness. Because of the low UV absorption of the resist a standard UV mask aligner can be used for exposure, even for thick layers. Processing of SU-8 includes the following steps:

a. Deposition of the resist by spray- or spin coating
b. Softbake
c. Exposure
d. Post exposure bake: Crosslinking of exposed resist
e. Development: unexposed resist is dissolved
f. Hardbake: The remaining structures are completely crosslinked. The resist gets its final mechanical strenght and chemical stability.

2 Flow cell for infrared detection in capillary electrophoresis systems

To use FTIR-spectroscopy as a powerful detection method in capillary electrophoresis [1] an infrared transparent flow cell had to be designed because the fused silica capillaries normally used in CE are not transparent to IR. An appropriate material for infrared transparent devices is CaF_2 because of its excellent optical properties. The cell consists of two plates of CaF_2, each 1 mm thick (see Fig. 1). On one of these plates there is a Titanium layer which acts as an optical aperture. The 200 nm thick titanium layer is deposited by evaporation and patterned by conventional lift-off technique. This metal structure must be completely isolated from the liquid to prevent the formation of gas bubbles.

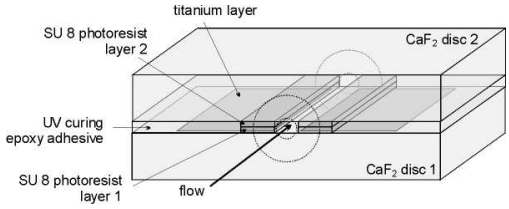

Fig. 1 Schematic drawing of the CE-cell

The channel is formed by two lines of SU-8 on each CaF_2 plate, each of them 100 µm wide. The distance between these two lines is 150 µm. Their height is 7.5 µm, half of the desired height of the cell. The CaF_2 wafers are spin-coated with SU-8 and softbaked. After UV-exposure the resist is post-exposure-baked (10 min at 90°C) and developed. Two wafers (one with metal structure and one without) are superimposed, aligned and pressed against each other during the hardbake process. Consequently the corresponding SU-8 structures are bonded together because the temperature of 200 °C induces complete crosslinking of the SU-8. Finally the area outside the SU-8 lines is filled with epoxy adhesive and the waferstack is diced. The final dimension of each cell is 2 x 5 x 2 mm^3. The capillaries (I.D. 50 µm) are coupled to the cell by means of a metal support and an elastic gasket that is applied to the tip of each capillary [1].
Results obtained with the help of this setup are discussed elsewhere [1,4].

3 Micromixer for FTIR-Spectroscopy

This mixing device is used for the investigation of chemical reactions by FTIR-spectroscopy combined with in-situ mixing of two reactants. The IR-beam directly passes the mixing chamber with an optical pathlenght of 10 µm (see Fig. 2).

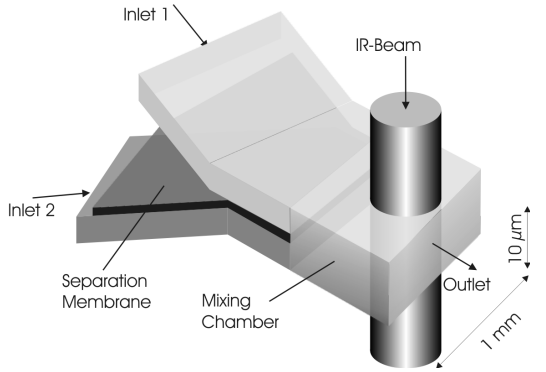

Fig. 2 Principle of the Micromixer (drawing not to scale)

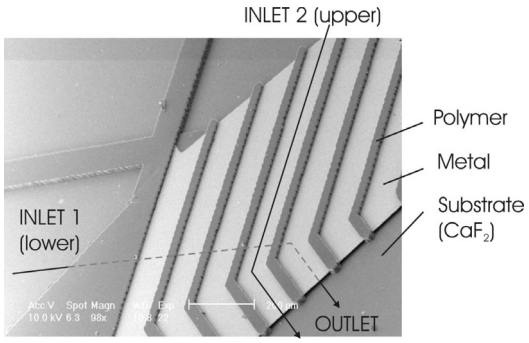

Fig. 3 SEM-Micrograph of Mixer (without Wafer #2)

The mixing device is Y-shaped. Two sheets of liquid are superimposed inside the mixing chamber and mixed by diffusion. Because of the cross-section of the outlet channel (1 mm wide, 10 µm high) the mixing time is approx. 50 ms. The mixer is used in the "stopped-flow-mode", i.e. the two liquids are injected by means of a double syringe pump. Then the flow is stopped, the reactants are mixed by diffusion and the chemical reaction takes place. This reaction is investigated by time resolved FTIR-spectroscopy [2,3].

Fabrication of the micromixer is performed by means of a 2-layer lithography, combined with a polymer-based wafer bonding technique.

Preparation of the Micromixer:

Calcium Fluoride is used as substrate material. A 4 µm thick layer of SU-8 is deposited by spin-coating, softbaked, exposed, post-exposure-baked, but not developed. On top of this layer a 2 µm thick layer of Ag is deposited by evaporation. This metal layer is covered by positive photoresist AZ 1512 HS. The photoresist is patterned as usual and the Ag-layer is wet etched to obtain the structure of the "separation membrane" (see Fig. 2). As an etchant a 45 % (WT) solution of $Fe(NO_3)_3$ in water is used. This solution does not attack the SU-8. Finally the SU-8 is developed with PGMEA. To dissolve unexposed SU-8 under the metal structure takes quite some time (approx. 2 hours for channels of 1 mm lenght). Wafer #1 now carrys the structures of Inlet 1 and the Separation Membrane (see Fig. 2). On wafer #2 the structure of Inlet 2 is fabricated as usual from a 4 µm thick layer of SU-8. This wafer contains the holes for 2 inlets and 1 outlet per mixer. So far the SU-8 on both wafers is not hardbaked and therefore the polymer is not completely crosslinked. Both wafers are super-imposed to form a sandwich, and aligned. Hardbaking is done in an EVG 501 wafer bonder. The wafers are pressed against each other with a force of 1700 N and heated to 200°C for 1 hour. Because of this high temperature the polymer is completely crosslinked and a bond is established between SU-8 and the Ag-structure (see Fig. 3).

The SU-8-"lines" above and under the metal membrane are necessary to maintain the position of the membrane halfway between both wafers.

However, with this simple wafer bonding method the bonding yield is not very high, especially if the height of the SU-8-structures is relatively low (below 20 µm). It is virtually impossible to achieve 100% uniform layer thickness of the SU-8 layers. Consequently gaps remain between the structures. To overcome this drawback an improved wafer bonding technique has been developed.

4 Wafer Bonding with SU-8

To avoid gaps between bonded SU-8 structures or between SU-8 structures and bonded wafer we combine exposed and unexposed SU-8. The unexposed SU-8 is thermoplastic. Nevertheless it is crosslinked at temperatures above 150 °C. Consequently it "flows" during the bonding process and no gaps remain. Areas of unexposed SU-8 have to be surrounded by narrow lines of exposed SU-8 and covered by a metal layer during development of the SU-8. This metal layer (Ag) is etched away prior to the bonding process.

References

[1] M. Kölhed, P. Hinsmann, P. Svasek, J. Frank, B. Karlberg, B. Lendl:
Anal. Chem., 74 (2002), 3843 - 3848.

[2] P. Hinsmann, J. Frank, P. Svasek, M. Harasek, B. Lendl:
Lab on a Chip, 1 (2001), 16 - 21.

[3] B. Lendl, P. Hinsmann, P. Svasek, J. Frank:
"Proceedings of the µTAS 2002 Symposium";
(2002), ISBN: 1-420-1009-5; 221 - 223.

[4] B. Lendl, M. Kölhed, P. Hinsmann, M. Haberkorn, P. Svasek, B. Karlberg:
"Proceedings of the µTAS 2002 Symposium";
(2002), ISBN: 1-4020-1009-5; 599 - 601.

Thermal Characterisation of a Direction Dependent Flow-rate Sensor

P. Fürjes[1], G. Légrádi[2], Cs. Dücső[1], A. Aszódi[2] and I. Bársony[1]

[1] Research Inst. for Technical Physics and Materials Science
MFA, H-1525 Budapest, P.O.Box. 49, e-mail: furjes@mfa.kfki.hu
[2]Budapest University of Technology and Economics, Institute of Nuclear Techniques
Műegyetem rkp. 3., H-1111 Budapest, Hungary

Summary: *A calorimetric flow sensor for detection of gas flow and direction was constructed by sacrificial porous silicon micromachining technique. The sensor structure contains four sensing resistors formed symmetrically around a central heater element. Predictions of flow and thermal simulations aimed at the optimum geometric design were compared with the results of functional tests measured by the realised structure.*

Keywords: *calorimetric gas flow meter, direction dependence, thermal simulation, characterisation*
Category: *Fluidic devices (7)*

1. Introduction

Calorimetric type gas-flow sensors analyse the temperature distribution around a central heater element built up by conduction and convection of the ambient. In a properly designed calorimetric sensor structure these phenomena must play determining role in heat transfer. In a single channel two sensing elements formed at the two side of a central heater detect flow rate and distinguish the two possible directions. A two dimensional direction dependent flow sensor requires additional sensing elements for appropriate temperature profiling.

2. Sensor design

A central heater element in the point of intersection of two perpendicular channels and four platinum resistors in symmetric positions were suspended as shown in Figure 1. The size of the four beam suspended heater and the sensing elements is $100\times100\times1\mu m^3$. Due to the small dimensions and the effective thermal isolation the power consumption of the heater was reduced to 2-20mW for the operation temperature of 100-500°C.

The heater and the sensing platinum resistors are encapsulated by two non-stoichiometric silicon-nitride layers forming the suspension bridges over the channels. The 80μm deep channels were formed by sacrificial porous silicon technique. Higher sensitivity and quick response can be obtained by minimising thermal loss via suspension beams.

3. Thermal characterisation

FVM (Finite Volume Method) was used for modelling flow and thermal conditions of the sensor to predict functional characteristics of the device. CFX-5.5, a high performance CFD (Computational Fluid Dynamics) code, is capable to simulate flow and heat transfer processes in complex structures by solving the Navier-Stokes and the energy equations in combined tetrahedral-hexahedral volume mesh.

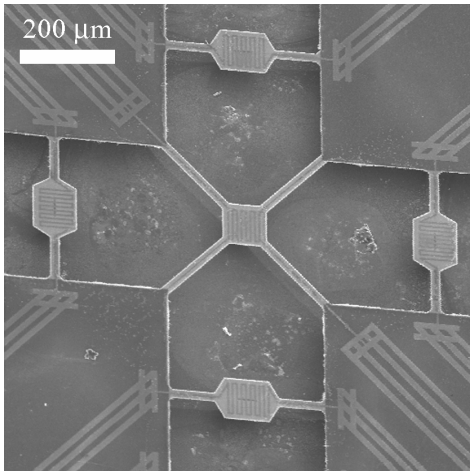

Figure 1. SEM view of the sensor structure

Temperature and flow-vector distribution over the surface of the structure were analysed in order to determine adequate geometry and dimensions of the structure. Temperature distributions presented in Figure 2 were calculated for a selected heater power of 18mW (heater temperature of cc. 480°C) and average nitrogen flow rate of 150cm/s. From the shape of temperature maps predicted by the model for different flow directions one may conclude that combined flow rate – flow direction values can be determined by the five element sensor structure.

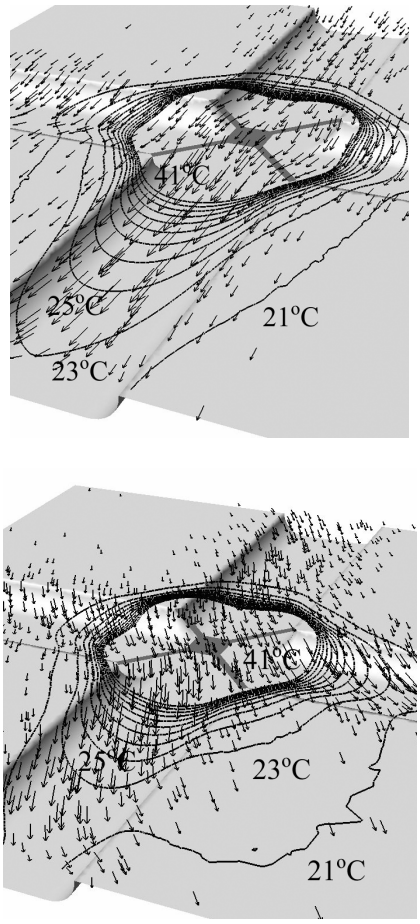

Figure 2. Temperature distribution modelled at different flow directions (a180° top, and 150° bottom) and average flow rate of 150cm/s. Arrows and isoterms (from 21°C to 41°C) represent the local flow direction and temperature values respectively.

To investigate the direction dependence of the realised sensor the temperature of single sensing resistors were measured as the function of flow direction. Flow is presented by the angle between the flow direction and one of the etched channels (180° represents the flow pointing from the heater to the sensing resistor). Graphs in Figure 3 correspond to the simulated temperature distribution shown in Figure 2.

Out of balance voltages of two Wheatstone bridges formed by the opposite sensing resistors in the same channel were used for measuring flow directions at various flow rates. Preliminary investigations resulted in nice correlation between the sensor signal and the flow angle**,** however, further investigations are essential for determination of combined flow rate and direction detection.

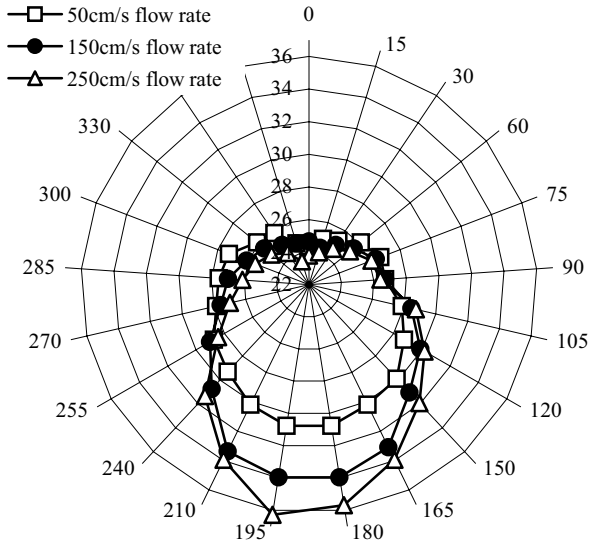

Figure 3. Measured temperatures (from 22°C to 38°C) of a sensing resistor as the function of flow direction with heater temperature of 480°C and different flow rates of N_2.

4. Conclusions

A low power flow direction dependent micro-calorimetric thermal flow sensor was designed and manufactured by using porous silicon sacrificial layer.

Flow and thermal conditions of the operating structure were investigated by FVM simulation using the CFX-5.5 code. Flow conditions and developing temperature distribution around the heater element were modelled and verified by measuring the temperatures of the sensing resistors.

According to the preliminary investigations the sensor is capable for simultaneous determination of flow-rate and direction.

Acknowledgement

This research was supported by „TeleSense” project No 2/035/2001 of the National Research and Development Program, and by the grants T 034821 and T 033094 of the Hungarian Scientific Research Found OTKA.

References

[1] P. Fürjes, G. Légrádi, Cs. Dücső, A. Aszódi and I. Bársony: „Modelling and Characterisation of a micro gas-flow sensor”, Proceedings of MME 2002, Sinaia (2002) 157-160

Towards a *"Quasi-Digital"* Magnetic Microvalve

M. Duch[1], R. Pérez-Castillejos[1], N. Yaakoubi[1], J.Esteve[1], E. Gómez[2] and E. Vallés[2]
J. Martin[3]
[1] Centre Nacional de Microelectrònica, (CSIC), Campus UAB, E-08193-Bellaterra, SPAIN
[2] Departament de Química Física, Universitat de Barcelona, E-08028- Barcelona, SPAIN
[3] Leventon, S.A., E-08740-Sant Andreu de la Barca, SPAIN
E-mail: Marta.Duch@cnm.es

Summary: *A new concept of micromachined "quasi digital" magnetic microvalve for integrated microfluidic systems [1] have been developed. Two external magnets, with on/off mode of operation principle, control the microvalve elements. The idea is to obtain a low cost, small size and low consumption prototype that allows to automatically controlled the dispensed doses.*

Keywords: *Microfluidics, microvalve, Magnetic microactuators*

Category: *Fluidic devices*

1 Introduction

Microfluidics is one of the major application areas in Microsystems technology. Microfluidics systems include miniaturized devices able to sense, microvalves and micropumps, to mix and control small volumes of fluids (gas or liquid). The main actuating principles that have been used in microvalves and micropumps are piezoelectric, thermopneumatic, electrostatic, electrochemical, bimetallic, shape memory alloy and electromagnetic [2]. In this paper, we present a new concept of "quasi-digital" magnetic microvalve based on an array of magnetic microactuators. Advantages of developed microvalves are simplicity, robustness, low power consumption and non-electrical contacts. Therefore, the proposed device is very suitable for low cost and disposable applications as flow regulator for drug delivery systems.

2 Fabrication Process

The fabrication process combines the silicon micromachined technology and the electrodeposition process of the Co-Ni alloys. The magnetic properties of this alloy [3] allow controlling the valves by applying and external magnetic field.

The magnetic microvalves consist of two silicon wafers, which are held together as shown in Figure 1. The valve cap is made of a silicon layer cover by a Co-Ni alloy. The fabrication is carried out by means of two steps of micromachining of the silicon 3D structure. The first step is to fabricate the valve caps, in this process the anisotropic wet etching of the silicon to obtain the silicon membranes is combined with the electrodeposition of a soft magnetic material as Co-Ni.

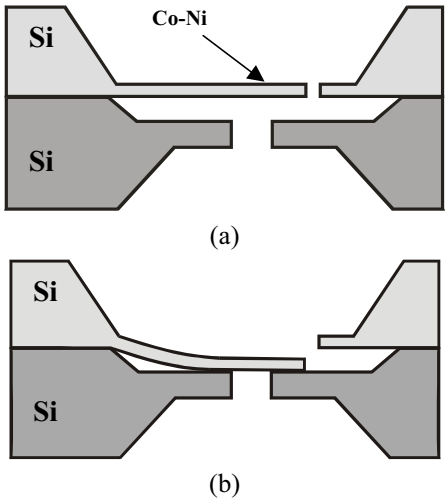

Fig. 1. Schematic cross-section of the magnetic microvalve made of Co-Ni capped Si. (a) no Field applied, (b) With Field applied.

An 8μm thick silicon membrane, a Ti/Ni seed layer (1000Å Ti/500Å Ni) deposited by sputtering and a 2μm thick electrodeposited Co-Ni film (60% Co-40% Ni) formed the body of the valve caps. Different shapes of the caps have been tested in order to optimize the behavior of the device. Some of these designs are shown in Figure2.

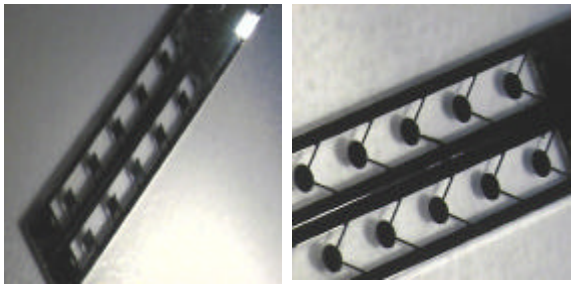

(a) (b)

Fig. 2. Photographs of two different series of valves. (a) square design valves and (b) round design valves.

The miromachinig of the second wafer combines the anisotropic wet etching of silicon with the dry etching by RIE to obtain the body of the valve. Different dimensions of the holes have been included in the design in order to characterizise the microvalve system for a wide range of flows.

Once the two wafers were processed they were glued together to obtain the complete "quasi-digital" magnetic microvalve.

3 A *"Quasi-Digital"* Magnetic Microvalve

The "Quasi-digital" magnetic microvalve consists of an array of magnetic elements as shown in Figure 3. Each valve element is controlled by means of two external magnets. When the magnet is up, the valve opens up. On the other hand, the microvalve closes when the second magnet is underneath.

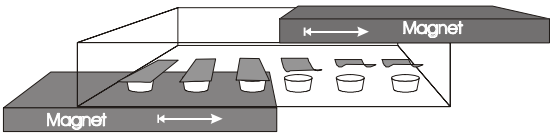

Fig. 3. A schematic illustration of the actuation principle of a quasi-digital magnetic microvalve

The flow is regulated by the number of valves elements open and closed, which depends on the magnets position. Therefore, an external magnetic field is always applied to the valves. This valves array was designed as a flow regulator and it is very suitable for low cost and single use applications, due to its simplicity. The magnet control can work either in a battery mode or connected to an external power supply.

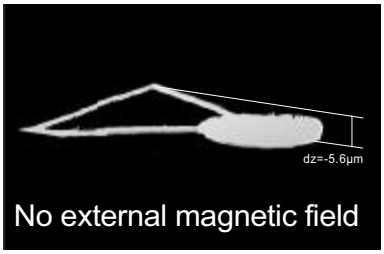

(a)

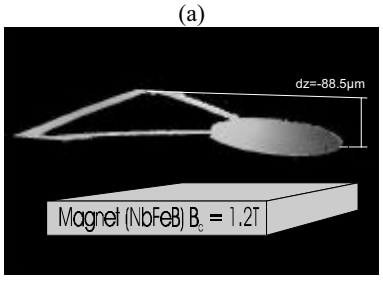

(b)

Fig. 4. Images obtained by a confocal microscope showing (a) the Co-Ni cap without external magnetic field and (b) the displacement of the Co-Ni cap when an external magnetic field is applied.

Some test devices were previously developed to study the magnetic response [3-4] of the Co-Ni caps in front of an external magnetic field. During the experiments, the external magnetic field was generated by a NbFeB magnet (M_s= 1.2, H_c= 890 kA/m), as is shown in Figure 4 a high response of the Co-Ni structure was observed. Figure 4 (a) presents the structure when no external magnetic field was applied, in this case, the structure was a little bended downwards. In figure 4 (b) a high displacement (around 80µm) of the structure was observed when an external magnetic field was applied. Furthermore, these structures present high robustness and flexibility. All these results confirm the suitability of the system.

4 Conclusion

A new concept of "quasi-digital" magnetic microvalve was developed in this work. The capability of controlling different flows by using an only one design gives to this system a high versatility and a low cost. Low power consumption, high robustness and high simplicity are other advantages of this new concept of microvalve.

Good results have been obtained in the characterization of a single valve. Last results concerning the characterization of a novel "quasi-digital" magnetic microvalve will be presented in the extended paper.

References

[1] Patent pending

[2] Melvin Khoo, Chang Liu: Micro magnetic silicone elastomer membrane actuator, *Sensors and Actuators A*, 89 (2001) 259-266.

[3] M. Duch, J.Esteve, E.Gomez, R.Perez-Castillejos and E.Vallés: Development and Characterization of Co-Ni Alloys for Microsystems Application, *Journal of the Electrochemical Society*, 149 (4) (2002), C201-C208.

[4] M.Duch, J.Esteve, E.Gomez, R.Perez-Castillejos and E.Vallés: Electrodeposition Co-Ni Alloys for MEMS, *Journal of Micromechanics and Microengineering*, 12 (2002), 400-405

Microfluidic device constructed from photosensitive BCB for erythrocyte membrane deformability measurement

P. Turmezei[1], A. Polyakov[2], J. R. Mollinger[1], M. Bartek[2], A. Bossche[1], J.N. Burghartz[2]

[1] Delft University of Technology, Electronic Instrumentation Laboratory, Mekelweg 4., 2628CD Delft, The Netherlands
email: p.turmezei@its.tudelft.nl
[2] Delft University of Technology, DIMES, Mekelweg 4., 2628CD Delft, The Netherlands

Summary: *In this paper a disposable microfluidic device intended to use for erythrocyte membrane deformability measurement is demonstrated. The prototype device is constructed from photosensitive benzocyclobutene (BCB), which was found an attractive material for constructing microchannels. The main advantage of using BCB is that after the photopatterning process step it can still be used as an adhesive material for the subsequent wafer to wafer bonding. Designs with different layer thicknesses were created and compared.*

Keywords: *adhesive bonding, BCB, Microchannel*
Category: *7 (Fluidic devices)*

1 Introduction

Erythrocytes having diameter of 8μm at rest can pass through much smaller capillaries due to the high deformability of their cell membrane. A number of diseases [1] affect this property causing serious circulatory problems. This, however, gives one way to detect these diseases by mimicking capillaries with microchannels on chip. Microdevices which measure cell membrane deformability using microchannels were successfully fabricated and reported [2]. Deformation of the cells was observed via a high speed camera in a laboratory.

In this paper a device is demonstrated which does not require laboratory conditions for the measurement. The prototype device was fabricated from photosensitive benzocyclobutene (BCB). Channels with different layer thicknesses were fabricated and channel design rules were deduced.

2 Design

The microfilter structure intended to measure the percentage of the stiffened cells is described below. The operation of the device can be seen in Fig 1.

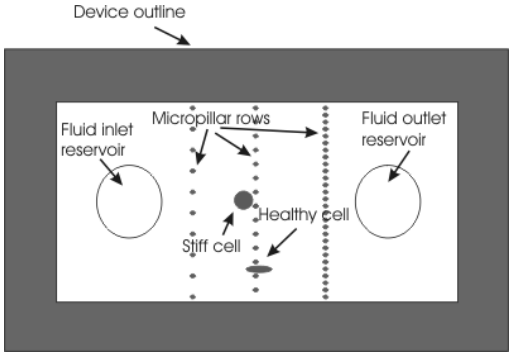

Fig.1. Schematic view of the microfilter

The instrument is centered around a flow device, which consists of a microchannel with rows of micropillars across it, forming a one dimensional filter array. The spacing in between the pillars decreases gradually row by row. A diluted blood sample is pumped into the device through the inlet hole. In the channel the pillars obstruct the movement of the cells, and as the spacing between them is decreasing the cells have to deform more each time they move to the next stage. Healthy blood cells are flexible enough to travel through the whole device, however the stiff erythrocytes get blocked at a certain stage. Deformability distribution of the blood sample can be determined by counting the cells at different stages.

Fabrication

Photosensitive BCB was used to create 4mm long, 1mm wide and 4μm deep microchannels on a silicon wafer capped with a glass cover plate. In the channel 15 rows of micropillars were also formed from this material. In the first row the spacing between the pillars is 15μm, the subsequent rows have a gradually decreasing spacing down to 5μm in the last row.

The process flow for fabrication of the device can be seen in Fig.2. In the first step the BCB was spun.

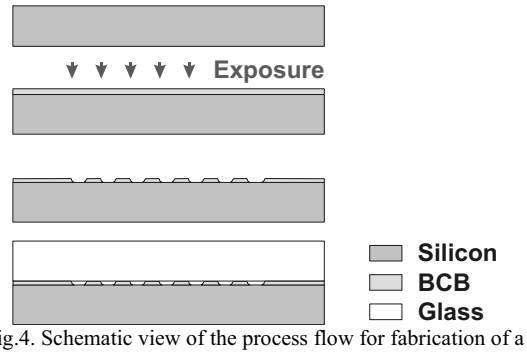

Fig.4. Schematic view of the process flow for fabrication of a microfilter.

In the next step the BCB was exposed on an Electronic Visions Group EV-420 manual mask and bonding aligner. After development, the BCB film can be still used as an adhesive material for the subsequent bonding process. A Logitech Wafer Substrate Bonding Unit was used to bond an AF45 glass wafer to the BCB coated silicon wafer. Inlet and outlet holes were drilled after bonding with a Proxxon MICROMOT 40/E precision drilling machine. Drilling did not cause any difficulties, the abraded particles could be removed from the holes without blocking the channels.

Test channels were also included in the design to be able to investigate BCB layer properties.

Results

Cross section SEM pictures of the wafers before and after bonding are shown in Fig. 3 left and right respectively.

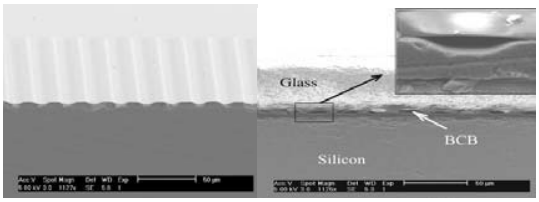

Fig.3. SEM photograph of the test structure before (left) and after (right) bonding

The effect of the bonding process on the structure can be determined by comparing the cross section of the structures before and after bonding. No significant change in BCB thickness can be observed. The slope of the sidewall of the channel is due to the lithography process and some deformation during bonding. This has to be taking into account during the design. To determine the design criteria channels with decreasing width were implemented (see Fig 5.). On the left side the BCB layer thickness is 4µm. 20, 10, 5 and 3µm channels are clearly visible, while the 2µm channel partially obscured and the 1µm wide channel completely disappeared. On the right side using 7µm thick BCB the 3µm wide channel has also disappeared.

Fig. 5 Test structures for determining the minimum channel width. BCB thickness 4µm (left), 7µm (right)

Fig. 6 Line deformation due to stress (middle) in 7µm thick BCB; wider (left) or thinner (right) structures have no such problems

Another limitation on using thick layer BCB is the minimum applicable line width. Figure 6 shows that the 5µm wide structures constructed from 7µm thick BCB (in the middle) have wavy lines. The same line width constructed from 4µm thick BCB has no such deformation (right). A thicker line width also solves the problem as can be seen in the left side. Figure 7 and 8 shows five rows from the devices constructed from 4µm and 7µm thick BCB respectively. The pillars in the thicker BCB bend due to the stress generated in the material. This would cause malfunction of the device, however the device constructed from 4µm thick BCB have no such deformation and are usable for testing with real blood samples.

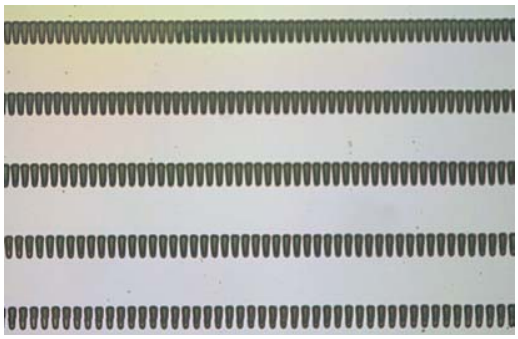

Fig. 7 Photograph of the device (BCB thickness 4µm)

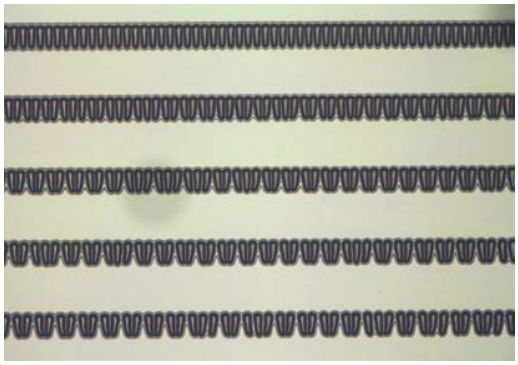

Fig. 8 Photograph of the device (BCB thickness 7µm); the pillars are bended due to stress in the photoresist

Acknowledgement

The work was supported by the Dutch Technology Foundation (STW), project DPC.5521.

References

[1] Dobbe, J.G.G., Hardeman, M.R., Streekstra, G.J., Ince, C., Strackee, J., and Grimbergen, C. A., (2002) Analyzing Red Blood Cell-Deformability Distribution, *Blood Cells, Molecules, and Diseases* 28(3) pp. 373-384

[9] Tracey, M. C., Greenaway, R. S., Das, A., Kaye, P. H., and Barnes, A. J. (1995). A silicon micromachined device for use in blood cell deformability studies. *IEEE Trans. Biomed. Eng.* 42(8), 751–761.

Characterization of wall shear stress sensors

M. Laghrouche[1], D. Meunier[1] and S. Tardu[2]

[1]Institute of Microelectronics, Electromagnetism and Photonics
IMEP, ENSERG, 23 rue des Martyrs, 38016 Grenoble Cédex France
[2]Laboratoire des Ecoulements Géophysiques et Industriels, LEGI, INPG-UJF-CNRS
B.P. 53 X, 38402 Grenoble Cédex-France
email: laghrouche@enserg.fr http://www.imep.enserg.fr

Summary: *a new type of hot wire anemometer was developed by using surface micro machining techniques. The reduction of the microprobes section and the development of a cavity below the hot polycrystalline silicon film reduced considerably the thermal exchanges and dynamic response time of these probes. This will make possible to measure fast fluctuations and turbulent phenomena in fluid mechanics.*

Keywords: *wall shear stress sensors, MEMS*
Category: *7 (fluidic devices)*

1 Introduction

The control of turbulence in mechanics of fluids is a subject which interests several industrial fields, the economic stakes are enormous, mainly in the civil and military aviation. The use of the conventional anemometer (with Platinum wire) cannot quantify any swirling structure responsible for parietal friction. These structures are a few hundred microns of width and a few millimetres length [1] and have a very short lifespan, about the millisecond.
Microsystems, thanks to their integration capability and the optimization of geometrical structure, are of a great interest in this field and seem adapted to these needs. Several microsensors of various geometries were produced by surface micro machining, by using thermally sensitive material like polycrystalline silicon.
In this article, we present the first results of electric characterization obtained from the first prototypes.

2 Realization of a simple shear stress sensor

Figure 1 shows the technological process adopted for the realization of the sensors. PECVD (Plasma Enhanced Chemical Vapor Deposition) silicon nitride was first deposited on 4" wafers to a thickness of 0.3 µm. Then the silicon nitride film was patterned, and wet thermal oxidation of silicon made through the nitride window. Oxidation time was adjusted to achieve flat surface. A 0.3 µm depth silica cavity was obtained. Polycrystalline silicon was deposited (LPCVD – thickness 0,5 µm) and doped by boron ion implantation. After the thermal annealing, polycrystalline silicon was patterned into variable section wire, (in this abstract, the hot wire dimensions are: 50 µm x 2 µm^2). Electrical contacts were finally taken with chromium pads. Releasing of the wire was performed by wet-etching of the silica cavity after dicing the sensors.

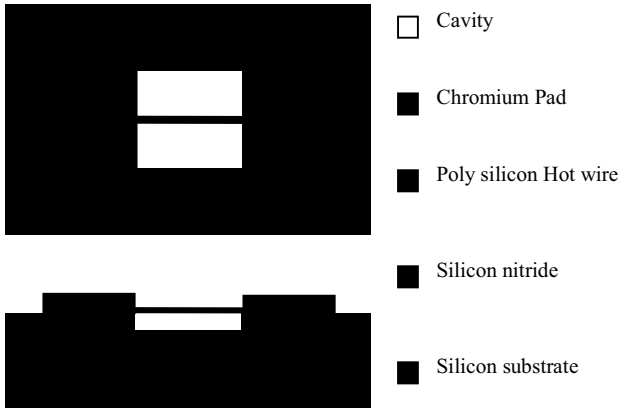

Figure 1 Technological realization of the hot-wire probe suspended on a micro-cavity.

3 Static and electric sensitivity of the sensors

The sensors were first characterized under 2 points prober, in order to determine their behavior with temperature and to estimate the polarization current needed. Two types of measurements were done for each type of sensors: the resistance measurement in function of the temperature for determining the TCR (Temperature Coefficient Resistance = $\frac{1}{R_0}\frac{\partial R}{\partial T} = -5.9.10^{-4}/°C$) where R_0 is room

temperature resistance ; and the voltage measurement in function of the polarization current. The variation of the resistance in function of the temperature was linear and in order to have an 70°C overheating, the polarization current has to be about 235µA.

4 Dynamic sensitivity

Although static measurement is founded on a simple principle, it is now accepted that the frequency response of such sensors is in general complex because of convective and conductive heat exchanges. An electric circuit based on the internal heating method was designed and carried out for the dynamic response time determination of the sensors (Fig.2)

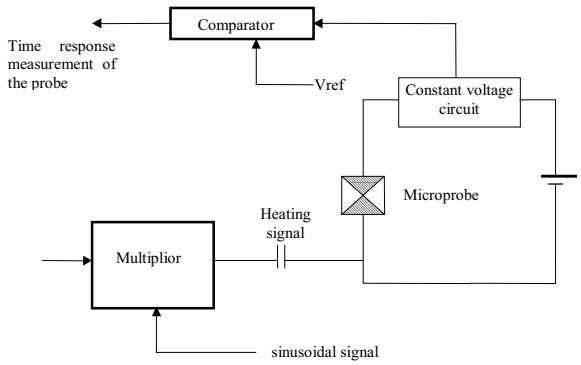

Figure 2 Time response measurement circuit

The circuit makes possible to simulate, on the sensor level, the fluctuations of temperature by carrying out an internal modulation of heating of the probe created by a D.C. current (rated current of the probe). To this current, a AC current of 1 MHz frequency modulated by a square signal of 1 KHz frequency is superimposed.
Figure 3 shows the time response of the sensor, which is about 150µs.

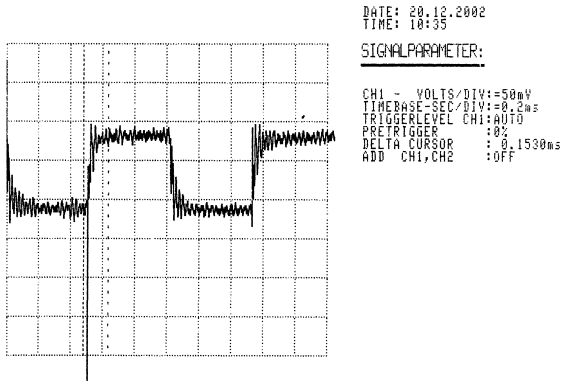

Figure 3 Time response measurement of a 50x2x0.5µm^3 wall shear stress sensor

5 Static speed calibration

The sensor was also characterized in a wind tunnel in order to calibrate it in static speed. This calibration was done from 7m/s up to 15m/s.
With this constant temperature configuration, we can find the various parameters α β and n of the electrical calibration of the sensor described by a law as: $E^2 = \alpha.(\overline{u_\tau})^{2n} + \beta$, where E is the output voltage and $\overline{u_\tau} \approx u_\infty / 22$ the friction speed. According to Levêque solution, n coefficient has to be close to 1/3.
In the figure 4, one can see that the above mentioned law fits perfectly the experimental values when n is taken equal to 1/3.

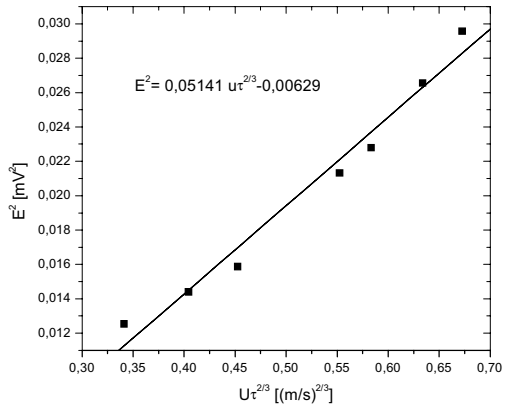

Figure 4 Static speed calibration in wind tunnel : E^2 in function of $(u_\tau)^{2/3}$.

Conclusion

We have characterized a wall shear stress sensor with several methods, and we expect to provide comparisons between various hot wire geometry by the venue of Eurosensors XVII.

Reference

[1] S Tardu; *Near wall turbulence control for local periodical blowing*, Experimental thermal and fluid science, Vol 16 n°1-2, pp.41-53,1998.
[2] D. Meunier, D.Tsamdos, J.Boussey, S.Tardu; *Simulation of wall shear stress integrated sensors.* Therminics,02, Madrid (Spain), Oct 02.
[4] Löfdahl *The influence of temperature on the measurements of Reynolds Stresses in shear free turbulence near a wall*, 1998

Development of an microfluidic system for integration with an optical detection chip

D.Brennan[1], A. O'Neill, J. Kruger and P. O'Brien
[1]NMRC, Lee Maltings, Prospect Row, Cork, Rep. Of Ireland
email: dbrennan@nmrc.ie http://www.nmrc.ie/

Summary: *This paper looks at the issues encountered in developing a microfluidic module for integration with a silicon based optical detection system. The output from a micro-HPLC system is integrated with the fluidic module for peak detection on a chip based detection system. The design, fabrication and test of an integrated micro-fluidic and the key area of packaging are addressed. Wafer and chip integration startegies using anodic and polymer bonding for the fluidic module and the optical transducer were investigated. The impact of the micro-fluidic module on the performance of the micro-HPLC system is also addressed*

Keywords*: Micro-fluidics, Micro-HPLC, Packaging.*
Category: *Fluidic Devices*

1 Introduction

HPLC is a chemical analysis method widely used for separation in the chemical, pharmaceutical and food industries. A number of systems exist for peak detection depending on the characteristics of the analytes, with electro-chemical or optical detection being the most common. A number of optical detection methods exist from absorption to refractive index. In recent years there has been increased research in the area of Surface Plasmon Resonance (SPR) and Resonance Mirror (RM) detection systems and others, these detection methods are suitable for R.I detection in chromatography units.

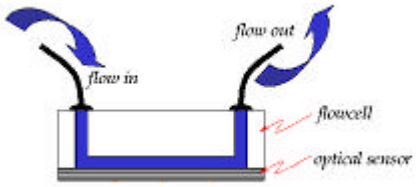

Figure 1. Integrated fluidic system with optical detection chip.

Such systems use silicon fabrication based techniques and lend themselves to integration with microfluidic platforms using similar microelectronic fabrication technologies. Thus there exists the possibility of using low cost microfabrication technology to integrate a fluidic component directly with sensor component.The issues involved in design, fabrication and integration of such a system is addressed poses issues in processing and performance. Standard CMOS may be modified to get optimised to minimise the effect on sensor surfaces and to performance from these integrated devices. The performance of the HPLC system with integrated fluidics is investigated for peak broadening and tailing effects. The fluidic sytem was integrated with the output of a C18 micro-HPLC separation capillary, of 5cm length and 300 ? m internal bore. Thecapillary column packing was 5 ? m diameter silica beads coated with C18 chemistry. Standard HPLC tests were used to determine the performance of the integrated system.

2 Fluidics Design

The fluidics system was simulated with Coventor, a software package used to model MEMS and microfluidic systems. This is a finite element package that uses the full Navier-Stokes equations [1]. The system modelled consisted of an inlet silica capillary of diameter of 75? m and the microfluidics channel which formed the interface to the optical detection chip, this had two corners on the inlet and outlet, as illustrated in figure 2. Four channel sizes were designed to investigate the effect of dead volume on the HPLC peaks.

Figure 2. Simulation of a plug injection into the micro-fluidic module, is investigated. Peak distortion and diffusion effects are evident over plug injection lifetime.

3.Fluidics Fabrication techniques

Photo definable polymers were investigated as adhesion layers between the optical sensor chip and the fluidic chip. This approach is a chip level

bonding technique with thin layers of polymer (3? m) deposited on the sensor wafer as an ahhesion layer. The polyamide underwent a Pre-bake to 120?C. A photoresist was spun on and patterned with UV exposure. The mask pattern defined windows on the sensor surface, from which the polymer was removed. A HF etch was used to remove the exposed polymer.The remaining polyamide formed a gasket type structure to seal to the sensor wafer. A number of pre-bake temperatures and 60, 85,100 and 120?C were tested to investigate the adhesion properties of the polymer layer. The fluidic channels were defined on a glass wafer in SU8. After the polymer processing each wafer was diced, the fluidic and sensor device were thermally bonded, for 4 hours at 90?C. Devices were found to fail at 400 – 500 psi with trials on a HPLC pump. The fluidics systems is located on the outlet of a micro-HPLC column and pressures greater that above are not encountered. Silica fused capillary of 75? m internal bore and 200? m outer diameter was integrated to the inlet and outlet port of fluidic chip. Standard Peek fittings were used to connect the micro-HPLC column to the inlet capillary and onto the chip, as outlined in figure 3.

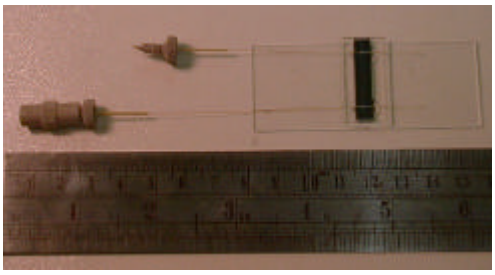

Figure 3. Polymer bonded flui dics component to a device with integrated fluidics.

4. Integrated system performance

The output from a micro-hplc system was integrated with the integrated device to determine the impact on HPLC peak separation performance. A standard test solution with a UV detector was used to determine performance.

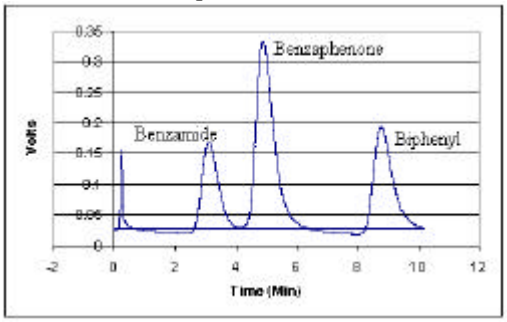

Figure 4. Outlined is the chromatogram from the three component test sample, obtained on the set-up with integrated flow-cell.

Six Repeated injections were carried out with the test solution giving a variation of 3% in the peak elution time. The test components were Benzamide, Benzaphenone and Biphenyl in a 60: 40, MeOH : D.I, buffer solution. The back-pressure on the micro-HPLC column varied over the repeated injections, this was due to the test setup. Absorption data was obtained at 254nm on a Shimadzu U.V detection system. The flow-rate of buffer solution was 5? l/minute. Test data outlined in figure 4 as was obtained with this HPLC setup.

Test	Peak1 (Min)	Peak 2 (Min)	Peak 3 (Min)	Pressure PSI
Test 1	N/A	N/A	N/A	1100
Test 2	4.05	6.23	10.76	1100
Test 3	3.89	5.95	10.26	1070
Test 4	3.77	5.86	10.37	1100
Test 5	3.82	5.86	10.36	1050
Test 6	4.07	5.74	9.98	1000

Table 1. Six repeated tests of the same test mixture was carried out on the fluidic system, the peak retention times are outlined and the pressure at which the HPLC column operated.

5. Conclusion

The design and fabrication of an integrated microfluidic platform has been demonsratted using microelectronics technology. The impact of dead volume on HPLC performance has been shown to be minimal and tailing of fluidic plugs due to corner effects has also had minimal impact of the HPLC performance.

6.References

[1] Coventor CAD software, Microcosm Technologies

[2] Kruger J, O'Brien P, Morrissey A, Alderman J, O'Neill A: Materials, Processing ,Component Integration, Assembly and Packaging Issues, Microtech IMAPS, 2001.

Direct Numerical Inversion of Ellipsometric Data to Determine Refractive index and Thickness for Real-time Sensing Applications

S. Otsuki and K. Tamada

Photonics Research Institute, National Institute of Advanced Industrial Science and Technology (AIST), Midorigaoka, Ikeda, Osaka 563-8577, Japan
email: otsuki-soichi@aist.go.jp http://www.aist.go.jp

Summary: *A direct numerical inversion for the determination of the refractive index and the thickness of the outermost layer of a thin transparent film on top of a multilayer was developed for real-time sensing applications. The algorism is based on the 2 × 2 matrix method without any approximation nor any a priori assumption. It is effective for both external and internal reflection geometries. The method is fast, takes less than 0.3 ms per one calculation for a new layer in typical cases, and is capable of single- and multiple-wavelength inversion of continuous as well as discontinuous-index profiles.*

Keywords: *ellipsometry, real-time sensing, direct numerical inversion, refractive index, thickness*
Category: *2 (Materials and technology)*

1 Introduction

Ellipsometry is a powerful tool for real-time sensing of the refractive index and the thickness of films preexisting or being newly deposited. Recently simultaneous determination of both the refractive index and the thickness of the outermost layer has been attempted by direct numerical inversions [1–3] and fitting procedures [4,5] of ellipsometric data. Especially the 2 × 2 matrix method is useful because it is so flexible to hold good both for reflection and transmission configuration and also to be easily extended to optically anisotropic systems in some simple cases [6,7]. However, algorisms reported so far using this technique rely on complicated approximations and a high order (eighth) polynomial to be solved [3], or need a fitting procedure [5], leading to insufficient calculation speed to allow simultaneous data acquisition.

2 Theory

The optical response of the isotropic stratified planar structures was analyzed by the 2 × 2 matrix method according to the formalism developed by Azzam and Bashara [8].

The scattering matrix is written as Eq. (1). In the case of external reflection configuration a new layer is formed at the interface of the first layer and light-incident (0) media. For direct numerical inversion of the refractive index and the thickness of the new layer, it is convenient to define a pseudo scattering matrix **S'** for representation of the effect of the existing layers as Eq. (2) and to multiply it by a factor $\mathbf{L}_j\ \mathbf{I}_{j(j+1)}$ for representation of an additional layer as Eq. (3). There, $\mathbf{I}_{j(j+1)}$ represents a matrix characteristics of the jth interface, $\mathbf{L}_j$ represents a matrix characteristics of the jth layer. In Eq. (3), r_j and t_j are the Fresnel reflection and transmission coefficients, respectively. The film phase thickness β_j also in Eq. (3) is represented by Eq. (4) for the jth layer in terms of the wavelength λ, the layer thickness d_j, the layer complex index of refraction N_j, and the layer complex angle of refraction ϕ_j. Therefore, the scattering matrix for the whole structure including the additional layer is given by Eq. (5).

The overall reflection coefficient R, which is

$$\mathbf{S}=\begin{bmatrix} S_{11} & S_{12} \\ S_{21} & S_{22} \end{bmatrix}=\mathbf{I}_{01}\mathbf{L}_1\mathbf{I}_{12}\mathbf{L}_2\cdots\mathbf{I}_{(j-1)j}\mathbf{L}_j\cdots\mathbf{I}_{(m-1)m}\mathbf{L}_m\mathbf{I}_{m(m+1)} \quad (1)$$

$$\mathbf{S'}_{j+1}=\begin{bmatrix} M_{11} & M_{12} \\ M_{21} & M_{22} \end{bmatrix} \quad (2)$$

$$\mathbf{S'}_j=\mathbf{L}_j\mathbf{I}_{j(j+1)}\mathbf{S'}_{j+1}=\left(\frac{e^{j\beta_j}}{t_{j(j+1)}}\right)\begin{bmatrix} M_{11}+M_{21}r_{j(j+1)} & M_{12}+M_{22}r_{j(j+1)} \\ \left(M_{11}r_{j(j+1)}+M_{21}\right)e^{-j2\beta_j} & \left(M_{12}r_{j(j+1)}+M_{22}\right)e^{-j2\beta_j} \end{bmatrix} \quad (3)$$

$$\beta_j=2\pi\left(d_j/\lambda\right)N_j\cos\phi_j \quad (4)$$

$$\mathbf{S}=\mathbf{I}_{01}\mathbf{L}_1\mathbf{I}_{12}\mathbf{S'}_2=\left(\frac{e^{j\beta_1}}{t_{01}t_{12}}\right)\times\begin{bmatrix} M_{11}+M_{21}r_{12}+r_{01}\left(M_{11}r_{12}+M_{21}\right)e^{-j2\beta_1} & M_{12}+M_{22}r_{12}+r_{01}\left(M_{12}r_{12}+M_{22}\right)e^{-j2\beta_1} \\ r_{01}\left(M_{11}+M_{21}r_{12}\right)+\left(M_{11}r_{12}+M_{21}\right)e^{-j2\beta_1} & r_{01}\left(M_{12}+M_{22}r_{12}\right)+\left(M_{12}r_{12}+M_{22}\right)e^{-j2\beta_1} \end{bmatrix} \quad (5)$$

$$R=\frac{S_{21}}{S_{11}}=\frac{B_1+B_2\ e^{-j2\beta_1}}{A_1+A_2\ e^{-j2\beta_1}} \quad (6)$$

$$\begin{aligned} A_1&=M_{11}+M_{21}r_{12} & A_2&=r_{01}\left(M_{11}r_{12}+M_{21}\right) \\ B_1&=r_{01}\left(M_{11}+M_{21}r_{12}\right) & B_2&=M_{11}r_{12}+M_{21} \end{aligned} \quad (7)$$

related to the elements of the matrix **S**, is given for s and p polarization by Eq. (6), where the coefficients A_i and B_i (i = 1 or 2) are written by Eqs. (7). These coefficients only include the refractive index (n) of the additional layer in question as an unknown variable. Thus it becomes possible to decouple the thickness (d) from the unknown value of n as an exponential function of the phase thickness β, as is true for the case of a single nonabsorbing layer [9–11].

In the internal reflection configuration, a new layer is formed at the interface of mth layer and light-transmiting (m+1) media. Similar formulas are derived also in this case (not shown).

Ellipsometry is based on the determination of the ratio ρ of the complex Fresnel coefficients R_s and R_p for s and p polarization respectively as a function of the ellipsometric measures Ψ and Δ.

$$\rho = \frac{R_p}{R_s} = \tan\Psi e^{-j\Delta} \qquad (8)$$

Using a substitution as

$$X = e^{-j2\beta_1} \qquad (9)$$

from Eqs. (6) and (8) a polynomial in X is obtained.

$$aX^2 + bX + c = 0 \qquad (10)$$

The coefficients of the polynomial are all complex functions of n of the additional layer in question as a sole unknown variable. When the light-incident phase and the additional layer are transparent, the film phase thickness β_1 becomes real so that the complex exponential function X satisfies the condition

$$\ln|X| = 0 \qquad (11)$$

Now n can be numerically determined as a root of Eq. (11). Then, d is obtained by Eq. (9). Otherwise a fifth-degree polynomial in the dielectric constant can be derived and directly solved as has been reported for a single layer [11].

3. Numerical Results

The Newton-Raphson method was used for the root finding with the initial value of 2.0 for n. The function, ln $|X|$ [see Eq. (11)], was adapted as a function to be solved, which worked much better than the function, G, used by Charlot and Maruani [10]. For multi-wavelength data d was determined as an average of values having converged not too late and larger than zero. The d value thus obtained was used to determine n for the wavelengths where the root finding failed. The inversion algorism was implemented with Visual C++®.

Results of the numerical inversion are shown in Fig. 1 for abruptly changing and linear gradient index profiles at three wavelengths. The accuracy is better than ±0.001 for n and better than ±0.01% for d. For the unoptimized code the inversion for a layer took 0.26 ms on the average on a 800-MHz

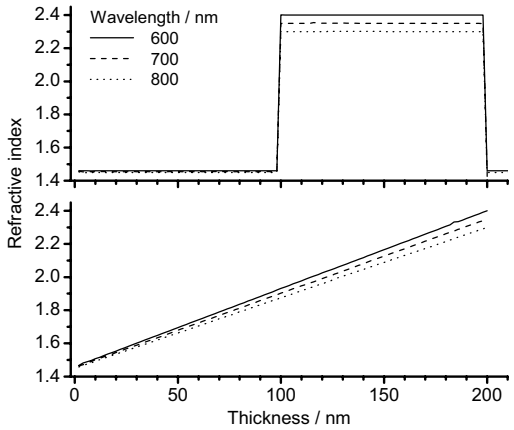

Fig.1 Inversion of simulated refractive index profiles at a thickness step of 2nm. Refractive index: 3.876–j0.02124 (substrate). Ambient: air. Incident angle: 70°.

Pentium® processor, which is more than 100 times faster than the other methods [3,5].

In conclusion, a method for the direct numerical inversion of the ellipsometric values for the real-time sensing of the refractive index and the thickness. It is proven effective for not only the ordinary external reflection ellipsometry but also the internal reflection ellipsometry (IRE), which is very attractive for in situ characterization of the film in solutions or special gas since the optical system is completely separated from the analyte phase by the prism [12].

References

[1] I-F. Wu, J. B. Dottellis, and M. Dagenais, *J. Vac. Sci. Technol. A* 11 (1993) 2398–2406.

[2] G. M. W. Kroessen, G. S. Oehrlein, E. de Frésart, and M. Hverlag, *J. Appl. Phys.* 73 (1993) 8017–8026.

[3] D. Kouznetsov, A. Hofrichter, and B. Drévillon, *Appl. Opt.* 41 (2002) 4510–4518.

[4] M. Kildemo, *Appl. Opt.* 37 (1998) 113–124.

[5] T. Heitz, A. Hofrichter, P. Bulkin, and B. Drevillon, *J. Vac. Sci. Technol. A* 18 (2000) 1303–1307.

[6] H. Wöhler, M. Fritsch, G. Haas and D. A. Mlynski, *J. Opt. Soc. Am. A* 8 (1991) 536–540.

[7] M. Schubert, *Thin Solid Films* 313-314 (1998) 323–332.

[8] R. M. A. Azzam and N. M. Bashara, Ellipsometry and Polarized Light, North-Holland, Amsterdam, 1977.

[9] A. R. Reinberg, *Appl. Opt.* 11 (1972) 1273-1274.

[10] D. Charlot and A. Maruani, *Appl. Opt.* 24 (1985) 3368–3373.

[11] J. Lekner, *Appl. Opt.* 33 (1994) 5159–5165.

[12] S. Otsuki and S. Wakida, *Book of Abstract Euroanalysis-12*, pp. 394, Dortmund, Germany, 8–13 September 2002.

Molecular Immobilization and Detection in a Photonic Crystal Fiber

Poul Erik Hoiby[1], Lars Bjarne Nielsen[1], Lars Hagsholm Pedersen[1],
Jesper Bo Jensen[2], Anders Bjarklev[2] and Theis Peter Hansen[2,3]
[1]*Biotechnological Institute*, Department of Molecular Characterisation, DK-2970 Hørsholm, Denmark.
Email: peh@bioteknologisk.dk http:// www.bioteknologisk.dk
[2]*Research Center COM*, Technical University of Denmark, DK-2800 Lyngby, Denmark.
[3]*Crystal Fibre A/S*, Blokken 84, DK-3460 Birkerød, Denmark.

Summary: *Molecules has been immobilized on the inside surface of a Photonic Crystal Fiber (PCF), and molecular interactions such as DNA hybridization and protein binding has been performed. The interactions were detected by fluorescence labeling. The experiments indicate that PCF's are suitable for biosensor applications.*

Keywords: *Molecular immobilization, DNA hybridization, protein binding*
Category: *6 (Biosensors)*

Introduction.

Photonic Crystal Fibers (PCF's) are silica based optical fibers with air holes running along the length of the fiber. These fibers allows for a close proximity of the light guided in the fiber and molecules positioned in the air holes. The penetration of the optical field into the air holes can be significant [1], making PCF's suitable for sensor applications. In the present work we have used a hollow-core fiber from Crystal Fibre A/S, which has a large center hole of approximately 17µm in diameter, and a cladding with smaller holes, each of approximately 3µm in diameter.

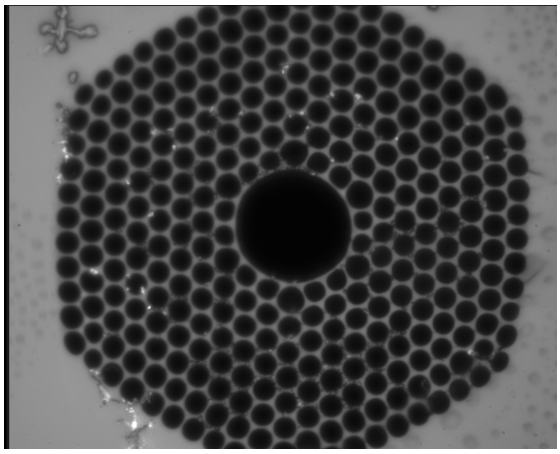

Figure 1. A hollow core Photonic Crystal Fiber seen from the end.

Here we report on the coating and immobilization of the biotin binding protein, streptavidin, to the inner surfaces of a PCF, by pumping the appropriate liquids through the fiber. The immobilized streptavidin was subsequently used for:
1) DNA hybridization between an immobilized biotin-labeled DNA-oligo and a mismatch- and a match Cy3-labeled DNA-oligo, respectively.
2) Protein-Antibody interaction between the immobilized streptavidin and a Cy3-labeled nonspecific antibody and a specific anti-streptavidin antibody, respectively.
The molecular interactions were detected in a microscope obtaining a fluorescence micrograph.

DNA hybridization

Since DNA hybridization is a well-characterized molecular process, it was chosen as the experimental setup inside the fiber. A fiber was coated with streptavidin and the hybridization was performed as illustrated in Figure 2. The experiment confirmed that a true hybridization took place inside the fiber, as only the perfect match probe hybridized to the immobilized biotin-DNA-oligo.

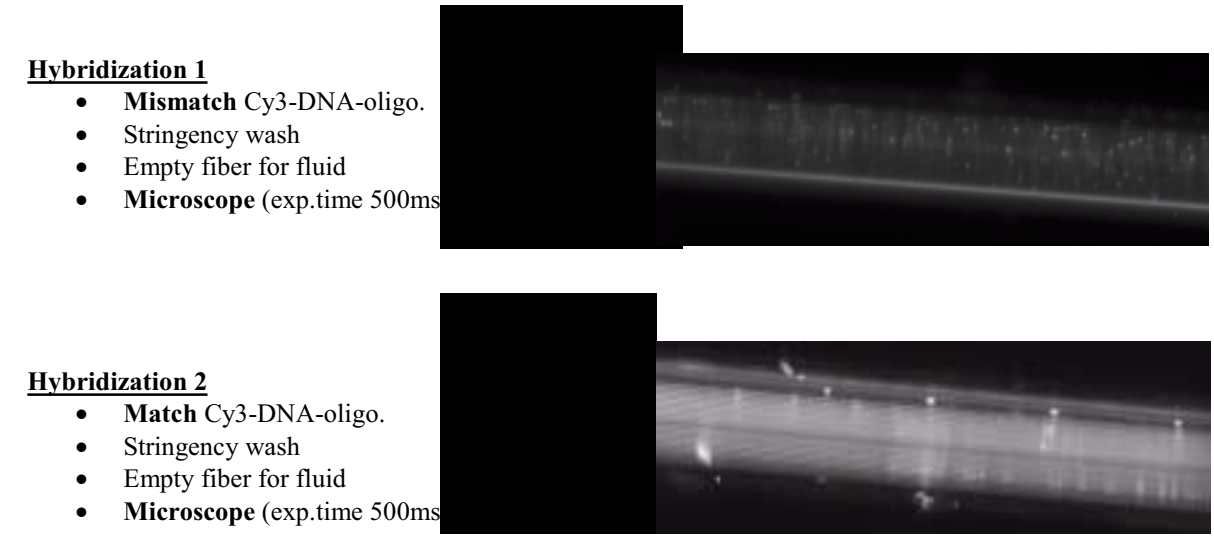

Figure 2. Mismatch- and match DNA hybridization inside a PCF.

Protein binding

Another well-characterized biological process is protein-antibody interaction. Figure 3 illustrates the experiment as it was carried out. As seen on the micrographs the unspecific antibody does not bind to the immobilized streptavidin, whereas the streptavidin specific antibody does.

These experiments show that it is possible to perform well-known biological interaction experiments inside the air holes of a PCF, extending its possibilities in sensor applications.

References:

[1]: T.M. Monro *et al.* "Developing holey fibers for evanescent field devices", Electron. Lett. **35** (14), (1999).

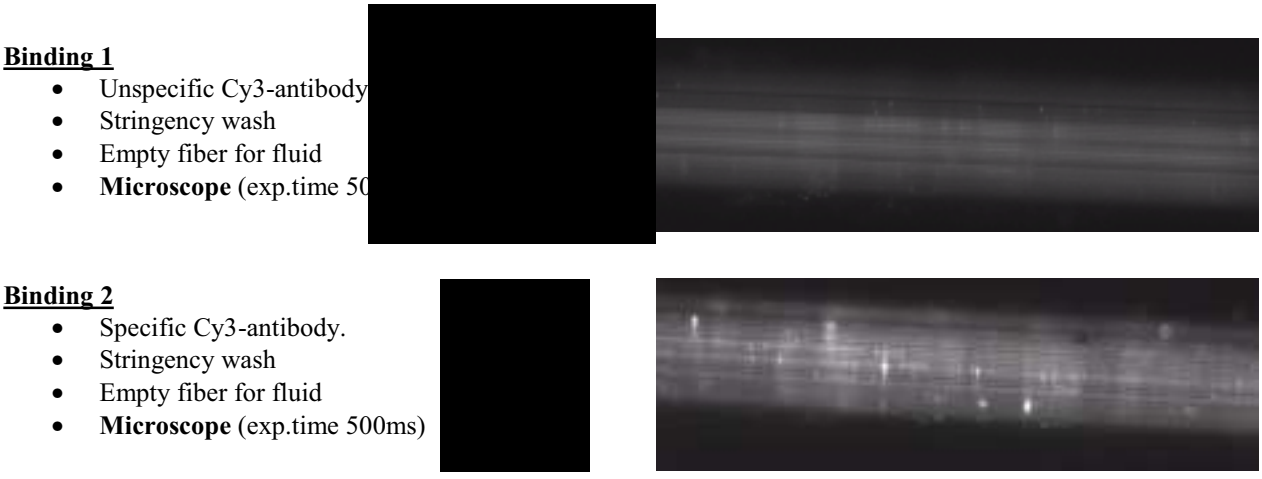

Figure 3. Unspecific- and specific protein binding inside a PCF.

Development of a Micro Gas Turbine For Electric Power Generation

J. Peirs, D. Reynaerts and F. Verplaetsen

Katholieke Universiteit Leuven, Dept. of Mechanical Engineering, Celestijnenlaan 300B, 3001 Leuven, Belgium
email: Dominiek.Reynaerts@mech.kuleuven.ac.be http://www.mech.kuleuven.ac.be

Summary: *A miniature gas turbine is under development with the aim to generate electrical energy from fuel. This system consists of a compressor, combustion chamber, turbine, and generator. The turbine is a single-stage axial impulse turbine with a rotor diameter of 10 mm, made of stainless steel using die-sinking electro-discharge machining (EDM). It has been tested with compressed air to speeds up to 160,000 rpm and air supply temperatures up to 360°C. When coupled to a small generator, it generates up to 44 W of electrical power with a total efficiency of 16 %. A 20 mm diameter centrifugal compressor matching the pressure and flow characteristics of the turbine has been designed and is currently under construction.*

Keywords: *microturbine, microcompressor, microgenerator, powerMEMS*
Category: *10 (Applications)*

1 Introduction

Portable devices like laptops and cellular phones have a limited autonomy because of the limited energy density of their batteries which is about 0.5 MJ/kg for Li-ion batteries. As fuel has an almost 100 times higher energy density (about 45 MJ/kg), it would be interesting to power these devices with fuel. However, this requires miniaturised energy conversion devices based on fuel cells, thermo-electric devices, Stirling engines, internal combustion motors, or gas turbines [1]. To take advantage of the high energy density, these generators should be as compact as possible. K.U.Leuven is developing a micro power generator based on a micro gas turbine as this is expected to offer the highest power density [2]. This paper reports about improvements in turbine performance and efficiency, high-temperature tests, and the design of the compressor.

2 Turbine design

Figure 1 shows an exploded view of the microturbine design. A single-stage axial impulse turbine (Laval turbine) was chosen because of its simple construction. The nozzles are designed for subsonic flow and therefore have a converging cross-section. Sonic speed is reached for a supply pressure of 1 baro.

The compressed air enters via a standard pneumatic connector (1) and expands over the stationary nozzles (3) where it is deflected in a direction tangential to the turbine rotor (5). The air is deflected again by the rotor blades where no expansion takes place. Finally, the air leaves the device through the openings in the outlet disc (6). The rotor has a diameter of 10 mm and is supported by two ball bearings (4). The nozzle disc and rotor are monolithic stainless steel parts, produced by turning and die-sinking EDM [2]. Figure 2 shows a subassembly of nozzle disc, rotor, and bearings.

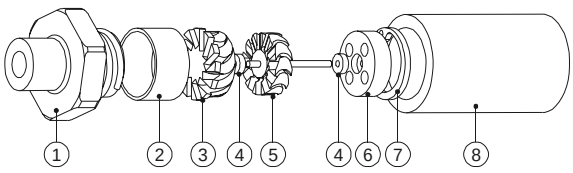

Fig. 1. Microturbine design.

The turbine has been coupled to a small brushless DC motor that is used as a 3-phase generator [2]. The generator is connected to a variable 3-phase load consisting of 3 potentiometers.

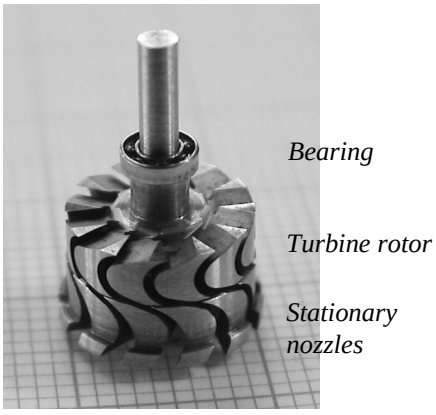

Fig. 2. Subassembly of nozzle disc, turbine rotor, and bearings. The rotor has a diameter of 10 mm.

3 Turbine performance

Previously, the turbine has been tested with compressed air at room temperature, for pressures up to 1 baro and speeds up to 160,000 rpm [2]. The turbine consumed 8 Nm^3/h and the maximal torque, power and efficiency were respectively 3.7 Nmm, 28 W, and 18 %. When coupled to the generator, 16 W of electrical power was generated, corresponding

to a maximal total efficiency (compressed air to electricity) of 10.5 %.

The performance of the turbine has been improved by using better ball bearings and adjusting the gap between the nozzle disc and rotor. This distance is very critical. For a too small distance, the rotor blades repeatedly block the exit of the nozzles causing an increased flow resistance and pulsed flow. For a too large distance, the losses increase due to turbulence at the nozzle exits.

This improved turbine has been tested in combination with the generator at different temperatures of the supplied air, ranging from 23°C to 360°C. Figure 3 shows that the electrical power varies with temperature between 30 and 44 W for a supply pressure of 0.8 baro. The volumetric flow is inversely proportional to the square root of the temperature and decreases from 11 Nm^3/h at 23°C to 7.4 Nm^3/h at 360°C. Figure 4 shows the total efficiency (from air to electricity) of the turbine-generator combination, not taking into account the heating of the compressed air. The maximum lies around 16 % and varies slightly with temperature. The improved turbine clearly shows lower flow resistance and higher efficiency.

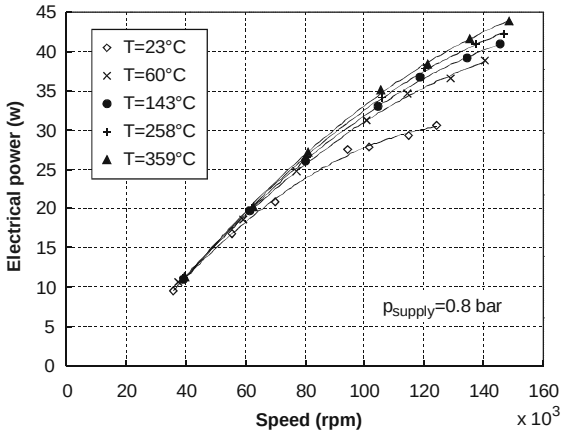

Fig. 3. Electrical power generated by the turbine at different air supply temperatures.

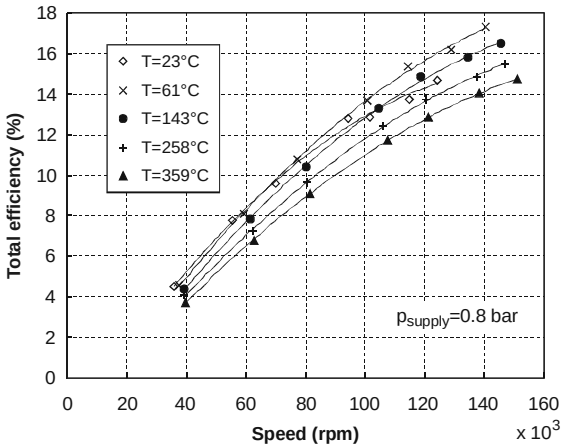

Fig. 4. Total efficiency of turbine and generator at different air supply temperatures.

4 Compressor design

A single-stage radial compressor design was chosen because radial compressors can generate high pressure ratios in a single stage and are relatively easy to realise. Axial compressors on the other hand need several stages to reach the required pressure ratio, and the geometry of the blades is more critical.

A stainless steel prototype of the 20 mm diameter rotor disc is shown on the right half of figure 5. The blades are created by die-sinking EDM using the copper electrode shown of the left side of figure 5. The electrode, which has the negative shape of the rotor, is produced by wire-EDM.

The flow in centrifugal compressors is limited to subsonic speeds due to compressibility effects. Therefore, the compressor has been designed to operate at 80 % of the sonic speed, resulting in a pressure ratio of 1.8. The dimensions are chosen such that it can realise a flow rate of 6 Nm^3/h at 0.8 baro, corresponding to the expected working characteristics of the turbine at 600°C. To attain the required pressure, the rotor has to rotate at 250,000 rpm. Therefore it will be mounted on special high-speed ball bearings allowing speeds up to 400,000 rpm.

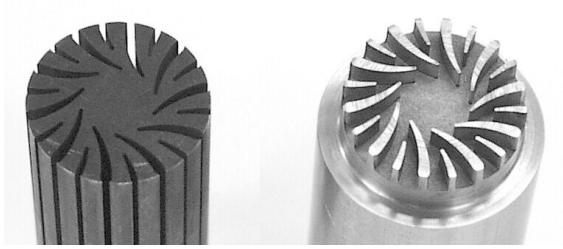

Fig. 5. Compressor disc prototype (right) and copper EDM-electrode (left) used to produce it.

Acknowledgement

This research is sponsored by the Belgian programme on Interuniversity Poles of Attraction (IAP5/06: AMS) initiated by the Belgian State, Prime Minister's Office, Science Policy Programming. The authors assume the scientific responsibility of this paper.

References

[1] A. H. Epstein et al. Shirtbutton-Sized Gas Turbines: The Engineering Challenges of Micro High Speed Rotating Machinery. In: *Proc. 8th Int. Symp. on Transport Phenomena and Dynamics of Rotating Machinery*, 2000.

[2] J. Peirs, D. Reynaerts, F. Verplaetsen, M. Poesen and P. Renier. A Microturbine Made by Micro-Electro-Discharge Machining. In: *Proc. Eurosensors XVI, 16th European Conf. on Solid-State Transducers*, pp. 790–793, Prague, Czech Republic, 15–18 Sept. 2002.

Novel comb-type differential pressure sensor with silicon beams embedded in a silicone rubber membrane

C.T Seo[1], S.S Kong, J.K Shin[1] and J.H Lee[1]

[1]School of Electronic and Electrical Engineering, Kyungpook National University,
Taegu, 702-701, Korea
email: ctseo@lycos.co.kr

Summary *A novel differential pressure sensor has been developed with silicon beams embedded in a silicone rubber membrane. The transducer is usable for most applications involving exposure to harsh media. A piezoresistive differential pressure sensor using silicone rubber membrane has been fabricated on the selectively diffused (100)-oriented n/n+/n silicon substrates by a unique silicon micro-machining technique using porous silicon etching. The pressure sensitivity is about 0.66 μV/mmHg and the non-linearity is less than 0.1 %.*

Keywords: *pressure sensor, silicone rubber, porous silicon layer*
Category: *4 (Non-magnetic physical devices))*

1 Introduction

Solid-state pressure sensors have been developed for a wide range of applications, including those in automotive systems, biomedicine, and automated process control. In spite of recent progress, conventional differential pressure sensors suffer from relatively low sensitivity and low burst pressure [1]. In order to solve this problem, we have developed a novel comb-type differential pressure sensor with silicon beams embedded in a silicone rubber membrane. It is well known that silicone rubber exhibits a very low modulus, good compatibility with IC process, high elongation, and good sealing properties on rough surfaces [2]. Therefore, silicon beams embedded in a silicon rubber membrane can withstand higher burst pressure than conventional silicon diaphragms.

In many applications, pressure sensors are required to function reliably during exposure to harsh media. As a result, it is important to isolate media-sensitive elements of the device from harsh media. Commonly media isolation has been addressed at the packaging level using oil-filled, metal-can packages and polymeric protective coatings. It is well known that silicone rubber membrane is resistant to alcohol, positive photo-resist developer, KOH and buffered hydrofluoric acid for short periods of time. Therefore, silicone rubber membrane can properly operate during exposure to harsh environment.

2 Fabrication

Figure 1 shows the structure of the proposed differential pressure sensor.

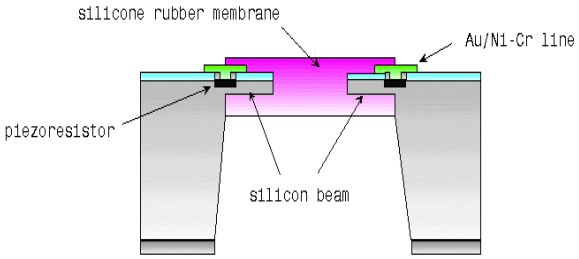

Fig. 1. Structure of the differential pressure sensor

Proposed differential pressure sensor has been fabricated on the selectively diffused (100) oriented n/n+/n silicon substrates by unique silicon micro machining technique using porous silicon etching. Fabrication process of the differential pressure sensor is shown in Figure 2. Porous silicon layer is formed in the heavily doped n+ layer by anodic reaction in 10% aqueous solution of HF for 40 minutes by applying a constant voltage of 0.6 V.

This layer is etched away by subsequent etching process in 5% aqueous solution of NaOH for 20 minutes. Since anodic reaction does not proceed to the lightly doped n-type substrate, the reaction stops automatically after complete conversion of the n+ region to porous silicon. The resultant microstructure is thus well defined and uniform without a cusp or undercutting phenomenon. This indicates that the silicon beam thickness and the air-gap height of the microstructure can be well adjusted by controlling the thickness of the n-epitaxial layer and n+-diffused layer. After etching the porous silicon layer, a silicone rubber membrane is formed by coating. Backside of the wafer is etched in KOH to complete the fabrication process.

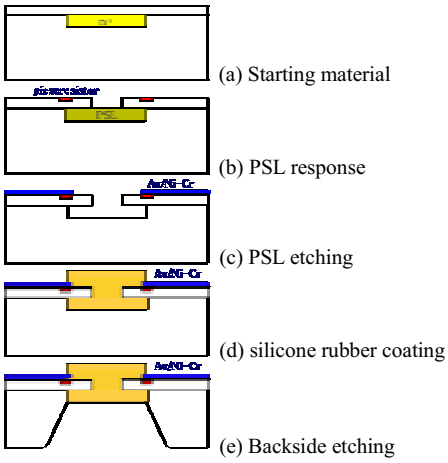

Fig. 2. Fabrication process of the differential pressure sensor.

Fabricated sensors consist of a silicone rubber membrane, four silicon beams embedded in a silicone rubber membrane, four piezoresistors located on the beams, and four fixed resistors near the beams.

A photomicrograph of the fabricated sensor is shown in Figure 3. The photomicrographs of the fabricated differential pressure sensor without silicone rubber membrane and with it are shown in (a) and (b), respectively.

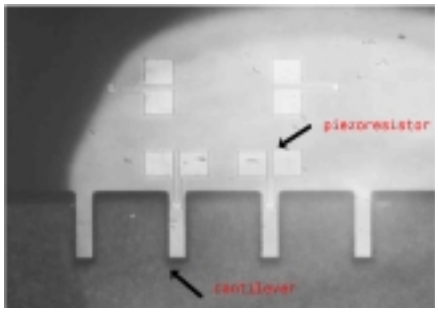

(a) Without silicone rubber membrane

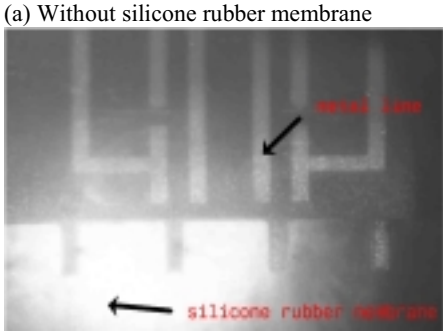

(b) With silicone rubber membrane

Fig. 3 Photomicrographs of the fabricated sensor.

3 Results

The output response of the fabricated sensor have been measured with four outputs of the half-bridge, which is designed to symmetrically locate two piezoresistors located on the opposite sides of the beams. A typical output voltage versus applied pressure characteristics over 100mmHg of pressure difference is shown in Figure 4. The measured sensitivity is about 0.66μV/mmHg at positive differential pressure and about 1.22μV/mmHg at negative differential pressure. The non-linearity is less than 0.1% at positive differential pressure.

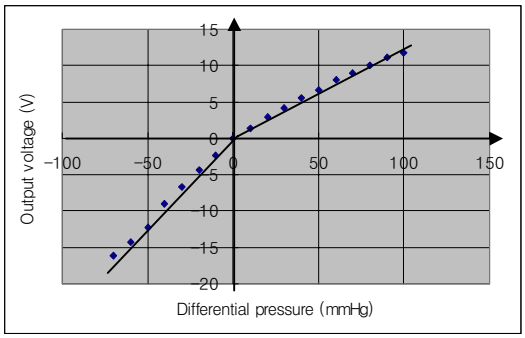

Fig. 4. Output characteristics of the fabricated differential pressure sensor.

3 Conclusion

A novel comb-type differential pressure sensor with silicon beams embedded in a silicone rubber membrane using selective porous silicon etching and dispensing mass loading methods has been designed, fabricated and characterized. It was demonstrated that porous silicon etching method has made it possible to precisely define dimensions of the beam and the air-gap of the microstructure by controlling the thickness of the n-epitaxial and n+ diffusion layers. The measured sensitivity is about 0.66μV/mmHg at positive differential pressure and about 1.22μV/mmHg at negative differential pressure. Increasing the number of silicon beams, hence the number of piezoresistors and optimizing the thickness of the silicone rubber can further increase sensitivity of the sensor.

References

[1] Tetsuya Watanabe, Satoshi Fukuhara, Hideo Tsukamoto, Takahiro Kudo, and Kyoichi Ikeda, "*Differential pressure sensor with micromachined overrange protectors*," Transducers'95, EurosensorsⅨ, 381-C9 (1995) 578-581.

[2] Christian Vieider, Ove hman, and H kan Elderstig, "*A pneumatically actuated micro valve with a silicone rubber membrane for integration with fluid-handling systems*," Transducers'95, EurosensorsⅨ, 303-B7 (1995) 284-286.

Dynamics of CMOS-based Thermally Actuated Cantilever Arrays for Force Microscopy

T. Volden[1], M. Zimmermann[1], D. Lange[2], O. Brand[3] and H. Baltes[1]

[1]Physical Electronics Laboratory, ETH Zurich, Hönggerberg HPT-F9, CH-8093 Zurich, Switzerland
email: volden@iqe.phys.ethz.ch http://www.iqe.ethz.ch/pel
[2]Stanford University, USA (current address)
[3]Georgia Institute of Technology, USA (current address)

Summary: *Arrays of CMOS-fabricated cantilevers with integrated thermal actuators and piezoresistive stress sensors have been fabricated and characterized. The performance variations within an array, and between different arrays, were measured in order to quantify the influence of the process variations. The sensor-actuator crosstalk (SAC) was studied. A model for the frequency response of the cantilever actuation is proposed, which corresponds well to the measured behaviour. The model has been used to design a compact controller for constant-force imaging. Initial images obtained with this controller are shown.*

Keywords: *thermal actuation, CMOS, AFM*
Category: *4 (Non-magnetic physical devices)*

1 Sensor Design

The CMOS chip comprises an array of 10 identical cantilevers designed for force microscopy together with signal conditioning circuitry (see Fig. 1). An industrial CMOS process is followed by micromachining in order to release the cantilevers with dimensions 500 µm x 60 µm x 4 µm [1].

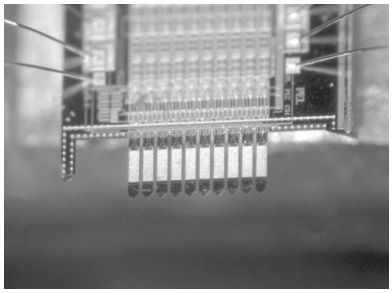

Fig. 1. Photograph of the 10-cantilever array.

The thermal actuator consists of a p-diffusion resistor heating a bimorph structure [2, 3] made from the silicon n-well and the aluminium layer (see Fig. 2).

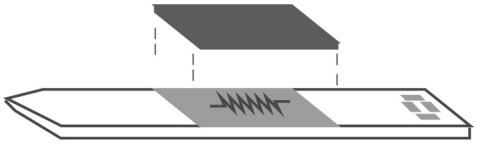

Fig. 2. Schematic of the cantilever with the bimorph actuation structure in the centre, and the piezoresistive Wheatstone bridge close to the clamped edge.

The piezoresistive stress sensors for deflection detection are located near the clamped edge of the cantilever. Three different sensor designs were studied: on the first two the piezoresistors are made from a p-well, with connecting leads made in p-diffusion or metal, the third type uses p-diffusion resistors and metal interconnections.

2 Measurements

The mechanical frequency response measured with an optical vibrometer and the signal from the integrated sensor were simultaneously recorded. A large number of cantilevers were tested and statistics on the parameter spread could be established. The cantilevers show a resonance frequency of around 20 kHz. The superposition of the resonance peaks from all cantilevers in an array is shown in Figure 3.

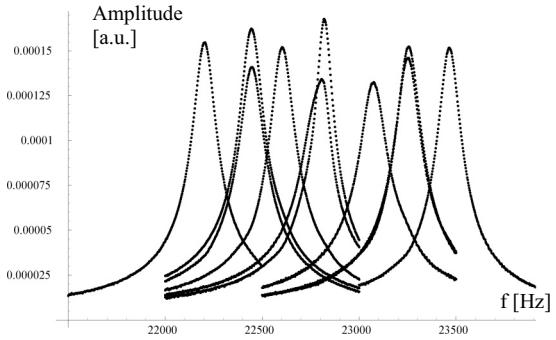

Fig. 3. Vibration amplitude as a function of frequency, around the fundamental resonance frequency for 10 cantilevers of one array.

The variations between arrays are larger and can be attributed to a spread in the thickness of the fabricated silicon membrane from which the cantilevers are released. A typical amplitude transfer characteristic of the thermally excited cantilever is shown in Figure 4. Beyond a corner frequency of around 100 Hz the vibration amplitude decreases with 1/f. This distinct low pass characteristic stems from the thermal actuation.

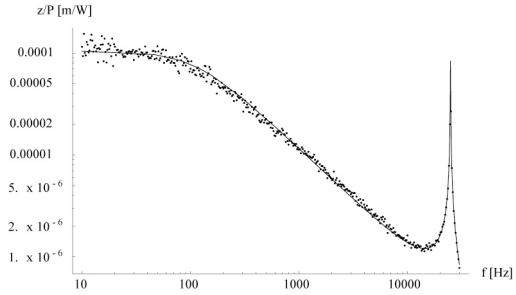

Fig. 4. Vibration amplitude per heating power as a function of frequency. Measured data (dots) and fit model (solid line).

3 Crosstalk

The heater is confined to the middle part of the cantilever and creates a bending moment over the length of the bimorph. Bending or stress caused by heating should be minimal outside this area. Still, a sensor signal is observed during actuation. This sensor-actuator coupling can be explained in terms of the thermal gradient that extends outside the heater and affects the piezoresistors. Comparing the sensor signal with the mechanical amplitude we see this crosstalk is constant up to a frequency of about 1 kHz (see Fig. 5).

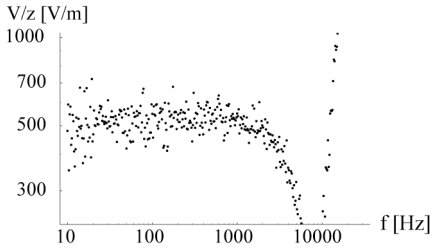

Fig. 5. The stress sensor signal (crosstalk) divided by the mechanical amplitude as a function of frequency.

4 Model

A precise model of the cantilever response to a thermal excitation is desirable for designing the control circuitry. The model combines the low pass characteristic of the thermal actuator with the mechanical response of the vibrating cantilever, which can be treated as a harmonic oscillator. The parameters of the model were fit to the measured data. Figure 4 shows the measured vibrating amplitude from one cantilever together with the fitted model. The proposed model agrees well with the measured data and allows the precise extraction of key parameters for a controller for constant-force imaging. The collected specifications have been successfully implemented in a stand-alone analogue controller and evaluated. An example constant force image taken is shown in Figure 6.

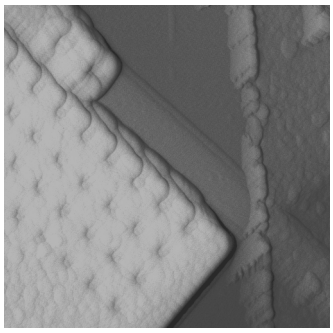

Fig. 6. Constant-force image (30µm by 30µm) showing a row of vias on a 0.8µm CMOS chip.

Acknowledgements

The work was supported by the Swiss programme TOP NANO 21.

References

[1] D. Lange et al. CMOS 10-Cantilever Array for Constant-Force Parallel Scanning AFM. *Transducers'01*, (2001) p. 1074.

[2] T. Akiyama et al. Fast driving technique for integrated thermal bimorph actuator toward high-throughput atomic-force microscopy. *Review of Scientific Instruments* 73 (2002) 2643-2646.

[3] T. Akiyama et al. Integrated atomic force microscopy array probe with MOSFET stress sensor, thermal bimorph actuator, and on-chip CMOS electronics. *Journal of Vacuum Science & Technology* B 18 (2000) 2669-2675.

A low volume electrostatic inchworm microactuator with high-resolution and large force

E. Sarajlic, E. Berenschot, G. Krijnen, M. Elwenspoek

Transducers Science and Technology Group, Mesa+ Research Institute, University of Twente
P.O. Box 217, 7500 AE Enschede, The Netherlands
email: e.sarajlic@el.utwente.nl http://www.el.utwente.nl/tt

Summary: *A novel electrostatic inchworm microactuator, which employs a built-in mechanical transformation and a large number of contraction units to generate large force and sub-micrometer resolution step, is presented. The actuator is fabricated in a single polysilicon device layer using a trench isolation technology. The entire actuator, including the clamps and the contraction element, fits in an area of 440 x 286 μm. Tests on the first prototype show an effective step size of 13 nm and a generated force of 0.55 mN. A driving voltage of 55 V has been used both for clamping and contraction.*

Keywords: *electrostatic microactuator, inchworm motion, vertical trench isolation*
Category: *4 (Non-magnetic physical devices)*

1 Introduction

Diverse MEMS applications require low volume, low power, large stroke, large force and high-resolution microactuators.

This paper presents a novel electrostatic microactuator with a potential to satisfy all these requirements. The actuator employs a built-in mechanical transformation [1] and a number of contraction units operating in parallel [2] to generate large force and sub-micrometer step within a small volume. A large stroke is achieved by adding small steps in sequence using the inchworm principle.

2 Working principle

A schematic view of the novel inchworm microactuator with the operation sequence is depicted in Fig. 1. The actuator consists of two electrostatic clamps and an electrostatic contraction element [2], which are electrically separated allowing individual biasing. A basic unit of the contraction element is composed of two parallel, mutually insulated, conducting beams. The number of basic contraction units operating in parallel can be chosen freely by design to increase generated force.

To create a single motion step the front clamp is first activated. On application of a potential difference on the contraction element a deflection of the beams occurs. This lateral deflection induces, due to a built-in mechanical transformation, a small but powerful longitudinal contraction moving the clamps closer together. Next, the back clamp is activated and the front clamp and the beams are released. The stretching of the beams pushes the front clamp forward. A large stroke motion can be achieved by adding the small single steps by repeating the operational sequence.

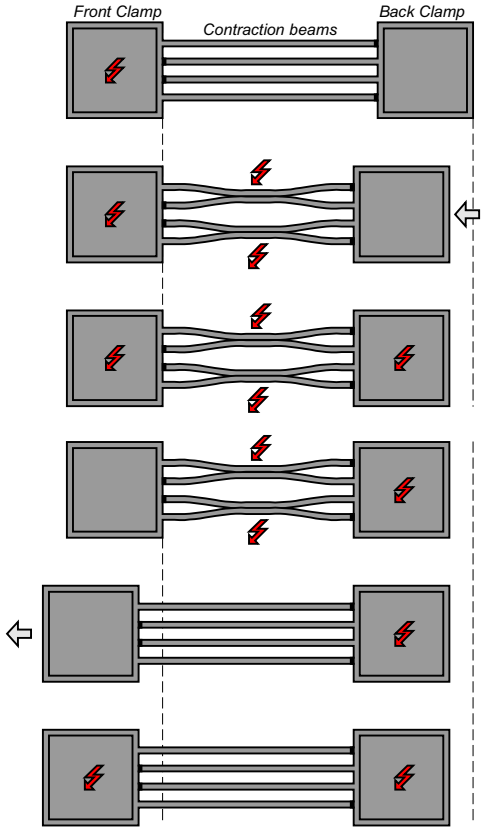

Fig. 1. Actuation sequence

3 Fabrication process

A vertical trench isolation technology [3,4] is used to successfully fabricate the inchworm microactuator. The technology employs trenches refilled with dielectric material to create, in a single device layer, electrical insulation and mechanical interconnection between released components (clamps and contraction beams). Hollow isolating bumps [4] are employed to reduce stiction during

release and operation, to prevent the short-circuiting between the clamps and the grounded substrate, to limit the charge accumulation and to serve as etch holes at the same time. The three-mask fabrication process is illustrated in Fig. 2.

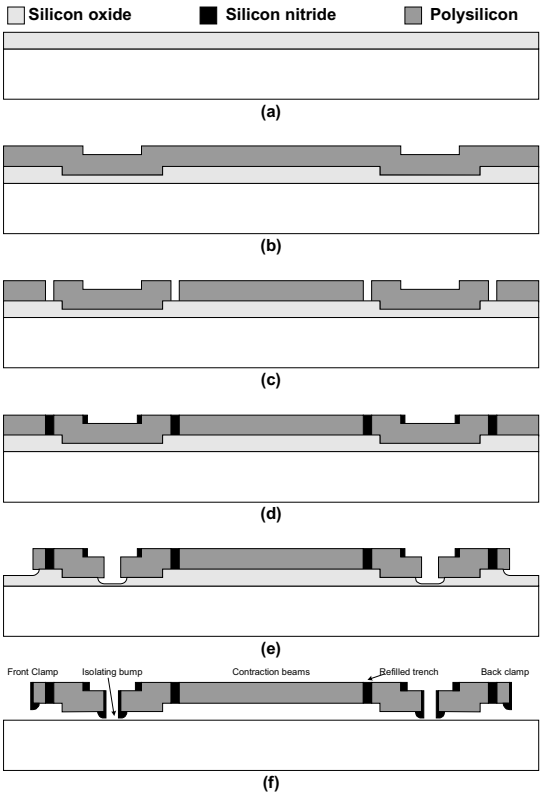

Fig. 2. Fabrication sequence.

4 Results

A SEM photograph of a fabricated actuator is shown in Fig. 3. A doped 4.8 µm thick polysilicon layer was used. The contraction element contains 16 parallel beams, 212 µm long, 2 µm wide with a 2 µm distance in between. Isolation trenches, 2 µm wide, were refilled with a low-stress silicon nitride layer to create distinct electrical domains, clamps and contraction beams. The gap between an activated clamp and the grounded substrate is determined by 150 nm high isolating bumps evenly spaced on the clamp surface. The actuator is supported by springs, which also provide driving signals to the clamps and the contraction element. The whole actuator including the clamps and the contraction element fits in an area of 440x286 µm.

The inchworm motion of the actuator is successfully performed. The driving voltage of 55 V was used both for clamping and contraction. The tests are performed at a maximum stepping frequency of 200 cycles/s due to the limitation of the driving electronics. The maximum obtained stroke of 11 µm, limited by physical constraints, corresponds to a force of 0.55 mN. An effective average step size of 13 nm was calculated.

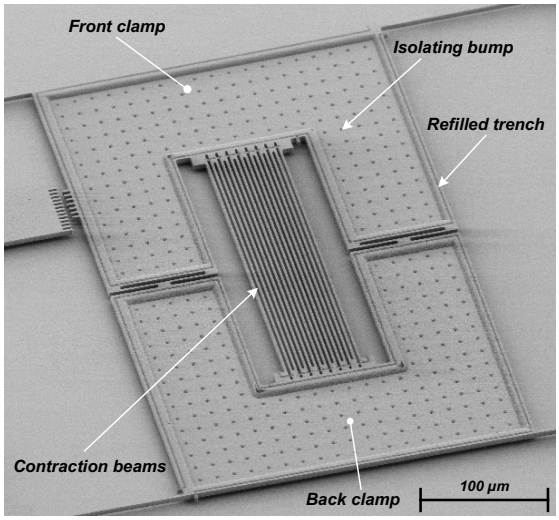

Fig. 3. SEM photograph of the inchworm microactuator.

4 Conclusion & Outlook

Design, fabrication and characterization of a low volume electrostatic inchworm microactuator with sub-micrometer stepping resolution and large force have been presented. Through successful generation of a large stroke motion a great potential of the microactuator is demonstrated.

Even better performance of the actuator, in terms of larger force (>1 mN), larger stroke (100 µm) and higher speed (>1 mm/s), is expected but have not yet been achieved due to encountered fabrication inaccuracies and limitations of the driving electronics. The current effort is focused on solving these issues.

Acknowledgements

This work is part of the research program of the 'Dutch Technology Foundation STW'. The invaluable contributions of M. de Boer, R. Sanders, J. Haneveld and MESA+ clean room staff are gratefully acknowledged.

References

[1] N. Tas, J. Wissink, L. Sander, T. Lammerink, M. Elwenspoek, Sensors and Actuators A 70 (1998), pp. 171-178.

[2] E. Sarajlic, E. Berenschot, G. Krijnen, M. Elwenspoek,, Proceedings Nanotechnology 2003, San Francisco, USA, February 2003, Vol. 1, pp. 392-395.

[3] T.J. Brosnihan, J. M. Bustillo, A.P. Pisano, R.T. Howe, International Conference On Solid State Sensors and Actuators (TRANSDUCERS97), Chicago, June 1997, pp. 637-640.

[4] E. Sarajlic, E.Berenschot, G. Krijnen, M. Elwenspoek, The paper is accepted for publication in Microelectronic Engineering, Ref. MEE 3466.

Self-Aligned Vertical Electrostatic Comb-Drive Actuators

E. T. Carlen, K.-H. Heng, S. Bakshi, and C. H. Mastrangelo

Corning Intellisense, Corp., 36 Jonspin Rd., Wilmington, MA, 01887, U.S.A.
email: carlenet@corning.com http://www.corning.com

Summary. *We report a novel self-aligned vertical electrostatic comb-drive actuator. Key to the actuator design is the self-aligned, offset comb-drive fingers, which are fabricated with very narrow gaps using a single lithography step. The offset comb-fingers are fabricated using two thick conducting layers separated by a thin dielectric layer. The lower fingers are formed with the device layer of the SOI substrate, while a thick, doped polysilicon layer is used for the upper comb-fingers. The actuator has been implemented in a compact actuator-flexure design combined with a staggered micromirror array arrangement with a high optical fill-factor (> 90%) for optical scanning applications. Large continuous scan angles (± 10 °) with actuation voltages < 60 Volts have been measured with no pull-in phenomena observed.*

Keywords: electrostatic vertical comb-drive, self-aligned process, Epipoly
Category: 4 (Non-magnetic physical devices)

1 Introduction

Vertical comb-drive actuators are attractive devices for applications requiring large out-of-plane (vertical) displacements due to their high force density [1]. In this paper, the design, fabrication and testing of a novel, self-aligned vertical electrostatic comb-drive actuator structure is reported. **The novel aspect of this device is the self-aligned fabrication process where the comb-drive gaps are formed in one fabrication step; thus minimizing the pull-in effect due to gap asymmetries**. This process allows for the fabrication of self-aligned vertical comb-drive actuators with very narrow gaps defined by a single lithography step in contrast to other vertical comb devices [2, 3] which use more than one lithography. The vertical comb-drive actuator has been implemented as the drive for a one-dimensional torsional element for a 1xN micromirror array.

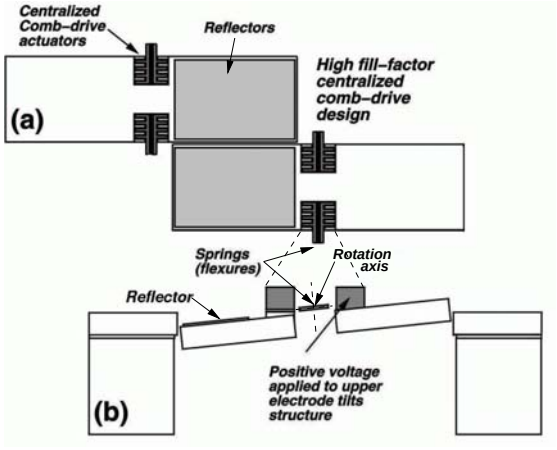

Fig. 1: Schematics (a) portion of staggered mirror array (b) cross-section of single device showing rotation about the central flexure.

2 Design

The compact comb-drive actuator structure, which surrounds the restoring spring, combined with a staggered mirror arrangement is shown in Fig. 1(a). An electrostatic potential applied between the upper and lower comb-fingers on one side of the devices results in torsional rotation due to the attractive force, shown in Fig. 1(b). Figure 2 shows the capacitance C_v and change in capacitance $\partial C_v/\partial t$, where *t* is the rotation angle, between the upper and lower comb-fingers. When the upper and lower fingers are not engaged (A) the capacitance is due entirely to fringing fields. As the fingers are partially engaged (B) the capacitance changes approximately linearly with angle. When the fingers are fully engaged (C), the capacitance is maximum and thus $\partial C_v/\partial t = 0$. Therefore the maximum rotation angle is located at position (C). The electrostatic torque is $\tau = N/2V^2\partial C_v/\partial t$, where N is the number of comb fingers and V is the applied voltage. The corresponding torsional spring constant is $k_t = \tau/t$. For the

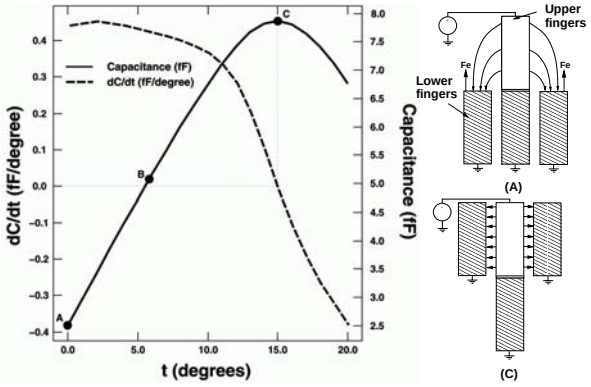

Fig. 2: C_v and $\partial C_v/\partial t$ as a function of rotation *t* for a single comb-finger pair with g = 2 μm and l_o = 87.5 μm.

design presented here $N = 5$, gap spacing $g = 2\mu m$, and comb-finger overlap $l_o = 87.5\mu m$. For $V = 50$ Volts,

$\tau \approx 1.1 \times 10^{-9}$ Nm corresponding to $k_t \approx 1.2 \times 10^{-8}$ Nm/rad at $t = 5^o$. A typical resonant frequency for these devices is 150 Hz.

3 Fabrication

The comb-drive actuators are fabricated using a new fabrication process, shown in Fig. 3. The device layer of the SOI substrate is used as the optically-flat platform for the reflective element. Conventional LPCVD low-stress

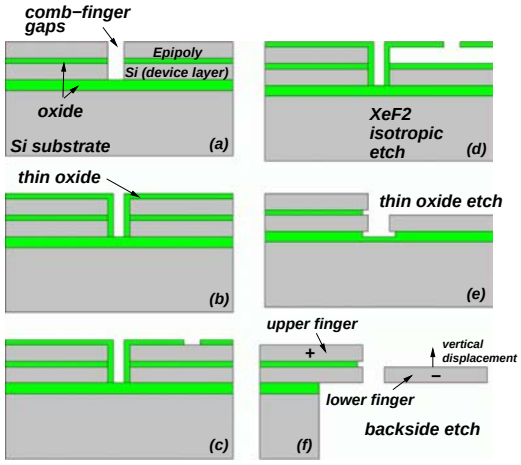

Fig. 3: Simplified process flow for self-aligned gaps. A single lithography step defines the gap between the upper and lower fingers.

polysilicon is used for the mirror flexures and electrode interconnections. The upper electrodes are constructed from a thick, doped polysilicon layer deposited in an atmospheric pressure epitaxial reactor (Epipoly). Following the Epipoly deposition, a thin (3000 Å) silicon nitride etch

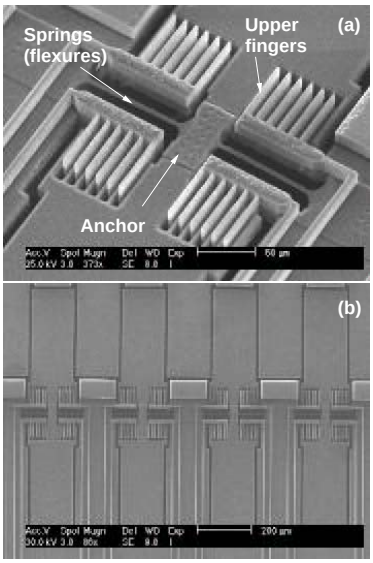

Fig. 4: SEM micrographs of array and device with straight flexures and 150 μm wide mirror platforms.

mask is formed with a single lithography step. The symmetric comb-finger gaps are etched through the Epipoly and device layers using a conventional ICP etching system; thus forming the self-aligned fingers. The remaining Epipoly is removed using a XeF_2 isotropic etch. A 1000 Å-thick thermally grown silicon dioxide mask is used to protect other silicon areas from the dry silicon etch. The reflectors and contact pads are formed (Cr/Au) using a lift-off process. The bulk silicon is then removed from the backside of the mirror array using an ICP etch. Finally, a protective polymer coating is removed from the front side of the sample using an oxygen plasma; thus releasing the devices. Figure 4 shows SEM micrographs of the fabricated devices. The devices shown have 20 μm thick upper and lower electrodes.

4 Results

Static rotation angle as a function of applied voltage has been measured on several devices. Figure 5 (Left) shows the static rotation of two different size devices, both with straight flexures. A rotation angle of 10^o is achieved with 60 Volts or less. Figure 5 (Right) shows the static rotation for a 150 μm wide mirror device with folded flexures, shown in inset. A rotation angle of 10^o is reached with 50 Volts.

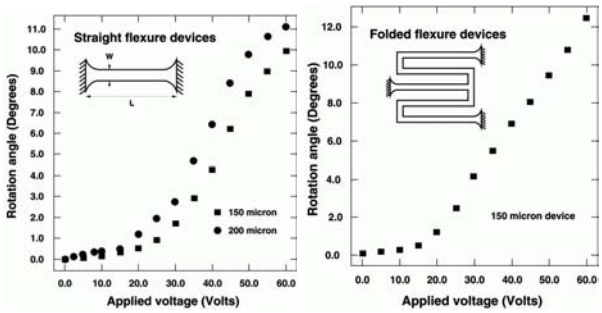

Fig. 5: (Left) Measured rotation angle as a function of applied voltage (DC) for different size devices (150 and 200 μm wide) with straight flexures (L=85 μm and W=5 μm) (Right) Measured rotation angle as a function of applied voltage (DC) for a 200 μm wide device with folded style flexures.

References

[1] A. Selvakumar et al. High density vertical comb array microactuators fabricated using a novel bulk/polysilicon trench refill technology. *Proc.. IEEE Solid-State Sens. Actuator Workshop* pp. 138–141, Hilton Head, SC, June 1994, IEEE.

[2] S. Kim et al. Vertical microlens scanner for 3D imaging. *Proc. IEEE Solid-State Sens. Actuator Workshop* pp. 227–230, Hilton Head, SC, June 2-6 2002. IEEE.

[3] D. Hah et al. A low voltage, large scan angle MEMS micromirror array with hidden vertical comb-drive actuators for WDM routers. *Proc. IEEE Solid-State Sens. Actuator Workshop* pp. 11–14, Hilton Head, SC, June 2-6 2002. IEEE.

[4] M. Kirstena et al. Deposition of thick doped polysilicon films with low stress in an epitaxial reactor for surface micromachining applications. *Thin Solid Films* **259** (1995) 181–187.

Advanced Thermal Vertical Bimorph Actuators for Lateral Displacement

H. Sehr, A. G. R. Evans, A. Brunnschweiler, G. J. Ensell, C. G. J. Schabmueller

Dept. of Electronics and Computer Science, University of Southampton, UK
Highfield Southampton SO17 1BJ
email: h.sehr@ecs.soton.ac.uk http://www.micro.ecs.soton.ac.uk/mems

Summary: *Vertical bimorph actuators perform lateral displacement using the bimetal effect. They consist of silicon beams side-coated with aluminium, which bend when heated. In this paper, we present an advanced design of the actuator based on a meander geometry, which enables higher displacements compared to prototype actuators presented previously. The design, fabrication and the characterisation are presented including static displacement, thermal time constant and lateral resonant frequencies.*

Keywords: *thermal actuation, vertical bimorphs.*
Category: *10 (Applications)*

1 Introduction

Prototype actuators based on thermally excited vertical bimorphs have been fabricated and characterised at the University of Southampton [1, 2]. They use a clamped-clamped geometry for the silicon beam. In this paper, the design, fabrication and characterisation of an advanced thermal vertical bimorph actuator are described. The advanced design has a higher actuation range than the prototype at a comparable input power.

Thermal vertical bimorph actuators consist of silicon beams side-coated with aluminium (figure 1). When heated they bend due to the different thermal expansion coefficients of silicon and aluminium, performing movement in the wafer plane. Obtaining lateral displacement using the bimetal effect [3] is a new concept for micro-actuators, which makes vertical bimorphs an interesting alternative for micro-positioning applications. Compared to electrostatic actuators [4], they only need small voltages (in the range of a few volts) and compared to thermally actuated compliant structures [5], only a small temperature change (up to 100 ˚C) is required.

2 Working Principle

The advanced bimorph actuator consists of a meander shaped silicon beam with sidewalls partly covered by aluminium as shown in figure 1. The silicon beams are 8 μm wide and 30 μm tall. The bimorphs are 1000 μm long. The aluminium fillets on the sidewall are 1.5 μm thick.

To heat up the actuator, a voltage is applied between the contact pads, which causes an electrical current through the silicon beam and hence heat dissipation. The bimorphs bend causing a linear movement of the front plate in the direction of the contact pads. A 200 nm oxide layer provides the electrical insulation between the silicon and the aluminium layer. The resistance of the silicon beam is 6.1 kΩ.

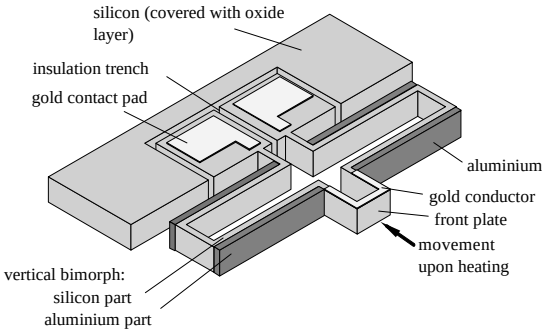

Fig. 1. Meander shaped thermal vertical bimorph actuator**.**

3 Static Deflection

In an SEM, static deflection of the front plate was measured as a function of the electrical input power, as shown in figure 2. With an input power of 6 mW (input voltage: 6.1 V), a deflection of 13.2 μm was obtained. The graph is linear with a small hysteresis for the increasing and decreasing power branches. The measurement is compared with an ANSYS simulation based on constant material parameters (figure 2).

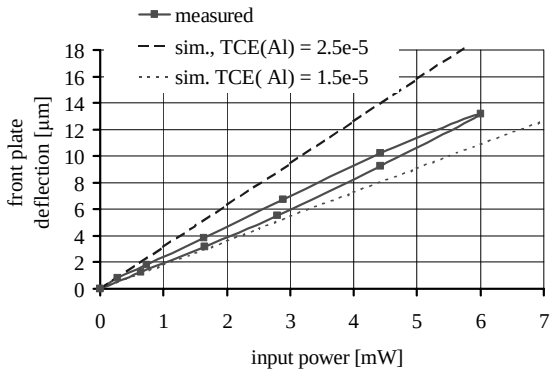

Fig. 2. Static deflection of the front plate as a function of input power, measurement compared with ANSYS simulation based on different thermal coefficients of expansion for aluminium TCE(Al).

4 Thermal Time Constant and Lateral Resonant Frequency

Using a pulsed input power, the thermal time constant of the actuator was measured to be 49 ms, which is in good agreement with the Ansys simulation predicting 48 ms. Lateral resonances were excited thermally and were found to be at 3576 Hz for the first harmonic and at 7148 Hz for the second harmonic. Figure 3 shows a plot of vibration amplitude versus frequency. The simulation predicts 3899 Hz for the first harmonic.

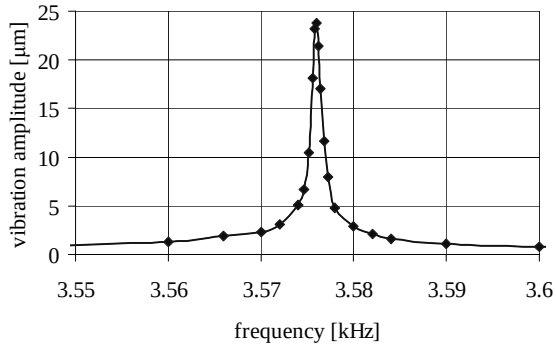

Fig. 3. Vibration amplitude versus frequency plot.

5 Fabrication

The fabrication process is based on the use of SOI substrates with a device silicon thickness of 30 µm. The patterns of the silicon beams are defined by DRIE. For the contact pads, gold evaporation is used.
To deposit aluminium fillets on the sidewalls of the silicon beams, a specially developed process based on angled evaporation and wet-etching is carried out [6]. The bimorphs are released by dry-etching the handle silicon and the buried oxide layer from the back. Figure 4 shows an SEM image of the actuator.

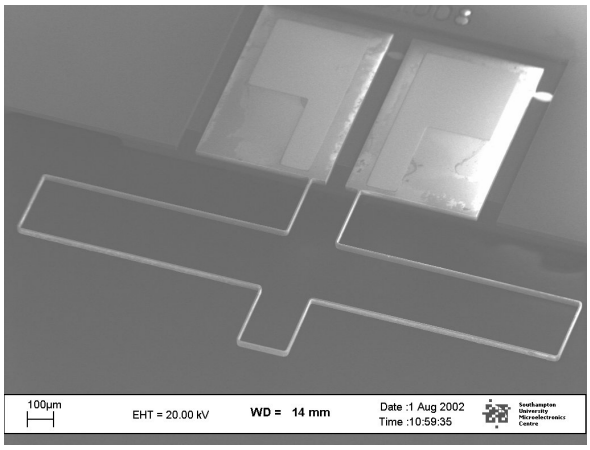

Fig. 4. SEM image of the actuator.

6 Conclusion

An advanced design of a thermal vertical bimorph actuator has been presented. It allows larger displacement compared to prototype actuators based on a clamped-clamped beam geometry. To characterise the actuator, static deflection, thermal time constant and lateral resonances were measured. The fabrication process is based on SOI substrates, DRIE and aluminium sidewall evaporation. Applications in micro-positioning and micro-robotics are envisaged.

References

[1] H. Sehr, A. G. R. Evans, A. Brunnschweiler, G. J. Ensell, T. E. G. Niblock, *Journal of Micromechanics and Microengineering*, Vol. 11, No. 4, pp. 306 –310.

[2] H. Sehr, I. S. Tomlin, B. Huang, S. P. Beeby, A. G. R. Evans, A. Brunnschweiler, G. J. Ensell, C. G. J. Schabmueller, T. E. G. Niblock, *Journal of Micromechanics and Microengineering*, Vol. 12, No. 4, pp. 410 –413.

[3] W. Riethmueller, W. Benecke *IEEE Transactions on Electron Devices*, Vol. 35, No. 6, 1988, pp. 758 – 763.

[4] P.-F. Indermuehle, V. P. Jaecklin, J. Brugger, C. Linder, N. F. de Rooij, M. Bingelli, *Sensors and Actuators*, A 46 - 47, 1995, pp. 562 – 565

[5] T. Moulton, G. K. Anathasuresh, *Sensors and Actuators*, A 90, 1995, 2001, pp. 38 – 48,

[6] H. Sehr, A. G. R. Evans, A. Brunnschweiler, G. J. Ensell, Micromachining and Microfabrication Process Technology VI, SPIE, Vol. 4174, Santa Clara, 2000, pp. 290 –298.

Exploitation of a pH-sensitive hydrogel for CO_2 detection

S. Herber, W. Olthuis, P. Bergveld, A. van den Berg

MESA+ Research Institute, University of Twente, P.O. Box 217,
7500 AE Enschede, The Netherlands
email: S.Herber@el.utwente.nl url: http://www.bios.el.utwente.nl

Summary: *In this paper is described how hydrogel is exploited as sensor material for the detection of carbon dioxide (CO_2). A pH-sensitive hydrogel disc, which swells and deswells in response to pH changes, was clamped between a pressure sensor membrane and a porous metal screen together with a bicarbonate solution. Bicarbonate reacts with CO_2 resulting in a pH change. The enclosed hydrogel will generate pressure as a response to the pH change. This pressure is a measure for the partial pressure of CO_2. The main advantage of this sensor principle is the lack of a reference electrode as required for potentiometric sensors.*

Keywords: hydrogel, Pco_2 sensor, Severinghaus
Subject category: 5 (Chemical sensors) & 6 (Biosensors)

1. Introduction

Stimulus-sensitive hydrogels are cross-linked hydrophilic polymers which undergo a volume change in response to changes in stimuli, such as pH, temperature, electric field, ion concentration or light [1]. This research project aims at exploring the possibilities of detecting the pressure built-up generated by a hydrogel contained under isometric conditions for sensor applications.

2. Sensor design

The first goal is to develop a gastric Pco_2 sensor for measuring the partial pressure of CO_2 in the stomach to determine whether a person has Gastrointestinal Ischemia [2]. To realize this, a pH-sensitive hydrogel disc is used. This type of hydrogel will swell with a decrease in pH and deswell with an increase in pH. A miniature pressure sensor is used to observe hydrogel swelling. In figure 1 a schematic representation of the hydrogel-based Pco_2 sensor is shown.

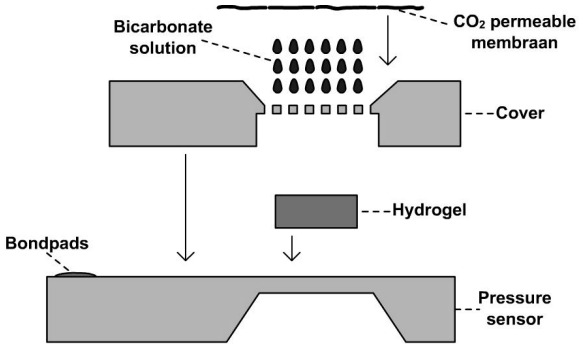

Fig. 1. Schematic representation of the hydrogel-based Pco_2 sensor.

CO_2 will diffuse through the membrane and react with the bicarbonate solution resulting in a pH decrease (Severinghaus principle [3]). In response to the pH decrease the hydrogel would like to swell, but since its volume is fixed by the porous cover (isometric conditions), a pressure will be generated. This pressure is measured by the pressure sensor and is thus a measure for the partial pressure of CO_2.

3. Experimental

The hydrogel disc was prepared from 2-hydroxyethyl methacrylate (HEMA, Acros) and 2-(dimethylamino)-ethylmethacylate (DMAEMA, Acros) by UV-polymerization. A monomer mixture of HEMA and DMAEMA was made with a mole ratio of 95:5 and to the total mole amount, 1.5% cross-linker tetraethyleneglycol diacrylate (TEGDA, Fluka) and 3% photoinitiator 2,2-dimethoxy-2-phenylaceto-phenone (DMPAP, Aldrich) was added. The solution was pipetted on a silicon mould with a cavity of 50 µm and covered with Mylar foil. On top a mask was placed with an aperture (diameter = 750 µm) through which the UV light can pass. The hydrogel was polymerized by 366 nm UV for 90 seconds. The principle is shown in figure 2. By using this method a hydrogel with a thickness of 50 µm can be made.

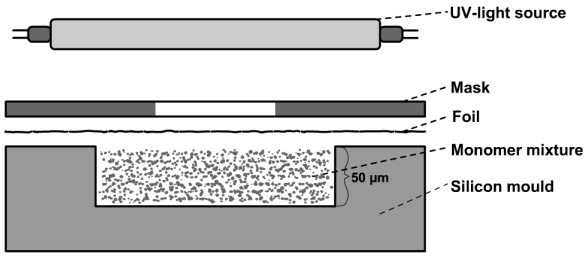

Fig. 2. Schematic representation of the setup that is used to obtain hydrogel discs with a diameter of 750 µm and a thickness of 50 µm.

The hydrogel disc was placed on the pressure sensor membrane of a bare Honeywell pressure sensor. The pressure sensor was glued on a PCB stick and wirebonded. On top of the sensor a porous metal screen was glued (for the initial experiments a metal screen was used instead of a silicon cover).

4. Results

For the initial experiments the sensor was first placed in different 100 mM pH buffers to measure the pressure the hydrogel generates as a function of pH. The result is shown in figure 3. As expected the pressure increases with decreasing pH.

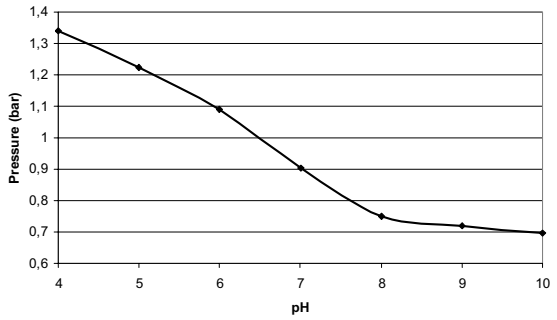

Fig. 3. Plot of the measured pressure versus pH.

Next, a CO_2 measurement was performed. The sensor was placed in a 100 mM $NaHCO_3$ solution together with a pH electrode. Gas was bubbled through the solution starting with 100% N_2, then 100% CO_2 and again 100% N_2. During the experiment the pH and pressure were measured versus the time. The result is shown in figure 4.

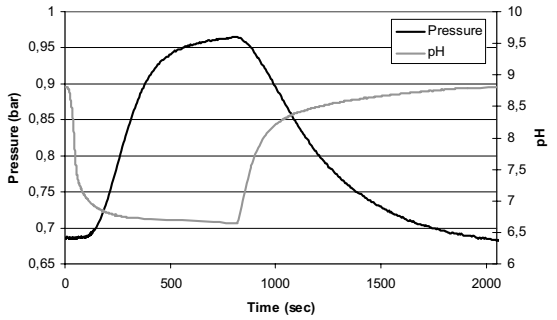

Fig. 4. Plot of the pH change of a 100 mM sodium bicarbonate solution and the pressure change of the hydrogel based sensor as result of a gasflow change from 100% N_2 to 100% CO_2 and back to 100% N_2.

As can be seen in the plot, the pH decreases first by the CO_2 and then increases again by the N_2 removing the CO_2. The pressure at start is 0.68 bar caused by the clamping of the hydrogel. At t = 800 seconds the pH is decreased to 6.7 by the CO_2. Due to this pH decrease, the hydrogel wanted to swell, but since it's volume is fixed it generates an additional pressure of 0.29 bar resulting in a pressure of 0.97 bar. By interpolating the plot from figure 3 the pressure at pH 6.7 can be found which is around 0.95 bar. This agrees reasonable well with the pressure measured during the CO_2 experiment.

Compared to the previous experiments with a Pco_2 sensor holding hydrogel microspheres, the use of a very thin layer of hydrogel gave a faster response [4].

5. Conclusions

A sensor concept is demonstrated where the swelling of a thin pH-sensitive hydrogel layer is measured with a miniature pressure sensor. With the addition of bicarbonate it is shown to be possible to measure CO_2. The principle showed in this article could also be used for other stimulus-sensitive hydrogels, such as a glucose-sensitive hydrogel to construct a glucose sensor.

References

[1] Heiko J. van der Linden, Sebastiaan Herber, Wouter Olthuis, Piet Bergveld, Stimulus-Sensitive Hydrogels And Their Applications In Chemical (Micro)Analysis, *The Analyst*, 2003, Accepted for publication.

[2] A. Groeneveld , J. Kolkman, Gastointestinal ischemia and splanchnic tonometry: a review of physiology, methodology and clinical implications, *J. Critical Care*, 9, 1994, pp.198-210.

[3] J. Severinghaus, F. Bradley, Electrodes for blood Po_2 and Pco_2 determination, *J. Appl. Physiol.*, 13, 1958, pp.515-520.

[4] S. Herber, W. Olthuis, P. Bergveld, A swelling hydrogel based carbon dioxide sensor, *Sens. Actuators, B*, 2003, Accepted for publication.

Structural characterization and gas sensitivity of nanoscaled tin oxide

N. Rosman[1], T. Pagnier[1], M. Rumyantseva[2], E. Makeeva[2] and A. Gaskov[2]

[1]LEPMI-ENSEEG BP 75 F-38402 Saint Martin d'Hères France
e-mail Thierry.Pagnier@lepmi.inpg.fr
[2]119899 Chemistry Department. Moscow State University, Moscow, Russia

Summary: *Nanocrystalline tin oxide powders have been prepared by different routes and characterized by X-ray diffraction, Raman spectroscopy and BET nitrogen absorption-desorption. The electrical response to CO (900 ppm in N_2) or NO_2 (90 ppm in N_2). was measured on thick films prepared from the corresponding powders. Structural characteristics and sensitivity are discussed as a function of thermal treatment of the samples.*

Keywords: Tin oxide, chemical sensor, Raman spectroscopy
Category: 5 (chemical sensors)

1. Introduction

Tin oxide SnO_2 is an interesting material for chemical gas sensors, because of the existence in air of an electron depleted layer due to oxygen adsorption. Modulation of this depleted layer by foreign gas adsorption gives rise to large changes in SnO_2 resistance.

The Raman spectrum of nanocrystalline tin oxide is also rather unique, with very intense specific bands, which have been anayzed in terms of phonon confinment and amorphous layer around nanocrystals [1], but also in terms of free surface vibrational states [2].

Despite similar grain size, nanocrystalline SnO_2 prepared by different routes may display different gas sensor abilities. We therefore intended to study the structure and sensing characteristics of SnO_2 prepared by different routes. X-ray diffraction was used to measure the crystallite size of the powder. BET adsorption-desorption allowed us to measure the specific surface area of tin oxide powders. Raman spectra were collected to better understand the origin of the new bands due to nanocrystalline state.

2. Sample preparation

Four kind of samples were prepared by variations of a wet chemical method. Starting from an $SnCl_4$* $5H_2O$ solution, gels were obtained by precipitation with NH_4OH (samples g and k), N_2H_4*H_2O (samples h), or NH_4OH+cetyltrimethylammonium bromide (CTAB) (samples s). For samples g, drying was conventional (100°C), while final powders of samples k were obtained by cryo drying.

After drying, the resulting powders were calcinated at 300, 500 700 and 1000°C for 24 hours in air. For electrical measurements and sensing characterizations, thick (0.5 mm) films were deposited by screen printing onto alumina substrates where gold electrodes had been pre-deposited. Films were dried at 100°C for 24 hours and calcinated at 500°C for 6 hours.

3. Results

Fig 1 shows the electrical conductance sensitivity towards CO at 380 °C for samples g, h and k. S(CO) is defined by

$$S(CO) = (G - G_0)/G_0$$

where G_0 is the sample conductance in dry air and G the conductance in the 900 ppm CO in N_2 atmosphere.

The general trend is the sensitivity growth with specific area as measured by BET.

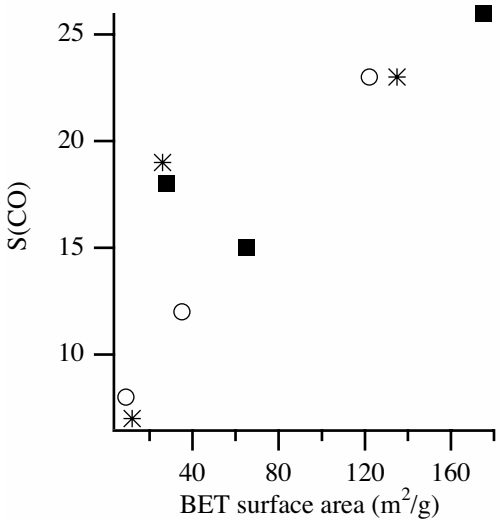

Fig. 1. Sensitivity towards CO S(CO) as a function of BET surface area for samples g(circles), h(stars) and k(filled squares). Measurements performed at 380°C

On the contrary, the sensitivity towards NO_2 at

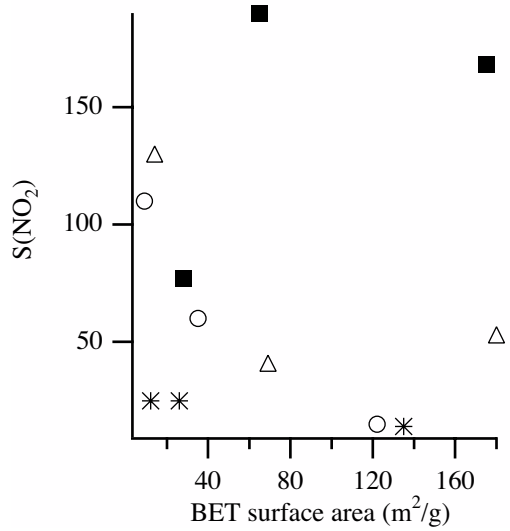

Fig.2. Sensistivity towards NO_2 $S(NO_2)$ as a function of BET surface area for samples g(circles), h(stars), k(filled squares) and s (triangles). Measurements performed at 200°C

200°C, defined by :

$$S(NO_2) = (R - R_0)/R_0$$

where R_0 is the sample resistance in dry air and R the resistance in 90 ppm NO_2 in N_2, decreases when surface area increases (Figure 2). This behaviour cannot be understood if one takes only into account the adsorption of NO_2. Moreover, very different values are observed depending upon the sample preparation: the sensitivity of samples k is much higher, and the sensitivity of sample h much lower than that of samples g and s.

This high sensitivity to sample k for samples heat-treated at 300 and 500°C could be due to a large amount of residual OH groups at the surface of the grains. Thermogravimetric analysis has shown that powder k had a much more important weight loss below 600°C, indicating that many water molecules remain in the sample up to 600°C.

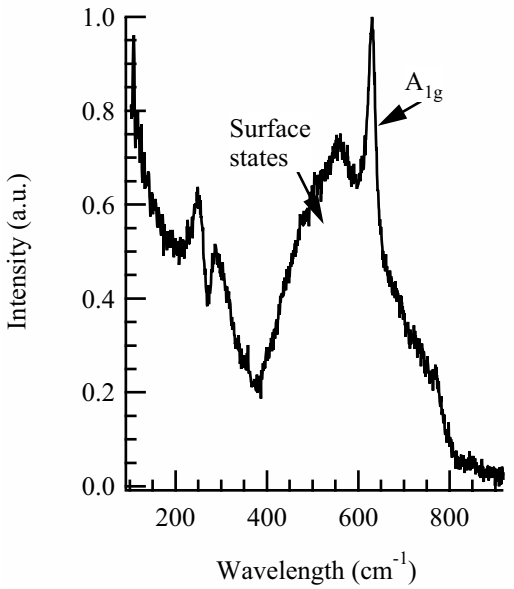

Fi.g 3. Raman spectrum of sample h heat-treated at 500°C. Excitation 514.53 nm.

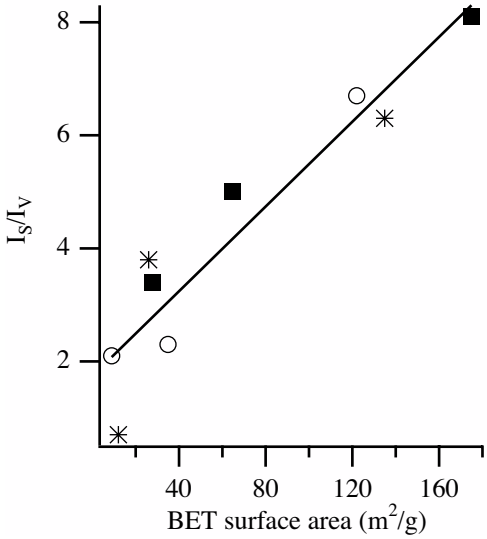

Fig. 4. Correlation between the Raman characteristics and BET results. I_S : intensity of the surface states band. I_V: intensity of the A_{1g} band. The straight line is a linear best fit through data.

A typical Raman spectrum is shown in Figure 3. The two major features are the A_{1g} band and the very broad «surface states» band. An indication of the relative strength of this «surface states» band is obtained by dividing its (integrated) intensity by the (integrated) intensity of the A_{1g} band. Figure 4 shows this ratio vs surface area measured by BET, showing a good correlation between these two results. This is an indication that the «surface states» band is strongly correlated to the free surface, i.e. that which can be in contact with the atmosphere, and to a lesser extent to the nanocrystal size, as one would expect if this band was due to phonon confinement or to the presence of an amorphous layer around each nanograin.

References

[1] A. Dieguez, A. Romano-Rodrıguez, A. Vila , J. R. Morante, J. Appl. Phys. 90(2001) 1550-1557

[2] L. Abello, B. Bochu, A. Gaskov, S. Koudryavtseva, G. Lucazeau, M. Roumyantseva, J. Solid State Chem. 135(1998) 78-85

This work was supported in part by the European Community in the framework of the INTAS programme.

Novel Carbon Dioxide Gas Sensors based on Field Effect Transistors

E. Simon, U. Lampe, R. Pohle, M. Fleischer, H. Meixner
H.-P. Frerichs*, M. Lehmann*

Siemens AG, Corporate Technology, Otto-Hahn-Ring 6, D-81739 München
* Micronas GmbH, Hans-Bunte-Str. 19, D-79108 Freiburg

Summary: *In the present work a new gas sensor technology used for the detection of CO_2 gas will be described. The new sensor technology is based on the signal read out of the work function change on sensitive layers. The sensor device consists of a field effect transistor (FET)with suspended gate electrode prepared in hybrid flip chip technology (HFC-FET). For the detection of CO_2 we present improved sensor layers based on $BaTiO_3$. In comparison to $BaCO_3$ layers these materials showed better response times (lower than one minute) and a good sensitivity (20-45 mV/decade). Especially the stability and adhesion of the layer could be improved. The results of the Kelvin probes can be transferred to the CO_2 HFC-FET measurements concerning sensitivity and response time. Further characterizations will follow.*

Keywords: *carbon dioxide, field effect transistor, work function type gas sensor*
Category: 5 (*Chemical sensor)*

1 Introduction

In the present work we describe a new carbon dioxide sensor based on work function type gas sensors. The detection of CO_2 gas is normally performed using optical devices or electrochemical cells. Now, we use a novel sensor principle - the change of the work function on the sensor layer surfaces. This gas signal can be read out using a field effect transistor with air gap (GasFET or HFC-FET) (see figure1) [1].

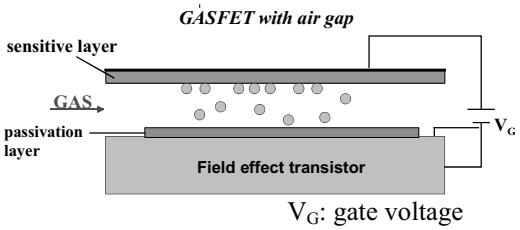

Fig 1: Scheme of a work function type gas sensor based on field effect transistors

Therewith, a low power and low cost gas sensor for CO_2 detection will be established. The development of CO_2 sensors is of great interest as for some applications especially in the low power and low cost area are great needs. For example the detection of fire can be improved due to the use of CO_2 sensors. Also, the control of the air quality or the detection of CO_2 leakages can be important applications.

In previous work it was found out that the CO_2 reaction with $BaCO_3$ as sensitive layer will lead to a change of the work function [2] [3]. The sensor reaction already occurs at room temperature or slightly increased temperatures (~50°C) but is dependent on the presence of humidity [4].
In the flollowing investigations we present another CO_2-sensitive layers based on $BaTiO_3$. $BaTiO_3$ can exists with a low excess quantity of Ba. The excess of Ba is not compensated by Ti – or O – vacancies or by forming of low amounts of a new barium titanate phase with a higher stoichiometry of Ba. Also a mixture of $BaTiO_3$ with CuO is reported as a high sensitive material for CO_2 sensing using the capacitance change in a temperature range of 200 – 1000 °C.

2 Experimental

The sensor layers were prepared using screen printing technique on a gold or platinum metalized alumina substrate. These substrates serve as the layer carrier for the Kelvin probe measurements and they represent the suspended gate electrode of the GasFET. On the backside of the alumina wafers there is a heater which is prepared by Pt thick film technique .
On the one hand the changes of the work function signal were detected by the use of the Kelvin probes made by Besocke [11] with a gold grid of 3 mm diameter as reference electrode. On the other hand HFC-FETs were used. The GasFET sensor set up was prepared by using polymer flip chip bond techniques. With conductive polymer bumps and a bond pressure of 15N, a HFC-FET with a small air gap (between 3-5µm) can be established. The Fet device was then wire bonded on a PCB board and connected to a circuit board (see figure 2). Gas measurements were carried out with a constant gas flow of 1l/min or 500 ml/min. The different gas concentrations were controlled by a mass flow controller.

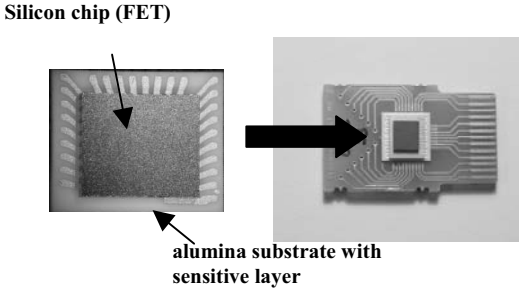

Fig 2. Picture of the HFC-FET sensor device(left) and on a PCB board (right).

3 Results

Using Kelvin probes the sensitivity of the $BaTiO_3$ thick films with excess of BaO to CO_2 gas are measured in the temperature ramge of 30 – 300 °C. Both types of electrodes, platinum and gold are used for the measurements. The humidity was normally set to 65 – 70 %rh.

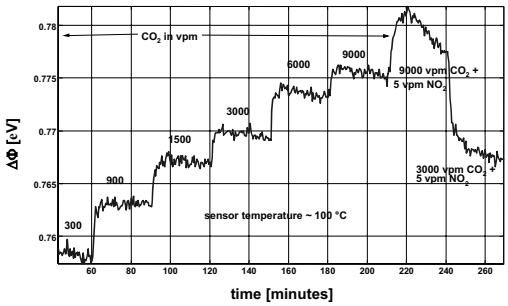

Fig 3. Work function signal of a $Ba_{1.05}TiO_{3.05}$ thick film at 100°C with gold electrode.

The gas measurements in synthetic/wet air in figure 3 showed that the $Ba_{1.05}TiO_{3.05}$ layer has a fast response time and a sufficient sensitivity to CO_2 (20 mV/decade). In comparison to $BaCO_3$ layers - the response time is lower than one minute whereas for $BaCO_3$ several minutes have been detected [4]. Analogue to the $BaCO_3$ Kelvin probe measurements, the sensitivity to CO_2 is dependent on the presence of humidity. First tests concerning the reaction of the $Ba_{1.05}TiO_{3.05}$ layer to other gases seems to be promising low. Only the reaction with NO_2 gas showed a significant cross sensitivity and additionally drift effects tend to increase (see figure 3). The sensitivity of a $BaTiO_3$/CuO thick film on a platinum electrode is higher (45mV/decade) than the CO_2 signal of the pure $BaTiO_3$ thick film with BaO excess. However the response time is increasing (3 min. for t_{90} at 40°C). Also the cross sensitivity against NO_2 is much higher than in the case of the pure $Ba_{1.05}TiO_{3.05}$ films. Further steps to eliminate this unwanted reaction will follow.

First tests has been carried out with a thick film $Ba_{1.05}TiO_{3.05}$ -layer used in a HFC-FET set up. Using gold as gate electrode metalization the sensitivity of the CO_2 GasFET is comparable to the results of the Kelvin probe measurements with $Ba_{1.05}TiO_{3.05}$.

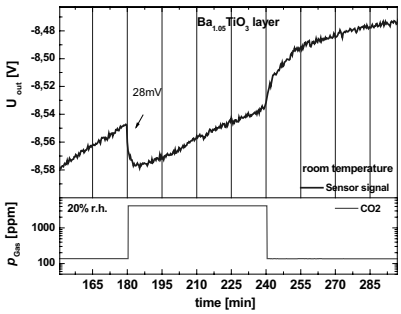

Fig 4. Signal read out of a CO_2 GasFET with $BaTiO_3$ as sensor layer at room temperature.

The change of the work function is in the range of 28 mV per decade for room temperature measurements (see figure 4).

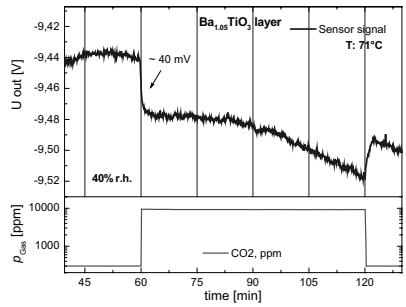

Fig 5. Signal read out of a CO_2 GasFET with $BaTiO_3$ as sensor layer at 70°C.

At 71°C the sensitivity is about 30 mV per decade (see figure 5). The response times, in both temperature ranges, are fast and lower than one minute. Unfortunately in both cases, the drift of the sensor is high.

References

[1]. Fleischer, M., et al., *Low-power gas sensors based on work function measurement in low-cost hybrid flip-chip technology.* Sensors and Actuators B, **80** (2001) 169-173.
[2] Ostrick, B., et al., *Adsorbed water as key to room temperature gas-sensitive reactions in work function type sensors: the carbonate-carbon dioxide system.* Sensors and Actuators B, **57** (1999) 115 - 119.
[3] Ostrick, B., et al., *Investigation of the reaction mechanisms in work function type sensors at room temperature by studies of the cross-sensitivity to oxygen and water: the carbonate-carbon dioxide system.* Sensors and Actuators, **B68** (2000) 197-202.
[4] Ostrick, B., *Die Untersuchung der Karbonat-Kohlendioxid-Wechselwirkung im Feuchtefilm der Oberfläche*, Dissertation, University of Gießen, 2000.

Preparation of grain size-controlled tin oxide sols for gas sensor application

Dang Duc Vuong[1], Go Sakai[2], Kengo Shimanoe[2], Noboru Yamazoe[2]

[1] Department of Molecular and Material Sciences, Graduate School of Engineering Sciences, Kyushu University, Kasuga-shi, Fukuoka 816-8580, Japan
email: vuong@mm.kyushu-u.ac.jp
[2] Faculty of Engineering Sciences, Kyushu University, Kasuga-shi, Fukuoka 816-8580, Japan

Summary: Sols of SnO_2 with a mean grain size controlled between 6 and 10 nm were prepared from SnO_2 gel by a hydrothermal treatment in ammonia or TMAH solution. Thin films of SnO_2 were prepared on an alumina substrate by spin-coating from the sol dispersions. The thin films showed different sensing behavior to H_2 gas depending on the grain sizes of the starting sols. Remarkably large sensor response to H_2 was observed with the grains of 8.5 or 10 nm in size, reaching a maximum at 400°C or 350°C, respectively.

Keywords: hydrothermal treatment, SnO_2, gas sensor
Category: 5 (Chemical sensors)

Introduction

Oxide semiconductor gas sensors have been extensively studied in order to understand or improve their sensing properties to inflammable and toxic gases. Recently, the importance of micro-structural control for semiconductor gas sensors has been disccussed [1]. The gas in problem (target gas) diffuses in the sensing body while it reacts with the surface oxygen of oxide grains included. Knudsen diffusion coefficient D_K is given by $D_K = 4r/3\,(2RT/\pi/M)^{1/2}$, where r is pore radius, M molecular weight of target gas, R gas constant and T temperature [2]. It follows that D_K is proportional to r, which would increase with increasing grain size. It is thus of interest to investigate how the grain size affects the gas sensing properties of thin film devices. On this background, we tried to grow SnO_2 grains in sol dispersion under controlled hydrothermal conditions. The SnO_2 grains thus grown were tested for H_2 sensing properties. This paper aimed at reporting the results of these studies.

Experimental

Stannic acid gel was synthesized by hydrolyzing 0.2 M solution of tin chloride ($SnCl_4$) with ammonia. The resulting precipitate was washed thoroughly with deionized water to remove Cl^-. The obtained gel was suspended in water and, after adjusting the pH of the suspension with ammonia or tetra methyl ammonium hydroxide (TMAH) solution, hydrothermal treatments were carried out in an autoclave under various conditions. Each sol dispersion thus obtained was subjected to measurement of particle size by a laser particle distribution analyzer (LPA). Part of it was dried at 120°C for 24h to determine the crystallite size based on the x-ray diffraction (XRD) method. To obtain SnO_2 thin films, the above sols were spin coated (1000 rpm) on an alumina substrate attached with a pair of comb-type Au electrodes, and sintered at 600°C for 3h.

Results and discussions

Figure 1 shows the distribution of particle size for 7wt.% SnO_2 sol dispersion after a hydrothermal treatment at 250°C for 3h under pH=12. The average particle size of this sol was 13 nm in diameter while the crystallite size based on XRD was 10 nm. The LPA particle size and XRD crystallite size changed significantly depending on the conditions of hydrothermal treatment. For example, Figure 2 shows the growth of crystallite size with a lapse of time under milder conditions, i.e, 200°C and pH=10.5. Under these conditions, the crystallite size of SnO_2 could not exceed 9 nm. Anyway it was possible so far

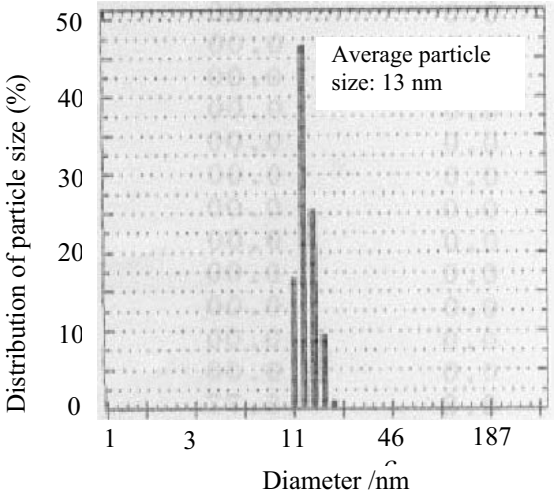

Fig. 1. Particle size distribution of 7wt.% SnO_2 sol after hydrothermal treatment at 250°C and pH=12 for 3h

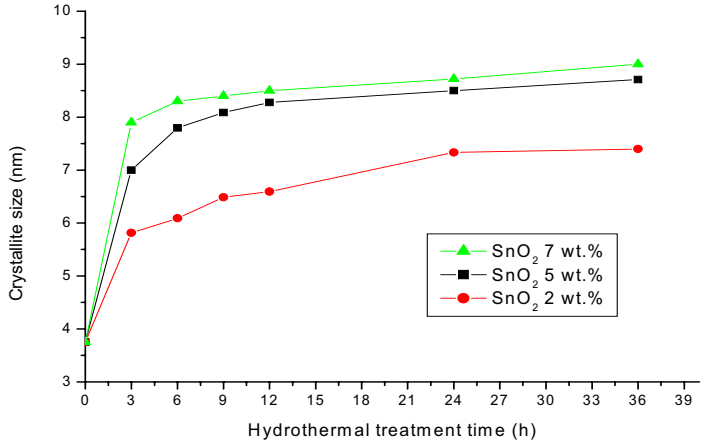

Fig. 2. Growth of SnO_2 crystallite size with time at 200°C and pH=10.5
Tin oxide content: 2wt.%, 5wt.%, 7wt.%

to control the grain (crystallite) size between 6 and 10 nm by changing the conditions of hydrothermal treatment. We are still trying to extend the upper limit of the range of controlled grain size.

Figure 3 shows the response transients of thin film devices to switching-on and off 200 ppm H_2 at 500°C. The response and recovery were very sharp. Figure 4 shows sensor response (Ra/Rg) to 200 ppm H_2 for the thin films devices derived from three different sols as a function of operating temperature. The sensor response exhibited a volcano-shaped relation with the operating temperature, giving a maximum at 350 or 400°C. The device derived from the SnO_2 sol with 8.5 or 10 nm in grain size exhibited remarkably large sensor response, as compared with the device derived from the sol with 6 nm. The origin of such a difference in sensing properties is under investigation and will be discussed in the presentation

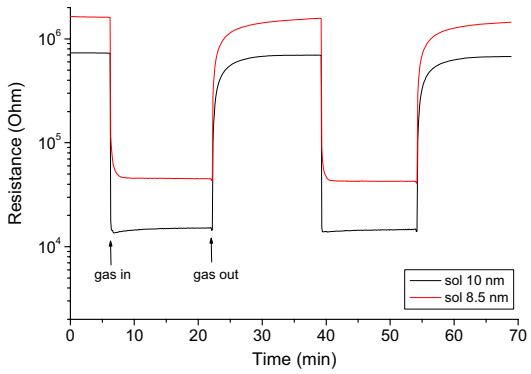

Fig. 3. Response transients of thin film devices derived from two different sols to 200 ppm H_2 at 500°C

a. Sol containing 10 nm- sized SnO_2,
b. Sol containing 8.5 nm- sized SnO_2,

Conclusion

The sol dispersions containing nanometer sized SnO_2 particles were prepared by a hydrothermal treatment. The crystallite size of SnO_2 included could be controlled in the range of 6-10 nm. Thin films of SnO_2 derived from these sols showed largely different sensing properties to H_2 in air, depending on the crystallites size of SnO_2 in the sols.

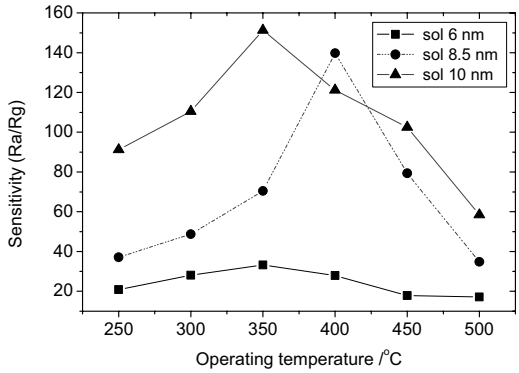

Fig 4. Sensor response of the thin film devices to 200 ppm H_2 as a function of operating temperature

References

[1]. Nam Seok. Baik, Go Sakai, Norio Muira, Noboru Yamazoe. *Sensors and Actuators B*, 63 (2000) 74-79
[2] Go Sakai, Naoki Matsunaga, Kengo Shimanoe, Noboru Yamazoe, *Sensors and Actuators B*, 80 (2001) 125-131

Portable gas chromatograph with integrated components

J. A. Dziuban[1], J. Mróz[2], M. Szczygielska[2], M. Małachowski[2], A. Górecka-Drzazga[1], R. Walczak[1], W. Buła[1], D. Zalewski[1], L. Nieradko[3]
[1]Wroclaw University of Technology, Faculty of Microsystem Electronics and Photonics, Janiszewski Str. 11/17, 50-372 Wroclaw, Poland, email: jad@wemif.pwr.wroc.pl
[2] The Center EMAG Katowice, Leopolda Str. 31, 40-189 Katowice, Poland
[3] Present address: Laboratoire d'Optique P. M. Duffieux, 16 Route de Gray, 25-030 Besancon Cedex, France

Summary: *The portable gas chromatograph with integrated micromachined flushed injector and thermal mass detector (TCD) has been developed. The silicon/glass injector operates in fixed volume (2 x 7 μL) or electronically operated mode. In the injector, an integrated, pneumatically operated, fast cross-valve is applied. TCD detector consists of two Pt microspirals packaged in silicon/glass micromachined chip. Temperature of two capillary molecular sieve separation columns is controlled by thick film heater made on polyimide foil. The chromatograph is equipped in two 16-bits microprocessors communicating to external controlling-steering portable PC. The chromatograph operates in on-line continues analyses mode.*

Keywords: *portable gas chromatograph, integrated injectors, silicon micromechanics*
Category: *5 (Chemical sensors)*

1 Introduction

The first integrated gas chromatograph was developed at late 70's of XX century by Angell, Terry and Jerman [1]. After several years of redesigning, the portable gas chromatograph has been introduced to the production by MTI Inc. (USA) in the period of late 80's and beginning of 90's, followed after, by wide expansion of the instrument under Hewlett Packard (Agilent USA) name [2]. The most important parts of the gas chromatograph being actually produced by Agilent Inc. are gas injectors and mass detector made by use of micromechanical engineering.
At the moment, there are few existing projects in Europe [3, 4] on integrated gas chromatograph development, although many companies have been developing theirs own custom-designed gas meters based on solutions of Agilent. Among them, natural gas meter of Actaris/SRA (F) seems to be the most advanced [5]. The lack of independent market of key components and/or of assembled portable gas chromatographs is the most important barrier blocking wider application of miniature gas chromatographs for on-line analysis in environment protection, gas systems electroengineering systems etc.
In our work results of a long-lasting research program carried out under auspices of Polish Research and Science Committee on portable gas chromatograph will be shown. The main goal of the work is to obtain miniature gas chromatograph with flushed gas injector and nano-dead-volume fast TCD, equipped in software and analog/digital circuits, able to provide continuous detection of combustible atmosphere in deep coal mining industry.

2 Experiment

The portable gas chromatograph developed by us (Fig. 1) consists of two micromachined parts: fixed or electronically adjusted gas injector and thermal-mass-detectors (TCD). Capillary columns ID 0.32 mm Rt-Msieve 5A of Restek (USA) each 10 m long are positioned in the thermally isolated chamber. Thick-film heater made on elastic polyimid foil surrounds columns and ensures proper temperature adjusting and stabilization (50°C – 120°C).

Fig. 1. The portable gas chromatograph: left - the instrument, carrier gas bottle, and PC, right - inside parts.

Injector assembled in the specially designed metallic case, is connected to pressure/flow regulators, filters and pumps. Four TCD sensors are located inside of the thermally isolated chamber (Fig. 2).

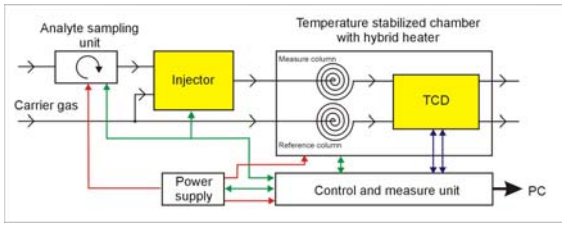

Fig. 2.The scheme of the gas chromatograph with integrated micromachined components – gas injector and TCD sensor.

The injector (Fig. 3) consists of two Borofloat 3.3 glass substrates, silicon (100) double side polished deep-micromachined substrate and polyimide, Teflon® coated foil.

a) b) c)

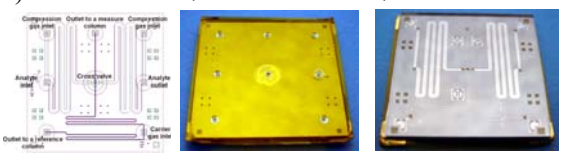

Fig. 3. The injector chip: a) the gas circuit of the injector, b) upper side of the chip, c) back side: micromachined fixed volume chambers, gas lines and cross-valve may be seen.

The gas circuit of the injector includes one integrated pneumatically operated fast cross-valve (1 ms), two fixed-volume chambers (7 µl each) and two narrow channels for active and reference gas column supplying. Some of injector characteristics are shown in the figure 4.

a) b)

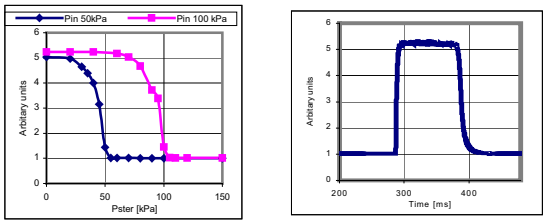

Fig. 4. The main injector characteristics: a) shut-down of the cross valve, b) injection of a gas sample.

The TCD applied in the gas chromatograph is based on a previously reported by us (Eurosensors XIV, Copenhagen, 2000) solution in which two microspirals 1000 x 400 µm^2, ∅15 µm Pt wire are located in channels and vias micromachined in a silicon substrate. After assembling of spirals, glass cap with machined channels are bonded to the substrate. In the reported here solution, four double-spiral sensors (Fig. 5a) are fabricated in single chip, double Wheastone's bridge configuration in a self-compensating mode is used. Main TCD characteristics are shown in figure 5b.
In the chromatograph the printed board circuit with two 16-bits processors with specialized software is used.
Tests have shown very good immunity of TCD detectors against carrier gas stop-flows. The typical result of the gas mixture analysis is shown in the figure 6.
Technical parameters of the gas chromatograph are similar to the well known Agilent/HP instruments.

a) b)

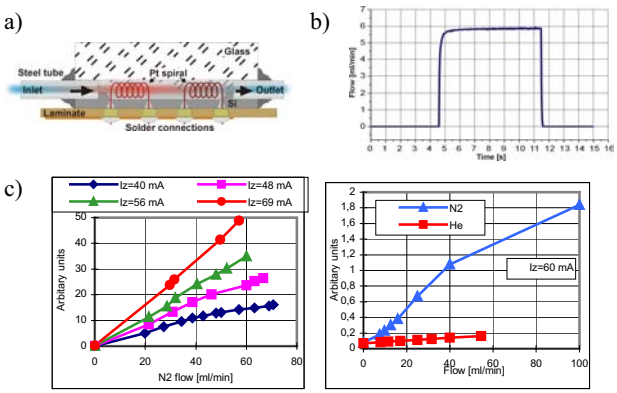

Fig. 5. The TCD detector: a) the scheme, b) dynamic characteristic – transit time below 7 ms, c) main characteristics – output signal vs. flow of N_2 for different current of heater Iz, and output signal vs. flow of N_2 and He for Iz=60 mA.

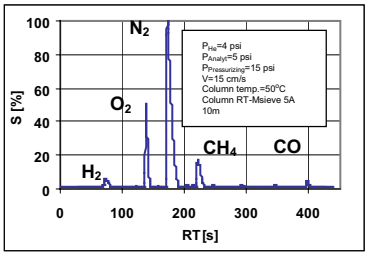

Gas	C_{nom} [%]
H_2	2
O_2	15
N_2	55
CH_4	20
CO	8

Fig. 6. The chromatogram of a gas mixture.

3 Results and discussion

We have obtained portable gas chromatograph weighting aprox. 3.5 kg for continuous analysis of a gas mixture. The lowest detection level obtained is about 1 ppm, average analysis time is below 6 minutes (depending on a column applied), repetition time is 10 seconds. All parameters of set up of GC may be electronically adjusted, the results of analysis may be visualized immediately.
At the moment it seems that our gas chromatograph is the only one European complex solution comparable to Agilent/HP standards.

The works have been financed by Polish Research and Science Committee PBZ 01915 and 9T11A03710. We would like to thank to K. Malecki, PhD, for TCD tests.

References

[1] S. Terry, J. Jerman , J. Angell, A gas chromatographic air analyzer fabricated on silicon wafer, *IEEE Trans. El. Dev, ED26*, 2 (1979) 1880–1886.
[2] http://www.chem.agilent.com
[3] M. B. Stone, J. A. de Mello, Life, the universe and microfluidics, *Lab Chip*, 2 (2002), 58-64
[4] Actaris: The Meter of Natural Gas
[5] http://www.sra-instruments.com

Enhancement of the Hydrogen Peroxide Quartz Crystal Biosensor using proteins

S.P. Martin, J. M. Lynch & S.M. Reddy

School of Biomedical & Life Sciences, University of Surrey, Guildford,
Surrey, GU2 7XH, UK, email: s.reddy@surrey.ac.uk

Summary: The development and optimisation of a quartz crystal acoustic wave sensor for hydrogen peroxide is described. Dimethoxybenzidine was used in the presence of horseradish peroxidase to detect hydrogen peroxide. This reaction produces an insoluble precipitate, the production of which was monitored using a quartz crystal. The presence of GOx and β-amylase in the reaction mixture increased impedance responses by about 10-fold and 2 fold, respectively at the concentrations used. The inclusion of either of the enzymes used was found to reduce the response time to 15 minutes from 68 minutes. Rapid and sensitive peroxide detection has implications for metabolite determination via peroxide-producing oxidase-based enzymatic processes.

Keywords: quartz crystal, biosensor, hydrogen peroxide
Category: Biosensors

1. Introduction

An approach has recently been described in which the surfactants, Triton X-100 and Tween 80 were used to enhance the detection of hydrogen peroxide, using the quartz crystal acoustic wave sensor (Martin et al., 2002). The technique uses 3,3'-dimethoxybenzidine (DMOB) and 3,3'-diaminobenzidine (DAB), with horseradish peroxidase, which in the presence of hydrogen peroxide produces an insoluble product (see the reaction sequence below). The product precipitates out and attaches to the quartz crystal surface resulting in a corresponding frequency (f_s) and impedance (Z_s) change.

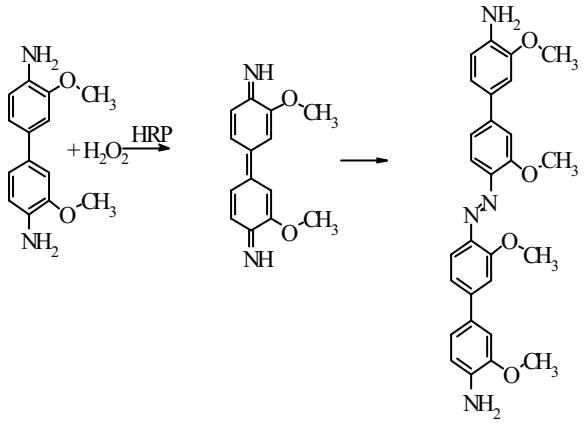

The proteins used during this study are listed in table 1, along with a number of their key characteristics. Most of the proteins are enzymes, which have a FAD active centre (GO_x, ChOx, β-amylase, and SO), while pepsin has a number of amino acids which form its active centre. BSA is a protein with no enzymatic activity.

Protein	MW (Da)	P_I
GO_X	160	4.2
BSA	65	4.7
ChOx	56	4.6-5.2
Pepsin	35	<1.0
β-Amylase	152	4.58-4.83
Sarcosine oxidase	42	7.8

Table 1. The proteins and their major characteristics.

2. Methods

2.1 Crystal preparation. Gold-on-chromium electrodes (100 nm and 5 nm respectively) were vapour-deposited onto either side of a blank AT-cut quartz crystal (IQD, Crewkerne, UK). The crystals had a fundamental resonance frequency of 10 MHz, and diameter of 8.2 mm. The crystals were cleaned with acetone and isopropanol, and dried with vacuum suction, prior to electrode deposition. The crystal was then sealed in the sample chamber as previously described (Reddy, 2000). A HP4194A impedance

analyser coupled to a PC was used to record resonant frequency and impedance changes.

Measurement procedure. For all experiments, a 300 µM DMOB solution was added to the test cell, to which was added a 360 U/ml HRP solution, giving a final concentration of 0.2 U/ml, and an appropriate concentration of protein to give a concentration between 0 and 0.14 % (w/v). A concentration of 300 µM hydrogen peroxide was used throughout all experiments. The test solution was stirred, during all experiments. After each experiment, the crystal was cleaned thoroughly with *N*, *N* dimethylformamide and deionised water. The use of the organic solvent removed the film adsorbed to the crystal during the experiment, and this was confirmed by the crystal frequency returning to its original value. All experiments were performed at room temperature.

3. Results & Discussion

A variety of proteins and enzymes were studied with the DMOB-HRP-H_2O_2 reaction. Some were tried with DAB reagent, but it was found that they had no enhancing effect upon this benzidine reaction. This is believed to be due to the additional amino groups, which could bind to any exposed carboxyl groups on the proteins, leading to solubilisation of the oxidised DAB.

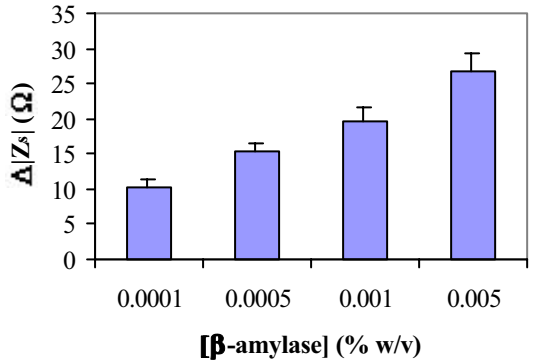

Fig. 1. Effect of β-amylase on the DMOB-HRP-DAB. H_2O_2 reaction, with H_2O_2 at 300 µM.

In the absence of any additional proteins, DMOB gave an impedance response of 14.75 ± 0.6 Ω at 300 µM hydrogen peroxide, in the presence of horseradish peroxidase. The response time was 68 mins. When the same experiment was performed with the proteins, a different response was seen. All the enzymes gave a reduced response time of 15 minutes, while BSA had no beneficial effect. Only β-amylase (Fig. 1) and Gox (Fig. 2) had an effect upon the response size, as well as the response time. GOx gave an improved response of 138.4 ± 26.3 Ω at 0.056 % (w/v), and β-amylase a response of 26.7 ± 2.7 Ω at 0.005 % (w/v).

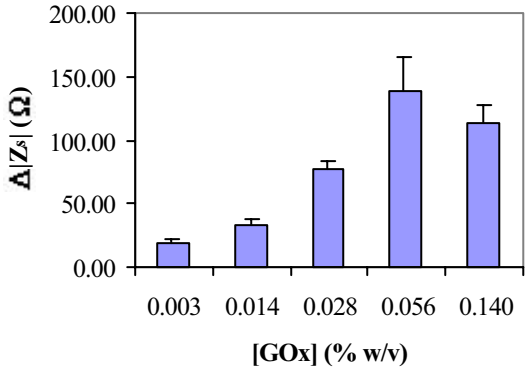

Fig 2. Effect of GOx on the DMOB-HRP-H_2O_2 reaction with H_2O_2 at 300 µM.

Both of these enzymes have a similar pI and molecular weight. A further experiment was performed to study the effect of pure FAD with this reaction, and it was found that this decreased the response time, but not the response size, as was the case with SO, ChOx and pepsin. So, it would appear the response time was reduced due to the FAD component of the enzymes, and the response size due to the pI and molecular weight. It is also likely that that the protein is adding to a mass/viscoelastic effect by surface-entrapment within the adsorbed precipitate.

4. Conclusions

In the present work, it was found that the presence of GOx and β-amylase had a beneficial effect upon the impedance response, and the time taken to reach the end of this response. The decreased response time is due to the presence of the FAD or amino acids of the enzymes, which are behaving as cofactors to HRP. The increased response size is due to either the pI or MW of the enzyme, which leads to increased deposition of oxidised DMOB at the crystal surface.

References

Reddy SM. (2000) Detection of phenol in aqueous solution using an AT-cut quartz thickness shear mode sensor. *Materials Science & Engineering C-Biomimetic and Supramolecular Systems*; **12**: 23-28.

Martin S.P., Lynch J.M. & Reddy S.M (2002) Optimisation of the enzyme-based determination of hydrogen peroxide using the quartz crystal microbalance. *Biosensors & Bioelectronics* **17**: 735-739.

Numerical Analysis of Contact Problems in MEMS by Homotopy Methods

E.-R. König, A. Mayr, and G. Wachutka

Munich University of Technology,
Institute for Physics of Electrotechnology, D-80333 Munich, Germany
email: koenig@tep.ei.tum.de http://www.tep.ei.tum.de

Summary: *Mechanical contact problems in electromechanical microdevices (MEMS) are of high technical relevance, but difficult to treat in numerical simulation, in particular for flexible contact beams, because the operating area near contact exhibits an inherent instability. We employ a homotopy algorithm to achieve a stable and accurate treatment of contact problems in MEMS for rigid as well as flexible structures from the open position to full nestling of a flexible electrode against the counterelectrode, including the initial touch–down and the following stages of shape snapping.*

Keywords: *MEMS, contact, homotopy, simulation*
Category: *1 (General, theoretical and modeling)*

1 Introduction

Contact problems such as, e. g. the touch-down of an electrode to its counterelectrode, are encountered in almost every electromechanical microdevice. Very often, the contact is a functional part of the device structure, e.g. in microrelays of rolling wedge type [1] or in micromembrane drives [2]. For these devices, the simulation of closing and opening the contact is indispensable for design and optimization. Even in devices, where making a contact is not a desired integral part of the device function, as it is the case in micromirrors, comb actuators or gyrators [3] it is necessary to know the exact landing voltages and energies with a view to to extracting macromodels which realistically cover the full range of operation.

2 Devices under consideration

Getting neighbouring structural parts in mechanical contact is an inherent feature of rigid-body devices such as micromirrors (fig. 1), characterized by one or a few degrees of freedom (DOFs), as well as of flexible devices like microrelays (fig. 2), characterized by an infinite number of DOFs. As it will be shown below, these two classes of devices can be treated within the same theoretical framework used for setting up efficient algorithms for numerical simulation.

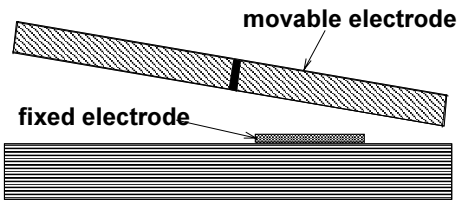

Fig. 1. Example of a rigid device : micromirror

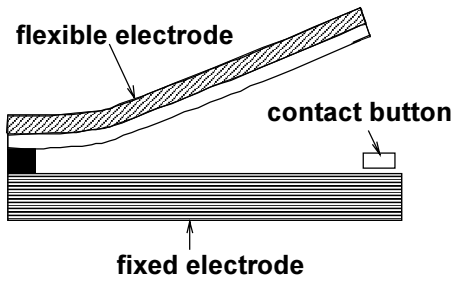

Fig. 2. Example of a flexible device : microrelay

3 Problems during contact simulation

Electromechanical microdevices exhibit an inherent instability in operation regions far from the zero position. As a consequence we observe touch-down, contact and sticking in nearly all cases of practical interest, which has a strong impact on simulation. Unstable operating areas can be treated in a robust and efficient way by the use of homotopy methods, as long as no contact is attained [4]. Making contact, however, constitutes a difficulty for homotopy methods for the following reason :
A static operating point, albeit stable or unstable, is calculated comprising a modified relaxation scheme between a Finite Element solver for the mechanical energy domain and a Boundary Element solver for the electrical energy domain. These solvers are treated as black boxes; neither a system matrix is extracted nor is the internal solving process controlled by the homotopy algorithm. The Finite Element solver is already equipped with a built-in contact algorithm, capable of detecting and treating contact correctly, but due to the unstable electromechanical equilibrium a straightforward solution cannot be achieved. In order to obtain convergence also in the unstable operating area, we apply a homotopy algorithm.

The part of the homotopy algorithm, which brings the relaxation scheme to convergence, assumes that the problem is smooth in a vicinity of the solution point. This implies that a well-defined relation between force and position F(x) exists and is a smooth function in the vicinity of x_0.

After having attained contact, this assumption is violated. A unique force/position relation exists only for $x < x_0$ but is not defined for $x \geq x_0$.

As a consequence, the homotopy algorithm described in [4] may produce artifacts by converging to wrong solutions as displayed in fig. 3.

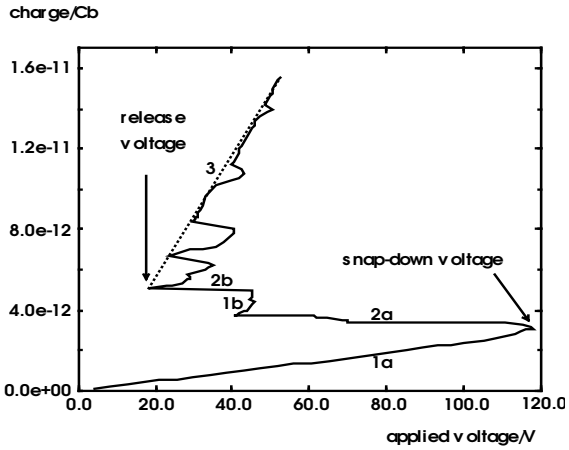

Fig. 3. Simulated characteristics of a microrelay (voltage vs. device charge). Under contact conditions, artifacts are produced in branch 3. The dotted line shows the true contact branch without artifacts.

4 Integrating a contact algorithm in the homotopy method

We developed a modification of our homotopy algorithm, which is able to converge under contact conditions and thus allows for a uniform treatment the whole operating area of an electromechanical microdevice, including contact, unstable and stable areas, for both rigid and flexible device structures.
The essential modification has been made in that algorithmic part which ensures convergence of the FEM/BEM relaxation scheme. In the new algorithm smooth behavior is required only in a half-space adjacent to the solution point. Figure 4 shows a part of the force/position relation F(x) with some selected equilibrium points. The circle indicates an omnidirectional vicinity of a solution point before contact is attained, while the half-circle denotes a half-sided vicinity of a solution point after contact is made.

As the above-mentioned continuity restrictions are dynamically detected, the convergence rate for operating points without contact is equal to that of the original algorithm. The modified algorithm can be used for both single-parameter homotopy (using, e.g., the device charge or the geometrical displacement as control variables), as well as for multi-parameter homotopy [4], which adaptively selects the locally best suited parameter.

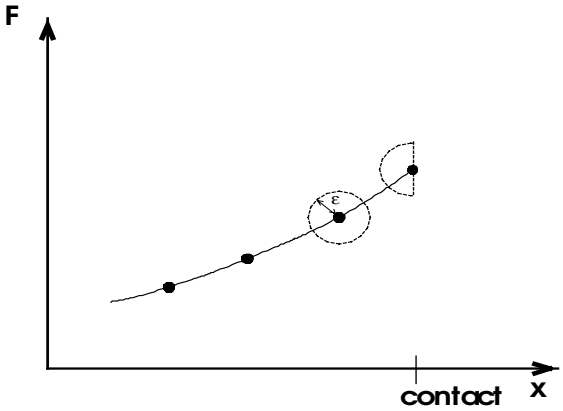

Fig. 4. Omnidirectional and half-sided vicinities of solution points with and without contact condition, respectively.

5 Conclusion

For the robust and accurate numerical analysis of electromechanical microdevices subject to contact constraints, we combined a contact algorithm as implemented in a FEM solver with a modified homotopy algorithm. This enables the efficient and stable simulation over the whole operating area, including contact, unstable and stable solution branches and multiple snap-points, for rigid as well as for flexible devices structures. The modified homotopy algorithm can be used in combination with single-parameter and multi-parameter homotopy methods, and allows for nearly arbitrary resolution of the device characteristics.

References

[1] J. Schimkat. Grundlagen und Modelle zur Entwicklung und Optimierung von Silizium-Mikrorelais. Dissertation, Technical University of Berlin, Germany, 1996.

[2] R. Zengerle. Mikro-Membranpumpen als Komponenten für Mikro-Fluidsysteme. Dissertation, University of the Armed Forces. Shaker publishers, Aachen, Germany 1994.

[3] V.P. Jaecklin, C. Linder, N.F. de Rooij, J.-M. Moret, R. Vuilleumier. Line-addressable torsional micromirrors for light modulator arrays. *Sensors and Actuators*, A41-42, pp.324-329, (1994)

[4] E.-R. König, G. Wachutka. Multi-Parameter Homotopy for the Numerical Analysis of MEMS. In: *Proc. 16 Eur. Conf. On Solid-State Transducers*, pp. 96-99, Prague, Czech Republic, 15-18 September 2002.

Novel stress test structures for surface micromachining applications

A.Bagolini, B.Margesin, A.Faes and G.Turco

ITC-irst, via Sommarive, 16, 38050 Povo (TN)
email: bagolini@itc.it
http:\\www.itc.it

Summary: *A novel set of microstructures for on-wafer stress measurement is presented, based on a lancet principle, with dedicated design for the amplification of the dimensional variations induced by the internal stress of the structural material. A tilted arm geometry was adopted in order to obtain a maximum of strain induced movement, keeping the design relatively simple and robust and the lancet on the wafer plane.*
A set of simulations, as well as an analytical examination of the structure was performed, to establish the optimal geometry: different tilt angles were simulated in a stress range between –300MPa and 300 MPa, obtaining good linearity. Test structures were then realized by means of surface micromachining, adopting photoresist as a sacrificial layer and electroplated gold as structural layer: the novel geometry was sided by traditional lancet structures [1] and wafer curvature measurements to confirm the readout.

Keywords: *stress, test structures, surface micromachining*
Category: *General, theoretical and modeling*

1 Introduction

In plane intrinsic stress of the deposited layers induces strain of the structures and subsequent movement of their released parts. This movement can be amplified so to produce an indication of the internal stress of the film. Several different layouts are available for in situ direct measurement of the stress of deposited layers [1,2,3]: the aim of these test structures is to provide a quick and reliable information which can become vital for micro-mechanical devices fabrication.

Traditional array structures such as buckling beams offer a discrete means of measuring stress, but with some limitations:

- different structures are needed to measure tensile and compressive stress.

- measurement is discrete, with poor resolution.

- wide test area is needed, with chains of structures.

The lancet layout offers a solution to all these limitations, providing a single structure for both tensile and compressive stress, with continuous readout and small wafer area encumbrance. The main effort in lancet layout concerns the possibility to magnify the lancet displacement: this work presents a novel layout for the lancet test structure based on geometrical amplification.

1 Lancet layout

The lancet conceptual and effective layout is reported in fig. 1:

Fig. 1. Conceptual (left) and effective (right) lancet layout.

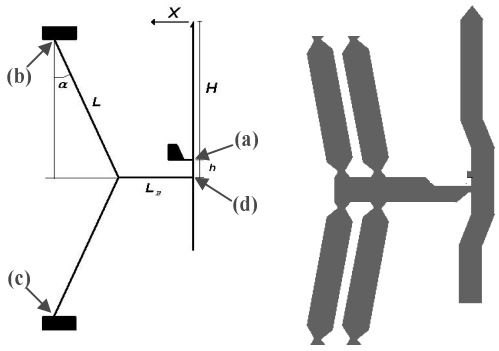

The lancet is fixed at point (a), with length *H* and a distance *h* between the anchor (a) and the junction (d). The tilted arms are fixed at points (b) and (c), with length *L*, inclination α and they are connected with the lancet by an horizontal arm of length L_B . The analytical equation that governs the movement of the lancet *X* deriving from a strain ΔL in the arms can be calculated by simple geometrical relations as follows:

$$X = \frac{H}{h}\left\{\Delta L_B + (L+\Delta L)\sin\left[\arccos\left(\frac{L\cos\alpha}{L+\Delta L}\right)\right] - L\sin\alpha\right\}$$

eq. 1

This equation considers small displacements only, since it does not take into account the non ideality of the junctions involved in the lancet's movement. The layout of the structure to be fabricated was drawn using Tanner Tools L-Edit™ software: a double arm set was implemented to grant a higher momentum to the horizontal beam and the lancet.

2 Lancet simulation

A complete set of finite element simulations was performed using Ansys™ simulation software, assuming the following gold characteristics:
E = 78 GPa, ν = 0.42
An image of the grid and the displaced lancet is reported in figure 2.

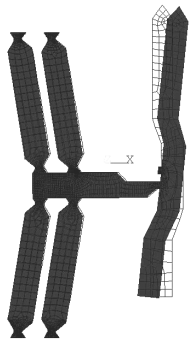

Fig. 2. Meshed structure (α = 10º) with displaced lancet for a simulated stress of 200 MPa.

Different α tilt angles were analyzed, obtaining an optimal tradeoff between potential movement (deriving from eq.1) and real movement which is reduced by non-ideality of the junctions: the maximum movement is obtained with α = 6º. Linearity of the displacement as a function of internal stress was verified both for compressive and tensile regime, as shown in figure 3.

Fig. 3. Simulated stress-displacement curve for a α = 10º arm tilt angle

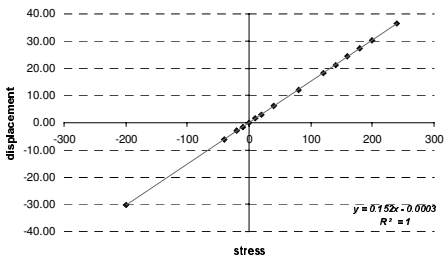

3 Lancet fabrication

A set of prototype lancets with 10º tilt angle was realized using surface micromachining techniques, on 4" diameter (100) oriented silicon wafer substrates. Oxide was initially thermally grown on the substrate, then conventional positive tone photoresist was deposited and patterned as a sacrificial layer. After that, wafers were deposited with a chromium adhesion layer (10nm) and gold seedlayer (150nm) by PVD technique. Then a second photoresist was deposited and patterned, to work as a mould for the electroplating. The structural layer, consisting of gold, was plated by using a commercial sulfite bath solution (AURUNA 591 ™ ammoniumsulfite-gold(I)). After the second photoresist removal, the seedlayer was wet etched. The final release of the structure was performed by removing sacrificial photoresist with dry etching in oxygen plasma, at a temperature of about 190 ºC for 20 min. A photograph of the released structure is reported in figure 4.

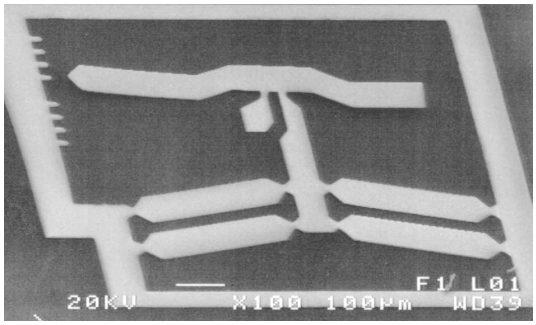

Fig. 4. Photograph of a released structure (α = 10º) with estimated internal stress of about 240 MPa.

4 Results

A novel lancet for in situ stress measurement was designed and fabricated with surface micromachining techniques. Optimization of the geometry was performed by a series of simulations, determining the optimal angle for the tilted arms at 6º. A correction factor of about 0.5 between the theoretical model equation and the simulated values of displacement was obtained, in a range of stress from 10MPa to 200MPa. Linear relation between stress and lancet displacement was confirmed by simulation in a range from highly tensile to highly compressive internal stress. A good agreement between classical lancet and amplified lancet was experimentally verified for stresses about 240 MPa.

References

[1] B.P. van Drieenhuizen, J.F.L. Goosen and P.J. French. "Comparison of techniques for measuring both compressive and tensile stress in thin films", *Sensors and Actuators A.* 37-38 (1993) 756–765.

[2] L. Elbrecht, U. Storm and R. Catanescu. "Comparison of stress measurement techniques in surface micromachining", *J. Micromech. Microeng.* 7 (1997) 151–154.

[3] Yogesh B. Gianchandani and Khalil Najafi. "Bent Beam strain sensors", *Journal of Microelectromechanical Systems* vol.5, no.1 march 1996.

Robust DC Model for the Offset Trimming of an Integrated Thermal Wind Sensor

S. Matova[1], P. Matov[2] and J. Huijsing[1]

[1]Delft University of Technology, ITS/EI, Mekelweg 4, 2628 CD, Delft, The Netherlands
email: s.p.matova@its.tudelft.nl
[2]Technical University – Sofia, EF, 8 Kl.Ohridski Blvd, Sofia 1000, Bulgaria

Summary: *Imperfection of the packaging of an integrated wind sensor causes disturbance of the thermal conditions around the sensor. As a result an offset is added to the measured thermal signals. The offset could be compensated for by adjustment of the heating powers of the sensor. In order to find an efficient way to calculate the compensating powers, using the electro-thermal analogy, a set of models was built. A regulation circuit for automatic compensation was built-in in the models. With its help an analytical expression was found that helps the calculation of the compensating powers. The accuracy and stability of the models was investigated in order to prove the adequateness of the obtained analytical expression.*

Keywords: *automatic compensation, wind sensor, DC bridge*
Category: *1 (General, theoretical and modeling)*

1 Introduction

An integrated wind sensor works on the hot wire principle. The integrated wind sensor consists of four integrated heaters, four thermopiles and a diode [1] (see figure 1). The four heaters ensure the heating of the device above the ambient temperature. Next to the heaters, at the sides of the chip, are positioned the thermopiles. They are connected serially two-by-two. In this manner they measure temperature differences between two opposite sides of the chip and perpendicularly to each other. An airflow passing above the measurement structure would cause temperature difference in the structure. This temperature difference is measured by the thermopiles. The magnitude of the temperature difference gives information about the flow speed. Since two orthogonal components of the temperature difference are measured, the direction of the flow can be easily obtained.

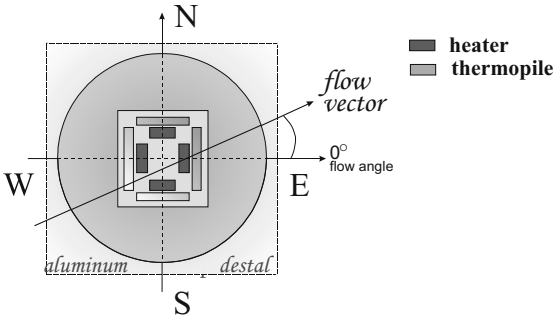

Fig. 1. Schematic view of the sensor.

The chip is turned upside-down and glued to a circular ceramic disc. The disc is placed in the middle of an aluminum pedestal in such a way that the disc and the pedestal form a flat plane. Hence, the chip stays under the ceramic disc shielded from the environment, and the ceramic disc provides the interface with the airflow.

In a perfectly performed packaging the chip is placed exactly in the middle of the ceramic disc. Thus, the thermal conditions around the chip are equal and in the absence of an airflow there is no temperature difference between any points of the structure, which are symmetrically positioned from the center of the structure. The device measures no flow. Because of imperfection of the packaging accomplishment the symmetry in positioning could be disturbed, which in turn causes an asymmetry in the thermal conditions around the sensor (change in the thermal resistances). This means that because of the uneven thermal dissipation, in the device would be temperature differences even in absence of airflow. This offset temperature difference would cause disturbance of the measured flow-thermal signal. Practically the offset signal can be compensated for by adjustment of the power dissipated in the four heaters.

2 Models of the wind sensor

We have developed a robust method for fast calculation of the proper amount of the dissipated in each heater power that compensates for an asymmetry [2]. Firstly, a numerical model was built using CoventorWare and used for the investigation of the thermal asymmetry. It appeared that the numerical investigation is rather time consuming and cumbersome. For speeding up of the process, we used the electro-thermal analogy to built simplified electrical DC models (figure 2.a.). Further, in order to automate the derivation of the heating powers, a negative feedback control circuit was built-in in the PSpice models (figure 2.c.).

An unexpected behaviour of the PSpice models appeared. In theory, the gain and the sign of the feedback determines the accuracy and stability of a

loop. Never the less, these models appeared to produce accurate results even when the feedback coefficient *k* was altered from +1E6 to -1E6 (the gains of E1, E2, E3 and E4 were +1 while those of E5, E6, E7 and E8 were altered from +1E6 to -1E6). An additional theoretical investigation was carried out and a system of 8 Kirhoff equations was made up for the electrical bridge from figure 2.b. The numerical solution of this system of equations showed that the DC bridge is not always balanced and this will result in at least two values of *k* at which the compensation is impossible or fails close to the poles of the transfer function. These values appeared to be quite different compared to the above-mentioned ±1E6. Hence, the proposed PSpice electrical models are always adequate regardless the sign of the feedback coefficient, except for some particular values for which the compensation was found impossible.

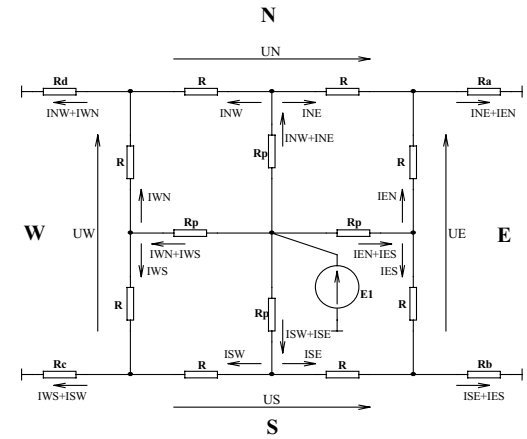

a.

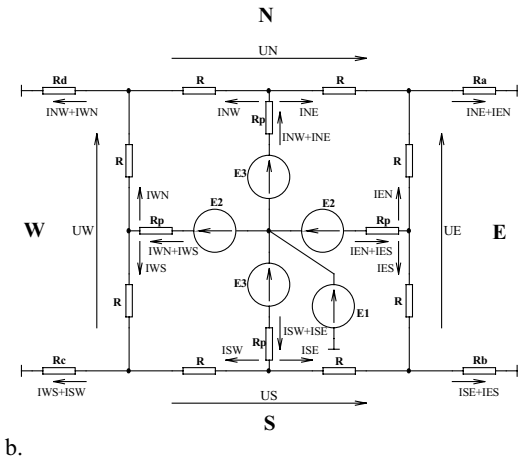

b.

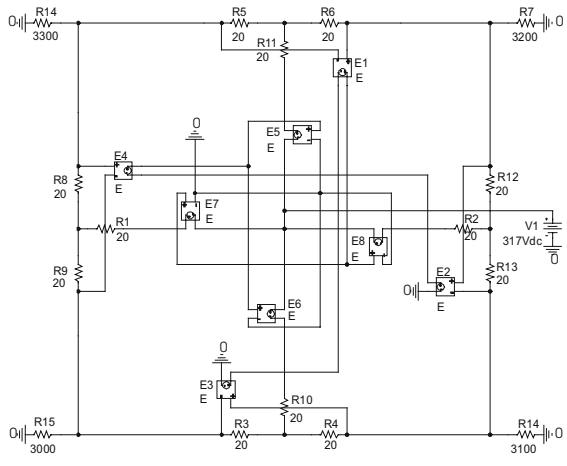

c.

Fig. 2. DC model of the wind sensor.

3 Conclusions

Using the results, obtained from the electrical models for different displacements, an analytical expression was found for a fast calculation of the required compensating powers [2]. With the help of this expression in the numerical model a compensation of displacements was achieved with inaccuracy |6.4|% in the flow speed and |1.6|° in the flow angle. For comparison, in the real device the amplitude inaccuracy is |4|% and the angle inaccuracy if |3|° after a manual trimming of the compensating powers. Also, measurements with the real device showed that the required compensating powers obey the derived analytical dependency.

References

[1] Van Oudheusden, B. W., Silicon thermal flow Sensor with a two-dimensional direction sensitivity, *Measurement Science and Technology V.1* (1990) pp.565-575

[2] S. Matova, K. Makinwa, J. Huijsing, Modeling and compensation of packaging asymmetry in a 2-D wind sensor, *Proc. 8th THERMINIC,* pp.70-73, Madrid, Spain, 1-4 October 2002.

Analytical and Finite Element Modelling of a Capacitive Accelerometer

R. Houlihan[1], K.-L. Chee and M. Kraft

[1]University of Southampton, ECS Dept., Highfield, Southampton, UK
email: rh00r@ecs.soton.ac.uk

Summary. *A three-degree of freedom accelerometer is presented which employs differential capacitance sensing and electrostatic force feedback. Empirical models for the capacitance and the electrostatic force are derived and compared with finite element results. Both conventional and MEMS dedicated finite element software are employed and comparisons between the two are made. The damping force due to the squeeze film effect has been extracted from the simulations and is to be incorporated into a system level model of the accelerometer. The accelerometer has been designed and fabricated and initial test results will be included in the final paper.*

Keywords: acclerometer, force-feedback, electrostatic levitation, finite element modelling
Category: 1 (General, theoretical and modeling)

1 Introduction

An accelerometer is presented which employs as its proof mass an electrostatically levitated micro-disc. Above and beneath the disc are arrays of pie-shaped electrodes with which the differential capacitance is measured and the electrostatic feedback force generated. Figure 1 shows the disc in its nominal position between the electrodes i.e. with the three actively controlled degrees of freedom, z, ϕ and θ, equal to zero. The pick-off and feedback signals are time-multiplexed and the figure illustrates both scenarios.

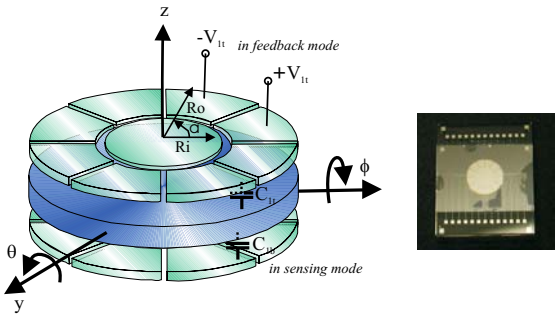

(a) (b)

Fig. 1: (a) Disc and electrode configuration showing both feedback and sensing modes of operation and (b) assembled device comprising a sandwich of three wafer layers.

2 Modelling of the Accelerometer

Determination of the capacitances between the disc and the electrodes and of the electrostatic force applied to the disc by energising the electrodes is non-trivial. Analytical expressions have been derived [1] and are given by Equations 1 and 2 respectively.

$$C_{1t} = \varepsilon_0 \Big(\frac{\pi(Ro^2 - Ri^2)}{4z_t} + \frac{(Ro^3 - Ri^3)(\theta - \phi)}{3z_t^2} + \frac{(Ro^4 - Ri^4)(\pi\theta^2 + \pi\phi^2 - 4\phi\theta)}{16z_t^3} + \ldots \Big) \quad (1)$$

$$Fz_{1t} = \frac{\varepsilon_0 V_{1t}^2}{2} \Big(\frac{\pi(Ro^2 - Ri^2)}{4{z_t}^2} + \frac{2(Ro^3 - Ri^3)(\theta - \phi)}{3z_t^3} + \frac{3(Ro^4 - Ri^4)(\pi\theta^2 + \pi\phi^2 - 4\phi\theta)}{16z_t^4} + \ldots \Big) \quad (2)$$

The use of a Taylor's expansion and corresponding approximations in deriving the equations were validated using finite element simulations. To this end, two finite element tools were considered: ANSYS, a generic simulation software package which, in recent releases, has included elements and analysis methods to facilitate modelling of MEMS devices [2] and Coventorware, a specific MEMS-dedicated simulation tool [3]. The model for the former is shown in Figure 2. A simple quarter model of the airgap between the electrodes and the disc is considered. The gap is modelled with a tetrahedral electrostatic solid element and by applying voltages to the electrode surfaces, an electric field is generated. The Coventorware model, shown in Figure 3 is more involved. By defining masks and performing a series of deposition and etch steps, a full model of the accelerometer is achieved.

A comparison between the capacitance results of the two finite element models and the empirical model is shown in Figure 4. The disc modelled has a radius of $500\mu m$ and the capacitive gap between the electrodes and the disc is $5\mu m$. It can be seen that the only significant variation between the analytical and ANSYS

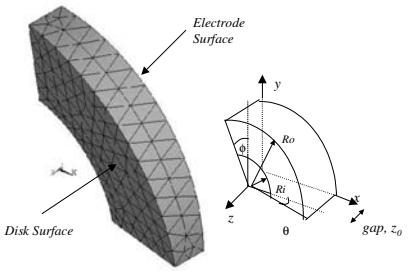

Fig. 2: The ANSYS quarter model of the accelerometer in which only the airgap between the electrodes is modellec

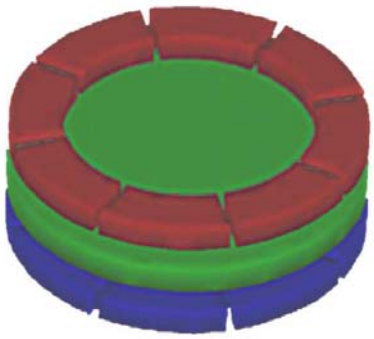

Fig. 3: The Coventorware model of the accelerometer which is built based on a series of deposition and etch steps

models occurs for large angles of rotation. This is a consequence of assumptions made in the derivation of the analytical model [1] and of taking expanding the Taylor series to a finite number of terms. The discrepancies between the ANSYS and the Coventorware results are thought to be attributable to the fact that the latter accounts for fringe capacitances whereas its generic counterpart does not. That the greatest deviation between the two occurs when the disc is at its maximum tilt towards the electrode provides evidence for this. From Figure 5(b), it can be seen that disagree-

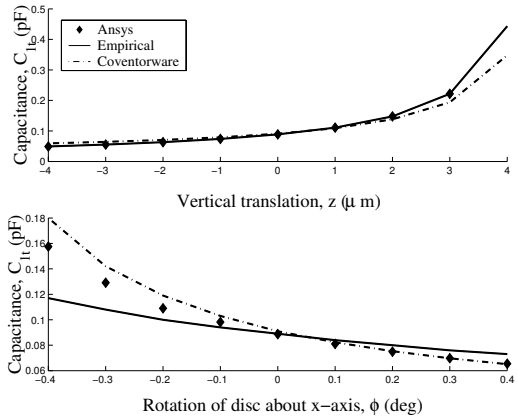

Fig. 4: Comparison between capacitance results as determined by ANSYS, Coventorware and the analytical model given by Equation 1.

ment between ANSYS and Coventorware results for the electrostatic force acting on the disc when all of the upper electrodes are energised, is approximately 10%. The feedback signal to the disc is a high frequency sig-

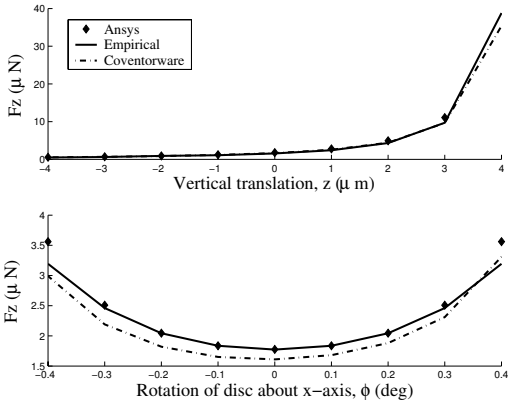

Fig. 5: Comparison between the electrostatic force, Fz on the disc when all of the upper electrodes are energised. ANSYS, Coventorware and the analytical model given by Equation 2 are compared.

nal ($\sim 100kHz$) which will cause the disc to fluctuate very rapidly about its nominal position. Squeeze film damping must be included therefore in any system level model of the accelerometer. Figure 6 shows the variation in the spring and dashpot contributions to the overall squeeze film damping force with increasing frequency. In the final paper, a system level Simulink model will be used to establish the effect of the damping on the device performance.

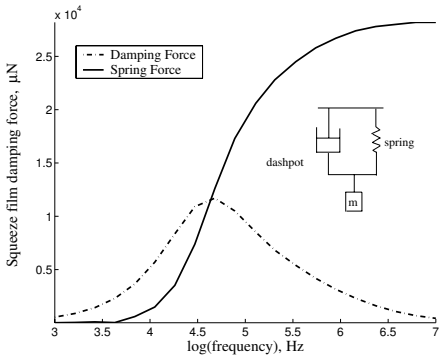

Fig. 6: Variation of spring and damping components of squeeze film damping force with frequency and at atmospheric pressure

References

[1] R. Houlihan, A. Kukharenko, M. Gindila and M. Kraft. *Proc. 2001 Symposium on Micromachining and Microfabrication* **4558**, pp. 277–286, San Francisco, 22–24 October (2001) SPIE.

[2] http://www.ansys.com/ansys/mems/applications.htm

[3] http://www.coventor.com/mems-software/

Backscattering Properties for Red Blood Cell Imaging System with High Frequency Ultrasonic Transducers

Shih-Jeh Wu[1], Ihyuan Kuo[2] and K. Kirk Shung[3]

[1]I-Shou University, M.E. Dept., Kaohsiung, Taiwan, email: wsj007@isu.edu.tw
[2]LeDron Technology, Chiayi, Taiwan, email:ledron.corp@msa.hinet.net
[3]University of Southern California, BioEng. Dept., Los Angeles, California

Summary: *High frequency ultrasonic imaging from blood is difficult due to its tenuous backscattering backscattered pressure. To increase the sensitivity focused transducer has to be used, thus raising the complexity of interpreting the received signals. A numerical simulation of the ultrasonic scattering property from erythrocyte and rouleau based on boundary element method was performed with experimental results based on a modified substitution method. The results (proportional relationship between backscattered pressure and frequency and the frequency limit for Rayleigh scattering) closely coincide with experimental data for erythrocyte. Rouleaux model results also show the dependence of degree of red cell aggregation on backscattering properties.*

Keywords: *focused ultrasonic transducer, red blood cells, boundary element method.*
Category: *1 (general, theoretical and modeling)*

1 Introduction

Nowadays, the application of high frequency medical ultrasound imaging has gained wide popularity in recent years for its superiority in resolving tissue structure. Ultrasonic microscope for biological tissues has also been proposed in numerous different clinical applications from intracascular imaging, Doppler flowmeter to ophthalmological and dermatological diagnostics since it can detect superficial blood flow down to capillary vessels [1,2].

The ultrasonic backscattering coefficient from blood is proportional to the fourth power of frequency. When the ultrasound frequency increases the ultrasonic backscattered signal from blood may increase dramatically and interfere with the backscattered signal from surrounding tissues. In high frequency intravascular imaging this can cause the blurring of vessel images and make it difficult to distinguish the tissue-blood boundary. Better understanding of high frequency scattering property of blood is necessary for designing the imaging system. However, experimental measurement of scattering coefficient of blood at frequency higher than 30 MHz is difficult to perform because of the increased attenuation. It's imperative to use focused transducer. This raises the problem of how to define and measure the backscattering coefficient since the incoming wave was assumed to be planar in the well known substitution method [3].

2 Methodology

Simple analytical solution of scattering from blood or other tissue cells has been obtained by Born approximation assuming spherical shape and uniform acoustical properties of scatterers. In this paper a three dimensional boundary element method [4,5] based on integral Helmholtz equations is used to calculate the scattering field from erythrocyte and rouleaux along with T-matrix method from planar and spherically focused wave. The simulation results were compared with experimental data by modified substitution method.

A single red blood cell is modeled as a fluid filled region enclosed by a surface S (as illustrated in Figure1).

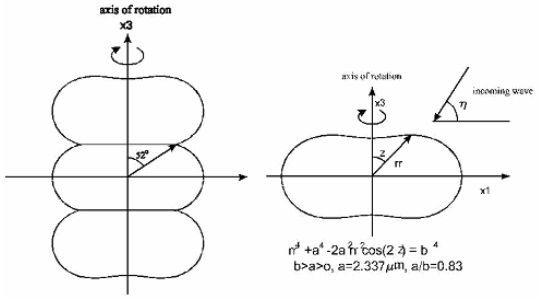

Figure 1 Erythrocyte and rouleaux models used in BEM.

The effect of the cell membrane is assumed to be negligible. Consider the region outside of the cell, the Integral Helmholtz Equation governing the pressure p and velocity v [5] distribution for the points on the surface can be expressed as

$$\int_S \{p(\sigma)\frac{\partial G(x,\sigma)}{\partial n_\sigma} + i\omega\rho v(\sigma)G(x,\sigma)\}ds(\sigma) = \frac{1}{2}p(x) - P_{inc}(x)$$

where ρ is the density of the fluid media, P_{inc}(x) is the incident pressure and p(x) is pressure distribution on surface S at point x. $G(x,x')$ is the Green's function at x with respect to x'. C is the speed of sound in exterior region, k is the wave number. On the other hand, if the region inside the

cell is considered, the equation governing the surface pressure distribution in a source free region is

$$\int_s \{p(\sigma)\frac{\partial G_i(x,\sigma)}{\partial n_\sigma} + i\omega\rho_i v(\sigma)G_i(x,\sigma)\}ds(\sigma) = -\frac{1}{2}p(x),$$

and the surface is divided into many small area elements. From these two equations the pressure and velocity distribution on each element can be solved. The scattered pressure field P_s(x) at any field point can then be obtained as

$$P_s(x) = P(x) - P_{inc}(x) = \int_s \{p(\sigma)\frac{\partial G(x,\sigma)}{\partial n_\sigma} + i\omega\rho v(\sigma)G(x,\sigma)\}ds(\sigma).$$

With this approach the scattered pressure from arbitrary scatterer and incident pressure can be obtained.

Backscattering coefficient is a measure of the scattereing capability of certain object and it requires the assumption of planar incident waves. We used a modified substitution method[6] to obtain the backscattering coefficient from focused transducer experimentally and Figure 2 is the schematic of the spherically focused transducer.

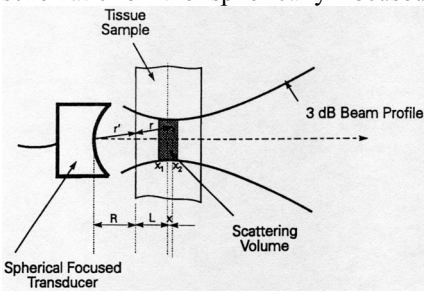

Figure 2 Schematic of the spherically focused transducer.

2 Results and Discussion

Figure3 shows the results of planar incident waves from single cell. The data shows linearity at frequency lower than 100MHz and good match with experimental data performed with red cell solution.

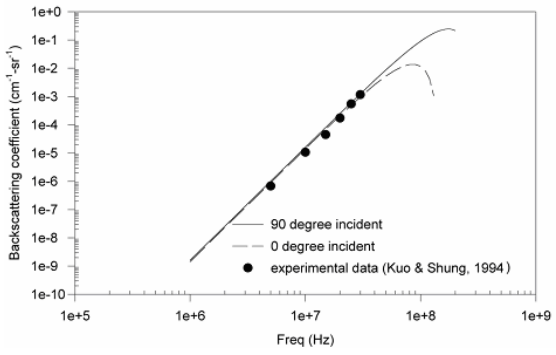

Figure 3 BEM backscattering results at 0 and 90° incident planar wave compared with experimental data.

Figure 4 is the comparison of measurements and computational results from two different focused transducers. The linearity is slightly skewed from planar wave cases but generally the numerical and experiment data matched well. Figure 5 shows the results from rouleaux and effect of the angle of incidence is more significant for longer aggregation. This information could potentially be used to estimate degree of cell aggregation.

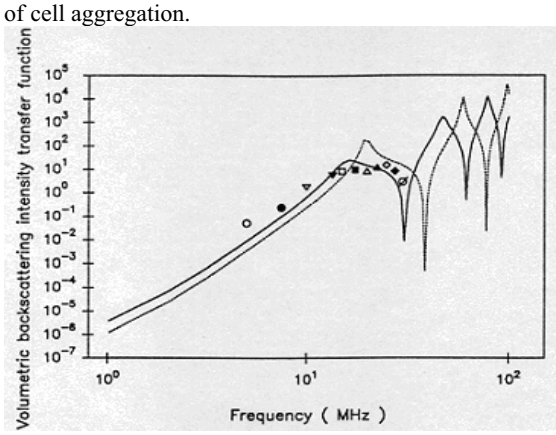

Figure 4 Experimental and theoretical backscattering results from porcine erythrocytes by focused transducers.

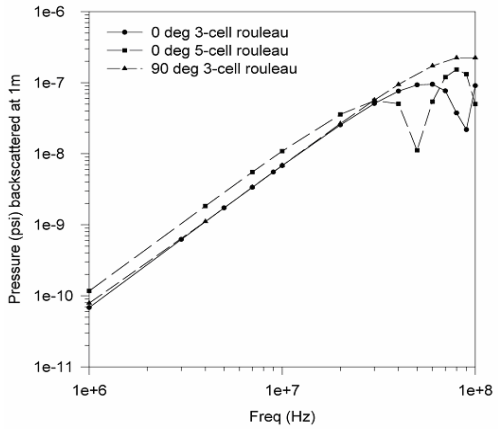

Figure 5 BEM backscattering results from rouleaux at 0 and 90 ° incident planar wave compared with experimental data.

References

[1] K. H. Ferrara, B. G. Zagar, J. B. Sokil-Melgar R. H. Silverman, and I. M. Aslanidis, "Estimation of Blood Velocity with High Frequency Ultrasound," IEEE Trans. UFFC Vol. 43, No. 1 (1996) 149-57.

[2] S. Maravada, K. K. Shung, and S. H. Wang, "High Frequency Backscatterer and Attenuation Measurements of Porcine Erythrocyte Suspensions Between 30-90 MHz," Ultrasound in Medicine and Biology, (2002) 1081-8.

[3] R. A. Sigelmann and J. M. Reid, "Analysis and Measurement of Ultrasound Backscattering from an Ensemble of scatterers excited by Sine-wave Bursts," J. Acoust. Soc. Am., 53 (1973) 1351-5.

[4] W. Tobocman, "Calculation of Acoustic Wave Scattrering by Means of the Helmholts Integral Equation," J. Acoust. Soc. Am., 76(1984) 599-607.

[5] R. D. Ciskowsky and C. A. Brebbia *Boundary Element Methods* in Acoustics, (1991) Elsevier New York.

[6] I. Y. Kuo and K. K. Shung, "High Frequency Ultrasonic Scatterering from Erythrocyte

Flow study in both turbulent and laminar flow with a system of thermal flow and capacitive pressure sensors

G. Kaltsas[(1)], D. Goustouridis[(1)], A. G. Nassiopoulou[(1)], D. Tsoukalas[(2)], S. Chantzandroulis[(1)]

[(1)] IMEL/NCSR Demokritos, P.O. Box 60228, 15310 Aghia Paraskevi, Athens, Greece
Tel: +30-1-6503247, Fax: +30-1-6511723
Web: http://www.imel.demokritos.gr e-mail: G.Kaltsas@imel.demokritos.gr
[(2)] School of Applied Mathematics and Physics/NTUA, Iroon Polytexneiou 9, 15780 Zografou, Athens, Greece

Summary: *A combination of a silicon thermal flow and two capacitive pressure sensors on the same substrate, in a specially designed housing, is proposed for high sensitivity flow measurements in both laminar and turbulent flows. The system of the 3 sensors can determine the transition point between laminar and turbulent region with sufficient accuracy. Good agreement between experimental results and theory was found.*

Keywords: *flow sensor, pressure sensor, laminar flow, turbulent flow, transition point*
Category: *8 (Packaging, chip handling, test and reliability)*

1. Introduction

Exact determination of gas flow is a critical parameter in many applications. Various gas flow sensors have been presented in the literature, most of them being of the thermal type. With these sensors one can measure with high accuracy laminar or turbulent flows, but there is limitation in measuring with the same sensor the flow in both laminar and turbulent regions. These limitations are intrinsic to the sensors principal of operation. In the present work we propose to combine a gas flow and a pressure sensor on the same substrate for sensitive flow measurement in both laminar and turbulent region.

2. Experimental set-up

The gas flow sensor [1] is of the thermal type and it is based on the differential temperature measurement principal. It consists of two thermopiles, situated symmetrically on both sides of a heating resistor. The thermal isolation from the silicon substrate is assured by a thick porous silicon layer [2]. A constant power is applied to the heater and the sensor signal is measured as the voltage difference between the two thermopiles. The sensor is described in detail elsewhere [1]. With zero flow the temperature distribution around the heater is homogenous, so the two thermopiles indicate the same value. When flow is applied the upstream thermopile is cooled down and the downstream thermopile is heated up. Flow is determined by measuring the differential output from the two thermopiles.

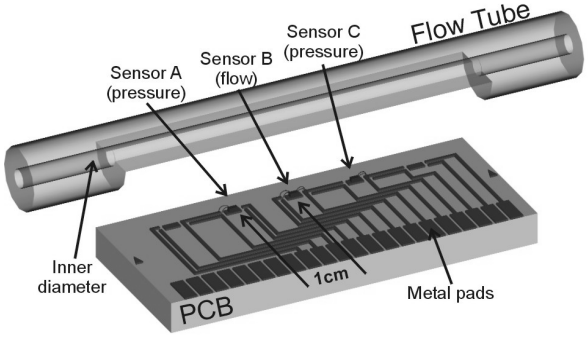

Figure 1: Sensors configuration and packaging.

The pressure sensor is of capacitive type and it is fabricated by bulk micromachining, using silicon fusion bonding and anisotropic wet etching techniques. It consists of an array of 6 membranes with diameter and thickness 250 μm and 3.5 μm respectively. The sensitivity of the sensor is 1.2fF/mbar, and its response in the range 0 – 200mbar is linear with accuracy better than 2%. The sensor is described in detail elsewhere [3].

The two types of sensors were mounted and bonded on the same printed circuit board (PCB), as in fig. 1. Two pressure sensors (A, C) and one flow sensor (B) were used. The flow sensor was situated in the middle of the two pressure sensors, in 1 cm distance from each of them. The PCB was hermetically sealed with a specially designed semi-cylindrical housing. The sensors were wall mounted in the bottom of the flow tube. The effective diameter and the length of the tube were 1.71 mm and 6 cm respectively. With this configuration we can measure flow and pressure difference simultaneously. The PCB is designed to hold another two sensors (fig. 1), for more precise determination of the flow profiles and parameters.

The flow measurement set-up is described in detail elsewhere [1]. It consists of the gases, a set of mass flow controllers (MFCs) and a network of pipes and valves. Three different flow ranges can be used, 0-1, 0-10 and 0-200 SLPM, depending on the selected MFC. The reference flow can be set with an accuracy of ±1% for each region. Pure nitrogen was used in all the experiments.

3. Results

The flow sensor response is shown in fig. 2. The sensor signal increases with flow, up to a value of about 3 SLPM, due to the increase of the heat transfer between the fluid and the sensor and then decreases for higher flows. This effect is due to the change from laminar to turbulent flow. Indeed, with the current experimental set-up the value of 3 SLPM corresponds to a Reynolds number (Re) of 1750, which is according to theory, close to the maximum number for laminar flow (Re=2000). From this behavior it is clear that the flow sensor can be used for the determination of the transition point between laminar and turbulent flow region, which is critical in many application and especially in aeronautics. The exact determination of the transition point, in combination with flow control, can contribute to the reduction of the flight cost.

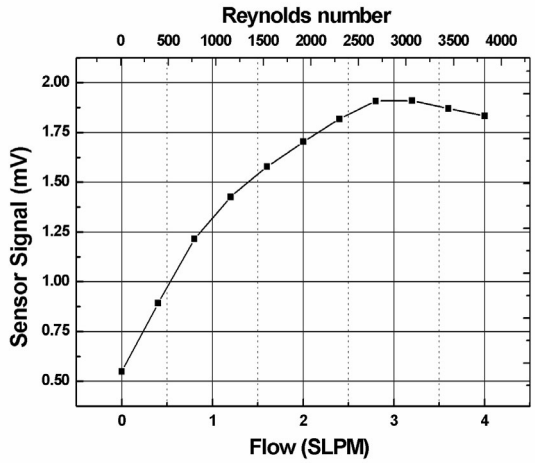

Figure 2: Flow sensor response.

The responses of the two pressure sensors are illustrated in fig. 3. The flow direction is from A to C. We can observe that the signal from sensor A is higher than that of C, as expected, since the pressure drops along the flow direction. The Bernoulli's equation predicts that the pressure difference should be given by the following formula:

$\Delta P = \gamma h_L$,

where γ is the fluid specific weight and h_L represents the energy losses due to friction in pipes. The energy losses are expressed through Darcy's equation [4]:

$$h_L = f \frac{L}{D} \frac{u^2}{2g},$$

where f is the friction factor (dimensionless), L and D are the length and the diameter of the tube respectively and u is the flow velocity. The friction factor is determined experimentally and it can be extracted from Moody's diagram [4]. Generally it depends on the Reynolds number and on the roughness of the pipes.

Fig. 3 illustrates the pressure sensors signal as a function of the square root of flow velocity. An almost linear relation is extracted for pressure difference, as well as for each sensor for the region above Re=9000, which is in agreement with the

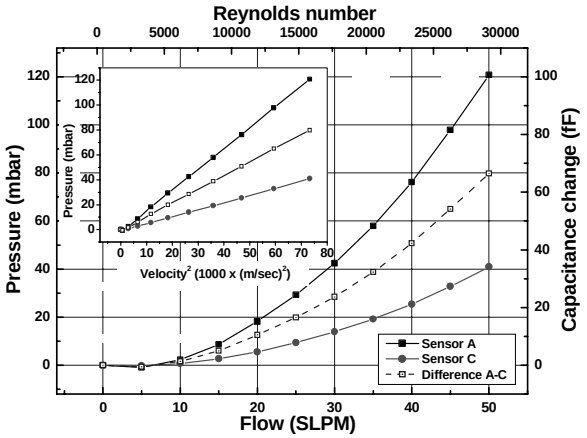

Figure 3: Pressure sensor response.

Bernoulli's equation. For the specific flow region the friction factor changes from 0.032 (Re=9000) to 0.023 (Re=29000), assuming that we use smooth pipes.

In the case of pressure sensor we can observe that the sensitivity is low in the laminar region but it increases as the flow passes in turbulent region. It is clear that using a combination of thermal flow and pressure sensors, we can obtain high sensitivity through the whole flow region with the same flow tube. The thermal flow sensor assures high sensitivity in the laminar flow region and the pressure sensor assures high sensitivity in the turbulent flow region. Obviously, with the present configuration there is no need to measure pressure difference, since the pressure sensor structure involves a differential pressure measurement between the fluid and the reference cavity. So, only one thermal flow and one pressure sensor are enough in the whole flow range.

4. Conclusions

A combination of a thermal flow sensor and two pressure sensors was used in order to obtain high sensitivity in both laminar and flow regions. The sensors were mounted on the same PCB and packed with a specially designed housing. Flow measurements were performed with pure nitrogen for Re up to 29000. The transition point can be also determined from the thermal flow sensor response. The results were in exact agreement with theory.

References

[1] G. Kaltsas, A. A. Nassiopoulos and A. G. Nassiopoulou, "Characterization of a Silicon Thermal Gas-Flow Sensor With Porous Silicon Thermal Isolation", IEEE Sensors Journal, 2, No 5, (2002).

[2] A. G. Nassiopoulou and G. Kaltsas, patent application, priority No PCT/GR97/00040.

[3] D. Goustouridis, S. Chatzandroulis, P. Normand ad D. Tsoukalas, "A miniature self-aligned pressure sensing element", J. Micromech. Microeng. 6 (1996) 33-35.

[4] R. L. Mott, "Applied fluid mechanics", Merrill publishing company, London, 1990

3D flow speed imaging system for polymer processing industry

X. Raoul, J. Balcaen, Y. Béreaux, J.Y. Charmeau, D. Graebling & M.Moguedet

Ecole Supérieure de Plasturgie, Laboratoire de Recherche Pluridisciplinaire en Plasturgie (LR2P),
85 rue Henri BECQUEREL – BELLIGNAT, BP 807 - 01108 OYONNAX Cedex
email : raoul@esp-oyonnax.fr http://www.esp-oyonnax.fr

Summary : *The study presented in this article is conducted within a European EUREKA project with industrial partners specialized in polymer processing and academic partners. The part of the project studied in the LR2P deals with the development of new theoretical models to determine the properties of material (glass fibre filled or not) when coming out of an injection barrel/screw unit before being injected into a mould. Developing theoretical 3D models requires experimental validation capabilities. The experimental set-up presented here is constituted of a fluorescent particle detected with cameras coupled to a data processing algorithm to monitor the particle 3D-displacement and flow-speed inside the screw device.*

Keywords : *3D vision, flow speed, platicising stage, injection molding, polymer processing application*
Subject category : *mechanical sensors*

1 Introduction

In polymer processing industry, one of the most interesting aspects is the low weight of the material and the possibility to manufacture complex objects. In addition to the gain in weight, there is also a possibility to produce low-cost objects. Those objects can as well be toys or air injectors in car engines. Applications of interest for the industrial pool concerned by the project are external parts of car (bumpers, wings). Therefore constraints applied on those objects can be very different from one to another. Hence raw material used shall be finely selected (fibres filled or not). The injection moulding process [1] consists in manufacturing a part from polymer pellets, after a passage in a molten state. During plastication, the polymer is subjected to the combined action of the screw in rotation and to an external heating by electric heater bands. At the present moment there exists no theoretical model to design a screw/barrel system given the material chosen. So we propose a dedicated set-up able to monitor in 3D the flow velocity during industrial production.

2 Industrial production concerns

The raw material to be used in the production step is chosen depending on objects to be manufactured (for example, whether it is necessary or not to reinforce the polymer with any kind of fibres to gain in robustness). Once the choice on raw material is done, engineers have to determine the shape of the screw unit. This device is an important part in the material transformation process, because it is supposed to guarantee the conversion of the feedstock of plastic pellets into a molten polymer ready to be injected into a mould. At the present moment to determine the shape of the injection screw engineers have an empirical approach because there exist no theoretical model able to connect the shape of the injection screw and the final properties of the polymer, [2]. Actually, one concern deals with fibre filled polymers and the physical effect of the screw on those fibres (if broken, the polymer loses its expected properties). Another aspect of concern is the homogeneity of the polymer depending on the time spent inside the screw/barrel unit and the shape of the screw. Homogeneity of the melt polymer with fillers is important for final objects' mechanical property. Time spent by the material inside the barrel coupled with temperature (>200°C), [3], are major parameters in the perspective of chemical degradation of the polymer.

3 The experimental set-up proposed

To try to solve the problem, once usually uses some extruder with transparent window and a single camera to monitor the displacement of a particle, [4], in this given window. This kind of systems presents the inconvenient of a partial 2D-estimation of the flow speed. In our laboratory we are developing a new system able to give the 3D displacement and velocity of a particle in a fluid even during industrial production (cf figure 1).
It is constituted of an extruder (cf figure 2) fixed on a rigid structure and of a displacing system of 4 digital cameras (BASLER® A301f at 80 fps each) along the structure.
Having 4 cameras guarantees the fact that the particle is always seen by 2 cameras and allows to estimate the 3D-displacement of a fluorescent particle. The particle is injected in the fluid and

illuminated by UV light sources. Data acquired by cameras (cf figure 3) are transferred in real time to PC to be processed.
Post signal processing extracts displacement and estimates velocity of the particle (cf figure 4). Each circle in the figure represents the barycentre of the particle detected and located by image processing. We notice two speed states : the first one corresponding to a high speed state (short distance between two consecutive points) due to a displacement of the particle along the bottom of the flight of the screw and a low speed state due to a displacement of the particle near to the inside surface of the barrel.
This first interesting result highlights the necessity to monitor in 3D the displacement of the particle.

4 Conclusions & Perspectives

The system presented in this abstract proposes a new possibility to estimate polymer's properties while being molten and verifying models for screw design. The ability to monitor in 3D the displacement and velocity of a particle in the polymer without any information or manipulation on the screw/barrel unit allows to run this estimation in industrial units.

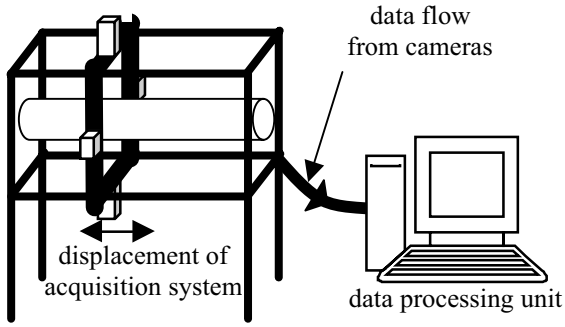

figure 1 : 3D vision system of flow speed in an industrial extruder with 4 cameras fixed on mobile structure around the screw/barrel unit

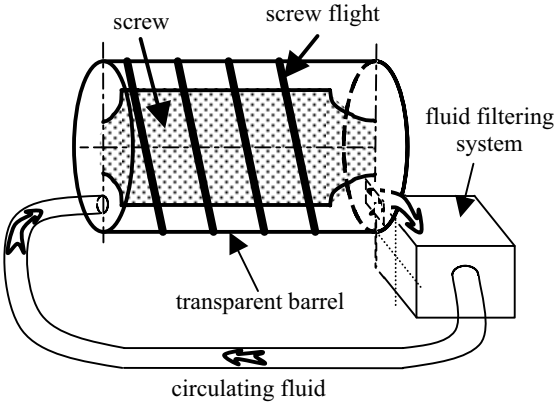

figure 2 : complete cycle of the fluid in the screw/barrel unit

We can already imagine that the difference in refraction indexes of polymer and extruder's plexiglass® will have to be taken into account during the image processing to calculate the 3D-position of the particle.

Acknowledgements

Support granted from Plastic Omnium, Dow Chemical and Engel.

References

[1] : J.F. Agassant, P. Avenas, J.P. Sergent , B. Vergnes et M. Vincent, "*La mise en forme des matières plastiques*", Technique et Documentation, Lavoisier, Paris, (1996,) 3° édition

[2] : G.A. Campbell, S. Bomma, S. St John & S. Chempath, ANTEC2002, pp 1441-1445, San Francisco, USA, May 2002

[3] : N. Pierre, Y. Bereaux, D. Graebling, J. Balcaen & J.Y. Charmeau, Int. Conf. on Industrial Tools, ICIT 2003, 08-10 April 2003, Bled, Sloveny

[4] : W. Song, J. Perdikoulias, M.Planeta, ANTEC2000, Orlando, USA, 7/11 May 2000

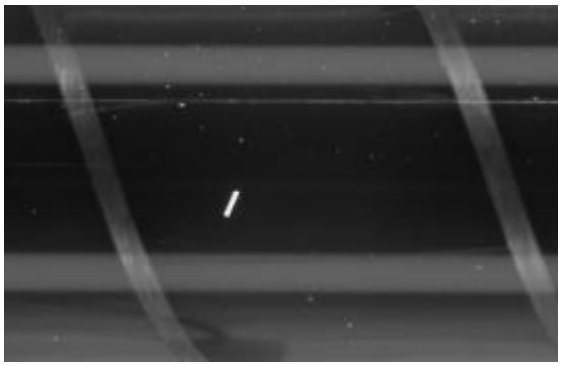

figure 3 : example of raw data recorded by one camera

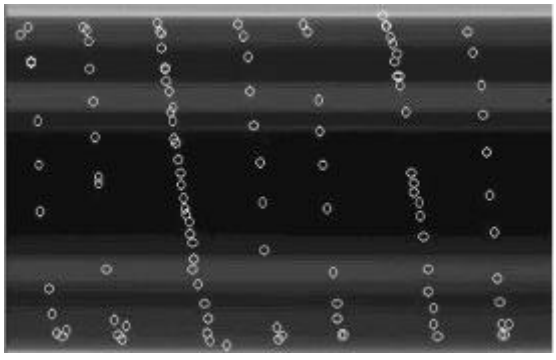

figure 4 : first estimation of successive positions of the particle along the screw in 2D with a single camera

Effect of photoresponse non-uniformity on light spot centroid detection

Anssi Mäkynen and Juha Kostamovaara

University of Oulu, Department of Electrical and Information Engineering,
FIN-90014 University of Oulu, Finland
email: anssi.makynen@ee.oulu.fi

Summary: *Experimental results of the effect of CMOS photodetector photoresponse non-uniformity (PRNU) on light spot centroid detection are presented. The results show, that for spot sizes below 0.1 mm the effect of PRNU remains clearly below 1 μm (standard deviation). This means that although CMOS photodetectors typically have quite high PRNU it is possible to implement accurate position-sensitive devices (PSDs) using standard CMOS technology.*

Keywords: *CMOS photodetector, photoresponse non-uniformity, position-sensitive detector*
Category: *4 (Non-magnetic physical devices)*

1 Introduction

An optical position-sensitive photodetector (PSD) identifies light spot position by detecting its centroid position. Good accuracy presupposes among other things that the spatial photoresponse of the PSD must be fairly uniform. Uniform photoresponses (non-uniformity << 1 %) are achieved using technology tailored for photodetector production. In case PSDs are implemented using non-tailored technologies such as CMOS, the large photoresponse non-uniformity (PRNU), which is characteristic for CMOS photodetectors, may lead in serious deterioration of the position sensing accuracy. This paper deals with the quantity of position sensing error caused by the PRNU of a typical CMOS photodiode.

2 CMOS PSD

Implementing PSDs using standard CMOS technology instead of dedicated photodetector processes has two potential advantages: first, the compactness of the sensor can be improved by implementing all the electronics and the detector on a single chip, and secondly, the sensor's overall performance may be improved using special PSD structures not probably realizable in conventional photodetector processes [1]. The obvious drawback of CMOS technology is that it is not designed for light detection and thus does not provide best possible performance in that sense.

CMOS photodetectors, such as well-substrate photodiodes, are suitable for optical sensing applications where a responsivity ranging from 0.1 to 0.4 A/W (quantum efficiency <50 %) is sufficient, and a relatively large spatial and spectral non-uniformity in responsivity can be tolerated, and where high speed and low crosstalk are not of importance [2]. The fairly large PRNU of CMOS photodetectors, which directly alters the sensed centroid position of the light spot, may be detrimental to PSD linearity. However, experimental studies have shown that the linearity offered by CMOS PSDs are equal to the best quality commercial (non-CMOS) PSDs the nonlinearity error being only a few micrometers (standard deviation) at most [1,3].

This paper reports experimental results of the CMOS photodetector PRNU and its effect on light spot centroid detection. The contribution of the PRNU on centroid error as a function on spot size, wavelength and wavelength bandwidth is calculated from the measured spatial responsivity data of a BiCMOS compatible diffusion-well photodiode.

3 PRNU of CMOS photodetector

The simplified cross-sectional construction of a BiCMOS compatible diffusion-well photodiode and its typical spectral and spatial responsivities are depicted in Fig. 1. The quantum efficiency of the detector is relatively low especially at longer wavelengths due to the narrow depletion region located near the surface. The distances of the upper and lower edges are approximately 0.3 μm and 0.8 μm from the Si/SiO_2 surface, respectively. The maximum quantum efficiency (~50 %) is typically achieved at the center of the visible range. Light interference within the protection layers cause fluctuations in both spectral and spatial photoresponses. The magnitude and spatial shape of the fluctuations depend on the wavelength bandwidth and spot size used.

The PRNU scanning of a 200 μm x 200 μm diffusion-well photodiode was performed with 2 μm steps using 2.5 μm spot size (FWHM) and wavelength bandwidths of 5 nm and 32 nm (FWHM) and center wavelengths of 630 nm and 850 nm. The average values of responsivity

corresponded to those measured with spectral scanning (0.052 A/W at 850 nm and 0.155 A/W at 630 nm). The relative standard deviations of the measured PRNU varied from 1 to 5.3 % (Table 1.) within the central region of the photodiode (side length 80 % of the total side length of the active area). Narrowband illumination and shorter wavelengths seem to result in higher PRNU than broader and longer ones. The above suggests that near infrared LEDs should be used as the light source instead of visible laser diodes in order to get small PRNU.

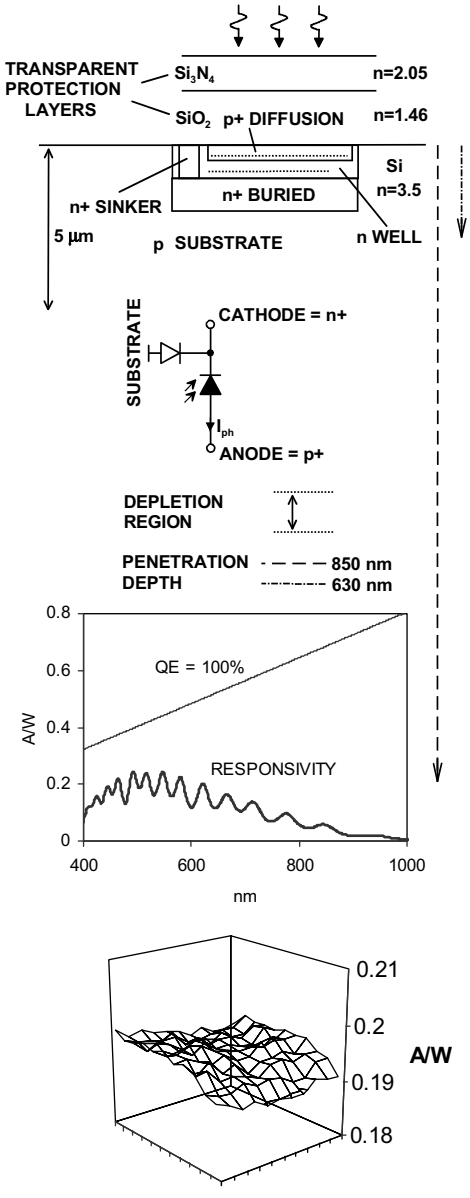

Fig. 1. Cross-section of a diffusion-well photodiode in a 0.8 µm BiCMOS process. Light interference within the protection layers cause fluctuations in spectral and spatial responses.

4 Centroiding error

The spatial responsivity results were used to calculate the error in the centroid position of a uniform round light spot of 10, 20, 30, 50, 100 µm in diameter by moving the spot vertically and horizontally around the detector active surface in 2 µm steps. The portions used for the spot movement were 30 % of the active area side length in case of 50 µm and 100 µm spots, and 65 % of the length in case of the smaller spots. The results are presented in Table 1. Centroid error depends on spot size, PRNU and bandwidth of illumination. A large spot size, high PRNU and narrowband illumination increases the error. According to the results, however, the error (<< µm) due to the PRNU is clearly less than what is typically measured for high quality PSDs (> µm). This means that it should be possible to implement highly accurate PSDs (position sensing error < µm) using standard CMOS technology. Note, however, that this presumes relatively small spot size (<< mm) and that optimum performance is achieved using relatively wideband illumination source such as an LED. Note also that centroid detection accuracy does not depend on wavelength (although PRNU seems to increase towards shorter wavelengths). This means that visible illumination providing the best quantum efficiency and hence best precision can be used without deterioration in accuracy. Results presented in Ref. [1] support the above conclusions.

Table 1. Standard deviations of the photoresponse non-uniformity (PRNU) and the centroid error for a round uniform spot of diameters 10, 20, 30, 50 and 100 µm.

Wavelength / bandwidth	PRNU	Standard deviation [nm] (Spot diameters in µm)				
	[%]	10	20	30	50	100
630 / 5 nm	5.3	11	34	88	140	300
630 / 32 nm	2.5	4	9	22	37	110
850 / 5 nm	1.9	4	13	31	59	160
850 / 32 nm	1.0	3	8	20	38	105

References

[1] A. Mäkynen, T. Ruotsalainen, T. Rahkonen and J. Kostamovaara. CMOS-compatible position-sensitive devices (PSDs) based on photodetector arrays. Provisionally accepted for *Sensors and Actuators A* (2003).

[2] P. Aubert, H.J. Oguey and R. Vuilleumier. Monolithic optical position encoder with on-chip photodiodes. *IEEE J. Solid State Circuits* 23 (1988) 465–473.

[3] J. Kramer, P. Seitz and H. Baltes. Industrial CMOS technology for the integration of optical metrology systems (photo-ASICs). *Sensors and Actuators A*, 34 (1992) 21–30.

Miniaturized solid state dye lasers based on a photo-definable polymer

Søren Kragh and Anders Kristensen

Mikroelektronik Centret (MIC), Technical University of Denmark (DTU)
Building 345east, Ørsteds Plads, DK-2800 Kongens Lyngby
email: ak@mic.dtu.dk http://www.mic.dtu.dk

Summary. *For the first time the widely used photo definable polymer SU-8 has been functionalized with optical gain. This is achieved by doping the polymer with a commercially available laser dye, Rhodamine 6G. We demonstrate this by realizing and characterizing two types of optically pumped micron-sized solid polymer dye lasers. The lasers are designed with lateral emission and have furthermore been integrated with SU-8 polymer waveguides, demonstrating the potential for applications within e.g. lab-on-a-chip microsystems.*

Keywords: SU-8, micro laser, Rhodamine 6G
Category: 4. Non-magnetic physical devices

1 Introduction

The functionality of microsystems, e.g. "lab-on-a-chip" systems, can be enhanced by integration of optical transducers on the chip. Polymer based solid state lasers are attractive devices for such applications, since polymer based micro-chips are widely used for lab-on-a-chip microsystems. Hu et al. [1] demonstrated a millimeter-sized solid state dye laser already in 1976, by casting a commercially available laser dye into a matrix of polyurethane. Li et al. [2] has more recently used modern microfabrication techniques for making similar devices in poly-methymethacrylate (PMMA) by casting and peel-off.

In this paper we present a new type of optically pumped solid polymer dye lasers, which can easily be integrated with polymer based microsystems. The solid state lasers are realized by doping a photo-definable polymer, SU-8, with a commercially available laser dye, Rhodamine 6G. This approach allows for fabricating miniaturized solid polymer dye lasers on any suitable substrate, by applying standard UV lithography to the dye doped photo definable polymer. By using photolithography, a large degree of freedom in design is achieved. Another attractive feature is the simple design, where total internal reflections on the vertical polymer cavity walls are exploited.

The laser dye Rhodamine 6G has optical gain in the wavelength range from app. 550 nm to 620 nm, when it is optically pumped by a pulsed, frequency doubled Nd:YAG laser at a wavelength of 532 nm.

2 Design

We have made two different lateral designs of the micro laser. One is trapezoid shaped, Fig. 1(a), the other is triangular shaped, Fig. 2 - both designs have been scaled to different sizes. The idea is to make a dye doped cavity of SU-8, supporting a mode by total internal reflection at points on all but one side. The point with partial reflectance is used for the output coupling. The critical angle for the SU-8/air interface is $\theta_c = 38.97^\circ$ ($n_{\mathrm{SU-8}} = 1.59$). In the triangular design the desired cavity mode is reflected three times per round trip. The geometry allows for an angle of incidence above the critical angle, θ_c, at two of the reflection points. The angle of incidence at the third reflection point, where the output coupling takes place, is then restricted to be less than 10 degrees, resulting in a reflectance of app. 5 percent in this point. The desired cavity mode in the trapezoid shaped cavity is reflected four times per round trip. This design allows for an angle of incidence, $\alpha = 47.29^\circ$, above θ_c at three reflection points, and an angle, $\beta = 38.14^\circ$, close to but below the θ_c at the fourth reflection point. This allows for a design with a reflectance of 37 percent at the output coupling. It is difficult to obtain much higher values of reflectance at the output coupling, without exceeding the critical angle due to the steep increase in reflectance as the critical angle is approached.

3 Fabrication

The Rhodamine 6G (Sigma-Aldric, R4127) is dissolved into SU-8 thinner, which is mixed into the SU-8 10μm photo-resist, both from MicroChem. The SU-8 based micro laser cavities can then be defined on any suitable substrate using the standard photo-lithographic process steps: spin-coating, soft-baking, i-line UV exposure, post-exposure baking, and development. The structures presented in this paper are fabricated on a glass Pyrex substrate and the height is 4.2μm.

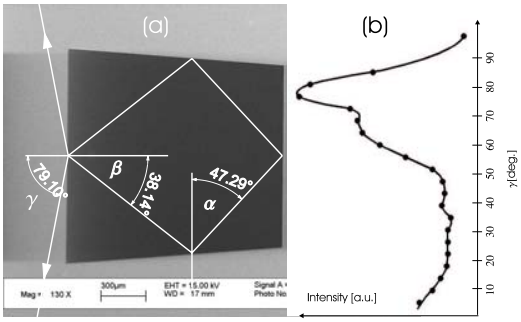

Fig. 1: (a) SEM photo showing the geometry of the trapezoid laser. There is total internal reflection on three of the sides and a reflectance of 37 % at the fourth side where the output coupling is placed. The critical angle of the SU-8/air interface is $\theta_c = 38.97°$. (b) Measured angular distribution of laser emission from the trapezoid laser.

4 Characterization

The lasers are optically pumped by a pulsed, frequency doubled Nd:YAG laser, and the emitted light is collected by an optical fiber connected to a spectrometer. Fig. 3 shows a series of emission spectra from the triangular devices, measured at different levels of pumping power. A lasing peak appears at a wavelength of 562 nm. Fig. 4 shows a similar set of spectra from the trapezoid shaped device, where the peak appears at a wavelength of 598 nm. According to the design, the triangle and trapezoid lasers should emit at an angle of 17 degrees and 79 degrees, respectively. This has been verified in the trapezoid design, where it was possible to measure the output from a single cavity, see Fig. 1(b).

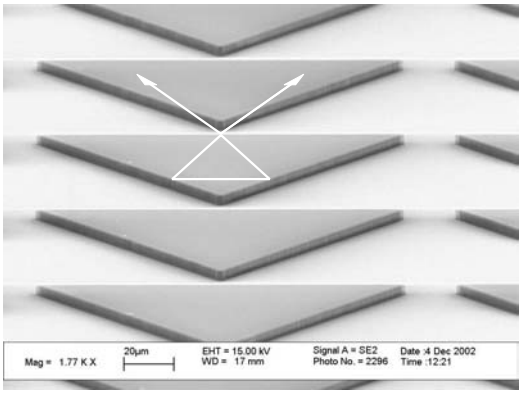

Fig. 2: SEM photo showing the triangular laser design. The round trip is superimposed and is 190 μm long. The reflectance at the output interface is approximately 5 %.

5 Conclusion

We have demonstrated a new type of optically pumped solid polymer dye lasers, by doping the commonly used photo-resist SU-8 with Rhodamine 6G laser dye. Laser

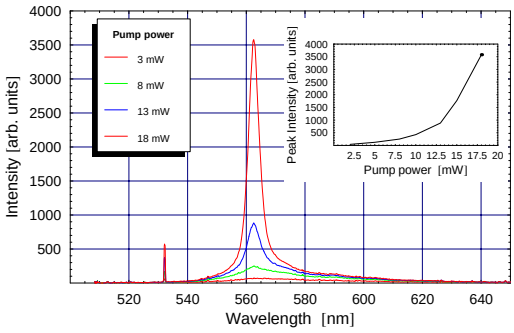

Fig. 3: Spectra measured from an array of laterally emitting triangular shaped lasers. The laser peak is established at 562 nm and the peak at 532 nm is scattered light from the Nd:YAG pump laser.

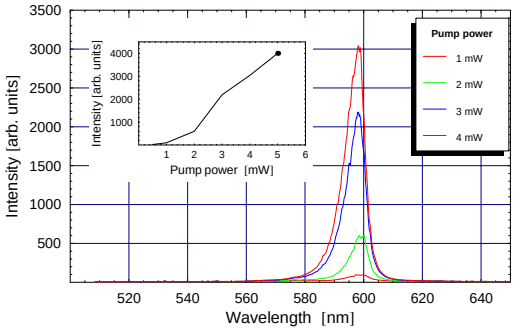

Fig. 4: Emission spectra from the laterally emitting trapezoid laser, see Fig. 1(a). The peak wavelength is 598 nm and is measured in the plane of the laser at an angle $\gamma = 79°$.

cavities of triangular and trapezoid shape with lateral emission were fabricated on a Pyrex glass substrate by standard photolithography, and lasing was demonstrated. As illustrated by the two emission spectra,Fig. 3 and Fig. 4, it is possible to vary the peak wavelength more than 30 nm by change of the lateral design only. Furthermore, by utilizing the good planarization properties of SU-8 we have integrated a laterally emitting dye laser with a SU-8 waveguide. The integrated optical system is realized by two successive UV lithography steps, defining the laser in dye doped SU-8 and the waveguide in normal SU-8. The latter two facts makes the polymer laser very attractive for the development of lab-on-a-chip micro systems.

References

[1] *Thin-film dye laser with etched cavity*, C. Hu and S. Kim, Appl. Phys. Lett. **29**, 582 (1976)

[2] *Fabrication and testing of solid polymer dye microcavity lasers based on PMMA micromolding*, Y. Li, M. Sasaki, and K. Hane, J. Micromech. Microeng. **11**, 234, (2001)

Comparison Between Bulk Micromachined and CMOS detectors for X-ray Measurements

J. G. Rocha[1] C. G. J. Schabmueller[2], N. F. Ramos[3],
S. Lanceros-Mendez[4], M. V. Moreira[4] A. G. R. Evans[2],
R. F. Wolffenbuttel[5], J. H. Correia[3]

[1]University of Minho, Dept. Ind. Electronics, Campus de Azurem, 4800-058 Guimaraes, Portugal.
Tel: +351 253 510190 Fax: +351 253 510189 Email: gerardo@dei.uminho.pt
[2]University of Southampton, Dept. Electronics and Comp. Sci.,
Microelectronics Centre, Southampton SO17 1BJ, UK.
[3]University of Minho, Dept. Ind. Electronics, Campus de Azurem, 4800-058 Guimaraes, Portugal.
[4]University of Minho, Dept. Physics, Campus de Gualtar, 4710-057 Braga, Portugal.
[5]Delft University of Technology, Lab. Electr. Instr., Delft, The Netherlands

Summary: *This paper compares two x-ray detectors fabricated using two different technologies: one is based on a bulk micromachined silicon photodetector and the other is based on a standard CMOS photodetector. The working principle of the two detectors is similar: a scintillating layer of CsI:Tl is placed above the photodetector, so the x-rays are first converted into visible light ($560\ nm$) which is then converted into an electrical signal by the photodetector. The different aspects of the fabrication and the experimental results of both x-ray detectors are presented and discussed.*

Keywords: *x-rays, scintillator*
Category: *4 (Non-magnetic physical sensors)*

1 Introduction

The two detectors reported and compared in this article are based on the same working principle: a scintillator material is placed above a photodetector. When the x-ray photons reach the scintillator, they are absorbed and converted into visible light. This visible light is then transformed into an electrical signal by the photodetector. One of the photodetectors is based on a sn-sub junction placed inside a bulk micromachined cavity [1]. The other one is based on a CMOS standard sn-sub junction [2].

2 Bulk micromachined x-ray detector

A cavity with $2\ mm \times 2\ mm$ square size and $400\ \mu m$ depth is fabricated in a p-type silicon substrate using KOH etching. Inside the cavity, arsenic is implanted in order to form the sn-p junction of the photodiode. After that, the cavity is filled with a scintillating material (CsI:Tl) and finally, a reflective layer is placed above the scintillating material [1]. Figure 1 shows a schematic cross section of the device. Figure 2 shows a picture of the device before the placement of the scintillating material and the reflective layer.

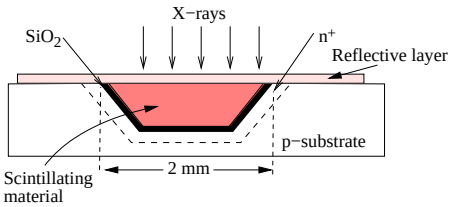

Fig. 1: Cross-section of the BMM x-ray detector.

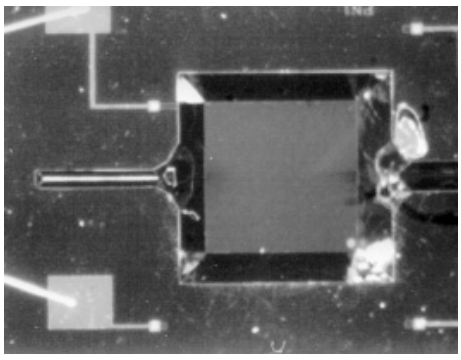

Fig. 2: Picture of the BMM x-ray detector before the placement of the CsI:Tl.

3 CMOS x-ray detector

The second device that is described here consists in four $400\ \mu m \times 400\ \mu m$ photodiodes fabricated in a standard CMOS process. In this case, an aluminum dye is used, where some cavities were opened. The cavities were then filled with a scintillator material and the set was placed above the CMOS photodetectors [2] as is shown in figure 3. Figure 4 shows a picture of the CMOS device before the placement of the aluminum dye with the scintillating material.

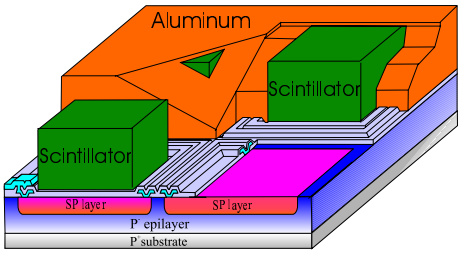

Fig. 3: Structure of a 2×2 CMOS x-ray detector array.

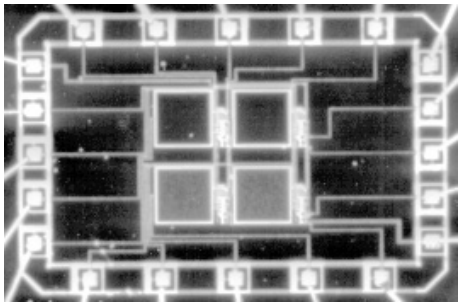

Fig. 4: Picture of the 2×2 CMOS photodetector array before the placement of the CsI:Tl layer.

4 Experimental results

The experiments on the two devices were performed using a didactic x-ray tube with a molybdenum anode from Leybold. In both cases, the tube was powered with a voltage of $35\ kV$ and a current ranging to $1\ mA$. This tube produces x-rays whose energy peak is near $20\ keV$. The results of these measurements are shown in figure 5 for the BMM detector and in figure 6 for the CMOS detector.

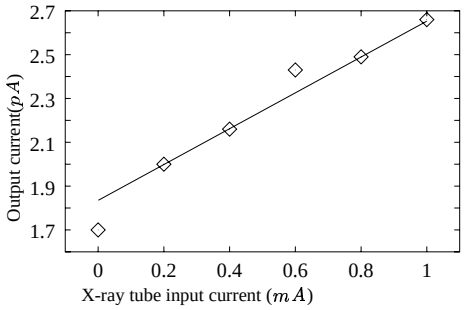

Fig. 5: Output current of the BMM x-ray detector with a x-ray tube input voltage of $35\ kV$.

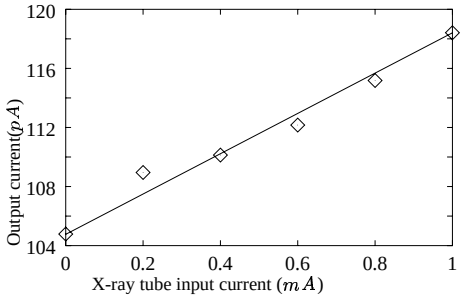

Fig. 6: Output current of the CMOS x-ray detector with a x-ray tube input voltage of $35\ kV$.

5 Comparison between the two x-ray detectors

- The BMM detector do not use a standard fabrication process in the photodetector construction. This fact permits the optimization of the junction depth in order to obtain a spectral response that matches the emission peak of the scintillator. Nevertheless the fabrication of the CMOS detector is cheaper as it make use of a standard fabrication process.
- The fabrication of the cavities in the BMM detector is easier due to the use of anisotropic chemical etching of the silicon instead of the mechanical methods used for the CMOS detector.
- The dimensions of the pixels in the CMOS detectors can be smaller than in the BMM one due to the fact that the side walls of the cavities fabricated with KOH etching in the BMM detector are not vertical (figure 1).
- Due to the standard fabrication of the CMOS prototype it is possible to integrate the electronics with the photodetectors without additional fabrication steps. This integration is more difficult in the BMM one.
- Both detector prototypes show a linear response up to $1\ mA$ of x-ray tube input current (figures 5 and 6).
- The CMOS detector has a higher sensibility, but a larger offset (figure 6).

6 Conclusion

Two x-ray detector prototypes were fabricated using two different technologies, one is based on a bulk micromachined silicon photodetector and other is based on a standard CMOS photodetector. The fabrication process and the performance of the two prototypes were presented and discussed comparatively. Whereas the CMOS detector has advantages in the integration of the photodetectors with the electronics and the detection sensibility, the BMM detector shows advantages in the fabrication of the cavities and the lower offset.

References

[1] J. G. Rocha, C. G. J. Schabmueller, et. al., “X-ray detector based on bulk micromachined photodiode,” Proc. MME’2002, (2002) pp. 323-326.

[2] J. G. Rocha N. F. Ramos, et. al., “CMOS X-rays Microdetector Based on Scintillating Light Guides,” Proc. Eurosensors XVI, (2002) pp. 525-528.

Towards a 1mm^3 Camera -- The Field Stitching Micromirror

M Last[1], L Zhou[1], V Milanović[2], JM Kahn[1], KSJ Pister[1]

[1]Berkeley Sensor and Actuator Center – University of California, Berkeley
email: lzhou@eecs.berkeley.edu http://www.eecs.berkeley.edu/~lzhou
[2]Adriatic Research Institute, Berkeley, CA 94709
email: Veljko@adriaticresearch.org http://www.adriaticresearch.org

Summary: *The concept of a movable mirror that can be used to extend the field of view and effective resolution of any camera is introduced. For millimeter-scale and smaller cameras, this is especially important since the number of pixels in the imaging array is severely limited. MEMS micromirrors are well suited for this application. Proof of concept using a 1-axis SOI micromirror is presented. Scaling laws for small cameras are discussed.*

Keywords: *post objective scan, field stitching, micromirror, MEMS, SOI, gimbal, electrostatic, camera*
Category: *4 (Non-magnetic Physical Devices)*

1 Introduction

1.1 Field Stitching Camera

CMOS imaging arrays have shrunk the size of commercially available cameras to just a few cubic centimeters. While small by most metrics, this is still much too large for envisioned microrobotic applications. Eventually, these cameras will shrink to just a single chip with an imaging lens with a minimal amount of packaging holding the system together [2]. The volume of this type of device is limited by the number of pixels, the pixel size, and the diameter of the imaging lens. Increasing resolution (# pixels), field of view (pixel size), or light sensitivity (lens diameter) will be attainable only by increasing the total volume of the system. We propose building a hybrid camera consisting of a very small imaging array and lens coupled with a movable mirror used to choose the field of view of the camera, similar to [1]. The mirror therefore multiplies the effective number of pixels in the array. The cost of this approach is a reduction in the effective sensitivity of the camera since each pixel is time multiplexed across multiple fields of view. However, this tradeoff might be required for extremely small cameras. For instance, using 10μm pixels, a 0.5mm x 0.5mm imaging array would have only 50x50 pixel resolution. In order to achieve high resolution for a camera this small, either the pixel pitch must be reduced substantially or field stitching must be used. This paper describes the optical setup and system design considerations for a field stitching camera. Proof of concept using a custom MEMS micromirror is demonstrated.

1.2 MEMS Micromirror

MEMS micromirrors have several features that make them uniquely suited for this application. Due to their small mass, they can be moved from field to field in milliseconds, enabling camera full-scene frame rates limited only by the sensitivity of the photodiode pixels. The extreme flatness (<30nm max deviation from mean) of the SOI (Silicon-on-Insulator) micromirrors developed in our lab (fig. 1) add negligible amounts of aberration to the optical system. Electrostatic actuation requires only microwatts; this is critical for power-limited applications such as sensor networks and microrobotics. Ongoing research in our lab focuses on reducing the mirror step response time and power consumption while increasing accuracy and range of motion.

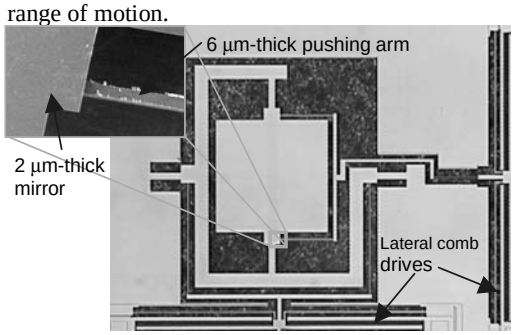

Fig. 1: A 2 axis scanner realized by a SOI/SOI bonding process. The central mirror is suspended by a double-axis gimbal structure that rotates about the two in-plane axes using orthogonally oriented torsion springs. A single-axis version was used for proof of concept experiment.

2 Proof of Concept

Fig. 2 shows the concept of the field stitching camera. A small camera consisting of an objective lens and an imaging array has a limited field of view and resolution. A mirror, placed *closer* to the camera than the focus is used to steer the camera's field of view. The original field of view of the camera becomes one of several sub-fields that

selected with the mirror and stitched together to form a complete image.

This concept was tested using a long working distance inspection microscope coupled to a digital still camera. A mask constructed using a laser printed transparency was used to block rays bouncing off of the shiny substrate surrounding the mirror. Imperfect blocking of these alternate paths creates superimposed "ghost images" that do not move when the field stitching mirror rotates. The image in fig. 3 was acquired using this system and the final image consisting of three mirror positions was stitched together in photoshop.

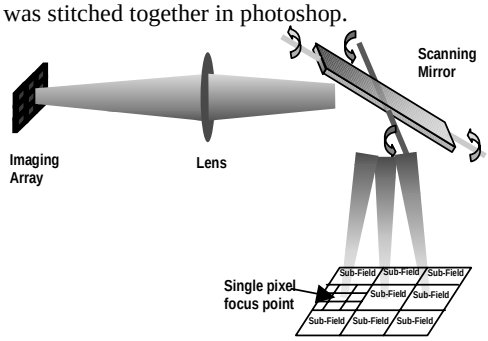

Fig. 2: Diagram of field stitching camera. A static camera field of view ("sub-field") is scanned in a 3x3 grid, increasing the field of view and effective resolution of the camera by a factor of 9.

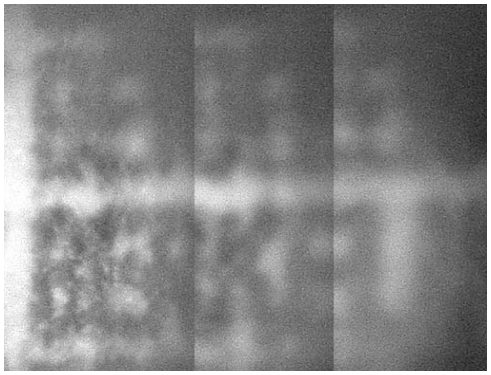

Fig. 3: Image formed using a 3x1 field-stitching camera. Field of view extended using MEMS field stitching mirror. Top row of text is reflection off substrate (note only "BER" visible), bottom row is reflection through mirror ("BERKELE" visible). Blurring is caused by field curvature and camera autofocus.

Field curvature is an issue with this type of camera. Because the mirror rotates the field of view instead of translating it, the field of view is spherical instead of flat. A variable focus lens can be used to flatten the field if necessary.

3 Scaling Considerations

The ideal way to shrink a camera is to scale every dimension down by the same factor until the either the diffraction-limited resolution is the same as the pixel resolution, or technology-imposed limits on pixel size preclude shrinking each pixel any further. Once this scaling limit has been reached, a ray-optics analysis shows any further reduction in the imager-lens distance results in a reduction angular resolution of each pixel. However, from a diffraction perspective, the increase in NA as the imager gets closer to the lens increases the angular resolution of the system. Setting the size of the pixels equal to the diffraction limited spot formed by the lens, the optimal location for the back focal length of the camera is found to be $f = \frac{0.61\lambda}{2NA\tan\left(\frac{\theta_{fov}}{2}\right)}$, where λ is the wavelength of light, θ_{fov} is the angular field of view of a pixel, and NA is the numerical aperture of the lens. In this way, an upper bound on resolution sets the lower bound on the length of the camera.

While diffraction and pixel size limit the resolution and length of the camera, the lens aperture limits the light collecting ability of the camera. Operating the imager at a constant signal-to-noise ratio (SNR), linear downward scaling of the aperture diameter results in a quadratic increase in exposure time. The field stitching mirror compounds this low-light problem, since each pixel is time-shared amongst the subfields of the camera. For an NxN field stitching camera, there is an N^2 increase in exposure time when SNR is kept constant.

4 Conclusion and Future Work

As we scale cameras to smaller sizes, diffraction and pixel pitch issues limit the resolution available in a standard camera. By adding a field stitching micromirror, this resolution can be recovered at the expense of increased exposure time. Our current work focuses on building an integrated system consisting of an 8x8 photodiode array and microlens.

5 References

[1] Colonna R., "Post-objective scanning. An image acquisition alternative." *Photonics Spectra*, vol.19, no.4, April 1985, pp.101-4. USA.

[2] K Itakura, T Nomusada, N Kokusenya, R Nagayoshi, M Ozaki, "A 1-mm 50 k-Pixel IT CCD Image Sensor for Miniature Camera System", *IEEE Trans. On Electron Devices*, vol 47, no.1, Jan. 2000

[3] S. Kwon, V. Milanović, L. P. Lee, "A High Aspect Ratio 2D Gimbaled Microscanner with Large Static Rotation," *IEEE/LEOS Optical MEMS 2002*, Lugano, Switzerland, pp. 149-150, Aug. 2002.

[4] V. Milanovic, M. Last, K. S. J. Pister, "Torsional Micromirrors with Lateral Actuators," *Proceedings of the 11th International Conference on Solid-State Sensors and Actuators, Transducers 2001*, Munich, Germany, 2001.

Vertical Comb Driven 1D and 2D Optical Scanning Mirrors Using Epi-Si Micromachining Process

Chengkuo Lee and Chun-Kai Liu
Optical Communication Division, Asia Pacific Microsystems, Inc.
No. 2, R&D Road VI, Science-Based Industrial Park, Hsinchu, Taiwan
Tel: +886-3-6121188, Fax: +886-3-6121199, email: mems@apmsinc.com

Summary: *A new process concept and experimental results of making optical scanning mirrors with large mirror size and deflection angle are presented in this paper. Stepped vertical comb drive actuators and thinned torsion springs are used to enlarge the deflection angle under moderate voltage load. The electrochemical etching technology is applied to release the epitaxial Si layer to serve as the micromirror plate. Preliminary results of both one dimensional (1D) and two dimensional (2D) optical scanning epi-Si mirrors are presented. For devices with a 1500x1500x27μm^3 mirror plate and 400x10x22.5μm^3 torsion spring, the dynamic optical scanning angle is measured as large as ± 16° under 40 Volts pulse load for electrostatic excitation.*

Keywords: *Epitaxial Si, Micromirror, Comb Drive*
Category: *4 (*Non-magnetic physical devices*)*

Introduction

Recently combining the SOI, DRIE and wafer bonding processes with the design of vertical comb drive actuators has been reported to be very attractive to the applications need large mirror size and tilting angle [1-2]. However, such processes and techniques are either very expensive approach, need of precise double side alignment, or need of precise wafer bonding alignment. In this paper, we report a new method to design and prepare a flat mirror with large size and deflection angle by using vertical comb drive actuators and electrochemical etching derived epi-Si structure. The mirror devices derived by this new approach seem to be promising to the above mentioned applications.

Design & Fabrication

Without using SOI based process, we apply the epitaxial silicon wafer as starting materials, and the well-known electrochemical etching technique is used to release large mirror and to precisely control the thickness of released mirror plate.
Vertical comb drive actuators of angular tilted structure, and comb drive configuration composing upper and lower comb-teeth have been demonstrated [1-3], while H. Schenk et al reported that mirror with in-plane comb finger structure still can be excited by periodically applying rectangular pulse load [4]. To gain in simpler process design and precisely comb alignment control, we propose a 4-mask process to fabricate our devices. As shown in Fig.1, the process starts with patterning thermal oxide and Al electrode layer to form the comb finger pattern. The backside LPCVD SiN hard mask is defined for KOH electrochemical wet etching. After the underneath bulk Si is removed away, the mirror and comb fingers are defined from the front-side by Si deep reactive ion etching (DRIE) to etch through the epi-Si layer, and thereby the mirror structure is released. At the initial stage of DRIE process, the torsion spring is only covered by photo resist (PR). We may divide the DRIE process into two major steps, the PR pattern can be removed between these two steps, and the torsion spring will be etched and thinned in the second step. We can also use the above method to make vertical comb drive with step height between inside and outside comb fingers for static displacement actuation.

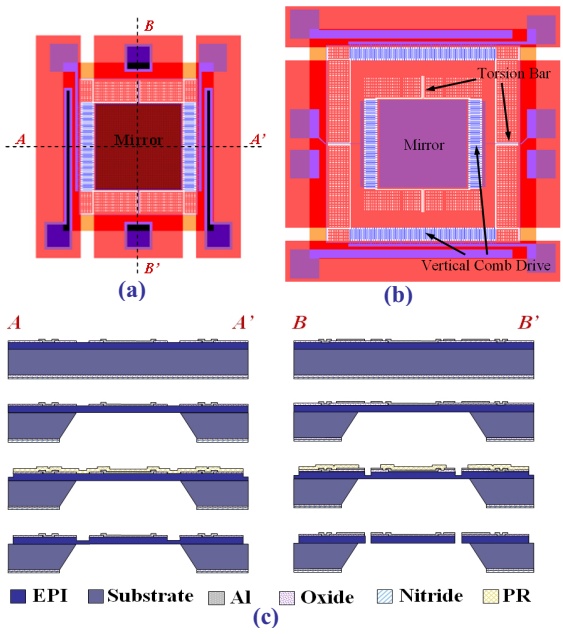

Fig. 1. Schematic drawing of (a) 1D epi-Si mirror; (b) 2D epi-Si mirror; and (c) cross sections of 1D epi-Si mirror process flow

The fabricated epi-Si mirror devices have a 1500x1500x27μm^3 mirror plate, and the 400x10x22.5μm^3 torsion spring. The thickness of torsion spring has been etched to become 4.55μm

thinner than mirror plate. The SEM photos of fabricated epi-Si mirror device are shown in Fig.2. With similar process, 2-D epi-Si optical scanning mirror can also be accomplished.

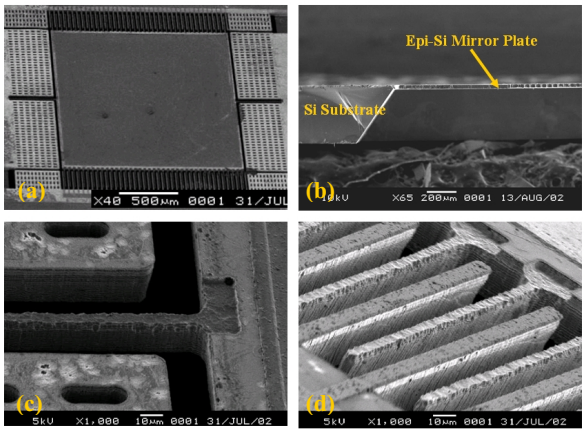

Fig. 2. SEM photos of (a)fabricated epi-Si mirror; (b)cross section view of epi-Si mirror plate; (c)thinned torsion spring; (d) stepped com fingers

Characteristics & Measurement Results

If we apply rectangular pulse load periodically to vertical comb drive actuators as steps shown in Fig.3, the mirror structure can be excited by this way. As the excitation frequency of the periodical pulse load reaches twice value of mechanical resonance frequency, the deflection angle jumps up.

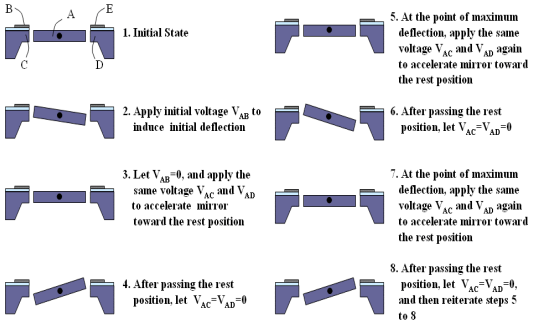

Fig. 3. Schematic drawing of steps of operation scheme for electrostatic excitation

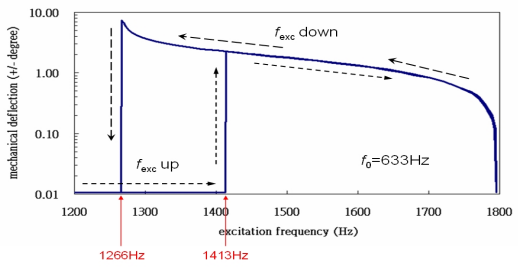

Fig. 4. Curve of mechanical deflection angle versus excitation frequency of applied voltage 40 Volts

Fig.4 shows the curve of mechanical deflection angle versus the excitation frequency. The dynamic optical scanning angle and mechanical deflection angle are measured as large as ±16° and ±8° under 40 Volts pulse load by using the present designed comb drive for electrostatic excitation. The behavior observed of vibration curve is similar to the results of Ref. [5]. By using the present design, the thinned torsion spring can result larger deflection angle under the lower electrical load. Fig.5 shows the schematic drawing of epi-Si scanning mirror optical measurement system and the scanning pattern of 1-D epi-Si mirror, and Fig. 6 shows the scanning patterns of 2-D epi-Si mirror with rectangular pulse voltage load at various frequencies.

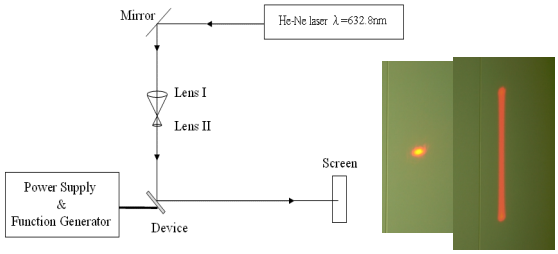

Fig. 5. Schematic drawing of epi-Si scanning mirror optical measurement system and the scanning pattern of 1D epi-Si mirror

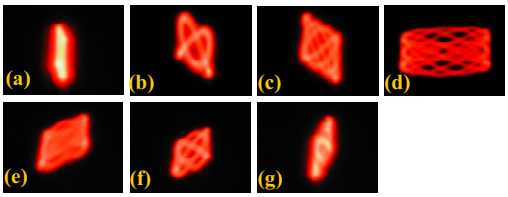

Fig. 6. Scanning patterns of 2D epi-Si mirror at various excitation frequencies (Outside frame Vpp=40V, Freq.=2985Hz; Inner frame Vpp=60V, and (a)Freq.=1650Hz; (b)Freq.=2247Hz; (c)Freq.=2250Hz; (d)Freq.=2328Hz; (e)Freq.=2375Hz; (f)Freq.=2385Hz; (g)Freq.=2500Hz)

Conclusions

Basically this process shows good yield of mirrors and perfect thickness control of mirror plate by means of KOH electrochemical etching stop mechanism. The thickness control of thinned torsion spring is determined by the etching rate selectivity during final DRIE process step. The preliminary 1D and 2D scanning pattern results of epi-Si mirror with large size are presented. Comparing with SOI and surface micromachining Poly-Si based processes, this process is promising for making micromirror devices to meet application markets where the extreme cost budget is crucial.

References

[1] O. Tsuboi, et al, IEEE Proc. of the 15th Intern. Workshop on MEMS, pp.532-535, Las Vegas, 2002.

[2] J. H. Lee, et al, Proc. IEEE/LEOS Intern. Conf. On Optical MEMS 2000, pp. 13-14, Kauai, 2000.

[3] V. Milanovic, et al, Proc. IEEE/LEOS Intern. Conf. On Optical MEMS 2001, pp. 135-136, Okinawa, 2001.

[4] H. Schenk, et al, IEEE JSTQE, Vol.5, No.5, pp.715-722, 2000.

Unsupervised scanning light pulse technique

H. Uchida[1], D. Filippini[2] and I. Lundström[2]

[1]Faculty of Engineering, Saitama University, 255 Shimo-Okubo, Urawa 338, Japan
[2]Division of Applied Physics, Institute of Physics and Measurement Technology, Linköping University, S-581 83 Linköping, Sweden. E-mail: danfi@ifm.liu.se

Summary: *A scanning light pulse technique (SLPT) operating in a totally unsupervised way suitable with screening purposes is demonstrated. The procedure automatically determine inflexion points (optimum biasing condition) and photocurrent amplitudes from locally acquired i-V characteristics that enables to display optimum biased measurements properly re-scaled to avoid spurious amplifying effects.*
Additionally, the procedure allows composing flat band voltage shift patterns within the same experiment, and avoiding feedback mode measurements. Optimum bias patterns when used to modulate subsequent measurements allow fast recording mode.

Keywords: *scanning light pulse technique, chemical sensors, field effect sensors, MOS capacitors.*
Category: *5 (Chemical sensors)*

1 Introduction

The scanning light pulse technique for chemical sensing purposes allows both: the generation of spatially distributed chemical images for practical applications [1,2] as electronic noses or functional materials screening, and fundamental research of chemical sensing mechanisms in field effect devices.

The generation of chemical images demands the use of extended gates with spatial modulation of the chemical properties induced by gradients in thickness, composition, temperature or geometry [3].

A common problem with this technology is the acquisition of partially fragmented and incomplete information due to the differences in the amplitudes of the local photocurrents and the pristine flat band voltages. Typically the measurements are performed at constant bias voltage or constant photocurrent (feedback mode [1]), which demand expert inspection of local responses to determine the conditions that retrieve the most substantial information for the experiment, that in any case is partial. Consequently, the screening of sensing materials may become unpractical with this technique.

In the present work, we demonstrate an enhanced approach for SLPT that enables to acquire all the relevant information and display normalized chemical images operating totally unsupervised.

Additionally, the technique allows composing optimum photocurrent or flat band voltage response indistinctly within the same experiment, but avoiding time consuming and electrically disturbing feedback mode measurements.

2 Experimental

Fig.1a shows the structure of the MOS sensor capacitor used for the SLPT measurement. A first SiO_2 layer (100 nm) was grown by thermal oxidation of the p type Si wafer (500 μm, 10 Ω.cm), followed by a second SiO_2 layer (90 nm) electron beam evaporated. Under the Al contact pad and central tip additional 300 nm of SiO_2 were deposited. Pd (70 nm) and Pt films (35 nm) were thermally evaporated to conform the layout depicted in Fig. 1a. The Si backside was coated with 200 nm of Al.
The SLPT measurement was made with the device placed in a tight gas cell, where a chopped laser beam (650 nm wave length, Melles Griot DLD203, LD in Fig.1b) illuminates the sensor though a glass window. A current preamplifier (Stanford Research Systems SR570) and a phase lock-in amplifier (Stanford Research Systems SR830) complete the setup.
The sensor was fixed in the gas flow cell and heated by a halogen lamp to 110°C. The laser beam was modulated by a reference sinusoidal wave from the lock-in amplifier (and reduced by an aperture plate), locally exciting the MOS structure at a frequency of 1 KHz.

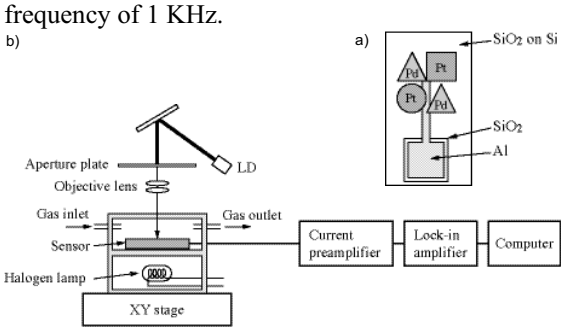

Fig. 1a. MOS capacitor layout, b) SLPT measuremt setup.

3 Results and discussion

Fig. 2a illustrates two different photocurrent vs. bias voltage characteristics and their shift upon hydrogen exposure. If the bias voltage in the inflexion point of signal 1 is chosen as constant (v) for the whole measurement, regions with the characteristics of signal 2 will be underrepresented in the final chemical image. Equivalently, when measuring in feedback mode, e.g. at the indicated constant photocurrent (i), the responses form signal 2 regions would be ignored.

Additionally to the proper choice of the monitoring bias voltage for each position, a local re-normalization of the photocurrent response (Δi) is required to avoid displaying spurious amplifying effects specially close to the metal edges (Fig. 2b).

In practice, counteractions demand exploratory measurements and expert inspection before to run the SLPT experiment, which in the best case determines which partial part of the response is observed in the final experiment. For screening purposes, an unsupervised procedure able to display all the available information in a common scale would be a great advantage.

In the present contribution, a 21 x 21 steps scanning is performed, for 31 different bias voltages between –5 and +5 volts in atmospheres of synthetic air, hydrogen and ammonia. With the measurement in air the inflexion point of each local photocurrent characteristic is detected, and the optimum bias voltage for each step of the laser beam is determined. Simultaneously the local photocurrent amplitudes are recorded and used later to re-scale the corresponding chemical responses.

Fig. 2b, depicts the photocurrent response to hydrogen and ammonia (calculated by the subtraction of the target gas photocurrent profile minus the air pattern) for a measurement at constant bias voltage and the corresponding enhancement using optimum and re-normalized responses (Fig. 2c).

Proceeding similarly, with the local photocurrent characteristics for hydrogen and ammonia, the optimum bias voltages for these can be calculated and consequently a truly flat band voltage shift map, avoiding feedback measurements, can also be computed.

Naturally the technique is more time consuming than the regular SLPT, but since the information provided is not partial and also completely unsupervised the trade off is fair and for screening purposes becomes key.

Additionally, faster alternatives, still retaining the enhancements are possible. Just one complete scanning in bias voltage for air is required to construct a map of optimum bias voltages for each position (Fig. 2d), which is then used for subsequent environments in regular SLPT measurements but at locally modulated biases. This alternative also allows re-scaling in the same way discussed above, only loosing the flat band voltage mapping.

In this way the unsupervised SLPT also becomes more friendly to the user and allows non-expert users to exploit its benefits, e.g. home tests, which is particularly attractive considering that the technique can be dramatically simplified replacing the micro-positioned laser beam by and standard computer screen [2].

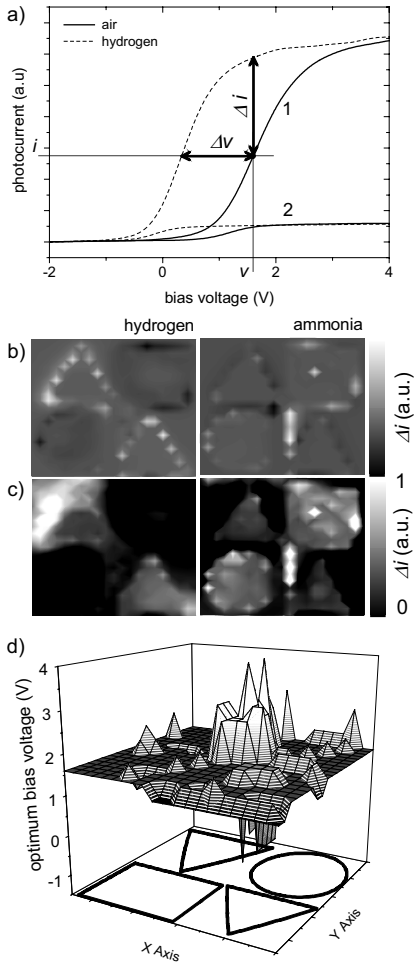

Fig 2a) Photocurrent vs. bias voltages shift characteristics in two different parts of the sensor and their corresponding shift with hydrogen. b) Photocurrent response patterns measured at a constant bias voltage of +1.6 V. c) Unsupervised renormalized maps for the same gases. d) Optimum locally modulated bias voltage pattern measured in air.

References

[1] I. Lundström, et. al., *Nature* **352** (1991), 47.

[2] D. Filippini, I. Lundström, *Appl. Phys. Lett.* **81** (2002), 3891.

[3] D. Filippini, I. Lundström, *J. Appl. Phys.* **91** (2002), 3896.

Evidence of band bending flattening of 10 nm polycrystalline SnO_2 using scanning tunnelling microscopy/spectroscopy techniques.

C.Malagù[1], M.C. Carotta[1], H. Fissan[2], V.Guidi[1], F.E. Kruis[2], M.K.Kennedy[2], T.G.G. Maffeis[3], G. Martinelli[1], G.T. Owen[3], and S.P. Wilks[3]

[1]University of Ferrara and INFM, via del Paradiso 12, 44100 FE, Italy
[2]Gerhard-Mercator University Duisburg, Bismarckstr. 81,47057 Duisburg, Germany
[3]University of Wales Swansea, Singleton Park, Swansea, SA2 8PP, UK

Summary: *We developed a model for n-type metal-oxide semiconductors, which allows one to calculate the density of surface-chemisorbed oxygen on nanostructured grains, once the Schottky barrier height is known. We collected scanning tunnelling images and spectroscopy on two sets of polycrystalline SnO_2 particles with grain radius of 30 nm and 10 nm respectively. The purpose of these experiments was to observe the flattening of the band bending and the corresponding decrease in the density of those surface states responsible for the pinning of the Fermi level.*

Keywords: *Nanostructured powders, Schottky barrier, Scanning tunnelling spectroscopy*
Category: *Chemical sensors*

1 Introduction

To successfully substitute conventional gas sensing systems with chemo-resistive gas sensors, it is obvious that sensitivity, selectivity, reliability and reproducibility are of paramount importance. In order to fabricate sensors with the required characteristics, the research has to focus on the improvement of the device, both through an upgrading of the technological processes involved and through the theoretical understanding of the fundamental mechanisms of electron transport within the chosen materials [1]. This calls for a fine control of the nanoparticles dimensions, the porosity of the sample and the thickness of the deposition.

As a result, the application of fundamental transport models to these devices is possible due to the achievement of uniform Schottky contacts between the particles, the homogeneity and symmetry of the grains.

Eventually, a complete understanding of the sensing mechanism requires an extensive characterization from a structural and electrical point of view. Scanning tunnelling microscopy (STM) and spectroscopy (STS) proved an essential tool in fulfilling this goal [2]. As an example of the described approach, we report the case of SnO_2, i.e., the most investigated material for chemo-resistive sensors.

2 Modelling

We have modelled in Eq. (1) the Poisson's equation in spherical coordinates together with the continuity law. The numerical solution of Eq. (1) predicts the flattening of the band bending inside the nanostructured grains when the grain radius, R, is comparable with the depletion length, Λ.

$$\begin{cases} \dfrac{1}{r}\dfrac{d^2}{dr^2}(r\Phi(r)) = -\dfrac{eN_d}{\varepsilon} + \dfrac{eN_d}{\varepsilon}e^{\frac{e\Phi(r)}{k_bT}} \\ -\dfrac{d\Phi(r)}{dr}\bigg|_{r=0} = 0 \\ \Phi(r)|_{r=R} = -V \\ -\dfrac{d\Phi(r)}{dr}|_{r=R} = \dfrac{eN_t}{\varepsilon} \end{cases} \quad (1)$$

The charge density used in the first part of this equation is a function of the electrostatic potential inside the grain Φ(r), for which the zero level is chosen in the conduction band minimum in the bulk. The first boundary condition states that the field inside the grain must be zero for symmetry. The second condition sets the surface potential Φ(R) to the value of the built-in potential, V. The latter is the Schottky barrier height reduced by the difference between the Fermi level and the conduction band minimum in the bulk. The Schottky barrier height depends weakly on R, whereas the band bending tends to decrease significantly when $R<\Lambda$. The flattening of the band bending is highlighted by the comparison of Fig. 1 (a) and (b), which represent the numerical solution of Eq. (1) in the two cases: $R<\Lambda$ and $R>\Lambda$. This flattening leads to a decrease of the density of chemisorbed oxygen, N_t, due to the decrease of the surface field. The relation between N_t and the surface electric field is in fact expressed in the last equation of Eq. (1), which represents the neutrality of the grain together with the Gauss law. Therefore, we expect that the fundamental difference between the behaviour

of SnO_2 particles with $R<\Lambda$ with respect to those with $R>\Lambda$ is a decrease in the density of surface states in the band gap. The surface states are attributed to chemisorbed oxygen [5] and they are responsible for the pinning of the Fermi level. Consequently, a lowering of their density is expected to improve the performances of a semiconductor as a gas sensor.

A value for Λ of 20-25 nm for our SnO_2 samples has been calculated from the model. We then pursued STS on polycrystalline particles both larger and shorter than this length in order to observe a variation in the measured band gap induced by the presence of surface states.

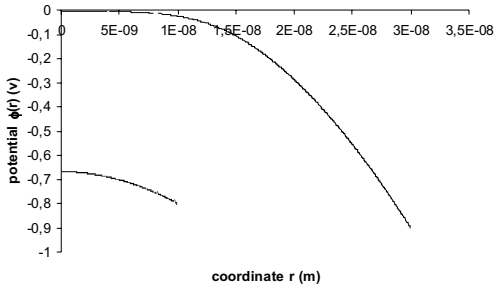

Fig. 1. Calculated band bending inside the SnO_2 grains, N_d=5x10^{18} at/cm^3; ε=10^{-10} F/m, T=120 ^{o}C. a) 10 nm SnO_2, b) 30 nm SnO_2.

3 Results and discussion

SnO_2 powders were prepared via a gas-phase synthesis method described elsewhere [3]. Two sets of nanosized SnO_2 particles in the cassiterite phase, with R=30 nm and R=10 nm, respectively, were deposited onto a 110 silicon substrate. STM images at room temperature, providing information about the morphology and the crystalline arrangement of the samples are presented in Fig. 2.

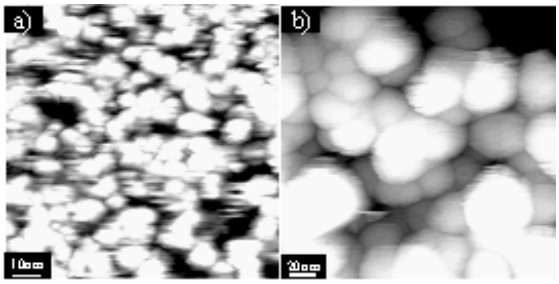

Fig. 2. SnO_2 nanoparticles, STM images at room temperature. a) R=10 nm. b) R=30 nm.

Additionally, STS spectra were acquired from the two samples. To perform STS measurements, the tip of the microscope records local (nanometer scale) current voltage (I-V) curves. The logarithmic derivative dlnI/dlnV of these I-V curves is proportional to the local surface density of states [4]. Fig. 3 shows the STS spectra from the two samples. Each spectrum is an average of over 6000 I-V curves, taken from a 100x100nm^2 surface area. The zero conduction region of the 10nm sample spectrum (bottom curve) gives an electronic surface band gap of 2.5eV. By contrast, the 30nm sample spectrum shows virtually no region of zero conduction, indicating a continuum of surface states in the band gap. This result clearly shows that the density of surface states is much higher for the 30nm particles than for the 10nm particles, in accordance with the predictions of the model regarding the important flattening of the band bending as $R<\Lambda$.

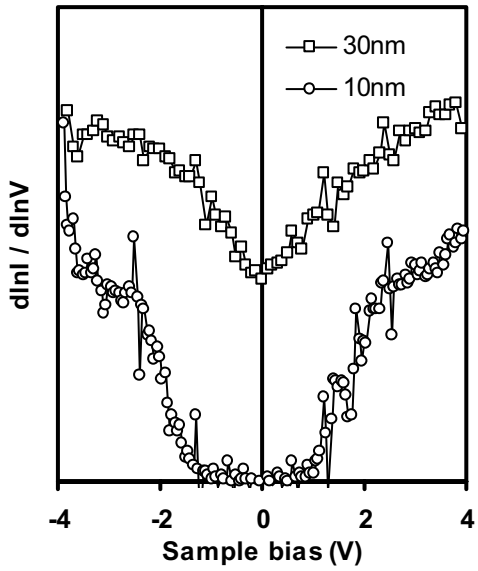

Fig. 3. Comparison between the surface density of states in 10 nm and 30 nm particles. The high density of surface states in large grains induces a virtually zero band gap.

References:

[1] C. Malagù et al., *J. Appl. Phys.*, **91** (2002) 808.
[2] J. Arbiol et al., *Sens and Act B* **78** (2001) 57.
[3] F.E. Kruis, K. Nielsch, H. Fissan, B. Rellinghaus, and E.F. Wassermann, *Appl. Phys. Lett.* **73**, (1998) 547.
[4] R.M. Feenstra, *Phys. Rev. B* **50**, (1994) 4561.
[5] T. T. Rantala, T. S. Rantala, and V. Lantto, *Surf. Sci.* **420**, (1999) 103.

Interferometric Porous Silicon Vapor Sensor with Fiber Optic Control

L. Pancheri[1], C. J. Oton[2], Z. Gaburro[2], L. Pavesi[2] and G. Soncini[1]

[1]Department of Information and Communication Technologies,
University of Trento, Via Sommarive 14 38050 Povo (TN), Italy
email: pancheri@dit.unitn.it
[2]INFM and Department of Physics,
University of Trento, Via Sommarive 14 38050 Povo (TN), Italy

Summary: *We show an experimental study for an optical vapor sensor based on the change of reflectivity of a thin porous silicon layer. In presence of vapors the reflectivity spectrum, which shows interference fringes, is modified, owing to the variation of the effective refractive index. We enlighten the PS layer with a monochromatic laser light and detect the reflected light intensity with a photodiode, using optical fibers to transmit the light. In this way we avoid the presence of electrical contacts, which could be dangerous in the presence of flammable vapors. We show a characterization of sensor response with ethanol and relative humidity.*

Keywords: *porous silicon, vapor sensor, fiber optic*
Category: *5 (Chemical sensors)*

1 Introduction

It has been demonstrated that many electrical and optical properties of Porous Silicon (PS) are sensitive to the presence of different gases and vapors due to the large specific surface of this material [1]. As PS is not stable, it needs to be stabilized to be reliably operated as a sensor. Different thermal and electrochemical oxidation treatments have been proposed to stabilize porous silicon.

Porous silicon films can be grown with a good control of thickness and porosity [2], so it is a suitable material to form well characterized thin films that can act as interference filters. The effective refractive index of porous silicon is related to its porosity and changes if a vapor is adsorbed on its internal surface or condenses into the pores.

Gao et al. [3] demonstrated that a porous silicon thin film can be used in a simple system to monitor the concentration of vapors in the environment. On the base of this principle, we realized an optical vapor sensor which employs fiber optics for the readout.

2 Experiment

Porous silicon samples were produced with an anodization treatment in a hydrofluoric acid solution. The thickness of porous silicon layers was measured with SEM micrographs and the index of refraction was estimated from the reflectance spectrum. We performed a thermal oxidation in order to stabilize the samples.

We characterized the variation of the refractive index in the presence of different concentrations of ethanol and relative humidity levels by measuring the fringe shift in the reflectivity spectrum of the samples.

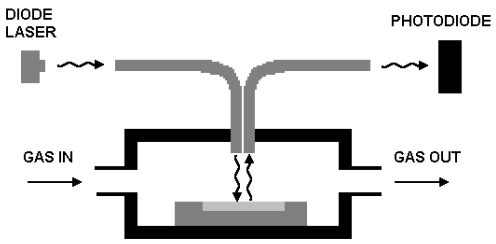

Fig. 1. Scheme of the system.

We designed a system which employs the variation of reflectance with vapor concentration at a single wavelength. The scheme of the system is shown in Figure 1. The light source is a semiconductor laser operated at a constant power, which emits infrared monochromatic light at 780 nm. The sample is put into a sealed chamber in which gas mixtures were flown, and enlightened by an optical fiber. Another fiber collects the reflected light and delivers it to a photodiode. The variation of the reflected light intensity in the presence of vapors causes a variation in the photodiode current.
We characterized the sensor response in the presence of ethanol vapor and humidity. As can be seen in Figure 2, with this system we could measure ethanol concentrations spanning three orders of magnitude and as low as 25 ppm in dry air.

The sensor showed a response time of about 10 seconds and a good reversibility and repeatability.

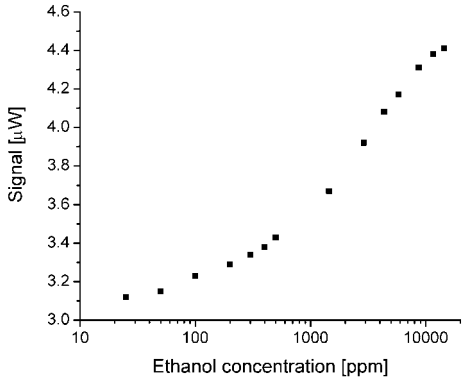

Fig. 2. Sensor response under different ethanol concentrations.

We evaluated how the presence of humidity affects sensor response. The sensor signal varies reversibly with humidity, but the response time is slower, especially at high relative humidity levels. However, the sensitivity to ethanol vapor is at least partially retained in the presence of humidity, as can be seen in Figure 3. The oscillations in the signal are due to the laser.

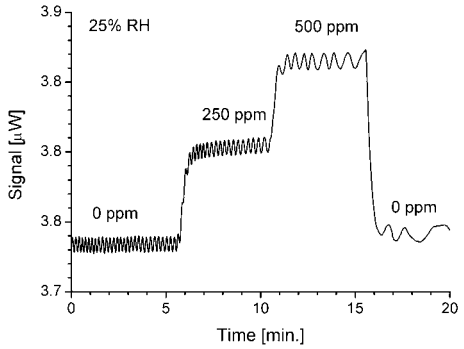

Fig. 3. Sensor response to ethanol in the presence of 25% relative humidity.

Preliminary tests show that the sensor is sensitive also to other organic vapors like acetone, hexane and trietilamine.

3 Conclusions

The sensor realized shows a good sensitivity, fast response and good reversibility to ethanol. It is also sensitive to humidity and other vapors, but it lacks selectivity.

This sensor could be used together with a humidity sensor to monitor the concentration of solvent vapors in industrial environments. The system realized has the advantage to be free of electric contacts, so it can be safely used to control the concentration of highly flammable vapors.

Other things to characterize are the long term stability of the sensor and the effect of temperature, which will be the object of future work.

References

[1] M. J. Sailor, in *Properties of Porous Silicon*, ed. L. T. Canham IEE Inspec – London U. K., 1997, p. 364.

[2] O. Bisi, S. Ossicini, L. Pavesi, Porous silicon: a quantum sponge structure for silicon based optoelectronics, *Surface Science Reports,* 38 (2000) 1.

[3] J. Gao, T. Gao, M. J. Sailor, Porous-Silicon vapor sensor based on laser interferometry*, Appl. Phys. Lett.,* **77** (2000) 901-903.

Organic Solvent Vapors Sensor Based on Diode Structures with Porous Silicon Layer

Vladimir M. Aroutiounian, Armen P. Hakhoyan, Arsen Z. Adamyan, Zaven N. Adamian, Robert S. Barseghyan

Dept. of Physics of Semiconductors, Yerevan State University,
Alex Manoogian 1,Yerevan 375049, Armenia, varou@semicond.ysu.am

Summary: *The porous silicon layers were formed in the outer part of n^+ emitter of n^+-p junction by the electrochemical anodization technique under different technological regimes. The sensitivity of the porous silicon layers to different chemical gases in the environment was investigated on the basis of analysis of the current-voltage characteristics. Certain correlation was observed between gas sensitivity and the dipole moment of the gas molecule.*

Keywords: *Sensor, porous silicon, diode.*
Category: *Chemical sensors*

1 Introduction

The discovery by Canham of the intensive photoluminescence of porous silicon (PS) in the visible range of spectrum at room temperature has attracted attention of many research and development groups. There are number of works devoted as to the study of the physicochemical properties of this new material, so and to the investigation of regularities of its formation [1-3].

Despite the considerable number of papers devoted to the study of the electro- and photo-luminescent properties of this material, the physical properties PS have not been determined so far. First of all, it refers to the localization mechanism of the charge carriers and the adsorptive sensitivity of the material.

The search for technological methods and regimes of the creation of gas sensors based on porous silicon is highly topical, which is stipulated by the following advantages of this material: simple and inexpensive technique of the porous layer formation; compatibility with common microelectronic techniques, and very large specific surface of contact with the gas environment [1-5].

The possibility of creation of the PS based gas sensors, operating on the basis of the phenomenon of changes in the photoluminescence intensity as a result of the adsorption of gas molecules on the PS surface was reported in [3,4]. However, the cost of such sensors is very high and they are not practical.

It is known, that the electro-physical properties of the PS, strongly depend on the features of its porous structure and technological conditions of its formation.

The results of investigation of the sensitivity n^+-p silicon diode structures with upper PS layer, to the mixtures of various organic vapors with air as well as the influence of the technological regimes of the PS formation on sensitivity are presented in this paper.

2 Results and discussion

The formation of the porous layer on the n^+ top layer of initial silicon diode n^+-p structures of 15 × 7 × 0,8 mm size was carried out by the electrochemical anodization method in the solution of fluoric acid (HF- 49%), pure ethyl alcohol and distilled water at a ratio of 1: 2: 1 (samples of group I) or with the addition to this mixture 5% methanol (samples of group II).

Depending on the anodization regimes (the current density varied in 10-50 mA/cm^2 range, duration: 2 - 6 minutes, with or without illumination from fundamental absorption range) the samples of both groups with the formed PS layer could either possess or lack photoluminescence at excitation by an intensive line 365 nm from a mercury lamp.

It is known [3,5], that the current-voltage characteristics of diode structures are the sensitive tool for the detection of adsorbed gases. Therefore, for the sensitivity study of both groups samples, the current-voltage characteristics of these structures were investigated. It is noteworthy, that after forming the PS layer under identical conditions, the dark and light current-voltage characteristics of the samples of either group did not display any observable differences.

It was shown, that after the anodization the dark current-voltage characteristics almost do not change, while the light performances change noticeably. At the same time a considerable increase of the short-circuit current and an insignificant change of the open-circuit voltage was observed. The invariability of the dark current-voltage characteristics means that under the conditions of anodization described above, the thickness of the porous layers does not exceed the depth of the n^+-p junction (d ~ 1,2 μm).

For the study of the sensitivity of group I and II samples to the mixture of vapors of organic substances (ethanol, acetone, benzene, toluene) with

air, the dark current-voltage characteristics of the structures in pure and gas containing atmospheres were measured at room temperature and at atmospheric pressure. The necessary concentration of the gas in a darkened hermetic camera was created by the thermal vaporization of the above-mentioned liquid substances.

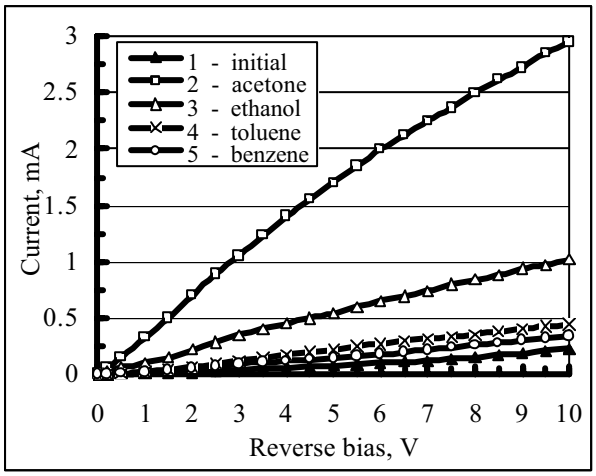

Fig. 1: I(V) characteristics of diode structures under saturation concentration of various organic solvent vapors.

These studies revealed considerable differences in sensitivity to the organic solvent vapors between the samples of both groups. If the current-voltage characteristics of group I samples in pure air and in the atmosphere of the vapors almost did not change, the current-voltage characteristics of group II samples underwent considerable changes as a result of organic solvent vapors adsorption. As distinct from the results observed in paper [3] the detected sensitivity of our samples to the vapors of the reducing gases under investigation, is manifested in the considerable increase of currents at reverse bias of the diode structures, whereas at forward biases the currents almost do not change. The results of this investigation at saturation concentrations of adsorbing vapors are depicted in Fig. 1, where the reverse branches of current-voltage characteristics before (curve 1) and after (curve 2-5) the adsorption of different vapors are presented.

The observable changes in the reverse branch of the current-voltage characteristics are connected with the adsorption process on the surface of the PS layer, because such changes were not observed on the reference samples (without PS).

It is known, that at room temperature chemisorption of the investigated vapors practically does not happen because of the high adsorption heat. This means that the reason of the change of electrical parameters of the structures is the physical adsorption of dipole molecules of the gases.

It is worth mentioning, that the last statement is well conformed to the observable correlation of the sensitivity of structures to vapors with different electrical dipole moments of molecules (Table 1). However, the electrical dipole moment is not the only physical factor affecting the change of conductance of structures with the PS layers at the adsorption of gases.

Table 1. The values of dipole moment and saturated vapor pressure of different solvents.

	Electrical dipole moment, (*Debye*)	Pressure of saturated vapors, (*Torr)*
acetone	2,88	233
ethanol	1.69	59
toluene	0.36	29
benzene	0	110

For example, it is well manifested in the adsorption of benzene or water vapors. Factually at the adsorption of benzene vapors, insignificant changes of the current-voltage characteristics of the structures are observed (Fig. 1, curve 5), though the electrical dipole moment of benzene molecules equals zero, and in the case of adsorption of water vapors no changes in the current-voltage characteristics are observed, in spite of the great value of the electrical dipole moment of water molecules.

The above-presented data clearly demonstrate that PS is a promising material for the creation of chemical sensors. To understand the mechanism of change of conductance fully, it is necessary to have an understanding of both charge transfer and the responses at conversion, which occur at the adsorption of gases on the surface of porous silicon.

This work was carried out in the framework of the ISTC A-322 grant.

References

[1] A.G. Cullis, L.T. Canham and P.D. Calcott: The structural and luminescence properties of porous silicon, *J Appl. Phys*., 82 (3) (1997) 909-965.

[2] O. Bisi, S. Ossicini, L.Pavesi, Porous silicon: a quantum sponge structure for silicon based optoelectronics, *Surface Science Reports,* 38 (2000) 1-26.

[3] I. Schechter, M. Ben-Chorin and A. Kux: Gas sensing properties of porous silicon, *Anal. Chem.*, 67 (1995) 3727-3732.

[4] J.M. Lauerhaas, M.J. Sailor: Chemical modification of the photoluminescence quenching of porous silicon, *Science*, 261 (1993) 1567-1570.

[5] A. Foucaran, F. Pascal-Delannoy, A. Giani, A. Sackda, P. Combette and A. Boyer: Thin Solid Films 297 (1997), 317-320.

Investigation on Cavitand-Coated PZT Resonant Piezo-Layer and QCM Sensors at Different Temperatures Under Exposure to Organic Vapors

M. Ferrari[1], V. Ferrari[1], D. Marioli[1], A. Taroni[1], M. Suman[2] and E. Dalcanale[2]

[1] Dipartimento di Elettronica per l'Automazione and INFM, Università di Brescia
Via Branze 38, 25123 Brescia, Italy - email: vittorio.ferrari@unibs.it http://ntweb.ing.unibs.it/deaweb/
[2] Dipartimento di Chimica Organica ed Industriale, Università di Parma
Parco Area delle Scienze 17A, 43100 Parma, Italy

Summary: *AT-cut thickness-shear mode quartz crystal microbalance (QCM) sensors and resonant piezo-layer (RPL) sensors made by lead zirconate titanate (PZT) thick films on alumina were sensitized with cavitand coatings (Qx-Cav and Me-Cav) and exposed to organic vapors of environmental interest. Responses at different temperature are compared. Effects due to the temperature dependence of the partition coefficient and the porosity of RPL sensors are also considered.*

Keywords: *QCM, resonant piezo-layer, acoustic-wave sensor, partition coefficient, cavitand, temperature*
Category: *5 Chemical sensors*

1 Introduction

AT-cut thickness-shear mode quartz crystal microbalance (QCM) sensors are commonly used as gravimetric elements due to their good mass resolution at comparatively low operation frequency. Recently, bulk acoustic-wave resonant piezo-layers (RPL) sensors made by lead zirconate titanate (PZT) thick films screen-printed on alumina substrate have been proposed as gravimetric sensors for chemical detection in air [1,2]. Comparative experiments on cavitand-coated RPLs and QCMs are here firstly reported on the response to some organic analytes of environmental interest. The capability of variable-temperature operation of the RPL arrays easily allows evidencing the temperature dependence of the partition coefficient and exploiting it to modulate the sensitivity. Film porosity also seems to play a role in the response.

2 RPL sensors

RPLs offer similar mass sensitivity at parity of frequency with respect to QCMs and can easily and cost-effectively manufactured as multisensor arrays on the same substrate. The RPL structure is made by the superposition of nonpiezoelectric substrate, specifically alumina, a bottom-electrode layer, a screen-printed PZT layer poled along its thickness, and a top-electrode layer (Fig.1).
The RPL substrate also includes a resistive element that can be used as a thermostating heater to modulate temperature effects by adjusting the sensor temperature to different values (Fig.2).

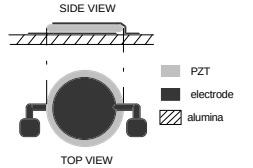

Fig. 1: Structural view of a RPL.

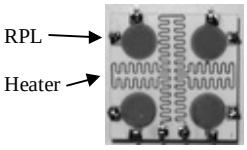

Fig. 2: RPL array.

3 Receptors

Cavitands used in this study exhibit supramolecular host proprieties which permit to incorporate guests with a suitable polarity and shape (Fig.3).

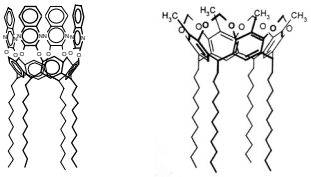
Fig. 3: *Qx-Cav* (left) *Me-Cav* (right)

Me-Cav has a more accessible and electron-rich cavity and can interact preferentially with analytes having "acidic" methyl groups. *Qx-Cav* presents a larger and deeper cavity formed by four quinoxalines; it is more adapted to interact with liphophilic organic guests, especially of aromatic origin [3]. Differently from QCMs (where cavitands are deposited onto the Au electrode surface), RPLs, due to their porosity, tend to let the coating receptors penetrate in the bulk, which fact, somewhat unexpectedly, produces an increase in sensitivity.

4 Experimental set-up

10-MHz QCM sensors and 7-MHz RPLs were sensitized with *Me-Cav* and *Qx-Cav* (starting from a 1% solution in methylene dichloride) either by spray coating technique with an air-brush or by dropping with a micro-syringe. Four QCMs and four RPLs were arranged into a stainless steel chamber with a volume of 175 ml, equipped with inlet and outlet for vapors (Fig.4).
The test vapors were generated from a bubbler at ambient temperature using nitrogen as the carrier gas and then diluted to known concentrations by computer-driven mass flow controllers. The sensors

were connected to dedicated oscillator circuits whose output frequencies were taken as the sensor signals. The sequential acquisition of the sensor signals and the vapor flow were controlled by a PC.

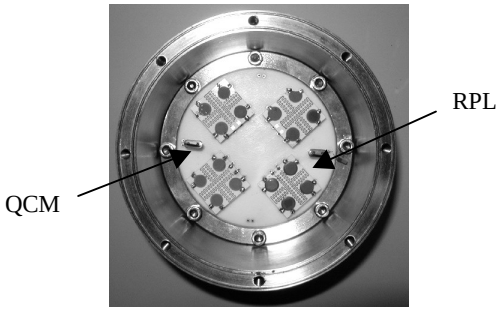

Fig. 4: Stainless steel sensor chamber.

5 Results

Typical experiments consisted of repeated exposure to the organic analytes with an exposure time of 20 min, followed by 10 min purging with nitrogen. The frequency outputs of all the sensors were recorded every 2 s. The temperature of the RPL arrays was set to selected values by properly adjusting the driving of the built-in heater by a dedicated thermostating circuit. For both types of sensors, baseline compensation was applied to the raw data to correct for residual thermal drift.

Fig.5 shows a typical response of a RPL (*Me-Cav*) sensor to 4000 ppm of toluene at different temperatures. As expected, it can be noticed that the amount of sorption decreases with increasing temperature. The temperature dependence of the partition coefficient shows an exponential trend in the case of nonspecific polymeric layers [4]. On the other hand, in our case it is necessary to take into account specific interactions (CH-π and hydrophobicity) with analytes and potential swelling-induced modulus changes of the cavitand receptor layer on the RPL device.

Fig.6 reports the frequency shifts of a RPL (*Me-Cav*) sensor versus toluene concentrations measured at different temperatures. It can be noticed that the ratio of the frequency shifts at the two temperatures, which is related to the partition coefficient of the cavitand-analyte pair, is independent from analyte concentration.

Fig.7 shows the response of a QCM (*Me-Cav*) sensor to 2000 ppm of toluene. In this case, a small increase of the chamber temperature (2-3°C), caused by the heating of the nearby RPL array, determined an unexpected and favourable improvement of the sorption kinetic without any significant modification of the frequency shift.

Both RPL and QCM sensors have shown suitable sensitivity to detect organic vapors down to concentrations in the order of 100 ppm. The RPL sensors can easily vary the array temperature to modulate the sensitivity and obtain higher-order sensing [5], and also to promote analyte desorption.

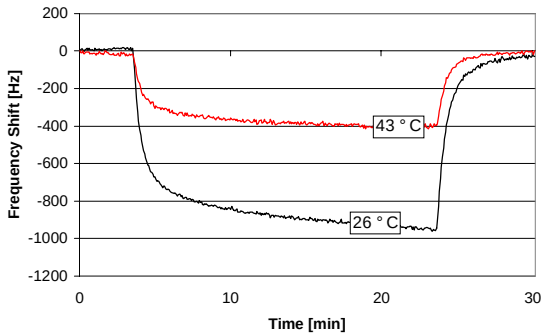

Fig.5: Response of a RPL (Me-Cav) sensor to 4000 ppm of toluene at different temperatures.

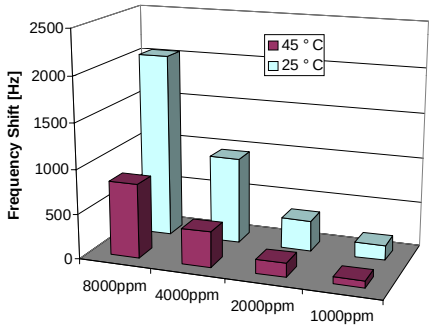

Fig.6: Response of a RPL (Me-Cav) sensor versus toluene concentrations at different temperatures.

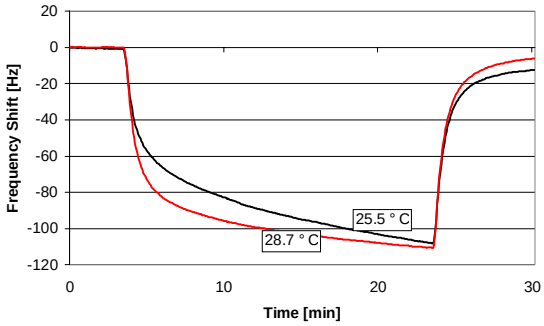

Fig.7: Response of a QCM (Me-Cav) sensor to 2000 ppm of toluene at slightly different temperatures.

References

[1] V.Ferrari, D.Marioli, A.Taroni, *Sensors and Actuators A*, 92, 1-3, (2001) 182-190.

[2] A.Depari, M.Ferrari, P.Ferrari, V.Ferrari, A.Flammini, D.Marioli, A.Taroni, *Proc. of ISA-IEEE SIcon 2002 Conference*, Houston, TX, USA, November 19-21, 2002, 25-31.

[3] M.Ferrari, V.Ferrari, D.Marioli, A.Taroni, M.Suman, E.Dalcanale, *Proc. 8th National Conference on Sensors and Microsystems*, pp. 156, Trento, Italy, 12–14 February 2003.

[4] J.W.Grate, A.Snow, D.S.Ballantine, Jr., H.Wohltjen, M.H.Abraham, R.A.McGill and P.Sasson, *Anal. Chem.*, 60 (1988) 869-875.

[5] T.Nakamoto, K.Sukegawa, E.Sumitomo, *Proc. of IEEE Sensors 2002 Conference*, Orlando, FL, USA, June 11-14, 2002, 33.3.

Planar LiSICON-based potentiometric CO_2 sensor

F. Ménil, B. Ould Daddah, P. Tardy, H. Debéda, C. Lucat

Laboratoire IXL, Université de Bordeaux I, 33405 Talence, France
email: menil@ixl.u-bordeaux.fr http://www.ixl.u.-bordeaux.fr

Summary: *A better ventilation control of buildings could lead to a substantial reduction of the greenhouse effect. Planar CO_2 potentiometric sensors based on lithium conductor LiSICON and made by use of thick films microelectronics technologies have been developed for this application. The imperfections of the original sensors, with regard to the instability of the baseline, the influence of humidity and the long recovery times were strongly improved by optimizing both physico-chemical and geometrical parameters, in the design and in the fabrication process.*

Keywords: *thick films, carbon dioxide sensor, lithium conductor, ventilation control*
Category: *5 (Chemical Sensors)*

Introduction

The reduction of the greenhouse effect will certainly be one of the major priorities of the next years. A better ventilation control of dwellings and industrial buildings should in theory make it possible to reduce of about 10% the production of carbon dioxide. Two contradictory factors have to be taken into account :

- minimize the air renewing, which saves energy and concomitantly decreases the CO_2 emission,
- bring fresh air for obvious health reasons.

Such an optimization requires the use of CO_2 sensors. Thick film sensors made by hybrid microtechnologies well respond to this application.

Sensor principle and design

The principle selected is that of a potentiometric sensor of type IIIa, according to the classifications defined by Weppner [1] and Miura et al.[2]. The basic elements of the sensor are the layer of lithium ion conductor LiSICON (Li^+ Supra Ionic CONductor), the pseudo-reference electrode, only sensitive to O_2 and the working electrode, sensitive to both CO_2 and O_2 thanks to the presence of the auxiliary phase based on lithium carbonate.

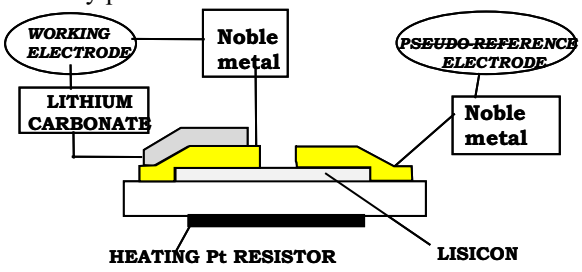

Fig. 1. Design of a thick-film CO_2 sensor

Assuming the formation of a thin layer of lithium oxide at the interface between the LiSICON and the pseudo-reference electrode, enables to derive a theoretical e.m.f. between both electrodes following the Nernst law with the CO_2 partial pressure. The sensor is normally selective to CO_2.

The design of the present sensor is inspired from the original proposal of a thick-film planar sensor based on NaSICON by Leonhard et al. [3]. The advantages of using LiSICON are a better resistance to humidity at the operating temperature of 500-550°C as well as better sintering properties during the fabrication process. Moreover, in order to ensure the continuity of the electrochemical chain, the use of LiSICON as ionic conductor implies that of lithium carbonate instead of sodium carbonate as auxiliary phase. Again, lithium carbonate offers a better resistance to humidity.

Results and discussion

The feasibility of such a sensor was first demonstrated. Fig 2 shows the variation of the e.m.f. with the logarithm of the CO_2 concentration, which follows the Nernst law with a slope of 73mV per decade at 500°C. This slope corresponds to an experimental value of 2.1 electrons per CO_2 molecule implied in the electrochemical reaction, in good agreement with the theoretical value of 2.

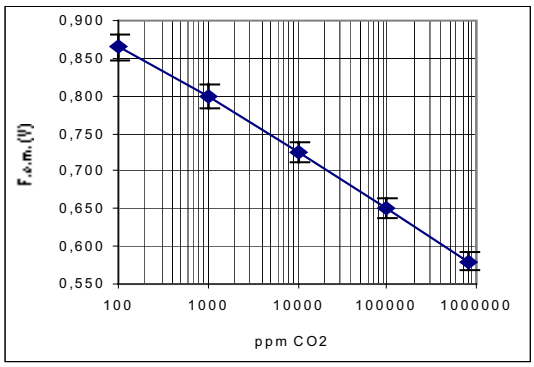

Fig. 2. E.m.f. provided by the sensor at 500°C, as a function of CO_2 concentration in dry air

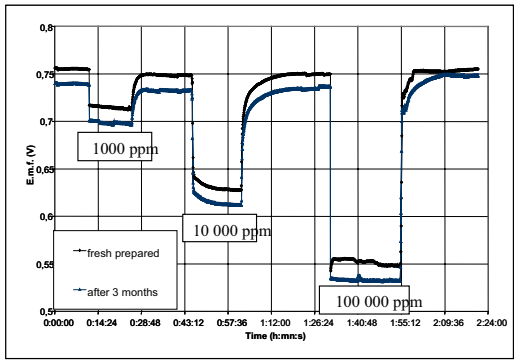

Fig. 3. Response of a CO_2 sensor freshly prepared and after being stocked 3 months in ambient air.

However, the first sensors suffered many imperfections :

- instability of the baseline
- influence of the humidity on the e.m.f.
- very long recovery times

The following steps consisted in attempting to solve the above problems, by modifying the physico-chemical parameters on one hand and the geometrical ones on the other.

The replacement of platinum originally used as electrode metal by gold permitted to stabilize the baseline. The adjunction of calcium or barium carbonate to the auxiliary lithium carbonate phase, practically suppressed the influence of humidity. The fabrication of a composite working electrode by mixing the gold ink with that of the auxiliary carbonate phase, apart from simplifying the sensor fabrication process, also improved its performances, especially regarding the recovery times after exposures to CO_2.

As for the geometrical parameters, the most unexpected result was certainly the very strong effect of the asymmetry of the electrodes on the response of the sensor. As soon as the surface of the pseudo-reference electrode becomes smaller than that of the working electrode, the sensor does not operate properly (baseline instability, decrease and even inversion of the sign of the e.m.f.). A possible simple explanation based on lithium carbonate diffusion from the working electrode to the pseudo-reference electrode, was ruled out by various spectroscopic methods (EDX, PIXE). A tentative explanation based on asymmetrical accumulations of charges at the interfaces will be proposed.

All previous improvements of both physico-chemical and geometrical parameters led to a satisfactory operating CO_2 sensor for the ventilation control, especially with regard to the reliability and the recovery times, as shown in Fig. 3.

References

[1] W. Weppner, *Sens Actuators*, B12 (1987) 107–119.

[2] N. Miura, S. Yao, M. Sato, Y. Shimizu, S. Kuwata, N. Yamazoe, *Chem. Lett.* (1993) 1973-1976.

[3] V. Leonhard, D. Fischer, H. Erdmann, M. Ilgenstein, H. Köppen, , *Sens Actuators*, B13-14 (1993) 530-531.

Polysilicon Surface Micromachining for the Fabrication of Thermally Isolated Micro-Igniters

P.Q. Pham, D. Briand and N. F. de Rooij

Sensors, Actuators and Microsystems Laboratory, Institute of Microtechnology, University of Neuchâtel, Rue Jaquet-Droz 1, P.O. Box 3, CH-2007 Neuchâtel, Switzerland
email: phuong-quyen.pham@unine.ch http://www-samlab.unine.ch

Summary: *This paper presents the fabrication and the characterization of surface micromachined polysilicon micro-igniters. Designed to ignite the propellant in solid-state propellant micro-thrusters, they consist in parallel suspended polysilicon bridges, which are heated up by Joule effect. Thermal losses through the substrate are minimized by suspending the micro-heaters above the substrate. The micro-igniters were fabricated by surface micromachining with an APCVD silicon oxide as sacrificial layer. The developed process is compatible with the integration of the diverging part of the nozzle composing the micro-thrusters. The micro-igniter electrical resistance value ranged from 200 Ω to 1.4 kΩ depending on the number of bridges. The current-voltage relation followed a linear characteristic at low power; at high bias voltages, a drift of the electrical power was observed after a few I-V cycles. A temperature of at least 450°C was reached with a power of 130 mW per beam. The electrical characteristics of the fabricated micro-igniters meet the power requirements for the ignition of solid propellant micro-thrusters.*

Keywords: *micro-heater, micro-igniter, polysilicon, surface micromachining*
Subject category: *2 (Materials and Technology)*

1 Introduction

With the emergence of micro-propulsion systems integrating MEMS technology, micro-thrusters based on the ignition and combustion of solid-state propellant has appeared [1,2]. Due to the major role played by the igniter in the device functioning, special attention should be paid to its design and to its characteristics in order to achieve successful ignition of the propellant. Current technology uses polysilicon micro-heaters as igniters, which are thermally insulated from the substrate by means of a thin dielectric membrane and fabricated by bulk micromachining [1,3].

Both bulk and surface micromachining of polysilicon have been used as fabrication technology for various applications. On one hand, polysilicon micro-heaters fabricated by bulk micromachining are already commonly used for gas sensors, gas flow sensors and igniter applications. On the other hand, the investigation and exploitation of polysilicon surface micromachining has been performed for mechanical, electrostatic or piezoelectric micro-actuators and -sensors. However, the surface micromachining of polysilicon used for heating applications is still under development and has been reported lately. Thermal simulation of a surface micromachined micro-hotplate has been performed and has shown that temperatures up to 400°C could be reached with an input power of 100 mW [4]. Polysilicon micro-igniters fabricated by surface micromachining have been integrated in a gas turbine microengine [5]; it presented a consumption power between 3 and 6 W for a bias voltage of 90 to 260 V.

In this paper, we report on the use of surface micromachining to fabricate freestanding polysilicon micro-igniters on silicon with the aim of reducing the ignition power consumption and the bias voltage. The electrical resistors, heated up by Joule effect, were thermally insulated from the substrate by being suspended above the bulk with an air gap. This was performed by using surface micromachining technology. The electrical power that could be delivered by the micro-igniters was measured. Infrared measurement was done to investigate the temperature reached by the devices. The instability of polysilicon electrical properties operated at high temperature was also examined.

2 Design and Fabrication

The micro-igniters were composed of 2 to 16 parallel polysilicon heating bridges, fabricated on a silicon substrate. The beams width was set to 20 μm; their length ranged from 180 μm to 240 μm. The design as well as the fabrication process of the igniters allowed the integration of a divergent nozzle through which the combustion gas can be evacuated (Fig. 1).

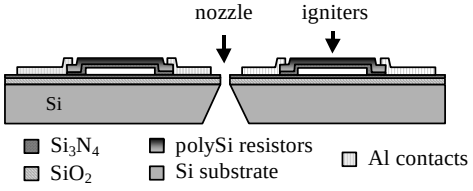

Fig. 1. Schematic cross-section view of suspended micro-igniters surrounding the nozzle throat.

The igniters were fabricated on 525 μm-thick silicon wafers, polished on the topside. The fabrication process started with the passivation of the substrate by a thermally grown SiO_2 and a LPCVD Si_3N_4. The sacrificial layer consisting in 1.2 μm-thick layer of partially doped APCVD SiO_2 was then deposited, densified and patterned. On top of it was deposited a double layer of 200 nm of LPCVD Si_3N_4 and 700 nm of LPCVD polysilicon. Polysilicon was doped by the phosphorous diffusion from a layer of doped APCVD SiO_2. The next step consisted in patterning the double layer of silicon nitride and polysilicon by RIE to form the electrical resistors. The release of the polysilicon resistors was performed by etching the SiO_2 sacrificial layer in HF 50%. Then aluminum interconnections were deposited through a shadow mask in order to prevent the stiction of the structures to the substrate. Finally, the aluminum was annealed in order to form ohmic contacts with the polysilicon.

An additional process step can be performed to integrate the nozzle during the igniter fabrication. This is achieved by etching the divergent nozzle by DRIE before the release of the resistors.

4 Results

Polysilicon micro-igniters have been successfully fabricated by surface micromachining (Fig. 2). The bridges were completely released after the etching of the SiO_2 sacrificial layer. No stiction of the structures on the substrate could be noticed and the structures were freestanding.

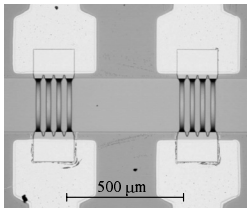

Fig 2. Picture of a micro-igniter composed of 2 × 4 free-standing polysilicon bridges (single beam dimensions: 20 μm × 180 μm).

A polysilicon electrical resistivity of 250 Ω/□ was obtained. The resistance of the micro-igniters varied between 200 Ω and 1.4 kΩ depending on the number of parallel beams that constituted the micro-heater. The current-voltage relation followed a linear characteristic at low power.

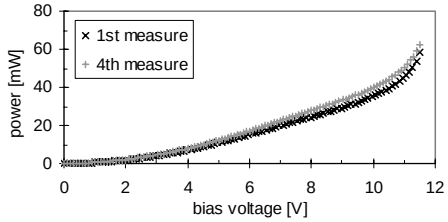

Fig. 3. Electrical power per beam versus bias voltage of a 2 × 2 polysilicon bridges resistor: a drift of the resistance value after several I-V cycles results in an electrical power change.

After a few I-V cycles at high bias voltages, a decrease of the resistance value was measured, which causes a power drift (Fig. 3). This is probably due to the instability of polysilicon resistivity at high current densities operation. Power up to 200 mW per beam could be delivered by the igniters for a few seconds, for a total power greater than 1 W. Infrared measurement showed that a minimum temperature of at least 450°C could be reached with a single beam power of 130 mW (Fig. 4). Despite the instability of polysilicon resistivity at high current densities, the micro-igniters fulfill the ignition requirements of the propellant (temperature, energy) and meet the electrical characteristics needed for the application.

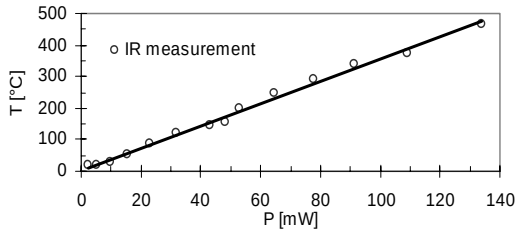

Fig. 4. Temperature as a function of electrical power per beam for a polysilicon resistor of 2 × 1 beams (IR measurement).

5 Conclusion

This paper described the fabrication and the characterization of freestanding micro-igniters for solid propellant micro-thrusters. The realization of polysilicon micro-heaters was successfully achieved by silicon surface micromachining. A single beam could deliver 200 mW and a temperature of 450°C could be reached with 130 mW. The thermal and electrical characteristic of the micro-igniters makes them suitable for the ignition of solid propellant. Further investigation would consist in studying the polysilicon mechanical behavior during operation and its material properties changes at high temperature.

References

[1] C. Rossi et al., "Solid Propellant Microthrusters on Silicon", submitted to *Journal of Propulsion and Power* (2003).

[2] D.H. Lewis Jr, S.W. Janson, R.B. Cohen and E.K. Antonsson, Digital Micropropulsion, *Sensors and Actuators* A80 (2) (2000) 143-154.

[3] C. Rossi, P. Temple-Boyer and D. Estève, "Realization and Performance of Thin SiO_2/SiN_x Membrane for Microheater Applications", *Sensors and Actuators* A64 (1998) 241-245.

[4] M. Dumitrescu et al., Thermal Simulation of Surface Micromachined Polysilicon Hot Plates of Low Power Consumption, *Sensors and Actuators* 76 (1999) 51-56.

[5] X. Zhang, A. Mehra, A.A. Ayon and I.A. Waitz, Development of Polysilicon Igniters and Temperature Sensors for a Micro Gas Turbine Engine, *15th Annual IEEE International MEMS 2002 Conference*, pp. 280-283, Las Vegas, Nevada, USA, 20-24 January 2002.

Reliability analysis of Pt-Ti micro-hotplates operated at high temperature

J. Puigcorbé[1], A. Vilà[1], D. Vogel[2], B. Michel[2], N. Sabaté[3], I. Gracia[3], C. Cané[3], J.R. Morante[1]

[1]Electronic Materials and Engineering-EME, Department of Electronics,
University of Barcelona, Martí i Franqués 1, E-08028-Barcelona (Spain)
email: anna@mercuri.el.ub.es http://nun97.el.ub.es
[2]Fraunhofer Institute Reliability and Microintegration (IZM), Berlin, Germany
[3]Centre Nacional de Microelectrònica-CNM, Campus UAB, E-08193-Bellaterra, Barcelona, Spain

Summary: *This work on microsystem reliability is devoted to the study of the degradation due to high temperature operation of silicon micro-hotplates, in order to optimise their design. The micro-structural variations of the films such as the grain growth and the formation of hillocks have been analysed using AFM techniques. Moreover Auger electron spectroscopy has been applied to measure the interdiffusion of Pt/Ti/Si_3N_4 during the high-temperature working mode of the micro-hotplate. These measurements have been correlated and completed with mechanical and electrical characterisation of Pt-Ti thin films in order to investigate the factors that influence on the reliability of micro-hotplates.*

Keywords: *Reliability, degradation, micro-hotplate, high temperature*
Category: *2 (Materials and Technology)*

1 Introduction

In MEMS devices, temperature regulation usually plays an important role, as the behaviour of their components is drastically influenced by temperature. In general, this control is reached by means of integrated parts or structures as micro-hotplates or micro-heaters, widely used in pyrotechnic actuators, flow and gas sensors, IR emitters, microTAS, and other applications. The market acceptance of these devices depends on the solution of problems associated with material and device degradation, which mainly involves their active parts. The reliable mechanical properties of the materials and thin films in the MEMS are critical for the appropriate behaviour and safety of these complex systems.

Micro-hotplates are usually made by integrating heater resistors into micro-machined membranes or more complex structures, which provide low power consumption, good temperature distribution and thermal isolation from the surrounding elements. However, the operation principle for most applications implies large temperature gradients, and even a rapid and frequent change in temperature, what cause important thermal stresses able to damage the device [1-2]. As a consequence, the materials that compose it suffer micro-structural changes and degrade producing defects such as cracks, hillocks or film delamination.

This work examines the reliability and degradation due to high temperature operation of micro-hotplates that present Pt-Ti as a metallisation defining a structure similar to those used as electrodes in micro-mechanised gas sensors. It also discusses how designs can be improved.

2 Experimental

Two support structures have been investigated for the micro-hotplates, one consisting on a complete dielectric membrane and another one as a square suspended from 4 arms (shown in Fig. 1). Both were fabricated on double side polished p-type <100> Si substrates, 300µm thick. A layer of 0.3µm of LPCVD Si_3N_4 over SiO_2 has been used as membrane. Over it, a sputtered Pt (300nm) film plus a 20nm Titanium layer for adhesion were used as metallisation in both micro-hotplate structures.

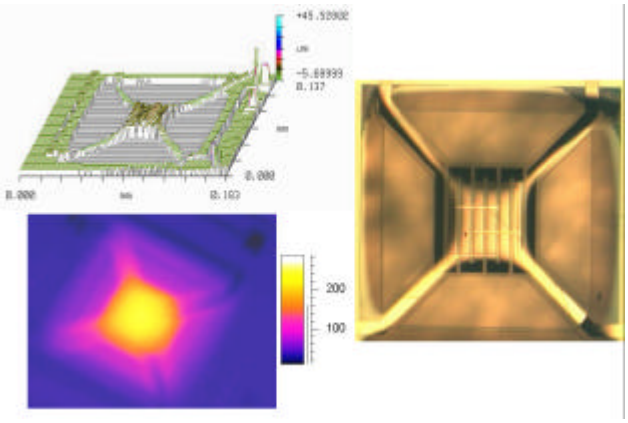

Fig. 1: Design (right), vertical residual deflection (left up) and temperature distribution during operation (left down) for the suspended micro-hotplate.

3 Results

The operation at high temperature of the two first micro-hotplate configurations gives to an evidently degraded appearance (Fig. 2), evidently showing that destructive processes take place and design optimisation is highly convenient.

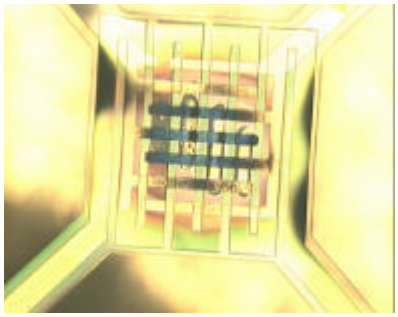

Fig. 2: Surface appearance of the suspended micro-hotplate after high temperature operation (>500ºC).

The micro-structural variations that occur in the Pt-Ti metallisations during post-process thermal treatments, such as grain growth and formation of hillocks, have been analysed using AFM techniques in order to evaluate its influence on the strength and on its mechanical behaviour. Observations show very important degradation in several edges of the Pt-Ti films (Fig. 3). These measurements have been correlated and completed with thermal, mechanical and electrical characterisation of Pt-Ti thin films in order to investigate the factors that influence on the reliability of the micro-hotplates. Nanoindentation measurements have revealed that the higher the grain size, the lower the hardness and the yield strength of the Pt-Ti thin films leading to affect the mechanical reliability of the micro-hotplate.

Moreover, Auger electron spectroscopy has been applied to measure the interdiffusion in the Pt/Ti/Si_3N_4 active area during the high temperature operation of the micro-hotplate. Experiments over the stacked configuration reveal that the Ti from the adhesion layer and the Ni from the Si_3N_4 membrane migrated into the Pt micro-heater, thus changing its electrical properties (Fig. 4). If high temperature is maintained enough long time, Ti and Ni can reach the Pt surface. This phenomenon has not been observed in samples heated externally (in an oven), suggesting that the diffusion is induced by the high currents and temperatures produced in the active area of the micro-hotplate during operation (electro-thermomigration). This change in the micro-heater properties modifies its electrical resistivity thus affecting the electrical performance of the device.

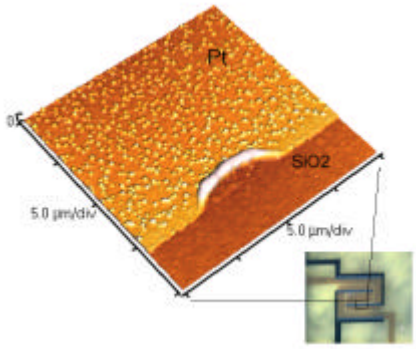

Fig. 3: Hillocks and delamination of Pt-Ti metallisation after high temperature operation.

3 Conclusions

The reliability and the degradation of high temperature operated Pt-Ti based micro-hotplates have been investigated experimentally. The structures studied are good enough to work up to 450-500ºC, but for higher operation temperatures several degradation mechanisms have been identified, such as grain growth, formation of hillocks, delamination and softening of the Pt-Ti films. Even, the operation of the micro-heater at these high temperatures has shown to produce electro-thermomigration of Ti and Ni into the Pt in the Pt/Ti/Si_3N_4 stacked configuration. The results obtained from all these analyses will be used to optimise the definitive design of the micro-hotplate in order to improve its reliability and lifetime.

References

[1] A. Götz, I.Gràcia, C.Cané, E. Lora-Tamayo, *J. Micromech. Microeng*. 7, 247-249, (1997).

[2] J. Puigcorbé, A. Vilà, J. Cerdà, A. Cirera, I. Gràcia, C. Cané and J. R. Morante, *Sensors and Actuators A,* Vol 97, 379-385, (2002).

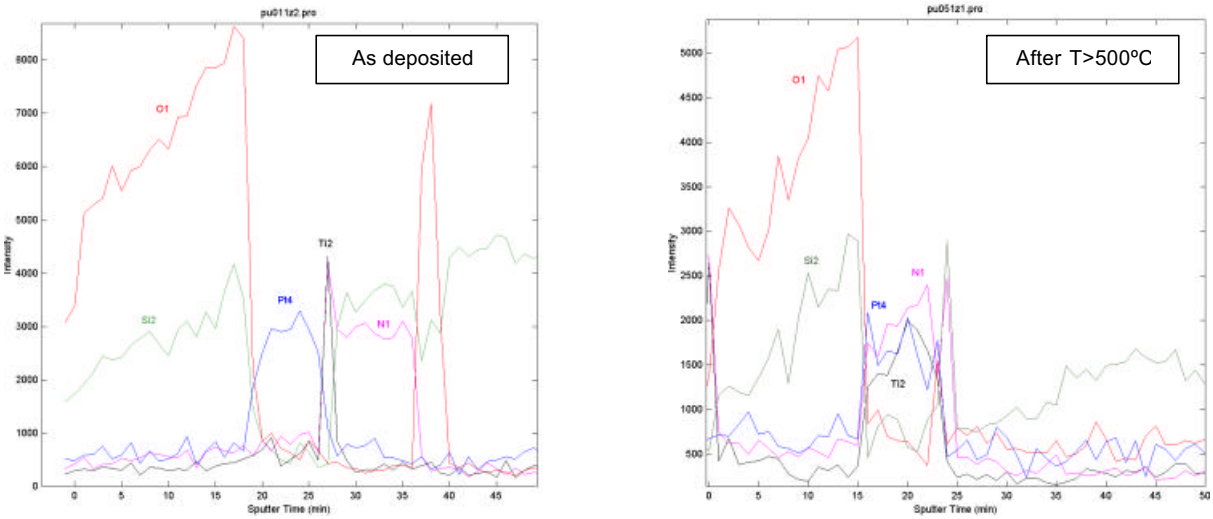

Fig. 4: Auger measurements of the electro-thermomigration of Ti-Ni into the Pt film after the high temperature operation.

Robustness of Silicon Microneedle Arrays Penetrating Bulk Materials

A. Trautmann, R. Haug, P. Ruther and O. Paul

IMTEK - Microsystem Materials Laboratory (MML), University of Freiburg,
Georges-Köhler-Allee 103, D-79110 Freiburg, Germany
e-mail: trautman@imtek.de phone: +49 761 203 7196 fax: +49 761 203 7192

Summary: *We report on the characterization of silicon microneedle arrays penetrating different solid materials. The microneedles are fabricated by deep reactive ion etching in an inductively coupled plasma etcher using the suspended etch mask technology. The penetration capability of differently shaped microneedles is verified in metals as well as plastics with a Vickers hardness between 4 HV and 73 HV. Microneedle shape dependent penetration behavior was extracted from load - displacement curves, enabling a direct comparison between various needle types.*

Keywords : *Microneedle arrays, robustness, mechanical stability*
Subject category : *8 (Packaging, chip handling, test and reliability)*

1 Introduction

The microneedle arrays presented here are intended to supply medical liquids into the human skin in a painless and minimally invasive manner. Since the human skin is covered by the resistant epidermis, consisting mostly of dead cells, transdermal drug delivery (TDD) applications require mechanically robust structures. Due to the soft and flexible characteristic of the skin, penetration of microneedles is not guaranteed. Thus, microneedles should be as slender and sharp as possible to enhance the penetration capability.

Solid microneedles with high aspect ratio can easily be fabricated in silicon [1, 2]. The needle shape is adjusted in sequences of isotropic and anisotropic dry etching in an inductively coupled plasma etcher using the suspended etch mask technology [2]. These slender needles have proven fluid access into the skin by means of their concave sidewall profile [2]. Their mechanical robustness is of major interest with respect to medical applications and is investigated in this study.

2 Microneedle shape

Arrays with different needle shapes were fabricated to characterize their penetration behavior. Figure 1 shows a microneedle array, where square etch mask openings with a width of 80 µm were applied. The distance between the openings was 50 µm. Basically three different microneedle geometries were fabricated to distinguish the penetration capability in view of the needle shape. Dimensions of the mask layout were kept the same. Individual needles are connected to each other by partition walls, four of these walls define a possible reservoir for liquids. Figure 2 shows an enlarged view of a single microneedle, in the following referred to as type 1. The tip shape of this needle is a pyramid (height ≤ h_1), supported by a cuboid with a side length of b. Type 2 consists of microneedles shown in Fig. 3. This needles have a concave sidewall

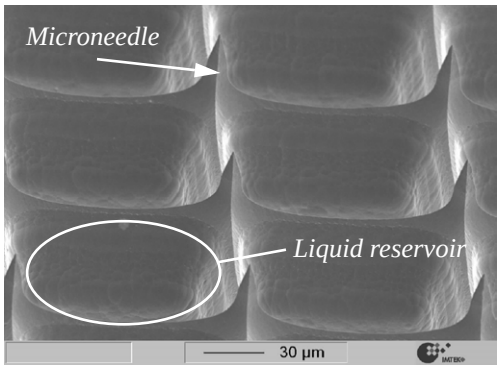

Fig. 1: SEM micrograph of a microneedle array. The square mask opening for the etching sequences had a side length of 80 µm, pitch was 130 µm.

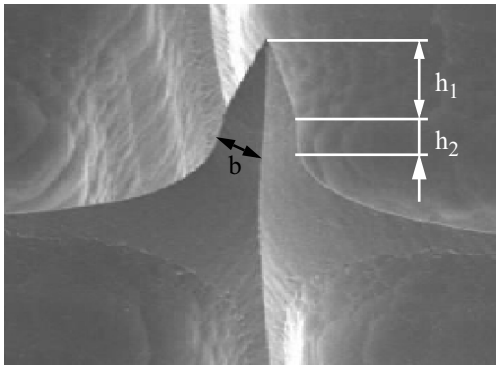

Fig. 2: Enlarged view of a single microneedle of type 1 with a height h_1 = 24 µm, h_2 = 16 µm.

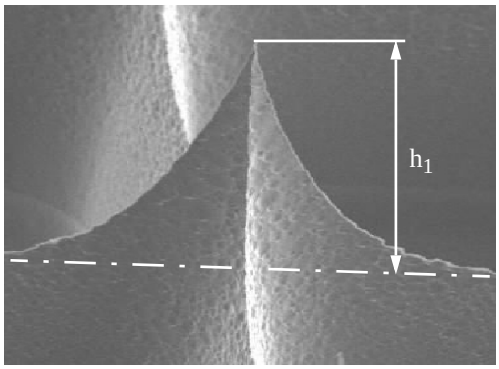

Fig. 3: Enlarged view of a single microneedle of type 2 with a height h_1 = 72 µm.

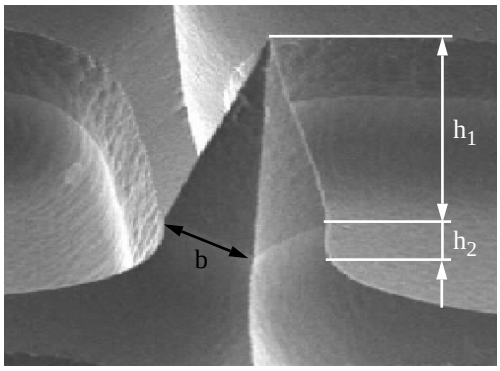

Fig. 4: Enlarged view of a single microneedle of type 3 with a height h_1 = 47 µm, h_2 = 18 µm.

profile with auxiliary cutting features. The sidewall profile of microneedles (type 3) shown in Fig. 4 is also similar to a pyramid with a slight undercut.

Table 1. Dimensions of a single microneedle of type 1, type 2 and type 3.

Dimension	Type 1	Type 2	Type 3
h_1	24 µm	72 µm	47 µm
h_2	16 µm	-	18 µm
b	11 µm	-	21 µm

3 Experimental

The microneedle arrays were diced into chips with side lengths of 2×2 mm^2. They are fixed to a metal rod mounted on a load cell (KD 40 from ME-Systeme, Germany). Chips and load cell are driven into the material by a high precision linear stage (Physics Instruments, 25 mm traveling range). Thus, the setup enables the measurement of displacement and load acting on the microneedle array during penetration into and withdrawal from the material under test. In a first test the chips were penetrated into lead with a hardness of 4 HV until a maximum force of 15 N. This enables a direct comparison of the penetration behavior between the needle sidewall shapes.

In a second test the chips were penetrated into five different materials; (i) Lead with a hardness of 4 HV, (ii) PC with a hardness of 13 HV, (iii) PMMA with a

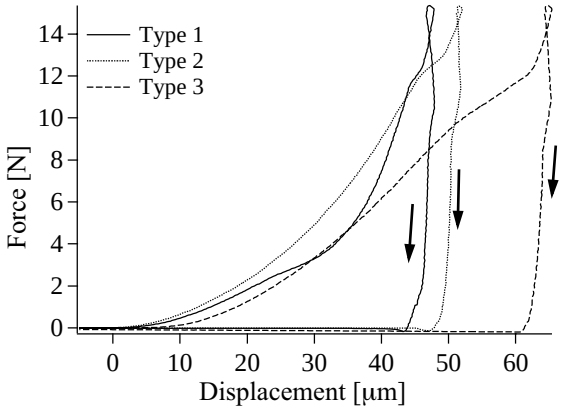

Fig. 5: Force vs. displacement. Type 1, type 2 and type 3 penetrated into and withdrawal from lead.

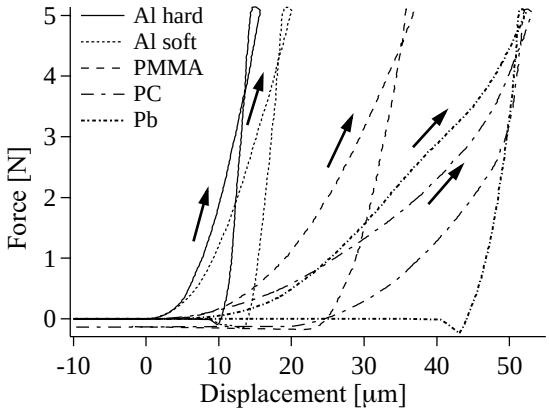

Fig. 6: Force vs. displacement of type 1 needles penetrated into and withdrawal from five materials.

hardness of 19 HV, (iv) Aluminum with a hardness of 39 HV, and (v) Aluminum with a hardness of 73 HV. The needle arrays were penetrated into the solid materials until a maximum force of 5 N.

4 Results

Figure 5 shows the forces acting on the needle arrays as a function of chip displacement during the penetration into and withdrawal form the lead bulk material. The influence of the needle shape results in changes of the measurement slopes. Since the penetrated material is plastically deformed, a hysteresis is obtained. Negative force values seen in the experimental data are caused by a sticking of the needle sidewall to the pierced material during withdrawal. Figure 6 shows the result of penetrating with type 1 into the five different materials. The needle arrays were capable of penetrating even into aluminium with a hardness of 73 HV. Plastics show a less steep withdrawal slope resulting from their more elastic behavior. After the chips were withdrawn from the materials under test, no visible damage was found on any needle.

5 Conclusions

Chips containing high aspect ratio microneedles with different geometries were fabricated. The microneedle arrays were mounted to a test rig capable of piercing various solid materials with the microneedles to verify the penetration capability in view of the needle robustness. Microneedle arrays have been pressed into both, solid metals and plastics, without suffering any damage. Needle shape dependent penetration behavior has been extracted from load - displacement curves.

6 References

[1] P. Griss, P. Enoksson, H. Tolvanen-Laakso, P. Meriläinen, S. Ollmar, G. Stemme, *Spiked Biopotential Electrodes*, Proc. MEMS '00 Conference, (2000), pp. 323-328.

[2] A. Trautmann, P. Ruther, O. Paul, *Microneedle Arrays Fabricated using Suspended Etch Mask Technology Combined with Fluidic Through Wafer Vias*, Proc. MEMS '03 Conference, (2003), pp. 482-485.

Characterization of MEMS Pressure Sensor Packaging Concept using O-rings as Hermetic Sealing

C. Pedersen[1], S.T. Jespersen[2], K.W. Jacobsen[1], J.P. Krog[1],
C. Christensen[1] and E. V. Thomsen[2]

[1]Grundfos A/S, Sensor Division, Poul Due Jensens Vej 7, 8850 Bjerringbro
email: capedersen@grundfos.dk http://www.grundfos.com
[2]Mikroelektronik Centret (MIC), Ørsteds Plads, Build. 345 East, DTU, 2800 Lyngby

Summary: *We present an in-depth characterization of a novel O-ring packaging concept for piezoresistive differential pressure sensors. The use of O-ring clamping as a hermetic sealing on coated MEMS pressure sensors provides a very powerful packaging concept applicable in various environments including wet aggressive media. Even relatively large misalignments of the die and O-rings only show a small influence on the sensor output signal (<4 mV). Furthermore, the sensor output shows a clear linear dependency on absolute media pressure with a maximum contribution smaller than 1% of maximum output. This is supported by 3D FEM stress analysis also showing a linear dependency on absolute pressure.*

Keywords: *O-ring, packaging, absolute media pressure, FEM, pressure sensor*
Category: *8 (Packaging, test and reliability), 1 (Modeling)*

Introduction

Corrosion resistant coatings have shown great promise in achieving wafer level packaging of MEMS pressure sensors for use in aggressive media [1]. In such environments several approaches are available for the encapsulation of coated pressure sensor dies [2]. As a novel approach in the field of MEMS pressure sensor packaging, O-ring clamping have now shown to be a promising candidate; see sketch in Fig. 1. By using O-rings as a hermetic sealing on coated MEMS pressure sensors, a direct media exposure of the MEMS device is possible. This results in a very simple, effective and cheap packaging concept applicable in various environments [3].

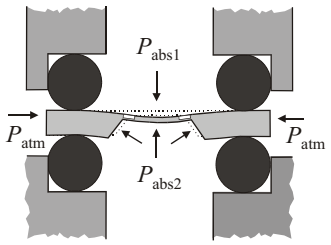

Fig. 1. A MEMS pressure sensor die clamped between two O-rings.

Alignment of die and O-rings

The first topic investigated was the influence of relative positions of the pressure sensor die and each of the two O-rings as shown in Fig. 1. Three separate alignment experiments, illustrated in Fig. 2, were performed on O-ring clamped sensor dies. In each of the three alignment experiments, the sensor output was measured for a range of relative displacements *x*. All measurements were performed at atmospheric pressure. Fig. 3 shows an example of sensor output behavior for each displacement situation in Fig. 2. The data indicates, that when the two O-rings are concentric (situation (1)) the induced output offset is less than around 1 mV for a misalignment of the sensor die up to 500µm. On the other hand, for non-concentric O-rings (situation (2) and (3)) a somewhat larger offset contribution up to 3-4 mV is induced. This larger contribution results from the moment acting on the sensor die, when applying non-concentric O-ring clamping (situation (2) and (3)). However, even relatively

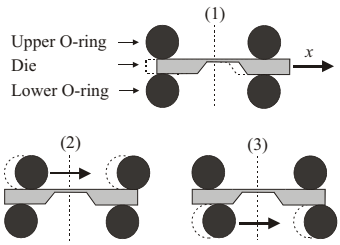

Fig. 2. Sketch of the die/O-ring alignment measurements.

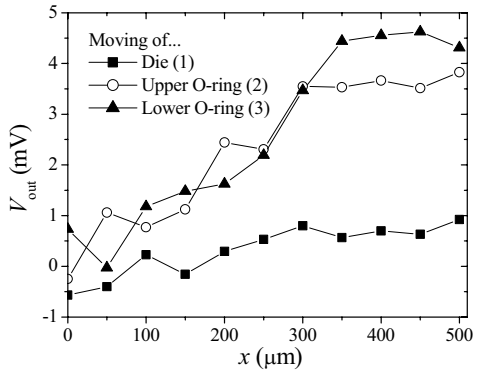

Fig. 3 Voltage output as function of displacement for the situations in Fig. 2.

large die/O-ring misalignments does not induce significant contributions to the output offset. This further emphasizes the power of the O-ring packaging concept.

Absolute media pressure dependency

In applications such as water supplies and central heating systems, the absolute media pressure can vary as much as 15 bars, leading to considerable stress contributions in the packaged sensor. We have found these stress contributions to be of importance when performing high accuracy calibrations on O-ring clamped MEMS pressure sensors.

Experimental results

For a wide range of absolute media pressures, a series of differential pressure characteristics were performed on O-ring clamped differential MEMS pressure sensors. In Fig. 4 a V_{out}-P_{abs} plot is shown for $P_{diff} = P_{abs1}$-P_{abs2} = 1bar. The plot is a blow-up of the smaller inserted plot containing data for all applied differential pressures. In addition to the usual linear dependency on differential pressure, the sensor output also has a clear linear dependency on the absolute media pressure. When using O-ring clamping, the pressure sensor die is free to expand or contract in the die plane as the media pressure acting on the etched edges of the sensor die varies. This effect is illustrated in Fig. 1.

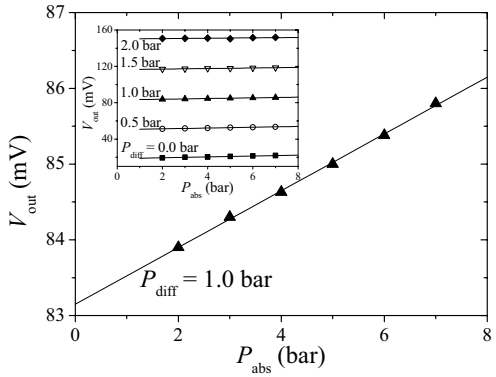

Fig. 4. Sensor output as function of absolute media pressure (blow-up of smaller inserted plot), $P_{abs} = P_{abs2}$.

3D FEM analysis

To further explore the dependency on absolute media pressure, an extensive 3D FEM analysis was carried out. The model shown in Fig. 5 include the sensor die and O-ring contact area from the packaging of the sensor. In Fig. 6 is shown a stress profile in the top layer of the sensor die as function of distance from the center of the membrane along the symmetry line perpendicular to the membrane edge (at atmospheric pressure). As a result of the O-ring clamping, a distribution in tensile stress is induced in the top layer of the die. The inner edge of the O-ring contact area at 1200 μm is clearly visible from the increase in tensile stress in the region 1000-1200 μm. The stresses induced by the O-ring clamping are however small compared to stresses induced by the media pressure (P_{abs} > 1bar, P_{diff} > 0bar). The smaller inserted plot in Fig. 6 show the stress for varying absolute pressure at the position of the piezoresistors, 475 μm from the membrane center (P_{diff} = 1bar). These and similar data for other P_{diff} values, all showed the same linear dependency on absolute pressure and thus were in good agreement with the experimental findings in Fig. 4.

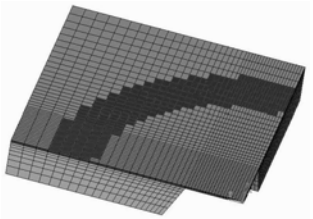

Fig. 5. 3D FEM model developed in this work. The O-ring contact area is shown in dark gray.

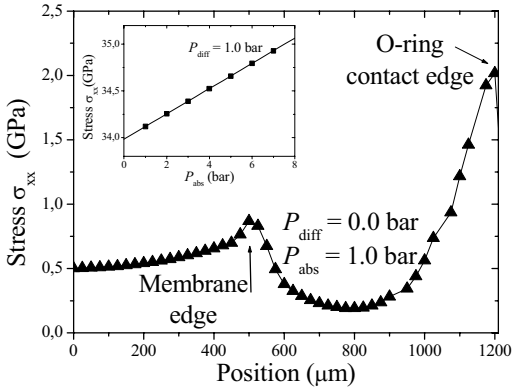

Fig. 6 Simulated stress (component along the symmetry axis perpendicular to the membrane edge) distribution relative to the center of the membrane.

Conclusion

A novel O-ring packaging concept for MEMS pressure sensors was investigated, showing only a small output dependency on relative die/O-ring positions. Furthermore, the influence of absolute pressure on sensor output showed a clear linear dependency with a maximum contribution smaller than 1% of maximum output. These findings were supported by 3D FEM analysis showing a linear stress dependency on absolute media pressure.

References

[1] C. Christensen, R. de Reus and S. Bouwstra, In: Technical Digest of 12th IEEE International MEMS'99 Conference, pp. 267-272, USA, 17-21 Jan. 1999.

[2] R. de Reus, C. Christensen, S. Weichel, S. Bouwstra, J. Janting, G.F. Eriksen, K. Dyrbye, T.R.. Brown, J.P. Krog, O.S. Jensen and P. Graversen, *Microelectronics Reliability* 38 (1998) 1251-1260.

[3] Grundfos. Pressure sensor or differential pressure sensor. Patent EP00801293B1.

Stress Isolation Chip for a Resonant Pressure Sensor

P. K. Kinnell[1], Dr. M C L Ward[2]

[1,2] The University of Birmingham, School of Mechanical & Manufacturing Engineering, University of Birmingham, Edgbaston, Birmingham, B15 2TT
Email: PKK618@bham.ac.uk

Summary: *This paper presents a stress isolation structure for resonant sensor applications. The structure is designed to selectively decouple a resonant strain gauge from the effects of unwanted packaging stress. A resonant pressure sensor is proposed that incorporates the stress isolation chip to allow a resonant strain gauge to be mounted to a large pressure sensitive silicon diaphragm. The chip behavior has been modeled using finite element analysis, and initial testing of the stress isolation chip has been carried out to verify its potential.*

Keywords: *Stress, isolation, resonant, strain gauge*
Category: *8 (Packaging, chip handling, test and reliability)*

1 Introduction

Resonant MEMs devices are now widely exploited in many sensor applications. While it is relatively easy to produce stable high Q resonators, packaging these devices in such a way that they are sensitive to the measurand but not affected by packaging stress presents a challenging problem[1, 2].

In the case of resonant pressure sensors a resonant structure is typically mounted to the back of a pressure sensitive diaphragm. This paper presents a novel stress isolation structure that allows a micro engineered resonant strain gauge to be selectively coupled to a large silicon diaphragm, to form a high sensitivity low-pressure sensor.

2 The Resonant Strain Gauge

The principle of using a resonant strain gauge mounted on a pressure sensitive diaphragm has been well documented[1, 2, 3]. For the purposes of this work a double-ended tuning fork (DETF) resonator is being used as the strain gauge. It will be excited electro-statically using a parallel plate actuator. The change in capacitance of a second parallel plate electrode will be used to pick-off the frequency of the device, see Fig 1. A DETF structure was chosen because it may be driven in a dynamically balanced mode, allowing a high mechanical Q to be developed[1].

3 Stress Isolation Chip

Previous work has been done to develop on-chip stress reduction zones, which shield sensitive structures from the unwanted affects of packaging or thermally induced stress [4, 5].

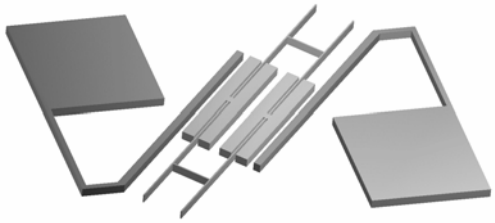

Fig. 1 Schematic of a double ended tuning fork resonator with drive and pick-off electrodes.

In the case of a resonant strain gauge the stress isolation must be selective. The affects of packaging stress must be decoupled from the resonator, however the resonator must still remain sensitive to the strain it was designed to measure. To achieve this a novel selective stress isolation structure is proposed.

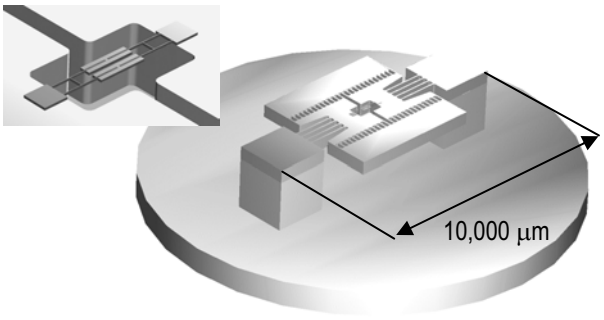

Fig. 2. Schematic of resonant pressure sensor assembly, the cut out shows an enlarged view of the double ended tuning fork resonator.

The aim of this structure is to act as a coupling between the resonant strain gauge at the heart of the device and the pressure sensitive diaphragm. By using such a structure it is possible to mount a micro-engineered resonator to a macro scale diaphragm, allowing high sensitivity low-pressure measurements. Fig. 2 shows a schematic of the

proposed resonant pressure sensor. The stress isolation chip can be seen mounted on a silicon diaphragm. In turn, mounted on the stress isolation chip is the strain sensitive resonator (note, drive and pick-off electrodes have been omitted from the schematic).

4 Finite Element Analysis

The Finite element analysis software Abaqus CAE was used to design and model the behavior of the stress isolation chip. Analysis shows the structure couples longitudinal displacement to the DETF strain gauge well, while lateral in and out of plane displacements generate much less strain in the DETF.

Fig. 3 shows the strain developed in the DETF as a result of displacements made to the stress isolation chip supports. Displacements were made in the longitudinal direction of the resonator, laterally (in plane with the stress isolation chip), and vertically (out of the chip plane). From the chart it can clearly be seen that longitudinal displacements of the stress isolation chip develop approximately 50 – 100 times more strain in the resonator than displacements in other degrees of freedom.

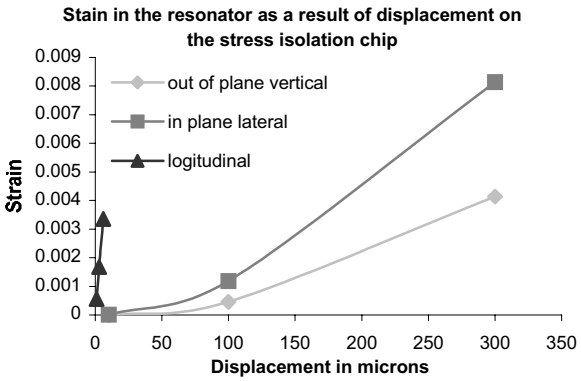

Fig. 3. Shows the strain developed in the resonator as a result of displacements made to the stress isolation chip.

As well as reducing strain developed in the DETF resonator as a result of non-longitudinal stress, the chip also ensures the DETF always stays correctly aligned and is only subjected to plain longitudinal strain: this is crucial to maintain optimum performance of the resonator. Fig. 4 shows the exaggerated deformation of the stress isolation chip after being subjected to non-longitudinal displacements. From the figure it can clearly be seen that the central area of the chip stays flat and aligned, only causing longitudinal strain in the DETF.

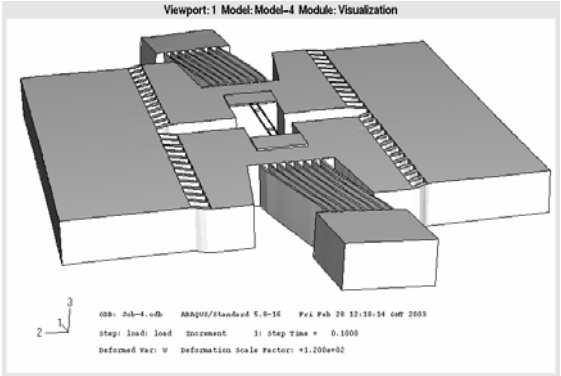

Fig. 4. Shows the affect of non logitudinal loading, the central area of the chip with the resonator stays aligned.

5 Fabrication & Testing

As a first step towards the final device a test stress isolation chip etched in bulk silicon was fabricated using an STS inductively coupled plasma etching machine. Rather than mounting a resonator on the chip, for the purpose of initial testing a pseudo resonator was built in to the stress isolation chip. This allowed a prototype stress isolation chip to be fabricated easily so mechanical testing could be done to verify the performance of the chip.

6 Conclusion

A novel stress isolation structure was presented, with a view towards mounting a micro resonator on to a macro scale pressure sensitive diaphragm. The potential to create selective stress isolation structures using deep reactive ion etching was demonstrated by finite element analysis, and verified through physical testing of a prototype stress isolation chip.

References

[1] S.P. Beeby, G. Ensell, N.M. White. *Micromachining Technologies for Industry (Ref. No. 2000/032), IEE Seminar,* 2000, Pages: 2/1 -2/4

[2] S.P. Beeby, G. Ensell, N.M White. *Engineering Science and Education Journal*, Volume: 9 Issue: 6 , Dec 2000, Pages: 265 -271

[3] J.C. Greenwood, D.W. Satchell.. *IEE Proceedings-Control Theory and Applications.* Volume: 135 Issue: 5, Jul 1988 Pages: 369 -372

[4] H.L. Offereins, H. Sandmaier, B. Folkmer, U. Steger, W. Lang. *Digest of Technical Papers, TRANSDUCERS '91*. 24-27 Jun 1991 Pages: 986 – 989

[5] V.L. Spiering, S. Bouwstra, R.M.E.J Spiering, M. Elwenspoek. *Digest of Technical Papers, TRANSDUCERS '91*, 24-27 Jun 1991 Pages: 982 –985

AFM Thermal Imaging of a Bulk Micromachined Thermopile

L. Fonseca[1], F. Pérez-Murano[1], C. Calaza[2], R. Rubio[1], J. Santander[1], E. Figueras[1], I. Gràcia[1], C. Cané[1], M. Moreno[2] and S. Marco[2]

[1]Centro Nacional de Microelectrónica (IMB-CSIC). Campus UAB. 08193 Bellaterra. Spain
email: luis.fonseca@cnm.es http://www.cnm.es
[2]Universitat de Barcelona. Departament d'Electrònica. Martí i Franqués 1. 08028 Barcelona. Spain

Summary. *The thermal characterization capabilities of an AFM has been applied in a bulk micromachined thermopile, showing its suitability to obtain the temperature distribution of micromachined devices.*

Keywords: AFM, thermal measurements, thermopile
Category: 8 (Packaging, chip handling, testing and reliability)

1 Introduction

Nanotechnology tools include successful scanning probe techniques, such as AFM, that allow to reduce the spatial range of the detail that can be obtained for the characterization of critical parts of sensors, actuators or microsystems. In this work, we have focused in one application of the AFM technique: thermal imaging, which has not been widely used for this purpose until now [1]. In this work this approach has been used to characterize a microdevice whose operation relies in a temperature contrast: a micromechanized thermopile.

2 AFM Thermal Measurements

The AFM thermal imaging approach has proven to be a very suitable technique to obtain the dimensional, structural and functional characteristics of a thermopile. A deeper insight of the thermopile operation can be gained with the aid of these advanced scanning probe based tools. Thermal information with a temperature resolution of 0.5ºC and a spatial resolution below 150nm can be obtained. Several factors may influence AFM thermal imaging, so that it may prove difficult to precisely determine the absolute local site temperature. However, an excellent contrast between sites having minor differences is expected.

3 Device Architecture

Our micromachined thermopile sensor chip consists of a series of thermocouples made of n-doped polysilicon and aluminum that are placed in a thin and freestanding nitride membrane [2]. The hot contacts of the thermocouples are formed on the thermally insulating membrane and the cold contacts are placed on the silicon rim of the structure, which acts as a heat sink. An underplatform silicon slab has been added in order to, taking advantage of the infrared absorption properties of heavily doped silicon (thus converting the IR radiation into thermal energy), define the sensitive area acting as an absorber (Fig. 1). The high thermal resistance membrane assures the temperature isolation between the hot and cold junctions thus allowing a temperature difference to develop when IR radiation reaches the absorber layer. Finally, an integrated self-test resistance has been included in the active area to swiftly electrically test the thermopile performance by Joule dissipation.

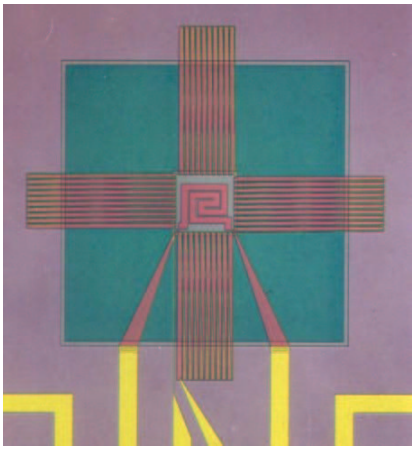

Fig. 1: Photograph of a micromachined thermopile. The nitride membrane, the silicon absorber, the self-test heater and thermocouples can be seen.

4 Measurement Results

After first checking that the AFM thermal characterization yields sound results (Fig. 2,3), we have ther-

mally measured the thermopile at different locations, proving the good isolation provided by the membrane (Fig. 4) and the uniformizing properties of the silicon absorber (Fig. 5). The different results have been cross-checked with the thermoelectrical characterization of the thermopile, and in some cases the AFM characterization has offered an explanation of otherwise puzzling thermoelectrical results (Fig. 6). The advantages of the modified AFM tip over other thermal probing are its small size and controlled applied force, thus allowing safe (less risk of breaking fragile parts such as the freestanding nitride membrane), truly local (nanometer scale, enabling pinpoint temperature determination) and undisturbed (low thermal mass) probing of an established temperature distribution.

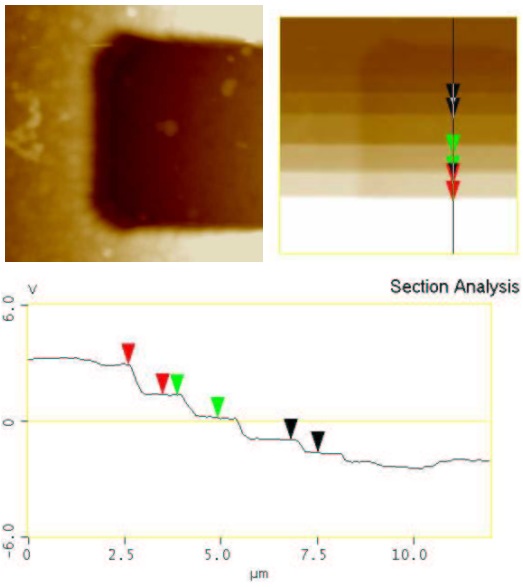

Fig. 2: Topographic image of a portion of the central heater, c-shaped rim (*up left*). Thermal image of the same area while changing the heater voltage (*up right*). Changes in the image and analysis steps (*bottom*) are evident.

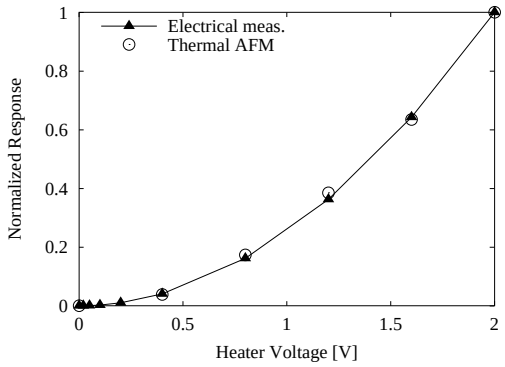

Fig. 3: Normalized thermogenerated voltage and AFM signal as a function of heater voltage. Functional identity is clearly seen.

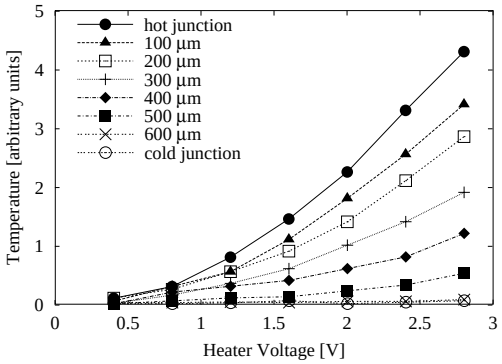

Fig. 4: AFM signal as a function of heater voltage along one thermocouple from hot to cold junction.

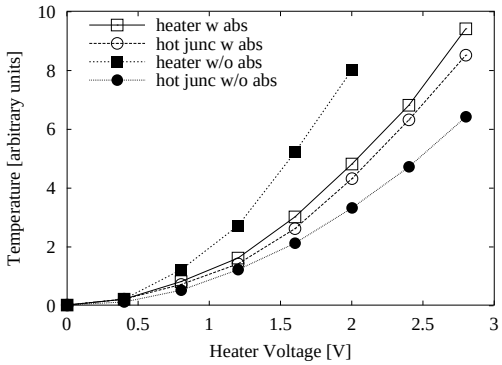

Fig. 5: AFM signal as a function of heater voltage at different locations within the active zone: the heater itself and close to the hot junctions. A thermopile with and without absorber is represented. The heater temperature is higher in the case without the absorber, but the hot junction temperature is higher when the absorber is in place.

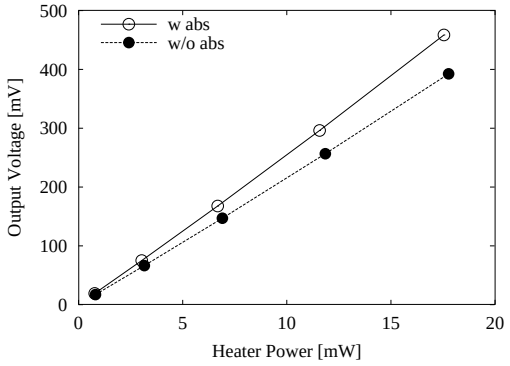

Fig. 6: Thermogenerated voltage as a function of the dissipated power in the heater for a thermopile with and without absorber. It is larger in the absorber case pointing to a higher hot junction temperature in accordance with the AFM measurements.

References

[1] A. Majumdar *Annu. Rev. Matter Sci.* **29** (1999) 505–585

[2] C. Calaza et al. *IRS2*, Erfurt, 2002.

RF MEMS Switches with Damascened Coplanar Waveguides

Dongha Shim, Eun-sung Lee and Insang Song

Samsung Advanced Institute of Technology, P.O. Box 111, Suwon, Korea
email: enJoee@hotmail.com

Summary: *This paper presents MEMS switches with damascened coplanar waveguides (DCPW) for commercial wireless applications. The proposed DCPW transmission lines with gap-fill dielectrics are fabricated using the dual damascene CMP (Chemical Mechanical Polishing) process. Therefore, the t-lines have very small surface thickness variations and alleviate the process problems from severe topography due to the thick t-lines in RF MEMS switches. Series metal-to-metal contact switches with DCPW t-lines are fabricated and evaluated. The switches exhibit the low loss (<0.25 dB @ 5 GHz) with good isolation (47 dB @ 5 GHz).*

Keywords: *RF MEMS, switches, damascened coplanar waveguide (DCPW), CMP*
Category: *10 (Applications)*

INTRODUCTION

RF MEMS (Micro Electro Mechanical Systems) is emerging technology for reconfigurable RF circuits. Recently, various kinds of RF MEMS switches have been developed and exhibit high performances [1], [2]. Most RF MEMS switches are composed of movable plates and transmission lines like coplanr waveguides (CPW) or microstrip lines.

This paper details design and fabrication of damascened coplanar waveguides (DCPW) using dual damascene CMP (Chemical Mechanical Polishing) technology [3]. The thickness of CPW is designed to be thicker than skin depths to reduce losses and is comparable in thickness with that of sacrificial layers in RF MEMS switches. The resultant severe topography of devices not only makes difficult photolithographic and film processes, but causes complexity in processes and associated designs as well.

The proposed DCPW with gap-fill dielectrics have very small surface thickness variations and alleviate the process problems associated with fabrication of RF MEMS switches. With the DCPW t-lines, metal-to-metal contact series switches are fabricated with 3 μm thick Au movable plates. Furthermore, pull-in voltages and RF performances of the switches are evaluated.

DESIGN AND FABRICATION

CPW is one of the most popular t-line structures in RF MEMS devices due to its easy accessibility to grounds. The basic structure of CPW with a signal line and ground planes is shown in Fig. 1(a) and the proposed DCPW with a planarized surface with gap-fill dielectrics in Fig. 1(b).

The DCPW t-lines with dimensions of S/W/S = 18/150/18 μm (50 Ω) are fabricated on 500 μm thick quartz substrates (ε_r = 3.8, tanδ = 0.0001). The thickness of CPW t-lines should be designed to at least 3 skin depths so as to minimize conductor losses. A 3 μm thick Au is used for conductor lines because the skin depth of Au is about 1 μm at 5 GHz. The tetra-ethylorthosilicate (TEOS) oxide is used to fill the gaps in DCPW t-lines.

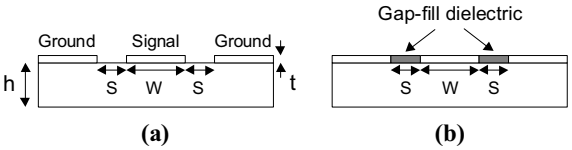

Fig. 1. Cross-sectional schematic diagram of (a) CPW and (b) DCPW t-line.

The magnitude of characteristic impedance Z_0 and the attenuation of CPW and DCPW with above-mentioned dimensions are calculated using Ansoft HFSS software and shown in Fig. 2. There is decrease in $|Z_0|$ of DCPW t-line due to gap-fill dielectrics which increase the shunt capacitance of t-lines. The figure also shows that there is very little difference in attenuations, 0.35 and 0.36 dB/cm at 5 GHz, in CPW and DCPW t-lines respectively.

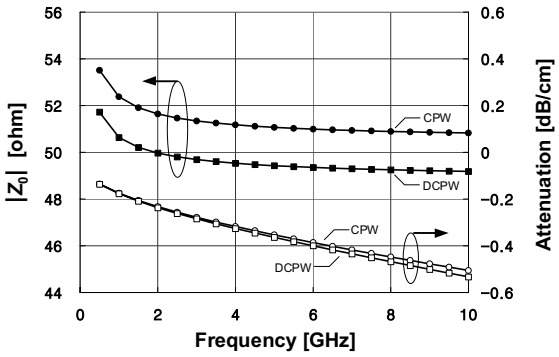

Fig. 2. Calculated magnitude of characteristic impedance $|Z_0|$ and attenuation of the designed CPW and DCPW t-lines respectively.

The fabrication process flow of DCPW t-line is shown in Fig. 3. (a) A thick TEOS oxide layer (5 μm)

is deposited and patterned to form gap-fill dielectrics with a dry RIE etch. (b) A thick Au layer (4-5 μm) is sputtered for conductors of signal and ground lines. (c) CMP of Au to form DCPW t-lines with thickness of 3 μm. The cross-sectional view of a fabircated DCPW t-line is shown in Fig. 4. The flat and residual free surface after CMP is clearly seen in the figure.

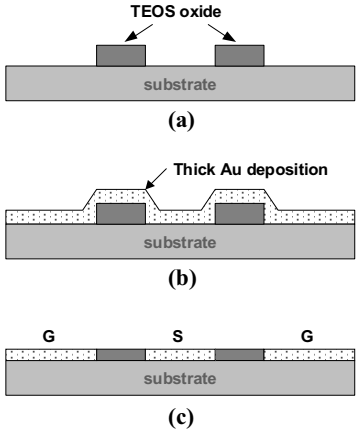

Fig. 3. Fabrication process flow of DCPW t-lines.

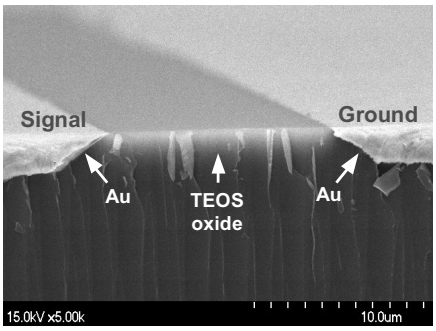

Fig. 4. Cross-sectional SEM micrograph of the gap filled with TEOS oxide between a signal and ground line of a DCPW t-line after CMP.

RESULTS AND DISCUSSION

An RF MEMS switch fabricated above DCPW t-lines is shown in Fig. 5. A circular movable plate is used to minimize the deflection of the plate from its stress gradient. The switch has a series topology with metal-to-metal contacts. The movable plate is fabricated using Ti/Au sputter deposition with total thickness of 3 μm. The plate is anchored to the substrate at the end of the flexures and the anchor is connected to the ground through a bias line of a high impedance. The lines are made of high resistivity material (doped poly-Si with 500 Ω/square sheet resistance). A pull-down electrode is placed under the movable plate and connected to supply voltage through the bias line. It is isolated from the plates using 1500 Å PECVD silicon oxide layer. The size of a fabricated switch is 1.5×1.4 mm^2.

The pull-in voltages are measured for 81 samples and averaged 18.3 V. Fig. 6 shows the insertion loss and reflection of ON-state, and the isolation of OFF-state. The switch possess an insertion loss of better than 0.25 dB up to 5 GHz and an isolation of over 40 dB up to 10 GHz due to a very low OFF-state capacitance of 1.5 fF.

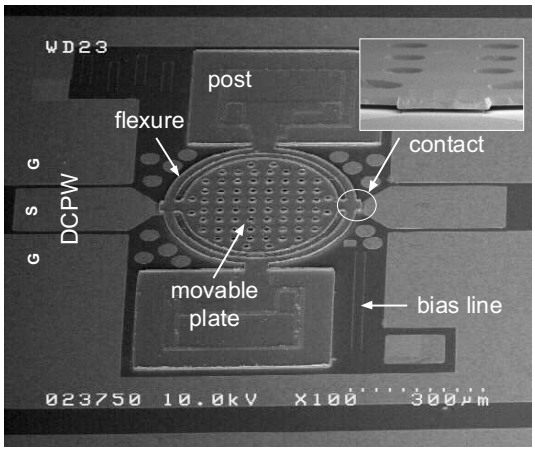

Fig. 5. SEM micrograph of a fabricated MEMS switch with DCPW lines.

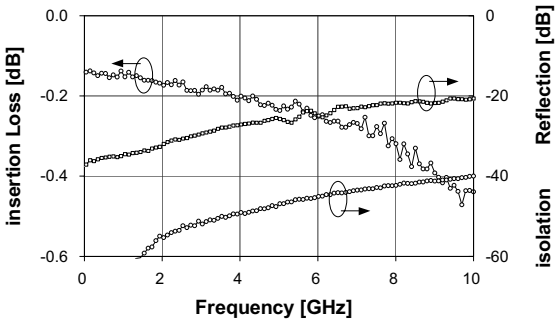

Fig. 6. Measured RF performances for a MEMS switch.

CONCLUSIONS

In this paper, series metal-to-metal contact RF MEMS switches with DCPW t-lines are designed and fabricated. The RF measurement shows that these switches possess low insertion loss and high isolation up to 10 GHz.

REFERENCES

[1] C. L. Goldsmith, Z. Yao, S. Eshelman, and D. Denniston, "Performance of low-loss RF MEMS capacitive switches," *IEEE Microwave Guided Wave Lett.*, vol. 8, pp.269-271, Aug. 1998.

[2] J. B. Muldavin and G. M. Rebeiz, "High isolation MEMS shunt swtiches; part 1: Modeling," *IEEE Trans. Microwave Theory Tech.*, vol.48, pp.1045-1052, Jun. 2000.

[3] C. Kaanta, S. Bombardier, W. Cote, W. Hill, G. Kerszykowski, H. Landis, D. Poindexter, C. Pollard, G. Ross, J. Ryan, S. Wolff, J. Cronin, "Dual Damascene: A ULSI Wiring Technology," *VLSI Multilevel Interconnection Conf.*, Santa Clala, CA, Jun. 1991, pp.144 -152.

A High Aspect Ratio, Low Voltage Tunable RF Capacitor

Arda D. Yalçınkaya, Søren Jensen and Ole Hansen

Mikroelektronik Centret (MIC), Technical University of Denmark, B 345 E, DK-2800 Lyngby, Denmark.
http://www.mic.dtu.dk, E-mail: ady@mic.dtu.dk

Summary: *We report a low-voltage, high-aspect ratio, widely tunable capacitor fabricated using a simple single-mask fabrication process. The low tuning voltage range is compatible with the supply ranges of the current transistor circuits and enables the device to be used in radio frequency integrated circuits. Characterizations with respect to electrical quality factor, time-domain response and tuning ratio were performed and it was found that the device can be used in VHF and UHF tunable filters and impedance matching applications.*

Keywords: *Tunable capacitors, radio frequency, ICP, DRIE*
Category: *10 (Applications)*

1 Introduction

The tunable capacitors considered in this paper are comb structures, where the capacitance is realized through a number of interdigitated finger electrodes on a fixed and a movable part – the shuttle. The shuttle is suspended by a couple of folded beam springs with a low effective spring constant for motion in the intended direction and a high spring constant for motion in other directions. The present device, shown in Figure 1, makes use of high-aspect ratio comb fingers for obtaining high device capacitance, and the folded suspensions enable linear in-plane actuation at large displacements with low voltages. Since the device has a height of 50 μm and air-gaps of 2.5 μm between the fingers, the air-film damping control issue is easily resolved. The hollow spine of the movable section not only helps to reduce the effective mass but also eases the release process and reduces the probability of stiction to the substrate [1]. A combination of light mass and heavy damping reduces the vibration sensitivity of the device.

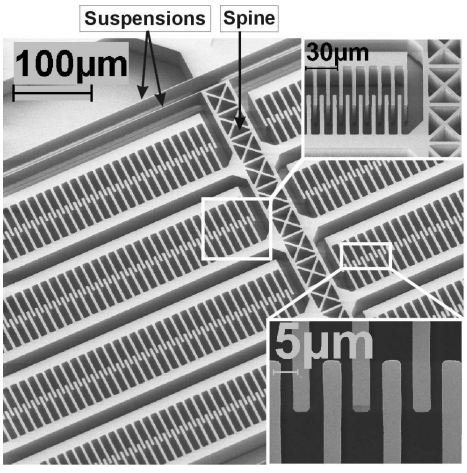

Fig. 1: Overview SEM picture of the tunable capacitor. At the top, the suspensions and the hollow spine are indicated. The insets show comb finger details.

2 Fabrication

The device was fabricated using dry deep reactive ion etching (DRIE) followed by a wet isotropic release etch of a sacrificial silicon dioxide layer. The starting material was a 4″ (100) silicon-on-insulator substrate with a 50 μm thick, highly doped device layer on top of a 1 μm thick oxide layer. The process sequence is illustrated in Figure 2.

First, the geometry of the structures was patterned onto the substrate using 1.5 μm thick AZ5214 photoresist, whereafter the masked substrate was etched anisotropically in an STS ASE® DRIE tool [2] until the buried oxide was reached (Figure 2-A). Due to the high aspect ratios of more than 1:20 and the narrow air gaps needed to obtain a high capacitance between the fingers, a novel etch recipe was developed. The recipe uses short etch/passivation cycle times to reduce mask undercut and sidewall roughness, and to push the DRIE tool beyond its standard 1:10 aspect ratio performance, the process parameters were changed during the etch to compensate for the change in etch conditions with increasing aspect ratios. Next, the photoresist was stripped in an O_2/N_2 plasma, and the narrow structures released in 40% hydrofluoric acid (Figure 2-B). Finally, a layer of 200 Å/5800 Å Ti/Au was evaporated on top of the devices to enhance the electrical quality factor (Figure 2-C). SEM images of the fabricated devices can be seen in Figure 1.

3 Characterization

The tunability of the device was characterized using a probe station and a HP-4280A CV plotter. Open circuit calibration was performed before the measurements in order to compensate for the probe and pad capacitances [3]. The measurements, along with a numerical calculation based on the measured device dimensions, are given in Figure 3, which evinces that the capacitance can be tuned between 1 pF (static capacitance) and 2 pF by increasing the control voltage from 0 V to 3.15 V where maximum deflection is obtained. The dynamic behavior of the mechanical system was explored at at-

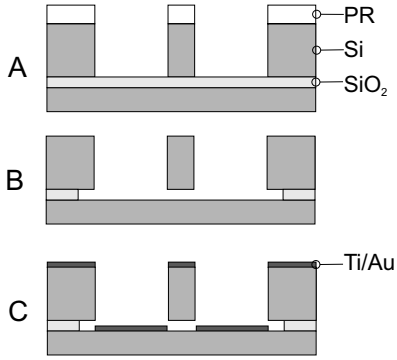

Fig. 2: Tunable capacitor fabrication sequence.

mospheric pressure to extract the settling time using the C-t mode of the HP-4280A, with an external pulse biasing for fast measurements. A pulse voltage of 1.2 V was applied and the measurement was performed after the falling edge of the pulse. As can be seen from Figure 4, the capacitor settles in about 0.2 ms with a desired over-damped response. This is essentially the signature of a low mechanical quality factor (≤ 0.707), enabling the atmospheric operation of the device without overshoot and with a fast settling time. Finally, scattering parameters of the device at microwave frequencies were measured, using a Cascade probe station together with a HP-8510 network analyzer / HP-8515A fixture, resulting in Figure 5. The graph, showing s_{11} on a Smith chart, reveals that, by taking the pad capacitances into account, the electrical quality factor is approximately 100 at 100 MHz and the self-resonance frequency was found to be 4.08 GHz. For application purposes, the pad capacitances can be eliminated by using an insulating handle substrate and an identical fabrication scheme. The quality factor can further be increased by predeposition of metal layer as the first step and utilizing lift-off. This layer can also serve as a mask for the DRIE step.

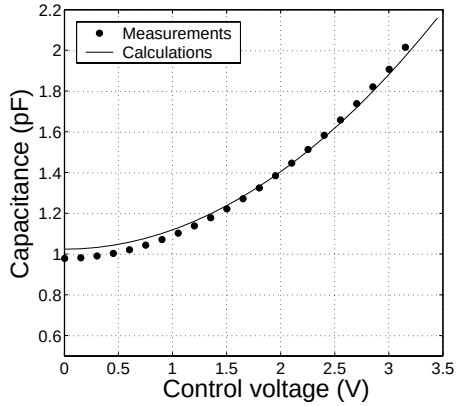

Fig. 3: Capacitance-voltage tuning characteristic of the comb-driven tunable capacitor. Measurements performed at 1 MHz agree well with the curve calculated using measured (SEM) device dimensions.

4 Conclusion

A high-aspect ratio tunable capacitor that combines low-voltage actuation and wide tuning range was successfully fabricated through a simple process in which an aspect ratio of 1:20 was obtained with vertical sidewalls. Performance characterizations have shown that the present device can be utilized to implement VHF and UHF tunable filters with the electrical quality factors well above 100. A tuning ratio of 2:1 was achieved by changing the control voltage by only 3.15 V, enabling the compatibility with the state of the art supply voltage range of integrated circuit technologies. The device has proven not to require any special treatment for a desired, fast transient response with no overshoot or oscillations.

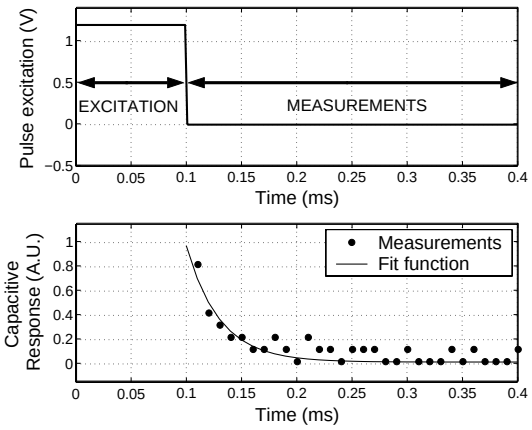

Fig. 4: Transient response of the tunable capacitor. Measurements were performed after the falling edge of the excitation pulse (digitization of the capacitance value after 0.2 ms is due to the resolution of HP-4280A in C-t mode).

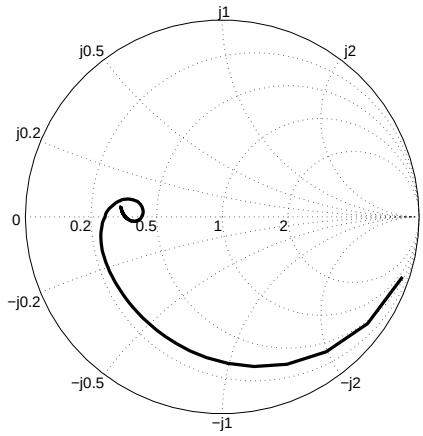

Fig. 5: Reflection coefficient (s_{11}) of the MEMS tunable capacitor measured from 45MHz to 10GHz. (The measured two-port parameters were used to calculate one-port s_{11} at the first port with shorted second port).

References

[1] R.L. Borwick III *et al.*, Sensors and Actuators A, **103**, pp. 33-41 (2003).

[2] Hynes, A.M. *et al.*, Sensors and Actuators A, **74**, pp.13-17, (1999).

[3] A. Dec and K. Suyama, IEEE Trans. Microwave Theory and Tech, **46**, pp. 2587-2596 (1998).

Integrated Chip-Size Antenna for Wireless Microsystems: Fabrication and Design Considerations

P.M. Mendes, A. Polyakov*, M. Bartek*, J.N. Burghartz*, J.H. Correia

Dept. of Industrial Electronics, University of Minho, Portugal
*Lab. of ECTM/DIMES, Delft University of Technology
Phone: +351-253510190 Fax: +351-253510189
E-mail: paulo.mendes@dei.uminho.pt

Summary: This paper reports on fabrication and design considerations of an integrated folded shorted-patch chip-size antenna for applications in short-range wireless microsystems and operating frequency of 5.7 GHz. Antenna fabrication is based on wafer-level chip-scale packaging (WLCSP) techniques and consists of two adhesively bonded glass wafers with patterned metallization and through-wafer electrical interconnects. Two different fabrication options based on via formation in glass substrates using excimer laser ablation or powder blasting are presented.

Keywords: *chip-size antenna, WLSCP, wireless microsystem, laser ablation, powder blasting.*
Category: *8, 9, 2.*

1 Introduction

Monolithic solutions to small-size distributed systems equipped with short-range wireless communication capabilities will highly be facilitated if cheap and easy-to-use 'on-chip' or 'in-package' solutions would be available. A chip-size antenna is the key element in order to obtain a fully integrated wireless microsystem on a single chip. On-chip integration requires the antenna to be small and to be realised on a low-loss substrate compatible with integrated circuits operation and fabrication [1, 2]. A folded shorted-patch antenna (FSPA) can be used as a compact solution for the on-chip antenna integration [3]. Due to its rather complicated structure, its implementation is not trivial. In this paper, design and process considerations for on-chip implementation of an FSPA are presented.

2 Antenna Design

The proposed, on-chip integrated, folded short-patch antenna is shown in Fig. 1. It consists of three horizontal metal sheets that are electrically connected by two vertical metal walls. All this is embedded in a dielectric substrate having certain electrical permittivity and dielectric losses. These two parameters together with the antenna geometry and its actual dimensions will determine its radiation characteristics and overall performance.

For the best performance, the metal sheets should have minimum resistivity and the dielectric should be a low-loss material with high electrical permittivity. This allows achieving small antenna dimensions and high efficiency.

At frequencies above 1 GHz, glass becomes a very attractive option. Its main advantages are low losses, reasonable ε_r, availability in a form of wafers with any required thickness and diameter, and last but not least low cost. There is also sufficient experience in processing of glass wafers from MEMS and WLCSP applications [4].

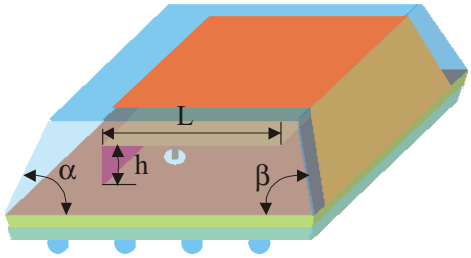

Fig. 1: Proposed folded shorted-patch antenna.

An FSPA can be realised as a stack of two glass wafers with patterned metal layers and through-wafer interconnects in the form of metallized vias. High antenna efficiency requires thicker substrates (>300 µm) and therefore high aspect ratio vias in glass are required.

Fig. 2 shows return loss of the proposed FSPA, considering the use of two stacked, 500 µm thick Corning Pyrex #7740 glass substrates and dimensions of 4.5x4x1 mm^3. The simulated radiation efficiency of 60 % and bandwidth of 50 MHz at -10 dB return loss have been achieved. The predicted far-field radiation diagrams (Fig. 3) shows that the power is being mainly radiated upwards and the antenna interference with backside devices is minimized.

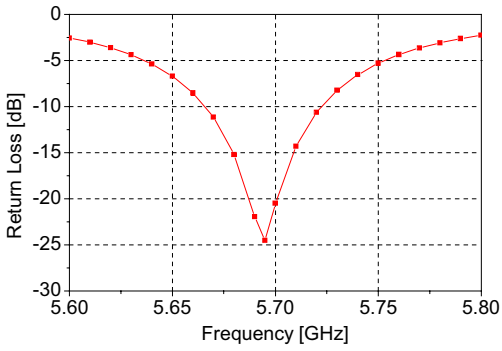

Fig. 2: Simulated return loss of the FSPA.

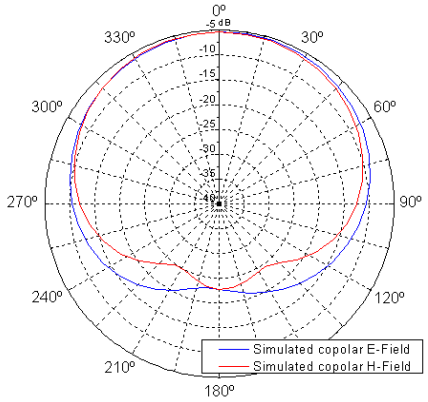

Fig. 3: Simulated co-polar far-field gain patterns for FSPA operating at 5.695 GHz.

3 Fabrication

We have proposed and currently investigate two different fabrication options for realization of an on-chip integrated FSPA. Both are based on WLCSP techniques and are schematically shown in Fig. 4. The first one is based on laser drilling of high aspect ratio vias in glass with subsequent electroless plating and patterning of the bottom and middle Cu layers, followed by glass-to-glass adhesive bonding. The second fabrication option starts with deposition and patterning of Cu layer on a glass wafer followed by adhesive bonding to the upper glass wafer. The encapsulated middle Cu patch is then reached by powder blasting followed by plating and patterning of the bottom Cu layer. In both cases, the fabrication sequence continues by bonding to a temporary carrier and a V-groove trenching using shaped dicing blade [5]. Finally the upper Cu layer is deposited and patterned. The processing sequence is completed by singulation into individual dies by dicing.

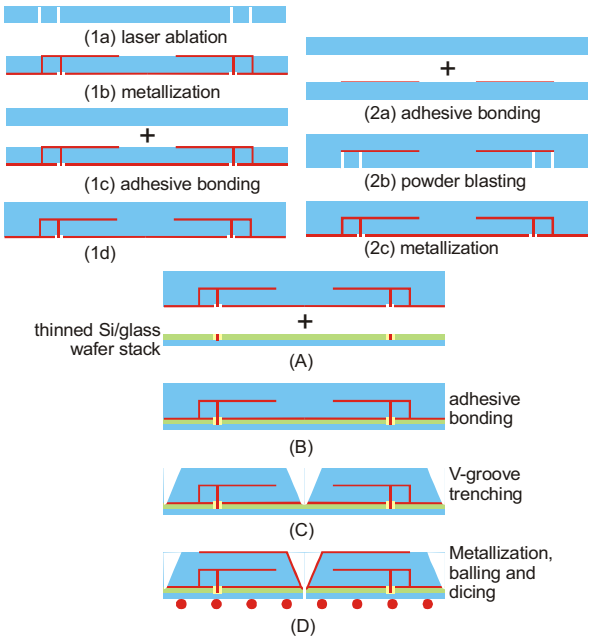

Fig. 4: Schematic fabrication sequence using laser ablated vias (left); using powder blasted vias (right).

3.1 Laser ablation

Glass starts to loose its transparency in the UV region and therefore excimer lasers are needed for glass ablation to form through wafer vias. Due to the limitations of the focusing system, direct ablation of the required pattern is not possible and an intermediate hard mask between the laser beam and glass wafer was required. Fig. 5a shows SEM photograph of 80 µm diameter vias formed in a 500 µm thick glass wafer using a 193 nm excimer laser. Note that no protection layer has been applied and therefore contamination on the wafer surface resulting from the ablation process is clearly visible.

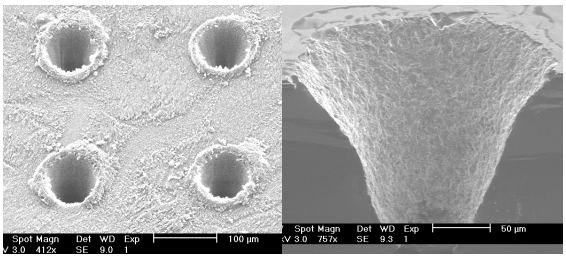

(a) (b)

Fig. 5: SEM picture of (a) 80 µm circular vias in a 500 µm glass substrate fabricated using a 193 nm excimer laser; (b) cross-section of a 200 µm diameter powder-blasted via.

3.2 Powder blasting

Powder blasting is a widely used method in glass processing. Its main disadvantage is that the typical side-wall slope is about 75° which results in rather limited achievable aspect ratio of powder-blasted vias of ~2.5:1. Fig. 5b shows a cross sectional SEM photograph of a powder-blasted, 200 µm diameter via in a 240 µm thick substrate.

4 Conclusions

This work demonstrates that folded shorted-patch antennas operating at 5-6 GHz are feasible using WLSCP techniques and suitable for microsystems aiming wireless short-range links. A folded shorted-patch antenna was designed and possible fabrication options were analysed.

Acknowledgements

The authors would like to thanks the Portuguese Foundation for Science and Technology (POCTI / ESE / 38468 / 2001 and SFRH/BD/4717/2001) and EU (IST-2000-10036) for funding this work.

References

[1] P.M. Mendes, et al., Integrated 5.7 GHz Chip-Size Antenna for Wireless Sensor Networks, *Transducers'03*, Boston, USA, June 8-12, 2003.
[2] P.M. Mendes, et al., Design and Analysis of a 6 GHz Chip Antenna on Glass Substrates for Integration with RF/Wireless Microsystems, *IEEE APS Int. Symp.*, Columbus, Ohio, USA, June 22-27, 2003.
[3] R.L. Li, et al., Novel Small Folded Shorted-Patch Antennas, *IEEE APS Int. Symp.*, Vol. 4, pp. 26-29, 2002.
[4] A. Polyakov, et al., Processability and Electrical Characteristics of Glass Substrates for RF WLCSP, *ECTC 2003*, New Orleans, USA, May 27-30, 2003.
[5] http://www.shellcase.com/

Metal patterning on high topography surface for 3-D RF devices fabrication

Nga P. Pham, E.Boellaard, W.Wien, L.D.M.van den Brekel*, J. N. Burghartz, P. M.Sarro
Delft University of Technology, DIMES
Laboratory of Electronic Components, Technology and Materials
P.O.Box 5053, 2600GB Delft, The Netherlands
Tel: + 31 15 278 1237 Fax: + 31 15 278 7369
* MECO Equipment Engineers B.V., The Netherlands
Email: nga@dimes.tudelft.nl

Summary
Electrodeposision (ED) of photoresist is a promising method to transfer fine patterns onto non-planar, high-topography surfaces. It is especially suited for patterning metal layers to fabricate three-dimensional (3-D) structures. A newly developed MECO coating system is employed and commercially available photoresists are used. The coating process developed to improve the resolution of the printed images in and across cavities ≥375µm deep is described and the effect of several parameters investigated. Examples of fabricated truly 3-D and novel RF structures on silicon wafers are presented.

Keyword: Electrodeposition of photoresist, lithography, 3D-patterning, micromachining

Subject category: Applications, material and technology

Introduction
For the realization of 3D structures, lithographic steps over large topography surfaces are of crucial importance. The quality of the patterns in and across micromachined structures such as anisotropically etched cavities or multi-level etched surfaces is greatly influenced by the conformity of the photoresist layer. Several coating methods like modified spin coating or spray coating have been explored [1-3] and reasonable results achieved. However, the flowing effect of photoresist can often result in local non-uniformity of the resist layer, especially at top and bottom corners of etched cavities [4]. Thus patterned lines running over these regions may be deformed or even interrupted Although there are some ways to reduce the flowing effect [3], it is still difficult to control it when too many different designs are present on the same wafer, as often the case for truly 3D RF devices. ED of photoresist is a suitable technique to overcome this problem as it can create a conformal layer regardless of the geometry and size of the structures. The requirement of a conductive layer as plating base layer in this method makes it especially suited for metal patterning. In this paper, we present experimental results on ED coating aimed at patterning metal layers over large topography surface. Examples of novel 3-D RF structures fabricated using ED resist coating are presented as well.

The ED coating process
The ED resist coating experiments are performed in a coating system developed by MECO Equipment Engineers B.V. using Eagle 2100 ED negative resist. The resist coating is based on the electrodeposition of a negative organic acrylate-type photoresist onto a cathodic polarized conductive substrate. The coating set up consists of a bath with photoresist in the form of emulsion solution containing micelles with 100nm in size. The wafer is placed in a cathode with a conductive surface facing to the stainless steel anode. A schematic view of the electro-deposition cell illustrating the coating principle is depicted in fig 1.

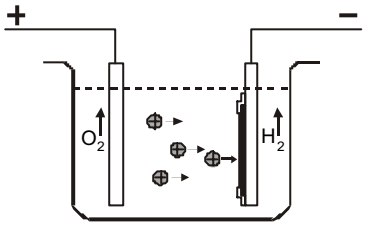

Fig 1: *ED coating set up*

Both flat wafers and wafers with etched cavities coated with an Al layer (1-4µm thick) are used. The Al layer will be the active device metallization layer and at the same time will act as a plating base. The wafers are first immersed in a MECO Surclean solution at 50°C for 30s, rinsed in DI water, activated for 10 sec in a 15% H_2SO_4 and again rinsed in DI water. Then they are transferred to the bath for an average 90 sec deposition step at voltages between 20 and 160V. After a rinsing step in a permeate cell to remove adhering coating liquid, they are finally baked at 70°C for 60s. To evaluate the layer thickness and uniformity, the resist is exposed in an UV contact aligner and then developed in MECO AMS developer at 40°C. Resist thickness is measured through the openings by means of a Tencor 200 profiler.

Results and Discussion
The influence of bath temperature on resist thickness has been characterized at different voltages as illustrated in Fig 2. The temperature where a minimum resist thickness is obtained is called T_{min}

and is around 40°C-45°C. As thin but uniform layers are highly desirable for better pattern transfer on large topography surfaces, we have chosen 45°C as a coating temperature for further experiments. More over, as can be seen in fig 2, at temperature lower than $T_{min,}$ it is more difficult to control the expected resist thickness as a minor change in temperature can lead to a large variation on resist thickness. On the other hand, higher bath temperatures result in a faster degradation of the emulsion [5].

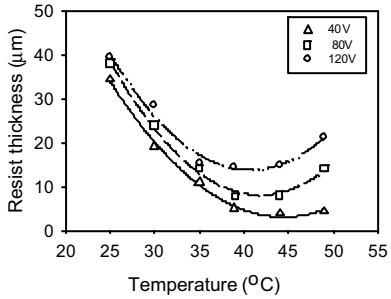

Fig 2: *Resist thickness vs. bath temperature*

Resist thickness also depends on applied voltage and increases with increasing applied voltage at a fix coating temperature. Fig 3 shows the resist thickness vs. applied voltage for a coating temperature of 45°C.

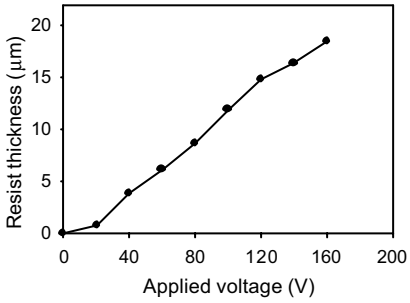

Fig 3: *Resist thickness vs. applied voltage*

After exposure and development the patterned lines are evaluated. As can be seen in fig 4a, the patterned sidewalls are steep and adhere well to the substrate, but exhibit a shoulder at the edge and a thin fringe is observed at the bottom of the opened features. This phenomenon certainly will degrade the pattern resolution. An improvement has been made by adding an extra hot water rinse at 70°C after development. The improvement can be seen in fig 4b in which the shoulder is rounded and residues are removed at the bottom edge of the pattern.

The developed coating process described above has been used for patterning structures in and across deep cavities. Smooth layers with rather conformal coverage have been obtained. The resist uniformity of ± 5% has been obtained on wafer with cavity's depth of 390 µm. In particular a good coverage at very critical parts like an obtuse corner of an etched cavity (see Fig.5a), the week point for spin or spray coating methods, is a strong point of this method.

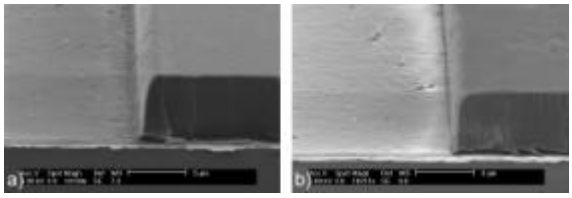

Fig 4: *Patterned ED resist: a) after standard development; b) after the extra hot water rinse*

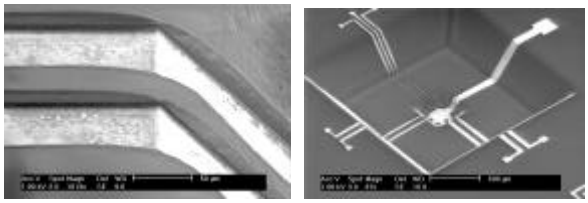

Fig 5: *Patterned ED resist lines: a) at the top corner of a deep etched cavity; b) over 370 and 150 µm deep cavity*

Another example of the potential of this method is given by a patterned resist over two-level micromachined structures as shown in Fig 5b Patterned lines 100µm to 20µm wide over deep cavities of 370µm and 150µm are illustrated.

We have used this ED coating procedure to fabricate several novel 3-D RF devices. This coating method is used as the last step in the process for patterning metal layer. In fig 6a, a 3-D solenoid inductor is shown. Very fine line running over two-level micromachined surface can be patterned. The other structure (see Fig.6b) is a 4 µm Al through-silicon-chip transmission line (TCT), particularly interesting for novel packaging concepts.

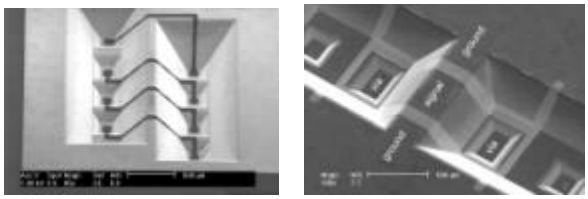

Fig 6*: 3D RF devices: a) 3D solenoid inductor with turns running from the front to the backside of the wafer; b) Through-chip transimission lines after ED resist patterning and Al etching*

Conclusions

ED resist coating is a suitable method to pattern metal on wafers with very large topography with a high-resolution image. A process for consisting of pre-treatment, coating, exposure and development has been developed. For cavities ≥375µm, the minimum line width is ~ 20µm. Several 3-D and RF structures have been realized illustrating the potential and flexibility of this technique.

References

[1] V.G.Kutchoukov et al., Sensor &Actuator A85(2000), 377-383.
[2] N.P.Pham et al., Proc. SPIE conf. vol.4174 (2000).390-397.
[3] N.P.Pham et al., Proc. EUROSENSOR 02 (2002).182-
[4] A.Suriadi et al, Proc. SPIE 4404 (2001).
[5] P.Kersten et al, Sensor &Actuator A51 (1995), 51-54.

A Wireless RF CMOS Interface for a Soil Moisture Sensor

Raul Morais[1], A. Valente[1], C. Couto[2] and J.H. Correia[2]

[1]University of Trás-os-Montes e Alto Douro, Engineering Department,
Ed. Engenharias II, Quinta de Prados, 5000-911 Vila Real, Portugal
email: rmorais@utad.pt http://www.utad.pt/~aci
[2]University of Minho, Department of Industrial Electronics,
Campus de Azurém, 4800-058 Guimarães, Portugal

Summary: *This paper describes a wireless RF CMOS interface for a soil moisture sensor. The mixed-signal interface is based on a 2nd-order switched capacitor, fully differential sigma-delta modulator with an effective resolution of 17-bit. The modulator bit stream output is applied to a counter as a first order decimation filter and encoded as a pulse width modulated signal. This signal is then transmitted by means of an amplitude shift keying modulation, through a power amplifier operating at 433.92MHz in class-E mode. The soil moisture sensor is based on Dual-Probe Heat-Pulse method and is implemented using an integrated temperature sensor and heater. After applying a heat-pulse, the temperature rise that is a function of soil moisture, generates a differential voltage that is amplified and applied to the mixed-signal interface input. The described interface can also be used with other kinds of environmental sensors in a wireless network for agricultural environments such as greenhouses. The CMOS mixed-signal interface has been implemented in a single-chip using a standard CMOS process (AMIS 0.7µm, n-well, 2 metals, 1 poly)*

Keywords: *Wireless, Sigma-Delta, Soil-Moisture Sensors*
Category: *9 (System architecture, electronic interfaces, wireless interfaces)*

1 Introduction

The control of physical and chemical variables in agriculture fields require the use of several sensors, as soil temperature and relative humidity, CO_2 concentration, solar radiation, soil moisture, among others.

An important goal in agricultural exploitations it is the need to minimize natural resources over-consumption, namely water supply in irrigation systems. Irrigation management systems should have information about soil moisture at the plant root level. With such information, only the necessary water could be provided in an efficient way.

Today a large number of sensors based on different methods are available for measuring soil moisture. However, they present a few drawbacks: as inaccuracy, high-cost and soil dependency.

Integrated microsensors, with on-chip interface circuitry, are currently replacing discrete sensors due to their inherent advantages, namely, low cost, high reliability and on-chip processing. To accomplish small, robust and inexpensive microsystems, it is desirable to integrate the soil moisture sensor with digital signal processing and wireless front-end. Therefore, this microsystem can be installed near plants roots for measuring real plant water needs.

2 System overview

The complete system is divided in two blocks, as depicted in figure 1: the sensing system and the mixed-signal interface.

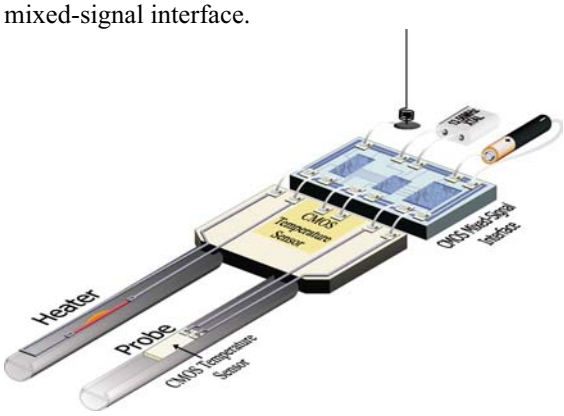

Fig. 1. System overview.

The implemented CMOS mixed-signal interface, outlined in figure 2, includes a 2nd-order switched-capacitor fully differential sigma-delta (ΣΔ) modulator, a first-order decimation filter, a shift register, a pulse width encoder, an amplitude-shift-keying (ASK) modulator and a RF switch. The 433.92 MHz carrier is generated by the on-chip phase-locked loop (PLL).

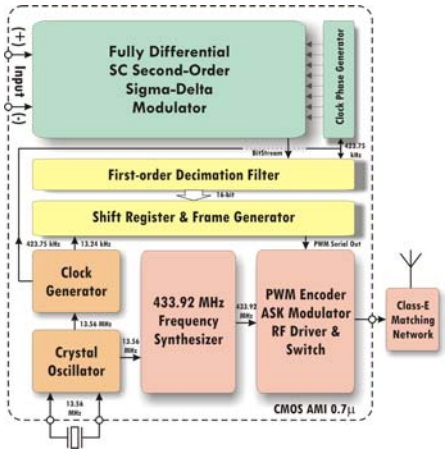

Fig. 2. Mixed-signal interface architecture.

2 Mixed-signal interface

The water in the soils must be measured with a resolution better than 1%. The sensing system has a differential output of about 330 µV/% and signal bandwidth is typically a few Hz.

Previous studies have showed that a second-order ΣΔ modulator is a suitable architecture for converting this kind of signal to digital domain. The second–order architecture is preferred to the simpler first–order one because it is less sensitive to the correlation between the input and the quantization noise, which reduces the presence of pattern noise [1].

The 2nd-order ΣΔ modulator has been implemented using switched capacitor techniques. In addition to robustness of these techniques, the use of fully differential topology minimizes common mode interferences, switches charge injection and clock feedthrough. The two integrators are based on fully differential folded-cascode amplifiers biased by a constant-gm wide swing circuit. Also, for reducing the influence of the first-amplifier offset and low-frequency noise, a chopper scheme has been implemented. The modulator reference is external and set to ±0.5 V.

The bit stream output is applied to a counter as a first decimation filter. For each counting, a sample is generated, stored and transmitted. Data is first encoded as a pulse width modulated signal and afterwards transmitted by the on-chip RF transmitter by means of an amplitude shift keying modulation.

2.1 RF transmitter module

The RF transmitter module includes a crystal-controlled frequency synthesizer, a PWM encoding circuit, an ASK modulator, a RF driver and a RF switch.

To ensure carrier stability, the frequency synthesizer was implemented as a phase-locked loop (PLL) using a 13.56 MHz crystal reference oscillator. The PLL features a 300 µA charge pump with current matching and a 4th order loop filter. The voltage-controlled oscillator has a constant of about 80 MHz/V.

3 Results and conclusions

Simulations from the extracted layout have shown that it can be expected an effective resolution of about 17-bit (DR=105.4db) for the ΣΔ modulator with a conversion time of 38.8 ms for a clock frequency of 423.75 kHz. The PLL has a lock time of about 6 µs.

Figure 3 shows a binary pattern '011' PWM encoded signal (A) and transmitted signal (B) in a 50 Ω load. In this first prototype, the class-E matching network is off-chip and it is intended to integrate it on-chip in the next prototype.

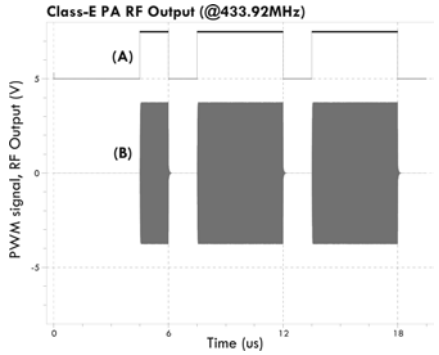

Fig. 3. PWM signal and RF output signal.

Figure 4 shows the layout of the implemented mixed-signal interface. Die area is 3.79 mm^2.

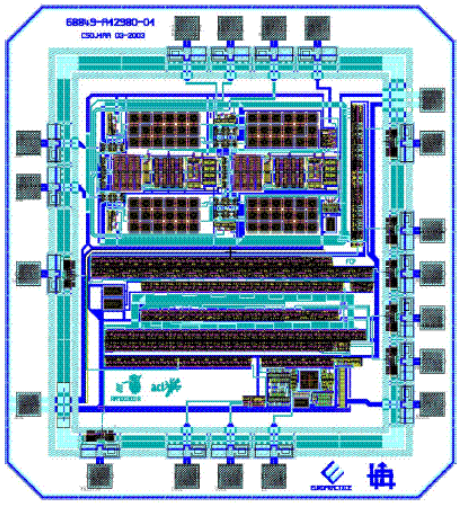

Fig. 4. The layout design of a wireless RF CMOS interface for a soil moisture sensor.

References

[1] J. C. Candy. A Use of Double Integration in Sigma-Delta Modulation. *IEEE Transactions on Communications,* 33 (1985) 249–258.

Displacement Model for Dynamic Pull-In Analysis and Application in Large-Stroke Electrostatic Actuators

L.A. Rocha, E. Cretu and R.F. Wolffenbuttel

Delft University of Technology, Faculty ITS,
Dept. for Micro-electronics, Mekelweg 4, 2628 CD, Delft, The Netherlands
Email: L.Rocha@its.tudelft.nl

Summary: *AC-operation of an electrostatically actuated microstructure enables a displacement beyond the quasi-static pull-in voltage and the associated limitation at 33% of gap. When considering dynamics of the actuator structure, displacements of the order of 70% of the full gap become possible by using sine waves as the actuation voltage. A large-displacement model for electrostatic actuators is presented in this paper and the results are compared with measurements. Operation up to 70% of gap has been confirmed at frequencies between 300 and 700 Hz, depending on the gas type and gas pressure of the surrounding medium.*

Keywords: *Pull-In voltage, MEMS modeling, electrostatic actuators*
Category: *1 (General, theoretical and modeling)*

1 Introduction

The inherent instability associated with electrostatic actuators is an extensively studied phenomenon [1,4]. In the quasi-static regime, the model describing the displacement of a MEMS structure due to voltage applied reduces to finding the equilibrium between mechanical and electrostatic forces (the damping is neglected). This results in a sudden pull-in at a well-defined pull-in voltage at 1/3 of the gap for 1DOF displacement structures [4].

When the changes in the applied voltage are sufficiently fast, the quasi-static regime does not apply and the static pull-in analysis becomes inaccurate. The damping forces and mass inertia need to be included in the model for a meaningful study of the dynamic pull-in behavior of the structure.

The analysis of pull-in at dynamic conditions demonstrates that the structure displacement is not necessarily limited to 1/3 of the gap. Displacements in the order of 70% of the full gap have been obtained by using sine waves as the actuation voltage. This property has huge potential for the construction of large-stroke electrostatic actuators for use in e.g. variable capacitors.

A large-displacement model for electrostatic actuators is presented in this paper and compared with measurements. The changes of the pull-in voltage and pull-in displacement are also checked for various frequencies and signals. As large displacements have been achieved, this study could yield a significant advance in large-stroke electrostatic actuator design.

2 Large Displacement Model

The structure used for analysis and experimental verification is basically a planar movable beam with folded suspension on both ends and electrodes extending perpendicular to the axial direction. One set of stator electrodes in the same plane is used for electrostatic actuation and another set of electrodes is used for capacitive displacement measurement.

The movement of such a parallel plate electrostatic actuator is defined by the equation:

$$F_m + F_b + F_k = F_{elec} \tag{1}$$

where F_m is the mass contribution ($m\ddot{x}$), F_b is the force caused by the damping, F_k is the spring force (kx) and F_{elect} is the electrostatic force ($\frac{1}{2}C(x)V^2$), with x the displacement.

The damping force for large displacements can be modeled as a series of nonlinear inductances and resistances controlled by the displacement x. The values for the resistors and inductors [5] are:

$$R_{m,n} = (mn)^2\left(\frac{m^2}{w^2}+\frac{n^2}{l^2}\right)\frac{\pi^6 d(x)^3 Q_{pr}(d(x),P)}{768lw\eta} \tag{2}$$

$$L_{m,n} = (mn)^2\frac{\pi^4 d(x)}{64lwP} \tag{3}$$

where η is the viscosity, P the pressure, m and n odd integers, w and l are the width and length of the surface, respectively. The gap d is a function of the displacement ($d(x) = d_0 - x$, being d_0 the initial displacement) and as the Knudsen number ($K_n = \frac{\lambda}{d(x)}$, where λ is the gas mean free path) also varies for large displacements, its dependence to the displacement is included on the function:

$$Q_{pr} = 1 + 9.638(K_n)^{1.159} \tag{4}$$

Each of the RL sections used in [5] behaves like a first order system with variable gain and time constant. The total damping force can be modeled as a sum of several forces of the type:

$$F_{m,n} = \frac{\dot{x} - \dot{F}_{m,n}L_{m,n}(x)}{R_{m,n}(x)} \tag{5}$$

The all non-linear system can be written in the form $\dot{X} = f(X,V)$ as:

$$
\begin{aligned}
y &= \dot{x} \\
\dot{y} &= -\tfrac{1}{m}((F_{1,1} + F_{3,1} + ... + F_{m,n}) + kx - \tfrac{1}{2}C(x)V^2) \\
\dot{F}_{1,1} &= \frac{y - F_{1,1}R_{1,1}(x)}{L_{1,1}(x)} \\
\dot{F}_{3,1} &= \frac{y - F_{3,1}R_{3,1}(x)}{L_{3,1}(x)} \\
\dot{F}_{m,n} &= \frac{y - F_{m,n}R_{m,n}(x)}{L_{m,n}(x)}
\end{aligned}
\qquad (6)
$$

and can be implemented in any simulation program using simple integrators, and displacement controlled parameters.

3 Simulations and Experimental Results

The model was implemented in Simulink, and several simulations were done at different operating conditions (different pressures and gas type) and compared with actual measurements at the same conditions (Fig. 1).

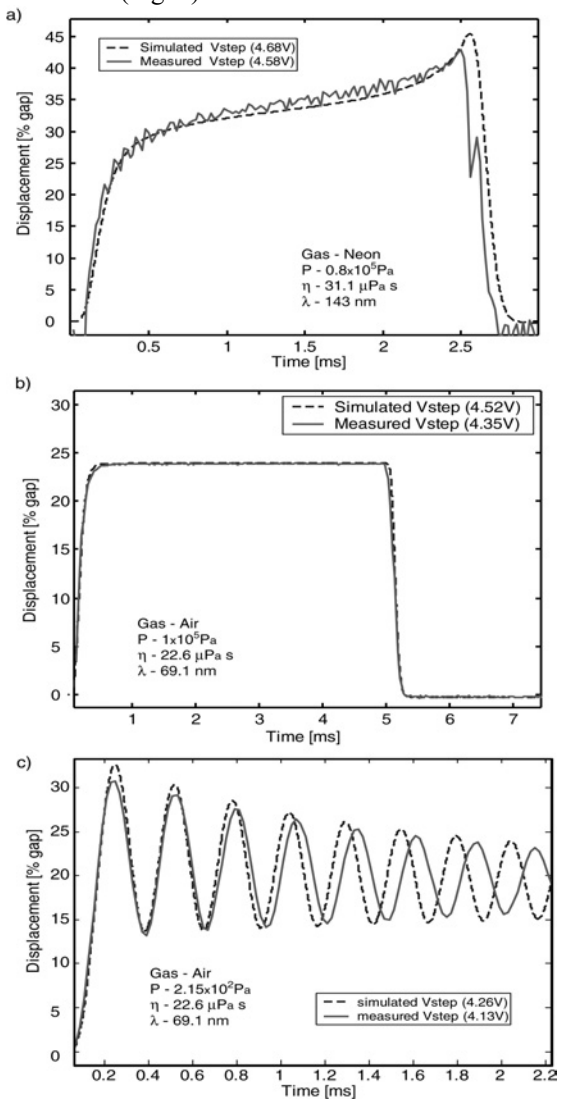

Figure 1. Simulated and measured response to different electrostatic signals. a) 200Hz square wave b) and c) 100Hz square wave.

Sinewave voltages of different frequency have been used for actuation. The results of simulated and measured pull-in voltage and pull-in displacement are shown in Fig. 2.

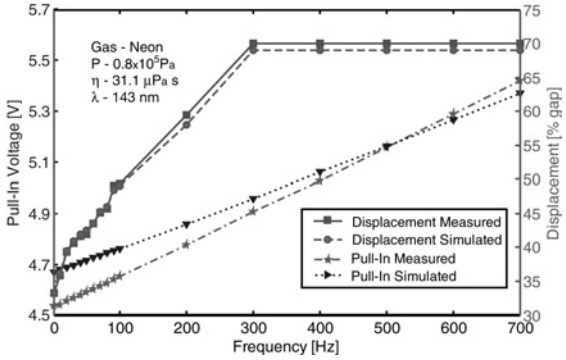

Figure 2. Simulated and measured dynamic pull-in and dynamic displacement.

4 Conclusions

A dynamic model that accurately describes the voltage-to-displacement characteristic of an electrostatic actuator is presented. The analysis and experimental results demonstrate that the electrostatic actuator can be dynamically operated beyond the static pull-in displacement provided that the appropriate AC voltage is applied. There is an operating point in the statically unstable region where the spring and damping forces are equal to the electrostatic force [6], thus enabling the application as electrostatic actuator beyond the static pull-in displacement limit. A thorough understanding of the damping effect and the dependence on gas type and pressure is required. Operation up to 70% of gap has been demonstrated using AC voltages in the 300 Hz range.

References

[1] S.T. Cho, K. Najafi and K.D. Wise, "Internal stress compensation and scaling in ultra-sensitive silicon pressure sensors", *IEEE Tr. ED*, vol. 39, pp. 836-842, 1992.

[2] P.M. Osterberg and S.D. Senturia, "M-TEST: A test chip for MEMS material property measurement using electrostatically actuated test structures", *J. Microelectromech. Syst*., vol. 6, pp. 107-118, June 1997.

[3] H.A.C. Tilmans, and R. Legtenberg, "Electrostatically driven vacuum-encapsulated polysilicon resonators, Part 2, Theory and performance", *Sensors and Actuators*, vol A45, pp. 67-84, 1994

[4] E. Cretu, L.A. Rocha and R.F.Wolffenbuttel, "Using the Pull-in Voltage as Voltage Reference", *in Proc. Transducer01*, 2001, vol. 1, pp. 678-680.

[5] T. Veijola, H. Kuisma, and J. Lahdenperä, "Compact Large-Displacement model for capacitive accelerometers", *in Proc. Conference on Mod. and Sim.of Microsystems, Semiconductors, Sensors and Actuactors,* (San Juan), Apr. 1999.

[6] L.A. Rocha, E. Cretu, R.F. Wolffenbuttel, "Hysteresis in the Pull-In of Microstructures", *in Proc. MME02,* 2002, pp. 335-338.

A flow-through potentiometric sensor for an integrated microdialysis system

D.G.Pijanowska[1,2], A.J.Sprenkels[1], H. van der Linden[1], W.Olthuis[1], P.Bergveld[1]

[1] MESA+ Research Institute, University of Twente, P.O.Box 217,
7500 AE Enschede, The Netherlands
[2] Institute of Biocybernetics and Biomedical Engineering, Polish Academy Sciences
ul. Trojdena 4, 02-109 Warsaw, Poland
depijano@ibib.waw.pl

Summary: *In this paper, the performance of a flow-through potentiometric sensor based on a semi-permeable dialysis tubing implemented in silicon, is presented. The sensor is designed as part of a lab-on-a-chip system and has been successfully incorporated into an integrated microdialysis system. Results of a potassium sensor, operating stand-alone, and as part of the integrated system are presented.*

Keywords: *potentiometric sensor, flow-through system, potassium sensor, microdialysis, Lab-on-a-chip, µTAS,*
Category: 5 (*Chemical sensors)*

1 Introduction

A generic flow-trough potentiometric microsensor based on a semi-permeable tubing made in Perspex® has been described previously by Böhm [1]. As proposed in this paper the microchannel itself is an integral part of the sensor geometry and is formed by a tubular semi-permeable membrane. The major advantage of this geometry is the fact that commercially available ion-selective cocktails can be applied, yielding sensors for different analytes. The sensor based on this concept is designed in the form of an integral component of lab-on-a-chip systems.

The sensor fabrication and the performance of the potassium microsensor operating stand-alone, and as part of an integrated microdialysis system are presented.

2 Experimental

2.1 Materials

The dialysis tube from regenerated cellulose with MW cut-off of 20 kDaltons was adapted from an artificial kidney Filtral® 6, AN69 HF, Hospal France. Epoxy resin (Hysol®, Dexter, USA) was used to fix the dialysis tube. The sensors windows were closed with a piece of Pyrex fixed with UV curable glue (Loctite 350).

To form the electrodes, a conducting silver-silver chloride paste (Electrodag® 6088 SS, Acheson Colloiden B.V., The Netherlands) was used.

Components of hydrogel: acrylamide AAm, N,N-bisacrylamide (crosslinker) 2,2-dimetoxy-2-phenylacetophene DMPAP (photoinitiator) obtained from Fluka, and DMSO.

2.2 Sensor fabrication

Originally, the sensors were designed to be filled with two liquids: internal electrolyte and ionophore cocktail. However, it was found that due to specific configuration of the sensor, it was difficult to form well defined interface between the two liquids. To solve the problem a UV sensitive hydrogel based on polyacrylamide was applied for entrapment of the internal electrolyte.

A cross section of the potentiometric flow-trough microsensor is shown in Fig. 1.

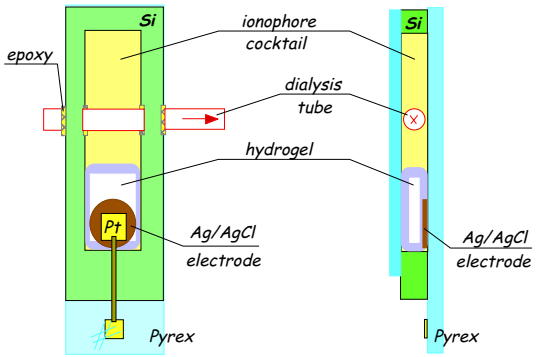

Fig. 1. Layout of the flow-trough potentiometric microsensor implemented in silicon.

The estimated swelling capability of the hydrogel containing 3.6% of a crosslinker vs. AAm was about 45%. The photographs in Fig. 2 show the pAAm hydrogel after drying at room temperature for 30 min and in a swollen state.

Before use the hydrogel was soaked in the internal electrolyte for at least 24 hrs. Prior to placing the hydrogel into the sensor cavity, it was cut to the proper square size. Then the hydrogel was placed in the sensor cavity and dried for about 15 to 30 min. Afterwards the cavity was closed with a piece of Pyrex and fixed with the UV curable adhesive.

Next the cavity was filled with the internal electrolyte to allow the hydrogel swell again for at least 1 h. Finally the excess of internal electrolyte in the surrounding of the dialysis tube was removed

and replaced with an ionophore (valinomycin) cocktail (60031 obtained from Fluka).

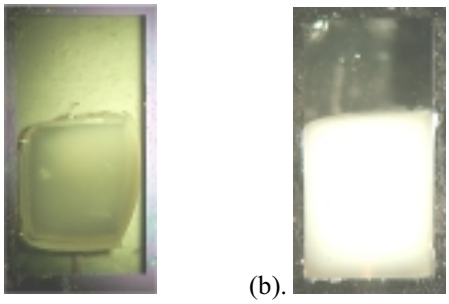

(a). (b).

Fig. 2. The pAAm hydrogel in a dry state (a), and in a swollen state (b).

To form a reference electrode, the sensor cavity located next to the ion-selective one was completly filled with pAAm hydrogel saturated with 3 M KCl.

2.3 Measurements

The stand-alone sensors were operating at a constant continuous flow rate of 2 ml/h. The concentration of the potassium ions was changed by a standard addition method using 0.1 M and 1 M KCl aqueous solutions. As a background electrolyte 100 mM NaCl was used.

Sampling was performed using the integrated microdialysis probe under continuous flow at a flow rate of 2 µl/min for 60 sec.

The potential of the detecting electrode was measured against the integrated reference electrode, using a home-made high-impedance instrumentation amplifier. Before measurements the sensors were allowed to stabilize by flowing with 50 mM KCl solution for about 2 hrs.

3 Results and discussion

The results presenting the dynamic response of the sensor and calibration curves for the continuous flow at a constant flow rate of 2 ml/h are shown in Fig. 3 a and b respectively. The sensitivity of the sensors varied from 50 to 55 mV/dec. The sensitivity depends on the time of the sensor conditioning (stabilization) before measurements. The minimal time for the sensor conditioning is 2 hrs.

The activities of the cations in the aqueous solution were calculated according to the Debye-Huckel approximation [2]. The potentiometric selectivity coefficient for the sensor for potassium over sodium (K^{pot}=161.5) was estimated according to the fixed interference method (FIM) [3] by increasing the concentration of the activity of the primary ion in the solution in steps of about 0.7 decade.

The sensor has been successfully integrated in a microdialysis system [4]. A calibration curve for the sensor operating in the microdialysis system for 60-second sampling through a microdialysis probe at a flow rate 2 µl/min is shown in Fig 3.b (upper curve).

4 Conclusions

A flow-trough potassium potentiometric microsensor based on semi-permeable tubing has been implemented in silicon, and exhibit satisfactory parameters: near Nernstian response and a good selectivity over sodium.

The sensors have been successfully integrated into a chip resulting in lab-on-a-chip type device for microdialysis, consisting of several functional blocks: microdialysis probe and sensor array.

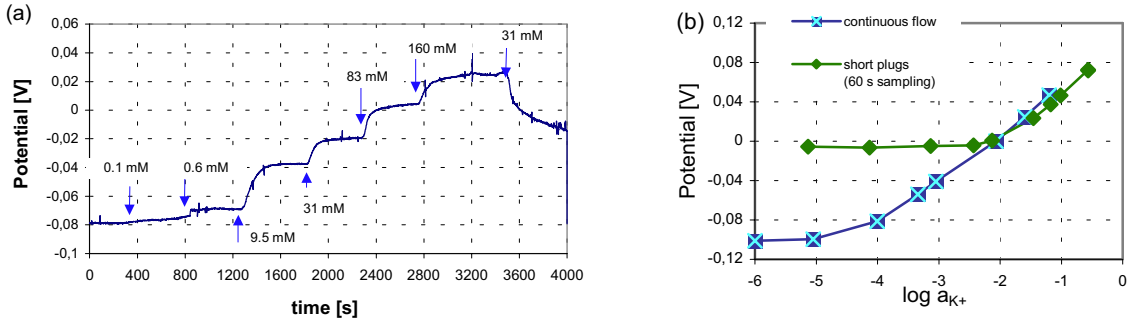

Fig. 3. Time response (a) and calibration curve (b) for the potassium sensor for continuous flow. Background electrolyte was 100 mM NaCl. In the upper curve of fig. (b) also the calibration curve for the sensor as integrated in the microdialysis system is shown.

References

[1] S.Böhm, W.Olthuis and P.Bergveld, *Proc.of the SPIE Conf. on Industrial and Environmental Sensing, Boston, USA, Sept.19-20*, (1999) 24-30.

[2] Y.Umezawa, K.Umezawa and H.Sato, *Pure Appl.Chem.*, 67 (1995) 507-518.

[3] K.Umezawa and Y.Umezawa, CRC Handbook of ion-selective electrodes: selectivity coefficients, *CRC Press* (1990) 3-9.

[4] D.G.Pijanowska, A.J.Sprenkels, J.Bomer, W.Olthuis, P.Bergveld, *Proc. of micro TAS,* Nara, Japan, Nov. 4-7, (2002) 34-36.

Array of voltammetric sensors for the discrimination of bitter liquid solutions

C. Apetrei[1], M.L. Rodríguez-Méndez[1], V. Parra[1],F. Gutierrez[2], M.L. Gomez[2], J.A. de Saja[3]

[1]University of Valladolid, Inorganic Chemistry Dept., E.T.S. Ingenieros Industriales, Pº del Cauce s/n, 47011 Valladolid, Spain. email: mluz@eis.uva.es
[2]Instituto de la Grasa, CSIC, Avda. Padre García Tejero, 4, Sevilla, Spain
[3]University of Valladolid, Condensed Matter Physics Dept. Prado de la Magdalena s/n, 47011 Valladolid

Summary: *Novel voltammetric sensors based on conducting polymers and on phthalocyanine complexes have been developed. Polymeric sensors obtained by electrodeposition of the corresponding monomers (3-methylthiophene, pyrrole and polyaniline) in presence of different doping agents (surfactants and redox anions) and carbon paste electrodes based on phthalocyanines have been immersed in model solutions of bitterness. These model solutions included $MgCl_2$, quinine, and four phenolic compounds (monoaldehydic form of oleuropein, dialdehydic form of oleuropein, monoaldehydic form of ligstroside and dialdehydic form of ligstroside), which are the main responsible of the bitterness detected in some foods and beverages such as olive oils. The influence of the chemical characteristics of each electrode in its electrochemical response has been evaluated. Finally, an array has been constructed using those sensors with the best performances. The Principal Component Analysis (PCA) of the obtained signals has allowed the discrimination of the studied bitter solutions.*

Keywords: *Electrochemical sensor, conducting polymer, phthalocyanine, electronic tongue, bitterness*
Category: 5 *(Chemical sensors)*

1. Introduction

The search of materials whose sensing properties could be chemically modified to form electrochemical sensors with sufficient cross-selectivities is crucial for the development of electronic tongues [1-3]. Conducting polymers and phthalocyanines are promising class of materials to fabricate voltammetric sensors because they have a rich electrochemical behaviour and their properties can be tuned by chemical methods [4].
The objective of this work is to develop new voltammetric electrodes able to be used as sensing units of an electronic tongue and in particular, to discriminate bitterness. For this purpose, polymeric sensors have been obtained by electrodeposition. One of the novelties of the work is the use of large surfactant and redox anions as doping agents aiming to obtain films with improved electrochemical properties. Sensors based on different phthalocyanines have been prepared using the carbon paste electrode technique (CPE).
A multichannel taste sensor constructed with those sensors with the best performances has been exposed to six bitter solutions prepared from compounds responsible of bitterness in foods and beverages (for instance, the bitterness of olives is caused by oleuropeins). The capability of discrimination of the array has been evaluated by using Principal Component Analysis (PCA).

2. Experimental

Lutetium bisphthalocyanine ($LuPc_2$) and octatertbutyl praseodymium bisphthalocyanine ($PrPc_2^t$) were synthesised in our laboratory. The CPE were prepared by mixing the corresponding phthalocyanine with carbon powder and Nujol.
Sensors based on polypyrrole (Ppy) poly-3-methyltiophene (P-3-MET) and polyaniline (PANI) were obtained by electrochemical polymerization of the corresponding monomer using potassium ferrocyanide (FCN), p-toluenesulfonic acid (pTOL), sodium 1-decanesulfonate (SDS) and tetrasulfonic nickel phthalocyanine (NiPcTs) as doping agents. Once prepared, the sensors were used as the working electrode in a conventional three electrode cell.
The artificial bitter solutions were obtained by solving $MgCl_2$, quinine, monoaldehydic form of oleuropein, dialdehydic form of oleuropein, monoaldehydic form of ligstroside and dialdehydic form of ligstroside in ultrapure water.
The PCA was carried out using Matlab V. 4.2

3. Results

Each sensor produced a characteristic response when immersed in the model solutions. This is illustrated in Fig.1 where the cyclic voltammograms of the electrodes immersed in ligstroside are shown. As expected, the cyclic voltammogram of the bisphthalocyanine based electrodes (Fig. 1.a and 1.b) showed two definite anodic waves corresponding to the one electron ring oxidation and the one electron ring reduction of the phthalocyanine molecule. When the scanning potential is reversed, opposite reactions take place. The electrochemical behaviour is directly correlated to the nature of the metal complexed in the phthalocyanine core and to the presence of substituents in the phthalocyanine ring.

The redox transformations observed in phthalocyanine CPE electrodes are accompanied by ion movements between the solution and the bulk material necessary for preserving the macroscopic electroneutrality of the electrode. For this reason, the peak positions and their sharpness depend on the nature of the test solution and the electrochemical responses can be used to distinguish the model bitter solutions.

Ppy, p-3MET and PANI films electrosynthetized in the presence of conventional doping agents, did not show redox peaks in the range studied (-1.0 V to 0.5V). In order to obtain polymeric sensors with improved electrochemical response, a series of Ppy electrodes doped with surfactants and redox ions were prepared.

An interesting type of Ppy is Ppy(FCN) where a redox anion, hexacyano-ferrate is used as dopant. This film not only behaved as a good redox electrode but displayed the electroactivity of the dopant anion and showed sensitivity to the size of cations present in the solution phase (Fig 1.c).
The electrochemical behaviour of polypyrrole films electrosynthetized in the presence of surfactants and NiPcTs is illustrated in Fig. 1.d and 1.e.
The process of reduction and oxidation of these PPy films is understood in terms of the transport of ions in and out of the polymer. For this reason the polymeric sensors produced characteristic electrochemical responses to each model solution which could be used as a fingerprint to discriminate the six types of bitterness.
Finally, the sensors with the best performance characteristics were selected (stability, reproducibility, variety of responses)
In order to evaluate the discrimination capabilities of the sensor array, PCA was conducted using the anodic wave as the input variable. The results indicate that the electronic tongue is able to discriminate different types of bitterness (Fig.2).

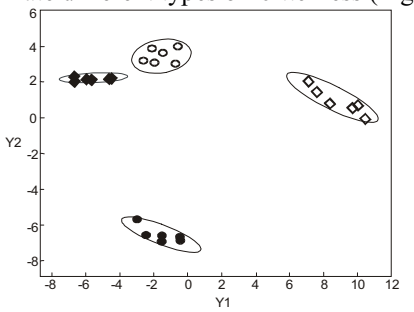

Fig. 2. PCA of the response of the array of sensors towards ■) monoaldehydic form of oleuropein, □) dialdehydic form of oleuropein, •) monoaldehydic form of ligstroside ○) dialdehydic form of ligstroside.

Summarizing, the rich and characteristic electrochemical response observed when the selected sensors are exposed to the bitter solutions makes doped Ppy and bisphthalocyanines appealing materials for the preparation of electrodes for bitter taste.

Acknowledgments

Financial support provided by the CICYT (Grant nº AGL2001-2104-C02) and UE CRAFT-1999-70722 is gratefully acknowledged.

References

[1] K. Toko. *Electroanalysis* 10 (1998) 657-669.
[2] A. Legin, A. Rudinitskaya, Y. Vlasov, C. Di Natale, F. Davide and A. D´Amico. *Sens. And Actuators B* 44 (1997) 291-296.
[3] F. Winquist, P.Wide and I. Lundstrom *Anal. Chim. Acta*, 357 (1997) 21-31
[4] A. Arrieta, M.L. Rodríguez and J.A. de Saja. *Proc. Eurosensors XVIII. Prague 2002.pp245-247*

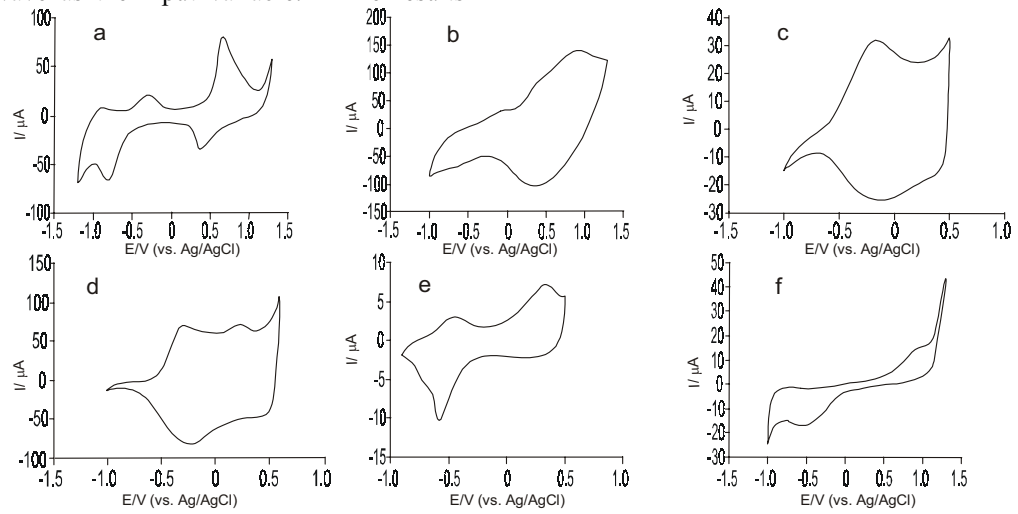

Fig. 1. Cyclic voltammetry of (a) $LuPc_2$ (b) $PrPc_2^t$ (c) Ppy-Tol (d) Ppy-FCN (e) Ppy-SDS (f)Ppy-NiPcTs electrodes immersed in 0.2 M solution of *di*aldehydic form of ligstroside. Scan rate 50 mV s^{-1} .

Advantages of Monitoring Mass Changes in Voltammetric Experiments

Alzira Yamasaki, João A. B. P. Oliveira, Armando C. Duarte and M. Teresa S. R. Gomes
Department of Chemistry, University of Aveiro, 3810-193 Aveiro, Portugal
email: mtgomes@dq.ua.pt http://www.dq.ua.pt/ingles/index_mem.htm

Summary: *Voltammetric experiments were performed in aqueous copper and lead solutions. The working electrode was a gold electrode of a quartz crystal, which allowed recording the mass deposited and lost on and from the electrode. Mass plotted vs. potential is in many cases easier to interpret than current, as some processes, like oxidations or reductions involving gases, do not contribute to the mass. Besides, mass deposition rate can be related to the deposited metal, which allows interpreting the voltammogram even in the absence of potential information. Both currents and mass losses in anodic stripping processes can be used for quantitative analysis.*

Keywords: *electrochemical quartz crystal microbalance, copper, lead*
Category: *5 Chemical Sensors*

1 Introduction

Voltammetry produces information about chemical species through the measurement of the current as a function to the applied potential between a working electrode and a counter electrode. The third electrode is a reference electrode, which remains at a constant potential throughout the experiment. The counter electrode is often a platinum coil, but several types of mini and micro electrodes, in a variety of shapes and forms, have been employed as working electrodes. If the working electrode is on a piezoelectric crystal, mass changes can also be recorded.

Copper and lead in aqueous solutions have been analyzed by voltammetric methods. The plots of current and mass *vs.* potential were studied and used to elucidate the reduction and oxidation processes.

Anodic stripping is a technique suitable for analysis of species in trace amounts, as analyte is pre-concentrated on the working electrode for a certain period of time. The stripping current obtained by the application of an anodic potential is then measured. Experiments employing the electrodes of quartz crystals were performed and mass measurements used in quantitative analysis.

2 Experimental

Apparatus

An electrochemical quartz crystal nanobalance EQCM 700 from Elchema was used. Quartz crystals were 10 MHz AT-cut HC-6/U with gold electrodes deposited over a chromium layer (ICM-International Crystal Manufacturing Co, Inc). Quartz crystal cells were made of Teflon and allowed easy crystal assembling. A glass cup appropriate for holding volumes around 10 or 20 mL was easily connected to one face of the cell. Both crystal cells and cups were home-made according to a design conceived to allow changing of cups and crystal face in contact with the solution without dismounting the quartz crystal.
The counter electrode was a platinum coil and the reference was an Ag/AgCl electrode.

Procedure

Volumes of 10.0 mL of aqueous samples were introduced in the glass cup and contacted with one of the crystal gold electrodes. Solutions were deaerated with nitrogen prior to the cyclic voltammetric experiments. A constant nitrogen blanket was maintained over the solution during measurements. In anodic stripping voltammetry, deposition times of 3 minutes were made and nitrogen bubbled during two and half minutes, not only to prevent oxygen from entering into the solution, but specially to stir the solution and to favour mass transport through convection.

Electrolyte solutions of acetic acid / sodium acetate with different pH buffer capacities were employed.

Results and discussion

Fig. 1 shows the cyclic voltammogram of an electrolyte solution of pH 6.0 containing 63.82 mgL^{-1} of copper and 85.10 mg L^{-1} of lead.

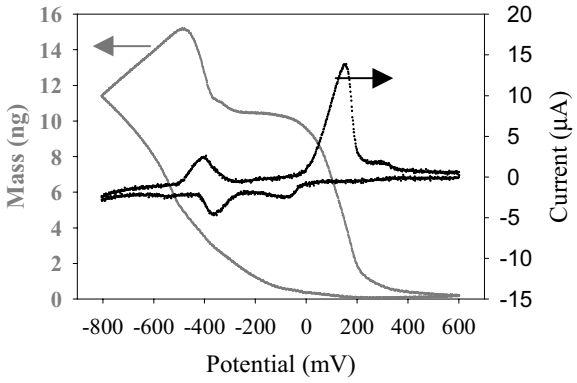

Fig.1 Cyclic voltammogram of a solution of copper and lead at pH = 6.0.

Potential was linearly scanned between 600 mV and -800 mV with a velocity of 5 mV/s. Starting at 0 V and decreasing the potential, a cathodic peak around -75 mV could be found, which was attributed to copper reduction. A simultaneously deposition of copper was also visible from the mass deposited onto the electrode.

Around -300 mV the mass curve shows a change in the slope, as lead starts also to be deposited. A peak in the current confirms the reduction of lead. Mass deposition rate remains constant after the reversal of the scan voltage, until the sign of current is reversed and an anodic peak is formed, corresponding to lead oxidation. Copper oxidation and loss of mass on the electrode start around 0 V.

As limit current is attained, mass deposition rate is a constant for each metal (0.0744 ng/s for copper and 0.118 ng/s for lead, calculated in separate using a single metal in each experiment). Deposition rate for solutions where both copper and lead are simultaneously present, show the same deposition rate for copper before lead reduction takes place, after which a deposition rate equal to the sum of individual copper and lead deposition rates occurs. This behavior allows finding out which metal is being deposited without knowing the potential.

Fig. 2 and Fig. 3 show the cyclic voltammograms obtained under similar experimental conditions, at pH 4.75 and pH 3.0, respectively.

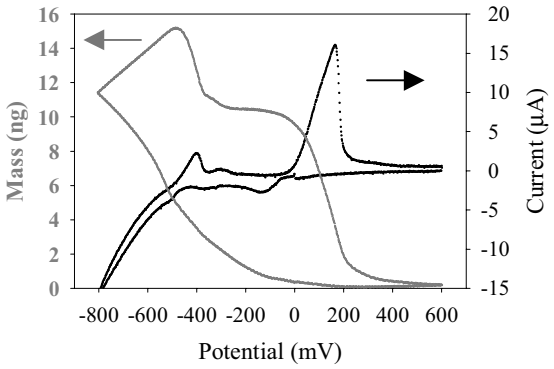

Fig. 2 Cyclic voltammogram of a solution of copper and lead at pH = 4.75.

In spite of the mass *vs.* potential plots being equal for the three situations, marked differences can be noticed on the current *vs.* potential plots. For instance, an inverse current peak, which increases in magnitude as pH decreases, can be noticed after the oxidation peak of lead. Current peaks corresponding to oxygen (-500 mV) or proton reduction (-800 mV) are also present in Fig. 1 or Fig. 2, although these processes do not disturb the mass signal.

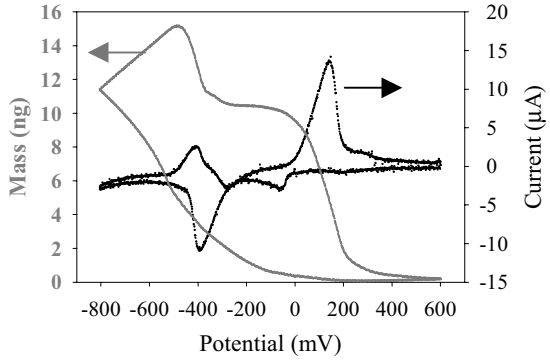

Fig. 3. Cyclic voltamogram of a solution of copper and lead at pH = 3.0.

The fact that oxidation or reductions involving gases is not a mass contributing reaction constitutes a clear advantage of the monitorization of mass in respect to the current. The mass is however sensitive to some other important structural features, which are also shown in the current plot, as for instance a small mass loss after the lead anodic peak current, which is probably due to the lead and copper interaction.

For quantification of trace metals, anodic stripping should be performed. Fig. 4 shows the results obtained with a pre-concentration performed holding the potential at -800V for 3 minutes.

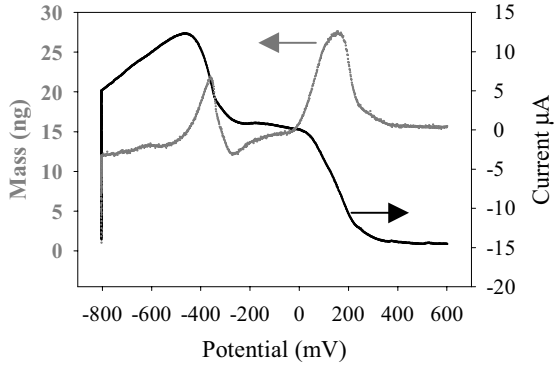

Fig. 4. Anodic stripping voltammetry of a solution containing copper and lead.

The graph was obtained for the same solution with copper and lead concentrations in the mg L^{-1} range, for which no pre-concentration was necessary. However, the methodology was also applied for the quantification of copper in natural waters, where values between 3.6 and 5.3 µg L^{-1} were found.

A complete understanding and interpretation of the voltammetric behavior of metal solutions is still being pursued, for which experiments with different voltage scan rates have been obtained.

Analyses of real matrices operated by a metalloporphyrin based electronic tongue

R. Paolesse[1,3], C. Di Natale[2,3], M. Burgio[1], E. Martinelli[2], E. Mazzone[2], G. Palleschi[1], A. D'Amico[2,3]

[1]University of Rome 'Tor Vergata', Dipartimento di Scienze e Tecnologie Chimiche, via della Ricerca Scientifica 1, 00133 Rome, Italy,
[2]University of Rome 'Tor Vergata', Dipartimento di Ingegneria Elettronica, via del Politecnico 1, 00133 Rome, Italy
email: dinatale@ing.uniroma2.it
[3]CNR-Istituto per la Microelettronica e i Microsistemi, sezione di Roma, via del Fosso del Cavaliere 100, 00133 Rome, Italy

Summary: *The development of chemical sensors operating in the liquid phase has been performed by deposition of thin film of metalloporphyrins onto glassy carbon electrodes by electropolymerization technique.* ***An array of the developed potentiometric sensors have been exploited for the analysis of real matrices. This array was able to discriminate among different brand of commercial mineral waters and among model sample contaminated by heavy metal salts. The*** *developed electronic tongue was also successfully exploited for the discrimination among pharmaceutical drugs belonging to the same active principle but differing for excipients.*

Keywords: *Electronic tongue, Porphyrin, PLS*
Category: *5 (Chemical sensors)*

1 Introduction

In the last few years the need to control both the safety and the quality of environmental and food matrixes has becoming more and more urgent. Chemical sensors are an advantageous solution to these demands, because they can allow both on line and remote control of different environments. Furthermore the integration of chemical sensors in array configurations has greatly expanded the exploitation fields of such a devices. In fact, in this configuration sensors should not be necessarily specific for a target analyte, but they can be broadly selective or even not selective at all, with the only necessary requisite to behave differently from each other, i.e. to furnish not correlated responses. According to this approach, the chemical pattern of the matrix, i.e. the concentration of the different analytes present in the mixture, is reduced to a pattern formed by the sensor responses. Suitable Pattern Recognition procedure is then in charge to assign these patterns to their relevant classes of pertinence. This classification is the final response of the array. For the analogy of this approach with the working mechanism of the mammalian "chemical" senses, olfaction and taste, these sensor arrays have been generally called electronic noses (vapor phase sensors) and electronic tongues (liquid phase sensors). Starting from the first approach of Persaud and Dodds, [1] the development of electronic noses is a well consolidated field of research and several examples of these arrays have been reported in the literature and different instruments are now commercially available in the market [2].

We have contributed to this field by developing sensor arrays based on quartz crystal microbalances (QCM) coated with different metalloporphyrins as sensing materials. This electronic nose has been successfully exploited in different fields, ranging from food analysis to clinical applications [3].

Quite surprisingly, only few examples of electronic tongues have been reported in the literature, although the need of liquid samples control is urgent as much as that of vapor matrices. The excellent performances of metalloporphyrins as sensing materials in vapor phase chemical sensors led us also to explore the development of liquid phase sensors based on metalloporphyrins as sensing material.

Among the different possible transducers, CMEs (Chemical Modified Electrodes**)** represent an attractive approach for the development of liquid phase sensors. Among the different possible choices used to fabricate the CMEs, the electropolymerization is an elegant, attractive, and easy strategy for the immobilization of metal complexes on the electrode surfaces. The principle is based on the electrochemical oxidation (or reduction) of a suitable designed monomer to form a polymeric film incorporating the metal complex.

The Chemical Modified Electrodes (CME) have been obtained by electropolymerization of metal complexes of the 5,10,15,20-*tetrakis* (3-methoxy-4-hydroxyphenyl)porphyrin, TMHPP, on glassy carbon electrodes. The resulting devices have been used as potentiometric sensors and they were firstly characterised in terms of stability, sensitivity and reproducibility towards the detection single model analytes, such as for example NaCl, ethanol and

triethylamine, in the concentration range of 10^{-6} to 10^{-3} mol/l.

These CME sensors showed very promising stability, reproducibility and sensitivity properties and these encouraging results led us to integrate five CME, coated with the different TMHPP metal complexes, in an array together with a reference electrode (Ag/AgCl), to develop a metalloporphyrins based electronic tongue [4]. The developed electronic tongue was able to discriminate and to correctly classify the five classes of sensations that traditionally have been assigned to the human taste.

In this paper we present the exploitation of the developed electronic tongue to test a mixture solutions and real sample as mineral waters, pharmaceutical drugs and pollutants environment.

2 Experimental

The CMEs were obtained by deposition of the following monomers: Mn(TMHPP)Cl, Fe(TMHPP)Cl, CoTMHPP, NiTMHPP, H_2TMHPP. The electronic tongue was formed with five porphyrin electrodes and a conventional Ag/AgCl reference electrode. The measurements were done as standard potentiometric ones and electrical potential across each electrode and the Ag/AgCl reference electrode was measured using a very high input impedance amplifier (10^{13} Ω).
Electronic tongue measurements were carried out by immersion of the porphyrin electrodes into the liquid samples, held at constant temperature (25 °C) and gently stirred to maintain sample uniformity. Sensors reached the stable potential in the samples within about 15 minutes.
The developed array was firstly tested for the discrimination of different brands of commercial mineral waters. The experiments were carried out using distilled water as reference, measured before and after each mineral water sample. Data analysis was carried by Partial Least Square (PLS) technique and the results obtained are reported in Figure 1.

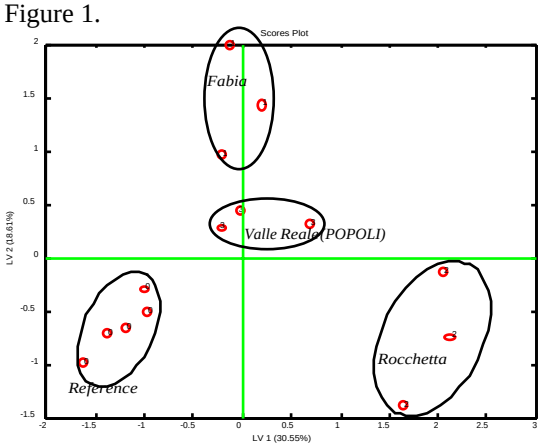

Figure 1. Plot of the first two latent variables of a discriminant PLS model in mineral water experiments.

It is worth mentioning that the array was able to classify each sample and that discrimination can be correlated to the ionic composition of the mineral waters, as reported by the chemical analysis carried out with conventional techniques.
This result led us to explore the ability of the developed electronic tongue to detect water samples pollution by heavy metals, such as Cd, Pb or Hg. In this case known amount of salts of the above cations were added to a model solution. Also in this case the array was able to discriminate among the different solution and a satisfying correlation was observed between separation and heavy metal cation concentration.
A different field of applications was that of pharmaceutical drugs, with the aim to discriminate among samples containing the same active principle (at the same concentration), and that differ only for excipients. The analyzed drug classes have been those of the Diclofenac® and the Lorazepan®. The results in the case of anti-inflammatory (the Diclofenac®) are shown in Figure 2.

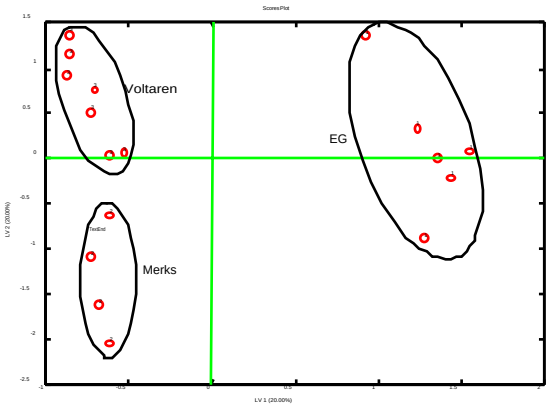

Figure 2. Plot of the first two latent variables of a discriminant PLS model in Diclofenac experiments.

More detailed characterisation of the array and its exploitation in the analysis of real matrices will be presented in the final paper.

References

[1] K.C. Persaud, G. Dodd, *Nature*, 299 (1982) 352-355.

[2] Handbook of Machine Olfaction, editors: J. Gardner, T. Pearce, T. Nagle, S.S. Schiffmann, Wiley-VCH, 2002.

[3] J.A.J. Brunink, C. Di Natale, F. Bungaro, F. Davide, A. D'Amico, R. Paolesse, T. Boschi, M. Faccio, G. Ferri. *Analytica Chimica Acta*, **325** (1996) 53-64

[4] R. Paolesse, C. Di Natale, M. Burgio, E. Martinelli, E. Mazzone, G. Palleschi, A. D'Amico *Sens. Actuators B* in press.

The Fabrication of Scalable Nanosensor Arrays in CMOS Technology

M. J. Milgrew, D. R. S. Cumming and P. A. Hammond

University of Glasgow, Department of Electronics and Electrical Engineering,
Rankine Building, Oakfield Avenue, Glasgow, G12 8LT, Scotland
E-mail: mark@elec.gla.ac.uk http://www.elec.gla.ac.uk

Summary: *A scalable nanosensor array fabricated in an unmodified CMOS process is presented. The design employs a differential circuit and novel multiplexing to make ISFET/REFET measurements in each cell of the array – while being biased by a common reference electrode. All signal processing is performed in-situ and all readout circuitry is located on-chip. The FET-based sensors employ a floating gate electrode structure and are sensitive to pH. On return from the foundry, the devices must be exposed to UV light to eliminate any difference in threshold voltage. The circuit gives a linear range that allows the FET devices to potentially operate as pX sensors in the array.*

Keywords: *sensor, array, CMOS*
Category: *5 (Chemical Sensors)*

1 Introduction

There is considerable interest in developing solid state based sensors for integration with medical diagnostic devices [1]. A single-chip pH sensor fabricated in a standard CMOS process has been demonstrated [2]. In this work, we describe a scalable nanosensor array that can perform both temporal and high-resolution spatial measurements on an analyte. These devices have the potential to be integrated into a 'lab-on-a-chip' system.

2 Nanosensor Arrays

A pH-sensitive ISFET can be fabricated using a floating gate electrode and a Si_3N_4 passivation layer. This technique is adopted here to develop a scalable array with an unmodified CMOS process. Each cell in the array makes a differential potentiometric measurement between an ISFET and a REFET – biased by a common reference electrode.

An nxn array is designed by considering a single column of n electrochemical half-cells (Fig. 1). The resultant circuit maintains a constant source-drain voltage v_{sd} and a constant drain current i_d for the ISFET in the enabled row. The source voltage v_s varies with changes in pH of an analyte. A Kelvin four-terminal multiplexing configuration is used to isolate the measurement of v_s from the current source.

For each column of n electrochemical cells, the circuit is employed for both ISFETs and REFETs. The source voltages $v_{s(ISFET)}$ and $v_{s(REFET)}$ are connected to an instrumentation amplifier to measure and amplify the voltage difference. This signal is used to establish the pH value of an analyte.

We have developed a 2x2 array which has been fabricated in a standard 0.35µm CMOS process (Fig. 2). Each cell comprises an ISFET, a REFET, and minimal addressing circuitry. This results in a

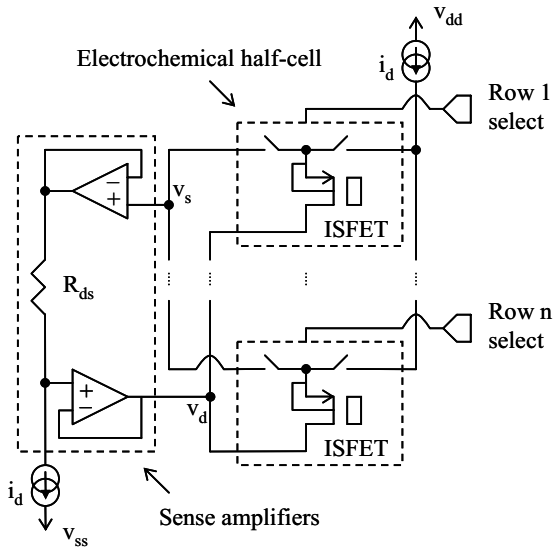

Fig. 1. A column of n electrochemical half-cells.

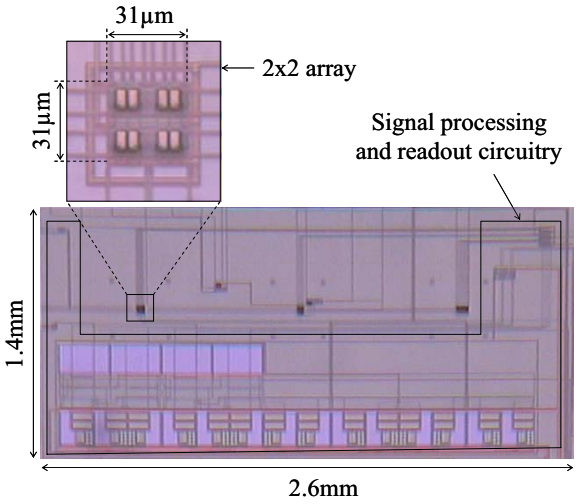

Fig. 2. Micrograph of the nanosensor array circuit.

geometrically square cell with each side no greater than 15.5µm in length. The ISFET and REFET devices have a gate length of 0.3µm and a gate width of 1µm. The readout circuitry for the array is incorporated on-chip and consists of a row decoder, a column sequencer, and a 10-bit ADC.

3 Experimental

In order to facilitate testing, a customized probe is used to deposit solution on the sensitive area of packaged chips and act as a reference electrode (Fig. 3). An unbuffered 0.1M NaCl electrolyte solution (under the control of a syringe) is applied to the chip surface via silicone rubber tubing connected to a capillary. A silver wire inside the capillary makes an electrical connection to a conventional probe arm to establish the reference electrode potential.

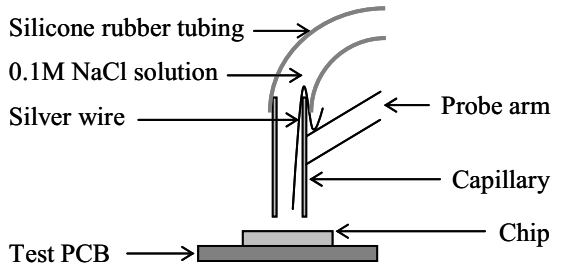

Fig. 3. Modified probe used as a reference electrode.

4 Results and Discussion

The FET-based sensors are p-channel transistors that conduct when the reference electrode-source voltage (v_{RE} -v_s) is less than -V_T. We have found that there is a significant difference in the threshold voltage between ISFETs and REFETs in the cells of the array (Fig. 4). The magnitude of V_T for the fabricated devices can vary from 1V to 4V.

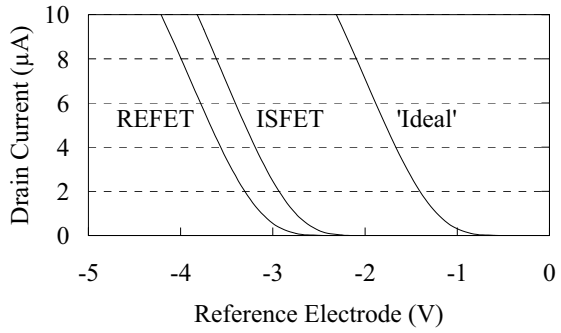

Fig. 4. Transconductance characteristic for a single ISFET/REFET cell (v_s=0).

This anomaly is a result of trapped charge that accumulates on the floating gate electrodes during fabrication. In order to bias the array with a common reference electrode and make differential measurements, the transconductance must be identical for all ISFETs and REFETs. Consequently, it is necessary to eliminate the trapped charge with exposure to UV radiation. As the time of exposure increases, the mismatch between the FET threshold voltages is reduced. The transconductance approaches an 'ideal' curve that corresponds to applying the voltage directly to the gate of the FET devices.

The source voltage of an ISFET is found to vary linearly with the reference electrode voltage for a range of 1.75V (Fig. 5). Consequently, for a theoretical sensitivity of 57mV/pH, the ISFET is in principle capable of detecting a range of 1→14pH. The device can also potentially be used as a pX sensor if an ion selective membrane is deposited on the surface above the floating gate electrode.

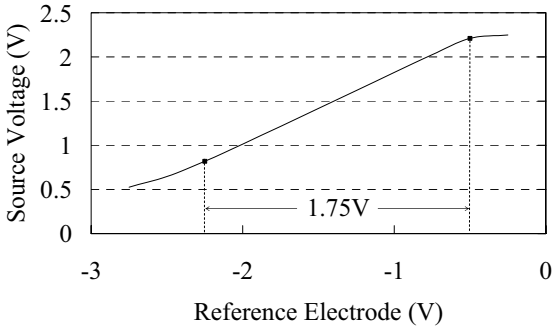

Fig. 5. Source-reference electrode voltage characteristic for an ISFET.

All of the components in the nanosensor array circuit have been characterized and are in good agreement with simulation results. The whole array circuit consumes no more than 15mW from a 3.3V power supply.

5 Conclusions

A complete nanosensor array integrated circuit has been designed and fabricated in a standard CMOS process. For correct circuit operation, it is necessary to expose the FET-based sensors to UV light to eliminate any variations in threshold voltage. The design is scalable and although the array is initially sensitive to pH, it can potentially be functionalized for various ions. We envisage that the final array devices will be integrated into a 'lab-on-a-chip' system and applied to areas such as tissue engineering.

References

[1] S. R. Manalis, E. B. Cooper, P. F. Indermuhle, P. Kernen, P. Wagner, D. G. Hafeman, S. C. Minne and C. F. Quate, "Microvolume field-effect pH sensor for the scanning probe microscope", *Applied Physics Letters*, 76 (2000) 1072-1074.

[2] P. A. Hammond, D. Ali and D. R. S. Cumming, "A single-chip pH sensor fabricated by a conventional CMOS process", *Eurosensors XVI*, Book of Abstracts (2002) 489-490.

Development of a creatinine-sensitive biosensor based on chemical field effect transistors for medical analysis

W. Sant[1,2], M.L. Pourciel[1], J. Launay[1], T. Do Conto[1], A. Martinez[1], P. Temple-Boyer[1]
F.Montiel-Costes[2], J.Montoriol[2]
[1] LAAS-CNRS, 7 avenue du colonel Roche, 31077 Toulouse Cedex 4, France, temple@laas.fr
temple@laas.fr http://www.laas.fr
[2] HEMODIA S.A., Rue du chêne Vert, BP 148, 31676 Labège Cedex, France

Summary: *low-cost, disposable, chemical field effect transistor (ChemFET) microsensors including a SiO_2/Si_3N_4 pH-sensitive gate have been fabricated for pH measurements and adapted to biochemical applications by using polyvinyl alcohol (PVA) enzymatic layers. Application has been performed through the development of a creatinine-sensitive biosensor using immobilized creatinine deiminase as bioselective element. Creatinine detection properties have been characterised in dialysate, evidencing linear response on the [20-450 µmol.L^{-1}]concentration range. The microsensor will be used for blood analysis and more precisely for haemodialysis.*

Keywords**:** *ChemFET, creatinine detection, medical analysis*
Category: *Chemical sensors*

1 Introduction

Chronic end-stage kidney failure affects many patients in the world. Since it was developed in the 1960s, kidney dialysis has allowed a great number of patients to survive the illness. Up to now, these techniques, and more precisely haemodialysis, have been constantly developed to improve the quality of health care and the patients' life expectancy.

In order to further improve the comfort of the haemodialysis patient, the dialysis effectiveness should be continuously monitored. This goal can be reached by developing disposable, low-cost, chemical microsensors for the detection of the H^+, K^+ and Na^+ ions, urea and creatinine. This involves the use of mass manufacturing techniques deviated from microelectronics and therefore the development of ChemFET (chemical field-effect transistor) microsensors.

This work deals with the development of such standard, technological process for the manufacturing of low cost pH-sensitive field effect transistors (pH-ISFET) and creatinine sensitive enzymatic field effect transistors (C-EnFET).

2 Experiment

N-channel ion sensitive field effect transistors (ISFETs) were fabricated on <100>-oriented N-type (500 Ω.cm) silicon substrate using a standard P-well technology [1]. A 50nm thermally grown SiO_2 layer and a 50nm Si_3N_4 layer deposited on top formed the pH-sensitive gate structure. Finally, the sensor applications have been extended to enzymatic detection by using a photosensitive polyvinyl alcohol (PVA) layer [1] containing creatinine deiminase. This PVA layer was deposited on the pH-sensitive gate either by dip coating (thickness around 10 microns), either using spin-coating and photolithography techniques. Thus, by optimising the deposition and photolithography stages, it was possible to pattern 1-micron thick PVA layers (figure 1).

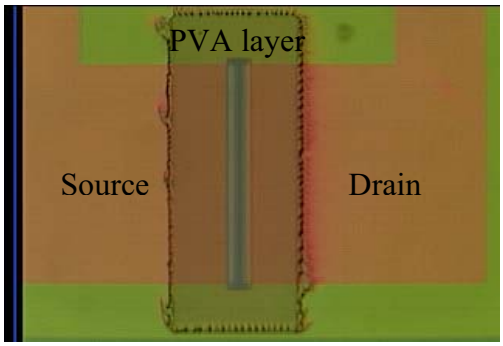

Fig. 1. Deposition of the creatinine deiminase based PVA layer on top of the SiO_2/Si_3N_4 pH sensitive gate

Two structures of chemical sensors were manufactured. The first structure is a single ISFET realized on a 2 x 5 square millimeters chip. The second structure encloses a ChemFET/ReFET structure on a 5 x 5 square millimeters chip. The chips were stuck thanks to an epoxy insulating glue on specifically coated printed circuit. After wire bonding, encapsulation was performed thanks to a biocompatible silicone, leaving the sensitive parts uncovered.

The gate voltage being applied to the solution by a "gold wire" pseudo-electrode, ChemFET sensors were characterized by I-V measurements, the V_{GS} voltage variations being monitoring for a constant drain-source current I_{DS}.

PH measurements were studied using three standard buffer solutions (pH = 4.01, 7.00 and 10.01). The performances of the SiO_2/Si_3N_4 ISFET

chemical sensor have been studied thanks to the H^+ ion detection. Linear non-nernstian (sensitivity: 40 mV/pH) pH responses have been obtained while using the "gold wire" pseudo-electrode.

Creatinine detection was studied in dialysate (pH ≈ 7.6). The enzymatic microsensor was dipped in the solution (2 mL volume) and measurements was performed after 30 seconds of immersion, at room temperature (about 20°C).

3 Results

Creatinine has been detected thanks to the pH variations induced by the creatinine deiminase enzymatic reactions [2]. Thus, The C-EnFET detection properties are obtained on the [20 - 450 µmol.L^{-1}] concentration range, evidencing an equivalent pH increase (figure 2). Higher voltage variations were obtained for the thick PVA micro-drops compared to the thin PVA photolithographic patterns. This phenomenon should be related to the higher PVA volume, i.e. to the higher amount of creatinine deiminase, deposited by dip coating.

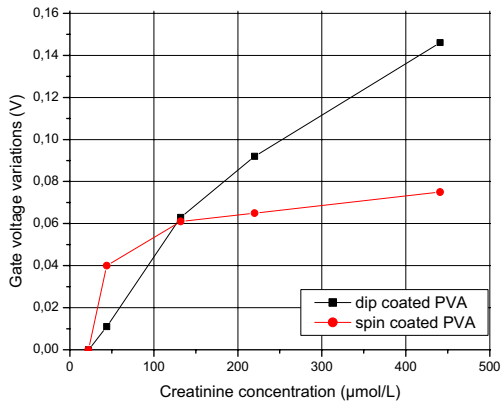

Fig. 2. Creatinine detection in dialysate solutions for a PVA enzymatic layer deposited by dip coating and spin coating/photolithography

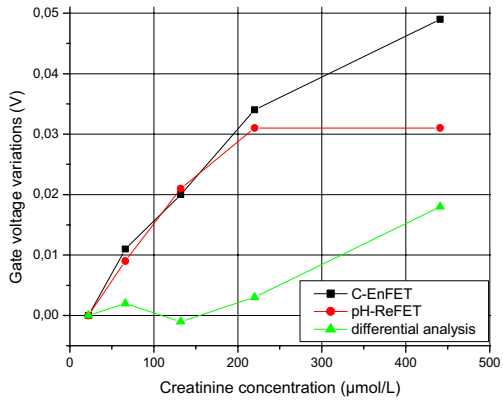

Fig. 3. Differential measurement of creatinine in dialysate solutions with a creatinine-PVA droplet

In a previous study, we showed that the dialysate was not buffered enough to prevent pH variations [1]. Thus, the ChemFET/ReFET structure has been used in order to take into account this phenomenon. In this case, The C-EnFET and the pH-ReFET undergo similar variations. Nevertheless, differential analysis evidences a quasi-linear relation for creatinine concentrations ranging from 130 to 450 µmol.L^{-1} , and the creatinine sensitivity has been finally estimated around 35 mV/pCréatinine.

4 Conclusion and perspectives

Low-cost, disposable, SiO_2/Si_3N_4 pH-chemical microsensors have been fabricated and adapted to creatinine detection by using photosensitive polyvinyl alcohol (PVA) enzymatic layers. The pH and creatinine detection properties have been studied while using a "gold wire" pseudo-electrode. Thus, creatinine detection has been obtained between 20 and 450 µmol.L^{-1} in dialysate solution. Since pH variations were also evidenced, a differential analysis between the C-EnFET and a pH-ReFET has been developped. Thus, linear response has been shown in the same concentration range, the sensitivity being estimated to 35mV/pCreatinine.

These works will be continued by studying by differential analysis the detection of the creatinine in dialysate with an enzymatic PVA layer deposit by photolithography. The sensors will then be developped for blood analysis and more precisely for haemodialysis.

Acknowledgement

These Research and development works are supported by the french society HEMODIA S.A. (Toulouse, France)

References

[1] W. Sant, M.L. Pourciel, J. Launay, T. Do Conto, A. Martinez, P. Temple-Boyer: "Development of chemical field effect transistors for medical analysis", Proceedings of the 16th European Conference on Solid-State Transducers, EUROSENSORS XVI, September 15-18 2002, Prague, CZECH REPUBLIC, p.619-620

[2] A.P.Soldatkin, J.Montoriol, W. Sant, C.Martelet, N. Jaffrezic-Renault: "Creatinine sensitive biosensor based on ISFETs and creatinine deiminase immobilised in BSA membrane" *Talanta*, 58 (2002), 351-357

Fabrication and characterization of membranes actuated by a PZT thin film.

C. Zinck[1], D. Pinceau[1], E Defaÿ[1], E. Delevoye[1] and D. Barbier[2]

[1]CEA-DRT - LETI/DTS - CEA/GRE - 17, rue des Martyrs, 38 054 GRENOBLE CEDEX 9 - France
Email: czinck@cea.fr http://www.cea.fr
[2]LPM INSA-Lyon, Build. 502, 20 av. Albert Einstein, 69621 Villeurbanne cedex, France

Summary: *Piezoelectric and ferroelectrics films are very promising materials for micro-actuators in MEMS applications (micro-actuators). In this paper, we present the fabrication and characterization of silicon membranes actuated by thin piezoelectric films. The influence of the electrodes implementation has been carefully analyzed. Si/SiO2/PZT square membranes have been elaborated by DRIE etching, and a sputtering process for PZT thin films has been specifically developed. We have investigated the dynamic and static behavior of our Pt/PZT/Pt/Ti/SiO2/Si membranes. Sputtered PZT on 4" wafers lead to high quality material well suited for large membrane deflection up to several microns. Detailed process will be given*

Keywords: *PZT, actuators, membranes, electrodes configuration.*
Category: *2, Materials and technology.*

1 Introduction

Piezoelectric thin films present a great interest for the microsystems thanks to their reversible effect [1]. Combining micromachined silicon membranes with piezoelectric (or ferroelectric) thin films has resulted in novel micro-devices such as motors [2], accelerometers [3], pressure sensors [4], micropumps [5], actuators [6], or acoustic resonators [7]. In this work, we present the fabrication and the characterization of square membranes (Si/SiO_2) actuated by a thin PZT layer.

2 Fabrication

Table 1 summarizes the process used to fabricate the membranes. The piezoelectric membranes were micro-machined out of 4 inches SOI wafers. The device is constituted by a 10 µm thick silicon layer, 2 µm of thermal oxide layer, the bottom electrode (50 nm of Titanium and 200 nm of Platinum), the piezoelectric thin film (700 nm) and the top electrode (200 nm of platinum). The piezoelectric thin film ($PbZr_{0,5}Ti_{0,5}O_3$) was deposited by RF magnetron sputtering at low temperature, therefore in the amorphous state. Then, in order to obtain a good crystallization in the perovskite phase, we performed a Rapid Thermal Annealing ; 30s at 675°C under a N_2+O_2 atmosphere. The bottom electrode contact was wet etched in the PZT layer. Then we have patterned the top electrode by lift-off using a negative photoresist. And finally square apertures were opened from the backside of the SOI wafer by a Deep Reactive Ion Etching. Figure 1 shows a 3 mm square membrane without any excitation. The free deformation due to stress is shown.

	SOI thick wafer (10µm/1µm/525µm) with a 2µm thermal SiO_2 layer on both sides.
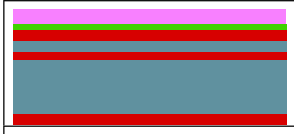	Evaporation of the bottom electrode (Ti/Pt). Annealing at 400°C. Sputtering of 700 nm PZT thin film and RTA.
	Top electrode: ✓ Evaporate ✓ Patterning
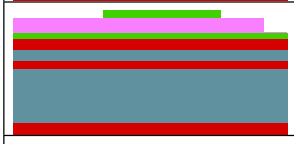	Wet etching of the PZT layer.
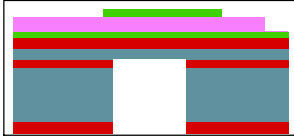	Dry etching of the oxide layer on backside and DRIE of Si to release the membranes.

Tab 1. Process flow short description.

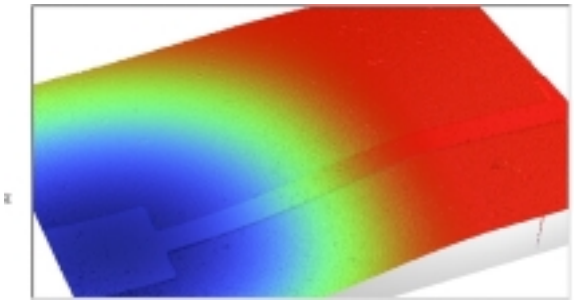

Fig 1. 3D map of a 3 mm square membrane, with a 700 µm square centered electrode (measured by optical interferometer) without excitation.

3 Characterization of the PZT thin film

We have developed and investigated the elaboration of PZT thin films by RF magnetron sputtering. The stoechiometry of the film has been checked by Rutherford Backscattering Spectrometry. The film is 10% deficient in lead. X-ray characterization (fig 2) shows a film crystallized the film in the perovskite phase without any traces of the pyrochlore phase (Pb-Ti-fluorite).

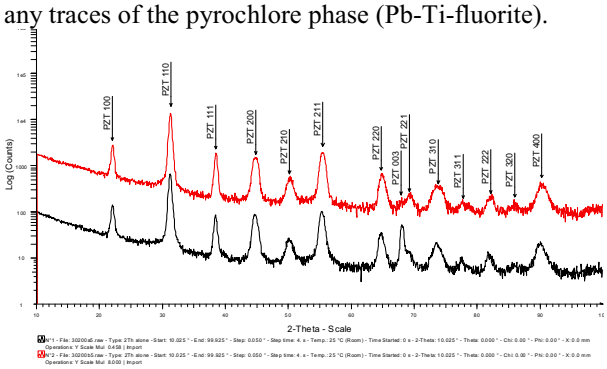

Fig 2. X-ray diagram of the PZT layer.

4 Characterization of the devices

1. Static and quasi-static behavior

We have first studied the behavior of the membrane when a PZT thin film is excited with an AC voltage (square or sinusoidal) at low frequency excitation. The figure 3 shows the response of a 7 mm square membrane with a 1 mm square centered electrode to a square voltage (-10 V to 10 V) at 50 Hz. Measurement were made with a laser vibrometer. Total deflection is about 5 µm.

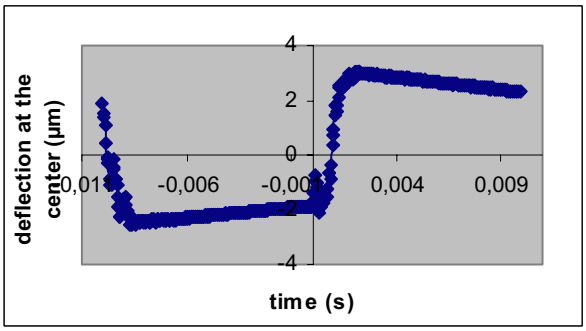

Fig 3. Response of 7 mm square membrane to a square volatge at 50 Hz.

2. Dynamic behavior

We have evaluated the frequency of the first mode for different geometries of the actuators. We present the evolution of the first mode with the following parameters : the membrane length and the electrode length. Vibration frequencies were characterized by using the laser vibrometer. The membranes were actuated by an AC sinusoidal voltage of 10V amplitude. Typical response is presented on the figure 4. This device exhibits a first mode (B_{00}) at 13 kHz with a sensitivity of 0,87 µm/V.

We have compared the FEM results to our measurement. We used two FEM software's for the design of the devices ; ATILA provided by Cedrat technology* and ANSYS. Table 2 compares the first results not including the stress in the layers. Further analyses will be detailed.

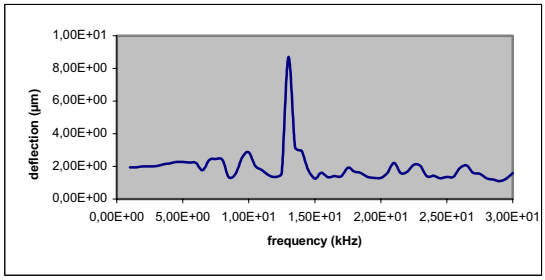

Fig 4. harmonic characterization of a 5 mm square membrane with a 1 mm square electrode.

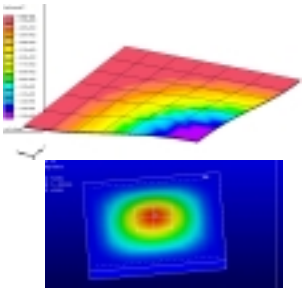

ATILA: 5,6 kHZ

ANSYS: 6,1 kHz

Experimental :13 kHz

Tab2. Comparison FEM vs. experimental measurement.

5 Conclusion

We have demonstrated the behavior of our PZT thin film as an integrable actuator in MEMS technologies. Membranes actuated by the PZT show good deflection and can be used in a quasi static or in a resonant mode.

* http://www.cedrat.com/

References

[1] P. Muralt,, "Piezoelectric thin films for MEMS". http://www.elsevier.com.

[2] M.-A. Dubois and P. Muralt, "PZT thin film actuated elastic fin micromotor", IEEE Trans. Ultrason., Ferro., and Freq. Cont., vol. 45, no. 5, 1998, 1169.

[3] G. Li, Z. Li. Z. Wang, Y. Hao, T. Li and G. Wu, "Design and simulation of a novel Highly symmetrical piezoelectric triaxial accelerometer", http://www.ansys.com.

[4] E. Defaÿ, C. Millon, C. Malhaire and D. Barbier, "PZT thin films integration for the realization of a high sensitivity pressure microsensor based on a vibrating membrane", Sensors and Actuators A , 2002; A99(1-2), 64.

[5] M. Koch, N. Harris, A. Evans, N. M. White and A. Brunnschweiler, "A novel micromachined pump based on tick-film piezoelectric actuation", Sensors and Actuators A, vol. 70, 1998, 98.

[6] M. J. Mescher, M. L Vladimer and J. J. Bernstein, "A novel high-speed piezoelectric deformable varifocal mirror for optical applications", IEEE, 2002, 511.

[7] H. H. Kim, B. K. Ju, Y. H. Lee, S. H. Lee, J. K. Lee and S. W. Kim, "A noble suspended type thin film resonator (STFR) using the SOI technology", Sensors and Actuators A, vol. 89, 2001, 255.

Direct-Write Asymmetric Y-branch Waveguides on Flame Hydrolysis Silica for Sensing Applications

A. Cleary[1], S. García-Blanco[1], A. Glidle[1], J.S. Aitchison[2], P. Laybourn[1], J.M. Cooper[1]

[1]Dept. of Electronics and Electrical Engineering, Oakfield Avenue, University of Glasgow, G12 8LT, Scotland, UK.
[2]Dept of Electrical and Computer Engineering, 10 Kings College Road, University of Toronto, M5S 3G4, Canada.

Summary: *Asymmetric Y-branch waveguides with different branching ratios were written on Ge doped Flame Hydrolysis Deposited (FHD) silica using electron-beam irradiation. Power splitting ratios were modelled using the 2D Beam Propagation Method (BPM) and the theoretical ratios compared with the experimental ones. We show that this type of waveguide is suitable for use in a sensor chip to make fluorescence measurements by integrating microfluidic channels with these waveguides.*

Keywords: *silica-on-silicon; electron-beam; Y-branch.*
Subject Category: *2 (Materials and Technology)*

1. Introduction

Planar silica devices using FHD silica have long been of interest to the Telecommunications industry due to the robust nature of the high optical quality glass waveguides produced [1]. FHD silica has also found interesting applications in optical sensing at visible wavelengths [2,3]. Waveguides were originally defined using standard photolithography and dry etch techniques, but this method can be time-consuming and reproducibility poor. A further FHD silica layer needs to be deposited after the dry etching of the core in order to allow integration of the microfluidic channels.

Electron-beam directly written optical waveguides have been demonstrated before as a technique that allows the fabrication of directly-buried low-loss waveguides, leaving a perfectly planar surface suitable for further integration of microfluidics [4]. An upper cladding layer of glass is not needed to protect the guides, allowing the use of more convenient materials such as polymers. Writing times are significantly shorter than the corresponding dry etch times required.

This work demonstrates the applicability of electron-beam written waveguides in FHD silica to fluorescence measurements for biological applications. Single-mode asymmetric branching waveguides with varying branch angles have been written and their performance compared with that predicted by 2D BPM simulations. A sensor chip is proposed, in which microfluidic channels are etched through the waveguides and sealed with a silicone polymer.

2. Theory

FHD of Ge doped silica uses an oxy-hydrogen flame to synthesise soot particles from $SiCl_4$. Dopants are added to alter the refractive index and to lower the sintering temperature of the glass. The soot is deposited onto a silicon wafer with a layer of thermal oxide as undercladding. The soot is then consolidated in a furnace at 1350 ºC.

Electron-beam irradiation of FHD silica has recently been reported [5]. The increase in refractive index observed is believed to be mainly due to compaction of the material, while the addition of Ge to the glass produces a greater effect than is observed in thermal silica [6]. Figure 1 shows an approximation of the waveguide profile after irradiation. The FHD silica layer is 2.4 μm thick, the width of the waveguides written is 2 μm and the thermal SiO_2 is 7 μm.

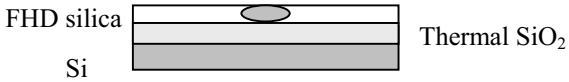

Figure 1: Profile of an electron-beam written waveguide

Asymmetric Y-branch structures in silica for optical interferometers were reported by Takato [7], and have recently been employed in sensors [2, 3]. At shorter wavelengths, the waveguide dimensions required for single-mode guiding decrease to the point where they reach the limits of photolithographic possibilities. Therefore, the use of electron-beam irradiation, which can write with nanometre precision, should result in more reliable waveguide structures.

Figure 2 shows a schematic of the proposed chip, where d, the final distance between the output

waveguides, was varied to produce a branching angle change, which varies the splitting ratio.

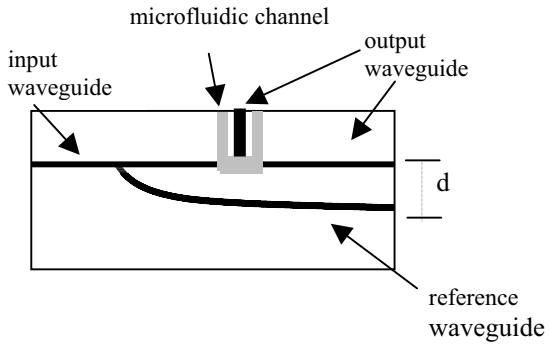

Figure 2: Top view of the sensor chip layout

Preliminary tests have been conducted to establish the feasibility of integrating microfluidic channels into the waveguide chip to allow fluorescence measurements to be made. These channels are defined by photolithography and dry etching using CHF_3. The channels are etched through the waveguide to allow direct excitation. PDMS (Polydimethylsiloxane) is used to seal the channels and to provide an upper cladding for the waveguides. This polymer was chosen due to its suitable refractive index (1.43) and low autofluorescence.

3. Fabrication and Characterisation

FHD silica wafers were grown in-house with a core/undercladding index difference of 0.75%. The wafers were diced into 1 x 1.5 cm pieces using a fine diamond saw. All waveguides were written on substrates deposited in the same run. A thin layer (30 nm) of NiCr was evaporated onto the substrate prior to electron-beam irradiation to prevent charging. The refractive index change produced in the irradiated area was $5x10^{-3}$ for a dose of 0.01 Ccm^{-2} and electron energy of 50 keV.

End-fire coupling was used to excite the waveguides. A x40 lens with a numerical aperture (NA) of 0.65 was used to focus the light into the guides, while a x20 lens with a NA of 0.40 was used for collection. Measurements were made using a LabMaster optical power meter.

4. Analysis

Table 1 shows the waveguides that were written, the predicted percentage output power of each branch and the measured percentage output powers.

Final distance d (μm)	Predicted branch 1 output (%)	Predicted branch 2 output (%)	Measured branch 1 output (%)	Measured branch 2 output (%)
57.5	59	41	56	44
65	61	39	63	37

Table 1: Comparison of predicted (BPM) and measured branch outputs

The measurement error is estimated to be ±4%. Excess losses are attributed mainly to leakage into the slab and to the roughness of the waveguide facets. A good agreement between the measurements and simulations can be observed.

5. Conclusion

We have demonstrated that asymmetric branching waveguides can be accurately written on FHD silica using electron-beam irradiation, and that predicted branching ratios can be consistently achieved. We propose that this method of creating waveguides will provide a route to fluorescence sensing systems by incorporation of microfluidic circuitry.

Acknowledgements

The authors wish to thank the EPSRC for funding this research.

References

[1] M. Kawachi, *Optical and Quantum Electronics* 22 (1990), pp. 391-416.
[2] J.M. Ruano, V. Benoit, J.S. Aitchison, J.M. Cooper, *Anal. Chem.* 72 (2000), pp. 1093-1097.
[3] J. M. Ruano, A. Glidle, A. Cleary, A. Walmsley, J. S. Aitchison and J. M. Cooper, *Biosensors and Bioelectronics* 18 (2003), pp. 175-184.
[4] R.A. Syms, T.J.Tate, R.J. Bellerby, *J. Lightwave Tech.* 13 (1995), pp. 1745-1749.
[5] S. Garcia-Blanco, A.Glidle, J.H. Davies, J.S. Aitchison, J.M. Cooper, *Applied Physics Letters* 79 (2001), pp. 2889-2891.
[6] S. Garcia-Blanco, T.C. Kleckner, A. Glidle, J.H. Davies, J.S. Aitchison, J.M. Cooper, *Proc. ECIO*, pp. 121-124 Paderborn, Germany, 2001.
[7] N. Takato, K. Jinguji, M. Yasu, H. Toba, M. Kawachi, *J. Lightwave Tech.* 6 (1988), pp. 1003-1010.

Piezoelectric AlN thin films grown by reactive sputtering for MEMS applications

E. Iborra, J. Olivares, M. Clement, L. Vergara, A. Sanz-Hervás, and J. Sangrador

Dpto. de Tecnología Electrónica, E.T.S.I. Telecomunicación, Universidad Politécnica de Madrid, Ciudad Universitaria, 28040 Madrid, Spain.
e-mail: eiborra@etsit.upm.es

Summary: *In this work we investigate the suitability of piezoelectric AlN films deposited by RF sputtering for MEMS applications. The morphological and piezoelectric properties of the films are analysed in relation with the sputtering parameters (substrate bias voltage, pressure and gas composition). c-axis oriented films with adequate piezoelectric response and controllable residual stress were obtained. Preliminary results on the fabrication of micromachined suspended structures are presented.*

Keywords: *AlN, sputtering, piezoelectric, stress, MEMS*
Category: *2 (Materials and technology)*

1 Introduction

Aluminium nitride (AlN) is an interesting material for the fabrication of sensors and actuators [1]. It is used as the piezoelectric layer in surface and bulk acoustic wave (SAW and BAW) devices [2], which are the basis of some chemical and biological sensors. The feasibility of piezoelectric MEMS actuators, such as RF microswitches, which make use of PZT and ZnO as actuating materials is currently being investigated [3]. Aluminium nitride exhibits several advantages compared to those two materials, such as excellent insulating properties, a large breakdown field and a better compatibility with silicon technology [2].

To fabricate AlN-based MEMS it is necessary to obtain films with *c*-axis orientation, controlled residual stress and grain size, and good adhesion to the substrate. RF sputtering is the most common technique to grow AlN films with those characteristics at low temperature. In this work we report the procedure to obtain films with crystal quality and residual stress suitable for the fabrication of MEMS suspended structures (cantilevers and bridges).

2 Experimental techniques

Aluminium nitride films have been deposited by RF sputtering of an Al target in an Ar/N_2 gas mixture on silicon and oxidized silicon wafers. The total pressure, the gas composition and the substrate bias voltage have been varied over a wide range. X-ray diffractometry (XRD) has been employed to assess the preferred orientation and grain size. The residual stress has been measured by the *bow* technique. To evaluate the piezoelectric response, SAW structures have been fabricated by depositing metallic IDTs transducers on the AlN films. The electromechanical coupling factor (k^2) was derived from the frequency response of the SAW structures. Bulk and surface micromachining technologies are being developed to fabricate suspended test structures.

3 Results

Our results on the sputtering of AlN films are summarized as follows. When the bombarding energy of the species that impinge on the substrate is sufficiently high, films with *c*-axis orientation are obtained. If the bombardment is very directional, the residual stress becomes too high. Increasing the pressure allows to reduce the directionality of the impinging particles and, therefore, the stress of the films. However, the bombardment energy is also decreased. This effect can be compensated by adjusting the substrate bias voltage. This way, it is possible to maintain the c-axis orientation while controlling the residual stress.

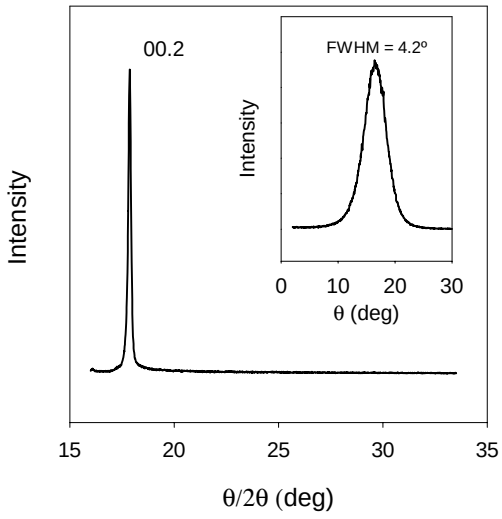

Fig. 1. XRD pattern of a representative AlN film. The inset shows the rocking-curve.

As an example of the crystal quality attainable, figure 1 shows an XRD pattern of a *c*-axis oriented AlN film with a large grain size (approximately 60 nm) and a compressive residual stress of 500 MPa. The inset shows the rocking-curve with a full-width-at-half-maximum of 4.2º.

Figure 2 shows the dependence of the residual stress on the pressure for two different substrate bias voltages. The residual stress decreases as the pressure is increased or the substrate bias voltage is decreased. The stress also depends on the nitrogen content. By adjusting the deposition conditions we obtained layers with stress ranging from large to very low compressive (or even tensile) values.

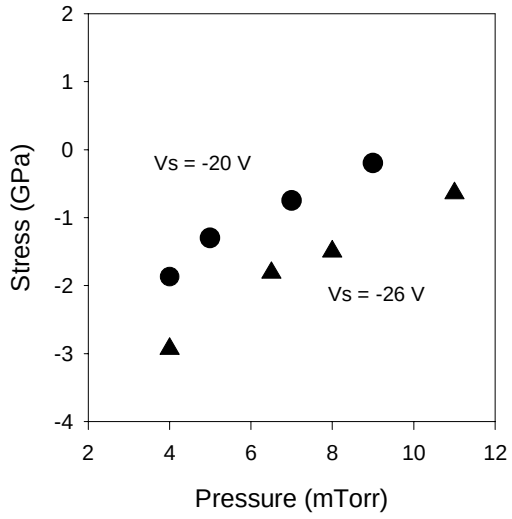

Fig. 2. Variation of the residual stress with the pressure for two values of the substrate bias voltage .

The frequency response of a representative AlN SAW structure is presented in Figure 3. The piezoelectric coefficient was derived from the value of the electromechanical coupling factor (k^2), which was determined by analysing the SAW response.

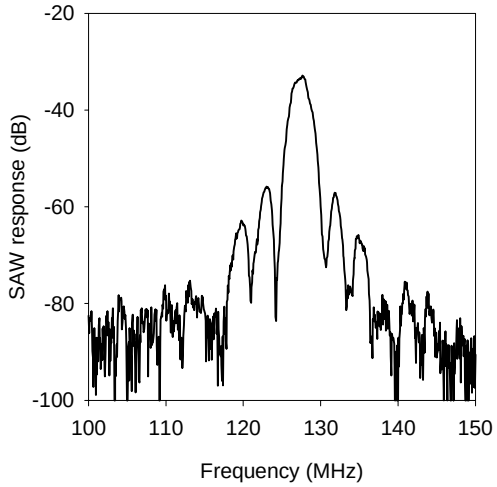

Fig. 3. SAW frequency response of a test structure.

To evaluate the viability of the material for MEMS applications, preliminary test structures consisting in suspended bridges and cantilevers have been fabricated. As an example, a silicon-bulk micromachined structure is shown in figure 4. Experiments are currently underway to produce piezoelectrically-actuated MEMS.

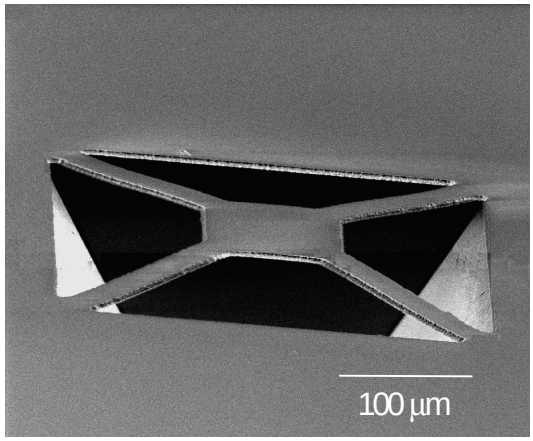

Fig. 4. Suspended structure consisting in a SiO_2/AlN/SiO_2 sandwich on a Si substrate.

Acknowledgements

This work has been supported by the Ministerio de Ciencia y Tecnología of Spain through project no. MAT2001-350.

References

[1] B. Cunninham. M. Weinberg, J. Pepper, C. Clapp, R. Bousquet, B. Hugh, R. Kant, C. Daly, and E. Hauser. Sensors and Actuators B 3629 (2000) pp.1-12.

[2] T. Laurent, F. O. Bastien, J. C. Pommier, A. Cachard, D. Remiens, and E. Cattan. Sensors and Actuators A. 87 (2000) pp. 26-37.

[3] B.Piekarski, D. DeVoe, M. Dubey, R. Kaul, and J. Conrad. Sensors and Actuators A. 91 (2001) pp. 313-320.

PMMA to SU-8 Bonding for Polymer Based Lab-on-a-chip Systems with Integrated Optics

B. Bilenberg[1], T. Nielsen[1], D. Nilsson[1], B. Clausen[2] and A. Kristensen[1]

[1] Mikroelektronik Centret (MIC), Technical University of Denmark
[2] The Department of Manufacturing Engineering and Management (IPL), Technical University of Denmark
email: bbo@mic.dtu.dk http://www.mic.dtu.dk

Summary. *We present an adhesive bonding technique developed for SU-8 based "lab-on-a-chip"-systems with integrated optical components. Microfluidic channels and optical components (e.g. waveguides) are defined in SU-8 photoresist on a Pyrex glass substrate. The microfluidic channels are sealed by a second Pyrex substrate, bonded on top of the cross-linked SU-8 structure using an intermediate layer of poly-methylmethacrylate (PMMA). Due to a lower refractive index of PMMA, this bonding technique offers good sealing of the microfluidic channels in combination with optical waveguiding in the SU-8 structures. The bonding technique is optimized with respect to temperature, and at a bonding force of 2000 N on a 4-inch wafer. A maximum bonding strength of ∼18 MPa is achieved.*

Keywords: PMMA, SU-8, Bonding, Integration
Category: 2 (Materials and technology)

1 Introduction

The integration of optical components and microfluidic components in polymer-based "lab-on-a-chip"-systems requires the use of new materials for sealing of the microfluidic systems. SU-8 is a widely used photo definable material for microfluidic and microoptical systems [1]. However, when integrating microfluidics and microoptics, SU-8 is not the optimal choice of intermediate material for bonding due to optical losses to the bonding layer. The use of poly-methylmethacrylate (PMMA) as an intermediate material solves this problem because the refractive index of PMMA is smaller than that of SU-8, whereby light can be confined in the SU-8.

In this paper we present an adhesive wafer-bonding technique for SU-8 based "lab-on-a-chip"-systems with integrated optical components. The bonding technique is optimized with respect to temperature at a bonding force of 2000 N distributed over a full 4-inch wafer. We have focused on optimizing the bonding temperature, because this is a critical processing parameter for polymer based optics due to thermal aging of polymers [2], which leads to increased optical losses.

2 Experimental work

In the study of the bonding strength of PMMA to SU-8 a series of sample Pyrex wafers were processed. The wafers were bonded in a homebuilt pressing machine and pull-tested to measure the bonding strength.

2.1 Processing

The fabrication of the samples relies on standard cleanroom processes. Prior to fabrication the Pyrex wafers are cleaned in Triton X100 soap and 7-up etch (sulphuric acid and ammoniumperoxodisulphate at $80°$C) before they are dehydrated for 12 hours in an oven at $220°$C. A 10 µm thick SU-8 layer is spun onto the bottom wafer, prebaked at $90°$C for 2 min on a hotplate, flood exposed and post-baked on a hotplate at $90°$C for 15 min to cross-link the SU-8. A 5 µm thick PMMA [3] layer is spun onto the top wafer and prebaked in an oven at $170°$C for 30 min. Finally the two wafers are put on top of each other with the SU-8 and PMMA layers face to face.

2.2 Bonding

The sandwiched wafers are pressed together in a homebuilt pressing machine with pressure- and temperature control. Initially three different bonding sequences with varying bonding time were tested to assess the influence on the bonding strength. The choice of bonding time showed no significant influence on the bonding strength. The following sequence was chosen for the further studies of the temperature dependence: The wafers are heated to bonding temperature before the bonding force is applied. The bonding temperature is kept for 10 min before active cooling is turned on, and the bonding force is released when the temperature drops below $75°$C.

A number of bonding experiments were performed at different temperatures between $50°$C and $150°$C, with a constant bonding force of 2000 N.

Furthermore a preliminary study of the bonding strength dependence on bonding force was performed. In this series of experiments the temperature was constant, 150°C, while the bonding force was varied between 1000 N and 2000 N.

2.3 Pull-testing

The pull-testing experiments were performed in a standard pull-testing machine capable of recording load-extension curves within a load range of 0-415 Kg. The bonded wafers were diced into 10 mm × 10 mm squares which were glued in between two metal bolts with an Epoxy based glue from Loctite©. The bolts fitted into the pull-testing machine. From the load-extension curves the bonding strength of each sample was extracted. By visual inspection it was checked after each pull-test that the fracture actually occured between the bonded wafers.

3 Results and discussion

The investigation of the bonding strength dependence on the bonding temperature is shown in Fig. 1. For

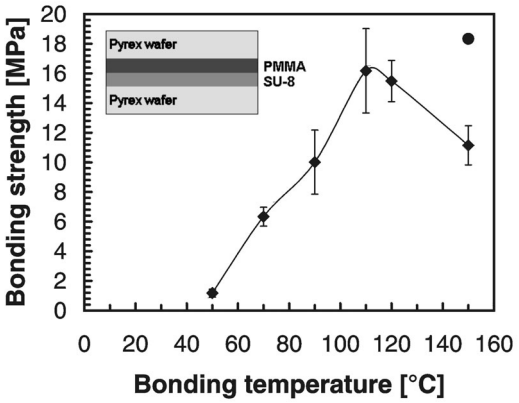

Fig. 1: Bonding strength obtained with different bonding temperatures. The bonding force was 2000 N (diamonds) and 1000 N (circle). The error bars indicate the standard deviation on the measuring points.

a bonding force of 2000 N the maximum bonding strength of ∼ 16 MPa is reached at a temperature between 110°C and 120°C. This is just above the glass transition temperature, T_g, of 105°C for PMMA.

The preliminary study of the bonding force dependence showed that the bonding strength actually increases with decreasing bonding force within the available range of 1000-2000 N. At 1000 N the bonding strength is ∼ 18 MPa while at 2000 N it is ∼ 11 MPa at a bonding temperature of 150°C. Therefore it is actually possible that the bonding strength of PMMA/SU-8 increases further at lower bonding strengths and thereby becomes comparable to the maximum bonding strength of SU-8 to SU-8, which earlier has been measured to be ∼ 21 MPa [4].

The PMMA bonding technique has not been investigated systematically with patterned SU-8 layers. However, the technique has been used to produce a work-

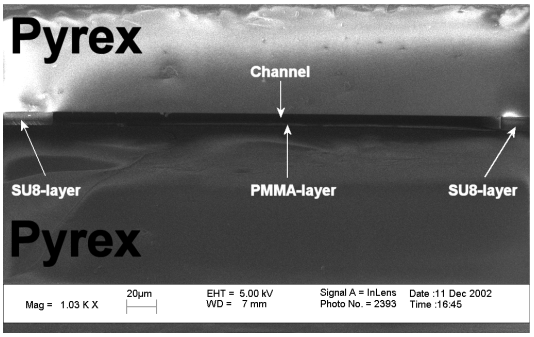

Fig. 2: Scanning electron micrograph of a cross section of a SU-8 based device with a 300 µm wide and 10 µm high micro-fluidic channel patterned in SU-8 and bonded with the poly-methylmethacrylate (PMMA) bonding technique, presented in this paper.

ing microfluidic device with a channel width down to 100 µm and channel height of 10 µm without any indication of PMMA clogging the channels, see Fig. 2.

4 Conclusion

A new adhesive bonding technique using PMMA as an intermediate material has been demonstrated. This technique improves the possibilities for integration of optical components with microfluidic devices. The results indicate that the optimum bonding temperature is just above the glass transition temperature of PMMA. The maximum achieved bonding strength is ∼ 18 MPa.

References

[1] *Microfluidic systems with on-line UV detection fabricated in photodefinable epoxy*, R. J. Jackman, T. M. Floyd , R. Ghodssi, M. A. Schmidt, K. F. Jensen, J. Micromech. Microeng. **11**, 263 (2001)

[2] *Advances in polymer integrated optics*, L. Eldada, L. W. Shacklette, IEEE J. of selected topics in quantum electronics. **6**, 54, (2000).

[3] PMMA 950K A13 from MicroChem Corp.

[4] *A low-temperature wafer bonding technique using patternable materials*, C. T. Pan, H. Yang, S. C. Shen, M. C. Chou and H. P. Chou, J. Micromech. Microeng. **12**, 611, (2002).

A Spectrally Resolved Multi-Point Optical Fibre Ultra Violet Sensor Using Cladding Luminescence

C. Fitzpatrick[1], C. O'Donoghue[1] and E. Lewis[1]

[1]Department of Electronic & Computer Engineering, University of Limerick, Limerick, Ireland
email: Colin.Fitzpatrick@ul.ie

Summary: *A multi-point sensor for ultra violet detection is presented. The sensor is a polymer optical fibre which has had sections of its cladding stripped and replaced with phosphor doped epoxies. Two points on the fibre have been coated with phosphors of different emission spectra (red & green) when stimulated by ultra violet radiation. The spectral emission intensity is dependent on the strength of the incident ultra violet radiation. Part of the emissions are coupled to the fibre's core. The fibre's output is monitored using a spectrometer which can determine localised areas of varying ultra violet intensity. Results are included in the form of spectra (400nm to 900nm) under different ultra violet stimulation conditions.*

Keywords: *optical fibre sensor, multi-point sensor, ultra violet sensor, spectrally resolved measurement*
Category: *2 (Materials & Technology)*

1 Introduction

The multi-point sensor presented here is based on the cladding photoluminescence of an optical fibre which has had its cladding replaced with a phosphor doped epoxy. These have been reported previously in single point probe form [1]. When the fibre is irradiated by ultra violet light the cladding luminesces and part of the emission is coupled to the fibres core. This has been shown to have a direct dependence on the fibre's V-number [2]. A diagram showing this sensing principle is shown in Figure 1.

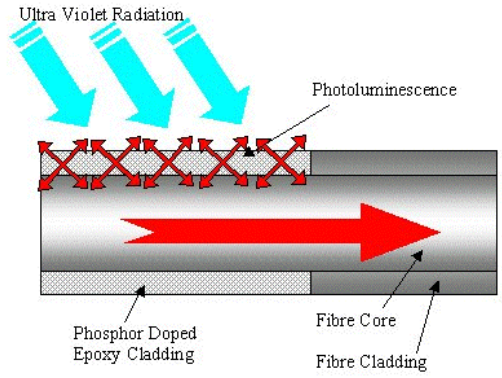

Fig. 1 Ultra Violet Sensor Based on Cladding Photoluminescence

This paper reports a expansion on this probe design whereby two different points on the fibre have been coated with phosphors with different peak emission wavelengths which correspond to the red (630nm) and green (525nm) sections of the visible spectrum. When the fibre's output is monitored using a spectrometer it is possible to determine the intensity of the ultra violet irradiation at localised areas by observing the recorded intensity levels of the emission wavelengths on a Microspectrometer detector. In this paper the ultra violet emission from the lamp is simulated by an array of L.E.D.s with a peak emission wavelength of 370nm. This was done to enable isolated stimulation conditions of the individual coated regions of the fibre. This sensor has applications in monitoring the uniformity of microwave plasma ultra violet discharges for water sterilisation units

2 Sensor Materials & Preparation

Phosphor selection is an important parameter in the system design process. It is crucial to the sensitivity of the measurement that there is a large overlap in the spectrum of the ultra violet radiation being monitored and the phosphor's absorption. Also in order to make a comparison between the phosphors photoluminescent emissions it is important that the sensitivity and quantum efficiency are matched for the two phosphors involved. One final point for consideration when selecting phosphors for such a sensing system is that their peak emissions must be sufficiently separated in wavelength in order that the peaks may be resolved by the spectrometer and that any spectral overlap is minimised.
The epoxy host for the phosphor also takes specific consideration. It is necessary for the epoxies transmission spectrum to include the UV radiation under investigation in order for the stimulating photons to be able to penetrate the cladding and interact with the phosphors. The fibre used for the sensor must also have a refractive index larger that the epoxy in order to create the conditions for a positively guiding waveguide.
The coating is applied pneumatically using a process developed at the University of Limerick [3]

3 Experimental Setup

The sensor was tested using two separate arrays of three ultra violet LEDs from Optosource (260019 series). These LEDs have a domed lens which produces a narrow viewing angle of 10 degrees. This focuses the emitted radiation thus increasing the intensity of the ultra violet on the fibre. Each array has its own power source making it possible to control the individual currents and hence the emission intensity on each of the individual sections of the fibre independent of the others. The spectrometer used to monitor the fibre's output was the Ocean Optics S2000. This is a low-cost, high-performance system sensitive in the UV-VIS-NIR region from 200-1100 nm. It has a high-sensitivity linear CCD array that provides high response and excellent optical resolution in a miniature package. It is suitable for use with large core diameter optical fibres. The spectrometer communicates with a PC through a data acquisition card. The spectral outputs are displayed using a LabVIEW V.I. A graphical user interface is constructed in LabVIEW where the output may be analysed or manipulated. A schematic diagram showing the experimental set-up is shown in Figure 2.

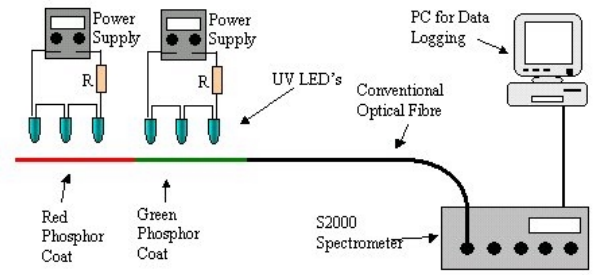

Fig 2. Experimental Set-up for Multi-Point Sensor.

4 Results

The fibres were tested under three conditions. One time when the ultra violet stimulation was identical on both points on the sensor, once when the ultra violet was withdrawn from the green section but not the red and once when the ultra violet was irradiating the green section only. These results for the first two conditions are shown in Figures 3 & 4.

5 Discussion

It is clear from Figures 4 & 5 that a system capable of distributed or multi-point sensing based on spectrally resolved information has been developed. This sensor gives the user clear information on the spatial distribution of incident ultra violet radiation along the fibre. Due to the good spectral separation between the two peaks of interest it may be possible to replace the S2000 spectrometer with a less expensive detection device. This may take the form of a low cost on chip micro-spectrometer or the use of a colour sensitive photodetector.

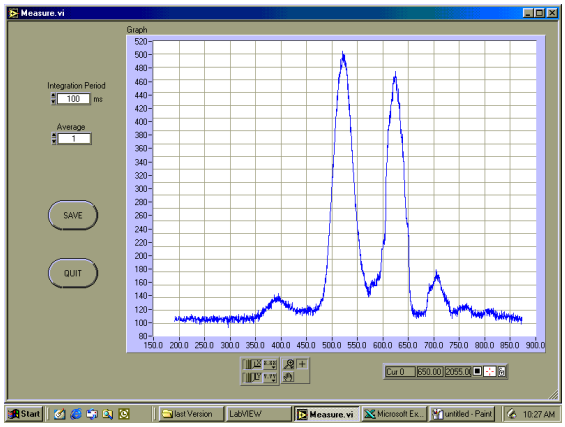

Fig. 3. Spectrometer Output For Both Green & Red Coated Sections Under Irradiation

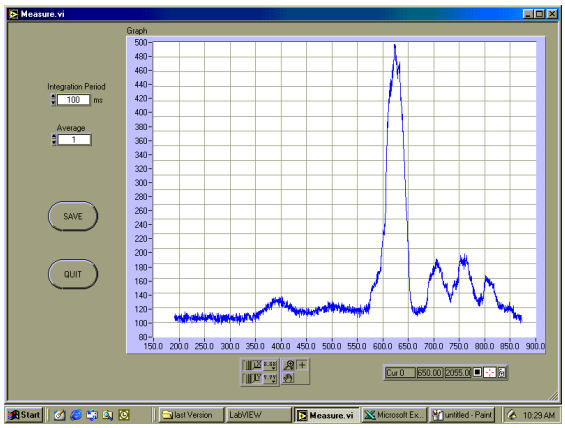

Fig. 4. Spectrometer Output For Red Section of the Fibre Under Irradiation

References

[1] Fitzpatrick C. Lewis E. Al-Shamma'a A. Lucas J., "An Optical Fibre Sensor for Germicidal Microwave Plasma Powered UV Lamps Output With Potential For On-Line Temperature Control" OFS 2002 (15th Optical Fibre Sensors Conference), Portland, Oregon, 6-10 May 2002, pp 455 - 458.

[2] Marcuse D., "Launching light in fibre cores from sources located in the cladding", J Lightwave Technology Vol. 6 No. 8, August 1988, pp 1273-1279

[3] O'Donoghue C. Fitzpatrick C. Lewis E. Grout I., "A fabrication process for luminescent clad fibre optic sensors", ODF2002 (3rd International Conference on Optics-photonics Design & Fabrication), October 30th -November 1st 2002, Tokyo, Japan, pp 107-108.

Integration of Self-Assembled 3-D RF Passive Components with Thin-Film Microstrip Lines

G.W. Dahlmann[1], M.M. Ahmad[1], E.M. Yeatman[1], A. Boughriet[2] and I.D. Robertson[2]

[1]Department of Electronic & Electrical Engineering, Imperial College London, U.K.
email: e.yeatman@imperial.ac.uk http://www.ee.imperial.ac.uk/optical/
[2]School of Electronic Engineering and Mathematics Department, University of Surrey, Guildford, Surrey, U.K

Summary: *A fabrication process has been developed which allows the combination of thin film microstrip transmission lines with released metal structures which can then be rotated out-of-plane by surface tension self assemby. The transmission lines allow low-loss feeds to the lumped element components. The use of self-assembly allows decoupling from lossy substrates, which can greatly improve the Q and operating frequency range. This is demonstrated for inductors, where Q of up to 70 is achieved on low resistivity silicon, with no self resonance up to 30 GHz. The process technique avoids all substrate modification and high temperature steps.*

Keywords: *high-Q inductor, microelectromechanical systems (MEMS), RF-MEMS, self assembly*
Category: *2 (Materials and technology)*

1 Introduction

Fabrication of more 3-dimensional structures, in a way compatible with low-cost batch production and standard semiconductor process steps, is a key challenge in many fields of MEMS. Previously, we have developed a technique of rotating parts defined by photolithography to out-of-plane orientations, using the surface tension force in molten hinges [1], [2], and have applied this technique to metal parts in order to create vertical inductors on silicon [3],[4]. In this way, magnetic and capacitative coupling to the substrate can be much reduced, lowering losses and raising the maximum operating frequency. Integration of high Q, high frequency inductors and other passives on silicon is very attractive for lowering cost and raising performance of tuned radio frequency circuits, particularly for low power applications such as sensor networks. However, achieving the full possible benefit of such an approach to passive components requires the use of interconnects which themselves do not have high losses or parasitic coupling. Thin film microstrip (TFMS) transmission lines are an attractive choice for this requirement, being of compact size and offering the possibility of fabrication over previously processed active silicon. This paper reports on the integration of TFMS with vertical, self-assembled RF structures.

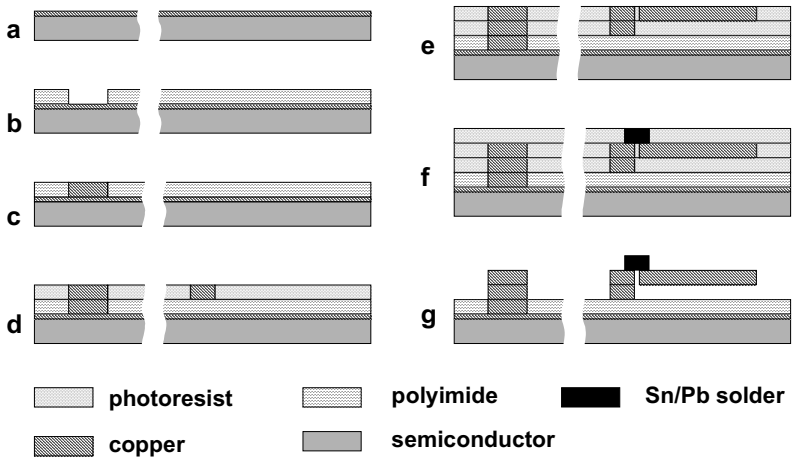

Fig. 1. Fabrication process flow. For each step the left side shows TFMS lines and vias, the right side the inductors and anchors.

2 Fabrication

Fig. 1 shows the process flow. A Cu ground plane is first deposited (a) on a low resistivity (5 Ω·cm) silicon substrate. The transmission line dielectric is photo-imageable polyimide (HD Microsystems HD4010), in which vias are opened for ground points for RF probing (b). The via metalisations are formed by Cu electroplating (c). Further processing is as reported in [4]; anchor (d) and inductor layers (e) are electroplated in photoresist molds, the signal lines of the TFMS being formed simultaneously.

Eutectic Pb-Sn solder hinges are then added in a further lithography and plating step (f), and the sacrificial resist layers are removed in proprietary resist solvent (g). The solvent is removed by freeze drying, to prevent stick-down of the released parts. Solder reflow is then carried out, just above the eutectic melting temperature at 200ºC, in a reducing atmosphere to avoid oxidation of the solder hinge material. The melted hinges cause the inductors to rotate into the vertical plane, after which the temperature is reduced, and the hinges cool and solidify. Examples of the final structures are shown in Fig. 2. The TFMS dielectric height was 9 μm, track widths were 60 μm, and meander and hinge metal thicknesses were 5 μm and 10 μm respectively. No substrate modification is involved; polishing steps are also avoided.

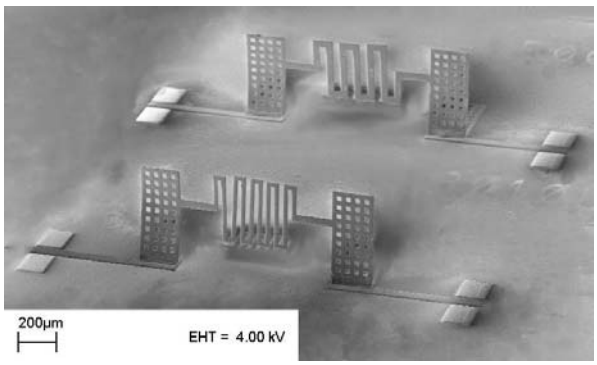

Figure 2. Meander inductors with TFMS lines and probe points.

3 Results

The S parameters of the meander inductors were measured using an Agilent 8510C vector network analyser, with 100 μm pitch ground-signal-ground probing on a Cascade probe station. The feed lines were de-embedded from the measured response, using fits of the TFMS parameters from measurements of test structures, to obtain the results given in Fig. 3. For comparison, meanders of equal dimensions not released or rotated were also measured, as shown. Inductances obtained were about 1.5 nH.

The obtained Q values and peak frequency greatly exceed those achieved previously for rotated inductors. The maximum Q of 70 approximates to the best reported for any high frequency inductors on silicon. In [5] Q values up to 85 are reported for 3D coils, but measurements above 1 GHz are not given and the inductors are relatively large. In [6] peak Q values of 70 are also achieved, for similar L, with peak frequency at 6 GHz well below the 10 GHz obtained in this case. No resonance is seen in our measurements up to 30 GHz. Other applications of this technique will be possible, such as spiral inductors.

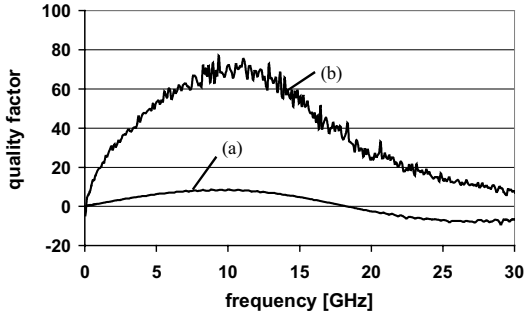

Fig. 3. Q vs. frequency for (a) in-plane meander and (b) out-of-plane meander

References

[1] R.R.A. Syms and E. M. Yeatman, Electr. Lett., 1993, 29(8), pp.662-664.

[2] P.W. Green, R.R.A. Syms and E. M. Yeatman, J. Microelectro-mechanical Systems, 1995, 4(4), pp.170-176.

[3] G. W. Dahlmann & E. M. Yeatman, Electr. Lett. vol. 36, pp. 1707-1708, 2000.

[4] G. W. Dahlmann, E. M. Yeatman, P. Young, I. D. Robertson & S. Lucyszyn, Sensors & Actuators, vol. 97-98, pp. 215-220, 2002.

[5] K. Van Schuylenbergh, C.L. Chua, D.K. Fork, J-P. Lu & B. Griffiths, in *IEEE Lester Eastman Conf. on High Performance Devices*, 2002, pp. 364 –373.

[6] J-B. Yoon, Y-S. Choi, B-I. Kim, Y. Eo & E. Yoon, IEEE Electron Dev. Lett., vol. 23, pp. 591-593, 2002.

Impedance Spectroscopy modelling of porous SnO_2 gas sensing ceramics

P. M. Faia[1], C.S. Furtado[2] and A.R. Ferreira[2]

[1,2]ICEMS Coimbra - Department of Electrical Engineering and Computers, LTMEU/FCT, University of Coimbra, Polo 2, Pinhal de Marrocos, 3030 Coimbra, Portugal.
[1]Email: faia@deec.uc.pt http://www.deec.uc.pt/

Summary: *Monitoring particles in the gas phase by electronic charge-transfer reactions at semiconductor surface is a concept aimed by R&D in recent years. The advantages of the use of semiconductor oxides are high sensitivity, simple design, low weight and cost. However, the range of applications is sometimes limited by the narrow knowledge that researchers have about conduction mechanisms behaviour of the oxide ceramics. Improvement of these properties cannot be achieved simply by experimentation, but requires a better understanding of the reactions with the gases.*

In this paper we describe undergoing work on Impedance Spectroscopy modelling of SnO_2 samples. Model construction is based on samples spectra obtained at various working temperatures in the presence of different gas atmospheres. The model being constructed is intended for a better understanding of the porous ceramics conduction mechanisms evolution on the SnO_2 porous ceramics.

Keywords: porosity, chemical semiconductor sensors, impedance spectroscopy, modelling.
Category: General, theoretical and modelling.

1 Introduction

It is known that predominant mechanisms influencing the variation of the electrical conduction, due to the presence of gases, occur at the contact surface of the materials [1]. This fact gives even more importance to the study of the involved processes in the production of reproducible sensors with higher surface areas.

The sequence of adsorption/desorption reactions that take place at the semiconductor surface requires ionic bonds to be formed, which influence the concentration of the conduction electrons in the solid. Consequently it is desirable for the sensing ceramics to have a large contact surface with the gas [2].

The introduction of porosity in the metal oxide ceramics improves the response in relation to sensors made out of dense compact bodies. With this approach, a greater contact surface with the gas is obtained, enhancing the surface reactions.

2 Impedance spectroscopy modelling

The technique of complex impedance spectroscopy gives information on the transport mechanisms in the materials, by which the charge distribution influenced by the structure can be characterised. This information when crossed with the ceramic porous structure of the crystals makes possible a better understanding of the mechanisms of physical and chemical adsorption. In this context it can be assumed that the total answer in the frequency domain of a ceramic material can be modelled in terms of simple electric circuits, with the representation of the separate contributions of the grains, the grain boundaries and the interfaces electrodes/material. Usually it is assumed that each of the processes is well represented by a parallel of a resistance and a capacitor. The resistance accounts for the opposition to the flow of the current and the capacitance to the charge storing. The relevant resistance/capacitance parallels are then associated in series.

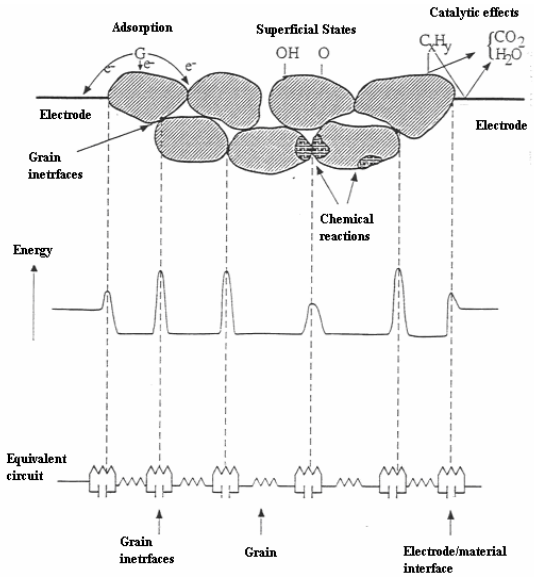

Fig. 1 - Schematic representation of a material.

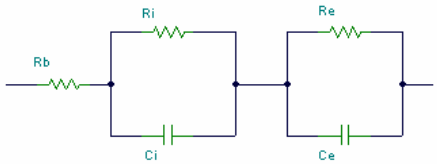

Fig. 2 - A.c. model under development.

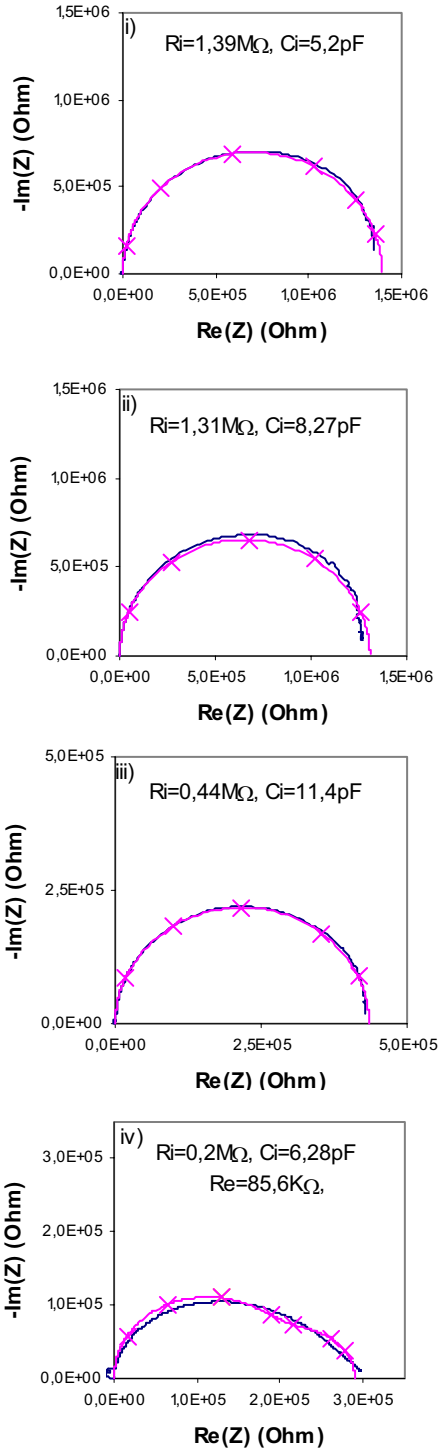

Fig. 3 - IS spectrums and respective simulations (×), using *Winfit*, of SnO_2 samples (in air at 25ºC) sintered at: i) 600ºC; ii) 700ºC; iii) 800ºC; iv) 1000ºC.

Taking for base this model, the materials are electrically represented by the scheme in figure 1. SnO_2 samples have been characterised under various atmospheres: dry and wet synthetic air; CO dilution in dry synthetic air. Based on the obtained IS spectra, an equivalent circuit model is being developed. Previous work [3], recommended the adoption of a model exhibited in figure 2, where R_b, R_i and C_i stand for the bulk resistance, grain boundary resistance and grain boundary capacitance, respectively, and R_e and C_e represent the electrode-sample interface. This model has been used as a first approximation to characterize SnO_2 samples: simulations obtained, using a impedance analysis software (*winfit*), have been based as much as possible on this model. When simulations show to be unsatisfactory, a geometrical method is used: sometimes various iterations are performed, until the best approximation is reached. Figures 3 and 4 present modelled spectra in dry synthetic air. From the spectra is very clear that there is a significant variation of the grain boundaries properties between 700 and 800ºC. It is also visible that, for the highest sintering temperature, the electrode influence is not negligible.

It can also be noticed that: a) as the sintering temperature increases the grain boundary resistance decreases, confirming the expected decrease on the porosity of the samples; b) the bulk resistance is very small and almost imperceptible on the diagrams; c) the bulk capacitance has been neglected since it does not show on the experimental data.

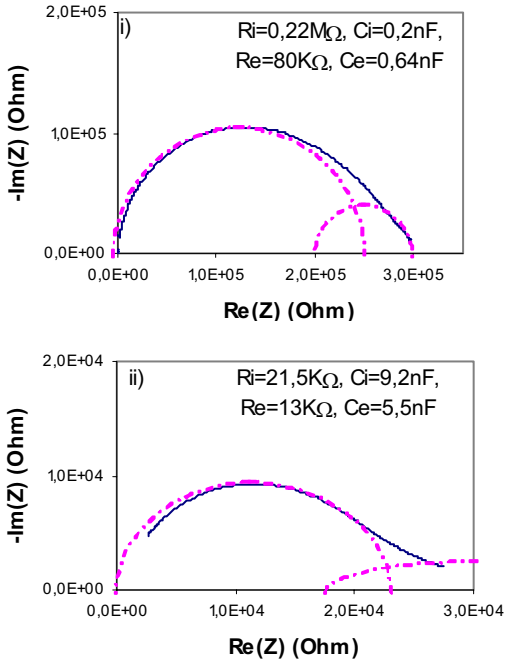

Fig. 4 - IS spectrums and respective simulations (- -), using the geometric method, of SnO_2 samples (in air at 25ºC) sintered at: i) 1000ºC; ii) 1200ºC.

References

[1] H. Baltes, W. Göpel, J. Hesse, *Sensors Update*, Vol. 1, VCH.

[2] P. Faia, C. Furtado, A. Ferreira, J. Perdigão, *Porosity influence on SnO_2 oxide ceramics sensitivity to CO*, Key Engineering Proceedings, vol. 230-232, pp420-423, 2002.

[3] M. Labeau, U. Schmatz, A. Gaskov, *Capacitance effects and gaseous adsorption on pure and doped polycrystalline tin oxide*, Sensors and Actuators, vol. B26-27, pp.49-52, 1995.

3-D Modeling and Simulation of Deep Isotropic Gas Phase Etching

Behraad Bahreyni and Cyrus Shafai

Dept. of ECE, The University of Manitoba, Winnipeg, Manitoba, Canada, R3T 5V6
email: behraad@ieee.org http://home.ee.umanitoba.ca/~spm/

Summary: *This paper describes our achievements in three dimensional simulation of gas phase etching of a substrate. Movement of gas molecules inside the etching chamber is simulated. Individual substrate atoms are removed upon the reaction between the etchant molecules and substrate material. Unlike most other etch simulation methodologies, the motion of the etchant gas molecule is continuously simulated, and not predicted by algorithm. This is required for deep undercutting of the etch mask. The simulator is capable of duplicating experimental results for xenon difluoride etching of silicon, which often involve complicated phenomena such as trenching and loading. The small number of simulation parameters makes it possible to use the described method for simulation of isotropic etching of various substrates.*

Keywords: *etch simulation, etch profile, XeF_2*
Category: *1 (General, theoretical, and modeling)*

1 Introduction

Gas phase etching of substrates is of great importance in microfabrication industry. Generally, anisotropic etching is used to transfer the mask pattern to the underlying substrate and isotropic etching is performed as the last step to release the micro-structures. Due to the widespread use of silicon in microfabrication industry, gas phase isotropic etchants of silicon have been employed extensively for fabrication of MEMS. Among these etchants are xenon difluoride (XeF_2) and bromine trifluoride (BrF_3). Both of these materials etch silicon isotropically in their gaseous form (non-plasma) and both are very selective to silicon compared to other materials which are commonly used in micro-fabrication.

One problem with using these etchants is poor control over etch parameters and non-uniformity among the final etch profiles. This is particularly troublesome in the early stages of process development due to the varying etch rates across a wafer.

This work is extending and improving our previous achievements in two dimensional simulation of isotropic gas phase etching [1,2]. In addition to adding 3-D simulation capabilities to our simulator, the simulation algorithms have also been improved to decrease the simulation time and increase the versatility of the simulator.

2 Etching model

A common etch simulation method, especially for anisotropic etch simulation, is to calculate (or use a look-up table to load) the etch rate along different crystallographic directions. Many algorithms exist which use this data and remove layers of atoms from the substrate based on the mask opening geometry. These methods usually do not take into account the effects of adjacent mask openings on each other's profiles, or minute irregularities such as surface roughness and trenching phenomenon [3]. Furthermore, in the case of isotropic etching, undercutting of the etch mask modifies the the etch profile as a function of etch depth. Thus, algorithms which determine the etch rate based on the mask geometry will become inaccurate for deep isotropic etching.

In our simulator the etch process is simulated by following the trajectory of individual etchant gas molecules inside the etching chamber. The simulation starts by *generating* an etchant molecule above the substrate surface possessing random direction of motion. Since the etchant molecule is not subject to an external force, it will change direction only after colliding with another gas molecule. Therefore, the direction of movements is completely random (Brownian) and the radius of movement will be about one mean free path (MFP) of the etchant gas at the etching pressure. The etchant molecule continues its movements until it impinges on the surface of the substrate or on the masking material. If the gas molecule impinges on the mask, it bounces back and continues its movements in space. If the etchant molecule hits the substrate surface, it may either bounce back or react with the substrate material, depending on the reaction probability between the etchant and substrate materials. If the reaction does

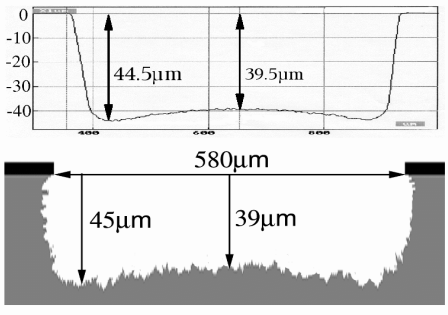

Fig 1. Comparison of simulation and experimental data. Simulated trench depth is 6µm vs. 5µm for the measured value.

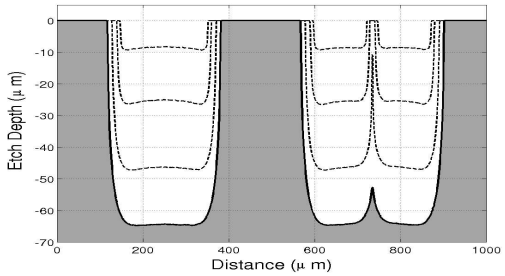

Fig 2. Changes in etch profile with etch depth. Initial hole diameters were 200μm, 120μm, and 120μm.

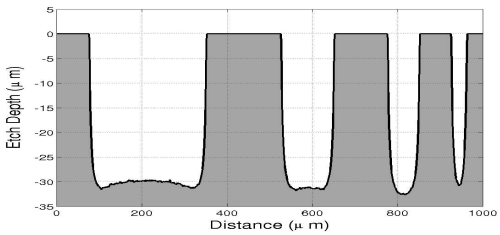

Fig 3. Dependence of etch profile and depth on the ratio of MFP to mask opening diameter. Initial hole diameters were 250μm, 100μm, 50μm, and 10μm.

occur, the corresponding substrate molecule is removed and another etchant molecule is generated.

This model is valid when the effect of an existing boundary layer can be neglected and the flow dynamics inside the chamber are not complicated. These conditions are met for many of the non-plasma gas etchants, such as XeF_2.

3 Simulation results

Simulation results were compared against experimental data obtained from etching silicon by XeF_2 gas. XeF_2 etches silicon isotropically (and selectively) in its gaseous form at etching pressures of around 1Torr. At such pressures, the MFP of gas molecules is between 10μm and 20μm, which can be found from:

$$\lambda = \frac{RT}{\sqrt{2}\,\pi\, d^2\, P\, N_A} \qquad (1)$$

where R is the universal gas constant, T is the temperature, d is the molecule diameter, P is pressure, and N_A is Avogadro's number.

As shown for the case in Fig 1, good agreement exists between simulation and experimental data and the simulator had closely predicted the trench depth.

Fig 2 shows the predicted changes in the etch profile as the etch depth becomes larger. As can be seen, when the etch depth is around a few MFP's, trenching effect can be observed at the edges of the profile. This figure also illustrates the loading effect between two neighboring holes and final release of the overhanging mask. The MFP for all simulation results is set to 20μm.

Our simulator shows that the etch profile and depth for simple mask openings mainly depend on the ratio of the mask opening diameter to the MFP of the etchant gas. This can be observed in the simulation results of Fig 3. This result was found to closely agree

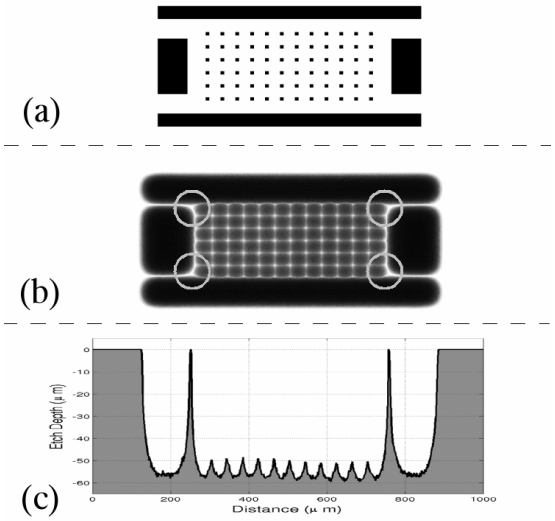

Fig 4. Application of the 3D simulator for process development: (a) original mask (black color represents mask opening); (b) top view of etched sample (darker colors are deeper etches); (c) vertical cut along two of the spots which have not released for the case in (b).

with experimental XeF_2 etching [2].

Finally, Fig 4 illustrates the application of the simulator for identifying critical spots on a mask pattern. This knowledge will help MEMS designers identify potential problems in mask designs. Also, the release step in microfabrication is often performed by continuous monitoring of the whole microstructures. Identifying critical spots which will release last, helps to concentrate the monitoring process to a few locations rather than whole wafer.

4 Conclusions

A new algorithm was proposed for 3D simulation of isotropic gas phase etch processes. The simulation results were verified by comparing them against experimental data. Since isotropic etching is often used for releasing purposes, the simulator can be employed to spot those points on microstructure which will release last, or to assist the process designer in deciding on proper etch depth for microstructure release.

Future research will include adding capabilities for anisotropic etch simulation and applying similar methodologies to thin film deposition simulation.

References

[1] B. Bahreyni, C. Shafai, and C. M. Card, *Technical Proceedings of NanoTech 2003*, vol. 3, San Francisco, USA, February 2003, pp. 9-12.

[2] B. Bahreyni and C. Shafai, *J. of Vacuum Science and Technology A20 (6)*, (2002) 1850-1854.

[3] E. W. Scheckler and A. R. Neureuther, *IEEE Transactions on Computer-Aided Design of Integrated Circuits and Systems*, vol. 13, no. 2, (1994) 219-230.

The Effects of Conductivity on the Scattering Characteristics of SAW Liquid Sensors

Ruyen Ro[1], Hsin-Yuan Tung[1], Shih-Jeh Wu[2], Yun-Ju Chen[1]

[1]Deparement of Electrical Engineering

[2]Department of Mechanical Engineering

1, Section 1, Hsueh-Cheng Rd. Ta-Hsu Hsiang, Kaohsiung, Taiwan 840, R.O.C.

email: ryro@isu.edu.tw

***Summary**: In this paper, reflection and transmission coefficients of a SAW liquid sensor subjected to different conducting loadings are investigated theoretically. In terms of SAW phase velocities and attenuation constants, the liquid loading region can be represented as an equivalent transmission medium. Subsequently, a transmission matrix method is proposed in this study to calculate the frequency responses of the loaded SAW device composed of a pair of input and output interdigital transducers. The effect of conductivity on the scattering characteristics of Rayleigh and leaky SAW liquid sensors will be demonstrated. Numerical results in this study can be employed to design the state-of-the-art SAW liquid sensor.*

Keywords: SAW liquid sensor, transmission matrix method, conductivity, scattering characteristics
Subject category: 1, 5, 6

Introduction

SAW (Surface Acoustic Wave) devices have been widely used as RF filters and their application on sensing liquid/gas has also been studied [1,2]. Previously complicated neural network scheme has to be used to recognize specific liquid properties in our laboratory. In this paper we developed a transmission matrix method to directly relate the conductivity of carried liquid to the measured phase change. In this way, the loading liquid can be accurately figured from conductivity property without complicated computation.

Methodology and Results

Figure 1 shows the schematics of the SAW liquid sensor studied in this paper [3]. By directly solving Christoffel's equations subjected to appropriate boundary conditions at the interface, the phase velocity and attenuation constant of SH leaky SAW propagating over 36°YX. $LiTaO_3$ under different conducting loadings (conductivity, σ) of the liquid media were obtained and illustrated in Fig. 2. The corresponding transmission matrix block diagram is depicted in Fig. 3. The matrix [T] is a 3×3 transmission matrix representing the scattering characteristics of the IDT. Both the substrate transmission line and liquid loading region are two-port devices and can be represented by 2×2 matrices, matrices [D] and [L], respectively. $|U_i^+|^2$ and $|U_i^-|^2$ are the acoustic powers in the forward and backward directions at reference plane i . I_i and V_i are the resultant current and voltage, at the corresponding electrical port of the IDT. After some matrix manipulation and enforcing the appropriate boundary conditions (no reflection), the currents I_1 and I_5 can be determined in terms of the voltages V_1 and V_5, and vice versa. It follows that the admittance matrix as well as the scattering matrix of the liquid sensor can then be evaluated.

The phase differences of the transmission coefficients versus frequency for various conductivities are shown in Figs. 4 and 5. θ_{21} is the phase angle of S_{21} and each curve represents the difference ofθ_{21} as σ changes. The width of the liquid loading region in the case was 2 mm and the piezoelectric materials selected were 128°YX. $LiNbO_3$ and 36°YX.$LiTaO_3$. The wave propagation mode for the former one was a Rayleigh wave and SH leaky SAW for the other. The center frequency for the Rayleigh wave device was about 39.2 MHz and 3dB bandwidth was from 37.6 to 40.8 MHz. On the other hand, for the leaky SAW device, the center frequency was about 99.5 MHz and 3dB bandwidth ranged from 93.5 to 105.4 MHz. The reference value in Fig. 4 or 5 was the calculated phase angle of the transmission coefficient as the conductivity of the liquid loading was set to be zero. In both figures, the absolute value of the phase difference increases as the conductivity increases in the frequency range of interest (shown in the direction as the arrow pointed). It is also noticeable that the value of the phase difference for each curve (~40°) in Fig. 5 for 36°YX.LT is greater than the other case (~8° for 128°YX.LN) shown in Fig. 4. Typical phase error of commonly used measurement system is about ± 2° (e.g. HP 8719ES

network analyzer). From the results we obtained in this study, as we can measure the phase accurately enough, 36°YX.LT is sensitive enough and very suitable to be applied to detect conductivity of certain loading liquid and to recognize specific liquid. Experiments have been conducted to verify our numerical results and will be presented later.

References

[1] J. Kondoh, T. Muramatsu, T. Nakanishi, and S. Shiokawa. Development of surface acoustic wave liquid sensing system and application for Japanese tea measurements, *Proc. 2001 IEEE Int. Freq. Ctrl. Symp. and PDA Exhibition*, pp. 497-501, 2001.

[2] B. S. Ballantine, R. M. White, S. J. Martin, A. J. Ricco, E. T. Zellers, G. C. Frye, and H. Wohltjen. *Acoustic wave sensors-theory, design, and physico-chemical applications*, Academic Press, San Diego, 1997.

[3] R. Ro, S. Yang, H. Lee, and C. Shen. Effects of conducting liquid loadings on propagation characteristics of surface acoustic waves, *Proc. Natl. Sci. Counc. ROC(A)*, 25, 131-136, 2001.

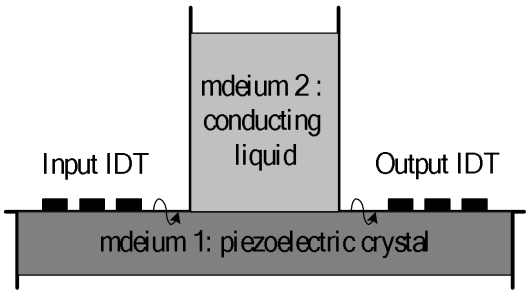

Fig.1 Schematics of the SAW liquid sensor

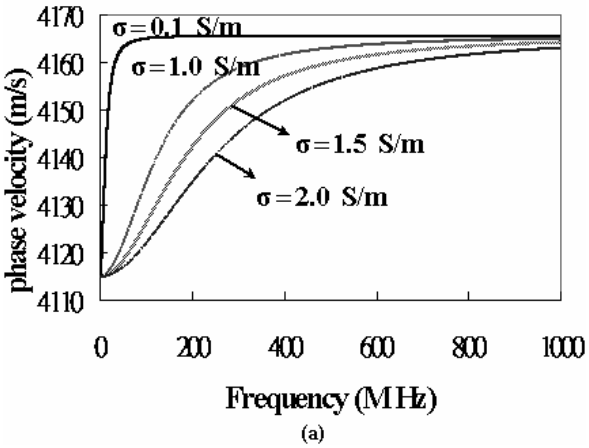

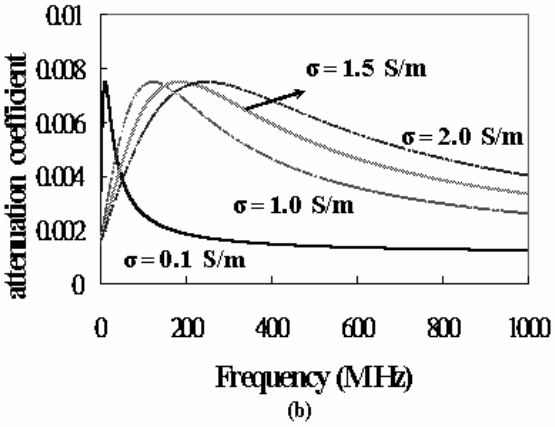

Fig.2. (a) Phase velocity and (b)attenuation constant of SH leaky SAWs versus frequency. The piezoelectric crystal is 36°YX.LT.

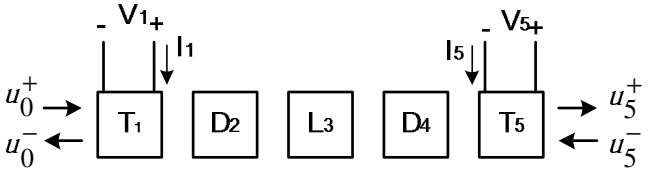

Fig. 3.The matrix block diagram of SAW liquid sensor

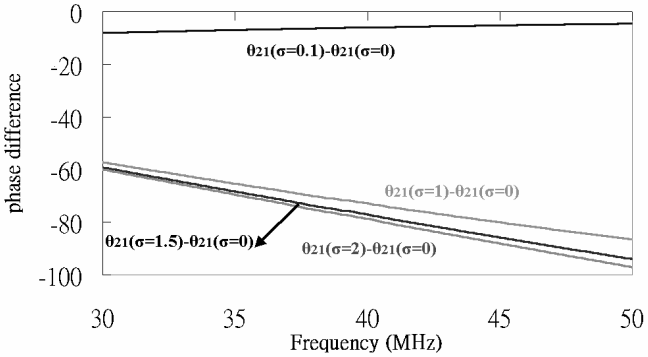

Fig.4.The phase difference of the transmission coefficients versus frequency with various conductivity. The piezoelectric crystal is 128°YX.LN.

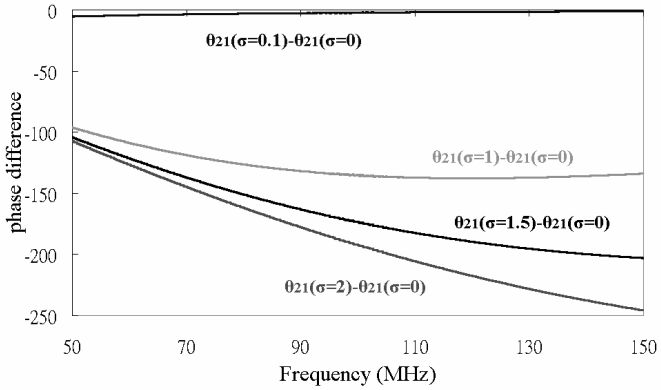

Fig.5. The phase difference of the transmission coefficients versus frequency with various conductivity. The piezoelectric crystal is 36°YX.LT

Geometrical optimization of an acoustic thermal flow sensor

J.W.van Honschoten[1], P.Ekkels, G.J.M. Krijnen and M.C. Elwenspoek[1]

[1]Transducers Technology Group, University of Twente, P.O. 217, 7500 AE Enschede, the Netherlands
email: j.w.vanhonschoten@el.utwente.nl

Summary: *In this paper a thermal acoustic flow sensor that measures particle velocity (the 'Microflown') is analyzed. A model is developed that calculates the sensor sensitivity and its frequency dependent behavior, as a function of material parameters and device geometry. Consequently, improved devices could be fabricated, with a new geometry consisting of three wires of which the central wire is relatively most heated. These are the best performing sensors up to date with a frequency range attending over 5 kHz and signal-to-noise ratios improved by 10 dB to more than 20 dB over previous designs.*

Keywords: *thermal flow sensors, acoustic, optimization*
Category: *1 (General, theoretical and modeling); 2 (Materials and technology)*

1 Introduction

The Microflown is a micromachined acoustic sensor that measures particle velocity instead of sound pressure, which is usually measured by conventional microphones [2, 3, 4]. Originally a flow sensor [1], it is optimized for sound measurements.
The sensor usually consists of two closely spaced thin wires of 1500 µm (spacing 100-350 µm) of silicon nitride with an electrically conducting platinum pattern. This metal pattern acts as temperature sensor *and* as heater. The wires are electrically heated to about 600 K. When subject to a particle velocity, the temperature distribution around the resistors is asymmetrically altered. The temperature difference, and therefore the temperature dependent resistance difference, of the two sensor wires is in first order proportional to the particle velocity.

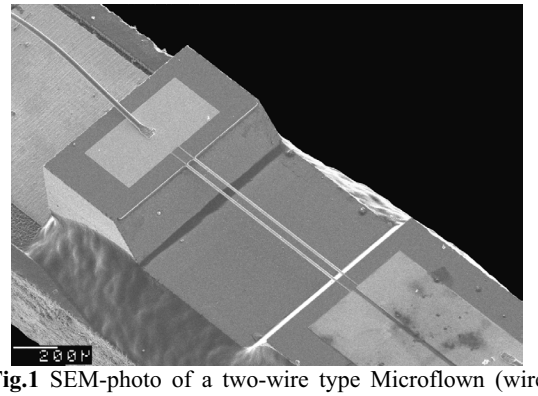

Fig.1 SEM-photo of a two-wire type Microflown (wire lengths 1 mm)

2 Sensor optimization

Using a numerical version of the model described in former work [5,6], a program was developed to calculate the sensitivities of geometrically different devices. Parameters such as the channel depth (l_z), the wire length (l_y), their mutual distance ($2a$), and the dissipated power are taken into account in this model, as well as a three-wire configuration.

3 Experimental

Many geometrically different devices were fabricated, with $40<l_z<300$ µm, $80<2a<300$ µm and $500<l_y<1500$ µm according to the process flow describe in [6]. In particular several three-wire sensors of different geometries were designed, and the sensitivity as a function of the dimensions and the relative power in the central wire was investigated. The total dissipated power was varied from 0 to 75 mW.

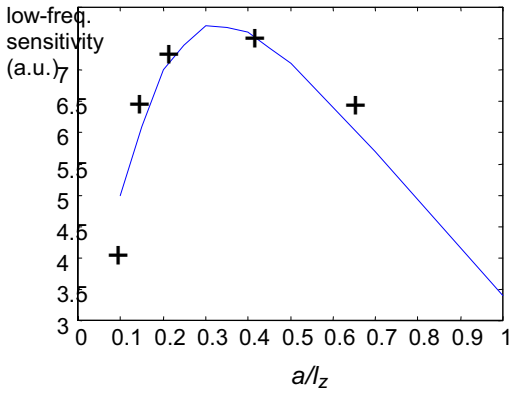

Fig.2 Low-frequency sensitivity $S(f=0)$ as a function of the ratio a/l_z (line represents the calculations). The crosses show experimentally obtained results, from devices with l_z=240 µm; $2a$=50, 80, 100, 200, 300 µm.

The sensitivity of all devices was experimentally determined using a standing-wave-tube, together with a loudspeaker and a reference microphone. The most relevant characteristics of the sensitivity are the low-frequency('DC'-)sensitivity and a characteristic frequency f_c [6], a measure of the bandwidth. Their dependences on a/l_z (Fig.2), l_z/l_y (Fig.3), a (Fig.4), and P (Fig.5) were compared to the model calculations; good agreement was found.

One sees that for given l_y, the sensitivity increases with l_z, up to $l_z \approx l_y$. See Fig.3. The optimum a at given l_z, is about $a \approx 0.3\ l_z$ (Fig.2). However, to obtain a broadband, flat, frequency response, a should be as small as possible (Fig.4). Both requirements cannot be fully satisfied simultaneously, but a very well performing device is obtained when $a \approx 100$ µm at $l_y = 1$ mm.

4 The three-wire configuration

A significantly better performing device is made of *three* instead of two wires. The central wire, the heater, is heated up to ~780 K, while the other two wires, acting as sensors, are relatively cold and thus attain lower noise levels.

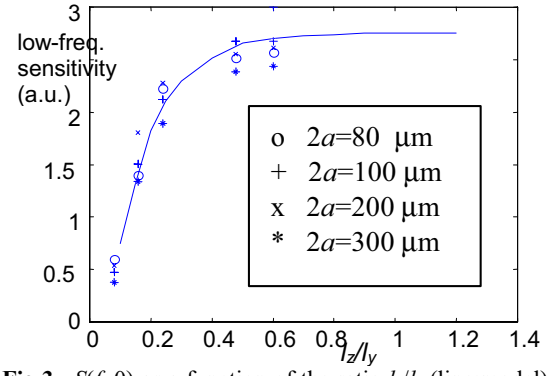

Fig.3. $S(f=0)$ as a function of the ratio l_z/l_y (line:model). The marks indicate experimentally obtained results from devices with l_y=500 µm; l_z=40, 80, 120, 240 or 300 µm and $2a$=80, 100, 200 or 300µm.

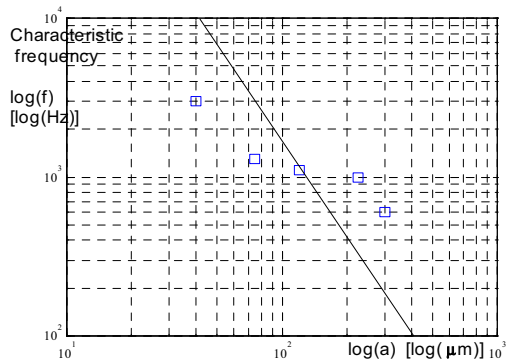

Fig.4. Characteristic frequency f_c of the sensitivity curve, as a function of the distance between the sensing wires, mutual wire distance=$2a$, plotted logarithmically. The line shows the theoretical dependence $f_c \propto a^{-2}$.

The sensitivity, however, is proportional to the total dissipated power. A three-wire device, with a relative heater power of 0.85, has a two times higher sensitivity than a two-wire sensor of the same dimensions and power. The optimal geometry, see Fig.6, is found to be near l_y=1 mm, l_z=300 µm, a=50 µm and P_{total}=70 mW. In the frequency bandwidth 1.0-4.0 kHz, its signal-to-noise ratio (at 1 Pa) is then about $1.3 \cdot 10^4$ to $3.3 \cdot 10^4$ √Hz.

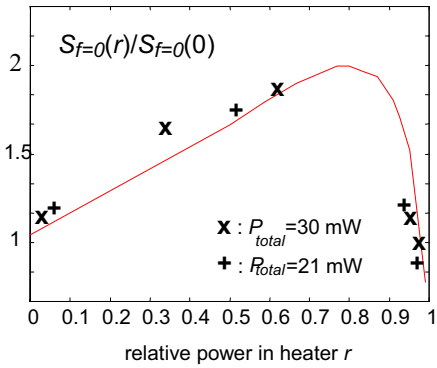

Fig.5 . Low-frequency sensitivity $S_{f=0}$ as a function of relative heater power $r=P_H/(P_H+2P_S)$ normalized to the sensitivity $S_{f=0}$ at r=0, according to the model calculations (line), and the experimentally obtained points (crosses).

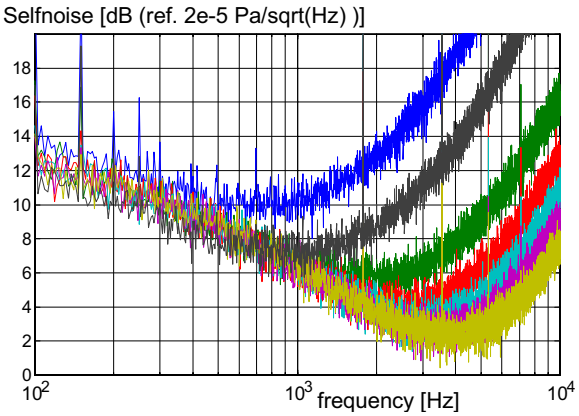

Fig.6. Selfnoise levels of the best up to date three-wire type Microflown, a=100 µm, l_z=200 µm, a sensor power $P_{S2}+P_{S1}$=11mW and a heater power P_H=0 mW (upper curve), 5, 10, 20, 32, 44 and 58 mW (lowest curve). The upper curve corresponds to the two-wire configuration.

5 Conclusions

Using a numerical model, two and three wire acoustic thermal flow-sensors have been geometrically optimized. Model and experiment showed good agreement and the resulting Microflowns are found to improve the frequency range to 5 kHz while improving the signal to noise ratio by 10-20 dB.

References

[1] T.S.J. Lammerink et al, "Micro Liquid Flow Sensor", *Sens. and Act. A*, pp.37-38, 45-50, (1993).
[2] H-E. de Bree et al., The Microflown: a novel device measuring acoustical flows, *Sens. And Act.* A 54 (1996) 552-557
[3] www.microflown.com
[4] W.F. Druyvesteyn et al, A new sound intensity probe; comparison to the Bruel & Kjaer p-p probe, 104th AES Conv. Amsterdam; pre-print 4651, 1998
[5] V.B. Svetovoy, I.A. Winter, Model of the μ–flown microphone, *Sens. and Act.* 86 (2000), 171-181.
[6] J.W. van Honschoten, Optimisation of a two-wire thermal sensor for flow and sound measurements, MEMS '01.

Modeling of Sensitivity for Sensors Based on Surface Plasmon Resonance

V. Chegel, Yu.Chegel and Yu.Shirshov

Institute of Semiconductor Physics, National Academy of Sciences of Ukraine
41 pr. Nauki, 03028 Kiev-28, Ukraine
email: che@isp.kiev.ua http://www.isp.kiev.ua

Summary: *The computer modeling is carried out for parameter of sensitivity of optoelectronic sensors, using phenomena of surface plasmon resonance (SPR). The SPR-sensor's physical model is described in view of probable modifications of sensitive surface with a dielectric layer. The variants of optimization of sensitivity for SPR-sensors, constructed on the principle gold - dielectric are considered. With the purpose of comparison of processing techniques two methods of SPR-curve treatment - traditional with estimation of sensor's response on shift of the curve minimum and proposed, using calculating of derivative in the SPR-curve half-width point are compared.*

Keywords: *Surface Plasmon Resonance, modeling, sensitivity, sensor.*
Category: *1 (General, theoretical and modeling)*

1 Introduction

A number of works to modeling of SPR-sensors sensitivity is devoted [1,2,4] . SPR-curves with a sufficient accuracy are simulated with using of the formalism for matrix of scattering in the multilayers structures. In work [1] was simulated the sensitivity of gas sensor with presence of dielectric layerr above the gold layer, that results in dependence of sensitivity on the form of SPR - curve and height position of its minimum. Really, form of curves and height position of SPR-curve minimum play in this case significant role, but they are only a result of combination of the index of refraction n_i, index of absorbtion k_i and thickness d_i for each from i layers of multilayer system (Fig.1). For more complex determination of SPR-sensor sensitivity it is

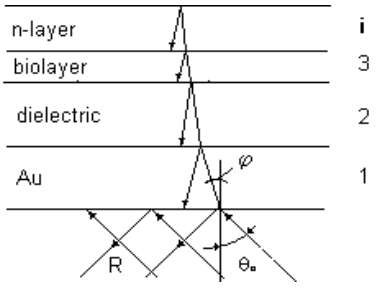

Fig.1. The scheme of multilayer system.

necessary to know the character of dependence $S_i = f(n_i, k_i, d_i)$, where S - sensitivity of sensor. In work [2] is simulated sensitivity of SPR-sensor without a dielectric layer, but with use the gel matrix as a layer - sorbent of biomolecules. The modeling of sensitivity of SPR-sensor, based on «particle linkage» technology (technology with linked metal particles) is carried out in work [3] Technology is based on the effect of increase of SPR-response, if on the sensor's surface is sorbed the layer of biomolecules connected with little particles of optically active substance with high refraction, for example, colloidal gold or titan dioxide.

More universal is proposed variant of modeling for multilayer system with gold, dielectric layers and layer of investigated molecules, adsorbed directly on the gold or dielectric. The proposed model theoretically allows to consider system with n-layers.

For study of SPR-sensor sensitivity the original program, allowing step by step varyation of the n_i, k_i and d_i in wide range of technologically possible values was developed. For all variants the SPR-response $d\theta_{min}$ is calculated for registration of the tested layer with thickness d_{mol} and optical parameters close to biomolecules layer (N_{mol} = 1.46, d_{mol} = 2, 5 or 10nm). Accordingly, the sensor sensitivity is:

$$S = d\theta_{min}/d_{mol}$$

As base values the following parameters, describing above mentioned layers, were taken: Au-complex index of refraction N_{Au} = 0.15 + 3.6i, d_{Au} = 45nm; dielectric - N_d = 1.5 + 0i; glass prism - N_g = 1.51; ambient - N_a = 1.334.

The program is based on the calculating of integral Fresnel coefficient R for p-polarization of incoming laser light [3]. In case of i layers is convenient to calculate R, using a formalism of the scattering matrix S [4],

$$S = I_{01} L_1 I_{12} L_2 \cdots I_{(i-1)i} L_1$$

where matrix of interface between layers

a and b: $$I_{ab} = \begin{bmatrix} 1 & r_{ab} \\ r_{ab} & 1 \end{bmatrix}$$

where r_{ab} - Fresnel coefficient of reflection for the apropriate interfaces,

and matrix of the layer: $$L = \begin{bmatrix} e^{\beta_i} & 0 \\ 0 & e^{-\beta_i} \end{bmatrix}$$

where β - phase thickness of appropriate layer:

$$\beta = 2\pi\left(\frac{d}{\lambda}\right)N\cos\varphi$$

Where d -thickness of the appropriate layer, φ-angle of refraction for the appropriate layer (Fig.1), λ-length of a wave (632,8 nm), N-complex coefficient of the refraction for appropriate layer. The reflection coefficient of multilayer structure is determined by elements of first column of a scattering matrix:

$$R = S_{10}/S_{00}$$

2. Analysis of results

The results of modeling reveal, that sensitivity of considered SPR-biosensor changes depending on parameters of multilayer structure in the significant range of values, especially for layers of biomolecules with a large size. Maximal theoretical sensitivity of SPR-sensor without a dielectric layer should be observed with thickness of a gold layer approximately 70-80 nm with minimal possible value of k_{Au}. The index of refraction n_{Au} don't reveal noticeable influence on sensitivity in this case.

In case of model with a dielectric layer the more complex dependence on SPR-response from thickness and index of refraction of a dielectric layer is observed. Sensor's sensitivity with presence of a dielectric layer (N_d = 1.45) for all thickness of biomolecules layer grows fluently up to some critical thickness of a layer, and then sharply (Fig.2) decreases. Exception is the case, when value of index of absorption k_d of dielectric increases up to 0.2, were sensitivity decreases with presence of a dielectric layer of any thickness (curve 4 Fig.2). The critical value of thickness of dielectric layer, at which sensitivity of SPR-sensors begins to decrease, also depends on dielectric characteristics of gold and dielectric layer as well as on the size of biomolecules and in our case can changes from 32 nm up to 62 nm for k_d = 0. For value k_d = 0.02 amplifier property of a dielectric layer is reduced to minimum, and with k_d = 0.2 sensitivity decreases always.

The observable peak character of dependence of sensitivity for SPR-sensor is explained by increasing of tangential component of wave vector of light as well as increasing of value of wave vector of surface plasmon, that expressed in changing of the form of SPR -curve. Really, if for thickness of a dielectric layer d_d=10nm the form of SPR-curve differs from a classical form a little, with the further increase of d_d the minimum of curve is displaced to the right upwards, SPR-curve extends and with some threshold value of dielectric thickness occurs significant changes of the SPR-curve's form, results in decreasing of sensor's sensitivity. In this case is possible, especially for large values of dielectric thickness, to present function of sensor's sensitivity depending on the

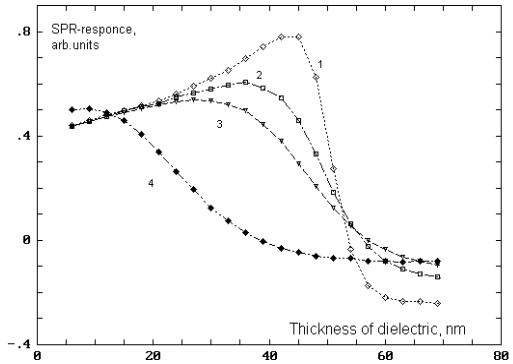

Fig.2. Dependence of SPR-response on the index of absorption and thicknes of dielectric layer (N_d = 1.45). 1-for registration of biomolecules layer (N_{mol} = 1.46, d_{mol}=2nm). 1-(k_d=0.0i), 2-(k_d=0.02i), 3-(k_d=0.04i), 4-(k_d=0.2i).

form SPR- curve as derivative $S = dR/d\theta$ in certain point, for example, in a point of half-width of SPR-curve, that results in increasing of sensitivity with comparison on traditional method, were SPR angle shift is calculated. With thickness, far from critical, both methods reveal similar sensitivity.

The presented results of modeling allow not only to find optimal parameters of SPR-sensors, but also to specify researched parameters of bioobjects, due to direct dependence of SPR-response on values of dielectric constants and thickness of layers structure. Actually, it is necessary to have a number of specific nomograms for calculating of the SPR-response which are taking into account real values of materials, that applied.

References

[1]. Jiri Homola. Model of a chemo-optical sensor based on plasmon excitation in thin silver films. *Sensors and actuators B*, 11 (1993) 481-485.

[2]. B.Liedberg, I.Lundstrom, E. Stenberg. Principles of biosensing with an extended coupling matrix and surface plasmon resonance. *Sensors and Actuators B*, 11 (1993) 63-72.

[3]. P.T.Leung, D.Pollard-Knight, G.P.Molan, M.F.Finlan.Modelling of particle-enhanced sentitivity of the surface-plasmon resonance biosensor. *Sensors and actuators B*, 22 (1994) 175-180.

[4].R.M.A.Azzam and N.M.Bashara, Ellipsometry and Polarized Light, North-Holland, Amsterdam,1977.

Design of thick film initiators for car safety units by means of FEM

W. Smetana, R. Reicher and H. Homolka

Vienna University of Technology, Institute of Industrial Electronics and Material Science,
Gusshausstrasse 27/3666 , A-1040 Vienna, Austria
email: walter.smetana@tuwien.ac.at http://www.iemw.tuwien.ac.at

Summary: *Finite element method has been proved as an useful tool to design thick film initiators for automotive safety unit application as well as a method of rapid prototyping of such devices. Parameters like the thermophysical properties of the explosive, physical properties of the substrate and the resistor as well as diffusion effects occurring at the termination of the resistor element have to be taken into account during the design of the thick film initiator element. Ignition tests conducted with an explosive on the base of $Sb/KMnO_4$ have demonstrated the validity of the design process on the base of FEM.*

Keywords: *thick film, initiator, design, FEM, actuator*
Category: *1 (General, theoretical and modeling)*

1 Introduction

Seat belt pretensioners and airbags protecting passengers of cars against risks of injury in the case of an accident are equipped with detonators. They are typically activated by electro-explosive devices where resistive wire elements, bridge elements realised in semiconductor or thin film technology are acting as initiator systems. Crash sensors in cars induce, in the case of an accident, a current pulse in this resistive initiator element. As the device is heated up to a critical temperature the explosive detonates and consequently the airbag or the retention system will be released. Thick film initiator elements can be considered as practical alternative to these systems with regard to their excellent immunity to externally generated electric currents induced by radio waves, static electricity or radar which may cause an undesired, premature ignition, as well as to their mechanical robustness which is required when the explosive is compacted and pressed against the initiator element in the order to provide an intimate contact responsible for a low thermal contact resistance and consequently a reliable ignition.

2 Thick film initiator element

The thick film bridge device appears as a simple resistor. The thermal characteristics of the bridge element have to be adjusted to certain ignition requirements that are also strongly related to the performance of the applied explosive. Heating occurs internally within the bridge volume when the current passes through the device. Two operation conditions may be distinguished: „No-fire" is a safety test of conventional nature where constant current is applied for a certain period without exceeding the ignition temperature of the pyrotechnic powder. Depending on the value of firing currents, in the „all-fire" region, consistent bridge operation is governed by the occurence of distinct phases in the bridge element: the metallisation is heated through melt, vaporisation, and finally into an ionised plasma. In the solid phase state of the resistive element which is considered in our design process the temperature of the initiator is heated up finally exceeding the critical temperature of explosive. Conduction is the dominant heat transfer mechanism. In the case of ignition the bridge is either destroyed by the reaction or eventually fused (burned open) by the firing. Operation characteristics, firing sensitivities and tolerances to electrical hazards and no-fire currents can be modified by adjusting bridge geometry and selection of materials with appropriate thermophysical properties.

3 Design

Relevant performance characteristic data, which ignition elements generally have to meet, are a resistance of 2 Ohm +/- 10%, a „no-fire" current of 500 mA for 10 s and an „all-fire" current of 1,2 A. between a response time time of 500 µs and 2 ms respectively.

A thermal distribution analysis using the finite element method (ANSYS FEM-package) has been carried out in order to evaluate the performance of a thick film initiator element realised with a commercially available Au-resinate paste terminated with a Pd doped silver conductor paste applied on a conventional 96% Al_2O_3-substrate as well as on a glass ceramic coated substrate where the coating-layer is acting as a heat barrier. The applied explosive was a pyrotechnic powder on the base of $Sb/KMnO_4$ with an ignition temperature of 506 K. Typically, the device has an overall rectangular shape (Fig. 1). Materials property data to be considered for numerical simulation are summarised in Table 1.

Table 1. Materials property data [1], [2], [4]

	Density kg/m^3	Thermal conductivity W/(mK)	Specific heat J/(kgK)	Resistivity Ohm-m
Al_2O_3-substrate	3 780	24	800	$1 .10^{18}$
glass ceramic dielectric	3 200	1,1	710	$2 .10^{13}$
Au	19 300	317	129	$2{,}25 . 10^{-8}$
Ag	10 500	429	235	$1{,}617 . 10^{-8}$
$Sb/KMnO_4$	2 070	0,3	540	$1 .10^{12}$

Ignition tests carried out on bare bridge elements show that in a very restricted zone nearby the termination pad the resistor path burns open which must be related to an increase of resistivity as a result of diffusion effects. A theoretical evaluation has proved this assumption: The Ag-concentration profile in the resistor element has been calculated applying 2nd Fick`s law. Based on the resultant concentration profile and the resistivity vs. concentration data reported in the literature [3], it was possible to calculate the resistivity profile of the diffusion zone as demonstrated in Fig. 2.

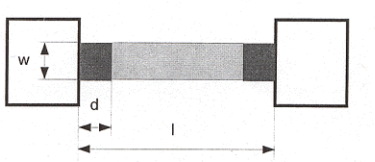

Fig. 1. Initiator model with diffusion zone d at Ag-Au termination

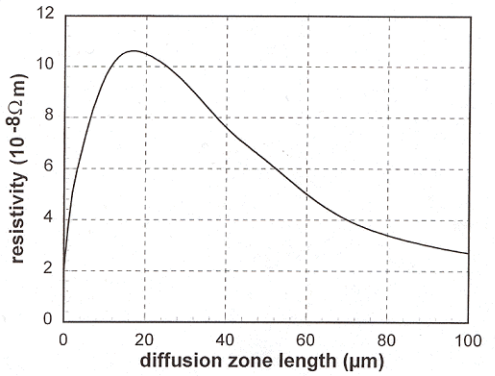

Fig. 2. Resistivity distribution within diffusion zone

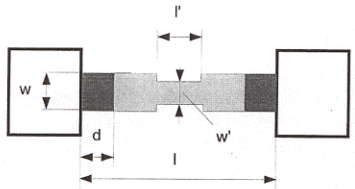

Fig. 3. Element with diffusion and contraction zones

In a very restricted region of the diffusion zone nearby the termination pad the resistivity peak may develop a hot spot. This zone is too small to provide a reliable ignition of the explosive. A new model of an initiator element, comprising an adequate reduction of the resistor within the resistor element provides a nearly uniform temperature level already exceeding the peak temperature of diffusion zone (Fig. 3). By alteration of the geometrical proportions of the model it has been provided that the area of peak temperature is always encountered in the center of the resistor element within a settling time of 2 ms as shown in Fig. 4.

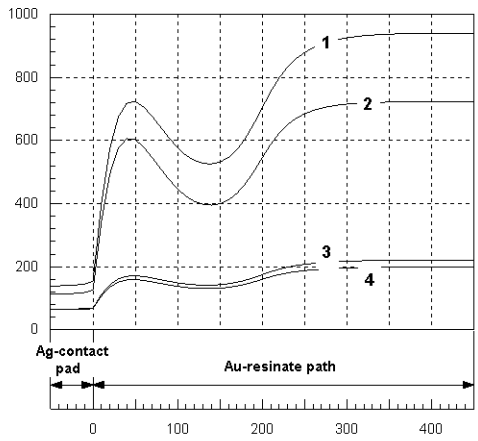

Fig.4. Temperature distribution for different modes:
With explosive: 2 "all-fire", 4 "no-fire"
without explosive 1 "all-fire", 3 "no-fire"

The performance of the initiator element in the "no-fire" as well as in the "all-fire" mode is governed by the thermophysical properties of the applied explosive. Consequently the design of the bridge element must be always adapted to the specific properties of the selected pyrotechnics. The modified thick film device shows an excellent no-fire characteristic and is capable of igniting the explosive powder at substantially less energy than required for ordinary wire bridges. It has been found that the bridge behaves well under both firing and subthreshold conditions.

References

[1] D. R. Lide, *Handbook of Chemistry and Physics*, 1992-1993, pp. 12-34-12-35 and 12-130.
[2] C. Y. Ho, R. W. Powell and P. E. Liley, *J. Phys. Chem. Ref. Data*, 2(1972) 340 and 395.
[3] R. W. Berry, P. H. Hall, M. T. Harris, *Thin Film Technology*, 1968, pp. 306-307.
[4] M. W. Beck and M. E. Brown, *Combustion and Flame*, 65(1986), 263.

Sensitivity Analysis of Novel ZnO/$LiTaO_3$ SAW Transducers

D. A. Powell[1], K. Kalantar-zadeh[1] and W.Wlodarski[1]

[1]RMIT University, School of Electrical and Computer Engineering, Melbourne, Australia.
email: david.powell@ieee.org

Summary: *Surface Acoustic Wave (SAW) devices for sensing applications were fabricated on 36°-YX $LiTaO_3$ with a ZnO guiding layer. The capability of these transducers for gas and liquid sensing applications was shown by studying parameters such as mass sensitivity and electromechanical coupling coefficient. Devices were fabricated with film thicknesses ranging from 0 to 4μm yielding operating frequencies between 94 and 104MHz. Phase velocity was calculated as a function of ZnO guiding layer thickness by searching for singularities of the generalised Green's function. This was confirmed by measuring the change in centre frequency. Electromechanical coupling coefficient was calculated and shown to have a maximum of 10% at thickness of 3.5μm. Mass sensitivity was calculated as a function of layer thickness, and was found to reach a maximum of 6.9m^2/kg for a ZnO thickness of 6μm. However, the measured value for 4μm ZnO layer was ~10m^2/kg. This is greater than the sensitivity of conventional Love mode devices fabricated on 36°-YX $LiTaO_3$ with SiO_2 guiding layers.*

Keywords: *SAW Sensor, $LiTaO_3$, ZnO, sensitivity*
Category: *1 (General, theoretical and modelling)*

1 Introduction

Layered SAW devices have previously been proposed as high sensitivity gravimetric sensors suitable for operation in both gas and liquid media, due to their shear-horizontal particle displacement and high level of surface acoustic energy trapping. For example, [1, 2] demonstrate numerical and experimental analysis of "Love mode" devices fabricated on 90° rotated ST-Quartz with SiO_2 guiding layer.

2 Fabrication

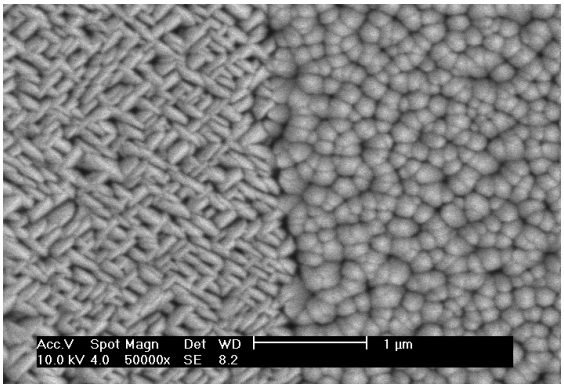

Figure 1: ZnO growth on bare $LiTaO_3$ (left) and metallised area (right)

Devices were fabricated on 36°-YX $LiTaO_3$ wafers, using Al metallisation layer deposited onto a Cr adhesion layer by electron beam evaporation. Electrodes and reflectors with a periodicity of 40μm were fabricated using a wet-etch process to create a 2-port resonator device. Such devices offer reduced noise in an oscillator system due to their higher Q factor. ZnO films were deposited by RF magnetron sputtering. Figure 1 shows an SEM micrograph of the growth of ZnO films on $LiTaO_3$. As was previously reported [3], the grain growth and corresponding crystal orientation of ZnO can be seen to differ on the metallised and free regions.

3 Velocity

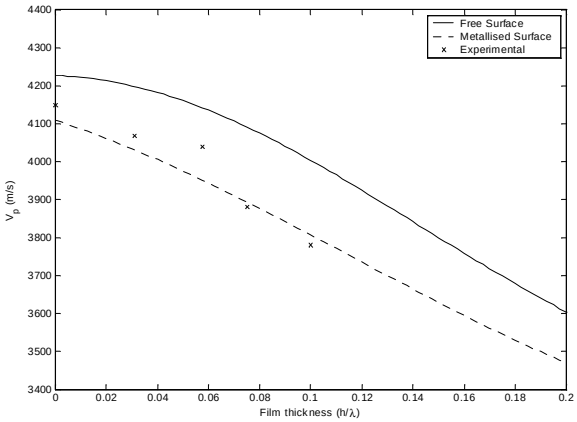

Figure 2: Measured phase velocity and calculated free and metallised velocities

Figure 2 shows the theoretically derived phase velocity for ZnO layers on $LiTaO_3$. Free and metallised surface velocities were determined by searching for the poles and zeros of the Green's function, whilst holding λ constant at 40μm. This was calculated at the boundary between the substrate and the ZnO guiding layer [4], taking into account the differing orientation of the film over the free and metallised regions. It was found that the propagation velocity was closer to the velocity in the metallised region.

4 Electromechanical Coupling

The electromechanical coupling coefficient (k^2) is a measure of the interaction between electrical and mechanical fields in a piezoelectric material. In the case of SAW sensors, it is particularly important to have high k^2 for conductivity-based measurements [5]. The values presented in Figure 3 were calculated from the difference between the pole and zero of the Green's function.

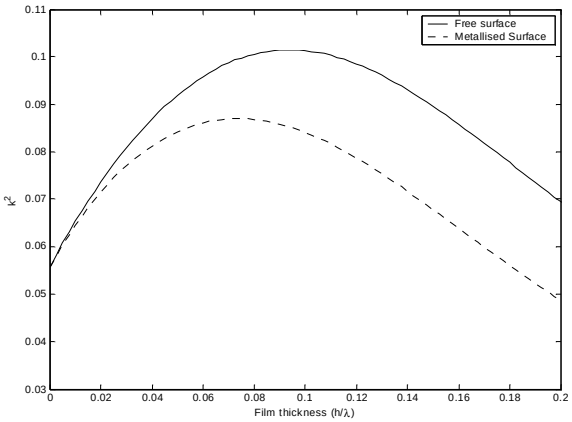

Figure 3: Electromechanical coupling coeffecient

The high electromechanical coupling has been confirmed by the high sensitivity of the devices when used for conductometric gas sensing [4]. For devices operating at 165MHz with a 1.25μm ZnO layer, the response to 1ppm NO_2 gas with WO_3 selective layer was 40kHz.

5 Mass Sensitivity

Figure 4 shows the theoretically derived and measured mass sensitivity of the devices. Calculation was based on the velocity shift (determined by the Green's function analysis) caused by the addition of a thin layer of SiO_2 onto the surface of the substrate. The theoretical sensitivity was identical for both free and metallised surfaces.

To verify these results experimentally, a ~22nm SiO_2 layer was sputter-deposited onto the surface of the sensor. The frequency shift was measured and from this the velocity shift was derived.

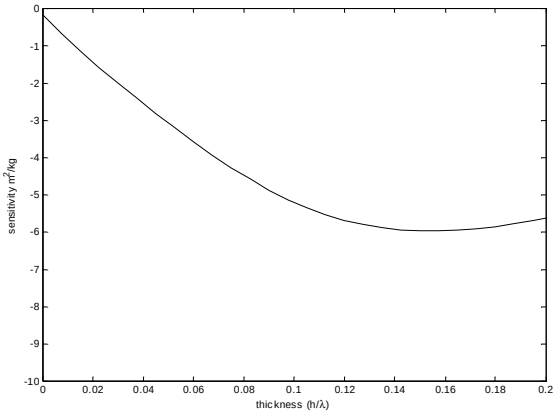

Figure 4: Calculated mass sensitivity

The measured sensitivity was ~10m^2/kg for 4μm ZnO, which is greater than the calculated value. We believe that this is due to the non-uniformity of the ZnO surface as well as the difficulties related to the modelling of the polycrystalline ZnO guiding layer. Ogilvy [2] describes similar difficulties in reconciling the theoretically derived mass sensitivity of SiO_2/Quartz devices with that obtained by deposition of Au thin films.

References

[1] G. Kovacs, G. W. Lubking, M. J. Vellekoop, A. Venema, "Love waves for (bio)chemical sensing in liquids", *Proc. 1992 IEEE Ultrasonics Symposium*, pp. 281-285, Tucson, USA, 20-23 October 1992.

[2] J. A. Ogilvy, "The mass-loading sensitivity of acoustic Love wave biosensors in air", *J. Phys D: Appl Phs*, 30 (1997) 2497-2501.

[3] D. A. Powell, K. Kalantar-zadeh, S. Ippolito, W. Wlodarski, "A Layered SAW Device Based on ZnO/LiTaO3 for Liquid Media Sensing Applications", *in Proc. 2002 IEEE Ultrasonics Symposium*, Munich, Germany, 8-11 October 2002, *to be published.*

[4] V. Y. Zhang, J.-E. Lefebvre, C. Bruneel, T. Gryba, "A Unified Formalism Using Effective Surface Permittivity to Study Acoustic Waves in Various Anisotropic and Piezoelectric Multilayers", *IEEE Trans. UFFC*, 48 no 5 (2001) 1149-1461.

[5] S. J. Ippolito, K. Kalantar-zadeh, A. Trinchi, W. Wlodarski, "Layered SAW Nitrogen Dioxide Sensor with WO_3 Selective Layer", *to be presented at SPIE International Symposium on Microtechnolgoies for the New Millenium 2003*, Canary Islands, Spain, 19-21 May 2003.

Resistance thermometers based on Ge films on GaAs substrates: low-temperature conduction and magnetoresistance mechanisms

V.F. Mitin[1], G.G. Ihas[2], C. McKenney[2], V.K. Dugaev[3] and M. Vieira[4]

[1]Institute of Semiconductor Physics, NASU, pr. Nauki 45, 03028 Kiev, Ukraine, E-mail: mitin@isp.kiev.ua
[2]University of Florida, P.O. Box 118440, Gainesville, Florida 32611, USA
[3]Institute for Problems of Materials Science, NASU, Vilde 5, 58001 Chernovtsy, Ukraine
[4]ISEL-DEETC, Rua Conselheiro Emidio Navarro, 1949-014 Lisbon, Portugal

Summary: *The main characteristics of thermometers for low temperature (0.03 to 400 K) measurements are presented. These thermometers are based on Ge films on GaAs substrates. Low-temperature conduction and magnetoresistance mechanisms in Ge films used as temperature sensors are investigated. The magnetoresistance of the Ge film temeperature sensors is usually very small. A new giant negative magnetoresistance effect in Ge films at ultralow temperature (T < 0.2 K) and in weak magnetic fields (H < 1 Tesla) has been observed. We discuss the physics of this phenomenon and present the results of the modeling. We also discuss the possibility to use this effect for detection of weak magnetic fields at ultralow temperatures.*

Keywords: *low temperature thermometry, magnetic sensors, Ge films, disordered semiconductors*
Category: *1 (General, theoretical and modeling)*

1 Introduction

There are several types of commercially available temperature sensors, which are traditionally used for the low-temperature measurements. It was shown recently [1-3] that a new type of resistance thermometers based on Ge films on GaAs substrates can be used for temperature measurements in a wide range of temperature from 0.03 to 400 K. The low sensitivity to the magnetic field and gamma radiation makes Ge/GaAs thermometers very promising for various applications [4]. The main advantage of the Ge/GaAs sensor fabrication technology is the ability to construct thermometers for operation in different temperature ranges, with temperature and magnetic field characteristics tailored to meet specific user demands. This is possible by careful control of the technical conditions of Ge film preparation [1]. From this point of view, the study of the conduction and magnetoresistance mechanisms in Ge films that are responsible for the termo- and magnetic field sensitivity is very important.

In this paper we report on main characteristics of Ge/GaAs temperature sensors and analyze the conduction and magnetoresistance mechanisms in Ge films at low temperatures.

2 Description of the sensors and their main characteristics

The thermometers are based on Ge film resistors deposited on semi-insulating GaAs substrates using the vacuum technology [1]. The sensitive thermochips (0.3 mm × 0.3 mm × 0.2 mm) are made by using microtechnology and placed in non-magnetic micropackages [3]. The microsensor, including the micropackage, measures 1.2 mm in diameter by 1.0 mm long. These microsensors can be also placed in a second package (3 mm diameter by 5.0 mm long copper can) for ease of handling while mounting in a number of cryostats.

Shown in Fig. 1 is the typical resistance as a function of temperature for different models of thermometers.

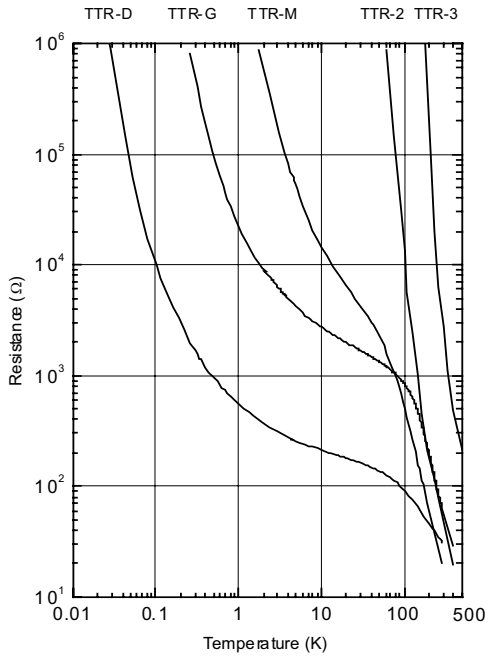

Fig. 1. Resistance vs. temperature curves for different thermometer models.

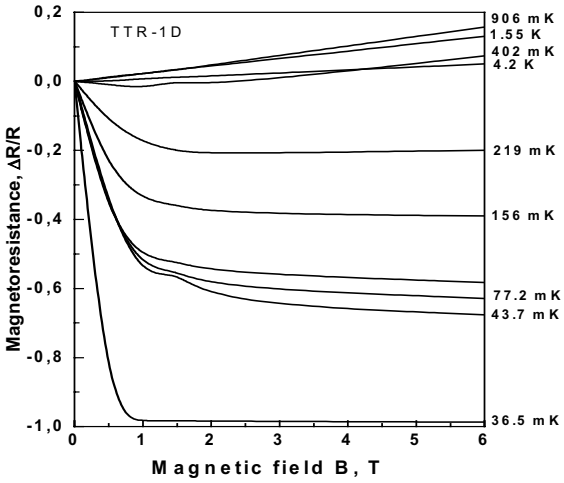

Fig. 2. Giant negative magnetoresistance effect in Ge films at ultralow temperatures.

There is a problem of temperature measurements in magnetic field. The magnetoresistance effect causes an error in the temperature reading. Depending on impurity composition and the temperature range, the magnetoresistance in Ge films can be positive and negative, very small and extremely large. Here we discuss the giant negative magnetoresistance effect, which has been found in Ge films at ultralow temperatures [5] and shown in Fig. 3.

3 Theory and modeling

The analysis of the experimental data shows that the main mechanism of conductivity is hopping in the regime of Coulomb interaction [5]. The corresponding theory contains necessary formulas for the resistivity with an exponential accuracy, and some phenomenological parameters. We used the theories of transport in strongly disordered and heavily doped semiconductors, such as weak localization [6], variable-range hopping [7], and scaling theories of localization [8]. In the framework of variable range hopping, the negative magnetoresistance at low temperature, $T < 0.5$ K, can be attributed to the quantum correction mechanism – suppression of the interference of hopping trajectories by magnetic field. This explains the dependence of the negative magnetoresistance on temperature (quantum correction increases when the temperature decreases) and also the saturation of magnetoresistance at $H > 1$ T (this magnetic field is strong enough to suppress the quantum correction).

For modeling, we used a combination of the scaling theory of localization and variable-range hopping suitable to describe the conductivity and magnetoconductivity close to the mobility edge [8].

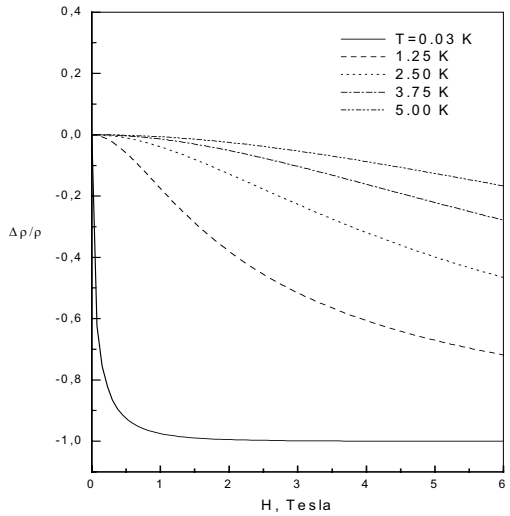

Fig. 3. Calculated dependence of magnetoresistance on magnetic field for different temperatures.

The dependence of the mobility edge on magnetic field is at the origin of the negative magnetoresistance caused by suppression of the quantum localization correction in a magnetic field. The agreement between experiment and theoretical modeling is rather good. The results for the magnetoresistance as a function of magnetic field and temperature are presented in Fig. 3.

Acknowledgement

This work is partially funded under European Commission INTAS Contract No. 2000-0476.

References

[1] V.F. Mitin, Yu.A. Tkhorik and E.F. Venger, *Microelectronics Journal* 28 (1997) 617–626.

[2] V.F Mitin, *Semicond. Physics, Quant. Electron. & Optoelectronics* 2 (1999) 115–123.

[3] N.S. Boltovets, V.V. Kholevchuk, R.V. Konakova, V.F. Mitin and E.F. Venger, *Sensors and Actuators A* 92 (2001) 191–196.

[4] V.K.Dugaev, G.G.Ihas, C.McKenney, V.V.Kholevchuk, V.F.Mitin, I.Yu.Nemish, E.A.Soloviev, and M.Vieira, *Proc. of 1st IEEE Int. Conf. on Sensors (IEEE Sensors 2002)*, pp. 1275-1280, Orlando, USA, June 12-14, 2002.

[5] V. Mitin, J. McFarland, G.G. Ihas and V.K. Dugaev, *Physica B* 284-288 (2000) 1996–1997.

[6] B.L. Altshuler and A.G. Aronov, In: *Electron-Electron Interaction in Disordered Systems*, Elsevier, 1985, pp.1-153.

[7] A.L. Efros and B.L. Shklovskii, *J. Phys. C* 8 (1975) L49.

[8] D.E. Khmelnitskii and A.I. Larkin, *Solid State Commun.* 39 (1981) 1069–1070.

Integrated Optical Generalized Mach-Zehnder Interferometer Sensor

Romeo Bernini

National Research Council CNR-IREA, via Diocleziano 328, 80124 Napoli, Italy
email: bernini.r@irea.cnr.it http://www.irea.cnr.it

Summary: *A new integrated optical refractometer based on generalized Mach-Zehnder interferometer (GMZI) is described. GMZI is a multiple arms-multiple outputs interferometer that, with a suitable design, permits to realize highly sensitive, and wide measurement range, integrated optical refractometer. The sensor operates over N outputs so that, as far as the refractive index of the external media changes, the output intensity moves through the different outputs. This configuration permits a simpler data analysis and avoids the need for a separate reference arm. Furthermore, in some applications a direct digital readout is possible.*

Keywords: *Integrated optics, Refractometer, Mach-Zehnder interferometer*
Category: *1 (General, theoretical and modeling)*

1 Introduction

In the integrated optical field, the Mach-Zehnder interferometer (MZI) represents the most widely used detection scheme. Mach-Zehnder devices permit to realize integrated optical refractometers that exhibit high sensitivity [1] and are straightforward to design and fabricate. However, a high sensitivity corresponds to a small measurement range due to the periodic output of MZI. In order to overcome these limitations several MZI with different sensitivity can be integrated on the same chip so to remove the ambiguity [2].

In this work, a new integrated optical refractometer based on generalized (multiple arms-multiple outputs) Mach-Zehnder interferometer (GMZI) is presented. The GMZI has been used in several applications for optical telecommunications like wavelength division multiplexing (WDM) [3], wavelength selective switching, and variable-ratio power splitter [4]. In the following we show that this device, with a suitable design, can be easily used in sensing applications with performances comparable to multiple MZI, but with a simpler geometry and data analysis. Furthermore, in some applications, where a lower resolution is required, a direct digital readout is possible.

2 Sensing principle

Figure 1 shows a schematic representation of the sensor. It consists of two multimode interference (MMI) couplers connected by a waveguide array. The first MMI coupler acts as 1×N power splitter, dividing the input power equally in the N waveguides of the array. The waveguides are the arms of the interferometer and have different lengths L_j due to different sensing pad lengths ΔD_j .

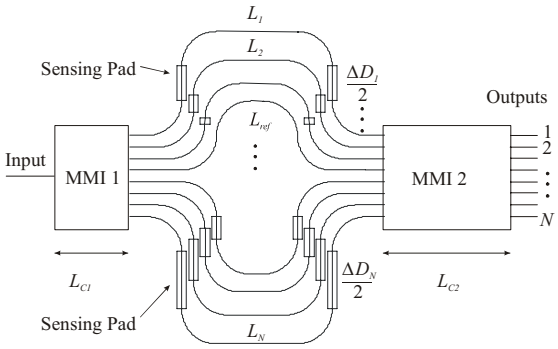

Fig.1 Schematic view of the GMZI sensor.

The shortest arm is the reference one. The sensing length differences are obtained by the straight part of the waveguides, whereas the waveguide bends equally long. The second MMI coupler is a N×N combiner and is the key element of the GMZI. This MMI distributes the power incident at each of its inputs to all the outputs where interference occurs between the relatively delayed optical fields. By suitably choosing the lengths of the sensing pads, it is possible to achieve constructive interference (or phase match) for N different refractive index values of the external medium n_o at different outputs of the combiner. So, as far as the refractive index of the external medium changes, the output intensity moves through the different outputs.

A phase match condition at an output of the second MMI is obtained if the relative phase delays through the array arms compensate for the phase relations of the MMI couplers. Using the analysis given in [5], the sensing pad length of the *j*th arm of an N-channel GMZI can be written as:

$$\Delta D_j = L_j - L_{ref} \cong d_j \Delta L \qquad j = 1, \cdots, N \qquad (1)$$

where L_{ref} is the length of the reference arm. d_j is an integer parameter called the array arm factor determined by the phase relations on the N×N

output MMI, and ΔL is the length that produces a phase shift of $2\pi/N$ between two adjacent refractive index channels and is equal to:

$$\Delta L = \frac{\lambda}{N\Delta n_{eff}} \quad (2)$$

where λ is the device operating wavelength, equal to 632nm, and Δn_{eff} is effective refraction index channels spacing. Following the procedure given in [5], it is possible find an optimum set of the array factor (d_j) resulting in a small device with the best response.

3 Sensor design and performance

Beam propagation simulations have been performed using guided-mode propagation analysis (MPA) in two dimensions of the MMI couplers and introducing phase delays corresponding to the relative sensing pad of the array arms. The reduction from three to two dimensions has been obtained by the effective index method. In particular, we have considered a rib waveguide with a silicon oxinitride core (SiON n=1.58) surrounded by a cladding region of SiO_2 (n=1.46). This stronger guiding of the modes allows a small bending radius enabling the realization of a compact device.

Assuming N=8, we have chosen the width w of both the MMI couplers equal to 60μm, and the optimum length of the first coupler L_{C1} and of the second coupler L_{C2} is found to be respectively 1146μm and 4584μm. Finally, the length of the optimum set of the array arm factor d_j is found using the procedure given in [5]. For N=8 this set is $\{d_1,\ldots,d_N\} = \{6,3,1,0,4,5,7,10\}$.

We have considered an external refractive index n_o ranging between 1.33 and 1.40. So the effective refraction index channels spacing Δn_{eff} is 2.7e-5. The sensor operates over N equally spaced effective index channels $n_i = n_{min} + i\Delta n_{eff}$ for $i=0,\ldots,N-1$, where n_{min}=1.5682.

The normalized power of the mth output is due to the interference of N optical fields. As an example, in figure 2 the behavior of the power of the second output as a function of n_o is depicted. As can it be seen the output intensity is maximum when n_o realizes the condition $n_{eff}=n_i=n_4$. The overall sensor response is reported in figure 3. As the refractive index of the external medium changes, the output power moves through the different outputs without ambiguities. Note that, in general, in a GMZI adjacent outputs do not correspond to neighboring refractive index values. The output channels are slightly non-uniform spaced respect to external refraction index n_o, due to non-linear relation between n_o and the effective refractive index of the waveguide array.

Assuming that a change in the normalized output power equal 0.01 can be detected, the resolution around to n_0=1.39 is 6.6e-5.

In this device fluctuations and drift in input light power can be referenced to the sum of all outputs, that is constant, producing significant improvements in signal-to-noise ratio (SNR) and stability and eliminating the need for a separate reference arm.

Finally, if a lower resolution is required, the output readout can be simplified using a direct digital scheme. In fact, connecting the signal of the single output to a comparator with a reference level of about 0.41, it happens that only one output at time was at high level.

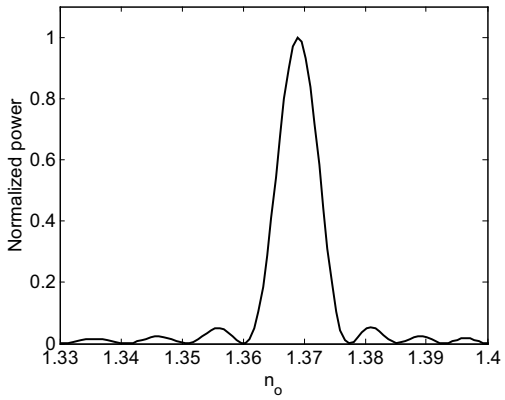

Fig.2 Normalized power of ouput 2.

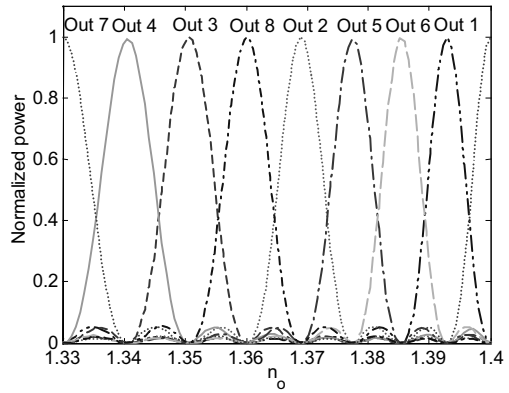

Fig.3 Normalized sensor response.

References

[1] R.G. Heideman, P.V. Lambeck, *Sensors Actuators B*, 61 (1999), 100-127.

[2] P. Hua, B.J. Luff, G.R. Quigley, J.S. Wilkinson, K. Kawaguchi, *Sensors Actuators B*, 87, (2002), 250-257.

[3] L.O. Lirstuen, A. SudbØ, *IEEE Photon. Technol. Lett.,* 7, (1995), 1034-1036.

[4] N.S. Lagali, M.R. Paiam, R.I. MacDonald, *IEEE Photon. Technol. Lett.,* 11, (1999), 665-667.

[5] M.R. Paiam, R.I. MacDonald, *Appl. Opt.*, 36, (1997), 5097-5108.

The Influence of Electrothermal Feedback on Metal Film Microbolometers

F. Kohl[1], F. Keplinger[2], A. Jachimowicz[2], Rainer Fasching[3]

[1]Ludwig Boltzmann Institute of Biomedical Microtechnology, Gusshausstr. 27,Vienna, Austria,
franz.kohl@tuwien.ac.at
[2]Vienna University of Technology, Institute of IEMW, Vienna, Austria,
[3]Rapid Prototyping Laboratory, Stanford University, CA 94305 Stanford, USA

Summary: *Using the electro-thermal coupling equation the bolometer performance can be described as a function of a single operating parameter, the self heating ΔT. The related model comprises the impact of electro thermal coupling on sample impedance, responsivity and time constant. The main simplifications of the model are a linear dependence of the electrical resistance, $\Delta R = R \cdot \alpha_\rho \cdot \Delta T$ on temperature as well as lumped thermal conductance G and heat capacity C, whose values are chosen as independent of operating temperature. Furthermore, we suppose perfect absorption of incident infrared (IR) radiation, $\eta = 1$, and current controlled operation. Within this frame estimates of the achievable responsivity and detectivity D^* for a given bolometer design remain valid even for strong electrothermal feedback. The assumption of a constant TCR lead to significant deviations, if $\Delta T \cdot \alpha_\rho$ exceeds 0.1.*

Keywords: *electrothermal feedback, Bolometer,*
Category: *1 (Modelling)*

1 Introduction

Miniaturized metal-film resistors on micromachined carriers are attractive candidates for room temperature bolometers from a technological point of view. Although metals in general suffer from a comparable low temperature coefficient of resistivity (TCR) they offer low 1/f noise making them attractive as bolometer material for very low frequency applications. Recently, we presented a model for room temperature resistance bolometers based on a TCR, $\alpha = (1/R)dR/dT$, that is independent of temperature [1]. In the case of metal film bolometers this approximation is applicable only in the weak self heating regime. However, in practical devices metal film bolometers are operated with strong self heating [2]. We introduced a temperature dependence that fits closer to the behavior of metals. Since the electrothermal coupling effect is inherent to the model used its results remain valid even for strong self heating.

2 Outline of the model

The temperature dependence of the electrical resistivity of metals is reasonable described by $R(T) = R_0 \cdot (1 + \alpha_\rho \cdot \Delta T)$. In contrast, the TCR decrease with temperature. The coefficient α_ρ and the corner frequency f_0 for 1/f are all material parameters of the model. It is assumed that 1/f noise is a volume property of the resistor material and that interface effects, e.g. of the electrical contacts, do not contribute to the noise. The model uses the bolometer resistance R_0 at a reference temperature T_0, the thermal conductivity G of the bolometer to the heat sink and the heat capacity C as design dependent specifications. Following the treatment of [1] we obtain the temperature sensitivity $\frac{dT}{dP_{IR}} = \frac{1}{G - I^2 \alpha_\rho R_0} = \frac{1}{G} \cdot \frac{1}{1 - a_0}$, where dP_{IR} means a static change of *absorbed* IR radiation power. The parameter $a_0 = I^2 \alpha_\rho R_0 / G$ reflects the strength of electrothermal feedback effect and $a_0 \to 1$ causes thermal instability. To describe the self heating connected with the device current I it is convenient to use the dimensionless bias parameter $a = \alpha_\rho \cdot \Delta T = \alpha_\rho \cdot \frac{I^2 \cdot R}{G} = \frac{a_0}{1 - a_0}$. Thus, within the frame of the model, thermal instability does not occur for useful self heating.

For a constant bolometer current I the voltage responsivity at zero frequency may now be expressed as a function of the bias parameter only.

$$S_V\big|_{\omega=0} = \frac{d(I \cdot R)}{dP_{IR}} = I \cdot \frac{dR}{dT} \cdot \frac{dT}{dP_{IR}} = \sqrt{\frac{a(1+a)\alpha_\rho R_0}{G}}$$

Due to the heat capacity C a harmonic variation of the absorbed IR power leads to a frequency dependence of the voltage responsivity according to $S_V(\omega) = \sqrt{\frac{a(1+a)\alpha_\rho R_0}{G}} \cdot \frac{1}{1 + j\omega C(1+a)/G}$. Thus the electrothermal feedback increases the thermal time constant C/G by a factor $(1+a)$. Electrothermal coupling causes a frequency dependent

impedance leading to a power spectral density $V_J^2(\omega) = 4k_B TR_0(1+a)\cdot\frac{1+2a+(\omega\tau(1+a))^2}{1+(\omega\tau(1+a))^2}$ of the thermal noise. The power spectral density of the 1/f noise is modeled as $V_{1/f}^2 = 4k_B TG\cdot\frac{a}{\alpha}\frac{\omega_0}{\omega\cdot I_0^2}$ where I_0 is the reference bias current leading to a intersection of $V_{1/f}^2$ with $4k_B TR_0$ at a frequency ω_0. The derivation of these quantities is analogous to the treatment in Ref. [1]. The concept of noise equivalent power (NEP) refers all sources of electronic noise to an equivalent noise of the power of the IR radiation. We obtain $NEP^2 = NEP_P^2 + NEP_J^2 + NEP_{1/f}^2$, neglecting all other possible contributions. Here $NEP_J = |V_J| / |S_V|$, $NEP_{1/f} = |V_{1/f}| / |S_V|$ and NEP_P refer to the noise equivalent power of Johnson noise, 1/f noise and phonon noise (thermodynamic temperature fluctuatons), respectively.

3 Results

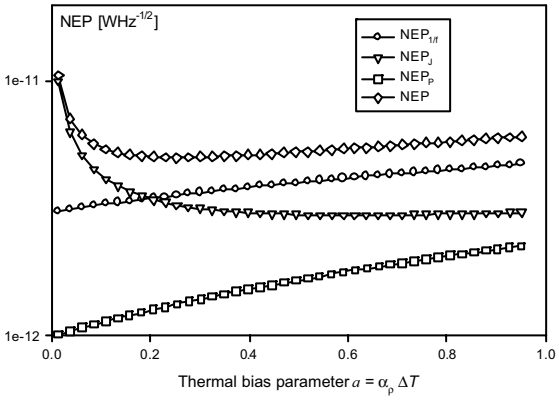

Fig. 1: Calculated NEP and the related individual contributions for a Ti bolometer ($\alpha_\rho = 0.0025\,K^{-1}$, operating frequency 1Hz, τ = C/G = 20 ms [3],[1]).

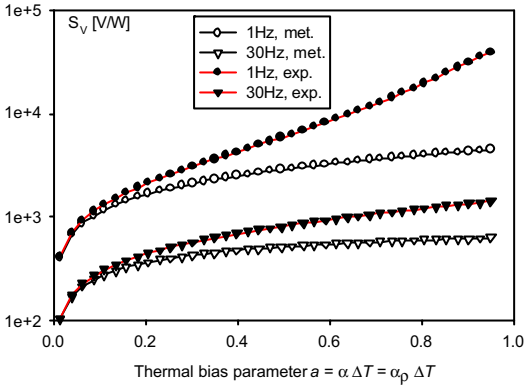

Fig. 2: Calculated dependence of the voltage responsivity on the thermal bias parameter for a Ti bolometer [3] and for an equivalent temperature independent TCR α. Two operating frequencies were studied, situated well below and above the thermal corner frequency (C/G = 20 ms).

Fig. 1 shows calculated results for a Ti bolometer [3], [1] that are typical for very low operating frequencies.

As Fig. 2 shows the constant TCR bolometer shows a higher responsivity than the metalfilm device. However, the former exhibits thermal instability for $a \to 1$, whereas the latter remains stable. Fig. 3 presents calculated bolometer detectivities, given by $D^* = \sqrt{A}/NEP$, taking the detector area A from Ref. [3]. The Ti bolometer exhibits an maximum detectivity, that is mainly composed from opposite slopes of the bias dependences of thermal and current noise (see Fig.1).

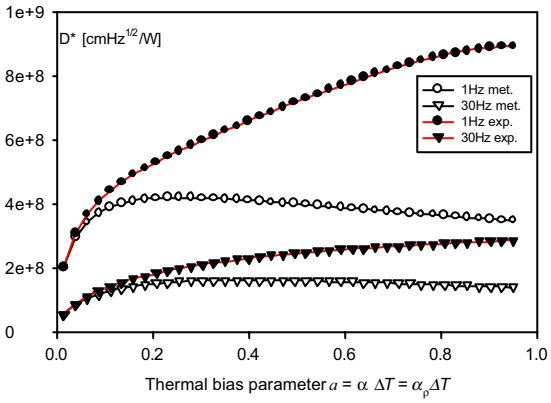

Fig. 3: Calculated detectivity for a Ti thin film bolometer [3] and the results for equivalent temperature independent TCR [1].

4 Conclusions

The operating characteristics of metal film bolometers are conveniently expressed as a function of the self heating. We compared our results for metalfilm devices with those resulting from the standard approximation i.e. a temperature independent TCR for a comparable construction. Both devices have similar characteristics only in the low self heating regime, i.e. for $a < 0.1$. In general the constant-TCR model overestimates responsivity and detectivity values that can be reached with a metal film bolometer. With respect to the thermal bias these devices exhibit an optimum of the detectivity, whose position depends on the operating frequency because of the 1/f noise. Benefits from the metallic temperature characteristic are thermal stability for $a \to 1$ and a slightly higher bandwidth

References

[1] F. Kohl, F. Keplinger, A. Jachimowicz, R. Chabicovsky, *Proceedings of IEEE Sensors 2002*; Sheridan Printing Co. Inc., (2002), ISBN 0-7803-7455-X; S. 1290 - 1293.

[2] A. Tanaka et al., *Proc. of the SPIE*, vol. 3061; (1997) 198-209.

[3] M.V.S. Ramakrishna et al., *Proc. of the SPIE*, vol. 3666; (1999) 415-420.

Modeling of Thermally Isolated Micromechanical Thermo Converter

Jiri Jakoveko[1], Miroslav Husak[1], Tibor Lalinsky[2]

[1]Czech Technical University, Dept. of Microelectronics, Technicka 2,
166 27, Prague 6, Czech Republic, jakovenk@feld.cvut.cz
[2] Institute of Electrical Engineering, Slovak Academy of Sciences, Bratislava, Slovakia

Summary: *This report discusses the design of Thermo-mechanical converter that creates heart of the RF power sensor microsystem. The conception of absorbed power measurement is based on thermal conversion, where absorbed RF power is transformed into thermal power, inside a thermally isolated system. Micromechanical Thermal Converter (MTC) spatial temperature dependences, thermal time constant and power to temperature characteristics are calculated from the heat distribution. The temperature changes induced in the MTC by electrical power dissipated in the HEMT (High Electron Mobility Tranzistor) are sensed using the temperature sensor. The temperature distribution, over the sensing area, and mechanical stress was optimized by studying different MTC sizes, and layouts of the heater and temperature sensor.*

Keywords: *Thermo-mechanical simulations, MEMS, Power sensor*
Category: *1 (General, theoretical and modeling)*

1 Introduction

Transmitted power is the main quantity measured in RF systems. The classical approach to transmitted power measurement is based on the measurement of absorbed power waves (incident and reflected) that requires sophisticated multiple power meter structures and need complex calibration of the measured data. A better method of the absorbed power measurement is based on thermal conversion where, absorbed radio frequency (RF) power is transformed into thermal power inside of a thermally isolated system.
Thermo-mechanical numerical modelling and simulation has a significant influence on the optimal topology of the Micromechanical Thermal Converter. The main characteristics which optimise The MTC devices are the temperature distribution over the sensing area, time response, sensitivity analysis and evaluation of the mechanical stresses.

2 Micromechanical Thermal Converter

A new micromechanical island structure design concept of MTC have been proposed.
Micromachining technology of mechanically fixed and thermally isolated cantilevers, bridges and islands MTC devices [1] is fully compatible with GaAs HEMT technology. The micromachining technology enables mechanical fixing and thermal insulating of the very thin MTC structures by thin polyimide membrane. Low mechanical stress and thermal conductivity makes polyimide applicable.

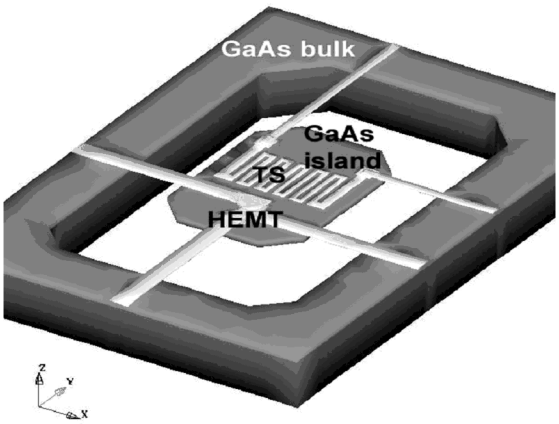

Fig. 1. Model of the Island MTC structure. GaAs island is "floating" in Polyimide 1um thick layer (not visible). The meander-shaped TS is also shown. *Z*-direction is 20times magnified.

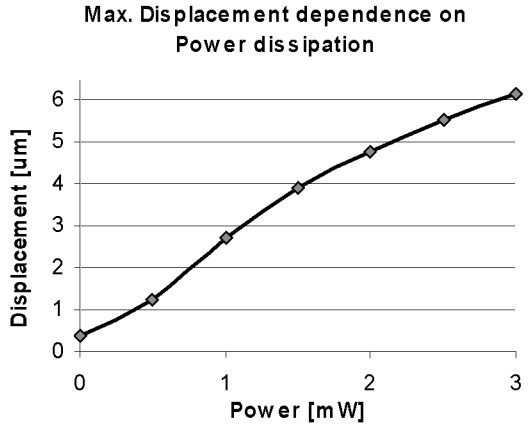

Fig. 2. Maximal Displacement dependence on Power dissipation simulated for Island structure.

3 Results

The power to temperature (P-T) conversion characteristics of the MTC structures, were investigated by simulation and were compared with the real micro-machined devices. High electro-thermal conversion efficiency defined by extracted thermal resistance values (R_{th}) 24 K/mW was obtained for island MTC.

The 3D graph gives good overall visualization of the temperature distribution (fig.3) in the island MTC structure for the power dissipation of 2 mW generated by the HFET heater. The island is "floating" in the polyimide layer that mechanically and thermally isolates the MTC structure. HEMT heater and zig-zag temperature sensor is integrated within the island structure. Polyimide layer is not shown, but was considered in simulation. The island structure floating in polyimide is well thermally isolated and the heat flux goes only through the metallization lines.

The thermal analyses were performed for both vacuum ambient and non-convective gaseous medium around the MTC structure. The heat losses, due to radiation, were viewed as negligible.

Transient on/off power characteristics for island structure are depicted on fig. 4. At the beginning there was power of 2mW switched ON. In the time of 2ms the power was switched OFF. Thermal time constant of the island structure arrangement is 2ms. There are two transients on the fig. 4. Upper is the temperature of the heater and the bottom dependence reflect average temperature of TS.

Stress and displacement magnitude evaluation were simulated using MemMech simulator. Outer substrate rim was set as rigid (non moveable). Fig. 2 shows the most extreme island structure displacement dependence on power dissipation.

4 Conslusion

Spatial temperature dependences, thermal time constant, thermal stress and displacement and power to temperature characteristics were calculated from the heat distribution. These indings were compared to results from thermo-mechanical measurement of real micromachined MTC devices. Temperature distribution, mechanical stresses and displacements of GaAs MEMS device have been simulated using CoventorWare. Using FEM simulations, the layout of HFET transistor, temperature sensor and MTC shapes and dimensions were also optimized

Acknowledgments

This research has been supported by the NATO SfP grant No. 974172, by the research programme of the Czech Technical University in Prague: No. MSM212300014 „Research in the Area of Information Technologies and Communications"

References

[1] T. Lalinsky, L. Matay, Z. Mozolova, S. Hascik, I. Kostic, E. Burian, M. Dzik, "Development of InGaP/Polyimide Bridges Fully Compatible with InGaP/InGaAs/GaAs Based HFETs", *Proceedings of the International MEMS Workshop – iMEMS*, July 4-6, Singapore, pp. 362-368, 2001.

[2] J. Kyncl, L. Kneifel, "Design and Modeling of Parts of Electroheat Devices Using MATHEMATICA SW", *First International Conference on Advanced Engineering Design*, Glasgow, 1999, p. 157-165.

[3] S.D. Senturia, Microsystem Design, *Kluwer Academic Publisher*, book, 2001.

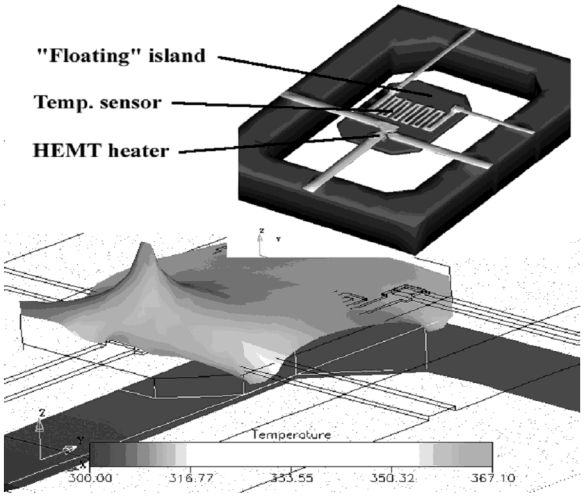

Figure 3. 3-D plots of temperature distribution of the island MTC structure. The island is "floating" in polyimide layer that mechanically and thermally isolates the MTC structure. Polyimide not shown.

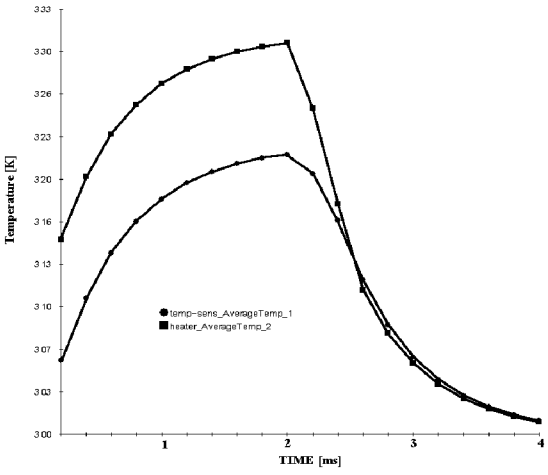

Fig. 4. The power on/off transient characteristics for island MTC structure for power ON of 2mW. At the beginning there was power of 2mW switched ON. In the time of 2ms the power was switched OFF.

Development of Comb Drive with New Compressive Suspension Spring for Large Static Displacement and Continuous Motion Applications

Chihchung Chen and Chengkuo Lee

Asia Pacific Microsystems, Inc., No.2 R&D Road VI, Science-Based Industrial Park, Hsinchu, Taiwan.
e-mail: gchen@apmsinc.com http://www.apmsinc.com

***Summary*:** New comb drives using compressive suspension springs are designed and developed to provide capabilities of large static displacement and continuous motion for applications, such as micro XY stage, two dimensional lens scanner, variable optical attenuator, and optical switch, etc. The maximum static displacement of conventional comb drive is constrained by the comb finger electrodes sticking effect. Because the lateral stiffness of spring is unable to resist the lateral disturbance, two new designs proposed in this paper are capable of enhancing the lateral stiffness against to the lateral disturbance. The new design can increase the lateral stiffness when the comb drive displacement increases, therefore the maximum static displacement can be enlarged.

Keywords: *actuator, comb drive, electrostatic actuator*
Category: *1 (General, theoretical and modeling)*

1 Introduction

Developing a comb-drive with large static displacement and continuous motion capability is a major research interest, actuators of such capability is crucial for pratical applications like micro XY stage, two dimensional lens scanner, and variable optical attenuator, optical switch, etc. In the conventional design of comb-drive the maximum static displacement of comb actuator is limited by the side sticking effect of comb fingers [1,2]. The tiny deviations of comb finger and gap width will cause the unbalanced force of both sides of finger electrode, and such deviation is easily induced by microfabrication process [3]. The unbalanced force of both sides of finger electrode is the major contribution factor to the side sticking effect. How to design and make a comb actuator that is more robust to the process induced deviation is very attractive to industrial pratical use. We have presented a comb drive with stepped structure between spring and comb finger electrode by using SOI-DRIE process [4], such approach let traditional comb drive can have enlarged static displacement. In this study, we present a new design concept for making comb drive with further improved maximum displacement of static movement under dc voltage load.

2 Design, Fabrication and Characterization

The configuration of comb-drives with springs of conventional design, and our new type I and type II designs are depicted in Fig. 1 (a), (b) and (c), respectively. The length, width, and thickness of each beam of spring in Fig. 1 are 800μm, 1.6μm, and 45μm, while comb electrode spacing, electrode thickness, number of electrode finger are 4μm, 92μm, and 100, respectively. The made type I device is shown in Fig. 2 by using the reported process technology [4].

Let the spring constant of moving direction as k_x, and the spring constant of in-plane direction perpendicular to moving direction as k_y. The sticking of comb electrode fingers occurs when k_y being less than the stability criteria k_e, which represents the sufficient stiffness to keep the electrodes of rotor moving at center axis between two electrodes of stator nearby [1,2]. The k_y of conventional comb-drive design is decreasing as the actuated displacement increasing, in the mean time the k_e is increasing. The maximum displacement can be predicted by calculating when k_y being equal to k_e. In order to have enlarged travel distance of comb drive, the k_y should be designed to be increased as the actuated displacement increased. Since the k_y of the parallel spring comb-drive is decreasing while the spring is extended, a compressive spring is therefore considered in our present design to alter the characteristic of k_y. Compressive spring can naturally increase the lateral stiffness so as to provide more robust behavior, and larger static displacement.

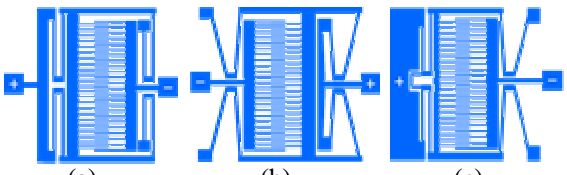

(a) (b) (c)

Fig.1 Schematic diagrams of (a) conventional com-drive with parallel normal folded spring, (b) comb-drive with a pair of compressive spring, and (c) comb-drive with one normal folded spring and one compressive spring.

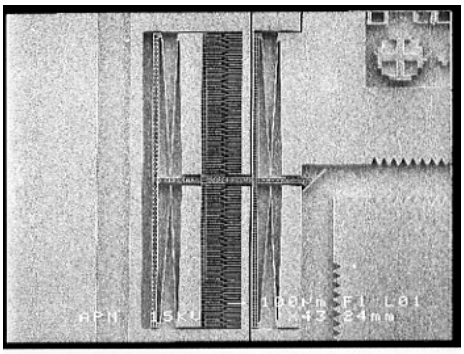

Fig.2 SEM of comb drive actuator with compressive spring

3 Simulation and Discussion

Based on the analytical model, and FEM analysis results via ANASYS, we may derive the curves of actuation displacement versus electrostatic force along with the moving direction, as shown in Fig. 3. The calculated result of comb drive with conventional 2-folded spring is confirmed with the measured data that is published elsewhere [4]. Fig. 3 illustrates the k_x of our new designed compressive spring resemble to the k_x of parallel 2-folded spring. These curves point out a factor that our new designs will not deteriorate the force output in moving direction, comparing with the conventional design; this is an important performance requirement to actuator.

Additionally, Fig. 4 presents the k_y of conventional comb drive with 2-folded spring decreased rapidly and the value of k_y coincides with the k_e at 32 μm displacement. Regarding to the type I comb drive, in spite of that the k_y of comb drive with a pair of compressive springs is increased as spring being compressed, the k_y still coincide with the k_e at 18 μm displacement. Because the initial k_y of type I comb is too small. To further enhance the lateral stiffness of comb-drive with compressive spring design over initial actuation period, one of the compressive springs is replaced by a normal folded spring, and then this type is the type II comb drive. Besides, an n-bridge structure connected the two normal 2-folded springs, as shown in Fig. 1(c). This type II comb is proposed to provide the necessary lateral stiffness of the parallel spring over large displacement period. As shown in Fig.4, similarly, the initial k_y of type II comb has been promoted by such modification, the k_y keeps increasing as the displacement increasing as the trend observed in the type I case. As a result, the k_y of type II comb meets with the k_e at actuation displacement approximate 58μm. By using our new design, we are able to increase the static displacement performance about 81%.

4 Conclusion

A novel comb drive design, consisting an compressive spring, and a normal 2-folded spring connected with an n-bridge spring, is presented to reach higher value of the maximum static displacement than the one of conventional comb drive using normal 2-folded spring. The preliminary simulation results show a better static displacement and robustness to environment disturbance, such as shock, and unbalanced electrostatic force coming from process-induced feature size variations, etc. The characterization of made devices is undergoing now.

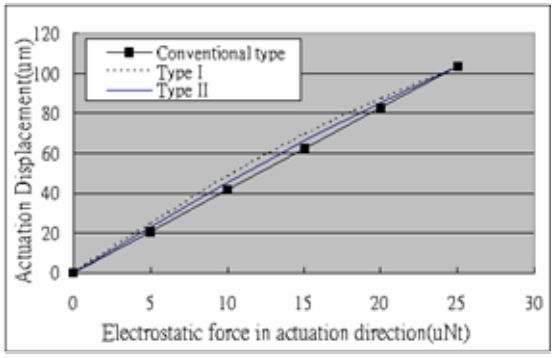

Fig.3. Actuation displacements of comb actuators with parallel spring, compressive spring and hybrid spring versus electrostatic force driving in actuation direction

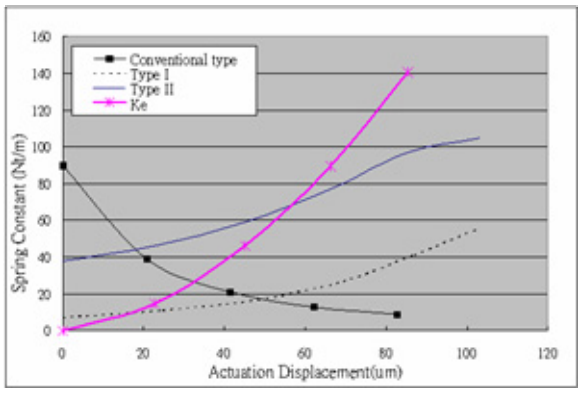

Fig.4. Lateral spring constant k_y of parallel spring, compressive spring, and hybrid spring and stability criteria k_e versus various actuation displacement

References

[1] T. Hirano, et al., "Design, Fabrication, and Operation of Submicron Gap Comb-Drive Microactuators," *J. Microelectromechanical Systems,* Vol. 1(1992), 52-59.

[2] V. P. Jaecklin, et al., "Micromechanical comb actuators with low driving voltage," *J. Micromech. Microeng.* , Vol.2(1992), 250-255.

[3] R. Liu, et al., "MEMS resonators that are robust to process-induced feature width variations," *J. Microelectromechanical Systems,* Vol.11 (2002), 505-511.

[4] C. Chen, et al, "Study of Lateral Comb Drive Actuator with Large Displacement and Low Actuation Voltage," *Proc. of Microprocesses and Nanotechnology 2002,* pp.304-305, Tokyo, Japan, Nov. 6-8, 2002, IEEE Catalog No. 02EX589.

Robustness of ToF estimators – an Empirical Evaluation

F. van der Heijden[1], P.P.L. Regtien[1] and T.S.Beneder[1]

[1]University of Twente, Faculty EEMI, Laboratory for Measurement and Instrumentation, PO Box 217, 7500 AE Enschede, The Netherlands
email: F.vanderHeijden@el.utwente.nl http://www.mi.el.utwente.nl/

Summary: *The performance of ToF estimators for acoustic tone bursts is empirically evaluated. In indoor applications, the observed waveform is likely to be disrupted by multiple echoes. These echoes can cause complex interference patterns. The paper presents the results of a comparison study of the robustness of various ToF estimators against such type of disruptions.*

Keywords: *ultrasonic position measurement, time-of-flight, performance evaluation, multiple reflections.*
Category: *1 (General, theoretical and modeling)*

1 Introduction

The determination of the time of flight (ToF) of an acoustic tone burst is a key issue in position and distance measurement systems. In reflective environments, e.g. indoor applications, the ToF measurement is often difficult. Multiple echoes cause complex interference patterns. In the example of fig 1, the second peak of the interference pattern is larger than the first peak [1]. Most methods for ToF estimation rely on simple models where the shape of the observed waveform is assumed to be known in advance. The only parameters that are considered as unknown are the magnitude and the Tof. However, the occurrence of interfering echoes breaks down the validness of these models, and the methods may suffer from performance degradation.

This paper studies the robustness of ToF estimators, i.e. their ability to cope with waveforms that are disrupted by multiple echoes. The aim of this paper is to empirically evaluate this quality aspect of the various methods.

Some literature exists that addresses the performance evaluation of ToF estimators [2], [3]. The usual performance criterion is the RMS plotted against the SNR of the observed waveform, thus providing information about the noise sensitivity of the estimators. However, these evaluations do not address the problem of having multiple echoes.

2 ToF estimators considered

The tone burst that we consider consists of a few cycles of a sinoidal wave. The frequency of the sine wave is the carrier frequency. The envelope of the observed waveform, in the absence of multiple echoes, is a smooth function (for which different models have been proposed in the literature).

The ToF estimators that we evaluate are tabulated in Table 1. Some methods use the envelope of the waveform. We use quadruple filtering and Rice's representation to calculate it. This method is considered as optimal [4]. The covariance model based method is a new method presented in [5]. The other methods are discussed in [2], [6]. (The curve fitting method will be included in the final paper).

3 Evaluation Procedure

The first step of the empirical evaluation is the tuning of the adjustment parameters of all the estimators. We recorded 150 waveforms acquired under different conditions (different rooms, ToFs, and heights above the floor, etc.). Figure 1 is an example of a waveform obtained in this way.

For each record, we manually determined the ToF. For that, we used knowledge usually not available, e.g. the geometry of the setup. But in this experimental situation, such knowledge can be exploited. These manually obtained ToFs are considered as the conventional true values. As an criterion for the tuning of the adjustment parameters we used the sample standard deviation of the estimation errors calculated over the 150 records. A bias compensation guarantees that the bias (calculated as the mean error over all 150 records) of all operators is zero. Table 1 shows the performance of the various operators obtained in this way. Note that in this case, the matched filter – theoretically the best one – scores worst. Apparently, this method is not able to deal with unmodelled phenomena.

A simple model of the occurrence of multiple echoes in a waveform is

$$z(t) = a\,h(t-\tau_{tof}) + \sum_i d_i h(t-\tau_{tof}-\tau_i) + n(t) \qquad (1)$$

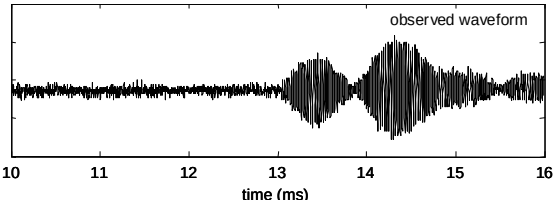

Fig. 1. An example of an observed waveform.

Table 1. Standard deviation of the estimation errors

method	std. dev. (ms)
Covariance model. based filtering	0.027
Thresholding the envelope with threshold adaptive to the maximum of the waveform	0.034
Thresholding with threshold adaptive to the maximum of the waveform	0.038
Envelope thresholding	0.044
Thresholding	0.053
Matched filtering on the envelope	0.107
Matched filtering	0.120
Curve fitting on the envelope (not yet implemented)	

The first term is the direct response whose ToF τ_{tof} should be estimated. a is the corresponding amplitude. The second term represents the multiple echoes with amplitudes d_i and delays τ_i (relative to τ_{tof}). $n(t)$ is the noise. Usually, only one of these echoes is dominant. We silently ignore the existence of the others.

In order to assess the robustness of the operators, we selected one record whose multiple echoes were small relative to the direct response. The model for this record is: $a\,h(t-\tau_{tof})+n(t)$. We also recorded a waveform obtained in an anechoic room. Since the SNR for this record is large, we model this record with $h(t)$. Using these two records we are now able to simulate the occurrence of a second echo in a controlled fashion:

$$z(t) = a\,h(t-\tau_{tof}) + D\,h(t-\tau_{tof}-T) + n(t) \qquad (2)$$

D and T are the parameters that control the simulation. The simulated waveforms are used to measure the influence of the second echo on the accuracies of the various ToF-estimators.

4 Results

We measured the RMS of the simulated waveform either with fixed delay T and varying amplitude D, or vice verse. Preliminary results are shown in fig 2. The graph on the top shows the RMSs with varying D with T fixed to 0.5 sec. The second graph shows the RMSs with varying T and with D fixed to a.

5 Conclusion

From fig 2 and table 1 we conclude the following:

- The non-adaptive threshold methods are robust except when the second echo occurs almost directly after the first. However, these methods have a large standard deviation.
- The adaptive threshold methods are robust except when the amplitude of the second echo becomes large (influencing the maximum of the wave)
- Matched filtering in either form is not robust.
- The covariance model based method combines a small standard deviation with good robustness. The adaptive envelope threshold method performs slightly worse, but is much easier to implement.

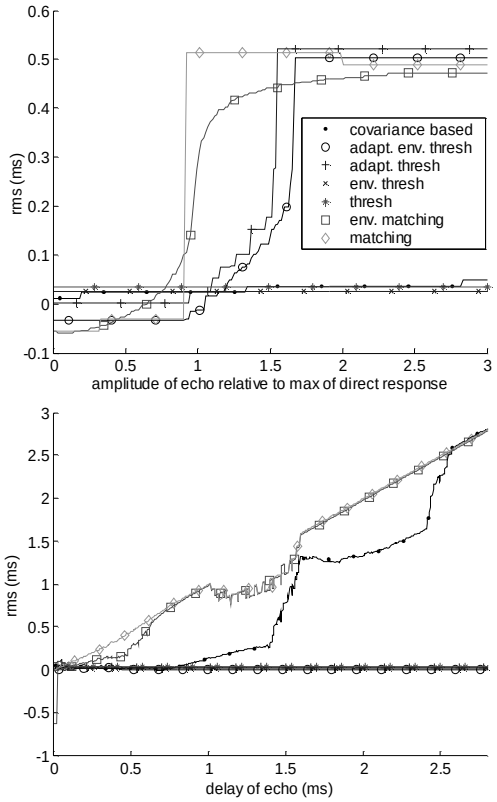

Fig. 2. RMS versus relative amplitude (top) and delay (bottom) of second echo.

References

[1] F. van der Heijden, G. Túquerres, P.P.L. Regtien, "A Reflection Model for Ultrasonic Position Measurements for Indoor Applications", to appear in Proc. XVII IMEKO 2003, June 2003

[2] B. Barshan, "Fast processing techniques for accurate ultrasonic range measurements", Meas. Sci. Technol. 11 (2000) 45-50.

[3] H.W. When, P.R. Bélanger, "Ultrasound-Based Robot Position Estimation", IEEE Trans on Robotics and Automation, Vol. 13, No. 5, p. 682-692, October 1997.

[4] A. Papoulis, Probability, Random Variables, and Stochastic Processes – Third Edition", MacGraw-Hill, 1991.

[5] F. van der Heijden, G. Túquerres, P.P.L. Regtien, "Acoustic Time-of-flight measurements in a reflective room", to appear in Proc. XVII IMEKO World Congress, June 2003.

[6] M. Parrilla, J.J. Anaya, C. Fritsch, Digital Signal Processing Techniques for High Accuracy Ultrasonic Range Measurements, IEEE Trans on Instrumentation and Measurement, Vol 40, No. 4, pp 759-763, August 1991.

Study of an Elastic Surface Deformation by Piezoelectric Actuator: Model Formulation, FEM Analysis, and Experimental Investigation.

P.J. Costa Branco[1], A. Oliveira[1] and P. Sousa[1]

[1] Mechatronics Lab, Instituto Superior Tcnico (IST), A. Rovisco Pais, 1049-001 Lisboa, Portugal
email: pbranco@alfa.ist.utl.pt http://pbranco.ist.utl.pt

Summary. *Unimorph design of a piezo bonded to a surface is the most common structure used to induce deformations. Analytic models by Park and Agrawal have been extensively used. However, they are based on different strain distribution hypothesis that must to take into account the relative thickness size between piezo and surface. To evaluate the two models, results from analytic models and FEM simulations revealed the importance of the assumptions for strain distribution at the piezo actuator foreach model. An experimental prototype matching a clamped surface actuated by a piezo has been built. Experimental results are compared with the models.*

Keywords: piezoelectric actuator, surface deformation, modeling
Category: 1 (General, theoretical, modeling)

1 Introduction

The models developed by Park [1] and Agrawal [2] have been extensively used to determinate the induced strain on piezo actuated surfaces. Park's model considers a constant strain distribution through the piezo actuator and a linear distribution through the surface material. This approach can only be valid when the piezo thickness is is much smaller than the surface thickness, as shown in Fig. 1(a). Agrawal's model instead assumes a linear distribution through the actuator and the surface. When the piezo thickness is of same size order than the surface one, a linear extension approach becomes more adequate as shown in Fig. 1(b). The two models have been evaluated by FEM and experimental tests based on a cantilever beam structure-actuator shown in Fig. 2.

2 FEM model and experimental prototype

FEM analysis used the Ansys software. The adhesive was a cyanoacrylate with a Young modulus of $5{:}17 \pounds 10^{9}$ N/m^2. The surface was aluminium with width equal to the piezo and length of 25:2 cm. The aluminium had a Young's modulus of $7{:}31 \pounds 10^{10}$ N/m^2 and a Poisson constant of 0:3. Two beam thicknesses tb were considered 0:5 and 1:0 mm and a piezoceramic with a thickness of $tc = 0{:}19$ mm. An experimental prototype has been built. The beam structure was placed in a vertical cantilever position as shown in Fig. 3. A high precision potentiometer taken out of an aeronautic sensor (angular ratio gyroscope) has been used to measure the beam tips displacement.

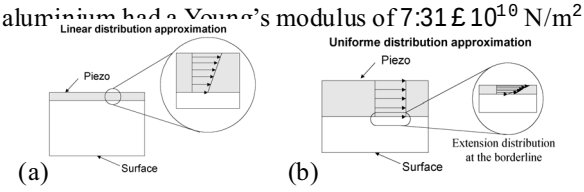

Fig. 1: (a) Uniforme strain distribution and (b) linear strain distribution in the piezoelectric actuator.

3 Results

3.1 Analytic and numerical analysis

FEM results are reference by which analytic models were judged. In Figs 4(a-c), FEM results show the linear strain (¤) and the uniform strain model (4). They produce identical results for a 1 mm thickness beam. When compared with FEM model, analytic ones are only able to accurately predict the slope at the end of the piezo, showing worse results for the slope at the end of the beam. Concerning the slope at the end of the piezo, theoretical models underestimate the slope relative to the FEM model, leading to the differences observed in the beam's slope predictions. Theoretical models do not accurately predict the slope at the end of the piezo and differences grow with increasing voltage. For a 0:8 mm thickness beam (Fig. 5), differences

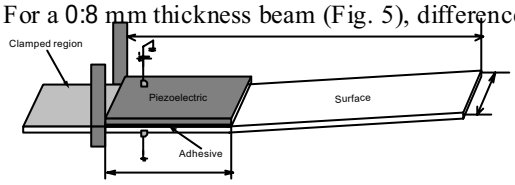

Fig. 2: Cantilever beam structure-actuator.

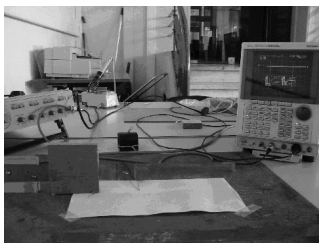

Fig. 3: Surface mounted piezo actuator: AC voltage source, piezo, aluminium, and digital oscilloscope.

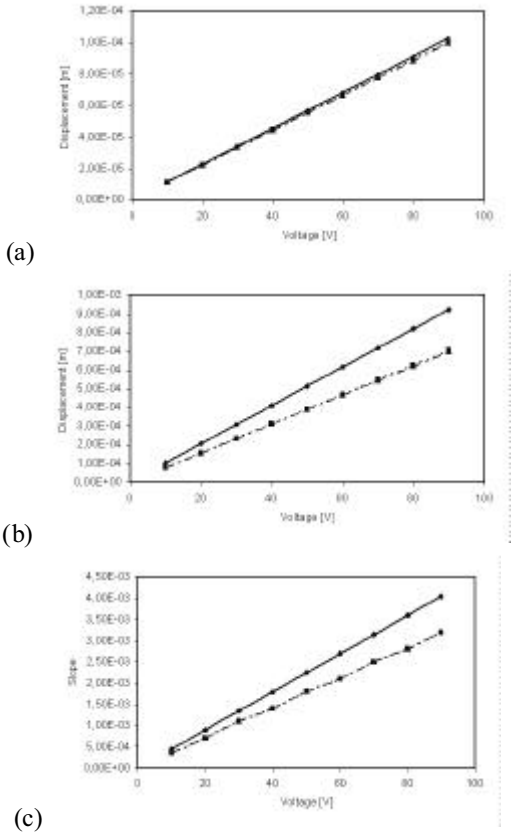

Fig. 4: Beam thickness 1 mm. Slope at a) end of the piezo, b) free end of the beam, c) end of the piezo.

between theoretical models become signi cant. The slope at the end of the piezo is overestimated by the uniform strain model and underestimated by the linear strain model. Still, regarding the beam's free end slope, the uniform strain model shows results closer to those obtained in FEM simulation. Experimental tests were carried out for an intermediate 0:8 mm thickness beam. Figure 6 shows how, for the 0:8 mm thickness tested, the FEM model results represent a good approximation of reality.

4 Conclusions

Despite being more simplistic, the uniform strain model can be used for higher thickness ratios, which is an advantage since it is a simpler model to use. The Agrawal's model is the one that best estimates the slope of the piezo and is not constrained by thickness considerations. Thus it is a very solid model for estimating

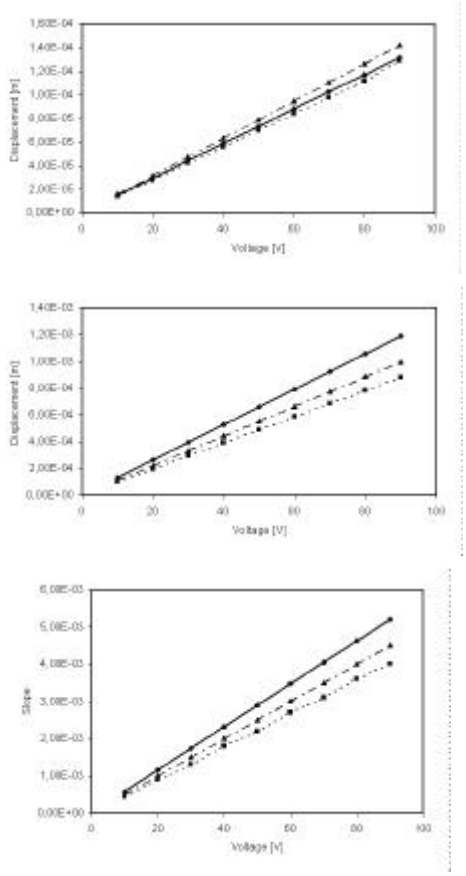

Fig. 5: Beam thickness 0:8 mm. Slope at a) end of the piezo, b) free end of the beam, c) end of the piezo.

the slope of areas covered by the actuator but should not be used for predicting the beam's slope when its thickness is small.

References

[1] Park, C., Waltz, C. & Chopra, I.: *Bending and Torsion Models of Beams with Induced-Strain Actuators*, Smart Materials and Structures 5 n^{o}1, IOP Publishing Ltd, 1996

[2] Agrawal, N. Brij, Treanor, Kirk K.: *Shape Control of a Beam using Piezoelectric Actuators*, Smart Materials and Structures 8 n^{o}6, IOP Publishing Ltd, 1999

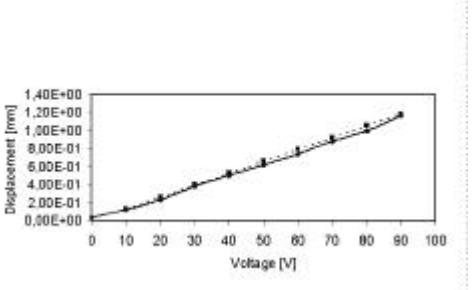

Fig. 6: Experimental (continuous line - experimental points in diamonds) and FEM results.

Experimental introduction of Rayleigh damping in analytical models of piezoelectric transducers

J.L. Pons[1], H. Rodríguez[1], J.F. Fernández[2] and M. Villegas[2]

[1]Instituto de Automática Industrial, CSIC, Ctra. Campo Real km. 0,200, 28500 Arganda del Rey, Madrid, Spain
email: jlpons@iai.csic.es http://www.iai.csic.es/sam
[2]Instituto de Cerámica y Vidrio, CSIC, Camino de Valdelatas s/n, 28049 Madrid, Spain

Summary. *A number of papers address the analytical modelling of piezoelectric transducers and, in particular, of travelling wave ultrasonic motors. Most of them focus on the complex electromechanical modelling of the motor stator. In this paper, an the experimental introduction of structural damping in analytical models is introduced. The proposed approach is based on a two-coefficient Raylaigh model. Experimental verification is reported through an integral model used for design, optimisation and simulation purposes.*

Keywords: Ultrasonic Motors, Piezoelectric transducers, Rayleigh damping, Analytical model
Category: 1 (General, theoretical and modeling)

1 Introduction

Analytical models of the so-called Travelling Wave Ultrasonic Motors, TWUMs, have been approached during the last decades. TWUMs belong to a relatively new class of electromechanical devices, which use the inverse piezoelectric effect to obtain linear or rotary motion. Their simple structure, high power density, high torque/low speed operation and its solid-state nature, with no generation of electromagnetic fields, have attracted a widespread interest, see *Rodriguez et al.* in [1].

A number of papers have addressed the issue of improving the stator analytical models. Friend et al., [2], introduced a closed-form solution of the vibration of an anular plate without considering shear deformation and rotary inertia. Hagedorn et al., [3], model the plate thickness as a function of the radius and include both shear and rotary inertia but the piezoelectric domain was not considered. A quite accurate model of the non-uniform electric field in the piezoelectric domain is included in [4] and [2]. In addition, the teeth dynamic behaviour is also considered in [5].

Analytical modelling of piezoelectric transducers requires the introduction of material parameters. This involves the experimental characterization of the piezoelectric specimen in terms of electromechanical coefficients as well as the introduction of structural parameters, in particular system damping. Several approaches can be found in the literature, both viscous and structural models are reported, see [6, 7].

This paper introduces the experimental application of Rayleigh damping approaches in analytical models of piezoelectric transducers. In particular, the application to analytical models of travelling wave ultrasonic motors, TWUM, is addressed. First, an intergal TWUM model will be briefly introduced. Following, the theory behind structural damping will be given to lead to the experimental introduction of damping coefficients in a third section.

2 Experimental introduction of Rayleigh damping

The forced vibration of the utrasonic motor stator can be described according to the following expression:

$$[M]\{\ddot{u}\} + [C]\{\dot{u}\} + [K]\{u\} = \{F_v\} \qquad (1)$$

It is particularly interesting the formulation to include the structural damping, $[C]$, in equation 1. Usually, viscous and structural models are used to describe the damping behaviour of mechanical continuum, [6, 7]. Structural damping is generally used in the frequency domain while viscous damping, i.e. Rayleigh damping, can be used in the time domain, with acceptable results when the damping level is low, [7].

2.1 Viscous damping

In our approach, a two-coefficient Rayleigh model has been used. This approach maintains modal shapes, leading to relatively simpler solutions [7, 8, 9].

The Rayleigh damping matrix has a general structure as shown below:

$$[C] = [M] \sum_{k=0}^{p-1} \alpha_k ([M]^{-1}[K])^k \qquad (2)$$

For the simpler case, when $p = 2$, the damping matrix becomes:

Damping parameter	USR30
ξ for n=4	0.39%
ξ for n=5	0.85%
α_0	-1.457×10^3
α_1	7.148×10^{-8}

Table 1: Experimental determination of damping parameters

$$[C] = \alpha_0[M] + \alpha_1[K], \tag{3}$$

where, α_0 and α_1 are the damping coefficients. This damping approach keeps orthogonality with respect to the system eigenvectors, $[\tilde{U}]$. As a consequence, system equations can be completely uncoupled through a modal expansion, [8], for the i-th vibration mode, we have:

$$m_i\ddot{\Lambda} + c_i\dot{\Lambda} + k_i\Lambda = v_i \tag{4}$$

where,

$$m_i = |\tilde{u}|_i[M]\{\tilde{u}\}_i, \qquad c_i = |\tilde{u}|_i[C]\{\tilde{u}\}_i,$$
$$k_i = |\tilde{u}|_i[K]\{\tilde{u}\}_i \quad \text{and} \quad v_i = |\tilde{u}|_i^T\{v\}.$$

After normalisation, i.e. $m_i = 1$, we have:

$$\ddot{\Lambda} + 2\xi_i\omega_i\dot{\Lambda} + \omega_i^2\Lambda = v_i \tag{5}$$

where, ξ_i is the damping ratio.

Coming back to the determination of the damping coefficient, we end up with:

$$c_i = 2\xi_i\omega_i = \alpha_0 + \alpha_1\omega_i^2. \tag{6}$$

It can be easily seen that, by experimerimentaly obtining the damping ratio, ξ_i, for two different vibration modes, the Rayleigh coefficients, α_0 and α_1 can be worked out.

2.2 Experimental determination of Rayleigh coefficients

The Rayleigh damping coeeficients (α_0 and α_1) have been experimentaly determined for the Shinsei USR30 TWUM according to the method described in the previous section. The resulting damping coefficients and damping ratios are summarised in table 1.

The experimental damping ratios corresponding to two vibration modes were obtained from the system resonance curve. In order to do so, the damping ratio was determined according to $\xi = (\omega_b - \omega_a)/2\omega_r$, where, ω_r resonance frequency of the vibration mode being analysed, and ω_a and ω_b are frequencies for which the amplitude of the resonance curve is 3dB below the resonance value respectively, [10]. Figure 1, shows the resonance curves as obtained for modes $n = 4$ and $n = 5$ for the commercial motor Shinsei USR30.

The forced response of the USR30 was measured by a high resolution laser interferometer (VF300 by Politek). In addition, the experimentaly verified low damping ratio, $\xi < 0.01$, made it possible to validate

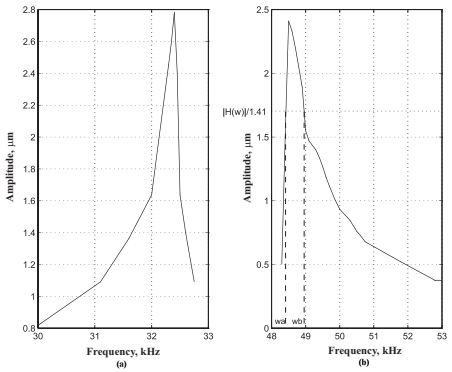

Fig. 1: Resonance curves for a) fourth and b) fifth vibration modes. Experimental determination of damping ratio for USR30

the assumption that the forced response of the motor at the resonance frequency is effectively very close to the corresponding modal shape.

References

[1] H. Rodríguez, J.L. Pons, R. Ceres, L. Calderón, *Smart Materials and Structures* in press. Modelling of the Travelling Wave Piezoelectric Motor Stator: An integrated review and new perspective, (2002).

[2] J.R. Friend and S. Stutts, The dynamics of an annular piezoelectric motor stator *J. Sound and Vibration* 204 (3): 421-437, (1997).

[3] P. Hagedorn and J. Wallasheck, Travelling wave ultrasonic motors, part I: working principle and mathematical modeling, *J. Sound and Vibration*, 155 (1):3-46, (1992).

[4] S.V. Gopinathan, V.V. Varadan and V.K. Varadan, Detailed study ofelectromechanical fields in piezolaminates, *Proc. of the SPIE*, 1: 438-448, (1999).

[5] J.L. Pons, H. Rodríguez, F. Seco and R. Ceres, Novel Modeling Technique for the Stator of Traveling Wave Ultrasonic Motors, submited to *IEEE Trans. on Ultras., Ferr. and Freq. Control*, 2002.

[6] D. L. Cronin, Eigenvalue and Eigenvector Determination of Nonclassically Damped Dynamic System, *Computers and Structures*, 36:133-138, (1990).

[7] M. Liu and D. G. Gorman, Formulation of Rayleigh Damping and its Extensions, *Computers and Structures*, 57(2): 277-285, (1995).

[8] I. H. Shames and C. L. Dym, Energy and Finite Element Methods in Structural Mechanics, *Taylor and Francis*, USA, (1991).

[9] N. Zabaras and T. Pervez, Viscous Damping Approximation of Laminated Anisotrpic Composite Plates Using The Finite Element Method, *Computer Methods in Applied Mechanics and Engineering*, 81(3): 291-316, (1990).

[10] D. J. Inman, Engineering Vibration, *Prentice Hall*, USA, (1994).

Finite Element Analysis of Spurious Compressional Wave Excitation by Transverse-Shear-Mode Liquid Sensors

J. Kuntner and B. Jakoby

Vienna University of Technology, Industrial Sensor Systems E366
Gusshausstrasse 27-29/366, A-1040 Vienna, Austria
email: jochen.kuntner@tuwien.ac.at http://iss.iemw.tuwien.ac.at

Summary: *Microacoustic sensors have proven to be powerful tools in a number of applications ranging from chemical sensing to viscosity and density sensing in fluids. For liquid media, transverse shear mode resonators have been utilized as they do not lead to an unwanted excitation of compressional waves in the liquid, which would lead to a serious damping of the sensor. Although the microacoustic modes are dominantly shear polarized, compressional waves are excited as well. This is related to the non-uniform distribution of the shear discplacement and to spurious normal discplacement components at the sensitive surface. The effects associated with these compressional waves recently have been investigated experimentally. In this contribution we present a finite element analysis of the oscillating device leading to an identification of the mechanisms causing the excitation of the spurious compressional waves.*

Keywords: *Microacoustic Sensor, Viscosity Sensor, Transverse Shear Mode Resonator*
Category: *1 (General, Theoretical and Modeling)*

1 Introduction and Theory

Shear polarized acoustic wave sensors are very well suited for sensing tasks in the liquid phase, like, e.g. viscosity sensing or chemical sensing (where the sensitive surface is covered with a selectively adsorbing chemical interface). In principle a pure shear displacement at the sensitive surface avoids the excitation of compressional waves and merely leads to an evanescent shear wave in the adjacent viscous liquid (see Fig. 1). Compressional wave excitation would lead to unwanted acoustic radiation losses which would drastically reduce the performance of the sensor. The remaining viscous loading can either be used, e.g. for viscosity sensing, or it represents a cross-sensitivity that needs to be compensated, e.g. in case of chemical sensors.

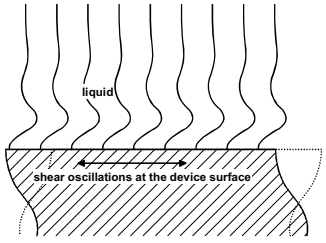

Fig. 1: A shear oscillating surface in contact with a viscous liquid.

In this contribution we consider transverse shear mode (TSM) resonators where a shear polarized mode is excited in a quartz disk by means of electrodes deposited on both sides of the disk (see Fig. 2). The shear polarization is achieved by using proper crystal cuts like singly rotated cuts in quartz, e.g., the so-called AT-cut. In this case, the displacement ***u*** is oriented in the crystalline X-direction lying in the cut plane of the disk.

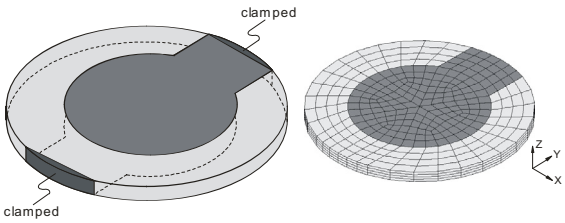

Fig. 2: TSM resonator: basic structure (left) and FEM model (right).

Due to the finite extension of the electrode, a so-called trapped mode is excited, which leads to additional small displacements in other directions than X and to a non-uniform distribution of the dominant displacement component u_x across the sensing surface. Both effects potentially lead to the excitation of spurious compressional waves in the adjacent liquid. (In case of the nonuniform distribution of u_x this can be seen by considering the continuity equation in the liquid as described in [1].) The effect of compressional wave excitation has been investigated experimentally in a number of works [1,2,3,4,5,6]. In [3,4,5] the impact on the equivalent circuit model of the resonator is also considered. In this contribution, we present a rigorous finite element (FE) analysis of the resonator to numerically analyze the compressional wave excitation.

2 Analysis Approach

As sample structure we consider a 4MHz AT-cut resonator featuring disk and electrode diameters of 8 and 5 mm, respectively (see also Fig. 2). The thickness of the (gold) electrodes was assumed to be 500 nm. The analysis also accounts for the effect of mounting the disk in a holder by clamping the respective areas at the disk circumference (Fig. 2).

The structure has been modeled using the software ANSYS, where 1224 brick elements for the quartz disk and 372 shell elements for the electrodes have been used.

3 Results

To discriminate the different excitation mechanisms mentioned above, it is instructive to consider the behavior of the resonator in air. To investigate the displacement distributions, the resonator is excited slightly off the resonance frequency (as no damping was assumed at this stage). Firstly it is found that the peak values for $|u_z|$ are two orders of magnitudes below those for $|u_x|$. As expected, the dominant shear displacement u_x approximately depends on the radial coordinate only. Fig. 3 shows its distribution along the X-axis yielding a Gaussian-like distribution as it also has been found experimentally. Note that irregularities in the numerical data can partly be attributed to the interaction of u_z with the non-vanishing normal displacement component u_z.

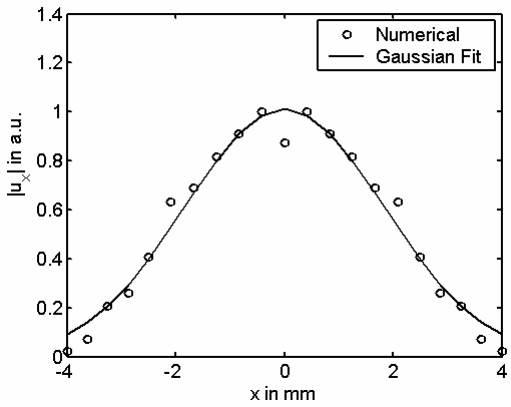

Fig. 3: Distribution of u_x at the resonator surface along the X-coordinate.

Fig. 4 shows a contour plot for u_z across the disk surface and a cross-sectional view of the deformation in the Y-Z plane compared to the undeformed structure (drawn displacements are exaggerated). The positive and negative peaks in the contour plot (bright and dark spots) indicate possible excitation centers for compressional waves when the device is loaded with a liquid. Considering the second mechanism of excitation, i.e. the non-uniformity of u_x, one can expect only two excitation centers. These are approximately located at those positions on the X-axis, where the slope of the distribution $u_x(x)$ reaches its maximum. This can be simply shown by considering the continuity equation in the adjacent liquid [1]. In our example these locations would be at about $x = \pm 1.5$mm on the X-axis (see Fig. 3). In experiments, the dominant excitation centers found correspond to the ones obtained from considering the non-uniformity of u_x. [4,6]. Thus it can be concluded, that the major effect being responsible for the excitation of compressional waves is the non-uniformity of the shear displacement component across the sensitive surface.

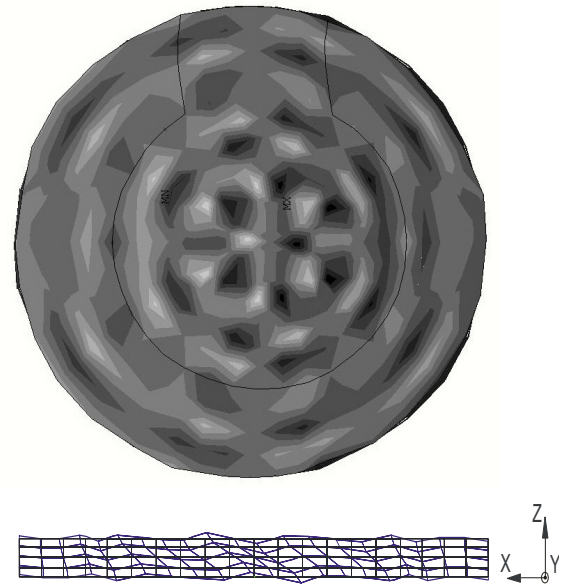

Fig. 4: Contour plot of u_z (upper) and cross section of the deformation in the XZ plane (lower).

4 Discussion and Conclusions

In this contribution we present a finite element analysis of a transverse shear mode resonator for the operation in liquids. Due to mode trapping, TSM resonators also excite spurious compressional waves, which can be firstly attributed to normal displacement components u_z and secondly to the non-uniform distribution of the dominant shear displacement u_x at the sensing surface. In our analysis we identified patterns of compressional wave excitation centers corresponding to both mechanisms. Comparing these results to experiments we find that the dominant cause for compressional wave excitation is the non-uniformity of the shear displacement. In our final contribution we will further discuss the effect of liquid loading by means of simulation results and comparisons with experiments.

References

[1] B.A. Martin, H.E. Hager, *J. Appl. Phys.* 65 (7), 1989, 2627-2629.
[2] Z. Lin, M.D. Ward, *Anal. Chem.* 67 (4), 1995, 685-693.
[3] T. Schneider, S.J. Martin, *Anal. Chem.* 67 (18), 1995, 3324-3335.
[4] R. Lucklum, S. Schranz, C. Behling, F. Eichelbaum, P. Hauptmann, *Sens. Act.* A 60, 1997, 40-48.
[5] H, Välimäki, J. Lekkala, H. Helle, *Sens. Act.* A 60, 1997, 80-85.
[6] L. McKenna, M.I. Newton, G. McHale, R. Lucklum, J. Schroeder, *J. Appl. Phys.* 89 (1), 2001, 676-680.

Mechanical behavior simulation of an electrostatic actuated Fabry-Perot cavity

C. Tibeica, R. Muller, D. Cristea

National Institute for R&D in Microtechnologies (IMT), 32B Erou Iancu Nicolae Street, PO Box 38-160, 72996, Bucharest, Romania
email: catalint@imt.ro http://www.imt.ro

Summary: *A tunable optical filter using a Fabry-Perot air gap resonant cavity has been modeled in order to optimize the mechanical behavior. The performed simulation optimizes design parameters and is able to predict the effects of residual stress gradient induced in structure during technological processes. Two different membrane layer geometries and materials have been considered.*

Keywords: *FEM simulation, Fabry-Perot cavity, optical filter, electrostatic actuation, residual stress*
Category: *1 (General, theoretical and modeling)*

1 Introduction

A tunable Fabry-Perot cavity based on MEMS technology is a versatile microstructure used in many applications (optical filters, modulators, sensors).
It consists of a resonant microcavity composed by two flat, parallel, high quality mirrors separated by a gap.
We consider a micromachined microcavity, where the distance between the two mirrors can be change by applying an electrostatic force on the top mirror which is also a suspended thin membrane.

The paper is focused on the simulation, based on Finite Elements Method (FEM), of the behavior of mechanical parts of the Fabry-Perot micro-cavity resonator. The analysis includes the coupled electro-mechanical simulation that can be performed to optimize the performances of device, and reduce the technological iterations.

An electrostatically actuated mirror, in two different designs, is analyzed using Coventorware software tool.

2 Basic considerations

The device can be modeled as a square parallel-plate actuator with four connecting flexures that acts as tensile and/or torsional springs.
Assuming a linear spring force with the spring constant k, the balance of the mechanical and electrostatic forces is determined by the implicit equation [2]:

$$F(U,x) = \frac{1}{2}\frac{\varepsilon U^2 A}{(d-x)^2} - k'x = 0 \qquad (1)$$

where
ε - is the electric permittivity of medium
U – is the voltage between plates
A – is the area of capacitive plate
d – is the initial distance between plates (without voltage)
k' – is the effective spring constant
x(U) – is the stationary displacement at voltage U

From equation (1) it results that a low voltage actuation and a wide range displacement can be obtained by two ways:
- increasing the plates area, and
- reducing the effective spring constant

A general design rule for MEMS tunable optical filters says that the mechanical excursion of movable mirror at maximum voltage be no larger than 1/3 of the gap. In our simulation, a maximum voltage of 50V was imposed.

3 Design

Two different designs of the movable mirror were demonstrated.
The first consists in a square polysilicon membrane suspended by four flexures in the corners (Fig. 1). The initial geometrical parameters for simulation are the thickness of polysilicon layer, set to 0.75 μm, and the gap between fixed electrode and the membrane, set to 2 μm.
For the second structure (Fig. 2), the geometry of flexures is modified, and the material of membrane is gold with a central titanium window having a thickness of 0.015 μm. In this configuration only the central area of membrane play an optical role.
To prevent an exaggerate deformation of the thin titanium window, a rectangular shape with the same dimensions, was cut in the bottom actuation electrode The stiffness of the second structure is lower than that of the first because this configuration decreases the effective spring constant allowing a large range of motion at low voltage. The initial parameters were the same as in the previous design.

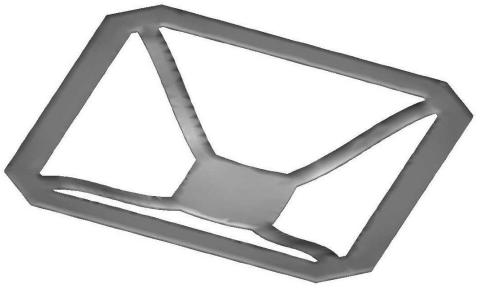

Fig. 1. View of displacement for the polysilicon mirror under electrostatic actuation (50X exaggerated deformation)

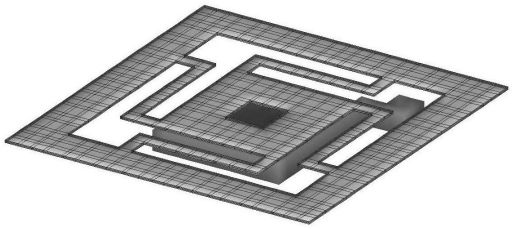

Fig. 2. The meshed model of mirror for the second design, with a thick central window

High-quality flatness is needed for the central area that plays the role of mirror, because of optical reasons.

4 Simulation results

The simulations have been performed in two steps:

(1) an electro-mechanical analysis to obtain the mirror displacements under a set values of gap and applied voltage

(2) static analysis considering only the residual stress action (uniform biaxial stress)

Coventorware software utilizes an iterative approach to couple the electrostatic and mechanical solvers together. The Simulation Manager create a set of simulation solutions for a set of variable parameters. In our analysis, the voltage was fixed to 50V, and the gap is ramped up from 1.0 to 2.0 μm.
In each case, the simulation predicts a 0.01 μm deviation from planarity of a central square with 10x10 μm area.

An assumption is made namely that the residual stress in titanium and gold is constant in each layer. For polysilicon a typical value of -450 MPa (a compressive stress) is considered, and +70 MPa for gold.

Values that are more exact can be determined by measurements on test structures made in the same process conditions as the mirror because the residual stress is a function of technological conditions [3].

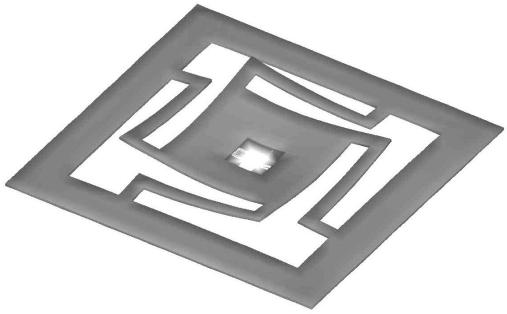

Fig. 4. View of displacement under residual stress in the titanium-gold layered mirror (300X exaggerated deformation)

5 Conclusions

Finite element analysis has been performed to analyze and optimize an electrostatic actuated mirror in Fabry-Perot cavity. A deflection of 0.6 μm (~35% of 1.5 μm gap) is obtained with a 50V applied voltage. A bi-layered configuration has been simulated in order to minimize the residual stress effects.

References

[1] J. A. Walker, K. W. Goossen, S. C. Arney, N. J. Frigo, P. P. Iannone, *J. of Lightwave Technology,* 10 (1996) 2382-2386

[2] E.-R. Konig, G. Wachutka – "Analysis of unstable behavior occurring in electro-mechanical microdevices" – Proc. Of 2nd Int. Conf. on Modeling and Simulation of Microsystems, Sensors and Actuators (MSM-99); San Juan, Puerto Rico, 330-333

[3] W. Fang, J. A. Wickert – "Determining mean and gradient residual stresses in thin films using micromachined cantilevers" – *J. Micromech. Microeng*. 6 (1996) 301-309.

Micromachined capacitive long-range displacement sensor

Toon A.A.Kuijpers, Gijs J.M.Krijnen, Theo S.J. Lammerink, Remco J. Wiegerink, Miko C. Elwenspoek

Transducer Science & Technology group, MESA+ Research institute, University of Twente, PO box 217, 7500AE,Enschede, The Netherlands. email: a.a.kuijpers@el.utwente.nl

Summary: *First measurement results are presented for a surface-micromachined long-range (50– 100 μm) periodic capacitive position sensor. The sensor consists of two periodic geometries (period = 10 μm) sliding along each other with minimum spacing of about 1.5 μm. The relative displacement between the two, results in a periodic change in capacitance. An electrostatic comb-drive actuator is employed to generate displacements. Measured maximum capacitance change ΔC=0.72 fF corresponds to simulation results but needs better shielding from external noise sources. The results show this sensorconcept can potentially lead towards long-range nano-positioning control of microactuator systems.*

Keywords: *periodic capacitive position sensor, displacement transducer, periodic geometry, surface-micromachining, MEMS, comb-drive, microactuator, nano positioning,*
Category: *1 (General, theoretical and modeling) & 10 (Applications)*

1 Introduction

Accurate positioning is of paramount importance for many applications of micro-systems. Microactuators for example have a high potential in probe-microscopy and future probe memory applications [1] provided that nm position accuracy can be obtained over 10's of μm displacement range. In many cases such accuracies cannot be obtained using open loop operation and, thus, position sensing is required. In order to make such systems both economically viable as well as compact, on chip position sensing appears to be a requirement.
In this work we investigate a capacitive position sensor integrated with a micromachined electrostatic microactuator to facilitate nano-position control. The aim is to develop a position sensor with nm-range accuracy over a displacement range of 50 -100 micrometers. To achieve this while keeping the demands on the dynamic sensing range of the sensor modest, a combination of discrete (counting) and analog measurement techniques is investigated.

2 Measurement concept

Capacitive metrology systems and capacitive displacement transducers using phase read-out with mm-scale electrode plates are known to be able to achieve nm-accuracy or better with large dynamic range [2,3,4]. For micro-scaled MEMS devices a capacitive position sensor becomes a challenge because of small sensor capacitances with relative large influence of parasitics and noise-sources (e.g. kT/C).
The concept for the surface-micromachined capacitive position sensor presented in this article is given in Figure 1. The sensor consists of a slider driven by two electrostatic comb-drive actuators and sliding along a fixed sense-structure. Both slider and sense-structure have opposing periodic patterns. As the slider-beam moves (x-direction) the capacitance between slider and sense-structure changes periodically. By counting the number of periods as well as measuring the change in capacitance within one period, one will in principle be able to obtain a long-range position measurement with high resolution and high accuracy.

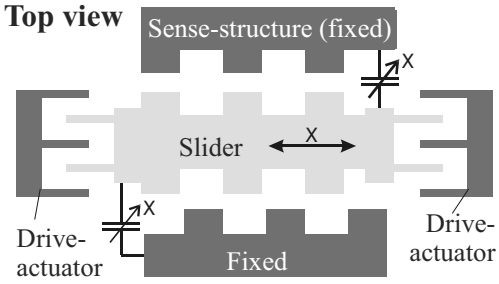

Figure 1: Concept of a capacitive long-range position sensor. Dark parts are fixed, light part moves.

Pedrocchi et al [5] have demonstrated a PC board 10x model for a long-range micromachined capacitive position sensor with an optimized electrode pitch-to-spacing ratio. Measurement results were limited by Johnson noise to 63 nm sensitivity. Because of the geometry of the capacitance this concept suffers from out-of-plane forces. Cheung et al [6] and Legtenberg [7] have used micromachined comb-sensors to detect displacements. Cheung was able to measure lateral positions with 0.01 μm estimation error using Kalman state-variable feedback. Legtenberg measured a linear change $\Delta C/\Delta x \approx 2.67$ [fF/μm] with initial capacitance $C_{comb} \approx 300$ fF ($\Delta C_{max} \approx 80$ fF) over a deflection range of 30 μm. Kung et al [8] have reported an air-gap-capacitor pressure sensor with integrated NMOS circuits where a 100 fF air-gap-capacitor could be measured with a resolution of less than 30 aF. These figures indicate that measurement of the capacitance-changes of the periodic capacitive sensor and micromachined devices is feasible. To our knowledge the combination of long-range, high accuracy and micromachined devices as presented in this work has

not been addressed before. Previously, various pattern combinations were investigated numerically with respect to maximum performance (i.e. large capacitance and large capacitance changes) [9]. In this paper we describe the first experimental results.

3 Design and experimental

An example of a realized device is given in Figure 2. It is fabricated in a one-mask surface micromaching process as described by Legtenberg [10]. In this symmetric design electrostatic forces on the slider are balanced. The symmetric periodic electrode patterns we use inherently cause ambiguities in position detection and a periodic sensitivity. Hence, in our design we intend to use quadrature detection combined with two geometrically shifted sense-structures so that a minimum in sensitivity for one sense-structure is balanced by a maximum in sensitivity of the other (see Figure 2).

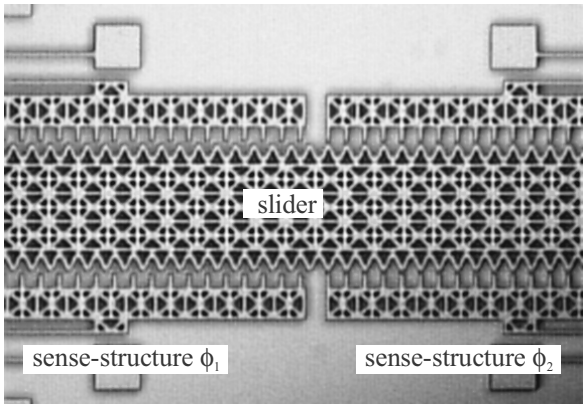

Figure 2: Photograph of a micromachined long-range capacitive position sensor with a slider beam with sinusoidal 10 µm-period and 2 pairs of sense-structures with rectangular 'fingers'. Minimum gap is 1.5 µm.

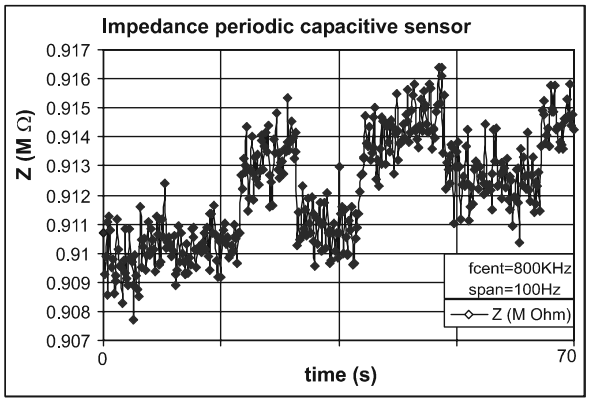

Figure 3: Impedance of 1 sense-structure as measured with the HP4194A impedance analyzer for the structure of Figure 2. The impedance is measured while the slider is step-wise displaced.

We performed measurements with a HP4194A impedance analyzer and compared results with 2D-Finite-Element simulations [9] for various periodic geometries. Measurement results for the micro-machined device in Figure 2 are presented. The impedance of one sense-structure at f=800 kHz was measured, while the slider is driven by a comb-drive microactuator between a position of minimum capacitance (sense-structure bottom-left) and a position of maximum capacitance (bottom-right). The sliderbeam has a sinusoidal pattern and the sense-structures have rectangular-fingers by design but are rounded by the micromaching processes. The period of the pattern is P_x = 10µm and the minimum gap is g=1.5µm. Each point in the graph was obtained by averaging 8 measurements, each obtained using an integration time set to 'medium'.

The steps in impedance in Figure 3 correspond to a change in capacitance $\Delta C \approx 0.72$ fF around a nominal capacitance value of $C_{nom} \approx 218$ fF. FE-simulations of the capacitance between a 10µm-period sinus-pattern and rectangular fingers on slider and sense-structure respectively, show a ΔC_{max} = 2.4 fF for a minimum gap of 1 µm and ΔC_{max} = 0.7 fF for 2 µm gap. This is a clear indication that the measured changes in capacitance are indeed due to the displacements. Figure 3 also shows that the measurement set-up needs further improvement to decrease external disturbances and noise sources. Naturally, the first next step is to measure with all 4 sense-structures and implement proper shielding. Future work will also encompass different measurement techniques.

4 Conclusions

We have shown first experimental results for micromachined capacitive long-range displacement sensors based on electrode patterns with periodic geometry. Measurements clearly show the potential of this method.

References

1 P.Vettiger, M.Despont, U.Drechsler et al., The "Millipede" - More than one thousand tips for future AFM data storage, IBM J RES DEV 44 (3): 323-340 MAY 2000

[2] L.K.Baxter et al., Capacitive Sensors: design and applications, IEEE Press, New York, 1997.

[3] P.D.Atherton, T.R.Hicks, The Nano-positioning book, Queensgate Instruments, Berkshire, 2000.

[4] K.B.Klaassen, C.L.van Peppen, Linear capacitive microdis-placement transduction using phase read-out, Sensors & Actuators, **3**, (1982), 209-220.

[5] A.Pedrocchi, S.Hoen *et al*, Perspectives on MEMS in Bioengineering: A novel Capacitive Position Micro-sensor, IEEE Trans. On Biomedical Eng., **47**-1, (2000), 8-11.

[6] P.Cheung, R.Horowitz, Design, Fabrication, Position Sensing and Control of an Electrostatically-driven Polysilicon Microactuator, IEEE trans. Magnetics, **32**-1, (1996), 122-128.

[7] R.Legtenberg, A.W.Groeneveld *et al*, Towards Position control of electrostatic comb drives, *Proc. 6th Workshop on Micromachining Micromechanics and Microsystems (MME'95)*, Copenhagen, Denmark, 3-5 Sept.,1995.

[8] J.T.Kung, H.S.Lee, An integrated Air-Gap-Capacitor Pressure sensor and digital readout with sub-100 attofarad resolution, J. of Microelectromechanical systems, **1**, no.3, 121-128, 1992.

[9] A. A. Kuijpers et al. 2D-Finite-Element simulations for long range capacitive position sensor, invited for publication in J. Micromech. Microeng, July 2003.

[10] R.Legtenberg et al., Comb-drive actuators for large displacements, J.Micromech. Microeng., **6**, (1996), 320-329.

Modeling and simulation of a silicon soil moisture sensor based on the DPHP method for agriculture

A. Valente[1], R. Morais[1], C. Couto[2] and J. H. Correia[2]

[1]UTAD University, Dept. Engenharias, Quinta de Prados, 5000-911 Vila Real, Portugal
email: avalente@utad.pt http://www.utad.pt/˜aci
[2]University of Minho, Campus de Azurém, 4800-058 Guimarães, Portugal

Summary. *A silicon soil moisture sensor, based in the dual-probe heat-pulse (DPHP) method, was modeled and simulated for achieving, with low cost, accurate and reliable measurements. This method is based on the application of a heat pulse during a fixed interval of time. The maximum rise in temperature ($\triangle T_m$) is monitored by the measurement probe, placed at a certain distance of the heater source. A low-cost high-performance and small temperature sensor (a dynamic V_{PTAT} generator) is required to be placed into the probe which have 0.912 mm in diameter and 20 mm long. If one considers the range of water contents, ratio of water mass to dry soil mass, in a typical agricultural soil (0.05 to 0.35 $m^3\ m^{-3}$), the average sensitivity of the dual probe is about $1.95°C$ per unit change ($m^3\ m^{-3}$) in water content for $q = 400\ Jm^{-1}$.*

Keywords: Soil moisture sensor, DPHP method, CMOS temperature sensor
Category: 1 (General,Theoretical and modeling)

1 Introduction

Efficient short and long-term management of irrigation systems requires the use of reliable and accurate soil moisture sensors. Today, a large number of sensors, based on nuclear, electromagnetic, tensiometric, capacitance, among others, techniques are available for measuring soil moisture. Generally, these methods have several limitations that restrict their integration in the management of irrigation systems. The main disadvantages are: soil dependency, inaccuracy and high-cost sensors.

2 Theory

The heat capacity of soil, ρc_p, is evaluated by adding the volumetric heat capacities of soil constituents:

$$\rho c_p = 1.92X_m + 2.51X_o + 4.18\theta_v \qquad (1)$$

where X_m, X_o, and θ_v are the mineral, organic, and water fractions of the soil, respectively. The leading coefficients represent the volumetric heat capacity (MJ$m^{-3\circ}C^{-1}$) of each soil constituent. When a pulse of heat is applied during a fixed interval of time to the heater probe, the maximum rise in temperature ($\triangle T_m$) at some distance from the heater is measured. As mentioned by Campbell *et al.* [1] the relationship between the ρc_p and $\triangle T_m$ is,

$$\rho c_p = \frac{q}{e\pi r^2 \triangle T_m} \qquad (2)$$

where, *q* (Jm^{-1}) is the heat applied per unit length of the heater, *e* is the base of natural logarithms, and $r(m)$ is the distance between the heat and temperature probes. Substituting Eq. 1 into Eq. 2 and rearranging yields an expression that shows the relationship between θ_v and $\triangle T_m$,

$$\triangle T_m = \frac{q}{e\pi r^2(1.92X_m + 2.50X_o + 4.18\theta_v)} \qquad (3)$$

or,

$$\theta_v = \frac{\frac{q}{e\pi r^2 \triangle T_m} - (1.92X_m + 2.50X_o)}{4.18} \qquad (4)$$

Although $\triangle T_m$ varies with ρc_p and θ_v, *q* can be selected to produce an adequate temperature signal for the expected range of θ_v for a typical agricultural soil (0.05 to 0.35 $m^3 m^{-3}$).

3 Projected system

The system consists of two needle probes mounted in parallel to provide a heater and a sensor probe. The needles will be made from stainless steel tubing, 0.912 mm in diameter, which will protrude 20 mm beyond the edge of the acrylic mounting.

The heater will be made from Stablohm 800A wire and placed in the middle of 'heater' needle. A high-accuracy CMOS temperature sensor with amplifier will be placed in the center of the 'probe' needle. The needles will be filled with high-thermal-conductivity epoxy glue to provide water-resistant, electrically insulated probes. The complete projected system is illustrated schematically in Fig. 1.

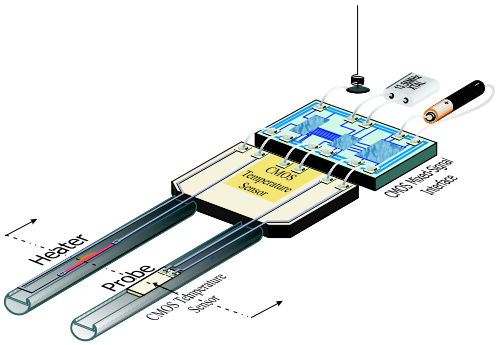

Fig. 1: The complete soil moisture sensor system.

4 Heat-pulse simulations

Experimentally, it is not possible to heat the line source instantaneously, so a short-duration heat pulse is used. Fig. 2 shows the calculated temperatures at a distance *r* following application of equivalents amounts of energy via instantaneous and short-duration heat pulses. The short-duration heat pulse causes a significant delay in time at which the maximum temperature change is obtained, but has very little effect on $\triangle T_m$. Because of this minimal effect on $\triangle T_m$, it is possible to use the instantaneous theory with short-duration heat pulses to obtain accurate heat capacities, and hence soil moisture.

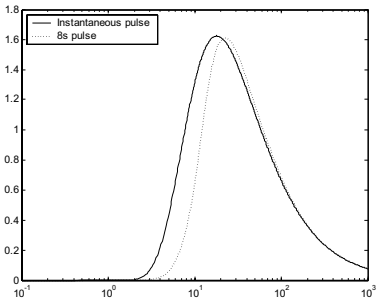

Fig. 2: Simulated temperature for instantaneous and pulsed line source models.

For a given θ_v, the sensitivity of $\triangle T_m$ increases as more energy is applied to the probe (q), but decreases with larger probe spacing and higher bulk densities. The $\triangle T_m$ distribution were simulated, using FEMLAB, and the Fig. 3 shows these results.

5 Temperature sensor simulations

A low-cost, small and high-performance temperature sensor is required to be placed in a stainless steel needle with 0.912mm in diameter and 20mm long. A proportional to absolute temperature (PTAT) circuit with bipolar devices fabricated in the CMOS process meet these criteria. Meijer *et al.* [2] showed that the application of dynamic voltage processing, using dynamic element matching (DEM) and dynamic amplification,

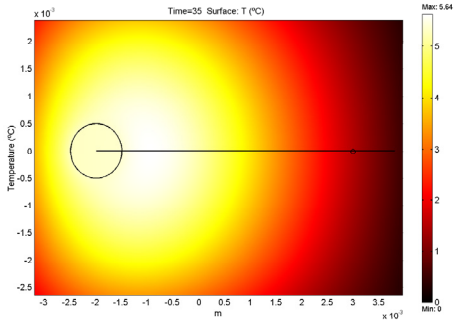

Fig. 3: Simulated $\triangle T_m$ distribution at 35s.

will enable to get a very high performance temperature sensor.

The high-performance CMOS temperature sensor is composed of a dynamic V_{PTAT} generator with thirty two switching stages that produces an average value of V_{PTAT} over these states almost equal to $(nkT/q)\ln 15$ (Fig. 4) and a dynamic switched capacitor amplifier with a DC gain of fifteen. These gives a sensor sensitivity of $0.234mV°C^{-1}$.

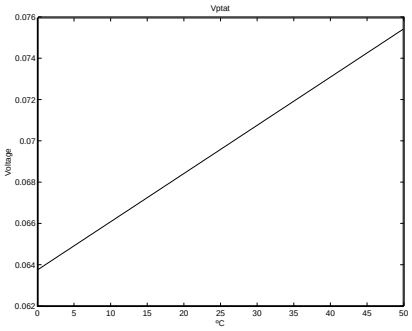

Fig. 4: Simulated PTAT voltage.

6 Conclusions

The modeling and simulation of a soil moisture sensor using the dual-probe heat-pulse method were achieved. Simulations shown that an accurate PTAT voltage can be generated with the implementation of dynamic element matching techniques. It is also shown that the sensitivity of the dual probe is about $1.95°C$ per unit change ($m^3\ m^{-3}$) in water content for a heat strength of q of 400 Jm^{-1}.

References

[1] G. S. Campbell, C. Calissendorff and J. H. Williams. Probe for measuring soil specific heat using heat-pulse method. *Soil Sci. Soc. Am. J.*, **55** (1991) 291–293.

[2] G. C. M. Meijer, G. Wang, F. Fruett. Temperature Sensors and Voltage References Implemented in CMOS Technology. *IEEE Sensors Journal*, **1(3)** (2001) 225–234.

A miniaturized self-calibrated pyrometer microsystem

L.M. Gonçalves, L.G. Gomes, S.F. Ribeiro, C. Couto and J.H. Correia

University of Minho, Industrial Electronics Dept.,
Azurém – Guimarães - Portugal
email: lgoncalves@dei.uminho.pt

Summary: *This paper describes the design, modeling and optimization of a miniaturized self-calibrated pyrometer to detect infrared radiation (in 5-20 μm range of wavelengths) in order to measure the real temperature of objects without contact. The microsystem consists of a thermally insulated absorbing area and two thermopiles with the hot junctions in the absorbing area and the cold junctions on a heat sink (i.e. the silicon bulk). The complete microsystem is in silicon planar technology and each thermopile has a different reference temperature, biased by a Peltier microstructure near to the cold junction of the thermopile. A silicon die passivated with a silicon nitride membrane is the ground floor of all microsystem. The absorbing area, a black gold strip on the silicon nitride membrane is obtained by anisotropic etching of the bulk silicon from the back of the wafer. The pyrometer microsystem is composed by: the IR optical filter on the top, the electronic system built in CMOS technology added by Multi-Chip-Module (MCM) techniques and the pyrometer. Application of a network of pyrometers in textile industry is the final goal.*

Keywords: *micropyrometer, IR radiation, thermopile, Peltier effect*
Category: *1-General, Theoretical and modeling*

1 Introduction

The pyrometers are equipments of great utility, since they allow to measure temperature of an object without contact. However, the pyrometers available on the market have a limitation, since the measured value depends on the emissivity of the target object surface. Also, the existing equipment is very expensive, becoming difficult its uses in production lines that requires control of temperature in real team as dyeing in the textile industry. A new method of contactless measuring the surface temperature and/or emissivity of objects is applied based on 2 thermopiles with 2 different reference temperatures (biased by the Peltier devices). Therefore, it is possible to measure the temperature of distant objects independently of the emissivity, based on these two readings.

The voltage obtained by a sensor at T_{s1} temperature, when this is exposed to a body at a certain T temperature, is obtained by (Stefan's Law):

$$U_1 = K.\sigma\left(T^4 - T_{s1}^4\right) \qquad \text{Eq. 1.1}$$

σ - Emissivity **K – Sensor constants**
T – Target temperature **T_{s1} – Sensor 1 temperature**

If another sensor is submitted at a different temperature T_{s2}, granting that both sensors are disposed in such way that they equally receive the same amount of radiation, the voltage on this sensor is given by:

$$U_2 = K.\sigma\left(T^4 - T_{s2}^4\right) \qquad \text{Eq. 1.2}$$

The ratio between the two values is:

$$\frac{U_1}{U_2} = \frac{T^4 - T_{s1}^4}{T^4 - T_{s2}^4} \qquad \text{Eq. 1.3}$$

That equation can be arranged to:

$$T = \sqrt[4]{\frac{U_1.T_{s2}^4 - U_2.T_{s1}^4}{U_1 - U_2}} \qquad \text{Eq. 1.4}$$

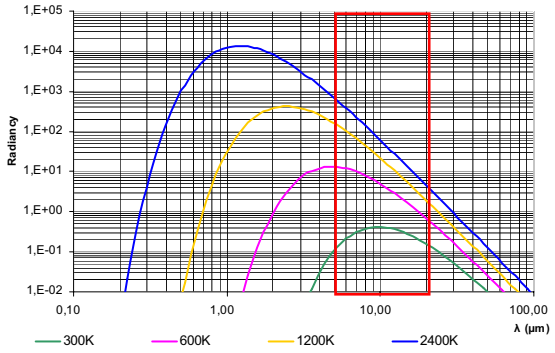

Fig. 1- Selected wavelength range.

The effect of the bandpass effect of the receiver and lens were not included in the equations (Plank's Law).

In order to get the maximum sensibility on the receiver, in the temperature between 0 ºC and 2500 ºC, based on the Plank's Law, the receiver should operate in wavelengths between 5 μm and 20 μm.

2 Simulation and design

The structure was modeled using Finite Element Analysis, in order to get the best dimensions for the Peltier converter and the Seebeck elements. These elements use a metal pair (like Nickel and Chrome) or polysilicon (type p and type n). The materials for the Seebeek thermopile are documented and compared on the references presented.

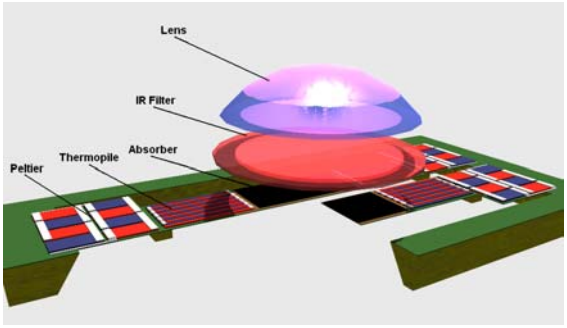

Fig. 2 - An artist impression of the complete microsystem with convex-planar lens and optical filter.

Each pyrometer can have a bandpass filter under the lens to filter a specific-wavelengths range. The compilation of the different values of the measured temperatures by a few pyrometers will compute the correct temperature of the target.

Metal	Seebeck coeff. at 273 K (μV/K)
Nickel	-18
Palladium	-9
Platinum	-4.45
Aluminum	-1.7
Lead	-0.995
Tungsten	0.13
Silver	1.38
Copper	1.70
Gold	1.79
Chrome	18.8

Table 1-The absolute Seebeck coefficient of metals.

3 Implementation

Bulk-micromachining technology in silicon (obtained through anisotropic wet chemical corrosion of the silicon wafer with an aqueous KOH solution, see Fig. 3) and deposition of thin-film layers allow to build a microsystem which integrates two thermopiles operating at two different temperatures biased by 2 Peltier structures. The silicon etching is done due to high-thermal conductivity of silicon. A silicon nitride (low-thermal conductivity) membrane is the ground-floor of the micromachined parts. A black gold strip, above the silicon nitride membrane, will absorb the IR radiation collected by a convex-planar lens including an optical filter (see Fig. 2) designed for a narrow band in the range of 5-20 μm wavelengths. This optical path eliminates the problems founded in previous research works with macroscopic pyrometers. The IR radiation absorbent area with thermal isolation and two thermopiles with the hot zone on the IR absorbent area and the cold zone on non-isolated thermal area. Each thermopile has a different reference temperature obtained through the act of a micro-structure based on Peltier effect (e.g. nickel and chromium strips) that is deposited on the cold junction of the thermopile.

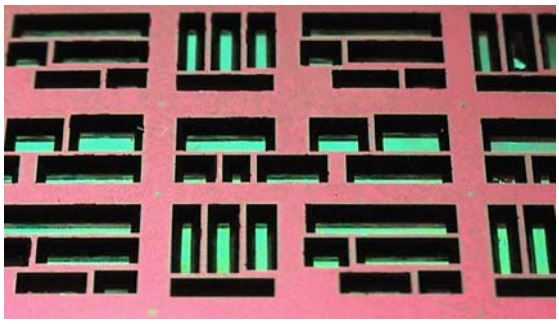

Fig. 3-The backside of a silicon wafer etched with an aqueous KOH solution. A silicon nitride membrane was used as etch-stop mask.

The electronics is merged with the micromachining parts by Multi-Chip-Module (MCM) techniques in the level of dies.

3 Conclusions

This new concept presents a miniaturized self-calibrated pyrometer microsystem with interface electronics to detect and quantify the IR radiation in the range of 5-20 μm wavelengths in order to determine the temperature of an object without physical contact. The use of a pyrometer RF network in production lines that requires control of temperature in real time as textile dyeing is the final goal of this project.

A few research has been done in order to make an RF network in 433 MHz, connecting many micro-pyrometers on a network.

References

[1] S.H. Kong. Infrared Micro-Spectrometer. *Phd Thesis, Delft University of Technology* (1995)

[2] P.M. Sarro. Integrated Silicon Thermopile Infrared Detectors. *Phd Thesis*, *Delft University of Technology* (1987).

[3] N.W. Schneeberger. CMOS Microsystems for Thermal Presence Detection. *Phd Thesis*, *Swiss Federal Institute of Technology Zurich* (1998).

Residual Stress Sensor for the Microelectronics Industry

J.M.M. dos Santos[1], N.G. Wright[1], A.B. Horsfall[1], S.M. Soare[2], A.G. O'Neill[1], S.J. Bull[2], A.J. Walton[3], A.M. Gundlach[3], J.T.M. Stevenson[3]

[1]School of Electrical, Electronic and Computer Engineering, University of Newcastle, NE1 7RU, UK
[2]School of Chemical Engineering and Advanced Materials, University of Newcastle, NE1 7RU, UK
[3]Scottish Microelectronics Centre, University of Edinburgh, EH9 3JL, UK
J.M.dos-Santos@Newcastle.ac.uk Tel +44 (0)191 222 7595 Fax +44 (0)191 222 8180

Summary: *The process-induced stress in interconnects' features have a direct influence on the reliability of the integrated circuit (IC). We have proven this localized stress in a particular interconnect feature, can be directly gauged by the use of a novel rotating stress sensor, fabricated in a CMOS compatible process. The developed sensor is able to display the residual stress in the feature as a rotation. The rotation is observable with a reflected light microscope and is compared with finite element computer simulations, using ANSYS. Due to the inherent structure's scalability it is suitable for state-of-the-art chips' environment production.*

Keywords: *Sensor, stress, interconnects, reliability*
Category: *8 (Packaging, chip handling, testing and reliability)*

1 Introduction

In this paper we report the first results of a rotating beam stress sensor for IC metallisation. A design study using finite element analysis, jointly with the fabrication process is outlined in section 2. It was used to demonstrate a range of stress sensors as shown in section 3.

The metal stress in the narrow IC interconnect lines, leading to premature track failure is largely caused by the thermal expansion mismatch, during the manufacturing process, between the track and the silicon (Si) substrate, with further constraint imposed by the intermetal dielectric. The processing can cause a tensile stress in the track larger than the yield stress in the metal. The metal tries to shrink but is prevented by its adhesion to the dielectric. Thus it must relieve the stress by void formation and growth [1, 2].

The techniques most widely used to quantify stress involve x-ray diffraction [3], but 1 μm is the state-of-the-art's smallest spot size. Measuring the wafer bowing cannot be applied to a single metal stripe, but would have to be averaged over a wafer patterned with many similar stripes. Routine in-line monitoring of stress is not realistic using these techniques. There is therefore a need for new methods of measuring stress in metal interconnect. Our proposal is a suitable test structure, which can be fabricated on the wafer along with devices and used to monitor stress generation and relaxation as a function of processing. A rotating beam sensor design, as shown in fig. 1 has potential for fulfilling this function for both aluminium (Al) and copper (Cu) technologies becoming an useful practical monitoring tool. Such a sensor will continue to work as critical dimensions reduce, and do not require expensive specialist measuring apparatus.

2 Sensor's Design, Functioning and Fabrication

The rotational sensor is shown diagramatically in fig. 1. As can be seen from the figure, when the fixed beams (arms) are freed from the underlying dielectric layer, they contract or extend in order to relieve the residual tensile or compressive stress. These two arms are connected off centre on opposing sides of the rotating beam (pointer with a length P). Any deviation in the length of the arms (A_1-A_2) exerts a torque about the centre of the sensor structure, causing a rotation of the pointer (given either by the deflection δ or the angle θ).

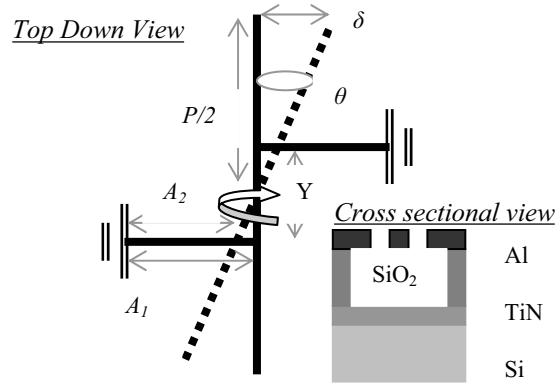

Fig. 1. Schematic diagram (arbitrary dimensions) of the sensor's structure and functioning. The most critical dimensional parameter is the arm separation (Y).

The sensors were fabricated on three inch n-type Si wafers of thickness 380 μm. 0.1 μm of TiN (titanium nitride) was sputter deposited to act as an etch stop layer, before 2 μm of PECVD SiO_2 (silicon dioxide). 1 μm of Al was then sputtered. After lithography, the Al was patterned by reactive ion etching (RIE). The wafers were then subject to a sinter process. The final process is the isotropic

RIE step, which is required to release the structures from the SiO_2 underneath. A process based on the use of as fluorine plasma has been developed for this purpose [6]. After processing, the rotation of the devices is measured using a CamScan scanning electron microscope with digitising frame grabber.

3 Results and Discussion

Fig.2 shows electron micrographs of the released sensors for devices fabricated with a 2μm feature width and 140μm arm length (A). The anticlockwise rotation of the pointer clearly shows evidence of tensile stress in the layer, which is as a result of the sintering process. The dark areas in the pictures show the detachment of the TiN etch stop layer, revealing the Si surface beneath, suggesting a small amount of over etch at the end of processing.

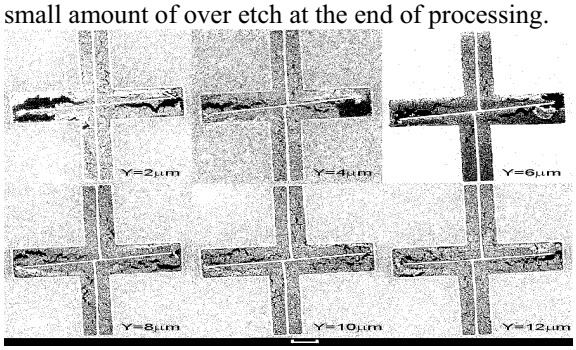

Fig. 2. Electron Micrographs of released sensors with A = 140μm, showing the effect of Y. The scale bar = 30μm.

Nanoindentation testing in conjunction with finite element modelling, using the software package ANSYS, has been used to model the rotation of the structure in terms of the process conditions and material properties of the Al layer [4]. The variation of deflection with physical dimensions is similar to that observed previously for polysilicon and silicon nitride [5]. However the plastic deformation of the soft Al has a much more significant effect.
Fig. 3 shows the angle of rotation (θ) of the sensor structure as a function of Y for two values of A.

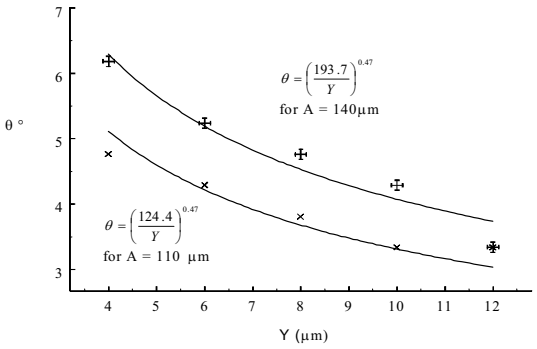

Fig. 3. Variation of θ versus Y for fabricated sensors. The trend lines on the fits have been calculated by using regression analysis based on the ANSYS results.

Sensor structures fabricated with Y= 2μm, as shown in fig. 2, have a lower θ than those with Y= 4μm. This is due to the excessive deformation of the arm / pointer intersection (hinge) with the release in stress. Because of this fact in the central region of the pointer, structures with this Y are considered to be more likely to fail mechanically; excess plastic deformation in this region will also reduce the sensor's sensitivity. For this reason, these structures are not considered any further.

The discrepancy between the fit equations for the simulated and experimental data arises from two main sources. The fit exponent (0.822 for simulated and 0.47 for experimental) is dependent on the geometry of the intersection between the arms and pointer. The simulated structure comprises perfectly sharp features at this intersection. Including a more realistic shape at these hinge points, by the use of a fillet defined by a radius of curvature, reduces the value of the exponent in the equation as summarised in table 1.

Table1. Variation of curve fitting parameters with radius of curvature (r.c.) of the hinge structures. The data suggests in order to achieve the experimental exponent of 0.47, would require a radius of curvature of 27.1 μm.

Radius of Curvature (μm)	Exponent
0	0.82
2	**0.73**
5	0.71
10	0.67

The r.c. for the fabricated sensor structures is close to 2 μm. Hence, although the modification of the hinge structure does not produce results equal to those observed experimentally, it can be seen that a more realistic behavior can be simulated.

4 Conclusions and Further Work

We have shown that the stress in sub-micron interconnect features, a potential roadblock for the microelectronics reliability, can be measured using a rotating sensor structure. This rotation, which is observable with an optical microscope, is suitable for use in a process environment. We have shown that the comparison of the rotation predicted by finite element simulation and that observed in experimental structures is critically dependent on the pattern transfer of the lithographic. The optimum device matches the one in which the arm separation is double the pointer width, as this offers the highest value of rotation and avoids excessive deformation of the structure in the hinge area.

References

[1] M. Iguchi, *et al*, IEDM Tech Dig, (1999), p615
[2] H. Shibata, *et al*, Jpn. J. App. Phys., **33**, p1814, (1994)
[3] P. Besser, AIP Conf. Proc. **491**, p229, (1999)
[4] S.M. Soare *et al*, submitted to Surface and Coatings Technology
[5] X. Zhang, *et al*, Thin Solid Films, **335**, p97, (1998)
[6] A.B. Horsfall, *et al*, submitted to J. Vac. Sci. Technol.

Fabrication of 3D MEMS Antenna Array for IR Detector Using Novel UV-Lithography, Plastic Micro Machining and Mesh Structure Bonding Technique

JONG-YEON PARK, KUN-TAE KIM, SUNG MOON and JAMES JUNGHO PAK*

Microsystem Research Center, Korea Institute of Science and Technology
SEOUL 130-650, Republic of KOREA, mems21c@empal.com
*Dept. of Electrical Engineering, Korea University, SEOUL, Republic of KOREA

Summary: This paper describes the novel UV-Lithography technique for fabrication of 3D feed horn mold structure array using implementation of mirror reflected parallel beam illuminator (MRPBI) system, fabrication of 3D feed horn MEMS antenna's plate using plastic micromachining (PMM) by Polydimethylsiloxane (PDMS) and the 3D MEMS antenna array are assembled using novel 3D MEMS bonding technique by mesh structure bonding (MSB) method.

Keyword: 3D MEMS, UV-Lithography, Mesh Structure Bonding, Plastic Micro Machining
Category: 2

INTRODUCTION

A 3D feed-horn-shaped Microelectromechanical systems (MEMS) antenna has some attractive features for array applications, which can be used to improve microbolometer performance and to enhance the optical efficiency for thin film transistor-liquid crystal display (TFT-LCD) and other display devices. Since MEMS technology has faced many difficulties in the fabrication of a 3D feed-horn-shaped MEMS antenna array itself, The purpose of this paper is to propose a new fabrication method to realize a 3D feed-horn-shaped MEMS antenna array by using a mirror-reflected parallel-beam illuminator (MRPBI) System with an very slowly rotated, inclined x-y-z stage.

NOVEL UV-LITHOGRAPHY METHOD

With a conventional UV lithography apparatus, it is very difficult to fabricate high-aspect-ratio structures (HARS) because a typical UV lithography apparatus cannot produce perfectly parallel light. From a theoretical analysis, a columnar illuminator over 6 m in height is required to achieve parallel light, but generally a laboratory height is not 6 m. An essential idea of this research is to make a light ray with long propagation by using a reflective mirror and a conventional UV-lithography apparatus for creating parallel light in a small lab space. Also, a novel method of lithography was tried to make a 3D structure array by exposing a planar wafer to the generated parallel light and rotating an inclined x-y-z stage at an ultra-slow rate. An optimization of the 3D structure array can be achieved by simulating a 3D feed-horn MEMS antenna using a high-frequency structure simulator (HFSS). Vertical sidewall array and 30º tilted sidewall array, we achieved a 300-um-high structure array using a MRPBI system, which was confirmed using scanning electron microscopy. A high-aspect-ratio, 300-um, thick structure with 30º tilted sidewalls was fabricated using a SU-8 negative photoresist, and a 100-um vertical sidewall structure array was fabricated using a PMER negative photoresist. The feasibility of fabricating both 3D feed horn MEMS antenna and a mold array was demonstrated. In order to study the effect of this new technique, we simulated the 3D feed-horn-shaped MEMS antenna array had been simulated with high frequency structure simulator (HFSS) and then compared the results with those from traditional 3D theoretical antenna models. As a result, it seems possible to use a 3D feed-horn-shaped MEMS antenna in the Tera-hertz range to improve microbolometer performance and to fabricate several optical MEMS devices.

FABRICATION FOR 3D MEMS ANTENNA ARRAY

We fabricated the 3D feed-horn-shaped mold structure array using a negative photoresist in the MRPBI system. It is necessary to control the 3D feed-horn antenna angle; hence, several experiments with mold structure of various angles were performed by controlling X-Y-Z stage and protecting it against UV reflection with a bottom anti-reflection coating (BARC)**.** 3D MEMS antenna array plate fabricated using plastic micromachining. It's thickness of about 30-40μm using Polydimethylsiloxane (PDMS) by capillary filling with clamping technique.

MESH STRUCTURE BONDING (MSB) TECHNIQUE

Micro assembly of 3D MEMS antenna array and IR detector array have many difficult to conventional MEMS bonding process. That is reason of IR detector array were 2.5 μm floated onto substrate, therefore thickness bonding material required under 2.5 μm for optimization of contact gap and all of IR detector array were bonded with 3D MEMS antenna at low temperature process. To overcome those limitations, the proposed to novel 3D MEMS bonding technique that is mesh structure bonding (MSB) using Microchannel with PDMS injection. This MSB technique can be used to produce low temperature bonding, thickness control of bonding material and detail bonding at mesh structure.

CONCLUSION

In this paper, novel techniques and methods have been described to fabricate a 3D feed-horn MEMS antenna by

using a new UV lithography apparatus called the mirror reflected parallel beam illuminator (MRPBI) system 3D MEMS antenna design was optimized for an enhanced performance microbolometer using HFSS.

REFERENCES

[1] R A Wood, "Uncooled thermal imaging with monolithic silicon focal plane," SPIE, Vol.2020 Infrared Technology, pp.322-329, 1993

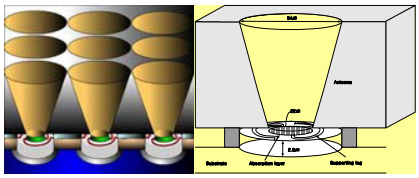

Figure 1: Schematic drawing of a 3D feed-horn MEMS Antenna coupled with a microbolometer.

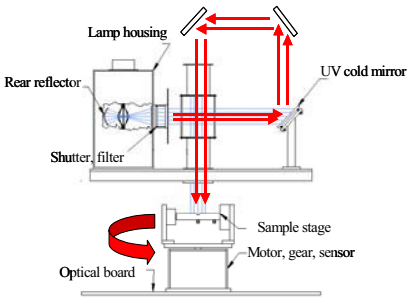

Figure 2: Schematic drawing of the MRPBI system

Figure 3: Inside photograph of MRPBI system

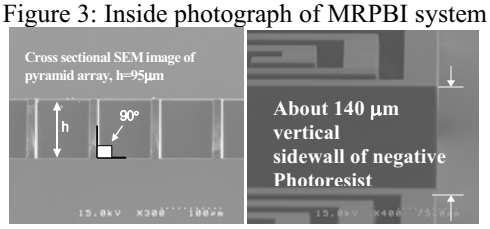

Fig.4 SEM images of a vertical sidewall array using a negative photoresist PMER, fabricate by MRPBI system

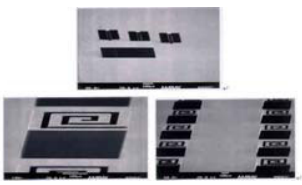

Fig.5 SEM images of an inclined sidewall array using a negative photoresist SU-8 fabricated by MRPBI system

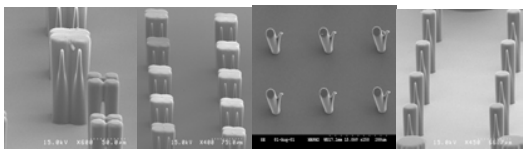

Fig.6 SEM image of quadruple shape arrays and teapot shaped arrays using negative PMER photoresist fabricated using the MRPBI system.

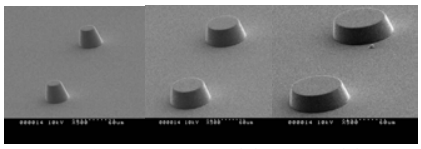

Fig.7 SEM images of feed-horn mold array.

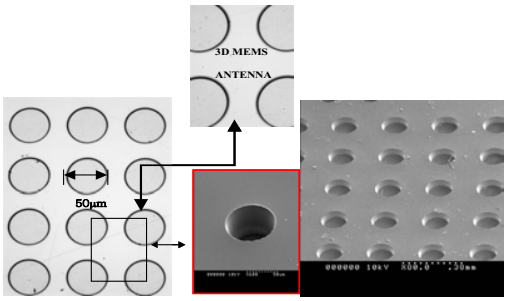

Fig.8 SEM images of 3D MEMS Antenna

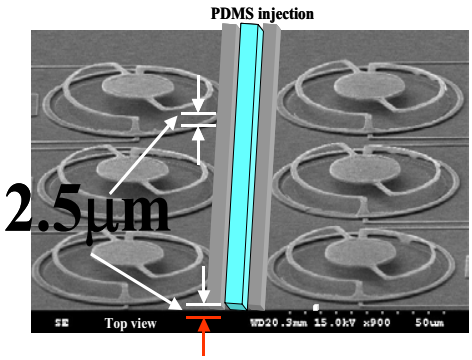

Fig.9 Mesh structure bonding (MSB) using Microchannel with PDMS

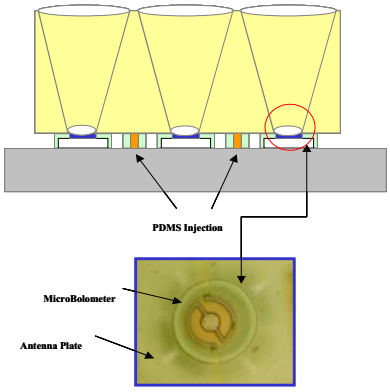

Fig.10 Micro assembly for 3D MEMS antenna with IR detector using mesh structure bonding (MSB) technique

Ferroelectric LTCC Tape for Piezoelectric Applications

Andrzej Łoziński[1], Jari Juuti[2], Johanna Honkamo[2] and Seppo Leppävuori[2]

[1/]Gdansk University of Technology, Dept of Optoelectronics, ul. Narutowicza 11, PL 80-952 Gdańsk, Poland
email: alozi@eti.pg.gda.pl
[2/]University of Oulu, Microelectronics and Material Physics Laboratories
EMPART Research Group of Infotech Oulu
FIN-90570 Oulu, Finland

***Summary**: The development of low temperature co-fired ceramic (LTCC) green tape for piezoelectric applications based on perovskite-type lead lanthanum zirconate titanate (PLZT) composition is reported. The green tape production process, the sample preparation, applied measurement methods and resulting dielectric and piezoelectric parameters of the PLZT samples produced from the green tape are described.*

Keywords: ferroelectrics, piezoelectrics, LTCC, PLZT.
Category: 2 (Materials and technology)

1. Introduction

Our former achievement in the production of good quality perovskite-type ferroelectric thick-films for utilization in piezoelectric devices [1] has promoted endeavours to produce low temperature co-fired ceramic (LTCC) tape for such applications. We utilized the tetragonal lead lanthanum zirconate titanate PLZT 7/62/38 composition. This notation means that the zirconium to titanium ratio Zr/Ti is 62/38 and 7 % of lead ions Pb^{2+} is substituted by lanthanum ions La^{3+}.
The paper reports the development of the green LTCC tape preparation process, the sample preparation, applied measurement methods and resulting dielectric and piezoelectric parameters of the PLZT samples produced from the green tape.

2. Green tape preparation

The used PLZT powders were prepared according to the process elaborated earlier [2]. The residual lead oxide excess was removed from the powders by washing them in acetic acid.
Green tape was prepared from 7/62/38 PLZT powder with 4% by weight of glass frit. The glass frit consists of 22.4 % SiO_2, 8.8 % B_2O_3, 66.6 % PbO and 2.2 % Al_2O_3. Properties such as specific surface area of PLZT powder were measured to optimise the amounts of additives and solvents for slurry preparation. PLZT powder and glass frit were mixed with solvents and dispersant in a ball mill for 24 hours, then plasticizers and binder were added and mixed for another 24 hours to obtain the slurry. The solvents were ethanol and xylene (50/50) and the dispersant was Blown Z-3 Menhaden fish oil, which also acts as a surfactant. The binder used was polyvinyl butyral (B98), and plasticizers were butyl benzyl phthalate (S160) and polyalkylene glycol (Ucon). The tape casting was done with a laboratory caster, Unicaster 2000, with a single doctor blade and a 250 μm wide gap. After drying, the thickness of the tape was ~60 μm with a smooth surface and flexibility enabling further handling for component preparation.

3. Sample preparation

Rectangular samples (14x12 mm) were prepared by cutting from the green tape. Ten layers were stacked and laminated together at 70 °C using 100 bar pressure and 20 min lamination time. After lamination, careful burnout of the organics was carried out before the sintering. Sintering was performed at 750-950 °C temperature in an alumina crucible and with the protection of a lead oxide atmosphere. The effect of increased sintering time was examined at the highest sintering temperature. After sintering, the AgPd electrodes were screen-printed and fired at 700 °C. Poling was carried out in silicone oil at 100 °C temperature and with 3.5 MV/m electric field.

4. Measurements and results

Dielectric hysteresis behaviour of the samples was investigated with a Radiant RTV6000HVS system. Remnant polarization was investigated at various electric fields and temperatures. Samples were poled with an E = 3.5 MV/m electric field and at T = 100 °C temperature.
A system based on a Michelson interferometer [3] was used to determine the piezoelectric coefficient d_{33} at 10 Hz frequency.
Table 1 presents the density, the relative permittivity ε' and dielectric loss tan δ (measured at 1 kHz frequency, 1 V_{rms}) of the samples in the virgin and poled state under various conditions of sintering.

Table 1. Density, relative permittivity and dielectric loss of the samples produced under various sintering conditions.

Sintering Conditions	Density [kg/m^3]	ε' virgin	ε' poled	tan δ virgin	tan δ poled
750°C; 30min	4882	214.77	216.26	0.0196	0.0209
850°C; 30min	5728	444.38	446.98	0.0219	0.0221
950°C; 30min	6244	503.74	502.93	0.0221	0.0191
950°C; 90min	6267	603.76	597.81	0.0223	0.0193

Shrinkage of the samples sintered at 950 °C for 90 min in X, Y, and Z directions was 15.1 %, 13.3 % and 17.4 % respectively.
Fig. 1. shows the temperature dependence of the remnant polarisation of the samples with different sintering conditions.

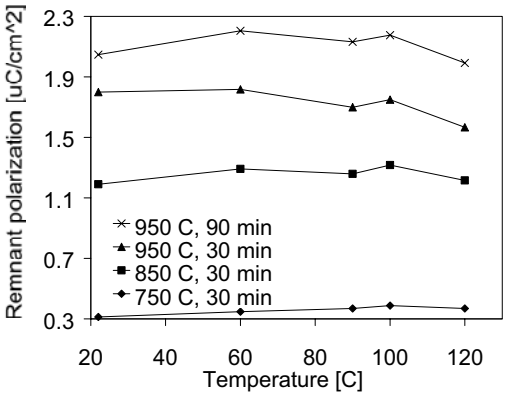

Figure 1. Remnant polarisation vs. temperature of samples sintered under various conditions, measured with 3.5 MV/m electric field.

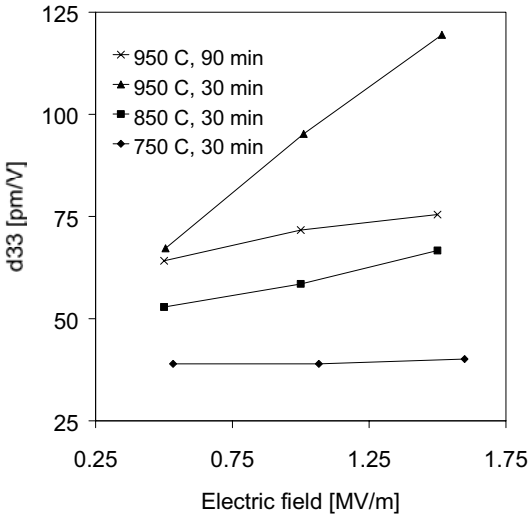

Figure 2. d_{33} coefficient vs. electric field of the samples sintered under various conditions.

Fig. 2 shows the dependence of the d_{33} coefficient as a function of the electric field applied to the samples sintered under various regimes.
The data from Table 1 shows that both the samples sintered at 950 °C gave reasonable results. However, the d_{33} coefficient shown in figure 2 points at the sample sintered for 30 min as the best one with the maximum value of 118 pm/V. The observed maximum value of d_{33} is higher than that obtained earlier with screen-printed samples (86 pm/V) [1].
Investigations to get optimum parameters are continuing.

5. Conclusions

The development of the LTCC green tape preparation process, the sample preparation, applied measurement methods and resulting dielectric and piezoelectric parameters of the PLZT samples produced from the green tape is reported.
Obtained results seem to be promising. Investigations, especially regarding the sintering and poling conditions, are continuing and the next, extended abstract will give more details and final results of the mature technology.

Acknowledgements

This work has been done within the 5th Framework Program of the European Community (project G5RT-CT-2001-05024, POLECER) and Polish State Scientific Committee (project Polar Films). The work is also part of the Finish Academy project 172304, TUKEVA programme and Finish National Technology Agency project 52059, PRESTO programme.

References

[1] A. Łoziński, J. Juuti, S. Leppävuori: LTCC compatible PLZT thick-films for piezoelectric devices, The 16-th European Conference on Solid-State Transducers, 15–18 Sept. 2002, Prague, Eurosensors 2002 - Proc (2002) 104-105. Czech Republic.
[2] A. Łoziński, F. Wang, A. Uusimäki, S. Leppävuori: PLZT thick-films for pyroelectric sensors, Mes. Sci. Technol. 8. (1997) 33-37. UK.
[3] H. Moilanen, S. Leppavuori: Laser interferometric measurement of displacement-field characteristics of piezoelectric actuators and actuator materials, Sensors and Actuators A 92 (2001) 326-334. Switzerland.

HgMnTe: a dual photodetective-magnetoresistive material

C. Reig[1], V. Muñoz-Sanjosé[2], I. Terry[3], L.A. Kosyachenko[4], Sun Weiguo[5]

[1]Universitat de València, Dept. d'Enginyeria Electrònica, Av. Dr. Moliner, 50, 46100-Burjassot, Spain
E-mail: candid.reig@uv.es http://www.uv.es/~candid
[2]Universitat de València, Dept. de Física Aplicada, Av. Dr. Moliner, 50, 46100-Burjassot, Spain
[3]University of Durham, Dept. of Physics, South Road, Durham DH1 3LE, United Kingdom
[4]Chernivtsy National University, Kotsyubinsky Street 2, 58012 Chernivtsy, Ukraine
[5]Optoelectronics Institute, PO Box 030, 471009 Luoyang, Henan, P.R. China

Summary: *HgMnTe, a promising diluted magnetic semiconductor material for magnetoelectronics, can be fitted to be used as IR photodetector in the range from 1.2 to 12μm. In this work we analyze the dependence of device performance on the growth method. Infrared detectors with p-n junctions formed by ion etching of p-$Hg_{1-x}Mn_xTe$ and Schottky barriers are reported. By using a new proposed highly efficient technique we have obtained an 'as grown' usable detector material, making the process economically attractive. The samples have been tested by means of electrical, optical and magnetoresistance measurements.*

Keywords: *semimagnetic semiconductors, magnetoresistance, photodetector, photodiode*
Category: *2 (Materials and technologies)*

1 Introduction

Spintronics and magneto-optics have become fields of increasing interest during the past decade. For long, diluted magnetic semiconductors (DMS) have been largely studied due to their unique magneto-transport and magneto-optical properties. We can name Faraday rotation and giant magneto-resistance (GMR) as the most important [1]. Recently, new discoveries have been carried out on the behaviour of these compounds, only reported for transition metals, before. In this sense, ferro-magnetism has been observed in zinc-blend III-V and II-VI Mn-based compounds, while new studies on Cr- and Co-based ones have highlighted new possibilities of these materials [2]. So, since 1990, several groups have tried to realise concepts comparable to GMR in a semiconductor device, so fitting better into the typical scheme of semiconductor very large scale integrated technology.

Among DMS's, $Hg_{1-x}Mn_xTe$ has specially attracted industrial interest due to its potentiality as a substitute of $Hg_{1-x}Cd_xTe$ photodetectors [2]. To achieve this, high quality material, with good transport and optical properties at device level, is need. In this work, we analyse such characteristics in diodes and samples obtained by different growth methods.

2 Photodiodes fabrication

Photodiodes were fabricated using bulk $Hg_{1-x}Mn_xTe$ ($x\approx0.1$) crystals prepared by both modified Bridgman (MB) technique [3], with a 4 weeks post-annealing process, and modified zone-melting (MZM) technique [4]. The diodes were prepared by Ar ion bombardment [3,4]. As a result, a p-to-n conversion takes place in the near-surface layer (~1 μm) with a sufficiently high electron concentration $n>10^{18}cm^{-3}$, i.e., n^+-p junction is formed (Fig. 1).

The diode structures exhibit appropriate rectifying properties and a typical photodiode behaviour. The contribution of diffusion, generation-recombination, tunnelling and avalanche processes to charge carrier transport in the photodiodes are reported. The detectivity of the photodiodes ($D^*=5\times10^{10}$ $cm\cdot Hz^{1/2}W^{-1}$ for the 10-11 μm wavelength cutoff) is competitive to that of $Hg_{1-x}Cd_xTe$ photovoltaic detectors and limited by the background irradiation 300 K, 2π FOV.

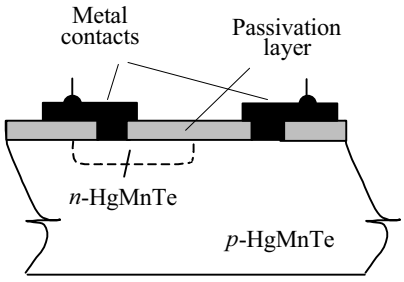

Fig. 1. Cross-section of HgMnTe photodiode

The electrical properties and detectivity of HgMnTe Schottky barriers have also been also studied. The principal parameters defining the characteristics of a diode structure, as well as the tunnelling and above-barrier (diffusion) carrier transport, are determined. The obtained experimental and theoretical data demonstrate the high detectivity of the Schottky diodes under study [5].

3 New material properties

Travelling zone (TZ) methods have at least four major advantages with respect to the common Bridgman method. The first is that the temperature of the process is about 150ºC lower. The second is that the TZ extracts the impurities and improves the purity of the so obtained material. The third is that

the segregation of Mn is overcome so improving the homogeneity of the ingot. The last advantage is that the lower temperature avoids the formation of Hg vacancies, that act as acceptors in HgMnTe.

$Hg_{1-x}Mn_xTe$ bulk crystals were produced by a variation of the travelling heater method (THM), consisting in the use, as a feed, of two segments of HgTe and MnTe with adequated sections for fixing the desired composition [6]. The growth was carried out at temperature of 600°C and rate of 2 mm/h. SEM and EDAX observations prove the crystals the shown an excellent axial and radial composition uniformity throughout the most of the total length (<1%). The yield of the process was about 80%.

The electrical characterisation was performed with the help of a closed cycle He cryostat embedded in a magnetic field of 0.3T. The samples were mounted in a Van der Pauw configuration. Both Hall and magnetoresistance measurements were carried out. In Fig. 2, we show the comparative results for several samples.

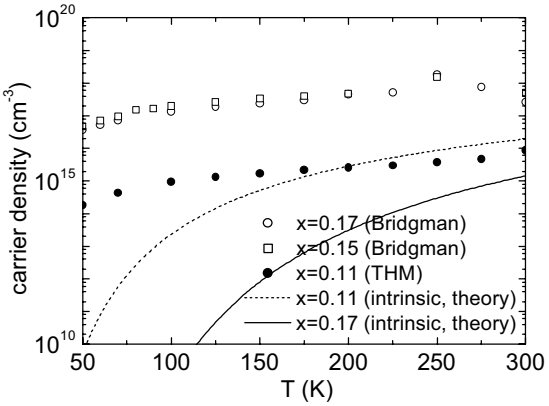

Fig. 2 Carrier density as a function of temperature

Calculated carrier concentration from this data were ~10^{17}cm^{-3} for MB samples, (2-5)×10^{16}cm^{-3} for MZM method and ~10^{16}cm^{-3} for THM samples. This latter value can only be achieved by MB material after long (several weeks) post-annealing processes in Hg high vapour pressure.

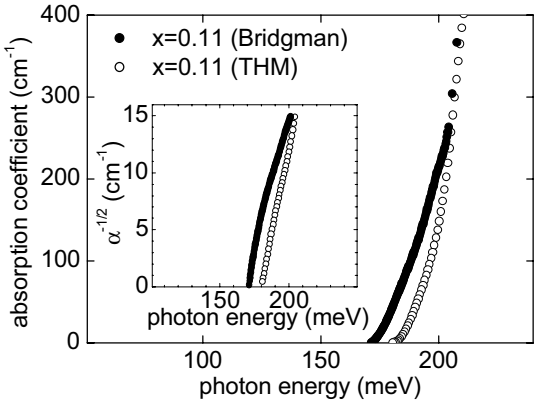

Fig. 3 FTIR optical absorption coefficient spectra

To analyse the optical behaviour, some samples were studied by means of FTIR. These samples were carefully ground to a thickness between 100 and 150 μm, while maintaining a mirror-like surface. A typical result of the FTIR measurement, from which absorption coefficient was calculated, is shown in Fig. 3. We can observe that the behaviour of the absorption coefficient follows that shown by the MB material for a comparable composition. The values obtained fell in the range of $0.110<x<0.113$, which highlights the excellent homogeneity of the whole ingot.

With alternative applications in mind, in Fig. 4, we present the dependence of the magnetoresistance with temperature of HgMnTe in a 0.3T magnetic field. As displayed in the graph, the use of this material as a magnetoresistive sensors should involve the use of a cooling system together with higher Mn concentration samples.

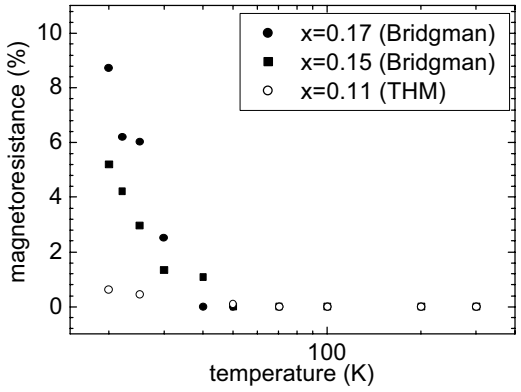

Fig. 4 Dependence of magnetoresistance on temperature

References

[1] G. Schmidt and L. W. Molenkamp. Dilute magnetic semiconductors in spin-polarized electronics. *J. Appl. Phys.* 89 (2001) 7443-7447.

[2] Piotrowski J and Rogalski A. New generation of infrared photodetectors. *Sens. Actuators A*. 67 (1998) 146-152.

[3] L.A. Kosyachenko, I.M. Rarenko, Sun Weiguo and Lu Zheng Xiong. Charge transport mechanisms in HgMnTe photodiodes with ion etched p-n junctions. *Solid-State Electron.* 44 (2000) 1197-2002.

[4] L.A. Kosyachenko, S.E. Ostapov, A.V. Markov and I.M. Rarenko. Electronic transport properties of HgMnTe n^+-p junctions. *Infrar. Phys. & Tech.* 44 (2003) 1-10.

[5] L.A. Kosyachenko, A.V. Markov, S.E. Ostapov, I.M. Rarenko, V.M. Sklyarchuk, Ye.F. Sklyarchuk. Electrical properties of narrow-gap HgMnTe Schottky diodes. *Semiconductors.* 36 (2002) 1138-1145.

[6] C. Reig, C. J. Gómez-García, V. Muñoz. A new approach to the crystal growth of $Hg_{1-x}Mn_xTe$ by the cold travelling heater method (C-THM). *J. Crys. Growth*. 223 (2001) 357-362.

The Optimization of High-Temperature Sensor Microhotplates Based on Thin Alumina Membranes

S.Yu.Gogish-Klushin[1], D.Yu.Kharitonov[1], M.Paranjape[2], A.V.Pisliakov[1], V.G.Pevgov[1], A.E.Senkin[3], A.A.Vasiliev[1]

[1] Russian Research Center Kurchatov Institute, Kurchatov sq. 1, 123182, Moscow, Russia
email: A-A-Vasiliev@yandex.ru, vasiliev@imp.kiae.ru, fax: +7-095-194-19-94
[2] Georgetown University, Washington, D.C., USA
[3] Novgorod State University, Velikii Novgorod, Russia

Summary: *The technology of the manufacturing of thin alumina membranes and microhotplates based on these membranes is developed. The optimization of the microhotplate layout and of the technology of the membrane fabrication permitted to obtain low power consumption at continuos heating (450^0C) of about 70 mW, "thermal" response time of the heater (63% level) of 50 ms, microheater resistance drift at 450^0C of less than 2 % per year; the microhotplate withstands more than $5 \cdot 10^6$ on-off cycles. The microhotplate was used for the deposition of semiconductor and thermocatalytic gas sensing inks and for the measurement of gas flow. Driving electronics for the gas sensor was designed.*

Keywords: *Alumina Micromachining, Microhotplate, Gas Sensor, Gas Flow Sensor.*
Category: *2 (Materials and Technology), 4 (Non-magnetic physical devices), 5 (Chemical Sensors).*

Introduction

Recent interest to the manufacturing of thin aluminum oxide film, different versions of micromachining with alumina films, and the fabrication of microhotplates using alumina membranes is due to the problems met by scientists and technologists working with silicon-based micromachining [1]. These problems are related with very big difference in mechanical and thermal properties of silicon and dielectric materials (that are silicon oxide, nitride and their combinations) used for the fabrication of thin membranes stretched on silicon frame.

Another problem, which is more important for high-temperature applications of microhotplates, for example for the fabrication of gas sensors, is poor adhesion of platinum and gold to the surface of silicon oxide. The application of titanium or chromium sub-layers does not solve this problem, because these metals are easily oxidized at high temperature. As a result, platinum adhesion is lost.

The last problem is related with the cost of silicon micromachined wafers, because the scale of sensor production is not sufficiently large.

Several research groups [2-4] tried to resolve these problems using an alternative solution, that is the application of aluminum oxide films.

The authors of papers [2] and [3] used anodic oxidation of aluminum for the formation of thin aluminum oxide. The film of alumina can be patterned using photoresist deposited on top of aluminum wafer before oxidation.

Free standing alumina film is obtained by selective etching of aluminum. The alumina film has rather good quality and can be used for the manufacturing of different sensors.

From our point of view, the main disadvantage of this film is that it contains amorphous phase, and therefore re-crystallizes at high temperature necessary for the annealing of gas sensing layers (700 – 800^0C).

We used another way, the formation of poly-crystalline membranes on alumina ceramic frame.

Experimental

Thin polycrystalline γ-alumina film was formed on top of the alumina ceramic substrate (48x60 mm). The diameter free-standing part of the membrane was equal to 3 mm, the size of the chip was 6x6 mm.

The view of the of the chip is given in Fig. 1.

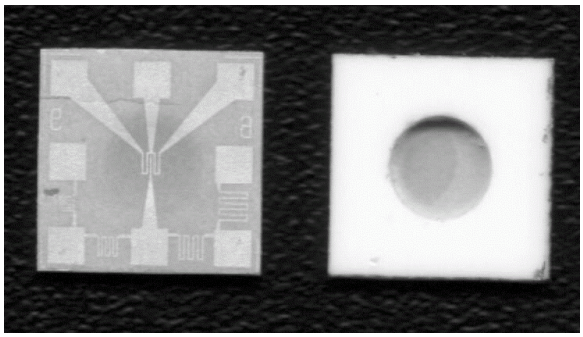

Fig. 1. The view of the chip with alumina membrane and platinum vacuum sputtered heater.

The optimal thickness of our membrane equals to about 30 μm. This thickness is a compromise between

sufficiently low heat conductivity from the heater and mechanical properties.

The membrane is porous. Its specific area equals to about 100 m^2/g, this enables the application of the polycrystalline material as a support for the catalyst for thermocatalytic gas sensors.

The heater was formed on top of the membrane by magnetron sputtering and patterned by photolytography and ion etching. The optimum size of the heater is about 300x300 μm. The sensor with this heater consumes about 70 mW at 450^0C.

Problems related with the impregnation of the membrane material with photoresist were avoided by the application of shadow masks using SU-8 technology.

Results and Discussion

Thermal properties of the microhotplates were tested. One of the most interesting applications of such membranes is related with its low heat capacitance, which enables the operation of gas sensors in pulsing mode and self-calibration of thermocatalytic gas sensors. "Thermal" response time of microheater ($\tau_{0,63}$) is equal to about 50 ms.

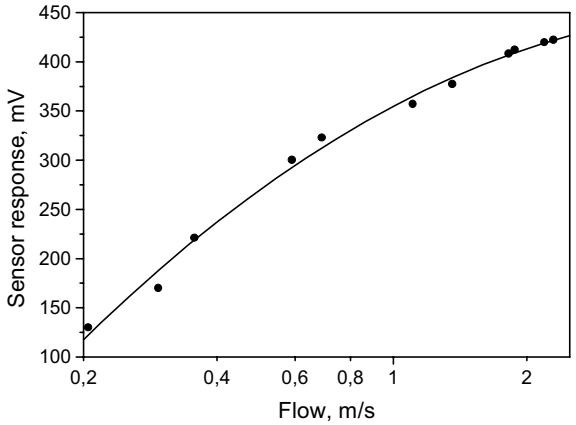

Fig.2. The calibration curve of air flow meter based on alumina microhotplate.

Another application of microheaters on alumina membranes is gas flow meters, in particular for natural gas and for car engines. In the last case, an important property of these microheaters, in contrast to silicon based elements, is the possibility of their heating up to high temperature necessary to burn out surface contamination. The calibration is given in Fig. 2.

For the compensation of the variations of ambient temperature, we placed reference resistor on the frame of the sensor chip. In the Fig. 3, the temperature dependence of both resistors is shown.

Long-term stability of platinum microheaters on alumina membranes was tested at 450^0C. This temperature is typical of both semiconductor and thermocatalytic methane gas sensors. The data are presented in Fig.4. The variations of heater resistance are correlated with changes in ambient temperature.

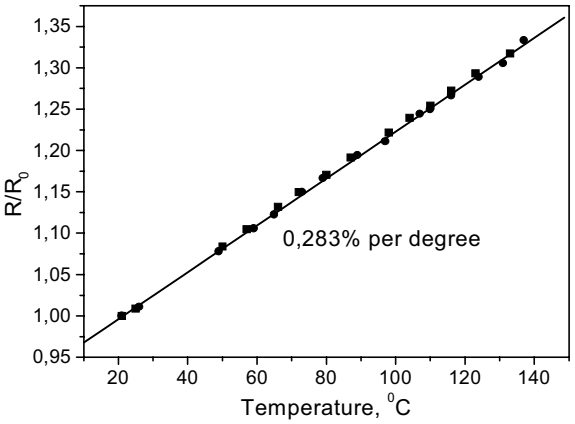

Fig. 3. TCR of platinum resistor on the alumina membrane (circles) and on the frame (squares).

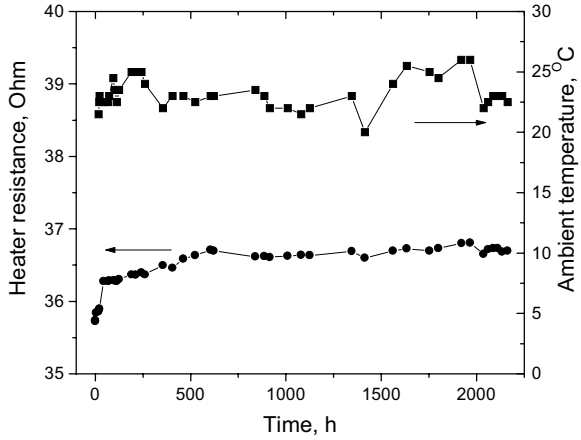

Fig. 4. Long-term stability of Pt heater on alumina membrane at 450^0C

After initial stabilization, the drift of heater resistance is below 2 % per year.

The deposition of thick SnO_2 and Al_2O_3/Pt/Pd permitted to obtain gas sensors with properties similar to described earlier [1]. Microprocessor based electronic controller taking into account the layout of the sensor was designed.

References

[1] D.Vincenzi, M.A. Butturi, A.Vasiliev, et al. Development of a low-power thick-film gas sensor deposited by screen-printing technique onto a micromachined hotplate. Sensors and Actuators B: Chemical, Vol. 77 (1-2) (2001) pp. 95-99

[2] A.Govyadinov, P.Mordilovich, et al. Anodic alumina MEMS: application and devices. MEMS - 2000, Nov. 5-10, 2000, Orlando, Florida, vol.2, ASME, New York, p.313 (2000).

[3] I.L.Grigorishin et al. Hydrogen sensor based on thermoelectric transducer. Russian Journal "Sensor", N 3, 2002, p.47.

[4] A.A.Vasiliev, S.Yu.Gogish-Klushin, et al. A novel approach to the micromachining sensors: the manufacturing of thin alumina membrane chips. "Eurosensors XVI", Prague, October, 2002, p.129.

A Novel Ultra Violet Assisted PET Micromachining

T. Maleki[1], S. S. Mohajerzadeh[2] and S. Mohammadi[3]

[1,2]University of Tehran, campus No.2, Electrical engineering Dept., North Karegar Street,. Tehran, Iran
[3]Dept of Electrical and Computer Eng., Purdue University, USA
email: smohajer@sun1.vlsi.uwaterloo.ca

Summary: *A novel ultraviolet assisted micro-machining is presented in which the etching of PET substrates is ani-isotropic in the direction of light illumination. The etching of plastic is performed in a DMF solution and desired pattern is obtained by photolithography. The effects of solution temperature and light intensity have been studied. An average etch rate of 10 µm/hr is achieved without any mask undercut. This technique has been applied to realize square membranes, 60 µm thick micro-gears and micromolds.*

Keywords: *PET, DMF, UV etching, micromachining*
Category: *2 (Materials and technology)*

1 Introduction

Poly-Ethylene-Terephthalate or PET is a suitable choice for many large area electronic applications. It can tolerate operating temperatures up to 120°C [1]. It has also been observed that the presence of ultraviolet illumination during the etching process enhances the removal of PET, accelerating the etching phenomenon [2]. The PET used in our experiments are transparent foils with 120 µm thickness. They are cleaned using an RCA#1 solution for 12mins followed by rinsing in DI water and blow-drying. We report a novel micro-machining of plastic substrates using solvent etching in the presence of ultra-violet illumination. While no dissolution of PET is observed in pure Di-Methyl-Formamide (DMF) solution, exposure of the sample to UV leads to dissolution of substrate in the direction of light. Also regions which have been masked from UV light remain intact.

2 Experimental setup

In figure 1, one can see the schematic setup used for this experiment. The setup consists of a water-cooled glass container with a controlled liquid solvent temperature. The top lid of the container is made from quartz to allow proper transmission of UV photons. Intensity of the UV light has been measured at a wavelength of 360nm and at the place of the sample. Normally DMF has been used as the chemical solvent, although a mixture of Di-Chloro-Methane (DCM) and DMF has been also exploited. Addition of DCM has degraded the chemistry of the etching by attacking the masking layer and roughening the crater surface. The masking layer in these experiments have been a bi-layer of germanium-copper alloys with four periods and typical thickness of 60Å and 300Å for copper and germanium layers, respectively. This combination has been found to be suitable as the masking layer to protect the PET from being exposed to UV as well as solvent in the unwanted areas. For the formation of masking layer, cleaned samples are loaded in a vacuum chamber and deposition is made at a substrate temperature of 110 °C and at base of 1×10^{-6} torr.

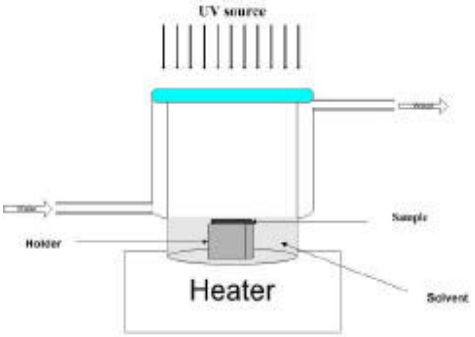

Fig1: Schematic of the setup used for ultraviolet assisted micro-machining. Quartz plate used to prevent evaporation of DMF.

2 Parameter optimization

There are two major parameters that influence the etch rate of PET. The first one is solvent temperature. Figure 2 shows the etch rate of PET as a function of temperature while UV intensity kept constant at 4 mw/cm^2. As shown, at temperatures lower than 50°C, etching will be stopped or is insignificant. At temperatures higher than 120°C considerable warping in the substrate is observed, hampering the etching process. At temperatures ranging from 70 to 120°C a reasonable and monotonic rise in the etch rate is observed without any damage to the substrate after extended etching periods. In Figure 3 one can see the effect of UV intensity on the etch rate of PET while solvent temperature remains at 120°C. Increasing the

intensity of UV leads to a monotonic and linear enhancement in the etch rate of substrate. Further increase in the intensity of UV light may degrade the PET itself. A maximum etch rate of 10µm/hr is obtained from the observed data by optimizing these parameters.

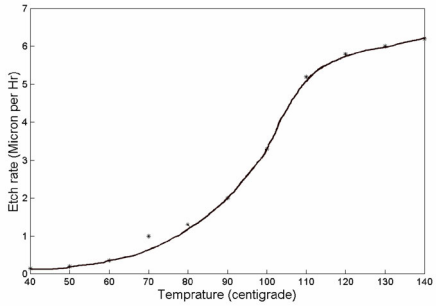

Fig2: Etch rate of the PET as a function of solution temperature

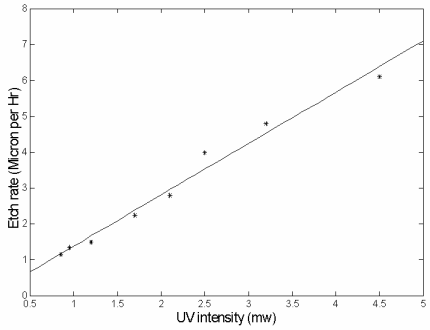

Figure3: Etch rate of PET as a function of UV intensity

3 Experimental results

In Figure 4 SEM image of a microgear, fabricated using this technique is demonstrated. The thickness of the gear is 60ìm and its diameter is 400ìm. Sharp edges of the gears indicate proper vertical etching of the substrate. The masking layer has survived a 6-hour etching process. Axel of the gear has been prepared using similar condition. In figure 5 SEM veiw graph of a plastic mold for fabricating a metal microgear is shown. Electroplating is needed to complete the fabrication.

Apart from microstructures, we have also realized Ge/Al thermocouples on PET substrates. Al has been used as a pair of thermocouple junction due to its compatibility with PET. Membranes with 20 µm thickness have been realized using UV-assisted etching technique, carried out from the back side of the thermo- arrays. Figure 6 shows a Ge/Al thermo-array fabricated on plastic under an intentional bent. The depth of the crater is about 100 µm and membrane thickness is about 20 µm. The electrical characteristics of the array show a seeback coeficient of 100 ìV/ºC for Al-Ge junction.

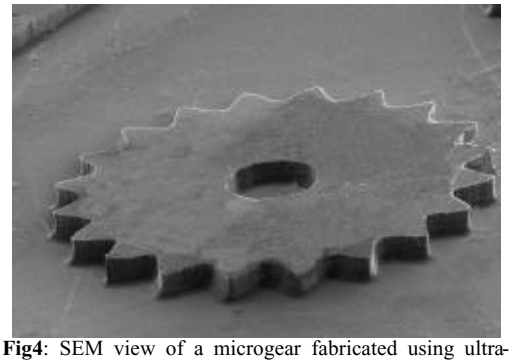

Fig4: SEM view of a microgear fabricated using ultra-violet assisted an-isotropic etching of PET.

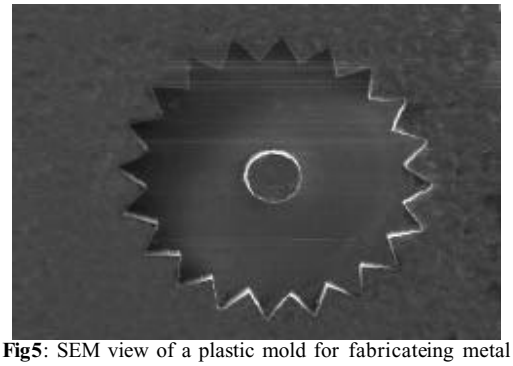

Fig5: SEM view of a plastic mold for fabricateing metal microgear using electrodeposition.

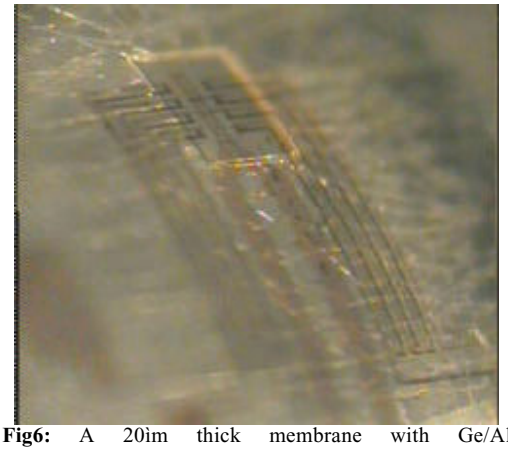

Fig6: A 20ìm thick membrane with Ge/Al thermocouples on its other side. Thinner membrane will increase the sensitivity of thermocouples.

References

[1] H.Dreuth, C.Hieden, "Thermoplastic structuring of thin polymer films", *Sensors and Actuators A. 78* PP. 198-204, 1999. Elseveir.

[2] P.Apel, "track etching technique in membrane technology" *Radiation measurements 34*, PP. 559-566 ,2001, Elseveir.

[3] A.i.Vilenskey, D.l.zagorski, S.A.Bystrove, "Investigation of latent tracks in poly-ethylene-terephthalate and their etching", *Surface Science 507-510*, PP. 911-915, 2002, Elseveir.

The influence of isopropyl alcohol on etch rates and roughness of silicon (hkl) surfaces

I. Zubel[1], M. Kramkowska[1]

[1]Wroclaw University of Technology, Faculty of Microsystem Electronics and Photonics,
Janiszewskiego 11/17, 50-372 Wroclaw, Poland
email: irenaz@wemif.pwr.wroc.pl

Summary: *Silicon wafers with untypical crystal orientations have been etched in KOH and KOH saturated with isopropyl alcohol solutions. Etch rates of different (hkl) planes were estimated. The effects of IPA additive on etch rates and surface roughness of considered planes were analysed. It was shown that IPA affects only the planes of (hh1)-type, causing both their etch rate reduction and surface quality improvement. The planes influenced by IPA feature with a specific bond configuration, different from the planes which are not sensitive to IPA effect.*

Keywords: *silicon, anisotropic etching, (hkl) planes, crystal orientation, surface roughness, etch rates*
Category*: 2 (Materials and technology)*

1 Introduction

Wet anisotropic etching of silicon substrates is commonly used in micromechanics for fabrication of different MEMS structures including membranes, "bossed-type" features, suspended beams, seismic masses, etc. The etching in KOH solutions makes up serious problems connected with undercutting of convex corners. Beneficial influence of isopropyl alcohol (IPA) on the reduction of convex corners undercut has been known for many years and reported in the literature [1,2]. IPA addition results in etch rate reduction of some crystal planes, especially those ones, which are prone to develop on the convex corners of etched structures. However, the effect of IPA on the roughness of different (hkl) crystal planes has not been considered yet.

2 Experimental

Silicon substrates with (100), (110), (311), (211) and (331) crystal orientations have been studied. The substrates were etched in 10 M KOH and 5 M KOH+IPA solutions since the both solutions give satisfactory quality of (100) Si surface. The process was carried out at the temperature of 75°C for the time assuring etching depth of several tenth of micrometer. The etched substrates were subjected to SEM observations. The etch depth was measured with a micrometric gauge, or in case of very rough bottom surface, by assessing the depth of cross-section from SEM observations.

3. Results

Etch rates in different [hkl] orientations in KOH solution have been evaluated by different authors. The most comprehensive database has been presented by Sato [3] on the basis of silicon sphere etching. The etch rates in KOH+IPA solutions are rather uncommon. The values of etch rates for particular crystal planes, especially those, which were prone to develop on the sidewalls of convex structures, have been presented in our previous works [4]. The substrates with different crystal orientations enabled us to measure the etch rates directly.

3.1 Comparison of etch rates in KOH and KOH+IPA solutions

The relative values of etch rates (V_{hkl}/V_{100}) in KOH and KOH+IPA solutions, obtained from direct measurements of etches depth on different (hkl) substrates, are shown in fig. 1. The angles between (hkl) and (110) planes are indicated on x-axis. The data for KOH solution show a good agreement with the results by Sato et al. [3].

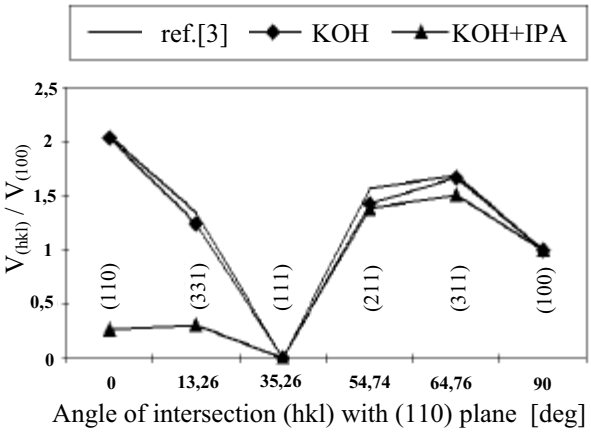

Fig. 1 Relative etch rates in KOH and KOH+IPA solutions for different (hkl) planes. Solid lines reperesent the results by Sato et al [3]; squares and traingles are the authors' experimental results

The plot for KOH solution shows clearly that etch rates of (hkl) planes are lower than of (100) one, only in the vicinity of [111] crystal orientation. For the other planes the relation of $V_{hkl}>V_{100}$ holds. The peak value of etch rate ratio $V_{hkl}/V_{100} \approx 2$ is located near (110) plane.

IPA addition to KOH solution results in dramatic reduction of etch rates of some crystal planes of hh1-type. The most pronounced effect of etch rate reduction (by 8x) can be observed for (110) plane. IPA does practically not affect the planes of h11-type. Fig. 2 shows etch rate ratios in KOH and KOH+IPA solutions versus the angle of inclination of (hkl) plane towards (110) one. Error bars represent the possible measurement error, which is especially large in the case of (111) plane due to its very low etch rate.

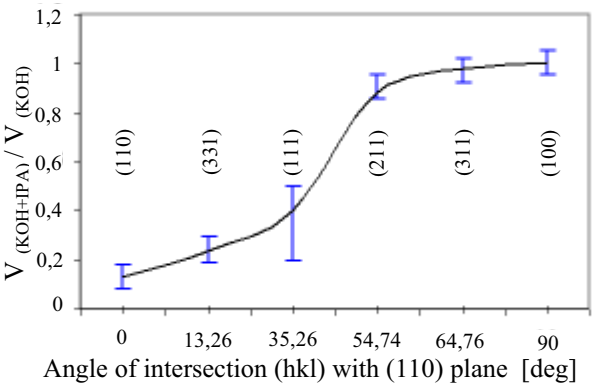

Fig.2 Etch rate ratio in KOH+IPA and KOH solution for different (hkl) planes

3.2. The roughness of surfaces etched in KOH and KOH+IPA solutions

SEM images of (211), (311), (331) and (110) surfaces, etched in both considered solutions, are shown in figs. 3 and 4. The images for (100) and (111) planes have been neglected because the surfaces were optically smooth both after KOH and KOH+EPA etching.

In pure KOH solution only (311) planes exhibit smoothness comparable with (100) surface. The (110) and (211) planes are remarkably inferior. The most distinguished roughness appears, however, on (331) planes.

IPA addition to KOH solution resulted in remarkable improvement of (331) surface quality. Slight improvement has been also observed in the case of (110) plane. The both of planes featured with distinguishable etch rate reduction due to IPA addition. The effect of IPA on the roughness of (311) and (211) planes, where the additive does not cause any etch rate reduction, is apparently negative. The whole surface is covered with bulky hillocks, which are typical for the surfaces etched in KOH+IPA solutions. SEM images, shown in figs. 3 and 4 indicate that the surface features reflect the layout of (111) planes, characteristic for the surface orientation. The correlation of surface relief with the type of surfacial bonds and the layout of (111) planes on a particular (hkl) surface is a key for the consideration of IPA effect on different (hkl) planes. The considerations will be carried out in the extended version of the work.

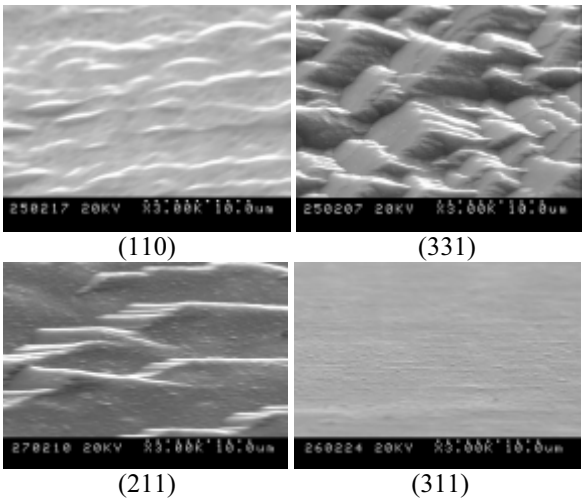

Fig.3 Different (hkl) planes etched in KOH solution

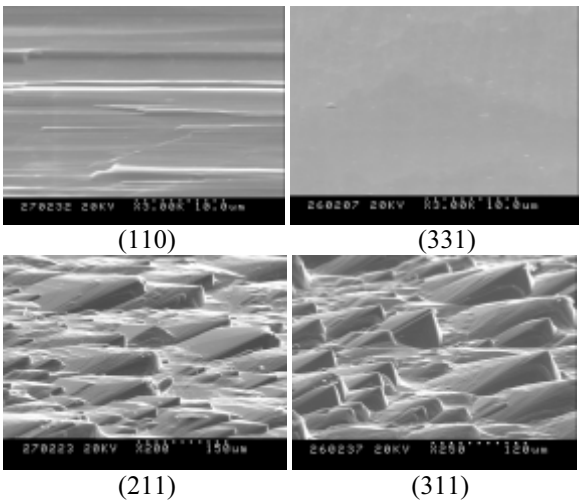

Fig.4 Different (hkl) planes etched in KOH+IPA solution

References

[1] J.B. Price. In: H.R. Huff, R.R. Burges, eds. Semiconductor Silicon, the Journ. Electrochem. Soc. Softbond, Proc. Ser. Princeton, NY, 1973 339-351

[2] I. Barycka, J. Dziuban , M. Kramkowska, I. Zubel. Compensation of convex corners in sensors with bossed structure etched in TMAH and TMAH+IPA solutions, Proc. SPIE, Optoelectronic and Electronic Sensors IV, 4516, 2000, 56-65

[3] K. Sato, M. Shikida, Y. Matsuhima, T. Yamashiro, K. Asumi, Y. Iriye, M. Yamamoto. Characterization of orientation-dependent etching properties of single-crystal silicon: effects of KOH concentration, Sens. Actuat. A 64 1998 87-93

[4]I. Zubel, M. Kramkowska. The effect of isopropyl acohol on etching rate and roughness of (100) Si surface etched in KOH and TMAH solutions, Sens. Actuat. A 93 2001 138-147

Chemiresistive properties of lead nanoparticles, covered by oxide layer

V. Bochenkov, V. Zagorsky and G. Sergeev

Lomonosov Moscow State University, Chemistry Dept., Leninskie gory, 119992, Moscow, Russia
email: boch@kinet.chem.msu.ru

Summary. *Nanostructured lead thin films were synthesized by vacuum deposition of metal vapors on the substrates at 80 K. Then samples were heated to room temperature and exposed to the air. High sensitivity to water and ammonia vapors in the air at room temperature was found for thus prepared materials. It is compared to that of the films, prepared previously by condensation of lead vapors on pre-deposited p-xylylene film [1, 2].*

Keywords: core-shell nanoparticles, gas sensors, lead oxide
Category: 2 (Materials and technology)

1 Introduction

Recently, the sensitivity of lead-containing poly-*p*-xylylene films to the presence of ammonia in the air was found [1, 2]. Films were prepared by the condensation of *p*-xylylene vapor on the substrate at 80 K, followed by lead vapors deposition. Polymerization of monomer was initiated thermally at 110-150 K, or by UV-irradiation at deposition demperature. Samples were as sensitive as conventional semiconductor sensors, with the operating temperature 20-25 °C instead of 200-300 °C. This work aimed at closer investigation of this system, clarifying the role of the polymer and studying its effect on sensitivity.

2 Experimental

Series of metal-polymer films with different quantity of lead were prepared by the technique and using cryostats, which were described in detail elsewhere [3]. Shortly, the technique involved of *p*-xylylene was synthesized by *in situ* pyrolysis of *p*-cyclophane in the gas phase and deposited on the substrate at 80 K. Lead was evaporated by resistive heating at 650 °C and condensed on *p*-xylylene film. After that the film was heated up to room temperature, undergoing the polymerization of *p*-xylylene.

Experiments without polymer included lead deposition on the substrate at 80 K and heating in vacuum up to room temperature. After that, lead particles were exposed to the air.

We used textolite supports with copper electrodes and ceramic supports with stainless steel interdigitated electrodes. Resistance measurements were carried out in DC-regime, in range from 10 to 10 V using Keithley 614 electrometer.

In all cases metal content was controlled by conductivity measurements during the deposition. Evaporation stopped after obtaining island film with the resistance about $2 \cdot 10^{10}$ Ω . This technique was described in detail recently [4].

3 Results

In order to distinguish the influence of different factors on the film conductivity, the experiments with dry ammonia nitrogen mixture and humid ammonia were carried out. It has been found that the film samples do not change their resistance in such conditions. Introducing water vapors in the dry ammonianitrogen gas mixture decreases the resistance dramatically.

At the next step the investigation of humidity influence on sample resistance were carried out. Different values of humidity were obtained using several saturated aqueous solutions of salts. Some preliminary results for the films with different lead content are presented in Table 1.

Table 1: The resistance of lead-poly(*p*-xylylene) films at different relative humidity at room temperature.

	Relative Humidity,%		
Pb, %	54	75	97
6	$1 \cdot 10^{16}$	$3 \cdot 10^{14}$	$1 \cdot 10^{13}$
10	$3 \cdot 10^{14}$	$1 \cdot 10^{14}$	$1 \cdot 10^{12}$
20	$8 \cdot 10^{13}$	$2 \cdot 10^{13}$	$3 \cdot 10^{12}$

We have found that only the value of relative humidity value higher than 54 % significantly influences the sample resistance. As a result, the co-operative effect of water vapors and ammonia on the resistance is much larger than the effect of the individual components. Thus, estimated values of film resistance of samples, placed in dry ammonia-nitrogen gas mixture or in the dry air are about 10^{15}–10^{16} Ω; in saturated

water vapors (97 %) - about 10^{12}–10^{13} Ω, and above the aqueous solution of ammonia - about 10^{11} Ω.

The morphology of such films was characterized by Atomic Force Microscopy. Fig. 1 presents an example micrograph. The nanoparticles about 50 nm in size agglomerate, yielding structures about 200 nm.

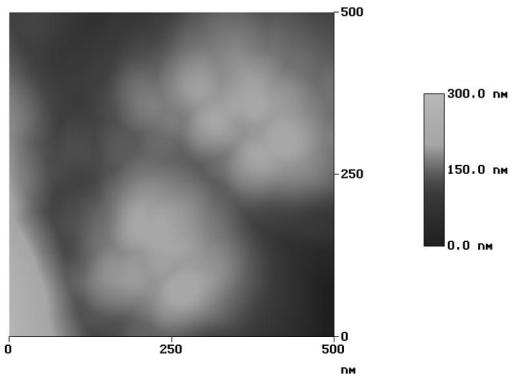

Fig. 1: Morphology of lead-poly-p-xylylene film.

Our next step was to investigate the role of the polymer in such nanostructured films. In order to do this a number of samples without polymer was prepared.

The resistance of the films at different relative humidity was studied in DC regime. Resulting dependence is presented in Fig. 2. Sensor response was found to be larger for such samples in comparison with those, containing isolating polymer.

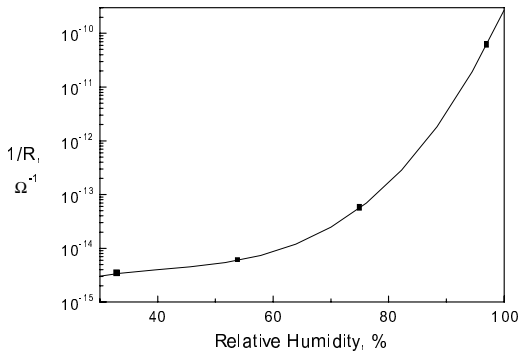

Fig. 2: Conductance of nanostructured lead film at various relative humidity at room temperature.

Lead nanoparticulate films, prepared on silica, were characterized by Scanning Electron Microscopy. Particle sizes, estimated from micrograph, are about 200 nm. The example of the micrograph is presented in Fig. 3.

We consider the chemiresistive effect on such films in frames of conventional metal-oxide semiconductor model, where the adsorption-desorption of oxygen takes a significant part.

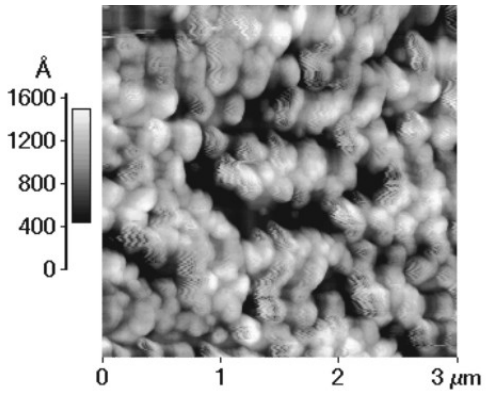

Fig. 3: Microstructure of lead island film.

4 Conclusions

The gas sensitivity of lead-poly-*p*-xylylene films is supposed to arise due to partial oxidation of the lead nanoparticles, thus producing semiconducting layer on the metal particle surface. Lead core works as electron dopant, increasing the concentration of electrons in conduction band and decreasing the operating temperature of the sensor.

The sensitivity of lead island films, formed without poly-*p*-xylylene matrix, is higher than that of metal–polymer films.

5 Acknowledgements

We thank Prof. L.Brehmer, Institute of Physics, Potsdam University and his team for help in electrical and microscopic measurements.

The work was partially supported by INTAS 2000-00-911 and RFBR 02-03-32469 grants.

References

[1] V.V. Zagorsky, M.A. Petrukhina, G.B. Sergeev, V.I. Rosenberg and V.G. Kharitonov. Patent RFN 2017547, 15 August 1994.

[2] G. Sergeev, V. Zagorsky, M. Petrukhina, S. Zav'ialov, E. Grigor'ev and L. Trakhtenberg. Preliminary study of the interaction of metal nanoparticle containing poly-*p*-xylylene films with ammonia. *Anal.Commun.* **34** (1997) 113–114.

[3] G. Sergeev, V. Zagorsky and M. Petrukhina. Nanosize metal particles in poly(*p*-xylylene) films obtained by low temperature codeposition. *J.Mater.Chem.***5**(1) (1995) 31–34.

[4] V.E. Bochenkov, N. Stephan, L. Brehmer, V.V. Zagorskii and G.B. Sergeev. Sensor activity of thin polymer films containing lead nanoparticles. *Colloids&Surfaces A* **198-200** (2002) 911–915.

Liquid crystal wavefront corrector with modal response

M. Loktev[1], G. Vdovin[1] and P. Sarro[2]

[1]Delft University of Technology, Electronic Instrumentation laboratory,
Mekelweg 4, P.O.Box 5031, 2600 GA Delft, the Netherlands
email: m.loktev@its.tudelft.nl http://guernsey.et.tudelft.nl
[2]Delft Institute of Microelectronics and Submicron Technologies (DIMES),
Feldmannweg 17, 2628 CT Delft, the Netherlands

Summary: *Development of a silicon-based liquid crystal phase modulator for adaptive optics applications is reported. The advantage of this technology is that low-order wavefront aberrations can be compensated in a continuous way and using a relatively small number of actuators. It is shown that the device can operate with one or two degrees of freedom per actuator, depending on requirements to the quality of correction. Design and technology of the reflective-type modal LC corrector with silicon backplane is described. Experimental investigation of the prototype, which was manufactured using different technology, is presented. Possibilities for further development are discussed.*

Keywords: *spatial light modulators, phase modulation, liquid crystals, adaptive optics*
Category: *2 (Materials and technology)*

1 Introduction

Classic adaptive optics system uses a wavefront sensor to measure random phase deformations induced by a distorting media and a wavefront corrector to compensate them in real time. Traditionally, deformable mirrors that exist in a number of modifications represent primary technology for wavefront corrector [1].

Liquid crystal phase modulators were suggested as a low-cost alternative to deformable mirrors for budget-sensitive industrial and medical adaptive optics applications. They have wide potential opportunities: low control voltages (units of volts), which makes this technology compatible with CMOS processes), large stroke range (tens of wavelengths), low power consumption (0.1 mW/cm^2), no moving parts and low cost of materials.

There are a number of commercially available LC correctors with pixelated structure of actuators, whose operation is similar to that of piston-type segmented mirrors [2]. But this type of device requires large number of pixels to produce a good approximation to smooth continuous wavefronts. This paper is devoted to the development of an LC corrector with modal response, which provides a spatially continuous phase modulation and a reasonable approximation to low-order aberrations even for a relatively small (several tens) number of actuators. It was shown that the device can operate with one or two degrees of freedom per actuator, depending on requirements to the quality of correction.

2 Design

Operation of a reflective-type modal LC corrector is based on change of the birefringence of a thin layer of nematic LC under applied electric field (Fig.1). The device is driven by AC voltages applied through a set of point-like contacts connected to a special resistive layer, which ensures continuous voltage variation across the aperture, resulting in a smooth phase response. The dielectric mirror covers the resistive layer improving the corrector's reflectivity.

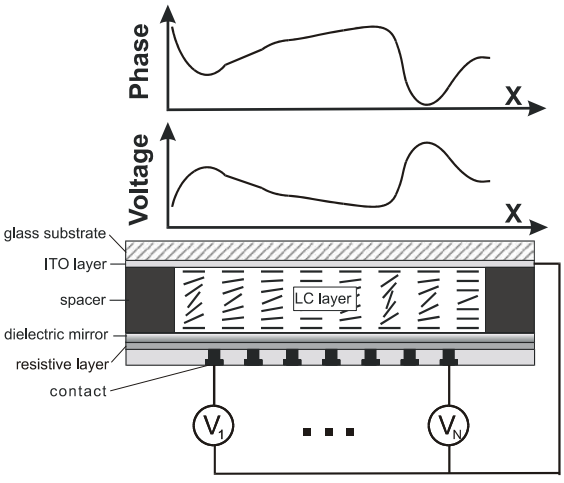

Fig. 1. Structure of a modal LC corrector

Series of 37-channel devices with 30-mm and 70-mm aperture were produced earlier using glass-based technology [3]. Nevertheless, this technology is quite expensive and is hardly suitable for serial production. Another option is offered by silicon technology, which allows to form required structure of actuators on the surface of a chip using standard IC manufacturing processes (Fig.2). An important

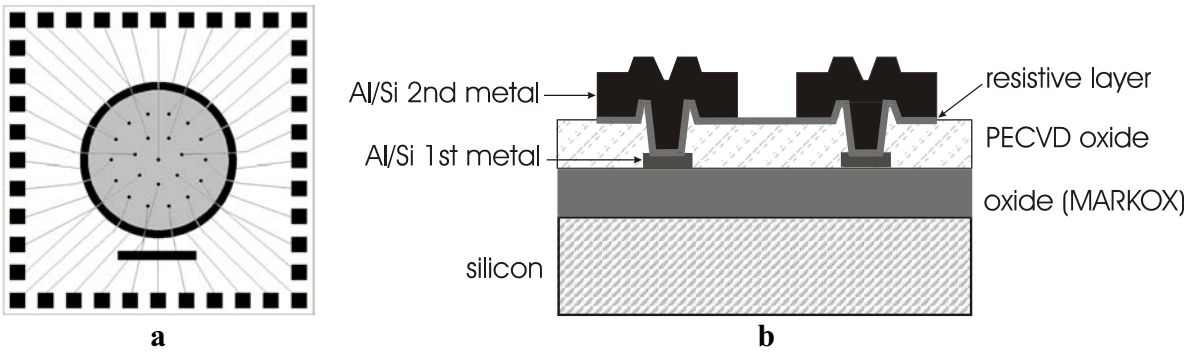

Fig. 2. Design of the backplane for 39-channel modal LC corrector; (a) view from top; (b) cross section.

advantage of silicon-based technology is in possibility to integrate of an optical part of the device and a part of control electronics in a single chip. It allows reducing the number of inputs of the chip relative to the number of actuators, which makes the technology scalable.

In the present design (Fig.2) the backplane of LC modulator contains the structure of control electrodes formed by two metal layers (Al/Si alloy). Contacts in the active area and contact pads at the periphery are formed in the upper metal layer, and the lower one provides wiring between them. A layer of silicon oxide ensures isolation between the metal layers. One of the main technical difficulties was in manufacturing of the resistive layer with sheet resistance in the range ~1-10 MΩ/sq. Recently these properties were demonstrated for thin films of *n*-type doped silicon carbide, which were deposited using PECVD technology and then annealed with an excimer laser operating in UV range. To improve electric contact between thin (~100 nm) carbide layer and thick (0.6μm) top metal layer, the second one is deposited on top of the carbide. This design is actually in process.

3 Methods of control

The modal LC wavefront corrector is unique among other types of modal correctors in that it can be operated with several degrees of freedom per actuator. Each of the driving AC voltages is characterized by several parameters; namely, amplitude, frequency, phase and harmonic structure of the wave. It is shown that variation of any of these parameters for a given contact changes either its electro-optic response or the result of its interaction with neighboring contacts. It is necessary to realize which set of control parameters provides the maximum flexibility of the device and the best correction quality.

With this purpose we performed investigation of several methods of control using numerical simulation and analytic approach; some of the results were verified experimentally using a prototype. Two methods were found to be the most useful.

1) *Single-frequency control (SFC) under which means that all contacts are driven with AC voltages of the same frequency; all control voltages are in phase.*

This method provides the correction quality close to that of deformable mirrors; efficiency of 37-channel corrector with hexagonal arrangement of contacts is estimated as 22 Karhunen-Loeve modes. Linear control algorithms can be implemented; it is already proved to work in experimental adaptive optical system.

2) *SFC with additional adjustment of phase shifts between the voltages.*

This method can be used for further improvement of the results obtained by the 1st method. Simulations have shown that the reduction of residual aberrations due to optimization of phase shifts can reach 65%. This method demonstrates the maximum flexibility.

4 Outlook

1) Realization of dynamic control and development of integrated electronics for demonstration of the scalability.

2) Application of a dual-frequency control technique for improvement of dynamic characteristics of the corrector.

References

[1] R. K. Tyson, Principles of Adaptive Optics, second edition, Academic Press, Boston, 1998.

[2] D. Dayton, S. Browne, J. Gonglewski and S. Restaino, Characterization and control of a multi-element dual-frequency liquid-crystal device for high-speed adaptive optical wave-front correction, *Applied Optics* **40**, 2345-2355 (2001).

[3] S. Kotova, M. Kvashnin, M. Rakhmatullin, O. Zayakin, I. Guralnik, N. Klimov, P. Clark, G. Love, A. Naumov, C. Saunter, M. Loktev, G. Vdovin and L. Toporkova, Modal liquid crystal wavefront corrector, *Opt. Express* **10,** 1258-1272 (2002).

Artificial Receptors of Nanostructured Monolayers Stabilized by the Spreader-bar Technique

Th. Hirsch, H. Kettenberger, O. S. Wolfbeis , V. M. Mirsky

Institute of Analytical Chemistry, Chemo and Biosensors, University of Regensburg, 93040 Regensburg, Germany. Email: thomas.hirsch@chemie.uni-regensburg.de

Summary: *Thiol modified purines and pyrimidines (template molecules) co-adsorbed together with dodecanthiol (matrix molecules) onto a gold surface, form self-assembled nanostructured monolayers showing recognition properties towards different purines and pyrimidines. These properties, measured as changes of electrochemical impedance on additions of analytes, depend on the type of the template used. An array consisting of a combination of five receptors formed by thiolated derivatives of adenine, thymine, uracil, guanine and cytosine as the templates, allows us to recognize any of these bases of nucleic acids. This technology provides a simple way to form a large variety of chemoreceptors with different selectivity and can be used for manufacturing of large sensors arrays.*

Keywords: *Chemosensors, artificial receptors, nanotechnology, monolayer*
Category: *2 (Materials and technology)*

One of the main trends in the modern sensors technology is focused on exploiting of pattern recognition principles [1,2]. A progress in this general approach, based on miniaturization of sensor devices and integration of single sensors into large arrays [3,4] is fast and impetuous. The main limitation in the development of this field is a requirement to form sensor arrays with large variety of receptors possessing different selectivity. Classical chemical synthesis is time-consuming and too expensive to be considered as a perspective way to solve this problem. Recently, we have modified a technology of patterned monolayers [5-7] and developed a novel type of artificial receptors based on nanostructured self-assembled monolayers [8-10]. This so-called spreader-bar approach based on creation of mixed monolayers of two different compounds, none of them exhibiting recognition properties alone. One component, called matrix, is an alkanethiol, the second component, called spreader-bar molecule (template), is similar to the analyte in shape and chemical structure. The matrix molecules must be able to form a thicker monolayer than template molecules do. Both molecules are co-adsorbed on the gold surface. The structures formed were found to be able to interact with analyte molecules in a solution.

Here the spreader-bar approach is applied for preparation of sensor arrays based on thiolated bases of nucleic acids as spreader bars (Figure 1). The results show, that in spite of limited selectivity of every single sensor element, the sensor array can be used for recognition of bases of nucleic acids as well as caffeine and uric acid.

Only small changes in capacitive current were observed for adsorption of adenine, cytosine, thymine, uracil, caffeine or uric acid onto self-assembled monolayers formed by pure dodecanethiol or pure thiolated purines and pyrimidines. The highest effect was displayed for adsorption of adenine: a relative decrease in the signal for adsorption on dodecanethiol on addition of 300 $\mu mol \cdot L^{-1}$ of adenine was 0.7%. The same experiments with the other analytes showed signal changes even less than 0.4%. A behavoir of mixed monolayers comprising of dodecanethiol and one of spreader bars was quite different. Adsorption of adenine, cytosine, thymine, uracil, caffeine or uric acid resulted in over 25% change of the capacitive current.

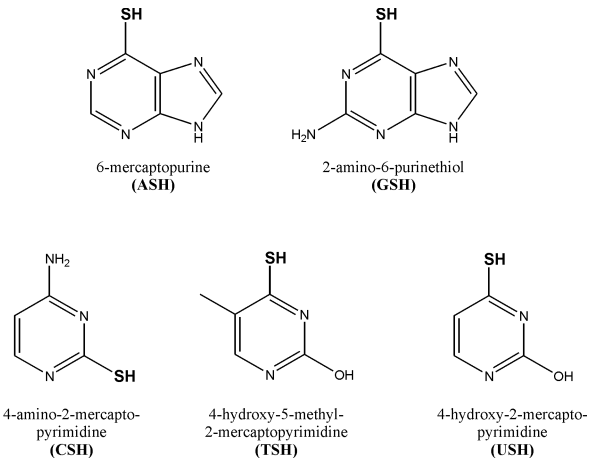

Fig 1. Overview of the spreader-bar molecules.

The response depended on a specific combination of template and adsorbate. For adenine as analyte the the signal decreased according to the order: TSH > USH > GSH > ASH > CSH (Table 1). This order can be explained by interactions between the template and analytes. It is well known that adenine binds its complementary bases thymine or uracil; most probably it is valid also for thiolated derivatives of the latter compounds. GSH and ASH have the same shape like the analyte thus providing conditions for adsorption of these molecules into cavities formed by the template molecules and for π-stacking interaction with these molecules. Due to the minor energetic

stabilization by π-stacking in contrast to the hydrogen binding [11], the binding of adenine to GSH and ASH six different purines and pyrimidines tested. For cytosine and uric acid the patterns are the same,

Table 1. Relative decrease (%) of the capacitive current on addition of analytes (250 μmol·L^{-1}) for different spreader-bar systems.

spreader-bar	adenine	cytosine	thymine	uracil	caffeine	uric acid
ASH	17.5	0.7	-0.1	6.5	1.7	7.0
CSH	10.0	-0.4	-2.0	10.4	1.0	5.5
GSH	16.2	1.2	0.0	4.6	0.7	8.0
TSH	26.0	0.4	-0.2	15.0	1.0	6.7
USH	19.6	1.8	-0.5	14.1	0.8	9.0

spreader-bar systems is less effective. In case of the CSH spreader-bar, no hydrogen binding can occur, and due to the smaller size of CSH, the surrounding dodecanethiol molecules hinder the analyte to come close enough to the template thus preventing a stacking interaction. Changes of the capacitive current on addition of adenine, uracil, caffeine, uric acid, cytosine or thymine to mixed monolayers formed by dodecanethiol and ASH are shown in Fig 2.

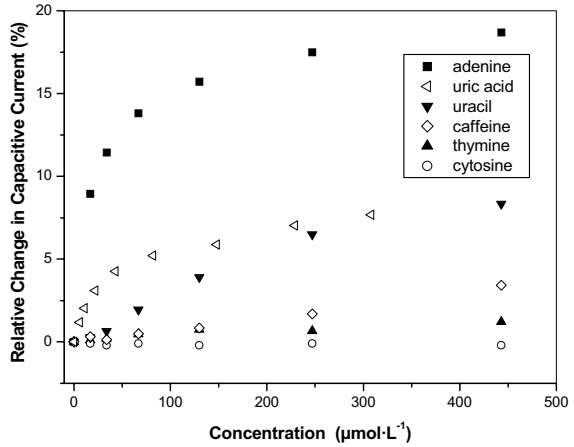

Fig. 4. Relative changes in capacitive current of gold electrode coated by dodecanethiol and ASH on addition of different analytes.

The influence of the hydrogen bonds on the binding of an analyte is illustrated by the comparison of uric acid and caffeine as analytes. Both, uric acid and caffeine have the same purine structure, but in contrast to uric acid, three potential hydrogen donors in caffeine are blocked by methyl groups. This may be a reason of 4 to 11 times lower signal changes in the case of caffeine. An investigation of relative signal changes on adsorption of the same concentrations of different purines and pyrimidines onto mixed monolayers formed with either ASH, GSH, TSH, USH or CSH, results in signal patterns which are typical for every specific analyte used. The sequences are valid for the whole concentration range studied. This set of five artificial receptors based on these mixed monolayers allows one to identify every of the however the magnitude of the signal changes for uric acid was 5 to 17 times higher.

The spreader-bar technique provides a simple way to manufacture almost a non-limited number of such receptors: practically every thiol derivative can be used. Here we demonstrated an application of this approach to form sensor arrays for recognition of purines and pyrimidines. The binding detection can easily performed by measurements of capacitive current, however one can suggest an application of other detection methods, for example quartz microbalance or cyclic voltammetry.

References

[1] C. Krantz-Rulcker, M. Stenberg, F. Winquist and I. Lundstrom. *Anal. Chim. Acta* 426(2), (2001) 217-226.

[2] B. K. Lavine. *Anal. Chem*. 70(12), (1998) 91-97.

[3] K. J. Albert, N. S. Lewis, C. L. Schauer, G. A. Sotzing, S. E. Stitzel, T. P. Vaid, and D. R. Walt. *Chem. Rev.* 100(7), (2000) 2595-2626.

[4] R. M. Crooks and A. J. Ricco. *Acc. Chem. Res.* 31(5), (1998) 219-227.

[5] J. Sagiv. *Isr. J. Chem.* 18, (1979) 346-353.

[6] M. Lahav, E. Katz, A. Doron. F. Patolsky and I. Willner. *J. Am. Chem. Soc.* 121, (1999) 862-863.

[7] O. Chailapakul and R.M. Crooks. *Langmuir* 9, (1993) 884-888.

[8] V. M. Mirsky, Th. Hirsch, S. A. Piletsky and O. S. Wolfbeis. *Angew. Chem., Int. Ed.*, 38(8), (1999) 1108-1110.

[9] H. L. Zhang, M. Chen and H. L. Li. *J. Phys. Chem. B*, 104, (2000) 28-36.

[10] Th. Hirsch, H. Kettenberger, O.S. Wolfbeis and V. M. Mirsky. *Chem. Commun.* (2003) 432-433.

[11] J. Sponer, J. Leszczynski and P. Hobza, *J. Chem. Phy.* 100, (1996) 5590-5596.

Self-assembling dual corner cube reflector fabricated in GaAs using the micro-origami technique

T. Fleischmann, K. Kubota, P. O. Vaccaro, S. Saravanan and T. Aida

ATR Adaptive Communications Research Laboratories,
2-2-2 Hikaridai, Keihanna Science City, Kyoto 619-0288, Japan
email: thomas@atr.co.jp http://www.atr.co.jp

Summary: *The fabrication of a GaAs dual corner cube reflector with vertical parallel plate actuation is demonstrated. A strain-driven self-assembly mechanism is used to fold GaAs mirrors into the vertical position The micro-origami hinges are formed by a strained bi-layer composed of InGaAs and GaAs. This allows the deposition of electrical contacts across the hinge giving the possibility to integrate electrically active components on free-standing structures. In the design of the corner cube reflector this is used to achieve parallel plate electrostatic actuation promising operation over a large force and distance range.*

Keywords: *MOEMS, GaAs, self-assembly, free-space optical communication, electrostatic actuation*
Category: *2 (Materials and Technology) or 4 (Non-magnetic physical devices)*

1 Introduction

Micro machined corner cube reflectors (CCR) are of significant importance in free-space optical communication systems. The basic principal relies on three orthogonal mirror plates which reflect light striking the CCR in the vicinity of the body diagonal back to the emitting source. In an integrated sensor system the shape of the CCR can be modulated in accordance with environmental changes and information about the sensor status is communicated without the need of power consuming transmitters at the location of the sensor [1]. Several considerable advantages arise from using III-V semiconductors instead of silicon. For instance, optoelectronic components or devices, such as Bragg-reflectors, optical filters, detectors or active diodes are easily integrated. Furthermore, the epitaxialy grown GaAs is expected to provide improved mirror flatness and reduced surface roughness when compared to poly-silicon. For fabrication of the GaAs CCR the micro-origami process was used, in which mechanical hinges are formed via the strain induced deformation of a bi-layer structure [2] providing a simple self-assembling mechanism. Depending on the growth structure hinges can be designed to fold in different directions, making the fabrication of complex 3D semiconductor structures possible [3]. In addition, using micro-origami hinges allows electrical connections across the hinge which makes it possible to integrate electronic or optoelectronic components on free-standing plates.

2 Design and fabrication

The device structure and operation is illustrated in figure 1. After assembly the mirrors are arranged in such a way that together with the substrate they form two CCRs with their body diagonal facing in opposite direction. Thus light striking the CCR from two opposite sources is modulated simultaneously and reflected back to its source. The two interlacing mirrors are arranged in a parallel configuration and thus the voltage required for actuation is expected to be reduced.

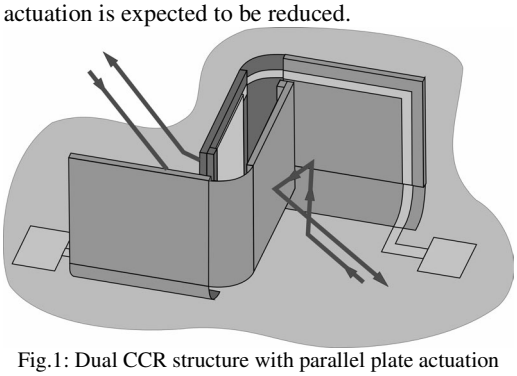

Fig.1: Dual CCR structure with parallel plate actuation

The origami-process used to fabricate the device is schematically illustrated in figure 2. The strain in the hinge region results in a deformation which lifts the mirror plates out of the substrate once the sacrificial layer is removed and thus the device is fully self-assembling. The completed structure is then dried employing a freeze-dry step.

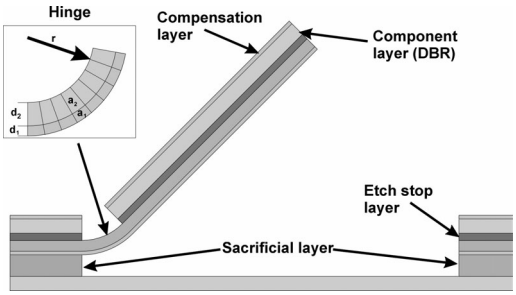

Fig.2: Micro-origami strain driven self-assembly technique

3. Results and discussion

Using Ansys we have modelled the hinge deformation in order to optimise the growth structure and dimensions. These calculations also include the effect the contact stripes on the hinge have on the bending angle of the mirror plate. In the device shown here a 40 nm Ti/Au layer was used which was found not to influence the curvature of the hinge and is of sufficient thickness for electrostatic applications. For applications where large currents are required on the free-standing plate, the strain in the hinge has to be adjusted in order to compensate the change in curvature. Also of importance is the thickness of the strain compensation layer on top of the mirror plates. In order to guarantee flat mirrors this thickness and indium concentration has to be matched to the strain resulting from the first InGaAs layer. Figure 4 shows the calculated curvature radius of the mirror as a function of the compensation layer thickness. The results obtained from these calculations are now used to optimise growth structure and hinge dimensions.

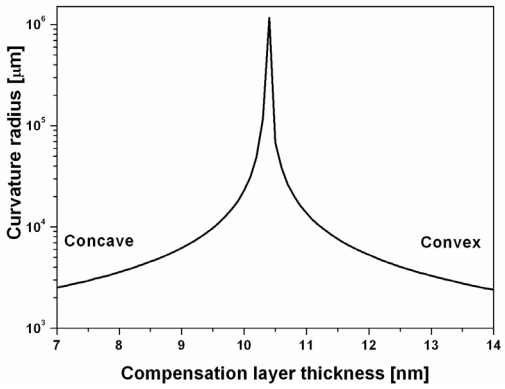

Fig. 3: Curvature versus compensation layer thickness.

Figure 4 shows the SEM photograph of a fabricated device with a mirror size of 100x100 μm^2. As can be seen from the picture, the angle of the plates is larger than 90° resulting in the CCR not being orthogonal. As a result, electrostatic actuation was not observed in this device. However, the curvature radius of the hinge, which together with hinge dimension defines the deflection angle, is easily adjusted by changing the growth structure. By adding locking mechanisms on the side of the plates it is also possible to fix a desired angle.

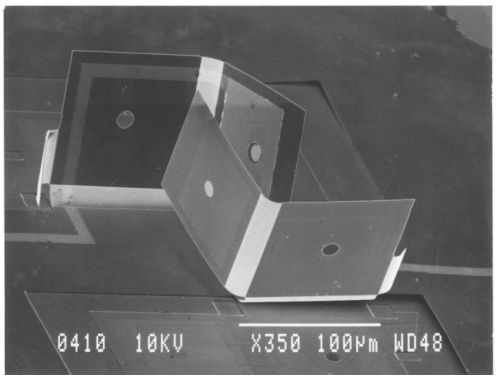

Fig. 4: SEM photograph of a dual CCR.

In conclusion, we have fabricated a self-assembling CCR structure based on GaAs. By using the micro-origami technique it is possible to fabricate electrical contacts across the hinge and therefore integrate electronic components on free-standing plates. For the CCR this can be used to achieve vertical electrostatic actuation with the mirror plates remaining parallel. This is expected to significantly reduce the voltage required for actuation.

References

[1] P. B. Chu, N. R. Lo, E. C. Berg and K. S. J. Pister, "Optical communication using micro corner cube reflectors", IEEE Proc. 10th Int. Workshop on MEMS '97, (1997), 350–355.

[2] P. O. Vaccaro. K. Kubota and T. Aida, "Strain-driven self-positioning of micro machined structures", Appl. Phys. Lett., **78**, (2002), 2852-2854.

[3] K. Kubota, T. Fleischmann, S. Saravanan, P. O.Vaccaro and T. Aida, "Self-assembly of micro-stage using micro-origami technique", JJAP Int. Micro processes and Nanotechnology Conference, (2002), Tokyo.

Mixed-Ligand Nanocluster-Based Chemoresistors: Synthesis and Selectivity

Young Jun Kim[1], Yong Shin Kim[1], Dae-sik Lee[1], Seung-Chul Ha[1], Yoonseok Yang[1], Young-sik Hong[2], Haesik Yang[1], and Youn Tae Kim[1]

[1]BioMEMS Team, Basic Research Laboratory,
Electronics and Telecommunications Research Institute (ETRI)
email: junkim@etri.re.kr
[2]Power Source Device Team, Basic Research Laboratory,
Electronics and Telecommunications Research Institute (ETRI)

Summary: *A series of gold nanoparticles stabilized with mixed thiolates were synthesized via exchange reactions by varying relative amount of the stabilizers, octanethiolate (OT) and 4-chlorobenzenemethanethiolate (CBMT). The nanoclusters were characterized by TGA and ^{1}H NMR. Thin film transducers of the monolayer-protected nanopartilces were formed on interdigitated electrodes. Upon exposure to organic vapors, toluene, n-hexane, cyclohexane, pentane, and chloroform, increase in film resistance was observed. The resistance dependence on relative amount of the thiolates encapsulating the metal nanoparticle revealed feasibility of diversifying chemical selectivity.*

Keywords: *nanoparticle, chemoresistor, mixed-ligand, selectivity*
Category: *2 (Materials and technology), 5(Chemical sensors)*

1 Introduction

Much research has been concentrated on developing sensor arrays that allow identification toward multi-component analytes as well as single-component analytes. Recently several examples of thiolate-capped gold nanoclusters as chemoresistors were reported due to some advantages, facile fabrication of the devices, operation at room temperature, and modest sensitivity reaching several-ppm detection. However no application of such chemoresistors in sensor arrays was reported. Small number of available chemical functionality of stabilizing ligands[1] is thought to be the major block limiting selectivity.

In this report possibility of diversifying chemical selectivity of nanocluster-based chemoresistors is described. The idea is to produce nanoparticles with diverse selectivity by varying relative amount different thiolates. In principle chemoresistors of innumerable combinations of mixed thiolates could be generated from relatively a few ligands (Figure 1). 'Place-exchange' reaction[2] was turned out to be an ideal method providing combinatorial synthesis. Thiolates with small polarity contrast were combined (4-chlormethylbenzenethiolate (CMBT, $ClPhCH_2S$-) and n-octanethiolate (OT)) and still produced selectivity even toward chemically similar hydrocarbon analytes.

2 Experimental

Mixed-ligand stabilized gold nanoclusters were prepared through exchange reactions between

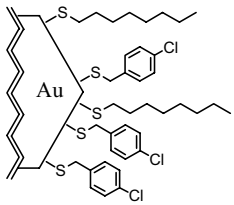

Figure 1. Simplified schematic view of a nanocluster with mixed-ligand comprised of CMBT and OT.

CMBT ($ClPhCH_2S$-)-capped gold nanocluster and octanethiol. Two-step synthetic method by Burst[3] was used to prepare CMBT stabilized nanocluster (2:1 molar ratio of $HAuCl_4$ and 4-chlorobenzenemethanethiol was used). The nanoparticles were characterized by TGA, and ^{1}H NMR (Table 1). Dip-coating each nanocluster solution on to interdigitated electrode produced a series of tranducers films (S_1, S_2, S_3, and S_4) (Table 1). The detection system was equipped with a laptop computer, mass flow controllers, a detection chamber, and a temperature controller. Responses of the chemoresistors to organic vapors were carried out by following vapor-induced change of resistance.

3 Results and Discussions

^{1}H NMR analysis confirmed successful synthesis of the nanoclusters and provided calculation of the molar ratio of the CBMT and OT ligands comprising the nanoclusters (Table 1). The characteristic aromatic and aliphatic hydrogens

from CBMT and OT were observed in the range of δ 6.2 to 8.0 and δ 0.9 to 1.8 respectively (Figure 2).

Table 1. Information of the nanoparticles constituting the transducer films.

Transducer symbols	Molar ratio (OT: CBMT)	Weight % of the ligands (%)
S_1	0.0 : 1.0	18
S_2	0.42: 1.0	19
S_3	0.79:1.0	17
S_4	1.36: 1.0	20

Absence of methylene protons adjacent to sulfur atom of the CBMT and OT and broadening of the aromatic hydrogens from CBMT is caused by surface tethering. Trace amount of tetra-octlyammonium bromide, TOAB (1:8.6 molar ratio compared to CBMT), used as a phase transfer catalyst for nanoparticle synthesis, was observed to remain in the product (δ 3.3). The leftover contamination of the film by TOAB doesn't seem to affect the signal responses to any significant degree (Figure 3 and 4).

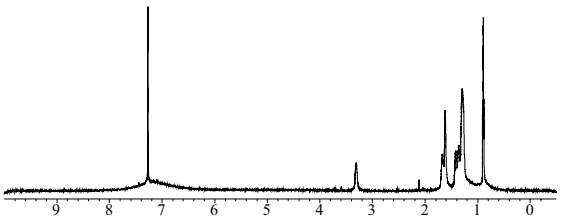

Figure 2. ^{1}H NMR (600 MHz) spectrum of the mixed-thiolate nanocluster used for preparing the transducer, S_2.

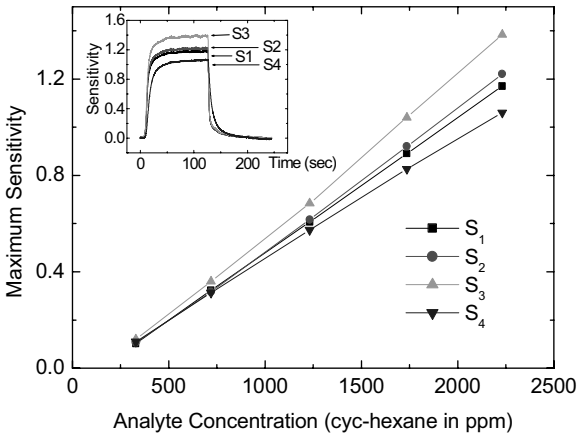

Figure 3. Maximum sensitivities (100 x $\Delta R/R_o$) of the mixed-ligand nanoparticle sensors in response to varying concentrations of cyc-hexane.

Fairly linear responses were observed for all the sensors toward cyc-hexane in the concentration ranges concerned (Figure 3). Such linearity was also observed toward pentane and n-hexane in the similar concentration range. Generally S2 and S3 produced higher sensitivity than S1 toward cyc-hexane, n-hexane, pentane and chloroform with concentrations ranging from a few hundreds to several thousands ppm. Sensitivity differences among the sensors tend to increase as the vapor concentrations increase. Inset in Figure 3 is response signals of the sensors at 2200 ppm of cyc-hexane.

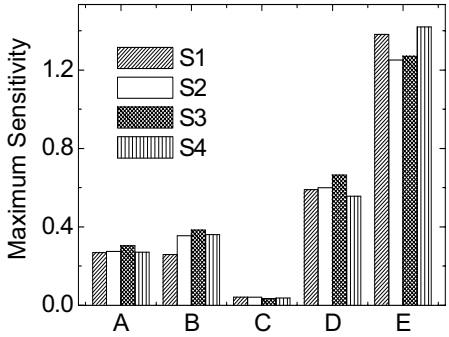

Figure 4. Maxium sensitivities (100 x $\Delta R/R_o$) of the sensors (S1-S4) toward a series of organic vapors (A: n-hexane, B: chloroform, C: pentane, D: cyc-hexane, E: toluene) (1200 ppm).

Diverse selectivities were generated among the mixed-nanoclusters (S1-S4) toward most of the organic vapors except C as observed from variation of the maximum sensitivities (Figure 4). Combination of polar and nonpolar ligand thiolates is expected to better expand the selectivity.

4 Conclusion

Variation of relative amount of the thiolates incorporated onto the gold nanoparticle was successfully accomplished through 'place-exchange' reaction. Diverse selectivities were generated through mixed-ligand nanoclusters. Future direction of this research would be to further widen the selectivity window using thiolates with pronounced contrast in their polarities.

References

[1] H. Wohltjen and A. W. Snow *Anal. Chem.* 70 (1998) 2856-2859.

[2] M. J. Hostetler, A. C. Templeton, and Royce W. Murray *Langmuir* 15 (1999) 3782-3789.

[3] M. Brust, M. Walker, D. Bethell, D. J. Schiffrin, R. Whyman, *J. Chem. Soc., Chem. Commun.* (1994) 801.

A study of powder size combinations for improving piezoelectric properties of PZT thick-film devices

R.N.Torah, S.P.Beeby and N.M.White

Department of Electronics and Computer Science, University of Southampton, UK
Email: rnt00r@ecs.soton.ac.uk http://www.ecs.soton.ac.uk

Summary: This paper details investigations into the effects of different powder size ratios on the d_{33} coefficient of thick-film PZT layers. The two powders used were 5H type PZT supplied by Morgan Electro Ceramics Ltd. These were prepared using ball milling for the large particles, ~2um, and attritor milling for the small particles, ~1um. These powders were mixed with 10% by weight of Ferro CF7575 lead borosilicate glass and an appropriate quantity of ESL 500 solvent to formulate a screen printable paste. The results show the optimum powder combination obtained and a final formulation for a practical thick-film paste. The highest d_{33} value, 63.5pC/N, was obtained with the 4:1 ball to attritor powder by weight paste formulation.

Keywords: piezoelectric, thick-film, d_{33}
Category: 2 (Materials and Technology)

1 Introduction

Screen printable piezoelectric materials were first reported in 1987 [1] and have since found use in many applications; including motors [2] and micromachined silicon devices [3].

Studies have shown [4] however, that the thick-film PZT samples have lower d_{33} coefficients than their bulk counterparts [5] due to differences in processing and composition.

Piezoelectric thick-film pastes are produced by mixing milled piezoelectric powders with a glass binder and organic vehicle. Several milling processes can be used to form the powder [6]. Previous work has shown that the large particle size of ball milled powder produces the highest d_{33} values, whilst the smaller, more evenly distributed, particles of the attritor milled powders produce the most consistent d_{33} values [6]. This paper presents details of the next stage in the paste development which is the combination of ball and attritor milled powders and determining the optimum ratios.

2 Theory

The larger particle size associated with the ball milled powder results in increased piezoelectric responses. Therefore, it was important to maintain the ball milled particle as the dominant particle within any powder combination. The smaller attritor milled particles can be used to fill the interstice between the ball milled particles. The increased mechanical density of the film improves both the mechanical coupling and subsequent piezoelectric properties of the film.

The attritor particles used in this investigation where milled 3 consecutive times and have been denoted attritor3. The combined ball milled and attritor3 milled powders were mixed with Ferro CF7575 lead borosilicate glass, which forms the binding matrix when fired.

3 Calculations

The initial calculations for the ratio of ball milled to attritor milled powders centred on a basic 2D model shown in figure 1.

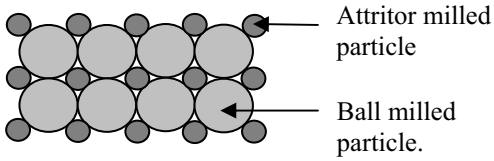

Fig 1: Ideal 2D model for particle distribution.

The limitations associated with this model are that it is a 2D representation of a 3D problem and it assumes the particles are spherical. The particle sizes used in the model are obtained from the size distributions identified in reference 6. The average particle size was used in the calculations but clearly in practice there is a range of particle sizes. The particle layout shown in figure 1 was used in the model since the calculated particle sizes closely match the actual particle size of the attritor3 powder.

Using the average ball milled particle diameter of 2μm, the largest particle size that will fit the interstice between the particles is 0.83μm. Using this value, the total area between the ball particles was calculated. A ratio of attritor particles to ball particles required to fill the total area was then calculated. The weight ratio of powders can be calculated using the density of PZT-5H [5], this gives an optimum powder ratio of 8.8:1 ball milled to attritor milled powder by weight.

In practice the attritor3 powder has an average particle size of 1μm, slightly above the ideal. Given this, and allowing for the other assumptions described above, a range of powder ratios from 8:1 to 2:1 were investigated. The calculated percentages of powders for each paste are shown in table 1. The

percentage of glass remained constant since 10% has previously been identified as the optimum [6].

Table 1. Percentages of Att3 and Ball powders

Paste	Attritor3 percentage weight	Ball percentage weight	CF7575 percentage weight
8:1	10%	80%	10%
4:1	18%	72%	10%
2.6:1	25%	65%	10%
2:1	30%	60%	10%

4 Processing

The four powder combinations in table 1 were mixed with ESL 500 solvent to create thixotropic screen printable pastes. These pastes were then mixed using a triple roll mill, which disperses the powders evenly throughout the paste.

The pastes were printed on a 96% alumina substrate using standard thick-film screen-printing process with a DEK 1200 printer. The substrates were dried in a DEK 1209 IR drier at 140°C and then fired on a belt furnace with a peak temperature of 890°C. Each sample was poled at 150°C with field strength of $4MVm^{-1}$ [4]. The d_{33} values were measured using a Take Control PM35 piezometer.

5 Results

Figure 2 shows the average measured d_{33} values and standard deviations for each of the powder combinations. Included are the previous results for ball and attritor3 milled powder for comparison [6].

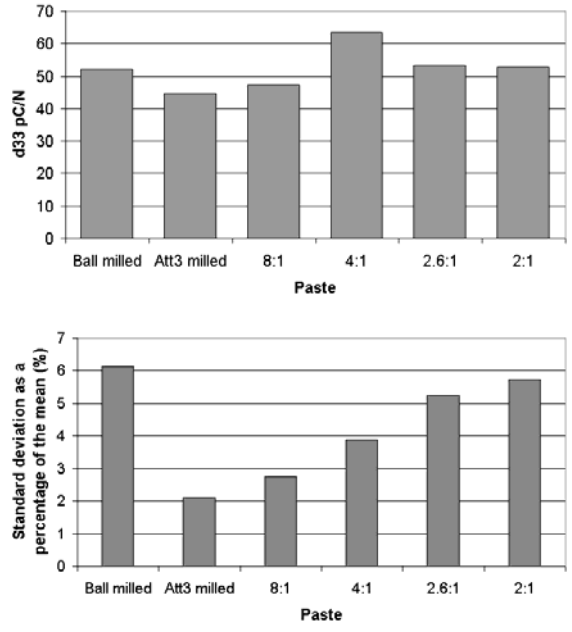

Fig 2 Average d_{33} and percentage standard deviation for each powder combination.

The results show that there is a clear improvement in the d_{33} value obtained by combining powder types together. In addition, there is an optimum ratio of powders which occurs at a ratio of 4:1 by weight. This gives a d_{33} value of 63.5pC/n and also shows an improved standard deviation when compared to the original ball milled paste.

6 Conclusions

The combination of 4:1 by weight of ball milled to attritor milled powder (i.e. 18% attritor3, 72% ball and 10% CF7575 powders) produces the highest d_{33} coefficient with an average measured value of 63.5pC/N. Figure 2 shows that the number of smaller particles added to the paste appears to have a saturating effect past ratios of 2.6:1 as the interstice gaps within the matrix have been already filled. This result agrees reasonably closely with the basic 2D model.

The previous optimum paste, obtained from purely ball milled powder, had a d_{33} coefficient of 52pC/N. The new 4:1 paste has resulted in an increase in piezoelectric activity of over 20%. The results also show that the percentage of deviation has decreased from 6.2% to 3.9% from the previous ball milled paste. This indicates the optimum paste not only produces a more active film, but also results in a more repeatable material.

Further work will develop a 3D model to seek further optimisation and confirmation of the experimental work. Also, the use of multilayer structures in combination with this new paste formulation will be investigated to further increase the effective d_{33} coefficient.

7 Acknowledgements

The authors wish to thank the support and assistance given to us by Morgan Electro Ceramics Ltd.

8 References

[1] Screen-printing piezoelectric devices, H.Baudry, 6th European Microelec. Cont. Proc, p456-463, 1987.
[2] A piezoelectric tactile sensor with three sensing elements for robotic, endoscopic and prosthetic applications, J.Dargahi, Sensors and Actuators A, Vol.80, 2000, pp. 23-30.
[3] Silicon micromechanical resonator with thick-film printed vibration excitation and detection mechanisms, S.P.Beeby, N.M.White, Sensors and Actuators A, Vol 88, 2001, pp.189-197.
[4] An investigation of the effect of poling conditions on the characteristics of screen-printed piezoceramics, P.Dargie, R.Sion, J.Atkinson, N.White, Microelectronics International, Vol. 15/2,pp. 6-10, 1998.
[5] Morgan Electroceramics Ltd.: Piezoelectric Ceramics Data Book for Designers.
[6] A study of the effect of powder preparation and milling process on the piezoelectric properties of thick-film PZT, R.N.Torah, S.P.Beeby, N.M.White, Eurosensors XVI Proc., Prague, 2002.

Pyroelectric Current Spectroscopy: a tool to control the quality of PZT ceramics for IR detection

L. Pintilie[2], M. Pereira[1], M.J.M. Gomes[1], and I. Boerasu[1,2]

[1]University of Minho, Campus de Gualtar, 4710-057, Braga, Portugal
email: mpereira@fisica.uminho.pt http://www.uminho.pt
[2]NIMP, Atomistilor 105bis, P.O. box MG-7, 76900, Bucharest-Magurele, Romania

Summary: *Pyroelectric Current Spectroscopy (PCS) was used to investigate the homogeneity of some PZT ceramics with potential for infrared (IR) detection. In case of non-homogeneous ceramics several peaks were obtained in the PCS spectra, suggesting the presence of PZT phases with different Zr/Ti ratio, thus having different transition temperatures. The non-homogeneity was confirmed by SEM-EDAX. PCS can be a useful tool in optimizing the calcination and sintering parameters (temperature and time) during ceramic preparation.*

Keywords: *pyroelectricity; PZT; ceramics*
Category: *2*

1 Introduction

Lead zirconate-titanate (PZT) ceramics are known to possess very good pyroelectric properties, making them attractive for the infrared (IR) detection [1]. The main parameter defining the quality of such a material is the pyroelectric coefficient [1]. Its value is dependent on the compositional homogeneity of the ceramic. In the specific case of PZT materials, a non-homogenous distribution of the Zr/Ti ratio can lead to different properties than those expected when the ceramic was prepared. The problem arises from the fact that different Zr/Ti ratios means different transition temperatures, thus different values of the pyroelectric coefficient in different regions of the samples [2]. All this means that pyroelectric IR detectors manufactured from the same bulk ceramic pellet could have different detection characteristics. Thus, such non-homogeneity is not desirable in case of mass production because it can decrease the yield and increase the costs.

In this communication we present a simple method to investigate the quality of a PZT ceramic from the point of view of its pyroelectric properties. The method is based on pyroelectric current measurement and is called Pyroelectric Current Spectroscopy (PCS).

2 Experimental

Several ceramic samples were prepared by conventional ceramic technology. The raw materials were $PbCO_3$, TiO_2 and ZrO_2. Nb_2O_5 was used in some cases to improve the densification. The Zr/Ti ratio reported in the present communication is 92/8, with up to 6 at.% Nb. The Nb-doped ceramics were compensated according to the formula: $Pb_{1-y/2}(Zr_{0.92}Ti_{0.08})_{1-y}Nb_yO_3$. No lead excess was used. The powders were calcinated at 875 ^{0}C for 2 hours. The sintering of the pressed pellets was performed at 1200 ^{0}C for 40 minutes. The structure and the morphology were evaluated by X-ray diffraction (XRD) and Scanning Electron Microscopy (SEM) respectively. The composition was investigated by EDAX on different regions of the sample.

Silver paste electrodes were used for pyroelectric current measurements. Prior the measurement each sample was poled by applying a dc field of about 20 kV/cm at high temperature. The pyroelectric current measurement was performed by inserting the sample into an oven and recording the current vs. temperature curve[3].

3 Results and discussion

A typical X-ray diffraction pattern for the prepared ceramic is presented in Fig. 1.

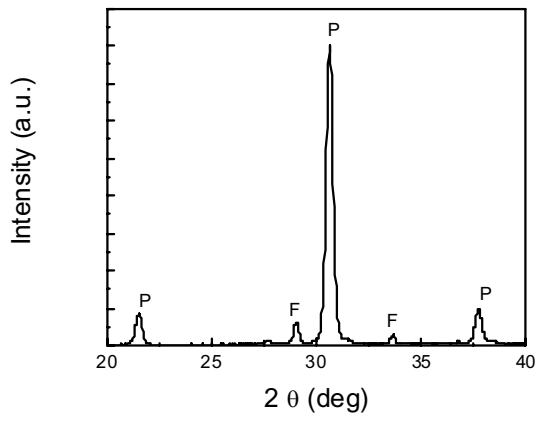

Fig. 1 XRD spectrum for PZT(92/8) ceramic with 6 at % Nb. (P – perovskite; F – fluorite phase).

The spectra for Nb-doped PZT compositions reveal the presence of perovskite structure, with some amount of fluorite phase at high Nb content [4]. From fig.1, the ceramic body seems to be quite homogeneous in terms of Zr/Ti ratio. However, the SEM-EDAX analysis (see Fig. 2) had revealed the presence of small "islands" of Ti rich phase in a matrix of Zr rich material. The EDAX analysis had also revealed that the Zr/Ti ratio is not uniform over the ceramic volume. It varies between 96/4 in the matrix and 13.5/86.5 inside the "islands". The above results show that most probably the calcination parameters (time-temperature) were not adequate to obtain a homogeneous distribution of Zr/Ti ratio. Initially it was thought that the Pb vacancies introduced by Nb doping will help the completion of the solid-state reactions and the densification of the ceramics, thus requiring shorter calcination and sintering times [4]. However, it seems that the calcination time was not long enough to complete the solid-state reactions. That will explain the presence of Ti rich "islands" inside the Zr-rich PZT phase. It is known that during the solid-state reaction the first to form is $PbTiO_3$ (PT), which then transforms into PZT [5]. Other causes for the non-homogeneous distribution of Zr/Ti ratio could be the short mixing time in the ball-mill before calcinations and the agglomeration capability of the highly reactive raw materials. The small average size of the grains and the relatively high porosity observed in the SEM photos are probably due to the short sintering time.

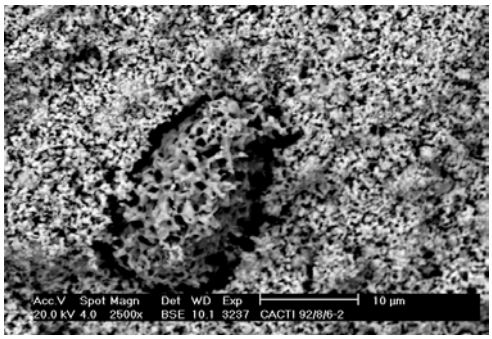

Fig. 2 SEM photo showing an "island" of Ti-rich phase in the PZT matrix.

The sample non-homogeneity was then tested by pyroelectric current measurements, as is shown in Fig. 3 for the sample with 6 % Nb. Several peaks are observed in the PCS spectra. At this Zr/Ti ratio only two transitions should exist, according to the phase diagram: 1) a secondary transition F_{RH}(LT) - F_{RH}(HT), that should be at about 65 ^{0}C; 2) the main transition F_{RH}(HT) - P_C at about 245 ^{0}C [2]. The Nb should increase the temperature of the secondary transition and decrease the temperature of the main transition [6,7]. It is reported also that increasing the Nb content both transitions become broader.

In the recorded PCS spectrum, five peaks are observed (temperature indicated on the graph). It can be assumed that the first broad peak at 173 ^{0}C is related to the secondary transition F_{RH}(LT) - F_{RH}(HT) and the next peak is related to the main transition F_{RH}(HT) - P_C. In the case of a ceramic with homogeneous Zr/Ti ratio these should be the only recorded peaks. However, there are three other peaks at higher temperatures, related with the presence of Ti-rich phases in the sample. According to the $PbZrO_3$ - $PbTiO_3$ phase diagram, the 3 transition temperatures correspond to Zr/Ti ratios in the range 55/45 – 5/95, i.e. intermediary phases formed during calcination. Thus, the Pyroelectric Current Spectroscopy confirms the results obtained from SEM-EDAX analysis. Similar results were obtained for the samples with 2 and 4 at %Nb.

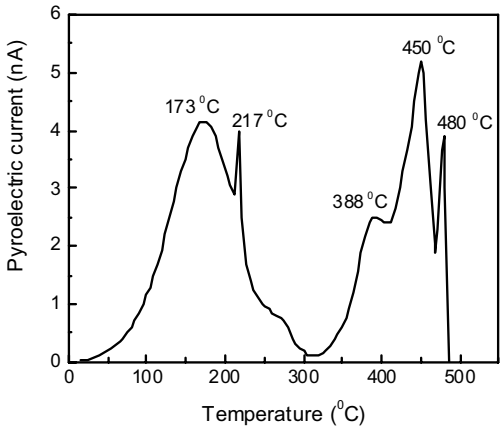

Fig. 3 PCS spectrum for a PZT(92/8) sample doped with 6 at % Nb.

The conclusion is that PCS, as a non-destructive technique, could be a useful tool in controlling the quality of the ceramics intended for IR detection.

The authors acknowledge financial support from FCT-Portugal (project POCTI/CTM/12140/1998). I. Boerasu thanks FCT for the grant PRAXIS XXI/BD/21539/99. L. Pintilie acknowledges the NATO grant at the University of Minho.

References

[1] A.M.Glass and M.E.Lines, "*Principles and Applications of Ferroelectrics and Related Materials*", (Clarendon Press, Oxford), 1977.

[2] B.Jaffe, "*Piezoelectric Ceramics*", (Academic Press, London), 1971.

[3] R.L. Byer and C.B. Roundy, *Ferroelectrics* 3 (1972) 333-338.

[4] M. Pereira, A.G. Peixoto, and M.J.M. Gomes, *J. Eur. Ceram. Soc.* 21 (2001) 1353-1356.

[5] O. Auciello, L. Mantese, J. Duarte, X. Chen, S.H. Rou, A.I. Kingon, A.F. Schreiner, and A.R. Krauss*, J. Appl. Phys.* 73 (1993) 5197-5207.

[6] J. Du, S. Lin, and M. Adachi, Jpn. *J. Appl. Phys.* 40 (2001) 4965-4968.

[7] Z. Ujma, L. Szymczak, J. Handerek, K. Szot, H.J. Penkalla, *J. Eur. Ceram. Soc.* 20 (2000) 1003-1010.

Photoimageable thick film metal oxides, on silicone substrates, for gas sensing applications

J. Wöllenstein[1], R. Stich[1], E. Moretton[1], H. Böttner[1], J. Beardon[2] and P. Smith[2]

[1]Fraunhofer Institute for Physical Measurement Techniques, Dept. Components and Microsystems,
Heidenhofstrasse 8, 79110 Freiburg i. Br., Germany
email: woellen@ipm.fhg.de http://www.ipm.fhg.de
[2]City Technology Ltd, Walton Road, Portsmouth, Hampshire, PO6 1SZ, United Kingdom

Summary: *Conventional commercial metal oxide gas sensors are fabricated by screen printing or dip coating. Neither of these techniques is suitable for use of Si-substrates and fragile 'microhotplate' type silicon devices. A novel method of depositing photoimageable metal oxide films has been developed. The material is spin coated onto the entire substrate and photolithographically patterned. The films thus produced can have thicknesses as low as a few microns, and can readily be patterned with a lateral resolution of tens of microns. Good control over powder morphology and photoresist rheology are required and have been achieved.One major advantage of this route when compared to techniques such as sputtering, is that the material is similar in properties to screen printed material, hence gas sensing behaviour is consistent with that of conventional commercial sensors.*

Keywords: *gas sensor, metal oxide, silicon substrate, thick film, photoimageable*
Category: *2 (Materials and technology)*

1 Introduction

In 1962 Seiyama and Taguchi demonstrated that semiconducting metal oxides, heated up to ~300°C in air vary their conductivity in a sensitive manner due to the presence of traces of reactive gases in the air. This has been the key to the commercial development of thick film sensors based mainly on SnO_2. However, the heating power consumption of these sensors is high and the manufacturability of the commercial thick film sensors on ceramic substrate is difficult to automate and requires costly manual operations. In contrast metal oxide sensors consequently fabricated on standard silicon substrates provide either compatibility with Si microelectronics and MEMS with the possibility to use common bonding and packaging. In particular, silicon micromachining offers potential for a reduction in power consumption.

2 Experimental

According to this concept — compatibility with Si-microelectronics — we present a novel technology for using porous oxides thick films on the CMOS technologies. This process is mainly characterised by its photoresist-matrix assisted deposition of oxides. The method can create a sensitive oxide area similar in size to those produced by use Si-substrates as a simple additional step to the processes involved in micromachining or thin film technologies, and thus smaller than conventional screen printing of thick films. The alternative inking techniques or "ink jet" method [1], [2], [3] can present problems such as not well defined oxide patterns as well as variations in oxide thickness. By using the novel method of photolithography for producing thick films, it is possible to both create a well-defined oxide pattern and control the oxide thickness.

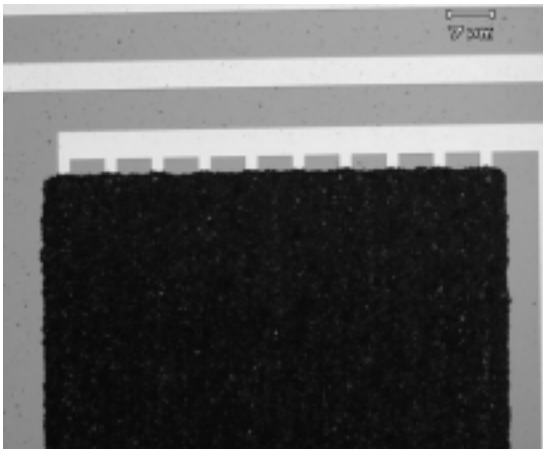

Fig. 1: Optical microscopic image of the photolithographically structured CTO thick films on structured silicon substrates.

The deposition process starts with the metal oxide powder preparation. The particle size was controlled using a ball mill. The photoimageable thick film metal oxides were deposited by spin coating an ink, comprised of the metal oxide powder and a photoresist, on silicon wafers with platinum heater/electrode structures. The resist matrix is based on a special photoresist, which becomes insoluble in water after an exposure to UV

radiation. The experiments were carried out with different metal oxide powders (e.g. SnO_2, chromium titanium oxide (CTO), $BaSnO_3$). After annealing at CMOS-compatible 400°C the resist matrix has been removed and the metal oxide appears as a well sticking highly porous film. EDX-analysis showed no or only little carbon residues from the photo resist in the metal oxide after annealing.

Figure 1 shows the patterned deposit of CTO over 200 nm thick Pt-electrodes. A SEM image of the microstructure of the photostructured CTO after annealing at 400°C is pictured in Fig. 2. The grain size of the 10 µm CTO-thick film amounts 300-500 nm.

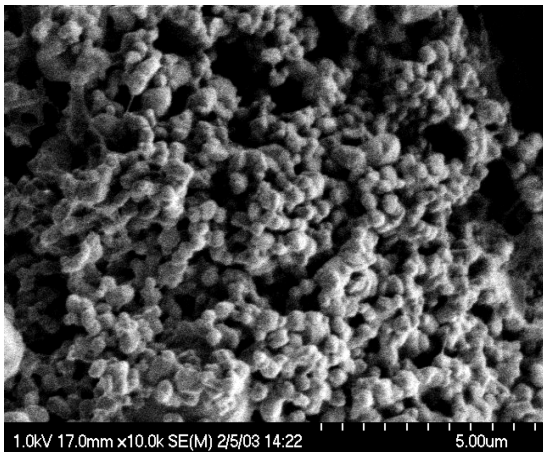

Fig. 2: Morphology of photolithographic structured CTO-layer after annealing at 400°C.

In the experiments the films were deposited onto 2 x 2 micro arrays. A silicon wafer was used as substrate, SiO_2 film of 1 µm thickness was prepared by thermal oxidation to insulate gas sensing elements from the substrate. A Ta/Pt film (25/200 nm thickness) was deposited and patterned to act as interdigital electrodes, heater and temperature sensor. The detailed processing steps used for fabrication of the array substrates are reported in [4,5].

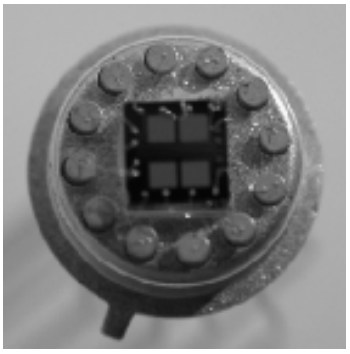

Fig. 3: Mounted fourfold sensor array in a TO5-housing

In order to measure the gas sensitive behaviour, the sensor chips were mounted in a TO5-housing. A mounted device can be seen in figure 3.

Characterisation of the sensors under trace gas exposure will be presented. Figure 4 shows e.g. the change of the sensor signals (i.e. resistance) of four sensors, with an approximate operation temperature of 380°C, during exposure to different test gases like H_2 (100 ppm), CO (100ppm), NO_2 (0.5 ppm) in synthetic air.

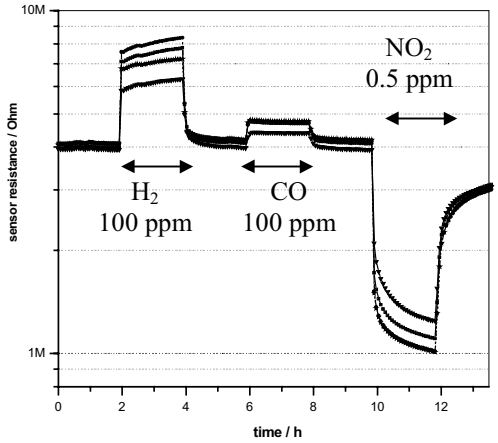

Fig. 4: Response of four photolithographically structured CTO-sensors to different test gases in synthetic air at 380°C (50% r.h.).

References

[1] I. Simon, N. Bârsan, M. Bauer and U. Weimar, Micromachined metal oxide gas sensors: opportunities to improve sensor performance, *Sensors and Actuators B 73*, 1-26, (2001)

[2] J. Cerda, A. Cirera, A. Vilà, A. Cornet and J. R. Morante, Deposition on micromachined silicon substrates of gas sensitive layers obtained by a wet chemical route: a CO/CH_4 high performance sensor, *Thin Solid Films 391*, 265-269, (2001)

[3] S. Capone, P. Siciliano, N. Bârsan, U. Weimar and L. Vasanelli, Analysis of CO and CH_4 gas mixtures by using a micromachined sensor array, *Sensors and Actuators B 78*, 40-48, (2001)

[5] J. Wöllenstein, H Böttner, M. Jaegle, W. J. Becker, E. Wagner, Material properties and the influence of metallic catalysts at the surface of highly dense SnO_2 –films, Sensor and Actuators B 70 (1-2) (2000) 196-2008.

[6] J. Wöllenstein, G. Plescher, G. Kühner, H Böttner, D. Niemeyer, D. E. Williams, Preparation, morphology and gas sensing behavior of $Cr_{2-x}Ti_XO_{3+Z}$ thin film on standard silicon wafers, IEEE-sensor journal Vol. 2 Number 5 (2002) p 403-408

Sensing properties of perovskite oxide $La_{1-x}Sr_xCoO_{3-\delta}$ (x=0.5) obtained by using pulsed laser deposition

Dam T.V. Anh, W. Olthuis and P. Bergveld

MESA+ Research Institute, University of Twente,
P.O. Box 217, 7500 AE, Enschede, The Netherlands.
E-mail: d.v.anh@el.utwente.nl, http://www.el.utwente.nl/mesa

Summary: *$La_{1-x}Sr_xCoO_{3-\delta}$ belongs to the group of perovskite oxides of the ABO_3 structure, with a trivalent rare earth in the A position (La) and a trivalent metal ion in the B position (Co). Doping with divalent Sr-ions at the trivalent La-positions creates oxygen vacancies which give the oxide catalytic properties to H_2O_2. However, the conventional techniques which are used to prepare this oxide such as chemical methods, are not suitable for making a thin film. In this paper, a thin layer of $La_{1-x}Sr_xCoO_{3-\delta}$ (x= 0.5) perovskite oxide is deposited on a Pt electrode by using the Pulsed Laser Deposition technique. The catalytic properties of this perovskite oxide to hydrogen peroxide due to the presence of the oxygen vacancies will be discussed. The results show the possibility to use this perovskite oxide as a sensing material for potentiometric hydrogen peroxide sensors.*

Keywords: *perovskite oxide, $La_{1-x}Sr_xCoO_{3-\delta}$, pulsed laser deposition, hydrogen peroxide*
Category: *2 (Materials and technology) or 5 (Chemical sensors).*

1 Introduction

$La_{1-x}Sr_xCoO_{3-\delta}$ belongs to a group of perovskite oxides of the ABO_3 structure with a trivalent rare earth in the A position (La) and a trivalent metal ion in the B position (Co). The structure of the $LaCoO_3$ perovskite oxide consists of CoO_6 octahedra and the La^{3+} ions, which are inserted between the CoO_6 octahedra. When the trivalent La^{3+} ions in $LaCoO_3$ are replaced by divalent earth alkaline ions Sr^{2+} to form $La_{1-x}Sr_xCoO_{3-\delta}$, a positive charge is generated. Because the Co^{z+} ions can have a different oxidation state, the charge neutrality is maintained by the formation of oxygen vacancies and a change in the valence state of the Co^{z+} ions. Therefore, the oxide has an oxygen deficiency, δ, due to the high oxygen vacancy concentration.

This type of perovskite oxides is a promising candidate for solid oxide fuel cells, oxygen separation membranes and sensor material [1]. Different types of the perovskite oxides, which are synthesized by chemical methods, have been used as a material for hydrogen peroxide sensing. However, the response time of the sensor is quite low due to the long time it takes for the hydrogen peroxide to diffuse into the thick layer of the perovskite oxide. Among the existing deposition methods, the Pulsed Laser Deposition (PLD) is a suitable technique for the fabrication of a perovskite oxide thin film. This technique allows the stoichiometric transference of the deposited material from target to substrate [2]. In this paper, we show the possibility to obtain a thin $La_{1-x}Sr_xCoO_{3-\delta}$ (x=0.5) perovskite oxide film by using the PLD technique and its sensing properties to hydrogen peroxide.

2 Experiments

The $La_{0.5}Sr_{0.5}CoO_{3-\delta}$ thin film is deposited on platinum electrodes which were sputtered on a $Ta_2O_5/SiO_2/Si$ wafer, using the setup as shown in Fig. 1. During the deposition process, a metallic shadow mask was placed on top of the substrate to shield the platinum electrical contacts from undesired deposition of the $La_{0.5}Sr_{0.5}CoO_{3-\delta}$. The ablation process of $La_{0.5}Sr_{0.5}CoO_{3-\delta}$ is realized by a spatial uniform 248 nm excimer laser beam. The deposition time was varied from 5 to 7 min depending on the required thickness of the film. The thickness of the film was estimated to be about 75 nm after 5 min of deposition. After deposition, the sample was cooled down to room temperature in an O_2 flow. The annealing in the oxygen environment is necessary to obtain a stable composition and to create the oxygen vacancies in the perovskite oxide film. Finally, the wafer was diced in separated devices and encapsulated with Hysol®.

The sensing properties of the $La_{0.5}Sr_{0.5}CoO_{3-\delta}$ thin film to hydrogen peroxide is characterized in a phosphate buffer (pH = 7.1) containing 0.1M KCl. All chemicals used (Merk, Fluka) were of analytical reagent grade.

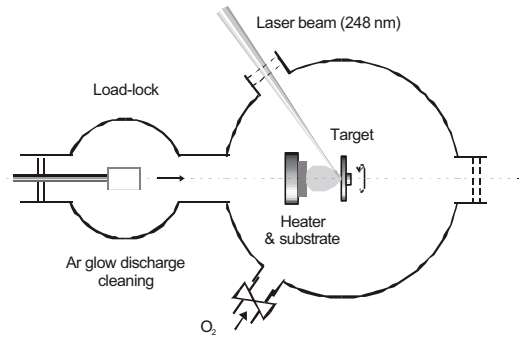

Fig. 1: Pulsed Laser Deposition system.

3 Results and discussions

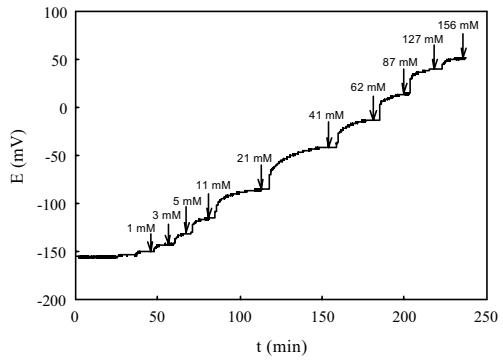

Fig. 2: Potential of the $La_{0.5}Sr_{0.5}CoO_{3-\delta}$ electrode depends on the hydrogen peroxide concentration.

The $La_{0.5}Sr_{0.5}CoO_{3-\delta}$ thin film shows catalytic properties to hydrogen peroxide. The potential response of the $La_{0.5}Sr_{0.5}CoO_{3-\delta}$ electrode to a change in the hydrogen peroxide concentration has been measured with respect to a saturated calomel electrode (SCE) and is shown in Fig. 2.

The response time of the electrode potential to hydrogen peroxide is estimated to be about 10 min. The electrode potential response depends on the

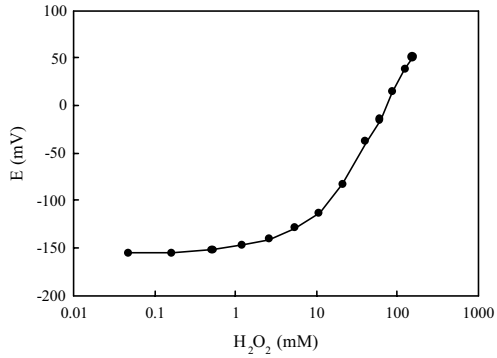

Fig. 3: Potential of the $La_{0.5}Sr_{0.5}CoO_{3-\delta}$ electrode as a function of the hydrogen peroxide concentration.

logarithm of the hydrogen peroxide concentration with a slope of 130 mV/dec (see Fig. 3). The high sensitivity of $La_{0.5}Sr_{0.5}CoO_{3-\delta}$ to hydrogen peroxide is suggested to be caused by a change in the oxygen vacancy concentration in $La_{0.5}Sr_{0.5}CoO_{3-\delta}$ during its reaction with hydrogen peroxide. The investigation of the oxide oxygen vacancy concentration by means of the corresponding work function measurement will be discussed.

Acknowledgements

The authors would like to thank Johan Bomer and Frank Roesthuis for technical support. The Dutch Technology Foundation (STW) is acknowledged for financial support.

References

[1] L.G. Coccia, G.C. Tyrrell, J.A. Kilner, D. Walner, R. J. Chater, I.W. Boyd, Applied Surface Science, 96–98 (1996) 795-801.

[2] E. A. F. Spans, F. J. G. Roesthuis, D. A. H. Blank, H. Rogalla, Pulsed laser ablation of $La_{0.5}Sr_{0.5}CoO_{3-\delta}$, Applied Surface Science, 150 (1999), 171-177.

Relative Humidity sensors using porous SiC membranes and Al electrodes

E.J. Connolly[1], H.T.M. Pham[2], J. Groeneweg[2] P.M. Sarro[2] and P.J. French[1]

[1]Laboratory for Electronic Instrumentation & DIMES, T.U. Delft, Mekelweg 4, 2628 CD Delft, The Netherlands, e.j.connolly@its.tudelft.nl
[2] DIMES, T.U. Delft, Mekelweg 4, 2628 CD Delft, The Netherlands

Summary: *We report the fabrication and characterisation of capacitive relative humidity (RH) sensors based on porous SiC membranes and Al electrodes. The idea of the SiC is that it is a very durable material and that it should at least be better than Si at withstanding harsh environments. We use 73% HF and anodisation current-densities of 1-50mA/cm^2 to make SiC porous. We make use of the fact that the etch-rate of Al in 73% HF is very low, therefore allowing the possibility to use Al electrodes instead of Au. This also facilitates our sensor fabrication, as Al is more cleanroom friendly than Au. Preliminary data including sensitivity, response time, etc are given for our devices in the range 10% - 90% RH. SEM images are used to show cross-sections of the membranes.*

Keywords: *relative humidity sensor, porous SiC, Al electrodes*
Category: *2 (Materials and technology)*

1 Introduction

Porous silicon has been demonstrated to be very effective as a humidity sensor [1]. A well known problem with porous Si, however, is that it is very 'reactive' and so sensors based on this material generally need to have an ageing treatment to have reliable and repeatable sensitivity. SiC with its well known ability to withstand harsh chemical environments, should in principle be a better material for relative humidity sensing in such environments. Membrane or thin film structures have also been demonstrated, which is a big advantage as regards ease of integration with standard processing, due to greater flexibility in choice of doping type and concentration. We have made sensors using porous SiC, which can also be made porous by electrochemical anodisation in HF, similarly to single crystal silicon [2, 3].

2 Experimental

Thin films of (p-type) SiC were deposited on standard Si wafers, using PECVD, and doped with Boron in-situ. The thickness' of the films were ~5000Å.
After the thin films were deposited, a SiN mask was deposited on the backside of the wafer as a KOH mask to make membranes. Then Al electrodes were deposited on the front side.
For KOH etching we used 33% KOH and we stopped etching before the SiC was reached. This was because we expected to get a better ohmic contact to the (bulk) Si instead of the SiC.
After KOH etching, Al was evaporated on the backside of the wafer, and the wafers were diced into 10mm x 10mm samples. The samples were then mounted on specially prepared holders for porous formation.
We made porous SiC by electrochemical etching/anodisation using 73% HF (including Triton X100 surfactant), anodisation current densities, J_A, in the range 1 – 50 mA/cm^2, and anodisation times, t_A, between 30 seconds and 10 mins.
Figure 1 shows a schematic similar to the devices used in this work.
The phase angles of the sensing capacitors were typically (at RH values of 10%) ~ - 85°, indicating reasonable quality capacitors.
Electrical contacts were made to the sensors by wire bonding, and they were then tested in a Vaportron H-100L humidity chamber, with temperature as well as RH control. A HP 4194A impedance/gain-phase analyser meter operated at frequencies between 100Hz-100KHz was used for capacitance measurements. The experimental set-up is described more fully in [1].

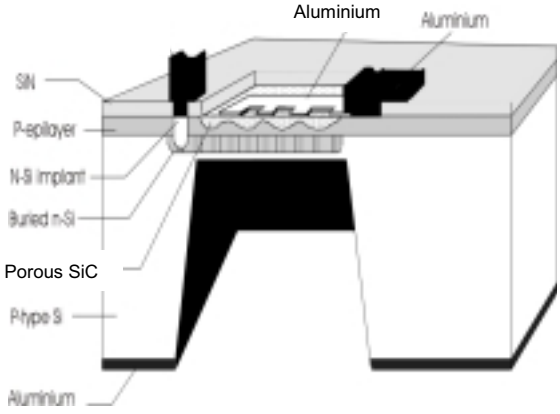

Fig. 1. Membrane RH sensor schematic

3 Results

Figures 2 and 3 show respectively the response of our sensors (at T=25˚C) as the RH is varied between 10% and 90% RH, and the response to step changes from 10% - 90% RH and 90% - 10% RH. We can see that the sensitivity is about 25%, it is slightly frequency dependant with the lower frequency having a little larger sensitivity. The lower frequency response also seems to be a little better for lower RH values. The response time is about 1.5-2 minutes for increasing RH and about 2-3 minutes for decreasing RH. Some drift to the final value is observed for the decreasing RH data.

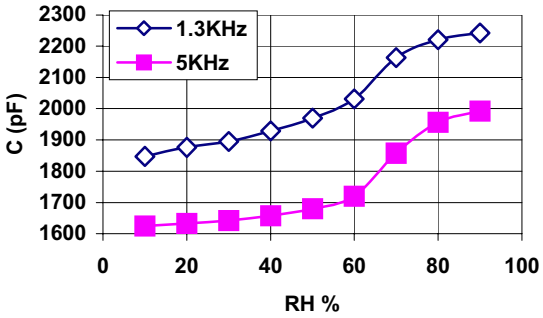

Fig 2 response of porous SiC to RH between 10% and 90% RH

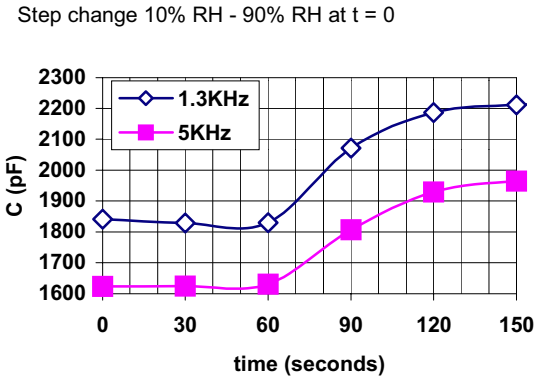

(a)

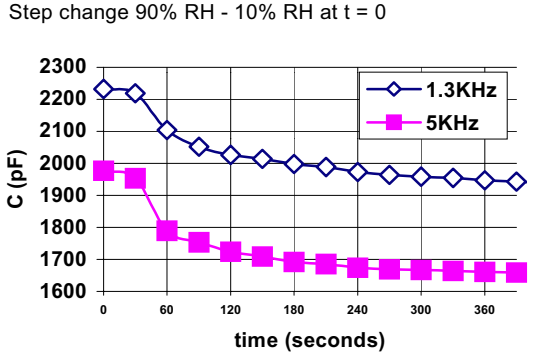

(b)

Fig 3 response times for (a) a step change 10% - 90% RH; (b) a step change 90% - 10% RH

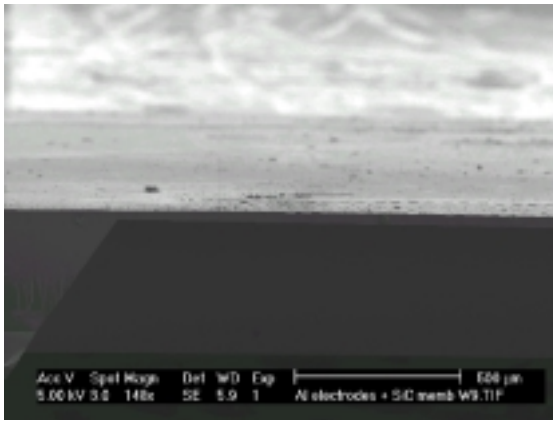

Figure 4 Cross-section SEM of the formed membranes. The thickness of the membranes is ~40µm (see also fig.5).

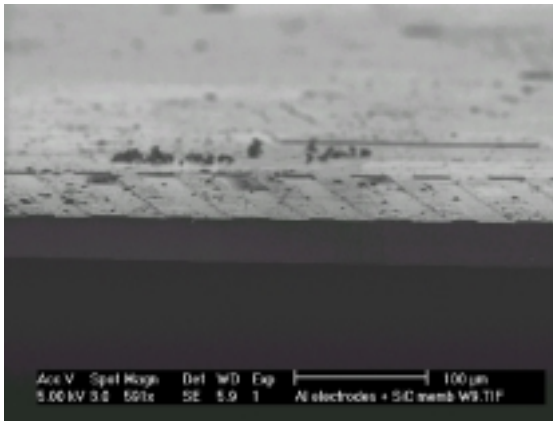

Figure 5 A higher magnification of a section of figure 4. The Al electrodes can be seen. Some sawing debris can also be seen.

References

[1] GM O'Halloran, "Capacitive humidity sensor based on porous silicon", PhD Thesis, TU Delft, 1999.

[2] AO Konstantinov, CI Harris, A Henry, E Janzén, "Porous silicon carbide: material properties, formation mechanism and techniques of material modification", Proc. Silicon Carbide and Related Materials Conference, Kyoto, Japan, 1995.

[3] EJ Connolly, GM O'Halloran, HTM Pham, PM Sarro, PJ French, "Comparison of porous silicon, porous polysilicon and porous silicon carbide as materials for humidity sensing applications", Sensors and Actuators **A 99** (2002) 25-30.

Fabrication Technology for Twin Nanochannels

V.G. Kutchoukov, L. Pakula, J.R. Mollinger, A. Bossche

Delft University of Technology, ITS/DIMES, Dept. of Microelectronics, Electronic Instrumentation Laboratory, Mekelweg 4, 2628 CD Delft, The Netherlands
email: v.g.kutchoukov@its.tudelft.nl http://titus.et.tudelft.nl/

Summary: *This paper presents a method for fabrication of nanochannels for fluidic applications. The nanochannels are created by etching the sacrificial layer located between two mechanical layers. The main advantage of the proposed technology is the use of standard UV lithography instead of e-beam lithography for defining the channels. The depth of the channels is controlled by the thickness of the sacrificial layer and the width by the etching time. The accuracy of the definition depends on the selected materials and the etching technique used. After the channels are created another mechanical layer is deposited to form completely the shape of the channels.*

Keywords: *nanochannels, fluidic devices*
Category: *2 (Materials and Technology)*

1 Introduction

In the past decade the interest in fabrication of micro- and nanochannels for fluidic devices has increased especially for biochemical applications [1]. However, scaling the dimensions of the channels down from micro- to nanoscale requires, in most cases, electron beam lithography to be used, which has high cost due to low throughput. Therefore, we propose a fabrication technology for nanochannels, which uses only a standard UV lithography. Moreover, the size of the nanochannels is not dependent on the resolution of the pattern, but only on the sacrificial layer thickness and its etching. An artist impression of the proposed nanochannels is shown in figure 1.

Another advantage of the technology described is that the nanochannels can be seen directly by using a transparent top-mechanical layer.

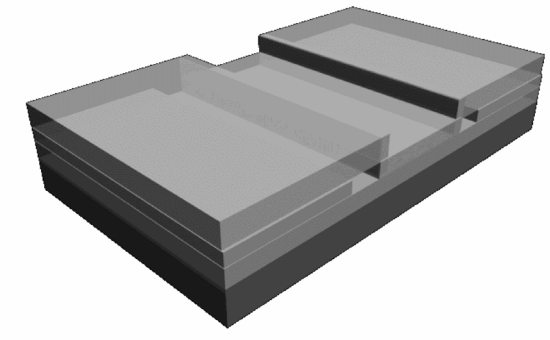

Fig. 1. Sketch of twin nanochannels created by sacrificial etching.

2 Fabrication Technology

The process flow, used for the fabrication of the nanochannels is shown in figure 2. As a substrate we have chosen a silicon wafer on which 300nm thermal SiO_2 was deposited in order to insulate the channels from the substrate [2]. In the next step we have deposited 150nm polysilicon as a sacrificial layer for the nanochannels. Afterwards a second SiO_2 layer is deposited by PECVD on the top of the polysilicon. The thickness of this layer in our experiment was 1μm. By using a photoresist and standard UV lithography a window is defined and the top SiO_2 is removed by dry etching. The sacrificial polysilicon layer was then etched by TMAH. TMAH was chosen instead of KOH due to its high selectivity to SiO_2 and low etch rate of the polysilicon layer [3].

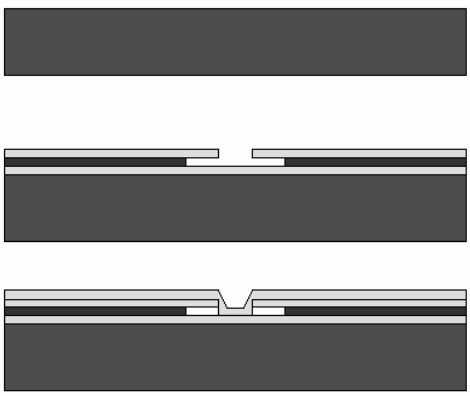

Fig. 2. Process flow for fabrication of twin nanochannels.

However, in order to remove the native oxide prior the etching with TMAH a short etch dip in BHF 1:7 for 1 minute is required. The sample was etched in TMAH 25wt% at 62°C for 3 minutes. SEM image of the resulting structure is shown in figure 3.

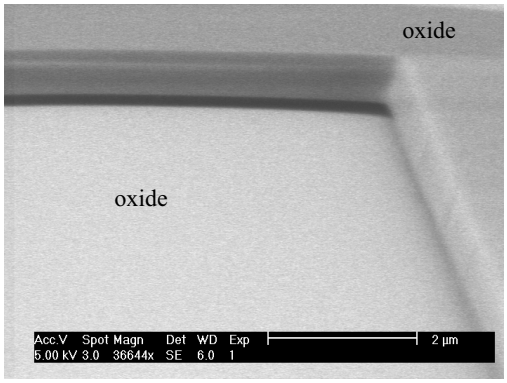

Fig. 3. SEM image of the sample after performing the etching of the sacrificial layer in TMAH.

In the last step an oxide layer was deposited on the top of the surface in order to close the nanochannels and to form their final shape. The thickness of the deposited oxide layer was 300nm. Figure 4 shows a SEM image of the cross-section of the realized channels.

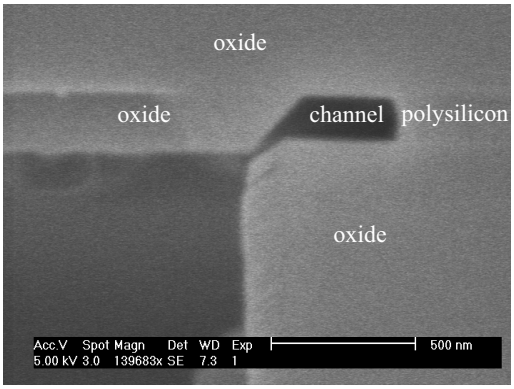

Fig. 4. Cross-section of the realized nanochannels.

3 Conclusions

We have demonstrated a simple process to fabricate twin nanochannels with controllable width and depth in the nanometer range. Normal UV lithography can be used to define the location of the nanochannels. The possibility to have transparent capping layers for the channels is demonstrated, allowing optical observation for biological experiments.

References

[1] J. Haneveld, H.V. Jansen, J.W. Berenschot, N.R. Tas, M.C. Elwenspoek, *The 13th Micromechanics Europe Workshop, MME'02*, October 6-8, 2002, Sinaia, Romania, pp. 47-50.

[2] J. Lichtenberg, G. Lammel, M. Oulevey, E. Verpoorte, Ph. Renaud, N.F. de Rooij, *Proc. 14th European Conference on Solid-State Transducers - EUROSENSORS XIV,* 27-30 August, 2000, Copenhagen, Denmark, pp. 463-466

[3] M. Shikida, K. Sato, K. Tokoro, D. Uchikawa, *Sensors and Actuators*, Vol. A80, 2000, pp. 179-188

Magnetotransport properties of nanostructured $La_{2/3}Sr_{1/3}MnO_3$ thick films

D.G. Lamas[1,*], L.B. Fraigi[2], A. Caneiro[3], D. Niebiskikwiat[3] and R.D. Sánchez[3,*]

[1]CINSO (Centro de Investigaciones en Sólidos), CITEFA-CONICET, J.B. de La Salle 4397, (1603) Villa Martelli, Pcia. de Buenos Aires, Argentina - email: dlamas@citefa.gov.ar
[2]CITEI, INTI, CC 157, (1650) San Martín, Pcia. de Buenos Aires, Argentina
[3]Centro Atómico Bariloche and Instituto Balseiro, CNEA, Pcia. de Río Negro, Argentina
[*]Member of CONICET, Argentina

Summary: *We report the magnetotransport properties of nanostructured $La_{2/3}Sr_{1/3}MnO_3$ thick films prepared by screen-printing technique. Nanocrystalline powders synthesised by liquid-mix with mean crystallite size of 25 nm were used as active material of screen-printable inks. A moderate firing temperature was used to avoid particle growth. High values of LFMR, of about 25-30% at 5K, were found due to the low crystallite size of the film. Ceramic samples prepared by uniaxial pressing and sintering in air were also studied for purpose of comparison.*

Keywords: *manganites, low-field magnetoresistance, thick films, nanostructured materials*
Category: *2 (Materials and technology)*

1 Introduction

In the last years, polycrystalline $LaMnO_3$-based materials have been intensively studied since they appear to be useful for magnetoresistive sensors. This is due to their large low-field magnetoresistance (LFMR), which is observed in the 0.1T range. It has been established that the LFMR increases as the grain size reduces, although in the case of $La_{2/3}Sr_{1/3}MnO_3$ it has been reported that the LFMR saturates at a value of 30% for a grain size of 400 nm. In addition, it has been reported that the high field magnetoresistance (HFMR) progressively increases when reducing the grain size and large values are obtained for grain sizes in the nanometric range [1,2].

Although nanostructured manganites have these interesting properties, magnetoresistive sensors are usually based on thick films sintered at relatively high temperatures (about 1100-1400°C), which results in large grain sizes [3,4]. In this work, we present the preparation of liquid-mix-derived nanostructured $La_{2/3}Sr_{1/3}MnO_3$ thick films and their magnetotransport properties.

2 Experimental Procedure

$La_{2/3}Sr_{1/3}MnO_3$ powders were synthesised by the liquid-mix method using appropriate amounts of La_2O_3 (99.999 %), $SrCO_3$ (99.994 %) and metallic Mn (99.99 %). The final thermal treatment was carried out in air at 600°C during 24 hours. The as-synthesized powders were studied by X-ray diffraction (XRD) employing a PW 1710 Philips diffractometer. The crystallite size was determined by means of the Scherrer equation. Powder morphology was studied by transmission electron microscopy (TEM), using a Philips CM200 microscope.

Standard screen printing methods were employed for obtaining nanostructured thick films on alumina (96% Al_2O_3). The screen printable ink was prepared by mixing the $La_{2/3}Sr_{1/3}MnO_3$ powder with an organic vehicle composed by a solution of ethyl cellulose in a blend of organic solvents (butyl carbitol acetate and terpineol). After drying the films for 10 min. at 110°C, they were fired at 850°C in air during 10 min, with heating/cooling slopes of ± 35°C/min. XRD was used to check the phases present in the films and to determine their crystallite size, as in the case of powders.

The magnetic characterisation of powders was performed using a Quantum Design SQUID magnetometer between 0 and 5T. M vs T measurements were carried out under a magnetic field of 0.5T in a temperature range of 10-370 K in order to determine the Curie temperature (T_c) from the maximum of $|dM/dT|$. The saturation magnetisation was measured at T = 5K and H = 5T.

The electrical resistivity of the films was measured by the usual four-probe method in the 5-300 K temperature range under a magnetic field between 0 and 9T. $\Delta\rho/\rho_o$ vs. H measurements were carried out for low magnetic fields (H < 0.7T). Ceramic samples, prepared by uniaxial pressing and heating in air at 600°C during 2 hs., were also studied for purpose of comparison.

3 Results and discussion

XRD study confirmed that nanocrystalline, single-phase powders are obtained by the liquid-mix synthesis method. The average crystallite size obtained from XRD data was of (25 ± 3) nm. This crystallite size was confirmed by TEM observations, and a very narrow size distribution was found

(standard deviation = 4 nm). The Curie temperature obtained by d.c. M-T curves was of (345 ± 5) K. The saturation magnetisation was about 64.6 emu/g (2.8 μ_B/Mn). The difference between this value and the one found for large grain materials, 93 emu/g (3.7 μ_B/Mn), can be attributed to the existence of a magnetically disordered surface, as proposed by Ll. Balcells *et al.* [1]. Considering that the magnetisation of this layer can be neglected, a thickness of 1.4 nm is deduced.

By means of XRD analysis, it was found that thick films and ceramic samples also were single-phased, with crystallite sizes very similar to that of nanopowders. In spite of this, significant differences were found in the transport properties. Fig. 1 shows the resistivity of thick films and ceramic samples as a function of temperature. The resistivity of ceramic specimens was one order of magnitude lower than that of thick films, although they presented a similar behaviour. A metal-insulator transition around 200 K and an increase of resistivity at low temperatures (T < 50 K) can be observed. The increment of ρ(T) at low temperature has been assigned to the existence of a Coulomb barrier at the grain-boundaries [1,5]. Within this temperature range, the resistivity follows a $\rho(T) = A\ exp[(\Delta/T)^{1/2}]$ law, where Δ is the Coulomb gap. By a linear adjustment of the $ln\ \rho(T)$ *vs.* $(1/T)^{1/2}$ curve for T < 50 K, the value Δ was obtained: Δ = (5.83 ± 0.06) K for films and Δ = (2.86 ± 0.06) K for ceramics.

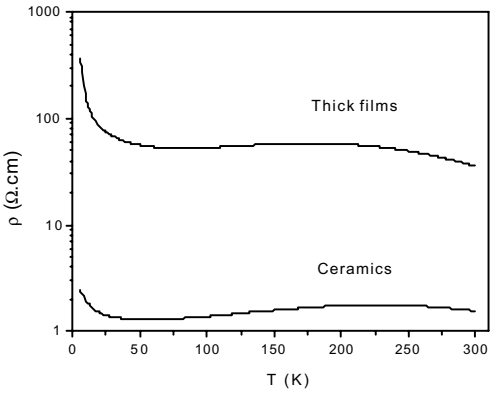

Fig. 1. Resistivity of thick films and ceramic samples as a function of temperature.

The important difference in resistivity and Coulomb gap of both materials is probably due to a larger number of 'good-conducting' paths [5] in ceramic bodies, favoured by the uniaxial pressing. However, different grain boundary composition due to the presence of a very small amount of carbonaceous residues in thick films (incomplete elimination of the organic solvents introduced for the preparation of inks) can also explain these results.

Fig. 2 shows the field dependence of the magnetoresistance, $\Delta\rho/\rho_o = (\rho - \rho_o)/\rho_o$ (ρ_o is the resistivity under H = 0) for both thick films and ceramic samples, plotted for different temperatures between 5 and 200K. As it can be observed, the LFMR of thick films is higher than that of ceramics for T = 5K, but the contrary is found for high temperatures. The LFMR was about 25-30% at 5K, but it decreased rapidly with increasing temperature. Similar results have been reported in the literature [1,2,5,6]. Differently, the HFMR was slightly higher for thick films and showed its maximum value around 100-150K.

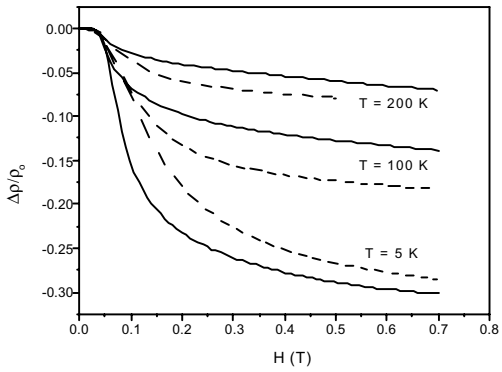

Fig. 2. MR of thick films (solid lines) and ceramic samples (dashed lines) as a function of magnetic field for different temperatures.

4 Conclusions

In this work, we report the preparation and magnetotransport properties of nanostructured $La_{2/3}Sr_{1/3}MnO_3$ thick films. High values of LFMR, of about 25-30%, were found due to the low crystallite size of the material (25 nm). Differences in the properties of thick films and ceramic compacts have been found, probably due to a larger number of 'good-conducting' paths in the ceramics.

References

[1] Ll. Balcells, J. Fontcuberta, B. Martínez and X Obradors. *Phys. Rev. B*58 (1998) R14697-R14700.

[2] Ll. Balcells, B. Martínez, F. Sandiumenge and J. Fontcuberta. *J. Magn. Magn. Mater.* 211 (2000) 193-199.

[3] Ll. Balcells, R. Enrich, A. Calleja, J. Fontcuberta, and X Obradors. *J. Appl. Phys.* 81 (1997) 4298-4300.

[4] Ll. Balcells, J. Cifre, A. Calleja, J. Fontcuberta, M. Varela and F. Benítez. *Sensors and Actuators* 81 (2000) 64-66.

[5] M. García-Hernández, A. de Andrés, J.L. Martínez, C. Prieto, A. Muñoz and L. Vazquez. *Thin Solid Films* 373 (2000) 94-97.

[6] D.G. Lamas, A. Caneiro, D. Niebieskikwiat, R.D. Sánchez, D. García and B. Alascio. *J. Magn. Magn. Mater.* 241 (2002) 207-213.

Micromechanical electrostatic field sensor for the detection of surface charges

M. Hanf and W. Dötzel

Chemnitz University of Technology, Faculty of Electrical Engineering and Information Technology, Reichenhainerstr. 70, 09126 Chemnitz, Chemnitz
email: hanf@infotech.tu-chemnitz.de http://www.tu-chemnitz.de

Summary: *Electrostatic driving and capacitive read out play an important role in MEMS. Because the electrodes are placed on insulating materials and in some cases they are coated with an insulating layer it has been observed that after electrical breakdown in the air gap or the contact of the movable element and the dielecric layer charges are deposited on the insulating materials which influence the characteristic of the MEMS. The article presents a novel electrostatic field sensor realized using micromechanical components. It was developed to characterize surface charges on dielectric layers mainly in the region of electrode structures.*

Keywords: *electrostatic field sensor, surface charge, extended*
Category: *2 (Materials and technology)*

1 Introduction

Electrostatic driving and capacitive read out play an important role in MEMS. These systems consist of the micromechanical component and the driving and the detection electrodes, respectively. The electrodes are placed on insulating materials and in some cases they are coated with an insulating layer to prevent short circuit. It has often been observed that insulating materials carry charges for a long time after charging. These charges affect the characteristics of micromechanical systems like an additional offset voltage []. An example of this influence is shown in Figure 1. The driving electrodes of this MEMS are coated with an insulating layer stack of SiO_2 and Si_3N_4. It is to be seen that after electrical breakdown in the air gap at high positive or negative voltages the whole curve of the static deflection of a cantilever tip is shifted along the x-axis. Furthermore it is known that an additional offset voltage leads to a change of the dynamic characteristic of the electromechanical system. In literature measurement methods to characterize surface charges are described. Some examples are given in [2]-[5]. The charge distribution on insulating materials is visualized by scanning electron microscopy (SEM) and the surface potential or the capacitance are measured using the Kelvin probe force microscopy (KPFM), the electrostatic field meter (EFM), electrostatic voltmeter (EVM) or the electric atomic force microscopy (EAFM).

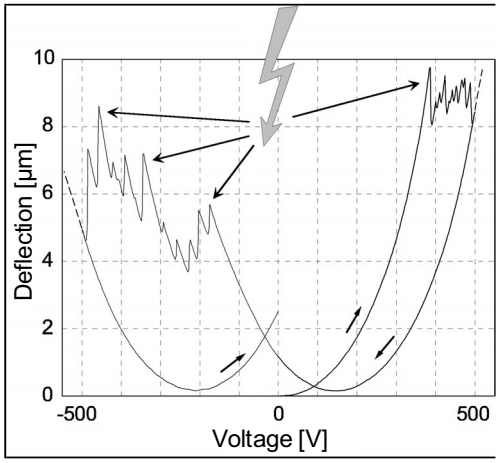

Figure 1: Influence of electrical breakdown in the air gap on the static deflection of a cantilever tip vs. the applied voltage []

2 Function principle

To characterize the behaviour of charges on dielectric layers in the region of driving or sensing electrodes of capacitive MEMS a measurement technique was developed that is related to the KPFM. Figure 2 shows a scheme of the realized electrostatic field sensor. It consists of a bending beam with a cubic tip whereby the lower surface is the sensing area with a size of about 50 µm x 50 µm. A sinusoidal voltage with the frequency ω and an adjustable offset voltage is applied between the sample and the beam. The calculation of the resulting electrostatic force on the sensing area will be presented in detail in the article. Without any additional offset voltage and no surface charges are present the final equation includes only a term with the frequency 2ω. Consequently the tip of the beam will oscillate with 2ω. If surface charges are present

the equation will consist of terms with the frequencies ω and 2ω. The velocity of the motion of the beam tip is detected by a laserdoppler interferometer and a signal analyzer calculates the FFT and integrates the signal to obtain the deflection amplitude vs. frequency. The amplitude at the frequency 2ω is used to adjust the distance between sensing area and sample surface and the amplitude at the frequency ω is used to control the offset voltage of the applied driving voltage that way that the detected amplitude at this frequency becomes zero. A computer controls the measurement setup, i.e. it drives the x-y-z-table with the sample, communicates with the signal generator and the signal analyzer and stores the obtained data for the topography and the surface potential which is equal to the applied offset voltage. The measurement setup will be explained in more detail in the article.

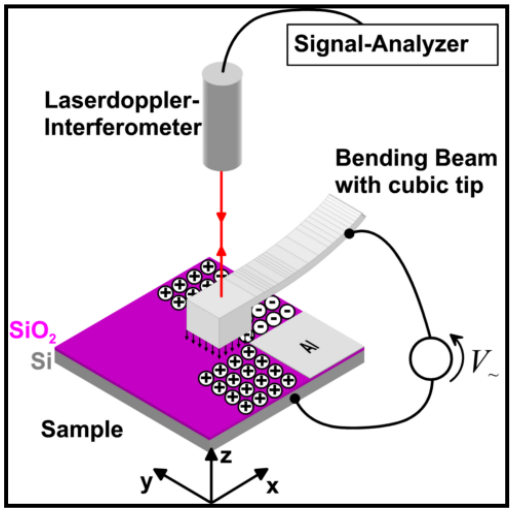

Figure 2: Scheme of the realized electrostatic field sensor

3 Results

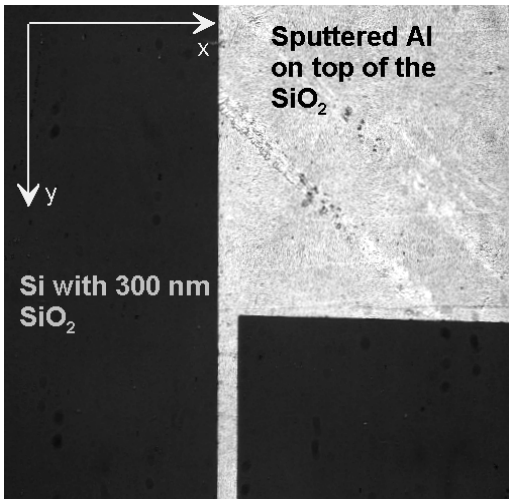

Figure 3: Top view of the used sample, Si with wafer thickness with 300 nm thermal grown SiO_2 and a sputtered Al-structure on top of the SiO_2

First measurement results were obtained with test structures which consist of Si with wafer thickness with 300 nm thermal grown SiO_2 and sputtered aluminum-structures, Figure 3. The capacitor created this way is charge to several voltages and the sample was scanned after that. Figure 4 shows a result measured after charging the Al to +5 V. Latest obtained results will be presented and discussed in the paper.

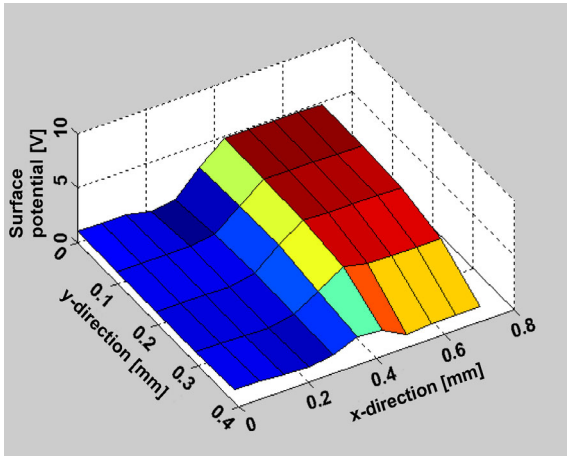

Figure 4:Measured surface potential distribution Al charged to +5 V, see also Figure 3

References

[1] Wibbeler, J. et al.: *Parasitic charging of dielectric surfaces in capacitive microelectromechanical systems (MEMS).* Sensors and Actuators A 71, 1998, pp. 74-80

[2] Hülz, H.: *Elektrische Charakterisierung der Oberfläche ferroelektrischer Schichten.* Dissertation, Dresden, 1998

[3] Riehl, P. S.: *Microsystems for Electrostatic Sensing.* Dissertation. Berkeley, 2002

[4] Schmutz, P.; Frankel, G. S.: *Characterization of Potential Inhomogeneities on Passive Surfaces by Scanning Kelvin Probe Force Microscopy.* The 8th International Symposium on Passivity of Metalls and Semiconductors, M. B. Ives, Jasper, Canada, 5/99

[5] Likodimos, V.; Labardi, M.; Allegrini, M.; Garcia, N.; Osipov, V. V.: *Surface charge compensation and ferroelectric domain structure of triglycine sulfate revealed by voltage-modulated scanning force microscopy.* Surface Sience, 490 (2001), 1-2, pp. 76-84

Fabrication of a CMOS compatible vertical accelerometer

L.S. Pakula, H. Yang and P.J. French

Delft University of Technology, ITS/EI, Mekelweg 4, 2628 CD Delft, The Netherlands
email: l.pakula@its.tudelft.nl

Summary: *This paper presents the fabrication process of a CMOS compatible surface micromachined vertical accelerometer. PECVD silicon carbide was used as mechanical layers due to its good properties. Aluminium was chosen for electrodes. As the maximum processing temperature is 400℃, the sensor can be made on top of the CMOS readout circuit as post-processing. The sensor is designed to operate in range -5/+5g with sensitivity 1.8Ff/g. The sensor has been fabricated and is under measurement. The initial measurement shows that the initial capacitance is 0.42pF.*

Keywords: *surface micromachining, silicon carbide, vertical accelerometer.*
Category: *Materials and technology*

1 Introduction

Microaccelerometers are one of the most important silicon sensors [1]. In this paper, we describe a CMOS compatible post-processing surface micromachined accelerometer.
The compatibility to CMOS process imposes material and technological limitation on the accelerometer fabrication process, like thermal budget and stress. By proper selection of materials it is possible to maintain cleanroom compatibility and simplify production process.
Surface postprocessing surface micromachining technology enables integration of the sensor with electronic read-out circuit on one chip.
It has many advantages, including reduction in size, simplification of packaging and therefore cost reduction.
Silicon carbide appears in many crystallographic forms and therefore with wide spectrum of properties finding its place in many fields like optoelectronics, microelectronics and MEMS. Due to its very good properties such as high mechanical strength, high thermal conductivity, ability to operate at high temperatures, resistance to harsh environment and extreme chemical inertness in several liquid electrolytes [2] has great potential in Micro Electro Mechanical Systems (MEMS).
The properties of PECVD amorphous SiC can be controlled over a wide range (for example, –400MPa to 400MPa for stress) by changing the deposition conditions, especially the ratio of the gases used [3].

2 Fabrication process

Presented sensor was fabricated using surface micromachining technology. Fig.1 shows the schematic drawing of the sensor. The mass consists of three layers SiC-Al-SiC suspended on four doubled-layer SiC-Al springs. The bottom electrode is divided in four parts, which enables the minimizing of the measurement error introduced by rotation of the sensor round x or/end y-axis.

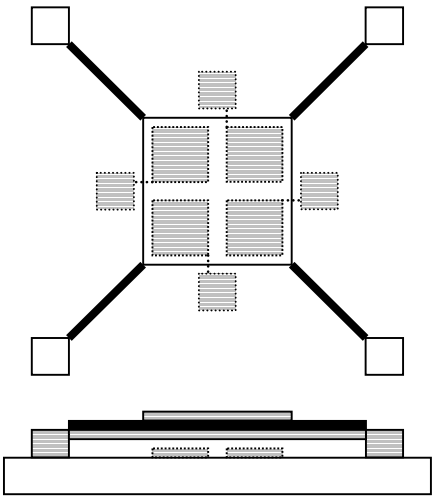

Fig. 1. Schematic view of vertical accelerometer.

The electrical and mechanical properties of the device have been calculated and simulated with ANSYS. The initial capacitance is calculated to be 0.58pF. The resonant frequency is simulated to be 5.6kHz. Special attention has been paid to the damping. The calculation shows that the critical damping can be achieved when the size of the damping holes is 6μm and the distance between two holes is also 6μm. The damping ratio is simulated to be 0.78 with ANSYS/FLOTRAN. The sensitivity is calculated to be 1.8fF/g.

Low stress PECVD silicon carbide [4] was used as a mechanical material, and aluminium for the electrodes. In order to avoid the problem of stiction the freeze-drying process step has been employed.
The process flowchart is presented below:
First Al was sputtered in Trikon Sigma sputter coater on Si/ox/SiN wafer. After lithography the

layer was patterned in Trikon Omega 201 plasma etcher, forming the first (bottom) electrode set.
Next sacrificial layer was processed: (see fig 2a.)

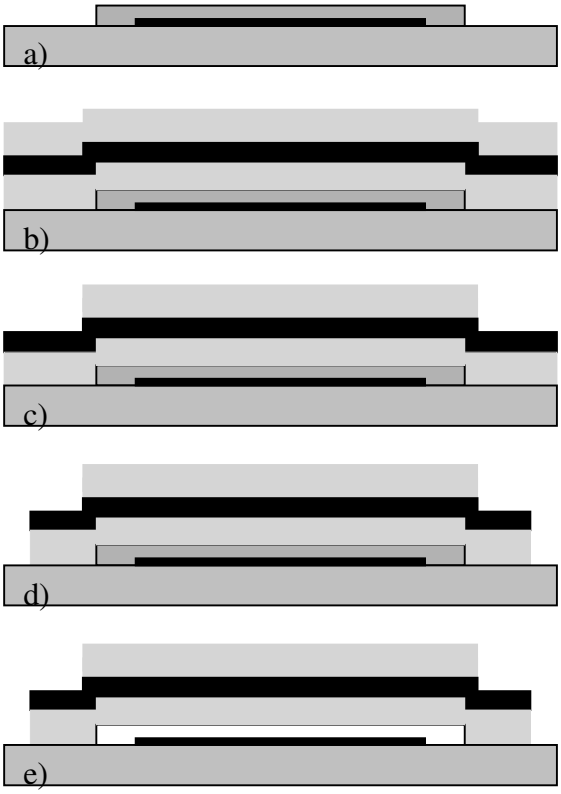

Fig. 2. Fabrication steps of vertical accelerometer.

1 µm 4% PSG (4% P in PSG) layer was deposited in Novellus PECVD system. Then the sacrificial layer was patterned using Drytek plasma system.
Now membrane has to be build. 1.8 µm of PECVD Low stress SiC was deposited in Novellus Concept One system. The condition of silicon carbide deposition are listed below:

SiH_4 flow:	0.25 slm
CH_4 flow:	3 slm
Pressure:	2 Torr
Temperature:	400°C
Power: HF	450W
LF	150W

Those conditions providing assure the deposition of SiC with 65MPa tensile stress.
Directly on top of silicon carbide, 1.4µm aluminium electrode layer was sputtered using the same system as for the first Al layer. Next to aluminium, second 1.8µm low stress PECVD SiC layer was deposited (fig 2b). After applying the mask the layer is patterned in Alcatel GIR300 fluorine etcher in CF_4:SF_6:O_2 = 70:10:10 sccm gas mixture to form top layer of membrane. (fig. 2c). Then next mask is applied to pattern both aluminium and silicon carbide beneath. Both layers are etched in the same plasma. The plasma conditions are:

Cl_2 flow:	30 sccm
HBr_4 flow:	40 sccm
Pressure:	5 mTorr
Temperature:	20°C
Power: RF	35 W

To prevent accidental removing of the bottom Al electrode, the process should be stopped before the SiC layer is etched thru. Then the chlorine based plasma is changed to fluorine based plasma:

SF_6 flow:	70 sccm
CF_4 flow:	10 sccm
O_2 flow:	10 sccm
Pressure:	0,05mBar
Power: HF	60 W

which stops etching on bottom aluminium.

The structure was released by removing PSG sacrificial layer in HF (fluoric acid) with addition of 2-propanol (fig 2e). To prevent problem of stiction the freeze drying step is applied after the sacrificial step.

3 Results

The device has been fabricated. The picture of fully released structure is presented on fig. 3. The initial capacitance is measured to be 0.42pF. The device is under measurement.

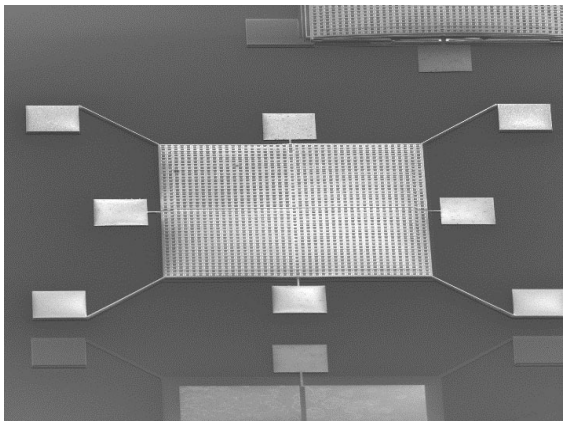

Fig. 3. SEM photo of fully released vertical accelerometer.

References

[1] N. Yazdi et al., "Micromachined inertial sensors", Proc. of the IEEE, , Vol.86, No.8, August 1998 pp. 1640-1659.
[2] H.T.M. Pham et al., Proc. Micromachining and Microfabrication Process Tech., SPIE 2001, Vol.4557, pp. 272-279.
[3] P.M.Sarro et al., *"Low-stress PECVD SiC thin films for IC-compatible microstructures"*, Sensors and Actuators A67 (1998), pp.175-180.
[4] H.T.M. Pham, C.R. de Boer, L. Pakula, P.M. Sarro, *"Influence of Deposition Parameters and Temperature on Stress and Strian of Insitu doped PECVD Silicon Carbide"*, Materials Science Forum vols. 389-393 (2002), pp. 759-762

NiO-based thin films with Pt surface modification for H_2 detection

I. Hotovy[1], J. Huran[2], P. Siciliano[3], S. Capone[3], L. Spiess[4]

[1]Slovak University of Technology, Microelectronics Department, Ilkovicova 3, 812 19 Bratislava, Slovakia, e-mail: hotovy@elf.stuba.sk
[2]Institute of Electrical Engineering, Slovak Academy of Sciences, Dubravska cesta 9, 842 39 Bratislava, Slovakia
[3]I.M.M.-C.N.R., Sezione di Lecce, Via Arnesano, 73100 Lecce, Italy
[4]Technical University, Department of Materials Technology, PF 100565, D-98684 Ilmenau, Germany

Summary: *In this work, the surface modification of nickel oxide thin films deposited by dc reactive magnetron sputtering using Pt is presented. The surface modified NiO thin films have been investigated with respect to structural, surface morphological and gas sensitive properties t. The Pt very thin overlayers with a thickness of about 3 and 5 nm were formed on top of NiO surface by sputtering. The electrical responses of the NiO-based sensors towards H_2 concentration (500-5000 ppm) have been measured.*

Keywords: Nickel oxide, thin films, surface modification, Pt, H_2 sensor
Category: *2 (Materials and technology)*

1 Introduction

A promising approach in this field is both to use novel materials based on semiconducting metal oxides, and to exploit the advantages of microelectronic and micro-mechanical technologies for the fabrication and production of a system compatible with current electronic information systems. Moreover, the surface properties and the deposition conditions of these materials play an important role in the properties of MOS-based gas sensors. Hence, a considerable interest is normally devoted to the preparation and characterisation of the sensing films.

Nickel oxide, that is usually taken as model for *p*-type, is an attractive material well known for its chemical stability as well as for its excellent optical and electrical properties. Indeed, NiO thin films have been studied for applications in electrochromic devices and also as functional sensing layers for MOS gas sensors. NiO films can be fabricated by different physical and chemical vapour deposition techniques, such as reactive sputtering and plasma-enhanced chemical vapour deposition. The preparation method and the deposition mode are fundamental in determining the properties of MOS thin films, but the effective dependence of the process parameters on the film properties is not well defined. Nevertheless, it is evident that the improvement of the material properties and performance as gas sensor can be reached by adding catalyst or promoters [1].

2 Experimental

The NiO films were deposited by dc reactive magnetron sputtering from a Ni target in a mixture of oxygen and argon. Two types of unheated substrates were used: Si and alumina substrates. A sputtering power of 600 W was used. Both argon inert and oxygen reactive flow were controlled by mass flow controllers. The relative oxygen partial pressure was 20 %. The total gas pressure was kept at 0.5 Pa. Details of these sputtering deposition conditions were given elsewhere [2]. The NiO film thickness under the above conditions was 100-150 nm and was measured by a Talystep. On top of these base films thin Pt overlayers (3, 5 nm) were deposited through photolithographic mask by magnetron sputtering. After deposition, the films were annealed in a tube furnace for about 4 h in dry air at 500ºC.

The crystal structure was identified with a Theta Theta Diffractometer D 5000 with Goebelmirror into Bragg-Brentano focusing with copper radiation. The surface morphology and the elemental distribution were observed by a LEO 1420 SEM with an energy dispersive X-ray (EDX) analyser based on a germanium detector and operating at 12 kV acceleration voltage. Different lateral parts of the sensor structure were thus analyzed in order to check the elemental distribution.

The sensor structures were mounted as suspended devices onto standard TO-8 packages and introduced into a test chamber in teflon for the sensing tests in controlled ambient. A gas flow controller (MKS mod. 647B) connected to mass flow meters (MFCs) and to certified gas bottles allows to dilute the target gas in dry air at different concentrations. The sensor working temperature was so controlled and varied in the range from 25 to 250° C. A dc voltage of 1 V was applied across the sensing films and the electrical current was measured by using a Keithley (mod. 6517A) electrometer equipped with a multiplexer.

3 Results

From XRD spectra of undoped NiO films it was found that they had polycrystalline structure (f.c.c. NiO phase). The diffraction pattern showed the presence of diffraction peaks from the (111), (200) and (220) lattice planes of the NiO lattice. Peak positions were present at angles smaller by around 0.7-1.2 degree, which means a bigger distance between the lattice planes than expected in theory. It was detected that these films have a strong (200) diffraction peak indicates a preferred orientation along [100] direction. In case of NiO films with a 3 nm thick Pt surface modification no peaks of Pt were observed due to the small amount of platinum applied. All NiO peaks were suppressed.

The SEM pictures obtained for undoped and NiO film with 3 nm Pt displayed in Fig. 1 show different porosity. The morphology of undoped NiO films is covered by a rough and compact granular structure, but in the case of Pt modifying it is less regular, showing the presence of pores.

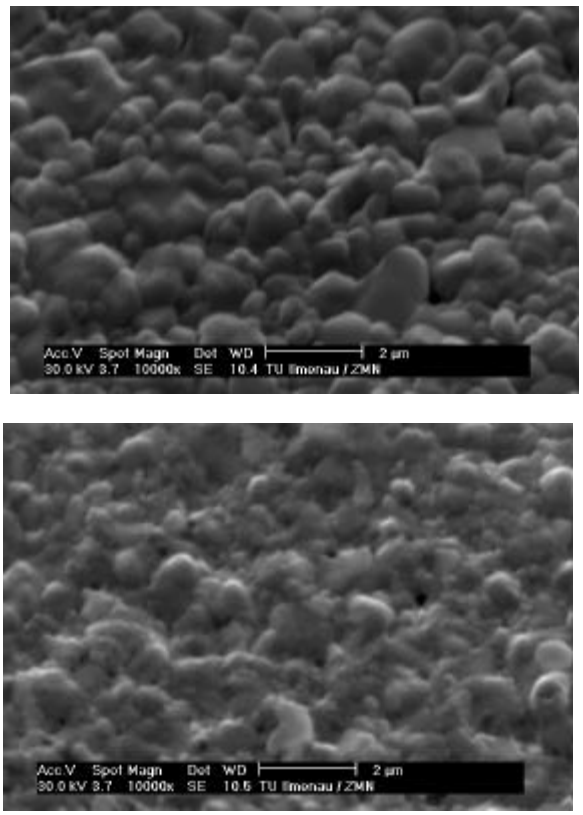

Fig. 1. SEM micrographs of NiO base film (top), NiO film with 3 nm Pt (botoom).

EDX microanalysis revealed that Pt is present on the NiO films modified with a Pt overlayer of 3 nm thickness. Fig. 2 shows EDX spectra obtained within this sample.

The response of NiO thin films to H_2 is improved by a factor of 1.6-2.0 using a thin Pt (3 nm) overlayer at 150-250ºC (Fig. 3). Compared to pure NiO films, NiO films modified using a thin Pt show a significantly enhanced dynamic response to H_2 at 150-250ºC (Fig. 4).

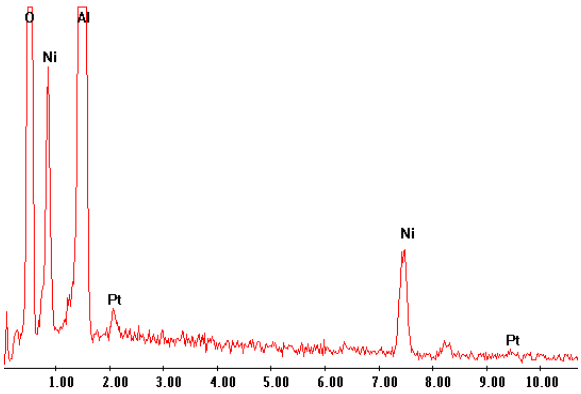

Fig. 2. EDX spectra from sample of NiO film with 3 nm Pt.

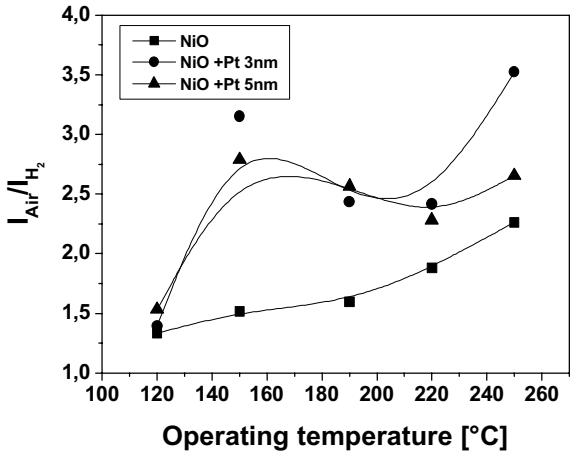

Fig. 3. Response to 1000 ppm H_2 for the NiO-based sensors as a function of working temperature.

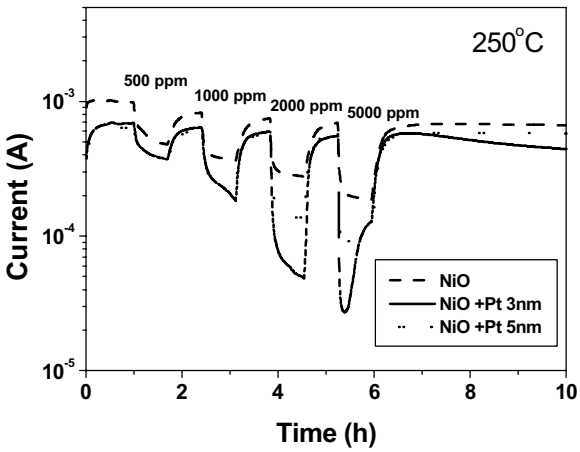

Fig. 4. Dynamic response of the NiO-based sensors to the H_2 measurement protocol at 250ºC.

References

[1] A. Salehi, M. Gholizade, *Sensors and Actuators* B89 (2003), 173-179.

[2] I. Hotovy et al., *Sensors and Actuators* B78 (2001), 126-132.

Investigation of a conducting polymer O-ring seal for microvalves

R. Tamadoni[1], P.N. Bartlett[2], D.G. Chetwynd[1] and J.W. Gardner[1]

[1]School of Engineering, University of Warwick, Coventry, CV4 7AL, UK
Email: j.w.gardner@warwick.ac.uk; Web: http://www.eng.warwick.ac.uk
[2]Department of Chemistry, University of Southampton, Southampton SO17 1BJ, UK

Summary *The gas-sealing properties of a novel electro-deposited poly(pyrrole) O-ring have been studied. The leakage flow rate through a polymer O-ring seal was determined using a vacuum system by measuring the change in the pressure dropped across it. The result suggested that the generalised leakage flow (q) through the poly(pyrrole) O-ring seal was proportional to the film thickness (d) and the film porosity. It was also found that the effectiveness of the polymer seal is increased by the application of an external load. This effect was most significant on the thickest poly(pyrrole) film of 2.7 μm.*

Keywords: *Poly(pyrrole) O-ring seal, thickness dependence, generalised flow, leakage rate, porosity*
Category: *2 (Materials and technology)*

1. Introduction

Although conducting polymers have been the subject of a large number of studies in different fields, for example as chemoresistor sensors [1], little work has been reported on their mechanical properties [2]. Novel properties of conducting polymers, such as their reproducibility, ability to be electro-deposited into small spaces in any shape and pattern [3], make them an attractive material for use in microengineering systems. This work is a continuation of preliminary studies being carried out by Warwick University to investigate the behaviour of the conducting polymers as electro-deposited seals in micro-valve systems [4].

2. Experimental

2.1 Test rig design

A low cost test rig has been designed and constructed to investigate the sealing properties of conducting polymer O-rings under different load forces. It measures leakage (rising pressure) into a partly-glass vacuum chamber through an electromechanical valve, controlled by commercial LabView™ software. The test rig consists of a stainless steel vacuum chamber (35 ml volume), a vacuum pump, a manual sealing valve and a digital pressure sensor to monitor the chamber pressure. A glass pentaprism with a 750 μm diameter through hole provided an ideal surface for the O-rings sealing contacts. Accurate alignment of the O-rings' centres over the hole was achieved using the pentaprism, a magnifying TV camera and an X-Y-Z positioner.

A solenoid with a saturated magnet attached to a spring beam provided a linearly controlled electromagnetic force to apply external pressure on the O-rings. This was achieved using a constant current source drive and a software program written in Labview. It supplied sufficient current for generating the desired magnetic field within the coil. Figure 1 illustrates the technical arrangement of the experimental test rig.

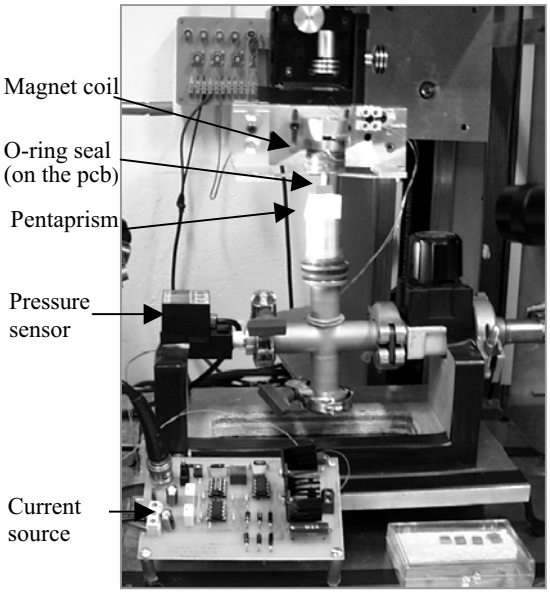

Figure 1. The photograph of the test rig designed to investigate the O-ring characteristic in vacuum condition.

2.2 Measurement procedure

Poly(pyrrole) with counterion 1-butane sulphonic acid (PPY-BSA)) was electrochemically deposited on the SRL 168 O-ring devices in the Chemistry department at Southampton University. Three different polymer thicknesses (1 μm, 2 μm and 2.7 μm) were used in the measurement. All testing was carried out under similar conditions at room temperature. The O-rings were subjected to a vacuum pressure of about 10^5 Pa each for leakage test. The rate of pressure change in the chamber was measured for different O-ring thickness, d.

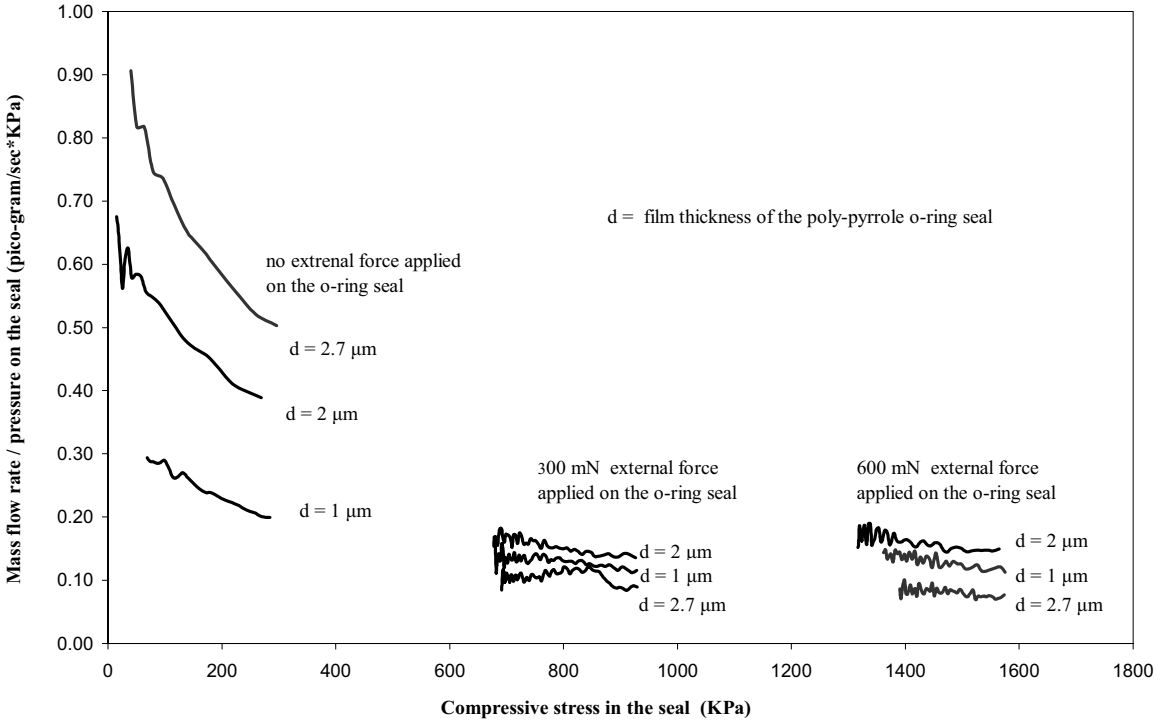

Figure 2. The effect of the closure force and the seal thickness on the leakage flow rate

Further experiments were carried out with the additional application of an external force to the O-rings of 300 mN and 600 mN, respectively. All the data were finally recorded and saved in a spreadsheet file using a Labview program.

3. Results and discussion

A simple mathematical model defines the leakage of a gas through a poly(pyrrole) O-ring as

$$\dot{q} = p_s \times 1/X$$

where $\dot{q}$ is the generalised flow, p_s is the differential pressure on the seal and X represents all the "resistive" parameters in the seal that have an effect on the leakage flow (e.g. average roughness, compressive stress, film porosity). Figure 2 illustrates the effect of the closure force and the film thickness on the seal resistivity (i.e. q/p_s). In natural seal conditions (i.e. no external force), the film thickness is almost inversely proportional to the resistivity ($d \propto 1/X$). This confirms that the leakage process is linear and partly through the pores within the polymer film. If thick films compress more, it does not overcome their greater porosity and surface roughness.

Applying external forces to the poly(pyrrole) seals increased the resistivity effect, improving the sealing property. The thickest film (2.7 μm) showed the best sealing action, while the middle one improved less with increased load. It appears that the external axial force on the thickest polymer seal (with the most pores) compresses the pores and hence restricts the leakage flow rate through the seal, but thinner films are too stiff for this to occur. We also expect that the application of an external force to control the leakage rate is more effective on less dense polymers (with more porosity). Thin films may be better if only natural sealing is used.

These findings may be considered as important factors in the design of an intelligent seal with controllable mechanism. The promising action with gases suggests that the seal will be very good with liquids and direct investigations are proceeding.

References

[1] J.W. Gardner and P.N. Bartlett, Application of conducting polymer technology in Microsystems, *Sensors and Actuators A,* 51, 1-10, 1995

[2] X. Liu, D.G. Chetwynd, J.W. Gardner, S.T. Smith, C. Beriet, P.N. Bartlett, Measurements of tribological properties of poly(pyrrole) thin film bearings *Tribology International*, **31**, 313-323, 1998

[3] W.R. Salaneck, D.T. Clark, E.J. Samuelsen, Science and applications of conducting polymers, *Proceedings of the Sixth Europhysics industrial Workshop,* Lofthus, Norway, (May 1990), 161-170

[4] Q. Fang, D.G. Chetwynd, J.W. Gardner, Conducting polymer as electro-deposited seals and glues for microvalves and micro structures, EPSRC Report, EPSRC Grant No GR/M60170, June 2001

Miniaturised Thermocouple For Simultaneous Temperature and Hydrogen Sensing

L. Sandro[1], A. Orsini[1], E. Proietti[2], R. Beccherelli[2], C. Di Natale[1,2], A. D'Amico[1,2]
[1]University of Tor Vergata - Department of Electronic Engineering Via di Tor Vergata 110 - 00133 Roma
Sensors and Microsystems Group - 00133 Roma (ITALY)
e-mail damico@eln.uniroma2.it
[2]IMM-CNR Sezione di Roma, Via Fosso del Cavaliere 100, 00133 Roma (ITALY)

Summary: *We will present vacuum deposited miniaturised Cu-Pd thermocouples. They show simultaneous sensitivity to temperature and gaseous hydrogen. They are realised atop a thin film Si_3N_4 membrane suspended on a micromachined substrates. This construction results in fast response and low insertion error in the temperature measure.*

Keywords: *thermopile, temperature, hydrogen sensing,*
Category: *2 (Materials and technology)*

1 Introduction

Thermocouples are self-powered highly sensitive and nearly linear temperature sensors. Several types have been coded as "standard ITS-90" and characterised [1]. The choice on the specific type to use in practical applications is determined by required temperature range, sensitivity and, often, by environmental conditions the thermocouple has to operate in.

Integration of a thermocouple on a substrate is needed in most applications where temperature is to be monitored simultaneously with other physical and chemical quantities. Use of conventional vacuum processes and simple lithographic steps allow easy manufacturing and relatively low cost per unit. However standard thermocouples are based on alloys. However when either evaporation or sputtering techniques are used, stoichiometric composition of deposited thin film thermocouples might not be fully guaranteed from run to run. This affects reproducibility. On the other hand vacuum deposited thin films of very high purity metals can be routinely obtained.

Thin films have a vanishing disturbance on heat transfer on the substrate. Further improvements can be achieved by shrinking their in-plane width. This miniaturisation allows die area savings. It also allows more precise temperature monitoring by placing the thermocouple in close vicinity to other sensors in a multisensorial system exposed to the environment. One could also envisage a thermocouples made of at least one chemically interactive metal. This was demonstrated for Pd and H_2 [2].

Thin film miniaturised thermocouples can also have short response time, in the 100 µs range [3]. This is often limited by thermal delay due to bulky substrates.

At this conference we will present a miniaturised Cu-Pd thermocouple capable of detecting hydrogen. Fast response is achieved by realising the thermocouple onto a thin dielectric membrane.

2 Fabrication of devices

We have chosen palladium because of its affinity to hydrogen. Indeed Pd:H and Pd are *different* materials having *different* absolute thermoelectric power (ATP)[2]. The ATP of Pd and Pd:H are positive. Hence a second metal with negative ATP is preferred. Several materials like Mo, W, Fe, Ag, Au or Cu can be used. However refractory metals are hard to evaporate and often alloy with the crucible. Iron is ferromagnetic, hence incompatible with electron-beam evaporation. Therefore we have focused our attention on copper and left more expensive gold for future investigation. While for Au a very thin film of Cr is needed as adhesion layer, we have found that Cu sticks satisfactorily on both Si_3N_4 and SiO_2.
First we have deposited Pd by electron-beam evaporation (pressure 10^{-5} Pa or lower) on LPCVD-grown Si_3N_4. The Pd film has been then patterned by conventional photolithographic techniques. A thin film of Cu has been evaporated atop by joule evaporation and similarly patterned. Both films are 100 nm thick. A top view of four thermocouples is shown in fig. 1.
Particular care should be paid when verifying electrical continuity of the thermocouples with conventional ohmmeters. The probe current flowing through the very narrow leads (the overlap area is as low as 9 μm^2) results in overheating and damage of the junction. We have therefore evaluated continuity by imposing current limitation.

First qualitative measurements reveal good sensitivity to temperature and hydrogen.
A thorough characterisation and calibration is under way.
We plan to integrate miniaturised thermopiles as a series of these thermocouples. This will increase sensitivity and make acquisition less keen to interference. These thermopiles will be realised onto a micromachined 1 µm thick suspended low stress Si_3N_4 membrane.

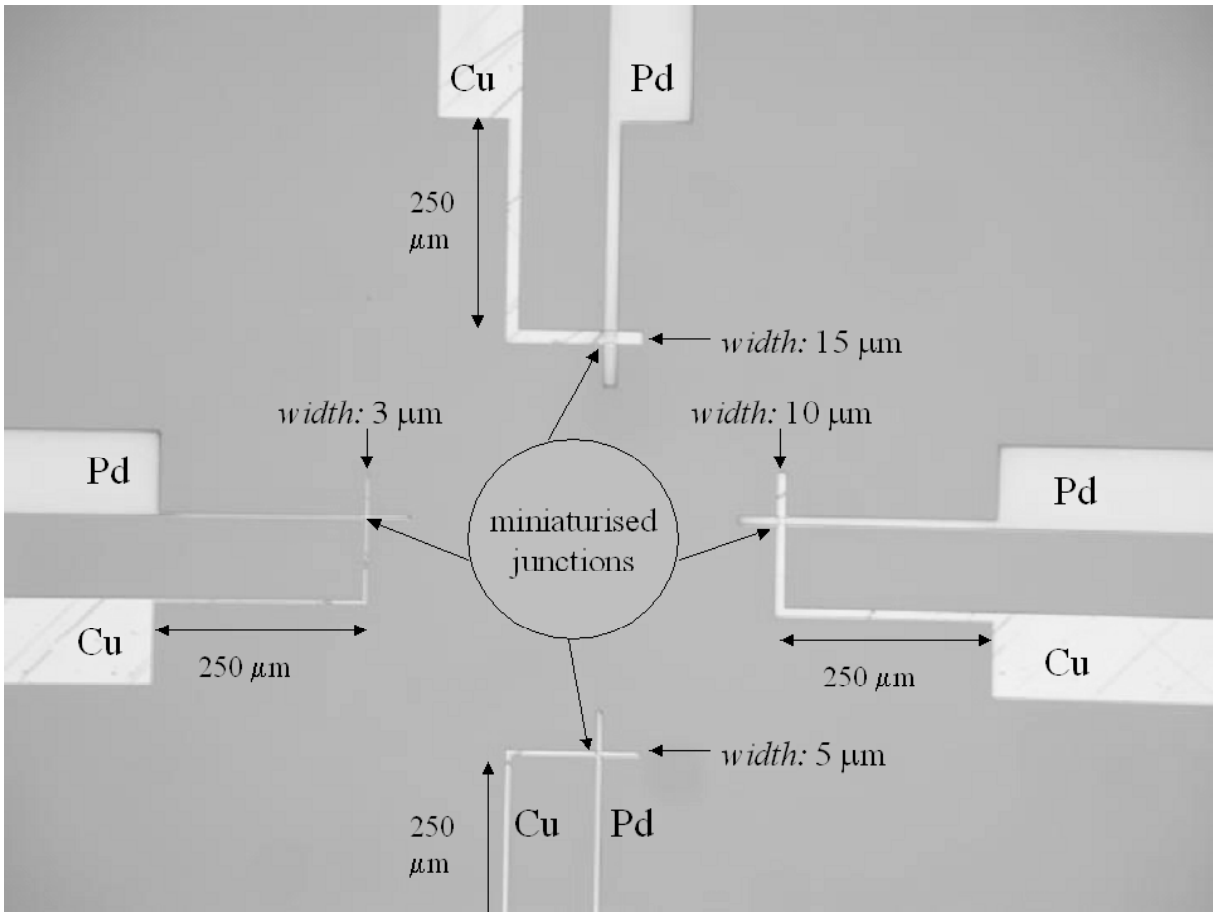

Fig. 1. Top view of four miniaturised thermocouples onto a Si_3N_4 coated silicon wafer.

References

[1] G. W. Burns, M. G. Seroger, G. F. Strouse, M. C. Croarkin, and W.F. Guthrie. Temperature-Electromotive Force Reference Functions and Tables for the Letter-Designated Thermocouple Types Based on the ITS-90, *Nat. Inst. Stand. Tech. (U.S.) Monogr*. 175, 1993.
[2] M. Baciocchi, A.Bearzotti, M. Gentili, A. Lucchesini, C. Caliendo, E. Verona, A. Damico. Cu/Pd Thin-Film Thermopile As A Temperature And Hydrogen Sensor, *Sensors And Actuators A-Physical* 22 (1-3) (1990) 631-635.
[3] B. Serio, H. Gualous, J.P. Prenel A gold–palladium thin-film microsensor array for thermal imaging of laser beam waists *Sensors and Actuators A- Physical* 84 (2000) 303–309.

Low Cost Accelerometers made from Selectively Metallized Polymer

W. Eberhardt[1] H. Kück[1], R. Mohr[2], D. Warkentin[2]

[1]Hahn-Schickard-Gesellschaft, Institut für Mikroaufbautechnik, Breitscheidstr. 2b, 70174 Stuttgart
[2]Institut für Zeitmesstechnik Fein- und Mikrotechnik, Universität Stuttgart, Breitscheidstr. 2b, 70174 Stuttgart
email:warkentin@izfm.uni-stuttgart.de, Phone:++49 711 121 3708, Fax: ++49 711 121 3705

Summary: *We report on an innovative low cost concept for the fabrication of micromechanical sensors and actuators, where three dimensional polymer devices with high aspect ratios are fabricated by micro-injection molding and covered by metal using electroless plating. To demonstrate the new approach, we fabricated an accelerometer device consisting of two metallized polymer parts.*

Keywords: *molded interconnect device, mechanical beam, accelerometer, composite*
Category: *2. Materials and technology*

1 Introduction

Silicon is well known as an excellent material for high performance sensor and actuator devices. But the cost of silicon chips are still enormous due to the complex fabrication technology in clean rooms. In addition packaging of the sensor and actuator chips in many cases generates high cost, since the standard packaging technologies for microelectronic devices are not suited for interfacing the devices to the macroscopic world. We report on an alternative new low cost concept for the fabrication of micromechanical devices, which is based on selectively metallized polymer structures, where the sensor or actuator is part of the plastic package as indicated in a schematic view of an accelerometer device given in figure 1.

Fig. 1. Schematic view of a polymer based accelerometer (top view, side view)

The full area shows seismic mass, springs, electrodes, conductors and connectors made of polymer which is metalized for electrical and mechanical purposes. The shaded areas show the mechanical support, which is part of the package and where no metal is deposited during electroless plating. Further more electronic devices for readout, e. g. an ASIC can be assembled on the polymer device.
The technology is similar to Molded Interconnect Device Technology using two shot micro injection molding, where the device consists of two types of plastics and the surface of the first type of plastic is metallized by electroless plating, while no metal is deposited on the surface of the second polymer constituting the device.

2 Polymer Beams

For the new approach it is essential to know about the molding behavior, the mechanical properties, geometrical limitations and thermal stability of such composites. Therefore we first investigated the behavior of miniaturized mechanical beams with different crossectional areas from 100 x 250 μm^2 up to 400 x 1000 μm^2 (fig .2). Mold making was done using conventional high speed cutting. Because of the finite viscosity of the polymer melt the length and aspect ratio of the molded beams depend on the beam cross section.

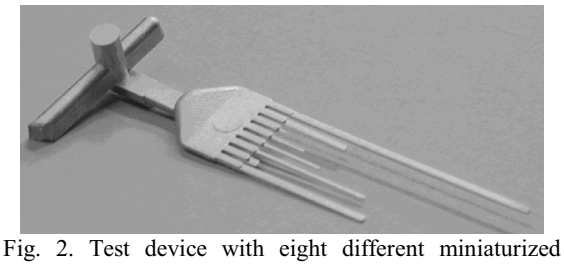

Fig. 2. Test device with eight different miniaturized beams

The metalization was done by electroless plating of copper, nickel-phosphorous and gold with a thickness up to 50 µm in total. We measured the bending behavior of the composite and developed a simple analytical model to describe the mechanical properties of such metallized polymer beams.

3 Accelerometer Device

To demonstrate the new approach, we fabricated an accelerometer device consisting of two metallized polymer parts, the seismic mass with electrodes and springs and a frame with electrodes and anchors for the springs (fig. 3) respectively.

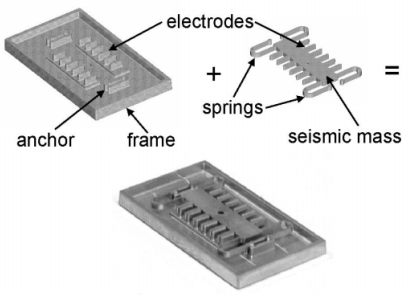

Fig. 3. Photo of the accelerometer device

The overall dimensions are 32 x 18 x 2 mm^3 at minimum dimensions of 310 µm. The gap between the electrodes is about 60 µm (fig. 4).

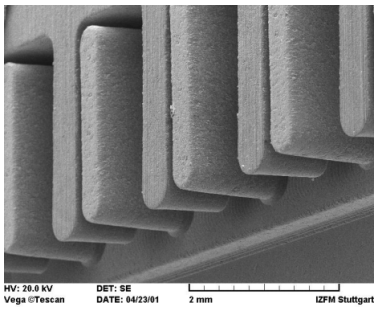

Fig 4. Electrodes of seismic mass and frame

Electrical insulation of the seismic mass electrodes and the two arrays of frame electrodes is done by laser ablating of the metal layer. To measure the capacitance change due to an acceleration a differential capacitance to voltage converter is used. The frequency and acceleration response of the sensor are shown in figs. 5 and 6 respectively.

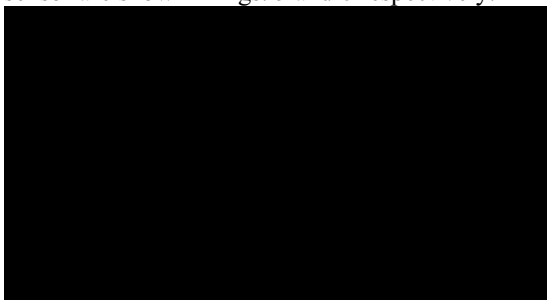

Fig. 5. Frequency response of accelerometer device

Fig. 6. Acceleration response of accelerometer device

We designed a second scaled demonstrator with overall dimensions of 13 x 10 x 1,1 mm^3 at minimum dimensions of 210 µm and a gap width of about 20 µm, which is fabricated and tested currently. Figure 7 schows a photo of the assembeld polymerparts.

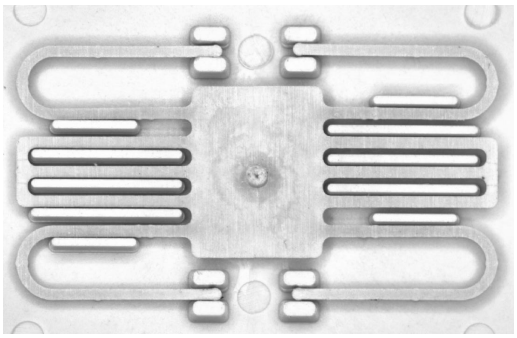

Fig. 7. Polymerparts of the scaled senor

4 Conclusion

Our new approach is not restricted to the fabrication of micromechanical sensors. Due to the comparatively large capacitance also electrostatic actuator devices e. g. microvalves are feasible. We report on our latest results on the behavior of miniaturized beams and accelerometer devices based on selectively metallized polymer devices fabricated by microinjection molding.

References

[1] Eberhardt, W., et al.: Innovative Concept for the Fabrication of Micromechanical Sensor and Actuator Devices Using Selectively Metallized Polymers, Sensors and Actuators A 97-98 (2002) 473-477

Passivation of electronic devices by electrophoresis

L.Grigore[1], G.J. Ensell[1] and D. Stavarache[2]

[1]University of Southampton, Dept od Electronics & Computer Science., Highfield, Southampton, SO17 1BJ, UK
email: lg@ecs.soton.ac.uk http://www.ecs.soton.ac.uk
[2]Baneasa S.A., 32 Erou Iancu Nicolae Str., sect.2, Bucharest, Romania

Summary: *Taking into account that glass is a mixture of oxides electrophoresis might be a suitable process for depositing passivation glass for electronic devices. In an adequate medium, the glass powder becomes a colloidal suspension of solid particles immersed in solvent that can migrate to one of the electrophoresis cell's electrodes under an external electrical field. Unlike the classical "doctor blading" process, electrophoresis is a modern, faster and economical procedure that obtains very uniform layers, adherent to the silicon substrate in optimum conditions (short time, lower current consumption, high efficiency).*

Keywords: *passivation glass, electrophoresis, suspension*
Category: *2 (Materials and Technology)*

1 Introduction

Nowadays, electrophoresis, the simplest separation process based on single particle migration or on electrical charged particle groups differential migration when an external electrical field is applied, has a lot of practical applications, from separation processes of organic or inorganic substances to flotation and painting [1].
Many researchers have attempted to achieve a technological process for depositing passivation glass by electrophoresis, which is why the literature shows a variety of parameters concerning both the composition of the working solution, the type of glass used and the working conditions.
For example, some attempts were achieved for glasses containing: ZnO 40-65%, ZnF_2 0.1-5%, Al_2O_3 1-6%, P_2O_5 1-10%, B_2O_3 2-40% and SiO_2 1-10% [2] or with ZnO 45-75%, B_2O_3 13-35%, SiO_2 2-20% and PbO 0-10% with the addition of $2ZnO.SiO_2$ 0.01-20% for improving the electrical and blocking characteristics [3,4]. These types of glasses were suspended in solution using mixtures of alcohol-acetone [2], ammonia-isopropyl alcohol-ethyl acetate in the presence of a surfactant [4] or ammonia-alcohol and nitrogen bubbling [5].

The suspension is prepared by mixing the solid glass powder into the solvents with an ultra sound (US) generator. Before applying the external field (for 3-5 minutes), the electrodes are introduced, then after the process they are removed and dried. Finally the glass passivated wafer is thermally annealed [4,5,6,7,8,9] for three hours at 1350°C [2], the obtained treated glass having a flow point of 720°C [2] or 680°C and a thermal expansion coefficient of $44.5x10^{-7}$/degree (at 30-300°C) [3].

2 Experimental part

The experimental set-up (figure 1) consists of a quartz electrophoresis cell with two electrodes: the cathode - represented by the working wafer on which the passivation glass is deposited (on the processed devices, in our situation) and the anode - a gold plated wafer.

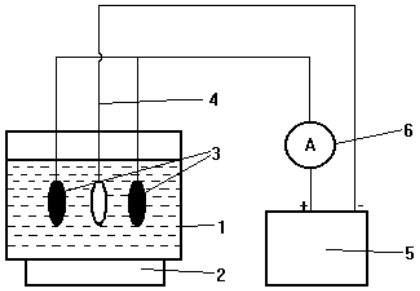

Figure 1. Experimental set-up for the electrophoresis process
1-electrophoresis cell; 2-US generator; 3-anodes; 4-cathode; 5-power supply; 6-A-meter

The type of glass used is Schott's G 017- 002 that contains: SiO_2 >2%, B_2O_3 >20%, ZnO >20%. This white powder is transformed into the suspension necessary for the process by mixing it with ethyl acetate and isopropyl alcohol and with a small amount of an aminic surfactant. For homogenising this mixture at a molecular size and obtaining a stable suspension, an US generator is needed. As completion of the electrophoresis process does not take a very long time, this mixing of the components just before the process is sufficient for providing a medium homogeneity throughout the deposition process.

After the deposition, glass passivated wafers are air-dried and then thermally annealed at 700°C in a furnace.

3 Results and discussions

The electrophoresis cell was operated at room temperature (20 - 25°C), with current densities (c.d.) in the range $0.5x10^{-3}$ - $1.9x10^{-3}$ A/dm^2 and deposition times of 2 - 5 min [10].
The glass is uniformly deposited in the channels between the pads on the wafer (as seen in the pictures in figure 2 taken with an optical microscope), the thickness measured with the optical microscope being 100-200 μm before the thermal treatment and of 30-80 μm after it, which means that the glass contraction coefficient is between 0.59 and 0.67. These values represent average values measured with the optical microscope at different points all over the wafer surface ($4.1x10^{-3}$ cm^2).

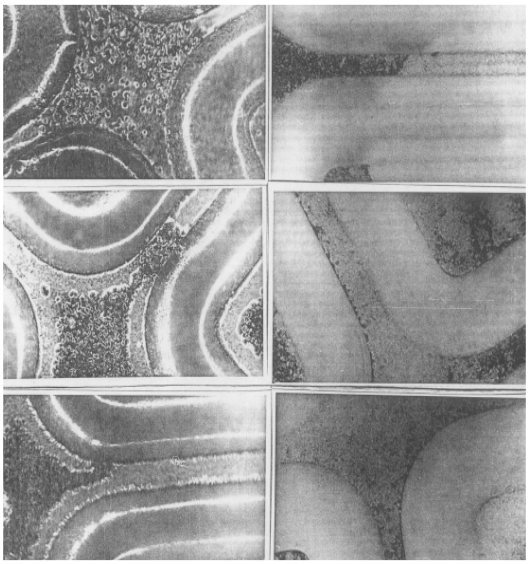

Figure 2. Passivation glass layers thickness while increasing current density (c.d.) in the electrophoresis process before (a) and after (b) thermal treatment

1 - c.d.: $0.5x10^{-3}$ A/dm^2, a) 100μm, b) 30 μm;
2 - c.d.: $0.8x10^{-3}$ A/dm^2, a) 115μm, b) 35μm;
3 - c.d.: $1.2x10^{-3}$ A/dm^2, a) 120μm, b) 40μm.

If the process is incorrectly operated two limit situations might be seen:

- *under-deposited glass*; in this situation the layer is very thin, non-uniform and even interrupted (this is obvious especially after treatment where the bottom of the channel is quite clear);

- *over-deposited glass*; in this case the layer is so thick that it exceeds the margins of the channel.

The third example deposited in optimum conditions fulfils all the exigencies with the layer structure and thickness, and achieves good passivation for the device.
Glass consumption was evaluated at 0.028 g per wafer with 98-99% efficiency of the process related to it.

4 Conclusions

Passivation glass deposition by electrophoresis is a modern, efficient, rapid and less current consumer process. The deposited glass layers are of the best quality (uniform and adherent to the silicon substrate) and they are also obtained with less glass consumption than the classical "doctor blading" process.

References

[1] E. Jercan, *Electroforeza* (1983) Ed. Tehnica, Bucuresti.
[2] JP 61 32, 431 86 32, 431 (Cl.H01L21/316), 15 Feb. 1986.
[3] JP 60 60, 944 85 60, 944 (Cl.C03C14/00), 08 Apr. 1985.
[4] *Electrophoretic Deposition Manual for Lead Silicate and Lead Borosilicate Passivation Glasses*, 3-rd ed., Nippon Electric Glass Co., Ltd., Japan.
[5] JP 59, 202, 639 84, 202, 639 (Cl.H01L21/316), 16 Nov. 1984.
[6] JP 61, 119, 043 68, 119, 043 (Cl.H01L21/316), 06 Jun. 1986.
[7] JP 61 31, 612 86 31, 612 (Cl.H01L21/316), 21 Jul. 1986.
[8] JP 59,167, 023 84, 167, 023 (Cl.H01L21/316), 20 Sep. 1984.
[9] JP 59, 123, 238 84, 123, 238 (Cl.H01L21/316), 17 Jul. 1984.
[10] Romanian Patent RO 114912C/2000 (Cl.C25D13/02): L. Grigore, D. Stavarache, *Process and Installation for Electrophoretic Deposition of Zinc Borosilicate Glass on Silicon*.

The influence of thermal treatment on the stress characteristics of suspended Porous Silicon membranes on silicon

D. Papadimitriou[1], C. Tsamis[2] and A. Nassiopoulou[2]

[1]National Technical University of Athens, Department of Physics, GR-15780 Athens, Greece.
email: dimitra@central.ntua.gr
[2]IMEL/NCSR "Demokritos", P.O. Box 60228, 15310 Aghia Paraskevi, Athens, Greece

Summary: *In this work, the mechanical properties of suspended porous silicon (PS) membranes on bulk silicon are investigated. Micro-Raman spectroscopy is used to characterize stresses in supported PS membranes, in the form of micro hotplates that are fabricated by a novel technique, based on the isotropic etching of silicon under a PS layer, in a high density plasma reactor. Important information is obtained for the stress evolution of PS as a function of porosity and the annealing conditions that can be used for optimization in device fabrication.*

Keywords: *Porous Silicon, suspended membranes, stress, micro hotplates*
Category: *2 (Materials and technology)*

1 Introduction

Over the last years, porous silicon (PS) has attracted significant interest, due to its potential usage in various fields of applications. PS layers have been effectively used as active elements for the fabrication of suspended micro hotplates for low thermal sensor applications, due to its very low thermal conductivity value [1], and as isolation material for radio-frequency (rf) applications because of its high resistivity and its compatibility with modern very-large-scale-integration VLSI [2].
Optimization of the mechanical properties of PS layers as well as stress control is a main issue that has to be considered for these applications.
In this work we investigate in a systematic way the evolution of the stress that develops in PS layers as a function of porosity and thermal treatment.

2 Experimental Procedure

As a starting material, p type <100> silicon wafers (c-Si) with resistivity 1-10 Ωcm were used. An ohmic contact was formed at the backside of the wafers by ion implantation at a dose of 8×10^{15}cm^2 and energy of 60 KeV. The samples were oxidized at 1050^{o}C for 30 min in O_2, which resulted in the growth of a 100 nm thermal oxide. Subsequently a 100 nm nitride layer was deposited in a Low Pressure Chemical Vapor Deposition (LPCVD) system and was patterned to define areas for PS layer formation. Anodization was carried out in an electrolytic cell at different current densities ranging from 10 to 80 mA/cm^2 and for a time chosen according to the wanted PS thickness. Subsequently, the PS layers were subjected to various thermal treatments in N_2 or O_2 ambient and for temperatures ranging from 300^o to 1050^o C. Micro-Raman spectroscopy was used for stress characterization in two cases : (a) for supported and (b) for unsupported PS layers. The test structures were in the form of micro hotplates used for thermal sensor applications. The micro hotplates were partially or fully released from the substrate by means of lateral isotropic etching of the bulk silicon substrate in a High Density Plasma reactor. The etching process is highly selective, both to porous silicon and to the photoresist used to protect the device. High lateral etch rates can be achieved (of the order of 6-7 μm/min) in a high-density plasma reactor. The details of the fabrication process of the micro-hotplates are reported elsewhere [3].
Figure 1 is a SEM image of a fully released porous silicon micro-hotplate. The dimensions of the membrane are $60\times60\mu m^2$, the width of the supporting beams is 20 μm, and their length 150 μm. The thickness of the PS layer is 4 μm. Strain measurements were performed in the central region of the micro hotplates, both in the case of fully released and partially released membranes.

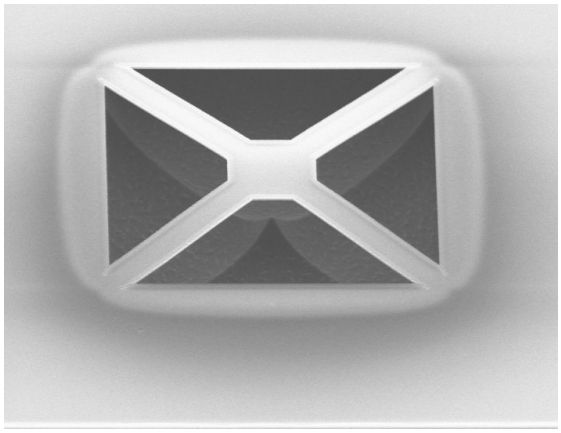

Fig. 1. Fully released porous silicon micro-hotplate used as test structure for the strain measurement. The thickness of the membrane is 4 μm.

3 Results and Discussion

Raman scattering was excited by the 488 nm line of an Ar^+-laser. It was spectrally analyzed by a Jobin-Yvon micro-Raman spectrometer (T-64000) equipped with a CCD-detector.

PS membranes with porosities ranging from 60% to 75% were investigated by micro-Raman spectroscopy after dry oxidation for 1 h at 300°C in O_2 ambient. Figure 1 shows the Raman spectra of PS membranes with 65% porosity for (a) supported and (b) unsupported membranes. A spectrum of the c-Si substrate is also shown. The observed Raman-frequency shifts of the porous layers are partially due to the porosity of the layer and partially due to the compressive stresses that the layer exhibits [4] because of the lattice miss-match between porous silicon and crystalline silicon. Strain generated frequency shifts were obtained by comparison of the Raman frequencies of supported and unsupported membranes with the same porosity. These shifts vary from 1.3 to 3.3 cm^{-1} for porosities ranging from 60% to 75% respectively. The corresponding stresses, calculated under the assumption of an in-plane stress distribution [5] by using the phonon deformation potentials of c-Si and the elastic constants of PS after extrapolation of values known from the literature [4], are in the range of 10–20 MPa.

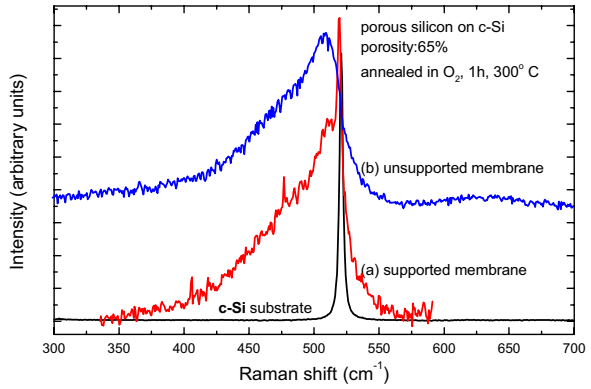

Fig. 2. Raman spectra of (a) supported and (b) unsupported PS membrane of porosity 65% after annealing at 300°C for 1h in O_2 ambient. A spectrum of the c-Si substrate is also shown.

PS layers of 60% porosity were treated further at various temperatures and ambient. Figure 3 shows the Raman spectra of PS layers with 60% porosity after a second oxidation at 900°C for 1h. We notice that the Raman frequencies of the unsupported membranes were shifted by almost 10 cm^{-1} with respect to the frequency of unsupported membranes treated in one-step. The spectra were broadened and almost two orders of magnitude less intense. This indicates that the nanocrystallites within the porous material were strongly oxidized and their sizes were highly reduced. On the contrary, the frequency change of the Raman spectra of supported membranes after a second oxidation was max. half the change of the unsupported ones. A calculation of the stress from the frequency differences of the spectra of supported and unsupported membranes after a two-step process yields stresses which are almost one order of magnitude higher than those of membranes treated in one-step.

Detailed analysis for the stress evolution in various conditions will be presented.

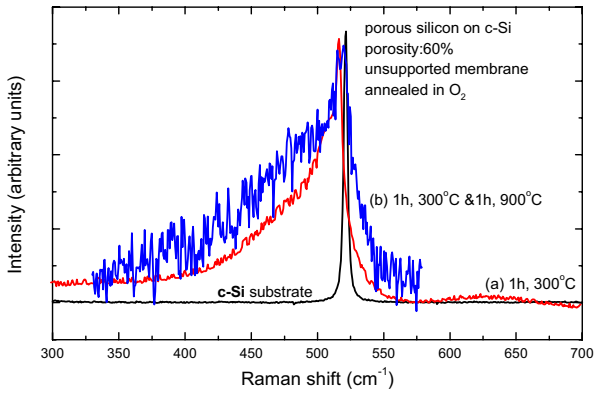

Fig. 3. Raman spectra of unsupported PS membrane of porosity 60% after annealing in O_2 ambient (a) at 300° C for 1h, and (b) at 300° C for 1h and at 900°C for 1h (in (b) the signal is magnified; the Raman signal of the c-Si substrate is superimposed to the signal of the PS layer, because light penetrates through the highly PS layer to the substrate).

References

[1] C. Tsamis, A. Tserepi and A. G. Nassiopoulou, "Thermal properties of suspended porous silicon micro-hotplates for thermal sensor applications", To appear in Sensors and Actuators A.

[2] H. Kim, K. Chong, and Y-H. Xie "The Promising Role of Porous Si in mixed-signal Integrated Circuit Technology", PSST 2002, March 2002, Tenerife, Spain.

[3] C. Tsamis, A. Tserepi and A. G. Nassiopoulou, "Fabrication of suspended porous silicon micro-hotplates for thermal sensor applications", Physica Status Solidi (a), Vol. 196, Issue 2, April 2003

[4] D. Papadimitriou, J. Bitsakis, J.M. López-Villegas, J. Samitier, J.R. Morante, "Depth dependence of stress and porosity in porous siliocn: a micro-Raman study", Thin Solid Films 349, 293-297 (1999).

[5] M. Siakavellas, E. Anastassakis, G. Kaltsas, A.G. Nassiopoulou, "Micro-Raman characterization of stress distribution within free standing mono- and poly-crystalline silicon membranes", Microelectronic Engineering 41/42, 469-472 (1998).

Analysis and Measurement of Cure Residual Stresses in a Thermoset resin

V.Antonucci[1], A.Cusano[2], M.Giordano[1], J.Nasser[3]

[1]Institute for Composite and Biomedical Materials Technology CNR, Italy
P. le Tecchio 80, 80125 Napoli
Tel: +39 081 2425936; Fax: +39 081 2425932
[2]Department of Engineering, University of Sannio, Benevento, Italy
[1]Department of Materials and Production Engineering, University of Naples, Italy

***Summary*:** Main focus of this work is the analysis and measurement of residual stresses in a thermoset polymer resin due to both temperature changes and shrinkage phenomena induced by the polymerization reaction of the resin. In particular, strain measurements have been performed by embedding a single Bragg Grating Fiber Optics (FBG) sensor into an epoxy resin placed into an aluminum mold and activating the cure reaction into an oven. The internal strains and temperature during the cure were monitored and recorded. Residual stresses and strains were computed also numerically by solving the mechanical equilibrium equations with an incremental transient approach. The numerical results showed a good agreement with the experimental measurements.

Keywords: *Cure stress, fiber optic, modeling*
Category: *2 Materials and Technology*

1 Introduction

The performances and quality of thermoset based polymer composites are affected strongly by the manufacturing cycle which involves several chemical and physical phenomena, such as heat transport, mass transport, rheological changes and chemical reaction. In fact, the composite consolidation is determined mainly by the development of the cure reaction which could induce strong exothermal peaks and thermal differences along the part if occurs non-uniformly. This would lead to the non uniform evolution of the mechanical properties and residual stresses in the composite part that are detrimental leading to cracking or dimensional tolerance problems [1]. Therefore, the prediction and the measurement of the processing induced residual stress and strains represent important issues to be addressed.
In general, numerous studies have been performed to predict numerically the residual stresses by using both elastic and viscoelastic approaches [2-5] focusing the analysis, in some cases, only on the cool-down phase of the processing cycle [2]. On the other hand, most of the experimental works have been concentrated on the measurement of the curvature and warpage of unsymmetrical laminates [1,6], while only more recently sensing techniques, based on fiber optic sensors, have been implemented to get local information about the strain fields [7-8]. In this work, the build up of strains during the non-isothermal cure of an epoxy resin in an aluminum mold has been investigated both numerically and experimentally. In particular, a finite element code has been developed to solve the stress analysis problem. On the other hand, a single fiber Bragg grating sensor has been used to measure the strain build evolution. The experimental data in terms of deformations showed similar behavior of the numerical results confirming the reliability of the developed model and the sensor capability.

2 Numerical Modeling

The mechanical equilibrium equations have been solved numerically by the finite element method using the Cauchy-Navier approach with the hypothesis of *Plain Strain* and considering the stresses induced by temperature and conversion gradients as volume forces.
In particular, an incremental transient formulation has been adopted: prior to the stress and deformation calculation for a single time step, the heat transport and the mass balance equations have been solved to give the temperature and conversion distribution, then, after evaluating the instantaneous mechanical properties of resin, stress and strain increments have been computed over each time step assuming the previous temperature and conversion as reference stress free conditions, finally the global stress has been computed by the sum of each time step increment.

3 Sample preparation and optoelectronic setup

The holder consisted of a rectangular aluminum mold (100 x 30 x 4 mm) having a cavity of 80 x 10 x 3 mm, shown in Fig.1. Two triangular grooves were made at both ends of the mould to permit the optic fiber to pass all through the cavity and to be maintained straight at its central line.

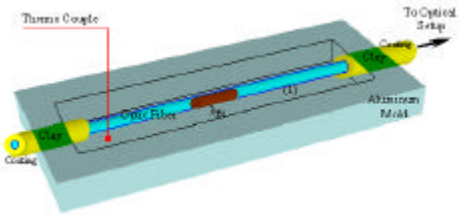

Fig. 1. Aluminum Mold with A Bragg Grating Fiber [not to scale].

The grooves were closed by clay to prevent the resin exiting from the mold. A K-Type thermocouple was used to measure the temperature. A 100÷10.6 per weight mixture of an Epoxy resin [DGEBA] and a Hardener [Esamethylentetra Amine] was used to fill the mold's cavity. The whole setup was then placed in an oven where there was an hole to permit the exiting of the fiber.
The fiber Bragg grating demonstrated a 0.3 nm bandwidth at approx. 1552 nm. The sensor was connected to the optical circuit consisting of a 2 mW Super-luminescent LED light source operating at 1550nm, of a fiber Y-optical coupler 1x2 and a Optical Spectrum Analyzer OSA. The optical spectrum analyzer ensures a wavelength resolution of 0.02nm, a proper signal processing based on interpolation method and centre of mass analysis have been implemented achieving a resolution less than 10pm. The Bragg's spectra were registered at every minute in synchronicity with temperature measurements.

4 Results

The numerical analysis has been performed with reference to a top view of the experimental set-up by considering the fourth part of the system. Figure 2 shows the analyzed section and the used triangular mesh.

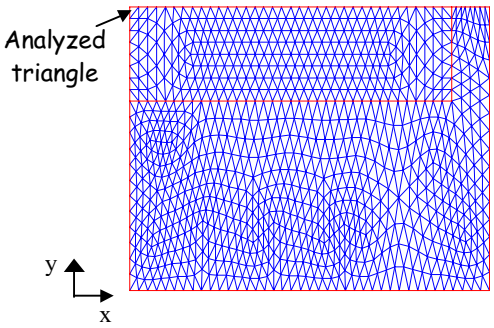

Fig.2. Adopted mesh for the numerical integration.

The numerical simulations have been performed by imposing on the external surfaces of the system the temperature profile used experimentally (heating to 130°C followed by cooling at 1.5°C/min). The computation of the stresses and strain for the resin has been performed as the resin attains the gel point (conversion 0.54). Figure 3 reports the x-component of the strain as function of the temperature for the triangle evidenced in figure 2.

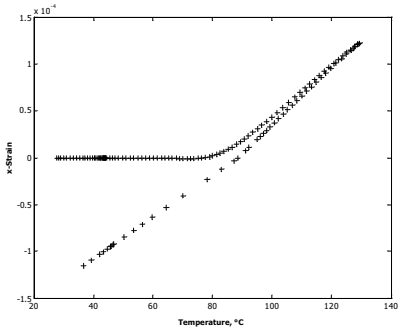

Fig.3. x-component of the strain as function of temperature for the evidenced triangle.
One should observe that the polymer resin is compressed during the heating, while in tension during the cooling. This is due to the constrains of the aluminum mold which is characterized by a thermal expansion coefficient lower than that of resin.
This result was confirmed by the experimental Bragg sensor measurements as shown in figure 4.

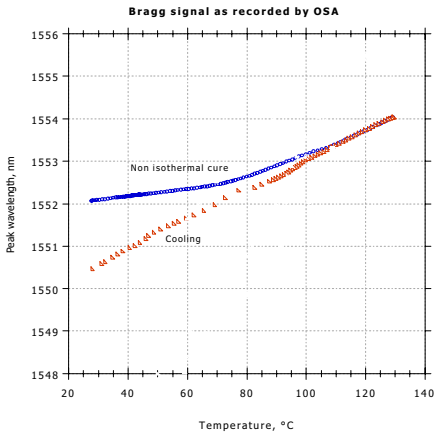

Fig.4. Bragg centre Peak as function of temperature.

References

[1] M.Gigliotti, M.R.Wisnom, K.D.Potter, Composites Science and Technology, 63 (2003) 187-197.
[2] A.S.D.Wang, F.W.Crosssman, J.Compos.Mater., 11 (1977), 300.
[3] T.A.Bogetti, J.W.Gillespie,Jr., J.Compos.Mater., 26 (1992), 626.
[4] S.R.White, H.T.Hahn, J. Composite Mater., 26 (1992) 2402.
[5] S.R.White, Y..Kim, Mechanics of Composite Materials and Structures, 5 (1998) 153-185.
[6] K.S.Kim, H.T.Hahn, Composites Science and Technology, 36 (1989), 121.
[7] A, Asundi, J. Leng, Smart. Mater. Struct., 11, (2002) 249-255.
[8] C.M.Lawrence. D.V.Nelson, T.E.Bennett, J.R. Spingarn, Proc.SPIE on Smart Strcutures and Materials, pp. 154-165, vol.3042 (1997).

Saturation Magnetostriction of FeCoSiB Glass Covered Amorphous Wires

M. Neagu[1,2], H. Chiriac[2], C. Hison[3]

[1]"Al. I. Cuza" University, Faculty of Physics, 11 Carol Blvd., Iasi, Romania, e-mail:mneagu@uaic.ro
[2]National Institute of Research and Development for Technical Physics, 47 Mangeron Blvd., Iasi, Romania
[3]Istituto Nazionale per la Fisica della Materia, Universita "Federico II", P.le V. Tecchio 80, Napoli, Italy

Summary: *Results concerning the saturation magnetostriction, λ_S, dependence on the tensile stress applied during annealing as well as during measurements for $Fe_{72.5-x}Co_xSi_{12.5}B_{15}$ glass covered amorphous wires before and after glass removal are reported. The increase of the tensile stress during annealing leads to an increase of saturation magnetostriction at zero applied stress, $\lambda_S(0)$, up to about 5% for highly magnetostrictive samples (Fe-based). For low magnetostrictive as well as for negative magnetostrictive samples (Co-based), when the value of tensile stress applied during annealing increases, changes up to 10% of $\lambda_S(0)$ absolute value were observed. Increasing the tensile stress value during measurements λ_S decreases.*

Keywords: *Amorphous materials, Magnetomechanical effects, Magnetostriction.*
Category: *2 (Materials and technology)*

1. Introduction

The new class of amorphous wires, the glass covered wires, offers new perspectives for the applications of amorphous magnetic materials due to their specific advantages in terms of outstanding magnetic, magnetoelastic and mechanical properties [1,2]. For applications, as well as for basic research of magnetoelastic materials, the saturation magnetostriction, λ_S, is an important characteristic [1-7].

The aim of this paper is to analyze the influence of tensile stress (applied during treatment as well as during measurements) on λ_S value, for positive, negative and nearly zero magnetostrictive $Fe_{72.5-x}Co_xSi_{12.5}B_{15}$ glass covered amorphous wires.

2. Experimental details

Samples having the diameter of the metallic core ranging between 10 and 25 μm and the thickness of the glass cover between 2 and 15 μm were investigated before and after glass removal, in as-cast state and after stress-current annealing. The glass cover was removed by chemical etching with a hydrofluoric acid solution. The annealing was carried out by means of Joule effect produced by an electric current passing through the amorphous wire under tensile stress. During treatments, the current density, tensile stress and annealing time values were varied up to $250x10^6 A/m^2$, 500 MPa and 250 minutes, respectively. The amorphous state of the samples was examined by X-ray diffraction. The saturation magnetostriction value was determined using small-angle magnetization rotation method [8]. The small-angle rotation of magnetization is generated by applying simultaneously to the samples a small a.c. transverse magnetic field, a saturating d.c. axial magnetic field and a tensile stress σ. For amorphous alloys with very low saturation magnetostriction, the measured magnetostriction $\lambda_S(\sigma)$ is dependent on the external tensile stress σ. In this case $\lambda_S(\sigma)=\lambda_S(0)+\alpha\sigma$, where $\lambda_S(0)$ is the saturation magnetostriction constant at zero applied stress and α (stress derivative) is a negative coefficient experimentally determined.

3. Results and Discussion

The obtained results show that for as-cast samples, the saturation magnetostriction at zero applied stress, $\lambda_S(0)$, is of the same order of magnitude as for conventional amorphous wires (with diameters between $80\text{-}200x10^{-6}$m) having the same compositions [3, 4, 8]. For x=0 the alloy exhibits the maximum positive value of saturation magnetostriction ($\lambda_S(0)=32x10^{-6}$), while the maximum negative value ($\lambda_S(0)=-2.8x10^{-6}$) is obtained for x=72.5 at. % Co. For 4.35 at. % Fe, the material is nearly zero magnetostrictive.

When an amorphous magnetic wire is subjected to external stress, a magnetoelastic anisotropy is induced, adding to the initial anisotropy caused by the residual internal stresses. Therefore the saturation magnetostriction value depends on the tensile stress applied on the specimen (during annealing as well as during measurements).

The obtained results for as-cast nearly zero magnetostrictive $Co_{68.15}Fe_{4.35}Si_{12.5}B_{15}$

amorphous wires, show that the values of $\lambda_S(0)$ and stress derivative, α, are about -0.11×10^{-6} and $-0.9\times10^{-10}MPa^{-1}$, respectively, for glass covered samples while for glass removed samples they are -0.05×10^{-6} and $-1\times10^{-10}MPa^{-1}$, respectively.

In the case of low magnetostrictive samples, increasing the value of tensile stress during measurements, λ_S decreases and its sign can be changed in the case of positive $\lambda_S(0)$. For these alloys, the value of α can reach about $-1\times10^{-10}MPa^{-1}$.

Fig. 1 presents the dependence of $\lambda_S(0)$ on the annealing current density for $Co_{72.5}Si_{12.5}B_{15}$, $Fe_{4.35}Co_{68.15}Si_{12.5}B_{15}$ and $Fe_5Co_{67.5}Si_{12.5}B_{15}$ glass covered amorphous wires annealed 180 minutes under 477 MPa.

Fig. 2 presents the dependence of $\lambda_S(0)$ on the tensile stress applied during treatments for $Fe_{4.35}Co_{68.15}Si_{12.5}B_{15}$ samples annealed 150 minutes, under 477 MPa, at $55x10^6A/m^2$ and $145x10^6A/m^2$ current densities.

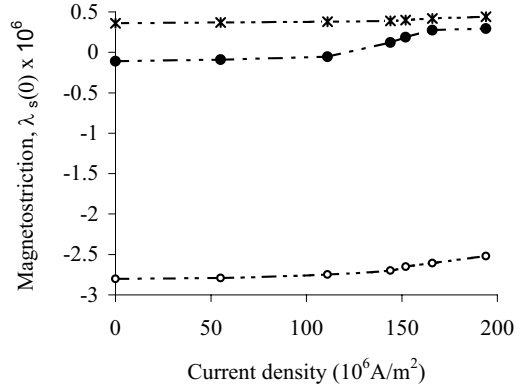

Fig. 1. Dependence of the saturation magnetostriction at zero applied stress, $\lambda_S(0)$, on the annealing current density for O $Co_{72.5}Si_{12.5}B_{15}$, • $Fe_{4.35}Co_{68.15}Si_{12.5}B_{15}$ and × $Fe_5Co_{67.5}Si_{12.5}B_{15}$ glass covered amorphous wires annealed 180 minutes under 477 MPa.

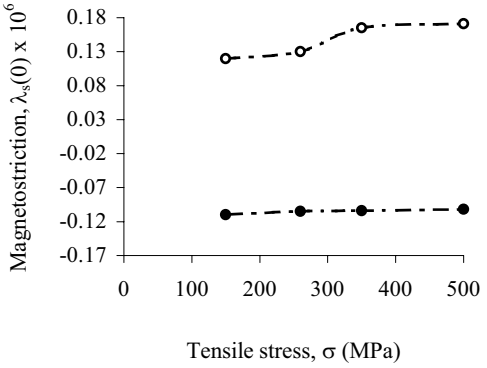

Fig. 2. Dependence of the saturation magnetostriction, $\lambda_S(0)$, on the tensile stress, σ, applied during treatments, for $Fe_{4.35}Co_{68.15}Si_{12.5}B_{15}$ glass covered amorphous wires annealed 150 minutes, under 477 MPa, at • 55×10^6 A/m^2 and O 145×10^6 A/m^2 current densities.

As can be seen, in the case of nearly zero magnetostrictive $Fe_{4.35}Co_{68.15}Si_{12.5}B_{15}$ wires an important variation of the saturation magnetostriction value and also a change in its sign can be obtained after stress-current annealing.

For low magnetostrictive as well as for negative magnetostrictive samples (Co-based), when the tensile stress applied during annealing increases, changes up to 10% of $\lambda_S(0)$ absolute value were observed (a decrease and an increase for negative and positive magnetostriction, respectively).

For highly magnetostrictive samples (Fe-based), $\lambda_S(0)$ increases up to about 5% after stress-current annealing.

All the variations in the saturation magnetostriction value are exhibited by both glass covered and after glass removal wires.

The obtained results present a special interest for basic research offering new perspectives for amorphous materials applications.

3. Conclusions

We focused our attention on analyzing the influence of tensile stress (applied during treatment as well as during measurements) on saturation magnetostriction for positive, negative and nearly zero magnetostrictive $Fe_{72.5-x}Co_xSi_{12.5}B_{15}$ glass covered amorphous wires.

In the frame of the increasingly stiff competition between the amorphous magnetic materials for magnetomechanical sensors, the glass-covered wires are attracting much interest due to their more convenient shape, dimensions, handy opportunities for tailoring their magnetoelastic properties, high mechanical and good corrosion resistant properties.

References

[1] H. Chiriac and T. A. Óvári, *Progress in Materials Science* 40 (1996) 333-407.

[2] M. Vazquez and A. Hernando, *J. Phys. D: Appl. Phys*. 29 (1996) 939-949.

[3] P. Squire, D. Atkinson, and A. Atalay, *IEEE Trans. Magn,* 31 (1995) 1239-1247.

[4] C. Gomez-Polo and M. Vazquez, *J. Magn. Magn. Mater*. 118 (1993) 86-92.

[5] J. Gonzalez, J. M. Blanco, A. Hernando, J. M. Barandiaran, M. Vazquez and G. Rivero, *J. Magn. Magn. Mater*. 114 (1992) 75-81.

[6] J. Gonzalez, A. Zhukov, J. M. Blanco, A. F. Cobeno, M. Vazquez and K. Kulakowski, *J. Appl. Phys.* 87 (2000) 5950-5952.

[7] H. Chiriac, M. Neagu and C. Hison, *IEEE Trans. Magn.* 38 (2002) 2823-2825.

[8] J. Yamasaki, Y. Ohkubo and F. B. Humphrey, *J. Appl. Phys*. 67 (1990) 5472-5474.

Nanoliter spectrofluorimetric detector for flow systems

S. Bargiel[1], A. Gorecka-Drzazga[1], J. Dziuban[1],
P. Prokaryn[2], M. Chudy[2], A. Dybko[2], Z. Brzozka[2]
[1]Faculty of Microsystem Electronics and Photonics, Wroclaw University of Technology, Wybrzeze Wyspianskiego 27, 50-370 Wroclaw, Poland
e-mail: bargiel@wemif.pwr.wroc.pl
[2]Department of Analytical Chemistry, Warsaw University of Technology, Noakowskiego 3, 00-664 Warsaw, Poland

Summary: *The Si-glass technology was used to fabricate the new spectrofluorimetric microdetector. During the detector designing the authors paid attention to its versatility. The microdevice was made as a separate module, which can be connected via tubings to any microanalytical system, in which the fluorescence should be measured. Moreover, by using the optical fibres,the authors were able to decrease the detecting volume to 17 nl, what in consequence enabled measurements of low-volume samples. The microdetector performances were verified during simple test measurements.*

Keywords*: anisotropic etching, fibre optics, microfluidic detectors, fluorescence measurements,*
Category: 2 *(Materials and technology)*, 7 *(Fluidic devices)*, 9 *(System architecture, electronic interfaces, wireless interfaces)*.

1 Introduction

Fluorescence is the most commonly used detection technique in μTAS due to its selectivity and high sensitivity [1]. Microfabrication with use of such techniques as anodic bonding, and deep etching enables the integration of separation microchannel with optical fibres system directly on a microchip. To get a good signal-to-noise ratio, the amount of excitation light reaching the detector must be minimised whereas the amount of fluorescence light emitted by the excited fluorophores must be maximised. A new optical microdetector integrated with microfluidic silicon-glass device is presented. Construction of the chip is optimised to obtain small detection volume, and to secure good connections of optical fibres with a light source and fluorescence detector.

2 Design

The goal of the project was to minimize detection volume of a sample on the order of nL. It has been achieved by the fabrication of the silicon-glass microchip with fluidic channel and two optical fibres (Fig.1). An anisotropically etched channel is 200 μm deep, 500 μm wide and 20 mm long. In order to form the channel a Pyrex-like glass cover was anodically bonded. A standard multimode 125/62.5 μm fibre was used to couple excitation light to the built-in optical cell. The excitation liquid volume was about 17 nL. The quartz fibre was positioned in the V-groove, etched perpendicular to the flow channel. The fluorescence signal was transmitted to the photodetector by a plastic fibre (PMMA, 0.75 mm in diameter) located on the glass cover, above the optical cell. Both fibres were fixed by optical UV curable epoxy.

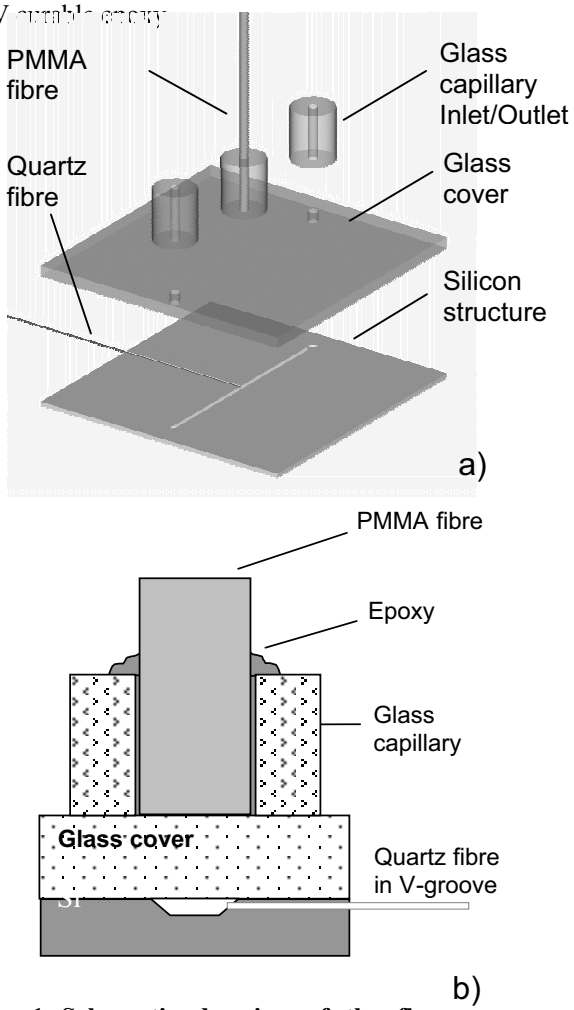

Fig. 1 Schematic drawing of the fluorescence detector: a) assembly drawing, b) cross section view

3 Fabrication

The channel and V-groove were produced on the 3", n-type, (100) oriented silicon wafer by deep, anisotropic wet etching in 10 M KOH. Thermal silicon dioxide mask was used. After removing the mask, the silicon wafer was thermally oxidized to obtain 0.3 μm thick SiO_2 layer. The 25x25 mm silicon chip was anodically bonded to glass cover at 450°C and 1 kV. Glass inlets were positioned over mechanically drilled vias (ϕ=0.9 mm) and fixed using UV epoxy.

The assembling of the fibres was performed in several steps. The quartz fibre was positioned in the V-groove under the microscope and carefully immobilised by small amount of UV curable glue. A glass capillary located on the glass cover, above the optical cell, served as a mechanical protection of the plastic fibre. Next, the plastic fibre with polished end-face was fixed inside the capillary.

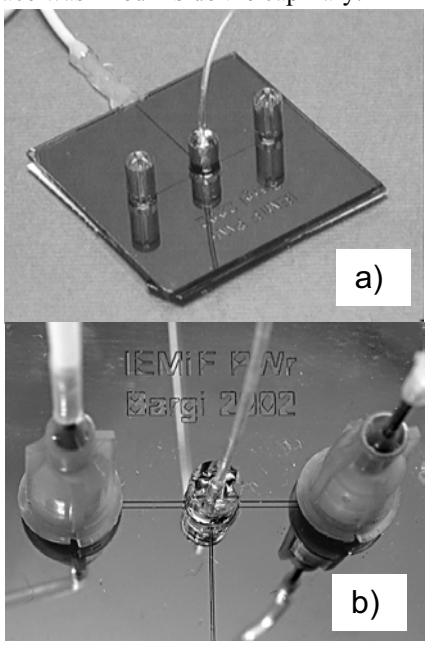

Fig. 2 Complete microfluidic fluorescence detector: a) general view; b) close-up of the detecting area

4 Test measurements

The spectrofluorimetric microdetector is a separate module, which can be coupled with any microanalytical system, in which there is a need of the fluorescence measurements. However, before the whole analytical microsystem assembling each of the single elements should be tested. The preliminary tests of the microdetector were performed in order to verify its analytical usefulness. First, the leakproofness of the microstructure and its resistance to liquid pressure were checked. During pumping (with the use of a peristaltic pump - Gilson Minipuls3) a liquid medium into the microdetector channel no sample leakage was not observed even when the flow rate was high. The maximum flow rate of the liquid for the constructed microdetector was estimated as 3 ml/min, this value could be even higher but tubing's connections are the limitation. The maximum flow rate value is comparable with total flow rate in the FIA (Flow Injection Analysis) systems, but in the case of presented construction is only the safety parameter. Generally, the spectrofluorimetric microdetector is adopted for flow chemical analysis at low flow rates. The exemplary spectra and the single-wavelength measurements of water solution of popular fluorimetric indicators (fluoresceine and erythosine - see Fig. 3) were performed at 100 - 150 μl/min.

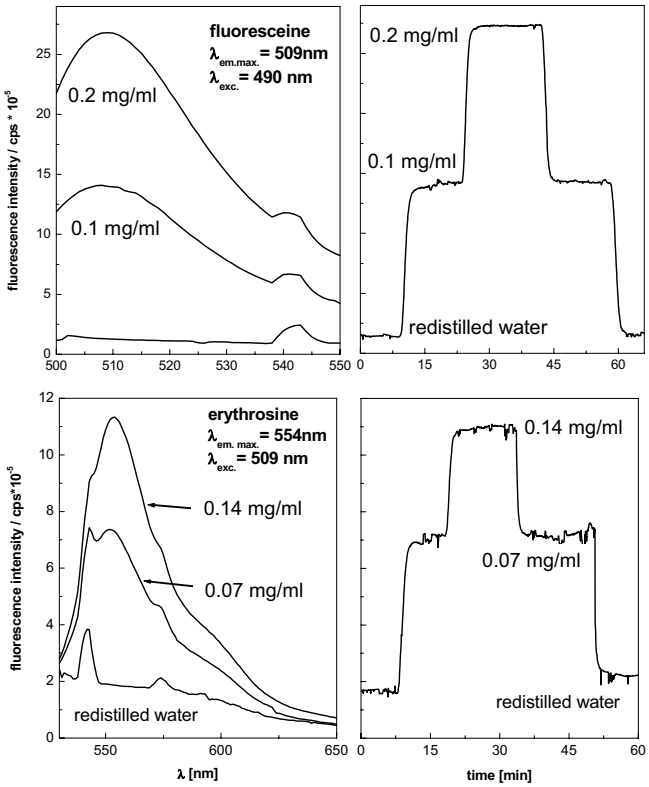

Fig. 3 Spectra and the single wavelength measurements of fluorescence indicators using designed microdetector

The high S/N ratio was observed during the measurements with the use of the microdetector and obtained results are comparable to those obtained in a classical spectrofluorimetric cuvette. The noise recorded during single λ measurements was caused by the flow pulses from the pump.

Acknowledgments

Michal Chudy wishes to thank The Foundation for Polish Science for financial support.

References

[1] J. C. Roulet, H. P. Herzig, E. Verpoorte, N. F. de Rooij, R. Dändliker, *Integration of micro-optical systems for fluorescence detection in μTAS application*, Micro Total Analysis Systems 2000, A. van den Berg, eds., pp. 163-166, Kluwer Academic Publishers, 2000.

New SOI technology for wall shear stress integrated sensors

D. Meunier, D. M. Tsamados and J. Boussey

Institute of Microelectronics, Electromagnetism and Photonics
IMEP, ENSERG, 23 rue des Martyrs, 38016 Grenoble Cédex France
email: tsamados@enserg.fr http://www.imep.enserg.fr

Summary: *In this paper we present a new technology for wall shear stress integrated sensor fabrication. Thanks to the use of appropriate SOI wafers and wafer bonding technique, we found out an innovative technology that provides ultraminiaturized array-sensors needed in numerous microfluidic applications.*

Keywords: *MEMS, SOI, pressure sensors, wall shear stress sensors*
Category: *2 (Materials and Technology)*

1 Introduction

Three parameters are fundamental for accurate understanding of complex phenomenon such as turbulence or separation occurring within the boundary layer of a fluid flowing through a microchannel or tangentially to a wing surface. These parameters are wall shear stress, pressure fluctuations and temperature. For Avionics and automotive applications, a big challenge is to simultaneously monitor these three parameters in order to actuate their evolution in time and space.

Nevertheless, the achievement of active control strategy requires the integrated sensors to fulfill very severe criteria. For instance, the dynamic response of the pressure and wall shear stress sensors should be fast enough to immediately detect the formation of local turbulence mechanisms of which the lifetime is of the order of the millisecond. Moreover, the use of these sensors is only interesting if they can be disposed in an array configuration with a small enough mesh to allow spatial resolution compatible with the length of the smallest boundary layer eddies, i.e. <200µm.

Since the early nineties, several teams have been working on the choice of the best available MEMS-based silicon technology providing highly sensitive sensor arrays. Most of them either report high integration density of wall shear sensors [1,2], or good dynamic performance for pressure fluctuation sensing [3], but all have failed to comply with the necessity to co-integrate the three types of sensor arrays with good performance on the same chip.

With the help of numerical simulations (microfluidic, thermal and mechanical FEA), we have outlined the optimal dimensions of the three adopted sensors. This simulation approach has been developed elsewhere [4] and proved that only SOI technology allows the realization of these prototypes briefly described in the following section.

2 Sensors properties

The wall shear stress sensor's operation is based upon the principle of hot wire anemometry. The sensing element is made of polysilicon resistors that must be thermally isolated from the substrate by a sealed or open cavity to minimize the heat exchange with the substrate [4,5]. On the other hand, pressure sensing is based on the use of piezoresistive gauges placed on very small diaphragms (100×100µm^2). In order to accurately sense pressure fluctuations, these sensors must operate in a differential configuration. This last option necessitates the design of a specific ventilation channel as well as a high degree of thin layer thickness uniformity and reproducibility when elaborating such sensors. Finally, simple miniaturized p-n diodes have been adopted for local temperature sensing.

In the following section, we present the flowchart of the technology we have defined for the co-fabrication of the above described sensors highlighting the specific contribution of selected technological parameters. A first run of this technology is undertaken and is expected to provide the first prototypes by the venue of the eurosensors XVII.

3 Fabrication

The starting materials are two standard SOI wafers. The first one, called "base" wafer, is a BESOI one with silicon layer thickness chosen equal to the pressure sensor cavity depth. This wafer should also be <100>-oriented and p-type doped (typical resistivity range: 14-20Ω.cm).

The second wafer, called "active" wafer, should be Unibond or SIMOX completed with epitaxial growth. It should present an SOI layer 1 to 2 µm thick, a 0.5µm-thick buried oxide layer and be n-type doped, allowing consequently boron-ion implantation to minimize the leakage current of the piezoresistive gauges. The first step (Fig.1&5) consists in elaborating the pressure sensor cavities

in the “base” wafer using a deep RIE silicon etching. The buried oxide of the “base” wafer presents an excellent etch stop layer with respect to the deep RIE selectivity between oxide and silicon. This guaranties a perfect reproducibility of the cavity depth upon the whole wafer surface. During this step we also patterned the vent channel for the pressure sensor. A double side lithography has to be applied to pattern appropriate alignment features on the back side of this “base” wafer, these alignment features will be required in step n° 3.

The second step (Fig.2) aims to pattern the thermal isolation cavities necessary for the hot wire anemometer operation. It is conducted under the same technological conditions than the first step and leads to a perfect reproducibility of the cavity depth. Indeed, this cavity depth becomes equal to the SOI thickness of the initial “active” wafer.

The two wafers are then thoroughly cleaned before being assembled in a substrate bonder tool. This wafer bonding is followed by a thermal anneal step that strengthens the bonded surface energy. Afterwards, removing all of the “active” wafer’s silicon substrate reduces the whole pair thickness. The latter has been made by wet selective etching (TMAH solution).

After that, the fourth lithography is performed to pattern the p-n junction and the piezoresistive gauge surfaces to be implanted. A boron ion-implantation (dose and energy are estimated by numerical simulation) is then conducted and followed by an activation annealing. Notice that one of the more important advantages of this technology is to allow piezoresistive gauges to be monocrystaline that confer higher sensitivity than for currently used polysilicon gauges. Follows a deposition of a polysilicon film, p-type doped in which a fifth lithography allows the hot wire resistor patterning.

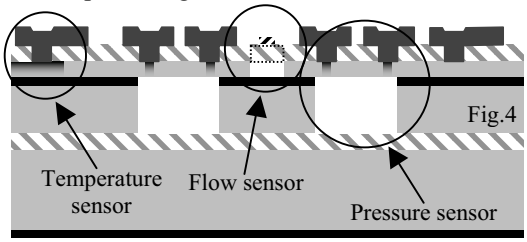

Fig.1: Pressure sensor cavity elaboration in the "base" BESOI wafer by deep RIE etching of <100> silicon.
Fig.2: Patterning within the "active" SOI wafer of the cavity underneath the hot wire anemometer.
Fig.3: A new substrate is obtained by bonding together the above-processed followed by thinning down the upper "active" layer.
Fig.4: Final structure showing the three types of sensors. (dotted lines show the hot wire releazing) are realized in step 1.
Fig.5: Deep RIE of cavity pressure sensors etching.
Fig.6: Profile of the pressure sensor’s membrane. A slight curvature (~85nm) is observed due to residual stress.

Another lithography will open the contact holes for the various sensors. A chrome layer is then deposited by sputtering and patterned to form the lead wires. The eighth lithography permits the release of the polysilicon resistors (by sacrificial attack of the underlying silicon dioxide film) for thermal isolation architectures requiring open (and not sealed) cavities.

4 Conclusions

This technology based on SOI wafer bonding requires only 8 photolithographies and masks. The principal advantage of such technology is to keep reproducible and constant pressure sensor cavity's depth and membrane's thickness. This is very important for the arrays configuration. Another advantage is that the pressure gauges will be in monocrystaline silicon and exhibit consequently very high sensitivity. Finally, this technology offers various thermal isolation architectures for the hot wire anemometer. In the future, signal processing integrated circuit will be integrated in this technology.

References

[1] Jiang et al., Flexible shear stress sensor skin for aerodynamics applications, MEMS'99.
[2] Löfdahl et al., Small Silicon Pressure Transducers for Space-Time correlation measurements in a flat plate turbulent boundary layer, J. Fluids Eng. 116, 457-463, 1996.
[3] Löfdahl et al., MEMS applications in Turbulence and Flow Control, Prog. in Aerospace Sci, 35, 101-203, 1999.
[4] Meunier et al., Realization and simulation of wall shear stress integrated sensor, Therminic 02 Workshop.
[5] Meunier et al., Fil chaud dans une micro cavité et capteur de pression en technologie MEMS, Congrès SHF "Microfluidique" - Toulouse - décembre 2002

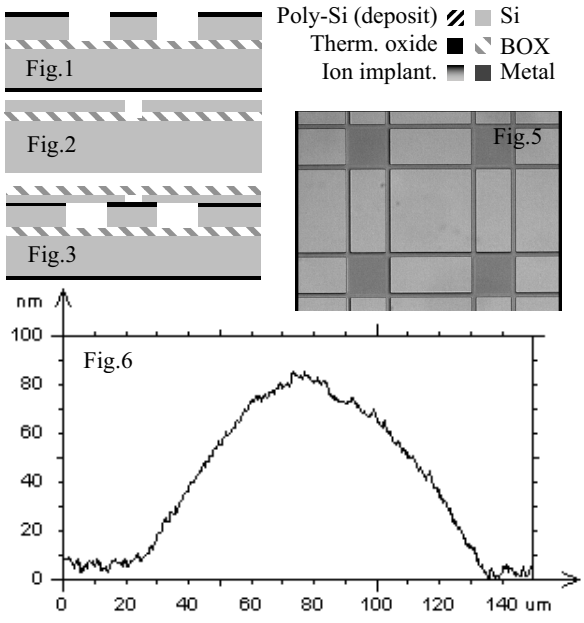

Thin Magnetic Amorphous Wires for GMI Sensor

H. Chiriac, M. Tibu, V. Dobre and I. Murgulescu

National Institute of Research and Development for Technical Physics,
47 Mangeron Boulevard, 6600, Iasi, Romania,
e-mail: hchiriac@phys-iasi.ro, http://www.phys-iasi.ro

Summary: *We performed a study of the giant magneto-impedance effect (GMI) and its characteristics in nearly zero magnetostrictive conventional amorphous $Co_{68.18}Fe_{4.32}Si_{12.5}B_{15}$ wires with diameters between 150-20 μm. The values of the impedance (Z) and GMI ratio (ΔZ/Z) were measured in the frequency range 100kHz – 10MHz for probes in as cast state and for probes obtained by cold drawn process. We obtained a four times higher GMI ratio for cold drawn wires with diameter 20 - 30μm after certain thermo-mechanical treatments in comparison with that measured for as cast wire 130μm in diameter produced by rapid quenching from the melt technique. The results are discussed considering the correlation between induced stress and modifications in circumferential magnetic domains configuration.*

Keywords: *GMI, magnetostriction, permeability, amorphous wires.*
Category: *2 (Materials and technology)*

Introduction

The GMI effect consists of a significant change in the impedance of a soft magnetic material, driven by a high frequency current, when it is placed in a static magnetic field. This effect arises mainly from the changes in the dynamic magnetization processes as the frequency of the driving ac current increases. Such changes (damping of domain wall motions, changes in the mode in which the magnetization proceeds on a given direction) affect the magnetic permeability and consequently, the magnetic penetration depth of the ac current through a magnetic conductor at high frequencies [1],[2].

Magnetic amorphous wires with nearly zero magnetostriction manifest high sensitivity of the GMI effect being promising for magnetic sensors applications. The GMI effect sensitivity in amorphous wires depend mainly on the wire composition which in our case ($Co_{68.18}Fe_{4.32}Si_{12.5}B_{15}$) is responsible for the negative nearly zero magnetostriction constant but also on the mechanical stress induced by fabrication process. The stress distribution determines the value of the circumferential magnetic anisotropy constant and the value of the magnetic permeability at the wire surface. The development of the new sensitive sensors based on the GMI effect requires high GMI effect sensitivity at low external magnetic field.

The aim of our work is to study the GMI effect sensitivity dependency on the wire diameter and on the thermo-mechanical treatments.

Experimental

Amorphous wires with diameters between 150-70μm, CoFeSiB in composition, were obtained by in rotating-water rapid quenching from the melt technique and also wires with the same composition were obtained by cold drawing in multiple steps from 130μm down to 20μm. The samples were subjected to heat treatments by anealing in conventional furnace in vacuum at 200 - 300°C using a certain heating rate and by passing a curent through the sample (effect Joule). Also mechanical treatments were performed for some samples during the anealing proces. The magnetic characteristics of the amorphous wires in as cast state, after cold drawn in multiple steps process and also after heat treatments were studied. The hysteresis loops both for axial and circumferential excitation field were traced and compared, the second one being related to the circular magnetization process as the effect of a circular magnetic field, produced by an AC driving current.

We performed impedance (Z) measurements in the frequency range 100kHz-10MHz for probes in as cast state, with diameters beween 90 - 150μm and for probes obtained by cold drawn process as a function of H_{dc} applied magnetic field. For the latters special mechanical treatments were performed in order to improve the surface quality of the wires.

Results and Discussion

The dependency of the impedance (Z) as a function of the H_{dc} applied magnetic field for the amorphous wires in the as cast state obtained by rapid quenched from the melt with diameters between 70 - 150μm is represented in fig.1. As it can be seen in fig.1. there is a variation in impedance value with the applied field for all diameters but the most important modification for low dc applied magnetic field is for thiner wires. More than that, by decreasing the wire diameters in multiple steps cold

drawing processes and after adequate heat and surface mechanical treatment we obtained a higher GMI ratio $\Delta Z/Z(\%)$ (defined as $\Delta Z/Z=(Z(H_{dc})-Z(H_{dc}=0))/Z(H_{dc}=0)$) for the wire with 30μm as it is shown in fig.2. Such a behavior can be explained by taking into consideration the internal tensile stress induced by cold drawn

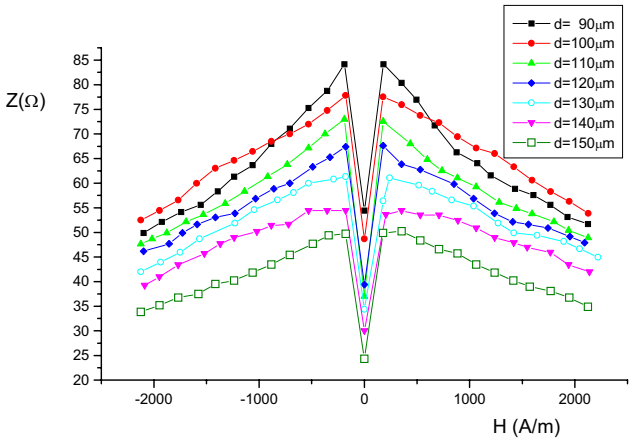

Fig.1.The impedance at 10MHz as function of DC applied magnetic field for CoFeSiB amorphous wires in as cast state.

process wich determine a modification in the magnetoelastic energy and cause an increasing of the outher shell thickness[3],[4].

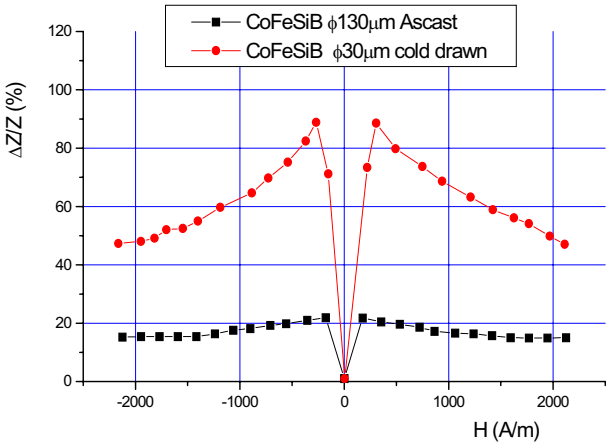

Fig.2. Field dependence of the GMI ratio for as cast 130μm and cold drawn 30μm in diameter wires

Due to the induced circumferential stress, the circumferential magnetic anisotropy constant increases and determines an increasing of the GMI ratio for low DC applied magnetic field.[5]

The increasing of the outher shell thickness with the decreasing of the wire diameter through a cold drawn process is confirmed by the circumferential hysteresis loops represented in fig.3. At low applied circumferential magnetic field the value of circumferential magnetic moment increases with the decreasing of wire diameter. The value of the coercive force in the case of circumferential magnetization process is about five times lower than that measured for longitudinal magnetization process.

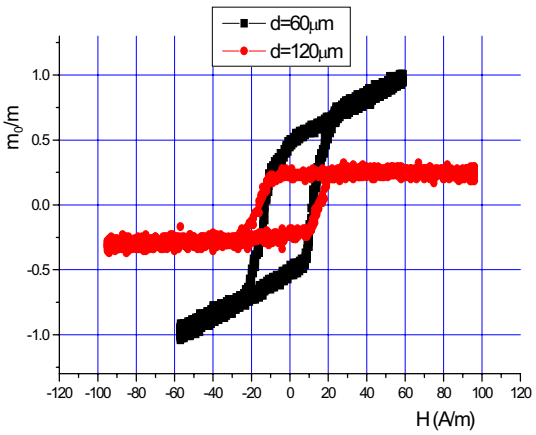

Fig.3. Reduced circumferential magnetic moment for cold drawn amorphous wires 60 and 120μm in diameter

The improvement of the wire surface quality, cause also modifications of the GMI ratio in the range of low DC applied magnetic field.

A controlled reduction by cold drawing of the wires diameter determines a significant increasing in GMI ratio in the range of low applied DC magnetic field making this kind of amorphous wires useful in development of new magnetic sensors based on GMI effect.

References

[1] L. V. Panina, K. Mohri, K. Bushida and M. Noda,"Giant magneto-impedance and magneto-inductive effects in amorphous alloys", *J. Appl. Phys*., vol. 76, pp. 6198-6203

[2] L. V. Panina, K. Mohri, T. Uchiyama, K. Bushida, and M. Noda, "Giant magneto-impedance effect in Co-rich amorphous alloys", *Eds. Singapore: World Scientific*, 1995, pp. 461-470.

[3] H. Chiriac, V. Finai, T. A. Ovari, C. S. Marinescu, F. Barariu and P. Tiberto, Mat. Sci. Eng. A 226-228 (1997), p.646

[4] M. Knobel, H. Chiriac, J. P. Sinnecker, S. Marinescu, T. A. Ovari, and A. Inoue, *Sensors and Actuators* A: Physical 59 (1997), p. 256.

[5] H. Chiriac, T. A. Ovari, Gh. Pop and F. Barariu, J. Appl. Phys. 81 (1997), p. 5817.

UV SENSITIVE GaN FILMS DEPOSITED BY CYCLIC PLD AT DIFFERENT SUBSTRATE TEMPERATURES

P. Sanguino[1], O.M.N.D. Teodoro[2], M. Niehus[1],
L. Melo[1], C. Boemare[3], M. J. Soares[3], T. Monteiro[3],
A.M.C. Moutinho[2] and R. Schwarz[1]

[1]Physics Department, Instituto Superior Técnico, Av. Rovisco Pais 1,
1049-001 Lisboa, Portugal
Fax: 21 841 9118, Phone 21 841 7775, Email: pesang@hotmail.com
[2]CEFITEC, Physics Department, New University of Lisbon
2829-516 Caparica, Portugal
[3]Physics Department, Campus Universitário de Santiago,
3810 Aveiro University

Summary: *GaN films were deposited by cyclic pulsed laser deposition at different substrate temperatures. Alignment of the films along the c-axis increased with substrate temperature but nitrogen loss also increased. Relative nitrogen concentration was determined by XPS and was smaller for films deposited at higher temperature. A decrease of the resistivity of the films agreed with higher metallic (Ga) concentration. Films with non-ideal stoichiometry already revealed* the typical donor-bound excitonic transition at 3.47 eV. This results suggests adjustments in the deposition conditions in order to have both perfect crystal alignment and good stoichiometry.

Keywords: *GaN, PLD, XPS, X-ray diffraction*
Category: *2 (Materials and Tecnhology)*

1. Introduction

The preparation of high quality semiconductor films of group-III nitrides (GaN, AlN, InN and their alloys) is a forefront task of the present technological research. The main reason is connected with the attractive applications of such films in "blue and UV" optoelectronic devices such as blue LEDs and blue laser diodes [1,2].

The Pulsed Laser Deposition (PLD) [3] is a promising alternative of the common MOCVD (Metalorganic Chemical Vapour Deposition) and MBE (Molecular Beam Epitaxy) techniques for preparation of these materials.

2. Abstract

In this article we report results on characterization of GaN grown on pre-nitridated sapphire substrates at temperatures between 400ºC and 600ºC by applying a two step cyclic PLD process. We compare them in terms of crystal structure, surface morphology, stoichiometry and resistivity.
The growth rate was around 0.05 μm/hour, which is smaller than reported by others.

Figure 1 shows the θ-2θ XRD scans for three 0.1 μm samples grown between 400ºC and 600ºC on c-axis oriented sapphire. As can be seen, the GaN (0002) peak intensity decreases with lower substrate temperature, which is an indication of the transition to the amorphous state. This is probably caused by the lower surface mobility of the deposited species at the reduced substrate temperature.

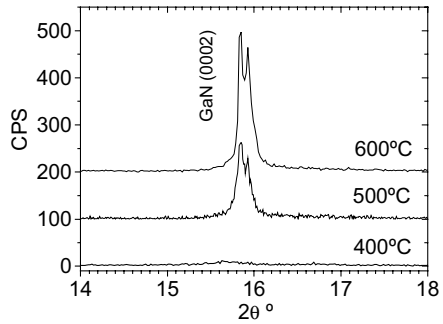

Fig. 1 θ-2θ XRD scans for three 0.1 μm samples grown at (a) 400ºC, (b) 500ºC and (c) 600ºC on c-axis oriented sapphire. Only the GaN (0002) peak is shown.

Figure 2 shows the variation of surface film morphology with substrate temperature. Images are plotted in a 4μm scale. The increase of the average domain size of the grains with deposition temperature is a clear indication of the transition from amorphous to crystalline material. This is in agreement with the XRD scans mentioned before. The mean roughness was measured to be 1nm, 4nm and 10nm for the substrate temperatures of 400ºC, 500ºC, 600ºC respectively.

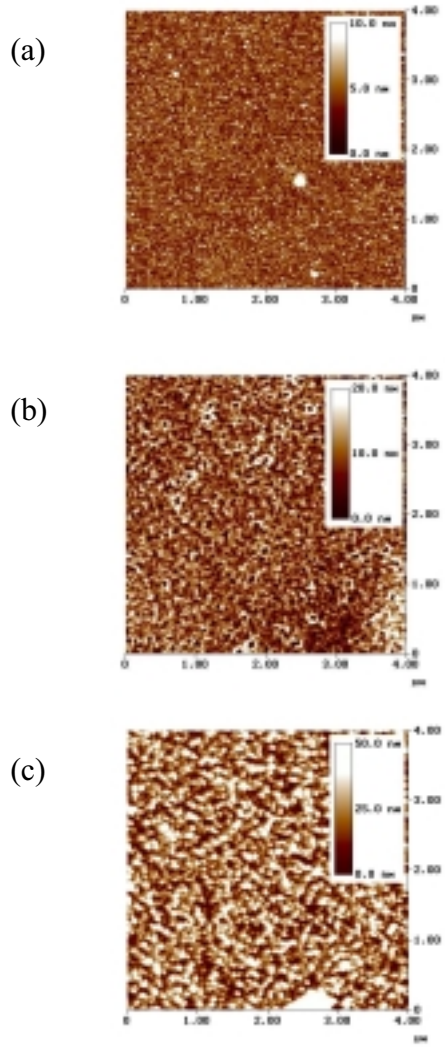

Fig. 2. Evolution of surface morphology of GaN samples deposited at (a) 400ºC, (b) 500ºC and (c) 600ºC. Pictures measured with AFM.

Film resistivity (fig 3a), measured with Van der Pauw 4 point probe technique, showed an increase in the conductivity with the deposition temperature. This seemed to indicate an increase in the metallic composition of the films at higher temperatures due to loss of nitrogen. Results from surface compositional analysis, performed by XPS, agreed with this assumption (fig 3b). The relative concentration of nitrogen at the surface of the film decreased with the substrate temperature.

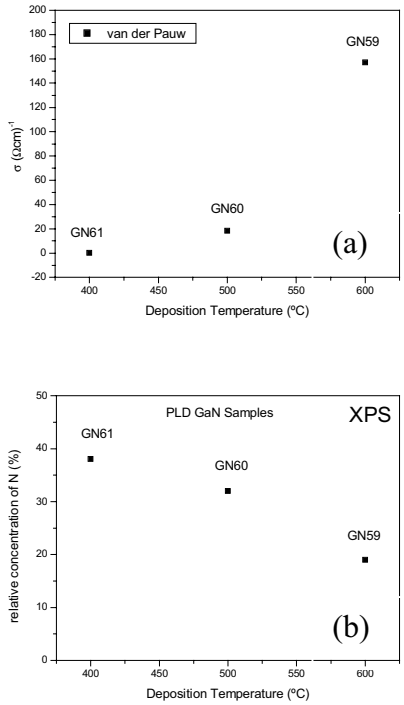

Fig.3. Film resistivity (a) and relative nitrogen concentration (b) for GaN samples deposited at different temperatures.

In conclusion, the films deposited at higher temperature showed an increased in the orientation of crystal grains along the c-axis but revealed a higher dark conductivity due to the loss of nitrogen.

Although chemical composition analysis points to a non-ideal stoichiometry, our best GaN samples already showed the typical donor-bound excitonic transition at 3.47 eV.

Comparison of the results obtained for samples produced under different conditions allow suggesting adjustments in the deposition parameters in order improve the quality of the films.

References

1. S. Nakamura, M. Senoh, N. Iwasa, and S. I. Nagahama, Appl. Phys. Lett., 1995 (13); 67: 1868-1870.
2. S. Nakamura, M. Senoh, S. Nagahama, N. Iwasa, T. Yamada, T. Matsushita, H. Kiyoku and Y. Sugimoto, Appl. Phys. Lett., 1996; 68 (15): 2105-2107.
3. V. Talyansky, R. D. Vispute, R. P. Sharma, S. Choopun, M.J. Downes, T. Venkatesan, Y. X. Li, L. G. Salamanca-Riba, M. C. Wood, R. T. Lareau, and K. A. Jones, Mat. Res. Soc. Symp. Proc., 468, 99-104 (1997).

A Novel two-output parallel-field Hall microsensor with low offset and temperature drift

Ch. S. Roumenin, D. Nikolov and A. Ivanov

Institute of Control and System Research, Bulgarian Academy of Sciences,
Bulgaria, Acad G. Bonchev Str., Blk. 2, Sofia – 1113, P.O. Box № 79
e-mail: roumenin@bas.bg

Summary: *A novel parallel-field four-contact Hall microsensor with two current supplies and two outputs is proposed and experimentally investigated. It is established that in case of the same supply currents, magnetosensitivities of the two outputs have equal values, but are opposite in sign, and the two offsets are nearly equal. The device structure is fabricated by standard silicon IC technology. By appropriate conditioning circuit, applied for the two output signals, a drastic reducing of the residual offset and its temperature drift more than two orders in a large temperature range* $-10 \le T \le 80$ *°C is achieved.*

Keywords: *Hall microsensor, offset reduction, output temperature drift*

Category: *3 (Magnetic physical devices)*

1 Introduction

In this paper is reported for the first time a novel parallel-field four-contact Hall microsensor with two outputs, where the offset and the offset temperature drift are simultaneously reduced with more than two orders. The origin of the offset phenomenon in Hall devices is due mainly to: crystal damage, geometrical errors in mask alignments, mechanical stress and strain, non-uniform temperature distribution and heat dissipation in the substrate, generation of a thermoelectric voltage across Hall leads, Peltiez effect, junction field effect, etc. Up to now overcoming of the offset, which is a major drawback of Hall plates, is achieved by improvement of the fabrication technology and device symmetry, variety of compensation static and dinamic techniques, spinning current method included, etc. [1-7]. Unfortunately they are not effective enough and increase considerably the cost.

2 Device structure and operation

The used for the first time in [1] four-contacts parallel-field Hall microsensor is particularly improved and is applied for overcoming of the offset problem. On Figure 1 is presented the novel silicon Hall microdevice. It consist of four contacts C_1-C_4, two constant current supplies I_1 and I_2 and two differential outputs $V_{C1,4}(\boldsymbol{B})$ and $V_{C2,3}(\boldsymbol{B})$. Specific feature of the biasing circuit is that the polarity of outer C_1 and C_4 terminals is the same as the one of the inner contacts C_2 and C_3, but opposite in sign. The inevitable even geometrical magnetoresistance is neutralized by the differential outputs and the device symmetry. The analysis of the new transducer showed that Hall signals $V_{C1,4}(\boldsymbol{B})$ and $V_{C2,3}(\boldsymbol{B})$ are *opposite in signs*, the magnetosenstitvities of the two outputs are equal $V_{C1,4}(\boldsymbol{B}) = V_{C2,3}(\boldsymbol{B})$ at currents $I_1 = I_2$, and the offsets $V_{C1,4}(B = 0)$ and $V_{C2,3}(B=0)$ are *nearly equal* too, $V_{C1,4}(0) \approx V_{C2,3}(0)$. However it is well known that the offset can not be distinguished from the Hall voltage. In our case the offset problem is resolved by *subtraction of the two output signals* ($V_{C1,4}(\boldsymbol{B})$ + $V_{C1,4}(0)$) and ($-V_{C2,3}(\boldsymbol{B})$ + $V_{C2,3}(0)$), or $V_{C1,4}(\boldsymbol{B})$ + $V_{C2,3}(\boldsymbol{B})$ + $V_{C1,4}(0)$ $-V_{C2,3}(0) = 2V_{C1,4}(\boldsymbol{B})$ + [$V_{C1,4}(0)$ – $V_{C2,3}(0)$] for a given magnetic field $\boldsymbol{B}$ orientation.

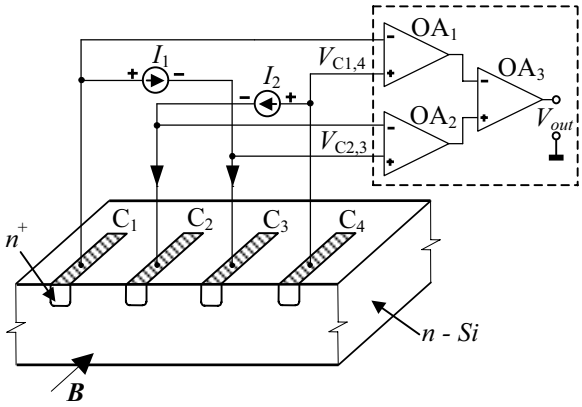

Fig. 1. A four n^+ contact parallel-field Hall microsensor with two outputs. The conditioning circuit, consisting of operational amplifiers OA_1, OA_2 and OA_3 for reduction of the offset and offset temperature drift is shown.

In the circuit on Fig. 1 the two sensor voltages after amplification by op-amps OA_1 and OA_2 are subtracted by op-amp OA_3. The output signal of OA_3 is defined as $V_{out} = 2V_H(\boldsymbol{B}) + V_{off}$. This is why in the novel Hall microsensor the residual offset V_{off} can be *very low*. At the same time the temperature offset drifts of the two outputs are equal, because they originate from

one and the same sensor zone. By this reason the residual temperature offset drift $V_{off}(T) = V_{C1,4}(0,T) - V_{C2,3}(0,T)$ should be dramatically reduced.

3 Experimental results

Experimentally investigated are silicon Hall microdevices fabricated in a standard planar technology on *n*-Si wafers with ρ = 7.5 Ω.cm., where the substrate serves as an active transducer region. In Figure 2 are presented the dependences of the two Hall voltages on the magnetic field ***B***.

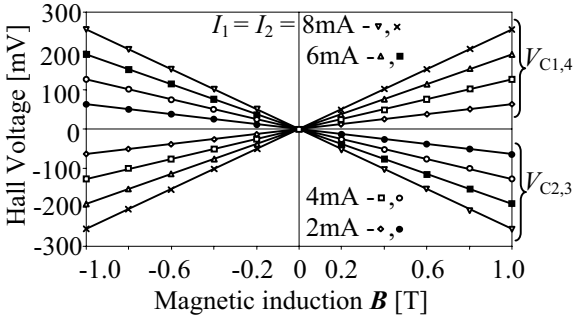

Figure 2. The magnetic response of the two output voltages $V_{C1,4}$ and $V_{C2,3}$, the current $I_1 = I_2$ as a parameter, T = 20°C. The initial offsets are nullified in advance.

The obtained relative magnetosensitivities are S_{RI} = 32 V/AT. The non-linearity of $V_{C1,4}(\boldsymbol{B})$, $V_{C2,3}(\boldsymbol{B})$ and $V_{out}(\boldsymbol{B})$ at induction $B \leq \pm 1$T does not exceed NL ≤ 1%. The determined temperature coefficient of magnetosensitivity of the two outputs is T.C. = 0.1 % /°C. On Figure 3 can be seen that the individual offsets at $I_1 = I_2$ = const. *are almost equal*.

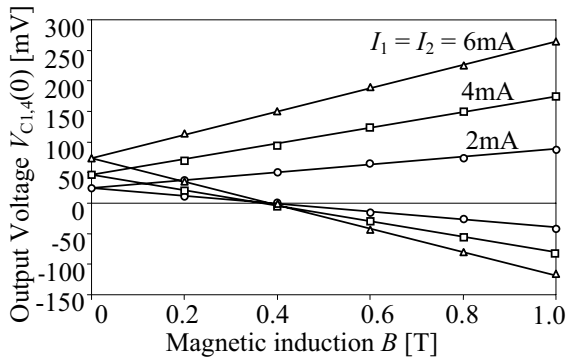

Figure 3. The output voltages $V_{C1,4}$ and $V_{C2,3}$ as a function of the magnetic field, the current $I_1 = I_2$ as a parameter. The respective initial offsets $V_{C1,4}(0)$ and $V_{C2,3}(0)$ are nearly equal, T = 20°C.

The residual offset V_{out} from op-amp OA3 is about *130 times lower* than the individual ones. Figure 4 presents separatly the temperature dependence of the offset voltages $V_{C1,4}(0,T)$ and $V_{out}(0,T)$. It is established that the offset drift $V_{off}(T)$ is about *150 times lower* than the drifts of the two signals $V_{C1,4}(0,T)$ and $V_{C2,3}(0,T)$. By calibration at any temperature T_0, a very low value of the offset V_{off} in a large temperature interval –10°C ≤ T ≤ 80°C is achieved.

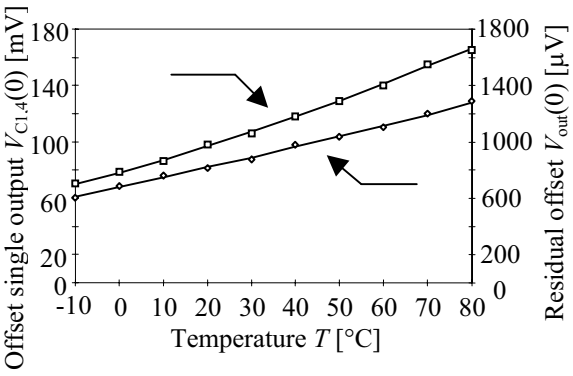

Figure 4. Temperature dependence of the offset voltage for one of the outputs as well as for residual offset voltage $V_{out}(0)$, $I_1 = I_2$ = 8 mA.

These results based on the new concept for offset reduction are very promising. If sophisticated IC technologies are used for the four-terminal device, the offset behavior and its temperature drift can be improved considerably. This solution presents an accurate microsystem for magnetic field with universal metrological applications.

References

[1] Ch.S. Roumenin. Parallel-field Hall microsensor. *Compt. Rendus Acad. Bulg. Sci*. 40(11) (1987) 59-62; Hall effect sensor. Bulg. Patent No 41974 (May 6, 1986).

[2] S. Middelhoek, S.A. Audet. *Silicon Sensors*. Acad. Press. London. (1989).

[3] Ch.S. Roumenin. Parallel-field Hall microsensors: an overview. *Sensors and Actuators.* A30 (1992) 77-87.

[4] C. Muller-Schwanneke, F. Jost, K. Marx, S. Lindenkreuz, K. von Klitzing. Offset reduction in silicon Hall sensors. *Sensors and Actuators*. A81 (2000) 18-22.

[5] Ch.S. Roumenin. *Solid State Magnetic Sensors*. Elsevier. Amsterdam. (1994).

[6] R. Steiner, C. Maier, M. Mayer, S. Bellecom, H. Baltes. Influence of Mechanical Stress on the Offset Voltage of Hall Devices Operated with Spinning Current Method. *Journal of Microelectromechanical Systems*. **8**(4) (1999) 466-472.

[7] R. Ernst, M. Hackner, H-P. Hohe. Realising Highly Symmetric Vertical Hall Sensor Elements on a Standard CMOS Process. *Proc. of the 16 European Confer. on Solid-State Transducers*, pp. 595-597 Eurosensors XVI, Prague, Czech Rep., 2002.

System Level Modelling of New Resonant MEMS Magnetometer in Simulink®

Zaki Izham[1], Michael C. Ward[2], Kevin M. Brunson[3] and Paul C. Stevens[4]

[1,2]University of Birmingham, School of Mechanical & Manufacturing Engineering, University of Birmingham, Edgbaston, Birmingham B15 2TT, UK.
email: Izham@gmx.net
[3,4]Microsystems & Microengineering Business Group, QinetiQ, St. Andrews Road, Malvern, WR 14 3PS, UK.

Summary: This paper describes an approach that allows the rapid analysis of a MEMS device at a system level using Simulink® by Mathworks. Parametric behavioural models are used to analyse MEMS structures and their response to changes in their drive-pickoff circuitry and environment. This method allows changes made at a system level to be analysed rapidly and hence greatly reduces development time and cost.

Keywords: *Resonant sensors, magnetometer, modelling*
Category: *3 Magnetic physical device*

1 Introduction

Resonant sensors have been developed and produced over the past decades but rarely take advantage of the high Q factor associated with MEMS resonators. This work has been performed to create a robust model to understand the dynamics of a high Q system in order to develop a new generation of resonant magnetic sensors that fully exploits the high Q. The modelling work done here will be compared to the experimental results obtained from the testing of a novel high Q MEMS resonator [1] and used to improve the design. This work is extremely timely considering the recent availability of high resolution direct digital synthesiser chips (DDS).

2 Modelling

Analytical models were assembled to obtain a first order estimate of the mechanical response of the device as shown in figures 1 and 2. The analytical models allow estimates to made for device resonant behaviour, change in capacitance with respect to displacement and electrical transform to an output voltage under a changing magnetic field. These models were compared to finite element simulations and are shown to agree within one percent. Device parameters such as the effective spring constant, drive frequency, damping and pickoff circuit parameters can be used to build a system level model in Simulink® (see figure 5). The dynamic modelling capability of Simulink is used to investigate the response of the MEMS resonant magnetometer in real time as shown in figures 3 and 4. By manipulating the input signal and tracing the resonant curve of the system it is possible to extract the resonant frequency, f_n, of the system. A ramped input (visible in figure 3) will give a direct current-displacement relation and hence spring constant k can be obtained by solving two simultaneous equations independent of magnetic field strength. Therefore compensation can be made for manufacturing variations and packaging issues. Furthermore, monitoring the decay of vibration (figure 4) enables the damping factor, c, to be determined. Figure 3 shows the excitation signal used to extract the system parameters f_n , k, and c. The system resonant frequency and spring constant can be used to determine the effective mass of the system, hence making available all the device parameters. A more complete solution will include second order effects such as cross axis coupling.

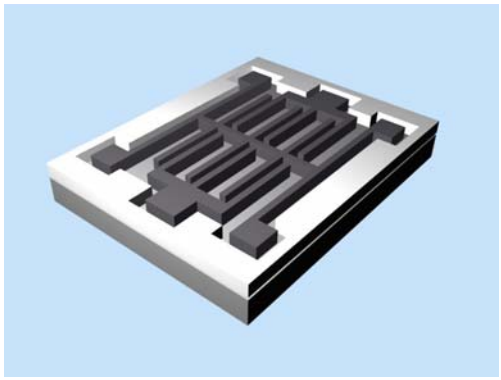

Fig. 1. Schematic of the resonant magnetometer.

3 Advantages

Once a robust system level model has been generated it will be possible to incorporate design changes at a system level to model changes in the device. Parametric modelling can be used to improve not only the design of the device but even the drive and pickoff electronics since it is possible to incorporate this in the Simulink® model.

Fig. 2. Manufactured prototype.

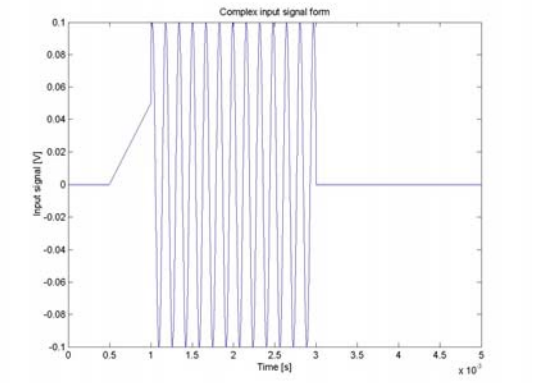

Fig.3. Excitation signal.

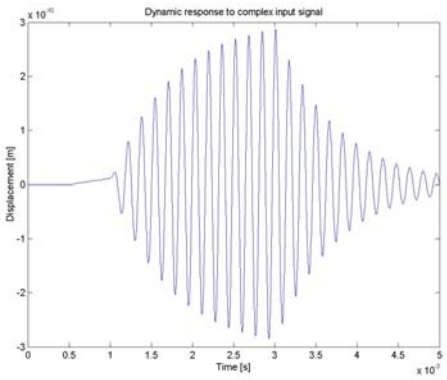

Fig.4. Device response to excitation signal.

3 Conclusion

This paper shows that it is possible to perform complex system level modelling of MEMS devices using Simulink® which is relatively cheap and simple to use. It is shown that simulations can be performed to extract device parameters vital to calibrate the output of the sensor.

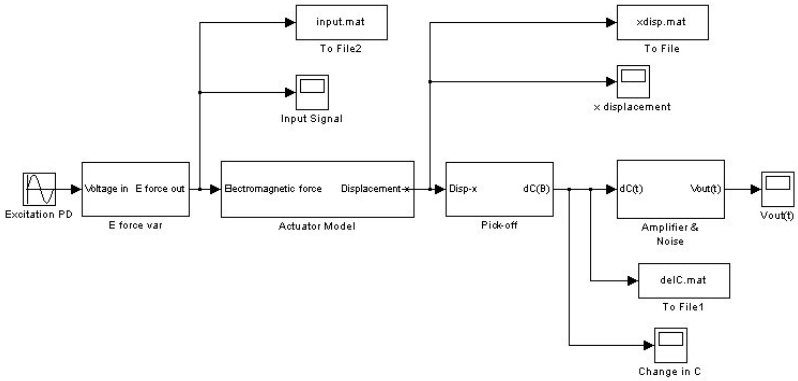

Fig. 5. System model with masked sub systems.

References

[1] Z. Izham et. al. Development of a Resonant Magnetometer. Proceedings of the 2003 Nanotechnology Conference and Trade Show February 23-27, Grand Hyatt San Francisco.

Spin-valve based high current sensors: a new IC/PCB design

C. Reig[1], D. Ramírez[1], F. Silva[2], J. Bernardo[2], P. Freitas[2]

[1]Universitat de València, Dept. d'Enginyeria Electrònica, Av. Dr. Moliner, 50, 46100-Burjassot, Spain
email: candid.reig@uv.es http://www.uv.es/~candid
[2]INES-MN, Rua Alves Redol, 9, 1000-29 Lisboa, Portugal

Summary: *We introduce a novel IC/PCB design of high current sensor, based in spin valve technology, with a full Wheastone bridge configuration. Two main advantages need to be highlighted. The first is that the four magnetoresistance sensing elements are deposited and patterned at the same time, so avoiding differences among them. The second one is that the IC fabrication process involves only three lithography steps, making the process cheaper and faster. Some prototypes have been fabricated and characterised in the range of [-5A, 5A]. Sensitivity and linearity have proved to be suitable for industrial applications.*

Keywords: *spin valve, magnetoresistance, current sensor*
Category: *3 (Magnetic physical devices)*

1 Introduction

Since the discovering of the GMR effect in 1988, a rapid development has taken place. GMR is now commonly used in sensors and read heads, and tunnel junctions are actually used in MRAM's. This devices utilise spin-polarised transport of electrons through a non magnetic material. In GMR, spin polarised electrons are injected from a ferromagnetic metal into a thin non magnetic metal layer. Tunnel junctions make use of a CPP configuration to drive the injected spin polarised current through a thin oxide layer. In spin valve systems a sandwich of ferromagnetic/non magnetic/antiferromagnetic layers forces the resistivity to follow an external magnetic field [1].

Spin valve based sensors have been successfully applied to: read elements in storage systems, rotational speed control devices, positioning control devices in robotic systems, high current monitoring devices for power lines, etc. [2]. For linear sensor applications, a four elements bridge configuration is preferred due to the null output in the absence of a signal field, the higher output signal and the minimisation of the temperature dependence [2].

Nevertheless, the Wheastone bridge configuration frequently displays offset voltage outputs in absence of magnetic field. This is mainly due to resistance mismatches among the magnetoresistors, produced during the fabrication process [3]. In order to overcome this handicap, a mixed PCB/IC design is presented. The main characteristic of the IC design is that the four resistors are deposited and patterned at the same time, so avoiding differences among them. Moreover, the fabrication process is, in this way, shorter and cheaper. The PCB for 'chip on board' encapsulation is designed in parallel. The current tracks are patterned for driving the current close to the sensing elements. Next paragraphs are dedicated to explain the details.

2 Sensor fabrication

A detailed scheme of the fabrication process is shown in Fig. 1.

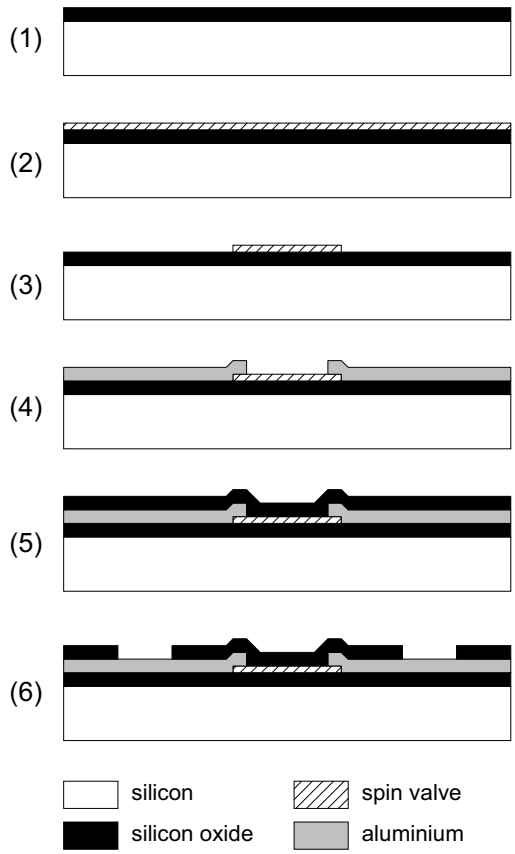

Fig. 1 Scheme of the fabrication process

The spin valve structure was deposited by ion beam sputtering (IBD) on 3" Si/SiO_2 1500Å (1) substrates with a base pressure of 5×10^{-8}–1.0×10^{-8}Torr. For IBD deposition, a Xe flow was used for a deposition pressure of 4.1×10^{-5}Torr. The spin valve structure was Ta(20Å) / NiFe(30Å) /

CoFe(20Å) / Cu(22Å) / CoFe(25Å) / MnIr(60Å) / Ta(40Å). This structure has demonstrated to give magnetoresistance responses of about 6%, linear ranges of about 25Oe and sheet resistivities of about 10-15(Ω·□) [1]. Deposition rates ranged from 0.3Å/s to 0.6Å/s. A 40Oe field was applied to the substrates during the deposition to ensure an easy axis in the pinned layer (2). The spin valve elements were then patterned by photolithography (direct laser writing on photoresist) followed by soft sputter etching, into elements with dimensions 200µm×3µm (3). The contact leads [0.150µm $Al_{98.6}Si_{1.0}Cu_{0.4}$/150Å TiW(N)] were defined by lift off (4). A 1500Å SiO_2 layer was used for passivation (5). Pads were finally opened for external contacts by wet etching (6).

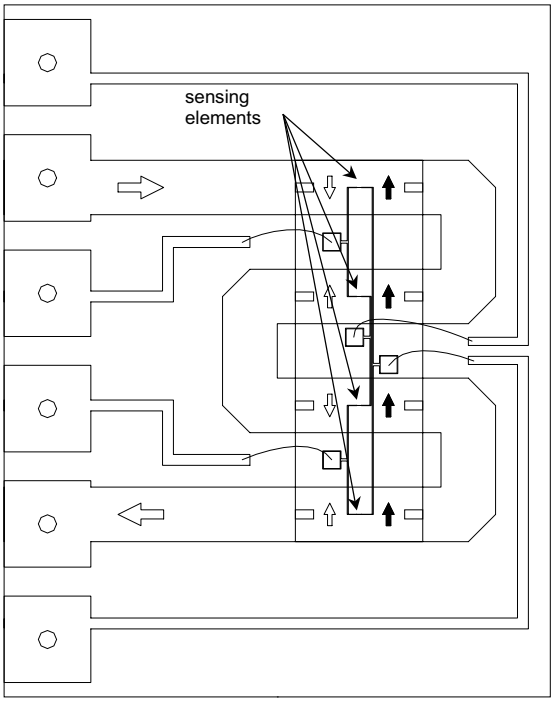

Fig. 2 Sensor function scheme. (Horizontal arrows: current; vertical hollow arrows: magnetic field; vertical filled arrows: spin valve easy axis). Sensing elements are highlighted

So fabricated sensors were then encapsulated 'chip on board' onto previously designed PCB's. The scheme is shown in Fig. 2. In this way, the current runs alternatively from-left-to-right and from-right-to-left through below the four sensing elements, and generates a magnetic field that increases the resistance in two sensors and decreases in the other two sensors. By an appropriate interconnection of the pads, we get a balanced Wheastone bridge.

3 Results

A photograph of first fabricated sensor is shown in Fig. 3. The IC dimensions are 7.2mm×18.0mm. The overall size was about 1.0in×1.2in, suitable for industrial electronics applications.

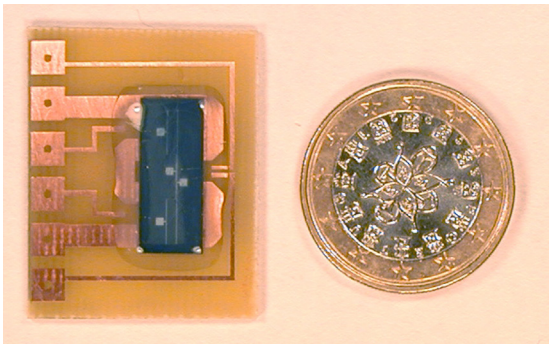

Fig. 3 Photograph of a sensor prototype

Preliminary I-V characteristic is shown in Fig. 4. Typical impedance of the sensor is about 1kΩ. The linearity has been demonstrated to be very good in the range [-5A, 5A], and no traces of saturation have been detected. The offset has been measured to be <1mV for a 1mA exciting current, so improving previously reported values [4]. The sensitivity has been calculated to be about 0.86mV/(V·mA), good enough for high current sensing.

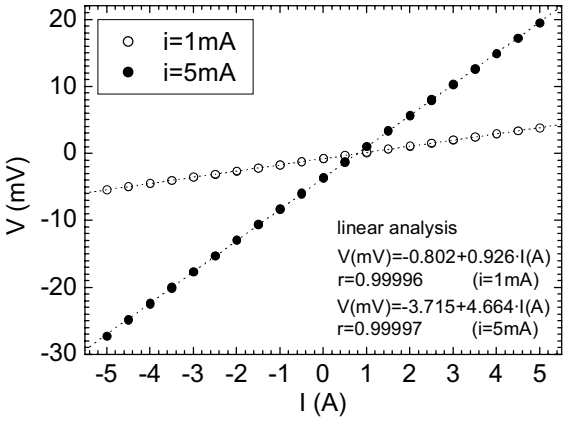

Fig. 4 Sensor I-V preliminary characteristic

References

[1] U. Hartmann (Ed.) Magnetic Multilayers and Giant Magnetoresistance. Springer (2000)

[2] P.P. Freitas, F. Silva, N.J. Oliveira, L.V. Melo, L. Costa and N. Almeida. Spin valve sensors. *Sens. Actuators A 81* (2000) 2-8.

[3] Wanjun Ku, F. Silva, J. Bernardo and P.P. Freitas. Integrated giant magnetoresistance bridge sensors with transverse permanent magnetic biasing. *J. Appl. Phys.* 87 (2000) 5353-5355

[4] J. Pelegrí, D. Ramírez, E. Sanchis, A.E. Navarro and S. Casans. Giant magnetoresistive sensor in conductance control of switching regulators. *IEEE Trans. on Magnetics*. 36 (2000) 3578-3580

On Chip Calibration of Hall Sensors Sensitivity

F. Tinfena [1], F. Mannozzi [1], V. Kempe [2] and L. Fanucci [3]

[1] Dipartimento di Ingegneria dell'Informazione.University of Pisa,Via Diotisalvi 2, I-56122 PISA (Italy)
[2] austriamicrosystems AG, Schloss Premstätten, A 8141 Unterpremstätten, Austria
[3] IEIIT, National Research Council, Via Diotisalvi 2, I-56122 PISA (Italy), E-mail: l.fanucci@iet.unipi.it

Summary: *A promising method to calibrate the Hall sensors sensitivity is based on the measurement of a stable reference magnetic field, which is generated directly on-chip by an integrated metal coil excited by a stable current. A mixed signal circuitry adjusts the sensitivity according to the reference magnetic signal measurement. In this paper we present a novel scheme for the small reference field detection in presence of the external magnetic field signal. This approach achieves an accurate continuous autocalibration procedure that is invisible from the outside and active during the entire lifetime of the sensor.*

Keywords: *Hall sensors, magnetic sensors, calibration, integrated coil*
Category: *3 (Magnetic physical devices)*

1. Introduction

In many particular high precision applications the unstable sensitivity of Hall devices represents a significant drawback. A method to correct the sensitivity changes is based on the generation of a stable reference magnetic field (normal to the die surface) directly on-chip. Sensitivity is regulated by a closed loop control system that compares the sensed value for the generated field with an expected value and adjusts the intensity of the sensor biasing accordingly [1], [2]. In principle this calibration approach is well known but it has never been realized in detail because of the difficult implementation. Reference field has to be measured in presence of the external magnetic field. This signal is the physical input quantity of the sensing device and it could be up to 3 order of magnitude greater than the on-chip generated one. On these conditions it is essential to find a valid solution that guarantees good selective detection capabilities of small reference field in presence of disturbances and noise. Various ways for field signal coding implementation are possible. In this work a solution based on the separation of reference and external signals in the frequency domain is proposed.
A Testchip that achieves a signal independent self-correction of its sensitivity has been realized on 0.8 µm CMOS austriamicrosystems technology.

2. Hall plates - Reference field actuators

The Hall sensors used in the integrated circuit including the calibration system are n-well active region plates in p-substrate with Greek cross symmetrical shape [3], ohmic contacted by 4 n^+ diffusions and current biased (I_{bias}). Active area is surrounded by an integrated metal coil, which is the actuator that generates the reference field (B_{ref}). It is fabricated with CMOS technology layers and it is excited by a current (I_{coil}) with low thermal drift.

If the accuracy of the current source is high enough only the geometry of the actuator defines the stability of the reference [4], [5]. Field amplitude is limited by the intensity of the current and by the small number of turns of the integrated coil.

3. Proposed solutions

3.1. Outband calibration

The on-chip calibration system should work during the normal operation and for all the lifetime of the device and in presence of the external magnetic signal (B_{ext}). This has a limited bandwidth, maximum amplitude much larger than the reference one and it acts like a disturbance in the measurement of the latter. A method to distinguish the two signals is needed. The proposed solution is based on the separation in the frequency domain (outband calibration). It is obtained by a modulation of the current flowing through the integrated coils of the actuators. The modulating signal could be sinusoidal or a particular sequence of impulses, but the use of a simple alternating square wave $c_p(t)$ allows an easy switch-based circuit implementation. Square wave modulation (frequency f_{ref}) generates a reference field with spectral components higher and far enough from the maximum external signal frequency. A synchronous demodulator detects the reference signal measured by the Hall sensors and conditioned by the Front End stage as in Fig.1.

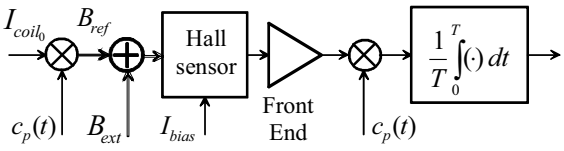

Fig. 1 Outband calibration scheme

Depending on the maximum external disturbance amplitude and on the modulating frequency, a valid selective detection of the small reference field could require too long filtering times (T).

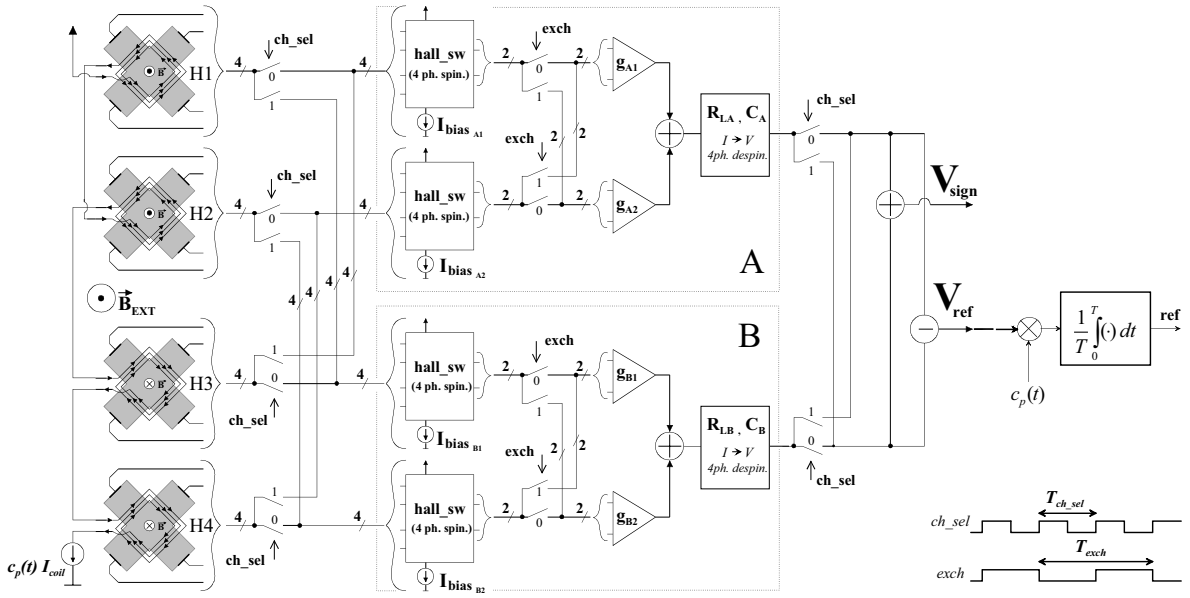

Fig. 2 Signal disturbance rejection scheme and timing of control signals

3.2. External signal disturbances rejection

A significant reduction of external disturbance and integration time is obtained with the innovative front-end structure of Fig.2. Like in [4] the measurement element consists of 4 Hall sensors divided in 2 pairs: one has the reference field in one direction (square wave modulated I_{coil} flows counter-clockwise), the other in the opposite direction (I_{coil} flows clockwise). There are 2 channels (*A,B*) for signal conditioning. Each includes switches (**hall_sw**), transconductive amplifiers (**g**) and charge storing elements (**C**) for sensors biasing, amplification and offset compensation based on four-phase spinning current method. A further spatial offset compensation is achieved placing the 2 sensors of a pair very close and biasing by currents with same intensity but flowing one in a 90°-direction respect to the other. Considering that the external field is the same for all sensors, if the two channels were really identical the sum of the two outputs would give two times the external signal, while the difference would give two times the reference. Because of the inevitable mismatches sensors, biasing currents and channels elements are not identical and the unwanted component can not be canceled out by the difference. A considerable reduction of the mismatch effects is achieved if the channels are periodically exchanged. Each pair of sensors is connected for half of the integration time *(T)* to a channel of biasing/amplification and for half to the other, as scheme and timing of Fig.2 show. The *ch_sel* signal is a square wave (period T_{ch_sel}) and it controls the switching between the two lines. Inside a channel also the 2 inputs of the transconductive amplifiers ($\mathbf{g_{A1}}$,$\mathbf{g_{A2}}$ and $\mathbf{g_{B1}}$,$\mathbf{g_{B2}}$) are switched by the *exch* signal to have a better offset compensation ($T_{exch}=2\ T_{ch\_sel}$).

4. Conclusion

In this work an outband autocalibration system is presented. It is based on a reference field generated by integrated coils and separated by the external field in the frequency domain. External disturbance is strongly reduced by the particular front-end structure adopted. Reference is selective detected by a synchronous demodulator, which analog output is converted to digital domain. Numeric samples are discrete-time integrated and obtained values are used in an externally closed loop to control the biasing current of the sensors. Measurement results on realized Testchip show good external field disturbance rejection and noise suppression. With $f_{ref} = 125\ kHz$ and *262 ms* of total integration time (analog $T = 256\ \mu s$, average on *1024* samples) sensitivity is measured with an accuracy in the order of 0.8 % of its absolute value.

References

[1] M. Demierre, S. Pesenti, R.S. Popovic, "Self calibration of a CMOS twin Hall microsystem using an integrated coil" *Proc. EUROSENSORS XVI,* Prague, September 2002.

[2] P.L.C.Simon, P.H.S.de Vries, S.Middelhoek "Autocalibration of silicon Hall devices", *Sensors and Actuators A52*, 1996, pp.203-207.

[3] R.S.Popovic, "Hall Effect Devices", Bristol: Adam Hilger, 1991.

[4] M. Demierre, S. Pesenti, J. Frounchi, P.A. Besse, R.S. Popovic, "Reference magnetic actuator for self-calibration of a very small sensor array", *Sensors and Actuators,* A 97-98 (2002) 39-46.

[5]] J.Trontelj, L.Trontelj, R.Opara, A.Pletersek, "CMOS Integrated Magnetic Field Source Used as a Reference in Magnetic Field Sensors on Common Substrate",*Proc.IMTC/94*,JAPAN,1994, 461-463.

Design and Fabrication of a Vibrational Micro-Generator for Wearable MEMS

Wen-Sheh Huang, Kung-Ei Tzeng, Ming-Cheng Cheng, and Ruey-Shing Huang

National Tsing Hua University, 101, Section 2 Kuang Fu Road,Hsinchu, Taiwan 300, Institute of Electronic Engineering, ROC
email: rshuang@ee.nthu.edu.tw

Summary: *This paper reports the development of a vibration-induced micro power generator with improved structural design and fabrication. The device consists of a thick electroplated planar copper coil of thickness 100um and plated nickel-iron alloy suspension spring. Thick plated copper coil has reduced the generator internal resistance to 2 Ω. Spring of nickel-rion alloy increases linear vibration amplitude up to 1mm. RMS output Power of 0.32uW was measured when shaked by tapping gentlely with finger tips, which demonstrates the feasibility of micro power gneration in wearable MEMS applications. Numerical simulation of magnetic field spatial distribution and spatial magnetic flux change rate of planar coil with respect to moving magnet are also presented. These simulation results facilitate the optimization of coil design.*

Keywords: *generator, micro power source, vibration*
Category: *3 (Magnetic physical devices)*

1 Introduction

Miniaturized micro power source devices are of great interest for a variety of wearable MEMS and distributed sensor system applications. Mechanical micro power source that converts natural environmental or parasitic vibration kinetic energy to electrical energy is superior to the chemical based power sources in the aspects of its perpetual life time and no need for replenishment of energy sourcing materials.

In this paper, a prototype vibrational micro-generator is fabricated and tested for the first time to investigate the feasibility of wearable micro power source. Numerical simulation of magnetic field spatial distribution helps the optimization of coil design. Thick electroplated planar coil and spring are designed to reduce the generator internal resistance and increase vibration amplitude of magnet.

2 Description

A schematic cross-section view of the micro-generator is shown in Figure 1. The magnet suspension spring is fabricated in one wafer, whereas planar coil is on another wafer and then bonded together with epoxy adhesive bonding.

Simulation results of flux change rate as a function of the coil location relative to the center of the magnet is shown in Figure 2. It is clearly shown that the flux change rate has a peak near the edge of the magnet. Faraday's Law predicts the voltage output to be proportional to the rate of changing magnetic flux, which shows that coil turns close to the magnet's edge are the most efficient power generation coils.

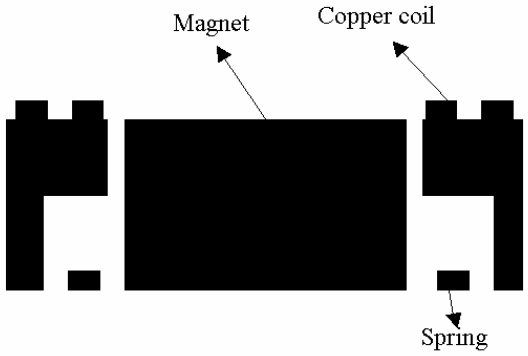

Fig. 1. Schematic cross-section view of the micro-generator

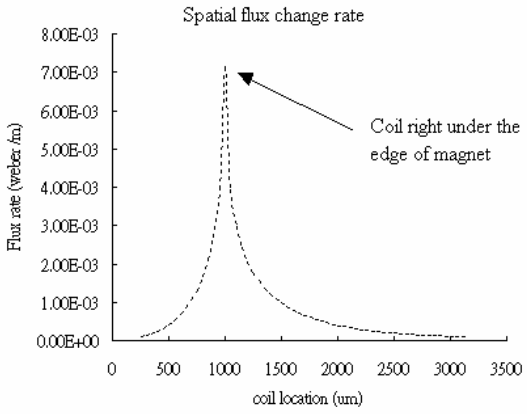

Figure 2: flux change rate vs. the location of the power generation coil, position 0 corresponding to the center of the magnet

The optimization is done by proper placement of coil and elimination of the less efficient power generation coil to reduce the number of coil turns, hence reduce the generator internal series resistance. Instead of inserting the spring between planar coil and the magnet, the electroplated spring that supports moving magnet is suspended right under the energy-collecting coil. This arrangement of energy collecting coil and suspension spring in different planes enables us to locate the coils at where the magnetic flux change is the largest.

Device fabrication has improvements from the previous reported results[1][2] in two aspects; one is applying the thick electroplated copper coils to significantly reduce the internal resistance; the plated coil thickness is about 100um and internal resistance is only 2 Ω as shown in Figure 3.

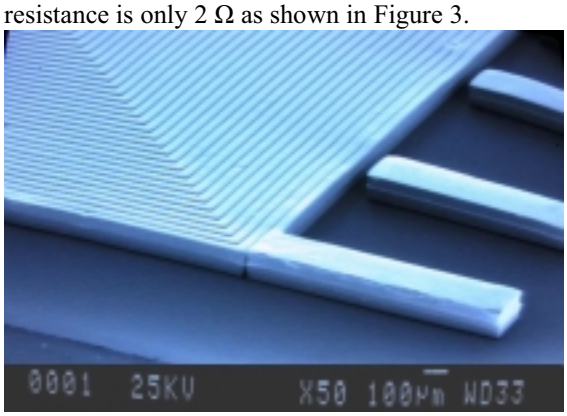

Figure 3: Electroplated 100um copper coil

The other improvement is spring fabricated with electroplated nickel-iron alloy. Nickel-iron alloy has higher yield stress as compared with that of copper and thus can sustain larger vibration amplitude.

3 Measurement

The most direct method to test the feasibility of wearable MEMS applications is to gently tap the device with fingers mimicking the vibration generated while the device is weared on a person. As shown in Figure 4, the rms output power is measured to be 0.32uW.

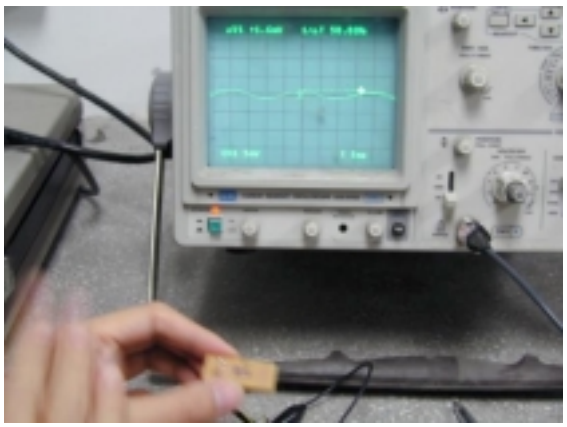

Figure 4: Feasibility of power generation test by direct finger tapping caused vibration

When the prototype micro-generator is placed on a sinusoidal vibration test bed with vibration amplitude of about 50um, the rms output power of our prototype device is about 1.44uW. Figure 5 is the rms output power when vibration frequency is sweeped from 50 Hz to 300 Hz. The peak output power appears at the frequency around 100Hz which can be shifted by design.

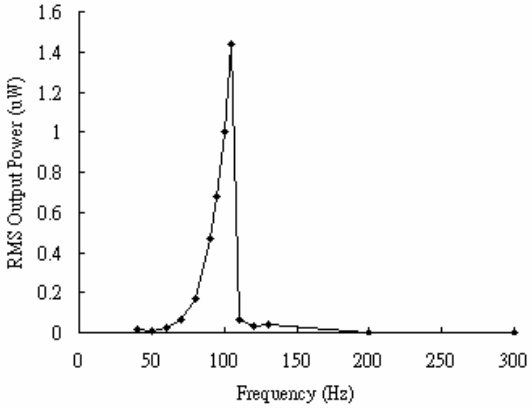

Figure 5 rms output power when vibration frequency is sweeped from 50 Hz to 300 Hz.

4 Conclusions

The improvement of coil's design and spring material will increase energy coupling and transformation efficiency from vibration to electricity significantly. Larger power generation was achieved by the increased energy transform efficiency from kinetic to electric. This makes the electric power generation directly from human body movement feasible and promising.

References

[1] C. Shearwood, C.B. Williams, and R.B. Yates, *Eurosensors XI*, pp. 767-770.

[2] Neil N. H.Ching, H.Y.Wong, Wen J.Li, Philip H. W. Leong, and Zhiyu Wen, *Transducers '01*. ,pp38-41

Micromachined Diaphragms with Integrated Actuation Coils

N.J. Grabham, S.P. Beeby and N.M. White

University of Southampton, Department of Electronics and Computer Science, Southampton, SO17 1BJ, UK
email: njg@ecs.soton.ac.uk http://www.ecs.soton.ac.uk

Summary: *This paper presents a process for fabricating diaphragms, suitable for use in micromachined pumps within the field of micro-fluidics. To enable the actuation of a thick-film deposited magnetostrictive material, actuation coils are fabricated onto the non-chamber face of the diaphragms. These actuation coils are fabricated using a multilayer deposition approach compatible with micromachining processes. The selection of diaphragm and actuation region dimensions has been achieved through the use of finite element modeling. The paper also describes the fabrication process used to realize the structures.*

Keywords: *Magnetostrictive, Thick-Film, MEMS*
Category: *3 (Magnetic physical devices)*

Introduction

There is interest in using magnetostrictive materials to actuate micromachined pumps for use in micro-fluidic systems. An example is the control of small amounts of substance, such as that typically used in DNA isolation. Published work, such as that of Quandt *et al* [1], mainly concentrates on the use of thin-film magnetostrictive materials for actuation with the magnetic field commonly provided through the use of externally mounted coils.

Current research at the University of Southampton is investigating the fabrication of a thick-film magnetostrictive material for use with micromachined devices. This paper describes a fabrication process, which enables the production of actuation coils integrated within the surface of the diaphragm pump, prior to the deposition of the thick-film magnetostrictive material [2]. The advantages of using an integrated coil approach, as opposed to an external coil, include device compactness and the ability to integrate several devices in close proximity to each other with minimal cross actuation.

Prior to fabricating the devices in single crystal silicon, the diaphragm and actuator dimensions have been determined through the use of finite element modeling, which is discussed in the subsequent section. This is followed by a description of the fabrication process.

Modeling of Diaphragm Shape

The shape and dimensions of the etched diaphragm have been modeled using the ANSYS finite element analysis (FEA) software package. The use of this modeling approach permits the effects of the geometry of the diaphragm on the resulting strain distribution within the device to be readily assessed.

For the purposes of speed of computation, the diaphragms were modeled as quarter devices, using the symmetry of the structures to extrapolate the results to those of the full device.

The effect of the magnetostrictive thick-film is modeled by the inclusion of a suitably dimensioned region on the upper face of the diaphragm; the magnetostriction of the thick-film material is simulated using thermal expansion of this material to yield suitable stresses for the simulation.

Two effects were examined in the test devices; firstly, the strain distribution was determined to investigate any strain concentrations. Secondly, the volume displaced by the whole diaphragm for a given strain in the actuator layer was calculated.

The use of a FEA approach also allows the resonant frequencies of the structure to be determined, so that the device can be driven at its mechanical resonance frequency.

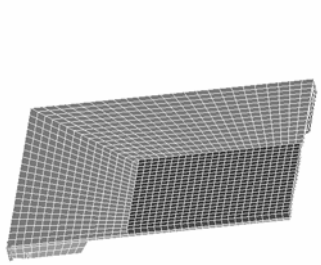

Fig. 1. Rectangular diaphragm quarter device model

The two diaphragm shapes evaluated were a plain rectangular diaphragm and an oval one. In both cases, the etched diaphragm is contained within a chip package of rectangular form. The ANSYS models used for the rectangular and oval diaphragms are

shown in figure 1 and figure 2, respectively. In both figures, the smaller, darker, region represents the magnetostrictive material and the larger, lighter, material the micromachined silicon forming the diaphragm and its associated surroundings and mountings.

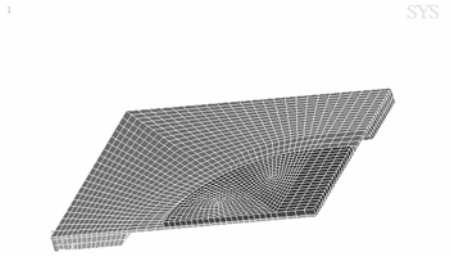

Fig. 2. Oval diaphragm quarter device model

Materials Used to Fabricate Devices

The main section of the device is formed by bulk micromachining of microelectronic grade single crystal silicon, in the form of double polished 100mm diameter wafers.

The conductors are formed using evaporated gold layers of 500nm thickness. To aid the adhesion of the gold to the silicon and silicon dioxide layers, chromium is also deposited to act as an interface layer between the silicon and the gold. It also provides a more reliable bond and reduces peel-off of the gold films.

Electrical insulation and mechanical protection of the integrated coils are achieved through the use of chemical vapour deposited silicon dioxide layers.

Fabrication Process

The micromachined diaphragms with integrated coils are fabricated in two phases. The first phase being to form the diaphragms, and the second to form the integrated coils.

To form the diaphragms, a KOH wet etch is used in conjunction with nitride / silicon dioxide masking layers to etch from the back of the wafer until a diaphragm thickness of 70µm is reached. Once the diaphragm has been successfully etched, the nitride masking layers are removed.

With the diaphragms formed, the processing enters the second phase with the start of the coil fabrication by the deposition of a 500nm thick layer of gold combined with a chromium adhesion promotion layer. This metal layer is then patterned using a lift-off technique to provide the first layer of coil turns. This initial metal layer is then covered with an insulating layer of silicon dioxide, which is then patterned and etched to provide access to the buried metal layer at the desired points. A further metal layer is then deposited onto the surface, and again patterned using the lift-off process to generate the second layer of coil turns which connect to the first layer through the vias etched into the underlying silicon dioxide layer. An additional layer of silicon dioxide is then deposited to insulate and protect the coils, and again patterned and etched to permit access to the two layers of metal at the required points for connection to external drive circuitry. This final layer of silicon dioxide also serves as a suitable interface layer to permit the thick-film magnetostrictive material to bond reliably to the device.

A simplified, non-scale, representation of a possible cross section of the diaphragm with two layers of integrated coils is shown in figure 3. The gold layers indicated in the figure also contain the chromium interface layer mentioned previously.

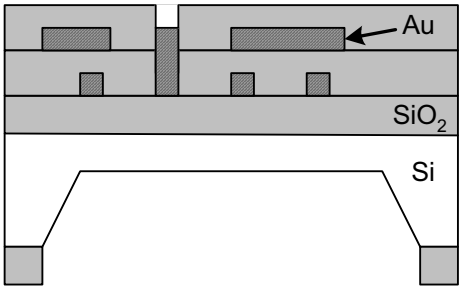

Fig. 3. Representation of structure of diaphragm with integrated coils

Acknowledgements

The authors wish to thank the Engineering and Physical Sciences Research Council (EPSRC) for their financial support under grant number GR/R43327. We also gratefully acknowledge the support and assistance given to us by Newlands Technology Ltd.

References

[1] E. Quandt and K. Seeman. Magnetostrictive thin film microflow devices. In *Proceedings of Microsystems Technology 96* (1996). pp. 451-456.

[2] N.J. Grabham, S.P. Beeby and N.M. White. The formulation and processing of a thick-film magnetostrictive material. *Measurement Science and Technology*. 13 (2002) 59-64.

MICROFABRICATION OF GOLD WIRES FOR ATOM GUIDES

E. Koukharenko[1], Z. Moktadir[1], D. Bagnall[1], M. Kraft [1], C. Vale[2], M. Jones[2], E. Hinds[2]
[1]University of Southampton, Dept. Department of Electronics and Computer Science, Highfield, Southampton, SO17 1BJ, UK, ak@ecs.soton.ac.uk
[2]Blackett Laboratory, Imperial College, Prince Consort Road, London SW7 2BW.

SUMMARY

The last few years have seen an enormous interest in the design of microscopic atom traps for manipulating neutral atoms. Miniature atom traps have potential applications in many fields including quantum computing and integrated atom optics. Microfabricated current carrying wires can produce magnetic fields suitable for trapping atoms that are laser cooled to μK temperatures (sketched in figure 1) . Recently, Bose-condensed atom clouds have been produced using micrometer-sized atom traps fabricated on chips [1, 2]. This paves the way to a field where microelectromechanical systems and coherent atom optics overlap. Microfabrication can bring a significant contribution to this field because of the advanced techniques used to fabricate micron scale structures. The overlap between the two fields will deliver devices for sensing applications such as atom-interferometry. The purpose of our work is the microfabrication of wires capable of carrying high density currents necessary to create high magnetic field gradients used for atom trapping.

Keywords: atom guide, gold wires, high density currents

Subject category: *Magnetic Physical devices*

RESULTS

Miniaturized atom optics is a new field allowing the control of cold atoms in microscopic magnetic traps and waveguides. Using microstructures (known as atom chips), the control of cold atoms on the micrometer scale becomes possible. This possibility will lead to the construction of integrated atom interferometers [3]. The realization of such structures requires high magnetic field gradients
The motivation of this work is to realize micromachined high-density current-carrying wires for atom guides [4, 5]. However, the process can be used for a variety of applications such as on-chip inductors and microtransformers. In order to realize the micromachined high-density current-carrying wires for atom guides a one-mask micromachining process was developed.

The fabrication process can be summarised in the following way: Silicon substrates <100>, p type, 17-33 Ω cm resistivity and 100 mm in diameter are cleaned in fuming nitric acid (FNA). Next, a thin electrical insulating film of silicon dioxide SiO_2 (600 nm) is deposited by wet oxidation. Then, Cr-Au layers (few hundreds of Angstroms Cr and 3, 5, 10, 25 μm of Au) were sputtered on a silicon wafer. Next, the wafers are primed using hexamethyldisilazane (HMDS) vapor for 3 minutes. This is followed by spin-coating step to deposit standard SPRT 510 photoresist using a hand spinner. Then, the gold layers are

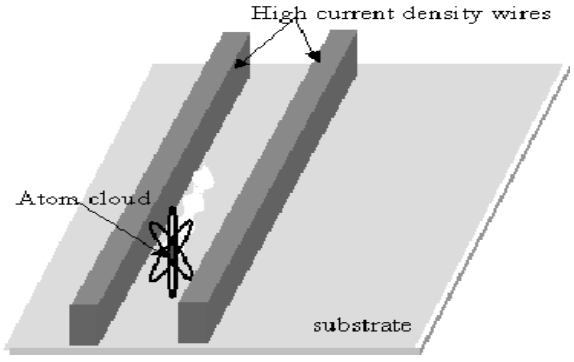

Fig.1: Schematic representation of an atom cloud in the vicinity of high current density carrying wires

photolithographically patterned with the mask to form the areas for contacts pads, golden wires of 3, 5, 10, 25 μm thick of Au, and golden mirrors (see figure 1). The exposure was done with a contact mask using a Hybrid Technology Group (HTG) aligner using UV lights source (350-450 nm spectrum, Mercury lamp) at 1.6-1.9 mW/cm^2 intensity. Next step was wet chemical etching of Au with aqueous KI_3 solution and Cr in a mixture of a

Ceric Ammonium Nitrate ($H_8CeN_8O_{18}$) with nitric acid. The mask design is shown in figure 2.

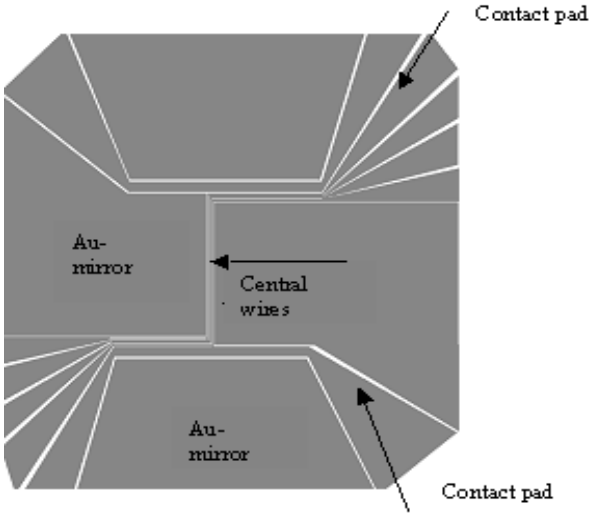

Fig. 2: The mask used for wires fabrication.

The mask defined four golden mirror areas, contact pads and four central wires of 100 and 50 µm wide separated by a gap of 30 µm.
The fabrication process is diagrammatically illustrated in figure 3. Figure 4 shows the SEM pictures of the view from the top an atoms guide prototype device. The full description of the design, experimental set up and results will be presented at the conference.

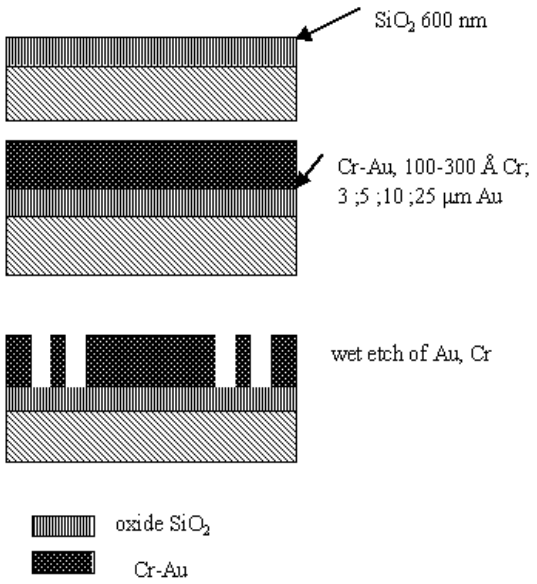

Fig3: Schematic diagram illustrating the fabrication process

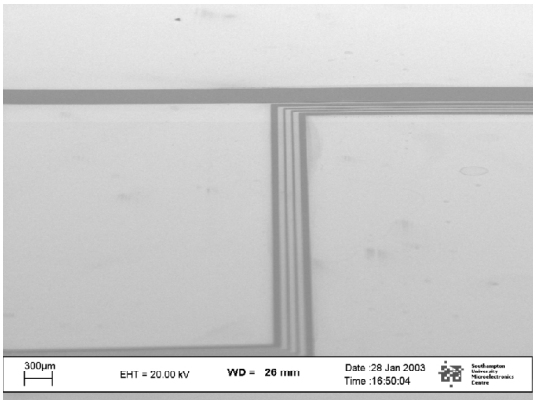

Fig.4 **:** SEM picture showing the central region the wires structure.

REFERENCES

[1] W. Hansel *et al*. Nature, **413,** 489, (2001).
[2] H. Ott *et al*. Phys. Rev. Lett. **87**, 230401 (2001).
[3] E. Anderson *et al*., Phys. Rev. Lett. **88**, 100401, (2002).
[4] R. Folman *et. al* Phys. Rev. lett,, **84**, 4749 (2000).
[5] E. Hinds *et al*. Phys. Rev. Lett., **86,** 1462 (2001)

Frontier Problems of Flux-gate Magnetometry

V. Korepanov, R. Berkman, A. Sukhyniuk and A. Marussenkov

Lviv Center of Institute of Space Research, 5-A Naukova Street, 79000 Lviv, Ukraine
email: vakor@isr.lviv.ua http://www.isr.lviv.ua

Summary: *The flux-gate magnetometers are widespread nowadays in different branches of science and industry. The state of the modern electronic components base and available manuals allow to build the flux-gate magnetometer with moderate level of parameters practically by every skilfull engineer. But if the rigid requirements of low noise level and/or power consumption are imposed the problem to create such magnetometer needs special study. The results of such study, both theoretical and experimental, are exposed in the report.*

Keywords: *flux-gate magnetometer, noise, power consumption*
Category: *3 (Magnetic physical devices)*

1 Introduction

The flux-gate magnetometers are probably the most widespread ones nowadays. This is because of high level of their metrological and operational parameters and high flexibility to the external conditions – they can operate in deep space, water, for industry, field geophysics etc. There are also many companies in the world producing flux-gate magnetometers (FGM), mostly with comparable level of parameters, satisfying majority of demands. But in some seldom cases there are the consumer's requirements which are not easy to satisfy, first of all it deals about very low noise level or sensitivity threshold and power consumption. The problems connected with the decreasing of these values are the most difficult to solve. The present state of research in these directions is reported below.

2 Noise study

The recent progress in electronic components and parts allowed to reduce the FGM electronic unit proper noise so considerably that the FGM sensitivity threshold is limited mainly by the flux-gate sensor magnetic noise (MN).

The problems of MN calculation and measurement require special approach both in theoretic analysis and practical implementation. In the result of intensive investigations following semi-empirical equations were proposed for the calculation of MN density b(f) and its root-mean-square value ΔB_{sq}:

$$b(f) = b_0 \left[1+(f_0/f)^{\alpha}\right], \qquad (1)$$

$$\Delta B_{sq} = \left\{ \int_{f_{min}}^{f_{max}} b(f)\, d f \right\}^{1/2} = \left\{ b_0 \left[f_{max} - f_{min} + f_0^{\alpha} \left(f_{max}^{1-\alpha} - f_{min}^{1-\alpha}\right)/1-\alpha\right]\right\}^{1/2}, \qquad (2)$$

where f_0 is corner frequency, f_{max} and f_{min} - correspondingly maximum and minimum frequencies of FGM operation band, b_0 - noise density at flat part of the noise plot.

It is seen from (1) that the shape of MN density frequency spectrum is determined by b_0, corner frequency f_0 and coefficient α. For modern FGM with ring-core and race-track sensor the value of f_0 in the majority of the cases was reduced to about 1 Hz.

It is evident also from the same expression that by its character MN is similar to flicker noise, for which $\alpha=1$ is usually taken. However our detailed research of MN frequency spectrum for different materials and designs in frequency band up to 1 mHz showed that the value of α for advanced FGM often can be accepted as low as 0.8.

The main term determining FGM noise is b_0 which, as experimental study gave it, can be expressed as follows:

$$b_0 = C_F \cdot V^{-1/2}, \qquad (3)$$

where C_F is an empirical constant $\approx 5 \cdot 10^{-28} T^2 m^3 Hz^{-1}$ for good permalloy material of the FGM sensor (FGS) core and V is FGS core volume.

As it is seen, the easiest way to decrease the noise is to use the cores with big enough volume V. But this possibility is very limited because of the necessity to have reasonable both sensor size and excitation power. More efficient is to try to get as low C_F value as possible. C_F is dependent on the quality of the FGS core material - its specific magnetic noise value is the main factor influencing C_F, but not only. The core excitation mode and also the processing mode of the sensor output signal also have great impact on C_F reducing [1]. The attempts in this direction are still continued and very optimistic estimation recently made as to the possible noise value gives about 0,1 picotesla at 1 Hz [2]. Unfortunately, it is not informed in the referenced paper whether the FGM or though the FGM sensor with such a low noise was practiced.

With the use of these theoretical and experimental results a set of advanced FGMs is created.

The technical parameters of main types of LEMI magnetometers as well as the results of their application for field geophysics are described in details at Lviv Center of Institute of Space Research web-site [3].

3 Power consumption

The modern electronic components base allows to create data acquisition and especially processing units with negligible power consumption in comparison with the power necessary for providing of FGS proper operation conditions. That is why the most important problem for FGM creation with low power consumption is to reduce the FGS excitation power. It is clear that the excitation power dissipates in two ways: the power P_c consumed for the magnetic core re-magnetization and the power P_w dissipating in the copper winding of FGS. Power consumption P_c in the magnetic core depends on parameters of hysteresis loop, magnetization frequency and core volume. For magnetic materials with rectangular shape of hysteresis loop this power can be defined as follows:

$$P_c = 4B_s H_{eq} V f = 0.8 B_s H_{eq} f \frac{l^3}{\mu_c} \qquad (4)$$

where B_s - saturation induction; H_{eq} - equivalent coercive force; $\mu_c = l^2/(5 \cdot 2s_c)$ - relative permeability of the core shape for bar-core and racetrack FGS, l – core length; s_c – core cross-section surface.

The equivalent coercive force H_{eq} value according to [4] can be presented as follows:

$$H_{eq} = H_c + \sigma \Delta^2 B_s f \frac{\pi}{2(\pi - 2\alpha_0)}. \qquad (5)$$

where H_c – coercive force of static hysteresis loop, σ - specific conductance of ferromagnetic material, Δ - thickness of ferromagnetic tape, $2\alpha_0$ – width of saturation pulse.

So, the power consumption for remagnetisation of FGS core can be defined as follows:

$$P_c = 4B_s H_{eq} f V = \left(4B_s H_c f + \frac{2\sigma \Delta^2 B_s^2 f^2 \pi}{(\pi 2\alpha_0)} \right) V . \qquad (6)$$

This expression also confirms low efficiency of noise level decreasing according to (3), i. e., using FGS core with big volume: the consumed power will proportionally increase and the noise will decrease proportionally to square root of core volume.

The power dissipation P_w in the FGS winding can be estimated using the obtained expression:

$$P_w = \frac{2\pi(k_d + 1)}{k_A^2 k_H^2 k_w (k_d - 1)} H_m^2 \rho l = K H_m^2 \rho l , \qquad (7)$$

where $k_A \approx \sqrt{\pi \cdot \alpha_0^{-1}}$ peak-factor of the excitation current, k_w - filling factor of the excitation winding, k_d - ratio between outer and inner diameters of the excitation winding, H_m - peak value of the excitation magnetic field strength, ρ - copper specific resistivity, $K = const$ for geometrically similar windings.

It is necessary to say that usually the power consumption of real excitation circuit is (4÷10) times more than the calculated value because of poor matching of excitation generator output and sensor impedance. For typical construction of FGS ($k_d = 1.1$ and $\mu_c = 700$) the major part of excitation power dissipates in the winding at wide range of sensor volume. So, the way to considerably decrease the power consumption is to increase the coefficient k_d or in other words, the volume of copper winding. It may be realized in the easiest way for bar-core FGS. Using this approach a set of super-low power consuming analog FG magnetometers was manufactured with the sensor length about 5 ÷17 mm and power consumption 1.5 ÷ 15 mW only.

4 Conclusion

As it was stated above, no specific problems arise when FGM with moderate level of parameters is necessary to manufacture. But special cases happen rather often when very low FGM noise level or power consumption is necessary. The semi-empirical relations are obtained which show with rather good matching to experimental results the ways how to proceed in these cases. The discussed results are physically transparent and can be useful for every expert in the field.

In conclusion it is necessary to emphasize still two aspects of high class FGM creation.

- Most important is to use magnetic material with as low as possible noise constant C_F. Unfortunately, due to the complicated technology of melting and rather low market demand the alloys with super-low C_F values are no more industrially produced.
- Even for very good magnetic core material the FGS excitation mode has exclusively high influence both on noise level and power consumption.

This work was partially supported by STCU grant NN-38.

References

[1] R. Berkman, V. Korepanov and B. Bondaruk. Advanced flux-gate magnetometers with low drift. In: *Proc. XIV IMEKO World Congress*, pp. 121-126, Tampere, Finland, vol. IVA, 1997.

[2] R. H. Koch, J. G. Deak and G. Grinstein. Fundamental limits to magnetic-field sensitivity of flux-gate magnetic-field sensors. *Appl. Phys. Letters.* 75, no. 24 (2000) 3862 – 3864.

[3] www.isr.ua

[4] M. Rozenblat. Magnetic amplifiers. *Soviet Radio.* 1 (1960) (in Russian).

GMI current sensor

M. Malátek, A. Platil and P. Ripka

Czech Technical University in Prague, Dept. of Measurement, Technicka 2, 166 27 Prague 6, Czech Republic
email: malatem@fel.cvut.cz http://measure.feld.cvut.cz

Summary: *GMI effect in Co-rich amorphous strip, which was thermally processed by temperature of 350°C, has been observed with maximum GMI sensitivity of about 230 % on the frequencies around 20 MHz. A simple contactless current sensor using GMI effect has been constructed. Basic measurements with and without biasing have been performed.*

Keywords: *GMI, current sensor, amorphous strip*
Category: *3 (Magnetic physical devices)*

1 Introduction

Giant magnetoimpedance effect (GMI) in soft magnetic materials has been systematically [1, 2] studied in last years. This phenomenon consisting of large relative change of HF-impedance under the application of dc magnetic field has been observed mainly in ribbons [3], thin films [4, 5] and microwires [6, 7]. In spite of growing interest in crystalline Mo – permalloy GMI materials [8-10], mainstream interest is oriented to amorphous and nanocrystalline materials.

2 GMI strip

Amorphous ribbon with $Co_{67}Fe_4Cr_7Si_8B_{14}$ composition was prepared by the planar fow-casting in the Institute of Physics, Slovak Adademy of Sciences in Bratislava.

Firstly, a short thermal processing of the strip was performed; the specimen was annealed in the air atmosphere at the temperature of 350°C for 10 minutes.

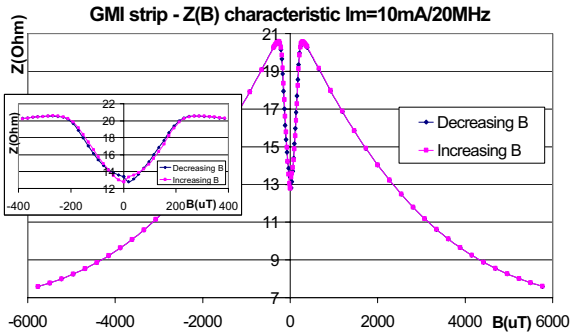

Fig. 1. Z(B) characteristic (I_m=10 mA/20 MHz) and detail of zero field area (inset)

Secondly, a set of Z(B) characteristics of 10 cm long, 1 mm wide and 20 µm thick strip has been obtained for the measuring current with constant amplitude and varying frequency. The characteristics in frequency range from 100 kHz up to 30 MHz of the measuring current I_m have been performed by the PC-controlled system comprising precise RLC bridge HP 4285A, Helmholtz coils and DC power supply HP 6642A.

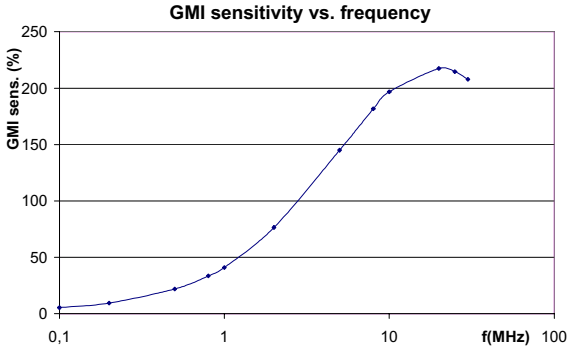

Fig. 2. Dependence of GMI sensitivity on frequency

The maximum of GMI sensitivity of about 230 % was observed in vicinity of 20 MHz (Fig 2). In our further experiments, 1 MHz current was used for the sake of simpler design. Fig. 1 shows Z(B) characteristic for measuring current I_m of 10 mA/20 MHz where the significant pinhole in zero magnetic field area can be seen (Figure 1 detail).

3 Current sensor

A simple contactless current sensor (see Fig. 3) using the GMI strip has been constructed in our laboratory. At first, the strip was wound around a nonmagnetic ring support, and then the biasing winding was coiled along the circumference of such a double-layer ring. The winding shifts working point out of the pinhole area to the "linear" (flank) part of Z(B), Z(I) characteristic when DC bias current is applied on it.

Initially, rough measurements with measuring current I_m=10 mA/1 MHz have been obtained with the sensor in both modes, with and without biasing. A PC-controlled system similar to the first one has been employed to measure the dependence of impedance Z on measured current I in range of ± 10 A. According to the assumptions, the Z(I) characteristic of nonbiased sensor (Fig 4)

and Z(B) characteristic of strip are alike in vicinity of zero currents (fields) even if the Z(I) characteristic is deformed due to bending stress that has arisen in coiled GMI strip. Thus, the biasing of the sensor must be used to work in bipolar linear mode. In lower current measurement range of ± 2 A (Fig. 5), the achieved linearity error is 4.4 %. To reduce nonlinearity, applying of compensation winding to perform negative feedback could be used.

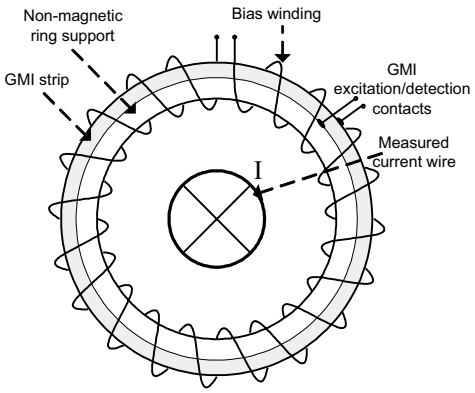

Fig. 3. Current sensor

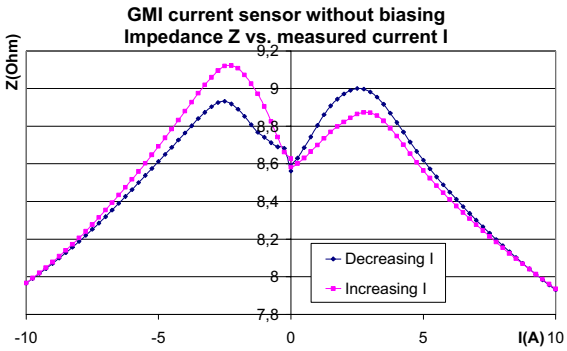

Fig. 4. Z(I) characteristic – sensor without biasing

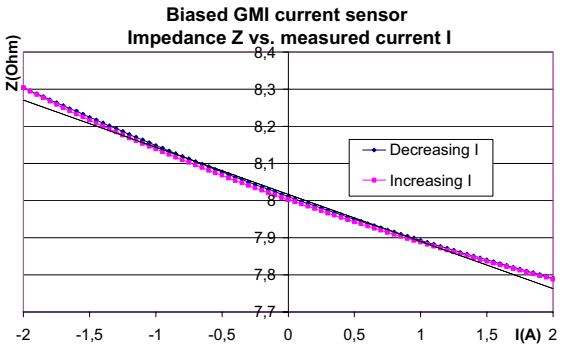

Fig. 5. Z(I) characteristic, small range – biased sensor

4 Conclusions

A simple contactless GMI current sensor developed in our laboratory has been tested. First measurements of Z(I) dependence on relatively low frequency of 1 MHz of the measuring current were accomplished. Following steps are aimed to measurements at higher frequencies, where the GMI sensitivity is higher (the maximum is predicted at the same frequency where the maximum of non-strained strip is).

Future work will be focused on improvements of the sensor; testing of thermal processing influence on properties of the strip, searching of optimal DC biasing, testing the possibility of AC biasing [7] and development of negative feedback using the biasing coil.

Acknowledgement

This work has been made in the cooperation with Institute of Physics of the Czech Academy of Sciences. Primarily we would like to thank to Mr. Ludek Kraus who supplied us with the sample of GMI material.

References

[1] J. Pokorný, L. Kraus: GMI effect in amorphous wires with creep-induced magnetic anisotropy, *In: Sensors and Actuators A* 59 (1997), 65-69

[2] P. Ripka (ed.): Magnetic Sensors and Magnetometers, *Artech House* Publ. 2001, ISBN 1580530575

[3] J. Hu, S. Zou, W. Chen, Y. Wang : Giant magnetoimpedance effect in Fe-Nb-B ribbon, *Solid State Comm.*, Vol. 109, 1999, 661-664

[4] Y. Nishibe, H. Yamadera, N. Ohta, K. Tsukada and Y. Nonomura: Thin film magnetic field sensor utilizing magneto impedance effect, *Transducers'99*, (1999), 594-597

[5] M.Yamaguchi, M.Takezawa, H.Ohdaria, K.I. Arai, A. Haga: Directivity and sensitivity of high-frequency carrier type thin-film magnetic field sensor, *Sensors and Act. A* 81 (2002), 102-105

[6] Kraus L., Knobel M., Kane S.N., Chiriac H.: The influence of Joule-heating on magnetostriction and GMI effect in a glass-covered CoFeSiB microwire. *J. Appl. Phys.* 85 (1999) 5435-5437

[7] K. R. Pirota, L. Kraus, H. Chiriac and M. Knobel: Magnetostriction and GMI in Joule-heated CoFeSiB glass-covered microwires. *J. Magn. Magn. Mater.* 226-230 (2001) 730-732.

[8] A. Platil, M. Malátek, P. Ripka, L. Kraus: GMI Sensor. In: *Eurosensors XVI*. Prague, 2002, vol. 2, 341-342. ISBN 80-01-02576-4

[9] P. Ripka et al.: Permalloy GMI sensor. *JMMM, Volumes 254-255*, January 2003, p. 633-635

[10] M. Vázquez, J.M. García-Beneytez, J.P. Sinnecker: Magneto-impedance effect in high permeability NiFeMo permalloy wires, *J. Appl. Phys.* 83: (11), Part 2 Jun 1 1998, 6578.

Microstrip impedance measurements for GMI sensors

D. de Cos, A. García-Arribas, and J. M. Barandiarán

Universidad del País Vasco, Departamento de Electricidad y Electrónica. Apartado 644, 48080 Bilbao, Spain.
email: dce@we.lc.ehu.es http://www.we.lc.ehu.es

Summary: *We present impedance measurements in magnetic samples as a function of the frequency, up to 500 MHz, and its dependence with the applied magnetic field, of high interest for magnetic sensors. The stress of the investigation is done in the experimental procedure, in order to get impedance values as accurate as possible. We describe an experimental configuration in which the sample is included in a microstrip line, like the ones used in RF applications, and the impedance is determined from the reflection coefficient. The results obtained in an amorphous ribbon are consistent with theory, indicating that the measurements are accurate. The measuring procedure allow us to follow in great detail the frequency dependence of the magnetization processes that influence the transport phenomena.*

Keywords: *microstrip lines, giant magneto-impedance.*
Category: *3 (Magnetic physical devices)*

1 Introduction

Giant magnetoimpedance (GMI) is the strong dependence of the electrical impedance on the applied magnetic field that experience high permeability magnetic samples. It is a completely classical effect that can be described easily using Maxwell equations. In short, it is based in the changes of impedance caused by the variations in the penetration depth of the AC current as a function of the applied magnetic field, due to its effect in the permeability of the magnetic sample. The GMI effect has been extensively studied in magnetic wires and ribbons during the last decade, and several sensing applications have been proposed to take advantage of its huge sensitivity to small magnetic fields. GMI based sensors could be considered as an alternative to other magnetic devices only if batch production is feasible. This implies that the samples must be prepared in thin films by atomic deposition techniques, with thickness in the micron range. The GMI effect is then noticeable only at elevated frequencies (tens of MHz to some GHz typically), where the penetration depth gets close to the thickness.

The impedance measurements as a function of the applied magnetic field that allow to characterize the GMI response in ribbons and wires are usually performed using a four point geometry. At higher frequencies, the external inductance of the measuring set-up can greatly reduce the effect. Besides, that unwanted contribution to the measured impedance hinders the interpretation of the results in terms of proposed theories [1].

To overcome this limitation, in this work we use an experimental approach taken from high frequency test set-ups.

2 Experimental

We have selected a 20 mm long ribbon of amorphous $(Fe_{0.06}Co_{0.94})_{75}Si_{15}B_{10}$ alloy. It has been glued to the transmission line using standard silver conductive paint. The transmission line used is a microstrip, made by a top conductor line printed onto a dielectric substrate covered in its bottom side by a ground conductor [3]. Impedance of the sample is obtained from the reflection coefficient of the line. Static magnetic field applied longitudinally to the sample and in its plane was provided by means of a pair of Helmholtz coils.

The test fixture configuration used in the present application is shown in Figure 1 (top). The sample is situated between two 50 Ω microstrip lines, both of them terminated in SMA connectors. One of these ports is loaded with a 50 Ω termination, and the other one is connected through a N-to-SMA transition to the Network Analyzer (Agilent 4395A), thus configuring the measurement plane. In Figure 2 (bottom) we show the electrical circuit corresponding to the described set-up. The microstrip line after the sample does not contribute to the reflection coefficient because its impedance

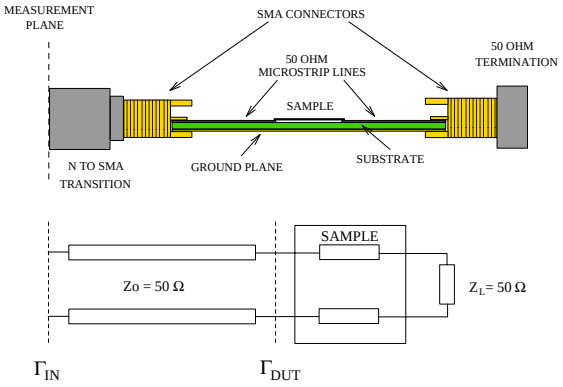

Fig. 1. Schematic view of measuring fixture (top) and its electrical model (bottom).

is matched with the 50 Ω termination. The propagative contribution to the impedance comes from the elements between the sample and the measurement plane (that is, the microstrip line, the connector and the transition). The relation between the reflection coefficients at the sample and at the measurement plane is

$$\Gamma_{IN} = \Gamma_{DUT} \exp(-2j\gamma l)$$

where $\gamma = \alpha + j\beta$, is the propagation constant, and l is the length of the transmission line. The exponential term of the equation can be easily determined (simply removing the sample and measuring the line in open termination) and afterwards numerically corrected to obtain Γ_{DUT}. Impedance is then obtained from

$$Z = Z_0 \frac{1+\Gamma_{DUT}}{1-\Gamma_{DUT}} - 50$$

where the subtracted 50 Ω come from the load termination.

The main shortcoming that would limit the use of this technique at very high frequencies is derived from the configuration of the fixture itself, where the sample, together with the ground plane below, can be viewed as another section of transmission line (in general with a characteristic impedance different from 50 Ω, and in this particular case depending on the applied magnetic field). This implies that the reflection coefficient is not constant along the sample, depending on the relation between its length and the wavelength associated to the measurement frequency. In the presented experiments the minimum wavelength is 60 cm (500 Mhz), which is much larger than the length of the sample (20 mm), so in this case the measured impedance is nearly unaffected by field propagation. A possible solution to this problem would be the use of coplanar waveguides or slotlines, where it is possible to connect circuit components in shunt from the conducting strip to the ground plane on the same side of the substrate. Then the sample could be connected not as a transmission line, but as a circuit termination.

3 Results

Figure 2 shows a typical measurement result, after line correction. It corresponds to the highest applied field (6 kA/m), where the sample is close to magnetic saturation, being its permeability nearly constant, close to μ_0. For this situation, it is easy to calculate theoretically the impedance of a ribbon as a function of the frequency using the Maxwell equations [2]. These calculations are presented in the inset. The similar overall shape of both experimental and calculated curves indicates that the measurement is essentially free of stray contributions. It is also possible to estimate the amount of external impedance to be about 5 nH (this value corrects the slope of Im(Z) that must coincide with Re(Z) at high frequencies).

In figure 3, we present some Z(H) curves corresponding to increasing frequencies. They show how different magnetization processes dominate at different frequencies, reshaping the curves. At low frequencies, changes in the permeability caused by wall displacement feature sharp peaks, whereas they disappear at higher frequencies because wall movement is hindered. A detailed analysis of the results will allow us to obtain a more profound insight of the magnetic behavior of the sample.

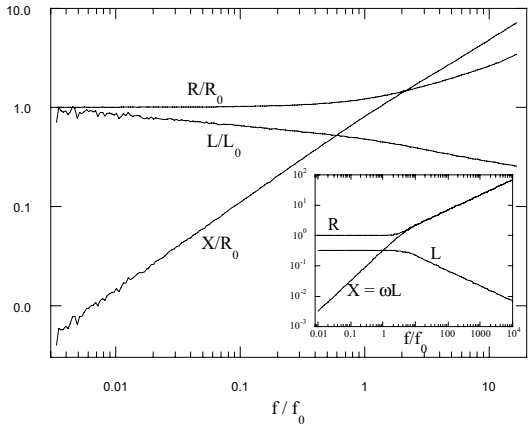

Fig. 2. Measured and predicted (inset) impedance Z=R+jωL. R_0 and L_0 are DC values.

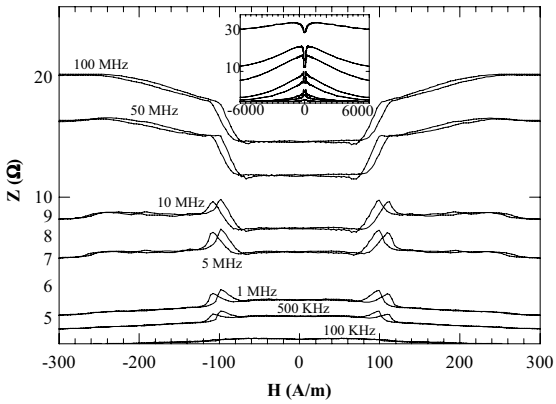

Fig. 3. Impedance as a function of applied magnetic field. Inset: same in a extended field range.

4 Conclusions

Using a measurement set-up based in a microstrip transmission line, we succeed in measuring impedance of a magnetic material up to 500 MHz, minimizing stray effects that worsen the results. It is anticipated that other line geometries could be more suitable at higher frequencies. The detailed features of the impedance measurements allow us to follow the frequency dependence of the involved magnetic processes.

References

[1] V. Raposo, M. Vázquez, A. G. Flores, M. Zazo, J. I. Iñiguez. *Proc. European Magnetic Sensors and Actuators 2002*. Athens, Greece.

[2] J. M. Barandiarán, A. García Arribas, J. L. Muñoz, and G. V. Kulyandskaya. *IEEE Trans. Magn.* 38 (2002) 3051-3056.

Magnetostrictive-bimorph sensor based on electrodeposited CoP.

M.D. Michelena[1,3], L. Perez[2], C. Aroca[1], E. López[2], M.C. Sánchez[2] and P. Sánchez[1]

[1]ISOM and Dpt. Física Aplicada. E.T.S.I.Telecomunicación, U.P.M., Ciudad Universitaria, 28040 Madrid, Spain
[2]Dpt. Física de Materiales. F. Física. U.C.M. Ciudad Universitaria, 28040 Madrid, Spain
[3]Dpto. C.C. del Espacio y T.T, Electrónicas, INTA, Ctra. de Torrejón a Ajalvir, km 4,2, 28850 Madrid, SPAIN.
email: diazma@inta.es

Summary. *Magnetostrictive magnetic materials traditionally used in piezoelectric—magnetostrictive sensors have been amorphous ribbons. The ribbons used to be stuck to the piezoelectric material by a viscous interface. To avoid the interface in order to improve the magnetomechanical coupling, magnetic materials have also been grown on the piezoelectric surface. The improvement of mechanical coupling has however a penalty in the sensitivity because of the small thickness of sputtered films. In this work we present the results of using thicker Co-P electrodeposited films as magnetostrictive elements of the sensor.*

Keywords: Magnetostrictive-piezoelectric sensor, electrodeposition
Category: 3 (Magnetic physical devices)

1 Introduction

The field of piezoelectric-magnetostrictive hybrid magnetic sensors was opened twenty years ago with the works of A. Pantinakis, D.A. Jackson, M. D. Mermelstein and A. Dandridge [1, 2, 3]. During these twenty years, almost all the magnetostrictive elements were amorphous ribbons. Amorphous ribbons seemed to present better magnetomechanical properties than other magnetic bulk materials[4], so they were appropriate candidates to be used in these sensors, based on the crossed piezoelectric and magnetostrictive effects.

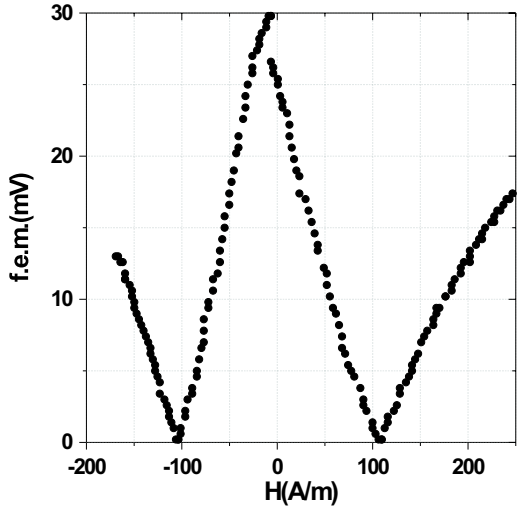

Fig. 1: Response curve of a bimorph-magnetostrictive magnetic sensor

There are however several reports about these hybrid sensors in which $Fe_{80}B_{20}$ magnetostrictive amorphous material had been grown on the piezoelectric surface by sputtering [5][6]. These sensors presented low signal response, low signal to noise ratio, poor reliability due to the small thickness of the magnetic material, and a high coercive force due to the roughness to thickness ratio (See figure 1). In spite of the surface of the piezoelectric element, sputtered films are not a good choice for these kind of sensors.

In relation to the piezoelectric element, it has been shown that the surface deformation obtained with bimorphs (exciting a flexion mode) is greater than that of the piezoelectric elements (in which just elongation-contraction mode was excited) [6]. Besides, mechanical resonance is reached at lower frequencies, which is more convenient if one faces the possibility of miniaturizing the sensors. In order to increase the thickness of the magnetostrictive element, electrodeposition seems to be a suitable technique to use.

2 Results

The sensors we present in this work are bimorphs of 50x2x0.06 cm^3 — acting as piezoelectric elements — in which a Co-P amorphous alloy with a thickness of several microns has been electrodeposited directly on the piezoelectric surface under the conditions described in [7]. The anisotropy of these alloys can be easily controlled during the electrodeposition process by controlling the current density[7]. Therefore, we are able to produce sensors in which the magnetic transducer has anisotropy perpendicular to the plane(see figure 2.a) and others with in plane anisotropy (see figure 2.b).

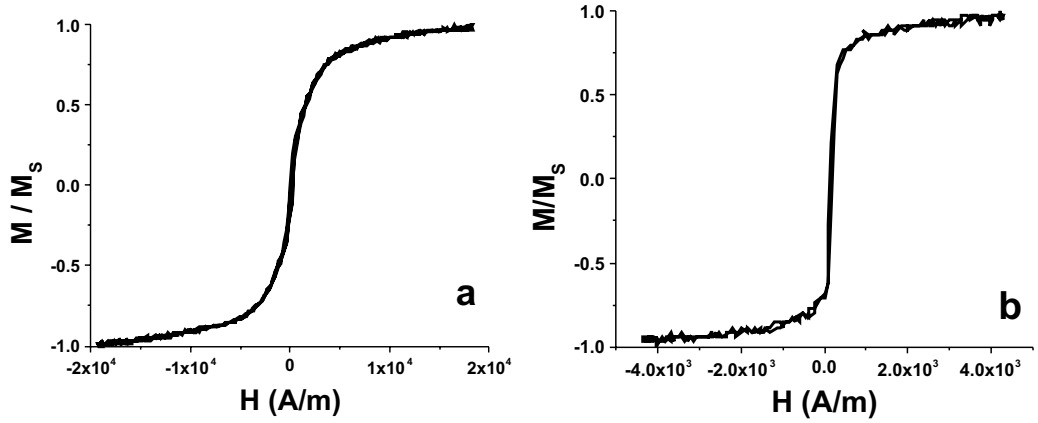

Fig. 2: Hysteresis loops of sensors in which the magnetic transducer has perpendicular (a) or in plane (b) anisotropy. Note the different scale in the H axis

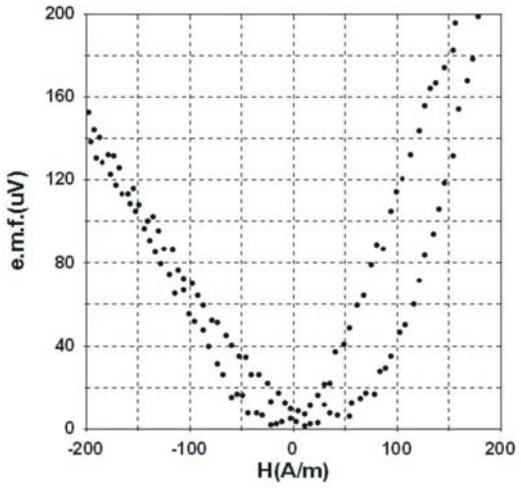

Fig. 3: Response curve of sensor in which the magnetic transducer has perpendicular anisotropy

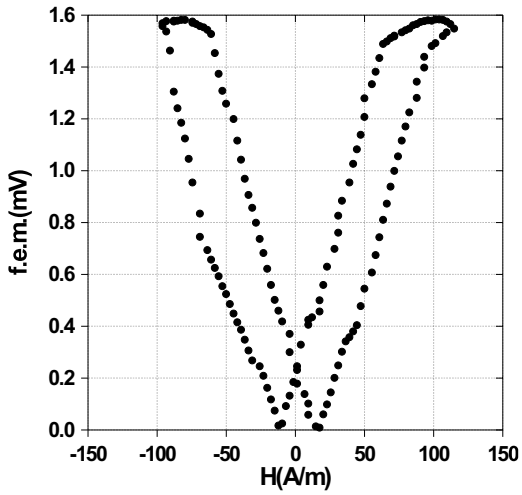

Fig. 4: Response curve of sensor in which the magnetic transducer has in plane anisotropy

In figure 3 and 4 it can be shown the response curve for the two sensors previously mentioned with sensitivities of tenths of μV/μT and 20 μV/μT respectively.

These sensors present higher sensitivity than the ones with sputtered magnetic films, they have high signal to noise ratio, reliability and a really low coercive force that can be avoided exciting the piezoelectric elements to a higher voltage.

References

[1] Pantinakis and D. A, Jackson, High-sensitivity low-frequency magnetometer using magnetostrictive primary sensing and piezoelectric signal recovery. *Electr. Lett.* **22** (14) (1986) 737

[2] M. D. Mermelstein, C. Askins and A. Dandridge, Streess-relieved magnetoelastic amorphous metal DC magnetometer. *Eletr. Lett.* 23 (6) (1987) 280

[3] M. D. Mermelstein and A. Dandridge, Low frequency magnetic field detection with a magnetostrictive amorphous metal ribbon. *Appl. Phys. Lett.* textbf51 (7) (1987) 545

[4] J. D. Livingston, Magnetomechanical Properties of Amorphous Metals. *Phys. Stat. Sol.* **70** (a) (1982) 591

[5] J.L. Prieto, C. Aroca, E.López, M.C. Sánchez, P. Sánchez Ó. de Abril and L. Perez, Improving the characteristics in magnetostrictive-piezoelectric sensors when the viscous interface is removed. *Sensors and Actuators* **84** (2000) 338-341

[6] M.D. Michelena, C. Aroca, E. López, M.C. Sánchez and P. Sánchez, New hybrid magnetometric sensor. *Sensors Actuators A* **100** (2-3) (2002) 153

[7] L. Perez, Ó. De Abril, M.C. Sánchez, C. Aroca, E. López and P. Sánchez, Co-P amorphous multilayers with high permeability *J. Magn. Magn. Mater*, **215-216** (2000) 337-339

PCB technology used in fluxgate sensor construction

A.Tipek[1], P.Ripka[1], Terence O'Donnell[2]

[1]Czech Technical University, Dept. of Measurement, Technická 2, Prague, Czech Republic
email: xtipeka@fel.cvut.cz http://measure.feld.cvut.cz
[2]NMRC, Lee Maltings, Prospect Row, Cork, Ireland http://www.nmrc.ie/

Summary: *Printed Circuit Board (PCB) integrated inductors have been adapted for operation as fluxgate sensors. The ring core is made from electrodeposited permalloy sandwiched between the layers of the PCB. The sensor excitation winding is also integrated into the PCB design. The pick-up coil is wound around the frame with the PCB core. The sensor characteristics as a function of the excitation frequency and the sensor sensitivity versus frequency are described. Achieved sensitivity was 2000V/T at 180 KHz with 60 turns of pick-up coil.*

Keywords: *fluxgate sensor, pcb technology*
Category: *3 (Magnetic physical devices)*

1 Introduction

The fluxgate sensor is one of the most popular precise magnetic field sensors [1]. The main disadvantage is a complicated construction of core and coils. Recently several research groups have been seeking solutions for how to reduce the size and price of fluxgate sensors using standard planar technology [2], [3] and pcb technology [4].

This article describes the basic parameters of a PCB technology fluxgate sensor. The sensor was adapted from previously developed PCB-integrated inductors in NMRC, Cork [5].

2 Construction

The construction is derived from the current sensor in PCB technology [6]. The magnetic circuit has the form of a 7mm/10mm ring made of electrodeposited permalloy. The core is sandwiched between the layers of the PCB. The sensor excitation winding is also integrated into the PCB design: individual conductor sections in the lower and upper copper layers are connected by vias, thus forming 40 turns with a total resistance of 700 mΩ. 1 A of excitation current creates a magnetic field intensity of 1.45 kA/m = 18 Oe. [6]

The pick-up coil of the fluxgate sensor was implemented using an external winding with 0.2 mm diam copper wire. The coil (60 turns) was wound around the frame with the PCB integrated core.

Figures 1 to 3 show the excitation current and the induced voltage in the pick-up coil for different excitation frequencies. In the diagrams;

Top trace is the excitation current (400mA/div)

Middle trace is the pick-up coil voltage for an external field, B=50μT

Bottom trace is the pick-up coil voltage for B=0μT, (i.e. sensor is shielded)

Fig. 1 - $f_{excitation}$=25KHz

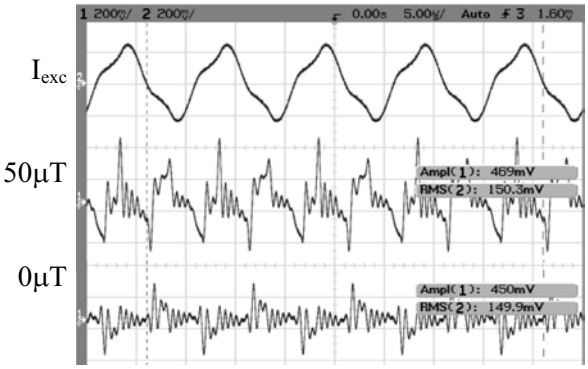

Fig. 2 - $f_{excitation}$=100KHz

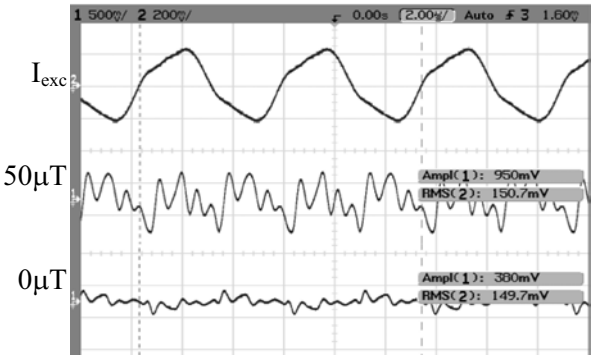

Fig. 3 - $f_{excitation}$=180KHz

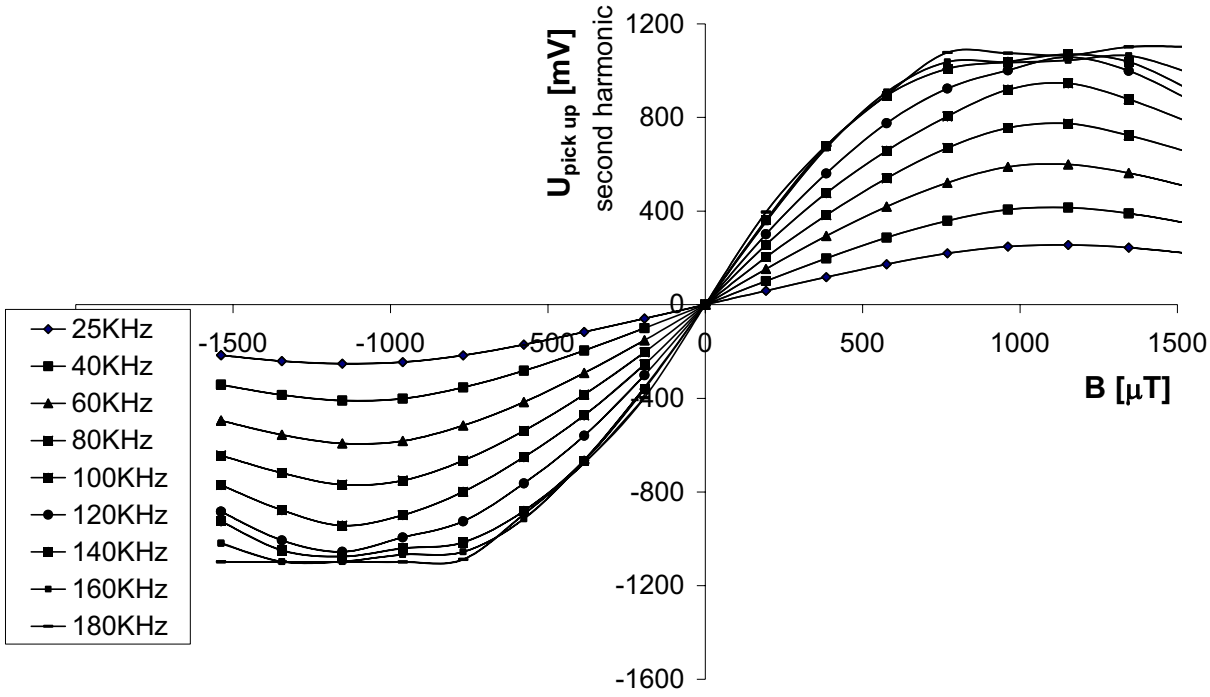

Fig. 4. – Sensor response versus excitation frequency

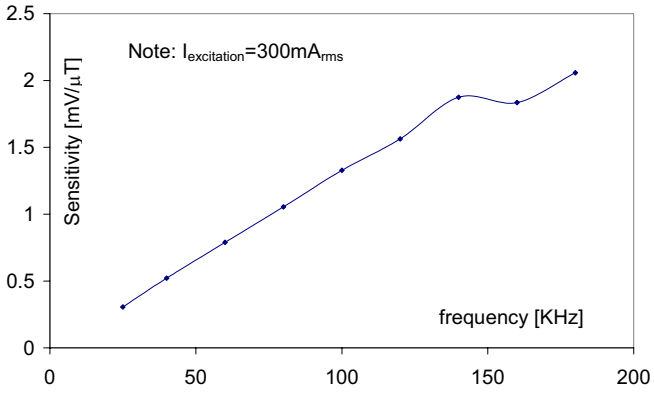

Fig. 5. – Sensor sensitivity versus frequency

3 Testing

The sensor characteristics were measured with a digital lock-in amplifier SR 844 in the LabCVI environment. The reference was set to 2nd harmonic; phase was always adjusted for maximum sensitivity.

Fig. 4 shows the sensor characteristics as function of the excitation frequency. Fig 5 shows the sensor sensitivity versus frequency.

4 Conclusion

A fluxgate sensor using PCB technology was introduced. The sensor response for different excitation frequency was determined. The sensitivity dependence versus excitation frequency was found. The excitation frequency of 100 KHz will be used in the sensor excitation.

In the full paper tuned excitation with the parallel capacitor and the noise parameters will be presented. The integration of the pick-up coil or the integration of a second pick-up coil for compass with the core material will be discussed.

References

[1] P. Ripka (ed): Magnetic sensors and magnetometers, Artech, London, 2001

[2] Kuchenbrandt, K., Huhnke, D., Lauckner, K., Schilling, M.: Preparation and Properties of Micro-Fabricated Fluxgate Sensors, Eurosensors XVI, Prague, 2002

[3] Chiesi L., Kejik P., Janossy B., Popovic R.S.: CMOS Planar 2D micro-fluxgate sensor, Sensors and Actuators A: Physical, 82 (1-30) (2000) pp. 174-180

[4] O.Dezuari, E.Belloy, S.E.Gilbert, M.A.M. Gijs: Printed circuit board integrated fluxgate sensor, Sensor and Actuators 81 (2000), p. 200-203

[5] S. O'Reilly, M. Duffy et al., "New Integrated Planar Magnetic Cores for Inductors and Transformers Fabricated in MCM-L Technology", Proc. of IMAPS-US , Chicago Oct. 1999., pp. 493-498

[6] P. Ripka, J. Kubik, M. Duffy, W. G. Hurley, S. O'Reilly: Current Sensor in PCB Technology, IEEE Sensors Conf., Florida, 2002 pp779-784

The Dose Rate Behavior of SOI Hall Sensor

P.K.Skorobogatov, A.Y.Nikiforov

Specialized Electronic Systems, 31 Kashirskoe shosse, Moscow, 115409 Russia, e-mail: pkskor@spels.ru

Summary: *The dose rate behavior of SOI (silicon-on-insulator) magnetic field Hall sensor was investigated under 1.06 μm laser irradiation. The sensitivity of Hall voltage deviation and recovery time to the sensor operation mode was obtained. In the voltage mode (constant voltage is applied to sensor) the increase of sensor current under pulse irradiation partially compensates the magnetic sensitivity deviation. However, the prolonged current decay tends to increase the sensor recovery time. In the current mode (constant current is applied to sensor) the initial magnetic sensitivity deviation becomes more deep. However the recovery process becomes shorter.*

Keywords: *Silicon-on-insulator, Hall sensor, dose rate*
Category: *3 (Magnetic physical devices)*

1 Introduction

SOI magnetic field Hall sensors are prospective because of their possible integration with SOI/CMOS read-out electronics. Dielectric isolation of elements provides their potential hardness to dose rate effects caused by accompanying radiation. In this paper we study dose rate behavior of a Hall sensor based on the original SOI Double Gate Field Effect Cross Resistor [1]. Numerical simulations and experiments were performed to investigate the Hall sensor magnetic sensitivity behavior under dose rate for different modes of operation.

2 Device under test description

Double Gate Field Effect Resistor (DGFER) is a SIMOX SOI structure depicted in Fig.1. The n-type <100> silicon layer has 0.2 μm thickness and the donor concentration near 10^{16} cm^{-3}. The thickness of the buried oxide layer (SiO_2) is 0.4 μm and the n-Si substrate's thickness is 500 μm.

DRFER is a Si - stripe (80 μm in length, 30 μm in width) on buried oxide layer, surrounded by thermal SiO_2 (LOCOS) regions.

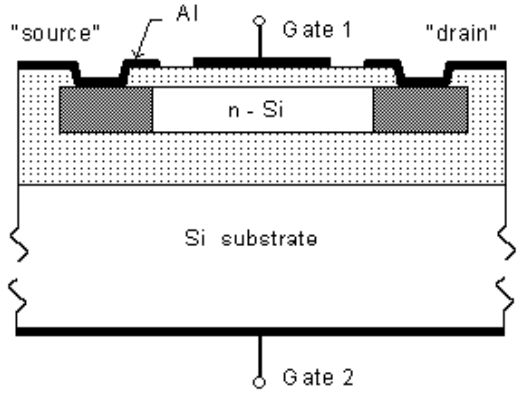

Fig. 1. DGFER cross-section.

3 Numerical results

In order to perform a dose rate analysis of DGFER behavior the "DIODE-2D" two-dimensional software simulator was used [2]. The DGFER behavior was simulated under 22 ns “Gaussian” ionization pulse.

The excess carriers generated by pulse radiation change the steady state electrons and holes densities and cause the additional photoconductivity current through sensor that tends to Hall sensitivity in opposite directions [3]. To define the optimal operating conditions under dose rate the numerical simulation was performed for two modes:

- voltage mode, where ideal voltage source of 5V is applied to structure;
- current mode, where ideal equivalent current source supplies the structure.

Voltage mode.

The results of magnetic sensor sensitivity transient numerical modeling under 10^9 rad(Si)/s ionizing pulse are presented in Fig. 2.

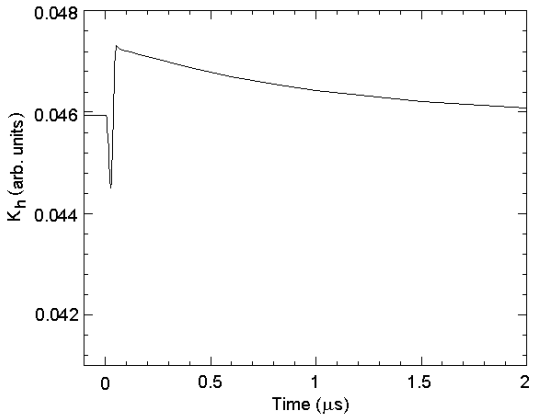

Fig.2. Numerical DGFER sensor transient magnetic sensitivity under 10^9 rad(Si)/s ionizing pulse and 5V bias

One can see that transient magnetic sensitivity behavior in voltage mode is not monotonous. Magnetic sensitivity reduces during the ionizing pulse

and just after it because of excess carriers growth due to dose rate effects.

Then the excess carriers recombination restores the initial density conditions and magnetic sensitivity becomes even more than initial. It is connected with different dynamic behavior of excess carriers density and additional photoconductivity current. After the photoconductivity current decay the magnetic sensitivity becomes equal to initial.

Current mode.

In this mode the current through sensor is constant during pulse ionization. This feature changed the transient magnetic sensitivity behavior of sensor. The results of magnetic sensor sensitivity transient numerical modeling under 10^9 rad(Si)/s ionizing pulse are presented in Fig. 3.

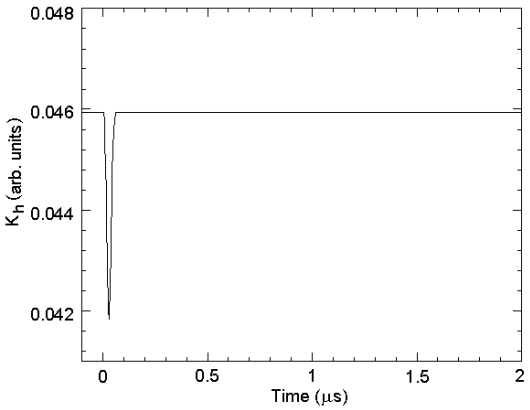

Fig.3. Numerical DGFER sensor transient magnetic sensitivity under 10^9 rad(Si)/s ionizing pulse in current mode

One can see that transient magnetic sensitivity behavior in current mode becomes monotonous. The initial loss of magnetic sensitivity tends to be more deep. However, the recovery process is not affected by current decay and finishes earlier than in voltage mode.

4 Experimental results

The experiments were performed using solid-state pulsed laser source with 1.06 μm wavelength and 15 ns pulse width. The laser pulse maximum intensity was enough to provide an average equivalent dose rate near 10^9 rad(Si)/s in silicon layer of DGFER sensor.

The measured Hall voltage transient response in a voltage mode under magnetic field of 50 mT is presented in Fig. 4. The same dependence for current mode is shown in Fig. 5.

We can see the increase of Hall sensitivity deviation under pulse ionisation in a current mode of sensor. The work in a voltage mode decreases the Hall sensitivity deviation. However the prolonged current decay increases the sensor recovery time.

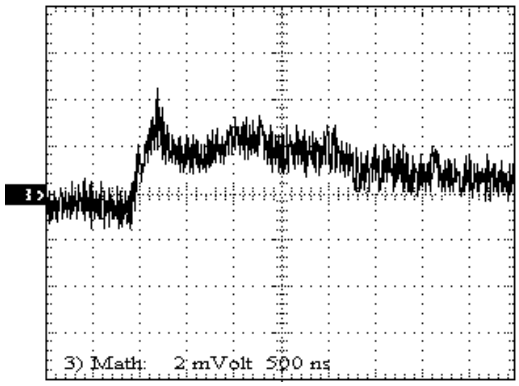

Fig. 4. The measured Hall voltage transient response of DGFER sensor in a voltage mode

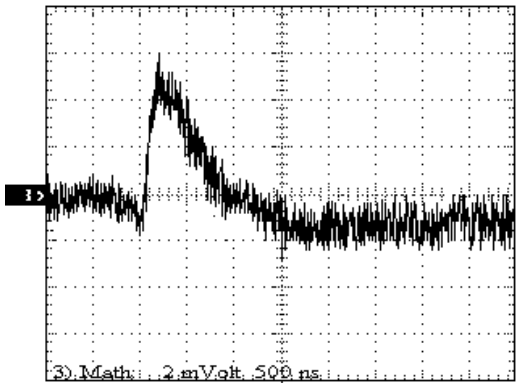

Fig. 5. The measured Hall voltage transient response of DGFER sensor in a current mode

Conclusions

It is shown that SOI Hall sensors transient magnetic sensitivity under dose rate depends on its electrical mode. In the voltage mode the increase of sensor current under pulse irradiation partially compensates the magnetic sensitivity deviation. However, the prolonged current decay tends to increase the sensor recovery time. In the current mode the initial magnetic sensitivity deviation becomes more deep. However the recovery process becomes shorter.

References

[1] A.V.Sogoyan, A.Y.Nikiforov, V.N.Mordkovich, A.S.Artamonov A.D.Mokrushin, N.M.Omelianovskaia, V.V.Belyakov, “Radiation Response of SOI Double Gate Field Effect Resistor”, Proc. of the Fourth Workshop on Electronics for LHC Experiments, Rome, 1998, pp. 480-483.

[2] A.Y. Nikiforov and P.K. Skorobogatov, "Dose rate laser simulation tests adequacy: Shadowing and high intensity effects analysis", IEEE Trans. Nucl. Sci., vol. 43, no.6, pp. 3115-3121, Dec. 1996.

[3] S.M. Sze, *Physics of Semiconductor devices. 2-nd ed*. John Wiley & Sons, N.Y., 1981.

Signal sensitivity versus noise sensitivity of magnetic measurement devices.

D.Blažek[1], J. Blažek[2], O.Blažeková[1]

[1]University of Žilina, Faculty of Science, Hurbanova 15, 01026 Žilina, Slovakia, email:blazek@fpv.utc.sk
[2]Air Force Academy, Rampová 7, 04121 Košice, Slovakia, email:blazek@dol.sk

Summary: *This contribution deals with the signal sensitivity and noise sensitivity of the devices for measurement of magnetic field. Presented ideas are valid for devices based on the induction method. The theory has origin in the Faraday induction law and the Nyquist theorem. The fact, that electric current is the measured quantity is assumed. Results of this article enable designers to optimize the winding of devices with respect to both the noise sensitivity and the signal sensitivity.*

Keywords: *magnetic devices, thermal noise, induction method, sensitivity*
Category: *3 (Magnetic physical devices)*

1 Introduction

Induction method is widely used for measuring a low frequency magnetic field. The serviceability of each device is conditioned by its signal sensitivity and noise sensitivity. The optimization of equipment Fig.1 consists of looking for the best combination of a material of core, a shape of core and a distribution of coils in winding. The aim of this article is the relationship between the winding and the signal sensitivity and the noise sensitivity, while the core properties are considered to be external parameters. This goal is reached by derivation of formula (11) which is valid for each core and winding.

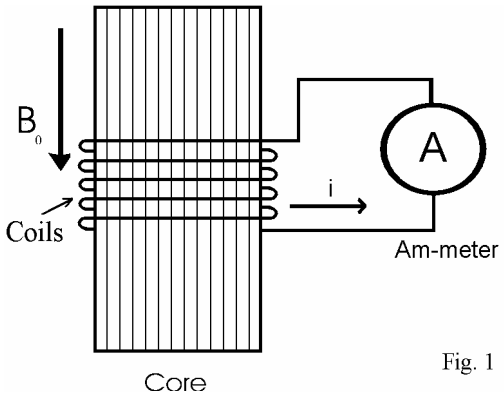

Fig. 1

Fig 1: The scheme of studied equipment

First, the analytical study based on Faraday induction law is done. In this step the signal sensitivity is determined. Investigation of thermal noise has origin in Nyquist theorem [1] and leads to the relation for noise sensitivity. Next the relation (11) is derived

2 Theory

2.1 Signal sensitivity

Magnetic flux linking the winding is proportional to an flux density of applied magnetic field B_o and a value of electrical current I in the circuit

$$\Theta = M B_o + L I , \qquad (1)$$

where self-induction L and mutual inductance M are functions of shape and material of the core and they depend on a distribution of the coils taken up on the core. The mutual-inductance M is proportional to a number of coils in the winding n while self inductance L is proportional to n^2, so one can introduce normed parameters

$$M_1 = M / n \qquad L_1 = L / n^2 . \qquad (2)$$

Periodical change of flux density with angular speed ω causes a circuit current with amplitude I_o. Signal sensitivity of the equipment is

$$k_S = \frac{I_o}{B_o} = \frac{n M_1 \omega}{\sqrt{R^2 + \omega^2 n^4 L_1^2}} \qquad (3)$$

with R as a circuit resistance.

2.2 Noise sensitivity

Each electric circuit in thermal equilibrium exhibits fluctuations. These fluctuations are superposed to the measured signal as a noise. Effective value of Nyquist thermal noise current is

$$I_{ef}^2 = \frac{k_B T}{2\pi} \frac{R}{R^2 + \omega^2 L^2} \Delta\omega . \qquad (4)$$

where Δω is bandwidth of the signal. The noise sensitivity is

$$k_N = \frac{I_o}{I_{ef}} = \sqrt{\frac{2\pi}{k_B T}} \frac{\omega B_o}{\sqrt{\Delta\omega}} \frac{M}{\sqrt{R}} \equiv \frac{M}{\sqrt{R}} . \qquad (5)$$

Temperature T, amplitude of measured flux density, frequency of signal and the bandwidth of amplifier have nothing common with the winding, so they are suspect to be external quantities to the winding. The winding resistance can be expressed as a

function of an electrical conductivity of used material σ, the cross area of used wire S and its length d. The optimal winding can be found under the condition that the volume of material used for wire $V = d\,S$, is a given constant parameter. Then, the winding resistance is

$$R_W = \frac{1}{\sigma}\frac{d}{S} = \frac{1}{\sigma}\frac{d^2}{V} = \frac{d_1^2}{\sigma V} n^2 \equiv \alpha\, n^2, \qquad (6)$$

where d_1 is length of one coil and α is appropriate substitution. Adding the resistance of ammeter R_A one get the total circuit resistance

$$R = R_A + \alpha\, n^2 . \qquad (7).$$

Substituting R into (5) one find that the noise sensitivity is monotonic increasing function of n and converges to its limit value $M_1/\sqrt{\alpha}$. Introducing a new parameter ε, $\varepsilon \in \langle 0,1 \rangle$ defined by relation

$$n = \sqrt{\frac{\varepsilon^2}{1-\varepsilon^2}\frac{R_A}{\alpha}} . \qquad (8)$$

and doing a substitution $p = \alpha\left(\omega L_1\right)^{-1}$ one gets a relation for noise sensitivity:

$$k_N = \sqrt{\frac{2\pi\omega}{k_B\, T\, \Delta\omega}}\,\frac{M_1\, B_o}{\sqrt{L_1}}\,\underbrace{\frac{\varepsilon}{\sqrt{p}}}_{x} . \qquad (9)$$

and for signal sensitivity

$$k_S = \frac{1}{R_A}\frac{M_1\sqrt{\omega}}{\sqrt{L_1}}\,\underbrace{\sqrt{\frac{p\,\varepsilon^2\left(1-\varepsilon^2\right)}{1 - \varepsilon^4 + p\,\varepsilon^2}}}_{y} . \qquad (10)$$

Most important is the relation between the noise sensitivity and the signal sensitivity which can be expressed in the form

$$y = \sqrt{\frac{x^2 - p\,x^4}{1 + x^4}} . \qquad (11)$$

The result (11) is demonstrated for different values of parameter p on Fig.2. One can see that decreasing of parameter p (i.e. using more material with better conductance) leads to growing of both the signal and the noise sensitivity. This effect is considerable until $p > 0.01$.

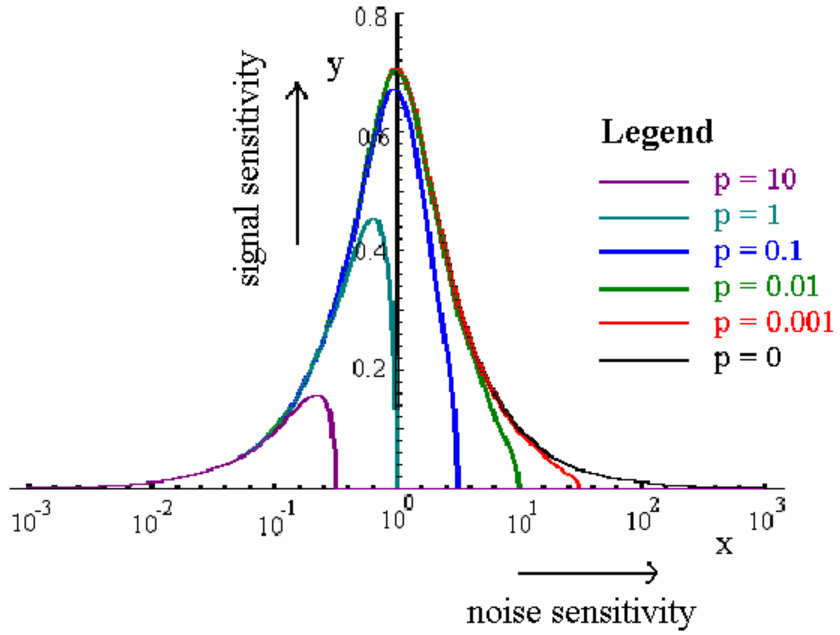

The black line (p=0) restricts the area of possible situations which can be achieved by changing the winding properties. Each chosen point on fig. 2. corresponds to some values of parameters p, ε. From p one can calculate the volume of material used for winding. The number of coils n in the winding is determined by the value of ε (8). Using the volume of material and number of coils one obtain the length and cross area of the wire. Resultant noise sensitivity and signal sensitivity is determined by relations (9) and (10). It is obvious, that quality of device is qualified by the value of ratio $M_1 / \sqrt{L_1}$, which depends on the material and shape of the core and depends on the distribution of coils on the core.

Acknowledgement

Research was supported by VEGA Grant 1/1714/20. Presented results are useful for implementation on ELF magnetic antenna produced by company for electronic digital systems EDIS, Košice. Authors are grateful to RNDr Jozef Kúdelčík for his aid.

Literature

[1] H. L. Pécseli, Fluctuations in Physical Systems, Cambridge University Press 2000.

Efficiency Improvement of a Chip-Size Antenna for Wireless Microsystems Using Bulk-Micromachining Technology

P. M. Mendes, D. A. Durães, M. Bartek* and J. H. Correia
Dept. of Industrial Electronics, University of Minho
*TUDelft/DIMES, The Netherlands
Phone: +351510190, Fax: +351510189, E-mail:paulo.mendes@dei.uminho.pt

Summary: *This work reports on the use of bulk-micromachining technology to increase the efficiency of a folded shorted-patch antenna. This antenna was designed on two stacked wafers (glass bonded on high-resistivity silicon). The analysis was carried out using the HFSS FEM tool. It was shown that bulk-micromachining technology could be used together with HRS to increase the antenna efficiency by ~20 %. Also, it can be used to allow the use of low-resistivity silicon for antenna substrate. Furthermore, bulk-micromachining technology can be used as an option to tune or to select the antenna operating frequency.*

Keywords: *Bulk-micromachining technology, chip-size antenna*
Category: 3

1. Introduction

A topic of growing interest is the concept of integrated antenna. Together with inductances, the on-chip antenna integration can be an added benefit in order to achieve a totally integrated RF microsystem. The antenna can be integrated if designed in an IC compatible substrate material. Patch antennas on high-resistivity silicon (HRS) or on glass are possible options [1, 2]. Concerning the antenna efficiency, the glass substrate is better, but the silicon substrate is desirable as it provides a way to directly integrate the RF circuitry. The problem of using HRS is the observed high losses, providing an antenna with low radiation efficiency [3]. To increase the patch antenna efficiency it has been proposed to use bulk-micromachining technology to remove selectively silicon underneath the antenna. Since removing the silicon underneath the patch leads to a larger antenna, a folded shorted-patch antenna can be used instead. This antenna can be built using two-stacked glass wafers [4], or with the bottom wafer substituted by HRS. In this stack the silicon has much higher losses than the glass. The solution is to remove the silicon underneath the middle patch to reduce the losses.

2. Fabrication

Bulk micromachining technology is used to selectively remove significant amounts of silicon from a substrate. A silicon nitride membrane is previously deposited in order to serve as etch-stop mask.

The bulk-micromachining setup is composed by a etch vessel connected to a thermostatic bath for temperature maintenance at 90ºC. The silicon wafer is etched with an aqueous KOH solution (1.5 Kg of KOH in 3 liters of water). The vessel is placed on the top of a magnetic stirrer with a magnet placed inside the vessel to stir the solution. The silicon wafer is mounted face down on an O-ring holder and is suspend inside the KOH bath. Keeping the temperature in the vessel at 85º C, the silicon etch rate is 1.4 µm per minute.

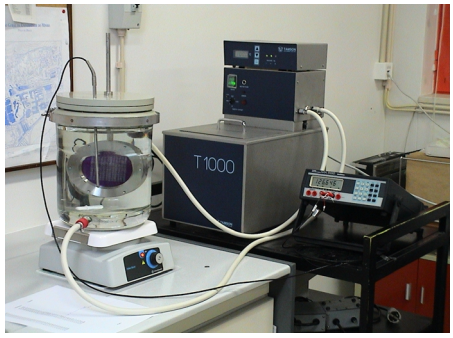

Fig. 1. Bulk-micromachining setup.

Fig. 2 shows the backside of a silicon wafer etched with an aqueous KOH solution. A silicon nitride membrane was used as etch-stop mask.

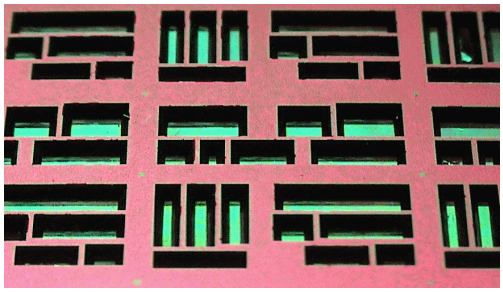

Fig. 2. The backside of a silicon wafer etched with an aqueous KOH solution.

3. Antenna design and analysis

The cross-section of the proposed antenna structure is presented in Fig. 3. It is built with a glass wafer on the top of a HRS wafer. This structure is favorable for size reduction and at the same time offers the possibility to have circuitry placed in the HRS wafer. The problem of increased losses should now be reduced with the use of bulk micromachining. This will partially remove the silicon underneath the middle patch.

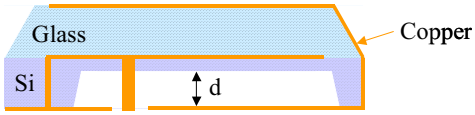

Fig. 3. Cross-section of the micromachined folded patch.

The following analysis was carried out with a model built in HFSS 8.5. This tool was previously used for successful patch antenna design (Fig. 4) on HRS and glass substrates [1-4].

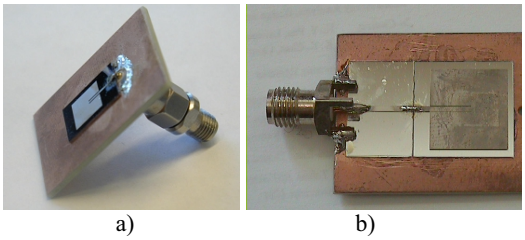

a) b)

Fig. 4. Patch antennas: a) on HRS; b) on glass.

Fig. 5 shows the added benefit of using micromachining for different values of silicon electrical resistivity. When the silicon is completely removed underneath the middle patch, the use of low-resistivity silicon together with micromachining is enough to obtain an antenna with ~50 % efficiency. Moreover, the use of micromachining can always have a benefit of ~10-20 % increase in efficiency.

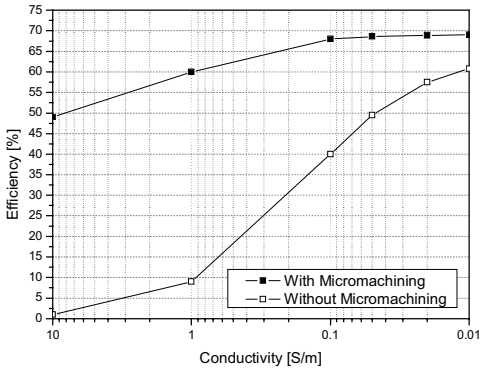

Fig. 5. Efficiency vs. conductivity for d = 500 µm.

Fig. 6 shows the effect on efficiency for different micromachined depths. As expected, the efficiency rises when the depth of the removed silicon is increased. Also, it is clearly shown the effectiveness of micromachining to enable the use of low-resistivity silicon as antenna substrate.

The Fig. 7 presents the return loss for different micromachined depths, when all the other dimensions are kept unchanged. As it can be observed, the drawback is the shift of the operating frequency for higher frequencies when the micromachined depth increases.

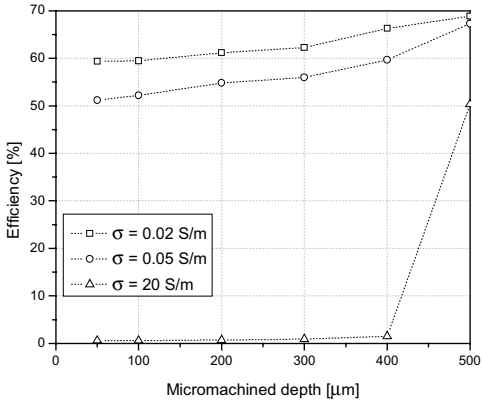

Fig. 6. Efficiency vs. micromachined depth.

This leads to larger antennas when using micromachining. On the other hand, we can take advantage of this effect. It can be used as a post-processing step to change, or to tune, the operating frequency of a previously designed antenna.

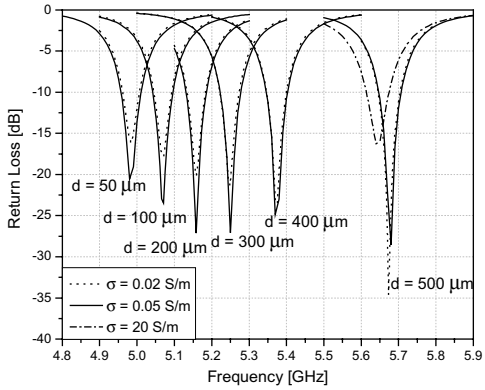

Fig. 7. Return loss for different micromachining depths.

4. Conclusions

This work shows how silicon bulk-micromachining technology can be used to increase the efficiency of a folded shorted-patch antenna. Also, it can be used as an option to tune or to change the antenna operating frequency. The use of bulk-micromachining technology allows the increase of the antenna efficiency approximately 20 %. It was also observed that the use of bulk-micromachining technology to etch completely the silicon wafer underneath the antenna allows to use regular silicon wafers instead of HRS wafers.

5. Acknowledgements

The authors would like to thanks the Portuguese Foundation for Science and Technology for funding this work (SFRH/BD/4717/2001 and POCTI / ESE / 38468 / 2001).

References

[1] P. M. Mendes, M. Bartek, J. N. Burghartz, J. H. Correia, “Design and Analysis of a 6 GHz Chip Antenna on Glass Substrates for Integration with RF/Wireless Microsystems”, to be presented at IEEE APS Int. Symp., Columbus, Ohio, USA, June 22-27, 2003.

[2] P. M. Mendes, M. Bartek, J. N. Burghartz, J. H. Correia, “Design and Tolerance Analysis of a 5.7 GHz Chip-Size Microstrip Antenna on High Resistivity Silicon”, to be presented at URSI-B, Columbus, Ohio, USA, June 22-27, 2003.

[3] P. M. Mendes, J.H. Correia, M. Bartek, J.N. Burghartz, “Analysis of Chip-Size Antennas on Lossy Substrates for Short-Range Wireless Micro Systems”, Proc. SAFE 2002, 8, Veldhoven, The Netherlands, pp. 51-54, November, 2002.

[4] P. M. Mendes, A. Polyakov, M. Bartek, J. N. Burghartz, J. H. Correia, “Integrated 5.7 GHz Chip-Size Antenna for Wireless Sensor Networks”, to be presented at Transducers’03, Boston, USA, June 8-12, 2003.

Expert System for Gas Sensor Array Configuration and Scenario Management

R.Traute[1], F.Haase[1], Dr. O. Kiesewetter[2], Dr. G. Müller[3] and Dr. T. Doll[1]

[1] Technische Universität Ilmenau, Dept. of Electrical Engineering, PO 100565, 98684 Ilmenau, Germany
email: Ruediger.Traute@tu-ilmenau.de http://www.e-technik.tu-ilmenau.de
[2]UST Umweltsensortechnik GmbH, Dieselstraße 2, 98716 Geschwenda, Germany
[3]EADS Deutschland GmbH, PO 801109, 81663 München

Summary: *We introduce an Expert System for gas sensor array assembly on a modular algorithm basis. It is open for various application specific scenarios and for all types of industrial gas sensors. The program package provides scenario and sensor input, array configuration, algorithm fusion and testing routines and compiles array evaluation code.*

Keywords: *Expert System, Sensor Data Base, Gas Mixture*
Category: *1 (General, theoretical and modeling)*

1 Introduction

Our work focuses on specific problems in the qualitative and quantitative analysis of gas mixtures for cross-sensitive sensors, e.g. metal oxide elements. To overcome these problems various methods of multicomponent analysis have been employed, like Principal Component Analysis or Artificial Neural Networks. However, such solutions can, in most cases, be only set up for specific applications (scenarios), i.e. they need training.

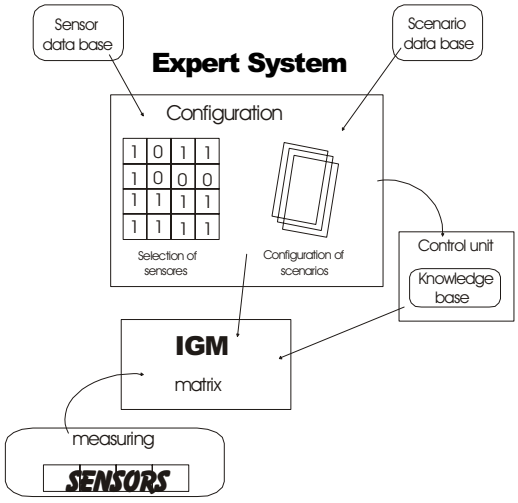

Fig. 1 System for measuring Gas mixtures

The objective of our work is to develop methods of forming gas sensor arrays for larger varieties of scenarios by analytical array evaluation methods that avoid expensive training, and provide software based array formation and testing routines.

Our goal was an easy to use system that connects the features of an advanced measuring and data processing system with a gas sensor database, which provides as much assistance as possible for the user.

.

2 Universal Modeling of Gas Sensors for Arrays

A new mathematical approach to handle signals from gas sensor arrays was the matrix method for individually composable sensor for algorithms implemented in the IGM earlier described [1].

The signal processing here is an iterative process. In the first step, the system evaluates the single signals only with the main sensitivity of the sensors used. Hence, a first estimation of the result is possible. After that reevaluation starts with the first result as an input. This iteration will continue until the result converges (Fig. 2) [2].
The matrix consists of logical rows. These rows are special for each gas sensor; so it is possible to store this information in a database and to build up the relevant output for each array of sensors.
For modeling a real gas sensor, the manufacturer has still to measure sensitivities towards various gases.

$$\begin{pmatrix} H(U_S^{(CO)}) & \oplus & f_{NO_2}^{(CO)} \cdot N_{NO_2}^{(CO)}(c_{n-1}[NO_2]) & \oplus & L & \oplus & L & \oplus & f_{H_2O}^{(CO)} \cdot N_{H_2O}^{(CO)}(c_{n-1}[H_2O]) \\ f_{CO}^{(NO_2)} \cdot N_{CO}^{(NO_2)}(c_{n-1}[CO]) & \oplus & H(U_S^{(NO_2)}) & \oplus & L & \oplus & L & \oplus & f_{H_2O}^{(NO_2)} \cdot N_{H_2O}^{(NO_2)}(c_{n-1}[H_2O]) \\ f_{CO}^{(O_3)} \cdot N_{CO}^{(O_3)}(c_{n-1}[CO]) & \oplus & f_{NO_2}^{(O_3)} \cdot N_{NO_2}^{(O_3)}(c_{n-1}[NO_2]) & \oplus & H(U_S^{(O_3)}) & \oplus & L & \oplus & f_{H_2O}^{(O_3)} \cdot N_{H_2O}^{(O_3)}(c_{n-1}[H_2O]) \\ L & \oplus & L & \oplus & L & \oplus & L & \oplus & L \\ L & \oplus & L & \oplus & L & \oplus & L & \oplus & H(U_S^{(H_2O)}) \end{pmatrix} = \begin{pmatrix} c_n(CO) \\ c_n(NO_2) \\ c_n(O_2) \\ L \\ c_n(H_2O) \end{pmatrix}$$

$H(\cdot)$	main sensitivity	$N_{CO}^{(NO_2)}(\cdot)$	cross sensitivity
$U_S^{(CO)}$	signal of the sensor	$c_n(CO)$	concentration of gas after iteration n
$f_{NO_2}^{(CO)}$	flag		

Fig. 2: Sensor matrix for signal processing

At the best these matrix rows consist of a sum of coefficients, that describes the individual responsivities of the Gas Sensor (complex mathematical forms are possible) [1].

$$c_n(NO_2) = H(U_S^{(NO_2)}) + N_{H_2O}^{(NO_2)}(c_{n-1}[H_2O]) + N_{CO}^{(NO_2)}(c_{n-1}[CO])$$

Fig. 3 Example of a matrix row for a Gas Sensor

Fig.3 shows the matrix row for a Sensor whose main sensitivity is NO_2 with cross sensibilities to CO and H_2O. A small paragraph of C-Code represents this row in our system.
By this, the entire configuration manager we develop puts these individual sensor files together and allows for convergence testing as well as scenario simulation.

3 Expert System for Gas Sensors

The Expert System is based on a Microsoft Access relational data base. It consists of several internal tables storing information, the relations between the tables and programmed code for managing, searching and the in- and output of the data.

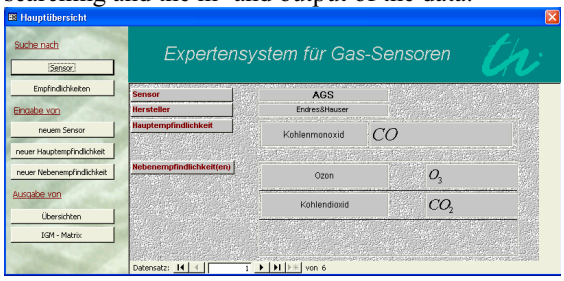

Fig. 4 User interface of the database

It is possible to store all the relevant informations in order to provide a model of used Gas Sensors to the testing system

The system supports the user to select the best possible array of gas sensors for his task. Therefore we implemented advanced search and rating routines.

For known scenarios like indoor monitoring, ozone measurements in urban locations or car cabin air quality control proposed solutions are stored in the system. Of course, the user can change the sensors used. The system will assist him to find the best configuration of sensors.

For unknown scenarios, the system will use a rating method to search for the suitable mix of sensors. After the input of the new scenario, the Expert System will dynamically evaluate the sensors and the possible arrays of them.

For that purpose we implemented a rating mechanism which assigns every sensor in the data base a rating number. This number depends on the mix of gases and the main- and cross-sensitivities of the involved sensors. For this reason this number has to be generated dynamically in the search- und selection process. The best choice for this particular task is the array of sensors with the lowest sum of rating numbers.

4 Implementation, results and conclusion

Our system is implemented as a relational data base. Several programmed modules working as user input, searching and assortment and output routines.

The Expert System is able to combine the matrix rows of the selected gas sensors, hence they can be used by the testing system. The arising files will be directly executable on the hardware, thus we are able to test and improve our analytical descriptions for a large variety of virtual scenarios.

References

[1] T. Doll, I. Eisele and H.-R. Tränkler. Intelligentes Gas-Multisensorsystem. *Geronimo Verlag Rosenheim.*(1998). ISBN 3-98106213-0-8

[2] T. Doll, A. Köster, H. Gerlach, F. Derbel, I. Eisele and H.-R. Tränkler. Konfigurations-, Auswerte- und intelligente Selbstüberwachungs-komponenten des modularen Gas-Multisensor-systems. *3. ITG/VDE-Fachtagung Sensoren und Meßsysteme. Bad Nauheim (1998)*

Electrochemical analysis of neuropathy target esterase activity by 1-methoxyphenazine methosulfate modified tyrosinase carbon paste electrode: progress in biomonitoring of organophosphate-induced delayed neurotoxicity

L.V. Sigolaeva[1], L.G. Sokolovskaya[1], A.V. Eremenko[1], G.F. Makhaeva[2], V.V. Malygin[2], I N. Kurochkin[1]

[1]Faculty of Chemistry, M.V. Lomonosov Moscow State University, Moscow, 119899, Russia;
lsigolaeva@genebee.msu.su http://www.enzyme.chem.msu.ru/ecobio
[2]Institute of Physiologically Active Compounds Russian Academy of Sciences, Chernogolovka, Moscow Region, 142432, Russia

Summary: *The 1-methoxyphenazine methosulfate modified tyrosinase graphite paste biosensor was developed. Electrode composition and measuring conditions were optimized allowing to detect phenol* at *–150 mB vs. Ag/AgCl reference electrode with the sensitivity of 0,8 A/M*cm^2 and the lower detection limit of 25 nM in a flow. The biosensor was applied for the assaying of the activity of toxicologically significant enzyme – neuropathy target esterase (NTE) produced phenol by the hydrolysis of the substrate, phenyl valerate. High sensitivity of the sensor enabled NTE to be assayed in whole blood, whereas the usual colorimetric assay is impossible. In vitro and in vivo correlation of NTE activity obtained in brain and whole blood show promise the biosensor NTE assay for whole blood as a biomarker of human exposure to neuropathic organophosphorus compounds.*

Keywords: *biosensor, phenol, tyrosinase, mediator, 1-methoxyphenazine methosulfate, neuropathy target esterase, NTE, blood, OPIDN*
Category: *6 (Biosensors), 10 (Applications)*

1 Introduction

Electrochemical phenol detection by tyrosinase biosensors is one of the most sensitive sensor systems. Theirs sensitivity to phenol can reach nunomolar and ever subnunomolar level. On this reason phenolic biosensors have a wide application mainly for phenols detection as common environmental pollutants. Phenolic biosensors are suitable as well for monitoring of enzymatic processes proceeding with the release of phenols.

We were first who offer to use tyrosinase biosensors for the bioelectrochemical analysis of toxicologically significant enzyme - neuropathy target esterase (NTE) [1-3]. NTE of vertebrates is a specific target for neuropathic organophosphates (OP). This neuronal enzyme is used as a biochemical marker for screening of OPs with respect to their ability to result in organophosphate induced delayed neuropathy (OPIDN). The inhibition/aging of neuronal NTE within hours of exposure to OP predicts potential for the development of OPIDN after a delay of 1-3 weeks. NTE is a convenient tool for assessment neuropathic potential of OPs and prediction of their possible neurotoxic hazard to humans as well for development methods of biomonitoring for neuropathic OPs exposure.

This report described our last achievements both in tyrosinase electrode preparation and NTE assay.

2 Results

2.1. Mediator modified tyrosinase carbon paste electrode

Mediator modified tyrosinase carbon paste electrode includes tyrosinase catalysis involving enzymatic oxidation of phenol *via* catechol into *o*-quinone, the latter being electrochemically reduced to catechol directly at the electrode when the required potential is applied. However, regeneration *via* mediator facilitates the electrode transport allowing the more sensitive phenol detection in a comparison to the direct electroreduction of *o*-quinone (Fig.1).

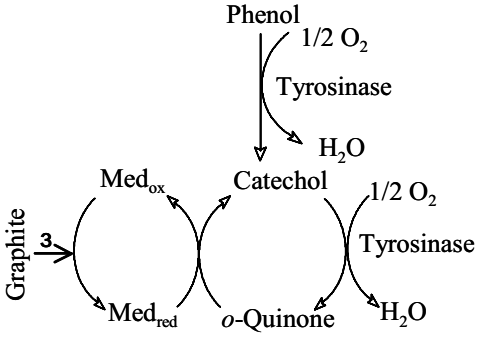

Fig. 1. Principle of amperometric phenol detection by MPMS-modified tyrosinase carbon paste electrode.

We use 1-methoxyphenazine methosulfate (MPMS) as a perspective light-stable mediator for the modification of tyrosinase carbon paste sensor. Various aspects concerning the electrode construction and operation have been studied and optimized. The optimum ratio of tyrosinase/MPMS was found. The dependences of the response on pH, buffer composition, ionic strength and applied potential were studied and the stability of the biosensor was also evaluated. The main analytical characteristics of the biosensor are summarized in the Table 1.

Table 1. MPMS-modified tyrosinase carbon paste electrode characteristics.

Analytical parameter	Value
Linear range	0,025÷20 μM
Detection limit (S/N=3)	25 nM
Sample volume	50 μl
Time of analysis	2 мин
Work stability	>90 % during 21 days
Storage stability (dry)	> 12 months
Reproducibility	25 %
Accuracy	5 %

2.2. NTE activity assay

By now lymphocyte NTE has been used as the only accessible biomarker of animal and human exposure to neuropathic OP compounds. Despite the potential utility of lymphocyte NTE as a biomarker, the time, resources and relatively high sample volumes required mitigate against using isolated lymphocytes routinely to monitor NTE activity. Thus, if the need were to arise to assess exposures of individuals to neuropathic OP compounds, it would be advantageous to be able to assay NTE in small volumes of whole blood.

We showed that the tyrosinase carbon-paste electrode improves remarkably the sensitivity of the NTE assay compared to the colorimetric method.

Due to high sensitivity of the biosensor method the influence of interfering blood components (ascorbic acid, tyrosine and others) is diminished by the high extent of sample dilution (1:200 or 1:500), thus allowing NTE to be detected selectively and with high sensitivity in whole blood where the usual colorimetric assay is impossible.

The *in vitro* specificity of whole blood NTE for a number of model neuropathic OP was close to that for neuronal and lymphocyte NTE.

Dose and time dependence of *in vivo* inhibition of whole blood NTE correlates strongly with that of brain NTE, as it was demonstrated for experimental animals (hens) in 4, 24, 48, 72 and 96 hr after acute i.m. treatment with increasing doses of neuropathic OP O,O-dipropyldichlorvinylphosphate.

The obtained results look promising for the development of monitoring system that could be routinely used for individuals exposed to neuropathic OPs.

2.3. NTE Analyzer

The pilot example of Analyzer for biosensor NTE assay was developed. The Analyzer consists of an internal microprocessor, flow-through electrochemical cell (supplied with working and reference electrodes), pump, sampler, vessels for work buffer and waste, liquid crystal display, and buttons for manual operation. All functions are controlled and monitored by an external computer. The software provides measurement monitoring, and showing the measured signal in real-time format. Data processing is also possible.

The application of this device is expected to enable more rapid assessment of human exposure to neuropathic Ops (as a result from occupational, environmental, accidental OP contacts or possible terrorists acts).

The research was supported by Project #1055.2 of the International Science and Technology Center (ISTC) and Award #RB2-2035 of the U.S. Civilian Research and Development Foundation (CRDF).

References

[1] L. Sigolaeva, A Eremenko, A. Makower, G. Makhaeva, V. Malygin and I. Kurochkin. A new approach for determination of neuropathy target esterase activity. *Chem.-Biol. Interactions.* 119-120 (1999) 559-565.

[2] L. Sigolaeva, A. Makower, A. Eremenko, G. Makhaeva, V. Malygin, I. Kurochkin and F. Scheller. Bioelectrochemical analysis of neuropathy target esterase activity in blood. *Analytical Biochemistry.* 290 (2001) 1-9.

[3] G. Makhaeva, L. Sigolaeva, L. Zhuravleva, A. Eremenko, I. Kurochkin, R. Richardson and V. Malygin. Neuropathy target esterase in whole blood: biomarker for exposure to neuropathic organophosphorus compounds. *Proc. of CBMTS-Industry II: The World Congress on Chemical and Biological Terrorism*, pp. 327-336, Dubrovnik, Croatia, 21-27 April 2002.

Inflammation Monitoring using a Lipid Bilayer Biosensor

J.A. Beddow[1], I.R. Peterson[1], C.Dwenger[2], R. Annamaneni[2], J.F. Bion[2], J. Heptinstall[1] and D.J. Walton[1]

[1] Coventry University SE, Priory Street, Coventry, CV1 5FB, UK
email: i.peterson@coventry.ac.uk http://www.nes.cov.ac.uk/research/cmbe
[2] Queen Elizabeth Hospital, Birmingham, B15 2TH, UK

Summary: *This study confirms a previous report of the detection of complement activation using an electrically monitored gel-protected bilayer lipid membrane system. Membrane conductivity increases on addition of blood serum together with a complement activator, lipopolysaccharide. It does not change if the activator is omitted or if the complement cascade is inactivated by heating. In a small clinical study involving 10 patients undergoing open-heart surgery, membrane porating activity was detected in all blood samples taken just after cardiopulmonary bypass. Apart from some anomalous cases (membrane failure), responses to patient serum were significantly higher immediately after the bypass procedure than just before or hours after surgery.*

Keywords: *Complement, Inflammation, Cardiopulmonary bypass, Biosensor*
Category: *6 (Biosensors)*

1 Introduction

Inflammation leads to activation of the complement cascade of human blood [1] culminating in the formation of membrane attack complex (MAC). There is a certain amount of evidence that the resulting membrane damage is the cause of negative outcomes of open-heart surgery [2]. The complement activity of blood can be estimated using time-consuming bioassays [3], but since the activation is transient, the result is not necessarily indicative of the state of the blood immediately after exposure to the unnatural environment.

There are a number of reports using bilayer lipid membranes (BLMs) to detect complement activation [4,5]. Pores even of molecular dimensions are readily detected electrically, but the membranes do not have the durability required for practical application. Recently lifetimes in excess of three months have been demonstrated for membranes produced by a new technique, with preliminary evidence that they respond to activated complement [6]. The present work rules out alternative interpretations and presents the results of a clinical trial on patients undergoing heart-lung surgery.

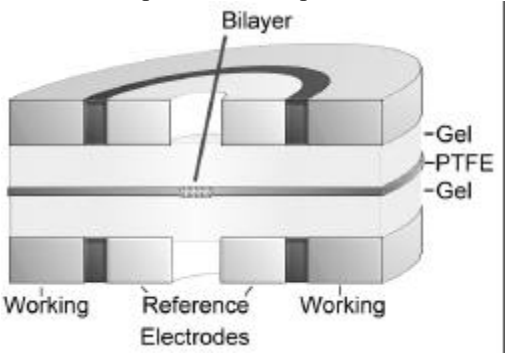

Fig. 1. Schematic of Gel-Protected Membrane.

2 Experimental

A schematic of the membrane-electrode configuration is shown in Fig. 1. Full details have been published previously [7]. The membranes were self-assembled from glycerol monooleate.

Whole human blood was collected by venepuncture, allowed to clot and then centrifuged. Decanted serum was used fresh. Complement activator solution was prepared by dissolving Lipopolysaccharide from *Klebsiella pneumonia* (Sigma L4268) in methanol and water, at a concentration of 10mg/ml.

Test membranes were allowed to stabilize for at least 10 minutes, and then droplets of test liquid were deposited on to the top agar layer. Using a bipotentiostat, a voltage of 50mV was applied and the time response of membrane conductivity logged.

3 Results

In the absence of activator or with heat-treated plasma no change in membrane conductivity was observed over at least 10 minutes.

Neither the anaesthetic propofol nor the anticoagulant heparin was found to affect membrane conductivity when added to test membranes with plasma.

Typically, when a membrane is exposed to serum plus complement activator solution, the conductivity starts to rise within 2 minutes of exposure to the test solution and increases in a series of small and large events.

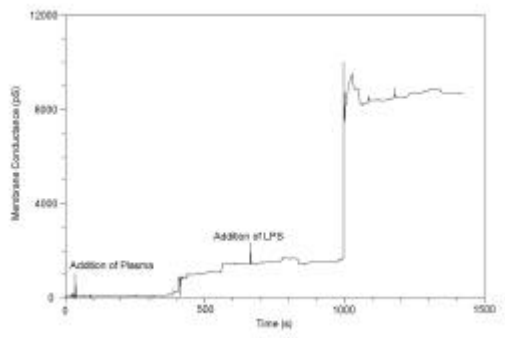

Fig. 2. Typical Clinical Response to Serum and LPS.

Fig. 2 shows a typical response during clinical testing. There was a large increase in membrane conductivity approx. 5 minutes after addition of LPS. Again, there were relatively few events, ranging in size between less than 1nS and greater than 1μS.

The results of 65 membrane tests on 10 CPB patients are summarised in Figure 3. Each graph represents a specific testing point during the CPB procedure, and shows the level of test membrane conductivity after exposure to a sample of the patient's plasma.

For all post bypass samples tested there was a significant increase in the test membrane conductivity, of between 3 and 500nS. For the other stages of the procedure there were far fewer membrane conductivity events. Some of the order of 10?S were consistent with the complete failure of the membrane.

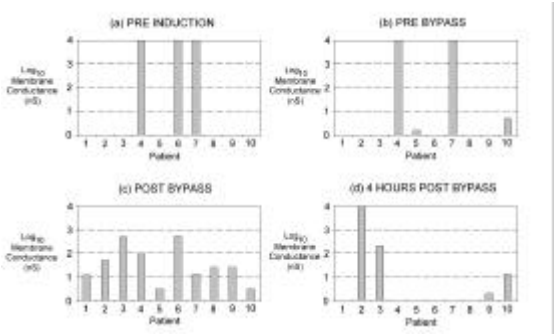

Fig. 3. Typical Clinical Response to Serum and LPS.

Discussion

Over and above membrane infant mortality, which occurs only within 24 hours after preparation, there was a level of failure for membrane elements during transport, which does not occur when the elements are kept stationary or handled normally [8]. It was therefore necessary to prepare the majority of the membrane elements on the site of clinical testing, meaning that some of the failures observed during testing were due to infant mortality rather than complement attack.

Since activated complement components only have short lifetime, activity is lost during the time it takes for the components to diffuse through the gel layer, but less so than during the time for an ELISA assay. The use of a thinner top gel layer is indicated. In the clinical trial there were membrane conductivity responses for all samples taken post bypass. This indicates the likely activation of some membrane active process, such as complement, during the CPB procedure. It also demonstrates the suitability of the membrane sensors for detection of such activity. Large variations in the total change in membrane conductivity were observed between samples. This may indicate variations in complement activity between patients.

Conclusion

A larger study linking more detailed patient information to the test data and results of other methods for the detection of complement activation, such as ELISA is needed before more detailed conclusions can be made. The clinical testing work has highlighted the need for a more robust membrane element and a thinner top gel layer.

The results presented here confirm a previous report of the response of gel-protected membranes to activated complement [6], most likely due to insertion of membrane attack complexes. Other interpretations have been ruled out. They indicate that membrane sensors can be applied to the analysis of membrane porating activity in blood samples in a clinical environment, and may be useful for monitoring the likelihood of organ failure in patients who have undergone CPB.

References

[1] B.P. Morgan, *Crit. Rev. Clin. Lab. Sci*. **32** (1995) 265-298.

[2] T.E. Mollnes, W.-C. Song and J.D. Lambris, *Trends in Immunology*. 23 (2002) 61-64.

[3] T.D, Jaskowski, T.B. Martins, C.M. Litwin and H.R. Hill.. *Clin. Diagn. Lab. Immunol*. **6** (1999) 137-139.

[4] P. Barfort, E.R. Arquilla and P.O. Vogelhut, *Science*. **160** (1968) 1119-1121.

[5] K.P. O'Boyle, F.A.Siddiqi and H.T. Tien., *Immunol. Comm.* **13** (1984):85-103.

[6] R.F. Costello, S.W. Evans, S.D. Evans, I.R. Peterson and J. Heptinstall.. *Enzyme Microbial Technol.* **26** (2000) 301-303.

[7] J.A. Beddow, I.R. Peterson, J. Heptinstall and D.J. Walton, *J.Electroanal. Chem* .**544** (2003) 107-112.

[8] J.A. Beddow, I.R. Peterson, J. Heptinstall and D.J. Walton, *Proc. SPIE* **4414** (2001) 62-69.

A Micro-machined Acoustic Sensor for Fuel Level Indication

R. Osborne, Dr M. Ward and K. Dawkins

University of Birmingham, Mechanical Engineering, Edgbaston,
Birmingham. B15 2TT roo007@bham.ac.uk.

Summary: A low cost and reliable acoustic sensor is to be used for the sending of fuel level information within a fuel tank. The micro-machined sensor is manufactured from n type doped single crystal silicon using electron beam lithography and deep etching techniques. The device will be designed to operate in the sub 20KHz frequency range. Post sensor signal processing coupled with mechanical filtering will analyse acoustic data and reference fuel volume by following the resonant frequencies within the tank.

Keywords: Acoustic devices, Mems devices.
Category: Non-magnetic devices.

Introduction

The automotive market has come under increasing pressure to raise standards of automotive sensors. An increase in life span is paramount; this has driven the industry to look at alternate technologies for sensor applications. The problem concerns the detection of fuel within a closed tank, allowing for slosh, background noise and a variety of fuel qualities. This device utilises an acoustic approach to the problem and relies on the natural phenomena of resonance within a closed end pipe. As the fuel level falls this results in a decrease in the frequency of the resonant modes in the tank. This scenario is used in the fuel tank utilising a small white noise source and micro machined silicon microphone.

Acoustic Sensor Development

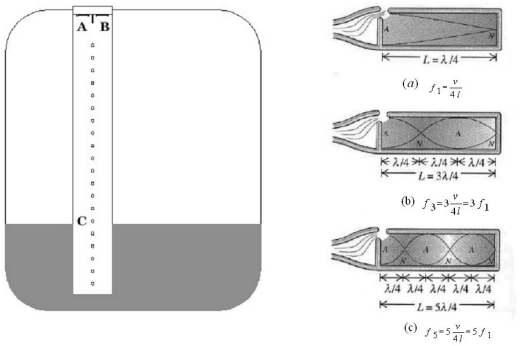

Fig 1. Sensor arrangement within the tank. A noise source is situated at point A, microphone at B and liquid level at C. The first three resonant modes are seen for the acoustic tube. [1]

White Noise excites the tube and induces resonant modes. Measurements of the modes are limited by the microphone sensitivity, which degrades above 16KHz and the processing electronics which has a sample frequency of 48KHz, implying that around 20KHz is the limiting frequency.

White noise within the tank excites acoustic tube or wave-guide will amplify resonating frequencies and dampen the rest. Successive modes of vibration will correspond to increasing frequencies and these will decrease as the liquid empties from the tank. Fourier Transform data showing this may be seen in fig 2. The reinforcing resonant modes may be seen in black the fundamental note may be seen at the bottom.

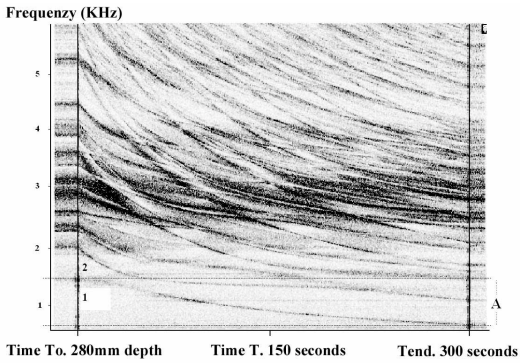

Fig 2. A Sonogram showing the fall in resonant frequency of each excited mode. Time on the x and frequency on the y-axis.

Electronics will examine the data and follow the trends of the strongest signals; these are the resonant modes of the excited space. Calibration problems are resolved through the use of a standard diameter resonance tube and final data output is made by use of a reference table in the processor of the device. A method to detect the fluid level could be achieved by providing many microphones each with a resonating frequency fig 5. As the frequency of the mode decreases each microphone will resonate in turn. The resolution of the system relies on the number resonating microphones. These devices are also subject to latching problems due to the bias voltage and electrostatic forces between the plates. Comparing the electrostatic forces with the deflection model data fig 7. A compromise between the need for proximity to increase capacitance and avoiding latching may be found. The electrostatic forces for differing sizes are seen in fig 3.

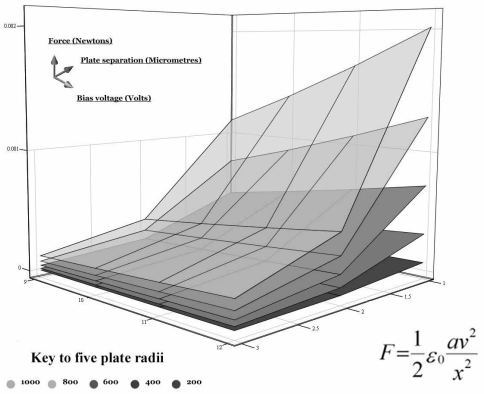

Fig 3. Plot of the electrostatic forces between the parallel plates of the microphone capacitor for a range of sizes.

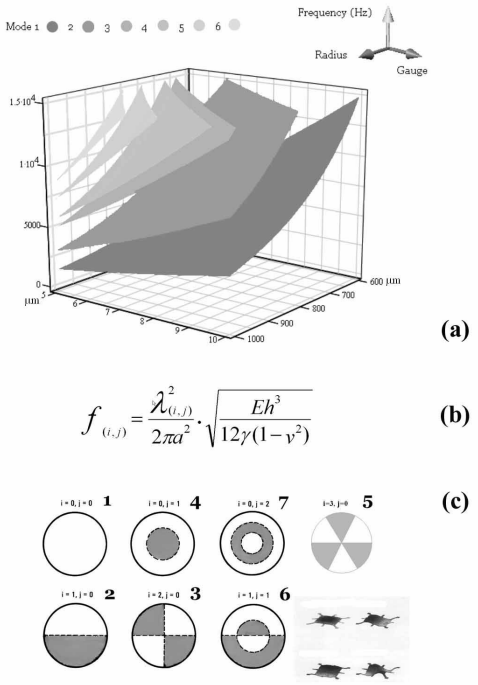

Fig 4. A plot of resonant frequency against microphone geometry (a). Planes correspond to the fist six resonant modes of excitation (c). Frequency determined using equation (b) [2] where, λ arbitrary transcendental value [2], the diameter, γ is the weight per unit area, h the thickness, E modulus and ν Poisson ratio. All standard SI units used.

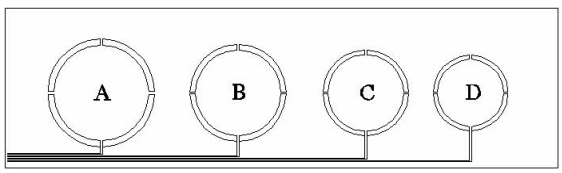

Fig 5. Four plate microphones in an array. As the size increases the resonant frequency decreases.

Design and Fabrication

The microphone will be fabricated from a buried oxide wafer. This enables the device layer to be fabricated using fewer manufacturing steps than conventional silicon microphones. An electro resist mask has been created with an electron beam lithographer. Developing a resist removes unwanted portions and exposing the wafer to a post bake then hardens the resist prior to etching. Dry etching removes silicon and a further wet etch removes the buried oxide layer freeing the structure.

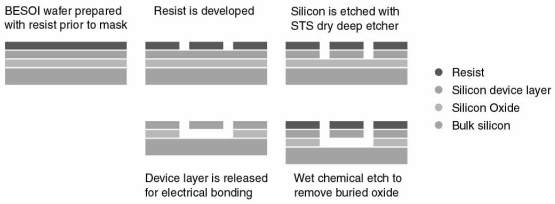

Fig 6. Process route for the microphone device using BESOI.

The initial design in fig 7 was used to identify the processing problems with the device. For instance this design does not allow for enough travel of the plate, the supporting structure has been developed further as in fig 8.

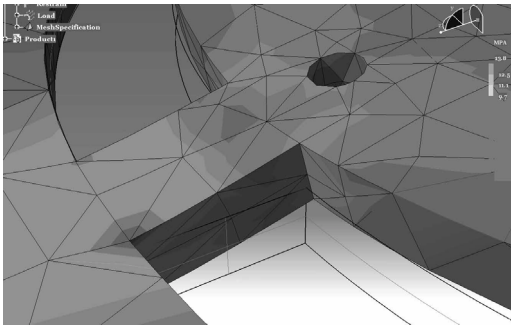

Fig 7. Microphone geometry showing moving plate, supporting arms and the surrounding bulk silicon.

Fig 7 shows the deflection response with application of 1mn to the acoustic plate. It is clear that there is not enough translation movement of the plate. Fig 8 shows an improvement in design.

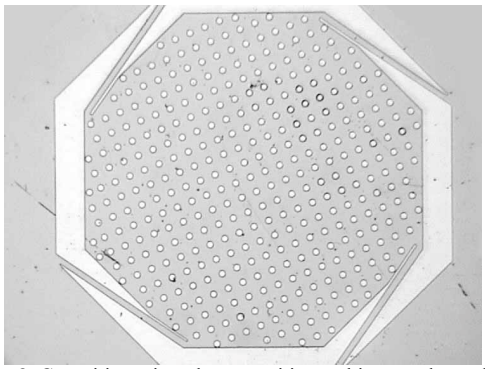

Fig 8. Capacitive microphone awaiting etching to release the surface acoustic plate. Total diameter is 800μm.

References

[1] A. Allen. A Textbook of Practical Physics. pp. 200-204 (1916). Macmillan and Co ltd.

[2] Blevins. Formulas for Natural Frequencies and Mode Shapes. 199 (1958). Krieger Publishing.

Correlation between structure of tungsten-oxide thin films and their performance characteristics for ozone and NO_x gas sensors

O.Berger[1], T.Hoffmann[1],W.-J.Fischer[1], V.Melev[2]

[1] Technical University of Dresden, Semiconductor and Microsystems Technology Laboratory, D-01062 Dresden, Germany.(berger@ihm.et.tu-dresden.de)
[2] Fraunhofer Institute of Nondestructive Testing (IZFP), EADQ, D-01326 Dresden, Germany

Summary: *Tungsten oxides thin films were obtained by electron beam deposition and annealed in the temperature range 350-800°C for 1-3 h. The structure, morphology and phase composition of the as-deposited and annealed films were characterized by X-ray diffraction and AFM. The electrical response towards NO_2 and O_3 was studied both experimentally and theoretically. In order to interprete the kinetic characteristics of tungsten oxide thin films upon exposure to different gases a model, based on surface adsorption/desorption processes coupled with bulk diffusion was used. All tungsten oxide thin films investigated in this work are suitable to detect very low concentrations of NO_2 (0.05-0.5 ppm in N_2 and synthetic air) and ozone (25-90 ppb) at very low working temperatures (80-160°C). The films annealed at 400°C for 1-2 h are very selective to ozone and the films annealed at 400°C for 3 h and at 800°C for 1 h are very sensitive to NO_2 (in N_2).*

Keywords: *Tungsten oxides, phase and structure transformation, NO_2 and O_3 sensors*
Category: *5 (Chemical sensors)*

1 INTRODUCTION

Nitrous oxides are typical air pollutants released by combustion facilities, automobiles and aircraft. In addition, decomposition of NO_2 by solar irradiation is a source of ozone (O_3) production. In recent years tungsten-oxide thin films have received considerable interest as promising materials for highly sensitive gas-sensing devices for NO_2 and ozone detection in ambient air [1].
The aim of this work was the characterization of the microstructure, morphology and phase composition of tungsten-oxide thin films prepared by electron-beam deposition in the as-deposited and annealed states as well as the investigation of the change in electrical conductivity of the films on exposure to NO_2 and O_3. The correlation between film structure and sensor properties was established, enabling the development of these films with high stability, sensitivity, selectivity and reversibility under low-temperature conditions. Such films are applicable as low-cost and low-power sensor devices for miniaturized gas monitoring, as described elsewhere [2].

2 RESULTS AND DISCUSSION

During film preparation the starting powder decomposes and as-deposited tungsten-oxide films are composed of a mixture of W_nO_{3n-2} phases, WO_3 and WO_2 as a result of the two follows reactions, i.e., $WO_{2.72} \rightarrow (W_nO_{3n-2}) + WO_2$ and $(W_nO_{3n-2}) \rightarrow WO_3 + WO_2$, that occur. These films consist predominantly of $WO_{2.92}$ crystallites.
Films annealed at 350°C for 3 h consist predominantly of $WO_{2.90}$ as a result of two solid-state reactions, i.e., $WO_{2.72} \rightarrow WO_{2.92} + WO_{2.90} + WO_2$ and $WO_{2.90} \leftarrow WO_3 + WO_2$, that occur. Annealing of the as-deposited thin tungsten- oxide films at 400°C for 1h leads to formation of predominantly $WO_{2.90}$ as a result of the two solid-state phase transformations, i.e., $WO_{2.72} + WO_{2.92} \rightarrow WO_{2.90} + WO_2$ and $WO_{2.90} \leftarrow WO_3 + WO_2$, that occur. Extended heat treatment (for 2-3 h) is responsible for an acceleration in the solid-phase transformation $WO_{2.72} \rightarrow WO_{2.90} + WO_2$ and promotes the solid-phase transformation $WO_{2.90} \rightarrow WO_3 + WO_2$. In the film annealed for 3 h, the relative amount of $WO_{2.90}$ decreases by a factor of 4.5 and the relative amounts of WO_2 and WO_3 increase by factors of 2.8 and 1.2, respectively, compared to the amounts in the film annealed for 1h.
Annealing at 500°C for 1h leads to a shift in the phase equilibrium $WO_{2.72} \leftarrow (W_nO_{3n-2}) + WO_2 + WO_3$ in the direction of formation of the $WO_{2.72}$. Annealing for 2h leads to a shift in the phase equilibria $WO_{2.72} \leftarrow (W_nO_{3n-2}) + WO_2$ and $(W_nO_{3n-2}) \leftarrow WO_2 + WO_3$ in the directions of formation of $WO_{2.72}$ and $WO_{2.92}$, respectively. In contrast to this, the equilibria $WO_{2.72} \rightarrow (W_nO_{3n-2}) + WO_2$ and $(W_nO_{3n-2}) \rightarrow WO_3 + WO_2$ are shifted to the formation of WO_3 and WO_2 for 3 h annealing time.
During annealing at 600°C for 1-3 h the solid-phase transformations $WO_{2.72} \rightarrow (W_nO_{3n-2}) + WO_2$ and $WO_{2.90} \rightarrow WO_{2.83} + WO_2$ occur, resulting in the formation of mixed W_nO_{3n-2} ($WO_{2.92}$ and $WO_{2.90}$), $WO_{2.83}$ and WO_2 phases. It can be assumed that the reaction $WO_{2.90} \leftarrow WO_3 + WO_2$ also takes place

under these annealing conditions.
During annealing at 800°C for 1-2 h $WO_{2.72}$ undergoes the complete solid-phase transformation $WO_{2.72} \rightarrow WO_{2.92} + WO_{2.90} + WO_2$. At the same time, the solid-phase transformation $W_nO_{3n-2} \rightarrow WO_3 + WO_2$ occurs, whereby the partial reaction $WO_{2.92} + WO_{2.90}$ is in progress after an annealing period of 1h. After an annealing period of 2h both solid-phase transformations are complete [3].
The direction of the phase transformations for different annealing conditions is influenced by the very high macrostresses that appear as an additional, independent thermodynamic factor.
The semiconductor phases are predominantly formed during annealing at 350-400°C for 1-3 h and at 800°C for 1h, whereas the thin films annealed at 500-600°C for 1-3h and 800°C for 2h consist mainly of phases with more pronounced metallic properties.
All investigated thin films can be divided into two main groups: compact (as-deposited and annealed at 350 - 500°C, for 1-3 h) and porous (annealed at 600-800°C for 1-3 h) layers.
The as-deposited thin films and films annealed at 350°C for 3 h have a relatively dense, smooth surfaces. The formation of new phases leads to an increase or decrease in the film volume and results in an increase in the tensile or compressive macro-stresses in the film. Due to adhesion between the film and the substrate, these macrostresses make an important contribution to the microstructural rearrangement of the film surface, namely, to the formation of agglomerates of crystallites of the different phases and boundaries between them at 400°C. Annealing for 2-3 h leads to an increase in grain size and smoothening of the polycrystalline film surface. Contrary to this, the agglomerates increase in amount, but their size decrease significantly, especially after an annealing period of 3 h [3].
The formation of the agglomerate boundaries at 500°C relieves the macrostresses in the thin film und can lead to microcrack formation. After 1 h these films have smooth surfaces, but the columns have loose boundaries between them. When the annealing time is increased to 2-3 h, the degree of fragmentation of the thin film increases. For an annealing time of 3 h, microcracks are formed on clearly defined, narrow agglomerate boundaries. The formation of pores through the entire depth of these films at the agglomerate boundaries is the next step in the process of reduction of the high-order macrostresses arising in the film as a result of the solid-phase transformations occuring at 600-800°C [3].
The gas sensitivity and response time of tungsten-oxide films are strongly dependent on the relations of the film thickness (H) and crystallite size (D_g) to the Debye length (L_d) of the electrons [4].
The transducer function of the microstructure of the compact thin films (annealed at 400°C) and macroporous thin films (800°C for 1h), consisiting mainly of semiconductor phases, is governed by the surface trap-limited model. This leads to a very high sensitivity and short response times to NO_2 and ozone [4].
In order to interprete the kinetic characteristics of tungsten-oxide thin films on exposure to different gases, a model based on surface adsorption-/desorption processes coupled with bulk diffusion was used. The best fit of the experimental curve I(t) for all these films is delivered using the sum of two exponentials functions. From this finding, it is evident that two adsorption/desorption "mechanisms" exist for sensor-gas interaction. The lattice defects in the grain boundaries and shear planes play the role of molecular sieves. The bulk diffusion of NO_2 molecules has a negligible effect on the sensitivity and response time of tungsten-oxide films annealed at 400°C. Chemosorption occur on the film surface on the least closely packed lattice planes of the semiconductor phases. At the same time bulk diffusion of ozone has a profound effect. For films annealed at 500-800°C, when the defect size in the grain boundaries and shear planes increases, the role of the bulk diffusion of NO_2 and ozone molecules becomes more significant [4].
All tungsten-oxide thin films investigated in this work are suitable for detecting very low concentrations of NO_2 (0.05-0.5 ppm in N_2 and synthetic air) and ozone (25-90 ppb) at very low working temperatures (80-160°C). The films annealed at 400°C for 1-2 h are very selective to ozone and the films annealed at 400°C for 3 h and at 800°C for 1 h are very sensitive to NO_2 (in N_2).

3 REFERENCES

[1] W.Göpel, J.Hesse, J.N.Zemel (eds), Chemical and Biochemical Sensors, Vols. **2** and **3**, VCH, Weinheim, 1991.
[2] M.Plötner, O.Berger, H.Stab, P.König, D.Beyerlein, W.-J.Fischer, Proc. IEEE Int. Frequency Control Symp., Seattle, 2001, 252-259.
[3] O.Berger, T.Hoffmann, W.-J. Fischer, V. Melev, Submitted to J. of Mater. Sci.: Mater. in Electronics.
[4] O.Berger, T.Hoffmann, W.-J. Fischer, V. Melev, Submitted to J.of Mater. Sci.: Mater. in Electronics.

Realtime Sensing while Drilling using the USDC and Integrated Sensors

Y. Bar-Cohen and S. Sherrit

Jet Propulsion Laboratory (JPL)/Caltech, Pasadena, California, USA
E-mail yosi@jpl.nasa.gov Web: http://ndeaa.jpl.nasa.gov

Summary: *The search for existing or past life in the Universe is one of the most important objectives of NASA's mission. In support of this objective, an ultrasonic based mechanism is being developed to allow probing and sampling of rocks and soil. The novel lightweight Ultrasonic/Sonic Driller/Corer (USDC) used in this study takes advantage of its ability to drill with low axial force and low power. These advantages overcome some of the major limitations of planetary sampling using conventional drills in low gravity environments. Sensors, such as thermocouple and fiberoptics, are integrated into the bit and used to perform real-time analysis while drilling.*

Keywords: *Ultrasonic drilling, piezoelectrics, sensors, fiberoptics*
Category: *10 (Applications)*

1 Introduction

Future NASA exploration missions to Mars, Europa, Titan, comets and asteroids are seeking to perform sampling, in-situ analysis and possibly the return of material to Earth for further tests. For this purpose effective instruments that can sample and conduct in-situ astrobiology analysis are being sought. As sampling devices, existing drilling techniques are limited by the need for large axial forces and torques, high power consumption and an inability to efficiently duty cycle. Lightweight robots and rovers have difficulties to accommodate the constraints of existing drills. To address these constraints and the challenges to the NASA objective of planetary in-situ sampling and analysis, an ultrasonic/sonic driller/corer (USDC) was developed [1 – 3].

1.1 The USDC as a piezoelectric based drill

The USDC consists of an actuator, free-mass and a bit. The actuator is a piezoelectric stack and a horn for the amplification of the displacement. The actuator is driven in resonance at 20kHz and a stress bolt holds it in compression to prevent fracture during operation. Unlike typical ultrasonic drill where the drill stem is acoustically coupled to the horn in the USDC the actuator drives a free flying mass (free-mass), which bounces between the horn tip and the drilling or coring bit at sonic frequencies. The impacts of the free-mass create stress pulses that propagate to the interface of the bit and the rock onto which the USDC is placed in contact. The rock fractures when its ultimate strain is exceeded at the rock/bit interface. Under a variety of conditions, this novel drilling mechanism has been shown to be more efficient and versatile than conventional ultrasonic drills. The low mass of a USDC device and the ability to operate with minimum axial load with near zero torque (see Figure 1) offers important capabilities for sample acquisition and in-situ analysis. Another important characteristic of the USDC is its ability to operate in the harsh environments of space, which include low or high temperature and/or pressure.

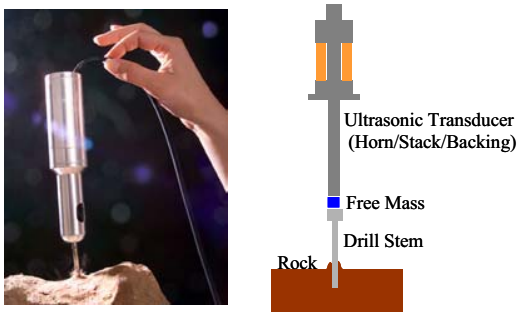

Fig. 1: The USDC is shown coring with minimum axial force and holding torque (left), and a schematic diagram of the USDC components (right).

1.2 Demonstrated characteristics

The USDC has been demonstrated to drill rocks that range in hardness from granite and basalt to sandstone and tuff. Other media that have been drilled include soil, ice and diorite, and limestone. This novel drill is capable of high-speed drilling (2 to 20-mm/Watt·hr for a 2.85mm diameter bit) in basalt and Bishop Tuff using low axial preload (<10N) and low average power (<12W). Drilling using average power levels as low as 5 Watts has

been demonstrated. The USDC has drilled 25-mm deep, 6-mm diameter holes in basalt in a little over 2-hrs from a 4-kg platform using 10W average and 25W peak power. It has also drilled 15-cm deep, 5-mm diameter holes in sandstone in just over an hour using similar power as for the basalt drilling.

2 Lab-on-a-Drill

The USDC novel characteristics allow it to be used not only as a sampling tool where cores and dust can be acquired but also as a probing device. The sonic and ultrasonic hammering action on the bit allows using it as a sounder for probing the drilled medium. Further, the longitudinal displacement of the bit without rotation allows mounting of sensors for real-time analysis of the drilled medium. The combination of sampling probing and sensing allows the USDC to be used as a lab-on-a-drill system. In order to allow effective design of the USDC it was analytically modeled and predicted drilling rates and power levels were corroborated experimentally with a reasonable accuracy [1].

3 USDC with integrated sensor suite

Since the USDC bit does not turn and its vibration amplitude is relatively small one can easily mount sensors on the bit and conduct real-time tests during drilling or coring. Two types of sensors were successfully demonstrated todate: thermocouple and fiberoptic. The thermocouple was used to measure the rate and maximum rise of temperature and these values were found to correlate to the hardness of the rock being drilled. Even though these thermal variables are dependent on the heat conductivity and capacity of the drilled object, one can assume with a reasonable accuracy that most rocks have thermal properties within a comparatively narrow range. Compiling temperature rise rate and maxima as a function of time for variety of drilled materials has demonstrated the feasibility of using a thermocouple-on-the-bit as a means of assessing the drilled medium hardness (see Figure 2).

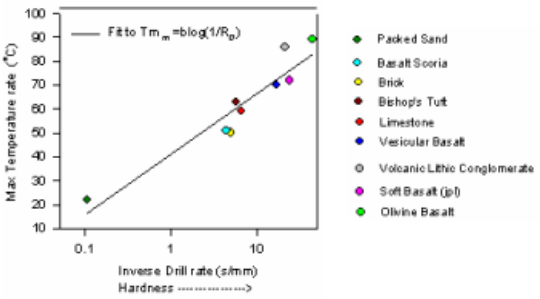

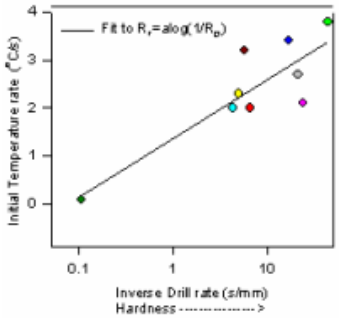

FIGURE 2: The measured temperature maxima and initial temperature rate as a function of hardness (inverse drilling rate) for variety of media.

Other tests using an optical fiber that was approximately 160 μm in diameter was imbedded into 10-mm diameter coring bit with a 1-mm wall thickness. Reflection data in the wavelength range of 400-1200 nm were recorded. The results of this study will be reported.

4 Summary

The USDC is being investigated for potential planetary applications as a Lab-on-a-drill. The capability to use it with integrated sensors was investigated and two type of sensors were examined including thermocouple and fiberoptics. The thermocouple was shown to assess the hardness of the drilled medium using the rate and maximum rise of the temperature. Further, reflection spectral data was examined using a imbedded optical fiber in a coring bit-. Other fibers using low wavelength UV excitation are being considered for detection of biological markers using biofluorescence.

Acknowledgement

Research reported in this manuscript was conducted at the Jet Propulsion Laboratory (JPL), California Institute of Technology, under a contract with National Aeronautics Space Agency (NASA).

References

[1] Bao X., Y. Bar-Cohen, Z. Chang, B. P. Dolgin, S. Sherrit, D. S. Pal, S. Du, and T. Peterson, "Modeling and Computer Simulation of Ultrasonic/Sonic Driller/Corer (USDC), Accepted for publication in IEEE UFFC.

[2] Bar-Cohen Y., S. Sherrit, B. Dolgin, T. Peterson, D. Pal and J. Kroh, "Ultrasonic/Sonic Driller/Corer (USDC) With Integrated Sensors," JPL New Technology Report, Docket No. 20856, Submitted on August 30, 1999, Patent was submitted on May 1, 2001.

[3] http://ndeaa.jpl.nasa.gov/nasa-nde/usdc/usdc.htm

Ignition and Combustion Investigation On Pyrotechnical Solid Microthruster

B. Larangot, A. Chaalane, V. Conédéra, P. Dubreuil, P. F. Calmon, C. Rossi

LAAS-CNRS, 7 avenue du Colonel Roche, 31077 Toulouse Cedex 4, France
email : blarango@laas.fr

Summary: *Within an European project [1], LAAS and its partners develop energetic microscale devices using energetic material with a Microsystem. Addressed applications for these kind of power MEMS are the micropropulsion for space (microthruster), military application (microrocket), smart gas generator or the electrical generation. The micropropulsion application has been chosen to demonstrate the capabilities of this pyrotechnical microsystem. The microthruster structure is composed of 4 parts: a silicon nozzle, a silicon igniter containing specific propellant mixture optimized for ignition, a chamber part containing a classic propellant and a back-side seal. The ignition process is a key point of this technology and needs a particular effort to provide the lowest energy to the propellant and constitutes a key for the miniaturization of this new kind of power MEMS in space applications.*

Keywords: *Power MEMS, microthruster, microrocket, micro ignition, microthrust*
Category: *10 (Applications); 2 (Materials and Technology)*

Abstract

Whatever the application, miniaturisation systems is a permanent effort to save mass, cost and energy. Following this perspective several research groups[1-3] in space technology design and develop new small spacecraft and missions concepts. In this context there is a real need in developing low cost, reliable microthruster. LAAS has chosen the solid propellant based thruster. Their high reliability, simplicity and long-term storability, make solid propellant thrusters an attractive solution for low ΔV micropropulsion module.

The principle of operation is very simple : a low electrical power feeds a thin film resistor producing the ignition of a GAP based propellant mixture contained in the millimetre scale igniters. Afterwards, the propellant stored in the micro machined chamber is ignited. The sustained combustion of this propellant produces energetic gas that are accelerated through the nozzle (see fig. 3) to generate a force. Technology of fabrication has already been published several time[4-5] . In this paper, we present the experimental results obtained for the validation of ignition energy and thrust characteristics. Both parameters seem important because that constitutes a valuable asset of this technology and system.

Ignition characterization

Different dimensions of resistors and different sizes of igniter have been investigated to find the dimensional ignition limits and to determine the optimal ignition energy and delay for each set of dimensions. Only one type of propellant will be considered.

To investigate ignition, a large number of tests samples (see Fig. 2) have been fabricated and tested. They are composed of 16 non-addressed polysilicon heaters with a resistance value of about 500 Ω. The serpentin shape of resistances is realized by Reactive Ion Etching of doped LPCVD polysilicon (see Fig. 1) placed at the center of a silicon nitride and thermal oxide membrane.

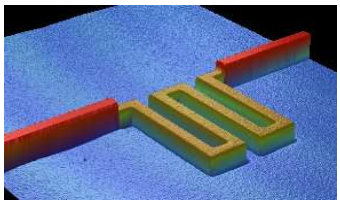

Fig.1. 3D view of a polysilicon resistance on a $SiNx/SiO_2$ membrane

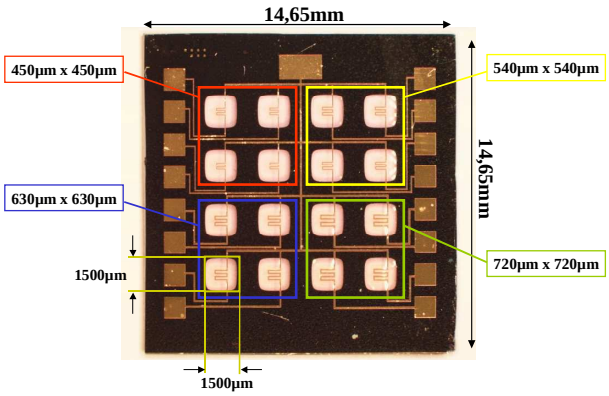

Fig.2. Sixteen non-addressed polysilicon heaters. An array of four size resistors: 450µm x 450µm, 540µm x 540µm, 630µm x 630µm and 720µm x 720µm.

[1]Micropyros : IST-99047
Partners : LAAS (CNRS laboratory-France), IMT (University of Neuchâtel-Switzerland), IMTEK (University of Freiburg-Germany), SIC (University of Barcelona-Spain), ASTC (University of Uppsala-Sweden) and LACROIX (France)

A Deep Reactive Ion Etching of the bulk silicon is used to liberate the membrane. The cavity thus fabricated is filled with the propellant.

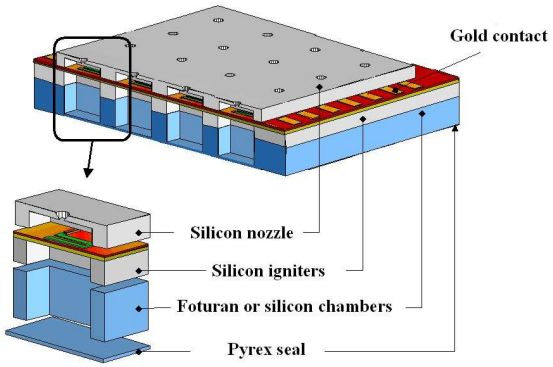

Fig.3. 3D view of the micropyrosystem

A programmable power supply delivers an electrical current to the polysilicon filament. The input current (I) and voltage (V) are monitored and saved via a PC in order to get the real ignition curves for each tests : I(t), V(t), I.V(t). Fig. 4 gives an example of igniters response. The propellant is ignited when the membrane breaks and the current becomes null.
The ignition time depends on the resistor and membrane sizes. For igniters with membrane of 2.25mm² , ignition power is of 150mW and time ranges from 250ms to 470ms.

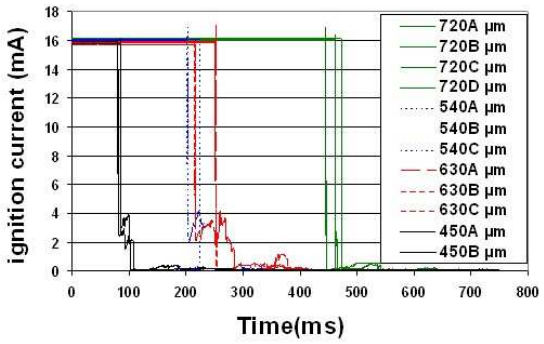

Fig.4. Example of ignition curve

Ignition investigations show that when the dimensions are reduced under the millimetre scale, the ratio between the chemical heat and the heat losses become unfavourable to the ignition and combustion. Several parameters can be optimised during the ignition phase, the most important are: the ignition source, the propellant composition, the surface of ignition point and the propellant surrounding material.

Combustion process and thrust generation

In the area of instrumentation, a thrust balance has been set up. Particular attention has been paid on the thrust balance calibration procedure to ensure that reliable measurements can be obtained.

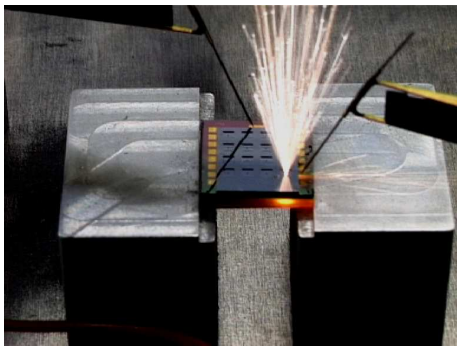

Fig.5.Photo of a thruster with a nozzle during the combustion

Fig. 5 represents a combustion for the millimetre scale device with a nozzle. This thruster has been tested with the thrust balance and thrust curve results are compared with modelling results.

Acknowledgements

We would like to thank the French group LACROIX for its collaboration for the propellant. The technological fabrication of the nozzle and chamber is realized by IMT-University of Neuchâtel.

References

[1] D. H. Lewis Jr, S. W. Janson, R. B. Cohen, E. K. Antonsson. Digital Micropropulsion. Sensors and Actuators A 80 (2) pp143-154, 2000.
[2] K. Takahashi, H. Ebisuzaki, H. Kajiwara, T. Achiwa, K. Nagayama. Design and Testing of Mega-Bit Microthruster arrays. Nanotech AIAA 2002-5758, Houston, 9-12 September 2002.
[4] C. Rossi, S. Orieux, B. Larangot, T. Do Conto, D. Esteve. Design, fabrication and modeling of solid propellant microrocket-application to micropropulsion. Sensors and Actuators, A99, 125 (2002).
[5] C.Rossi, B. Larangot et al. Solid propellant micro-rockets towards a new type of power MEMS. Nanotech 2002, Houston TX, 9-12 September 2002.

Development of a miniature optical tri-axial force sensor

J. Clijnen, D. Reynaerts and H. Van Brussel

[1]Katholieke Universiteit Leuven, Department of Mechanical Engineering,
300B Celestijnenlaan, 3001 Heverlee, Belgium
email: Dominiek.Reynaerts@mech.kuleuven.ac.be http://www.mech.kuleuven.ac.be

Summary: *This paper presents the design of an optical tri-axial force sensor that measures the forces on the pen tip of a computer pen during writing. The sensor consists of a mechanical structure, which converts the force into a linear displacement. This displacement is optically measured with three LED-photodiode pairs. To protect the sensor, an overload protection is provided. The design results in a sensor with the size of 8.4mm x 8.4mm x 45.6mm. The sensor has a range of ±2N, resolution of 0.5%, a sensitivity of 94.12mV/N, a relative accuracy of 1%, and a resonance frequency of 360Hz.*

Keywords: *miniature force sensor, optical*
Category: *4 (Non-magnetic physical devices)*

1 Introduction

This paper discusses the design of a cheap and mass-producible miniature force sensor for application in an advanced computer pen [1]. This computer pen behaves like a normal pen, but the written text will not only appear on the paper but also on a computer screen. Its working is based on the measurement of the pen tip forces during writing. The miniature optical tri-axial force sensor is designed to measure these pen tip forces. Its specifications are summarised in table 1. Although originally developed for a computer pen, the force sensor can also be used in robot surgery [2] and micro-assembly [3].

Table 1. The specifications of the force sensor.

Range	± 2N
Accuracy	0.5% or 0.01N
Frequency range	0…20Hz
Outside diameter	12mm
Inside diameter	> 4mm
Robustness	Overload protection
Temperature variations	20°±20°C

2. Principle in one dimension

The basic principle of the optical force sensor in one dimension is shown in figure 1. The force is applied onto a deformable structure. The resulting deformation is optically measured with an IR-LED and a photodiode. A plate, positioned between the IR-LED and the photodiode, moves together with the deformed structure. Its movement changes the amount of incoming light on the photodiode and, therefore, the electrical current signal of the photodiode.

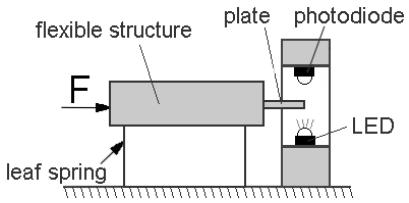

Fig. 1. The basic principle of the force sensor in one dimension.

3. Design of the force sensor

The basic principle in one dimension is extrapolated to the mechanical structure, shown in figure 2. To uncouple the forces, the structure consists of a four parallel bar mechanism for the x- and y-forces (figure 2a) in cascade with a two parallel leaf spring mechanism for the z-force (figure 2b). By gluing stiffening plates to the structure (figure 2c), the flexibility of the other parts of the sensor is negligible compared with the four bars and the two leaf springs. Consequently, the structure converts the pen tip forces into a pure three-dimensional translation of the cartridge holder.

The translation is measured with the optical displacement sensor, located at the back of the cartridge holder. A square beam, which is attached to the end of the cartridge holder, interrupts three light beams, as shown in figure 3. Besides these three light beams, an extra dummy light beam, which is not interrupted by the square beam, is provided to compensate for temperature effects.

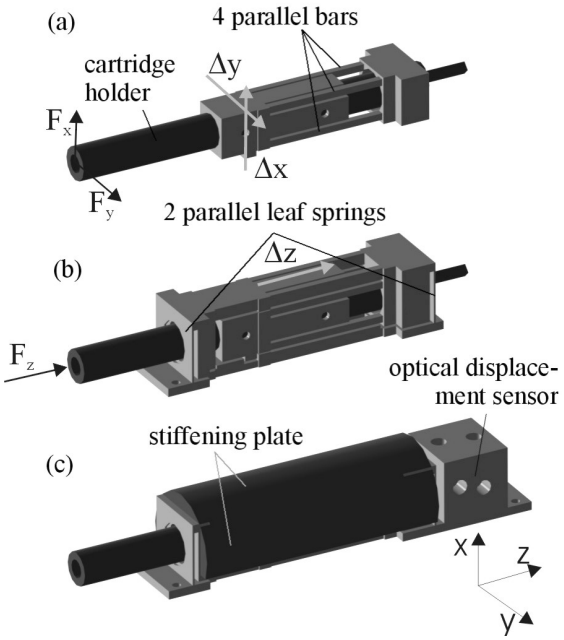

Fig. 2. The mechanical structure.

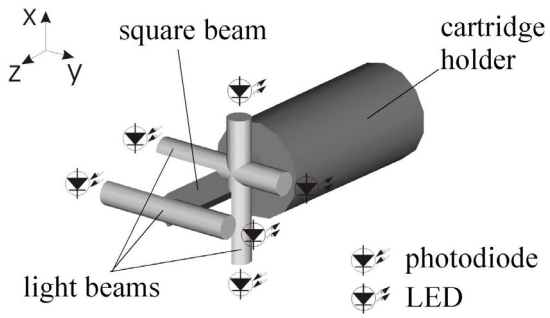

Fig. 3. The optical displacement sensor.

The sensor design has some characteristic features: an equal stiffness in all directions, an integrated overload protection, and integrated diaphragms to narrow the light beams.

Figure 4 shows the final sensor. Its size, without the cartridge holder, is 8.4mm x 8.4mm x 45.6mm.

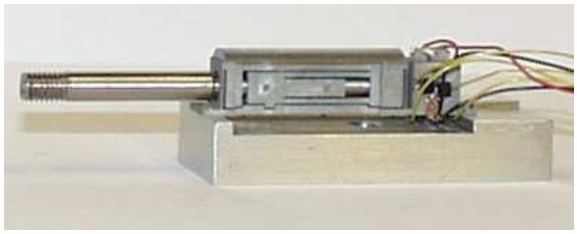

Fig. 4. The miniature optical tri-axial force sensor.

4. Test results

The sensor was extensively tested. The results for the x-axis are shown in table 2. Taking the cross-sensitivity into account, by using a 3x3 matrix relation between the sensor-signals and the forces, a relative accuracy of 1% was reached.

Table 2. The calibration results of the sensor (x-axis).

Resolution	0.5%
Repeatability	1%
Sensitivity	94.12mV/N
Cross sensitivity y-axis	3.73mV/N
Cross sensitivity z-axis	1.39mV/N
Relative accuracy	1%
Resonance frequency	360Hz
Temperature dependency	0.8mV/°C

Two methods to compensate the temperature dependency have been tested. The first method, based on a dummy photo-LED pair, does not give acceptable results. The reason for this is that the dummy pair does only detect changes in the optical components. A movement of the square beam, caused by the thermal deformation of the mechanical structure, is not detected. The second method, based on the direct measurement of the temperature, does not suffer from this problem. A linear thermal expansion model is then stabilising the sensor-signals.

5. Conclusion

The miniature optical tri-axial force sensor is designed to measure the contact forces on a pen tip during writing. The sensor is based on a flexible structure, which converts the force into a linear displacement. This displacement is measured with a simple optical principle: the light of the LED is partially blocked by a moving beam. The final design has a range of 2N, resolution of 0.5%, a sensitivity of -94.12mV/N, an accuracy of 1% and a resonance frequency of 360Hz

Acknowledgements

This research is sponsored by the Belgian program on Inter-university Poles of Attraction (IAP5/06), 'Advanced Mechatronic Systems', initiated by the Belgian State, Prime Minister's Office, Science Policy Programming.

References

[1] D. Reynaerts, H. Van Brussel, Design of an advanced computer writing tool, *Proc. 6th Int. Symp. on Micro Machine and Human Science*, pp. 229-234, Nagoya, 1995.

[2] G. De Gersem, E. Vander Poorten, and H. Van Brussel, Human machine interaction in endoscopic applications, in *BSMEE Conf. on Virtual Reality in Mechanical and Production Engineering VR-MECH'01*, (Brussels, Belgium), pp. 211–216, 2001.

[3] H. Van Brussel, J. Peirs, D. Reynaerts, A. Delchambre, G. Reinhart, N. Roth, M. Weck, E. Zussmann, Assembly of microsystems, *Annals of CIRP*, Vol. 49. (2), p. 451-472, 2000.

Digital Processing Technique Applied to a New Ultrasound System for Measuring Position and Orientation of Laparoscopic Surgery Tools

F. Tatar, J.R. Mollinger, P. Turmezei, A. Bossche

Delft University of Technology, DIMES/ITS Mekelweg 4, 2628 CD Delft, The Netherlands, E-mail: F.Tatar@its.tudelft.nl, http://ei.et.tudelft.nl/

Summary**:** *A new ultrasound wireless positioning system is developed that gives the surgeon the exact location and orientation of the instruments in the patient. The measuring system employ ultrasound markers placed on the instruments, outside of the human body. Knowing the dimensions of the usually rigid instruments it is possible to calculate their position and orientation inside the patient from the markers' positions. Using the cross-correlation method we obtained a resolution of 0.7 mm in determining the marker positions.*
To eliminate wiring to the tools a wireless radio wave (RF) system was used to trigger the ultrasound sensors.

Keywords: *ultrasound system, 3D-detection, cross-correlation*
Category: *10 (Applications)*

1. Approach

In minimal invasive surgery usually an endoscope is used to show the surgeon what is happening inside the human body. However, this view is very limited and gives no information of instrument positions outside the camera view.
We focused our efforts on the methods used for ultrasonic detection of position. The most widely used one is based on a pulse time-of-flight (TOF) estimation. In our set-up two pairs of ultrasound markers (transmitters) placed on each instrument are used to measure 3D position and orientation of the instrument [1]. The detection of the marker positions is realized by an array of ultrasound receivers.
The ultrasound transmitters are triggered by radio wave signals. For this purpose the marker modules include RF receivers that react on the correct identification code only. These RF trigger codes are sent by a central RF transceiver and are provided by a DSP unit, which controls the whole process and derives position information from the ultrasound signals. The schematic of the whole system is described in Fig .1
With preliminary TOF measurements we estimated the influence of temperature, humidity and air pressure on the velocity of sound, which is linearly correlated to the distance. While humidity and air pressure have only very little influence on the distance measurement, the temperature has a dominant effect. The temperature effect can be compensated with a simple equation that correlates variations in temperature in a surgical room with variations in sound velocity. [2]
Various methods have been developed to improve the TOF measurement accuracy. The simplest and most economical of them offer a poor resolution [3].
The goal is to investigate the possibility to improve our TOF acoustic measurements in a medical environment, using digital techniques. One of most used techniques for TOF detection is the cross-correlation method. [3]
Usually as known from literature the transmitted and the received ultrasonic signal are digitized and the maximum of the cross-correlation function between these two sequences yields the TOF.
The novelty of our approach is to replace the model for the transmitted signal with the last received digitized sequence memorized by the DSP. Since the time slot between two consecutive ultrasonic signals from the same marker is less than 100 ms, the signal envelopes will show only minor differences. This allows a more accurate correlation.

2. Results

The first measurements for the received ultrasonic signals were made for a distance marker-receiver of 1.69 m.
Two ultrasound transmitters react to two (different) RF trigger codes generated by the DSP.

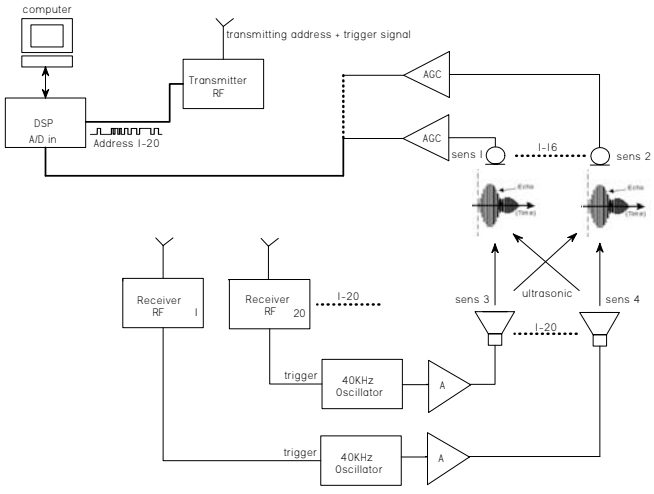

Fig 1. The schematic view of the localizing system

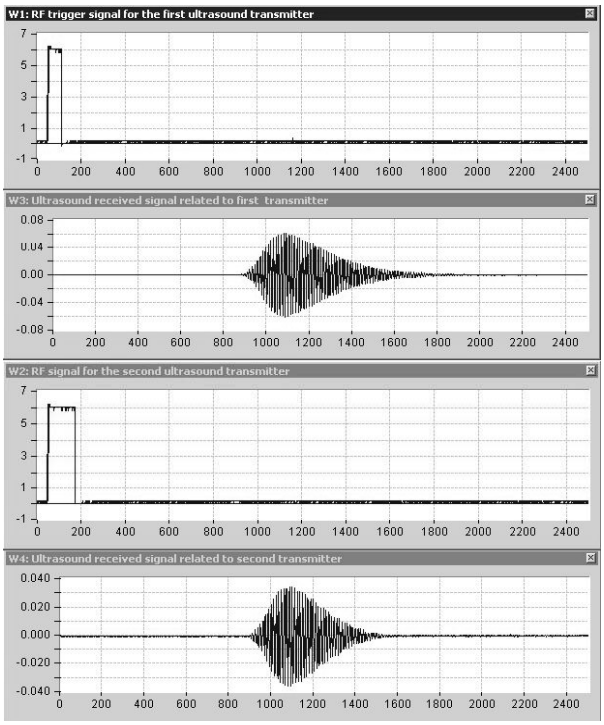

Fig.2 The ultrasound bursts received from different transmitters, triggered with different RF codes

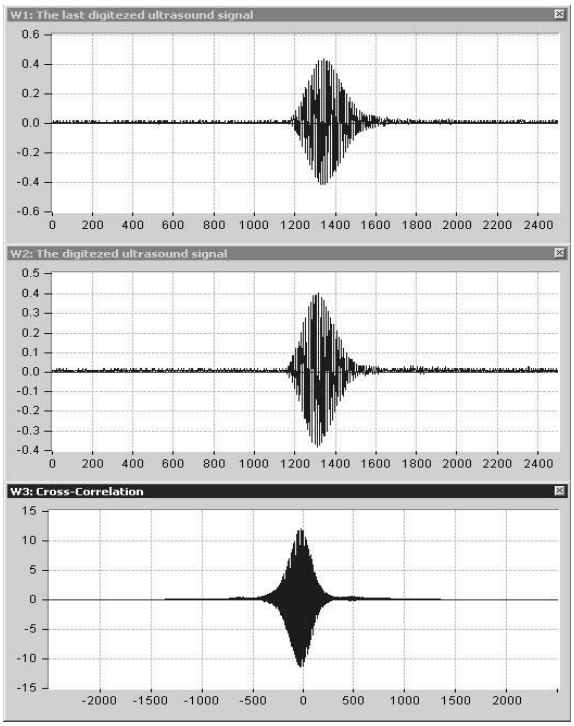

Fig 3.The cross-correlation function of two signals received after a change of 5 mm in transmitter position

Figure 2 shows the ultrasound signals acquired from the two different ultrasound transmitters. The ultrasound transmitters are reacting exactly to their specific code.

The distance transmitter–receiver for one transmitter was changed 5 times with 5mm steps and the received signals were acquired and sampled with a 500 kHz sample rate. Figure 3 is representing the two bursts for two consecutive sensor positions and the cross-correlation function between them. The cross correlation function is obtained using a DSP unit. The last graph from Fig. 3 shows the cross-correlation function for these two received signals. The maximum value of the function is correlated with 5 mm deviation of the transmitter position. Analyzing a set of consecutive cross-correlation sequences related to a set of 5mm standard deviations of the transmitter position we obtained a resolution of 0.7 mm with a sampling rate of 500 kHz of determining the transmitter position. Increasing the sampling frequency will increase the resolution. The maximum absolute error of measurements was about 2.8 mm for a distance of 1.69 m. The maximum of cross correlation function does not change the position for a relative rotation of transmitter and receiver of ± 15°. This shows that the distance between transmitter and receiver is accurately measured even for a large change of orientation.

In this setup the time slot between two measurements was 1-2 minutes, because displacements were made manually. In the final system the time slot will be 100 ms or less. This will decrease the relative error.

Furthermore advanced DSP filter algorithms could reduce the influence of noise and could increase the accuracy. E.g. replacing the noisy digitized samples situated before and after the ultrasound bursts with a constant value, we obtained more accurate results

3. Conclusions

The principle of a wireless ultrasound system for measuring the 3D position of laparoscopic instruments was discussed. By triggering the ultrasound transmission with an RF signal and cross correlating two consecutive bursts, the relative ultrasound transmitter position could be determined with a resolution of 0.7 mm. The maximum absolute error of measurements was about 2.8 mm for a distance of 1.69 m.

References

[1] Donald P. Massa , *Choosing an Ultrasonic Sensor for Proximity or Distance Measurement ,* Sensors Vol 16, No.2, February 1999.

[2] F.Tatar, J.R.Molinger, R.C. Den Dulk, W.A.van Duyl, J.F.L. Goosen, A.Boosche *Ultrasonic sensor System For Measuring Position and Orientation of Laproscopic Instruments in Minimal Invasive Surgery,* Proc EMBS Madison Wisconsin 2002 pag. 301-304

[3] Daniele Marioli, Claudio Narduzzi, Carlo Offelli, Dario Petri, and Andrea Taroni , *Digital Time of Flight Measurement for Ultrasonic Sensors* IEEE Transactions and Measurements , Vol .41 No.1 February 1992

POROUS a-Si:H FILMS PRODUCED BY HW-CVD AS ETHANOL VAPOUR DETECTOR AND PRIMARY FUEL CELL

Isabel Ferreira*, Elvira Fortunato and Rodrigo Martins

CENIMAT, Department of Materials Science, Faculty of Science and Technology of New University of Lisbon, and CEMOP/UNINOVA, Campus da Caparica, 2829-516 Caparica, Portugal

Abstract

In this work we show by the first time the possibility to use undoped porous silicon thin films produced by hot wire chemical vapour deposition (HW-CVD) as ethanol detector above 50ppm and as a primary fuel cell. Silicon thins films produced by HW-CVD technique, under certain deposition conditions, have a porous structure [1]. Therefore, in the presence of an alcohol, the OH group is adsorbed by the uncompensated bonds behaving as donor-like carriers leading to an increase in the current flowing through the material. This current enhancement is bias dependent in glass/ITO/i-a-Si:H/Al sensor and increases as the ethanol vapour pressure increases, from 10^{-1} mbar to atmospheric pressure. The response time of the current of the sensor and its recovery time are in the range of 10-50 seconds at room temperature. Apart from that, we also notice that this type of structure also behave as a primary fuel cell where a power of about 4 $\mu W/cm^2$ is by the first time report.

Keywords: HW-CVD technique, porous silicon, ethanol detector.

*T. 351 21 2948564, Fax. 351 21 2957810, e-mail:imf@fct.unl.pt

A Silicon Lab On Chip for DNA amplification and detection

Ubaldo Mastromatteo

ST Microelectronics, Italy
ubaldo.mastromatteo@st.com
http://www.st.com

Abstract:

Bio MEMS technology can be used in any chemical and biomedical application where analysis is performed on a sample of a living organism. This is likely to have a major impact on the medical world to detect human or animal diseases, but could also enable new products for checking food safety, detecting bacteria, toxins or allergens before food is prepared or consumed.

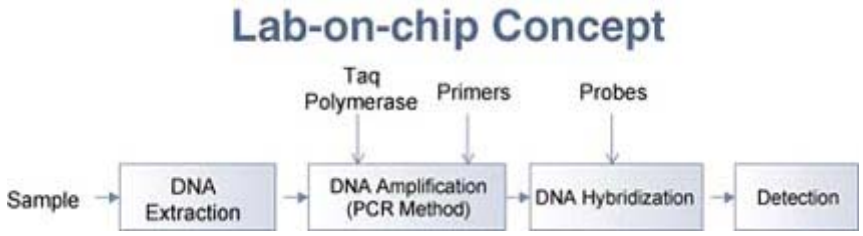

1 DNA Extraction

The genetic material (DNA) can be extracted from a sample of any living organism -- plant, animal, human, bacterium or virus. The template DNA to be amplified is extracted from chromosomes of the original cell. The DNA extraction technique include centrifugation, filtration, measuring, mixing and dispensing. By integrating all these complex steps, costs of the sample preparation would be drastically reduced and quality significantly improved.

2 DNA Amplification (PCR Method)

Concentration levels of DNA samples are often too low for direct analysis. Therefore the chemical amplification of the sample is necessary to increase the concentration.The Polymerase Chain Reaction method is one of the simplest techniques to amplify the number of copies of a specific region of DNA. Heating the sample, the DNA denatures and separates in two segments of single-stranded DNA. Building blocks called nucleotides bind to their complementary base on the DNA denatured.
Then the presence of an enzyme called Taq polymerase synthezises two new strands of DNA so to obtain two double-stranded DNA pieces. The original DNA is duplicated. Applying several times the particular cycle of temperature allowing denaturation and duplication processes, we get analizable quantities of DNA.

3 DNA Hybridization

The DNA obtained by amplification is denatured in single-stranded DNA and is mixed with a synthetic sequence of building blocks called probes. DNA probes complementary to genes of interest (target) are generated in the laboratory and deposited, or synthesized in-situ in microscopic quantities on the silicon (identification area). The DNA and the probe inserted bind together if the DNA contains the complementary base of the probe – this is the DNA hybridization.

4 Detection

One of the most common detection method is the Laser Induce Fluorescence (LIF) method where the presence of bound DNA is detected by fluorescence following laser excitation through a scanning microscope.
Thanks to the large quantity of DNA obtained the fluid becomes easily visible

Detection of the hybridisation of cystic fibrosis related DNA sequences using a magnetoresistive based biochip

D. L. Graham[1], H. A. Ferreira[1,2], L. A. Clarke[3], M. D. Amaral[3] and P. P. Freitas[1,2]

[1]INESC – Microsystems and Nanotechnologies, Rua Alves Redol 9, Lisbon, Portugal
email: dgraham@inesc-mn.pt http://www.inesc-mn.pt
[2]Instituto Superior Técnico, Physics Department, Avenida Rovisco Pais, Lisbon, Portugal
[3]Faculty of Sciences, University of Lisbon, Portugal

Summary: *On-chip detection of the hybridisation of cystic fibrosis related probe and target DNA sequences was demonstrated via the use of biotinylated target DNA and a post-hybridisation detection strategy using on-chip spin valve sensors and magnetically labeled streptavidin. A 50mer oligonucleotide probe corresponding to the anti-sense strand of the CFTR gene, exon 10, was immobilised over on-chip sensors and hybridisation was attempted using either a complementary (exon 10 target) or non-complementary (Rac1) DNA sequence. The detection of hybridised (biotinylated) DNA was shown using single 2x6um^2 spin valve sensors and two types of magnetically labeled streptavidin (2um microspheres and 250nm particles). In the case of the complementary target, visual verification of label binding across the chip surface and spin valve binding signals for both types of label were obtained The chips treated with the non-complementary target DNA showed no label binding and no binding signals were recorded.*

Keywords: *DNA chips, biochip, spin valve sensors, cystic fibrosis, superparamagnetic labels.*
Category: *6 (Biosensors) 3 (Magnetic physical devices)*

1 Introduction

The genomics research community has embraced the DNA-chip/microarray business to such an extent that the projected biochip market value for 2004 is $2.6 billion (US), with an associated revenue for related equipment, such as arrayers and scanners, set to top $2 billion by 2008.[1]However, fluorescence-based microarray systems for genetic diagnosis still face technical challenges, namely the lack of quantitative analysis, the difficulty encountered in comparing data collected from different microarray platforms and the often prohibitively high cost of equipment. Here we present a biochip technology based the use of magnetically labeled biomolecules and spin-valve sensors, primarily used in the read heads of hard disc drives. Although still in its infancy, this technology has already shown promise as a cheaper and possibly more quantitative means of diagnosis for genetic diseases. This example is taken from our work on the development of spin valve array chips for the diagnostic detection of cystic fibrosis.

2 Experimental methods

The spin valve metallic multi-layer was fabricated by an ion beam deposition system on a 3 in. Si wafer and have the structure Ta 20 Å/ NiFe 30 Å/ CoFe 25 Å/ Cu 26 Å/ CoFe 25 Å/ MnIr 60 Å/ Ta 30 Å/TiW(N) 150 Å. As deposited the spin valve coupon sample has a magnetoresistance ratio (MR) of ~7.5 %. The sensors were defined by standard photolithographic techniques and by ion milling. The spin valve sensors have dimensions of 2 μm × 6 μm (the spin valve stripe is 2 μm × 14 μm and the distance between the leads is 6 μm). Aluminum leads, 1μm thick, were used leading to wire-bond pads. After processing, the average MR of the sensor element is (5.5±0.5 %) due to contact and lead resistance. The average sensor sensitivity was found to be ~0.06%/Oe (~0.4 mV/Oe). Both sensors and leads were passivated with a 2000 Å thick sputtered SiO_2 layer for protection against fluid corrosion during experimentation.

The superparamagnetic labels used were 2um micro-coned, iron oxide filled, polyencapsulated microspheres (Micromer®-M,Micromod) and 250 nm particles of iron oxide bound in a dextran matrix (Nanomag®-D, Micromod). The moment per label was found to be ~2×10^{-12} and ~2×10^{-13} emu respectively for a 15 Oe magnetizing field.

The silicon wafer was cut into the individual 8x8mm^2 chips using a dicing saw. Unmounted chips were used to test oligonucleotide probe immobilisation using 50ul droplets of fluid applied to the passivated chip surface. Detection experiments were performed on chips mounted in 40-pin chip carriers. The contacts were made by wire bonding protected with a silicon gel (Elastosil E41), which also created an on-chip well in which to perform all of the fluidic steps of the experiment.

The chip surface was functionalized with amino groups using a 15% aq. solution of APTS, followed by cross-linking with a heterobifunctional spacer, sulfo-EMCS. The 50mer probe was then immobilised via a 3' thiol group. Verification of probe immobilisation was made using the same

probe with a 5'-fluorescein label, which could be observed by fluorescence microscopy.
The immobilised probe DNA was prehybridised in a 2.5% BSA solution for 2 hrs followed by hybridisation with the target DNA for 12 hrs at 37ºC. Evaporation of the fluid during hybridisation was prevented by reversibly fixing a glass coverslip to the chip carrier surface to create a low volume chamber. After hybridisation, the unbound DNA was washed away using 1xSSC containing 0.1% SDS and 1x SSC.
The chip carriers were then mounted in a small breadboard housed within an aluminum noise reduction box and co-axial cables were used to make the electrical connections to power sources and general-purpose interface bus (GPIB) controlled multimeters. A small (5 cm diameter) planar electromagnet with a $Ni_{80}Fe_{20}$ circular core was positioned over the chip carrier, in order to apply an in-plane magnetic field (-15 Oe) to induce a moment within the superparamagnetic particles. The experiments were performed by measuring the voltage drop across single sensors at 8mA sense currents with an 15Oe in plane applied field. All of the streptavidin binding experiments were made in 20ul volumes of 100mM phosphate buffer, pH 7.5

3 Results and Discussion

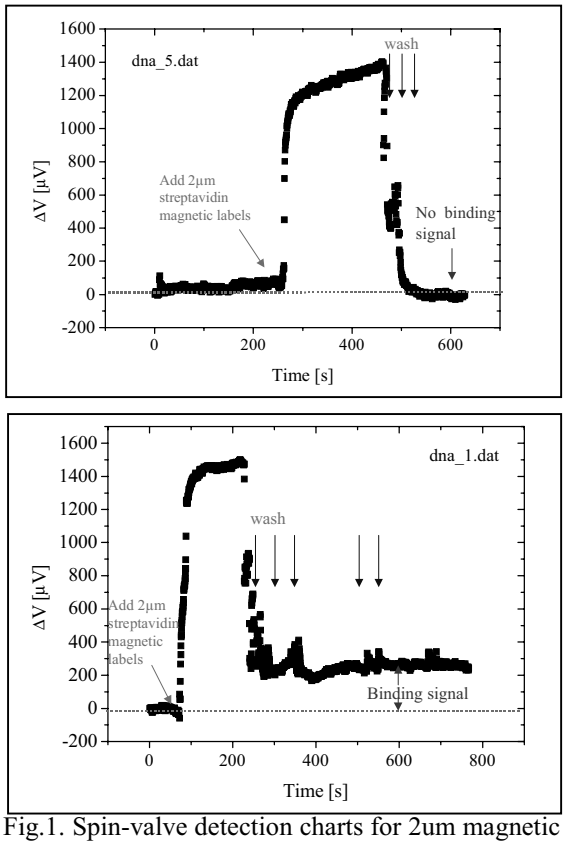

Fig.1. Spin-valve detection charts for 2um magnetic labels functionalised with streptavidin applied to chips hybridised with non-complemetary (top) and complementary (bottom) target DNA. The first signal peak represents the saturation of the sensor.

The residual signal after the washing away of unbound magnetic labels corresponds to the binding signal, equivalent to 2-3 bound 2um labels[2].

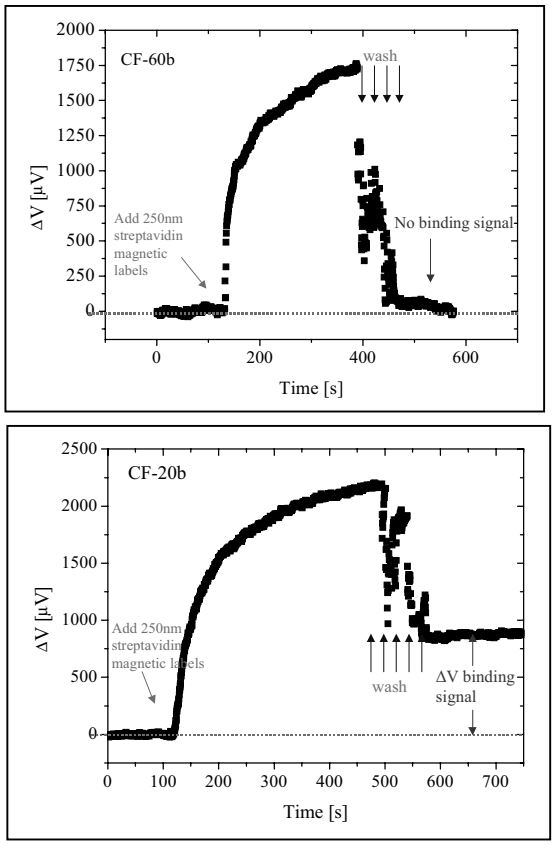

Fig.2. Spin valve detection charts for 250nm magnetic labels functionalised with streptavidin applied to chips hybridised with non-complemetary (top) and complementary (bottom) target DNA. The binding signal of ~1mV corresponds to ~100 labels bound to the sensor surface.

Conclusions

We have shown that a specific DNA probe can be hybridised on-chip and conveniently detected using a post-hybridisation detection method based on the binding of magnetically labeled streptavidin[3] to biotinylated hybridised DNA bound over a spin-valve sensor. Our present goal now lies with the successful integration of spin valve arrays on-chip to simultaneously detect hybridisation of target DNA at multiple different DNA probe sites.

References

[1] "Biochip World Market", Frost & Sullivan 2001

[2] D.L. Graham, H.A. Ferreira, J. Bernardo, P.P. Freitas and J.M.S. Cabral. J. Appl. Phys. 91(10), 7786-7788 (2002).

[3] D.L. Graham, H.A. Ferreira, P.P. Freitas and J. M.S. Cabral, Biosens. Bioelectron. 18(4),483-488 (2003).

A NEW COMPOSITE REDOX POLYMER-CLAY HOST MATRIX FOR THE IMMOBILIZATION AND ELECTRICAL WIRING OF NITRATE REDUCTASE

S. Da Silva[1], D. Shan[1], C. Mousty[1], S. Cosnier[1*], J. Pommier [2]and G. Giordano[2]

[1] Laboratoire d'Electrochimie Organique et de Photochime Redox, UMR CNRS 5630, Université Joseph Fourier Grenoble I, BP 53, 38041 Grenoble Cedex 9, France
[2] Laboratoire de Chimie Bactérienne, UPR CNRS 9043, 31 chemin Joseph Aiguier, 13402 Marseille Cedex 20, France

Corresponding author: e-mail: Serge.Cosnier@ujf-grenoble.fr, Tel: (33) 4 76 51 49 98 Fax: (33) 4 76 51 42 67

Summary: We describe herein a new bioelectrode design for the immobilization and electrical wiring of Nitrate Reductase (NR) in laponite clay combined with poly(pyrrole-viologen) films. The resulting biosensor performance for nitrate determination was investigated by cyclic voltammetry. The biosensor sensibility and its detection limit are 94.7 mA M^{-1} cm^{-2} and 0.5 µM respectively. The apparent Michaelis-Menten constant of the bioelectrode is 0.21 mM.
Keywords: *Biosensor, polypyrrole, nitrate reductase, viologen*
Category: *6 (Biosensors)*

1 Introduction

Nitrate is a well-known environmental contaminant largely encountered in ground, stream water and agro-alimentary. Besides conventional methods such as spectrophotometry, ionic chromatography, polarography, potentiometry, voltametry [1], some bioassays based on nitrate reductase have been developed. Nitrate Reductases (NR) are multiredox center enzymes responsible to the biological conversion of nitrate to nitrite. Since NR can use reduced methyl viologen as an artificial substitute for feredoxin and, these enzymes have been involved in the nitrate determination by electrochemical biosensors [2]. Nowadays the stable immobilization of macromolecular biomolecules on conductive materials with complete retention of their biological recognition properties still remains a crucial problem for the development of biosensors [3]. This paper presents here a new concept of enzyme immobilization that combines biocompatibility and electrical connection. This two-step procedure consists first in the physical entrapment of NR in highly hydrophilic inorganic clay. The latter was used as a template for the subsequent electropolymerization of a new water soluble pyrrole-viologen derivative assuring the electrical wiring of immobilized NR.

2 Electrode design

Glassy carbon electrodes were modified by electropolymerization of a hydrophobic pyrrole-viologen (1), *N*-methyl-*N'*-(12-pyrrol-1-yldodecyl)-4,4'- bipyridinium ditetrafluoroborate. Then an aqueous mixture of enzyme and laponite particles was spread on the underlying poly(pyrrole-viologen) film. Water was removed under vacuum, leading to the formation of an adherent NR/laponite film in which NR was entrapped. No cross-linking agent like glutaraldehyde was used. Finally, a new hydrophilic viologen, the *N*-methyl-*N'*-[*N*(13 pyrrol-1-yl-4',7',10' tri-oxatridecanyl)-propionamido)]-4,4' bi-pyridinium ditetrafluoroborate (2), was electrochemically polymerized on the resulting modified electrode.

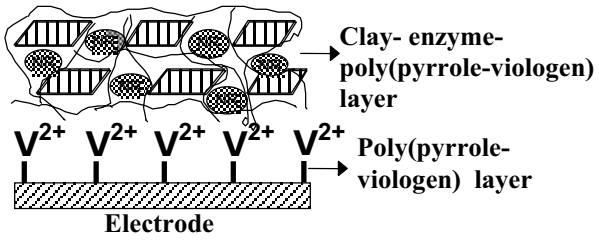

Scheme 1: The new NR modified electrode

3 Results

Thanks to the cation exchange properties of laponite, the dicationic viologen (2) was incorporated within the holes and microchannels of the bio-inorganic coating. The monomers were then polymerized around the immobilization NR in the interlamellas space of the clay that plays the role of a "template" for the electrogenerated redox polymer. The resulting electrode was studied by cyclic voltammetry in a 10 ml of 0.1 M Tris solution pH 7.5 (Figure 1). In the absence of nitrates, a stable quasi-reversible peak system appeared relative to the one-electron reduction of the polymerized viologen groups. In contrast, the presence of nitrates (5 mM) induces a marked increase in cathodic current associated with a decrease in anodic current of the dication / radical cation system of the polymerized viologen ($V^{2+/.+}$). Such

phenomenon unambiguously indicates an electrocatalylic reduction of nitrate by the laponite-NR-poly (2)/poly (1) electrode. Taking the increase in cathodic current (ΔI_{peak}) as an amperometric signal of the rate of the enzymatic reaction, figure 2 presents a calibration curve of ΔI_{peak} versus concentration of nitrates in the analyte solution. The cathodic ΔI_{peak} of the biosensor was linear with nitrate concentration from 5 to 163 µM, while a pseudo-plateau was reached for higher concentrations (above 2.5 mM). The detection limit of the bioelectrode is 0.5 µM and the sensitivity, calculated from the linear portion, is 94.7 mA M^{-1} cm^{-2}. K_M^{app} value, determined from the Lineweaver-Buck plot ($1/\Delta I_{peak}$ vs 1/C), is 0.21 mM.

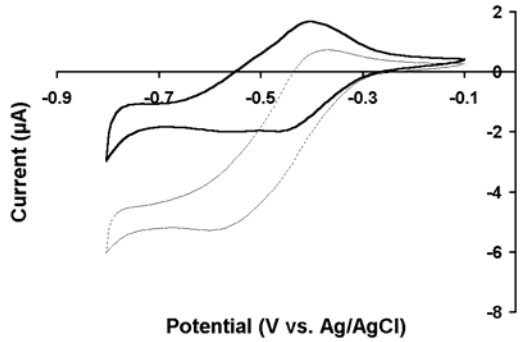

Figure 1: Cylic voltammetry of a new NR modified electrode in de-oxygenated 0.1 M of Tris solution (pH 7.5) in the absence (A) and presence (B) of 5 mM KNO_3; scan rate 5 $mV.s^{-1}$.

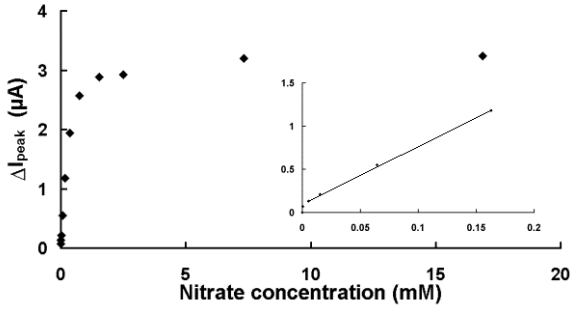

Figure 2: Cathodic ΔI_{peak} versus NO_3^- concentration resulting from cylic voltammetry performed in a de-oxygenated solution of 0.1 M of Tris solution pH 7.5 at a scan rate of 5 $mV.s^{-1}$.

4 Discussion

The observed catalytic behavior of the enzyme electrode in the presence of nitrate as well as the Michaelis-Menten shape of the related calibration curve demonstrate an electrical wiring of the immobilized enzymes. This indicates that the efficiency of the electrical communication between the underlying polymerized vilogens, poly (1) film and the viologens subsequently polymerized in the clay template, poly (2) film. These phenomena also illustrate the electron shuttle between the electrode surface and the NR molecules by electron happening between the polymerized viologen groups. Viologen dications are reduced into viologen radical cations at the electrode surface and re-oxidized by NR that catalyzes the reduction of nitrates (See reactions). The smaller K_m^{app} value than those encountered for similar biosensors means that the immobilized NR processes higher enzymatic activity and the present electrode exhibits higher affinity to nitrates. [4]. Then the clay template provides a biocompatible microenvironment around the enzyme molecules. Thanks to the hydrophilic character of the laponite particles and the absence of chemical reaction for the enzyme retention, no NR denaturation was thus observed. In comparison with other NR biosensors, this also reveals the absence of steric constants for the diffusion of nitrates and nitrites. The large permeability of the inorganic coating was not therefore decreased by the subsequent electrogeneration of the wiring polymer, poly (2). A preliminary study of the biosensor stability showed that it keeps 100% of its efficiency during 48 hours. Next, the loss of viologen signal and the enzyme denaturation decrease the efficiency to 68 % after 72 hours and 80.2 after 96 hours.

$$2\ V^{2+} + 2\ e^- \xrightarrow{\text{Electrode}} 2\ V^{+\bullet}$$

$$2\ V^{+\bullet} + NO_3^- + H_2O \xrightarrow{\text{NR}} 2\ V^{2+} + NO_2^- + 2\ OH^-$$

5 Conclusion

A new bioelectrode design providing the successful immobilization and electrical connection of NR was described. This biosensor fabrication was based on the "in situ" electrogeneration of a wiring redox polymer within an inorganic template allowing the soft enzyme immobilization. The final device represents in terms of biocompatibility and enzyme activity, a considerable advance over the previous designs of NR biosensors based on hydrophobic polymers.

References

[1] S. A. Glazier, E. R. Campbell and W. H. Campbell, *Anal Chem.* 70, (1998) 1511-1515

[2] B. Strehliz, B. Gründig, K.-D. Vorlop, P. Bartholmes, H. Kotte and U. Stottmeister, *Fresenius J. Anal. Chem.* 349, (1994) 676-678

[3] S. Cosnier, *Biosensors and bioelectronics* 14, (1999) 443-456

[4] D. Kirstein, L. Kirstein, F. Scheller, H. Borcherding, J. Ronnenberg, S. Diekmann and P. Steinrücke, *J. Electroanal. Chem.* 474 (1999) 43-51

[5] H. Borcherding,, S. Leikefeld, S. Frey, S. Diekmann and P. Steinrücke, *Anal. Biochem.* 282 (2000) 1-9

Acknowledgements

The authors wish to thank the Commission of the European Communities Research Directorate for their support under the PEBCAT project contract N° EVK1-CT-2000-00069.

Detection of proteins using a piezoelectric/biosensitive film

P. Inácio, J.N. Marat-Mendes, C.J. Dias
Dep. de Ciência dos Materiais, Secção de Materiais Electroactivos (CENIMAT)
FCT-UNL, Torre, 2829-516 Caparica, Portugal

Summary: *Most piezoelectric biosensors use thin piezoelectric crystals, either as longitudinal acoustic waves devices (e.g. quartz crystal microbalances, QCM), or as bulk/surface acoustic waves (SAW) devices. A system is described in which acoustic waves are launched in very thin (25 microns) polymer films to produce a transversal acoustic waves device. A film system, made of PVDF and a porous membrane, to be used in protein detection has been tested. Current work with this system is presented.*

Keywords: *Biosensor, Piezoelectricity, PVDF.*
Category: *Biosensors*

1 Introduction

Thin quartz crystals for the detection of small additions of bound mass to its surface have been used over a period of more than 40 years. This paper illustrates a related technique where a film system made of a piezoelectric polymer (PVDF Solef, from Solvay) and a porous membrane (Immobilon-P, from Millipore Co.), with a high protein binding capacity, are used to produce an oscillatory resonant device. The Immobilon-P membrane is a special type of porous PVDF.

2 Operating principle

Fig.1 shows a schematic of a generic piezoelectric film clamped between two pairs of electrodes: one set of electrodes acts as the transmitter and the other as the receiver. The central part (without electrodes) of this film will act as the biosensitive area. When a voltage signal is applied to the transmitter an acoustic wave is launched across the film, due to the piezoelectric effect, whose velocity is given by $v=(\rho s^E_{11})^{-1/2}$ [1], where s^E_{11} is the elastic compliance and ρ is the density of the film (for PVDF: $s^E_{11}=2{,}7x10^{-10}\ m^2/N$ and $\rho=1{,}8\ g/cm^3$). If L is the length of the film between the clamping electrodes, the resonance frequency of the film is given by:

$$f_o=(1/2L)\ (\rho s^E_{11})^{-1/2} \qquad (1)$$

The deposition of a small mass in the surface of the film has the effect of changing the film density. It can be shown [2] that there will be a change in the resonance frequency given by:

$$\Delta f/f=-(1/2)\Delta m/m \qquad (2)$$

Where Δf is the change in the original frequency f produced by an addition of a mass Δm to the surface of the film with a surface mass of m. By connecting this set-up to an appropriated electronic circuit, an oscillatory resonant device is obtained.

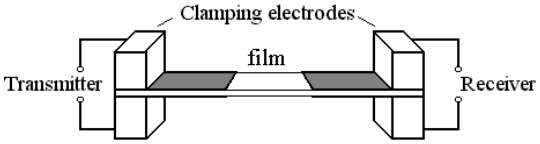

Fig. 1. *A piezoelectric film clamped between two pairs of electrodes.*

3 Polymer film system

Fig.2 shows a schematic of the film system used in our device. In the central part of a PVDF Solef strip (typical dimensions 7 cm x 1 cm x 25 μm) the aluminium electrodes are etched off. After cutting, a piece of Immobillon (length 5-20 mm) is thermally 'glued' in this central part by applying a very small pressure at a temperature of about 170°C. In the end,

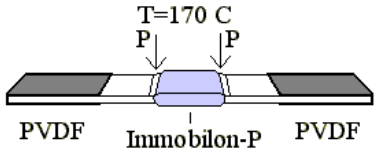

Fig.2. *PVDF/Immobilon/PVDF film system.*

film systems of PVDF/Immobilon/PVDF are obtained (typical dimensions are 7 cm x 1 cm). The areas of the aluminium electrodes that will be in contact with the solution are protected with a thin plastic layer. The Immobilon acts as the biosensitive area and the piezoelectric PVDF in the extremities is responsible for the film oscillation. Fig. 3 shows a schematic of the film container and oscillating circuit used with these films.

4 Oscillating circuit

A block diagram of the oscillator electronics is shown in Fig. 3. The charge produced in the receiver

goes to a charge amplifier where it is converted to a voltage and fed to a phase shifter. The phase shifter ensures that the signal being applied to the transmitter is at the correct phase so as to reinforce the acoustic wave travelling back and forth in the film. With the correct phase and sufficient gain in the feedback loop self-sustained oscillation in the film is achieved. The output from the circuit is its frequency of oscillation.

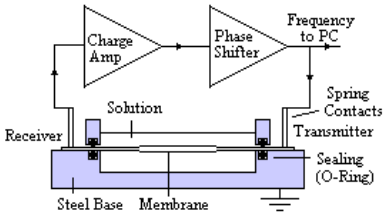

Fig. 3. *Oscillator schematic of the PVDF/Immobilon/PVDF system.*

5 Experimental

The response of the device illustrated in fig. 3 was tested with the protein bovine serum albumin (BSA). Fig. 4 shows typical results for the oscillation frequency of the device over time. The film starts oscillating in air. After stabilization of the oscillation frequency, the Immobilon-P (in the central part of the film) is wetted with methanol (to become hydrophilic, so it can adsorb proteins). As expected [2], a sudden drop in the oscillation frequency is observed. After 2 minutes the film is totally immersed in phosphate buffered solution (PBS) and again there is a small drop in the oscillation frequency. After frequency stabilization, a certain volume of a BSA solution of known concentration is added to the container. Immediately a rise in the oscillation frequency is observed (the inserted graphic in fig. 4 shows this more clearly). The absorption/adsorption of protein in the films was verified with a protein staining protocol. Several experiments of this type were made, where the BSA concentration was varied. Fig. 5 shows results obtained is these experiments, where it can be seen that this device has a frequency response related to the BSA concentration.

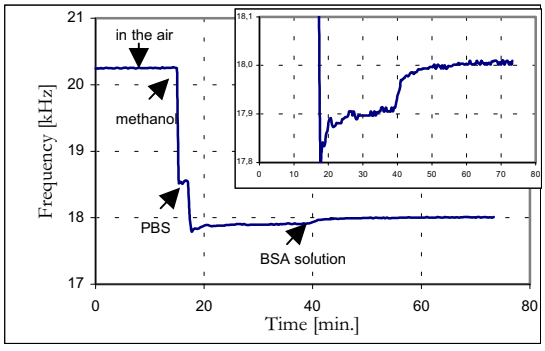

Fig. 4. *Typical results for the oscillation frequency over time in the experiments with BSA solutions. The inserted graphic shows an ampliation of the frequency scale.*

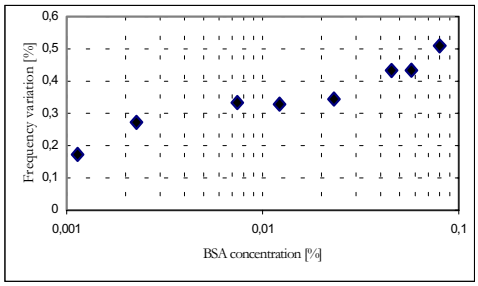

Fig. 5. *Frequency response of the device versus BSA concentration.*

6 Current work

Currently, work to ensure the reproducibility of results is being done by establishing well defined and precise measurement protocols. Also, the device is being tested with other types of proteins, like antibodies and antigens, in order to establish calibration curves for different proteins. After this step, work in the detection of antibody/antigen binding will be undertaken.

As it can be seen in the graphic of fig. 4, the device reacts to BSA with an increase in the oscillation frequency. However, as predicted by Sauerbrey equation (eq. 2) a decrease should be observed. But this equation can be applied if there is only adsorption of mass over the surface of the film. In our films there is not only adsorption of mass in the surface of the film, but also absorption of mass in the bulk of the film. Thus, a more complicated situation results, and other factors like the elastic properties of the film must be evaluated. Work in the development of a theoretical model that accounts for this behaviour needs to be done in the future. Towards this goal, electromechanical characterization of these films is currently being done.

7 Conclusion

We showed that the proposed device has a frequency response related to the BSA protein concentration. Therefore, this system can be suitable for protein detection (such as antibodies and antigens). After conclusion of current work we expect to be in a position that allows us to design and build a comercial prototype.

References

[1] - H. Ohigashi. " *Electromechanical properties of polarized polyvinylidene fluoride as studied by the piezoelectric resonance method*". J. of Applied Physics, Vol. 47, No 3, March 1976.

[2] - P.W. Walton, M.R. O'Flaherty, M.E. Butler, P. Compton. "*Gravimetric biosensors based on acoustic waves in thin polymer films*". Biosensors & Bioelectronics 8 (1993) pp. 401-407.

High Sensitivity detection of biomolecules by Microinductive Si technology based devices

S. Martínez[1], N. Yaakoubi[1,2], C. Serre[1], A. Pérez-Rodríguez[1], J. R. Morante[1], J. Esteve[2], R. Pérez-Castillejos[2] and J. Montserrat[2]

[1]EME- Departament d'Electrònica, Universitat de Barcelona, Martí i Franquès 1, 08028 Barcelona, Spain.
email: smart@el.ub.es
[2]Centre Nacional de Microelectrònica CNM-CSIC, Campus UAB, 08193 Bellaterra, Spain

Summary: *Inductive-based devices integrated with standard CMOS Si technology for high sensitivity bio-sensing applications have been designed and fabricated. Sensing principle is related to the changes of the coil inductance determined by the presence of a certain density of magnetic particles (MP's) in the device. These particles act as markers of the bio-molecule to be detected. The experimental data show that it is possible to detect less than 3 particles by 100x100 μm^2 active sensor surface, which is compatible with high sensitivity bio-sensing detection. The introduction of a ferromagnetic layer in the device design leads to an important increase in the sensitivity of the device.*

Keywords: *biosensor, magnetic particles*
Category: *6*

1 Introduction

The changes of the magnetic inductance determined by the presence of different densities of Magnetic Particles (MP's) in the active area of an integrated device can be used as source for sensor signal. This opens an interesting option for the detection of biomolecules. For it, both, MP's and the sensor surface, have to be functionalised with specific antibodies, and the MP's have to be fixed onto the surface by the formation of antibody-analite-antibody sandwich complexes [1]. In comparison with other kinds of magnetic biosensors [2], such as magnetic resistive or AFM based sensors, the proposed devices are characterised by their very high simplicity, a full compatibility with standard Si technology and materials, and a high flexibility. In this work, inductive-based integrated sensors fabricated using standard CMOS Si technology are presented for the development of low cost and high sensitivity biosensors.

2 Design and simulation

Figure 1 shows the simulation of the inductance variation for a device with a radius R=500 µm, 50 rings and two metal levels, versus the value of permeability µ. This simulation has been performed by finite elements (ANSYS) with the simple model reported in [3]. In this model, the presence of a certain density of MP's is modelled assuming a continuous layer with an effective magnetic permeability µ . As shown in the figure, changes in µ as small as 0.1 (in relation to µ=1) could be detected assuming an experimental resolution for the measurement of L of about 2 nH. This is related to the maximum device sensitivity of about 19 nH per unit change of µ, obtained at µ = 1. This suggests a high sensitivity of the device to the presence of a low number of MP's', for which the effective magnetic permeability would be close to 1.

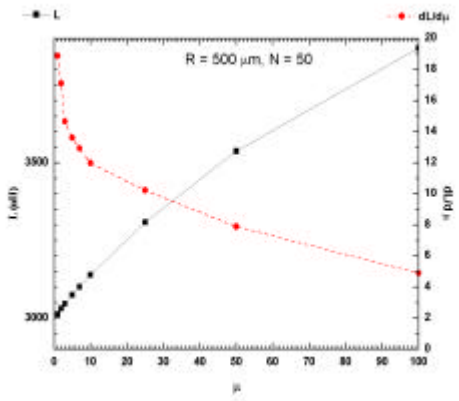

Fig. 1. L and dL/dµ simulated versus the effective magnetic permeability of the 1 µm thick active layer located on the coil.

An improvement in the device sensitivity can be obtained by the introduction of a ferromagnetic layer. Figure 2 shows the results of the simulation of the devices with and without a ferromagnetic layer (µ=1000, thickness 1µm) located at the back surface of the devices. This implies that the coils have to be fabricated onto a thin SiO_2 membrane. As shown, the maximum sensitivity of the device still occurs at µ= 1 and increases up to 40 nH per unity change of µ.

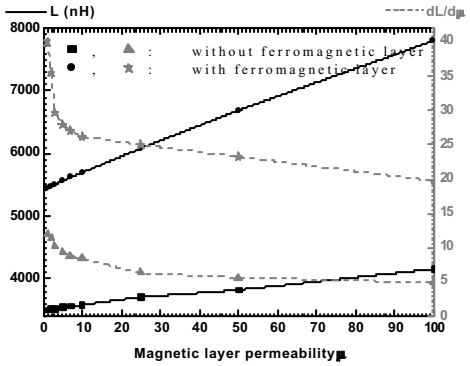

Fig. 2. Simulation comparison between the device sensitivity with or without the ferromagnetic layer

3 Fabrication and characterisation of the device

The devices have been fabricated with standard CMOS technology, using Al metal tracks and with the lowest separation between metal tracks technologically available in our laboratory (Figures 3, 4 and 5). The electrical analysis of the devices confirms the validity of the model developed for the simulations.

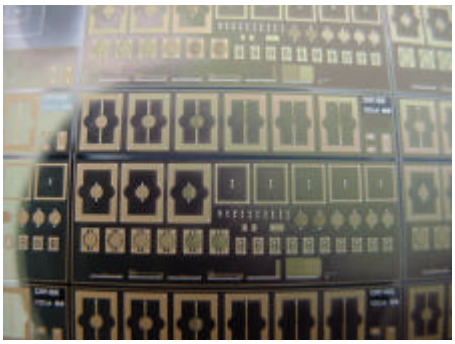

Fig. 3. Photographic view of a cell with the integrated devices

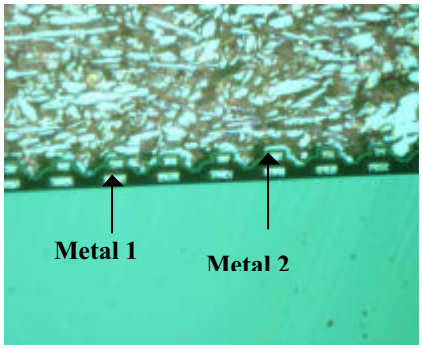

Fig. 4. Optical microscope cross-section image of the device

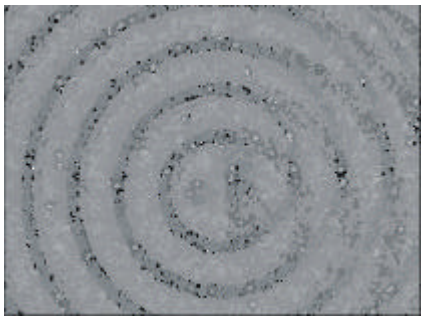

Fig. 5 Interferometric microscopic image of a coil with MPs.

The experimental data show that the biggest coils (R=500 μm) with the highest number of turns (N = 50) are sensitive to the presence of the MP's, being possible to detect up to 2,5 particles by 100 x100 μm^2 active surface. For this, commercially available paramagnetic particles have been used [4]. According to the sensitivity estimation proposed by Baselt et al [2], this would lead to a minimum detectable concentration of the analyte as low as $5x10^{-16}$M which is much better than sophisticated biological instrumentation. These first data corroborate the ability of the proposed sensor technology for very high sensitivity bio-sensing detection. First devices have also been fabricated onto micromachined Si membranes, for the electrochemical deposition of a ferromagnetic film (Fe, NiCo) at the back membrane surface. This has also required an optimisation of the process to minimise stress gradients in the membranes. The first data on the enhanced sensitivity of the devices to the presence of the MP's will be presented and discussed.

References

[1] K. Kriz, J. Gehrke, D. Kriz: Advance toward magneto immunoassays, *Biosensors & Bioelectronics*, 13 (1998),

[2] D.R. Baselt et al, "A High Sensitivity Micromachined Biosensors", Proc. IEEE **85**, pp. 672-680, 1997.

[3] S. Martínez, N. Yaakoubi, C. Serre, A. Pérez-Rodríguez, J. R. Morante, R. Pérez, J. Esteve, J. Montserrat, "Integrated inductances for Si-technology based high sensitivity biosensors", IECON 2002-28th Annual Conference of the IEEE Industrial Electronics Society/ 2002 International Conference on Industrial Electronics, Control and Instrumentation, (Sevilla, Spain, November 2002), The Institute of Electrical and Electronic Engineering , 2002 (IEEE Catalog Number: 02CH37363C)

[4] http://www.dynal.no

Silicon Microfluidic Devices Manufactured by Deep Reactive Ion Etching

Andreas Menz

Protron Mikrotechnik GmbH, Universitätsallee 5
D - 28359 Bremen / Germany
Phone: +49-421 / 22348-18 (-19), Fax: +49-421 / 22348-20
Email: menz@protron-mikrotechnik.de

1 High Aspect Ratio Etching

Deep Reactive Ion Etching (DRIE, Deep RIE, or ASE; patented by Robert Bosch GmbH) is a silicon etching process enabling the manufacturing of structures with high aspect ratios. The process bases on an alternating of ion etching and sidewall passivation of structures.
Protron's engineers have many years experience in development and manufacturing of MEMS with Deep RIE. The process is the most versatile silicon bulk micromachining process in microsystem technologies. It allows the realization of 3-dimensional structures with a high degree of design freedom. Protron uses the process for the realization of devices in almost every field of MEMS applications, such as microfluidics, microoptics, sensors, and actuators.

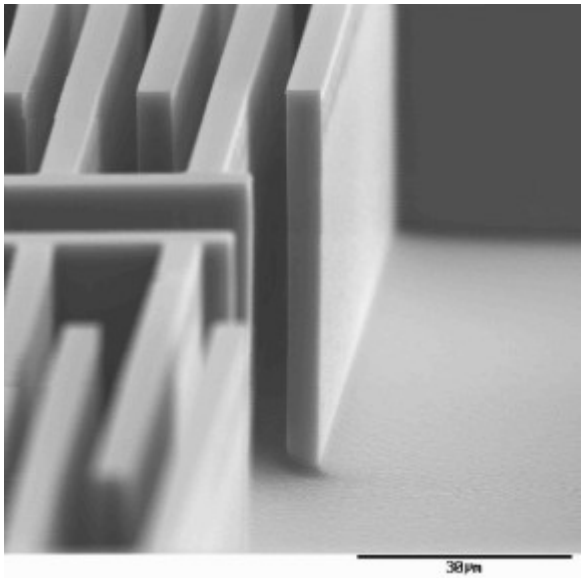

Fig.1 Comb drive manufactured with DRIE.

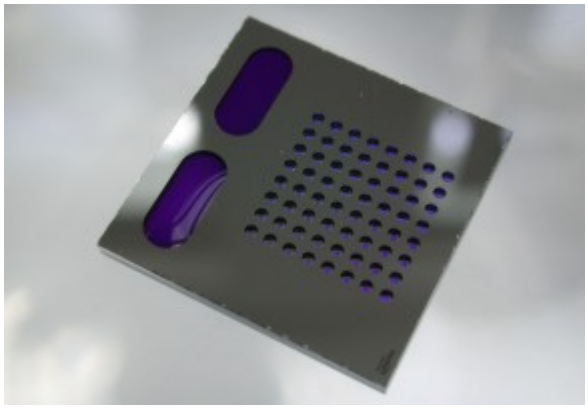

Fig. 2 Mircofluidic titerplate manufactured with DRIE.

New technology for the fabrication of a micropipette driven by ferrofluids

R. Pérez-Castillejos, J.A. Plaza, J.Esteve

Centre Nacional de Microelectrònica IMB-CNM-CSIC
Campus UAB, 08193-Bellaterra (Barcelona) SPAIN, e-mail: raquel@cnm.es

Summary: *This paper presents the fabrication process of a new micropipette driven by ferrofluids. The micropipette consists of a microchannel fabricated on polysilicon with a diameter of 4x1 μm. Perpendicular micropippette apertures are achieved by Focused Ion Beam. In addition, a new method based on controlled rupture of the microchannels due to stress concentration has been also developed, obtaining good and reproducible results. Advantages of ferrofluids are very suitable for disposable and easy replacement of micropipettes. First results will be presented during the conference.*

Keywords: *microfluidics, ferrofluids, Microsystems technology, FIB*
Category: *2 (Materials and technology); 7 (Fluidic devices)*

1 Introduction

During the last decade, traditional chemistry has been shaken up by the incorporation of microfluidics. Chemistry of the nano- and picoliter range takes advantage of the reduction of sample volumes and of response time, and especially the possibility of increasing the throughput and automation of the processes for it allows massive parallel chemistry to be performed.

In this paper, a novel micropipette is presented based in ferrofluidic pumping action. The pipette consists of a channel shared by both the ferrofluid and the reactant (fig. 1). When the volume of ferrofluid is shifted by means of an external magnetic field, over- and under-pressures are generated at the nozzle of the pipette, thus, shifting the reactant together with the ferrofluid. Under pressures can be used to grip micrometric bodies, e.g. cells. At the pipette end opposite to the nozzle, a reservoir is connected to the channel in order to allow the ferrofluid insertion. The length of the pipette was designed to prevent the ferrofluid and the reactant from contacting
.

2. Fabrication technology

Ferrofluids were chosen as the driving agent because, as a magnetic material, they can be controlled through an external magnetic field allowing to dynamically seal the channels up to pressures of 0.2bar, with minimum wear [1, 2]. As liquids, ferrofluids allow hermeticity of the sealing, independently of the channel shape and size, at least, down to a few microns -ferrofluid flowing in a 6μm-deep silicon cavity anodically bonded to glass due to a NdFeB magnet below is shown in fig.6.

The micropipettes were fabricated as described in fig. 2. First, the body of the pipette was built by structuring a layer of deposited PSG oxide (~1.5μm). Second, the oxide layer was protected with Si_3N_4 during the fabrication of cavities in the backside of the wafers (TMAH). Part of the cavities will be the ferrofluid reservoirs whereas the rest will serve to release the pipette nozzle, leaving it standing-alone (fig. 3). Then, the nitride was removed and a layer of polysilicon (0.5μm) was deposited. At this point, the body of the pipette is completely surrounded by polysilicon.

In order to obtain a channel, the PSG oxide has to be eliminated, leaving only the polysilicon walls. Hence, windows in the polysilicon layer have to be opened to allow the access to the PSG oxide layer. Three different approaches were proposed to open the windows: localized anisotropic wet-etching, Focused Ion Beam (FIB) etching, or simply causing the pipette nozzles to break at pre-determined points. The first technique is specially indicated to open windows at the insertion cavities for they are intrinsically reservoirs. The second (FIB etching) allows to etch extremely small and well-defined windows in the pipette nozzle (fig. 5) whereas the effectiveness of the controlled rupture technique is demonstrated in figure 4. FEM simulation (4a) and obtained results (4d) coincide perfectly.

3. Conclusions

A novel design of micropipette is presented, that have neither movable parts nor electric contacts. These two characteristics facilitate enormously the use and fabrication of the micropipette, even allowing to consider it disposable. The micropipette can generate both over- and under-pressures, thus, allowing it to operate in both dosing and gripping functions. Detailed results of the fabrication process and of the characterization of the multiple devices fabricated will be presented.

Acknowledgement: This work is funded by the Spanish Ministry of Science and Technology

through the MINAHE project (TIC2002-04280-C03-02).

REFERENCES

[1] R. Pérez-Castillejos, A. Baldi, J.A. Plaza, J.Esteve, A. Menz, W. Benecke, N. García, J. Higuero, T. Díez-Caballero, K. O'Grady, S. Wells, V. Patel, K. Johnson, D. Kriz, and D. Hurley, Procs. Nanotech'99, Montreux, November, 1999.

[2] R. Pérez-Castillejos, J. Esteve, M. C. Acero, A. Menz, and K. Kriz, Proc. Transducers'01, pp. 954, Munich, 2001, ISBN 3-540-42150-5 Springer-Verlag.

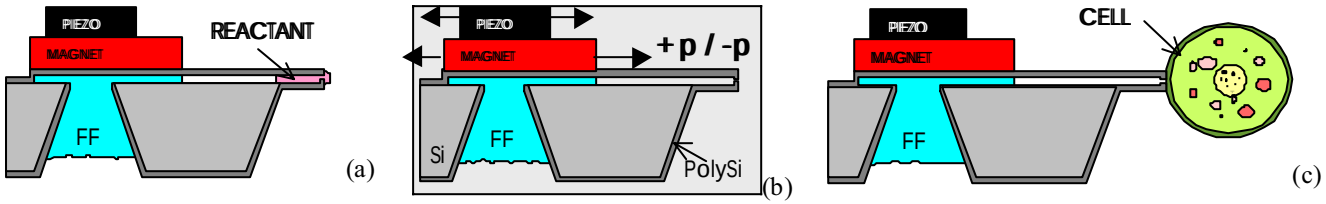

Figure 1. Micro/nanopipette proposed uses: the over- and under-pressures generated at the nozzle of the pipette (b) can be used in order to dispense liquids in controlled fashion (a) as well as to grip minute objects, e.g. cells (c).

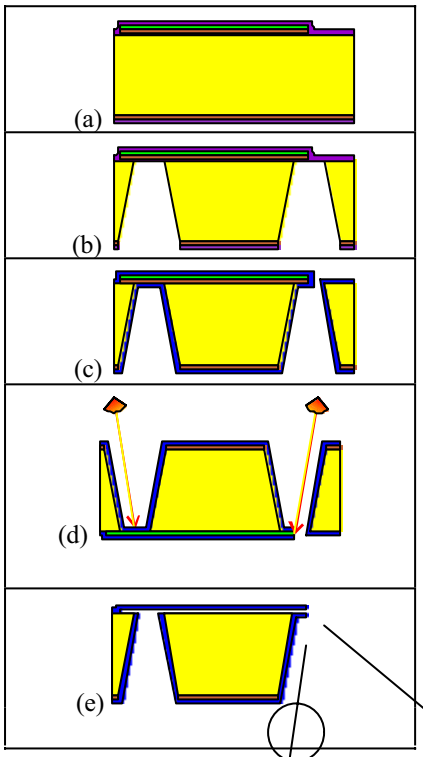

Figure 2. Fabrication flow-chart.

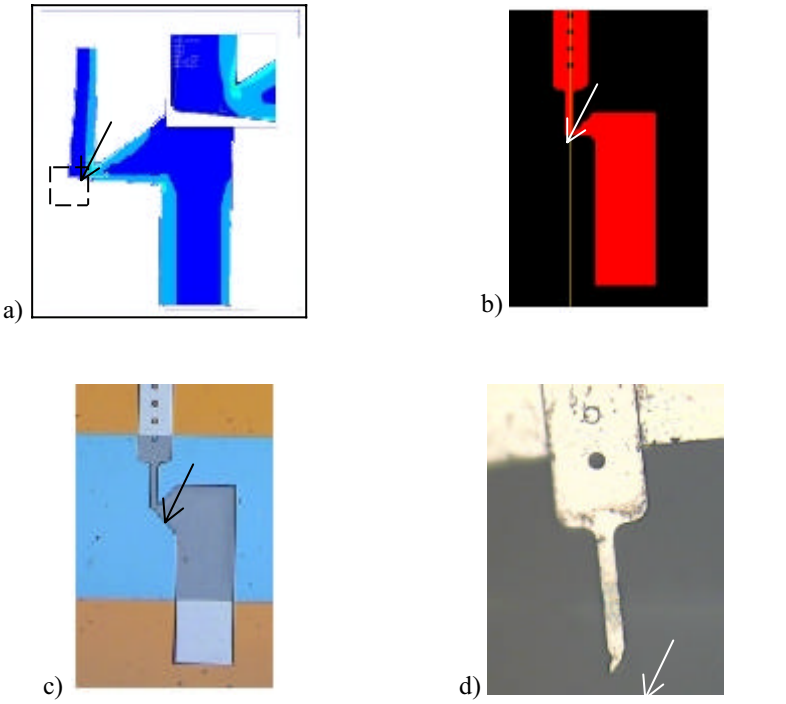

Figure 4. Pre-determined rupture of the nozzle: mechanical simulation (a), mask (b), prior to the polysilicon deposition (c), and obtained rupture (d).

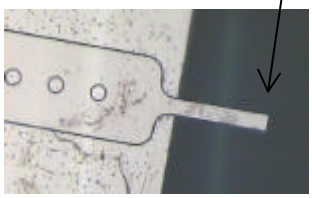

Figure 3. Photograph of a µpipette nozzle 11µm-wide and 2.5µm-high (inner diameter: 10 x 1.5µm^2)

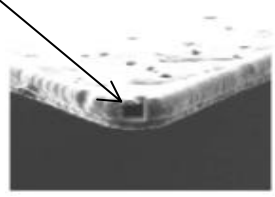

Figure 5. FIB perforation (1x1µm^2) of a PolySi nozzle.

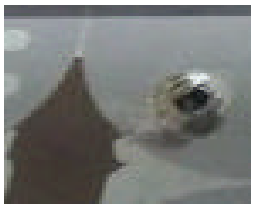

Figure 6. FF control in a 6µm-high cavity (NdFeB magnet).

Novel Low Temperature SOI-Based Fabrication Process of HF - Microelectromechanical Resonators

J. Bartholomeyczik, P. Ruther, A. Buhmann, K. Steffen[1], and O. Paul
IMTEK - Microsystem Materials Laboratory (MML), University of Freiburg
Georges-Koehler-Allee 103, D-79110 Freiburg, Germany
e-mail: bartholo@imtek.de phone: +49 761 203 7195 fax: +49 761 203 7192
[1]IMTEK - Process Technology

Summary: *We report on the fabrication, simulation, measurement setup, and preliminary testing of microelectromechanical high frequency filters (HF) using a novel micromachining technology. The fabrication process features the combination of (i) silicon-on-insulator (SOI) substrates, (ii) bulk silicon micromachining applying the ASE® process, and (iii) electroplating. Key features of the microelectromechnical filter are 200 nm wide transducer electrode gaps, a single crystal silicon (SCS) resonator structure and low temperature, CMOS compatible processing. In combination with an improved theoretical model these structures allow for the systematic analysis of damping effects of HF resonators.*

Keywords: *resonator, filter, SOI, equivalent network simulation*
Category: *(2) Materials and technology*

1 Introduction

Several approaches to fabricate microelectromechanical high frequency filters have been reported in the past. Most of the applied fabrication processes either use thick polysilicon layers in combination with electroplating [1] or SOI silicon electrode and resonator structures [2]. While yielding excellent high-*Q* resonators, the first approach is not post-CMOS compatible due to high processing temperatures. The second approach is not capable of producing high-*Q* resonators due to the fact that the relevant transducer gaps are limited by the available lithographic resolution and the maximum aspect ratio of the anisotropic etch process. Proposed concepts of post-processing gap adjustment [3] require high DC operating voltages to maintain the reduced transducer gap and so far have only been fabricated in combination with polysilicon structures. Thus none of these approaches is capable of producing CMOS compatible resonators that at the same time offer high-*Q* values.

2 Resonator Design

The realized microresonators feature 10 µm thick, SCS, clamped-clamped resonating beams. The beams are flanked by electroplated Au input and output electrodes. The beam is electrostatically actuated into mechanical resonance through the input electrode. The change in capacitance between the beam and the output electrode converts the mechanical oscillation back into an electrical signal. A large variety of resonator structures with designed resonance frequencies between 480 kHz and 526 MHz have been fabricated. To inspect the influence of different damping effects several resonators with different beam widths have been designed for each resonance frequency.

3 Fabrication

Figure 2 shows a schematic representation of the relevant process steps of the novel fabrication technology. A 10 µm thick SOI layer is structured using anisotropic silicon etching (ASE® process) to define beam and anchor structures (Fig. 2(a)). Afterwards a 200 nm thick sacrificial layer is deposited in a CVD process (Fig. 2(b)). To allow for electric contacting of the beam, this layer is patterned using thick DNQ/Novolak photoresist on top of the non-planar substrate (Fig. 2(c)). The seed layer for electroplating of the electrodes and beam contacts is deposited in a sputter process. As shown in Fig. 2(d), following thick resist pattering with critical dimensions in the micrometer range, a metal etch step is used to remove the seed layer covering the resonator beam. Finally, a

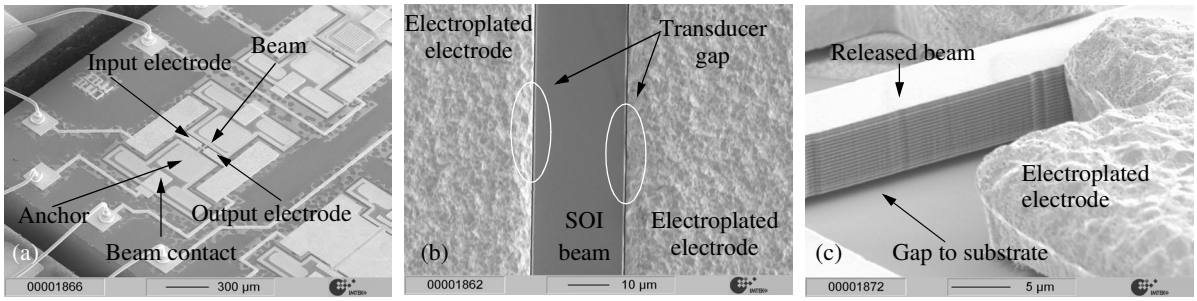

Fig. 1: SEM micrograph of (a) wire bonded resonator test chip, (b) top view of resonator with a 200 nm wide transducer gap, (c) clamped-clamped beam released from the substrate with part of an electroplated Au electrode.

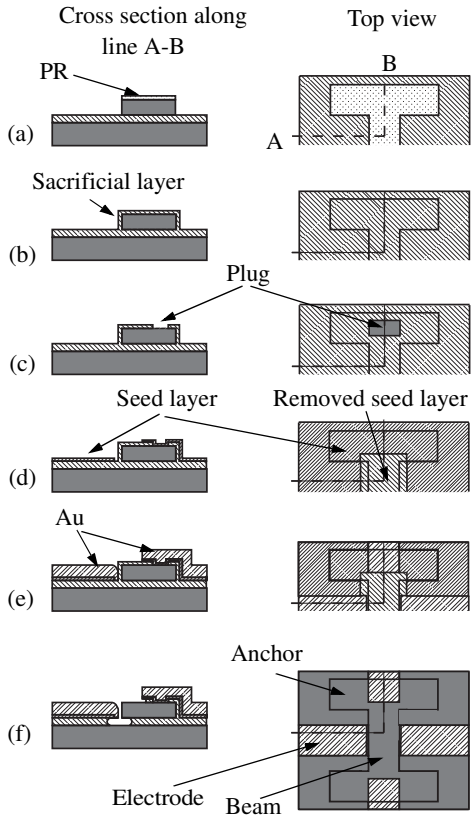

Fig. 2: Schematic representation of process steps for resonator fabrication: (a) ASE process to structure the SOI layer, (b), (c) deposition and patterning of a sacrificial layer, (d) seed layer deposition and pattering, (e) electroplating, and (f) seed layer and sacrificial layer removal. The cross section is given along line A-B.

20 µm thick photoresist is patterned for subsequent electroplating of the transducer input and output electrodes (Fig. 2(c)). To release the resonator beam and electrically isolate the electrodes, the seed and sacrificial layer are removed in a wet etching processes (Fig. 2(f)). The entire fabrication process uses standard clean room equipment. Figure 1 shows several SEM micrographs of realized microresonators.

4 Modelling and Measurement

The resonators and their measurement setup are simulated using an electrical network simulation program as described in [4]. The electromechanical device characteristics are extracted from an non-linear finite element simulation using ANSYS®. In contrast to [4] a coupled electrostatic and mechanical simulation in combination with anisotropic mechanical properties for silicon is used. This leads to higher non-linearities and slightly different resonance frequencies. The four dominant *Q*-factors Q_{TED}, $Q_{clamping}$, Q_{volume} and $Q_{surface}$ as described in [5] were modelled for the given structures.

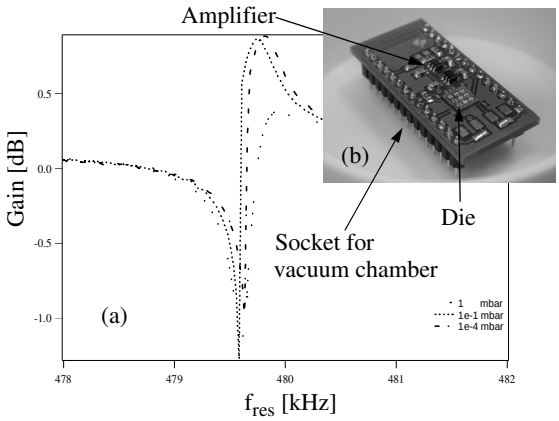

Fig. 3: (a) Diagram of the pressure dependence of a low frequency resonator and (b) PCB with a SMD, two stage amplifier and an attached resonator die.

Since simulation and preliminary testing showed that external amplification and measurement of the device does not allow for resonance detection, a small size, two stage, low noise amplifier circuit board as shown in Fig. 3 (b) has been fabricated. The resonator die is mounted directly onto the printed circuit board. All the electric paths are shorter than one hundreths of the signal wave length at the resonance frequency. Preliminary testing with a low frequency resonator to verify the working principle of the devices, using a voltage amplification at constant charge, have resonances shown as an example in Fig. 3 (a).

5 Conclusions

We have successfully developed a new low temperature fabrication process for HF microelectromechanical resonators. The designed resonators were systemically varied to allow for detailed analysis and modelling of the dominant dissipation phenomena which need to be well understood for optimal high-*Q* designs. After showing the functionality of these structures further evaluation is needed to characterize the behavior of the fabricated devices.

6 References

[1] W.-T. Hsu, J.R. Clark, and C.T.-C. Nguyen; Proc. Transducers'01, (2001) , pp.1110-1113.

[2] T. Mattila, O. Jaakkola1, J. Kiihamäki, J. Karttunen, T. Lamminmäki, P. Rantakari, A. Oja, H. Seppä, H. Kattelus, I. Tittonen; Proc. Transducers'01, (2001), pp. 1102-1105.

[3] D. Galayko, B. Legrand, D. Collard, L. Buchaillot, C. Combi; Proc. MEMS 2002, (2002), pp. 665-668.

[4] T. Vejola, T. Mattila; Circuit Theory Laboratory Report Series, Espoo (2000).

[5] K.Y. Yasumura, T.D. Stowe, E.M. Chow, T. Pfafman, T.W. Kenny, B.C. Stipe and D. Rugar; Journal of Micromechanical Systems, (2000), pp. 117-125.

High-aspect-ratio Three-dimensional Microstructures Fabricated by Two-photon-absorption Photopolymerization of SU-8

W.H. Teh[1,2], U. Dürig[2], M. Despont[2], U. Drechsler[2], R. Harbers[2], G. Salis[2], R. F. Mahrt[2], C.G. Smith[1] and H.-J. Güntherodt[3]

[1]Cavendish Laboratory, University of Cambridge, Madingley Road, Cambridge CB3 0HE, UK
Email: wht21@cam.ac.uk
[2]IBM Zurich Research Laboratory, 8803 Rueschlikon, Switzerland
[3]Institute of Physics, University of Basel, Klingelbergstrasse 82, CH-4056, Basel, Switzerland

Summary: We report the use of femto-second-pulsed near-infrared (λ = 796nm) laser for sub-diffraction-limit micro/nanofabrication via two-photon-absorption photopolymerization of SU-8. By scanning the focal volume through the interior of the thick (~1μm-500μm) SU-8 resist, high-aspect-ratio, three-dimensional (3-D) microstructures are fabricated on a shot-by-shot basis. Preliminary results suggest that even with low numerical-aperture optics (10x magnification, 0.30 NA) and off-the-shelf SU-8 resist, lateral spatial resolution of, but not limited to 950nm was realized, allowing photoplastic pillar structures with an aspect-ratio of up to 50 to be constructed. In certain cases, we have also exploited the low NA optics and high photopolymerization threshold to fabricate 3-D 'wavy' microflags, demonstrating real 3-D capabilities of the two-photon-absorption technique.

Keywords: *SU-8, Two-photon-absorption, Photopolymerization*
Category: *2 (Materials and technology)*

1 Introduction

The fabrication of high-aspect-ratio photoplastic micro/nano-structures based on SU-8 [1,2] are building blocks of many innovative devices, such as microgears, AFM/SNOM probes, microscanners, photonic crystals and microfluidic channels. However, it is difficult for conventional photolithography to fabricate high-aspect-ratio objects, especially real three-dimensional (3-D) structures smaller than the diffraction limit. This is solved by exploiting the non-linear absorption to femtosecond pulses through two-photon-absorption (TPA) photopolymerization. 3-D sub-diffraction-limit (SDL) resolution microstructures have been made previously [3-5] owing to the quadratic response of the TPA process. We further extend this method for the fabrication of SDL high-aspect-ratio 3-D photoplastic microstructures with the popular SU-8 ultrathick resist.

2 Results and discussion

For these experiments, we chose SU-8 2, 10 and 50 (Micro resist technology GmbH) to provide different thicknesses (~1-500μm) of SU-8, a negative resist consisting of a photoinitiator that polymerizes an organic resin. Here, we use an 80-MHz, 796-nm mode-locked Ti-sapphire laser oscillator as the light source, and a mechanical shutter to set the exposure time (4ms to 2s). The 69-70 fs laser pulses with a controlled average power of between 50 mW-400 mW, corresponding to laser pulse energies (LPE) of 0.63 nJ/pulse – 5.00 nJ/pulse and a peak power of 9.13 kW/pulse – 72.46 kW/pulse are used for the experiments. These laser pulses are focused by a 0.30 NA, 10x objective lens with a calculated Rayleigh diffraction limit of 3.24 μm. The SU-8/Si substrate is placed on a two-axis translation stage controlled by hand. BHF treated (100) Si substrates were used to improve the adhesion of SU-8.

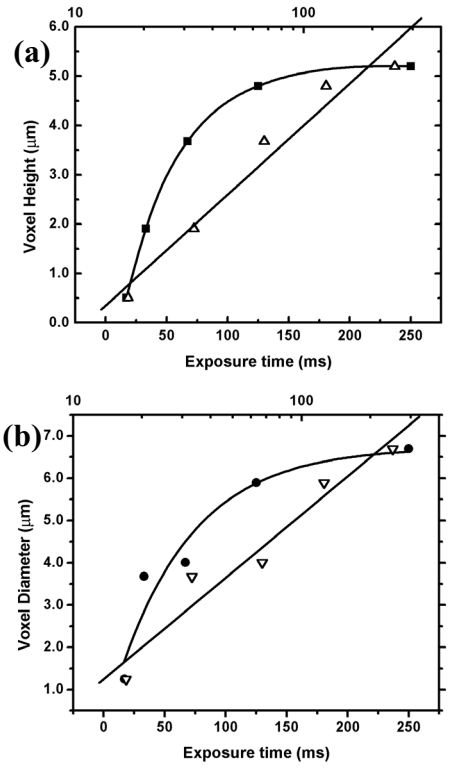

Fig 1. Voxel (a) height and (b) diameter as a function of laser exposure time. The same data are presented using both linear (solid symbols; bottom axis) and logarithmic (open symbols; top axis) coordinates.

Fig. 1 shows the characterization results (measured by atomic force microscopy) of TPA-exposed and PGMEA-developed voxels made by 1.88nJ/pulse (average power 150mW), 69fs laser pulses on a 5.4μm thick SU-8 10 as a function of exposure time. We see a threshold-like behavior of two-photon-photopolymerization, and a logarithmic dependence of the height and diameters on the exposure time similar to [3,5] for a different resin.

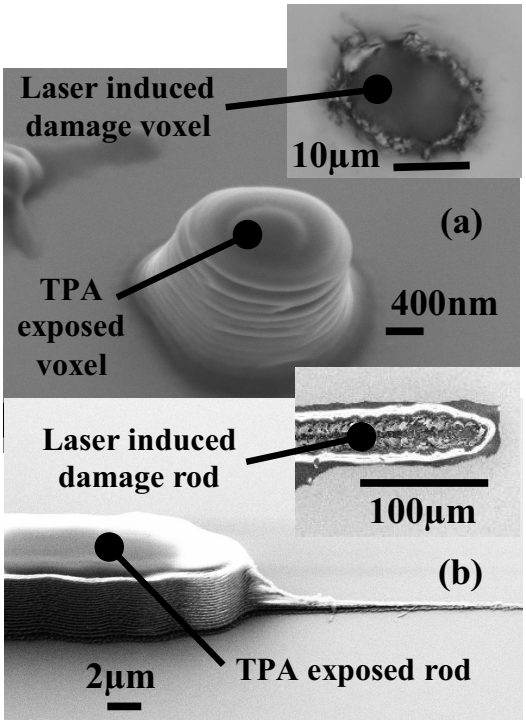

Fig 2. SEM micrographs of (a) a TPA exposed voxel with an LPE of 0.63nJ (Ave. P: 50mW) for 2 s. Inset: a typical laser induced damage to the SU-8 when using an LPE of 5.00nJ (Ave. P: 400mW) for 3 shots of 2 s exposure time, and (b) a TPA exposed rod with LPE of 3.09nJ/pulse (Ave. P: 247mW) moving at about 10-40μm/s. Inset: Laser-induced-damaged SU-8 when using LPE of 4.3nJ/pulse (Ave. P: 345mW) at the same speed.

Fig. 2 shows the SEM micrographs of TPA exposed voxels and rods, and compares them to typical laser-induced damage caused by high doses. Fig. 2 (a) shows voxel with a diameter of about 2.0μm, a dimension 62% of the diffraction limit imposed by the laser beam diameter. This opens up the potential of going far beyond the SDL in fabricating photoplastic microstructures, especially when higher NA optics and optimized SU-8 are used. We also see highly periodic (a periodicity of about 240nm) patterns caused by the standing waves of the laser light. Using the refractive index of SU-8 to be 1.67, this periodicity reveals an incident wave with $\lambda \sim 798$nm, similar to our laser wavelength. Fig. 3 shows the extremely high aspect-ratio (up to 50) of SU-8 pillars, made with an LPE of 3.75nJ with an average power of 300mW on a 500μm thick SU-8 50 resist. Here, the focal spot of the laser is moved up at a rate of about 1-3μm/s from the base. No pedestals around the pillars are found, verifying the sharp rise of the TPA threshold.

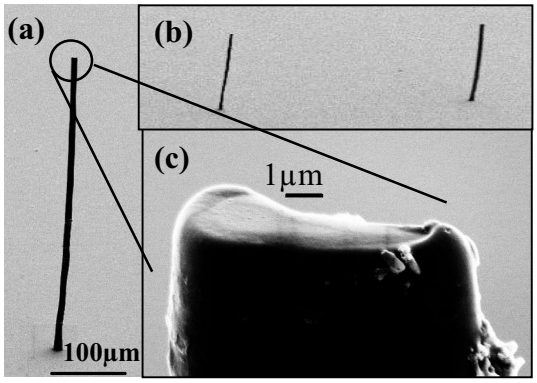

Fig 3. SEM micrographs of high-aspect-ratio SU-8 photoplastic pillars made by TPA photopolymerization with LPE=3.75nJ.

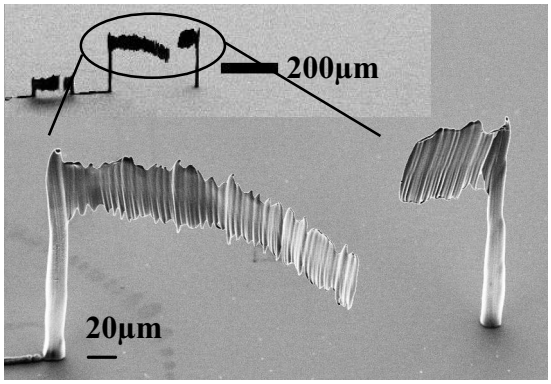

Fig 4. SEM micrographs of 3-D SU-8 photoplastic microflags made by TPA photopolymerization with LPE=3.75nJ.

Preliminary attempts to fabricate real 3-D microstructures are shown in Fig. 4. For these fabrications, we exploit the low NA optics and the high photopolymerization threshold to make suspended high aspect ratio vertical rods, which forms the 'wavy' flag. This is done with single shot exposures of the SU-8 by firstly scanning the laser focal spot in the vertical direction (to make the flag pole) and then followed by the horizontal direction (the flag). Because SU-8 is transparent to near-IR light, it allows the light to non-destructively penetrate into it, reinforcing the suitability for SU-8 as the transparent media. The quadratic dependence of the TPA rate on light intensity confines absorption to a highly localized area at the focal spot of the laser. This principle is used to fabricate real 3-D microstructures without the need to pile up 2-D layers to make a 3-D structure.

References

[1] N. LaBianca and J.D. Gelorme, *Proc. SPIE*, **2438** (1995) 846-852.
[2] M. Despont et. al., *Proc. MEMS '97*, pp. 518-522, Nagoya, Japan, 1997.
[3] S. Maruo, O. Nakamura and S. Kawata, *Opt. Lett.*, **22** (1997) 132-134.
[4] G. Witzgall et. al., *Opt. Lett.*, **23** (1998) 1745-1747.
[5] S. Kawata, H.-B. Sun, T. Tanaka, K. Takada, *Nature*, **412** (2001) 697-698.

UV photosensitive elastomer as a new mask for powder blasting microfabrication

A. Sayah, V.K. Parashar, A.G. Pawlowski, and M. A. M. Gijs

Institute of Microelectronics and Microsystems
Swiss Federal Institute of Technology Lausanne, CH-1015 Lausanne EPFL, Switzerland

Summary: *We report the use of a new photosensitive elastomer as a mask material for the three-dimensional microstructuring of glass using powder blasting technology. Spin-coated elastomer masks provide a promising alternative to metallic contact masks for the definition of microstructures. Mask thicknesses up to 100 μm with feature size down to 15 μm are obtained. We have investigated the resistance and selectivity of the elastomer mask to powder blasting and the effect of mask feature size on the glass micropatterning process.*

Keywords: *powder blasting, elastomer, mask technology*
Category: *2 (materials and technology)*

1 Introduction

The technique of powder blasting, historically used for glass decoration and surface cleaning from paint, has been introduced as a new advanced technology for microstructuring of brittle materials [1,2]. Powder blasting is a process, which removes material from the surface of a component by successive impact of abrasive particles. This technique has the advantage to extremely fast etch brittle materials such as glasses [1,2], ceramics [3] and ferrite materials [4]. There are only few other techniques that can be used to structure such materials in three dimensions. Figure 1 is a schematic diagram of the experimental set-up.

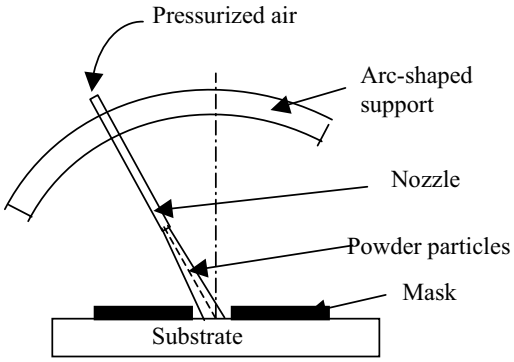

Figure 1. A schematic view of the powder blasting set-up.

The use of powder blasting to fabricate three-dimensional structures on the micrometric scale requires the use of a specific mask. It must have a good resistance and selectivity to the powder to allow the fabrication of micrometric structures. Metals have a good resistance to powder blasting and are favorable candidates to be used as a mask. Although metallic contact masks can be machined by laser ablation, only specific geometrical forms can be used. As the metal is not optically transparant, it is difficult to align the mask with respect to structures already existing on the substrat. To overcome this limitation, metallic masks have been fabricated by copper electrodeposition [5]. The main disadvantage of this solution is the time necessary to obtain a thick copper layer which resists well to the powder exposure. A third solution has been proposed which consists in using elastomer materials as a mask for powder blasting technology [6]. We have investigated in detail this last solution.

2 Photosensitive elastomer mask technology

We developed a mask technology based on a photosensitive elastomer material. In addition to its good resistance to powder blasting, the elastomer presents other very intersting properties: first, it is in liquid form and can be applied directly to the substrate by spinning. This allows to control the thickness of the masking layer. Second, its sensitivity to ultraviolet (UV) enables structuring by standard photolithographic techniques, third, it is a transparent material which makes alignment possible, and finally, arbitrary and disconnected objects can be microstructured in the glass substrate.

Different parameters have been optimised to obtain a very thick photoelastomer layer with a good photolithographic resolution. We use the flexopolymer LF55GN (a poly-urethane) [7]. This material is a photosensitive negative resist, which we pattern with standard UV radiation and is applied in thick layers as high as 100 μm. It is not a conventional resist, but a liquid elastomer, so before exposure, it needs to be protected with a cover layer of polypropylene (100 μm) to avoid mask contamination and to avoid direct contact

with oxygen, which inhibits the polymerization reaction. The process is schematically presented in figure 2. After exposure, the elastomer is simply developed in water as this exposed material is water-soluble.

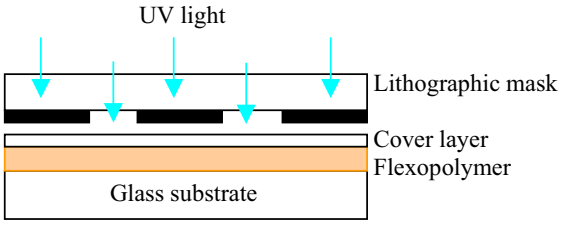

Figure 2. Schematic view of the elastomer masking technology.

3 Experimental results

Figure 3 shows clearly the high quality and good lateral resolution of the mask obtained using the photosenstive elastomer. The mask layer has a thickness of about 80 µm and has a vertical sidewall which is very smooth and straigth. This very intersting result can be explored to use this material for many applications where a thick resist layer and good lateral resolution are required.

The erosion rate of both the glass substrate and the elastomer mask has been investigated for different experimental parameters. The results demonstrate that the elastomer presents a high resistance to powder blasting. The ratio of the erosion velocity of the glass substrate to the elastomer mask, the selectivity, is as high as 1000.

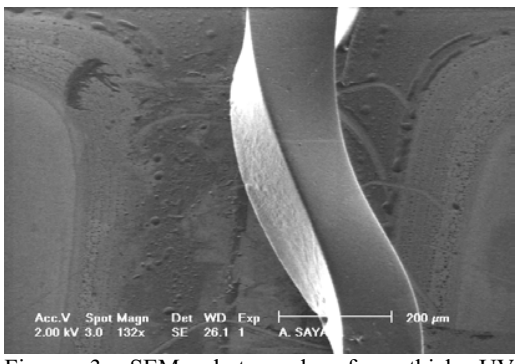

Figure 3. SEM photograph of a thick UV photosensitive elastomer layer after UV exposure and development.

The high quality of the photosensitive elastomer mask and its high erosion selectivity for etching brittle materials, have been combined to fabricate different sensors in glass, ceramics and magnetic materials. Accelerometers in glass have been realized by etching through 500 mm thick glass layer and are under test. Figure 4 presents an array of columns with square shape realized in a 1 mm thick soda lime glass substrate.

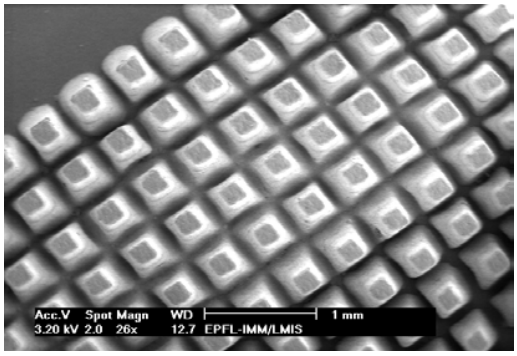

Figure 4. SEM photograph of an array of columns (100x100 µm^2 with interspacing of 100 µm) on glass material.

4 Conclusions

We have employed an elastomer material as a mask for powder blasting technology. We find that this material presents very interesting properties: direct application of the mask by spin coating, photo-sensitivity which permits the definition of arbitrary features, a high mask aspect ratio and an etching selectivity of 1000 with respect to glass, allowing to realize three-dimensional structures in mm thick glass substrate.

References

[1] E. Belloy, S. Thurre, E. Walckiers, A. Sayah, M. A. M. Gijs, Sensors & Actuators A, 84 (2000), 330-337.
[2] E. Belloy, A. Sayah, M.A.M. Gijs, Sensors & Actuators A, 92 (2001), 358-363.
[3] S. Ballandras. M. Wilm, M.A.M. Gijs, A. Sayah, E. Andrey, J.-J. Boy. L. Robert, J.C. Baudouy, W. Daniau, and V. Laude, in Proc. Of the IEEE Ultrasonics Symposium, Atlanta, Georgia, (2001), 871-874.
[4] M. Saidani, M. A. M. Gijs, J. Micromech. Microeng., 12, (2002), 470-474.
[5] H.Wensink, Henri V. Jansen, J.W. Berenschot, M.C. Elwenspoek. J. Micromech. Microeng. 10 (2000), 769-774.
[6] P. J. Slikkerveer, Mechanical Etching of Glass by Powder Blasting, Ph.D. Thesis, Eindhoven University of Technology (1999).
[7] See website, Mac Dermid (http:\\www. macdermid.com).

Sensor system to determine the supersaturation in industrial batch processes

Hanns-Erik Endres[1], Karl Neumeier[1], Eva Hammerl[1], Stephan Drost[1], Rudolf Müller[1], Michael Löffelmann[2], Alfons Mersmann[2]

[1] Fraunhofer-Institut für Zuverlässigkeit und Mikrointegration, Institutsteil München, Hansastraße 27d, D-80686 München, endres@izm-m.fraunhofer.de http://www.izm.fraunhofer.de
[2] Technische Universität München, Lehrstuhl für Feststoff- und Grenzflächenverfahrenstechnik, Boltzmannstraße 15, 85748 Garching

Summary: *The supersaturation is an essential parameter to control industrial batch crystallization processes. Until now a quantitative online measurement of supersaturation was not possible. A new sensor system consisting of an interdigitated capacitor (IDC) and a surface acoustic wave transducer is mounted on top of a peltier element, which allows a thermal cycling around the crystallization temperature. Together with a multivariate signal evaluation the online measurement of the supersaturation could be demonstrated.*

Keywords: *Interdigitated capacitor (IDC) sensor, surface acoustic wave (SAW) sensor, crystallization process, multivariate signal evaluation, Partial Least Square (PLS)*
Category: *10 (Applications)*

1 Introduction

Crystallization processes are widely spread in basic industries with a spectrum from adipic acid to pharmaceuticals. Most of the crystallization processes are batch processes with a certain supersaturation of the solution. The quality of the products (e.g. grain size and shape) is strongly dependant on the exact control of the supersaturation [1]. Until now an online measurement of the supersaturation was not possible.

2 Sensor head and measurement method

The measurement method is an anticipation of the crystallization in a certain volume and the detection of the beginning of the crystallization at the sensor's surface. The physical parameters of the fluid (viscosity, permittivity) affect the properties of the sensor. The sensor head consists of two planar sensors:

1) Interdigitated capacitor (IDC) with a grid width of 10 µm [2].
2) Surface acoustic wave element (SAW, resonance frequency of 52 MHz) [3].

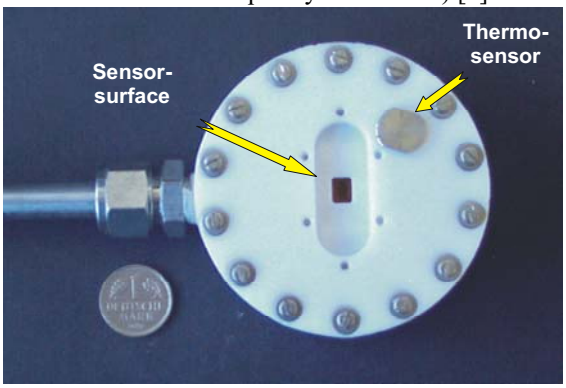

Fig. 1. Sensor head with SAW and IDC Sensor

Both sensors have an anticorrosive coating of SiC (silicon carbide) and are mounted on top of a peltier element, which allows a cyclic thermal process, which crosses the crystallization temperature T_C. The beginning of the crystallization process at the sensor's surface allows the determination of the crystallization temperature T_C. Using the known slope dC^*/dT of the solubility curve and measuring the solution temperature T_S with the sensor system, the supersaturation ΔC can be calculated [4]:

$$\Delta C = \frac{dC^*}{dT}(T_S - T_C) \qquad (1)$$

The sensors are mounted in a housing for crystallization vessels. Figure 1 shows the sensor head.

An experimental set up was mounted in a pilot plant station. The electronics is placed in a separate unit outside of the batch crystallization unit, shown in Figure 2.

Fig. 2. experimental setup with a crystallization vessel

The temperature cycle (shown in the solubility diagram Figure 3) has the following parts:

1. Equilibration
2. Cooling with phase transition
3. Heating
4. Equilibration

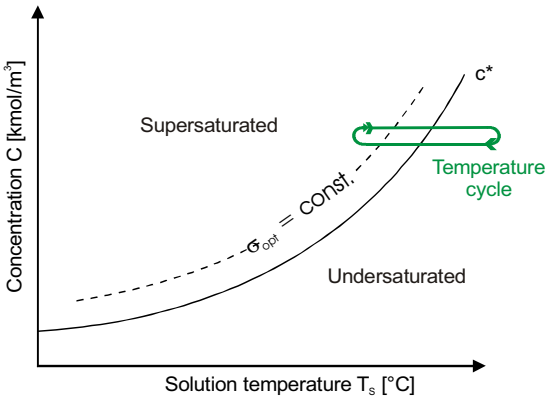

Fig. 3. temperature cycle of the sensor in the soluability diagram

During the heating step (3.) in the above mentioned temperature cycle the sensor's surface was sufficiently cleaned from crystals, deposited at the cooling step (2.). Throughout the temperature cycle the resonance frequency and the damping of the SAW sensor and the complex impedance of the IDC sensor (at ca. 16 kHz) are recorded.

3 Results

Most experiments have been performed with a solution of potassium nitrate (KNO_3) in water. An solution of 126.12 g up to 159.5 g KNO_3 in water achieves a crystallization temperature T_c from 14 up to 20 °C. Figure 4 shows typical sensor responses for potassium nitrate.

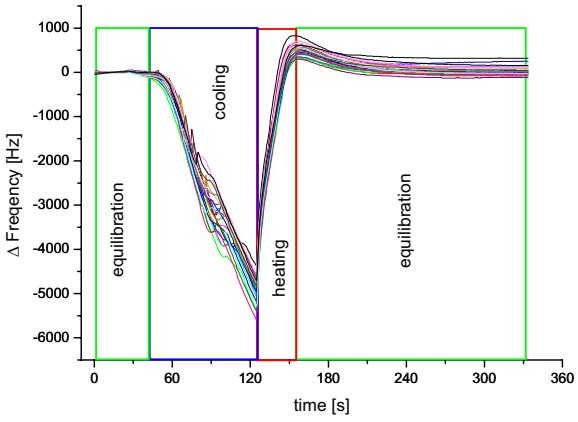

Fig. 4. typical sensor response (potassium nitrate with different concentrarions in water , SAW sensor)

The complexity of the physical and chemical processes around the crystallization temperature hindered an analytical calculation of T_C using the sensor signals. Therefore, a multivariate calibration with the partial least square method (PLS) was accomplished [5]. After some optimizing steps the Partial Least Square (PLS) evaluation delivers a reasonable result with an error within the needs of application (ΔT < ⅓ of the metastable temperature range). Figure 5 shows the evaluated / nominal comparison of the crystallization temperature T_C for 5 different solutions of potassium nitrate.

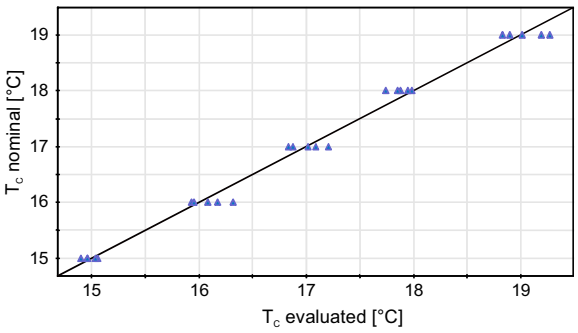

Fig. 5. Evaluated / nominal comparision for potassium nitrate

Experiments with 13 different substances proofed the results obtained with potassium nitrate.

4 Conclusion

The cyclic temperature variation of the sensor provides a sensor response ahead of the equivalent process in the batch reactor, so that an online control of the supersaturation is possible.

References

[1] Kühberger, M., Mersmann, A.; Improved product quality at a cooling crystallization process by measurement and control of supersaturation, Chemical engineering research & design 75-2(1997), 213-218

[2] Endres, H.-E.; Drost, S.; Optimization of the Geometry of Gassensitive Interdigital Capacitors, Sensors and Actuators B4(1991), 95-98

[2] Leidl, A.; Mader, B.; Endres H.-E.; Drost, S.: SAW and IDC devices as oil quality sensors, Analytica Conference '98, Abstracts, 544

[3] Mersmann A. ed.; Crystallization Technology Handbook, Marcel Dekker, New York 2001

[4] Beebe, K.R., Pell, R.J.; Seasjoltz, M.B.; Chemometrics – A practical guide, J. Wiley, 1998

Acknowledgement

This work was supported by the Bayerische Forschungsstiftung München.
The authors have to thank their industrial cooperator Grimm Labortechnik GmbH & Co KG, Ainring and several companies for measurements.

Improving the functionality of a prosthetic hand through the use of thick film force sensors

A. Cranny, P.H. Chappell, S.P. Beeby and N.M. White

University of Southampton, Dept. Electronics and Computer Science, Southampton, SO17 1BJ, UK
email: awc@ecs.soton.ac.uk

Summary: *A prosthetic hand has been instrumented with a range of sensors to measure grip force with the primary objectives of detecting touch and the onset of slippage of an item grasped by the hand. Two types of sensor have been used for this purpose: piezoresistive sensors to measure and monitor static forces and piezoelectric sensors to measure and monitor dynamic forces. All sensors have been fabricated using thick film printing techniques and their location and placement upon the prosthetic hand has been modelled for optimal performance.*

Keywords: *artificial hand, piezoelectric, piezoresistance, prosthesis, thick film*
Category: *10 (Applications)*

1 Introduction

An obvious problem with the majority of prosthetic devices is a lack of feedback control. In the case of a prosthetic hand, the user is unable to feel an item within its grasp – the user has no sense of what it is that they are holding beyond that which can be visually assessed. In certain situations, this could prove to be detrimental (e.g. the user would be unaware if they were holding a very hot or very cold item, possibly resulting in damage to the prosthesis or operator). More generally, the inability to monitor the grip force imposed on a grasped item means that the user can not be totally sure of the security of the grip and could be unaware (or have too little time to respond) should the object begin to slip from their grasp.

In attempting to remedy this problem, a number of dynamic and static force sensors have been located upon the inner surfaces of the mechanical digits and palm of a myoelectrically controlled prosthetic hand. Both piezoresistive and piezoelectric sensors have been utilised for this purpose, and both types of sensor have been fabricated using thick film printing techniques [1, 2].

When the hand closes around an object, the initial moment of first contact between the object and the inner surfaces of the prosthetic hand is detected by both the dynamic (near instantaneously) and static force sensors. As the hand continues to close, the static force sensors located in the mechanical finger tips directly measure the forces exerted upon the object. Continuous measurement of the grip forces allows the decision as to when the action of closing the hand should cease (and the current grip force be maintained) to be made by some local intelligence and thus remove the responsibility from the operator.

If the object begins to slip from the grip of the hand, the vibrations produced through friction are detected by the dynamic force sensors located in the palm of the prosthetic hand. This information is then used to re-activate the drive motors of the hand and increase the grip force, with the process being constantly monitored by the static force sensors.

2 Mechanics of the prosthetic hand

The prosthetic hand used in this project (see Fig. 1) is a prototype myoelectrically driven device designed at the University of Southampton and described elsewhere [3]. In use, the hand is controlled by the electrical signals produced by any convenient flexor-extensor muscle pair: one signal to open the hand and the other to close it. Each finger on the hand is individually controlled by its own dedicated motor, allowing independent flexion and extension of each mechanical digit.

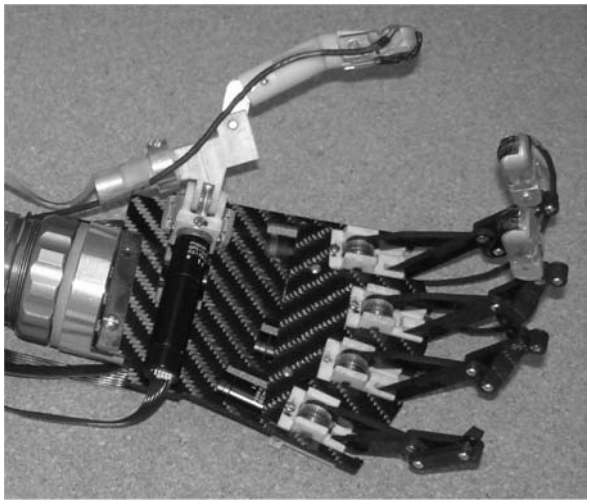

Figure 1. The Southampton-Remedi prosthetic hand [3].

The fingers are constructed from a number of interconnecting links, which when driven by the motors cause the finger to open or close in a natural curl pattern. The finger links are fabricated from a carbon fibre epoxy composite (to reduce the overall mass) except for the finger tip which is machined from stainless steel so that thick film sensors may be directly printed upon its surface.

The thumb is a two part assembly controlled by two orthogonal motors giving 2 degrees of freedom in movement. Moving the thumb in combination with any number of the finger units allows a range of natural grip postures to be adopted.

The palm of the prosthetic hand is also made from a carbon fibre epoxy composite to minimise the mass. The palm provides a common base for the location of all the finger motors as well as providing space for the attachment of force sensors and some electronic conditioning circuitry.

3 Sensor design

The static force sensors are used to directly measure the forces involved in a grip posture. The sensors exploit the piezoresistive properties of commercially available thick film resistive pastes. When printed and fired with electrically conductive end terminations in a planar configuration, these pastes form electrical resistors that exhibit a proportional change in their resistance with applied strain (gauge factor typically ranging from 8 to 10 [4]). The resistors are directly printed upon stainless steel cantilever structures located on the inner face of the distal tip of each mechanical finger. When a force is exerted upon the inner surface of a finger tip, the mechanical cantilever that supports the sensor is deflected and the resultant strain causes a proportional change in the sensor resistance which is easily detected by a simple resistance bridge circuit.

The piezoelectric sensors are used to monitor changes in grip force patterns. These sensors are fabricated from PZT (lead zirconate titanate) that has been rendered into a form that is suitable for thick film printing [5]. Multiple layers of this material are printed and fired upon an underlying electrically conductive pad on a separate supporting substrate before a final conductive pad is printed upon the top surface to yield a vertical stack. After polarization (electric field strength approximately 4 MVm^{-1} and temperature in the range 150C to 200C) these multi-layered devices exhibit a d_{33} piezoelectric coefficient of the order of 300 pCN^{-1}, which is somewhat lower than the equivalent bulk material coefficient. The piezoelectric sensors are located at various positions over the upper surface of the palm and respond directly to any vibration (e.g. as an object slips from the grip of the hand).

An estimation of an object's temperature held within the prosthetic hand can also be ascertained by the use of thick film resistors or thermistors printed upon the surfaces of the mechanical hand at locations of constant (or zero) strain. Such devices additionally provide first order temperature compensation for the other force sensors.

Acknowledgements

The authors wish to thank the Engineering and Physical Sciences Research Council (EPSRC) for their financial support under grant number GR/R95470.

References

[1] J.E. Brignell, N.M. White and A.W.J. Cranny, Sensor applications of thick-film technology, *IEE Proc. Part I, Solid State and Electron Devices*, 135 (1988) 77-84.

[2] N.M. White and J.D. Turner, Thick-film sensors: Past, present and future, *Measurement Science and Technology*, 8 (1997) 1-20.

[3] C.M. Light and P.H. Chappell, Development of a lightweight and adaptable multiple-axis hand prosthesis, *Medical Engineering and Physics,* 22 (2000) 679-684.

[4] N.M. White, Assessment of thick-film piezoresistors on insulated steel substrates, *Hybrid Circuits*, 20 (1989) 23-27.

[5] S.P. Beeby, A. Blackburn and N.M. White, Processing of PZT piezoelectric thick-films on silicon for MicroElectroMechanical Systems, *Journal of Micromechanics and Microengineering*, 9 (1999) 218-229.

A Low-g Accelerometer for Automotive Applications with Monolithic Multiple-Axes Integration

M. Rose, K. Kapser, M. Aikele, R. Gottinger, B. Hartmann, R. Burghardt*, H. Seidel**

Conti Temic microelectronic GmbH, MEMS Design & Technology,
Eugen-Sänger-Str., 85649 Brunnthal-Nord / München, Germany, konrad.kapser@temic.com
* Continental Teves, Guerickestr. 7, 60488 Frankfurt/Main, Germany, roland.burghardt@contiteves.com
** Saarland University, Chair for Micromechanics, 66123 Saarbrücken, Germany, seidel@lmm.uni-saarland.de

Summary: *In this paper, we present a low-g accelerometer for advanced automotive applications which is capable of monolithic multiple-axes integration. For the target application a high offset stability and an over-critical damping of the sensing element are required. With simple design changes the squeezed-film damping of the sensor can be adjusted within a wide range (5 Hz to 400 Hz) using atmospheric pressure inside the cavity. Due to its symmetrical design and the differential readout principle, an offset drift of less than 50mg over the full temperature range (-40°C ... 120°C) was achieved. The sensor principle presented in this paper can be utilized to realize a sensitivity axis parallel to the wafer surface as well as perpendicular to the surface. Furthermore, monolithic integration into a two-axis (x/z) or a three-axis (x/y/z) sensing element is possible. The tri-axial element exhibits a four-mass design providing redundancy and thus an ongoing self-test capability*

Keywords: *Accelerometer, low-g, multi-axial sensor, inertial measurement unit, bulk-micromachining*
Category: *10 (Applications)*

1 Introduction

The acceleration sensor presented in this paper consists of a silicon seismic mass suspended from two torsional beams. An applied acceleration results in a torque and thus in an inclination of the mass. The change in distance with respect to a pair of electrodes in the cap wafer is detected with a differential capacitive principle, thus reducing cross-axis sensitivity and enhancing offset stability. All readout electrodes are on one side of the seismic mass thus increasing the symmetry of the design, and reducing the influence of packaging stress. The electrical connection to the sensing electrodes is provided by a special feedthrough technology resulting in a hermetically sealed sensor and in a nearly standard setup for the bonding pads. The fabrication is based on a bulk micromachining process including KOH wet chemical etching for the seismic mass, RIE etching for the torsional beams, and anodic bonding of glass wafers for wafer level packaging of the device.

By introducing slight modifications in the design a sensor with a sensitivity axis in wafer plane (x- or y-sensor) or perpendicular to the wafer surface (z-sensor) can be realized, respectively. Fig. 1 shows the principle setup of such a sensor with a sensitivity axis parallel or perpendicular to the wafer.

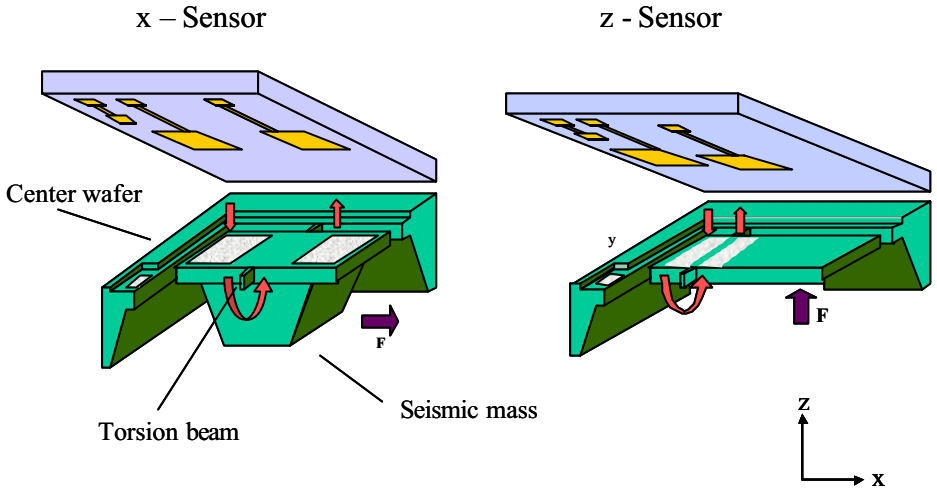

Fig. 1. Principle of the capacitive low-g sensor for a sensitivity axis in plane (x-sensor) and perpendicular to the wafer plane (z-sensor).

2. Multi-Axial Low-g Sensor

For future applications a major interest lies in the integration of several sensitive axes on one single chip in order to reduce size, cost, and alignment errors. The presented concept allows the integration of two or four sensing elements in a x/z or in a x/y/z configuration, respectively.

The basic idea as shown in [1] is a sensing element with a sensitivity axis which has an inclination with respect to the wafer surface. This is realized by an asymmetric suspension of the torsional beams with respect to the center of mass. Thus, the sensing element has a sensitivity in x-direction (parallel to the wafer surface) and z-direction (perpendicular to the wafer surface) as well. A design with equal sensitivities in x- and z-directions results in a sensitivity direction of 45° with respect to the wafer surface. For special applications it is also possible to implement a sensing element with different specified sensitivities in the different directions (resulting in a inclination angle different than 45°).

By using two sensing elements rotated by 180° with respect to each other two signals U1 and U2 are obtained from which the corresponding accelerations a_x and a_z in x- and z-direction can be calculated (Fig. 2).

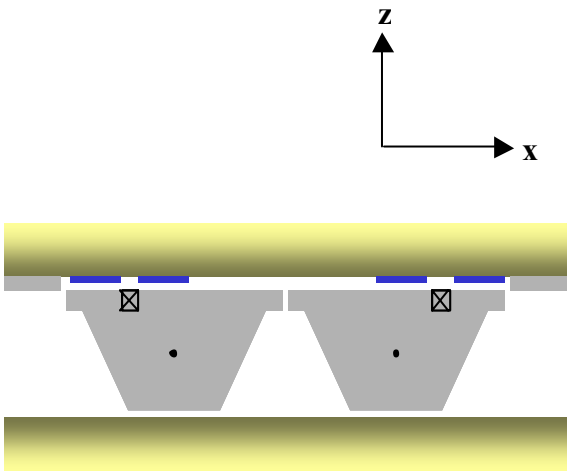

Fig. 2: Cross section of a dual-axis accelerometer.

The above concept is easily extended to a four-mass design which exhibits a pair of x/z and a pair of y/z sensing elements (Fig. 3). With this configuration the acceleration in all three directions x, y, z can be calculated with the shown principle. All sensors have identical layout and are monolithically integrated in plane on one chip. Due to the redundancy of the z-signal an ongoing selftest function can be implemented.

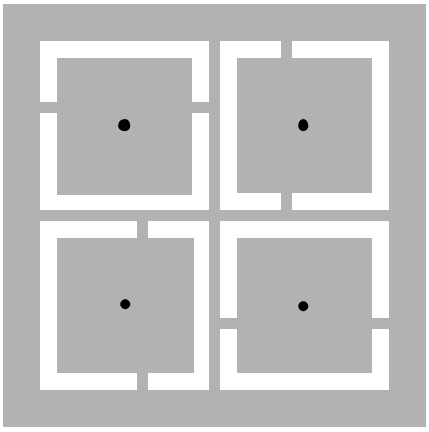

Fig. 3: Schematic top view of a tri-axis acceleration sensor with self-test capability consisting of one pair x/z and one pair y/z dual axis elements.

3. Conclusion

A new low-g acceleration sensor suitable for an inertial measurement unit was presented. The design allows a customization of the mechanical cut-off frequency between wide limits (5Hz to 400Hz). A small bandwidth is essential for some vehicle applications in order to suppress vibrational noise. The measured values for linearity error and offset drift over temperature are well within the specified limits of the target application. The sensor principle can be extended to realize planar dual axis (x/z and y/z) and tri-axis elements (x/y/z) based on the same fabrication technology. Due to the four mass design of the tri-axial sensor, an ongoing self-test capability is available

References

[1] M. Aikele, M. Rose, R. Gottinger, U. Prechtel, J. Schalk, T. Ohgke, M. Weinacht, H. Seidel, „A New Generation of Micromachined Accelerometers for Airbag Applications“, in Advanced Microsystems for Automotive Applications 99, D. E. Ricken and W. Gessner, edts., Springer, Berlin 1999, pp. 251-260

Comparative study between gas sensors arrays device, sensory evaluation and GC/MS analysis for QC in automotive industry

S. Garrigues[1], T. Talou[1] and D. Nesa[2]
[1] Laboratoire de Chimie Agro – Industrielle, ENSIACET, 118 rte de Narbonne, 31077 Toulouse cedex 4, France
email: talou@cict.fr
[2] Technocentre RENAULT, 1 av. du Golf, 78288 Guyancourt cedex, France

Summary: *Odours of new cars are important today for the consumers' comfort. Due to the interior trim parts' manufacturing process and to their petrochemical compounds based, many rubbers and foams used in automotive materials result in a "new car odour" mostly enjoyed but sometimes felt as unpleasant by customers. The use of olfactory sensory panels, especially trained to describe odours, is only one way of addressing that issue. Although they offer interesting characterisation methods, olfactory sensory panels may also have some drawbacks.*
The odours of several PVC skins were described by human assessors and the corresponding volatile organic compounds were also characterised by a commercially available electronic nose technique, based on QMB sensors, whereas their identification was carried out by GC/MS analysis. Finally, a confrontation of the three types of obtained data was performed and showed the existence of correlations as well as the interest of gas sensors device for automotive industry.

Keywords: *electronic nose, chemical sensor, automotive, PVC skin*
Subject category: *10 (Applications)*

1 Introduction

Since a few years, "electronic nose" technology has appeared in a new field of application : the car industry which is confronted with a lot of polymer-based elements that contribute to the "new car odor". Different types of chemical gas sensors have been already tested on this kind of materials : a first generation ones like MOS, MOSFET and CP sensors [1], as well as a second generation ones like QMB and MS-based chemosensors [2].

Quartz crystal MicroBalance gas sensors (QMB) is the chosen technology for our study. They present some advantages upon the above mentioned devices, as their smaller size.

Multiple gas sensors devices, abusively qualified "electronic noses", have long been supposed to react like artificial olfactory systems being able to mimicking the olfactory receptors mechanisms of human nose, with nevertheless a lower selectivity.

However, detection mechanisms of "electronic noses" are still difficult to predict. And the recurrent question remains, is to say : "Does gas sensors technology correctly transcribe the olfactory sensations perceived by human nose ?"

To answer this question, a sensory analysis of different PVC skins was performed by trained panel members using the olfactory referential "The Field of Odours ®" developed by Jaubert [3].

The present paper aims to evaluate the relevance of the discriminations between PVC skins obtained using gas sensors system. In this way, relationships between electronic nose measurements and sensory attributes were established and discussed according to chemical characterisation. The experimental procedure and the results obtained are reported below.

2 Materials & Methods

Materials & Sampling. 3 PVC skins (G, V and VO - cut up and sampled in the form of 12 mm circles), issued from different manufacturing processes, were analysed. Their characteristics are described in Table 1.

Table 1. PVC skin sample description.

Code	*Characteristics*
G	Charcoal grey polymer coating on a white tissue
V	Multicoloured polymer coating on a white tissue
VO	Multicoloured polymer coating on a white tissue Strong onion odour due to a migration product of the injected polyurethane foam

Static headspace optimisation. A central composite experimental design was set up (20 experiments), and carried out by using a HP 6890 GC / HP 5973 mass detector (Agilent Technologies) coupled with a headspace sampler (HP 7694). The column (DB-5MS (J&W), 30 m x 0.25 mm i.d., 0.25 µm d.f.) was programmed from 40 to 290°C (5 min isothermal) at 5°C/min. Injection port and detector temperatures were 150 and 290°C, respectively. Plastic samples were introduced in 22 mL vials and analysed as mentioned above.

The studied sampling parameters were : temperature (30 to 131°C), equilibrium time (120 to 960 min) and sample quantity, equalling to occupy a particular height in the vial (0.32 to 3.68 cm). Recorded responses were total peaks area and number

of peaks. Data were processed by using UNSCRAMBLER v7.5 (CAMO ASA, Oslo).

"Electronic nose" analysis. The analysis was conducted with VOCmeter device (AppliedSensors GmbH, Reutlingen) using 8 QMB gas sensors. The headspace generation was permitted by coupling a HS 40 XL sampler (Perkin Elmer) to the VOCmeter system, and realised under optimised conditions.

The sequence of the analysis was : sample acquisition time 60s; recovery time 540s. PVC skins were analysed in 10 replicates, averaged for data analysis

Sensory analysis. The sensory analysis was performed by an in-house expert panel composed of 8 assessors from RENAULT company, on the basis of the olfactory referential "The Field of Odours ®". The procedure of sensory analysis is detailed in [3].

The followed method is based on the D49 3001 [4] test method carried out by RENAULT. A six levels intensity scale is used to evaluate the perceived odour. The 3 PVC skins were analysed in 3 replicates. Then replicates assessments were averaged.

GC/MS analysis. Same instrumentation than the one used for static headspace optimisation was employed. Mass spectra were obtained by EI ionisation at 70 eV over the range of 35 to 550 a.m.u.

Each PVC skin was analysed in triplicates and replicate peaks were averaged.

Data Processing. The statistical data treatment was done by Multiple Factorial Analysis (MFA).

3 Results & Discussion

The drawing of isosresponse curves have allowed to determine the optima of the main parameters governing the headspace generation in the studied experimental field : one-third of the vial is filled by sample and heated at 80°C during 540 min. Theoretical model was successfully validate. Furthermore, the achievement of the thermodynamic equilibrium showed itself verified by the study of a kinetic follow-up [2].

A previous comparison of the distribution of an explained variance over dimensions of separated Principal Component Analysis (PCA) on each data set (sensory attributes, gas sensors and chemical compounds) were carried out. It showed that the information brought by electronic nose system is mono-dimensional whereas information delivered by sensory and physico-chemical analyses is shared among 2 dimensions regarding PVC skin samples.

Relationship between chemical QMB gas sensors measurements and sensory attributes are illustrated on the first plan of the MFA (Figure 1). The first plan showed 100% of the explained variance and firstly discriminated PVC skins between themselves according to their nature (PC 1). On the other hand, PC 2 allows, also, to distinguish them according to their olfactory perception, is to say "G" and "V" samples between "VO" malodorous sample.

QMB gas sensors (associated with PVC skin "G") were high correlated (r>0.7) with "methyl isobutyl ketone" and "phenol" chemical compounds. Sample "V" is correlated with "phenoled" descriptive term and "N,N-dimethyl formamide" and "2-ethyl hexanol" chemical compounds; while sample "VO" point out a good correlation with "sulphured" and "global intensity" sensory descriptors and "2,3,5-trimethyl 1,4-benzenediol" chemical substance.

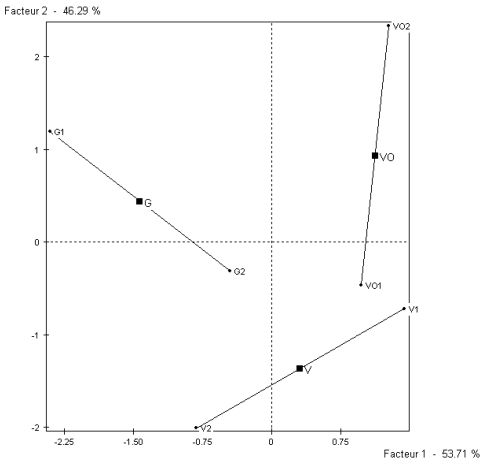

Fig. 1. PVC skin samples and gas sensors projections on the first plan of the MFA.

4 Conclusion

The chemical gas sensors device evaluated in this work transcribed only a part of the information provided by sensory analysis. Nevertheless, this study provided interesting correlation between QMB sensors type and sensory attributes, and especially between these electronic nose measurements and chemical identified compounds. However, much work needs to be done in the future to improve this situation.

References

[1] M. Morvan, *Caractérisation des odeurs de matériaux de l'habitacle automobile par "nez électronique", analyse sensorielle et analyse physico-chimique*, INPT PhD, 2001.

[2] S. Garrigues, *Étude des odeurs de matériaux polymères de l'habitacle automobile – Application des techniques de la métrologie sensorielle*, INPT PhD, 2002.

[3] J.-N. Jaubert, G. Gordon and J. C. Doré, *The field of odors : towards a universal language for odor relationships,* Perfumes & Flavors, 1995, pp. 1-16.

[4] D49-3001, *Émissions d'odeurs, pièces d'équipement intérieur – Mesure de l'intensité et caractérisation de l'odeur dans sa globalité*, Méthode d'essai RENAULT, 2001, pp.1-6.

Physical Sensors for Macro- and Microemulsions

B. Jakoby[1], A. Ecker[2], and M.J. Vellekoop[1]

[1] Vienna University of Technology, Industrial Sensor Systems E366
Gusshausstrasse 27-29/366, A-1040 Vienna, Austria
email: jakoby@iemw.tuwien.ac.at http://iss.iemw.tuwien.ac.at
[2]AC2T Research GmbH, Viktor Kaplan Strasse 2, A-2700 Wiener Neustadt, Austria

Summary: *Emulsions are used in various areas ranging from industrial applications to consumer products like foods. Besides the classically known (macro-)emulsions featuring droplet sizes of a few microns and above, artificially produced micro-emulsions gain increasing attention in colloid science. Recently we discussed the suitability of permittivity and microacoustic viscosity sensors for the monitoring of water-in-oil emulsions. It turned out, that permittivity sensors could be used to simply determine the water content of the emulsion whereas microacoustic viscosity sensors measure the viscosity of the oil phase instead of the averaged "macroscopic" viscosity of the emulsion. This behavior was attributed to the ratio of the size of the water droplets in the emulsion to the penetration depth of the ultrasonic wave excited by the sensor. In this contribution we validate this theory by investigating micro-emulsions featuring a much smaller droplet size. Moreover the results provide further insights into the applicability of these sensors for macro- and micro-emulsions.*

Keywords: *Microacoustic Sensor, Permittivity Sensor,Viscosity Sensor, Emulsion, Microemulsion*
Category: *10 (Applications)*

1 Introduction

In our recent work [1] we considered permittivity- and microacoustic viscosity-sensors as possible physical sensors for monitoring water-in-oil (W/O) emulsions. Both sensors are suitable for the implementation in small and compact on-line monitoring equipment. Potential applications range from the automotive field (water contamination of engine oil, fuel-water emulsions) to consumer applications (process monitoring in food production). In this contribution we describe further investigations with macro- and microemulsions, which were performed in order to achieve a better understanding of the underlying mechanisms and to explain the behavior that we observed earlier.

2 Theory

In [1] we found that a *permittivity* sensor can be used to determine the water content of a (macro-) emulsion as the permittivity $\varepsilon_{r,m}$ of the W/O emulsion can be obtained from the simple approximate formula

$$\varepsilon_{r,m} \cong \varepsilon_{r,o}(1+3f). \quad (1)$$

Here $\varepsilon_{r,o}$ is the permittivity of the oil and f denotes the water fraction by volume. This equation was derived from the Maxwell-Garnett mixing rule [2] and was verified experimentally.

Experiments with a microacoustic *viscosity* sensor (a "transverse shear mode" or "TSM" resonator) led to the surprising result, that the measured viscosity was hardly affected by the water content and only led to a slight decrease in the detected viscosity with increasing water content. This result is in contrast to the expected behavior requiring an increase of the viscosity with increasing water content (as can be verified using a classical viscometer). As a possible explanation we consider the ratio of the typical size of the water droplets in the emulsion to the penetration depth δ of the damped shear wave excited by the sensor [3]. If these two quantities are in the same order of magnitude or if the water droplets are even larger than δ, then the sensor possibly does not detect the macroscopically apparent increase in viscosity due to the interaction of the water droplets [1] (see Fig. 1).

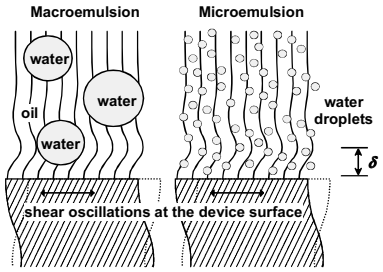

Fig. 1: Distribution of water droplets in the evanescent shear wave excited by the microacoustic sensor.

Instead, the sensor will measure the viscosity of the continuous phase, i.e. the oil. Occasionally in some experiments, water droplets may adhere at some spots of the sensor surface, which, due to the lower viscosity of water compared to oil, would effectively yield a lower viscous loading of the resonator compared to the case where no droplets adhere to the surface. These considerations would explain the behavior observed in our earlier

experiments. To verify this theory, we conducted further experiments with microemulsions featuring much smaller droplet sizes.

3 Experimental

For our experiments we prepared macro- as well as microemulsions consisting of water in diesel fuel. Such emulsions are considered as promising candidates for a novel type of fuel yielding increased engine power and lower emissions at the same time [4]. In contrast to cloudy or milky macroemulsions, microemulsions are typically clear solutions, as the droplet diameter is approximately 100 nanometers or less (see [4] for details on the preparation process).

For our experiments we used diesel/water emulsions based on two different diesel types (#1 and #2) having the same permittivity but different viscosities. Fig. 2 shows the resulting permittivities measured with a coaxial capacitive sensor. As in our previous experiments, the macroemulsion conforms to (1), whereas the microemulsions show an approximately linear increase in the permittivity with increasing water content, where the slope is somewhat larger than predicted by (1). Based on a linear fit, the factor 3 in (1) empirically would have to be replaced by 5.3. This different behavior for microemulsions could be caused by the influence of the surfactants and/or the microstructure, which apparently makes some of the assumptions underlying the Maxwell-Garnett rule [2] invalid.

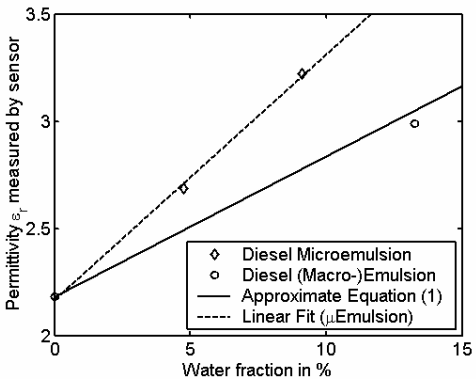

Fig. 2: Measured permittivity vs. water content in % for water-in-diesel micro- and macroemulsions.

For the viscosity measurements we examined microemulsions prepared on the basis of diesel #1 and diesel #2, and a macroemulsion prepared using diesel #1. To measure the viscosity, the damping of a 6HMz TSM microacoustic resonator has been evaluated. The upper graph in Fig. 3 shows the obtained viscosity in arbitrary units compared to the viscosity measured by using a classical rotational viscometer (both at 22.5°C). For the macroemulsion prepared from diesel #1, the rotational viscometer yields a slight *increase* compared to pure diesel #1, whereas the microacoustic measurement yields a slight *decrease*. This confirms to the anomalous behavior that has already been observed in [1]. However, for the microemulsion both measurement methods consistently yield a strong increase in viscosity. To confirm this behavior, microemulsions from a second type of diesel (diesel #2) have been measured yielding a distinct correlation between the two measured viscosities, which is also confirmed by the linear fit shown in Fig. 3 (lower graph).

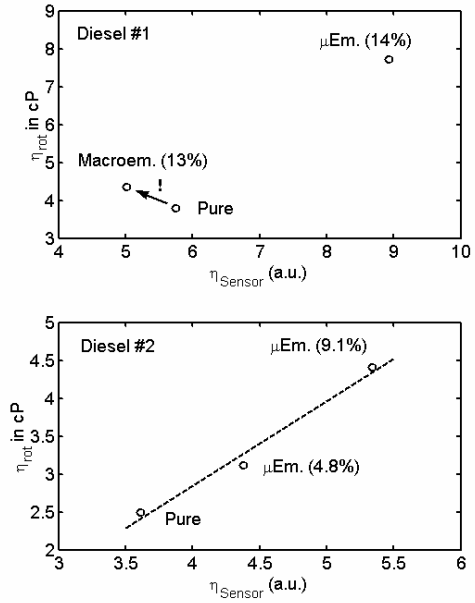

Fig. 3: Viscosities obtained from the TSM sensor (η_{Sensor}) compared to a rotational viscosity measurement (η_{rot}).

4 Conclusions

Based on our experiments, we conclude that the water content of W/O macro- and microemulsions can be determined using *permittivity* sensors, where in case of macroemulsions the Maxwell-Garnett rule can applied. For microemulsions a modified rule has to be considered. The results from *microacoustic viscosity* measurements strongly depend on the droplet size in the emulsions. For microemulsions, we found that the measured viscosity correlates well with classical viscosity measurements, whereas in case of macroemulsions the sensor yields values somewhat lower than the viscosity of the continuous phase (depending on droplet adhesion at the sensor surface).

References

[1] B. Jakoby and M.J. Vellekoop, *Proc. Eurosensors XVI,* Sept. 15-18, 2002, Prague, Czech Republic, p. 53-56.

[2] A. Sihvola: Electromagnetic Mixing Formulas and Applications, *IEE Publishing, Electromagnetic Wave Series*, London 1999.

[3] S.J. Martin, G.C. Frye, and K.O. Wessendorf, *Sens. Act. A,* 44 (1997), 209-218.

[4] M. Kacetl, R. Markl, and A. Ecker, *Petroleum and Coal*, vol. 43, 3-4 (2001), 143-148.

LCD aided computer screen photo-assisted technique for colorimetric assays evaluation

D. Filippini*, J. Manzano and I. Lundström

Division of Applied Physics, Institute of Physics and Measurement Technology, Linköping University, S-581 83 Linköping, Sweden. *E-mail: danfi@ifm.liu.se

Summary: *The ability of the computer screen photo-assisted technique (CSPT) to evaluate color samples through its light transmittance profiles is demonstrated by using liquid crystal displays (LCD) as light sources. Transmittance profiles are more drastically affected by angular dependencies than those obtained with CRT illumination. A local light reference computation is introduced to counteract this effect yielding equivalent profiles for both kinds of displays thus allowing for a broader universe of platforms to perform CSPT experiments, including mobile devices.*

Keywords: *colorimetric assays, (bio) chemical sensors, computer screen illumination*
Category: *10 (Applications)*

1 Introduction

Colorimetric (bio)chemical assays are typically evaluated with dedicated micro-plate readers, comprising monochromatic light sources and two dimensional micro-positioned detection. For the purpose of home tests, it has been recently proposed an alternative method that allows to measure distinctive light absorption features [1] at a fraction of the cost.

The computer screen photo-assisted technique (CSPT) uses a computer screen to display a controlled sequence of colors that illuminates a sample (evaluation of light absorbing bioassays of different nature has been demonstrated so far [1,2,3]). The sample is concurrently observed with a web camera. In this way, different sample colors within a constrained set of possibilities can be identified by their light absorption features enabling home assays evaluation with a broadly available platform.

The technique has been demonstrated with cathode rays tube (CRT) monitors, but the extension to liquid crystal displays (LCD) comprises additional advantages, as applications based on palmtops or mobile telephones.

In this contribution we evaluate an array of color samples with LCD aided CSPT. The results are contrasted with CRT measurements enabling us to determine inherent accuracies and to optimize calibration procedures.

2 Experimental

A CRT computer screen (NEC MultiSync FE950+) and a TFT-LCD monitor (Sony Vaio FX505, XGA), are used as light sources displaying a sequence of colors sorted to match the perception of the visible spectrum. The light source is a digital video file (AVI format) run with any commercial media player, which displays colors at 1 frame/s.

The sample, in this case an array of 24 different printed colors (Fig.1a), is placed in front of the light source, and a web camera (Logitech QuickCam Pro 3000) captures the light transmitted though it. The software provided by the manufacturer is used to capture 1 frame/s in synchronism with the illumination, and to compose a video file as result from the measurement.

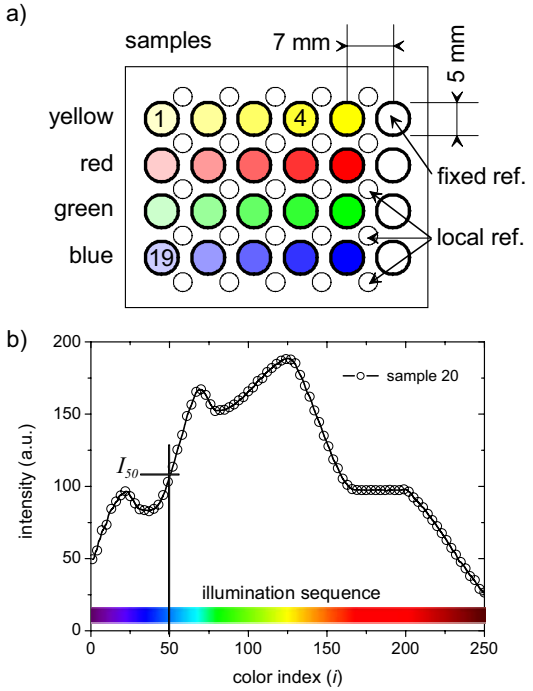

Fig. 1a) color samples and reference spots. b) Transmitted intensity profile through sample 20 as observed with the web camera for the 250 colors sequence used for illumination.

A MatLab program decompose the video file in individual frames extracting the information of light

intensity (evaluated as grey levels [1]) in all the pixels composing the image of each sample spot and calculates the average (I_i) value and standard deviation (evaluated over 314 pixels).

Repeating the procedure for all frames a distinctive intensity vs. color index (i) profile of each spot is composed (Fig.1b).

Taking a transparent spot as reference (I^{ref}_i) the transmittance profile can be composed according to:

$$T_i = \frac{I_i}{I_i^{ref}} \quad (1)$$

Typically the reference was taken as a fixed spot for the whole array of samples [1,2,3], which relates to measurements performed with CRT screen. In the present case, involving LCD displays as well, the references has been taken both in the traditional way and locally around each sample spot (four transparent spots around each sample spot).

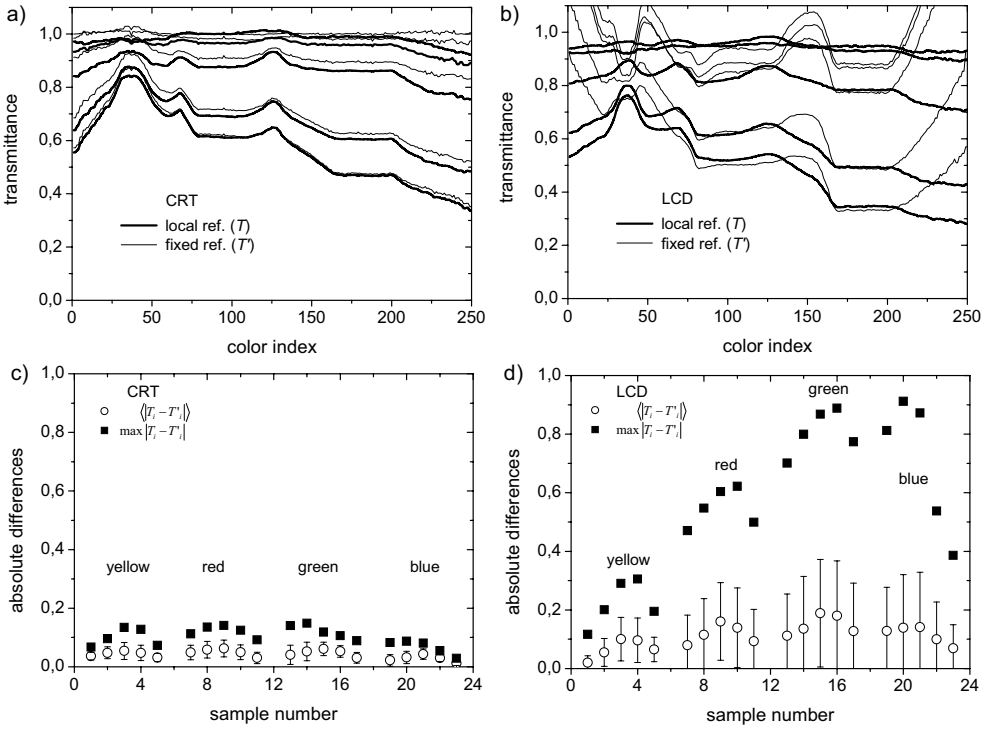

Fig. 2a) Transmittance profiles of blue samples with CRT illumination. Thick lines corresponde to local references and thin ones to a single reference (sample 6). b) Transmittance profiles of blue samples with LCD illumination. c) Average and maximum absolute deviation of the fixed reference measuremt with respect to the local reference for a CRT illuminations, d) idem as c) but for LCD illumination**.**

3 Results and discussion

Fig. 2a, shows the correction introduced in different absorption profiles of blue samples by taking the reference intensity close to each particular sample spot (local reference) instead of a single reference (sample 6 for all spots in the array, fixed reference).

For the CRT screen the effect of this correction is lower than 10% (20%) averaged along the whole profile (maximum), which shows the low angular dependency of the emitted light in this kind of screens (Fig.2c) (broad viewing angle).

In the case of LCD screens, even modern TFT displays like the present, have a narrower viewing angle, that if not corrected by approaching the reference illumination to each particular sample induces spurious features (like transmittances bigger than one) that disturb the ability of CSPT to recognize color substances.

The use of the present calibration procedure allows generating transmittance profile with LCD displays which are equivalent to those obtained with CRT screen. In this way the technique is made available to a broader universe of platforms which include even palmtop devices or mobile telephones as light sources.

References

[1] D. Filippini, S. P. S. Svensson, I. Lundström, *Chem. Commun.* (2003), 240-241.

[2] D. Filippini, I. Lundström, *Appl. Phys. Lett*. **81** (2002), 3891-3893.

[3] D. Filippini, I. Lundström, *Proceedings EMBEC'02, 2nd European Medical & Biological Engineering Conference* (2002), Part I, 310-311.

Implementation of sensors for on-line monitoring of diffuse pollution at the origin of river eutrophication

H.P. Beck[1], D. Bellefleur[2/3], F. Cuny[4], C. Josserand[5], C. Klein[1], N. Laurent[2], N. Le Nouveau[2/3], J.-P. Lickes[6], A. Meyer[1]

[1] University of Saarland, Institute of inorganic and analytical chemistry and radiochemistry, Postfach 151150, D-66041 Saarbrücken, Germany.
[2]G.E.M.C.E.A, 149 rue Gabriel Peri, 54500 Vandoeuvre-les-Nancy, France.
email : nathalie.le-nouveau@gemcea.u-nancy.fr http://www.gemcea.org
[3]CETE de l'Est – LRPC de Nancy 71 rue de la Grande Haie 54510 Tomblaine, France
[4]IRH Environnement, 11 bis rue Gabriel Peri54500 Vandoeuvre-les-Nancy, France.
[5]INERIS, Parc technologique ALATA BP2, 60550 Verneuil en Halatte, France.
[6]Administration de l'Environnement du Luxembourg, 16, rue Eugne Ruppert LU-2453 Luxembourg

Summary *: The project LIFE-Environment EUTROPH MONITOR (1/09/2001 – 31/08/2004) aims at the development of a suitable concept for on-line monitoring of characteristic parameters of river eutrophication, in the region SAAR-LOR-LUX. A net of on-line measurement stations is installed to monitor water quality parameters in a context of international cooperation. Stations are equiped with a datalogger that stores and transmits data to a central PC. The paper presents : the significance of sensors implementation for river eutrophication monitoring, the conception of on-line measuring stations and measuring methods, the quality assurance system implemented to ensure good measurements and the firsts results obtained.*

Keywords: *river, eutrophication, on-line measurement, sensor*
Category: *10 (Applications)*

1 Introduction

The goal of the project is to monitor continuously, with automatically working analysis stations coupled to a remote transmission system, the input of eutrophicating substances from various sources and their effects on the river water quality (growth of phytoplancton). The investigation area of the project covers the catchment areas of the cross-border river Nied on the German (SAAR) and French (LOR) sides, and the river Sauer on the Luxembourgian (LUX) side (see Fig.1).

Fig. 1. Investigation area and eutrophication of *la Nied Allemande* (France).

The data collected will be transmitted immediately to the authorities responsible for the surveillance of the environmental condition in chosen regions. A system of data evaluation will be implemented to provide a basis for decisions to be taken.

The project is to establish a means to comply with the guidelines of the EU especially according to the EU water Framework Directive 2000/60/EU.

2 Significance of sensors implementation for river eutrophication monitoring

Eutrophication results from excessive discharges of nutrients (nitrogen, phosphorus) from various origins (domestic, agricultural) in the river. The consequences are an abnormal growth of the river productiveness, the development of bloom algae, a disturbance of water uses (leisure, production of drinking water, etc.)[1]. The manifestations of river eutrophication are mainly speedy growth of phytoplancton, accentuation of the daily cycle of oxygen content, reduction of water transparency. Implementation of sensors is quite suitable to monitor river eutrophication because of the quickness of apparition of bloom algae according to environmental conditions (ambient temperature, period of sunshine). Thus we want to show that the nitrate and total phosphorus load as well the growth of the phytoplancton, can be continuously supervised , even in case of short term changes, with a combination of sensors and analysers.

3 Conception of on-line measuring stations and measuring methods

A net of several similar measuring stations is installed in the catchment area of the rivers Nied

and Sauer. The parameters measured in each station are the following ones :

- basic physicochemical parameters : pH, temperature, conductivity, dissolved oxygen,
- nutrients, cause of eutrophication : $NO_2^- + NO_3^-$, NH_4^+, PO_4^{3-} and P_t,
- effects of eutrophication : chlorophyll.

Some additional parameters are measured in the first station, in order to investigate their significance for eutrophication problems and their correlation with the basic parameters : TOC (total organic carbon), SAK (spectral absorbance coefficient), turbidity, redox.

Fig. 2. On-line measurement station for eutrophication.

The stations are containers where sensors and analysers are installed. River water is pumped continuously with an emerged peristaltic pump. Process analysers and probes measure continuously the different parameters. Every station is equipped with a data acquisition unit that stores all measured values on a data basis. They can be called upon and evaluated or deferred as data block to a central computer via broadcasting (see Fig.2).

The devices used for on-line measurements are systems available in trade. The measuring methods depend on parameters :

- probes for pH, conductivity, dissolved oxygen, nitrates (photometry), chlorophyll (fluorimetry),
- chemical analysers for phosphorus and ammonium.

4 Quality assurance system implemented to ensure good measurements

Some used analysers comply with normalised methods, however such systems are not yet available for all the parameters to be determined. Besides there is a general trend in favour of using probes, that present the advantages of low maintenance and no consumption of reagent. In order to guarantee the accuracy of measurements realised, various procedures are implemented, besides the auto-calibration of some analysers :

- weekly maintenance of the station, including check of probes by calibration with standard solutions,
- control analysis of water samples by normalised methods in the laboratory, at a precise frequency.

The data from on-line measurements will be assessed with respect to their accuracy. Fig.3 gives an example for such measurements in late autumn.

5 First results of data and interpretation

In conclusion, first measurements in various conditions will be done (rain event, dry period). We will try to bring to the fore some correlations between measured parameters and eutrophication phenomenona, by means of signal treatment algorithms.

The main guide lines of a model based on a G.I.S. that is being developed to help to interpret data will be presented [2]. The model calibration will be realised with on-line measurement data.

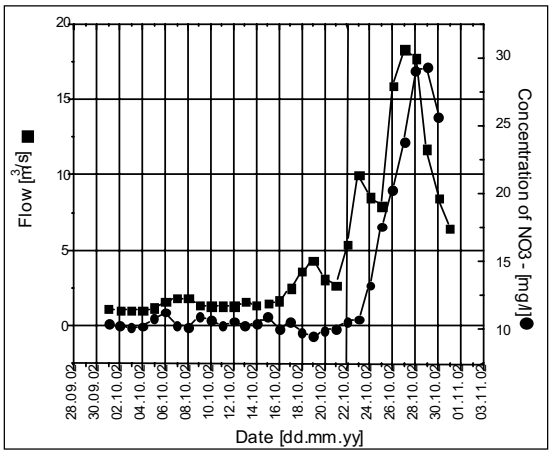

Fig. 3. Comparison of nitrates content in the Nied with flow after a raining period shows a one day lag-timefor washing out effects in the catchment area

This project is sponsored by financial and technical help of the following institutions :

- *European Union,*
- *Ministry of Environment of Saarland,*
- *Water Authority Rhin-Meuse.*

References

[1] J.-P. Benneton, *Eutrophisation des plans, Inventaire des principales sources de substances nutritives azotées et phosphorées, Etude bibliographique*, *Rapport de recherche LCPC n°130 (1984),* 72p.

[2] Agence de l'Eau Rhin-Meuse, Direction Départementale de l'Agriculture et de la Forêt de Moselle, *Eutrophisation des eaux superficielles en Moselle – Rapport technique (1993)*, 44p.

http://www.eutroph-monitor.com

A Portable Chlorophyll Sensor (PCS) for Predicting Chlorophyll Content in Potato Leaves

M.S. Borhan[1], S. Panigrahi[1], J. H. Lorenzen[2], H. Gu[1], C. Ulven[1]

[1]North Dakota State University, Ag & Biosystems Engineering Dept., Fargo, North Dakota
email: suranjan.Panigrahi@ndsu.nodak.edu
[2]North Dakota State University, Plant Science Dept., Fargo, North Dakota

Summary: *A prototype of handheld spectrometric sensor was developed and evaluated to predict chlorophyll content of potato leaves. The sensor consisted of a microspectrometer (MicroPac™CS600), with an integrated light chamber. Tests were conducted on 37 randomly selected leaves. A signal processing algorithm was developed to process the acquired signals and to obtain the second derivative of the spectral signature. Two statistical models were developed using principal component regression (PCR) and partial least square regression (PLSR). A hybrid neural network (NN) model was developed, optimized, and evaluated. The highest average accuracy (out of the three prediction model) obtained using the training data set was 99.3 %, while the highest average accuracy obtained using the test data was 78%.*

Keywords: *Portable sensor, spectrometer, neural networks, signal processing, Chlorophyll, PCR, PLS*
Category: *10 (Applications)*

1 Introduction and objective

Nitrogen is a very important nutrient for many crops including potato. Effective nitrogen management can have several benefits in terms of environmental as well as economical. Thus, it becomes improtant to determine the nitrogen (nitrate) content of plant leaves duirng their growing season. This information can allow the growers to selecetively apply the required amount of nitrogen at the specfic location in the field.

Lee et al. reported that chlorophyll is the primary absorber of light energy needed for photosynthesis, which relates to the N_2 availability to the crops [1]. Hence, chlorophyll can be used as an index of diagnosing the nitrogen status of the food crop. Generally, measuring red reflectance for canopy and branches is affected by both chlorophyll content and vegetation biomass. Previous works for estimating chlorophyll content used optical and radiometric techniques. Non-destructive techniques used leaf reflectance at 675 nm [2, 3, 4]. Previous researchers have identified leaf reflectance to be a good estimator of nitrogen content of sweet pepper leaves [5] and other crops, including maize [6]. They found the green band (550 nm) to be a better indicator of nitrogen content in leaves than either the blue (450 nm) or red (670 nm) bands. The reflectance was inversely correlated to the nitrogen broad-leaf with 73% reflectance variability [7]. The reflectance was also observed to be inversely correlated to leaf chlorophyll content of eight crops, including corn, cotton, cantaloupe, cucumber, lettuce, grain sorghum, spinach, and tobacco with 39 to 95% of the reflectance variability [6]. Optical sensor based crop indices (PNSI) are also accepted as a very useful means for evaluating crop nitrogen stress. Siza et al. collected spectral reflectance patterns under variable cloud cover and solar angles using a fiber optic spectrometer and SPAD (specialty product agricultural division of Minolta Corporation of Japan) meter [8]. The backpropagation neural network based model showed strong correlation between actual and predicted chlorophyll meter readings (R^2 = 0.91). However SPAD meter has limitations for real-time measurements. We developed a research project to develop a portable chlorophyll sensor that would use spectrometric system to obtain multiple wavelengths. Our initial goal was to develop a sensor that could be used both in the field and in the laboratory condition. This paper focuses on the development and testing of a portable sensor for predicting chlorophyll content of plant leaves (potato).

2 Methodology

A prototype of the portable chlorophyll sensor (PCS) was developed. A microspectrometer (MicroPac™CS600; OCLI, Inc., Santa Rosa, CA) enclosed in a metal box worked as the detector unit of the sensor and it was further integrated with a light chamber. The microspectrometer was placed at an angle of 40 degrees to the horizontal plane and a light source was placed vertically above the leaf. Additional design configurations were provided so that the reflectance signal from the leaf of the plant was received by the spectrometer. A laptop computer was used to acquire the digitized signals from the spectrometer.

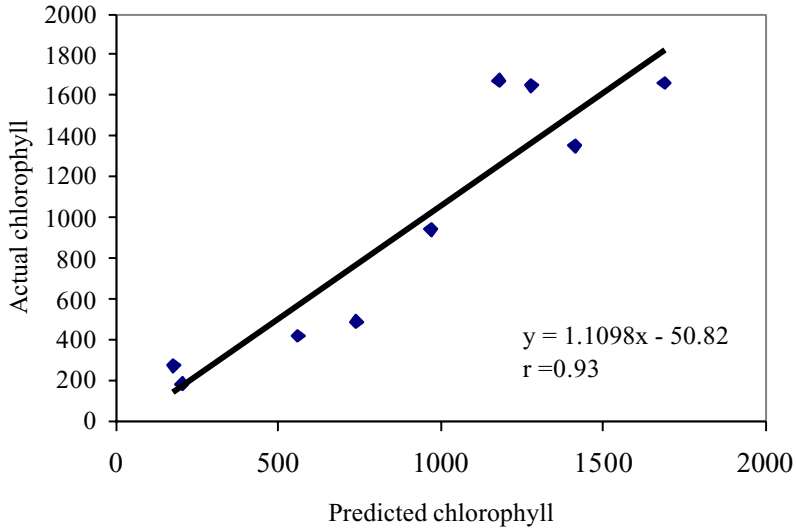

Fig 1. Comparison of actual versus predicted chlorophyll in conventional unit with the developed sensor predicted by the hybrid NN model (test data).

Potato plants (variety Russet-Burbank) grown in the research plot of North Dakota State University (NDSU, Fargo) were used for this experiment. Leaves were randomly selected based on color difference. Based on the visual color difference of the plant canopies (green to yellow), the spectral signature (reflectance) of 37 randomly selected plant leaves was taken. The actual chlorophyll contents of potato leaves were determined using the standard measurement methods in laboratory conditions.

The acquired signals were further processed suing different mathematical and statistical techniques including second-derivate technique. The second derivate reflectance values were used as the inputs to different prediction models. For this study, we used three different predictions models. They were: 1) Principal component regression (PCR), 2) Partial Least square regression and 3) Hybrid neural network model respectively. Out of a total of 37 samples, measurements from 28 leaf samples were used as the training data and those from other 8 leaf samples were used as test data set.

3 Results and Conclusions

PCR model provided an average accuracy of 84% and 63% on the training and test data respectively. One the other hand, the PLSR model provided average accuracies of 99% and 73% on the training and test data respectively. The hybrid neural network model consisted of two separate networks based on backpropagation architecture and they were called; primary and secondary neural network model. The hybrid neural network model provided average prediction accuracies of 91% and 78% on the training and test data respectively. Figure 1 shows the correlation between the actual and predicted chlorophyll contents on test data sets. A correlation coefficient of 0.93 with a slope of 1.1 (close to 1) shows the good performance of the hybrid NN model.

Reference

[1] W.S. Lee, W.W. Troyer, and T. Kataoka. Assessing nitrogen stress in corn varieties of varying color. *ASAE Paper No. 99-3034*, St. Joseph, MI, 1999.

[2] H.M. Bendict and R. Swidler. Non-destructive methods for estimating chlorophyll content of leaves. *Science*, 133 (1961) 2015-2016.

[3] K. Hardwick and N.R. Baker. In vivo measurement of chlorophyll contents of leaves. *New Physiology*, 72 (1973) 52-54.

[4] Y. Takano and S. Tsunoda. Light reflection, transmission, and absorption rate of rice leaves in relation to their chlorophyll and nitrogen content. *Tohoku Journal of Agricultural Research*, 21 (1970) 111-117.

[5] J.R. Thomas and G.F. Oerther, Estimating nitrogen content of sweet pepper leaves by reflectance measurements. *Agronomy Journal*, 64 (1972) 11-13.

[6] J.R. Thomas and H.W. Gausman. Leaf reflectance vs. leaf chlorophyll. *Agronomy Journal*, 69 (1976) 799-802.

[7] S.T. Jacques and C.P. Bellefleur. Determination of leaf nitrogen concentration of broadleaf tree seedlings by reflectance measurement. *Tree Physiology*, 8 (1991) 391-298.

[8] D.T. Siza, D.G. Wagner, and P.H. Heinemann. Hyperspectral input based neural network model for predicting chlorophyll status in corn. *ASAE Paper No. 00-1009*, St. Joseph, MI, 2000.

Direct determination of cyanides by potentiometric biosensors

M. Keusgen[1], M. Jünger[2,3], I. Krest[1], and M. Schöning[2,3]

[1]University of Bonn, Institute for Pharmaceutical Biology, Nussallee 6, D-53115 Bonn, Germany
email: M.Keusgen@uni.bonn.de http://www.uni-bonn.de/www/Pharmazeutische_Biologie.html
[2]Research Centre Jülich, Institute of Thin Films and Interfaces, D-52425 Jülich, Germany
[3]University of Applied Sciences Aachen, Division Jülich, Ginsterweg 1, Ginsterweg 1, D-52428 Jülich, Germany

Summary: *Cyanide and it derivatives are widely used in metal mining and metal plating industry. But also many medicinal and food plants are toxic for man because of their content of cyanogenic glycosides. In the present investigation, a cyanide-specific biosensor exploiting immobilized cyanidase (EC 3.5.5.1) has been developed. Enzymatically formed ammonia was detected by a potentiometric sensor based on an ammonia electrode or a pH-sensitive electrolyte / insulator / semiconductor (EIS) layer structure made of Al/p-Si/SiO_2/Si_3N_4. It could be demonstrated with both methods that this biosensor is sensitive enough to detect cyanide in sub-toxic concentrations. The detection limit was determined in the micromolar range.*

Keywords: *cyanidase, EIS structure, potentiometric ISE, silicon-based biosensor, cyanides*
Category: *6 (Biosensors)*

1 Introduction

Salts and derivatives of cyanide (CN^-) are worldwide used in metal mining and metal plating industry. For instance, sodium cyanide is employed in mining to release precious metals-gold and silver from the ore. But there are also natural sources for cyanide release. Because of their content of cyanogenic glycosides, many medicinal and food plants are toxic for man [1]. Cyanogenesis is known to occur in the plant genera *Prunus*, *Sambucus*, *Linum*, *Carica*, *Phaseolus* and *Manihot*. Mainly plants belonging to the genera *Phaseolus* and *Manihot* are widely used as food. Typical cyanogenic glycosides like amygdalin, linamarin, and lotaustralin, are shown in Figure 1. If plant material containing cyanogenic glycosides gets disintegrated, cyanide is liberated by the action of different enzymes. Cleavage of the glycoside residue by β–glycosidases is the most prominent step in this procedure. Especially in developing countries, chronic poisoning by cyanogenic plants after the consumption of "Manihot" is a serious problem. These poisonings are either cause by insufficient heating of food or by manihot with high levels of cyanogenic glycosides.

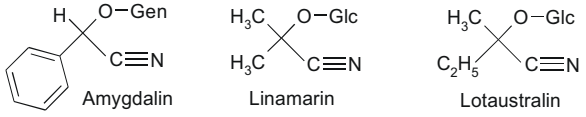

Fig. 1. Typical cyanogenic glycosides of plants.

Cyanide is acutely toxic to any animal and human. Very small amounts of cyanide can kill fish. For example, cyanide at a concentration as low as 20-80 ppb can take life of rainbow and brown trout. Therefore, cyanide in often used for fishing in Asia. Birds and mammals that drink water or feed on cyanide-poisoned wildlife can be killed if they are exposed to cyanide at between 40-200 ppm. The same amount would be lethally toxic to humans.

Because of this wide abundance of cyanide in the environment, a rapid and precise method for the determination of these compounds should be developed. A biosensoric system based on an ammonia electrode and the enzyme cyanidase [EC 3.5.5.1] seems to be an effective analytical method for this class of substances and a promising alternative to an ion-selective cyanide electrode [2]. Cyanide catalyses the hydrolysis of cyanide into ammonium and formiate. Moreover, a miniaturized sensor should be developed on the basis of a pH-sensitive electrolyte / insulator / semiconductor-structure.

2 Results and Discussion

In order to simplify treatment of cyanide containing samples and to reduce time of single measurements, a new method based on immobilized cyanidase and an ammonia-gas electrode as part of a flow-trough apparatus should be developed. The ammonia electrode was mounted on a specially designed flow-through cell with an adjustable inner volume of 2 µL [3]. In a first set of experiments, cyanidase (*Alcaligenes xylosoxidans*, Novo Nordisk SP 379) was filled into a small cartridge with an inner volume of 1 mL and operated at a flow rate of 0.5 mL/min using buffer solutions at pH 7.0 (60 mM). Shortly before the buffer stream reaches the electrode, pH was increase to pH 13 to allow ammonia detection. The

inner electrolyte of the electrode was diluted 1:9 with water. Temperature of the flow-through cell was stabilized at 36.0 °C. The analyzer was fully computer-controlled allowing automatic over-night measurements.

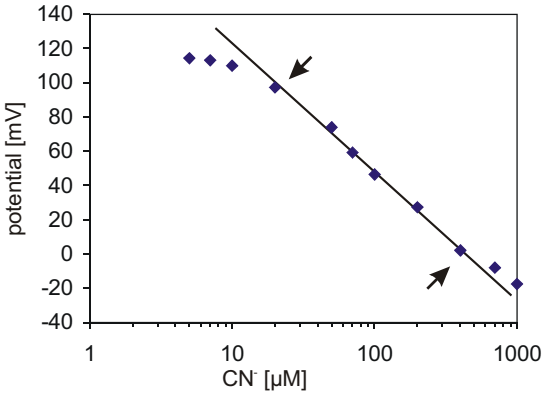

Fig. 2. Calibration plot of the cyanide biosensor based on an ammonia electrode. The linear calibration range is marked by arrows.

The detection limit of this sensor (see Fig. 2) was observed at 6 µM. Quantitative determination of cyanide could be carried out in the linear range between 20 µM and 300 µM. The detection limit corresponds to 0.16 mg/L cyanide (6 ppm). This sensitivity is sufficient for concentrations, which are toxic for humans.

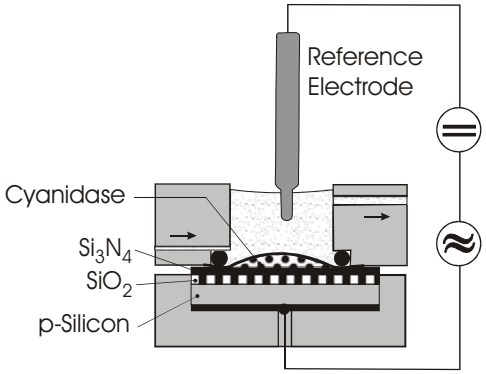

Fig. 3. Experimental set-up used for C/V and CONCAP measurements of the cyanide biosensor (EIS).

In order to further miniaturize this sensor, findings described above were transferred onto a further potentiometric sensor based on an EIS structure. The pH-sensitive layer of this semiconductor is formed by Si_3N_4. Fabrication and production of theses structures were described in ref. [4]. The detection principle can be explained by the presence of amine (NH_2) and hydroxyl (OH) groups at the surface of a hydrated Si_3N_4 layer. The ionization states of this layer depend on the surrounding H^+-ion concentration. The resulting potentiometric response was recorded and correlates with the pH, which is determined by the reaction products of the cyanidase.

With the intention to examine the potentiometric response of the sensors, the prepared EIS structures were mounted in a measuring cell sealed by an O-ring as shown in Figure 3. About 6 Units cyanidase (recombinant cyanidase from *Pseudomonas stuzeri*) were trapped by a semi-permeable membrane at the top of the pH-sensitive layer. The sensor was contacted on its front side by an Ag/AgCl reference electrode, and at the rear Al-contact by a gold pin. The characteristics of the biosensor were studied by capacitance/voltage (C/V) and constant capacitance (CONCAP) measurements.

Again, the sensor was operated in the flow-through mode with phosphate buffer, pH 7.5 (10 mM). In contrast to experiments described above, an open cell design was used. Good results were achieved with an inlet diameter of 1 mm, an outlet diameter of about 2 mm and a flow rate of 0.25 ml/min during measurements. The sensor was sensitive to cyanide concentrations as low as 1 µM (Figure 4). However, it must be assumed that the detection limit of the EIS sensor is in the nanomolar range. This sensitivity would be high enough even to perform analysis in the ppb-range.

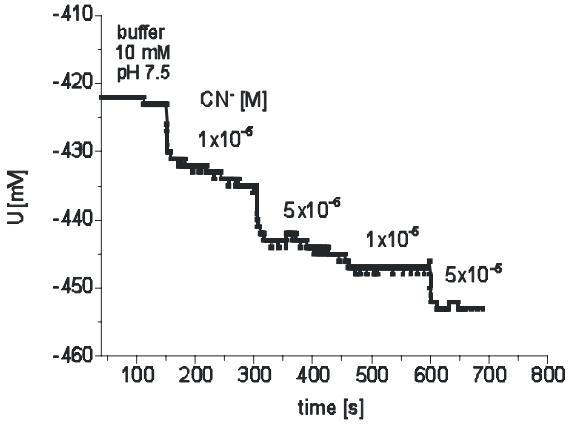

Fig. 4. Typical CONCAP plot of the cyanide biosensor with cyanide concentrations between 1 µM and 50 µM.

References

[1] J. Vetter. Plant cyanogenic glycosides. *Toxicon* 38 (2000) 11-36.

[2] A. Ipatov, M. Ivanov, S. Makarychev-Mikhailov, V. Kolodnikov, A. Legin, Y. Vlasov.Determination of cyanide using flow-injection multisensor system. *Talanta* 58 (2002), 1071-1076.

[3] I. Krest, I. M. Keusgen, M. Biosensoric Flow-Through Method for the Determination of Cysteine Sullfoxides. *Analytica Chimica Acta* 469 (2002), 155-164.

[4] M. Thust, M. J. Schöning, J. Vetter, P. Kordos, H. Lüth. A long-term stable penicillin-sensitive potentiometric biosensor with enzyme immobilized by heterobifunctional cross-linking. *Analytica Chimica Acta* 323 (1996), 115-121.

Fibroblast cell-based biosensor for sensing glucose

C. Tlili [1,3], K. Reybier [1], Alain Géloën[2], L. Ponsonnet[1], C. Martelet[1], H. Ben Ouada[3], M. Lagarde[2], N. Jaffrezic-Renault[1]

[1]Laboratoire d'Ingénierie et de Fonctionnalisation des Surfaces, UMR-CNRS 5621, ECL-Lyon, BP 163, 69131 Ecully Cedex, France; email : laurence.ponsonnet@ec-lyon.fr

[2] Laboratoire U352 Biochimie et Pharmacologie de la médiation lipidique, INSERM-CNRS, 20 avenue Albert Einstein, 69621 Villeurbanne CEDEX

[3] Laboratoire de Physicochimie des Interfaces, Université de Monastir, Avenue de l'Environnement, 5019 Monastir, Tunisie.

Summary: *The aim of this work is to demonstrate the feasibility of glucose sensing by fibroblast cells using impedancemetry analysis. Equivalent circuits are used to model the electrical flow through the interface. Cells are cultivated on Indium Tin Oxide (ITO) semiconductor electrodes. The variation of the electrical properties of fibroblasts as a function of glucose concentrations are measured by electrochemical impedance spectroscopy (EIS). This variation is not observed with carbohydrates not metabolized by cells such as D-mannitol. Moreover, inhibiting glucose uptake by cytochalasin B, a specific inhibitor of glucose transporters, abolishes the EIS signals. This demonstrates the specification of the sensor.*

Keywords: *cell-based biosensor, impedance spectroscopy, glucose*
Category: *6 (Biosensors)*

1 Introduction

Diabetes is diagnosed exclusively by demonstrating a persistent increased glucose concentration in the blood. Amperometric biosensors based on glucose oxidase are the most widely used biosensors. Biosensor response is generally based on the electrochemical oxidation of H_2O_2[1, 2]. This kind of biosensor is often used in short-term evaluation[3, 4] due to an activity loss of the enzyme and the relative toxicity of H_2O_2 for biological entities. The use of living cells as sensor elements provides the opportunity for high sensitivity in a broad range of biologically active substances which affect the response of the cells. This paper describes a new fibroblast based sensing device for the determination of glucose using impedance spectroscopy. Indeed, 3T3-L1 fibroblasts are able to metabolise glucose through the activation of specific glucose transporters (Glut 1 and Glut 4).

2 Results and discussion

2.1 Impedance spectra of fibroblast cell layer on ITO electrode

Figure 1 shows the Bode impedance plot corresponding to the cell monolayer covering the ITO electrode. These plots are interpreted in terms of equivalent circuits. The impedance spectrum of this system can therefore be analysed using an equivalent circuit that consists of a resistor and a constant phase elements (CPE) (replacing the capacitor) in series. The resistor R_0 is mainly due to the conductivity of the bulk solution and the wire connection whereas the C_{CPE} represents the dielectric properties of the electrode/electrolyte and additional qualitative information on the surface morphology of the ITO electrode. In the case of figure 1, R_0=486.8 and C_{CPE}=68 µF cm^{-2}. Moreover, R=6.5 KΩ cm^2, C=45µF cm^{-2} are the resistor and the capacity of an interfacial layer and R_c=5.425 Ω cm^2 and C_c=0.76µF cm^{-2} corresponds to the cell layer.

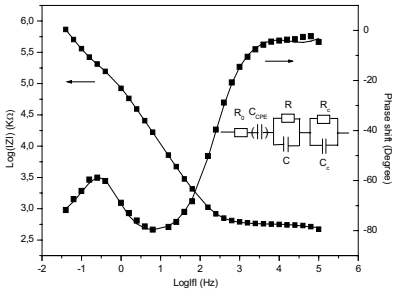

Fig. 1. Impedance spectrum of ITO electrode covered with fibroblast cells (3T3-L1).

2.2 Impedance measurements for glucose detection

Figure 2 shows the effect of glucose addition on the impedance spectra of the fibroblast cell monolayer. In this case, the Nyquist diagram representation is used since such a representation allows a more sensitive analytical treatment. Measurements are performed in a wide range of glucose concentrations (1 mmol to 23 mmol) which is wider than the physiological range. Each glucose addition induces a change of the Nyquist diagram, due to a change both in the resistance and in the capacity of the cell monolayer.

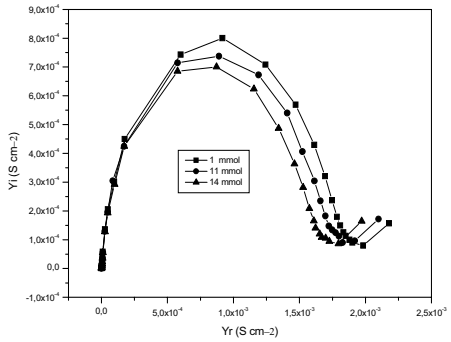

Fig. 2. Nyquist Diagram of the effect of D-Glucose on confluent monolayer of fibroblast cells.

Fig. 3 shows at glucose concentration below 14 mmol, a typical calibration graph of the absolute impedance response at 4 kHz of fibroblast/ITO electrode versus glucose concentration is produced. But when the concentration goes over 14 mmol, the system reaches a saturation. In order to highlight the specificity of the cells towards glucose and to reinforce the hypothesis of an impedancemetric signal correlated to glucose uptake by fibroblasts, the same experiments are performed with D-mannitol instead of glucose, a sweetener not metabolized by the cells. No variation is observed with D-mannitol additions in the range from 1 to 15 mmol.

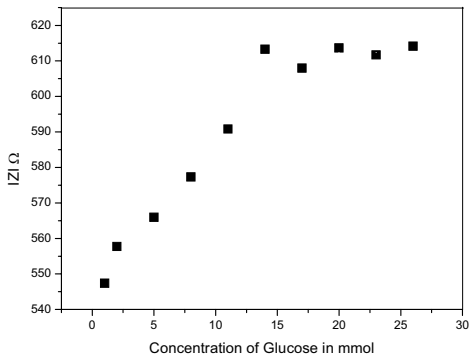

Fig. 3. Calibration plot of the glucose biosensor.

2.3 Impedance spectra of inhibited cells

To strengthen our hypothesis we inhibited the glucose transporters of the 3T3-L1 fibroblasts by using cytochalasin B which inhibits Glut 1 and Glut 4 mediated glucose uptake[32]. After glucose additions, the curves are superimposed which indicates that the resistance and the capacitance of the cell monolayer are not modified and consequently that glucose is no larger incorporated into the cells. These results demonstrate that the changes in the resistance and in the capacity of the cell monolayer directly result from glucose uptake and metabolization of glucose by the cells.

3. Conclusion

The present study shows for the first time the feasability and specificity of glucose sensing by fibroblasts over the physiological range of glucose concentrations, using impedancemetry analysis. Further studies, over a wider frequency range, are under way in order to improve the performance of the sensing device. Such biosensor could be applied to a more fundamental study of cell metabolism.

References

1. S. Cosnier, A. Senillou, M. Grätzel, P. Comte, N. Vlachopoulos, N. Jaffrezic-Renault, C. Martelet. A glucose biosensor based on enzyme entrapment within polypyrole films electrodeposited on mesoporous titanium dioxide. *J. Electroanal. Chem*. 469 (1999) 176-181.

2. S. Poyard, N. Jaffrezic-Renault, C. Martelet, P. Labbe, J. L. Besombes, S. Cosnier. A new method for the controlled immobilization of enzyme in inorganic gels (laponite) for amperometric glucose biosensing. *Sensors and Actuators B: Chemical.* 33 (1996) 44-49.

3. W. K. Ward, L. B. Jansen, E. Anderson, G. Reach, J. C. Klein, G. S. Wilson. A new amperometric glucose microsensor: in vitro and short-term in vivo evaluation. *Biosensors and bioelectronics*. 17 (2002) 181-189.

4. E. Wilkins, P. Atanasov, B. A. Muggenburg. Integrated implantable device for long-term glucose monitoring. *Biosensors and Bioelectronics*. 10 (1995) 485-494.

LTCC Manifold for Heavy Metal Detection System In Biomedical and Environmental Fluids

M. R. Gongora-Rubio[1], M. Bariatto Andrade Fontes[2], Z. Mendes da Rocha[2], E. Ritcher[3] and L. Agnes[3]

[1]Instituto de Pesquisas Tecnológicas do Estado de São Paulo - IPT, DITT/Laboratório de Instrumentação, Cidade Universitária, São Paulo, S.P., Brazil.
email: gongoram@ipt.br
[2]Universidade de São Paulo, LSI/EPUSP, Cidade Universitária, São Paulo, S.P., Brazil.
[3]Universidade de São Paulo, Instituto de Química, Cidade Universitária, São Paulo, S.P., Brazil.

Summary: *This work gives a short description of how LTCC (Low Temperature Cofired Ceramics) technology is a suitable material system for a FIA (Flow Injection Analysis) meso-analytical system fabrication of heavy metal detection system for biological and environmental fluids. The paper presents design and fabrication issues of a LTCC manifold integrated with sensor electrodes. The requirement of on-line measurement tests with high sensitivity for heavy metals has motivated the development of sensors for electrochemical stripping techniques in flow. Preliminary bench results, using a pre-concentration scheme, for mercury concentration, indicate a lower detection limit of 10 µg/, which is much lower than the maximum tolerable concentration for fresh waters and urinary fluids.*

Keywords: *LTCC, Chemical Sensors, FIA, Heavy metal detection.*
Category: 5

1 Introduction

In the Biomedical, Biotechnology & Chemical fields there are increased needs for analytical systems with new requirements and functionalities as: on-line in-flow measurement in decentralized fashion, better sensitivity, lower dead volumes, shorter response time, smaller sizes, lower power consumption, multi-sensor devices and low cost.
Flow techniques have been widely used in the analysis of environmental and Biomedical parameters, to which they are particularly adapted. In the E. Hansen [1] database with more than 700 citations related to the FIA practice we found several FIA approaches, but many of them are intended for off-line instrumentation. The meso-analytical system to be manufactured comprises a FIA for chemical sensing associated to other type of sensors as temperature, PH, DOB and a control, acquisition and transmission electronics integrated in a LTCC substrate to acquire the required environmental or biomedical data.
Our LTCC research has been focused on meso analytical system implementation in the last five years [2]. Such period has let us to design, simulate, fabricate and test several devices such as: flow sensors [3], passive flow controllers [2], micro-valves [2] and passive Mixers [4]. Fabricated devices may be integrated, using LTCC technology in a hybrid way, into a single meso system with enhanced functionality. The desired analytical meso-system is at present in development, so studies, simulations and tests are in progress, in order to develop remaining system parts.
At this time we would like to report a LTCC manifold with integrated sensor array for the proposed task.

2 LTCC Technology

LTCC ceramic tapes are glass - ceramic composite materials. They are produced in flat tapes of thickness usually in the range of 100 to 300 µm. One important feature of LTCC technology is the possibility of fabricating 3D devices using multiple layers fabricated in the green (before firing) with whatever feature in the form of vias, cavities, channels, internal electrical thick film elements are needed for the overall function of the structure.
The processing of the green ceramic tapes is usually done in three steps: 1) Machining and patterning of individual layers with via holes, cavities, resistors, conductors or dielectric pastes; 2) Collation and lamination of the tapes under pressure and temperature and 3) Co-firing of the entire laminate to sinter the material.

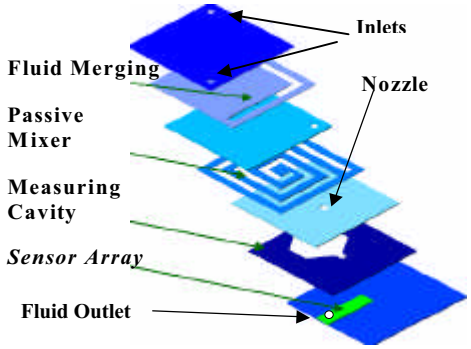

Fig. 1. LTCC layers for Manifold and sensor array.

3 Manifold and sensor array

A manifold for various tasks was designed, we include the possibility of mixing two fluids (if a reagent is needed) and implement a spiral coil used as a mixing/reaction chamber. DuPont 951 LTCC tapes with layer thickness of 250 µm were used to fabricate 1mm width microchannels, see figure 1.
A multi-electrode sensor array for electro-chemical measurement was fabricated using thick film deposition. The sensor array is composed of a silver/silver chloride reference electrode, a gold counter electrode and two gold detection electrodes (L=300µm, W=2mm). Figure 2 demonstrates electrode geometry for chemical sensing.

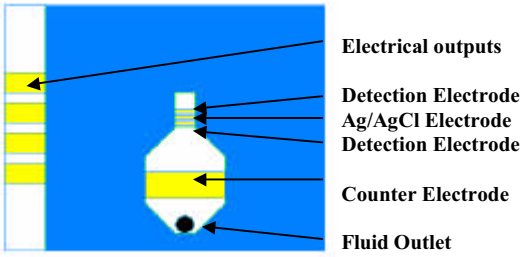

Fig.2. In flow sensor array geometry.

A ceramic green tape manifold will integrate the electrochemical detector using the auto-packaging capabilities of the LTCC technology. Figure 3 illustrates the fabricated manifold and integrated sensor array (four devices in a 3 x 3"LTCC tapes).

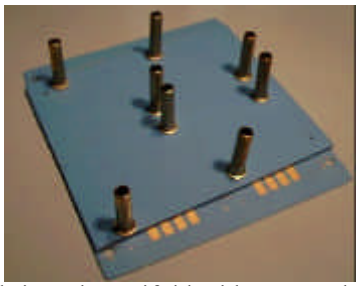

Fig.3. Fabricated Manifold with sensor electrodes.

3. Sample preparation, analytical techniques and results

All the solutions were prepared with deionized (18 MΩ) water obtained from a Milli-Q system (Millipore). The mercury stock solution (1000 mg/L, 1 wt. % nitric acid, atomic absorption standard solution, Aldrich) was diluted as required, just before their use. Hydrochloride acid solution (0.05 mol/L) was used as supporting electrolyte, prepared by dilution of Suprapur grade (Merck) concentrated hydrochloric acid. Nitric acid (suprapur) and hydrogen peroxide were purchased from Merck and used without further purification.
Potentiometric stripping analysis and cyclic voltammetry were performed with an Electrochemical System (Autolab PGSTAT 20, Eco Chemie - Utrecht) connected to a Pentium 200 MHz computer.
We added continuously 10µg/L of the stock solution to achieve 60µg/L. The pre-concentration potential was –0.35V, 30min, and sweep potential from 0.35V to –0,65V. We observed a mercury oxidation peak around 0.626V. The calibration curve obtained shown in figure 4.

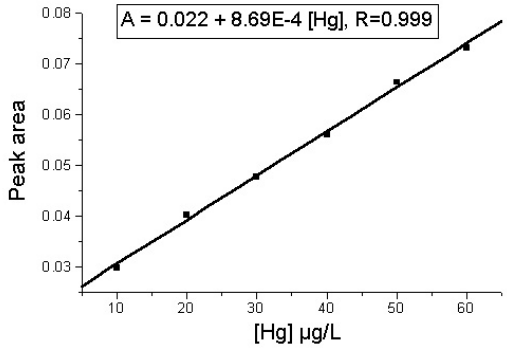

Fig.4. Manifold bench test results.

Conclusions

An LTCC manifold integrated with sensor electrodes for heavy metal detection meso-system suitable for biological and environmental fluids was fabricated and tested. Bench test indicates sensitivities for Hg of about 10 µg/l allowing biological and environmental fluids in-flow tests practicable.

Acknowledgements

M.R.G.R. and M.B.A.F. would like to acknowledge CNPq for partial support of this research.
We would like to acknowledge DuPont for provide Green Tape® materials for device fabrication.

References

[1] HANSEN E.H., http://www.flowinjection.com/search.html

[2] M. R. Gongora-Rubio, P. Espinoza-Vallejo, L. Sola-Laguna, and J.J. Santiago-Aviles. Overview of Low Temperature Co-fired Ceramics Tape Technology for Meso-System Technology, *Sensors and Actuators, A,* A89, pp. 222-241 (2001).

[3] M. R. Gongora-Rubio, Solá-Laguna L.M., P.J. Moffet & Santiago Aviles J. J., The utilization of low temperature co-fired ceramics -LTCC-ML - technology for meso-scale SEM, a simple thermistor based flow sensor, *Sensors-and-Actuators, A: Physical*. v. 73 n 3 1999, pp. 215-221.

[4] M. R. Gongora-Rubio, E. W. Simões, M. Bariatto A. F., R. Furlan, I. Ramos, M. T. Pereira & J. J. Santiago-Avilés. LTCC Hybrid Technology For Microfluidic Systems In Analytical Chemistry, *Proceedings of IBERSENSOR 2002,* Lima, Peru, 2002 pp.

Naphthalene Detection by a Bioluminescence Sensor

B. Valdman[1], F. Battaglini[2], S.G.F. Leite[1] and E. Valdman[1]

[1]Universidade Federal do Rio de Janeiro, EQ, Cid. Universitária, Bl. E, 21940-900, Rio de Janeiro, Brazil - email: belkis@eq.ufrj.br
[2]Universidade de Buenos Aires, INQUIMAE/DQIAQF, Buenos Aires, Argentina

Summary: *A bioluminescence detection system using* Ps. fluorescens *HK44 was applied for naphthalene measurement in a range 0 - 0.5 mg L^{-1}, lower than the maximum of 1mg L^{-1} recommended by EPA.. Diluted sample injections of naphthalene were added to 0.2 g L^{-1} or 0.4 g L^{-1} cellular concentrations used in the measurement medium. The same system was applied to a waste water effluent collected from a hydrocarbon contaminated site (2.4 mg L^{-1}) which includes naphthalene. The output signal of the biosensor system for the effluent was fully compatible with the results obtained for the naphthalene solutions.*

Keywords: *bioluminescence, effluent, naphthalene,* Ps. fluorescens *HK44*
Category: *6 (Biosensor)*

1 Introduction

Polycyclic aromatic hydrocarbons (PAH) are a well known group of carcinogenic compounds widely distributed in the environment. Naphthalene, one of those PAHs, enters the environment from industrial uses and incident spills. Exposure to large amounts of naphthalene may cause several harmful effects and possible damage or destruction of some of red blood cells. Due to the low level of exposure suggested by Environmental Protection Agency (EPA) of 1 mg L^{-1}, the quantification of this compound is of great interest.

Bioluminescence of genetically engineered microorganisms (GEMs) [1-5] is becoming a potential alternative to conventional technologies, where the bioluminescence response to naphthalene contamination is measured in real time *Pseudomonas fluorescens* HK44 represents the first GEM approved for field testing in the United States for bioremediation purposes. Strain HK44 harbors an introduced *lux* gene fused within a naphthalene degradative pathway [1], thereby allowing this recombinant microbe to bioluminescence as it degrades this specific PAH.

A biosensor using strain HK44 has been applied in this work for naphthalene detection at the concentration range 0-0.5 mg L^{-1}, lower than the maximum concentration recommended by EPA. This system has also been extended for the detection of naphthalene in contaminants present in a real waste water effluent.

2 Methods

2.1 Bacterial strain

A bioluminescent catabolic reporter strain, *Pseudomonas fluorescens* HK44 [1] was purchased from DMSZ, Germany. The bacterial strain is able to emit light as it degrades naphthalene, allowing this PAH compound catabolism to be monitored. *Ps. fluorescens* HK44 was incubated in YEPG medium [2] with addition of 15 mg tetracycline L^{-1} (pH 7.0). After growth at 28°C, cells were centrifuged and resuspended in 0.01% yeast extract solution.

2.2 Bioluminescence assay

Sampling lines of the cellular suspension (0.2 or 0.4 g L^{-1}) were continuously pumped (2 mL min^{-1}) through a flow cell (work volume = 0.4 mL) located in a black chamber to minimize background light (Fig. 1).

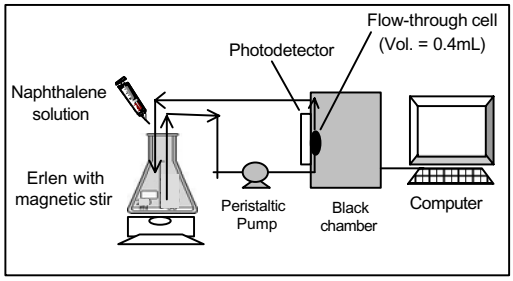

Fig. 1. Schematic diagram for bioluminescence sensor system

Time zero corresponded to the time of addition of a known volume of naphthalene solution to achieve 0-0.5 mg L^{-1} working range concentration [2].The light intensity signal for each sample was subtracted from the reference level signal of the aqueous cell suspension without naphthalene.

2.3 Light measurement

A PTI (Photon Technology International) digital display model 814 with a Hamamatsu photomultiplier tube model R4220 was used for all light measurements. Light detection was measured as a current (nA) from a photoelectric effect and

was sensitive to 10^{-9} A of induced current. The photomultiplier was connected to a computer through a National Instruments data acquisition card (model Lab-PC), allowing continuous sampling of photomultiplier output over long periods of time.

3. Results

In order to detect concentrations below the maximum value (1 mg L^{-1}) recommended by EPA for waste water, all experiments were conducted for a maximum of 0.5 mg naphthalene L^{-1} . On line measurements showed an increasing light emission until 0.28 mg naphthalene L^{-1} with a cell concentration of 0.2 g L^{-1} (Fig. 3).

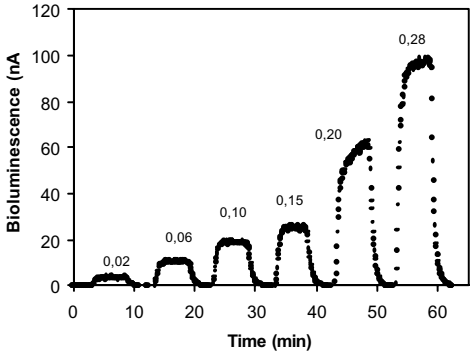

Fig. 2. Bioluminescence response to naphthalene (0.02-0.28 mg L^{-1}) with cell concentration = 0.2 g L^{-1}

Average values of output signals (bioluminescence) achieved at steady state light emission against naphthalene concentrations were plotted in Figure 3, showing a saturated response with 0.2 g cell L^{-1}.

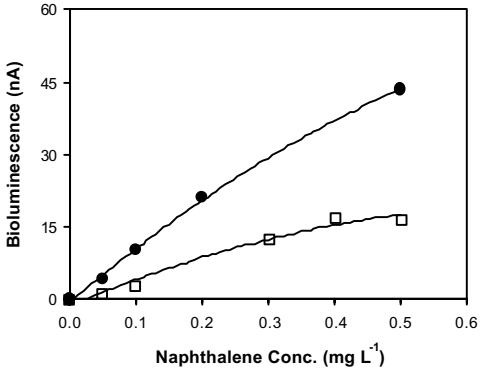

Fig. 3. Biosensor system calibration curves for ( ) 0.2 g L^{-1} and (λ) 0.4 g L^{-1} cell concentrations.

A real effluent was also collected from a hydrocarbon (HC) contaminated site (2.4 mg L^{-1}) to verify the bioluminescence response of strain HK44. As total HC concentration was low, cell concentration used was 0.2 g L^{-1}. As shown in Figure 4, output signals were obtained with diluted solutions of the effluent, for the range 0-1.2 mg L^{-1} of HC concentration.

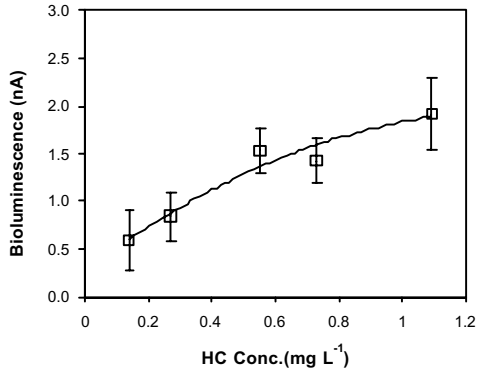

Fig. 4. Biosensor system response for a real effluent with cell concentration = 0.2 g L^{-1}

Considering that naphthalene concentration in this real effluent is in the range 1:10, the bioluminescence response obtained is in accordance with the calibration curve shown in Figure 3.

4. Conclusions

On line tests carried out using a biosensor system with a flow through cell and sample injections were successfully used to detect naphthalene in concentrations lower than 1 mg L^{-1}. A cell concentration of 0.2 g L^{-1} showed a good performance in the detection of low naphthalene concentrations present in a real effluent. Bioluminescence produced by *Ps. fluorescens* HK44 is a sensible analytical technique with potential to be used in the detection of PAH environmental contamination.

References

[1] J.M.H. King , P.M. DiGrazia, B. Applegate, R. Burlage, J. Sanseverino, P. Dunbar, F. Larimer and G.S. Sayler. *Science* 249 (1990) 778-781.

[2] E. Valdman, B. Valdman, S.G.F. Leite and F. Battaglini. *I Jornadas Nacionales AAQA* - Rosário, Argentina (2001) 27.

[3] C.J. Kelly, C.A. Lajoie, A.C. Layton and G.S. Sayler. *Wat. Environ. Res*., 71 (1999) 31-35.

[4] O. Bechor, D.R. Smulski, T.K. Van Dyk, R.A. La Rossa and S. Belkin. *J. Biotechnol.* 94 (2002) 125-132.

[5] B.M. Willardson, J.F. Wilkins, T.A. Rand, J.M. Schupp, K.K. Hill, P. Keim and P.J. Jackson. *Appl. Environ. Microbiol*. 64 (1998) 1006-1012.

A Low-Power CMOS Interface Chip for Data Logging Applications

Ulrik S. Wismar, Arda D. Yalçınkaya and Ole Hansen

Mikroelektronik Centret (MIC), Technical University of Denmark, B 345 E, DK-2800 Lyngby, Denmark.
http://www.mic.dtu.dk, E-mail: ady@mic.dtu.dk

Summary: *The interface chip presented in this paper is a dedicated chip designed for fish data loggers, that converts sensor signals from 7 sensors into an 11 bit digital signal. A full-custom prototype chip was fabricated in a 0.6 μm Complementary Metal Oxide Semiconductor (CMOS) process. Designed for a 5V battery supply, the chip has a power consumption less than 1.5 mW. The chip can be used to interface a large variety of sensors such as pressure, acceleration, temperature and light. In order to demonstrate the functionality, a hybrid system containing a pressure sensor and the interface chip was tested. This measurement showed a fine separation of different pressure levels and a linearity over a pressure range from 0 to 12 bar.*

Keywords: *Interfacing, multi sensor, ADC*
Category: *9 (System architecture, electronic interfaces, wireless interfaces)*

1 Introduction

Current demands on the data loggers for fisheries research have made it necessary to integrate multiple functionalities without sacrificing low power consumption, small size and portability. The original application of the present chip is to interface sensors placed on a fish to be used as a data logger. Some important physical parameters to be gauged in this task are pressure, temperature, acceleration/tilt, light intensity and conductivity. These parameters, for instance, can supply information about swimming depth, tail movement frequency, water salinity, hunting and escape behavior of the fish. A data logger on a fish is battery driven, and the interface is therefore optimized for battery supply and low power consumption. The chip could also be used in other applications, where a general sensor interface is needed [1].

2 Description of the Design

The chip can process seven external sensor signals and one internal temperature sensor signal, all of which are interfaced to high-impedance inputs. A block diagram of the interface chip is seen in Figure 1. The inputs are connected to an input multiplexer, and one of the inputs is passed to an instrumentation amplifier according to three input selection bits. If the first input is selected, the internal temperature sensor output is processed. In order to be able to communicate with a broad range of sensors, regardless their transduction styles and signal levels, the gain in the instrumentation amplifier can be set to 1, 10 or 100 times through two gain control bits. The output voltage from the amplifier is related to an internal reference voltage of 2.50 V below the supply voltage, which normally is in the range of 4.5 to 5.5 V. The amplified differential signal is then applied to the input of an 11-bit dual-slope integrating Analog Digital Converter (ADC) [2]. Since the conversion speed is not an issue, the obvious choice was a dual-slope ADC thanks to its precision and low-power consumption.

The ADC uses the same reference voltage as the amplifier meaning that the precision of the conversion is independent of changes in the supply voltage. Since the converter is an integrating type, an oscillator is needed for the internal counter of the ADC. In order to make the interface easy to use in a large variety of applications, an internal ring oscillator with a free-running frequency of 1 MHz is included in the chip. An external port allows to reduce the oscillation frequency, thereby increasing the resolution of the ADC. Since the data logger is a battery operated portable system, the interface circuit has to consume low-power. Using a supply voltage of 5V, the system is designed to consume 1.5 mW (drawing 300 μA of current) in the worst case. With this power consumption, the interface chip can fill 16 MB of data with a standard 5 mAh battery, corresponding to 16.7 hours of memory time.

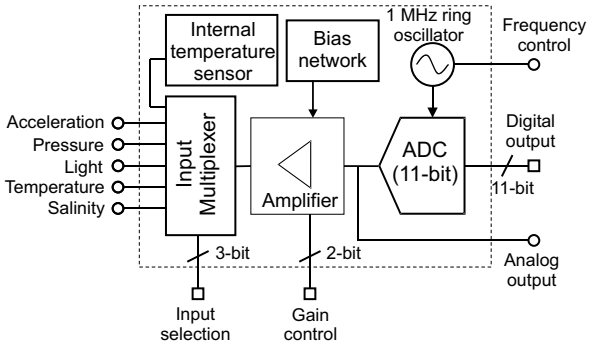

Fig. 1: Block diagram showing the contents of the interface chip.

In order to eliminate mismatch of the components, a common-centroid layout was designed for analog parts. Figure 2 shows a micrograph of the fabricated proto-

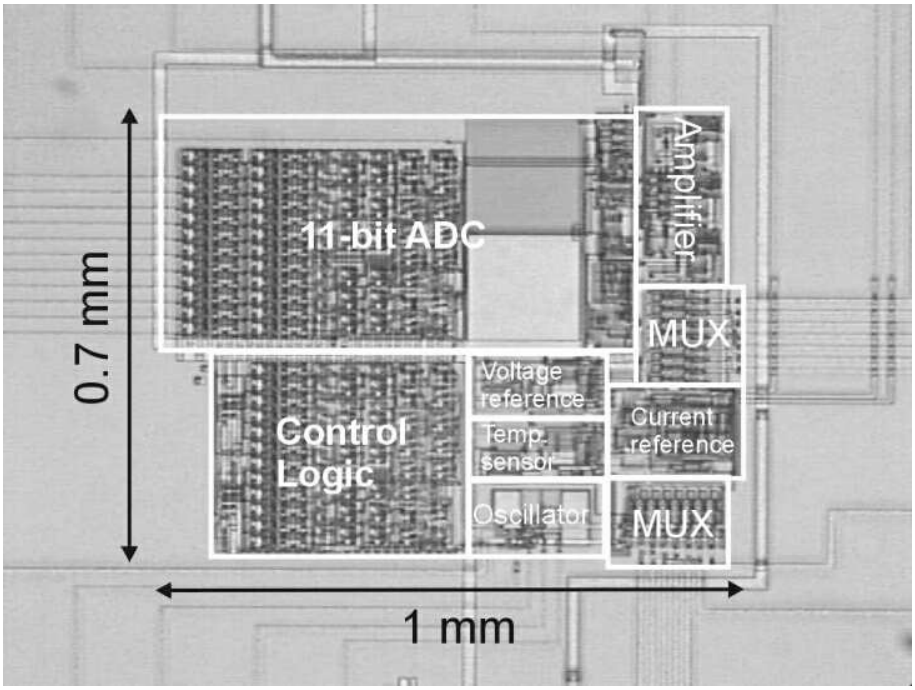

Fig. 2: Die micrograph of the fabricated prototype. Active chip area measures 1 mm×0.7 mm.

type using 0.6μm double poly, triple metal CMOS process from Austria Micro Systems. The layout is divided into two blocks containing analog and digital circuits respectively. This is done to avoid coupling of digital signals to the analog circuits. Separation of the supply voltages for the digital and the analog blocks helps to reduce the coupling and noise between these blocks. The chip die has an area of 0.7 mm^2 and the chip uses 43 bonding pads.

3 Measurement Results

As a measure of performance, the chip was interfaced to a differential pressure sensor with a piezoresistive Wheatstone bridge giving an analog output voltage in the range from 0 to 50 mV for pressure levels from 0 bar to 12 bar. The digital output from the interface as a function of the pressure applied to the sensor is shown in Figure 3. The digital words are converted into voltages to yield in Figure 3, where the 11 bit full scale value equals 2.500 V. The pressure applied to the sensor was measured in bar with three decimals of precision, and the digital result was found for pressures in the range from 0.5 bar to 12 bar, emulating a fish swimming at water depths from 5 m to 120 m. Taking the sensor signal level into account, an amplification of 10 and a clock frequency of 200 kHz were chosen for the best resolution. Three conversions were made at each pressure to find the maximum repetition error which was found to be 1 bit. Extrapolation over the experimental data reveals possibilities of separating pressures down to 0.05 bar in a pressure range from 0 to 93.4 bar.

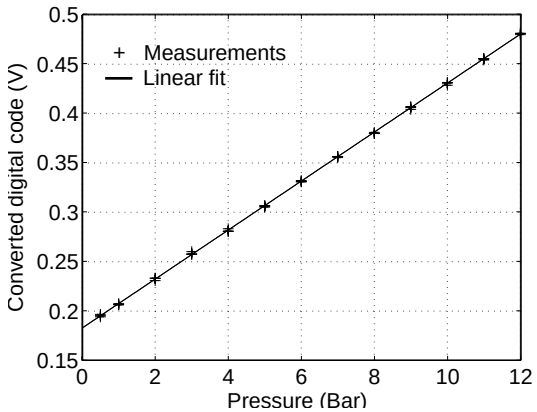

Fig. 3: Results from measurements with a pressure sensor applied to the interface chip.

4 Conclusion

A low-power, battery driven, portable sensor interface circuit was successfully designed and tested. Operating with a battery supply of 5 V and consuming 1.5 mW, the chip has shown to satisfy the requirements set by the fisheries research applications. Experimental characterization of the chip was performed along with a pressure sensor resulting in a maximum bit error of 1-bit.

References

[1] W. Claes et al., *IEEE J. Solid-State Circuits*, **37** (3) , pp. 293-301, 2002.

[2] S.M.R. Taha, *IEEE Trans. Instrum. and Measurements*, **34** (4), pp. 630-635, 1985.

A New Concept for the Linearisation of Sensor Bridge Circuits

G. de Graaf and R.F. Wolffenbuttel
Delft University of Technology, ITS/Et, DIMES,
Mekelweg 4, 2628 CD Delft, The Netherlands
Phone +31 15 278 4707, Fax. +31 15 278 5755
e-mail: G.deGraaf@its.tudelft.nl

Summary: *A general concept for the linearization of impedance bridges with circuit components changing in only one polarity is presented. A trans-admittance properly designed and matched to the nominal value of the bridge components reduces non-linearity from 9% to 0.4% over ±20% of bridge imbalance. This approach can conveniently be integrated with the readout circuit resulting in a highly linear sensor readout.*

Keywords: *Sensor bridge, linearisation, OFA*
Category: *Electronic Interfaces*

1 Introduction

Impedance bridges (Wheatstone bridges the in case of resistors) are universally applied for precision measurement and the read-out of sensors. A general feature of a bridge configuration is its simplicity. In case the nominal values of the components are well matched, the bridge also enables rejection of common-mode signals and improves power supply rejection. Moreover, parasitic transduction effects (notably temperature dependencies) can be compensated for. However, a linear output is obtained only in the fully-symmetric bridge configuration shown in Fig. 1a. The output voltage is described by: $U_o/U = \Delta Z/Z$, provided that the load impedance of the bridge (= the input impedance of the readout circuit) is much higher than the output impedance of the bridge. The main problem of this conventional Wheatstone bridge is that both an increasing and a decreasing (e.g. Z+ΔZ **and** Z-ΔZ) impedances have to be available in opposite bridge arms. This is achieved eg. in some differential capacitive transducers [1]. However, for practical or cost reasons often only increasing **or** decreasing component values (Z, Z+ΔZ **or** Z, Z-ΔZ) are available, for example piezoresistors in a membrane [2]. This paper demonstrates that linear readout can nevertheless be obtained by designing readout using a uniquely determined trans-impedance.

Non-linearity compensation concept

Figure 1b shows the non-symmetric half and full bridge configuration with Z+ΔZ elements only. The transfer function of this bridge can be derived as:

$$\frac{U_O}{U} = \frac{-\Delta Z}{Z + \left(\frac{2Z}{Z_b} + 1\right)(\Delta Z + Z)} \qquad (1)$$

For $Z = Z(1+\varepsilon)$ and $Z_b \gg 2Z$ the bridge transfer function can be written as: $\frac{U_O}{U} = \frac{-\varepsilon}{2+\varepsilon}$

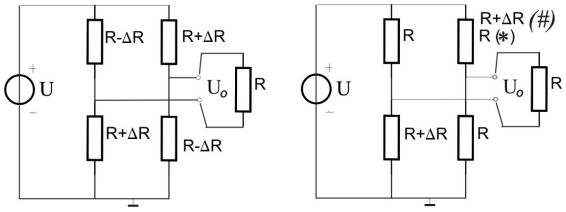

Fig. 1.a Conventional fully-symmetric impedance bridge.

1.b Full-(#) and half –bridge(*) only Z+ΔZ values.

A relative change of the active bridge components of 20% (ε= 0.2) results in a non-linearity in the output voltage of the bridge of about 9%. Equation (1) implies that the bridge non-linearity can be controlled by the load impedance Z_b. For a linear response Z_b should be equal to: $Z_b = -2Z$. This negative impedance can be electronically synthesized and combined with the bridge read-out, as is demonstrated in the next paragraph.

Read-out amplifier principle

Figure 2 shows the basic block diagram for bridge readout with simultaneous realization of a negative load impedance. The general transfer function of the differential input/output amplifier is given by:

$$\begin{bmatrix} U_o \\ i_o \end{bmatrix} = \begin{bmatrix} A_v & Z_i \\ Y_m & A_i \end{bmatrix} \begin{bmatrix} U_i \\ i_i \end{bmatrix}$$

Since $U_i = U_o$ and if the current gain A_i and the input impedance Z_i are designed for very high values, the desired transfer function is a trans-admittance with:

$$Y_m = \frac{i_o}{u_i} = -\frac{1}{2Z},$$

where Z denotes the nominal value of one of the four bridge impedances. A linearized Wheatstone bridge thus requires a voltage-to-current converter with a trans-conductance:

$$G_m = \frac{i_o}{u_i} = -\frac{1}{2R}$$

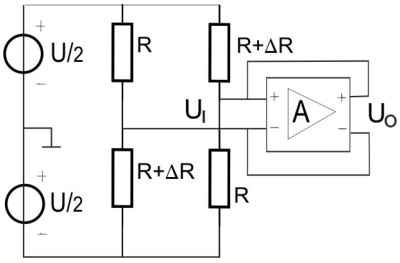

Figure2, Bridge and read-out amplifier.

Generally, it can be concluded that for a full bridge with linear output, the read-out amplifier should be realized using a floating voltage-current converter with a trans-conductance equal to twice the value of one of the bridge components.
Table 1 shows an overview of various bridge configurations with the required amplifier transfer function for a linear response.

	Bridge/Readout Transfer $[U_o/U]$	Required trans-admittance $[I_o/U]$
	Full bridge	
Resistive	$\Delta R/R$	$-1/(2R)$
Cap.$(\Delta\varepsilon,\Delta A)$	$\Delta C/C$ or $\Delta A/A$	$-j\omega(C+\Delta C)/2$
Cap.(Δd)	$2\,\Delta d/d$	$-j\omega C/2$
Inductive	$\Delta L/L$	$-1/(2j\omega L)$
	Half bridge	
Resistive	$-3/4\,\Delta R/R$	$-2/(3R)$
Cap $(\Delta\varepsilon,\Delta A)$	$\Delta C/4C$, $\Delta A/4A$	$-(2/3)\,j\omega(C+\Delta C)$
Cap (Δd)	$2\,\Delta d/d$	$-(2/3)\,j\omega C$
Inductive	$(3/4)\Delta L/L$	$-2/(3j\omega L)$

For capacitive bridges, devices with change in permittivity ($\Delta\varepsilon_r/\varepsilon_r$) or plate area ($\Delta A/A$) and sensors with plate distance variations ($\Delta d/d$) as the measurand can be distinguished. The bridge-amplifier combination provides a linear response in both cases, using the values of the trans-admittance from Table 1.

Realisation

The differential voltage-to-current amplifier can be implemented in many ways depending, on the required accuracy and frequency range of the bridge excitation signal. Figure 3 shows a full-floating voltage-to-current converter [4], using two differential input-output amplifiers (OFA's) for readout of a Wheatstone bridge. The circuit can operate at bridge excitation voltages between DC and several MHz,. The value of the trans-conductance should be set by two resistors that are well-matched with the nominal values of the bridge components, which is relatively easily achieved in integrated sensors. Positive feedback of the amplifier is required for synthesizing the negative trans-conductance.

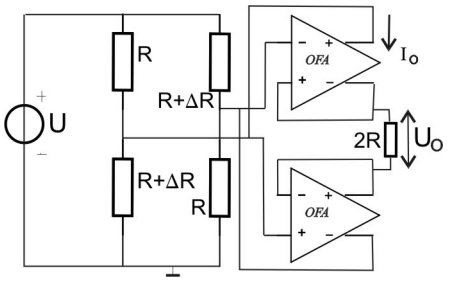

Figure3. Resistive bridge readout using two operational floating amplifiers (OFA's).

An important issue is therefore the stability of the entire system. The loop-transfer function is the product of the trans-conductance G_m of the read-out amplifier and the bridge output impedance Z_o. It can shown that it is a function of the bridge unbalance ε only and always smaller than –1 with maximum of -2/3 for ε= 1 (ΔR=R). The frequency response of the amplifier has to be carefully compensated to ensure a sufficient phase margin. The circuit has been implemented both for capacitive and resistive bridges in a CMOS process. The chip layout is shown in Fig. 5. The design predicts a non-linearity smaller than ±0.4% over ±20% bridge imbalance, which is an improvement by a factor 22 as compared to a conventional readout.

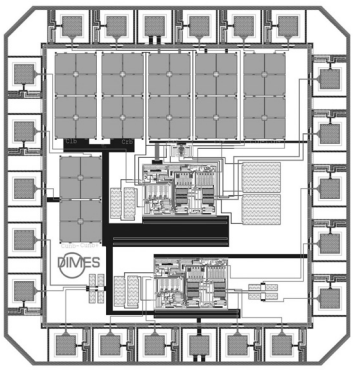

Conclusions

A technique for linearization of various half- or full impedance bridges is presented. The method presented can be implemented in a conventional bridge and is combined with basic readout. Accurate low-noise trans-conductance amplifiers in CMOS and floating voltage-to-current converters in bipolar technology have been designed and are now fabricated to experimentally verify operation.

References

[1] A novel combined redundant pressure sensor with self-test function**,** Sensors and Actuators A: Physical, Volume 60, Issues 1-3, May 1997, Pages 68-71, R. Puers, D. D. Bruyker and A. Cozma

[2] E. Kälvesten, L. Löfdahl and G. Stemme, Small piezoresistive silicon microphones specially designed for the characterization of turbulent gas flows. *Sens. Actuators A: Phys.* A46 (1995), pp. 151–155.

[3] Operational Amplifiers Theory and Design , J.H.Huijsing, Kluwer. Ac.Publishers, 101 Philip Drive Norwell, MA02060, USA.

Silicon photodiodes array for optical gas sensing

A. Tibuzzi[1], A. Macagnano[4], R. Paolesse[3], C. Di Natale[2], M. Zen[5], G. Soncini[1], A. D'Amico[2]

[1]University of Trento, Information&Communication Dept., Via Sommarive 14, 38050 Povo, Trento, Italy
email: arianna.tibuzzi@dit.unitn.it http://www.dit.unitn.it
[2]University of Rome Tor Vergata, Electronics Engineering Dept., Via del Politecnico 1, 00133 Rome, Italy
[3]University of Rome Tor Vergata, Chemical Sciences and Technologies Dept., Via della Ricerca Scientifica, 00133 Rome, Italy
[4]IMM-CNR National Research Council,Via Fosso del Cavaliere 110, 00133 Rome, Italy
[5]ITC-IRST, Microsystems Division, Via Sommarive 18, 38050 Povo, Trento, Italy

Summary: *A silicon integrated photodiodes array has been assembled, packaged and tested. Each photodiode has been coated by evaporation with a different metalloporphyrine. Both a blue LED and a white lamp with a monochromator have been used as light source with emission around 430nm, in the Soret band, where the absorption peak of the porphyrine is maximum. Porphyrine changes its adsorption spectrum in amplitude and wavelength peak in presence of VOCs; the transducer detects this with a variation in the generated current. Measurements in ethanol and tetrilammine vapors at different concentrations down to 1% have been performed. The system will be employed as an integrated electro-optical nose.*

Keywords: *silicon photodiodes, metalloporphyrins, optical sensing,*
Category: *5 (Chemical sensors)*

1 Introduction

The field of artificial olfaction has been significantly fruitful in the latest years with the introduction and study of new electronic noses and applications in several different areas, such as food and agriculture, industrial production and medicine. The need for a miniaturized nose, providing low cost, low weight, low power consumption, has driven our research on an innovative electro-optical system, made up of a photodiodes matrix, coated by metalloporphyrins as chemical interactive materials with interesting optical properties.

2 Metalloporphyrins properties and Transduction mechanism

The working principle of the optical sensor is based on the optical properties of the chemical sensing layer employed: in presence of a volatile compound, metalloporphyrins modify their absorption spectrum by shifting it towards higher/lower wavelengths and by changing the peak value amplitude (Fig.1) [1,2]. These CIMs are deposited by evaporation on silicon photodiodes (750μm×1010μm) able to detect the change in the light intensity they collect in their active depletion region (710μm×710μm). The devices employed in this first prototype have a responsivity peak around 900 nm, corresponding to 0.15 A/W in the Soret band. The photodiodes matrix is bonded in a dedicated package, with a glass transparent top to let the light of the blue led source pass and with two lateral holes for the gas flow (Fig.2); the transduction array is then included in a simple circuit that converts the generated reverse current output into an amplified voltage signal by using an operational amplifier with a 15MΩ feedback resistor (Fig.3).

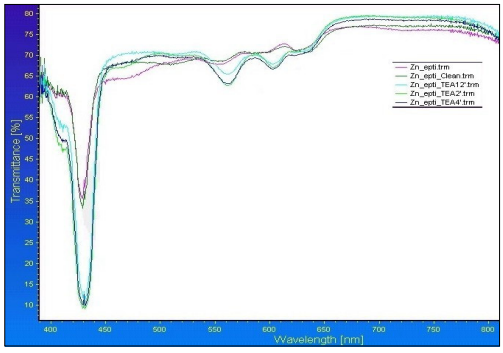

Fig. 1. Transmission spectrum of Zn-heptyloxy-TPP with no TEA and after 2',4',12' from TEA injection. The amplitude variation is reversible.

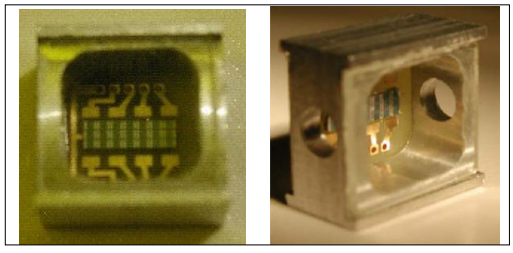

Fig. 2. Top and lateral view of the metal package containing the coated photodiodes array.

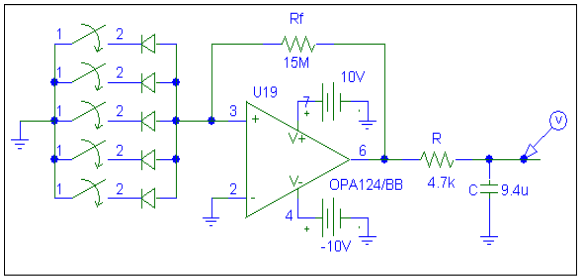

Fig. 3. Measurement circuit made up of the reverse biased photodiode as current generator, an operational amplifier to produce a voltage output and a low-pass filter to increase S/N ratio.

3 Experimental set-up and Results

The packaged chip has been lodged into a closed black PVC cylindrical chamber provided with holes for electrical connections to the circuit, for locating the light source in front of the matrix and for the tubes carrying the gas flux to be detected. The first experiments were performed with ethanol, using a two channels flux-meter to change the gas concentration and a bubbler. Nitrogen was employed as carrier and to clean the chamber after each cycle. Fig.4 and 5 shows the results obtained by employing, respectively, a Co-T(hexadodecyloxy)PP with a blue LED operated in continuous mode and a Zn-T(heptyloxy)PP with a white lamp followed by a monochromator, selecting the wavelength of 427nm. This second experiment allowed the detection of 5% EtOH, proving the importance of adjusting the source on the wavelength corresponding to the maximum variation in the transmission spectrum.

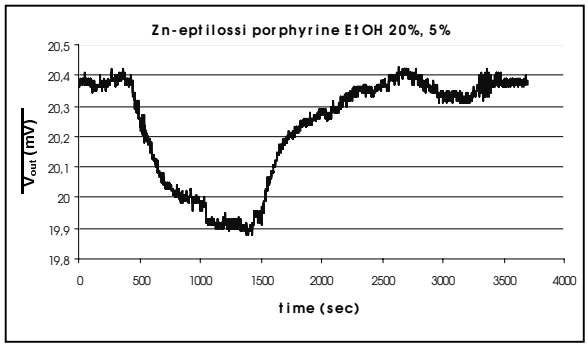

Fig. 5. Output voltage versus time while 2 measurement cycles at 20% and 5% EtOH concentrations are performed.

References

[1] C. Di Natale, D. Salimbeni, R. Paolesse, A. Macagnano, A. D Amico, *Porphyrins-based opto-electronic nose for the volatile compounds detection*, Sensors and Actuators B 65 2000 220-226.

[2] C. Di Natale, R. Paolesse, P. Bizzarri, A. Macagnano, A.G. Mignani, A. D Amico, *Optical transduction of the sensitive properties of an array of porphyrin films*, 9th International Meeting on Chemical Sensors Boston (USA), July 7-10, 2002.

[3] A. Tibuzzi, A. D Amico, C. Di Natale, R. Paolesse, A. Macagnano, G. Soncini, M. Zen, *A new prototipe of Electro-Optical Nose*, ISOEN 02 International Symposium on Olfaction and Electronic Nose, Rome, Italy, Sept. 29-Oct. 2, 2002.

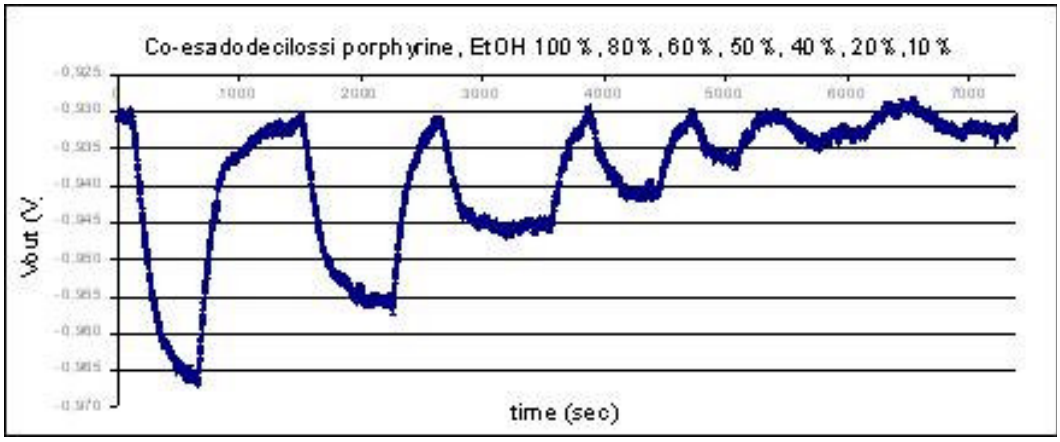

Fig. 4. Output voltage versus time while 7 measurement cycles at decreasing EtOH concentrations are performed.

An Inductive Powering System with Integrated Bidirectional Datatransmission

M. Catrysse, B. Hermans and R. Puers

K.U.Leuven, ESAT-MICAS, Kasteelpark Arenberg 10, B-3001 Leuven, Belgium
email: michael.catrysse@esat.kuleuven.ac.be http://www.esat.kuleuven.ac.be/micas

Summary: *An inductive powering system is presented, capable of powering implantable monitoring and stimulating devices. The system is capable of delivering at least 50 mW, with an efficiency of 36 % over a distance of 3 cm. The power transfer frequency is 700 kHz. Optimisation of the power transfer efficiency and the misalignment tolerance was obtained using a self-developed design tool. Moreover, a bidirectional datatransmission is integrated in the same system: amplitude modulation is applied for the downlink transmission, passive telemetry for the uplink transmission. Our new system is capable of a maximal bit rate of 60 000 bits/second is achieved.*

Keywords: *inductive powering, wireless datatransmission*
Category: *9 (System architecture, electronic interfaces, wireless interfaces)*

1 Introduction

In this paper, we present a new inductive powering system which is equipped with a bidirectional datatransmission. It has been optimised towards maximal power transfer efficiency and misalignment tolerance: a minimal amount of power transfer is guaranteed within certain limits for coil separation and lateral and angular misalignment. A new addition is the possiblity to use the inductive powering link also as a bidirectional communication tool, using ampiltude modulation of the downlink, and load variations for the uplink transmission. The system is developed for a "smart" orthopedic implant [1]: using this downlink datatransmission, the algorithms for the processing, storage and transmission of the measured data can be reprogrammed *in situ*, while the measured data can be transmitted to a PC base station, using the uplink data-transmission. In general, the proposed system, that consists of two coils only, can be used for the powering, control and data retrieval of both implantable monitoring and stimulation devices.

2 Inductive Link Principles

An inductive link consists of two coils, forming a loosely coupled transformer. The primary coil, placed outside the body, generates a magnetic field, that is partly picked up by the secondary, implanted coil. In this way, power is transferred transcutanously.
A design tool for the calculation of the electrical and magnetic properties of inductive links is implemented in MATLAB. The tool includes the influence of parasitic effects such as skin and proximity effect and parasitic capacitance. The design tool is used for the optimisation of the inductive link towards maximal efficiency and misalignment tolerance. Maximisation of the misalignment tolerance yields the optimal coil dimensions. A rule of thumb is that maximal efficiency is achieved for a primary coil diameter equalling twice the distance between the two coils. The operating frequency is set at 700 kHz in order to avoid biological tissue damage.

3 Design of the Complete Inductive Powering System

The inductive powering system with integrated bidirectional datatransmission is depicted in Figure 1. The primary coil is driven by a Class E amplifier. The Class E topology was chosen for its high efficiency. Taking into account the parasitic losses, such as the resistance of the RF Choke L_{RFC} and the on resistance of the switch S, an efficiency of up to 80 % is obtained.
The secondary circuit consists of a simple rectifier and regulator circuit. The capacitor C_2 is added to the secondary coil to form a resonant receiver circuit at the operating frequency. In this way, the power transfer efficiency is increased. The chosen topology consists of a minimal amount of components in order to minimise the dimensions of the implantable circuit.
The inductive powering system is designed to deliver 50 mW to the implantable device, at an internal regulated voltage of 5 V. The total power transfer efficiency, which is given by the multiplication of the primary circuit efficiency, the link efficiency and the secondary circuit efficiency, is 36 %. The supply voltage of the Class E amplifier is 2 V.

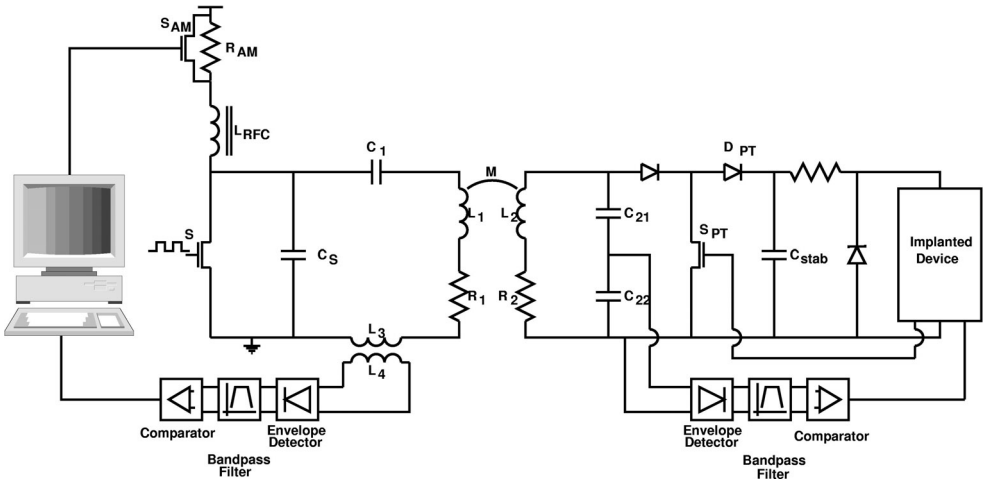

Fig. 1. Overview of the inductive powering system with integrated bidirectional datatransmission.

4 Integration of Bidirectional Datatransmission

For downlink datatransmission amplitude modulation of the Class E amplifier is applied, using a MOS transistor S_{AM}, acting as a switch and a resistance R_{AM}. The major drawback of this technique is the power dissipation. However, it is still preferred to frequency or phase modulation for its basic encoding and decoding circuits, as this approach allows the dimensions of the implantable circuit to be kept small. The decoding circuit consists of an envelope detector, a bandpass filter and a comparator. All blocks are built using commercially off-the-shelf compononents operating at 5 V, and can be powered by the inductive powering system. The capacitor C_2 from Figure 3b is split up into C_{21}-C_{22} and the high impedance input of the decoding circuit is connected to it.

Passive telemetry is used for uplink datatransmission [2]. A MOS transistor S_{PT} is introduced in the secondary circuit of the inductive powering system. By varying the gate voltage of the transistor S_{PT}, the input impedance of the link Z_{link} is varied. This impedance variation acts as a load variation on the Class E amplifier and can be 'sensed' by measuring the current through the primary coil L_1. Therefore, a transformer L_3-L_4 is introduced in the primary circuit. The current variation through the coils L_1-L_3 is now transformed to a voltage variation over L_4. This signal can then be decoded, using the same circuit as the decoding circuit for the downlink amplitude modulation. A second diode D_{PT} is also added in the secondary circuit to avoid the stabilisation capacitor C_{stab} to discharge through S_{PT} when it is conducting.

The major advantage of using passive telemetry for uplink datatransmission is the low power consumption: the secondary circuit is not acting as a transmitter and power transfer is still possible during datatransmission. The major drawback is a limited transmission range.

The gate voltage of S_{PT} is chosen in such a way that the modulation depth is 5 %. Due to the load variation, the Class E amplifier detunes from its ideal operation into Class CE regime. This reduces the efficiency of the amplifier, but an overall power transfer efficiency of 23.4 % is still obtained.

By integrating the downlink amplitude modulation and the uplink passive telemetry in the inductive powering system, a half-duplex communication link is achieved. The maximal bit rate achieved under test was 60000 bits/s, with a carrier frequency of 700 kHz. For practical applications however, the bit rate is set to 19200 bits/s such that an RS232 link to a PC can be connected.

5 Conclusion

This paper presents a unique inductive powering system, that combines power transfer with bidirectional data transfer. The design of the system has been highly automated, using a dedicated design tool. Although low cost commercial off the shelf components were used, an efficiency of 36% was obtained for the delivery of 50mW over a distance of 30mm. Moreover, bidirectional datatransmission at 60000 bits/s is integrated, which makes the system suitable for implantable monitoring and stimulating devices.

Acknowledgements

This research project has been supported by the IWT, in the framework of the STWW program, contract no. 000160.

References

[1] F. Burny et al, *Medical Engineering & Physics*, vol. 22, pp. 469-479, 2000.

[2] P.A. Neukomm & H. Kündig, *Sensors & Actuators A*, vol.21-23, pp. 258-262, 1990.

Evaluation of a Semi-Digital Readout Method for Reduced Crosstalk in Resonant Sensors.

Henrik Rödjegård[1], Peter Teichmann[2], Haris Kapidzic[1] and Gert Andersson[1]

[1] The Imego Institute, Arvid Hedvalls Backe 4, SE-41133 Göteborg, Sweden
email: henrik.rodjegard@imego.com http://www.imego.com
[2] Chalmers University of Technology, Göteborg, Sweden

Summary: *This paper presents a novel readout method for resonant sensors that is easily implemented in a digital CMOS process and which efficiently eliminate parasitic crosstalk between the excitation signal and the detection circuitry. Our method utilize a semi-digital excitation scheme that lacks the second harmonic and have an advantage in that it is more accurately generated, controlled and adjusted than a sinusoidal excitation signal. The novel readout method have been evaluated by the design of an excitation and detection ASIC manufactured in the 0.8-mm CMOS CXQ process from AMS. The functionality and the performance of the manufactured ASIC shows excellent agreement with theory.*

Keywords: *Resonant sensors, readout ASIC, low crosstalk readout*
Category: *9 (Electronic interfaces)*

1 Introduction and theory

The semi-digital excitation scheme presented in this paper is suitable for sensors with a resonant readout that is resistively or electrostatically actuated.

Figure 1 illustrates the working principles of the two commonly used methods to minimize the parasitic crosstalk, and the novel method presented in this work. First, Burst drive [1] that separates the excitation and detection signals in time, which only can be used for sensor with very high Q-values. Second, sinusoidal drive [2] that utilizes the inherent frequency doubling that appears in electrostatic and resistive actuators actuated symmetrical around a common bias.

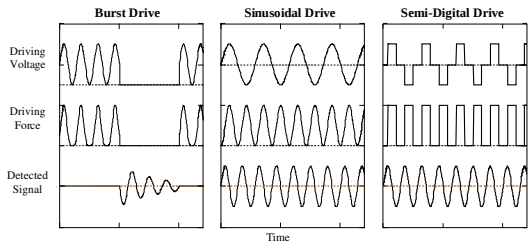

Fig. 1. Three ways to minimize parasitic crosstalk. The burst drive separates the driving and detection signals in time. The other two methods utilize the frequency doubling of the driving mechanism for frequency separation of the signals.

Third, the semi-digital drive method presented in this work, which also works according to the frequency doubling principle to eliminate the crosstalk, but having the additional advantage that the excitation signal is much more easily generated and adjusted. Since digital switches are used for signal generation and mixing the implementation becomes very robust and insensitive to fabrication process tolerances.

The Fourier coefficients of the semi-digital excitation signal are given by eq.1.

$$a_0 = \frac{1}{2}\left(V_{Hi} - V_{Lo}\right)$$
$$a_n = \frac{2}{n\pi}\left(V_{Hi}\sin\frac{n\pi}{4} + V_{Lo}\sin\frac{3n\pi}{4}\right), n \geq 1 \quad \text{Eq. 1}$$

Here V_{Hi} and $-V_{Lo}$ are the high and low excitation voltages respectively. From eq. 1 it is easily seen that the second harmonic (n=2) equals zero with V_{Hi} equal to V_{Lo}. The sensor, on the other hand, has its mechanical operation frequency on that frequency. Thus, the only double frequency signal on the chip is the one from the detection signal, and no traces from the excitation signal can electrically leak into the detection circuitry.

2 ASIC implementation

The architecture of the fabricated ASIC is outlined in Figure 2. The VCO is realized as a relaxation oscillator that is rough and fine-tuned by two analogue voltages. The VCO generates control signals for the power output as well as for the two mixers. The mixers operate with 90 degrees phase shift creating output signals that contain information of the amplitude as well as the phase of the sensor signal. Two individual analogue voltages control the V_{Hi} and V_{Lo} voltages, and thus the amplitude, of the excitation signal. The mixers as well as the power output circuitry are built from digital CMOS-switches. All amplifiers and filters are based on analogue standard-cell operational amplifiers provided by the manufacturer with added feedback netorks. The ASIC was fabricated in the 5

volts, 0.8 µm CMOS CXQ process at AMS (Austria Mikro Systeme International AG).

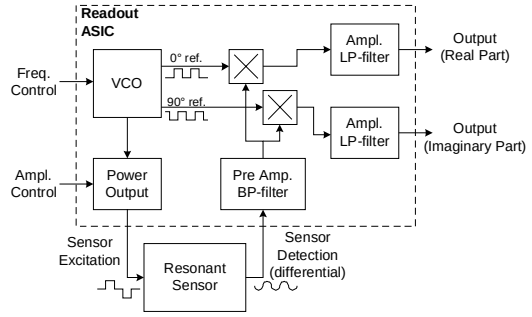

Fig. 2. The architecture of the readout ASIC.

3 Measurement results

The functionality and the performance of the ASIC have been evaluated, showing excellent agreement with theory. It can operate with detection frequencies from 50 kHz up to 300 kHz, corresponding to excitation frequencies between 25 kHz and 150 kHz. The gain of the detection circuitry (amplifiers, filters and mixer) was measured to 23 000 (RMS input to DC output), or 87 dB. The input-referred noise floor is 52 $nV_{RMS}/\sqrt{Hz}$ at a detection frequency of 100 kHz.

As a verification of the detection circuitry, Figure 3 shows the characterization of a Sallen-Key low-pass filter with a high Q-value using the ASIC as well as an HP4395A network analyser. The discrepancy between the two measurements is expected and can be accounted for since it reflects the band-pass characteristic of the ASICs preamplifier.

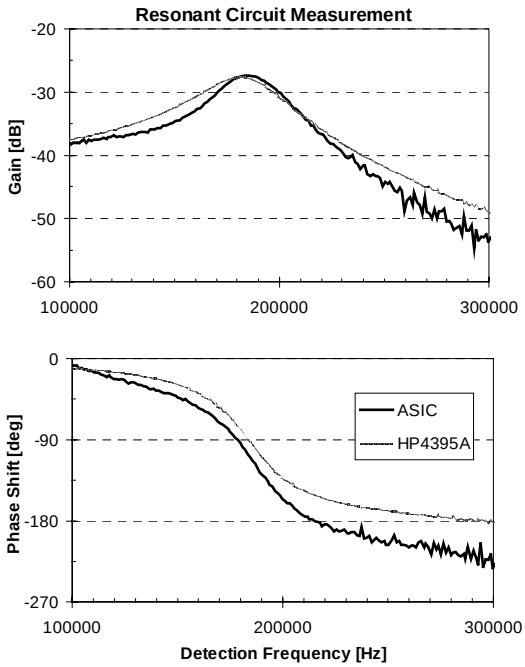

Fig. 3. Comparison between the fabricated ASIC and an HP4935A network analyser. The measured object is a Sallen-Key low-pass filter with Q=6. The discrepancy reveals the BP-characteristic of the ASICs preamplifier.

Conclusions

A novel low-crosstalk concept for readout of electrostatically or thermally actuated resonant sensors has been proposed, implemented, and evaluated. The readout principle provides high-resolution readout with robust electronics that is easily implemented in a low-cost CMOS process. A readout ASIC suitable for sensors with resonance frequencies ranging from 50 kHz to 300 kHz has been fabricated. Evaluations show that the principle works as expected. Due to the robustness and low cost this implementation it is a promising readout alternative for future resonant sensors applications.

References

[1] T. Corman, Vacuum-Sealed and Gas-Filled Micromachined Devices, Ph.D. thesis at the Royal Institute of Technology, 1999, Stockholm, Sweden, ISBN 91-7170-482-5, pp. 54-57

[2] D. Westberg, O. Paul, G. I. Andersson, and H. Baltes, A CMOS-Compatible Device for Fluid Density Measurements, Proc. MEMS ´97, January 26-30, Nagoua, Japan, pp. 278-283

All-Digital Interface ASIC for a QCM-Based Electronic Nose

James Beeley, Chris Mills, Andrew Glidle, Jon Cooper, David Cumming

Department of Electronics & Electrical Engineering, University of Glasgow, G12 8LT, UK.
Email: j.beeley@elec.gla.ac.uk http://www.elec.gla.ac.uk/

Summary: *An all digital interface application specific integrated circuit (ASIC) has been developed for the control and data sampling of a quartz crystal microbalance (QCM)-based electronic nose. The ASIC is capable of measuring QCM resonant frequency between 0 – 11 MHz with a resolution of 1 Hz and +/- 1 Hz precision. The ASIC has been used to control polymer coated QCM sensors, in conjunction with polymer/carbon-black coated microresistor (μR) sensors, in the detection of primary alcohols.*

Keywords: *Electronic nose, All-digital interface ASIC, Quartz crystal microbalance*
Subject Category: *9 (System architecture, electronic interfaces, wireless interfaces)*

1 Introduction

Several different electronic noses have been successfully developed based on Quartz Crystal Microbalance (QCM) sensor technology [1]. A variety of different interface electronics designs, based on multiple discrete components such as FPGAs and frequency-voltage converters, have been successfully constructed and implemented [2,3]. A QCM-based electronic nose interface digital application specific integrated circuit (ASIC) has been developed at the University of Glasgow. This offers advantages of compactness and reduced power consumption in comparison to existing implementations, and is of particular value in battery-powered portable applications.

2 ASIC construction

The ASIC is capable of measuring QCM resonant frequency over a range of 0 to 11 MHz, with a resolution of 1 Hz and +/- 1 Hz precision, and generates 10 frequency measurements per second. The ASIC interface is fabricated using Austria Mikro Systeme's CUP 0.6 μm mixed-signal complimentary metal oxide semiconductor (CMOS) process, and consists of three main components (Fig. 1). Firstly, a CMOS oscillator (a standard library component) to which the QCM sensor is connected. This is linked to a frequency counter block, consisting of a counter incremented by the oscillator, which rolls over to zero every 10^{11} counts. Finally, the counter's output is sampled every 100 ms and fed to an output block which converts the counter output to the measured frequency. This stores the 11 most recent counter values in a first in, first out (FIFO, S_n to S_{n-10}) and performs the following operation:

$$\textit{If } S_n >= S_{n-10} \textit{ then } \text{Frequency} = S_n - S_{n-10} \textit{ else } \text{Frequency} = S_n - S_{n-10} + 11\text{x}10^6$$

to obtain the frequency measured over 1 second. The output is generated as a 24-bit parallel output that is sent to an 8255 I/O card within a personal computer (PC) for data acquisition and logging.

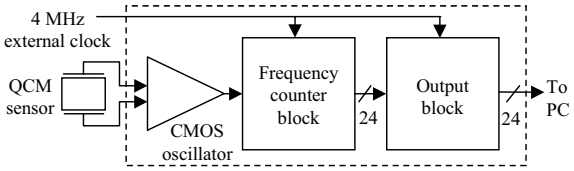

Fig. 1. ASIC block diagram.

3 Alcohol detection

The ASIC has been tested using a 10 MHz QCM sensor, in conjunction with a micro-resistance (μR) sensor, comprising interdigitated finger electrodes, within an electronic nose system (Fig. 2). Both sensors are polymer-coated with poly(ethylene-co-vinylacetate) (PE-co-VA), containing carbon black in the case of the micro-resistor sensor [5].

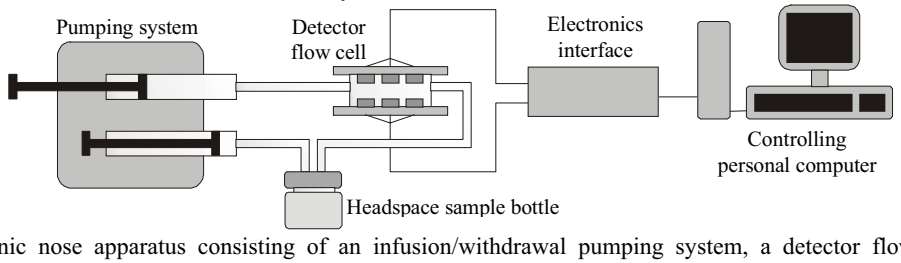

Fig. 2. Electronic nose apparatus consisting of an infusion/withdrawal pumping system, a detector flow cell, detector electronics interface and a controlling personal computer. Analyte gasses are introduced to the sensors from a headspace sample bottle.

The electronic nose system has been used to produce headspace analysis of alcohol vapors, $C_nH_{2n+1}OH$, where n = 1 to 8 and 10. Plots of the ratio of the response from the QCM and μR sensor pairs, S_{fr}, versus relative molecular mass (RMM) and alcohol liquid density (Fig. 3) show a linear relationship for alcohols where n > 2, despite the very non-linear response for Δf and ΔR produced by the respective sensors (inset).

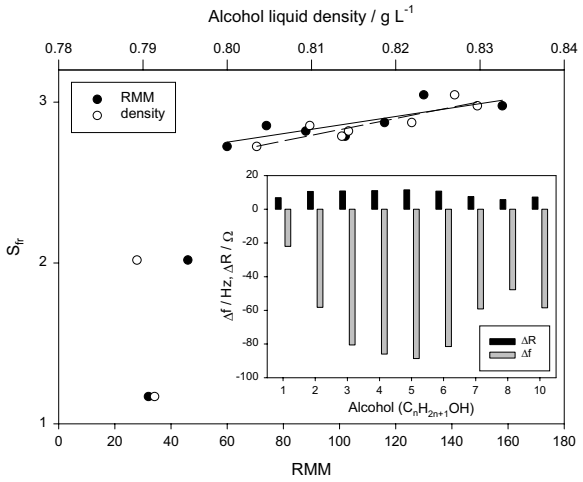

Fig. 3. S_{fr} versus RMM and alcohol liquid density calculated using, inset, ΔR and Δf upon the introduction of primary alcohols $C_nH_{2n+1}OH$ to QCM and μR PE-co-VA coated sensors (n = 1 to 8 and 10). A linear relationship is seen for both the RMM (solid line) and liquid density (dashed line) for alcohols where n > 2.

As the QCM response is proportional to a change in mass, and the μR response is proportional to a change in volume, S_{fr} can be defined as [4, 6],

$$S_{fr} = \frac{(\Delta f / f_c)}{(\Delta R / R_0)} \propto \frac{\Delta m}{\Delta V} \propto \rho_A \qquad (1)$$

where Δf and ΔR are the change in frequency and resistance of the QCM and μR sensors respectively, f_c and R_0 are, respectively, the QCM resonant frequency and the baseline resistance value, m and V are the mass and volume change of the polymer deposited on the QCM and ρ_A is the density of the adsorbed analyte. Also,

$$\frac{1}{S_{fr}} = \frac{Sk''\rho_p}{RMM_A} \qquad (2)$$

where, S is a gas/polymer sensitivity coefficient, k'' is a geometric constant related to the μR sensor electrodes, ρ_p is the polymer density and RMM_A is the relative molecular mass of the analyte.

Repeated measurement of methanol (n = 1) vapor at concentrations of approximately 800 ppm and 1600 ppm (Fig. 4) reveals that S_{fr} is independent of concentration change, in contrast to Δf and ΔR (inset). This concentration independence, allied to the linear properties of S_{fr} when detecting alcohols suggest that this system could be useful when designing electronic nose systems based on arrays of sensors for the detection of similar analyte gasses.

A full system on a chip (SoC) electronic nose is currently under development at the University of Glasgow, making use of IP from the nose ASIC, and featuring arrays of QCM and resistive sensors, along with on-chip processing and communications functionality.

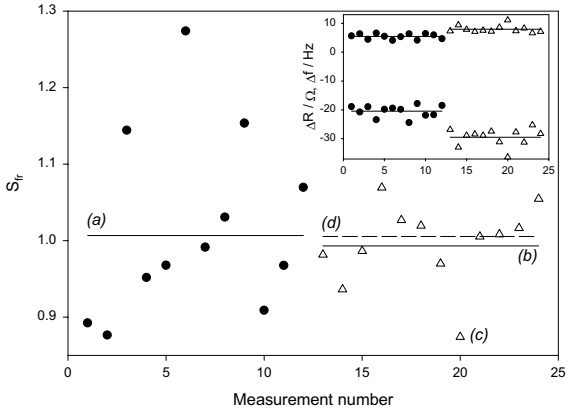

Fig. 4. S_{fr} for 12 repeat introductions of approximately 800 ppm (●) and 1600 ppm (Δ) of methanol to a pair of PE-co-VA sensors. The means (solid lines a and b) are plotted for each concentration. Upon removal of the outlier (c) using Dixon's Q-test, the mean of the 3.42×10^{-3} mol dm^{-3} measurements increases (dashed line d) to a value close to that of the 1.71×10^{-3} mol dm^{-3} measurements. Inset, ΔR and Δf for the 12 repeated introductions.

References

[1] K. J. Albert, N. S. Lewis, C. L. Schauer, G. A. Sotzig, S. E. Stitzel, T. P. Vaid, D. R. Walt, "Cross-Reactive Chemical Sensor Arrays", *Chem. Rev.* 100 (2000) 2595-2626.

[2] J Scroder, R. Borngraber, F. Eichelbaum, P. Hauptmann, "Sophisticated Interface Electronics for QCMs", In: *Transducers 01 Eurosensors XV, 11th International Conference on Solid-State Sensors and Actuators*, pp. 104-107, Munich, Germany, 10-14 June 2001.

[3] C. Di Nucci, A. Fort, S. Rochhi, L. Tondi, N. Ulvieri, V. Vignoli, F. Di Francesco, M Serrano-santos, "Study of the Dynamic Response of QCM Sensors by Means of a Fast and Accurate All-Digital Frequency Sensor", In: *IEEE Instrumentation and Measurement Technology Conference*, pp. 33-38, Anchorage, USA, 21-23 May 2002.

[4] L. Cui, M. J. Swann, A. Glidle, J. R. Barker, J. M. Cooper, "Odour Mapping Using Microresistor and Piezo-Electric Sensor Pairs", *Sens. and Actuators B: Chem.* 66 (2000) 94-97.

[5] M. C. Lonergan, E. J. Severing, B. J. Doleman, S. A. Beaber, R. H. Grubbs, N. S. Lewis, "Array-Based Vapor Sensing Using Chemically Sensitive, Carbon Black-Polymer Resistors", *Chem. Mater.* 8 (1996) 2298-2312.

[6] M. J. Swann, A. Glidle, L. Cui, J. R. Barker, J. M. Cooper, "The Determination of Gaseous Molecular Density Using a Hybrid Vapour Sensor", *Chem. Commun.* (1998) 2753-2754.

Sensing of CO in H_2-rich gases

O. Wurzinger, G. Reinhardt

University of Tübingen, Institute of Physical and Theoretical Chemistry,
Auf der Morgenstelle 8, D-72076 Tübingen, Germany
email: gr@ipc.uni-tuebingen.de http://www.ipc.uni-tuebingen.de/reinhardt/

Summary: *Differently doped thick film SnO_2 sensors were investigated in reducing atmospheres with high H_2 content. Such atmospheres appear in hydrogen reforming processes frequently used for the production of hydrogen for the operation of fuel cells. The thermodynamic stability of SnO_2 against reduction to the metal limits the operation temperature to temperatures below 320°C. Pt, Pd and Au doped SnO_2 -sensors showed sensitivity to CO at around 220°C. A maximum sensitivity was found for SnO_2 sensors doped with 2 wt% Pt. The cross-sensitivities to hydrogen, carbon dioxide, and water are much lower. Typical response time to changes in the CO content of about 2 sec were found.*

Keywords: *tin oxide, CO gas sensor, reformed gas, reducing gas*
Category: *5 (Chemical sensors)*

Introduction

SnO_2 based semiconductor gas sensors are widely used to measure CO in the presence of O_2. Only a few studies related to the operation in oxygen free or reducing atmospheres are available [1-2]. CO detection in H_2 rich gases originating from the reforming reactions of methanol or methane is an important task for the operation of PEM fuel cells. Since the PEM fuel cells operates satisfactorily only at very low CO levels, CO detection and control plays a major role. Our work was therefore focused on the detection of CO in reforming gases. Typical gas compositions for the steam reforming of methanol at 280°C and methane at 880°C are shown in Table 1. The sensing properties of differently doped SnO_2 sensors were tested in these environments.

Table 1. Typical gas concentrations behind a steam reforming reactor for methanol or methane operated at 280°C (methanol) or 880°C (methane).

gas	methanol reformer	methane reformer
MeOH	1%	-
methane	-	1%
CO	2%	15%
CO_2	22%	4,5%
H_2	68%	61,5%
H_2O	7%	18%

Experimental

Sensors were fabricated by screen printing electrodes and a sensitive layer on the front side and a Pt-heater on the back side of an Alumina substrate (thickness of 0.63 mm). One example is shown in figure 1. Different electrode geometries have been tested. The temperature was controlled by adjusting the heater resistance to constant values. Up to 20 sensors were measured in parallel. The whole measurement chamber was kept at 140°C to prevent water condensation. The gas mixing bench and data acquisition were driven by a Agilent VEE program. Changes of CO concentration were balanced with CO_2.

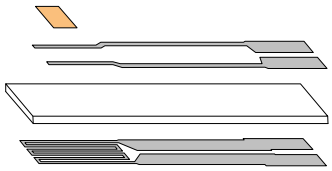

Fig. 1. View of the gas sensor structured by screen printing on Alumina substrate.

Results and discussion

1. Stability of SnO_2 versus reduction

It is important to maintain the SnO_2 phase during sensor operation. The reduction to the metal may occur by reaction with hydrogen or CO according to

$$0{,}5\ SnO_2 + H_2 \leftrightarrow 0{,}5\ Sn + H_2O \quad (1)$$

$$0{,}5\ SnO_2 + CO \leftrightarrow 0{,}5\ Sn + CO_2 \quad (2)$$

The calculated phase diagram (data sources from [3-4]) for the reduction with hydrogen is shown in figure 2. Up to about 320°C SnO_2 is thermodynamically stable in both reformer atmospheres with respect to the reduction with H_2. XRD-measurements with samples kept for 1 month in the stability area of Sn have confirmed the reduction to metallic Sn of our SnO_2-sensors.
The reduction with CO is critical in the case of a methane reformer, because SnO_2 is thermodynamically not stable. The reaction, however, seems to be strongly kinetically hindered. A similar behavior was found by another group in N_2 with

few % of CO [1-2]. With Mössbauer spectroscopy, the existence of Sn in the oxidation states +2 and +4 but no metallic Sn was found in nanocrystalline SnO_2 powder (undoped and Pd doped) at temperatures below 650 K.

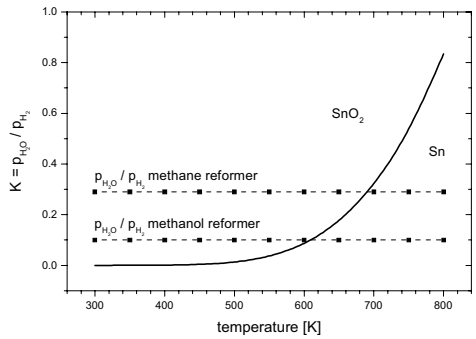

Fig. 2. Stability of tin oxide against reduction by hydrogen in two different gas mixtures.

2. CO sensing properties

The response of SnO_2 doped with Pt, Pd and Au are shown in figure 3. The Pt-doped samples show the largest sensitivity to CO.

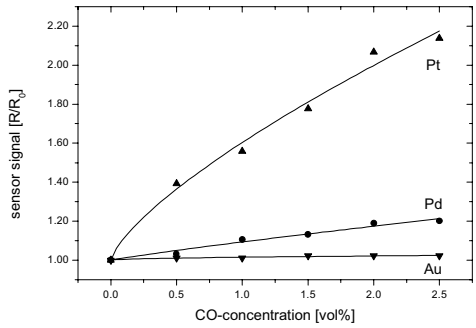

Fig. 3. Sensor signals of different 2 wt% doped sensors, operated at 220°C and 200 ml/min in the 1% methanol containing reformed gas.

Figure 4 shows the resistance of a Pt doped sensor over a larger CO concentration scale. In opposite to the operation in air, an increase in the sensor resistance with increasing CO content is generally observed. This behavior is finally not really understood, but it is evident that the sensing mechanism is different to the one in air. In air, chemisorbed oxygen species play a major role in the sensing mechanism. In the hydrogen rich gases chemisorbed oxygen species are absent due to the extremely low oxygen content (the calculated O_2 mole fraction is around 10^{-40}).
Cross sensitivities to CO_2, H_2O, methanol and H_2 are shown in figure 5 as a function of temperature. In order to minimize the cross-sensitivities an operation temperature of 220°C was chosen. Under this conditions cross sensitivities were 20 to 60 times smaller than the CO sensitivity. The response times (t_{63}-time) were found to be essentially constant in the temperature range 190°C – 250°C with values of approximately 2 seconds.

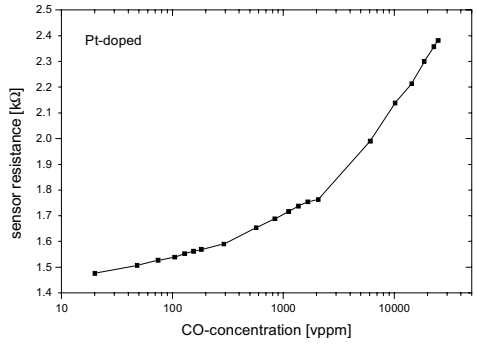

Fig. 4. Resistance change of 2 wt% Pt doped sensor, operated at 220°C and 250 ml/min in the 1% methanol containing reformed gas.

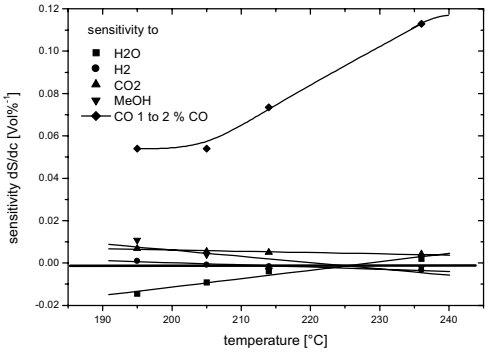

Fig. 5. Sensitivities of 2 wt% Pt doped sensor, 250 ml/min in the 1% methanol containing reformed gas. The gas whose cross sensitivity was measured was balanced with all gas components except CO.

Acknowledgements

We would like to thank J. Kappler and N. Barsan, for the preparation of thick film sensors, P. Reuse (EPF Lausanne) for the response time measurements and the German Federal Ministry of Education and Research (BMBF) for financial support.

References

[1] O. Safonova, I. Bezverkhy, P. Fabrichnyi, M. Rumyantseva and A. Gaskov. *Journal of Materials Chemistry*, 12 (2002) 1174-1178.

[2] A.G. Maddock, *Horwood chemical science series*, Chister 1997, ISBN 1-898563-16-0.

[3] I. Barin, *Thermochemical Data of Pure Substances*, VCH Verlagsgsellschaft mbH, Weinheim (1989)

[4] ChemSage 4.22. Thermodynamic software, GTT-Technologies, Germany.

H_2S Sensing with Nano-Structured WO_3 Films in Different Oxygen Atmospheres

L.F. Reyes[1,2], S. Saukko[1], A. Hoel[2], V. Lantto[1] and C.G. Granqvist[2]

[1]Microelectronics and Materials Physics Laboratories, University of Oulu,
Linnanmaa, FIN-90570 Oulu, Finland
email: vila@ee.oulu.fi
[2]Department of Materials Science, Ångström Laboratory, Uppsala University,
P.O. Box 534, SE-75121 Uppsala, Sweden

Summary: *Nanocrystalline WO_3 films were produced by advanced reactive gas deposition for gas-sensing applications. The metastable tetragonal crystal structure of deposited films changed gradually to a monoclinic phase as the sintering temperature increased from 400 to 600 ^oC. H_2S sensitivity in dry air of films sintered at 300 ^oC was highest at low operation temperatures. Maximum sensitivity was found at about 400 K. H_2S sensitivity was studied also in atmospheres having different oxygen concentrations. A decrease of the response time was found for intermediate oxygen concentrations. H_2S sensitivity was studied also in argon atmosphere with only a few ppm of oxygen. The temperature corresponding to the maximum sensitivity to H_2S was found to increase with decreasing oxygen concentration in the atmosphere.*

Keywords: *gas sensor, WO_3, electrical properties, nanocrystalline ceramics*
Category: *5 (Chemical sensors)*

1 Introduction

The gaseous pollutants from automobiles, industrial smoke-stacks and other sources have become a matter of urgent public concern. Several types of chemical detectors have been developed and many groups are working on research and development of new kinds of sensors and sensing materials for pollution monitoring. Semiconductor gas sensors serve as a posibility for the purpose. Nanocrystalline materials have been studied for various purposes during the last years owing to their many improved properties in comparison with those of conventional coarse-grained structures. The surface-to-bulk ratio for a porous nanocrystalline material is much greater than for a material with large grains which yields a large interface between the solid and a gaseous medium and may be very useful in the case of a semiconductor gas sensor.

Here, we apply a high-temeprature route employing advanced reactive gas deposition for structure engineering of WO_3 nanoparticles in making nanocrystalline films for gas sensing applications. WO_3 is an n-type semiconductor. Structure engineering is a possibility in the case of a very fine-grained n-type semiconductor oxide film to increase the electrical conductivity of the film up to a level which is useful for the room temperature operation. The reactive gas deposition as a high-temperature fabrication process makes it possible to produce nanocrystalline WO_3 films in matastable tetragonal crystal structure which has a stable layer structure with two formula units in the unit cell and terminal W=O bonds at the surface [1,2]. The films were found to be very sensitive to H_2S in air already at room temeprature [3,4].

2 Experimental

Nanocrystalline WO_3 films were made by reactive gas deposition using an Ultra Fine Particle equipment (ULVAC Ltd., Japan). Details on the method of deposition are available in Refs. 3 and 4. The nanocrystalline WO_3 films were deposited on alumina substrates with pre-printed gold electrodes and a Pt heating resistor printed on the reverse side. The average thinckness of the films was ~10 μm. The deposited nanocrystalline films were sintered at different temperatures up to 600 ^oC. When as-deposited films were sintered above 400 ^oC, the tetragonal phase started to change to a monoclinic phase. The average crystallite size for as-deposited films, derived by applying Scherrer's formula, was around 10 nm. After sintering at 600 ^oC, the monoclinic phase was dominating, and the crystallite size was ~35 nm. SEM observations from as-deposited nanocrystalline WO_3 films show about the same grain size of ~10 nm which was found for the average crystallite size from the line witdhs of x-ray diffraction patterns. This means that the WO_3 nanoparticles were grown without any agglomeration. In addition, the WO_3 nanoparticles show a porous network-like struture which is an important characteristic for gas sensing with the films. The electrical conductance as a function of temperature and its response to H_2S were measured using a gas blender connected to a test chamber. Synthetic air and argon as carrier gases flowed at a constant rate of 1 l/min through the chamber.

3 Result

Some result are shown here for a nano-structured tetragonal WO_3-film sample sintered at 300 ^oC. The conductance of the sample as a function of temperature in dry synthetic air is shown in the insert in Fig. 1. During heating the conductance starts to increase from the room-temperature value of about 5 nS and above about 400 K the increase is exponential with an activation energy of about 0.4 eV. After mixing of 5 and 10 ppm of H_2S with synthetic air, the conductance increases at room-temperature by factors of about 250 and 2000, respectively, as shown in the insert in Fig. 1. The maximum sensitivity of the sample to both 5 and 10 ppm of H_2S in dry air is at about 400 K where the conductance curves in Fig. 1 have sharp peaks. In addition, shoulders are shown in both conductance curves around about 500 K in Fig. 1 and also in the Arrhenius plots in the insert of Fig. 1. It is also see in Fig. 1 that the H_2S sensitivity of the sample is small above abount 600 K where the conductance values corresponding to the two H_2S concentrations of 5 and 10 ppm again start to increase with increasing temperature. In the case of 10 ppm of H_2S, the conductance decreases below the room-temperature value at its minimum temperature of about 650 K.

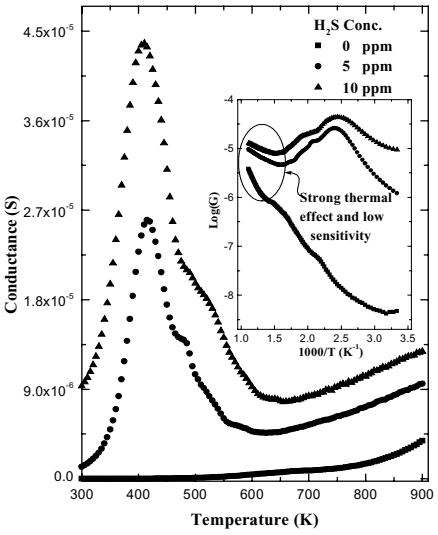

Fig. 1. Conductance of a tetragonal WO_3-film sample sintered at 300 ^oC as a function of temperature in synthetic air mixed with 0, 5 and 10 ppm of H_2S, respectively. The Arrhenius plots of the three conductance curves are shown in the insert.

The effect of oxygen content in the carrier gas mixed with H_2S was also studied with the sample sintered at 300 ^oC. Pure argon with only a few ppm of oxygen was now used as the carrier gas which was mixed with both oxygen and H_2S. It was found that the conductance increase with decreasing oxygen content in argon is related to a decrease of the activation energy of conductance with decreasing oxygen concentration. At 800 ppm of oxygen in argon, the activation energy of conductance was decreased to a value of about 3.6 eV. The behaviour of the conductance as a function of temperature is show in Fig. 2 for three gas mixtures where 10 ppm of H_2S is mixed with synthetic air, argon and with a mixture containing 800 ppm of oxygen in argon, respectively.

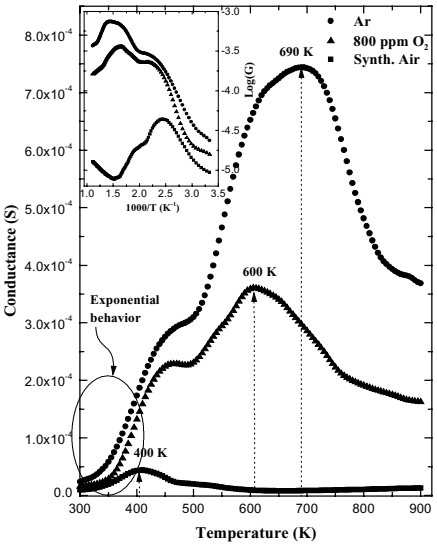

Fig. 2. Conductance of a tetragonal WO_3-film sample sintered at 300 ^oC as a function of temperature in gas mixtures where 10 ppm of H_2S is mixed with argon, a mixture of 800 ppm of oxygen in argon, and synthetic air, respectively. The Arrhenius plots of the three conductance curves are shown in the insert.

It is seen from the results in Fig. 2 that the sensitivity of the sample to H_2S increases with decreasing oxygen concentration. The temperature corresponding to the conductance maximum of the conductance curves in Fig. 2 also increases with decreasing oxygen concetration and the shoulders in the curves are now more pronounced at lower oxygen concentrations.

References

[1] Furio Cora, Atul Patel, Nicholas M. Harrison, Roberto Dovesi and C. Richard A. Catlow, J. Am. Chem. Soc. 118 (1996) 12174-12182.
[2] J.L. Solis, A. Hoel, V. Lantto and C.G. Granqvist, J. Appl. Phys. 89 (2001) 2727-2732.
[3] J.L. Solis, A. Hoel, L. B. Kish, C.G. Granqvist, S. Saukko and V. Lantto, J. Am. Ceram. Soc. 84 (2001) 1504-1508.
[4] L.F. Reyes, S. Saukko, A. Hoel, V. Lantto and C.G. Granqvist, J. Eur. Ceram. Soc, in press.

Thermal response of microfilament heaters in gas sensing

I. Bársony[1], P. Fürjes[1], M. Ádám[1], Cs. Dücső[1], J. Zettner[2] and F. Stam[3]

[1] Research Inst. for Technical Physics and Materials Science MFA, Hungarian Academy of Sciences
H-1525 Budapest, P.O.Box. 49, e-mail: barsony@mfa.kfki.hu
[2] Thermosensorik GmbH, D-91058, Tennenlohe, Am Weichselgarten 7, Germany
[3] National Microelectronic Research Centre, University College, Lee Maltings, Prospect Row, Cork, Ireland

Summary: *IR thermal imaging in the wavelength range of 3μm<λ<5μm with a comparable lateral pixel resolution had been used to study the dynamic behaviour of porous silicon micromachined, membrane-type microfilament structures for gas sensing application.*
Keywords: *microfilaments, calorimetric gas sensors, thermal response*
Category: *5 (Chemical sensors)*

1 Introduction

Calorimetric devices in gas sensing, flow and vacuum-metering require the accurate knowledge of the actual temperature, in order to assess the deviations from the set value. In case of combustion-type gas sensing the heat developed by the exothermal catalytic reaction on the active surface of the device will determine the actual temperature. In a pellistor [1] the temperature changes are detected indirectly, by measuring the change of the filament resistance, usually in a bridge arrangement. Nevertheless, it is absolutely required to know the thermal behaviour of the filament structure coated by the porous, usually ceramic matrix, containing the finely dispersed catalyst particles.

2. Thermal imaging

For characterisation of thermal response generally high-resolution thermal imaging is an emerging technique. Thermosensorik GmbH developed the technique used in this work. It is based upon the detection of the thermal radiation from the surfaces at elevated temperature. The thermographic technique operates with a cooled, highly sensitive mercury cadmium telluride (MCT) focal plane array detector of 384X288 pixels at T=70K, in the IR range of 3μm<λ<5μm. The image information of the camera is digitally captured by a frame grabber. The image is digitised in the detector head with an accuracy of 14 bit at a rate of 16 MPixel/s, allowing a full image frame rate of up to 140Hz.

Since the actual microdevice under test has dimensions in the μm range, the thermographic information at maximum lateral resolution had to be collected via a specially adjusted optics. Even so, all changes were restricted to a limited area of the array. This in principle allows an increase of the frame rate up to 800 Hz. The system is thereby capable of tracking fast changes in temperature. The method is of course prone to emissivity changes of the radiating surfaces; i.e. surfaces at equal temperature having black and bright appearance correspond to higher and lower detected intensity, respectively. Without an accurate calibration of the intensities vs. temperature, only surfaces of similar emissivity can be compared from the point of view of dynamic behaviour.

3. Microfilament structures tested

Single side bulk-micromachining with porous silicon sacrificial layers was used in fabricating the integrable membrane heater elements [1]. The microphotograph of a pellistor-type sensor element is shown in Fig.1. Note the pair of symmetric elements, one of, which is the active catalytic device, while the other serves as a thermal reference for the sensing.

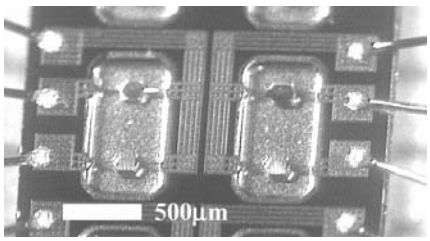

Fig. 1. Microphotograph of part of a sensor array chip with two pellistor-type sensors.

In the experiments three different isolation schemes have been used. The simplest makes use of the reduced thermal conductivity of porous silicon, formed underneath the SiN_x membrane, containing the Pt heater. The other two form suspended bridges, using full or partial air-gap isolation.

In Fig. 2 the SEM image of these both other methods for isolation are presented. After releasing the membrane-filaments by selective dissolution of the porous silicon sacrificial layer, the isolation airgap is formed, as seen under the filament in front. In order to increase the mechanical stability of the suspended hotplate a thin silicon support in the lengths axis was formed by a novel method [3, patent pending], as illustrated in the filament behind.

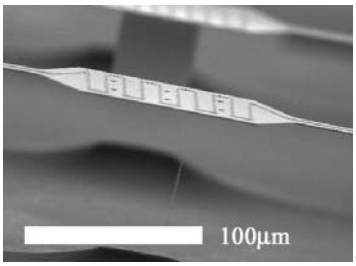

Fig. 2. SEM view of an unsupported, suspended bare Pt-heater resistor in front, and another one with a supporting vertical thin silicon pillar in the background.

The heat loss is controlled by heat transfer to the bulk silicon via heat conduction in the suspending beams, by heat conduction and convection in the surrounding gas and radiation from the hot surfaces. Latter mechanism is exploited in the thermographic technique used in the present study.

4. Filament thermal response

For the analysis of the thermal response of microfilaments a square wave heating of the resistors with an appropriate fill-factor was used. A narrow sampling window was than shifted "across the heating-pulse" for obtaining the IR information from the filament in the rising, stable and falling T regime. The sampling pulse width was 10ms, accordingly, the integration time, i.e. the number of sampling cycles had to be adjusted for the intensities detected. The amplitude of the heating current pulse was 5mA. The fill factor selection had to ensure the driving of the device to full temperature saturation with all compared structures. In this way temperature vs. time profiles of differently heated filaments could be recorded on the samples for a number of heating conditions.

Typical results are shown below for the three isolation schemes with a driving current amplitude of 5mA at 3V. In the free suspended filament in static mode this corresponds to T≅400°C. The driving pulse width of 100ms was set for reaching saturation. All presented results were obtained on bare filaments.

The rise and fall times of the temperature in the three cases for 90% of maximum and 10%, respectively are summarised in Table 1:

Isolation	rise time (ms)	fall time (ms)
unsupported	4	1.3
supported	4.2	1.4
PS	7	3.3

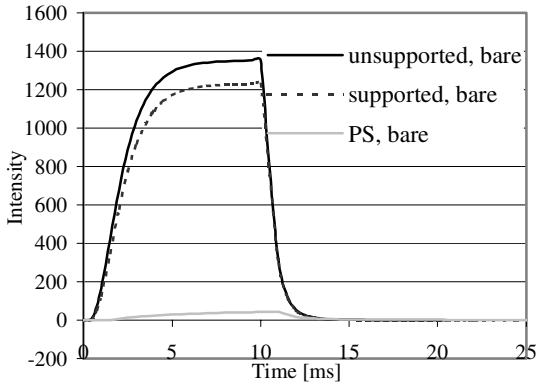

Fig.3. Time dependent response of the different heater filaments to a power drive of 18mW and 10ms.

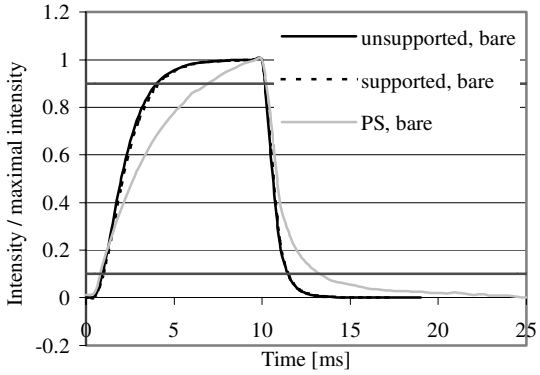

Fig. 4. Normalised time dependent response of the different heater filaments to a power drive of 18mW and 10ms.

Conclusions

The thermal response of bulk micromachined filament heaters, built with three different isolation schemes for calorimetric sensing applications, had been compared at similar driving conditions by means of fast thermometry. The use of Si support in released membrane heaters did not affect the speed of T setting. Mechanical stabilisation was achieved at the cost of a mere 10-15% temperature loss via the additional heat sink.

Acknowledgements

This study was partly supported by the EU FW5 project SAFEGAS and by the grant T 033094 of the Hungarian Scientific Research Found OTKA.

References

[1] Cs. Dücső, M. Ádám, P.Fürjes, M. Hirschfelder, S. Kulinyi and I. Bársony: „Explosion-proof Monitoring of Hydrocarbons by Micropellistor", Proceedings of Eurosensors XVI, Prague (2002) 605-606, Sensors And Actuators B, in press

Cross-sensitive polymeric materials on the basis of phosphine oxides for "electronic tongue" sensor systems

D. Kirsanov[1], A. Legin[1], S. Makarychev-Mikhailov[1], A.Rudnitskaya[1], V. Babain[2], Yu. Vlasov[1]

[1]Chemistry Department, St. Petersburg University, Universitetskaya nab. 7/9, St. Petersburg, 199034, Russia
email: andrew@sensor.chem.lgu.spb.su http://www.electronictongue.com
[2]Chlopin Radium Institute, St. Petersburg, Russia

Summary: *A variety of new sensing materials on the basis of phosphine oxides for solvent polymeric sensors have been developed and studied. It was found that phosphine oxide sensors exhibit good sensitivity to* Cu^{2+}, Zn^{2+}, Cd^{2+} and Pb^{2+} *ions in solutions, their sensitivity patterns being significantly different from those of solid-state sensors. Both polymeric and solid-state sensors were comprised into electronic tongue sensor arrays that demonstrated advantageous behavior in mixed solutions of these ions. Such sensor arrays are highly promising for environmental and industrial sensing.*

Keywords: *cross-sensitive chemical sensors, phosphine oxides, electronic tongue, heavy metals*
Category: *5 (Chemical sensors)*

1 Introduction

Chemical sensor arrays based on the principles of electronic tongue have been widely applied to the analysis of heavy metals, particularly metal ions (Cu^{2+}, Pb^{2+}, Cd^{2+}, Cr(IV), Fe(III), Tl^{+}, etc.) in the environment, industrial processes and waste treatment [1-2]. However, the sensors available for detection of most of heavy metals are traditionally based on solid-state materials, either crystalline or vitreous [2]. Along with obvious advantages, such as chemical durability, all solid-state materials exhibit certain drawbacks, e.g. sensitivity and selectivity patterns of these materials are rather similar. Since the selectivity of solid materials, either crystalline of vitreous, is determined mainly by the energy of metal interaction with chalcogenide sites, there is little hope that selectivity patterns can be changed more significantly by material modifications. On the other hand there is a number of sensing materials on the basis of organic polymers and especially solvent polymeric PVC membranes that were reported being sensitive to different heavy metals, but were scarcely used in multisensor arrays. Polymeric metal sensors may exhibit sensitivity and selectivity patterns very different from solid-state sensors, thus enabling new possibilities in heavy metal sensing in complex liquids, such as natural water or waste effluents. Of particular interest is utilization of a combined multisensor system, where solid-state sensors and polymer sensors might be fruitfully used together.

2 Experimental

2.1 Materials. Trioctylphosphine oxide (TOPO) and triphenylphosphine oxide (TPPO) were obtained from Fluka (Buchs, Switzerland). A number of different diphenylphosphine oxides with different third radical (ether (DPhOPO), thioether (DPhSPO), amine (DPhNDB), carbamoyl (DPhNCO)) were synthesized and purified in Chlopin Radium Institute (St. Petersburg, Russia). Bis(2-ethylhexyl)sebacate (DOS) and *o*-nitrophenyloctyl ether (NPOE) in Selectophore® grade; high molecular weight poly(vinyl chloride) (PVC), purum, were obtained from Fluka. Tetrahydrofurane (THF) from Merck (Darmstadt, Germany) was freshly distilled prior to use. All salts were obtained in p.a. grade from Ekros (St. Petersburg, Russia). Doubly distilled water was used throughout all experiments.

2.2 Membrane Preparation. The weighted amounts of membrane components: polymer (PVC), plasticizer (DOS or NPOE) and phosphine oxide were mixed in freshly distilled THF. The concentration of phosphine oxides was 0.1 mol/kg of plasticizer. Membrane cocktail was intensively stirred for approximately 15 min until all components were dissolved. Resulting homogeneous liquid was poured into Teflon beakers and left for 48 hours for solvent evaporation. Disks were punched from the resulted film and the sensors were made according to the conventional procedure. The membranes were mounted onto PVC tubes; 0.01 M solution of sodium chloride as internal filling and internal reference Ag/AgCl electrodes were used.

2.3 Potentiometric Measurements. Potentials were measured with a 30-channel mV-meter with high input impedance made in house, connected to PC for data acquisition and processing. Measurements were carried out in the galvanic cell:

Ag | AgCl, KClsat | sample | sensor membrane | NaCl, 0,01M, AgCl | Ag

Figure 1. pH-dependence of the electrode response of TOPO based sensors plasticized with NPOE in solutions of $Zn(NO_3)_2$.

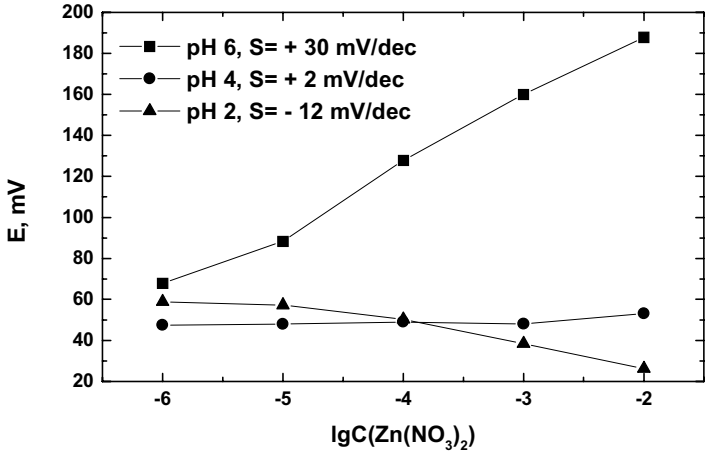

Calibration measurements were carried out in the range 10^{-6}–10^{-2} mol/L of heavy metal ions Cu^{2+}, Zn^{2+}, Cd^{2+} and Pb^{2+}. All presented data comprise averaged responses of 3 sensors of the same composition. All potentiometric measurements were performed at room temperature (20±1 °C).

3 Results and Discussion

All phosphine oxide sensors exhibited response in solutions of Cu^{2+}, Zn^{2+}, Cd^{2+} and Pb^{2+} (Table 1).

Table 1. Sensitivity of phosphine oxide sensors (sensor response slope, mV/dec) plasticized with DOS in solutions of heavy metal ions on 0.1 M KNO_3 background.

Phosphine oxide	Cu^{2+}	Zn^{2+}	Cd^{2+}	Pb^{2+}
TOPO	11.9	52.3	48.7	37.7
TPPO	11.2	3.0	2.5	13.6
DPhOPO	8.2	19.7	17.9	32.6
DPhSPO	11.5	9.4	10.2	31.3
DPhNDB	7.9	6.9	17.0	20.0
DPhNCO	16.5	9.1	7.2	25.1

Sensitivity pattern to the four heavy metals is distinctly different for different phosphine oxides, thus demonstrating a promise for applying the obtained sensors in multisensor arrays. The response in all solutions was stable and reproducible and the sensors did not exhibit memory effects depending on the sequence of measurements in metals.

Calibrations of phosphine oxide sensors in zinc nitrate solutions with different pH adjusted by hydrochloric acid were made and the slopes of the linear parts of the calibration curves were calculated. It was found (Fig. 1) that the response slope changes from slightly anionic at pH 2 to Nernstian cationic at pH 6. Anionic slopes can be attributed to the protonation of phosphine oxide at low pH values resulting in formation of positively charged complexes in the membrane that can act as ion-exchanging sites for NO_3^-. At higher pH values phosphine oxides display typical properties of neutral carriers and 'normal' cationic response is observed. This feature of phosphine oxide sensors' response can be also potentially valuable for multisensor arrays of "electronic tongue".

Sensors with phosphine oxides membranes displayed cross-sensitivity to heavy metals were comprised into the sensor array for determination of mixtures of aforementioned metal ions along with sensors with chalcogenide glass membranes. Measurements with the sensor array were made in the mixed solutions of copper, lead, cadmium and zinc. Compositions of the solutions were chosen using fractional and Taguchi design with the aim to reduce number of calibration solutions. Data processing was done by partial least square regression. It was demonstrated that sensors with membranes containing phosphine oxides allow to improve system performance.

References

[1] A. Legin, A. Rudnitskaya, Yu. Vlasov, Electronic tongues: sensors, systems, applications, in Sensor Update (G.K. Fedder and J.G. Korvink eds.), 10 (2002) 143-188, WILEY-VCH Verlag GmbH, Weinheim.

[2] C. Di Natale, A. Macagnano, F. Davide, A. D'Amico, A. Legin, Yu. Vlasov, A. Rudnitskaya, B. Seleznev, *Sensors and Actuators B* 44 (1997)423-428.

Monitoring of ethylene for agro-alimentar applications and compensation of humidity effects

A.Giberti, M.C. Carotta, V. Guidi, C. Malagù, G. Martinelli and M. Piga

University of Ferrara, Physics Dept., 12 Paradiso, 44100 Ferrara, Italy
email: giberti@fe.infn.it http://www.fe.infn.it/labsem/

Summary: *We used SnO_2 gas sensors for monitoring ethylene in the range of interest for fruits ripening. The effect of atmospheric humidity on the sensor conductance and rensponse towards ethylene was quantitatively measured. The results of our observations proved useful for the application of chemoresistive sensors for agro-alimentar monitoring.*

Keywords: *chemoresistive sensors, agro-alimentar monitoring, humidity*
Category: *chemical sensors*

1. Introduction

Ethylene monitoring is relevant for agro-alimentar applications. Feeding of this gas into storage chambers leads to rapid fruit ripening. The gas-concentration for monitoring highly depends on the kind of fruit of interest. As an example, a typical concentration level of ethylene for apples and pears is 100 ppm; for acid fruits the level is some ppm and only some ppb for kiwi. Quantification of ethylene concentration in a gas mixture is the aim of this work. Particular enphasis will be given to the study of interference with humidity, which has been recognized to play crucial role.

2. Experimental

We used a set of four SnO_2 gas sensors, two pure samples, annealed at 650°C and 850°C, and two Au-doped ones, annealed at 650°C and 850°C.

The sensing layers were deposited through thick-film technology onto miniaturized laser pre-cut alumina substrates equipped with a heater on the backside, a Pt-100 resistor for the control of the sensor operating temperature and a golden front interdigitated contacts. The pastes used for screen-printing were a mixture of the nanometric powders, an organic vehicle together with a small percentage of glass fritt to improve the adhesion of the layers to the substrates. SnO_2 powders were produced through sol-gel techniques [2]. The films were fired for 1h at 650 or 850°C in air. The thickness of the deposited layers was about 20-30 μm.

The flow-through technique was used to probe the sensors. Ethylene was supplied by certified bottles (100 ppm concentration) and fed into a test chamber. In order to control the environmental climatic parameters, we have equipped the test chamber with both relative humidity and temperature sensors. A device based on vapour saturation was used to humidify the carrier gas to a wanted level ranging within 0-70%.

The response to the gases has been defined as G/G_0, where G and G_0 are the conductance values in the air+gas mixture and in air, respectively.

3. Results

Ethylene measurements were performed in two different ways: the first one is obtained at a constant level of humidity; in the second one the amount of ethylene is kept constant and humidity was varied. A typical record of this second case is shown in Fig. 1 in the case of a pure SnO_2 for ethylene in the range 1-8 ppm with RH from 2% to 64%.

The mechanism of detection of ethylene at the surface of a metal-oxide semiconductor follows this route: after an initial physisorption stage, with several arrangements of the molecule, ethylene undergoes oxidation to acetic aldehyde according to the reaction [1]:

$$C_2H_4 + O_{ads} \rightarrow C_2H_4O$$

The influence of humidity in the ethylene response is evident: it does not change the shape of the curves but only affects their slope.

Basically humidity appears to damp the oxidation of ethylene probably because the formation of an hydroxilated layer decreases the surface concentration of the oxygen ions available for interaction with ethylene molecules.

The measurements on catalysed SnO_2 sensors show a qualitatively similar behaviour, but also an increase in the response with respect to the pure SnO_2 sample, for both ethylene and humidity; as an example at $RH=64\%$, G/G_0 is about 1.4 for the pure sensor, while is about 2.4 for the catalysed one. This is probably caused by the catalytic activity of gold at the surface.

Prior to on-field operation, an analysis aimed to determining the effect of temperature and humidity on the sensors response has been carried out. As one might expect, absolute humidity (AH) rather than RH does affect the sensor's conductivity.

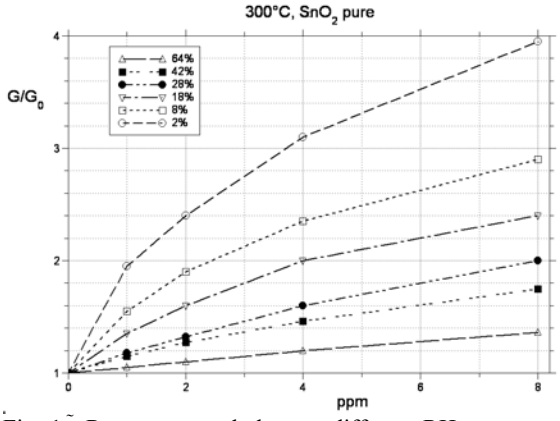

Fig. 1. Response to ethylene at different RH on a pure SnO_2 sensor annealed at 850°C. The effect of humidity results in a lowering in the response.

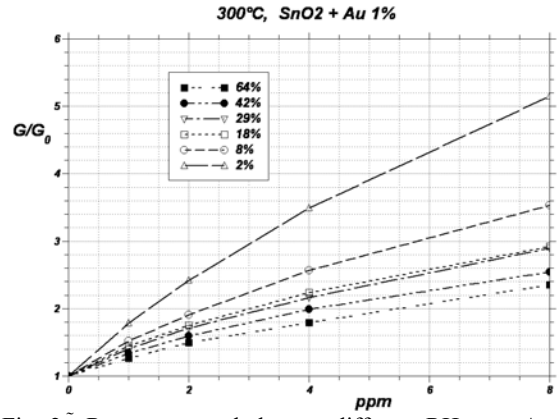

Fig. 2. Response to ethylene at different RH on a Au-catalysed SnO_2 sensor annealed at 850°C. The effect of humidity results in a lowering of the response.

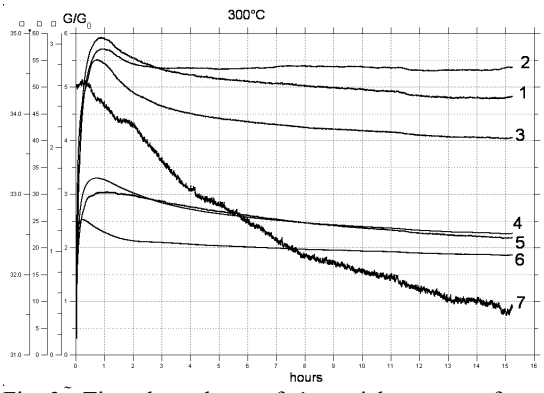

Fig. 3. Time dependence of: 1. partial pressure of water vapour (proportional to AH); 2. RH; 3. Au-cathalysed SnO_2 sensor, annealed at 650°C; 4. pure SnO_2 sensor, annealed at 850°C; 5. pure SnO_2 sensor, annealed at 650°C; 6. Au-cathalysed SnO_2 sensor, annealed at 850°C; 7. temperature inside the chamber. The responses of the sensors follow the trend of AH rather than that of RH.

A typical situation for four SnO_2 sensors exposed to humid synthetic air is reported in Fig.3: the chamber is subject to the natural overnight decay of temperature though RH is kept constant. This causes a decrease in AH, which can be calculated by Clapeyron equation and compared to experimental data.

Thus, the partial pressure of water, *p*, can be integrated in the form of Eq.1, with *a* and *b* as parameters to be fit with the saturated steam diagrams of water in the temperature range of interest.

$$p(T) = a \cdot e^{-\frac{b}{T}} \qquad (1)$$

Thereby, in Fig.3, the partial pressure of water, i.e., the absolute humidity, can be regarded as a function a function of time according to:

$$p(t) = RH\left[T(t)\right] \cdot a \cdot e^{-\frac{b}{T(t)}} \qquad (2)$$

where $RH[T(t)]$ is relative humidity vs. time. It comes out that the response of the sensors falls off with time during the night, following the trend of AH, as shown in Fig. 1.

Finally, compensation of the variation of the relative humidity and temperature, which are expected to take place in storage chamber, can be compensated for via a simple RH measurement unit. The algorithm for compensation can be easily implemented on a microchip in the control electronics of the sensors.

4. Conclusions

SnO_2 is a material suitable to ethylene monitoring in the range of interest. Humidity effects are important in spite that they are weakened by a catalyst. Moreover the catalyst leads to a larger response to ethylene.

Absolute humidity rather than relative humidity is the crucial parameter that determines the effects of humidity on the sensor's response.

A simple algorithm based on the Clapeyron equation allows the compensation of the humidity effects.

References

[1] A. V. Khasin, *React. Kinet. Catal. Lett.* 64 (1998) 289–294.

[2] B. Cavicchi, M. C. Carotta, M. Ferroni, G. Martinelli, M. Piga, S. Gherardi et al. "Au-, Pd-, Pt-doped thick films for gas sensing". *Proc. of 9th Int. Meeting on Chem. Sensors*, pp. 142-143, Boston, USA, 7-10, July, 2002.

Aqueous and alcoholic syntheses of WO_3 powders for NO_2 detection through thick film technology

B. Vendemiati, M. Blo, M.A. Butturi, M.C. Carotta, S. Galliera, S. Gherardi, V. Guidi, C. Malagù, G. Martinelli

INFM and Physics Dept. of Ferrara University, Via Paradiso 12, 44100 Ferrara, Italy
e-mail: vendemiati@ fe.infn.it

Summary: *Different methods for obtaining WO_3 powders suitable for gas sensing have been developed. Aqueous and alcoholic solvents proved to be the most promising media to grow nanometric particles. Morphological characterization highlighted that ethanol and a di-chetone, led to a finer grain with a more homogeneous size distribution. Thick films of WO_3 responded to NO_2 with high sensitivity. In particular the samples arising from ethanolic solution proved to be the most performing layers.*

Keywords: *Chemoresistive sensors, tungsten trioxide, NO_2 detection*
Category: *5 (Chemical sensors)*

Introduction

The new European environmental legislation, beginning from the Council Directive 96/62/CE, allows the assessment of air quality through alternative instruments with respect to the traditional analytical techniques. Thus innovative equipment based on a low-cost compact and mobile array of solid-state gas sensors could be useful for the purpose.

For this aim several transition metal oxides have been studied as potential candidates. In particular, WO_3 behaves as an n-type semiconducting oxide due to non-stoichiometry [1]; it has been proved as an excellent candidate material as far as chemoresistive sensors are concerned. Among the major pollutants, nitrogen dioxide is particularly harmful and its detection in the range of environmental standard (less than 100 ppb) has remained a challenging goal. In particular tungsten trioxide has been shown to be highly effective in NO_2 detection [2].

This work is devoted to the preparation of WO_3 powders through several routes and their deposition as thick films. Finally, the layers are comparatively tested towards NO_2.

Experimental

Preparation of nanometric WO_3 powders has been performed through several synthetical routes by using aqueous, hydrocarbonic and hydro-alcoholic solvents. Commercially available starting materials and solvents were used without further purification. A preliminary overview on the morphology of the whole set of powders showed that suitable nanomaterial candidates for gas sensing can be produced by a sol-gel process and precipitation, using water and short-chain alcohols as solvents.

1) Precipitation. **1a)** Water medium: 2.4 milli-moles of dodecilbenzensulfonic acid (sodium salt) were added to a 0.01 M solution of WCl_6 (Aldrich, 99.9+%; ultra pure water) and was subjected to ultrasonic treatment at 50°C for 3 h. The pale-green precipitate was cleaned and dried under vacuum, then annealed for 1 h at 850°C. The final yellow powder yielded a bimodal grain-size distribution ranging within 300-450 nm and >1μm. **1b)** Alcoholic medium: reaction of 8 milli-moles of WCl_6 with EtOH abs (Carlo Erba) and PTN (2,4 pentanedione, 0.08M in EtOH abs) resulted in a paramagnetic blue W(V) complex, whose stoichiometry has not been completely clarified. After a warm treatment in a sonic bath, the solution was stationary for 2 h at RT and a precipitate was formed. The blue powder was dried and then annealed at T=850°C for 1 h, leading to a yellow powder with more homogeneous and lower grain-size distribution than **1a)**.

2) Sol-gel, alcoholic medium: WCl_6 reacts with ROH (R=CH_3-, C_2H_5-, 0.02 M solutions) leading to a paramagnetic blue W(V) complex. After an ultrasonic treatment carried out at T=40°C for 2 h, 3.2 g of PTN was added and a blue gel occurs. The evaporation of the solvent yielded a dry blue gel which was crushed into a powder and annealed for 2 h at 850°C. The final yellow powder exhibited particle size ranging between 500 nm and 1μm.

Results

Powder and film characterisations have been carried out by means of TG-DTA, RBS, SEM, TEM and XRD. Fig.1 shows the TG-DTA curves performed on the **1b** precursor of pure WO_3. The

transformation from the precursor to the trioxide takes place through three different exothermic processes with a 24% weight loss. The powder **1b** has been calcinated at various temperatures ranging within 450-850 °C in order to study coalescence of the grains and porosity of the film. The othorombic phase for WO_3 was found in the range 450-550°C while the monoclinic phase occurs at temperature higher than 650°C. In the intermediate range of temperature the transition between the two phases takes place. TEM analysis showed considerable coalescence probably assisted by phase transition.

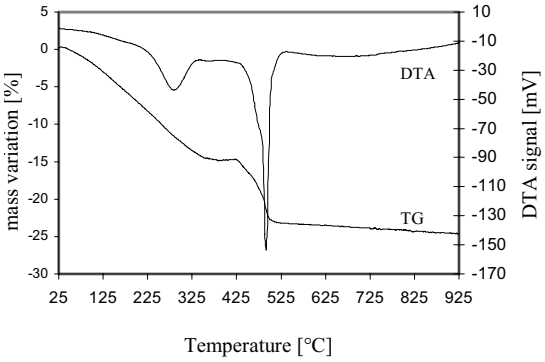

Fig. 1. TG-DTA analysis of **1b** WO_3 precursor.

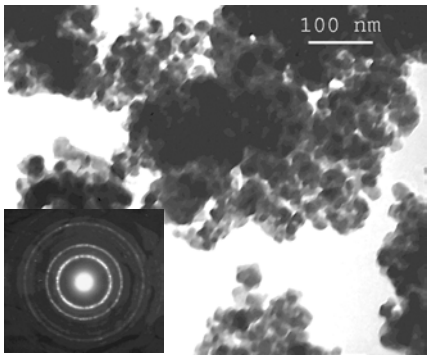

Fig. 2. TEM image of the nanosized WO_3 powder calcined at 450°C. The electron diffraction pattern shown in inset indicated the WO_3 orthorombic phase.

Fig. 3b shows the temperature dependence of conductivity in dry air of WO_3 **1b** and SnO_2 thick films. Measurements were carried out by changing the temperature from 100 °C to 500 °C at the heating rate of 3 °C/min. Both samples exhibited three regions of conductance as usual for SnO_2 sensors [3]; indeed WO_3 samples highlight a large increase in conductance and, in turn, a significant decrease in the energy barrier (see Fig. 3a). Such a difference could explain the ability of tin dioxide to sense either reducing agents at high temperature or NO_2 at low temperature, whilst tungsten trioxide is capable of sensing only oxidizing gases. In fact, it was previously observed that addition of W to SnO_2 resulted in a decrease of the response to CO and in an increase in respect to NO_2 [3]. Pure WO_3 shows no response to 100 ppm of CO within 200-250°C, a temperature at which the response to NO_2 is the highest (see Fig 4 at 200 °C working temperature)

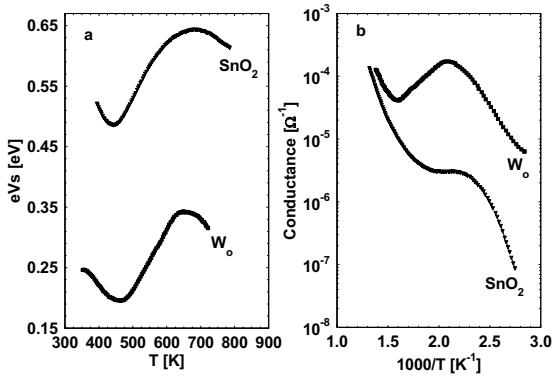

Fig. 3 a, b. Temperature dependence of the film conductance and the energy barrier.

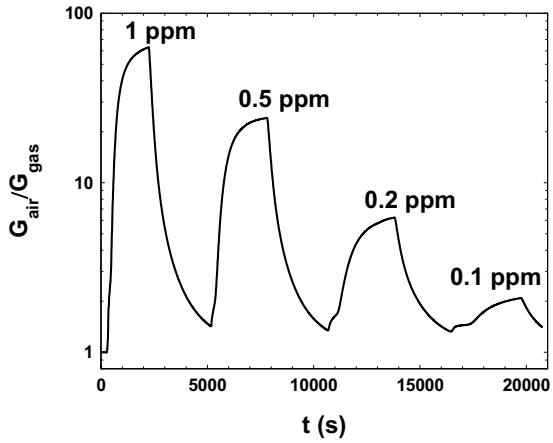

Fig. 4. Response of the **1b** film vs. NO_2, 200°C, dry air.

Conclusions

Different methods for obtaining nanometric WO_3 powders have been studied. A proper choice of the solvent act as a tailoring effect on the shape and the dimension of the grains. The ethanolic medium synthesis proved to be the best among the tested preparations. WO_3 material shows good responses versus oxidizing gases, without any interference from reductant gases, even in the environmental sub-ppm range concentration of NO_2.

References

[1] W. Noh, Y. Shin, J. Kim, W Lee, K. Hong, S. A. Akbar, J. Park Solid State Ionics 152–153 (2002) 827– 832

[2] M. Ferroni, V. Guidi, G. Martinelli, G. Sberveglieri, Journal of Material Research, 12 (1997) 793.

[3] A. Chiorino, G. Ghiotti, F. Prinetto, M.C. Carotta, C. Malagù, and G. Martinelli, Sensors and Actuators B, 78 (2001) 89-97.

Influence of Humidity on the CO Sensitivity of a New Gas Sensor Based on SnO_2 Nanoparticles Surface-Doped with Palladium and Platinum

P. Ménini[1], F. Parret[1], M. Guerrero[1], A. Martinez[1], K.Soulantica[2], L. Erades[2], A. Maisonnat[2], and B. Chaudret[2]

[1]Laboratoire d'Analyse et d'Architecture des Systèmes (CNRS-LAAS),
7 avenue du Colonel Roche 31077 Toulouse cedex 4, France.
e-mail: menini@laas.fr http://www.laas.fr
[2]Laboratoire de Chimie de Coordination (CNRS-LCC),
205 route de Narbonne, 31077 Toulouse cedex 4, France.

Summary: *In this paper, we show the influence of two doping agents Palladium and Platinum on the sensitivity for CO sensing of the nanoparticular SnO_2 sensors at an operating temperature of 450°C. It is well known that the evolution of the conductance of the sensitive layer is largely modified by doping. A study carried out to measure the influence of humidity demonstrates that if un-doped sensors show a variation of same sign but less important than in dry air, doped sensors display a very different behavior. Indeed, we obtain a point of null sensitivity between 0 and 10%RH (RH = relative humidity) and a strong inverse sensitivity above 15% RH. These results demonstrate the presence of unexpectedly different chemical operating modes for CO sensing according to the rate of humidity.*

Keywords: *gas sensors, SnO_2, nanoparticles, doping, sensitivity.*
Category: 5

1 Introduction

At present time, most of the gas sensors are either electrochemical or metal-oxide semiconductors in thick-film [1] or in thin-film [2] technology. The main problems of these techniques are : moderate level of sensitivity, low reproducibility, low selectivity, long stabilization periods and high power consumption for the thick layer. However, the sensor technology has integrated for a few years the development of nanomaterials.

This article deals with a new generation of nanoparticular SnO_2 gas sensors (Fig. 1). This new technology allows a very high surface-on-volume ratio and then may display a high level of sensitivity due to the reduction of grain size in agreement with Yamazoe et al.[3].

However different aspects of this kind of sensors have to be studied to acquire the sensing principles and to improve their actual performances.

A new technical method has been achieved to obtain a surface doping with nanocrystals of PdO and PtO_2 fixed on the tin oxide nanoparticles [4-5]. Electrical characterization under CO of these new sensors should produce a comparison of sensors' sensitivities according to the different doping agents. Then, the influence of moisture will be discussed.

2 Description of the sensor

The sensor used in this study is formed by a microhotplate platform and a nanoparticular SnO_2 sensing layer. The microhotplate architecture was initially developed for Motorola and presently exploited by Microchemical Sensors S.A. A SiO_xN_y membrane of 2 µm of thickness supports a polysilicon heater of 600µm x 430µm. Dimensions have been optimised to achieve good thermo-mechanical reliability and good homogeneity of temperature on the active area. The heater can reach temperatures of 500°C with a power consumption lower than 100mW.

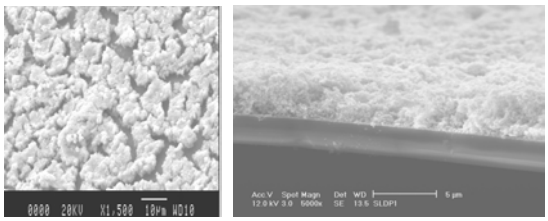

Fig. 1. SEM images of the sensing layer.

The metal-oxide used in this sensor is a crystalline SnO_2 nanomaterial synthesized by the decomposition and oxidation of a tin based organometallic precursor ($[Sn(NMe_2)_2]_2$), the mean grain size obtained is 15 nm of diameter. Doping is achieved by decomposing an organometallic precursor $M(dba)_2$ (M=Pd, Pt; dba = dibenzyli-deneacetone) under dihydrogen at the surface of the tin/tin oxide preformed particles. Upon heating in situ on the platform the tin material is transformed into SnO_2, whereas the doping agents are oxidized into PdO and PtO_2 nanocrystals which mostly remain at the surface of tin (Fig. 2). This material is then deposited using a microinjector technique over the two electrodes placed in the homogeneous temperature region of the heater. This heater permits the full oxidation into SnO2 with a controlled temperature cycle from ambiant to 500°C.

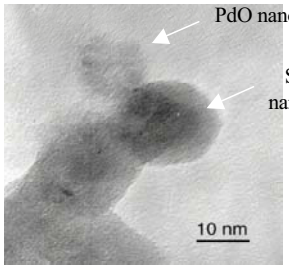

Fig. 2. HRTEM image of the Pd-doped SnO_2.

3 Experimental results

The experimental set-up consists of a gas delivery system, an exposure glass vessel and an electronic circuit for resistance determination through voltage measurements.

Before any test sequences, all sensors have to be subjected to several heating cycles in dry air.

The optimal operating temperature has been determined near 450°C for all tested sensors under 500ppm of CO. But, this temperature must not be exceeded to avoid electromigration problems from contact pads metal through polysilicon layer.

The sensitivity of the sensor is determined by $S = (R_{gas}-R_o)/R_o$ where R_o is the sensitive layer resistance without CO and R_{gas} the resistance measured under CO.

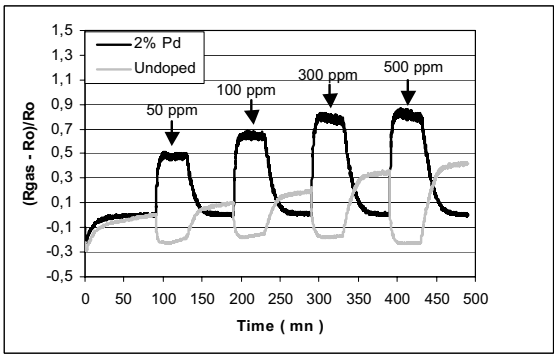

Fig. 3 : Undoped and Pd-doped sensor responses under CO injections in dry air.

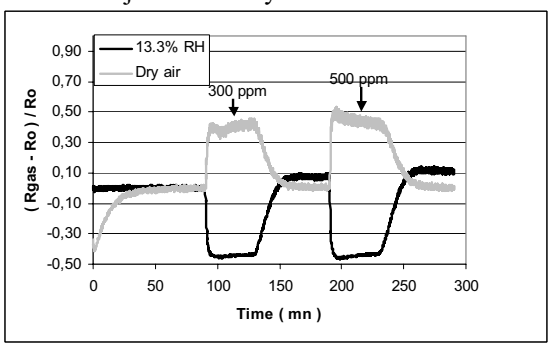

Fig.4 : Exemple of Pd-doped sensor responses in dry and humid atmosphere.

In figures 3 and 4 it can be seen that the response of doped sensors in humid air is inversed compared to that one in dry air. Secondly, doped and undoped sensors display the same variation (in term of sign) in humid atmosphere as it is observed in literature.

So, the doped-sensor sensitivity is null for a relative humidity about 5%.

4 Discussion

This inversion of sensitivity is surprising and, to the best of our knowledge unprecedented. The correlation with the rate of humidity is clear and the observation of a point of zero sensitivity confirms it. The origin of this behavior is as yet unclear but probably results from different catalytic properties of the doping nanoparticles according to the presence of humidity. The surface chemistry of this system has therefore to be studied in detail. An hypothesis would be the variation of rates of CO oxidation on the catalyst and absorption on SnO_2 according to the rate of humidity.

5 Conclusion

A new generation of gas sensors based on nanoparticular SnO_2 sensitive layer with two doping catalysts - Palladium and Platinum - has been elaborated and tested. The maximal sensitivity to carbon monoxide has been obtained at the upper temperature 450°C for all of the sensors. First results in dry air reveal that the palladium is the best doping agent for CO detection, but, at the moment, that in wet ambiant air, the best sensitivity is achieved for a Pt-doped sensor in agreement with the litterature [6].

The inversion of sensitivity from dry to wet air introduces firstly, a new concept of electrochemical operating mode between oxygenated gases and the superficially doped sensing layer and secondly, an opportunity to increase the selectivity using a sensor array.

Acknowledgments

Authors would like to thank Mr. P. Fau of Microchemical Systems S.A. which have provided us the micromachined platforms.

References

[1] K. Ihokura et al. The stannic Oxide gas sensor, principle and applications, *CRC Press, Boca Raton, Floride, 1994*.

[2] E. Leja et Al. *Thin solid film 59 (1979)*, pp147.

[3] N. Yamazoe. *Sensors&Actuators B5 (1991)* p 7.

[4] C. Nayral et al. Synthesis and use of a novel SnO_2 nanomaterial for gas sensing. *Applied Surface Science 164 (2000)* pp. 219-226.

[5] L. Erades, Phd Thesis, Nanoparticules d'oxydes metalliques semiconducteurs…, Toulouse, France, January 2003, CNRS-LCC.

[6] V.N. Mishra and R.P. Agarwal, Sensitivity, response and recovery time of SnO_2 based thick-film sensor array for H_2, CO, CH_4 and LPG, *Microelectronics Journal 29 (1998)* pp. 861-874.

Selective Gas Sensor Systems based on Temperature Cycling and Comprehensible Pattern Classification: a Systematic Approach

A. Schütze, A. Gramm

Laboratory for Measurement Technology, Saarland University, 66041 Saarbrücken, Germany
email: schuetze@lmt.uni-saarland.de http://www.lmt.uni-saarland.de

Summary: *Semiconductor gas sensors offer low cost solutions for many measuring problems but often lack selectivity. Temperature cycling greatly improves selectivity without requiring frequent recalibration like static sensor arrays. Optimization of the temperature cycle and of the subsequent signal evaluation is however difficult and very time consuming. We present a systematic approach allowing step-by-step design of intelligent gas sensor systems based on temperature cycling and hierarchical pattern classification.*

Keywords: *gas sensor system, selectivity, temperature cycling, pattern classification*
Category: *5 (Chemical Sensors)*

1 Introduction

Semiconductor gas sensors offer high sensitivity, good reliability and low cost making them attractive for a wide range of applications ranging from air quality control to safety applications like explosion warning or fire detection. Major drawbacks are the sensors lack of selectivity and poor long term stability. Sensor arrays offer better selectivity but lead to increased cost and require frequent recalibration. An attractive alternative is the extraction of multiple data from a single sensor (e.g. by temperature modulation or impedance measurements) leading to virtual multisensor systems. Temperature cycling especially has proven a very powerful approach improving both selectivity and stability [1]. However, development of a sensor operating mode requires comprehensive calibration and the subsequent signal evaluation to extract the required information offers a score of options (for an excellent overview see [2]). Design and validation of sensor systems based on temperature cycling is therefore a complex process restricting its use to high price applications even though hardware requirements are low [3]. In addition, many intelligent signal processing techniques present a kind of black box, where even small changes in the sensor characteristics lead to unpredictable results.

2 Systematic Approach

For efficient development of selective and stable sensor systems, our procedure for choosing operating modes and adapted comprehensible pattern classification is based on the following systematic steps:

2.1 Selection of gas sensors and operating mode

An automated test bench is used to closely simulate the conditions expected for the chosen application (i.e. temperature and humidity, gases and interferents at the expected concentration levels). Multiple sensors are operated with a complex temperature cycle (T-cycle) comprising several temperature levels and steps (based on manufacturer suggestions and users experience) and the resulting raw data are gathered in a data base. This process is speeded up considerably by using concentration ramps in a flow through test system providing a large data basis within comparatively short time. Then, linear discriminant analysis (LDA) [4] is used to ensure that the information content in the raw data is sufficient for the required task (i.e. discrimination between organic solvents). The LDA coefficients also allow the identification of the most relevant data for the classification, thereby making a selection of the most useful sensor(s) and operating temperatures possible.

2.2 Optimization of operating mode

For the most suitable sensor(s) the T-cycle is adapted by reducing it to those temperature levels and steps which are useful for classification. A high temperature phase often reduces sensor drift and should be included even if it is not necessary for classification [3]. Of course a compromise has to be found between required information content and cycle duration/ complexity based on the application. After calibration in the test bench, LDA is again used to check the validity of the T-cycle, i.e. its information content.

2.3 Comprehensible pattern classification design

Signal pre-processing (e.g. normalizing the response curves by division through their mean, Fig. 1) is used to achieve more stable data and to suppress the influence of relative humidity. Then, secondary features describing the shape of the response curves, which have proven superior to DFT and wavelet features [5], are generated. With these features a hierarchical decision tree is designed using LDA: Fig. 2 shows an example for the discrimination of six organic solvents over a concentration range from 2 to 200 ppm, where two solvents can be clearly separated from the other four. These are therefore grouped and the first deci-

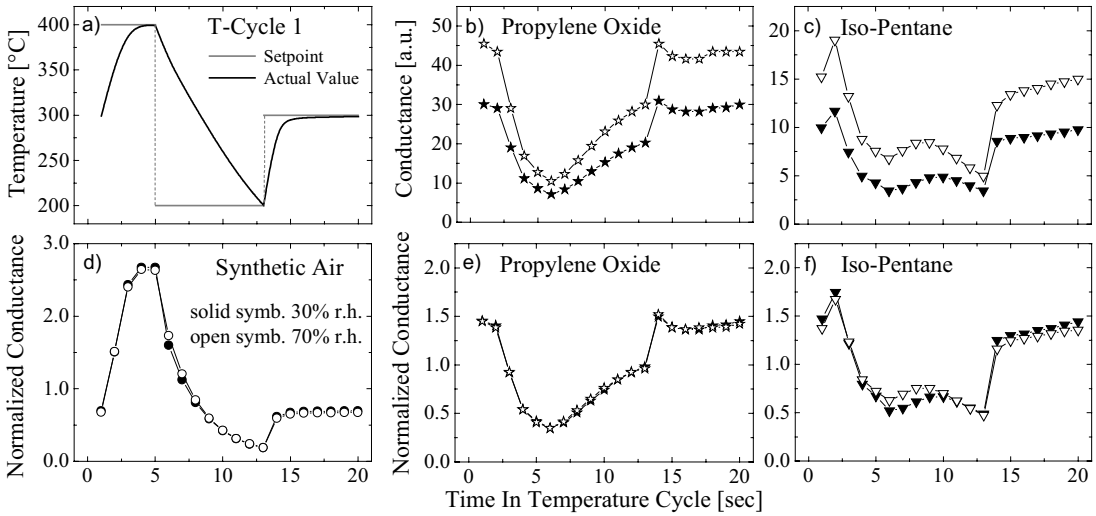

Fig. 1. T-cycle (a) and resulting exemplary response curves for a commercial metal oxide gas sensor (UST 1330) for 20 ppm Propylene Oxide and iso-Pentane in air (b, c). Normalization suppresses the influence of relative humidity in synthetic air (d) and Propylene Oxide (e), while some humidity induced changes in the curve shape are evident for iso-Pentane.

sion only separates between this group, iso-Pentane and Benzene (air has already been filtered out). The classification itself is performed using 2d-territorial plots of selected secondary features, as shown in Fig. 3 for the second decision (identification of Methanol). These plots offer simple visual control of classification performance, signal trends and eventual problems. By repeating this process for the remaining unidentified substances a complete decision tree is built for the desired application. Note that a quantitative estimate is easily possible after classification using a feature with good correlation to the concentration.

3 Conclusion and Outlook

The systematic approach presented here has proven very efficient for the development of intelligent sensor systems offering high selectivity and stability. It can also be used for microstructured gas sensors which allow much faster temperature cycling and therefore faster discrmination. Examples will be presented for different applications.

In case of insufficient classification quality, further improvement of the system is possible by switching on-line to a different T-cycle. Thus each decision can be based on a different T-cycle, which can also be designed on the basis of the first calibration run.

References

[1] A.P. Lee and B.J. Reedy: Temperature modulation in semiconductor gas sensing, Sens. & Act. **B** 60 (1999) 35-42.
[2] R. Gutierrez-Osuna: Pattern analysis for machine olfaction, IEEE Sensors, vol. 2, no. 3 (2002) 189-202.
[3] A. Schütze, A. Gramm and T. Rühl: Identification of organic solvents by a virtual multisensor system with hierarchical classification, *Proc. IEEE Sensors 2002*, pp. 382-387, Orlando, USA, 12-14 June 2002.
[4] R.O. Duda, P.E. Hart and D.G. Stork: Pattern classification, 2nd ed., Wiley, New York, 2000.
[5] A. Gramm and A. Schütze: High performance solvent vapor identification with a two sensor array using temperature cycling and pattern classification, *Proc. Eurosensors XVI*, pp. 609-610, Prague, Czech Rep., 15-18 Sep. 2002.

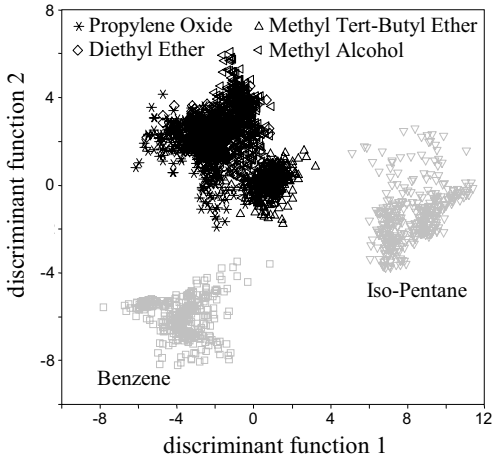

Fig. 2. LDA plot allowing separation of Benzene and iso-Pentane from four other organic solvents. For each gas 160 measurements with concentrations between 2 and 200 ppm are shown, 80 each for 30% and 70% r.h.

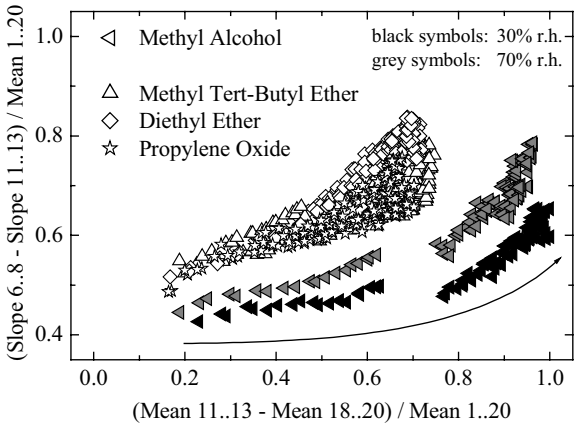

Fig. 3. Second decision of the classification discriminating between Methanol and three ethers; the arrow indicates increasing concentrations from 2 to 200 ppm. Changes in r.h. reproducibly shift the values for Methanol.

GaSTON – a Versatile Platform for Intelligent Gas Detection Systems and its Application for fast Discrimination of Fuel Vapors

T. Kammerer and A. Schütze

Lab. for Measurement Technology, Saarland University, P.O. Box 15 11 50, 66041 Saarbrücken, Germany
email: t.kammerer@lmt.uni-saarland.de http://www.lmt.uni-saarland.de

Summary: *Temperature cycling of semiconductor gas sensors is a very powerful tool for developing gas detection systems with high selectivity and stability. Microstructured gas sensors - due to their low thermal mass - have very low thermal time constants in the range of 10 ms. Based on these sensors, development of fast and highly selective gas detection systems is possible using temperature cycles with ten or more temperature levels and an overall duration of only a few seconds. For efficient evaluation of these systems, we have developed a versatile hardware platform which provides accurate temperature control for arbitrary temperature control and fast, high resolution data acquisition either in stand-alone operation or connected to a PC. Based on this hardware platform, we demonstrate a system consisting of a micro gas sensor and intelligent signal processing for fast discrimination between gasoline and diesel vapors.*

Keywords: *virtual multisensor system, temperature cycling, fuel discrimination*
Category: *5 (Chemical Sensors) or 10 (Applications)*

1 Introduction

Semiconductor gas sensors offer high sensitivity, good reliability and low cost making them attractive for a wide range of applications ranging from air quality control to safety applications like explosion warning or fire detection. In addition, modern microstructured sensors offer low cost and low power, opening new markets especially for mass applications and handheld devices. Major drawbacks today are the sensors lack of selectivity and poor long term stability, which prevent a wider use especially in safety relevant applications. To overcome these problems without multiplying cost and complexity of the resulting systems, temperature modulation of the gas sensors combined with intelligent signal processing is a very promising technique allowing vastly improved selectivity and significant drift reduction [1]. Discrimination between six organic solvents was possible over a wide concentration range using a single sensor [2]. For faster detection and identification microstructured sensors are very attractive, as they have very short thermal time constants due to the extremely low mass of their active membrane thus allowing much faster temperature changes.

2 Experimental

2.1 Hardware platform

To make full use of the potential offered by modern microsensors, accurate temperature control, arbitrary temperature cycles as well as fast high resolution data acquisition are necessary (at least during development to optimize sensor operating mode and signal evaluation). We have developed a versatile hardware platform named GaSTON (**Ga**s **S**ensor **T**-cycle **O**perating u**N**it) for the effective development of gas detection systems based on microsensors and T-cycling. GaSTON combines an analog temperature control circuit with a digital set-point and a data acquisition system allowing stand-alone operation as well as master-slave operation with a host PC. The control circuit regulates the heater resistance R_H and thereby the temperature of the sensor. The desired temperature

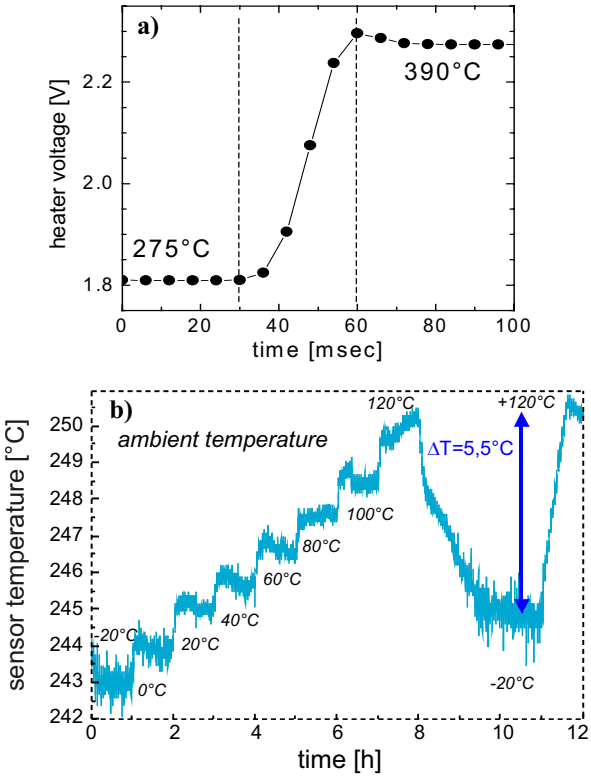

Fig. 1: Performance of the temperature control circuit with a microstructured gas sensor (MiCS 5110, [4]): (a) a new set point is reached within 30 msec even for large temperature changes, (b) a 100°C change in the ambient leads to a sensor temperature change of approx. 5°C.

is set by the micro-controller based on the known $R_H(T)$ characteristic using a digital potentiometer. This allows the definition of arbitrary temperature cycles (T-cycles) using nearly identical hardware for many different sensors as well as fast adaptation to new sensor elements. The hardware was tested with sensors based on alumina substrates with platinum heater [3] as well as microstructured sensors with thin film heaters [4]. Although the temperature coefficient of R_H is rather low for the microsensors, a high temperature stability was achieved. Fig. 1a shows the dynamic behavior (time required for a step change is 30 ms), Fig. 1b the accuracy of the temperature control during changes in ambient temperature.

The data acquisition offers two AD-channels with 16 bit resolution allowing measurement of either sensor resistance, heater voltage or heater current with a maximum rate of 150 Hz for one channel. Thus, the system can be used not only for resistive sensors but also for micro hotplate sensors measuring combustible gases by determining the heater power necessary for a given sensor temperature. Special emphasis was placed on data correctness and integrity, i.e. each measurement value is given an exact time stamp and missing values, which can be caused by timing errors, are logged. This is essential for intelligent signal processing, which extracts information from the time and temperature dependence of the sensor signal [2].

2.2 Fast discrimination of fuel vapors

The improved selectivity achieved by T-cycling is demonstrated in Figs. 2 and 3: a commercial microstructured metal oxide gas sensor (MiCS 5131, [4]) was operated using a simple T-cycle with 10 set points over a range of about 260°C. The temperature dependence of the sensor conductance shows a characteristic behavior in clean air and when the sensor is exposed to gasoline and diesel vapors, respectively, Fig. 2. Sensor raw data were normalized by dividing through their mean over the entire cycle. Note that

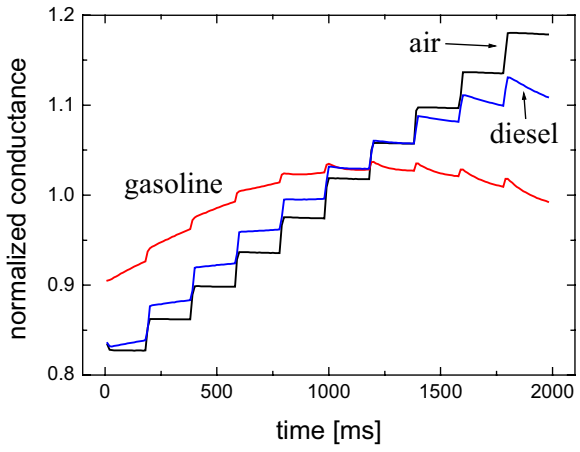

Fig. 2: Normalized response curves of a MiCS 5131 microstructured sensor in air and exposed to fuel vapors. The cycle consists of ten temperature levels between approx 160 and 420°C each held for 200 ms. The average value of each T-level is used for the linear discriminant analysis in Fig. 3.

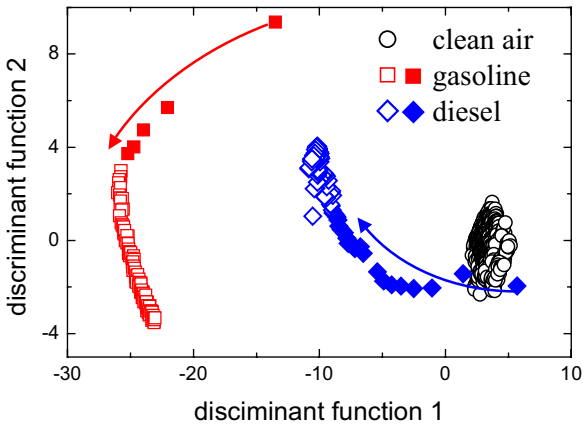

Fig.3: LDA plot showing the classification of fuel vapors in air with data extracted from the normalized T-cycle shown in Fig. 2 (average value for each T-level). Open symbols denote steady state conditions, solid symbols the run-in when the sensor is exposed to the fuel vapor.

this signal pre-processing often suppresses sensor drift considerably [2]. Using only the average value for each temperature of the normalized response curves, the vapors can be classified perfectly, for example using linear discriminant analysis (LDA) [5], Fig. 3. Note that the identification takes only a few seconds: even for the first cycles after exposing the sensor to the fuel vapors a clear signal trend is already visible as indicated by the arrows in Fig. 3. By shortening the cycle, i.e. using fewer T-levels with shorter duration, fuel identification will be possible in less then one second. This system could therefore be used to prevent filling a car tank with the wrong fuel.

3 Conclusion and Outlook

We have shown that temperature cycling of microstructured gas sensors allows fast identification of fuel vapors. Similarly, differentiation between H_2 and CO and even measurement of r.h. are possible by extracting suitable parameters from the T-cycles. Additional information, i.e. the slope of each T-level, could be used to further improve the selectivity, for example to suppress interferents. In addition to improving selectivity and stability, T-cycling can also reduce power consumption by turning off the heater between cycles while still achieving a data rate sufficient for most applications. We therefore expect many interesting new solutions based on this concept in the near future.

References

[1] A.P. Lee and B.J. Reedy: Temperature modulation in semiconductor gas sensing, Sens. & Act. B 60 (1999) 35-42.
[2] A. Schütze, A. Gramm and T. Rühl: Identification of organic solvents by a virtual multisensor system with hierarchical classification, *Proc. IEEE Sensors 2002*, pp. 382-387, Orlando, USA, 12-14 June 2002.
[3] UST GmbH, <http://www.umweltsensortechnik.de>
[4] Microchemical Systems SA, Corcelles, Switzerland, <http://www.microchemical.com>
[5] R.O. Duda, P.E. Hart, D.G. Stork, Pattern classification, 2nd ed., Wiley, New York, 2000.

Electromagnetic radiation effect (microwaves) on the ISFETs sensors feedback.

S. Casans[1], A. E. Navarro[1], D. Ramírez[1], C. Jiménez[2], A. Bratov[2]

[1]Laboratorio de Electrónica Industrial e Instrumentación (LEII), Departamento de Ingeniería Electrónica, Universidad de Valencia, C/ Doctor Moliner 50, 46100 Burjasot, Spain. Tel. int-34963160461, fax int-34963160461. E-mail: Silvia.casans@uv.es.
[2]Instituto de Microelectrónica de Barcelona (IMB-CNM), CSIC, Barcelona, Spain.

***Summary**: In this paper are presented the experimental results obtained in the preliminary study done about the effect produced by the use of the mobile telephones on the ISFETs (Ion Sensitive Field Effect Transistors) and MEMFET (Membrane Field Effect Transistors) sensors feedback. The mobile telephones emit an electromagnetic radiation that modifies the initial ISFET threshold voltage and also generates the sensor feedback instability. The experimental results presented show that this feedback instability can be eliminated when the sensor is exposed to ultraviolet radiation and besides the effect of this electromagnetic radiation can be minimised when the ISFET sensors are polarised with a high enough drain-source voltage (V_{ds}).*

***Keywords**: ISFET, MEMFET, electromagnetic radiation, sensing electromagnetic radiation.*
***Subject category**: 5 (Chemical sensors)*

1. Introduction

The ISFETs main drawbacks are the temporary drifts, the hysteresis and the thermal dependency, at least the main ones taken in account until now. All of them can be compensated or minimised to obtain a proper measurement interpretation. But the ISFETs feedback can be influenced by other external factors that they have not been considered until now. One of the external factors that it has not been considered until now is the electromagnetic radiation emitted by the mobile telephones. Nowadays is widely spread the use of the mobile telephones and the radiation effect on humans beings is a study priority area, but this radiation also can affect to other electronics devices modifying its working behaviour. As it can be seen in the experimental results presented later on, the electromagnetic radiation emitted by the mobile telephones deeply affect the ISFETs sensors modifying its inherent electrical characteristics and so on its feedback. This electromagnetic radiation effect on the ISFETs sensors was detected during our study to design and develop a novel ISFET conditioning circuit [1] and a novel ISFET measurement method [2]. In this paper are presented the main experimental results that allow to know how deeply the electromagnetic radiation affects the sensor feedback and how this effect can be avoided or, at least, minimized.

2. Experimental set-up.

The experimental measurement system used during the study can be seen on Fig. 1. The instrumentation system and the novel conditioning circuit used are explained in detail in reference [3]. The novel measurement method used to obtain a stable sensor feedback for long time measurements and temperature variations can be found in reference [4].

Fig. 1.- Measurement instrumentation system.

3. Experimental results.

The experimental study was done with ISFET and MEMFET sensors and in both of them the electromagnetic radiation had the same effect. The typical test stability MEMFET (sodium ion sensitive) feedback can be seen on Fig. 2. The stability test consist on studying the sensor feedback during long time periods maintaining constant the polarization conditions (voltage-V_{ds}-and current-I_{ds}-), the environmental temperature and the pH value of the solution in which the sensor is sunk. The experimental results show that the sensor feedback is stable. But when the mobile telephone is used close to the experimental measurement system (sensors included) (Fig. 1) and the same sensor pass again the same stability test, its feedback is completely unstable, as it can be seen on Fig. 3. On the radiated sensor feedback can be detected random peak voltages reaching values of 4 mV. These peak voltages are completely unacceptable in any of the measurements methods that can be used with ISFET/MEMFET sensors, because these peak

voltages means that the pH value of the solution has been changed and this fact is not true following the stability test. With any of the measurements methods [5, 6] that can be used with ISFET/MEMFET sensors we were misunderstanding the real meaning of the measurement done with the sensor.

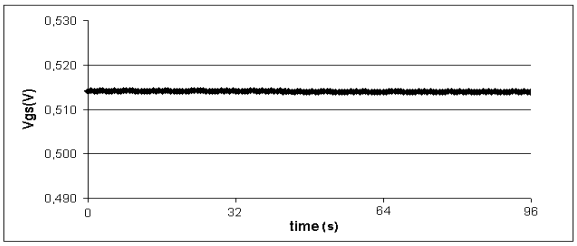

Fig. 2.- Sodium ion MEMFET (Na25) temporary feedback.

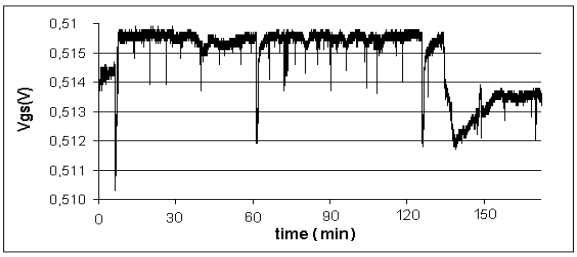

Fig. 3.- Sodium ion MEMFET (Na25) temporary feedback after it has been radiated with a mobile telephone electromagnetic radiation. .

When this unusual feedback was detected on the sensors it was decided to study again its transconductance graphs. In all the studied cases the initial sensors threshold voltage had suffer an important variation on its value. In some of the studied sensors the threshold voltage was increased in 200 mV.

The first step done in order to minimize the electromagnetic radiation effect observed on the sensors, was to increase the polarization voltage (V_{ds}) applied to the sensors. As it can be seen on Fig. 4 the transconductance graph is improved when the V_{ds} is increased.

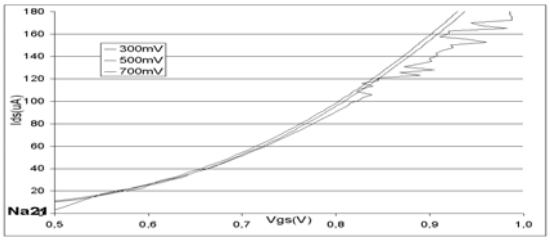

Fig. 4.- Na21 MEMFET sensor transconductace graph for different V_{ds}, after it has been radiated with a mobile telephone electromagnetic radiation

All the sensors radiated with electromagnetic radiation had the same effects: threshold voltage variation and instability feedback. The first effect made us think that both effects could be due to trapped charges in the gate dielectric generated by the electromagnetic radiation. Taking in mind this possibility it was decided to irradiate all the sensors affected by the electromagnetic radiation with ultraviolet light, like it is done with the CMOS memories. All the ISFET sensors irradiated with ultraviolet light almost recovered their initial feedback stability and threshold voltages, as it can be seen on Fig 5. After the ultraviolet radiation the ISFET voltage random steps were of 0.1mV instead of the previous 25mV after it was radiated with electromagnetic radiation.

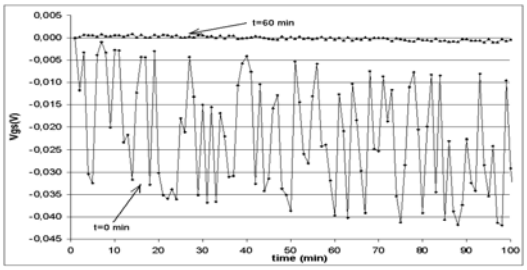

Fig 5.- ISFET test stability feedback before and after the ultraviolet radiation.

Conclusion

The electromagnetic radiation due to the widely spread use of mobile telephones, seriously affects the working behaviour of the ISFETs/MEMFETs sensors. This radiation changes the ISFETs/MEMFETs threshold voltage and causes a strong instability. The experimental results presented prove that there is a novel environmental factor to consider when the ISFET/MEMFETs had to be used: the mobile telephone electromagnetic radiation.

It has been outlined a possible explication to this effect and how it can be corrected.

Acknowledgements

This work was financially supported by PTR1995-0607-OP-02-02, DPI2002-04555-C04-02 and REN2002-04237-C02-02 from the Spanish goverment Comisión Interministerial de Ciencia y Tecnología (CICYT) and the CTIDIB/2002/248 from the Generalitat Valenciana.

References

[1] S. Casans, A. E. Navarro, D. Ramírez, J. Pelegrí, A. Baldi, N. Abramova: "Novel constant current driver for ISFET/MEMFETs characterization". Sensors and Actuators B 76 (2001) 629-633.

[2] S. Casans: "Desarrollo de una instrumentación electrónica para la medida y caracterización de sensores electroquímicos basados en ISFETs/MEMFETs: aplicación a la determinación de aniones en agua. Tesis Doctoral. Universidad de Valencia 2002.

[3] S. Casans, A. E. Navarro, D. Ramírez, E.Castro, A. Baldi, N. Abramova: "Novel voltage controlled conditioning circuit applied to the ISFETs temporary drifts and thermic dependency". 9th International Meeting on Chemical Sensors 2002.

[4] S. Casans, A. E. Navarro, D. Ramírez, N. Abramova, A. Baldi,: "Novel compensation method for absolute measurements using ISFETs". Eurosensors XVI, 181-182.

[5] Hendrik H.; Nicolaas F. de Rooy; Apparatus for determining the activity of an ion (pion) in a liquid. Patent 4,691,167. September, 1987.

[6] Ligtenberg, G; Leuveld, J.: Isfet-based measuring device and method for correcting drift. Patent, 4,701,253. October, 1987.

Development of potentiometric calcium sensitive biosensor based on ISFET

N.Zine[1], J. Bausells[1], I. A. Marques de Oliveira[2], J.Samitier[2] and A. Errachid[2]

[1]Centre Nacional de Microelectrònica (IMB-CSIC), Campus U.A.B., 08193 Bellaterra, Barcelona, Spain

[2]Centre de Bioelectrònica i Nanobiociencia - Parc Científic de Barcelona, c/ Josep Samitier 1-5, 08028 Barcelona, Spain
email: aerrachid@pcb.ub.es http://www.pcb.ub.es

Summary:
Calcium-selective CHEMFET devices based on plasticized membranes have been developed. The Diethyl N,N'-[(4R,5R)-4,5-dimethyl-1,8-dioxo-3,6-dioxaoctamethylene]bis(12-methylaminododecanoate) (calcium ionophore I (ETH 1001)) molecule has been used as the sensing. A new technique of treatment of surfaces has been used to increase the adherence between the gate of ISFET and the sensitive membrane. The designed sensors exhibit good linearity responses in the range 2-6,69 of pCa with a slope of 28,38 ± 1 mV decade^{-1}. These microdevices can be applied in the determination of the total calcium concentration in human blood serum.

Keywords: *Chemically modified field effect transistor (CHEMFET); Calcium; Functionalisation*
Category: *5 (Chemical Sensors)*

1 Introduction

The concentration of calcium ions in the blood is of great importance in a number of physiological functions, including the contractility of the heart, stability of the cardiac rhythm, neuromuscular transmission and blood coagulation. For the assessment of total calcium, atomic absorption spectrometry (AAS) and colorimetry predominate in daily use. However, AAS is rather complex for clinical environment and colorimetry necessitates an extended and involved sample treatment. Several components interfere with the colorimetry detection. Potentiometric sensors based on chemically modified field effect transistor (CHEMFET) [1-3] would offer an attractive alternative for the previously mentioned techniques, because these devices exhibit a fast response time, a low output impedance, small size and relatively high robustness.

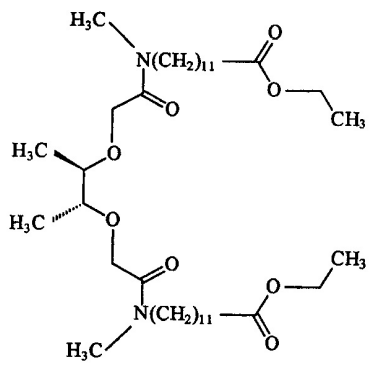

Fig.1: Calcium ionophore I (ETH 1001) [4]

In this work we study the behavior of Ca^{2+}-selective CHEMFET based on PVC plasticized membrane containing calcium ionophore I (ETH 1001) as cation-sensitive receptors (Fig.1).

2 Experimental

Membrane and CHEMFET preparation

ISFET

The ISFETs devices have been fabricated using a CMOS-compatible technology at Centro Nacional de Microelectrónica, Spain. The detailed manufacturing process has been described elsewhere [5]. The gate insulator of such devices is a combination of SiO_2 (800 Å) and Si_3N_4 (1000 Å). They were mounted on a specially designed printed circuit board, wire-bonded and encapsulated with an epoxy resin, leaving only the gate exposed to liquid solution. To improve the adherence of plasticized membrane, the ISFET gate in functionalised with a silane-based compound.

Process of the functionalisation

The method for functionalising the gate of the ISFET consists in mixing 95 % ethanol with 5% water. Later, this cocktail is adjusted to the pH 4.5-5.5 by means of the addition of acetic acid. The N-2-Animoethyl-3-aminopropylmethyldimethoxy-silane is added with stirring to yield a 2% final concentration. The ISFET devices are dipped into this solution, agitated gently, and removed after 2

minutes. Next, the excess silane is eliminated by dipping during 5 minutes in ethanol. Finally, the devices are cured to a temperature of 100 ºC during 8 minutes to eliminate the remains of the solvents.

CHEMFET preparation

The membranes have been prepared by dissolving the calcium ionophore I (ETH 1001) (Fluka, 10 wt%), 2-Nitrophenyl octyl ether (Fluka, 89 wt%) and Sodium tetraphenylborate (Fluka, 1 wt%) in tetrahydrofuran (THF, Merk). The membrane solution (approximately 4 µl) was deposited on the silalyted gate of FET using a transferpette. The introduction of such silane layer between a hydrophobic membrane and the gate nitride layer has the purpose to increase the adherence among Si_3N_4 and polymeric membrane. After membrane solvent evaporation the CHEMFETs were conditioned at least 24 hours in a 10^{-3} M $CaCl_2$ solution.

Results

Preliminary in vitro characterisation of the Ca^{2+}-CHEMFET has been performed by dipping this device in a solution having different concentrations of Ca^{2+}, together with a reference electrode using an HP4145B semiconductor parameter analyser. At the various pCa values, a series of single I_{ds}-V_{gs} ($G_m=\Delta Id_s/\Delta V_{gs}$) curves are registered as given in Fig.2. The shape of the curves is identical to a conventional MOSFET. It can be said that the Ca^{2+}-CHEMFET is still an electronic component which can be operated and used in a similar manner to the MOSFET.

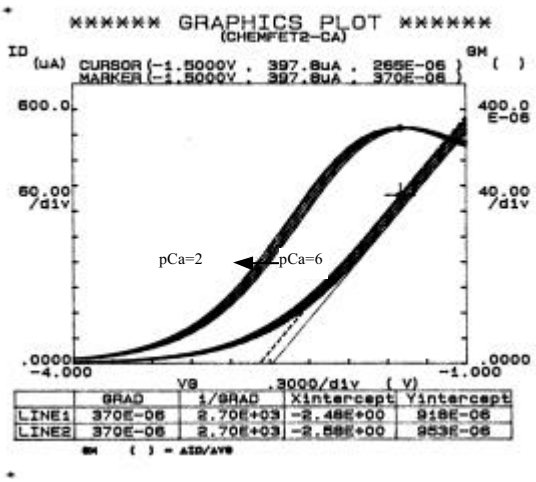

Fig.2: Electrical characteristics (drain current and transconductance as a function of gate-source voltage) of Ca^{2+}-CHEMFET in different concentrations (between pCa 2 and 6).

A sensitivity of 28,38 ± 1 mV decade^{-1} with a good linearity between pCa 2 and 6,69 has been obtained. The chemical characteristics on the Ca^{2+}-CHEMFET are comparable to the corresponding PVC-based microelectrodes devices [6-8], however, the detection limit of the microelectrodes are lower by about one order of magnitude.

In summary, the feasibility of fabricating a Ca^{2+}-CHEMFET using the N-2-Animoethyl-3-aminopropylmethyldimethoxysilane as a silanizing agent in order to increase the adherence between the gate of ISFET and the sensitive membrane has been demonstrated. Work will continue on studying the effect of pH and the interferences on the response of the devices before used in vivo.

Acknowledgements

This work has been supported by CICYT under projects TIC2001-3569-C02-01 and -02

References

[1] P. Bergveld, IEEE Trans. Biomed. Eng. 19 (1970) 70.

[2] S. D. Moss, J. Janata, C. C. Johnson, Anal. Chem. 47 (1975) 5.

[3] A. Errachid, A. Ivorra, J. Aguiló, R. Villa, N. Zine, J. Bausells, Sensors and Actuators B 78 (2001) 279.

[4] D. Ammann, R. Bissig, M. Guggi, E. Pretsch, W. Simon, I. J. Borowitz, L. Weiss, Helv. Clin. Acta, 58 (1975) 1535.

[5] C. carné, I. Gràcia, A. Merlos, M. Lozano, E. Lora-Tamayo, J. Esteve, Proc. Int. Conf. Solid-State Sensors and Actuators (transducers'91), San francisco, USA, 1991, pp. 225.

[6] P. Anker, W. Wieland, D. Ammann, R.E. Dohner, R. Asper, W. Simon, Anal chem. 53 (1981) 1970.

[7] F. Lanter, R. A. Steiner, D. D. Ammann, W. Simon, Anal. Chim. Acta 135 (1982) 51.

[8] P. Gehrig, B. Rusterholz, W. Simon, Chimia 43 (1989) 377.

Peculiarities of Response to CO of Pt/SnO_2:Sb Thin Films

O.V. Anisimov, N.K. Maksimova, N.G. Filonov, L.S. Khludkova, E.V. Chernikov

Siberian Physical Technical Institute, 634050, Tomsk, Russia, 1, Revolutsii
e-mail: Oleg73@mail2000.ru

Summary. *The gas-sensitive properties of carbon monoxide gas sensors based on thin (50 – 100 nm) tin oxide films have been reported. It was shown that temperature and gas concentration dependencies of sensitivity and response time have complicated shape. These peculiarities are caused by CO reaction with the different species of adsorbed oxygen on the surface of Pt/SnO_2:Sb thin films. The optimal operating temperatures (230 – 250 ^oC) providing fast response times and permitting to utilize sensors for measuring of gas concentrations in the range of 10 - 1000 ppm in air are determined.*

Keywords: *Gas sensors, tin oxide, thin films, CO, resistance*
Category: *5 (Chemical sensors)*

1 Introduction

In recently years SnO_2 thin films have been extensively investigated because of its applicability to an integrated gas sensor that has many advantages in terms of cost and reliability [1-4]. We studied gas-sensitive properties of tin oxide thin films with the additives in semiconductor volume and catalytic Pt on their surface in order to create reducing gas sensors [5,6]. In this study the research results of the sensitivity and response time of CO sensors in a wide range of temperatures and gas concentrations in air are reported.

2 Experimental

SnO_2 films with a thickness of 50 and 100 nm were prepared by cathode sputtering of the tin target with addition 1.5 at. % of antimony in oxygen-argon plasma. The films were deposited on Al_2O_3 substrates with a thickness of 150 μm. The contacts to tin oxide layer and a heater on a back side of a substrate were fabricated prior to the deposition of the semiconductor by a sputtering of platinum (Pt) with subsequent photolithographic processing. The area of a sensing element is 1 mm^2, whereas the area of all the sample - 1,5 mm^2. The superthin layers of catalytic platinum were received also by cathode deposition. After the sputtering process the films were annealed in an air for 24 h at 400 ^oC. The response is defined as relative variation of the electrical resistance at a given gas concentration level, that is (R_0/R_1 - 1), where R_0 is measured resistance of a sample in pure air, R_1 – resistance in CO-containing atmosphere. Response is measured in static conditions at introduction of air containing given gas concentration.

3 Results and discussion

The typical temperature dependencies of thin films resistance in pure air (curve 1) and response to exposure of 160 ppm CO mixture with air (curve 2) are shown in Fig. 1.

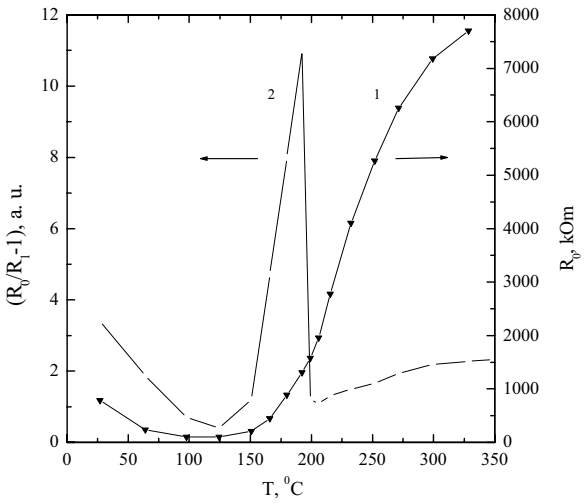

Fig.1. Resistance (curve 1) and response (curve 2) to 160 ppm CO of Pt/SnO_2:Sb thin films as function of operating temperature.

As one can see, at heating from room temperature up to 150-180 ^oC, the resistance is decreased due to ionization of shallow and deep impurity centers in part of a film, not depletion by charge carriers. At temperatures above 150-180 ^oC, there is a growth of resistance, which is resulted to surface transformations providing increase of a negative charge and depletion layer thickness : at 160 ^oC the transitions $O_2^- \rightarrow O^-$ are possible; at 230-300 ^oC - transitions $O^- \rightarrow O^{2-}$; at 250-400 ^oC there is a desorption of water [4]. At room temperatures the high response occurs (curve 2), that reduced at heating up to 100 - 120 ^oC. Apparently at these temperatures, there is a CO interaction with OH^--groups, which usually present on a surface of the semiconductor. The further increase of temperature is accompanied by sharp increase of response reaching maximum at 160-200 ^oC. Then the response again is

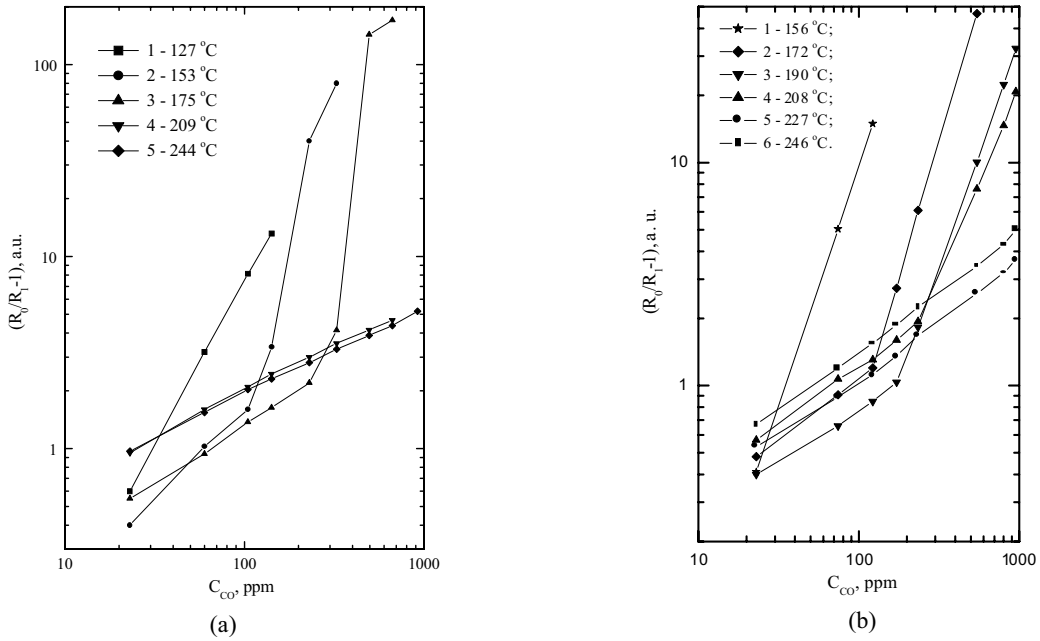

Fig. 2. Gas-sensing response as function of the CO concentration, for various thickness of Pt/SnO_2:Sb thin films: (a) 50 nm; (b) 100 nm.

reduced and other maximum takes place at 300-350 °C.

The concentration dependencies of response for Pt/SnO_2:Sb thin films by thickness 50 and 100 nm, measured at different temperatures, are demonstrated in Fig. 2a and 2b, respectively. The curves are built in a logarithmic scale, as it is known [4], that the relations have power character: $(R_0/R_1 - 1) = \alpha C_{CO}^m$, where the value of power low exponent $0 < m < 1$. It can be observed that in the temperature range of lower 200 -220 °C, the anomalies occurred: on curve 1-3 (Fig. 2a) and 1-4 (Fig. 2b) there are segments of sharp growth of response ($m > 1$) as increase of CO concentration in air. These features can be partially due to active participation of molecular oxygen O_2^- in oxidizing reaction of carbon monoxide. It is known that this reaction rate constant is decade two lower than that with atomic oxygen O^- [7].

It is probably, that in the high gas concentration range shortage atomic oxygen take place, O_2^-groups reacts with CO-molecules, and therefore sensitivity and response time are increased. The difference in thickness of researched structures (Fig. 2a and 2b) has an effect only for an absolute value of response, as the sensitivity of sensors is determined by a ratio between depletion layer width and thickness of film.

At temperatures above 200 °C, power law concentration dependencies of response are observed (Fig. 2a, curves 4-5 and Fig. 2b, curves 5-6), and parameter $m = 0.5$ is in some agreement with the literary data for detecting CO in air at 250-350 °C [4,5].

The response time does not depend on gas concentration and is equal 30 - 40 s, that corresponds to saturation time of gas concentration in the chamber. It is possible to assume, that in the temperature range above 200 – 220 °C, O^- and O_2^- balance on SnO_2 surface sharply varies, and reaction CO takes place with O^- exclusively.

That fact is interesting, that at realization of similar researches on interaction of tin oxide thin films with hydrogen, the concentration dependencies have a usual view with value $m < 1$.

These results indicates, that at operating temperatures 230 – 250 °C CO sensors based on thin oxide thin films have high sensitivity and fast response time and will be used for measuring gas concentration of 10 to 1000 ppm.

References

[1] D.E. Williams, *Sensors and Actuators B* 57 (1999) 1-16.

[2] C.-H. Shim, D.-S. Lee, S.-I. Hwang et al., *Sensors and Actuators B* 81 (2002) 176-181.

[3] M. Ivanovskaya, P. Bogdanov, G. Faglia et al., *Sensors and Actuators B* 77 (2001) 268-274

[4] I.A. Myasnikov, V.Ya. Sukharev, L.Yu. Kupriyanov. Semiconductor sensors in physic-chemical researches. *Moskow, Nauka.* 1991. 327 p.

[5] N.K. Maksimova, Yu.G. Katayev, E.V. Chernikov, *Journal of physical chemistry* 71 (8) (1997) 1492-1496 (in Russian).

[6] N.K. Maksimova, O.V. Anisimov, N.G. Filonov, L.S. Khludkova, E.V. Chernikov. *Proc. Int. Conf. on Thin Films and Layers Structures,* pp.153-155, Moscow, 26 - 30 November, 2002.

[7] V. Lantto, P. Romppainen, *Surface Sci.* 192 (1987) 243-264.

Small-size Thermoelectric Hydrogen Sensor based on Ni-induced Crystallized SiGe Film

Fabin Qiu[1, 2], Woosuck Shin[1], Masahiko Matsumiya[1], Noriya Izu[1], Norimitsu Murayama[1]

[1]Synergy Materials Research Center, National Institute of Advanced Industrial Science and Technology (AIST), Shimo-Shidami, Moriyama-ku, Nagoya, 463-8560, JAPAN
email: fabin-qiu@aist.go.jp http://www.unit.aist.go.jp/synergy/
[2]Department of Electronic Science and Technology, College of Electronic Science and Engineering, Jilin University, Changchun, 130023, P. R. China

Summary: *A small-size thermoelectric hydrogen sensor was prepared with the combination of thermoelectric effect of SiGe film and Pt catalyst reaction to hydrogen. Amorphous SiGe film was deposited by RF-sputtering method and transparent glass substrate was used for the convenience of aligning different patterns in the preparation of the small-size hydrogen sensor. SiGe film was crystallized with the Ni-induced effect at the glass-endurable temperature. The sensitivity to 3% H_2 at the operating temperature of 100 ℃ is 0.7 mV, and the detectable concentration is from 0.1% to 5%.*

Keyword: *thermoelectric effect, hydrogen sensor, glass substrate, Ni-induced SiGe film*
Category: *5 (Chemical Sensors)*

1 Introduction

Thermoelectric effect is one of highly reliable working principles. With the working mechanism, McAleer has fabricated the first thermoelectric hydrogen sensor with the basis of thermoelectric effect of SnO_2 bulk and hydrogen-catalyzing effect of Pt film [1]. During recent years, hydrogen sensors with normal-size based on thermoelectric effect of screen-printed Li, Na-doped NiO thick film or sputtered SiGe film was also successfully demonstrated by our research group [2, 3]. The successful application of SiGe film in the thermoelectric hydrogen sensor provided a good basis for the development of a new type micro-structured sensing element due to its simple structure and its high compatibility with lithography transfer technology. As the catalyst area was closely related to the heat generated by the hydrogen-oxidation reaction and in turn determined the available temperature difference in a certain extent, the performance of the sensing element with a small size become concerned before taking it into microfabrication development.

In this paper, a small-size thermoelectric hydrogen sensor was fabricated by using low-temperature crystallized SiGe film as thermoelectric material. The crystallization condition of the SiGe film with the Ni-induced effect and the hydrogen-sensing properties of the sensing element were investigated.

2 Experimental

For the fabrication of the sensing element, 3 μm thick SiGe film with L pattern was first sputtered on a glass substrate (corning 7059 sheet, 10mm × 10mm). The length of the pattern is 5 mm, and its width is 0.8 mm. Due to the amorphous state of the as-deposited SiGe film, a 30 nm-thick Ni-film was sputtered on the SiGe film so that it could be crystallized at a glass-endurable sintering temperature with the metal-induced effect. Transparent glass substrate was utilized for the convenience of aligning different patterns and simplifying the element fabricating process.

With the formation of crystallized thermoelectric SiGe film, a RF-sputtered Pt heater with thickness of 1 μm were formed on glass substrate by using a 50 nm thick Ti adhesion layer. And then a pair of Au electrodes connecting with the two end-sides of SiGe film for the measurement of sensing output voltage signal and the catalyst Pt film were in sequence sputtered. The deposition of different layers of SiGe film, Pt catalyst and Au connecting electrodes were conducted with the aids of metal-mask. The measurement of hydrogen-sensing properties were carried out in a gas flowing system, and an IR camera included in the measuring system was utilized to record the surface temperature variation for the evaluation of catalyst activity. The operating temperature of the sensing element is varied from 80 to 120 ℃.

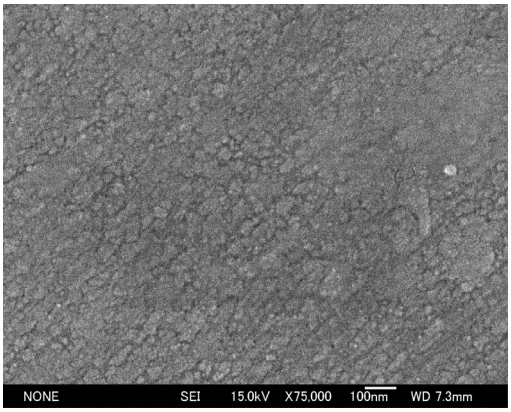

Fig.1 FE-SEM morphology of SiGe film

3. Results and discussion

XRD results indicated that the Ni-induced SiGe film could be crystallized when the sintering temperature was above 520 ℃. FE-SEM observation as demonstrated in Fig.1 shows that the grain size of the SiGe film sintered at 550 ℃ was about 70 nm.

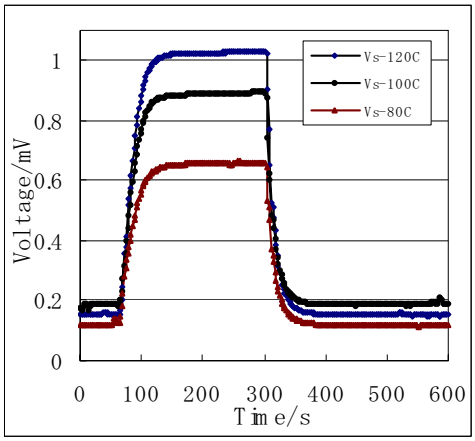

Fig.2 Hydrogen sensing properties for 3% H_2

The crystallization of thermoelectric SiGe film is essential for the enhancement of its thermoelectric properties, which was proved by the measurement of normal-size sensing element in our previous work [2, 3]. Due to the decrease of the mass of the present small size element, a high catalyst activity with a temperature increase of 60 ℃ at the catalyst side was observed. At the operating temperature of 100 ℃, the sensitivity related to 3% hydrogen was about 0.7 mV as shown in Fig.2. The detectable hydrogen concentration for the hydrogen-sensing element is from 0.1% to 5%. The response and recover time corresponding to 90% voltage change were all less than 50s. Based on the measured temperature difference between the two end-sides of the SiGe film and its output voltage signal corresponding to the element being exposed in hydrogen-contained atmosphere, the calculated Seebeck coefficient is about 140 μV/K.

The results obtained in this work indicated that the catalyst activity is much related to the mass which sharing the heat generated by the exothermic catalyst reaction. And the heat transfer from the hot side to the cold side has produced serious influence on the sensing properties. Its improvement could be expected by micro-fabricating the sensing element to optimize the sensor structure with the utilization of lithography transfer technology.

References

1. J. F. McAleer, P. t. Moseley, P. Bourke, J. O. W. Norris and R. Stephan, Sens. Actu. B 8 (1985) 251-257.
2. W. Shin, M. Matsumiya, F. Qiu, N. Izu and N. Murayama, J. Ceram. Soc. Jap. 110 (2002) 995-998.
3. F. Qiu, W. Shin, M. Matsumiya, N. Izu, N. Murayama, Jap. J. Appl. Phys. in press

SOI Gas Sensors with Low Temperature CVD films

J. W. Gardner[1], J. A. Covington[1], G. Shaw[2], I. P. Parkin[2] and F. Udrea[3]

[1]University of Warwick, School of Engineering, Coventry CV4 7AL, UK
e-mail: j.w.gardner@warwick.ac.uk; http://www.eng.warwick.ac.uk/SRL
[2]University College London, [2]Dept. of Chemistry, London WC1H 0AJ, UK
[3]University of Cambridge, Depart. of Engineering, Cambridge CB3 2PZ, UK.

Summary: *A novel gas sensor has been designed and fabricated using SOI technology. The device comprises of a thin SOI membrane in which has been embedded an FET heater. The device can operate up to a maximum temperature of ca. 350°C with a typical power consumption of 40 to 70 mW. Here we report upon a novel process that has been developed to deposit thin films of both vanadium and tungsten oxide at temperatures compatible with CMOS technology for use in resistive or FET based sensors. The CVD films are characterized and their response to CO and toluene investigated.*

Keywords: *SOI sensors, gas sensors, CVD films*
Category: *5 (Chemical sensors)*

1 Introduction

In the last two decades, there has been increasing demand for mobile, hand-held gas monitors with wide application in the environmental, automotive and medical industries. Presently, solid-state gas sensors tend to suffer from high power consumption (*ca*. 1 W) - especially for metal-oxide resistive gas sensors that require very high temperatures (e.g. 300 °C or more) [1]. In addition these sensors cannot detect accurately low levels (e.g. < 100 PPM) of some important hazardous gases. This makes them an impractical option for application in battery-operated units and less than ideal for automotive units. To overcome these disadvantages, we proposed and patented [2] a novel design of gas microsensors compatible with current CMOS technology, and have developed the concept within this joint EPSRC project. Our goal here is to combine an SOI CMOS resistive (or FET) gas sensor developed at the Universities of Warwick and Cambridge with a novel low-temperature post-CMOS chemical vapour deposition (CVD) process developed at University College London (UCL).

2 SOI Gas Sensors

Fig 1 illustrates the basic structure of the SOI CMOS gas sensor. In place of a passive resistive heater (e.g. platinum or polysilicon), an active *n*-channel MOSFET is used.

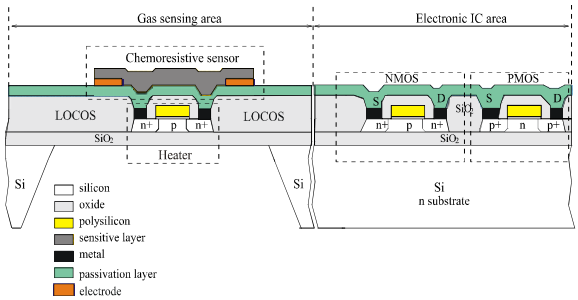

Fig. 1. Design of a smart SOI gas sensor employing an *n*-channel MOSFET heater (resistive type).

The MOSFET is ideal as a micro-heater because its power and hence its operating temperature, can be easily controlled via its gate potential. The MOSFET has a negative temperature coefficient (the current decreases at high temperatures due to reduced channel mobility) thus offering a good thermal stability. The SOI membrane and LOCOS provide vertical and lateral isolation respectively. Metal electrodes are placed above the micro-heater to form the resistor and isolated from it through subsequent IDLs (inter dielectric layers). In the FET sensor case the FET micro-heater surrounds the sensing element, with the gate oxide exposed through the IDLs.

The SOI device has been fabricated at SUMC (UK) and the resistive version is illustrated in Fig 2. The handle silicon was removed using either an isotropic dry deep RIE process or an anisotropic wet etch to leave a thin SOI membrane, shown in figure 3. The complete membrane comprises of a thin silicon layer together with an oxide/nitride passivation layers; the overall thickness being between 1 - 2 μm.

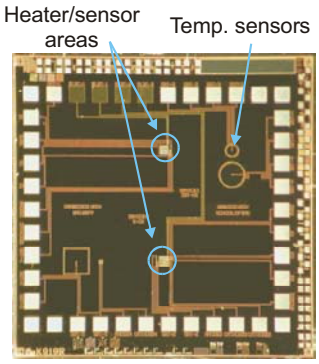

Fig. 2. Photograph SOI resistive gas sensing device and off-membrane temp sensors (5 mm by 5 mm)

The DC power consumption of the SOI devices has been measured and compared with other SOI devices fabricated via Europractice using a 0.8 μm MATRA process. The power consumption depends

upon the thickness of the SOI membrane; measured values range from 40 to 140 mW at 300 °C.

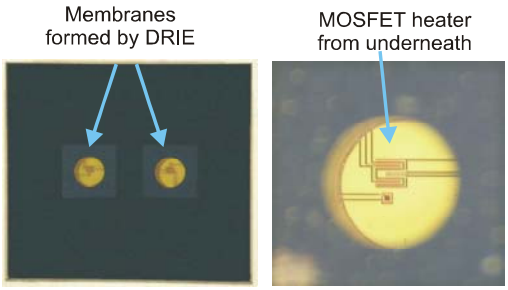

Fig. 3 Photograph of SOI MOSFET heater inside a thin translucent SOI membrane (DRIE process)

3 Thin Film Deposition

UCL have established reaction conditions for atmospheric pressure (AP) or aerosol assisted (AA) CVD that are attractive for large scale, rapid production of a variety of widely adopted gas sensing metal oxides (e.g. V_2O_5, WO_3, SnO_2) [3,4]. In addition, materials have been deposited *via* APCVD that are expected to exhibit interesting sensing and/or optical properties (e.g. VO_2, $Ti_{1-x}M_xO_2$ (M = W, Nb, V, Cr, N, Mo)). In each case, deposition using a cold-wall horizontal bed reactor was possible at 400 °C (in some cases as low as 350 °C), temperatures well below the melting point of aluminum. In general, the films showed good, uniform coverage across the substrate with high deposition rates (assessed by cross-sectional SEM to be *ca.* 0.5-1.0 μm/min).

We summarize here the results for the deposition of V_2O_5 (*via* APCVD) and WO_3 (*via* AACVD). Reaction of VCl_4 or $VOCl_3$ with water under APCVD conditions at 350-400 °C produced uniform, clear yellow films. Film characterization by glancing angle X-ray diffraction (XRD) showed only the *orthorhombic* phase of V_2O_5 (indexed unit cell dimensions a = 11.527(5), b = 4.382(5), c = 3.557(5) Å lie within ± 0.005 Å of literature). Depth profile studies of the film surface using X-ray photoelectron spectroscopy (XPS) showed the presence of vanadium and oxygen only (beyond the first few atomic layers). The binding energies recorded are in excellent agreement with literature (516.0 eV for V $2p_{3/2}$ and 530.5 eV for O 1s) and show a notable absence of chlorine contamination as well the presence of only one vanadium species (V^{5+}) residing in a single chemical environment. XRD/XPS analyses therefore suggest the direct, single step deposition of a single (orthorhombic) phase of V_2O_5. This is confirmed by Raman spectroscopy, which shows identical patterns to bulk and magnetron spluttered V_2O_5 (with bands at 697, 524, 478, 401, 300, 283, 194, 145 and 103 cm^{-1}). SEM showed the films to be comprised of sub-micron platelets, suggesting film growth proceeds from the substrate surface and *via* an 'island growth' mechanism. AACVD has been used successfully to deposit thin, uniform blue films at substrate temperatures of 300-400°C from the decomposition of a single source precursor tungsten hexa-phenoxide, $W(OPh)_6$ (see Figure 4). Characterization by XPS shows the films to be a single phase of WO_{3-x}, with the results being in excellent agreement (± 0.05 eV) with literature. Species present: $\mathbf{W^{6+}}$ $4f_{7/2}$ = 35.6 eV; W^{6+} $4f_{5/2}$ = 37.8 eV; **O** 1s = 530.0 eV; W 4f doublet shoulder at lower energies assigned to $\mathbf{W^{4+/5+}}$ cations). Carbon contamination was assessed to be low, at *ca.* 2 %, by XPS. Post-annealing the films in O_2 at temperatures ≥ 400 °C afforded pale yellow films within 30 min, characterized by XPS as WO_3 (i.e. **no** $\mathbf{W^{4+/5+}}$ cations present) with minimal carbon content (< 0.5 %).

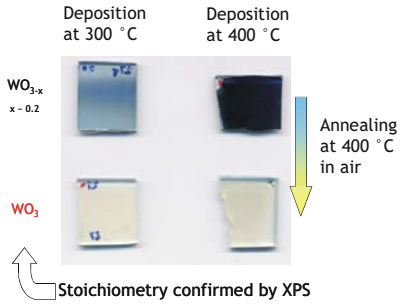

Fig. 4 Photograph of CVD films on glass substrate

Further characterization of film stoichiometry before and after annealing was carried out by XRD and Raman for films deposited at 300 & 400 °C. Raman spectroscopy shows bands of amorphous WO_{3-x} for deposition at 300 °C. At 400 °C a more crystalline film forms, with the WO_{3-x} spectrum dominated by *additional* bands that coincide with monoclinic γ-WO_3. Upon annealing at 400 °C, Raman confirms the presence of fully oxidized, crystalline monoclinic γ-WO_3 with removal of the bands assigned to the reduced species.

3 Conclusions

A low-temperature CMOS compatible process has been developed in order to deposit thin films of vanadium and tungsten oxide on to thin SOI micro-hotplates. Allowing circuit integration with metal oxide sensing materials. The response of these novel resistance and FET gas sensors to CO and toluene is reported. The low power, high temperature operation will make these sensors ideal for a range of gas detection applications.

References

[1] E. Jones, "The pellistor catalytic gas sensor", in P.T. Moseley and B.C Tofield (eds), Solid State Gas Sensors, A. Hilger, Bristol, 1987.

[2] F. Udrea and J.W. Gardner, Smart MOSFET gas sensor, UK patent GB2321336A, 1996, and World patent WO98/32009.

[3] M. N. Field and I. P. Parkin, *J. Mater. Chem.*, 2000, **10**, 1863-1866.

[4] W. B. Cross and I. P. Parkin, *Abstr. Pap. Am. Chem. Soc.*, 222: 355-Inor Part 1, Aug 2001; W. B. Cross and I. P. Parkin, *Abstr. Pap. Am. Chem. Soc.*, 222: 363-Inor Part 1, Aug 2001.

Analytical Model for Chemocapacitors

R. Igreja and C. J. Dias

Dep. de Ciências de Materiais
CENIMAT, Fac. de Ciências e Tecnologia
Univ. Nova de Lisboa, 2829-516 Caparica, Portugal.
email: rui@dcm.fct.unl.pt

Summary: *The present interest on the use of chemocapacitors with planar electrodes draw us to the need for a better understanding of how its capacitance changes with the geometric parameters of the electrodes and the properties of the medium surrounding the electrodes. In this work we present a conformal mapping based model to find analytical expressions for the sensor capacitance. This model can be applied for any electrode width and spacing as well for any thickness of the sensitive layer. The capacitance for a particular sensor configuration is a function of the dielectric permittivity of the materials, the electrode length and two geometric adimensional parameters: the ratio between the electrode width and the spatial sensor wavelength and, the ratio between the thickness of the sensitive layer and the spatial sensor wavelength.*

Keywords: *Chemocapacitors, interdigital electrodes, e-nose.*
Category: *5 (Chemical sensors).*

1 Introduction

Typical Chemocapacitors are made of an inert substrate over which the two comb electrodes are deposited. One chemical sensitive layer (usually a polymer) is then deposited over the electrodes (see Fig. 1). Polymers have been used for organic vapor sensing because they exhibit rapid reversible vapor sorption and are easy to applied as thin or thick films by a variety of techniques [1]. The polymer layer can be chosen according to its affinity to a particular molecule or set of molecules one wishes to detect. If several sensors with different polymer layers are used to make a sensor array it is then possible to evaluate complex organic vapor samples [1]. These sensor arrays can be part of an electronic nose for a particular application depending on the sensitive layers that are chosen.

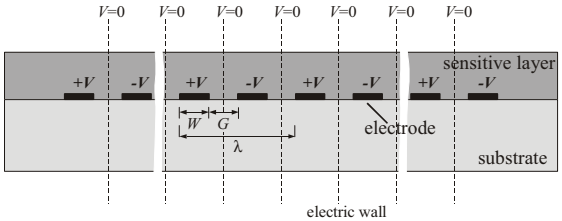

Fig. 1. Sensor cross-section.

The change in capacitance depends on the changes in the dielectric permittivity and on swelling of the polymer (sensitive) layer due to the ad/absorption of the analyte. The correct design of a Chemocapacitor requires closed form expressions for the computation of capacitance, based on the geometry of the electrodes and the properties of the substrate and chemical sensitive layer(s). These expressions enable the correct design of the sensor and they can be integrated into the chemical/physics of the analyte/polymer interactions to give an overall description of the sensor performance.

2 Modeling

The gaps between electrodes have a width of *G*while the fingers have a width of *W*. Each electrode is connected to a fixed potential (either $+V$ or $-V$) and has a number of fingers of length *L*. The sensor spatial wavelength is $\lambda = 2(W+G)$ and the sensitive layer as a thickness of *h*. For convenience two adimensional parameters are defined: (1) The metallization ratio $h = (2W)/\lambda$, and (2) the ratio between the sensitive layer thickness and the sensor spatial wavelength $r = h/\lambda$.

For symmetry reasons, the capacitance of one single semi-infinite layer can be evaluated as a function of (1) C_I - half the capacitance of one interior electrode relative to the ground and, (2) C_E - the capacitance of one outer electrode relative to the ground plane next to it (Fig. 2 shows an example for a sensor with six electrodes).

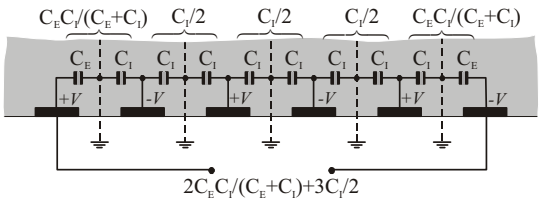

Fig. 2. Equivalent circuit for evaluation of the capacitance of a semi-infinite top layer.

Using network analysis to evaluate the equivalent circuit of Fig. 2 one can find the total capacitance between the negative and positive electrodes of a semi-infinite layer sensor to be equal to:

$$C = (N-3)\frac{C_{\mathrm{I}}}{2} + 2\frac{C_{\mathrm{I}}C_{\mathrm{E}}}{C_{\mathrm{I}}+C_{\mathrm{E}}},$$

provided that $N > 3$ where N are the number of electrodes. The capacitance for the lower half plane is calculated in the same way and adds to the capacitance calculated for the upper half plane to obtain the total capacitance of the sensor.

For the calculation of C_{I} and C_{E} we use conformal mapping techniques to map an appropriate space region of the sensor onto a parallel plate capacitor geometry (see Fig. 3) for which the capacitance value is known as well as the equipotential and electric field lines. Details of the conformal transformations were reported elsewhere [2].

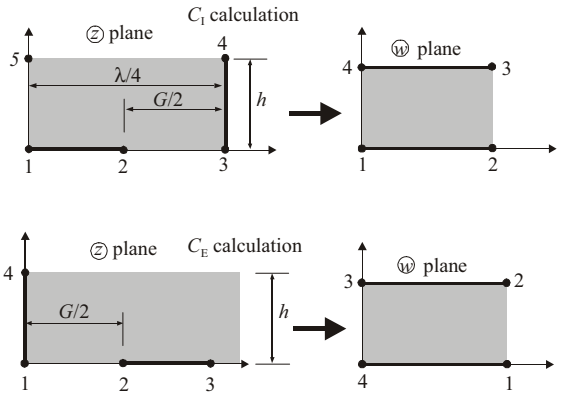

Fig. 3. Conformal tranformations on Argand plane for the calculation of C_{I} and C_{E}.

3 Results and Discussion

Figure 4 shows the dependence of the capacitance on the metallization ratio η (the simulation parameters are as written on graph).

In Fig. 5 is shown the capacitance of a sensor having a sensitive layer over the electrodes, as a function of the adimensionalized thickness r for the present model and with finite element methods (FEM) (the simulation parameters are written on graph). The capacitance reaches a saturation value for a value of r=0.5 (h=$\lambda/2$), which means that the sensor is not sensitive to changes in the permittivty occuring at a distance from the electrode plane greater than about half the sensor wavelength. The behavior of the capacitance value as evaluated by FEM is in agreement with our model, reaching the saturation [i.e. 99.5% of $C(h=\infty)$] for the same value of r.

To help the design of a particular sensor (fixing the sensor wavelength) one can make a contour plot for the capacitance density as a function of the parameters η and r (see Fig. 6).

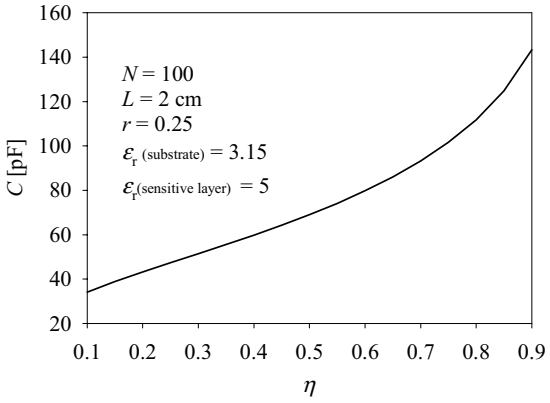

Fig. 4. Sensor capacitance as a function of the η.

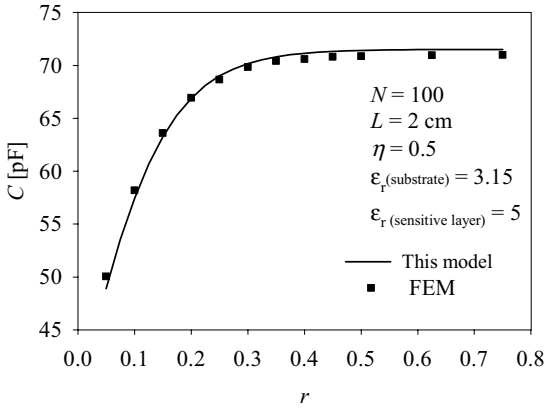

Fig. 5. Sensor capacitance as a function of r.

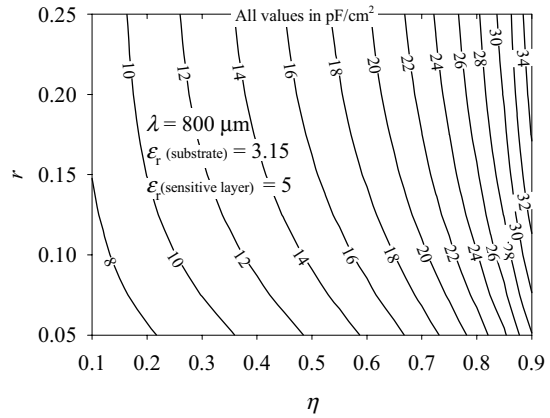

Fig. 6. Capacitance density as a function of η and r.

References

[1] J. W. Grate and G. C. Frye, *Sensors, update*, Edited by H. Baltes, W. Göpel and J. Hesse, vol. 2, chap. 2, John Wiley & Sons (1996).

[2] R. Igreja and C. J. Dias, *submited to the J. Appl. Phys.*

Optoelectronic Sensor for Chemical Sensing based on Syndiotactic Polystyrene Thin Film as Sensitive Layer

M.Giordano[1], M. Russo[1], A. Cusano[2] , G. V. Persiano[2], G. Mensitieri[3] and G. Guerra [4]

[1]Institute for Composite and Biomedical Materials , National Research Counceil, P. le Tecchio, 80, 80125 Napoli Italy email:gmichele@unina.it http://www.unina.it
[2]Engineering Department., University of Sannio, Corso Garibaldi 107, 82100 Benevento, Italy
e-mail: acusano@unisannio.it
[3] Materials and Production Engineering Department, University of Naples, P. le Tecchio, 80, 80125 Naples, Italy
[4] Chemistry Department, University of Salerno, 84081 Baronissi, Salerno,Italy

Summary: *In this work, the selective sorption property of sindyotactic polystyrene (SPS) in the nanoporous crystalline ? phase toward polluttants like chlorinated compounds and BTEX (benzene, toluene, ethylbenzene and xilene) has been used to develop an optoelectronic sensor based on fiber optic technology suitable for the monitoring of air and waters.*
In particular, a sensor probe has been made casting a thin SPS film in "delta" phase on the cleaved end of a standard fiber optic and reflectance measurements have been carried out to detect very low concentrations (ppm) of chloroform and toluene in water.

Keywords: *optoelectronic sensor, syndiotactic polystyrene, clathtrate, fiber optic*
Category: *Chemical sensors*

1 Introduction

A long standing challenge in the field of the chemical detection is the development of environmental microsensors higly selective to target chemicals. The combination of suitable sensitive materials and sensing techniques are the key points for the designing of microsensors based detectors. To this aim, attention has been focused on the use of polymeric materials as selective layers[1]. In particular, the sorbent polymers special tendency to collect and concentrate analytes molecules make them reliable materials to be employed in the microsensors designing

As sensing mechanism, an optoelectronic approach based on the use of fiber optic technology has been developed. This choice seems to be suitable in light of unrivaled advanatages associated to this class of sensors such as immunity to electromagnetic intereference, the dual functionalities related to their capability to serve as transducers and sensing data transportation systems.

In particular, thin film of "delta" phase syndiotactic polystyrene was cast upon the tip of a standard silica optical fiber. Reflectance measurements directly related to refractive index change have been, then, carried out to detect very small amounts of chemicals, in water concentrations of few ppm.

2 SPS in "Delta" chrystalline phase as sorption selective material.

Among the possible crystalline structures that SPS can form (for instance two forms, alfa e beta consisting in planar zig-zag chains and two others and gamma and delta consisting of s(2/1)2 TTGG helical chains)[2] special attention must be addressed to the "delta" phase that forms only when solvent are used. This is due to the fact that in this structure SPS can clathrate solvent molecules housing them between the helical chains. When suitable solvent treatment are imposed the removal of the guest molecules can be obtained. This results in the formation of a metastabile nanoporous structure able to absorb molecules of feasible size and shape, even present at very low activities, while the absorbing property in the other crystalline forms and in the amorphous phase is present at much lower extent. Thus allowing SPS in "delta" phase to be successfully used as polymeric coating for chemical sensing.

3. Experimentals

The sensor probe was prepared by stripping the fiber optic protection coating few centimeters from the fiber end and washing the nude part in chloroform in order to remove any residual of coating. Then the fiber was cleaved with a precision cleaver to obtain a uniform and plane cross section.
Following the cleaved fiber tip was dipped into a SPS chloroform solution (1%b.w.) and the clathrate

thus formed was finally exposed to acetone vapors in order to extract chloroform and obtain an empty delta chrystalline SPS layer.

Pellet-type of SPS was kindly supplied by Institute G. Donegani (inglese)" of Enichem .

Reflectance measurements have been performed by ligthing the sensing fiber with a broadband light source, to this aim a superluminescent diode (40nm bandwidth) operating at 1310nm has been used (fig. 1). A 2x2 in fiber coupler provides the necessary connections between light source, sensing interface and two receiving channel: one for reflected signal detection and the other one for power monitoring in order to obtain well compensated intensity measurements. To enhance system performances, sinchronous detection has been implemented. Here the light source has been externally amplitude modulated at 500Hz and the sensor outputs have been retrieved by using a dual channel lock in amplifier. Normalization procedure consists in taking the ratio between reflected signal and power monitoring one, in this hypotesis, normalization output is directly related to interface reflectance that in turn depends on polymer refractive index, thickness and external medium (air or water) refractive index[3].

Experimental measurements consisted in recording the change in the normalized sensor output as the sorption of the hazards in the nanocavities alters the polymer layer refractive index. The SPS sorption tendency toward chloroform and toluene in water was tested on the same sensor probe in two different successive solutions once ensured the reversibility of the probe.

Measurements were made immerging the SPS coated probe into a thermostated becker, (25°C) containing first pure distilled water. By successive additions of chloroform and toluene solution concentrations enriched of 5ppm per addition were obtained. Solutions were always magnetically stirred in order to ensure the maximum dispersion of the hazards in water.

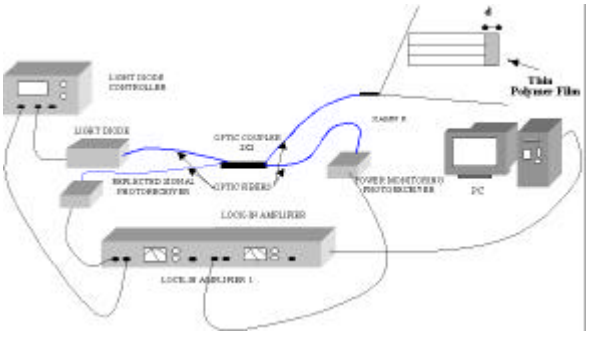

Fig. 1 Optoelectronic Set-up

3. Results and Discussion

Response of fiber optic sensor to sequential step changes of concentration (step changes of 5 ppm each) of chloroform and toluene in aqueous solution, are reported in figure 2. The different kinetics is related to the different mass transport behavior of the two substances in SPS: apparently sorption kinetics is faster for chloroform. This results in an overall increase of the signal in the order of 3.2 and 4.4 % for chloroform and toluene respectively, for a total concentration equal to 15 ppm. The behavior of the chloroform sorption curve shows a clearly visible progressive diminution of the equilibrium step response to each 5 ppm increment of concentration. For toluene the decrease in sensititvity is less pronounced. Such a behavior can be ascribed to the progressive saturation of the crystalline nano-cavities of SPS and/or to the thermodynamic of the water-solvent mixture. In fact, concentration could be misleading and it would be more appropriate to refer to solvent activity of the mixture.

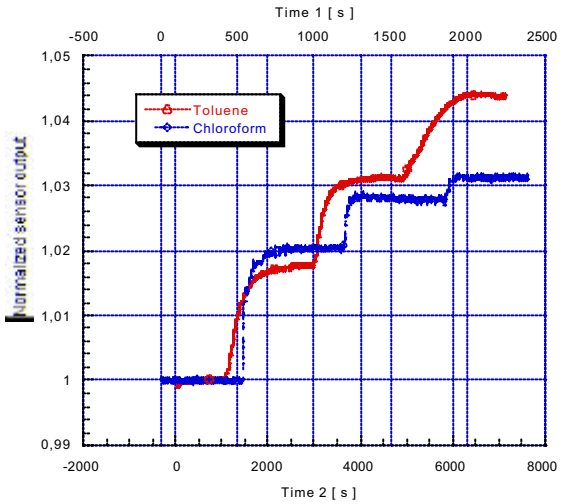

Fig. 2. Sorption curves of choroform and toluene. Each step corresponding to a 5ppm enhancing of the solute concentration in water.

References

[1] J. W. Grate and M. H. Abraham *Sensors and actuator B, 3* (1991) 85–111.

[2] G. Guerra, V. M. Vitagliano , C. De Rosa and P. Corradini *Macromolecules 23 (1990) 1539*

[3] A. Cusano, M. Giordano, L. Nicolais, J. Nasser, G. V. Persiano, M. Russo, "Optoelectronic Refractive index Measurements: Application to Polymer Smart Processing" *IEEE Sensors Conference (2002)* pp. 131-135

The performance of CO_2 and SO_x electrochemical gas sensors based on Y-ZrO_2 and $Na_3Zr_2Si_2PO_{12}$ (Nasicon) solid electrolytes

P. Pasierb, S. Komornicki, S. Koziński, R. Gajerski and M. Rękas

University of Mining and Metallurgy, Faculty of Materials Science and Ceramics,
al. Mickiewicza 30, 30-059 Kraków, POLAND
email: ppasierb@uci.agh.edu.pl http://www.agh.edu.pl

Summary: *Solid-state potentiometric CO_2 and SO_x sensors were fabricated using Nasicon ($Na_3Zr_2Si_2PO_{12}$) or ZrO_2:Y_2O_3 (8 mole% of Y_2O_3) as solid electrolytes, fused carbonates or sulphates as sensing electrodes and $Na_2Ti_6O_{13}$-$Na_2Ti_3O_7$ two phase system or porous platinum as reference electrodes. The influence of solid electrolyte on performance and long-term stability of sensors was determined. The CO_2 sensors with Nasicon as a solid electrolyte exhibited stable signal during long-term experiments. However, the unstable behaviour was observed in case of the SO_x sensors. This long-term instability of investigated cells is discussed in terms of possible reactivity of solid electrolytes with electrode materials.*

Keywords: *electrochemical gas sensors; CO_2; SO_x; Nasicon; stabilised ZrO_2; carbonates; sulphates*
Category: *5 (Chemical sensors)*

1 Introduction

The solid-state potentiometric gas sensors for the detection and monitoring gases emitted during combustion processes are the most promising ones. The simplicity of construction, low cost during serial production, compatibility with classical electronic devices, short response time, good selectivity and known dependence of measured signal on gas content (Nerstian behavior) are the best recommendation. The main disadvantage of the proposed electrochemical sensors for CO_2 or SO_x monitoring is the signal instability during the long-term use. Numbers of works have been done to propose the best systems exhibiting the stable behavior. Also, many papers concerned the theoretical aspects of working mechanism of investigated cells. Different solid electrolytes, sensing and reference electrodes were proposed and tested to the large extend [1-4].

The aim of this work was to compare the performance and working mechanism of potentiometric gas sensors prepared using two solid electrolytes: Na^+ ion conductor (Nasicon) and O^{2-} ion conductor (ZrO_2:Y_2O_3). The comparison was made for sensors designed for detection of CO_2 or SO_x.

2 Materials and measurements

Powders of ZrO_2:Y_2O_3 (8mole% of Y_2O_3, Tosoh Corp.) and sol-gel prepared [5] $Na_3Zr_2Si_2PO_{12}$ (Nasicon) materials were used. Powders were formed in pellet die (75 MPa), isostatically pressed (250 MPa) and sintered at 1673 K (5 h) in case of ZrO_2 and 1500 K (24 h) in case of Nasicon.

Both Li_2CO_3-$BaCO_3$ and Li_2SO_4-$CaSO_4$ (2:3 molar ratio) were used to form the electrodes sensitive to CO_2 and SO_x, respectively. Porous platinum or $Na_2Ti_6O_{13}$-$Na_2Ti_3O_7$ mixtures were used in construction of reference electrodes. $Na_2Ti_6O_{13}$ -$Na_2Ti_3O_7$ materials were prepared by solid-state reaction of TiO_2 (anatase, Cookson Technology) with sodium carbonate (Sigma-Aldrich). The details are given in [6].

The electromotive force (*EMF*) of prepared cells was measured as a function of temperature (300-500 ^oC), CO_2 (10-1260 Pa) or SO_2 (0.1-10 Pa) partial pressures and time. The details concerning the experimental setup are given in [7].

Additionally, XRD (X-ray diffraction), DTA & TG (Differential Thermal Analysis and Thermo-gravimetry), SEM (Scanning Electron Microscopy) and MS (Mass Spectrometry) techniques were used to assist the interpretation of obtained results.

3 Results and Discussion

3.1 CO_2 sensing characteristics

The CO_2 sensor has the following electrochemical cell structure:

$$CO_2, O_2^{(1)}, Ag| Li_2CO_3\text{-}BaCO_3| SE | B(Na), Pt, O_2^{(2)}$$

where SE is a solid electrolyte, B(Na) denotes $Na_2Ti_6O_{13}$ - $Na_2Ti_3O_7$ mixtures (used when Nasicon was as SE). Superscripts (1) and (2) denote sensing and reference electrodes, respectively.

The obtained results were fitted using Nernst equation. The determined parameter *n* (corresponding to the number of electrons in electrode reaction) was found to be between 2.2 and 2.8. The observed discrepancy of the parameter n from theoretical value

(n=2) may be explained by mixed conductivity either of sensing carbonates or electrolyte phases [7,8].

Short time experiments have indicated that the performance of sensors based on ZrO_2 and Nasicon as a solid electrolyte was comparable. For example, the determined response times ($t_{0.95}$) were below 60 s in case of both types of cells.

3.2 SOx sensing characteristics

The SO_x sensors were prepared analogously as in the case of CO_2 sensors. The following electrochemical cells were prepared:

$SO_x, O_2^{(1)}$, Me, Li_2SO_4-$CaSO_4$| SE | B(Na), Pt, $O_2^{(2)}$

where SE is solid electrolyte, Me denotes Ag, Au or Pt, B(Na) denotes $Na_2Ti_6O_{13}$ - $Na_2Ti_3O_7$ mixtures (used when Nasicon was SE).

It was found that in case of cells with silver (Me=Ag) no acceptable sensor characteristics was obtained. The observed *EMF* changes with the changes of SO_x partial pressure were not reversible, and most probably caused by SO_x gas corrosion of silver.

The replacement of Ag by Au was also unsuccessful, and typical sensor characteristic was not observed. Only use Pt at sensing electrode led to stable sensor characteristics. The Mass Spectroscopy indirect measurements has confirmed that used Pt connection catalyses completely oxidation of SO_2 into SO_3 above 673 K. The obtained results well correspond to thermodynamic data for the system SO_2+O_2.

Fitting obtained data of *EFM* to Nernst equation allowed determining the *n* parameter values. They were found to be above the theoretical value of 2, as in the case of CO_2 sensors.

The response time of investigated SO_x sensors was longer than in case of CO_2 sensors ($t_{0.95}$ = several minutes).

3.3 Sensors stability

The CO_2 sensors with Nasicon as the solid electrolyte showed stable behavior for long-time (above 6 months). On the other hand long-term drift of the sensing signal was observed for CO_2 sensors with stabilised zirconia as the solid electrolyte. Both thermodynamic considerations as well as DTA, XRD and SEM analysis indicate that observed instability may result from the chemical reaction between carbonate and stabilised ZrO_2 phases.

In case of both types of SO_x sensors a long-term drift of electromotive force was detected during the experiments carried out for several weeks.

The observed drift cannot be explained by the uncontrolled chemical reaction in solid state phase, as in the case of ZrO_2 based CO_2 sensors. The performed thermodynamic analysis excluded possibility of reaction of used sulphate phase with the solid electrolyte. So, further studies are necessary in order to explain observed instability of SO_x sensors.

4 Conclusions

The experimental results concerning potentiometric CO_2 and SO_x sensors have been described in this work. Most of the sensors exhibited reproducible signal during short-time experiments (<24 h). The measured electromotive force (*EMF*) of the investigated cells was found to be linear with the logarithms of CO_2 and SO_x concentration in the measured ranges of concentration (100-12600 ppm of CO_2 and 1-100 ppm of SO_x). The sensors exhibited quasi-Nernstian behavior, with the *n* parameter value higher than theoretical value (n=2). The operating temperature range was 300 ^oC - 500 ^oC and 500-550 ^oC for CO_2 and SO_x sensors, respectively. The response time was found to be below 60 s and several minutes for CO_2 and SO_x, respectively.

References

[1] M. Gauthier and A. Chamberland, *J. Electrochem. Soc.* 124 (1977) 1579-1583.

[2] T. Maruyama, Y. Saito, Y. Matsumoto and Y. Yano, *Solid State Ionics* 17 (1985) 281-286.

[3] N. Miura, S. Yao, Y. Shimizu and N. Yamazoe, *J. Electrochem. Soc.* 139 (1992) 1384-1388.

[4] M. Holzinger, J. Maier and W. Sitte, *Solid State Ionics* 86-88 (1996) 1055-1062.

[5] J.P. Boilot, J.P. Salanie, G. Desplanches and D. Le Potier, *Mat. Res. Bull.* 14 (1979) 1469-1479.

[6] P.Pasierb, S.Komornicki, R.Gajerski, S.Koziński, P. Tomczyk and M. Rękas, *J.Electroceramics*, 8 (1) (2002) 57-64.

[7] P.Pasierb, S. Komornicki, R. Gajerski, S.Koziński and M. Rękas, *Solid State Ionics* 157 (2003) 357-363.

[8] H. Näfe, *Sensors & Actuators* B21 (1994) 79-82.

Acknowledgments

The financial support of Polish State Committee for Scientific Research (KBN), Project No. 7 T08A 030 21 is acknowledged.

Fast Identification of Gas Mixtures Through the Processing of Transient Responses of an Electronic Nose

Nuno Almeida, Lino Marques and Aníbal T. de Almeida

Institute of Systems and Robotics,
Department of Electrical and Computers Engineering
University of Coimbra,
3030 290 Coimbra, Portugal
{nuno, lino, adealmeida}@isr.uc.pt

Summary. *Several gas sensing applications, such as odour source finding in mobile robotics, demand short time responses which at the present time lack on low price metal oxide gas sensors (MOx). This paper presents a processing technique that allows on line estimation of the present gas mixture, using transient data acquired from an electronic nose. Results showing the early estimate are presented.*

Keywords: Metal Oxide Gas Sensors, Electronic Nose, Wavelets, Artificial Neural Networks
Category: 5 (Chemical Sensors), 10 (Applications)

1 Introduction

Nowadays, it is completely accepted that electronic noses present the ability of recognising odours, identifying gaseous components of a mixture and quantify some of these components. However most of the existing algorithms for olfactory signal processing, present a considerable restriction to their utilisation in tasks that demand a very fast response because they are based on the processing of the steady state response of the gas sensor array. The ability to estimate the presence of a mixture from the first samples taken from the transient stage is a remarkable step for applications such as olfaction based mobile robot navigation [5], puff detection in air, automated cooking or real-time chemical process control. For other applications it may bring outstanding results because some gaseous mixtures cause a very slow change in the sensors resistances which leads to a considerable delay between the sample presentation and the return of classification results. This abstract reports a pre-processing technique that allows the estimation of the mixture presently in contact with the sensors independently of the initial (previous) mixture.

1.1 Previous Related Work

The problem of shortening the attainment of a classification/quantification of a gas mixture has already been addressed by other authors. Osuna [1] has modelled transient responses as a sum of exponential curves which are related to absorption, desorption, surface chemical reaction and free electron localisation in the bulk material. The process consists on fitting a function of form $f(t) = \sum_{i=1}^{M} G_i e^{-t/\tau_i}$ to each transient. Galdikas [2] successfully applied a similar method to evaluate meat freshness. Others [3][4] applied other discrete transforms to the identification problem and showed that the classification is clearly enhanced when compared to other methods.

The present setup is composed of four Figaro gas sensors, installed in a closed chamber, a vacuum-pump that was used to pull the air through one of the six bottles containing calibrated liquid mixtures.

2 The Data Processing

The pre-processing consisted of transforming each of the four transients using the continuous wavelet transform (CWT). Similarly to short time Fourier transform, a function (*wavelet*[1]) is multiplied with the signal at several scales (which allows the attainment of a frequency description) and at several moments (allowing the temporal localisation of the frequency occurrences). However, here the FT is not performed. Every peak is seen as corresponding to a sinusoidal signal in that frequency. The most remarkable fact related to CWT is that the window width varies with frequency enabling a good signal representation for all the spectra. The CWT can be summarised as:

$$CWT^{\psi}_{x(t),\gamma}(\tau, s) = \frac{1}{\sqrt{|s|}} \int x_{\gamma}(t) \psi^{*} \left(\frac{t-\tau}{s} \right) dt \quad (1)$$

in which γ is the sensor index, $x(t)$ is the transient signal, τ is the translation coefficient (defines shift in

[1]The term *wavelet* appears in literature as a word defining *small wave* or *well localised wave-like functions*

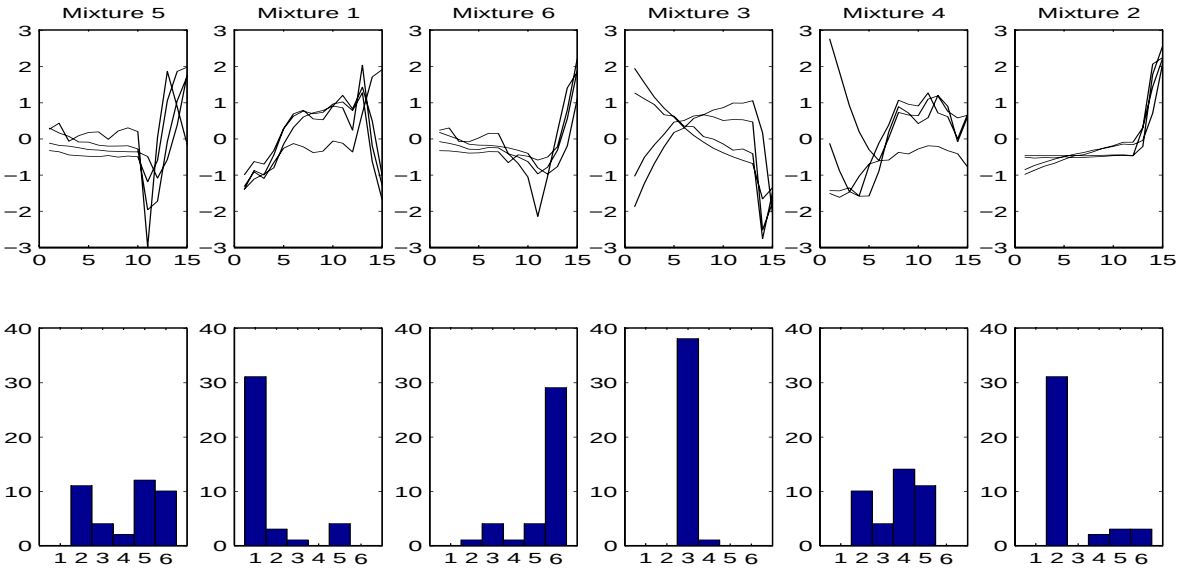

Fig. 1: Series of transients. The top row shows a random sequence of transient signals. The bottom row shows the probability returned by the classification algorithm

time), s is the scale coefficient (defines the support of the wavelet) and $\psi(t)$ is the mother wavelet (i.e. prototype for all window functions). For each transient between mixtures there will be a set of CWT matrixes containing the coefficients $\Psi^{\gamma}_{\tau,s}$ (one per sensor γ). In this case $\gamma \in \{1,\ldots,p\}$. Taking the vectors:

$$\Gamma_{\tau,s} = \begin{bmatrix} \Psi^{1}_{\tau,s} \\ \Psi^{2}_{\tau,s} \\ \vdots \\ \Psi^{p}_{\tau,s} \end{bmatrix} \tag{2}$$

i.e. we will have a matrix like:

$$\Gamma = \begin{bmatrix} \Psi^{1}_{1,1} & \Psi^{1}_{1,2} & \cdots & \Psi^{1}_{1,N} & \Psi^{1}_{2,1} & \cdots & \Psi^{1}_{M,N} \\ \Psi^{2}_{1,1} & \Psi^{2}_{1,2} & \cdots & \Psi^{2}_{1,N} & \Psi^{2}_{2,1} & \cdots & \Psi^{2}_{M,N} \\ \vdots & \vdots & \vdots & \vdots & \vdots & \ddots & \vdots \\ \Psi^{p}_{1,1} & \Psi^{p}_{1,2} & \cdots & \Psi^{p}_{1,N} & \Psi^{p}_{2,1} & \cdots & \Psi^{p}_{M,N} \end{bmatrix} \tag{3}$$

which will be the input to our recognition system. The first three main components obtained with principal component analysis (PCA) are presented in figure 2. Here we can see that there is a tenuous grouping that allow us to implement a classification algorithm over this data. A probabilistic neural network has been used. The training was performed using the coefficients provided by several transients between the six mixtures obtained randomly with varying time between mixtures. The sample rate was about 0.5 seconds. Figure 1 shows the classification (2^{nd} row) for the presented transients (1^{st} row).

Although the current algorithm presents some lack of robustness, the results are quite encouraging as it shows that it is possible to extract features from transient signals that constitute a unique pattern related to the present mixture in contact with the nose. Robustness with temperature, humidity and other external factors are yet to be tested.

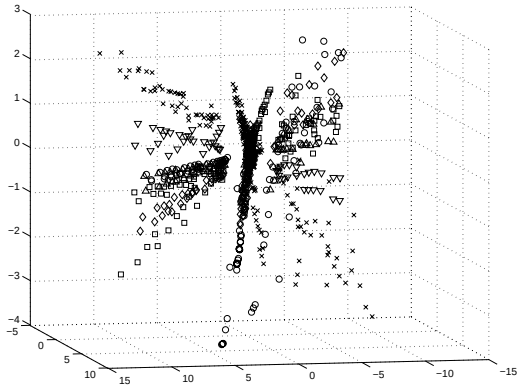

Fig. 2: Principal Component Analysis of Γ. $\times$ - water; $\circ$ - 25% ammonia, 75% water; $\bigtriangledown$ - 25% ethanol, 75% water; $\square$ - 10% ammonia, 10% ethanol, 80% water; $\diamond$ - 20% ammonia, 10% ethanol, 70% water; $\bigtriangleup$ - 10% ammonia, 20% ethanol, 70% water;

References

[1] Ricardo Gutierrez-Osuna, *et al.*, *Sensors and Actuators B* **61** (1999) 170–182.

[2] A. Galdikas, *et al.*, *Sensors and Actuators B* **69** (2000) 258–265.

[3] Cosimo Distante, *et al.*, *Sensors and Actuators B* **87** (2002) 274–288.

[4] Denise M. Wilson, *et al.*, *Sensors and Actuators B* **41** (1997) 63–70

[5] Lino Marques, *et al.*, *submitted to Eurosensors'03* (2003)

An impedentiometric electronic tongue

F. Di Francesco[1] , C. Domenici[1], R. Francesconi[1], A. Ahluwalia[2], A. Marchetti[2], G. Pioggia[2], W. Rocchia[2], G. Serra[2], D. De Rossi[2]

[1]Istituto di Fisiologia Clinica del C.N.R., Via G. Moruzzi 1, 56100 Pisa, Italy
email: ramsete@ifc.cnr.it http://www.ifc.cnr.it/

[2] Università di Pisa, Centro Interdipartimentale di Ricerca "E.Piaggio", Via Diotisalvi 2, 56100 Pisa, Italy

Summary: *An electronic tongue capable of discriminating the basic tastes by means of a chemical sensor array is presented. A purposely designed impedance meter was used to acquire data from sensors immersed in the testing solutions at a frequency of 150Hz. The whole measurement process was automated for an optimum control of experimental conditions and reproducibility. The sensor array was composed of six partially selective chemical sensors based on carbon nanotubes, carbon black dispersed in polymeric matrices and doped polythiophenes. A three-step data analysis process based on the principal component analysis and an artificial neural net allowed a fair discrimination of the solutions.*

Keywords: *Electronic tongue, chemical sensors, array, impedance measurement*
Category: *5 (Chemical sensors)*

1 Introduction

In the last fifteen years a new approach has been gaining importance within measurement technology based on the use of arrays of partially selective sensors and multivariate analyses techniques [1]. A fundamental stimulus to this kind of research was supplied by food industry, for its need to forecast consumer satisfaction for new products without using expensive, slow and unreliable human panels. A large amount of literature is available on electronic noses, but only recently similar concepts have been described for the analysis in liquids. Various measurement principles can be used for these so-called electronic tongues, such as voltammetric, potentiometric, conductometric or spectrophotometric techniques [2].

In the present work a different approach was chosen, based on the impedance measurement of various types of sensors.

2 Material and methods

Five sensors of three different types were prepared. In the first one, a gel system composed of a base material (polyvinyl alcohol) and a supplier of charged groups (polyacrylic acid and polyallylamine respectively) was added to single walled carbon nanotubes. In the second type carbon black, was dispersed in polymers (polyactide and 40% azobenzene substituted polylysine) according to the method described by Lonegarn [3]. In the third case, an alkoxy-substituted polythiophene was doped with sodium dodecyl sulphonate [4]. A reference sensor with the bare electrodes was also included in the array. The electric impedance of the sensor array was monitored at a frequency of 150 Hz, which had been previously chosen on the basis of a preliminary set of measurements as capable of guaranteeing the best discrimination. An automated measurement system composed of an impedance meter, a mechanical arm, a rotating platform and a data acquisition card was designed and realized.
A multiplexer allowed the sequential scanning of the sensors for the impedance measurement, while the array was automatically dipped into the baseline and test solutions by the coordinated movements of mechanical arm and rotating platform. The whole device was controlled by a PC running a software developed in a Labview™ environment. A block diagram of the system is shown in figure 1.

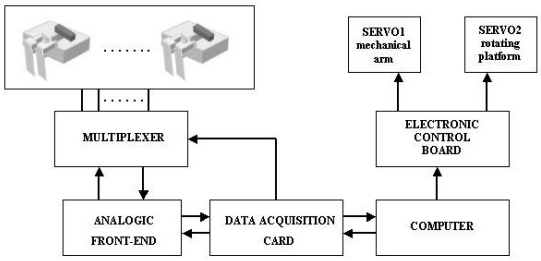

Figure1

3 Results and discussion

A high number of measurements was planned and carried out to assess the discrimination capabilities of the system and to avoid the risk of false classifications. In particular, 106 repeated measurements were carried out on each of fifteen test solutions in six measurement campaigns spanning a six month period.
The solutions represent the five basic tastes at three concentration levels, chosen as to cover the human sensitivity range:

	low	middle	High
Bitter-SodiumDehydrocholate	0.0001M	0.001M	0.01M
Sweet-Glucose	0.001M	0.01M	0.1M
Umami-Glutamic Acid	0.001M	0.01M	0.06M
Salty-Sodium Chloride	0.001M	0.01M	0.1M
Acid-Citric Acid	0.005M	0.05M	0.5M

so fifteen different samples were tested. Five solutions were measured at each run, while the sixth available position on the rotating platform was occupied by distilled water. The following measurement protocol was adopted:

a) Sensors in ambient air, start of data acquisition;
b) Sensors dipped in distilled water;
c) Sensors in ambient air;
d) Sensors in solution 1;
e) New cycles a)-d) for solutions 2 to 5;
f) Sensors in ambient air;
g) Sensors dipped in distilled water;
h) Sensors in ambient air, stop data acquisition.

At the end of this run of measurements, 36 values of both modulus and phase were acquired for each solution relevant to air (16 data), distilled water (10 data) and solution (10 data). All the solutions were repeatedly measured in random order, and the data were inserted in a database.

Data analysis was carried out in three successive steps, namely feature extraction, principal component analysis (PCA) and artificial neural net (ANN). Feature extraction was carried out by submitting suitable queries to the database. After a few trials, it was decided to use for all the sensors the steady state values of both phase and modulus, that were used as input variables for the PCA algorithm.

Results of a PCA analysis performed on 450 measurements belonging to one of the experimental campaigns are shown in figure 2. It can be seen that this algorithm allows a good separation of the different type of samples, notwithstanding the high number of measurements. Similar results could be obtained for each of the experimental campaigns, but if the whole set of data is considered the PCA plot becomes messy.

To overcome this problem and to obtain an idea of the number of possible correct classifications achievable by this system, a third data processing step was added.

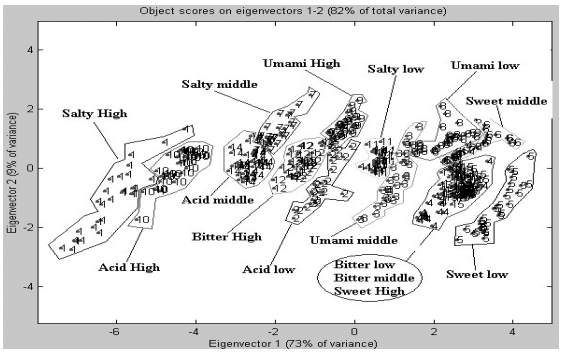

Figure 2

The values of the first 5 principal components were fed as input to a three-layer perceptron based on the back propagation algorithm. The whole set of 1590 measurements (106 repeated measurements × 15 solutions) was randomly split in three homogeneous subsets that were used to train and test the net and to evaluate the percentage of correct classification.

	Classified cases (%)	Recognition (%)
Umami High	62.9	86.4
Umami middle	80.6	89.7
Umami low	33.3	83.3
Salty High	66.7	100.0
Salty middle	62.9	81.8
Salty low	77.8	92.9
Sweet High	41.7	66.7
Sweet middle	50.0	83.3
Sweet low	54.3	78.9
Bitter High	66.7	87.5
Bitter middle	62.9	86.4
Bitter low	61.1	68.2
Acid High	41.7	66.7
Acid middle	45.7	56.3
Acid low	61.1	90.9
Average	57.9	81.3

Table II

Results are reported in table II. There are a significant number of cases in which the net was not able to give a response (2nd column), but the rate of correct answers in case of response is very promising. The system is currently under evaluation and the data set is being continuously increased.

Conclusions

An artificial tongue based on impedance measurements is reported. The device uses a variety of sensors which have different response mechanisms. Solution identification was performed using a three-step pattern recognition technique, with acceptable results. The authors are confident that solution discrimination can be improved through the use of a larger array and more sophisticated data processing methods.

References

[1] Gardner J.W. and Bartlett P.N., 1992, *"Pattern recognition in odour sensing"*, in Sensors and sensory systems for an electronic nose, Gardner J.W. and Bartlett P.N. Editors, pp. 161-180, Kluwer, Dordrecht.

[2] Winquist F., S. Holmin, C. Krantz-Rülcker, P.Wide, I. Lundström, "*A hybrid electronic tongue"*, Analytica Chimica Acta 406 (2000) 147–157

[3] Lonergan M.C., Severin E.J., Doleman B.J., Beaber S.A., Grubbs R.H., Lewis N.S., Array-Based Vapor "*Sensing Using Chemically Sensitive"*, Carbon Black-Polymer Resistors, *Chem. Mater.*, *8,* 2298-2312, 1996.

[4] De Rossi D. and Serra G., *"Process for preparing electro-conductive polymer films by doping with neutral polymers and chemical substances sensors obtained with this films*", European patent application EP 99200904.3.

HIGH SENSITIVE OZONE SENSOR BASED ON WO_3 MATERIAL

K. AGUIR, M. BENDAHAN, C. LAMBERT-MAURIAT, A. MALET

Laboratoire Matériaux et Microélectronique de Provence (L2MP, UMR 6137 CNRS),
Faculté des Sciences et Techniques de St Jérôme, case 152, 13397 Marseille Cedex 20,
France, Marc.Bendahan@L2MP.fr

SUMMARY
Thin films of tungsten trioxide (WO_3) have been deposited by reactive R.F. magnetron sputtering in view of exploiting their gas sensing properties. The electrical properties of oxide tungsten thin films are described and discussed. Ozone adsorption on films leads to a decrease of conductivity. This effect is used to design sensitive, fast and reversible ozone gas sensor, operating at different temperatures.

Keywords *: WO_3, gas sensor, Ozone*
Category *: 5 (Chemical sensors)*

1 – Introduction

The electrical properties of semiconductor oxides depend on the composition of the surrounding gas atmosphere. Based on this effect, the development of conductometric gas sensors using thin films of metal oxides, such as ZnO[1] and SnO_2[2], started in 1962. However, this type of gas sensor presents an inherent lack of selectivity, because more or less any type of reducing and oxidizing gases are detected by this mechanism.
Recents studies showed that WO_3 sensors seem to be very sensitive for ozone detection[3]. Tungsten oxide is an n-type metal oxide semiconductor, whose electron concentration is determined by the concentration of defects such as oxygen vacancy present in material. It is known that these vacancies play a significant role in the process of detection.
In this paper we report electrical responses of a metal oxide based gas sensor architecture : WO_3/SiO2/Si with Pt electrodes.

2 – Experimental

WO_3 films were sputtered on SiO_2/Si substrates with interdigitated platinum electrodes. The electrodes were obtained from a sputtered Pt film using photolithography and lift off processes. The experimental set-up used for the deposition of the WO_3 thin films was a reactive magnetron radio frequency sputtering device.

Grazing incidence X-ray diffraction (XRD) was applied to check the crystallinity and structure of the films.
The sensor characterization device was designed to measure the response of the sensors at various working temperatures and under different gas compositions.

3 - Results and discussions

Chemical Composition, Structure, and Morphology : after annealing at 400°C during one hour, X-ray diffraction patterns showed that the films were polycrystalline with the stable monoclinic structure.

Ozone Adsorption and Sensor Properties.
A typical dependence of the electrical resistance of the sensor on ozone partial pressure is shown in figure 1.
In presence of ozone the sensor resistance first increased very fast and then slowly.
The fast response is consistent with the hypothesis of a surface effect, especially related to ozone adsorption at the WO_3 surface. The time dependence of the slow one can be fitted with a square root law which is typical for a diffusion behaviour probably due to oxygen diffusion through the WO_3 thin film.

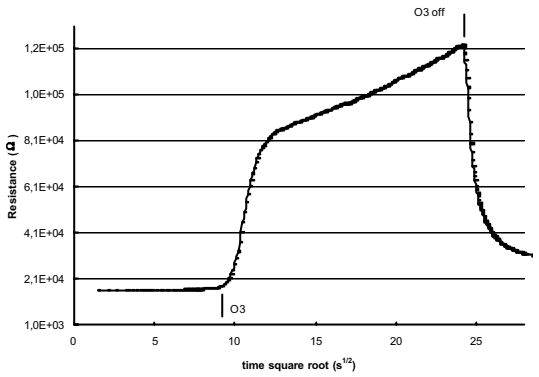

figure 1 : transient response of the sensor for 0.8 ppm of ozone at 200°C. Resistance versus time square root.

In order to design a very fast sensor, it will be so interesting to study only the first step transient response, and not to wait for the saturation.

The effect of temperature on the sensor performance, was also study. The sensor responses were measured between 150°C and 400°C. It appears, and with a good reproducibility, that the best answer was obtained at 300°C.

The sensor responses to different concentrations of ozone were then studied at 300°C (figure 2). The signal was reversible and proportional to the ozone concentration. The detection below 0.03 ppm is a crucial threshold. We can also notice the very fast response of the sensor which is about one second.

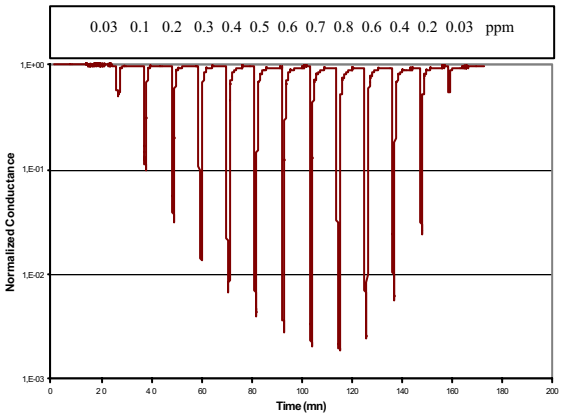

Figure 2 : normalized conductance variation versus time for WO_3 films exposed to small step-varying concentrations of O_3 at 300°C temperature.

4 - Conclusion

A high sensitive ozone gas sensor, can be designed using WO_3 thin films. The decrease of conductivity is the result of ozone reduction. The fast and reversible response and the high sensitivity of the developed ozone gas sensor make it clearly competitive with usual commercial sensors.

[1] T. Seiyama, A. Kato, K. Fujishi and N. Nagatani, Anal. Chem., **34**, 1502 (1962).

[2] N. Taguchi, Japanese Patent Application No. 45-38200 (1962).

[3] T. Maosong, D. Guorui, G. Dingsan, Appl. Surf. Sci. 171 (2001) 226,

Gas-sensitive properties of thin- and thick film sensors based on Fe_2O_3-SnO_2 nanocomposites

M. Ivanovskaya[1], D. Kotsikau[1], D. Orlik[1], G. Faglia[2]

[1]Scientific Research Institute for Physical and Chemical Problems, Belarus State University, Leningradskaya 14, 220050 Minsk, Belarus, E-mail: ivanovskaya@bsu.by
[2]INFM- Gas Sensor Laboratory, University of Brescia, Via Valotti 9, 25133 Brescia, Italy

Summary: *Influence of phase composition, structural peculiarities and grain size of Fe_2O_3-SnO_2 (Fe:Sn 1:9, 1:1, 9:1) nanocomposites on their gas-sensitive properties has been studies in this abstract. The characteristics of thin film sensors were obtained with regards to NO_2 and CO. Behaviour of thick film sensors were estimated in C_2H_5OH ambient. High sensitivity of Fe_2O_3-SnO_2 samples containing highly dispersive amorphous Fe_2O_3 phase has been revealed. The composites consisting of both α-Fe_2O_3 phase and Sn(IV)–α-Fe_2O_3 solid solution demonstrate maximum sensitivity to ethanol. Mechanisms of the processes which determine gas-sensitive behaviour of SnO_2-Fe_2O_3 composites are considered.*

Keywords: *Fe_2O_3-SnO_2 nanocomposites, structural characteristics, gas sensitivity*
Category: *5 (Chemical sensors)*

1 Introduction

The existing literature reports that the materials based on SnO_2-Fe_2O_3 composite possess high sensitivity to ethanol. As it has been established by Yamazoe, the metal cations which are characterized by electronegativity lower than electronegativity of Sn(IV), increase the sensitivity of SnO_2 based sensors to ethanol [1]. The value of electronegativity determines oxide activity in acid-base reactions. But the phase composition and the structural features of an oxide system and its activity in reduction-oxidation reactions are not taking into consideration [2].

The aim of the work was to elucidate the influence of structural peculiarities of SnO_2-Fe_2O_3 system on its gas-sensitive behaviour regarding certain gases.

2 Experimental

Fe_2O_3-SnO_2 samples (Fe:Sn 1:9, 1:1, 9:1) have been prepared by mixing Fe(III) and Sn(IV) hydroxides in required proportions followed by annealing of the dried species at different temperatures.

Structural investigations were carried out by XRD, ESR, TEM and Mössbauer spectroscopy.

Gas-sensitive properties of thick film sensors were studied regarding 1 ppm NO_2 and 50 ppm CO; thick film sensors were measured in humid ethanol vapors, modeling alcohol content in human being's expirated air.

The sensor response was calculated as $(I_{gas}-I_o)/I_o$ at fixed U value for thin films and as $(R_o-R_{gas})/R_{gas}$ in the case of thick film sensors.

3 Results and discussion

Fe_2O_3-SnO_2 nanocomposites of different dispersity and phase composition have been obtained by sol-gel technology. The samples with different Fe:Sn ratio have different structure (Table 1). Thus, annealing of Fe_2O_3-SnO_2 composite with Fe:Sn ratio 1:9 and 1:1 at 500-600°C leads to the formation of Fe(III)–SnO_2 solid solution, while in the case of Fe_2O_3-SnO_2 (Fe:Sn 9:1) composite, Sn(IV)–α-Fe_2O_3 solid solution is typical. Besides, amorphous highly dispersive Fe_2O_3 phase is also present in Fe_2O_3-SnO_2 (Fe:Sn 1:1) sample.

Table 1. Phase composition and grain size of simple Fe_2O_3 and SnO_2 oxides and Fe_2O_3-SnO_2 nanocomposites depending on temperature of annealing

T, °C	SnO_2 d, nm	Fe_2O_3 d, nm	Fe_2O_3-SnO_2					
			(Fe:Sn 9:1)		(Fe:Sn 1:1)		(Fe:Sn 1:9)	
			Phase	d, nm	Phase	d, nm	Phase	d, nm
300	2	Amorphous	Amorphous	–	SnO_2	2	SnO_2	2
500	6	15	Fe_2O_3	35	SnO_2	3	SnO_2	3
600	10	25	–	–	SnO_2	4	–	–
800	40	70	Fe_2O_3	50	SnO_2	10	SnO_2	10
			SnO_2	10	Fe_2O_3	25	Fe_2O_3	35

Thermal treatment of the composites at 800°C results in partial decomposition of sample structure and isolation of simple oxide phases – the species become heterogeneous.

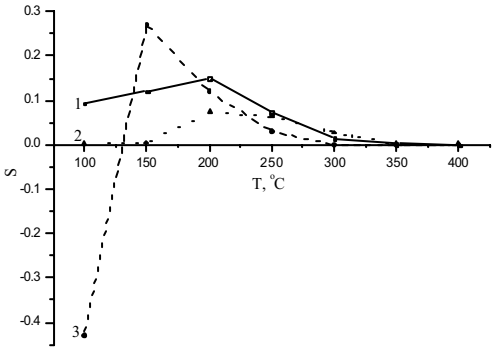

Fig. 1. Temperature dependent response (S) to 1ppm NO_2 of thin film sensors: Fe_2O_3-SnO_2 (Fe:Sn 9:1) (1), Fe_2O_3-SnO_2 (Fe:Sn 1:9) (2), Fe_2O_3-SnO_2 (Fe:Sn 1:1) (3), RH = 40 %.

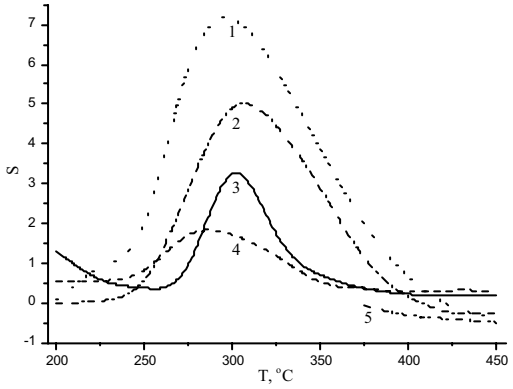

Fig. 2. Temperature dependent response (S) to humid ethanol vapors (0.025 ‰) of thick film sensors: Fe_2O_3-SnO_2 (Fe:Sn 9:1) (1), Fe_2O_3-SnO_2 (Fe:Sn 1:1) (2), SnO_2 (3), α-Fe_2O_3 (4), Fe_2O_3-SnO_2 (Fe:Sn 1:9) (5).

According to the available ESR data, two types of Fe(III) centers exist in Fe_2O_3-SnO_2 (Fe:Sn 1:1) composite: i) isolated Fe(III) ions within SnO_2 crystal lattice (signal g = 4.3, ΔB = 4 mT); ii) microinclusions of Fe_2O_3 amorphous phase (signal g = 4.3, ΔB = 4 mT). As it was found, the amorphous Fe_2O_3 only participates in NO_2 adsorption; isolated Fe(III) ions within SnO_2 lattice are inactive.

Mössbauer spectra of the samples represent a broadened doublet, which is the evidence of superparamagnetic Fe_2O_3 particles (d ~ 3-4 nm) formation. The parameters of Fe_2O_3-SnO_2 spectrum are different from the parameters, which are typical for the spectra of both α-Fe_2O_3 and γ-Fe_2O_3 bulk phases. However, the values of isomeric shift (δ) and induction of magnetic field (B) for amorphous Fe_2O_3 are closer to the parameters of cubic γ-Fe_2O_3 rather than trigonal α-Fe_2O_3. The coordination of Fe(III), which is specific for oxide/hydroxide iron compounds possessing cubic structure of unit cell (γ-FeOOH, γ-Fe_2O_3) preserves within Fe_2O_3 amorphous phase. This fact explains considerable activity of the mentioned species in gas adsorption process. Moreover, gas-sensitive and electro-physical properties of thin- and thick film Fe_2O_3-SnO_2 are substantially determined by Fe(III) state. Thus, isolated Fe(III) ions substituting Sn(IV) in points of SnO_2 lattice decrease considerably electrical conductivity of SnO_2 films and their sensitivity to both oxidizing (NO_2) and reducing (C_2H_5OH) gases. High sensitivity regarding NO_2 of Fe_2O_3-SnO_2 (Fe:Sn 1:1) is caused by the presence of highly dispersive Fe_2O_3 amorphous phase. The interaction between Fe_2O_3 and SnO_2 at the phase interface, which is accompanying with the formation of Sr–O–Fe and Sr–OH–Fe bonds leads to decreasing of contact resistance and increasing of electrical barrier transmissibility of the materials. Doping of Fe_2O_3 with Sn(IV) ions results in increasing of free electron concentration and enhancement of oxide layer conductivity. Fe_2O_3-SnO_2 nanocomposite which has a structure of Sn(IV)–α-Fe_2O_3 solid solution shows high response to ethanol vapors due to the presence of two types of adsorption centers – Sn(IV) and Fe(III). The two centers are characterized by different activity in the course of both reduction-oxidation and acid-base reactions. The mechanism of ethanol molecule detecting at the surface of the Fe_2O_3-SnO_2 composite is oxidizing dehydration, in which Sn(IV) functionates like a catalyst. Due to low Fe–O bonding energy and increased basicity of Fe_2O_3 in comparison with SnO_2, Fe(III) centers promote further oxidation of the intermediate products of ethanol molecule transformation. Moreover, high dispersity of Sn(IV)–α-Fe_2O_3 solid solution provides efficient electron exchange between the cations: Fe(III) $\leftrightarrow$ Fe(II). All this produces greater conductivity drop of an active layer and, consequently, improves sensor performance.

References

[1] N. Yamazoe. *Sensors and Actuators* B 5 (1991) 7-19.

[2] M. Ivanovskaya, D. Kotsikau, G. Faglia, P. Nelli. *Proc. Int. Conf. "Eurosensors XVI"*, pp 745-746, Prague, Czech Republic, 15-18 September 2002.

Acknowledgment

This work has been supported by INTAS program (project No 2000-0066).

Water detection in oily emulsions by means of a trapping electrode structure

M.G.H. Meijerink, E. Nieuwkoop

TNO TPD, P.O. Box 155, 2600 AD Delft, the Netherlands
email: meijerink@tpd.tno.nl http://www.tpd.tno.nl

Summary: *This paper presents the concept of a trapping electrode structure. This measuring concept can in general be used to increase the sensitivity when measuring impedance in emulsions of liquids with widely differing conductivities and/or dielectric constants. The increase in sensitivity is obtained by adapting the geometric structure of the measuring electrodes in such a way that they facilitate concentration of the species of interest on the electrodes. The trapping electrode structure method is demonstrated for oil-water mixtures.*

Keywords: *emulsions, trapping electrode structure, impedance*
Category: *5 (Chemical sensors)*

Introduction

Oil quality is a constant concern in various applications. Conditions vary from quality measurements in lubricating oil to well monitoring in the oil industry. Water presence in lubricating oil decreases the viscosity and compromises the lubricating properties of the oil. For the oil industry, water content is an issue for example in multi-phase flow meters [1], and in optimizing the efficiency of the oil well. Under certain conditions the salt concentration in water-oil emulsions may also be an issue to prevent corrosion in the system.

Known technologies for such detection challenges are for example ultrasonic detection of particles/droplets [2], or surface acoustic wave devices for measurement of viscosity.
In this article we propose the concept of a water-trapping electrode structure, which may be used to realize a high-sensitivity water in oil detecting device. We also demonstrate the limitations when this structure is used for salt measurements by means of conductivity measurements of the trapped water droplets.

Theory

Due to the high dielectric constant of water, capacitive measurements are an obvious way of assessing low quantity water presence in oil. Measurements with conventional probes however result in a limited sensitivity. This is caused by the formation of non-connected water bubbles in the oil. When measured with a macro-electrode, the droplets cause a local dielectric shortcut, but change the total dielectric path between the 2 electrodes only in a minor way, causing a very low sensitivity for capacitive measurements [3,4].

A way to circumvent the poor sensitivity caused by this effect is to choose an electrode configuration with a small enough spacing to trap water droplets between the electrodes. The droplets in direct contact with the 2 measuring electrodes allow for a much higher sensitivity for detecting water then macro electrodes.

Results

A 2-electrode probe with a surface area of 1.6*10 mm was realized with a spacing of 0.35 mm. This probe was positioned in a beaker with the emulsion on a magnetic stirrer. The stirrer was adjusted in a way that the flow in the beaker passes between the 2 electrodes of the probe.
The realized electrode structure visibly trapped the water droplets (Fig. 1). This mechanism worked for both the high viscosity of silicon oil as well as a crude oil fraction. Figure 1 shows an optical photograph with on the left clearly visible some trapped water droplets between the 0.35 mm spaced electrodes.

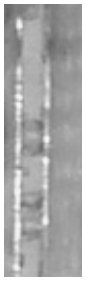

Fig. 1. The electrode structure with trapped droplets.

The probe electrodes were connected to a Rhode & Schwarz vector network analyser. The instrument displays the real part G and the imaginary part ωC of the conductivity independently.

Fig. 2 shows the real part of the conductivity measured on the probe with various oil-water emulsions.

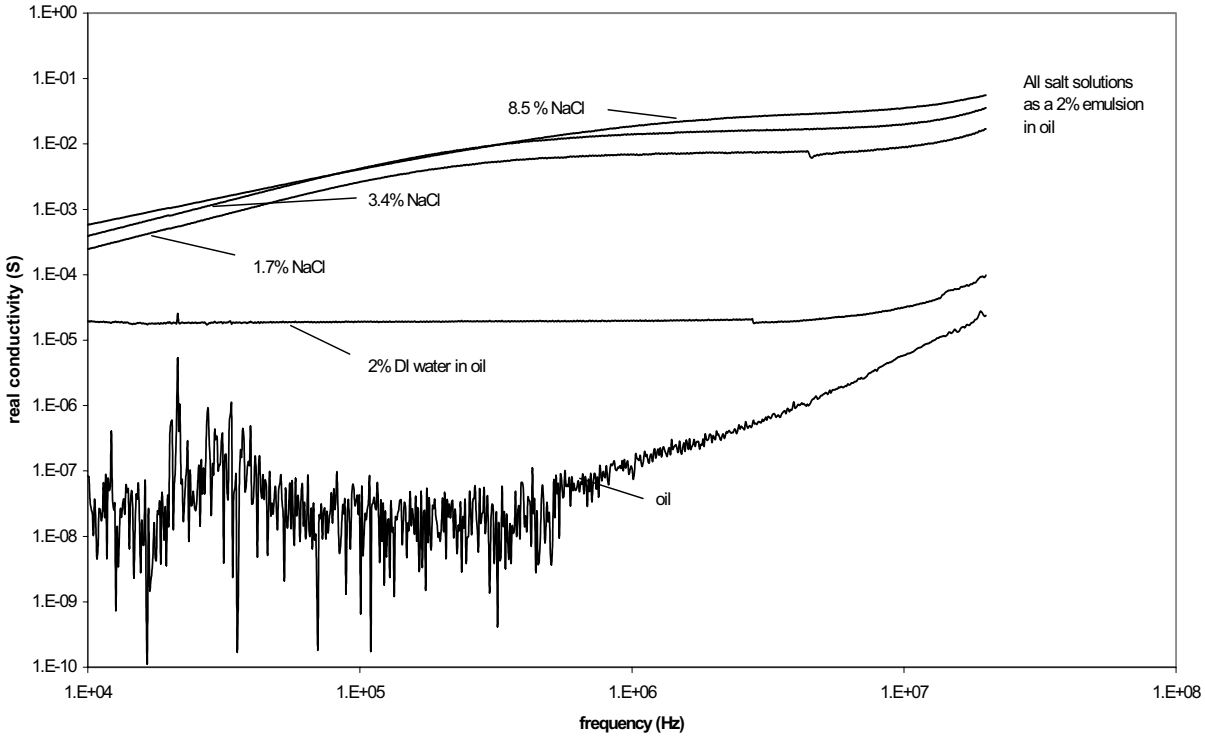

Fig. 2. The real part of the conductivity measured in samples of 2% water of various salt concentrations in oil.

Conclusions

The water trapping electrode structure is very suitable for a conductivity measurement on a water/oil emulsion. Impedance curves show a very good distinction between pure oil and oil containing small amounts of water. The presence of salt in the water dispersed in the oil can also be recognized on the experimental curves.

Acknowledgements

The authors would like to thank Mr. Philip Martin for fabrication of the electrode structure and assistance with the measurements.

References

[1] O.L. Bo, E. Nyfors, application of microwave spectroscopy for the detection of water fraction and water salinity in water/oil/gas pipe flow, *J. of Non-Crystalline Solids* 305 (2002) 345-353.

[2] A. Volker and de M. de Kroon, Characterization of suspensions by ultrasonic reflection measurements, *Ultrasonics* 36 (1998) 283-289.

[3] Jakoby and M.J. Vellekoop, Monitoring Water-in-Oil Emulsions Using Physical Sensors, *Eurosensors XV Conference proceedings* M2A4, Prague, Czech Republic, 2002.

[4] A. Sihvola, Electromagnetic mixing formulas and applications, IEE, Londen, 1999.

PORTABLE CHEMICAL GAS SENSOR PROTOTYPE FOR NITROAROMATIC COMPOUNDS DETECTION

F. THERY-MERLAND, E. PASQUINET, B. LEBRET, L.HAIRAULT.
CEA Le Ripault, BP 16, 37260 MONTS
Email : lionel.hairault@cea.fr

Summary: This poster presents the conception and development of portable gas sensor prototype for nitroaromatic compounds detection. It is based on Quartz Crystal Microbalance principle and a data processing. The sensitive material is a polymer which was choosen for his good sensibility and robustness. This prototype is able to detect 3 ppm of nitroaromatic compound with a high selectivity.
Keywords: gas sensor, nitroaromatic compounds, quartz crystal microbalance, prototype.
Subject category: Chemical sensors

For 10 years, many studies have been performed on the detection of nitroaromatic compounds using chemical gas sensors. The compounds that are the most often studied are trinitrotoluene (TNT), nitrobenzene or dinitrotoluene (DNT).

For each of these sensors, the sensitive material is a polymer (polypentiptycene [1], polysiloxane [2]) or a macrocycle (calixarene, phtalocyanine), which is deposited on an appropriate substrate.

In the CEA-Le Ripault research group, detection of other nitroaromatic compounds (scheme 1) by 9 MHz quartz crystal microbalance (QCM) transduction system, is studied.

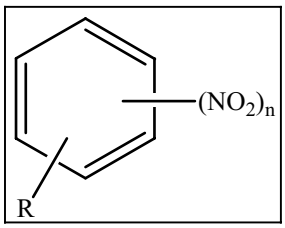

Scheme 1: Nitroaromatic compound A

Many sensitive materials were tested for nitroaromatic detection, but we have selected a polymer 1 for his good sensibility, reversibility and robustness. In fact, a 10 minutes exposure at 3 ppm of nitroaromatics, trigger a frequency shift of about 400 Hz (scheme 2). The selectivity is excellent. The compounds detected are nitroaromatic A (3 ppm), dichloromethane (580000 ppm), methyl-ethylketone (126000 ppm) and toluene (38000 ppm).

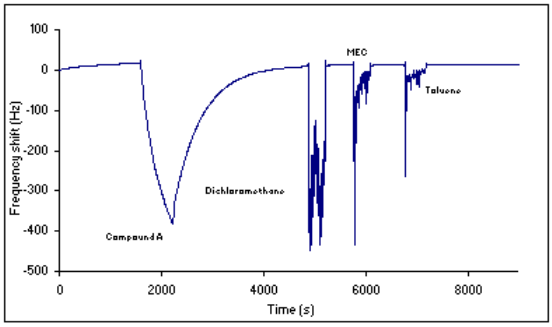

Scheme 2: selectivity results with polymer1 (after 100 days of storage under air)

After 6 months of ageing under ambient air, the polymer 1 can detect the compound A with a frequency shift of about 300 Hz (scheme 3).

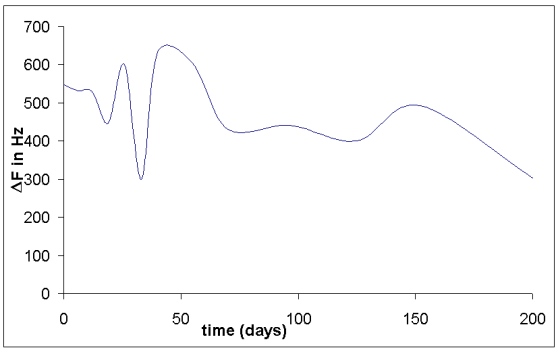

Scheme 3: Variation of the detection of the compound A during 6 months

We choose to develop an algorithm able to discriminate the compound A from the other gases

We can see that the shape of the gas response is different between compound A and solvents. We use this property to discriminate the gases with the derivative of frequency signal.

First, we must average the signal to erase the instability observed for solvents detection. The next step is the derivative of the frequency, which gives the result ΔF. If ΔF is included between two limits, the function returns ΔF else 0. One of the limits can be fixed by the user.

The returned value is saved in a turning buffer whose lengh can be adjusted. We look at the first and the last value of the buffer, if they are different from 0, we conclude that the gas A is present.

For this algorithm, we can adjust 4 parameters:

- Number of points for the average
- Frequency of the acquisition
- Limit value for the derivative
- Length of the buffer

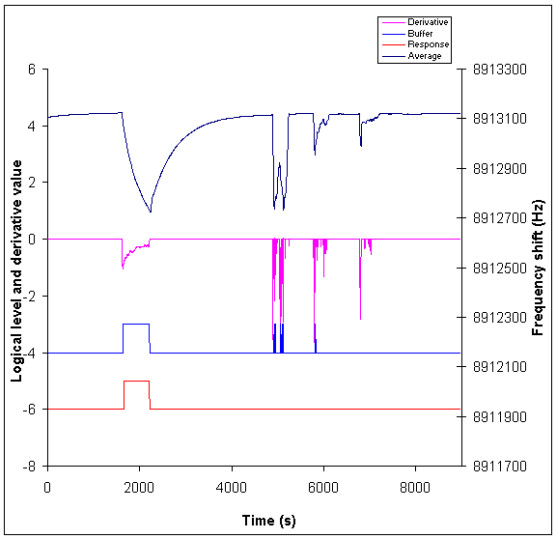

Scheme 4: Data processing from the average to the response

This model can be applied for other materials (which present the same type of response to A and solvents) with modification of the parameters.

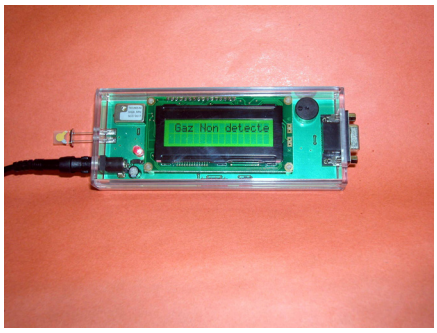

Scheme 5: The prototype

The prototype (scheme 5) has the size of a cellular phone and weights 225g. It is composed of a LCD screen, a buzzer, a 5V alimentation and a chip, which contains the program.

The validation tests are very heartening because we can verify that the response time is less than 60s. The solvents are not detected in the operational conditions. The response to the compound A gives a message on the screen with concentration detected and emits a sound.

At this time, the prototype is able to detect 3 ppm of A in fewer than 1 minute. In the future, we will add a battery to transform the system in a wireless system and we will study his performance for lower concentrations.

[1] M. La Grone, C. Cumming, M. Fisher, D.Reust, R. Taylor, *Proc. SPIE-Int. Soc. Opt. Eng.*, **3710**, 409-420, (1999). A. Rose, C.G. Lugmair, Yi-Jun Miao, J. Kim, I. A. Levitsky, V. E. Williams, T. M. Swager, *Proc. SPIE detection and remediation tech. for mines and minelike targets.*, **4038**, 512, (2000)

[2] R.A. Mc Gill and al., *Proc. SPIE-Int. Soc. Opt. Eng.*, **3392**, 384-389, (1998)

New design of thick film gas sensors with active filter

H. Teterycz, B. W. Licznerski[1], K. Nitsch, T. Sobanski, K. Wisniewski,

[1]Wroclaw University of Technology; Faculty of Microsystems Electronics and Fotonics
50 –370 Wroclaw, Wyb. Wyspianskiego 27, Poland
email: belicz@wemif.pwr.wroc.pl

Summary: *The authors present results of research studies on thick film gas sensors with SnO_2 and SnO_2/Rh multilayer gas sensing films. The use of planar sensor's construction with four measuring electrodes made it possible to investigate the electrical parameters of each layer and to evaluate the mechanisms of gas detection. Electrical parameters of different combinations of gas sensitive layers were measured using thermostimulated conductance and impedance spectroscopy. Preliminary long-term stability of sensors was also examined.*

Keywords: *thick-film; gas sensor; tin dioxide;*
Category: *5 (Chemical sensors)*

1 Introduction

Gas sensitive layers of chemical resistive sensors are made from different metal oxides of semiconductive nature [1]. However, regardless of the kind of used material, they have constantly had a problem with unsatisfactory selectivity and long-term stability [2].

During sensors performance, gas sensitive materials that constitute a catalytic-gas sensitive layer are subject to the influence of atmosphere with its very changeable content. They react to vestigial amount of substances which constitute air pollution and gradually lose their sensitivity because of the process of the blocking the surface active centres. References described methods [3] how to protect a gas sensitive layer from the influence of variouos harmful agent, but they are not satisfactory. Having analysed the processes occuring in gas sensors, the authors of the paper have come to the conlusion that if the layer protecting an active layer is to be the most efficient one, it should include an aditional layer made from different gas sensitive composition. This additional active layer should adsorb harmful substances while not desactivating an essential detecting layer. In the sensor of such a construction, the detecting layer made from pure SnO_2 is not directly subject to gas atmosphere. The first layer (SnO_2+Rh)selectively clean the gas that is measured on the second layer (SnO_2 pure).

The paper presents a new design of a gas sensor and measurement results of properties for constant and alternating current. The designed and executed multilayer sensors are characterised with different sensitivity. Additionally, as it is seen from conducted long-term research studies, the proposed design has enabled to improve long-term stability. The application for patent was filed for on 10 April 2002.

2 Experiment

Sensors of the new design were made according to standard thick-film technology. Gas sensitive layers were made from pure tix dioxide and tin dioxide doped with rhodium because of this material's interesting properties. Powders of tin dioxide were obtained with modified Okazaky method. Dopping with rhodium was performed with the impregnation process. The SnO_2 powder doped with rhodium chloride was dried at the temperature of 50ºC, then calcinated at the temperature of 600°C for 0,5h. The powders were mixed with organic vehicle, giving paste of rheological properties. No glass was added.

Sensors with the dimensions of 2,5·25mm^2 were made on 250μm thick alundum substrates (Fig. 1).

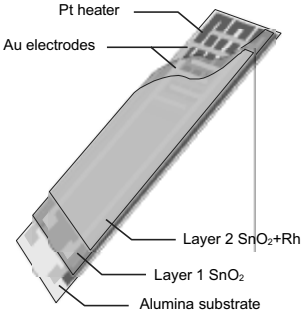

Fig. 1. Diagram of a multilayer gas sensors: a) appearance form the side of a heater, b) from the side of an active layer, c) cross section. D,G – golden electrodes.

The platinum heater that simultaneously played the role of a temperature sensor was placed on the bottom side of the substrate. Directly on the upper side of the substrate there were made two golden electrodes with the screen print method. A gas sensitive layer of pure tin dioxide was twice printed on them and fired in standard conditions at the temperature 850°C. Then, the whole area of the sensor, apart from the gas sensitive layer and contacts, was covered twice with a dielectric that

was fired in standard conditions. Two golden electrodes were again printed on such a prepared construction and covered twice with a printed layer of tin dioxide doped with rhodium. The main sensor was fired at the temperature of 850°C for 2h.

Measurements with the method of thermostimulated conductance and impedance spectroscopy were performed in a test chamber for the range of temperatures from 200 to 700°C. Long-term studies consisted in period control of parameters of sensors working in air (laboratory conditions) at the temperature of 550ºC.

The conductance or impedance of the sensor of presented design was measured between: lower electrodes found under the gas sensitive layer of SnO_2 (D-D), lower electrode found under gas sensitive layer of SnO_2 and upper electrode lying on SnO_2 (D-G) layer or upper electrodes found between SnO_2 layer and SnO_2+Rh layer which has direct contact with the atmosphere of the surroundings (G-G) (Fig.2).

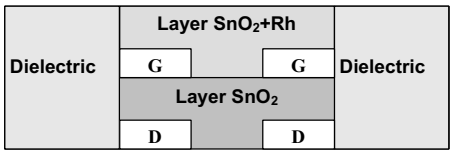

Fig. 2. Cross section of a thick film gas sensor

3. Results and Discussion

While analysing the structure of resistive gas sensors, it was noticed that their unstable work might have been caused by two elements: heater or gas senstive layer. Previous aging research studies of the layered heaters used in our sensors have shown that their resistivity changes by 1% during 1,5 year of constant work at the temperature of 550°C.

Research studies performed with the method of thermostimulated conductance and impedance spectroscopy have shown that changes in conductance and sensitivity clearly depend on the array of measurement electrodes.

Neither for synthetic air nor for methane, there were observed significant differences in the course of conductance measured between electrodes found under SnO_2 (D-D) layer and D-G electrodes. Impedance spectra known from measurements of alternating current have uncovered the existence of a single time constant which may be modelled by R(RQ) circuit. However, the course of measured impedance was significantly different between G-G electrodes found at SnO_2 layer. For measurements with alternating current, there was observed the existence of two time contants which were modelled by R(RC)(RQ) circuit.

In consequence, the sensitivity stated for electrodes found under SnO_2 (D-D) layer and D-G electrodes is very similar (Fig. 3). However, there has been observed a distinct decrease and expansion of sensitivity peak of the layer found between upper (G-G) electrodes (Fig. 3). It worth noticing that only SnO_2+Rh layer found on the surface of the whole construction has a direct contact with the atmosphere of the surroundings.

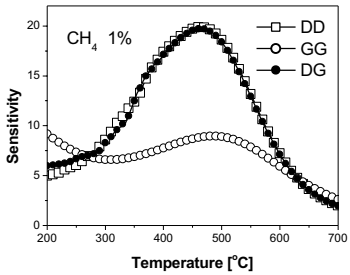

Fig. 3. Sensitivity dependence of a multilayer sensor on temperature for different configurations of measurement electrodes.

4. Conclusions

The SnO_2 sensitivity of the newly designed sensor with a gas sensitive layer as a filter was higher than in a sensor of standard construction. The SnO_2+Rh composition used as an active filter was also characterised by completely different sensitivity than for sensor of standard construction [5]. The sensor with presented construction was characterised with better stability in comparison to standard structure.

The authors think that presented solution with an additional layer playing the role of an active filter will also improve other electrical parameters of gas sensors. Currently there are being conducted further research studies to explain the processes ocurring first of all at the threshold of different layers that constitute the structure of a sensor.

References

[1] W. Göpel, K. L. Schierbaum: SnO_2 sensors: current status and future prospects, Sensors and Actuators B 1995 vol. 26-27 pp. 1-12.

[2] J. W. Gardner, V. K. Varadan, O. O. Awadelkarim, "Microsensors, MEMS, and Smart Devices" Eds. John Wiley & Sons, 2001.

[3] M. Sauvan, Ch. Pijolat: Selectivity improvement of SnO_2 films by superficial metallic films, Sensors and Actuators B vol. 58 (1999) pp. 295-301.

[4] H. Teterycz, B. W. Licznerski, K. Nitsch, K. Wisniewski, L. J. Golonka, Anomalous behaviour of new thick film gas sensitive composition, Sensors and Actuators B 47 (1998) pp. 152-156.

[5] B. W. Licznerski, K. Nitsch, H. Teterycz, K. Wisniewski, The influence of Rh surface doping on anomalous properties of thick-film SnO_2 gas sensors, Sensors and Actuators B 79 (2001) pp. 157-162.

The Impedance Analysis of Laser Deposited Sensor Layers

Milan Kovanda[a], Vladimír Myslík[a], Martin Vrňata[b], Miroslav Jelínek[c],

[a] Institute of Chemical Technology, Department of Solid State Engineering, 166 28 Prague 6, Czech Republic
[b] Institute of Chemical Technology, Department of Physics, 166 28 Prague 6, Czech Republic
[c] Czech Academy of Sciences, Na Slovance 2, 180 00 Prague 8, Czech Republic
e-mail: milan.kovanda@vscht.cz

Summary: *This work is concerned with both dc- and ac-measurements of gas sensors with active layers prepared by pulsed laser deposition (PLD) technology. The main interest was focused to following problems: measurement of real and imaginary part of complex impedance for frequencies ranging from 100 Hz to 10 MHz, construction of Nyquist diagrams, definition of an alternative phase-angle sensitivity S_{pa} (based on phase shift). The influences of S_{pa} vs. temperature and S_{pa} vs. frequency are also discussed.*

Keywords: *gas sensor, pulsed laser deposition, impedance spectroscopy*
Category: *5. Chemical sensors*

1 Introduction

The significant group of chemical sensors operates on the principle of surface dc-sensitivity changes. It is well known that the active layers of these sensors usually consist of three components: basic material (mostly metal oxides, some organic systems with delocalised π-electrons), dopants (metalic ions influencing above all resitivity and crystalinity of the active layer) and catalysts (noble metals in the form of small, non-aggregated particles reducing activation energy of the chemisorption and shifting of the Fermi level on the surface of the active layer).

A different approach considering properties of chemical sensors may be derived from ac-measurements [1]. These measurements are valuable tool for material characterization (grain size, conduction mechanisms, character of junction between the active layer and the metallic contacts).

In this contribution a new, alternative phase-angle sensitivity resulting from these ac-measurements is proposed.

2 Abstract preparation

The dc-sensitivity of the chemical sensor active layer (S_{dc}) was evaluated as a ratio of the layer resistance in air R_{air} and that in the atmosphere containing detected gas R_{gas} at given temperature [2].

$$S_{dc} = \frac{R_{air}}{R_{gas}} \qquad (1)$$

The ac-properties of these systems were classified by ac-impedance measurements. These measurements were carried out on a *HP 4194A impedance phase analyser* in the frequency range from 10^2 to 10^8 Hz with the voltage testing signal amplitude not exceeding 500 mV and with the help of the two-wire connection. This connection was selected from the practical point of view (the most common configuration of a sensor) although the results are affected by electromagnetic field non-homogeneities. The phase-angle sensitivity S_{pa} is evaluated at the given temperature of the active layer and the given concentration of the detected gas component. It was defined as a difference of phase angles Θ of complex impedance Z_{air} of the layer in "pure" synthetic air (Θ_{air} = arccos [Re (Z_{air}) /|Z_{air}|]) and complex impedance Z_{gas} of layer in a given concentration of detected gas (Θ_{gas} = arccos [Re (Z_{gas}) /|Z_{gas}|]).

$$S_{pa} = \Theta_{air} - \Theta_{gas} \qquad (2)$$

The definition of S_{pa} is illustrated on Figure1. This figure is a Nyquist diagram i.e. the imaginary part of the complex impedance vs. the real part of the complex impedance for different frequencies. From the Nyquist diagram, according to the definition (2) the dependence of the phase-angle sensitivity S_{pa} on frequency is constructed.

The following systems were investigated (basic material/dopant/catalyst): SnO_2, SnAcAc, SnAcAc /Pd (3.5nm), SnAcAc/FeAcAc(0.1%)/Pd (3.5nm) and SnAcAc/PdAcAc(1%)/Pd (3.5nm). These systems were selected according to reasons mentioned before [2,3]. The comparison between S_{pa} and S_{dc} values for various systems is in Table 1.

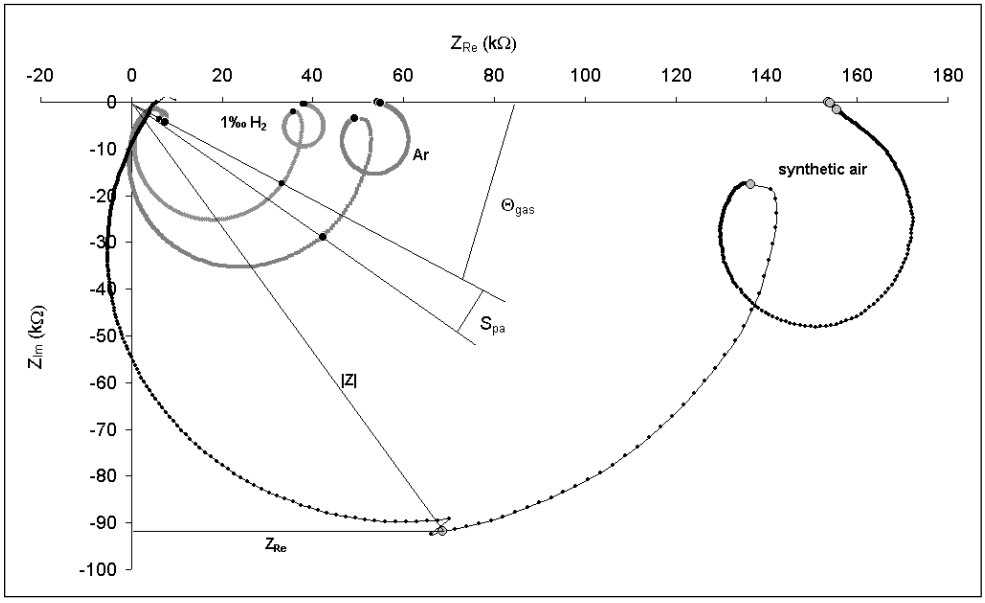

Figure 1**:** The response of SnAcAc based sensor to reducing (1000 ppm of hydrogen in argon), inert (argon) and oxidizing (synthetic air) atmosphere. The figure shows evaluation of S_{pa} according to equation (2). The S_{pa} values were evaluated at 1 MHz because of unambiguous graph interpretation and maximal method sensitivity.

Material	**S_{pa} (deg) at 22 °C**	**S_{pa} (deg)** ***{at T_{max} *}***	**S_{dc}** ***{at T_{max} *}***
SnO_2	~ 0	10.3 *{571 °C}*	5 *{571 °C}*
SnAcAc	~ 0	16.7 *{430 °C}*	28 *{430 °C}*
SnAcAc/Pd	3.5	10.2 *{383 °C}*	174 *{383 °C}*
SnAcAc/FeAcAc(0.1%)/Pd	12	36.7 *{413 °C}*	111 *{413 °C}*
SnAcAc/PdAcAc(1%)/Pd	4	6.0 *{310 °C}*	15 *{310 °C}*

Table 1: Overview of ac (at 1 MHz) and dc sensitivities to 1000 ppm H_2 for various material systems (***** T_{max} is a temperature of maximal dc sensitivity).

3 Conclusions

Some general comments to our results:

- The acetylacetonic systems shows lower temperature of maximal sensitivity T_{max}.
- The addition of Pd catalyst decreases temperature of maximal sensitivity T_{max} and hence working temperature of the sensor.
- The increase of the temperature leads to the increase of S_{pa} values in all cases.
- The SnAcAc and SnAcAc/FeAcAc/Pd systems give the absolute maximum of S_{pa} sensitivity.
- There is not significant correlation between S_{pa} and S_{dc} values.

Acknowledgements

This work was supported by Ministry of Education of Czech Republic, projects No.: MSM-223100002 and MSM-223400007 and Grant agency of Czech Republic (GAČR), projects No.: 106/01/P089, 106/03/P061 and 104/03/0406.

References

[1] U.Weimar, W.Göpel: A.c. measurements on tin oxide sensors to improve selectivities and sensitivities, Sensors and Actuators B 26-27 (1995) pp. 13-18

[2] M.Vrňata, V.Myslík, F.Vysloužil, M.Jelínek, J.Lančok, J.Zemek, The response of tin acetylacetonate and tin dioxide-based gas sensors to hydrogen and alcohol vapours, Sensors and Actuators B 71 (2000) pp. 24-30

[3] V.Myslík, F.Vysloužil, M.Vrňata, Z.Rozehnal, M.Jelínek, R.Fryček, M.Kovanda: Phase ac-sensitivity of oxidic and acetylacetonic gas sensors, Sensors and Actuators B 89 (2003) pp. 205-211

Optical Fiber Oxygen Sensor for *in vivo* NMR application

P. Caldas[1,2,3], P. A. S. Jorge[1,2], C.C. Rosa[1,2], A.G. Oliva[4], J. L. Santos[1,2]

[1]Unidade de Optoelectrónica e Sistemas Electrónicos, INESC Porto.
[2]Departamento de Física da Faculdade de Ciências da Universidade do Porto.
Rua do Campo Alegre, 687. 4169 007 Porto, Portugal.
email: pjorge@inescporto.pt http://opto.inescn.pt
[3]Escola Superior de Tecnologia e Gestão – Instituto Politécnico de Viana do Castelo.
4900 348 Viana do Castelo, Portugal.
[4]Instituto de Tecnologia Química e Biológica (ITQB), Universidade Nova de Lisboa.
Apartado 12, 2780 Oeiras, Portugal.

Summary: *An optical fiber sensor, for monitoring dissolved oxygen in in vivo Nuclear Magnetic Resonance (NMR) application, is presented. Oxygen detection is based on the dynamic quenching of the fluorescence of a Ruthenium complex trapped in the porous structure of a sol-gel silica film. Oxygen concentration is determined by phase-modulation fluorometry. A high brightness blue LED is used as optical source along with a standard high gain photodiode for detection. Preliminary results concerning the characterization of doped sol-gel thin films deposited by dip coating in glass slides and in optical fiber probes with different configurations are presented. Some considerations regarding optimal configuration are addressed.*

Keywords: *Optical fiber, oxygen sensor, phase fluorometry.*
Category: *5 (Chemical Sensors)*

1 Introduction

The on-line knowledge of dissolved oxygen (DO) concentration for *in vivo* NMR applications is crucial. Standard methods for O_2 detection are invasive and oxygen consuming. Also, the effect of an intense electromagnetic field in the NMR probe restricts the use of oxygen electrodes. The combination of recent fluorescence spectroscopy techniques with optical fibers has promising characteristics regarding remote monitorization of chemical parameters. A popular method for optical oxygen detection is based on dynamic quenching of the luminescence of Ruthenium complexes[1, 2]. The presence of oxygen quenches both the intensity, I, and the excited state lifetime, τ, of the flourophore. O_2 concentration is related to these parameters by the Stern-Volmer (SV) equation:

$$\frac{I_0}{I} = \frac{\tau_0}{\tau} = 1 + K_{sv}\left[O_2\right] \qquad (1)$$

where I_0 and τ_0 are respectively the intensity and the lifetime in the absence of quencher, K_{SV} is the SV constant and $[O_2]$ the concentration of oxygen. Direct measurement of either the intensity or the lifetime has problems associated that can be avoided using the phase modulation technique[3].

Applying a sinusoidal modulation to the optical source results in a phase delay, ϕ, in the fluorescent emission that can be related to the lifetime:

$$\tan\left[\phi\right] = 2\pi f \tau \qquad (2)$$

where f is the modulation frequency, which can be tuned, according to the luminescence lifetime, for optimum sensor sensitivity.

2 Proposed configuration

The proposed sensor can be seen in figure1.

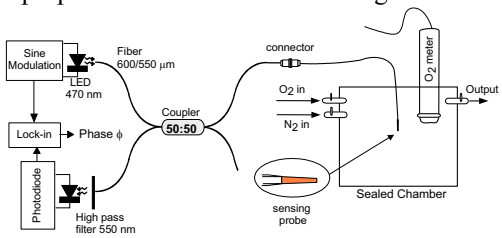

Fig. 1. Experimental set-up.

Light from a high brightness blue LED (*470 nm* - Nichia) was coupled to a silica glass multimode optical fiber (*550/600 μm*). The LED emission was sinusoidally modulated at *90 kHz* (lock-in limit). The sensing complex, Tris(2,2'-bipyridine) ruthenium (II) chloride hexahydrate [$Ru(bpy)_3$], was immobilized in a silica sol-gel film dip-coated on optical fiber probes. The resulting fluorescent signal was long pass filtered (λ_{cutoff} *=550 nm*) before detection. A reference signal, from the LED modulation, and the detected fluorescence signal were fed into a lock-in amplifier. The lock-in output was a phase signal proportional to the oxygen concentration. The sensing probes were placed in a gas chamber connected to O_2 and N_2 supplies. A standard O_2 meter monitored the oxygen level in the chamber.

The Sol-gel films were fabricated following standard procedure: a precursor, tetraethoxysilane (TEOS), was mixed with a solvent (Ethanol) in a volume ratio of *1* and with water (*0.01 M* HCL) in a molar ratio of *4*. After stirring, the ruthenium powder was added to this solution (*0.01 M*).

Films were dip-coated (*3 mm/s*) in glass slides, in the tip of multimode optical fibers and in optical fiber tapers. Drying of the films was performed at *20ºC*. The fiber tapers were fabricated by etching the fiber with *40% HF*. All sensing devices were tested as sensing probes in the set-up of figure 1. In order to compare the devices sensitivity the following parameters were evaluated:

$$Q = \frac{I_{N_2} - I_{O_2}}{I_{N_2}} \quad (3)$$

where I_{N2} and I_{O2} are the fluorescence intensities in N_2 and O_2 saturated atmospheres respectively, and:

$$\Delta\tau = \tau_{N_2} - \tau_{O_2} \quad (4)$$

where τ_{N2} and τ_{O2} are the excited state lifetimes in saturated atmospheres of N_2 and O_2 respectively. Lifetime was estimated by plotting *tan[ϕ]* as a function of modulation frequency.

3 Experimental results

Coupling radiation with maximum efficiency into the optical fiber is of critical importance. The best result was obtained by butt-coupling the fiber to an LED with a partially removed polished capsule. A *3*-fold increase in coupling efficiency was obtained as compared with standard coupling methods.

Preliminary tests were performed using coated glass slides. The up mentioned parameters were evaluated as a function of the solution aging time. Thermal treatments were also tested. The slides were placed inside the sealed chamber. The excitation and detection was performed trough the optical fiber coupler. In this configuration the detected fluorescence emission was very weak. Due to a low signal to noise ratio (SNR) the phase signal was unstable. *Q* parameters between *30%* and *40%* were obtained. Values for *Δτ* between *77 ns* and *176 ns* were recorded. These parameters increased with increased aging time. The unquenched lifetime decreased with increased aging time (mean value of *600 ns*). These behaviors result from increased film porosity and easier oxygen diffusion into the matrix[4]. The resulting SV plots were non-linear indicating film heterogeneity. After a thermal treatment for *3* hours *@ 80 ºC*, a great improvement in linearity was obtained at the expense of a slight decrease in *Q* values.

Some coated fiber tips were also tested. Because a solution drop formed in the tip of the fiber during the coating process, the resulting films were too thick and presented some cracks. In spite of that, due to increased thickness and a more efficient fluorescence coupling, a significant increase in SNR was observed (I_{N2} increased by *1.8*). Finally a fiber taper configuration was tested. The cladding was removed by etching the fiber with *40% HF*. Further etching, with slow immersion in the acid, allowed the fabrication of a fiber taper with thickness decreasing from *600 μm* to *300 μm* at the tip. The taper was then dip coated with the fluorescent solution. A uniform film resulted in the side of the taper. The 'drop effect' was greatly reduced because of the smaller tip area. A great improvement in the SNR was observed (I_{N2} increased by *3.5* relatively to glass slides). A *Q* value of *66%* was obtained. *Δτ* was increased to *350 ns*. The phase response to saturation with O_2 and N_2 can be observed in figure 2. The SV plot obtained from phase measurements with the taper configuration is shown in figure 3.

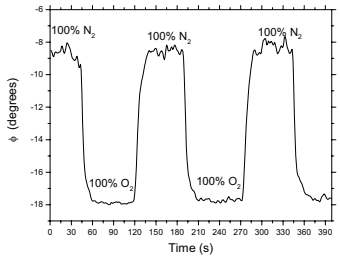

Fig. 2. Fiber taper response to O_2/N_2 saturation cycles.

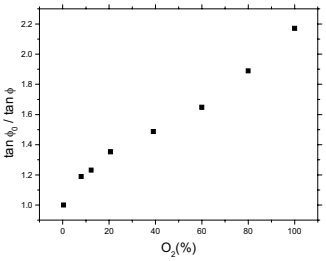

Fig. 2. Stern-Volmer plot obtained from the phase response of the fiber taper.

The SV response is clearly non-linear, indicating film heterogeneity. Linearity can be improved with an adequate thermal treatment. Encouraging results were obtained in gaseous O_2 measurements. To measure DO, several features can be improved. Fiber tapering is clearly a step towards sensor optimization. Work is in progress to determine optimal taper configuration. Hybrid precursors can be used in the sol gel process (better DO sensitivity). More sensitive, although more expensive, ruthenium complexes are available. Increasing modulation frequency to ideal value will improve sensor response[5]. Sensor response is temperature dependent, but work is in progress towards an all-optical temperature reference scheme.

References

[1] Aisling K. McEvoy, Colette M., McDonagh, B.D. MacCraith. *Analyst*, 1996. **121**: p. 785-788.

[2] M. K. Krihak and M.R. Shahariari. *Electronics Letters*, 1996. **32**: p. 240-242.

[3] M. T.Murtagh, D. E. Ackley, and M.R. Shahriari, Electronics Letters, 1996. **32**: p. 477-479.

[4] Colette M. McDonagh, et al. *Journal of Non-Crystalline Solids*, 2002. **306**: p. 138-148.

[5]. Vladimir I. Ogurtsov and D.B. Papkovsky. *Sensors and Actuators B*, 1998. **51**: p. 377-381.

Noise and resolution in quartz crystal oscillator circuits for high sensitivity microbalance sensors in damping media

L. Rodriguez-Pardo[1], J. Fariña[1], C. Gabrielli[2], H. Perrot[2]

[1] Dpto. T. Electrónica , IEA "Pedro Barrié de la Maza", Universidad de Vigo; 36200 Vigo, Spain.
E-mail : lpardo@uvigo.es
[2] Lab. Physique des Liquides et Électrochimie - CNRS - 4 Place Jussieu, 75252 Paris Cedex 05, France

Summary: *Four oscillators for their use like quartz crystal microbalance sensors in damping media have been designed. In order to increase the sensitivity, the four designs have been carried out to increasing frequencies. In this paper, a comparative study of the noise and the resolution of the circuits in function of the frequency and the quality factor is presented. Also, a calibration of the sensors has been made.*

Keywords: *Quartz crystal microbalance, electronic oscillator, frequency stability, mass sensitivity, resolution.*

Category: *5 (Chemical sensors).*

1. Introduction

In so much numerous scientific and industrial applications, measure instrumentation of very high precision is required to control and to study the evolution of different physical, chemical or biological processes. The piezoelectric oscillators are electronic circuits that fix their oscillation frequency by means of a piezoelectric crystal. The oscillation frequency depends on the characteristics of this material, on the associated electronic circuit and on the environmental conditions. At the moment, the frequency is the physical variable that can be measured with more precision. The sensitivity of the oscillation frequency to the temperature, humidity, pressure, acceleration and vibration, electromagnetic fields, electric fields, radiation, etc., allows to use the piezoelectric oscillators like sensors of high precision [1]. One of the well-known applications is the quartz crystal microbalance (QCM). In this case, the variation of the oscillation frequency is due to the variation of the mass deposition in the faces of the crystal [2] [3]. This type of sensor is used from the seventies in hole or in air to study the evolution of processes by observing the changes of associate mass. However, in liquid its use is quite more recent. Its main applications are the detection of chemical species, the biosensors of molecular recognition, etc.

2. Sensitivity, frequency noise and resolution

The sensitivity of a QCM resonator is proportional to its resonance frequency. With the objective of obtaining different sensibilities, oscillators at 2, 6, 9 and 27MHz have been designed for their use like mass sensors in liquid medium. The circuits are based on the Miller topology. The passive and active components have been optimized so that the oscillation condition stays with high losses (Q»500 for 2, 6 and 9MHz and Q»1000 for the 27MHz oscillator) in the resonator due to the liquid environment [4].

With the objective of determining the experimental sensitivity coefficients of the designed sensors, a calibration has been carried out observing the evolution of the oscillation frequency during an electrochemical deposition of copper (elastic deposition). The experiment has been realized for the four designed oscillators. The obtained results have been indicated in the table 1. In the figure 2 the evolution of the oscillation frequency during the deposition has been represented.

Table 1. Coefficient of experimental sensitivity.

Frequency	Teoric (Hz/(μg/cm^2))	Experimental (Hz/(μg/cm^2))
2MHz	9	6
6MHz	81	61
9MHz	183	167
27MHz	1650	1622

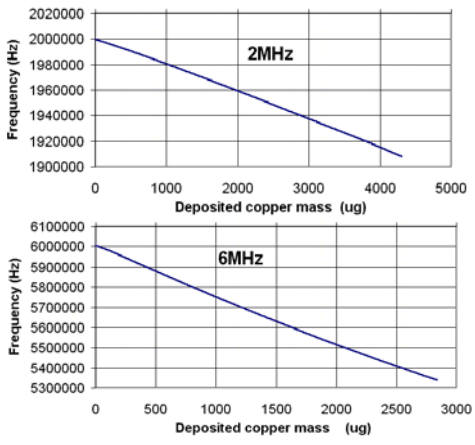

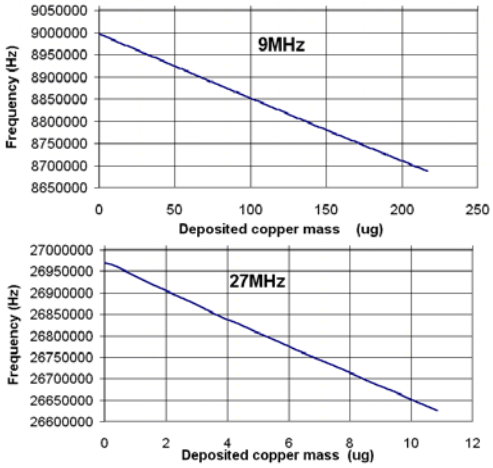

Fig.2. Calibration curves. Oscillation frequency during the deposition.

To determine the resolution of the sensors, the study of the short term stability has been carried out. For it, it has been realized a time domain characterization, by means of a direct measure of the oscillation frequency using a frequency counter. Later, the Allan variance has been calculated [5]. The study has been carried out with the resonator in air, in homogeneous liquid (distilled water) and in non homogeneous liquid (glicerol solution to 10% in water, of viscosity 1,274 centipoises at 20ºC). In the table 2 the resolution results obtained for the four oscillators in distilled water are indicated.

Table 2. Resolution of the sensors in distilled water.

Freq (MHz)	Q	$\sigma_y(\tau)_{max}$	Sensitivity (Hz)	Resolution
2	2040	$2\cdot10^{-7}$	0.40	67 ng/cm^2
6	2843	$3\cdot10^{-8}$	0.180	3 ng/cm^2
9	3238	$3\cdot10^{-9}$	0.036	161 pg/cm^2
27	1271	$3\cdot10^{-8}$	1.08	665 pg/cm^2

The frequency fluctuations of an oscillator increase when the quality factor of the resonator decreases. For the three oscillators with frequencies of the same order of magnitude, it can be observed that the oscillator sensitivity obtained starting from the variance of Allan increases when increasing the frequency, since the quality factor of the used quartz increases lightly.

Also, when using these oscillators like QCM sensor, because the sensitivity mass is inversely proportional to the resonance frequency, resolutions increase with frequency. In this way, with the oscillator at 2MHz superior variations at 66 ng/cm^2 can be measured, with the oscillator to 6MHz superiors at 3 ng/cm^2, and with the oscillator at 9MHz resolutions of 161 pg/cm^2 are reached.

On the other hand, the maximum quality factor is inversely proportional to the resonance frequency. In this way, in our case, the quality factor of the resonator of 27MHz decreases regarding the rest, being obtained a higher level of noise and therefore a smaller sensitivity (only changes superiors at 1.08Hz can be detected in the frequency). For it, although the sensitivity mass is bigger than in the other cases, the resolution will be of 665 pg/cm^2 in front of the 161 pg/cm^2 of the oscillator at 9MHz.

The table 3 summaries the resolution values obtained for the four oscillators in the three mediums. It can be observed that the non uniform load distribution on the surface of the quartz it doesn't affect to the present noise in the oscillator.

Table 3. Resolution in the tree medium. [1]:Air, [2]:Water, [3]:Glicerol 10%

2MHz	Q	$\sigma_y(\tau)_{max}$	Sensitivity (Hz)	Resolution (ng/cm2)
[1]	8662	$2\cdot10^{-8}$	0.04	6.7
[2]	2040	$2\cdot10^{-7}$	0.40	67.0
[3]	1898	$2\cdot10^{-7}$	0.40	67.0
6MHz	**Q**	$\sigma_y(\tau)_{max}$	**Sensitivity (Hz)**	**Resolution (ng/cm2)**
[1]	33332	$2\cdot10^{-9}$	0.012	6.7
[2]	2843	$3\cdot10^{-8}$	0.180	3.0
[3]	2585	$1\cdot10^{-8}$	0.060	0.983
9MHz	**Q**	$\sigma_y(\tau)_{max}$	**Sensitivity (Hz)**	**Resolution (ng/cm2)**
[1]	84195	$3\cdot10^{-9}$	0.012	0.161
[2]	3238	$3\cdot10^{-9}$	0.036	0.161
[3]	1703	$4\cdot10^{-9}$	0.036	0.215
27MHz	**Q**	$\sigma_y(\tau)_{max}$	**Sensitivity (Hz)**	**Resolution (ng/cm2)**
[1]	10662	$2\cdot10^{-8}$	0.54	0.333
[2]	1271	$3\cdot10^{-8}$	1.08	0.665
[3]	1065	$4\cdot10^{-8}$	1.08	0.665

3. Summary and Conclusions

Four oscillators for their use like QCM sensor in damping media have been designed. In order to increase the sensitivity, the four designs have been carried out to increasing frequencies.

It has been realized a comparative study of the noise and the resolution of the circuits in function of the frequency. It has been observed that when decreasing the quality factor of the crystal, the resolution of the sensor doesn't improve although the frequency of the oscillator has been increased. However, for frequencies of the same order of magnitude, resonators with similar quality factors can be used, so that the level of noise it doesn't increase practically with the frequency, and it is possible to improve significantly the resolution of the sensor.

References

[1] F. L. Walls and J.J. Gagnepain. *IEEE Trans. Ultrasonics, Ferroel. and Freq. Control*, vol. 39. N^o 2, (march 1992) 241-249.

[2]G.Sauerbrey, *Z. Phys*. 155 (1959) 206.

[3] V.E. Granstaff and S.J. Martin. *J. Appl. Phys*. 75 (3), (1994) 1319-1329.

[4] L. Rodriguez-Pardo, J. Fariña, C. Gabrielli, H. Perrot, R.Brendel, *to be published.*

[5] IEEE Standard. 1139-1999.

Synthesis of fluorescent 2-(2,2´-bithienyl)-1,3-benzothiazoles

Rosa M. F. Batista, Susana P. G. Costa and M. Manuela M. Raposo

Universidade do Minho, Departamento de Química, Campus de Gualtar, 4710-057, Braga, Portugal.
email: mfox@quimica.uminho.pt

Summary: *Seven new bithienyl benzothiazole derivatives **1** were synthesised by reacting various 5-formyl-5´-alkoxy- or 5-formyl-5´-amino-2,2´-bithiophenes **2** with ortho-aminobenzenethiol in good to excelent yields. Compounds **1a-g** were completely characterised by spectroscopic methods. Absorption and fluorescence spectra of these compounds were also recorded. In agreement with previous findings concerning the fluorescence studies of 2-(2´-thienyl)-1,3-benzothiazoles, the new compounds prepared can find application for additives in textile dyeing and plastics, tunable dye lasers, biological stains, fluorescent markers, materials science and optoelectronics.*

Keywords: *fluorescence, bithiophenes, benzothiazoles, bithienyl-benzothiazoles*
Category: *2 (Materials and technology)*

1 Introduction

Fluorescent compounds have found widespread use in scientific and industrial areas, for example as fluorescent brightening agents, for textile and plastics, additives in textile dyeing, inks and paints, tunable dye lasers and biological stains. Others applications include electroluminescent and liquid crystals displays, solar collectors, materials science and optoelectronics. The benzothiazole nucleus appears in many fluorescent compounds that have useful applications, which results from the ease of synthesis of this heterocycle and the high fluorescence quantum yields obtained when this small, rigid moiety is present in the compounds [1].

Thiophenes and oligothiophenes substituted by donor/acceptor groups have been extensively investigated. These compounds are often used as energy transfer and light-harvesting systems and for optical and electronic devices [2-4]. Oligothiophene derivatives are also characterised by important electroluminescence properties. Due to their strong fluorescence, these compounds can also find application as fluorescent markers [5-7].

2 Results and discussion

In recent years we have been interested on the synthesis and study of the fluorescence properties of a series of heterocyclic compounds of the benzothiazole type, substituted with several groups such as indolyl, carbazolyl, coumaryl and thienyl [8-10]. The most promising results were obtained for the 2-(2'-thienyl)benzothiazoles [8], substituted in position 5´ with electron donating groups, and these findings prompted us to evaluate the bithiophene moiety, with various groups such as alkoxy- or *N,N*-dialkylamino.

Our recent reported synthesis of 5-formyl-5´-alkoxy- and 5-formyl-5´-amino-2,2´-bithiophenes **2** made these compounds available in reasonable amounts, ready for further applications [11]. Indeed, we were able to use these compounds with sucess as substrates for the synthesis of 1,3-benzothiazole derivatives **1**.

Therefore the synthesis, UV/Vis and fluorescence properties of a series of heterocyclic fluorophores of the benzothiazole type containing a bithienyl moiety have been investigated. The benzothiazole moiety was obtained by the simple reaction of *o*-aminobenzenethiol with 5-formyl-substituted bithiophenes **2a-g**, in DMSO at 120 ^{o}C for 30-60 min. (Scheme 1). Purification of the crude products by column chromatography gave the pure benzothiazoles **1a-g** in good to excellents yields (57-96%).

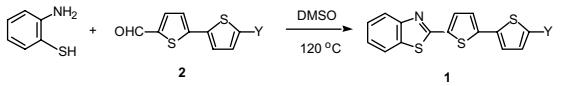

2 1

Y = OR or NR_1R_2

Scheme 1

The reaction is initiated by the formation of the corresponding imine that cyclises spontaneously, yielding the benzothiazoline, which is oxidised to the benzothiazole, aided by the oxidising character of DMSO. The new compounds **1a-g** were completely characterised by elemental analysis, ^{1}H and ^{13}C NMR spectroscopy and UV/Vis spectroscopy. The yields for compounds **1c-g** are lower than for compounds **1a-b**, due to the higher electron-donating character of *N,N*-dialkylamino groups. The fluorescence spectra of compounds **1a-**

g were measured, excitation and emission maxima and fluorescence quantum yields are also reported (Table 1). Absorption and emission spectra of 3 x 10^{-6} M solutions of compounds **1a-g** were run in degased absolute ethanol, using 9,10-diphenylanthracene as standard (ϕ=0.95 in ethanol). All the compounds are very fluorescent, especially **1a** and **1b** (ϕ= 0.71 and 0.53, respectively) and show large Stokes shift (the lowest being 98 nm for **1a** and the highest 148 nm for **1f**).

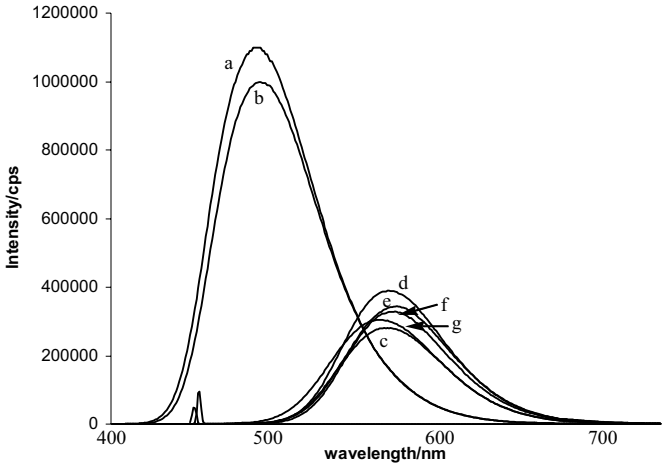

Fig. 1. Emission spectra for compounds **1a-g**.

Table 1. Yields, UV/Vis and fluorescence data for compounds **1a-g**

Compound	Y	Yield	UV/Vis		Fluorescence	
		(%)	λ_{max}/nm	log ε	λ_{em}/nm	ϕ
1a	OMe	96	393	4.14	491	0.71
1b	OEt	94	395	4.15	494	0.53
1c	NMe_2	65	443	4.08	576	0.32
1d	NEt_2	56	457	4.38	576	0.35
1e	N(Pr-*i*)$_2$	59	454	4.26	581	0.34
1f	piperidino	81	434	4.23	582	0.35
1g	morpholino	65	424	4.46	570	0.35

References

[1] B. M. Krasovitski and B. M. Bolotin. *Organic Luminescent Materials*, Weinheim, 1988, VCH.

[2] J. Roncali. *Chem. Rev.* 97 (1992), 711-738.

[3] F. Steybe, F. Effenberger, S. Beckman, U. Gluber, C. Bosshard, and P. Gunter. *Tetrahedron* 54 (1998), 8469-8480.

[4] H. A. M. Van Mullekom, J. A. J. M. Vekemans, E. E. Havinga and E. W. Meijer. *Mat. Sci. Eng*. 32 (2001), 1-40.

[5] N. Ikemoto, I. Estevez, K. Nakanishi and N. Berova. *Heterocycles* 46 (1997), 489-501.

[6] G. Barbarella, L. Favaretto, G. Sotgiu, L. Antolini, G. Gigli, R. Cingolani and A. Bongini. *Chem. Mat.* 13 (2001), 4112-4122.

[7] G. Barbarella *Chem. Eur. J.* 8 (2002), 5073-5077.

[8] S. P. G. Costa, J. A. Ferreira, G. Kirsch and A. M. F. Oliveira-Campos. *J. Chem. Research.* (1997) *(S)*, 314-315, *(M)*, 2001-2013.

[9] X. H. Luan, N. M. F. S. A. Cerqueira, A. M. A. G. Oliveira, M. M. M. Raposo, L. M. Rodrigues, P. Coelho and A. M. F. Oliveira-Campos. *Adv. Colour Sci. Tech.* 5 (2002), 18-23.

[10] P. C. R. Soares-Santos, M. M. M. Raposo, S. P. G. Costa and A. M. F. Oliveira-Campos. *Adv. Colour Sci. Tech.* 5 (2002), 94-98.

[11] M. Manuela M.Raposo and G. Kirsch. "Formylation, dicyanovinylation and tricyanovinylation of 5-alkoxy- and 5-amino-substituted 2,2´-bithiophenes". *Tetrahedron*, accepted for publication.

Desorption-ionization mass spectrometry on porous silicon dioxide

Jan Dziuban[1], Anna Górecka-Drzazga[1], Sylwester Bargiel[1], Rafał Walczak[1], Agnieszka Kraj[2], Tomasz Dyląg[2], Jerzy Silberring[2]
[1]Faculty of Microsystem Electronics and Photonics, Wrocław University of Technology, Wybrzeże Wyspiańskiego St 27, 50-370 Wrocław, Poland, jad@wemif.pwr.wroc.pl
[2]The Jagiellonial University, Faculty of Chemistry and Regional Laboratory, R. Ingardena St 3, 30-060 Kraków, Poland, silber@chemia.uj.edu.pl

Summary: *The silicon wafer with porous silicon dioxide spots for desorption-ionization mass spectrometry is presented. The test structures have been fabricated and tested for selected catacholamines. Desorption-ionization of the samples deposited on porous silicon dioxide spots does not require addition of a special matrix, and spectra in a low-molecular mass region can be clearly readable. Application of silicon wafer extends the operating range of a mass spectrometer for studies on metabolomics.*

Keywords*: MALDI, mass spectrometry, porous silicon dioxide, porous silicon*

1. Introduction

MALDI TOF (Matrix-Assisted Laser Desorption/Ionization Time Of Flight) mass spectrometry has been identified as a powerful tool for proteomic analysis. Usually, an analyte must be immobilized onto substrate in the matrix – a solid ultraviolet-absorbing organic material, usually sinapinic acid, dihydroxybenzoic acid for proteins, and 4-hydroxy-α-cyanocinnamic acid for peptides. Matrix with analyte is deposited on stainless steel plate in the form of small spots. Pulsed laser radiation vaporizes matrix, and ionises analyte (Fig.1).

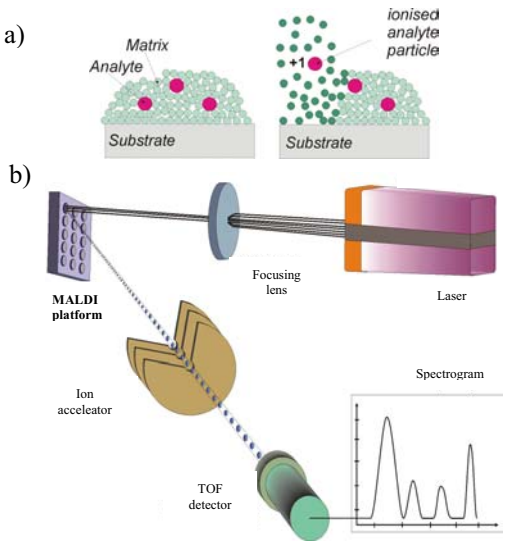

Fig. 1. MALDI TOF: a) matrix assisted ionisation, b) schematic view of mass spectrometry.

Then, ionised particles flow through spectrometer, where time of flight is measured. Detection limit of MALDI TOF spectrometry lays in femtomoles (10^{-15}M) region thus, the method seems to be the most attractive for post genomic investigation (gen expression analysis).

In their pioneer work (Nature, 1999, [1])Wei, Buriak, Siuzdak have shown that effective vaporization and ionisation of particles may be obtained in a porous silicon. The main advantage of porous silicon was an absence of interference between low-mass samples and matrix.

2. Experiments

The main goal of our work was to develop porous silicon-dioxide substrate for desorption-ionization spectrometry (DIOSD – Desorption-Ionization On Silicon Dioxide), and to investigate its applicability in a real-time research. Porous silicon dioxide quartz-like thick layer – according to our work – was fabricated on silicon substrate compatible to standard housing systems. A fabrication process of the DIOSD wafer, with a quartz-like porous thick layer, consisted of the several procedures is schematically presented in the Fig. 2. First, 3" (111) oriented, double side polished silicon substrate was thermally oxidized, and covered with Si_3N_4 CVD deposited layer. Next, dielectric layers were photolitographically patterned, Al layer was magnetron deposited on the back-side surface of the silicon wafer, and thick porous silicon layer was formed in C_2H_5OH:HF:water

solution (Fig.3). After porous silicon formation Al layer was removed, and wafer was rinsed in DI water.

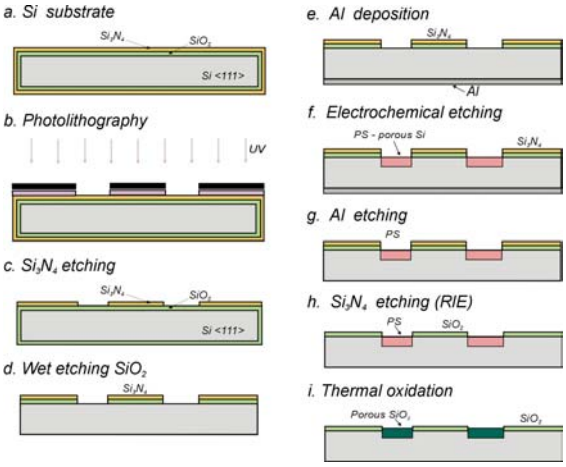

Fig. 2. DIOSD wafer step-by-step fabrication process.

Then, silicon dioxide porous layer was formed by wet high temperature oxidization, a wafer was divided into several DIOSD structures (Fig.4), and mass spectrometry tests were done.

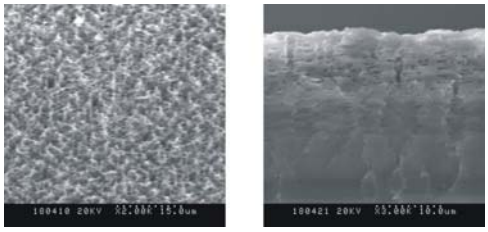

Fig. 3. Porous silicon layer 30 μm thick.

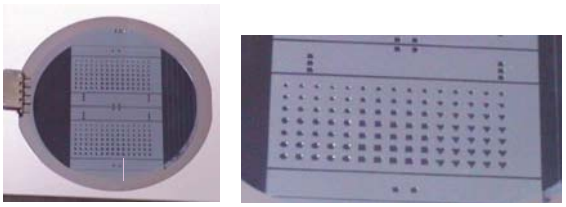

a) b)

Fig. 4. Porous silicon dioxide devices: a) 3" silicon wafer with two DIOSD structures, b) single structure with test spots.

3. Results

Desorption/ionozation mass spectrometry tests of selected catecholamines were done. Synthetic catecholamines were purchased from Sigma-Aldrich (Poland), and dissolved to the desired concentrations in water. Analyte was deposited into porous SiO_2 spots, silicon wafer was mounted on stainless steel plate, and positioned in apparatus (MALDI TOF Reflex IV mass spectrometer of Bruker Saxonia, Leipzig, Germany). The experiments were carried out in a positive-ion mode and in the reflectron mode (3 m flight path). High voltage was set to 20kV. Fig. 5 shows the example of the obtained mass spectra, very well defined peaks of low-mass peptides, no false signal may be seen.

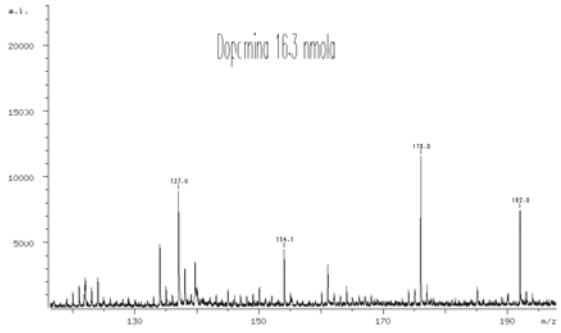

Fig. 5. Mass spectra obtained for sample of dopamine.

4. Summary

We have shown for the first time, that silicon dioxide porous quarz-like thick layer fabricated on silicon (111) oriented substrate, may be applied for the desorption-ionization mass spectrometry. This layer serves effectively – similar to the porous silicon layer reported prevuiously in the literature – as the matrix. The most advantageous feature of a new DIOSD wafer is an absence of interference between signals obtained from the matrix and low-mass analyte, and chemical inertness of silicone dioxide (quarz-like layer), important in biochemical investigations.

Acknowledgement

We would like to thank to our students Przemysław Szal and Tomasz Górecki for their help in technological works.

Works were financed by the Polish State Committee for Scientific Research (KBN) grant No PBZ 019-15 and 3 P04B 02024.

Literature

1. J. Wei, J. M. Buriak, G. Siuzdak, Desorption-ionization mass spectrometry on porous silicon, Nature, 399 (1999) 243-246

Nano-Structured Carbon Sensor for Simultaneous Measurement of Load and Temperature at Mechanically Strained Surfaces

Saskia Biehl, Holger Lüthje, Ralf Bandorf,
Fraunhofer-Institute for Thin Film and Surface Engineering, D-38108 Braunschweig, Germany

SUMMARY

Future innovations in important technical areas will depend on smart surfaces which combine protection against wear and corrosion with interactive control of the related system. Therefore multifunctional coatings with integrated sensors are needed, which will detect essential parameters of the surface like human skin is doing.

This paper deals with the development of novel multifunctional coatings based on nano structured carbon-hydrogen films. The layers were optimized with respect to mechanical and sensorical requirements. For the first time it will be reported, that diamond-like carbon films have been developed, which can be used simultaneously for force/pressure and temperature measurement. Moreover, the quasi monolithic layers showed excellent tribological properties with respect to wear protection and low friction. This new type of thin film sensor has the advantage over existing sensors that it can be used in areas under high mechanical load and therefore enables direct measurements in the contact zone of mechanical constructions. For layers of 5 MΩ base resistivity K-factors as high as 28 kΩ/N were obtained. The thermal variation of resistance resulted between 20 -110°C to 7,7 and 0,2 kΩ/K, respectively.

The diamond-like carbon films exhibits high hardness in the range of 15-30 GPa and therefore allowed measurement of normal forces without almost no deformation of the construction.

The fabrication was done by means of sputtering and plasma CVD techniques. The friction against steel was as low as 0,1.

It turned out, that the novel sensor layer can be used in various technical applications. Examples of characterization and applications will be discussed.

Keywords: force sensor, diamond like carbon, piezoresistive

Subject category: 5 or 1

Introduction

Whereas force detection typically will be performed by elongation of strain gauges or piezoresistive sensors, this paper describes a novel method, which enables the measurement of local temperatures and forces directly in the mechanical contact zone. This will be done by use of 1 µm to 5 µm thick hard and wear resistant coatings and with almost no deformation of the mechanical parts.

The piezoresistivity of graphitic carbon films was a research topic almost 50 years ago [1]. It was reported, that graphitic carbon films showed an piezoresistive behaviour with a negative k factor. Unfortunately this graphitic films were not wear resistant.

For the development of cheap but effective force sensors we therefore concentrated on a very innovative layer system. DLC layers can be deposited with an amorphous or nano-crystalline structure, depending on the preparation conditions. They can be doped with various elements, which will effect the mechanical and the electrical behaviour considerable.

It will be shown, that this type of coating can be used as a cheap but effective force, pressure and temperature sensor. Potential field of application will be the automotive and transportation industry as well as to the machining industry at the whole.

Experimental

For film preparation different plasma based methods have been used. Undoped carbon based hard coatings were fabricated by means of high frequency CVD processes, whereas metal doped films have been prepared by means of reactive dc sputtering as well.

As substrates hard materials were used. In particular plates of steel 100Cr6 and ceramic Al_2O_3 with a thickness of 5 mm and 1 mm, respectively. The substrates were polished on the coating side prior to deposition. RMS roughness was in the order of 30 nm. Analytical reference measurements were performed on Si wafer. The substrates have been coated with the above mentioned deposition processes. The thickness was in the range of 1 to 4 µm, preferable 2 µm. In all cases a conducting interlayer was deposited prior to the diamond like layers. For thermal measurements thin film electrodes were prepared locally by means of laser-direct micro-structuring.

The characterizations were performed by use of a flexible high load tester equipped with a heating station, were the samples were insulated to the base plate. Thus the resistivity could simply be measured by applying a defined current of a few µA through the load generating system. To this a static load up to 2000 N was used. As counterpart spherical and flat cylindrical tools have been used with diameters of 5 mm and 2 mm, respectively. Since roughness of the contact surfaces plays an important role, especially in the low load region, nano-topography of the amorphous carbon films and the counterparts was controlled by AFM. For elimination oft the contact problem, part of the samples were fabricated with thin film electrodes.

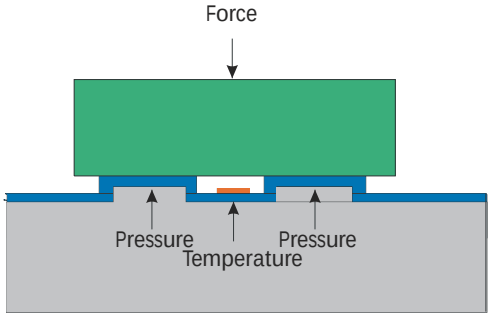

Fig. 1 Schematic of the measurement arrangement for simultaneously measurement of load and temperature

Results and discussion

By use of the above described characterisation technique different carbon based films have been tested. Whereas undoped layers of 2 µm in thickness showed at low force of 20 N a resistivity of 9 MΩ/µm, Ti and W doped films with 15At% and 5 At% ,respectively, only showed a normalized resistivity in the range of 1 to 5 Ω/µm. This holds for contact pad areas of 2 mm^2 and 3,2 mm^2.

Temperature sensor

Friction or other thermal loads on components can be determined with this multisensory diamaond-like carbon layer. Figure 2 shows the resistivity of a 2 µm thick carbon film with respect to sample temperature. The behavior shown in this example depends on layer structure and composition.

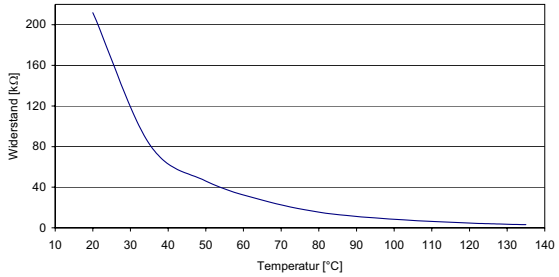

Fig. 2 Signal characteristic of the temperature sensor unloaded.

Load/force sensor

With increasing load we measured in all cases with doped or undoped carbon based films an enormous decrease of the resistivity. For undoped layers prepared by means of an rf-plasma CVD process, the characteristic of the electrical resistivity against the applied normal forces is shown in figure 3 at different substrate temperatures. In this case 2,5 µm thick coatings have been measured by use of flat cylindrical pins. The contact area was 2 mm^2 only. Thus the calculated pressure resulted in the high load region to some MPa, which is compatible to many mechanical applications.

The sensor characteristic showed an exponential variation of the resistivity versus normal forces. Two regions can be identified in general. In the low load region (up to ca. 100 N) the resistivity variations of more than one order of magnitude were observed, whereas in the high load region the variation was much lower, but became a more linear characteristic. However, also in this region we measured a reliable force depending effect, which can be used for the calibration of the sensor. We also see, that this behavior is independing on the substrate temperature. By increasing temperature the resistivity is decreasing but the two regions can still be identified.

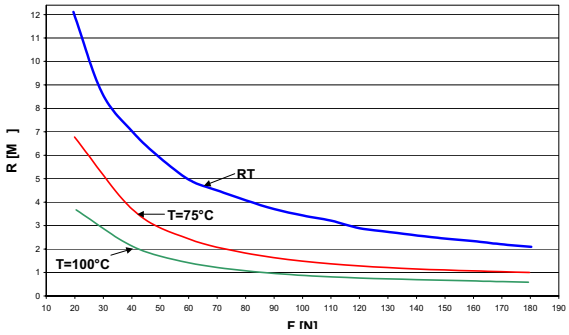

Fig. 3 Signal characteristic of the load sensor at RT, 75°C and 100°C. Contact area 2 mm^2. Dc measurement at 1 µA. Flat pin.

References

[1] A. Devenyi, A. Gheorghui, A. Belu, K.Korony: Electrical Transport and structure of vacuum deposited carbon films. Proc. Phys. & Chemistry of Semoconductors,Budapest, 11-17, 11.1970

A Calibration and Correction Method for Smart Sensors Based on Two-Dimensional Projective Interpolation

Henrique Serra, António Gano, João Correia, Nuno Especial

INETI-Estrada do Paço do Lumiar, Departamento de Electrónica, 1649-038 Lisboa. PORTUGAL
henrique.serra@ineti.pt http://www.ineti.pt/

Summay: *Sensor transfer curves have a non-linear behavior. The non-linearity can be structural and compensated through an appropriated design of the transducer and/or using analog or digital electronic circuits. The use of programmable electronic circuits makes possible the correction of sensors transfer curves and an automated calibration, with a decrease of their overall cost. Calibration and correction functions can be software implemented with the inclusion of a microcontroller in the sensor system. In this paper a calibration and correction method for smart sensors is described, which is based on two-dimensional projective interpolation algorithm. Test results of the method's implementation are also presented.*

KeyWords: *sensor calibration, sensor linearization, microcontroller based smart sensors, projective interpolation.*
Category: *9 (* System architecture, electronic interfaces, wireless interfaces*.)*

1-Introduction

In a batch of sensors, the transfer curve $z = f(x_1, x_2 ... x_n)$ [1] is affected by deviations resulting from the transducer and interface circuit's characteristics.

The aim of sensor calibration is to measure the static characteristic or transfer curve. The sensor correction makes possible the achievement of a linear static characteristic using the evaluated inverse transfer function.

There are both hardware and software-based correction methods. Hardware-based methods include analog and digital alternatives, using manual trimming [1] and/or digitally programmable circuits [2]. A microcontroller can provide an appropriate interface to different sensors elements and include generic software algorithms to correct the transfer curve. This solution allows the reduction of interface circuits and the automation of calibration procedures. There are basically three software methods to obtain the inverse of a transfer curve: EEPROM tables [3], polygonal interpolation [4] and polynomial interpolation [5][6].

Regarding software implementation, the polynomial methods need more RAM memory size in the calibration step but less EEPROM memory size in the measurement step.

In this paper a new approach for a polynomial projective interpolation method is implemented for applications in smart sensors with embedded low-cost microcontrollers. The method is set point deviation tolerant and is described in detail for a three-dimensional transfer curve.

[1] x_i is a physical/chemical variable and z is the electrical sensor output

2- Description of the Method

The algorithmic application of a two-dimensional projective based method to the sensors is divided in three distinct steps: pre-calibration, calibration and measurement. In the pre-calibration step, a reduced number of sensors transfer curves is analyzed and a calibration set with minimum number of points is achieved. In the calibration step, the transfer curve is obtained based on the previous set of calibration points. Also, a set of parameters of the inverse transfer function is evaluated. Finally, in the measurement step, the measured value of the primary variable is corrected using the inverse transfer function.

2.1 – Two-Dimensional Projective Interpolation

For a two-dimensional interpolation, it has been used the least squares regression method [7] that minimizes the error function:

$$S(a_0, a_2, ..., a_m) = \sum_{k=1}^{n} p_k \left| y_k - v(a_0, a_2, ..., a_m, x_k) \right|^2 \qquad (1)$$

where $v(a_0, a_2 ... a_m, x_k)$ is the interpolating function and y_k is the value of the two-dimensional transfer curve at point x_k.

The two-dimensional correction method is based on a projective interpolation of the transfer surface as shown in Fig 1.

The calibration reference values are (x_i, y_j) , i=1..n, j=1..m.

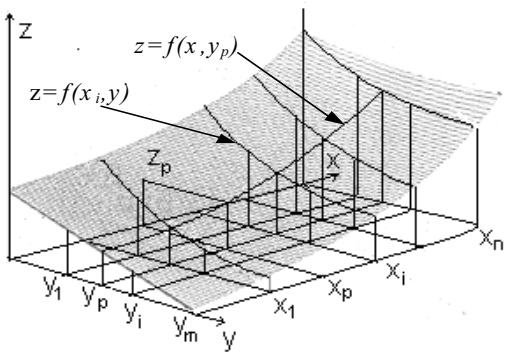

Fig.1 – Three-dimensional transfer surface reconstruction using the initial calibration points.

Each two-dimensional continuous function is reconstructed in each plane $x=x_i$ in order to get $z=f(x_i,y)$ and then $y=y_p$ in order to get $z=f(x,y_p)$. As shown in Fig. 1, at $y=y_p$ and $z=z_p$ the value x_p is evaluated using the inverse transfer function $x=g(z)$.

The transfer function relative error ε, in each point, is given by equation (2):

$$\varepsilon = \frac{f(x,y)\,g(x,y) - u(x)}{x_{\max} - x_{\min}} \qquad (2)$$

where $f(x,y)$ is the sensor transfer curve, $g(x,y)$ is the inverse sensor transfer function, achieved using the method described, and $u(x)$ is the ideal linear sensor transfer curve.

This projective interpolation method is applied in the pre-calibration, calibration and measurement steps.

The maximum degree of the two-dimensional correcting functions depends on the sensor transfer curve complexity. However, for the majority of sensors it is reasonable to use a maximum fourth degree polynomials [1].

The core of the method implementation is a subroutine that evaluates the two-dimensional functions based on least square method [7] This subroutine is used in all two-dimensional interpolations.

3-Test and Results

The method presented in this paper was tested for a humidity transducer transfer curve and other models that represent typical polynomial and exponential sensor transfer functions.

For this humidity sensor the typical transfer function is shown in equation (3).

$$v_{s1}(r_h,T) = 129.51e^{(0,05.(r_h-150))} + 4.16\times10^{-2}T - 1.24 \qquad (3)$$

where r_h is the relative humidity (%RH) and T the absolute temperature (ºC).

The voltage output v_{s1} varies between 0 and 5 volt, r_h in the range of 35%RH to 80%RH and T in the range of 20 ºC to 56 ºC.

The maximum initial relative error (related to the ideal transfer function placed in the middle of the temperature range) is about 50%.

With 10x10 calibration points, after pre-calibration points minimization and measurement correction, the results achieved are shown on *Table 1*, where n and m are, in that order, the primary variable and the secondary variable number of points; n_g and n_f are respectively the polynomial degrees of the interpolating functions $x=g(z,y_p)$ and $z=f(x_i,y)$.

Nº of points n/m	Degree of interpolating functions n_g/n_f	Error ε % of FSR
5/2	3/1	< 2.6%
5/2	4/1	< 1.13%

Table 1

4-Conclusions

The solution presented is systematic, flexible and generic and introduces added features:

- Easier implementation in low-cost microcontrollers with reduced embedded RAM/EEPROM memory size.
- Inclusion of the calibration and correction functions in the sensor with reduction of calibration costs.
- Minimization of calibration points.
- Increased tolerance to deviations in reference set-point, during calibration.

The algorithm can be extended to transfer curves with more than one secondary variable.

5-References

[1] Zbigniew Morón. "Can Analog Circuits Still Increase Sensors Smartness?". Sensors & Actuators A, Vol. 68, 1998, pp. 474-479.

[2] A. H. Taner, J. E. Brignell. *"Aspects of Intelligent Sensor Reconfiguration"*. Sensors & Actuators A, Vol. 46-47, 1995, pp. 525-529.

[3] P.P. L. Regtien, P. J. Trimp. *"Dynamic Calibration of Sensors Using EEPROMS"*. Sensors & Actuators A, Vol. 21-23, 1990, pp. 615-618.

[4] Peter Hille, Rainer Hohler, Hans Strack. *"A Linearisation and Compensation Method for Integrated Sensors"*. Sensors & Actuators A, Vol. 44, 1994, pp. 95-102.

[5] Gert Van der Horn, Johan H. Huijsing. *"Integrated Smart Sensor Calibration"*. Analog Integrated Circuits and Signal Processing, Vol. 14, 1997, pp. 207-222.

[6] Donald L. Ersland. *"A Consistent Mathematical Approach for Multiple Input Calibration*". Sensors, May 1999.

[7] Samuel D. Conte, Carl de Boor. Elementary *"Numerical Analysis. An Algorithmic Approach"*. McGraw Hill, 1981, pp. 251-267.

Long Detection Range for 2-D Bar-Code Detection System Using Unbalanced Masked Collimators and Wide-Opening Lens

Hiroo Wakaumi[1] and Chikao Nagasawa[2]

[1]Tokyo Metropolitan College of Technology, 1-10-40, Higashi-Ooi, Shinagawa, Tokyo, 140-0011 Japan, wakaumi@tokyo-tmct.ac.jp
[2]Tokyo Metropolitan University, 1-1, Minami-Ohsawa, Hachioji, Tokyo, 192-0397 Japan

Summary: A new two-dimensional bar-code detection system is proposed in which a wide-opening condensing lens is used to increase light incident on a photodiode reflected from a barcode, and also unbalanced masked collimators are employed to extend uniformly the depth of focus for three LDs. The proposed system provides a longer detection range while remaining compact and low-cost. The best performance was obtained using unbalanced masks with 2.5-mm and 3-mm hole diameters and a 28.5 mm-focal-length condensing lens with a 40-mm aperture, providing a practically usable great detection range of 13.7 cm for 0.25-mm 3-line bar codes. The maximum detection range of the proposed system is 1.33 times longer than conventional systems, and has potential application in high-speed, high-resolution bar-code systems.

Key words: *optical detection system, laser diode, collimator*
Category: *9 (System architecture)*

1 Introduction

Two-dimensional bar-code detection systems (2D BCDSs) for Code 49 and Code 16K 2D barcodes are highly useful in applications such as goods management in production lines and automatic warehouses where high-speed and high-resolution detection is required. The authors have already developed a high-speed 3-line 2D BCDS employing multiple laser diodes (LDs) with time-sharing light emission (TSLE) operation and have achieved a scanning speed of nearly 3 times that of conventional scanners [1]. They have also developed a high detection resolution system using the balanced masked collimators which provides a detection range of nearly 10 cm for 0.25-mm bar codes [2]. Bar-code detection systems that detect at a significant distance require the long detection range remaining narrow laser light beam. However, the detection range in this system is limited to nearly 10 cm by the simple masked collimator structure and the depth size of detection lens system. The standard approach for increasing detection range is the use of a combination of a non-spherical lens and a beam expander. This approach results in a large and expensive system.

In this paper, an unbalanced masked collimator system and a wide-opening condensing lens system are proposed for 2D BCDS, providing a long detection range while maintaining small system size and low cost.

2 Unbalanced collimator structure

The proposed 2D BCDS employs three LDs in TSLE operation, with non-spherical lenses and different hole diameter masks to give a longer detection range while remaining a distinct narrow beam (remaining coherent for greater distance). The BCDS is outlined in Fig. 1. The BCDS has different distances from three LDs to a barcode for allowing us to use a low height scanner mirror. Therefore, when the same diameter masks for three LDs are used, the depth of focus is different from each other in three LDs. In the proposed system, the depth of focus in each of LDs is adjusted successfully by selecting an appropriate combination of masks so that three laser beams remain uniformly narrow for a long detection range. Thin sheet masks (of vinyl chloride) with different hole diameters can be fabricated easily using an electric drill. These collimators can be fabricated at low cost and allows the LD unit be made compact, avoiding the use of large and expensive beam expanders.

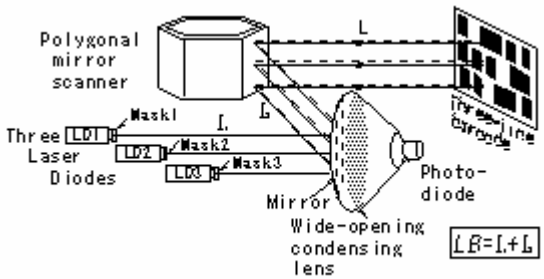

Fig. 1. 2D BCDS with TSLE operation and unbalanced collimator structure and wide-opening condensing lens.

3 Wide-opening condensing lens system

In a conventional BCDS, the aperture of a detection lens is almost equal to the height of the scanner mirror (25 mm). Therefore, the amount of light incident on a photodiode through the detection lens greatly decreases since a part of the

scattered reflected light from the scanner mirror passes outside the opening of the detection lens (25 mm).

The proposed BCDS employs a wide-opening condensing lens to increase the amount of incident light. A condensing lens with an aperture of 40 mm, considerably larger than the height of the scanner mirror (25 mm), was used. The focal length of the condensing lens is 28.5 mm, extremely short in spite of its large aperture. The depth of detection lens system with this condensing lens is 37 mm, 16 % shorter than that of the conventional system (44 mm), allowing the system be made compact in depth. Since the area of the wide-opening condensing lens is 2.6 times greater than that of the conventional system, this lens enables the photodiode to get enough light reflected outside the scanner mirror face. The condensing lens consisting of a single non-spherical lens is not expensive.

4 Experimental results

When the mask hole diameters Φ of LD1, LD2, and LD3 are 3 mm, 3 mm, and 2.5 mm, respectively, detection distance L versus LD light beam width ϕ is shown in Fig. 2(b). We can see that the depth of focus is longer, compared to that in balanced collimator systems (Fig. 2(a)). The maximum detection range at which ϕ remains narrower than 300 μm is almost 10.1 cm, whereas the maximum for the balanced masked collimator system is 8.3 cm.

A 3-line bar code with a minimum width of 0.25 mm was then detected using the unbalanced-masked-collimator 2D BCDS under TSLE operation. The maximum practical detection range using the proposed system was extended to 12.5 cm, compared to the maximum of 10.3 cm for conventional collimator systems (Table 1).

The wide-opening lens system was also added to the unbalanced collimator system to improve further the detection range. In this system, Φ of LD1, LD2, and LD3 were designed 0.3 mm, 0.25 mm, and 0.25 mm, respectively, and the focal length in each of LDs was optimized to achieve a longer detection range. As a result of the 3-line barcode detection, the maximum practical detection range was extended to 13.7 cm (Table 1). This represents a 1.33-fold increase in maximum detection range. This is due to the increase of incident light to the wide-opening condensing lens.

Table 1. 3-line bar-code detection range.

Type of 2D BCDS	Detection range [cm]
Conventional balanced masked collimator scanner [Φ(LD1~LD3)=3 mm]	5.5 - 15.8
Unbalanced masked collimator scanner [Φ(LD1,LD2)=3 mm, Φ(LD3)=2.5 mm]	3.5 - 16.0
Unbalanced masked collimator and wide-opening condensing lens scanner [Φ(LD1)=3 mm, Φ(LD2,LD3)=2.5 mm]	3.5 - 17.2

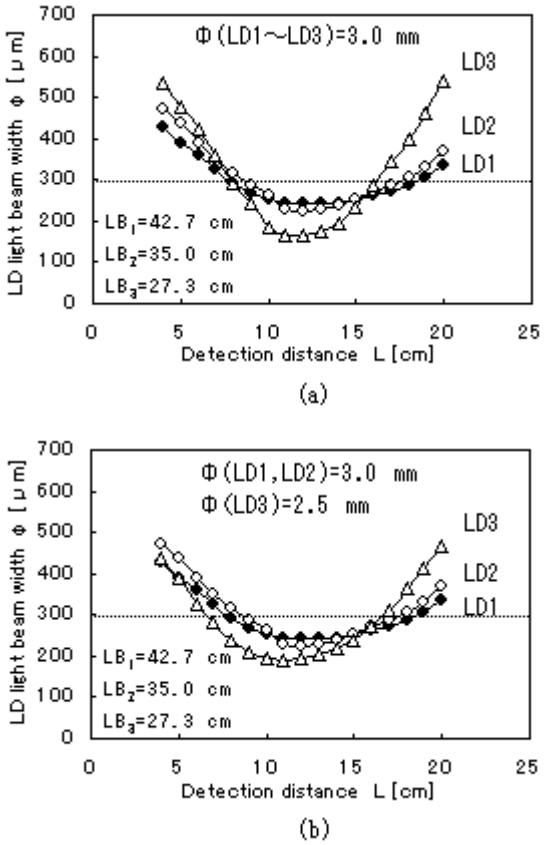

Fig. 2. Detection distance vs. LD light beam width. (a) Conventional balanced masked collimator system, (b) unbalanced masked collimator system.

5 Conclusion

A new 2D bar-code detection system with unbalanced masked collimators and a wide-opening condensing lens was proposed and shown to be capable of providing sufficient detection range over a practically usable detection range of greater than 13.5 cm for 0.25-mm barcodes. This long detection range was achieved without increasing the cost or size of the system. One reason for its long detection range is that the narrow laser light beam in each of LDs with the masked collimators is achieved for a longer range due to the individually optimized depth of focus of each LD. Another is that the wide-opening lens enables the photodiode to get enough light reflected from a barcode even when the barcode is near or far away at a distance from a scanner mirror.

References

[1] H. Wakaumi and C. Nagasawa. *Optical Review*, 8 (2001) 101-106.

[2] H. Wakaumi and C. Nagasawa. Proc. 16 European Conf. on Solid-State Transducers, pp. 353-356, Prague, Sep., 2002.

Feature Extraction for Yarn Evaluation

Vítor Carvalho[1], José G. Pinto[1], João L. Monteiro[1], Rosa Vasconcelos[2], Filomena O. Soares[1]

[1] Universidade do Minho, Dept. Electrónica Industrial, Campus de Azurém, 4800-058, Guimarães, Portugal, vcarvalho@dei.uminho.pt
[2] Dept. Engenharia Textil, Universidade do Minho, Portugal

Summary: *The aim of this paper is to present an experimental procedure to measure yarn evenness in real-time using capacitive sensors; samples with several millimetres are analyzed, depending on the type of sensor used. The new approach allows a direct measurement in 1mm range, with software sensitivity regions for yarn classification (considering Uster tables as a reference). This paper pays special attention to the importance of the spectral analysis in yarn evaluation and which procedures are needed to extract useful information.*
The final goal is to allow real-time actuation on a ring spinning frame when faults or other parameters exceed the maximum acceptable values for a given quality.

Keywords: *Yarn Evenness, Capacitive Sensor, Signal Processing, Spectral Analysis.*
Category: (9) *System architecture, electronic interfaces, wireless interfaces or (10) Applications.*

1 Introduction

Yarn irregularity is an important feature to assess its quality. This requires an arrangement of the fibres in which there is always the same number of fibres of a grouping in each cross section (longitudinal variation). Irregularity is used to evaluate variation in several characteristics along a strand (yarns, roving, sliver or tops) and unevenness measures the mean variation in linear density of a strand or part of it. Thus for purposes of yarn processing efficiency that influences final clothing appearance, there are levels of unevenness beyond which the yarn is unacceptable.

The final goal is to increase the quality specifying tough requirements. The use of the new solution developed improves quality control procedures during production.

For detection of such irregularities it is still applied nowadays electronic capacitance testers as a convenient and a reliable method of testing irregularity (determination of mass). Industrial systems use capacitors with 8mm length that allow mass measurements with 8 mm resolution. Mass yarn evaluated in 1 mm range is of utmost importance for a correct detection of irregularities as most of them have a short length (between 1 and 4 mm length) [1]. This paper presents a novel capacitive sensor that measures directly 1 and 4mm yarn mass. It also presents new software that, based on data acquisition and signal processing algorithms, allows the evaluation of all yarn relevant parameters.

2 Sensor design

A new capacitive sensor with parallel plates is developed, together with the electronic conditioning circuit, which allows 4 mm yarn mass reliable measurements. Based on the results obtained with this 4 mm capacitive some improvements were made in the 1mm length sensor. The studies undertaken show that a capacitance variation of 2,08E-17 F is expected when a 57 tex (0,057 g/m) yarn is used. Nevertheless, careful design of conditioning circuits was needed due to the low SNR.

As radiation is a major problem a solution with two sensors was used in a differential configuration (Figure 1). With this technique it would be possible to use the same equipment for two different yarn diameters. The use of a differential set-up makes the electric circuit more robust to temperature and air humidity variations, which are particularly important in textile industries.

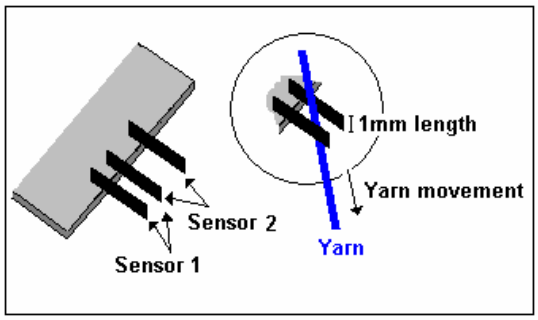

Fig 1. Representation of the two sensors

This system is to be used for on-line control of a ring spinning frame in order to evaluate the yarn evenness produced. Presently, in spinning mills this kind of evaluation is made off-line in laboratory using a small amount of yarn. The tests made with this system show good performance in laboratory environment. The experimental set-up used consists

on a PC with a data acquisition system together with a 4mm sensor and electronics.

2 Data Analysis

To classify yarn's quality tested it was developed a software using Labview™ 6.1. This software analyze the yarn in real time, depending of the input parameters for the acquisition: sensor input analog channels (up to 2 channels), yarn speed (m/min) or sample frequency (Hz), linear mass of yarn (Tex, Ne), set up of two groups of 4 values of sensitivity (%), one group for thin and thick points and other for neps, location of the results files, type of sensor (mm), sample length (m), output digital channel. Although there are established sensitivity values (thresholds) for classification of yarn faults (thin places - a decrease (50%) in the mass during a short length (4 mm), thick places - an increase in the mass, usually lower than 200% and lasting more than 4 mm and NEP's - huge amount of yarn mass in a short length (typically from 1 to 4 mm)), the user can define up to four sensitivities values, to perform a detailed analysis.

Sensitivity is the yarn mass threshold to detect a particular fault, regarding yarn mass average. For instance, sensitivity of 80% to detect thin points means that mass measurements below 0.8 of mass average is considered a fault. The output digital channel is used because the process of turning on/off the machine that controls the yarn speed is computer controlled, depending on the sample length to be analyzed and the yarn speed.

Several data is presented to users, namely: sensor input data (V), mass yarn variation (%), Spectrum, mean absolute deviation U(%), variation coefficient CV(%), deviation rate DR(%) and integral deviation rate IDR(%) for each sensitivity. The number of thin points, thick points and neps for each value of sensitivity, is also presented.

Complementary information is also available to users, as: FFT frequency peak and its power, sensor voltage without yarn (V), average voltage level of yarn (V), final and actual acquisition time (s), machine state (on/off), actual sample length (m), result files [5].

The developed software allows on-line processing, that is guaranteed using the buffer zero acquisition mode. The evaluation of the spectrum using FFT and result data files storage is only possible after the overall acquisition. Having the information of yarn linear mass, U (%), CV(%) and the faults measured for each sensitivity we are able to classify the sample in terms of quality, considering the tables published by the Switzerland label Uster for 8 mm sensors. However, the major innovation is the exact presentation of results with 1mm resolution.

Despite of the on-line version of this software, there is also an off-line version in which the inputs are the values of tension of the sensor during a previous run. This improvement makes also possible to perform new tests on already acquired samples.

Analyzing the magnitude spectrum obtained, it is very difficult to extract useful information, despite the presence of peak frequencies. Because of this we need to reproduce the FFT spectrum in energy bands, using its previous results. This approach is based on grouping samples of the magnitude spectrum in a selected number (n). The values extracted from the spectrum are summed and averaged for each group. With this procedure we are able to detect periodic imperfections caused by an incorrect processing in the mill despite of other information as the fibers constitution length[6].

3 Conclusions

The results point out that the evaluation of yarn mass, with this approach, is feasible at 1 mm range.

With this developed technique we are able to extract yarn mass values 1 to 4 mm range and using mathematical treatment is possible to compare the results with Uster standard tables (8mm yarn samples).

The main goal of this project is to develop a new technique that allows us to measure on-line 1 mm yarn mass in a spinning frame.

Acknowledgements

The authors are grateful to FCT project funding, contract n. POSI/P/EEI/13189/98.

References

[1] J.L. Monteiro and C. Couto, Pulse Frequency Calculation and Estimation in Yarn Evenness Analysis, *IECON' 95*, (pp. 985-989).

[2] S. Monteiro, R. Vasconcelos, F.O. Soares and J.L. Monteiro, Yarn Evenness Control in 1 mm Range, *Controlo 2000*.

[3] F.O. Soares, R. Vasconcelos and J.L. Monteiro, Influence of measurement length in yarn evenness control, *CA 2001*, (pp215-219).

[4] J.G. Pinto, R. Vasconcelos, F.O. Soares and J. L. Monteiro, High resolution yarn mass measurement, *ITM' 2001*, (pp425-430).

[5] V. Carvalho, J.G. Pinto, J.L. Monteiro, R. Vascocelos, F. O. Soares, On line measurement of yarn evenness, *ISIE'2003*.

[6] J.L. Monteiro, Sistema Distribuído de Análise da Regularidade de Fios Têxteis, PhD thesis, University of Minho, September, 1990.

Sensor Feature Extraction by Morphological Descriptors of Trajectories in Phase Space

E. Martinelli[1], G. Pennazza[1], C. Falconi[1], A. D'Amico[1,2] and C. Di Natale[1,2]

[1] Department of Electronic Engineering, University of Rome "Tor Vergata" via del Politecnico 1; 00133 Roma; Italy

[2] CNR-IMM, Via del Fosso del Cavaliere; 00133 Roma; Italy

Summary: *In this paper an alternative feature extraction from chemical sensor signal is introduced. The approach here presented is based on dynamic moments. The concept and its practical application is discussed through the illustration of practical examples.*
The alternative feature is compared with the more usual approaches using the classification performance in typical electronic nose applications as a comparison criterion.

Keywords: *feature extraction, chemical sensor, dynamic moments*
Category: *signal processing*

1 Introduction

Since sensing mechanisms of chemical sensor are still far to be completely understood, alternative approaches to sensor data representation may result in additional information improving the knowledge of chemical and physical processes at the sensor-environment interface.
The developments of the analysis of non-linear systems suggest that it is possible to investigate alternative strategies for signal modelling in a variety of applications.
In particular, the definition of new signal models may lead to new kinds of signal processing and feature extraction. In the case of chemical sensor, this kind of investigation could brings to the introduction of better descriptors of the sensor-analyte interaction resulting in an improved sensor accuracy. In this paper, we limit ourself to the definition of alternative features for qualitative analysis, namely the typical electronic noses applications aimed at classifying among a limited number of classes.
From this pattern recognition point of view a "feature" is any direct or derived measurement of the entities to be classified that helps differentiate between classes. In chemical sensor array, the individual measurements are the entities that have to be assigned to classes, and a measurement is a sequence of temporal ordered sensor signals taken during the exposure of the sensor to the sample.
The definition of the feature is then a fundamental step in data analysis process.
Feature extraction has been faced by several authors in the past years, and a manifold of features have been defined taking into consideration the sensor signal in the time domain. An almost exhaustive empyrical comparison of the feature that can be defined from the sensor signal can be found in ref. 1.
Recently a different approaches tried to describe the sensor signal in different domains, introducing a sensor phase-space [2].
In this paper, the sensor response is studied in a phase space and dynamic moments are introduced as descriptors of the sensor measurements. The practical use of moment descriptors will be illustrated through a typical electronic nose application where the moments are used as the features of a pattern recognition problem.

2 Dynamic Moments and chemical sensors array

Given a system whose state is completely described by n scalar variables, different states correspond to different points in a n-dimension vector space defined by an orthonormal basis where each direction corresponds to one of the scalar variables. The main property of such space, here called phase space, is in the univocal correspondence between points in the space and states of the system.
The dimension of phase space is based on Taken's Embedding Theorem [3]. with an appropriate choice of time delay τ, we can define this k-dimensional space as:

$$x(t)=\left[s(t)\ \ x(t+\tau)\ \ \ldots s\left(t+(k-1)\tau\right)\right] \qquad (1)$$

The representation of the system time series *x(t)* in this space produces a series of trajectories that expresses the underlying dynamical properties of the system. When these trajectories are bounded in a restricted zone of the space they are called attractors of the system.
The morphological descriptors of the attractors in the phase space can be used to obtain some information about the system dynamics. Such descriptors are used in the shape analysis of objects and are parameters analogous to the second

moments of the area of an geometrical figure in a 2-D space. It is possible the define different morphological descriptors, here called moment descriptors, in the phase space. Moments are calculated considering the coordinates and bisectors of the phase space and as depending of the time delay. For our applications we have considered the following moments:

$$MD2 = \frac{1}{n}\sum_{t=1}^{n} x_t y_t \quad (2)$$

$$MD3_{PB} = \frac{\sqrt{2}}{2n}\sum_{t=1}^{n}\left(x_t^2 y_t - x_t y_t^2\right) \quad (3)$$

$$MD3_{SB} = \frac{\sqrt{2}}{2n}\sum_{i=1}^{n}\left[2x_i^3 + 3\left(x_t^2 y_i + x_i y_i^2\right)\right] \quad (4)$$

$$MD3_X = \frac{1}{2n}\sum_{i=1}^{n}\left(x_i^3 + 3x_i y_i^2\right) \quad (5)$$

$$MD3_Y = \frac{1}{2n}\sum_{i=1}^{n}\left(x_i^3 + 3x_i^2 y_i\right) \quad (6)$$

where the number represents the moments degree, PB and SB the Principal Bisectors and Secondary Bisectors respectively, x and y indicate the time series x and y are related to the time series of the sensor signal s(k) in the following way: x=s(k) and y=s(k+τ). Each moment describes different morphological characteristic of the phase space trajectory that depends on system dynamic and on the time lag used for the moment calculus.
It is possible to apply this approach to the sensor response and extract the dynamic moments from the trajectories that these sensors spanned in the phase space.

3 Example of Application

In order to compare the performance of these novel features with the standard features, an electronic nose experiment related to the identfication of two different peaches farming, biological and standard, is considered. Measuerements have been performed with the enQbe electronic nose the last prototype developed at the University of Rome "Tor Vergata". From the signals four different features are calculated: integral of the response, steady-state signal shift, integral and steady-state shift together, and the dynamic moments.
As classification method the discriminant analysis solved by partial least squares (PLS) was adopted
In table 1 the results of the analysis are shown. The use of the dynamic moments improves the performance. For others features the prediction of correct classifications in the case of Biological cultivars is not adequate.
Figure 1 represents the score plot of the first two latent variables of PLS-DA model, built from dynamic moments, confirms the trend of the system to separate the two clusters using these features.

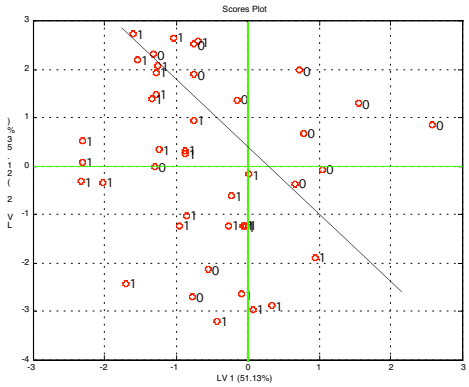

Fig. 1. The score Plot of the first two latent variable of PLS-DA model built with the dynamic moments as features.

Table 1. A comparison of Correct Classification rate for each classes obtained by PLS-DA using different features

Features	Standard farming	Biological farming
Integral of the response	100%	7%
Steady-state signal shift	96.78%	42.8%
Integral + Shift of Fequency	93.54%	42.8%
Dynamic Moments	96.78%	100%

References

1. T. Eklov, P. Mårtensson, I. Lundstrom; Selection of variables for interpreting multivariate gas sensor data, *Analytica Chimica Acta*, 381 (1991), pp 221-232.
2. E. Martinelli, C. Falconi, A. D'Amico, C. Di Natale; Feature extraction chemical sensors phase space, *Sensors and Actuators B* in print
3. F. Takens, "Detecting strange attractors in turbolence", in D. Rand and L.S. Young, editors, *Dynamical Systems and Turbulence*, Warwick 1980, pp 366-381.

Configurable Virtual Sensors with Image Processing Tools for a robotic football team

F. Ribeiro, P. Braga, J. Monteiro, I. Moutinho, P. Silva and V. Silva

Grupo de Automação e Robótica, Departamento de Electrónica Industrial,
Universidade do Minho, Campus de Azurém, 4800 Guimarães, Portugal
email: fernando@dei.uminho.pt http://www.robotica.dei.uminho.pt

Summary: *RoboCup is a scientific challenge created to foster research and development in fields like mobile and autonomous robotics, sensors, automation, electronics, computer vision and image processing, as well as other related areas. It consists of a football and/or rescue competition with several different leagues. The robot players use several different sensor types and sensorial fusion is of extreme importance. Sensors used by most team are described in this paper, as well as a new approach taken by this team which uses vision for the capture of most sensory data. Virtual sensors were developed using image processing and these proved extremely successful. Practical applications will be given in the paper.*

Keywords: *Virtual Sensors, Computer Vision, Image Processing, RoboCup, Robotic Football*
Category: *9 (System architecture, electronic interfaces, wireless interfaces)*

1 Introduction

For those unfamiliar with the RoboCup event, they can read the objectives and games rules on [1].

Compared with the Chess challenge launched in the middle twentieth century, RoboCup raises other more complex problems

Table 1. Chess versus RoboCup challenge.

	Chess	RoboCup
Environment	Static	Dynamic
State Change	Turn Taking	Real Time
Info Accessibility	Complete	Incomplete
Sensor Reading	Symbolic	Non-symbolic
Control	Central	Distributed

Therefore, the perception system and sensorial fusion needs a special attention since it is the basis of this challenge.

Although many teams prefer to buy a standard off the shelf robotic platform and implement changes in hardware/software or even adaptations, Minho team which has been participating on RoboCup since 1999 [2][3], builds its own platforms from scratch (see Figure 1). Being part of an Industrial Electronics Department they build the mechanics, the hardware and the software, bearing in mind that the budget is extremely low. This continuous participation in RoboCup has led to new developments in many fields especially in electronics and sensorial systems.

A Robotic football player is nothing else but a multi sensory system, a processor and a group of actuators. The information it perceives needs to be at a higher level due to the complexity of the game. Besides that, a team has several different robots, which complicates even more the game strategy. Cooperation is of extreme relevance since in a group of robots each individual shouldn't do the same task as others, otherwise they will importunate each other.

Fig. 1. Minho Team Robot.

The Robocup rules do not limit the use of any type of sensors, unless these are outside the football field or if they interfere with the opponent team. Therefore, teams tend to use many kinds of sensor like Lasers, Ultra-sounds, Infrareds, Computer Vision and Image Processing, Micro-switches, digital campus, and many others [4]. These are mainly used for Ball detection, Goal detection, opponents detection, collision avoidance, Self-Localisation within the field, Odometry, Communication between robots, Path planning, etc.

Many problems occur from the sensor readings like the precision and accuracy of the values read being not sufficient, lots of noise, low speed for the real time processing necessary, etc. The faster the robot perceives where the ball and the goals are, the faster it can act to score a goal. In systems with several different type sensors, sensorial fusion is extremely important and perception success depends upon it.

Minho team uses traditional sensors (infrared encoders specifically developed for that purpose) on each wheel in order to control each motor speed. But apart from that, all other parameters extracted from the game are taken from the vision system.

A group of standard routines were developed such that they can be configured in a configuration text file without the need for recompiling the game strategy code. These routines were written in Assembly language in order to optimize its processing speed.

Although many different vision head types are being used [5], Minho vision head is located in the robot's top center and consists of a camera pointing upwards on a parabolic mirror facing downwards. The camera can see itself on the mirror image but that part of the image is black and easily ignored. With this technique, the robot can see 360 degrees around it maintaining the ball and most game entities always in sight. The image is centered which simplifies the software build up but distorted although that is overcome by knowing the mirror curvature. The tools developed consist of three types: Histogram, Area and Colour. For each of these, a group of parameters is input to the system through a configuration text file, like the window coordinates, the threshold and the required colour. The structure of a Histogram type virtual sensor consists of:

```
struct HISTOGRAM {
    struct hist {
        int x1, y1, x2, y2;
        int peakCoordinate;
        int flag;
        int maximum;
    } H[MAX];
    int n_HIST;
    int colour;
    int flagHISTon;
    int flagSeeRectangle;
} HIST;
```

Fig. 2. Histogram Virtual Sensor Data structure.

Users without much programming knowledge can easily add virtual sensors to the game strategy, just by editing a SETUP text file. The main routines are Histograms, Areas and Colours. Parameters like the window coordinates, the threshold and the required colour are only examples. Figure 3 shows an example of a Histogram Virtual Sensor, which is used to detect peaks of a certain colour. This function return the coordinate with the highest value for the desired colour. The histogram is also displayed under the image to compare and check the results.

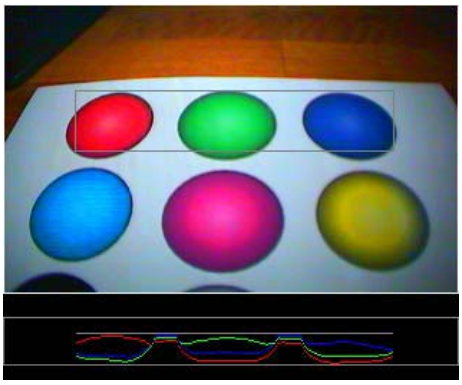

Fig. 3. Histogram Virtual Sensor in use.

These routines have been in use by this team and proved successful. This paper will describe all the virtual sensor routines, its usage, and its working basics. Several examples of its usage will be given.

References

[1] http://www.robocup.org

[2] C. Machado, S. Sampaio, B. Martins and F. Ribeiro. Minho robot football team for 2001. In: A. Birk, S. Coradeshi and S. Tadokoro, eds. *RoboCup 2001: Robot Soccer World Cup V*, pp. 657–660, Berlin, Germany, 2002. Springer LNAI 2377.

[3] C. Machado, I. Costa, S. Sampaio and F. Ribeiro. Robotic Football team from Minho University. In: M. Veloso, E. Pagello and H. Kitano, eds. *RoboCup 99: Robot Soccer World Cup III*, pp. 731–734, Berlin, Germany, 2000. Springer-Verlag.

[4] S. Monteiro, F. Ribeiro and P. Garrido. Problems, Solutions and Trends in Middle-Size Robot Soccer – A review. In: *Robotica'2001 – Festival Nacional de Robótica*, 25-28 April 2001, Guimarães, Portugal. Printed in CD-ROM.

[5] P. Lima, A. Bonarini, C. Machado, F. M. Marchese, C. Marques, F. Ribeiro and D. G. Sorrenti. Omni-Directional Catadioptric Vision for Soccer Robots. In: *Special Issue of the Robotics and Automation Systems Journal*, Amsterdam, Vol. 36, No.2, 31 August 2001. Elsevier.

Low Frequency Ultrasonic Transducers Based on Bimorph Ceramics

M. Santos[1], A. Ferreira[1], J. Perdigão[1] and J. Velho[2]

[1]Dep. Eng. Elect. Comp., ICEMS, FCTUC, Univ. Coimbra, Polo II, 3030-329 Coimbra, Portugal
email: marioj@deec.uc.pt http://www.deec.uc.pt
[2] Dept. GeoCiências, Univ. Aveiro, Aveiro, Portugal

Summary: *There is a growing interest for ultrasonic non-destructive technique that allows the characterization of various mechanical properties of paper. Due to the restrictions in the use of viscous fluids or bonding agents for coupling in this kind of material, new transducers have been developed to overcome these limitations. This article presents a simple way to use bimorph ceramics to construct transducers for ultrasonic velocity measurements in paper. In design and conception, impedance spectroscopy was used for transducer performance optimization. After, a multi-transducer measuring head that incorporates 18 transducers elements was developed and integrated in a final ultrasonic prototype, for strength and elastic in-plane properties evaluation.*

Keywords: *bimorph, ultrasonic, paper*
Category: *10 (Applications)*

1 Introduction

Ultrasonic trough transmission and pulse-echo techniques are widely used for inspection of materials. In a typically application the transducers are electrically pulsed and coupled to the test object. In paper, traditionally coupling techniques can't be used so, other type of transducers must be developed to overcome this problem. In our work a new transducer was constructed using lead titanate zirconate piezoelectric ceramics.

Bimorphs and unimorphs configurations that are widely used in many applications including position controlling, vibration damping, noise control, acoustic sensing, etc, [1] were studied and impedance spectroscopy analyze was used for electrical transducer behavior characterization. These transducers were integrated in a system that automatically determines the in-plane ultrasonic velocity of paper sheets. As tensile stiffness index (TSI) is a measure of the elastic property of paper [2] and is given by

$$TSI = v^2\, C \qquad (1)$$

it can be easily estimated, since v is the ultrasonic velocity and C a dimensionless constant related to the Poisson´s ratio of the material, that is approximately unitary for paper. Once TSI known for the different orientations, the tensile stiffness orientation angle (TSO) that is defined by the orientation of the maximum of the TSI plot and the paper machine direction can be evaluated.

2 Transducer design and characterization

In transducers conception were used ceramic multilayer bender (bimorph) manufactured by Ferroperm Piezoceramics. This ceramics [3] are built up from very thin layers of piezoelectric material and built-in internal electrodes. Internal electrodes extend to the rear end of the component and are connected to a set of 3 external electrodes. The selected material was lead titanate zirconate piezoelectric PZ29, due to its high strain with high dielectric constant and also low hysteresis and creep. The configuration used is of parallel type. The ceramics have a rectangular shape with dimensions of 21x7.8x1.8 mm (length/width/thickness).

Theoretical fundamental natural bending resonant frequency of a cantilever comprising a PZT bimorph [4], is given by

$$f_r = \frac{3.52\,t}{4\pi l^2}\sqrt{\frac{E}{3\rho}} \qquad (2)$$

where t is the thickness, l the free length, E the Young's modulus and ρ the density. From (2) we can easily see that we can control the resonant frequency of the cantilever by controlling the free length of the ceramic. As transducer housing is made by two aluminium pieces that hold the ceramic and are tied by 4 screws, unscrewing the screws can easily provide control of free length of the ceramic for test proposes.

In figure 1 is presented the ceramic behavior with free length increasing. Theoretical and experimental agreement for fundamental mode (A) is achieved for high values of the free length. Some discrepancies appear for low values of free length, probably due to imperfections on housing conception. The harmonic B only exists for values of l higher than 12mm. The harmonic C has a more or less constant value around 86 kHz.

Next step of our work was the selection of the working frequency, that must ensure a good S/N

ratio of the collected signals and by other side must lies above audio range to guarantee a less noisy system. Experimental tests were done using two transducers, one as transmitter the other as receiver, in contact with common sheet of paper. As transducer real part of impedance is very low (about 5 Ω) a matching circuit must be use to improve transducer energy delivery. Using a tone-burst excitation with a decreasing sweeping frequency it was verified that only near 30kHz the collected signal presents a reasonable S/N ratio. These experiments and practical considerations shown that the best compromise is obtained using a 21 kHz tone-burst excitation.

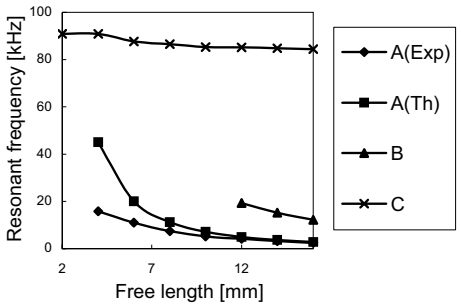

Fig. 1. Resonance frequency versus free length.

3 TSI measuring system

Paper is a highly directional material (anisotropic), meaning that its properties vary with direction. This anisotropy is related with fiber orientation due to the fabrication process.
One of the fundamental goal of paper makers is to minimize TSO angle, i.e. guarantee orientation of TSI plot coincident with machine direction. Measuring the ultrasonic velocity in several sheets directions determines TSI plot. This can be done using a pair of transducers and a rotation system. In our work a different approach was used. Instead of a rotation head, a multi-transducer prototype was employed (Figure 2).

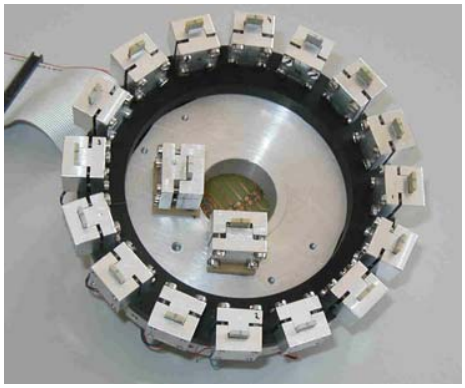

Fig. 2. Measuring head prototype.

The system integrates 9 pairs of transducers, analog multiplexing is used in both emitter and receiver stages and the system is PC controlled by means of an acquisition board and LabView software.
In figure 3 are presented two typical TSI plots obtained with this system, one corresponds to a common writing paper sheet showing its anisotropy and the other to a laboratorial hand made isotropic paper.

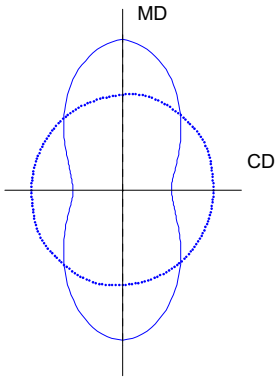

Fig. 3. TSI plots for common writing paper (-) and hand made paper (···).

3 Conclusions

The knowledge of TSI of the product being produced allows the papermaker to have a new way to optimize the process that is a time consuming task when using conventional rotation systems. This work describes a new measuring head that allows strength and elastic in-plane properties evaluation of paper. Bimorphs widely used as actuators, were successfully integrated in our prototype. Good accuracy, less time consuming and additional information can be obtained with this system.

References

[1] Q. Wang,X. Du, B. Xu and L. Cross, "Electromechanical coupling and output efficiency of piezoelectric bending actuators", *IEEE Trans. Ultrason., Ferroelect., Freq. Contr.*, 46, (3), 638-646, 1999.
[2] C. Habeger, R. Mann and G. Baum, "Ultrasonic plate waves in paper", *Ultrasonics*, 17, (1), 57-62, 1979.
[3] Ferroperm Piezoceramics A/S, "Ceramic multilayer bender", *Application Note*, 1-16, 2000.
[4] K Yao, W. Zhu, K. Uchino, Z. Zhang and L. Lim, "Design and fabrication of a high performance multilayer piezoelectric actuator with bending deformation", *IEEE Trans. Ultrason., Ferroelect., Freq. Contr,* 46, (4), 1020-1027, 1999.

Fiber Optic Sensors for Cracking Detection and Monitoring

P. Cruz[1], C. K. Y. Leung[2] and A. Diaz de León[1]

[1]Civil Engineering Department, University of Minho, 4800-058 Guimarães, Portugal
email: pcruz@civil.uminho.pt http://www.civil.uminho.pt
[2]Hong Kong University of Science & Technology, Hong Kong, China

Summary: *Advances in the production of optical fibers made possible the recent development of innovative sensing systems for health monitoring of civil structures. The main reasons of this development are the reduced weight and dimensions of fiber optic sensors, the strong immunity to electromagnetic interference, the improved environmental resistance and the scale flexibility for small-gage and long gage measurement. This paper provides an overview of the characteristics of the fiber optic sensors for cracking detection and monitoring. The application to reinforced concrete structures will be described.*

Keywords: *Fiber optic sensor, cracking, monitoring*
Category: *10 (Applications)*

1 Introduction

The existing healthy condition of many important concrete structures can be assessed through the detection and monitoring of cracking. For example, in concrete bridge decks, crack openings beyond 0.15 to 0.2 mm will allow excessive penetration of water and chloride ions, leading to corrosion of steel reinforcements.

Conventionally, crack detection and monitoring for bridges have been carried out by visual inspection. The procedure is time consuming, expensive and yet unreliable. Recently, various researchers have developed fiber optics based crack sensors for concrete structures. Existing optical crack sensors are, however, very limited in their applications. For example, sensing based on fiber breakage [1] can distinguish between the presence or absence of cracking but cannot provide information on gradual structural degradation. "Point" sensors developed by Ansari and Navalukar [2] can detect and monitor the opening of a crack only if the cracking occurs in a small region that is known a priori. The sensor employed in this study was based on measurement of intensity loss due to deformation. These sensors were calibrated and were embedded in a fiber reinforced concrete specimen.

Zako et al. [3] used an OTDR to measure the cracking point by Fresnel reflection of four optical fibers, which have been bonded to the surface of mortar beam with epoxy resin. In addition, the crack propagation in the mortar beam can be also measured by the breaking sequence of four optical fibers.

Gu et al. [4] developed a distributed fiber optic sensor consisting of individual segments spliced on one line. By measuring the Fresnel reflection at each splice between two pieces of fiber, the average strain within each piece can be obtained. Based on the strain reading, the severity of cracking within a certain region can be assessed. An optical time domain reflectometer (OTDR) was employed for interrogation of the sensor signal. Structural monitoring capability of the sensor was evaluated through experiments with reinforced concrete beams.

If the splices are placed very close to one another, cost will be high and also the forward signal may drop rapidly with distance (due to the presence of many reflection points), making the sensor inapplicable to real structures where a long sensing length is required [5].

Cai et al. [6] applied the distributed optical fiber sensing technology to detect the cracks in a small-scale plaster model test of an arch dam. By using OTDR the real time monitoring of cracks can be realized. The practice of this technology shows that the sensor network bonded to the downstream surface of the dam will not affect the stiffness of the model, but it must be correctly distributed.

Researchers at MIT and Brown University developed a sensor for the reliable detection and monitoring of cracks in concrete structure [7]. The sensor is based on a distributed optical fiber microbending sensor. An optical fiber is embedded in the concrete element in a "zigzag" shape (Fig. 1). Using OTDR equipment, the light intensity distribution along the fiber is measured.

Before the formation of cracks, the backscattered signal along the fiber should follow a relatively smooth curve. In the straight portions of the fiber, the small loss is due to absorption and scattering. In the curved portion (where the fiber turns in direction), macrobending loss may occur depending on the radius of curvature.

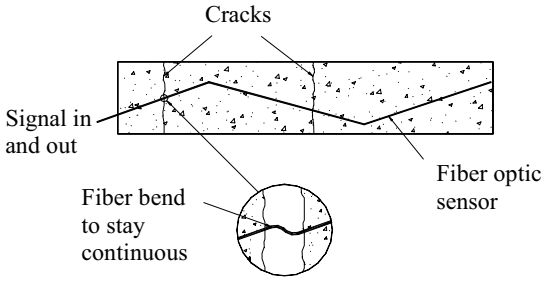

Fig. 1. Principle of operation of the "zigzag" sensor

When a crack opens in the structure, a fiber intersecting the crack at an angle other than 90º has to bend to stay continuous (Fig. 1). This perturbation in the fiber is very abrupt, and thus can be considered as microbending. This microbending results in a sharp drop in the optical signal (Fig. 2). This intensity loss is detected and located by means of the OTDR equipment. Also, from the magnitude of the drop, the crack opening can be obtained if a calibration relation is available.

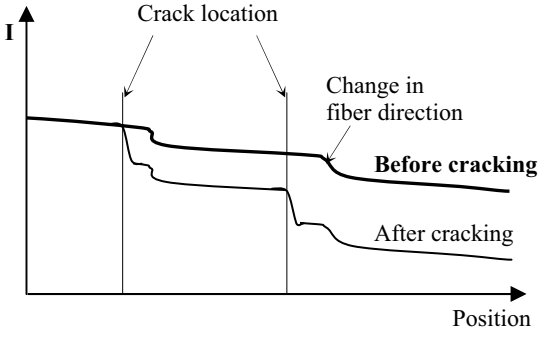

Fig. 2. Intensity along the fibre, measured by means of the OTDR equipment

The proposed technique does not require prior knowledge of the crack locations, which is a significant advancement over existing crack monitoring techniques. Moreover, several cracks can be detected, located and monitored with a single fiber. However, the crack direction is needed for measure the crack opening. An ideal application of the sensor is in the monitoring of flexural cracks in bridges, which may appear at arbitrary locations along the deck, but essentially perpendicular to the spanning direction. A method for applying the sensor to existing structures was recently proposed and is called the Sensor Plate [5].

To achieve the requirements in the monitoring of cracks on bridges the sensor plate is being now improved by researchers of the University of Minho, in Portugal, and of the Hong Kong University of Science and Technology.

This paper as first fruits present the results of laboratory test accomplished over material witch is utilized to make the sensor plate, the purposes of this test were related with the perform in behavior of the sensor plate to distinct cases in the field, taking into account different combinations of low and high temperature and crack opening, the last of this accomplished with the reinforced of the material with fiberglass.

References

[1] Rossi, P., and LaMaou, F. (1989). "New Method for Detecting Cracks in Concrete Using Fiber Optics." Materials and Structures, RILEM, 22(132), 437-442.

[2] Ansari, F., and Navalurkar, R. K. (1993). "Kinematics of crack formation in cementitious composites by fiber optics." Journal of Engineering Mechanics, ASCE, 119 (5), 1048-1061.

[3] Zako, M., Uragaki, H., and Kodate, K. (1995). "On intelligent structures using optical fiber (crack sensing with optical fiber)." Jour. of JSMS, 44(499), 493-497.

[4] Gu, X., Chen, Z., and Ansari, F. (2000). "Embedded Fiber Optic Crack Sensor for Reinforced Concrete Structures." ACI Structural Journal, 97(3), 468-476.

[5] Olson, N.G. (2002). "Mechanical and optical behavior of a novel optical fiber crack sensor and an interferometric Strain Sensor." PhD Thesis, Massachusetts Institute of Technology, September.

[6] Cai, D., He, X., and Zhang, L. (2001). "Distributed optical fiber sensing technology for crack detection in the small scale plaster model test of arch dam." Journal of Hydraulic Engineering, Chinese Hydraulic Engineering Society, Water Resources and HydroPower Press of China, 2.

[7] Leung, C., and Elvin, N. (1997). "Micromechanics Based Design of Optical Fiber Crack Sensor." Intelligent Civil Engineering Materials and Structures, edited by Ansari, F., Maji, A. & Leung, C., ASCE, 150-163.

Array of ISFETs for Express Environmental Monitoring

A.L. Kukla, Yu.M. Shirshov, A.S. Pavluchenko

Institute of Semiconductor Physics, 45 prosp. Nauki, 03028 Kiev, Ukraine
email: kukla@isp.kiev.ua http://www.isp.kiev.ua

Summary: *A multi-sensor based on array of ISFETs made by standard silicon technology with SiO_2-Si_3N_4 insulator layers have been developed for determination of toxic substances in drinking water and foods. The multi-sensor consists of a two thin silicon plates with a special enzyme tape between them. Basing on the enzyme activity measurements for acetyl- and butyrylcholinesterase, glucose oxidase and urease the investigation on determination of a number of heavy metals ions and phosphororganic pesticides in water solutions were carried out. The content of toxic elements was determined by estimation of the residual activity of enzymatic membranes after the injection of analysed samples.*

Keywords: *multi-sensors; ISFETs, enzyme membranes; toxic substances*
Category: *10 (Applications)*

1 Introduction

Determination of toxic substances (in particular heavy metal ions and organic pesticides) in drinking water and foods is of primary importance nowadays. Laboratory techniques, usually used for this, are rather cumbersome and expensive. Enzyme sensors, being compact and having small response time, are more suitable for simple measurements and express analysis.

In our previous papers [1,2] we described the 6-channel electrochemical enzyme sensor based on capacitance pH-sensitive EIS sensors. We investigated a possibility of using of a multi-enzyme sensor for recognition of heavy metal ions and phosphororganic pesticides in solutions. This paper deals with the development of an enzyme multi-sensor based on array of ISFET sensors, as well as with using of the multienzyme analysis to identify organic pesticides and different heavy metal ions in water solutions.

2 Multi-sensor design

The designed multi-sensor consists of a two special silicon plates with enzyme tape between them (Fig.1). The one Si-plate (the upper) contains the ISFET array made on standard silicon technology with SiO_2-Si_3N_4 insulator layers on surface. The source-drain contacts for each transistor are leaded to the outside edge of the plate. The other Si-plate (the lower) contains a row of cavity cells and zigzag flow channels obtained by silicon etching. A planar Ag/AgCl reference electrode is built into the flow-injection system. Before measurements one have to tightly close this structure and then to inject an analysed solution through the flow-injection system.

The feature of the above multi-sensor is that all enzyme membranes are integrated into a polyethylene film of about 0.5 mm thick by thermal compression. This film is arranged between the both Si-plates in such a way that the enzyme circles are situated exactly opposite to ISFETs gates at the one side and cell cavities at the other side. Additionally the flexible polyethylene film itself serves as a hermetic sealing in such a way that solution may contact only with the gates regions of transistors. Enzyme tape may be either in a form of a single strip or as a part of rotatable tape roll. Because of the fact that the enzyme membranes did not restore the initial activity value after its contact with the toxic solutions we assume that replaceable enzyme membranes are more preferable than the permanent ones. Nitrocellulose (NC) sheets are very suitable for their preparation.

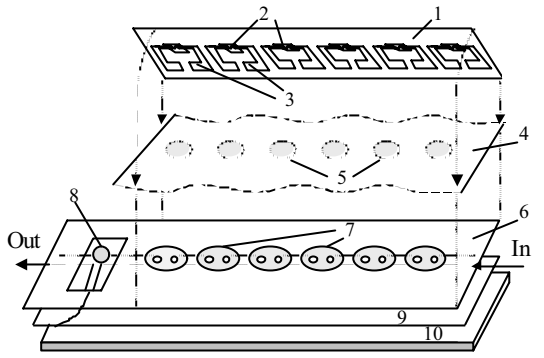

Fig. 1. Schematic view of sensor array: 1 – upper Si-plate with array of ISFETs, 2 – gate active area, 3 – connection to transistor contacts, 4 – polyethylene film, 5 – enzyme NC-membranes, incorporated in the film, 6 – lower Si-plate with inner flow-injection system, 7 – sensor cells, 8 – planar reference electrode, 9 – backside rubber sealing, 10 – support.

The enzyme membranes were prepared by deposition of 10% enzyme solutions with the 5-10

mg/ml concentration of enzymes on the NC-carriers. Glutaraldehyde was used for covalent grafting of enzymes to the carrier surface.

3 Results

With the above multi-sensor we perform the measurement of the enzyme activity for different forms of cholinesterase, urease and glucose oxidase. The conditions for enzyme sensors operation, such as buffer capacity, substrate concentration and time of incubation of enzyme membranes, were optimised to reach the maximal sensitivity of multi-sensor for analysis of heavy metal ions and organic pesticides in the investigated solutions.

Assuming the fact that enzymes used have essentially different sensitivity to metals and pesticides, and also noticeably distinguishing sensitivity to a row of different metals, we used a multienzyme analysis to recognize the heavy metal ions and organic pesticides in solutions as well as for determination of their content in the analysed samples [3,4]. To inactivate the enzymes, the chloride salts of the following heavy metals were used in our experiments: copper, cadmium, cobalt, nickel, tin, zinc, lead and strontium. Phasalone and 2,2-dichlorovinyl dimethyl phosphate were tested as organic pesticides.

Principal component analysis (ÐÑÀ) performed over the experimental data obtained from the sensor array was used to separate samples of toxic substances by their images. The base PCA matrix was formed of all data set for all tested substances in actual concentration range. It allows in the subsequent analysis of unknown substance (but from a number of previously calibrated ones) to detect not only type of substance, but also to determine its concentration.

Actual samples of solutions may contain also the mixtures of different toxic substances. In this case the PCA diagram does not allow to evaluate the contribution of separate elements to the given mixture. Therefore for more detailed analysis in mixtures we suggest the principle of dilution of investigated solution with the increasing degree (by 5, 10, 50 and 100 times) and multi-sensor measurement of residual activities of all enzymes followed by mathematical processing of obtained concentration curves. As a result of automatic comparison of these curves with the corresponding calibration ones some metals can be excluded from consideration, and as for the remaining ones, taking into account their relative weight in a general metal mixture, a conclusion of a possibility of presence in a solution in the certain concentration is made.

The threshold sensitivity of heavy metal ions detection was within the 10^{-4} to 10^{-7} mol/l range, depending on the type of the metal and the limit of detection of pesticides was 10^{-9} mol/l. Our experiments have shown that it is possible to detect all 8 types of heavy metal ions and 2 types of phosphororganic pesticides with help of above multi-sensor with accuracy of 10%, when it was a single substance, and of about 15-40%, when it was a mixture of different substances.

Our experiments have shown that developed sensor array in conjunction with the potentiality of multienzyme analysis followed by mathematical processing is well suitable for the environmental monitoring.

References

[1] N.F.Starodub, Yu.M.Shirshov, W.Torbicz, N.I.Kanjuk, V.M.Starodub, A.L.Kukla. Biosensor for in field measurements: optimisation of parameters to control phosphororganic pesticides in water and vegetables. In: D.P.Nikolelis et al, eds. *Biosensors for Direct Monitoring of Environmental Pollutants in Field*, Kluver Academic Publishers, 1998, pp. 209-219.

[2] N.F.Starodub, N.I.Kanjuk, A.L.Kukla, Yu.M.Shirshov. Multi-enzymatic electrochemical sensor: field measurements and their optimisation, *Analytica Chimica Acta*, v.385 (1999) 461-466.

[3] A.L.Kukla, N.I.Kanjuk, N.F.Starodub, Yu.M.Shirshov. Simultaneous control of phosphororganic pesticides and heavy metal ions by multi-enzymatic sensor, *Proc. of 9th International Fair and Congress for Sensors, Transducers and System,* v.2, pp. 105-110, Nurnberg, Germany, 18-20 May 1999.

[4] A.L.Kukla, N.I.Kanjuk, N.F.Starodub, Yu.M.Shirshov. Multienzyme electrochemical sensor array for determination of heavy metal ions, *Sensors and Actuators*, B57 (1999) 213-218.

Magnetic Field Sensor Application for the Measurement of Insulation Layer Thickness

A. Gasparics, G. Vértesy

Research Institute for Technical Physics and Materials Science, H-1525 Budapest, P.O.B.49, Hungary
email: vertesyg@mfa.kfki.hu http://www.mfa.kfki.hu

Summary: *A new, eddy current type measurement method has been developed, by applying a novel, high sensitivity magnetic field sensor, for the determination of the insulation layers' thickness, which cover the surface of conductive specimens. Insulation layer thickness up to 20 mm can be measured with good signal/noise ratio by this technique. It is also capable to take into account the probe tilting and the measurement process is fast enough.*

Keywords: *magnetic field sensors, eddy current measurement, insulation layer thickness measurement*
Category: *10 (Applications)*

1 Introduction

The quick, reliable and exact nondestructive determination of the thickness of insulation layers, which cover the surface of conducting materials is an important task in many areas of industry and research. The traditional inductive coil based method [see e.g. 1] is excellent up to some millimeters of the thickness. However, it is not possible to determine the thickness of thick (above 10-15 mm) layers by these devices, which is an important task in certain fields of application. The other drawback of these devices that they can hardly handle the probe tilting error, which often happens if the surface is rough. The aim of the present work is to show a new measuring principle, which is based on the application of a novel magnetic field sensor, and which provides high accuracy thickness measurement of the insulating layer in a wide range of its thickness.

2 Measuring principle

The schematic draw of the eddy current type experimental setup [2] can be seen in Fig.1. The exciting coil is used for generating ac electromagnetic field in the conductive material. This way the insulation layer is considered as a lift-off of the probe from the conductive surface. Between the sample and the exciting coil a Fluxset type magnetic field sensor [3] is placed. This sensor measures dc and ac (up to 100 kHz frequency) low level magnetic fields with high accuracy. The magnetic field resolution is 1 nT. Its principle of operation is close to the pulse-position type fluxgate magnetometers [4]. The device has small size, it is versatile, inexpensive and sufficiently robust to meet the demands of the industry. If the sensor is properly balanced, it measures only the axial component of the magnetic field, it is not sensitive to the perpendicular field. However, in this application, the sensor is not balanced exactly into the center position of the exciting coil. Therefore it measures the exciting field of the coil, too. This field is the result of the interaction between exciting coil and the conductive specimen. The specimen reflects the exciting field and modifies the field distribution around the exciting coil. The degree of this field modification depends on the distance between the coil and the specimen surface. As a consequence, the magnetic field detected by the Fluxset sensor depends on this distance as well.

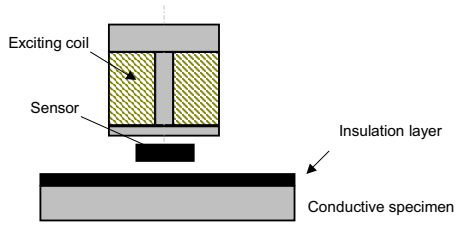

Fig. 1. Schematic draw of the experimental setup.

3 Numerical simulation

The results of the numerical simulation for 5 and 20 mm lift-off can be seen in Fig.2. It is easy to find out by comparing these figures, that the maximum of the B field (almost as well as the total energy of the magnetic field) is practically not modified in this range. Instead, the field distribution between the coil and the conductive specimen is changed slightly but in well visible way. Therefore, it is more reasonable to detect the change of the magnetic field distribution by using a magnetic field sensor, than to measure the change of the exciting coil impedance (i.e. the change of the total field energy).

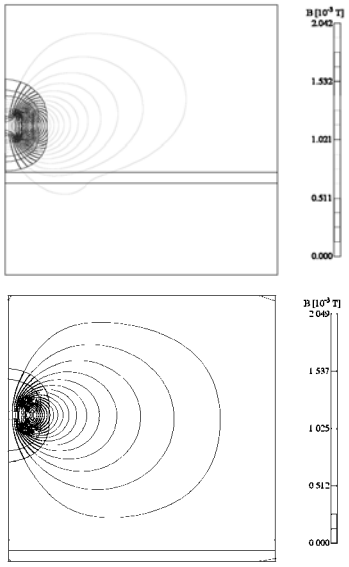

Fig.2: B field in case of 5 (above) and 20 mm lift-off.

Analyzing the differences of the magnetic field distribution 1mm below the coil and for the cases of 5 and 20 mm lift-off that results was found, which is illustrated in Fig 3. Here parallel (radial) and the perpendicular (axial) field components (with respect to the sample surface) are shown. Accordingly to this result, we can conclude, that measuring the radial field is much more expedient than the axial one. We got also that the sensor should have better field resolution than 10^{-4}.

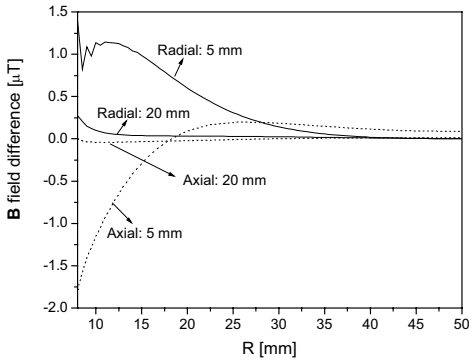

Fig. 3: Parallel (radial) and perpendicular (axial) field components (with respect to the sample surface) for 5 and 20 mm lift-off.

The Fluxset sensor measures only one component of the B field. This property makes this probe not sensitive for any tilting around the sensor axes, in contrast to the impedance type measurements. The inluence of the tilting was also analyzed perpendicularly to the sensor axes. It was found that the tilting of the probe caused different field distribution on the two sides of the exciting coil. This fact makes possible to detect the tilting independently of the lift-off and to take it into consideration this way.

4 Experimental results

Accordingly to the previously discussed requirements and also taking into account that the largest dimension of the recently used Fluxset sensor is 5 mm, it was found, that this sensor is one of the optimal choices for this application. A probe was developed without any further optimization and the experimental result, shown in Fig. 4, was obtained. The signal to noise ratio (of the whole signal processing chain) was better than 89 dB, which results better than 10^{-4} thickness resolution.

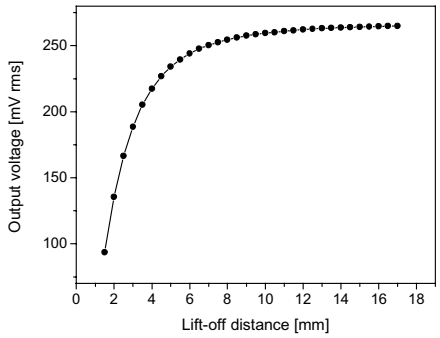

Fig.4: The measured change of the output voltage of the device as a function of the lift-off distance

4 Conclusions

A new measurement method has been developed for the determination of the insulation layers' thickness, which cover the surface of conductive specimens. By applying this method, insulation layer thickness up to 20 mm can be measured with good signal/noise ratio. Within the 0 - 5 mm lift-off range the reachable precision of the thickness measurement is ~0.12%. It is also capable to take into account the probe tilting and the measurement process is fast enough.

Acknowledgements
The financial support by Hungarian Scientific Research Fund (T-035264) and by EURATOM-EFDA Technology Workprogramme is appreciated.

References

[1] Siemens Testcenter, www.khe.siemens.de/IT/

[2] A. Gasparics, Cs.S. Daróczi, G. Vértesy, J. Pávó: Improvement of ECT probes based on Fluxset type magnetic field sensor, in *Electromagnetic Nondestructive Evaluation (II.),* pp. 146-151, R.. Albanese et al. (Eds.), IOS Press, 1998.

[3] G. Vértesy, A. Gasparics, J. Szöllősy: High sensitivity magnetic field sensor, *Sensors and Actuators A*, 85 (2000) 202

[4] P. Ripka: Review of fluxgate sensors, *Sensors and Actuators A*, 33 (1992) 129

An AC-based interrogation system for an hand-held electronic nose

V.D. Juncu, J.V. Hatfield

Department of Electrical Engineering and Electronics, UMIST, PO Box 88, Manchester M60 1QD, UK
email: John.Hatfield@umist.ac.uk

Summary: *Gas sensors based on organic polymers or metal oxide are widely used in gas, odor or aroma analysis. Electronic nose methods involved in these measurement systems use the multi-element array approach coupled with direct current (DC) interrogation techniques. Recently, experiments have been carried out where, with the help of a computer, an alternating current (AC) interrogation method produces an improved performance. This paper presents an AC-based interrogation system on a chip, using a single gas sensor to create the odor pattern, aimed for use in a hand-held electronic nose. Experiments upon volatile odors have been made and results are presented here.*

Keywords: *gas sensors, AC-based interrogation system, bandpass filter*
Category: *9(System architecture, electronic interfaces, wireless interfaces)*

1 Introduction

Gas sensors based on organic polymers or metal oxides are widely used in gas, odor or aroma analysis. By inputting a direct current (DC) into these sensors a certain resistance can be measured. When the sensor is presented with certain volatiles its resistivity changes, [1]. Thus, by using and array of sensors (for example, different conducting polymer materials for different sensors in the array), patterns of resistance change can be generated to characterize a volatile. In these measurements it has been considered that the only electrical property that exhibits change is the conductivity of the material. Recently, a more accurate model for metal and polymer based sensors have been developed, [2] which presents the sensor as a passive network of resistances, capacitances and inductances. Based on this model, experiments have been carried out where, with the help of a computer, an alternating current (AC) interrogation method produces an improved performance of the volatile reading, [3]. The method relies on the calculation of the Fast Fourier Transform of a signal coming from the sensor. This paper presents an AC-based interrogation system on chip, aimed for use in a hand-held electronic nose. Moreover, the number of sensors is reduced to a single one since it is possible to produce a volatile pattern consisting of readings taken at a wide range of frequencies. Essentially the system is a monolithic pseudo-spectrum analyzer, [4] which provides output voltage amplitudes in accordance with the frequency characteristics of the system under test (in our case the gas sensor). A noise-like signal is fed into the sensor and then a programmable bandpass filter is used to separate signals at different frequencies in a certain bandwidth. Further, the output from the band pass filter is input into a peak detector, which provides voltages proportional to the magnitudes of the frequency components selected by the previous circuitry in the system. The noise-like signal is needed because it exhibits a uniform power spectral density over a wide frequency range. Pseudo-random bit sequences (PRBS), [5] and chaotic signals, [6] have been used to generate such signal. The results show that gas sensors can readily be interrogated in a certain bandwidth, at different frequencies.

2 Architecture

The block diagram of the new AC-based interrogation system is shown in Fig.1.

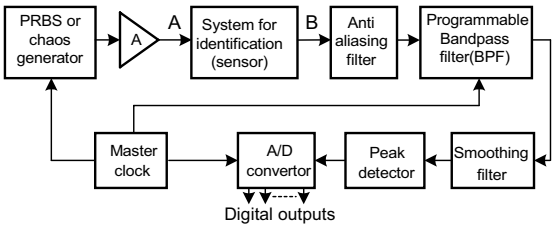

Fig. 1. Functional block diagram of the AC-based interrogation system

All the building blocks of this system have been implemented on a chip using a 0.6μm CMOS technology, and they perform the following operations. The PRBS or chaos generator provides the noise-like signal, which has components at almost all the frequencies in a certain range. These circuits are clock driven, and they exhibit an almost flat power density for frequencies up to one third of the clock frequency, [7]. Their outputs are conditioned through an amplifier, so the signal will have its amplitude limited to the input range subsequent circuitry can deal with. Moreover, one needs to insure that too high an amplitude won't drive the sensor into nonlinearity, [8]. In the system

chain we then put the sensor itself followed by a low pass filter, which will perform the antialiasing (a switched capacitor circuit will be used subsequently), and will limit the bandwidth of the signal to just over the highest center frequency the bandpass (BPF) filter can be programmed with. Programming the BPF, one can sweep its center frequency over a range up to the corner frequency of the antialiasing filter. A smoothing filter is then necessary after the BPF, which is followed by a peak detector. The DC voltage from the peak detector is converted into a digital number, which can afterwards be used in an automatic pattern recognition digital circuit. The clock frequency used was 3MHz (for the noise-like signals and for the BPF) and the highest center frequency of the bandpass filter (with 3MHz sampling frequency) was 85KHz. The corner frequency of the antialiasing and the smoothing filter was 100KHz.

3 Results

The center frequency of the BPF can be changed by 5 control pins, or by changing its sampling frequency. It was varied between 25KHz and 85KHz, and 6 different readings for 6 frequencies in this range have been performed. First, the system has been tested with a low pass filter with a corner frequency of 30KHz, placed where the sensor is supposed to sit (between points A and B in Fig. 1). This circuit was a simple RC filter which mimics the behavior of the sensor as it is modeled in [2]. The voltage in the output of the peak detector for the situation when point A in Fig. 1 is connected directly to point B (i.e. no system for identification is present) was measured. Then, the measurement was carried out with the RC circuit under test placed between the points A and B. A relative change in voltage between the two measurements is given in Fig. 2.

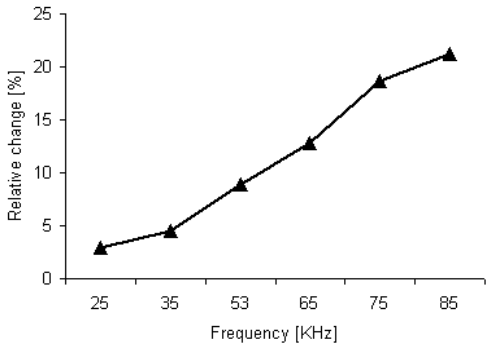

Fig. 2. Relative measurement of the RC filter spectrum

Introducing a tin oxide based sensor between points A and B, measurements for air, methanol and acetone have been performed. In this case, the base line has been considered to be the characteristic (the output voltage of the peak detector) of the sensor in response to air. The relative change of the sensor characteristic to saturated methanol and acetone vapor referenced to air is given in Fig. 3.

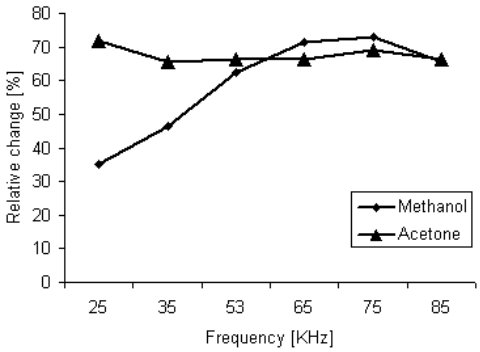

Fig. 3. Relative change in the voltage output to methanol and acetone

References

[1] J.V. Hatfield, P. Neaves, P.J. Hicks, K. Persaud and P. Travers, “Towards an integrated electronic nose using conducting polymer sensors“, Sensors and Actuators B 18-19 (1994), pp. 221-228.

[2] F. Musio, M.E.H. Amrani, and K.C. Persaud, “High frequency a.c. investigation of conducting polymer gas sensors”, Sensors and Actuators B 23 (1995), pp. 223-226.

[3] M.E.H. Amrani, R.M.Dowdesnell, P.A. Payne and K.C. Persaud, “Pseudo-random binary sequence interrogation technique for gas sensors”, Sensors and Actuators B 47 (1998), pp. 118-124.

[4] Y. Kuraishi, K. Nakayama, K. Miyadera, T. Okamura, “A single chip 20-channel speech spectrum analyzer using a multiplexed switched capacitor filter bank”, IEEE, Journal of Solid State Circuits, vol. SC-19, No.6, Dec. 1984, pp.964-970

[5] R.E.Zimmer, “Digital Communications and Spread Spectrum Systems”, MacMillan, 1985

[6] H. Tanaka, S. Sato and K. Nakajima, ”Integrated circuits of map chaos generators”, Analog Integrated and Signal Processing, 25, (2000), pp. 329-335.

[7] M. Delgado-Restituto, F. Medeiro and A. Rodriquez-Vazquez, "Nonlinear Switched-Current CMOS IC for Random Signal Generation", Electronics Letters, Vol. 29 (1993) pp. 2190-2191.

[8] J.W. Gardner, M. Vidic, P. Ingleby, A.C. Pike, J.E. Brignell, P. Scivier, P.N. Barlett, A.J. Duke, J.M. Elliott, “Response of a poly (pyrrole) resistive micro-bridge to ethanol vapor”, Sensors and Actuators, B 48 (1998) pp.289-296.

Theoretical Modeling of MIS Radiation Sensor with Giant Internal Signal Amplification

A. Malik, V. Grimalsky and A. Torres

National Institute for Astrophysics, Optics and Electronics (INAOE), Electronics Department,
P. O. Box 51 and 216, Puebla, Pue., 72000 Mexico,
email: amalik@inaoep.mx http://www.inaoep.mx

Summary: *Theoretical model of new silicon metal – insulator – semiconductor (MIS) based radiation sensor having a giant internal signal amplification is proposed to describe the experimentally obtained results. Numerical calculations have been provided for a circuit in which the MIS detector is connected in series with a constant voltage source, a pulse generator, and a load resistor. A constant voltage bias determines quasi-equilibrium inversion modes of the initial and final states of the detector. A non-equilibrium operating charge storage mode and readout mode occurs at applying a voltage pulse additionally to the bias. Duration of the pulse determines the integrated charge of photo generated minority carriers and readout process takes place at the pulse trailing edge. Theoretical modeling explains the giant value of the internal amplification of the signal that is determined as the ratio of peak values of readout currents and instantaneous photo current. At the integration time about 1 sec the amplification coefficient is in the order of 10^4 in the case of the external load 10 – 50 kΩ, and in the order of 10^6 when the external load is smaller than 1 kΩ.*

Keywords: *radiation sensor, MIS structure, signal amplification*
Category: *1 (General, theoretical and modeling)*

1 Introduction

A profound study of the physical processes in MIS structures under non-equilibrium conditions gives a new way of using an old and familiar device as a high sensitive radiation sensor with great internal amplification of an input signal. For the first time, the conception of this sensor has been reported on Eurosensors XVI [1]. According to this conception, an usual MIS capacitor may be used as a radiation sensor with significant internal amplification of an input signal, if it is working in non-equilibrium mode. For that, the sensor is connected in series with a constant voltage source, a pulse generator, and a load resistor. A constant voltage bias determines quasi-equilibrium inversion modes of the initial and final states of the detector. A non-equilibrium operating charge storage mode and readout mode occurs at applying a voltage pulse additionally to the bias. Duration of the pulse determines the integrated charge of photo generated minority carriers. Readout process takes place at the voltage pulse trailing edge. It is easy to understand our innovation from Figure 1. Here, the initial and final inversion quasi-equilibrium mode of the sensors is denoted as (A). A storage and readout processes under the applying of a time-dependent voltage (U) to the gate of p-MIS structure are denoted as (A→ B→ C) and (C→ A), respectively. At that, the current (I) in circuit is shown also. During the time interval t_0-t_1, the storage of photo generated holes occurs at the potential well at the silicon surface causing the augmentation of the inversion charge from Q_{p1} to Q_{p2}. Duration of the voltage pulse determines the integrated charge ($\Delta Q = Q_{p2} - Q_{p1}$). Readout process takes place at the pulse trailing edge at $t = t_1$, causing extraction of charge ΔQ into the substrate.

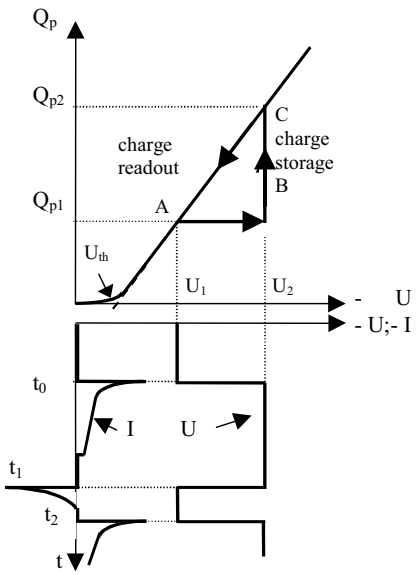

Fig. 1. The inversion charge density (Q_p) in p-MIS sensor as a function of the applied voltage (upper figure). Lower figure shows time-dependent voltage applied to the gate of the p-MIS sensor and a displacement current in circuit at the storage and readout processes.

The ratio of peak values of readout currents and instantaneous photocurrent obtained experimentally achieves giant values: about of 10^4 in the case of the external load 50 kΩ, and about of 10^6 when the external load is 50 Ω.

2 Model and Simulations

A description of a transient behavior of the MIS structure under investigations can be carried out within a framework of a circuit model, which is given in a Fig .2.

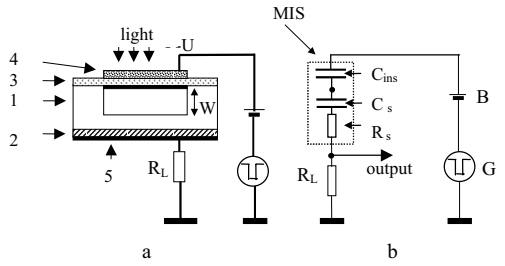

Fig.2. The MIS capacitor structure (a) and measuring circuit (b). 1 is n^- Si, 2 is n^+ Si, 3 is isolator, 4 is semi-transparent metal. The MIS capacitor equivalent is shown in dotted frame. R_s and R_L are the resistivities of the undepleted silicon bulk and load resistor, respectively.

In the case of relatively small concentrations of donors $N_D < 10^{14}$ cm^{-3}, the fully depletion approximation is valid, and the profile of electron concentration is sharp. The absorption length of the infra red radiation at wavelength $\lambda_0 = 0.93$ μm is $\alpha^{-1} \approx 5\text{x}10^{-3}$ cm.

The basic equations both for storing and readout are the equation for the charge of the holes in the inversion layer of the MIS capacitor and the second Kirchhoff's rule for the electric circuit. The temporal scales under storing are about 0.1 – 10 s at moderate levels of infra red irradiation, in a contrast with temporal scales 1 μs – 1 ms under readout. Therefore, the current in the circuit is essentially smaller under storing, than one under readout. The simulated and experimentally estimated values of the current are $|I(t)| < 0.2$ μA under the storage process. Thus, it is possible to neglect by the voltage drop at the external load and at the n^- layer. Because duration of readout stage is short, it is possible to neglect by an influence of thermo and photo generation at this stage. But the voltage drops at the external load $I \cdot R_L$ and at the n^- layer of semiconductor $I \cdot R_s$ are dominating there.

To simulate discharge process, it is necessary to solve the electric circuit equations jointly with diffusion-drift equations for concentrations of carriers and Poisson equation for electric potential within n^- layer. At the readout stage, a quick discharge of MIS capacitor takes place. The simulations of readout process have been done for a duration 1 μs of a voltage drop from $-|U_2|$ to $-|U_1|$. During the readout, the holes from an inversion layer move into n^- semiconductor layer. Simultaneously, an injection of electrons from n^+-n^- semiconductor junction takes place, too. Therefore, a double injection of carriers into n^- layer takes place and its resistance changes drastically. Thus, under the readout stage, MIS structure behaves as a 'virtual' p-i-n diode with a double injection of carriers. An influence of variable resistance of n^- layer on discharge depends on the value of external load. At the value of $R_L > 10$ kΩ, this influence is unessential, because the biggest value of the resistance of n^- layer is ~ 8 kΩ. Under smaller values of the external load, this influence is dominating (Fig.3).

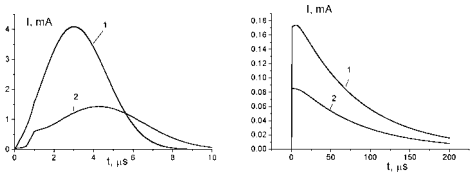

Fig.3. Dependencies of readout current the load $R_L = 50$ Ω (left) and $R_L = 50$ KΩ (right). Curve 1 is for the complete filled potential well, curve 2 relates to 75% filling of the well.

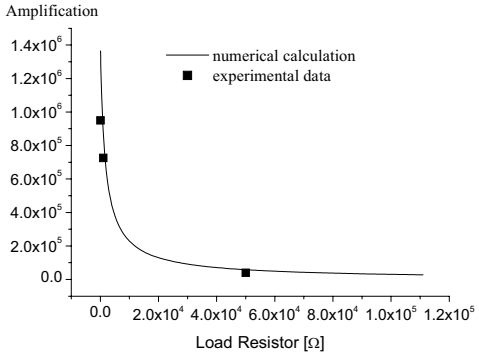

Fig.4. A comparison of the experimental and numerically calculated dependencies of the internal current amplification on a load resistor value R_L. The averaged value of the current under storage stage during 1 sec is 3 nA both in experiments and in simulations.

Under discharge, resistance of n^- semiconductor layer (base of virtual p-i-n-diode) is changed drastically, due to double injection of carriers. The initial value is about 8 kΩ and the minimal value may achieve 150 Ω. Thus, under smaller value of external load $R_L < 10$ kΩ, namely the resistance of n^- layer determines the dynamics of the current during discharge. Under greater values of $R_L > 10$ kΩ, decreasing the resistance of the n^- layer do not change the readout current.

Thus, using a storage (integration) of the charge in MIS structure under irradiation by small intensities of infra red light, it is possible to obtain essential values of output current under readout. The internal amplification coefficient may achieve the value about of 10^4 for the external load 10 – 50 kΩ and about 10^6 when the external load is smaller than 1 kΩ (Fig.4).

References

[1] A. Malik. Conception of optical sensors based on transient processes in MIS structures, *Proceedings of the International Conference Eurosensors XVI*, pp.731-734, Prague, 2002.

A fish-freshness sensor with flavin-containing monooxygenase type 3

K. Mitsubayashi[1], T. Kon[1], S. Nakakura[1], Y. Kubotera[1], Y. Hashimoto[1] and Y. Nishi[2]

[1]Tokai University, Dept. of Human and Info. Science, 1117 Kitakaname, Hiratsuka, Kanagawa 259-1292, Japan
e-mail: mitsu@keyaki.cc.u-tokai.ac.jp
[2]Tokai University, Dept. of Materials Science, 1117 Kitakaname, Hiratsuka, Kanagawa 259-1292, Japan

Summary: *A fish-freshness sensor was constructed by immobilizing flavin containing monooxygenase type-3 (FMO3) as, one of drug metabolizing enzymes in human liver, to a dissolved oxygen electrode. The FMO3 immobilized sensor was calibrated against trimethylamine solutions (TMA, putrefactive substance) from 1.0 to 50.0 mmol/l. As the results of the experiments with extractions of horse-mackerel, the sensor output increased with the holding time of fish samples at 25 °C because of their decomposition.*

Keywords: *freshness sensor, trimethylamine, flavin-containing monooxygenase, flow injection analysis*
Category: *10 (Applications)*

1 Introduction

An evaluation of food freshness is important in the field of food industries. In general, K value is widely used for the assessment of fish freshness. Convenient approach has been required because of its complicated operation for obtaining the K value. On the other hand, trimethylamine (TMA, fish odorous substance) is produced by the decomposition of trimethylamine N-oxide (TMAO) in sea creatures. Then, TMA is expected to be freshness index in fish.

In this research, a fish-freshness sensor was developed using flavin containing monooxygenase type-3 as a major enzyme for metabolizing TMA in human liver [1]. The sensor was also applied for evaluating the fish freshness with extract samples from horse-mackerel as sample fish.

2 Experimental

2.1 Construction of FMO immobilized biosensor

Flavin containing monooxygenase type-3 (FMO3, E.C.1. 14.13.8, P233, from *Adult human liver*; 30200pmol/mg・min, Gentest Corporation., MA, USA) catalyzes TMA with NADPH as coenzyme to trimethylamine N-oxide (TMAO) with following reaction.

$$TMA + NADPH + H^{+} + O_2 \xrightarrow{FMO3} TMAO + H_2O + NADP^{+}$$

The freshness sensor was constructed by attaching an FMO3 immobilized membrane onto a sensitive area of a dissolved oxygen electrode (Model BO-P, ABLE Corp., Tokyo, JAPAN) using a nylon net and a silicon O-ring [2].

To immobilize the enzyme, the FMO3 solution was mixed with photocrosslinkable polyvinyl alcohol containing stilbazolium groups (PVA-SbQ [stilbazole Quaternized]; Grade: SPP-H-13 [bio], Toyo Gosei Co. Ltd., Tokyo, Japan), the resultant mixture was placed onto a dialysis membrane (thickness: 15 μm, Technicon Chemicals Co., S.A., Orcq, Belgium) dried on a plastic-plate and then spread over the surface of the membrane until it had permeated (observed as a darkening of the membrane). The dialysis membrane was placed in the dark below 10 ºC for 1h and then irradiated with a fluorescent light for 30 min in order to photocrosslink the PVA-SbQ solution, thus immobilizing the enzyme into the dialysis membrane.

The FMO3 membrane was cut, and placed onto the sensing area of the dissolved oxygen electrode [3]. This membrane was covered with a supporting nylon net and secured with a rubber O-ring.

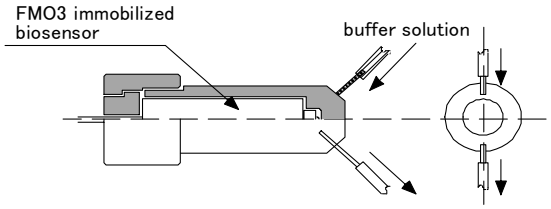

Fig. 1. FMO immobilized biosensor in reaction cell for flow injection analysis.

2.2 FIA for TMA and fish-extract solution

The behavior of the biosensor was evaluated using standard TMA solutions, as the typical putrefactive substance in fish, with a flow injection analysis system including a computer–controlled potentiostat (Model 1112, BAS Inc., Tokyo, Japan) at a fixed potential of –600 mV vs. Ag/AgCl as counter/reference (Figure 1). The TMA solution was injected in the flow system with a syringe (Hamilton Microliter Syringes, TYPE; 710, Hamilton Company, USA).

Then, fish extract samples of a horse-mackerel was also applied for the FIA system with the FMO3

immobilized biosensor. Figure 2 shows a procedure of the fish extracts and their preservation. Sample pieces of horse-mackerel kept at 25 ºC for several dozen hours were mashed and homogenized with a tenfold of buffer solution in a mortar. The resultant suspension solutions were centrifuged for 2 hours in twice, thus obtaining supernatant fluids as the fish extract solutions. The fish extracts were kept in refrigerator at -20 ºC except for the application to the FIA system.

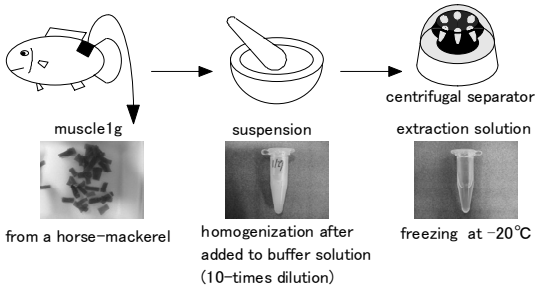

Fig. 2. Process of fish extraction and their preservation.

3 Results and Discussion

3.1 Evaluation of the FMO3 immobilized sensor

The typical response curves of the FMO biosensor to the injection of the standard TMA solutions is illustrated in Figure 3. The sensor output was presented by the change value from the initial current. As the figure indicates, the sensor outputs increased rapidly following the injections of the TMA solution, thus resulting in the peak currents 30 seconds after the injection, being dependent in the TMA concentration.

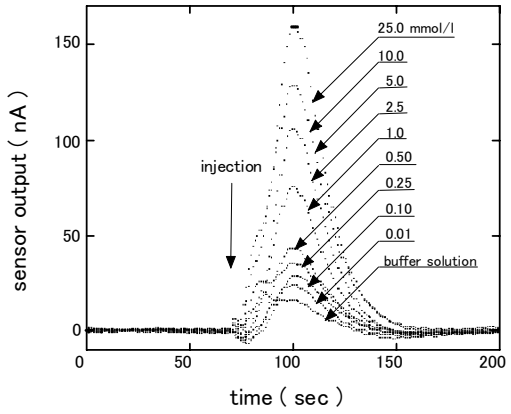

Fig. 3. Typical responses of the FMO3 immobilized biosensor to varying concentrations of TMA solution.

The sensor was possible to detect the oxygen consumptions induced by the oxidation of TMA as FMO3 enzyme reaction, thus obtaining the calibration range against TMA from 1.0 to 50.0 mmol/l, with a correlation coefficient of 0.994, deduced from regression analysis of the semi-log plots by a method of least squares according to the following equations:

sensor output (nA) = 26.1+ 87.2log[TMA (mmol/l)]

The reproducibility of the FMO3 biosensor in the standard TMA solution (10 mmol/l) is shown in Figure 4. As the figure indicates, the sensor performance was reproducible over multiple measurements, showing a coefficient variation of 4.39 % calculated by the peak output (average = 100.03 nA, n = 5) 30 sec after the injection.

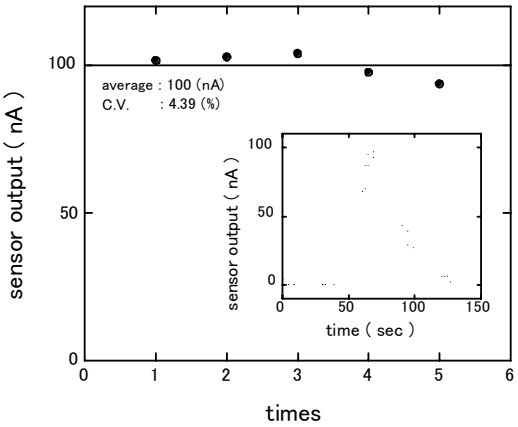

Fig. 4. This figure is positioned within a single column.

3.2 Evaluation of fish-freshness sensor

Figure 5 illustrates the peak outputs of the FMO3 biosensor in the FIA system to the extract samples of horse-mackerel kept at 25 ºC for various times.

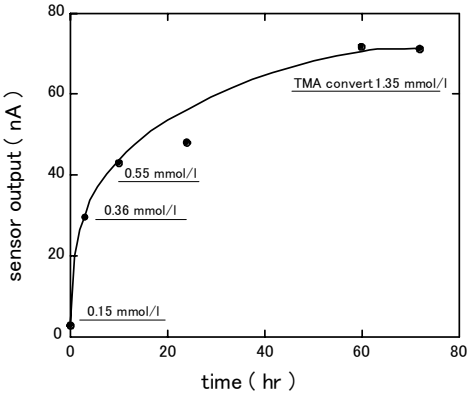

Fig. 5. Peak current change of the FMO biosensor to extract solutions from horse-mackerel kept at 25 ºC for several dozen hours.

As the figure indicates, the sensor peak currents increased in connection with their holding time because the putrefactive substances such as TMA in fish samples increased with time by the decomposition at 25 ºC.

References

[1] Dolphin C.T., et.al., *Nat. Genet.*, 17 (1997), 491-494.

[2] Mitsubayashi K., Hashimoto Y., *Electro-chemistry*, 68(No.11) (2000), 901-903.

Sensor Applications for a Piezo Stepper Motor

T. Hegewald*, M. Kaltenbacher, and R. Lerch

University of Erlangen, Institute of Sensor Technology, Paul-Gordan-St. 12, 91052 Erlangen, Germany
email: thomas.hegewald@lse.e-technik.uni-erlangen.de http://www.lse.uni-erlangen.de
* Supported by the Bavarian Research Cooperation (ForMikroProd)

Summary. *The exact alignment of opposing teeth is essential for the reliable operation of an inchworm piezo motor with interlocking micro-teeth. In this paper we are presenting different sensing technologies to detect the position of a row of micro-teeth in relation to another row of teeth with the same dimensions. A capacitive sensor, an optical technique, and an electromagnetic principle are investigated and compared.*

Keywords: position sensor, inch-worm-motor
Category: 10 (Applications)

1 Introduction

In 1975 Burleigh Instruments, Inc. introduced a concept of a translating motor based on piezoelectric actuators [1]. The motor consists of two clamping mechanisms and one main actuator. By controlling the driving voltage of the three actuators independently an inchworm like movement along a guiding rod can be achieved. Incrementally adding up those small displacements of the main actuator leads to large displacements of the entire structure.

The latest designs of inchworm motors employ an interlocking structure on clamps and rod. Compared to the conventional friction locking design much higher motor loads are possible while the clamping forces can be reduced. Figure 1 shows the principle of an inchworm motor with the interlocking micro-teeth on clamps and rod.

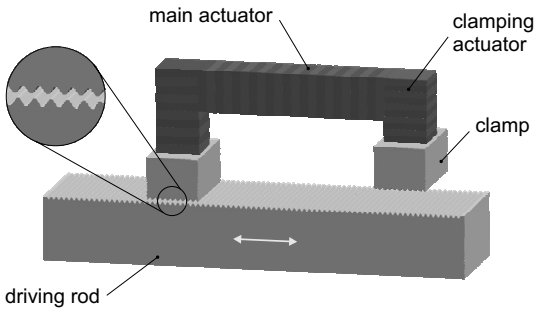

Fig. 1: Principle of an inchworm motor containing three piezo stack actuators and micro-teeth on driving rod and clamps.

The micro-teeth are manufactured by laser ablation with a tooth height a little smaller than the stroke of a clamping actuator and a tooth width corresponding to the stroke of the main piezo actuator. While those micro-teeth on rod and clamps increase the work load of the motor significantly they also require the main piezo actuator to position the clamps into a very exact configuration before pushing the clamps towards the rod. Any misalignment between the two rows of teeth will result in wear, shear forces in the structure, and even in missed steps. Therefore it is important to develop an inexpensive sensing system such that the correct alignment of the teeth can be ensured before the clamps are engaged.

The following section describes three different sensor principles for online monitoring of the alignment of the micro-teeth. The last section of this abstract paper discusses the measurement results from the different principles on the real structure.

2 Sensors

The goal of this project is to develop an inexpensive sensing technology which can easily be integrated into the control circuit of the stepper motor without requiring many additional parts. Using finite element simulations the general capacities of the different principles could be explored. Furthermore, a test setup was used to measure the sensitivity of the sensors for a driving rod with micro-teeth (about 60μm high and 120μm wide).

2.1 Capacitive sensor

The capacitive sensing principle fulfills the requirement of an inexpensive technology almost ideally. Besides an electronic circuit for signal processing no additional parts are needed.

When one of the clamping actuators is contracted, the small gap between clamp and rod forms a capacitor between the two metallic surfaces. Due to the micro-teeth on both sides, the capacitance of the structure is not only dependent on the gap width but also depends on the alignment of the teeth.

Finite element simulations with a simplified geometry of the structure have been performed to verify the general principle. The top diagram in Figure 3 shows the measurement results for the capacitive sensor.

2.2 Optical sensor

Optical position sensors and specifically linear encoders with high resolution and bandwidth have been successfully used in many industrial applications. A disadvantage of the optical principal is the need for additional sensor elements on the structure.

In our case the micro-teeth on the driving rod of the motor can be used as a base scale for the sensor. A very tiny scanning head containing a glass scanning reticle, a light source, and a light receiver are connected to each clamp of the inchworm motor. Using the imaging scanning principle the grating of the reticle needs to have the same period as the teeth on the driving rod. The principle makes use of the different reflection properties of the different teeth areas. The grating on the scanning head (grating period 120 μm) was manufactured in a photolithographic process. To eliminate the influence of ambient light the sensor light is modulated at about 22 kHz. The middle diagram in Figure 3 displays the measured sensor signal using the described optical sensor.

2.3 Electromagnetic sensor

Out of the broad range of electromagnetic sensors we look at devices which detect a change in the magnetic flux. Due to the magnetic properties of the driving rod material ($\mu_{rel} = 30$) an induced magnetic flux is influenced by the position of the teeth. Our first approach is to use an asymmetric u-shaped core with a sensing coil as illustrated in Figure 2.

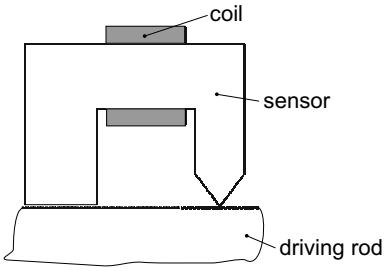

Fig. 2: Cross sections of the electromagnetic sensor.

The inductance of the coil depends on the position of the sensor tip. Finite element simulations revealed the highest sensitivity for read out frequencies around 1 kHz. The measurements on the test setup showed similar results. Figure 2 (bottom diagram) presents the normalized sensor inductance obtained at a frequency of 1 kHz.

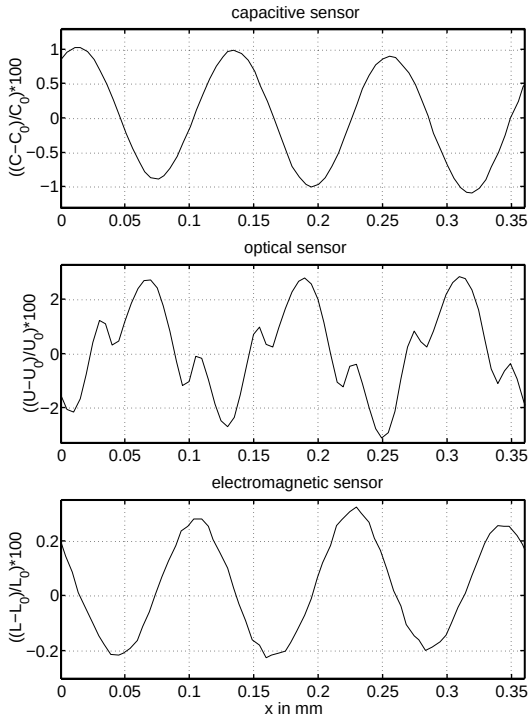

Fig. 3: Measurement data: capacitive, optical, and electromagnetic sensor (normalized signals in percent).

3 Conclusion

As Figure 2 illustrates, the capacitive sensor produces the smoothest output. The change in the signal compared to the total sensor signal is about 2 percent. However, the capacitive principle is very sensitive to any dirt particles between the surfaces.

The optical sensor generates the highest change-to-total-signal ratio (about 5 percent). However, this sensor is more complicated to adjust and contamination of the micro-teeth would also decrease the performance.

The smallest signal change (0.5 percent) was measured with the electromagnetic sensor. This change would not be enough to detect the alignment of the teeth reliably on the stepper motor. Nevertheless, the electromagnetic principle promises to be the most robust of the three discussed principles. Currently, a new concept for the electromagnetic sensor integrating a number of teeth into the measurement is under development. Furthermore, using a differential method and a Wheatstone bridge circuit to read out the signal will enhance the signal quality even more.

References

[1] W. G. May (Burleigh Instruments, Inc.). Piezoelectric Electromechanical Translation Apparatus. *United States Patent 3902084*, August 1975.

Application of biosensors based on ENFETs for fast detection of total solanaceous glycoalkaloids in potatoes samples

V. Arkhypova[1], S. Dzyadevych[1], E. Nazarenko[1], Y. Korpan[1], A. Soldatkin[1], A.El'skaya[1], J.-M. Gravoueille[2], C. Martelet[3], N. Jaffrezic-Renault[3]

[1]Laboratory of Biomolecular Electronics, Institute of Molecular Biology and Genetics, National Academy of Science of Ukraine, 150 Zabolotnogo St., Kiev 03143, Ukraine, E-mail: avalka@yahoo.com
[2]ITCF, Station expérimentale, Halle Technologique Pomme de Terre, 91720 Boigneville, France
[3]Ecole Centrale de Lyon, IFoS FRE 2608, 36 avenue Guy de Collongue, 69134 Ecully Cedex, France

Summary: *The possibility to apply of enzyme field effect transistors for detection of total glycoalkaloids content in real potato samples without any pre-treatment has been shown. Measurements protocols for such determination was developed. The effectiveness of total glycoalkaloids determination in juice samples from different variety of potato with biosensor was evaluated by using the method of standard additions and the calibration curves in the range 0.2 – 100 μM. A good correlation between results obtained with biosensor and routinely used method have been demonstrated. The method proposed is rather cheap, easy to operate and requires short analysis time compared with the traditional methods of glycoalkaloids evaluation.*

Keywords: *biosensor, enzyme inhibition, glycoalkaloids.*
Category: *10 (Application)*

1 Introduction

The cultivated potato is consumed daily throughout the world by millions of people as one of the major agricultural crops. Potatoes are grown in about 80 % of all countries, and worldwide production stands in excess of 350 million of tones per year, being exceeded only by wheat, maize and rice. Although the success of potato as a starchy staple has been enhanced by selecting varieties resistant to diseases and pests, early domestication was probably more concerned with reducing the level of natural bitter-tasting steroidal toxicants in tubers, known as glycoalkaloids, or eliminating them.

Commercially available potatoes destined for consumption contain about 20-150 mg of the total glycoalkaloids per 1 kg of tuber. Various factors, such as annual or regional variations, exposure to light (green potatoes) or to mechanical damage (harvesting) may result in a substantial increase in the initial total glycoalkaloids concentrations.

In general, testing potato samples is not a simple task. It consists of three steps: (1) extraction of all the compounds of interest; (2) elimination, if necessary, of all interfering species; and finally (3) determination of the specific analyte concentration [1]. All these procedures are complex. They need an expensive and bulky instrumentation with high power consumption and well-trained operators.

During our recent investigations biosensors for sensitive detection of the glycoalkaloids have been developed, characterised and optimised [2]. Further research concerning a possibility of application of the biosensor developed for real potato samples without any pre-treatment is presented in this paper.

2 Materials and Methods

Butyryl cholinesterase (BuChE), butyryl choline chloride (BuChCl), glutaraldehyde, α-solanine and α-chaconine were purchased from Sigma. The ion sensitive field effect transistors were fabricated at the Research Institute of Microdevices (Kiev, Ukraine) [3]. The biologically active membranes were formed by cross-linking of BuChE with bovine albumin in a saturated glutaraldehyde vapour on the transducer surface [2].

All measurements were performed in daylight at room temperature in an open vessel filled with a vigorously stirred 5 mM phosphate buffer solution, at pH 7.2. The level of inhibition due to the action of a definite concentration of alkaloids was evaluated by comparison of the biosensor response level with and without inhibitor.

Tubers of Monalisa, Pompadour and Elkana varieties were grown in Experimental station of ITCF. These potato varieties and two commercial ones (Caesar and Agata) were used. Harvested tubers were cleaned manually by washing under water and passed through a simple sieve to obtain the juices. The samples were analysed directly using the biosensor.

Reference measurements of the glycoalkaloids in potatoes were conducted by HPLC technique.

3 Results and discussion

The main analytical characteristics of the biosensors have been studied under different conditions.

Elaboration of a measurement protocol for real potato samples requires a preliminary transducer calibration, i.e. detecting the kind and proportion of glycoalkaloids to be used in the sensor under development. Mostly, the ratio between main potato alkaloids (α-solanine and α-chaconine) is known to be around 6:4, however, other ratios were quoted as well. Fig. 1 shows the dependence of immobilised BuChE inhibition on the α-solanine to α-chaconine ratio in the mixture.

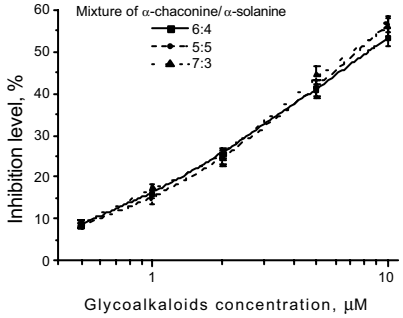

Fig.1. Calibration curves for the detection of the different mixture of α-chaconine : α-solanine. Measurements were conducted with 1 mM BuChCl in 5 mM phosphate buffer, pH 7.2.

Also, experiments were performed in order to study a possible effect of different procedures of sample pre-treatment on the sensor response (Fig.2).

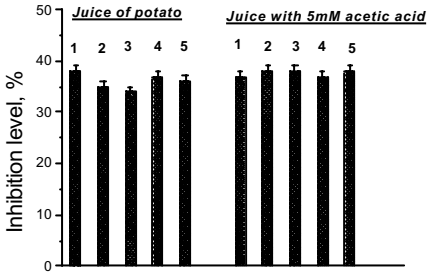

Fig.2. Inhibition of BuChE by potato juices prepared in different way before biosensor analysis (fresh juice (1), juice after centrifugation for 10 min at 10 000 rpm (2), for 20 min at 10 000 rpm (3), for 10 min at 5 000 rpm (4), for 10 min at 2 000 rpm (5)).

The optimal measurement protocol for glycoalkaloids determination in potatoes samples has been proposed. The effectiveness of total solanaceous glycoalkaloids determination in juice samples from different varieties of potatoes with biosensor was evaluated using the method of standard additions and calibration curves. The results of determination of the glycoalkaloids concentration in potato samples obtained by the biosensor are presented in Table 1 compared with the analogous data obtained by the method with standard complex pre-treatment procedure following by HPLC. Good correlation between those results has been shown.

Table 1. Levels of total glycoalkaloids content in different varieties of potato (metering error is about 5 %).

Potato variety	Biosensor method, mg/kg fresh weight		Reference HPLC method, mg/kg fresh weight
	Standard addition	Calibration curve	
Monalisa	145	157	138
Pompadour	250	212	253
Elkana	550	460	611
Agata	120	105	
Caesar	130	143	

The difference between the glycoalkaloids levels in various parts of the potato tuber was also shown. For example, the total glycoalkaloids content in the peel of Agata was about 234 mg/kg of fresh weight, in contrast to 105 mg/kg found in flesh. This result is in a good agreement with the results obtained by other authors.

A biosensor developed being well reproducible and sensitive will certainly provide a simple and fast method for screening great number of samples directly in fresh potato juice without any sample pre-treatment. The biosensor can work on a crude extract, or even directly on a suspension of potato or plant material. It can provide a way to save time and costs, with possibility of taking rapid assessment of total glycoalkaloids content in a variety of potato cultivars. In case of necessity, the selected samples can be then analysed more selectively by the standard methods for individual glycoalkaloids determination, which are more complex and need more time though.

This work was supported by INTAS Grant 00-00151 and PostDoc position from Grand Lyon (VA).

References

[1] M. Friedman, G. McDonald. Potato glycoalkaloids: chemistry, analysis, safety, and plant physiology. *Crit. Rev. Plant Sci.* 16 (1997) 55-132.

[2] V.N. Arkhypova, S.V. Dzyadevych, et al. Development and optimisation of biosensors based on pH-sensitive field effect transistors and cholinesterases for sensitive detection of solanaceous glycoalkaloids. *Biosensors Bioelectron.* 18 (2003) in press.

[3] A.A. Shul'ga, L.I. Netchiporouk, et al. Operation of an ISFET with non-insulated substrate directly exposed to the solution. *Sens. Actuators B* 30 (1995) 101-105.

Using Optical Spectra and Intelligent Pattern Recognition to Evaluate the Quality of Food in a large-scale Industrial Oven.

M O'Farrell[1], E. Lewis[1] and C. Flanagan[1], W.Lyons[1] and N. Jackman[2]

[1]University of Limerick, EC&E Dept., Castletroy, Limerick , Ireland
email: Marion.Ofarrell@ul.ie
[2]Food Design Applications Ltd., Newtown, Castletroy, Limerick

Summary: *An Optical fibre based sensor system has been developed for the purpose of examining the colour of food products online as they cook in a large-scale industrial oven. Spectroscopic techniques are employed to interrogate the sensor signal and the resultant output spectral patterns are examined by an Artificial Neural Network. A system based on pattern recognition has been developed which is capable of classifying colours that are favourable and those that are not optimum, in order to control the cooking process and optimise food quality.*

Keywords: *Optical Fibre Sensor, Artificial Neural Network, Pattern Recognition, Colour Classification, Food Processing Industry, Back Propagation Learning*
Category: *10 (Applications)*

1 Introduction

The food preparation industry is under increasing pressure to reach high standards and as well as maintaining production numbers. The throughput can be very high and the likelihood of occasional lower quality goods being erroneously produced is correspondingly increased. By inspecting food it is possible to grade the quality of the product e.g. in terms of colour [1] or shape and size [2], which adds value, consistency and allows producers to recover more end product.

The quality parameter assessed in this paper is colour. Examples of how colour affects the customer's decision in a purchase are evident from data obtained in customer surveys. In the case of cooked goods, customers often have preconceived notions of how a product should look e.g. roast chickens must be golden. It is vital that a customer sees the colour he/she expects, while also being able to return the following week and be guaranteed the same standard.

Further developments have been made to an existing Optical fibre based sensor system initially developed by the authors [3]. To date results have been obtained in collaboration with Food Design Applications Ltd. on meat products such as high meat content patti-burgers, minced beef and sausages and vegetables such as mushrooms. Further investigations have been made into high cereal content meat patties. This high cereal content means a less obvious colour change in the product as it cooks and therefore making it more difficult to classify. A neural network has been successfully trained to classify raw, undercooked, and overcooked patties.

2 System Set-up

The oven used for testing comprises a conveyor belt of approximately 15 metres in length (Fig. 1). The conveyor belt is heated from above to cook the food and a surface air-blowing technique is incorporated towards the end of the belt to colour the food.

Fig. 1. The Industrial Conveyor Belt Oven used in Tests

A white light source was used to illuminate the object. The source used in this investigation was a stabilised tungsten halogen lamp, which emits light in the range 400nm to 2µm in a continuous manner. The spectra of the food samples were recorded using an Oceanoptics S2000 spectrometer, and they were captured using LabVIEW software and subsequent analysis was done using the Stuttgart Neural Networks Simulator (SNNS), the Neural Network Software. The optical system comprises a purpose built optical fibre probe coupled to the spectrometer.

3 Spectroscopic Results

As explained in the introduction, the purpose of this work was to examine high cereal content meat patties. With high meat content patties as examined previously [3], the blood in the meat causes distinct colour changes from 68°C onwards but this is not the case with the high cereal type. Fig 2. shows

some patties at the various cooking stages. Here it is possible to appreciate how little colour change actually occurs.

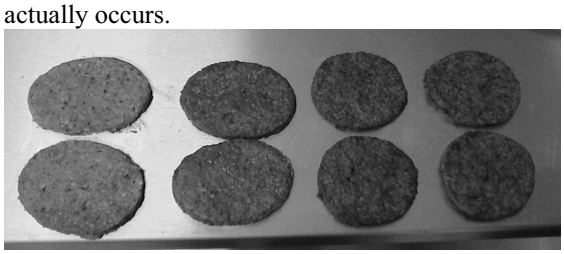

Figure 2: From left to right; Raw patties, Undercooked (65°C), Correctlycooked (78°C) and Overcooked (100°C).

Fig. 3 shows the variations in 390 spectra, 130 for each of the three classes i.e. raw, undercooked (65°C) and overcooked (100°C). It is clearly seen that the variations are so slight that it is quite difficult to segregate the colours. The raw patti poses the greatest problem as there are many dark flecks (slightly visible in Fig. 2) that cause quite a range of spectra for the one colour (the black lines in Fig 3.), whereas the other two colours are quite contained.

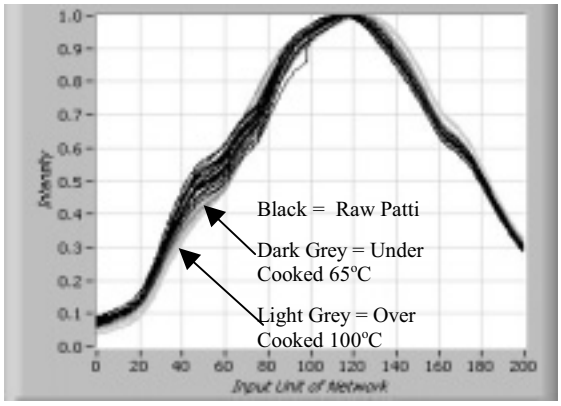

Figure 3: Spectral Variations in High Cereal Content Patties

4 Neural Network Design and Results

The spectrum of each food sample represents the distribution of received light across a wide spectrum of wavelengths in the visible and near infrared. These signals are complex and the patterns may be masked by interfering parameters, such as localised light absorption, due to fatty deposits. It is therefore necessary to apply advanced signal processing and pattern recognition techniques to categorise each sample and isolate interfering parameters. Neural Networks are becoming more popular as a means of pattern recognition [4] in the face of non-linearity.

A three layer Neural Network was used to classify the spectra into raw, undercooked (65°C) and overcooked (100°C). The input layer was made up of the 200 processing units. Into this was fed the 200 intensity readings for each spectrum (i.e. the x-axis of the graph in Fig. 3). 130 spectra were used for each colour, so that the training set was made of 130 x 3 (390 spectra). The learning function used was Back-Propagation with momentum and the following parameters were used as required by the Neural Network software, SNNS η(learning rate) = 0.8, μ (momentum term) = 0.6, c (flat spot eliminator) = 0.1 and δ (maximum error) = 0.1.

The ouput layer was made of 3 units one for each class (100, 010, 001). Table 1 shows the results of testing the trained network, using a Test Set of spectra not used in training. The Test Set was made up of 69 spectra, 23 for each class. Table 1. shows a sample of 6 results from the Test Set. It can be seen that the Network trained successfully.

Patti Coooking Stage	Ideal Output	Observed Activation Output		
Raw (too light)	100	0.880	0.056	0.000
Raw (too light)	100	0.901	0.000	0.000
Under Cooked	010	0.004	0.845	0.064
Under Cooked	010	0.004	0.909	0.093
Over Cooked (too dark)	001	0.000	0.003	0.893
Over Cooked (too dark)	001	0.000	0.023	0.880

Table 1: Sample of 6 (from 69) Results from the ANN Test Set after training the Network

5 Conclusion

A fibre optic based spectroscopic technique, coupled with Artificial Neural Network signal processing techniques, has been developed for the purpose of the recognition and classification of the various colours of high cereal content meat patties samples.

This paper further expands on previous research done by the authors [3]. It explores other food types whose colour change is not as obvious as pure meat, thus strengthening the viability of the system.

6 References

[1] McConnell RK Jr., Blau HH Jr. "Colour classification of non-uniform baked and roasted foods." *Proc. Food Processing Automation IV, pp.40 –46, 1995*

[2] Aleixo N., Blasco B., Molto E., Navarron F., "Assessment of citrus fruit quality using a real-time machine vision system", *Pattern Recognition, 2000. Proc. 15th International Conference pp. 482 –485 vol.1, 2000*

[3] O'Farrell M., Lewis E., "An Intelligent Optical Fibre based System for Monitoring Food Quality" *IEEE Sensors 2000. Proc. 1st International Conference pp. 308-311 vol.1, 2002*

[4] Lyons W.B., Lewis E., "Neural Networks and Pattern Recognition Techniques applied to Optical Fibre Sensors" *Transactions of the Institute of Measurement and Control 22, pp.385 – 404, 2000*

Optimised Integrated Magnetic Field Sensor

Marioara Avram, S. Nedelcu and Cecilia Codreanu

National Institute for Research and Development in Microtechnologies
Str.Erou Iancu Nicolae 32B, 7225 Bucharest, Romania, marioaraa@imt.ro

Summary: *An optimised integrated magnetic field sensor based on enhanced modulation of emitter injection and carrier deflection is presented. In the microfabrication of the magnetotransistor a standard n^+ buried layer, anisotropic etching protection and a split n^+ buried layer were alternatively used. The experimental measurement of the relative magnetosensitivity for the first two test structures showed an increased efficiency, although they resulted in lower magnetic field sensitivity. However, the latter structure showed a magnetosensitivity of approximately 18% higher than the first two structures. For collector currents of the order of 0.5 mA the measured relative magnetosensitivity is in the range of 15-30 % T^{-1}, with a good linear dependence between the magnetic field and the output signal.*

Keywords: *magnetic field, magnetotransistor, semiconductors*
Category: *10 (Applications)*

1 Introduction

The magnetic response of the bipolar magnetotransistors (BMT) is strongly influenced by the layout and the technological process design [1]. In the present paper an optimised bipolar magnetotransistor is presented. The basic test structure, which is a classical lateral dual collector p-n-p integrated transistor, is schematically shown in Fig. 1. The most important part of the emitter current is captured into the substrate due to the difference between the vertical and lateral pnp current gain. (The lateral pnp current gain is approximately 3 to 4 times smaller than the vertical gain, at the same structure.) In the presence of the applied field, the current I_S injected from the bottom emitter area cannot effectively reach the collector and influences negatively the magnetic response of the device.

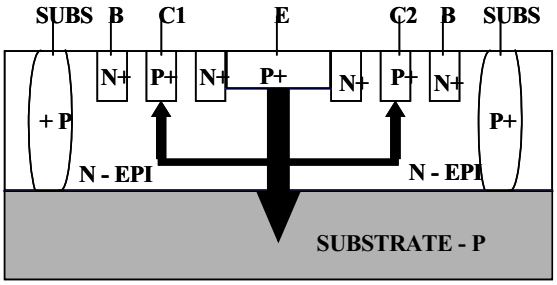

Fig. 1. The cross-section of the basic structure indicating the epi-layer (N-EPI), the substrate (SUBSTRATE-P) and the highly doped n+ regions of the base (E) and the collectors (C1, C2). The arrows show the emitter currents.

The Hall voltage developed along the base-emitter junction of the transistor modifies the bias conditions of the junction (its magnitude depends on the microfabrication process of the magnetotransistor [2]) and it is hard to be optimised. The reduction of the losses associated with the current component I_S is therefore highly desirable. In order to minimise the influence of the parasitic pnp transistor formed by the emitter, the epilayer and the substrate (EBS), three methods were investigated. In the next section the layout of each test magnetotransistor will be presented.

In order to compare the efficiencies of the test structures, the relative sensitivity S_r of the magnetotransistors is used. It is defined by the ratio:

$$S_r = \frac{\left|I_{C_1} - I_{C_2}\right|}{\left(I_{C1} + I_{C_2}\right)B} \qquad (1)$$

where B is the applied magnetic field, I_{C1} and I_{C2} are the collector currents and the $I_{C1} - I_{C2} = \Delta I_C$ is the relative imbalance current of the two collector currents. The experimentally measured magnetosensitivities $\Delta I_C/B$ are presented in the last section.

2 The Magnetotransistor Structure

The first test magnetotransistor has a n^+ buried layer under the active structure (Fig. 2), at the epi-substrate junction. Hence, the recombination level of the minority carriers increases in the base region. However, due to the reduction of the active collector currents and the Hall voltage there is also an unwanted reduction of the sensitivity of the device.

In the second magnetotransistor the parasitic EBS lateral transistor, at the collector–substrate junction underneath the active region (Fig. 3), is removed by anisotropic etching [3]. For this structure the minority recombination level is low, and the most

part of the collector current is captured to the contacts. The Hall voltage is not affected.

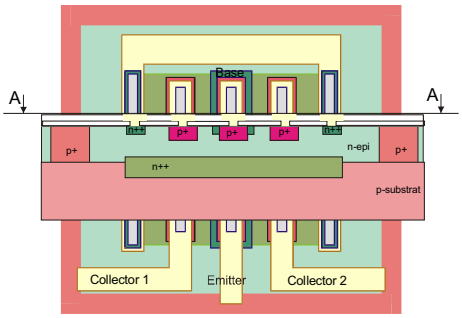

Fig. 2. Superimposed top view and cross-section view of the lateral pnp dual collector BMT with the n^+ buried layer protection.

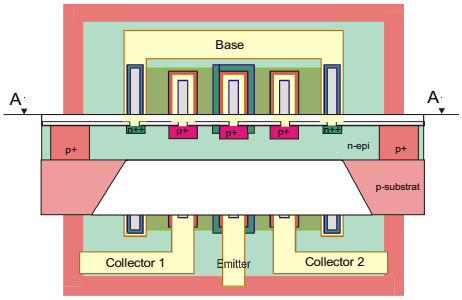

Fig. 3. Top view and cross-section view of the lateral pnp dual collector BMT with anisotropic etching protection.

Finally, the third magnetotransistor is similar to the first structure, but with the highly doped n++ region split in two halves. The parasitic EBS transistor becomes thus connected in parallel with the useful structure, and its electrical characteristics enhance the efficiency of the magnetotransistor [4]. It is first noted that for this structure the lateral pnp current gain is important and explains the observed high efficiency. Secondly, it should be noted that this structure cannot be used on the same chip with another bipolar structure.

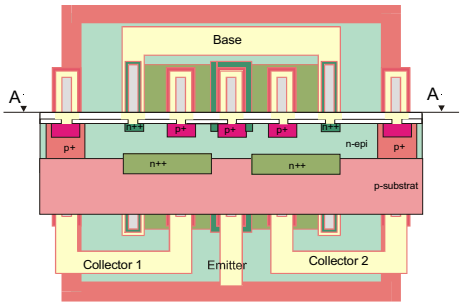

Fig. 4. Layout and cross-section view of the lateral pnp dual collector BMT with the n+ buried layer split.

3 Experimental Results

The basic test structure (see Fig. 1) is realised in an n-type epilayer on p-type silicon wafers, resistance $\rho \approx 7.5\ \Omega.cm$ ($n_0 \approx 10^{15}\ cm^{-3}$), (100) crystallographic orientation and 350 μm thickness. The doping level of the epilayer is approximately $6.10^{15}\ cm^{-3}$, with a thickness of approximately 12μm. The depths of the heavily doped n^+ diffusion regions have a 1.5 μm thickness.

For each test magnetotransistor discussed in the preceding section, the relative imbalance current ΔI_c as function of the applied field B has been experimentally measured, and the corresponding magnetosensitivities are shown in Fig. 3.

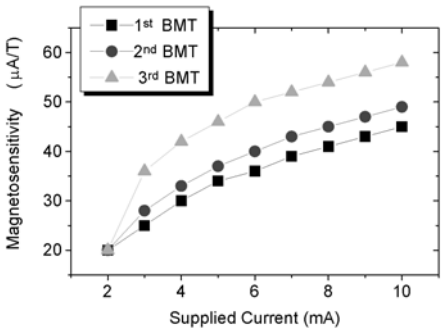

Fig. 3. The magnetosensitivity as function of the supplied current for the test bipolar magnetotransistors. The numbers 1 to 3 in the legend correspond to the magnetotransistors shown in Fig. 2, 3 and 4 respectively. The emitter current is $I_E = 2$ mA, and the base current is $I_B = 5$ mA.

It is observed that indeed the structure with the split n+ buried layer (noted 3rd BMT) has the greatest magnetosensitivity, almost 18% higher than the first two structures investigated. For collector currents of the order of 0.5 mA the measured relative magnetosensitivity is in the range of 15-30 % T^{-1}.

References

[1] Ch. S. Roumein. Sensors and Actuators. A 24 (1990) 83-105.

[2] M. Avram, O. Neagoe, Proc. Int. Conf. of Semiconductors (1997) pp. 456–459, Sinaia, Romania.

[3] R. Castagnetti, M. Schneider, H. Baltes. Sensors and Actuators A 46-47 (1995) 280-283.

[3] M. Avram, O. Neagoe. Proc. Int. Conf. of Semiconductors (1999) pp. 324–327, Sinaia, Romania.

Discrimination of different aromatic compounds in ethanol with a thin film sensor array

J. P. Santos, J. Lozano, M. Aleixandre, I. Sayago, M. J. Fernández, L. Arés, J. Gutiérrez, M.C. Horrillo

Laboratorio de Sensores (IFA-CSIC). Serrano, 144, 28006 Madrid, Spain
email: carmenhorrillo@ifa.cetef.csic.es http://www.ifa.csic.es

Summary: *A thin film solid semiconductor sensor array has been employed to discriminate several aromatic compounds in ethanol. These compounds are aromas or off-odors usually found in wines: acetic acid, ethyl acetate, acetaldehyde, trichloroanisole (TCA) and SO_2. The concentrations of these compounds were in the range of mg/l except in the case of TCA that was in the ng/l range. Principal component analysis (PCA) and radial basis neural networks (RB-NN) were performed in the data. The results showed that despite the strong influence of ethanol the system could discriminate correctly the compounds.*

Keywords: *aromatic compounds, thin film sensors, pattern recognition*
Category: *10 (Applications)*

1 Introduction

During last years quality wine has acquired a great importance as a high added value product. Research on wine and its constituents are of strong interest specially for winemakers. More than 600 volatile compounds have been identified in wines. Usually the study of these compounds is carried out with complex techniques such gas chromatography-mass spectrometry. In recent years electronic noses have been employed in wine applications [1]. One of the major drawbacks in this research is the strong influence of ethanol. The aim of this work is to study the discrimination capability of an electronic nose for several wine compounds in ethanol.

2 Experimental

2.1 Measurement setup

The main components of the measurement setup are shown in figure 1. The carrier used gas was nitrogen 99.998 % purity. The sampling method employed was static headspace followed by a dynamic injection. 10 ml of solution are kept in a Dreschel bottle at 30 °C for 30 minutes. Then the electrovalves are switched and nitrogen fluxes for 20 minutes carrying the volatile compounds to the sensor cell. Then the electrovalves are switched again to allow the sensors to desorb. This procedure is repeated several times, at least 8, for each compound. The first measurement correspond always to the blank solution (12% ethanol in deionised water). Measurements are carried out at a total gas flow of 200 ml/min.
The resistance of the sensors are measured with a Keithley 7001 multiplexer and a Keithley 2001 $7^{1/2}$ digits digital multimeter (DMM).

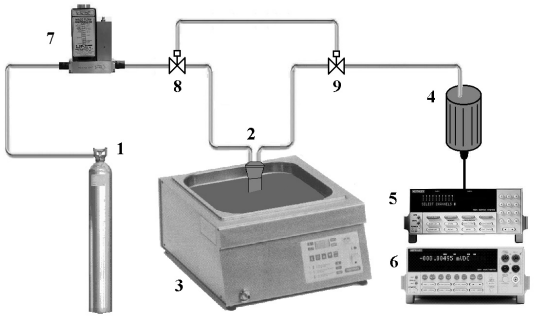

Fig. 1 Experimental setup. 1)nitrogen bottle; 2)Dreschel bottle with sample; 3)thermostatic bath; 4)sensor cell; 5)multiplexer; 6)DMM; 7)mass flowmeter controller; 8)and 9)Electrovalves.

2.2 Sensors

An array of 16 thin film tin oxide sensors was prepared in our laboratory by RF sputtering onto alumina and doped with chromium and indium. The details of the preparation are described elsewhere [2]. Sensors are put in a stainless steel chamber kept at 300 °C.

2.3 Aromatic compounds

The aromatic compounds measured were: acetic, acid, ethyl acetate, acetaldehyde, 2,4,6-trichloroanisole (TCA) and sulfur dioxide (SO_2). Their concentrations in 12% (v/v) ethanol solution are shown in table 1. At these levels they are usually considered off-odors in wine [3].

Table 1. Concentrations of the aromatic compounds

Compound	Concentration	Units
Acetic acid	200-800	mg/l
Ethyl acetate	50-300	mg/l
Acetaldehyde	50-400	mg/l
TCA	1-10	ng/l
SO_2	20-200	mg/l

3 Results and discussion

Responses of the individual sensors are defined relative to the minimum resistance to 12% (v/v) of ethanol:

$$r = \frac{R_{et}}{R_c}$$

where R_{et} is the minimum resistance of the sensor in ethanol and R_C is the minimum resistance of the sensor in the solution with the compound. The responses obtained can be as high as 200 % for some sensors and aromas.

Figure 2 shows the PCA plot for the compound dataset. The percentage of variance explained by each principal component is in brackets. Datasets are clearly separated. The PCA results are confirmed with the PNN analysis. The confusion matrix is showed in table 2. There is a 95 % classification success for the compounds.

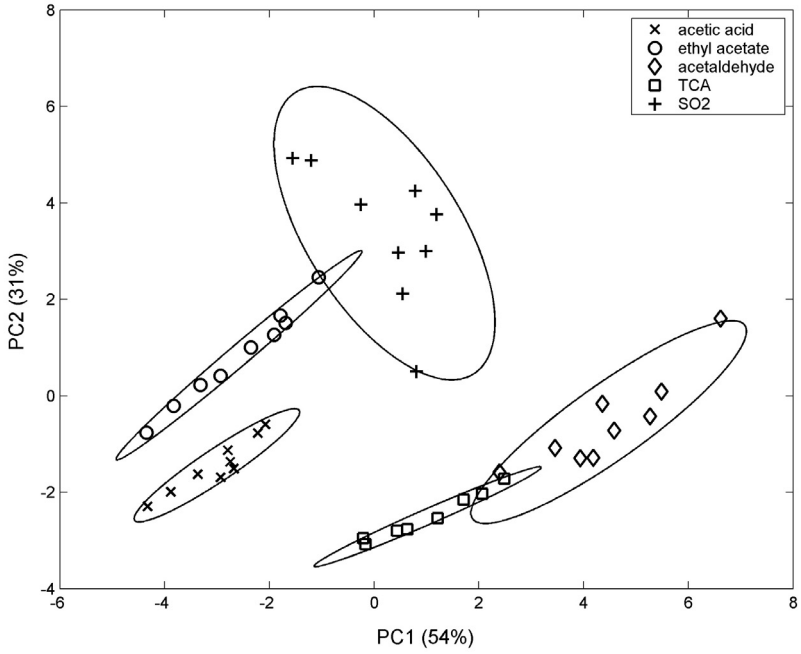

Fig. 2. PCA score plot.

Table 2. Confusion matrix of the RB-NN.

	Predicted compound				
Real compound	Acetic acid	Ethyl acetate	Acetaldehyde	TCA	SO_2
Acetic acid	9	0	0	0	0
Ethyl acetate	0	9	0	0	0
Acetaldehyde	0	0	8	1	0
TCA	0	0	0	8	0
SO_2	0	0	1	0	8

4 Conclussions

Discrimination of several aromatic compounds can be performed by a thin film sensor array even in the presence of a strong ethanol interference. The radial basis neural network classification results in a 95 % success rate.

References

[1] J. A Guadarrama et al., "Discrimination of wine aroma using an array of conducting polymer sensors in conjunction with solid-phase micro-extraction (SPME) technique", *Sensors and Actuators B 77* (2001) 401-408.

[2] M.C. Horrillo et al., "Design and development of an electronic nose system to control the processing of dry cured Iberian hams monitored via Internet". *Electronic noses and olfaction 2000,* pp.75-80. Bristol and Philadelphia: Institute of Physics publishing.

[3] R. S. Jackson, *Wine Science*, San Diego, California: Academic Press, (1994).

Surface Nanomachined Ni Tunneling Switch Using Electron Beam Crosslinked PMMA

W.H. Teh[1] and C.G. Smith[1,2]

[1]Cavendish Laboratory, University of Cambridge, Madingley Road, Cambridge CB3 0HE, UK
Email: wht21@cam.ac.uk
[2]Cavendish Kinetics Ltd., Statenlaan 57, 5223 LA 's-Hertogenbosch, The Netherlands

Summary: We demonstrate a three terminal electrostatically actuated 280nm thick Ni/Au bilayer cantilever with an insulated contact bump acting as a nanomechanical tunneling device, similar to a mechanical transistor. This near-zero curvature nanomechanical contact mode tunneling switch is fabricated using a combination of Ni plating and electron beam crosslinked PMMA surface nanomachining. It operates by modulating the tunneling current characteristics based on an elastic compressible contact surface model, which allows the gate voltage to independently control the electron flow through the metal-insulator-metal (MIM) junction. The force from the gate alters the contact area. Our results suggest a contact area change from 600 to 800 nm^2.

Keywords: *electrostatic NEMS, tunneling, insulator, nickel*
Category: *10 (Applications)*

1 Introduction

The sensitivity of tunneling current as a function of mechanical position and the many advancements of NEMS/MEMS technology into fabricating nano/micromechanical components have inspired work combining MEMS with tunneling junctions to produce novel devices. These devices include tunneling sensors for use as accelerometers as well as the possibility of a micromechanical tunneling transistor [1]. Here, we propose the combination of a NEMS switch with a built in tunneling junction to produce a nanomechanical contact mode tunneling switch. This is fabricated using a combination of Ni plating and electron beam crosslinked PMMA as the sacrificial layer. This device operates by modulating the tunneling current characteristics based on an elastic compressible contact surface model.

2 Results and discussion

The NEMS switch reported here is fabricated using an *electron beam crosslinked* PMMA surface nanomachining technique [2], combining with nickel electroplating. Here, we exploit the compliant nature of electron beam crosslinked PMMA as the sacrificial layer for the purpose of stress relaxation of the deposited mechanical film. This technique demonstrates curvature-free Ni/Au bilayer cantilevers measuring 10μm in length and 280nm in thickness, suspended over a 430nm gap, dimensions comparable to nanoresonators [3]. These near curvature free Ni switches [Figure 1] are highly scaled-down versions of previously reported cantilevers [4] and show reversible modulation of the tunneling current characteristics when applying different electrostatic pressure on the tunneling MIM junction. The electrostatic pressure comes from the excess potential applied on the gate after the cantilever has been switched on. More specifically, at an applied gate voltage of 36V or higher (pull-in voltage is 36V), the Ni beam switches due to instability, and as a result, the Al_2O_3 insulated bump at the tip contacts the underlying Au drain electrode creating a dielectric sandwich of $Au/Al_2O_3/Au$. The current-voltage characteristics at room temperature is non-linear and the contact can be modeled as a tunnel junction based on Simmon's theory[5] [Figure 2].

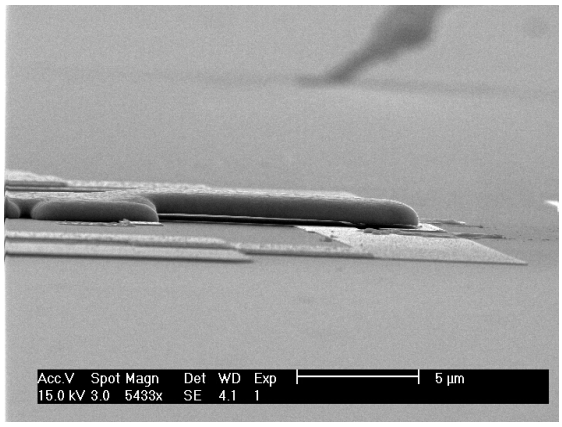

Fig 1. SEM micrograph of the switch in side view, demonstrating near zero curvature.

As the gate voltage increases, further compression of the contact asperities occur, resulting in higher tunneling currents. By plotting the drain current as a function of gate voltage (mutual characteristics), we find that the tunneling current is approximately linear with the gate voltage for the specific range in question [Figure 3].

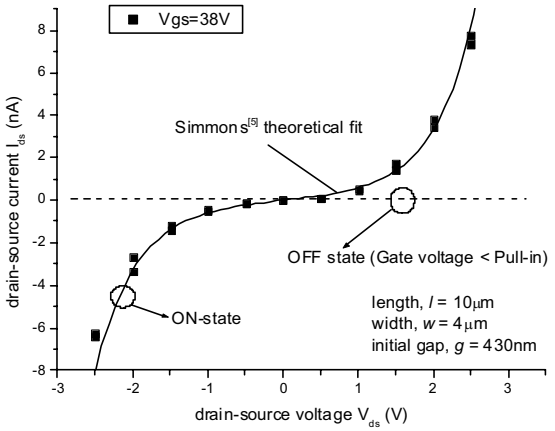

Fig 2. Measured I-V characteristics of the device demonstrates tunneling across the MIM junction.

In the present example, the softer Au asperity deforms under the pressure of the Al_2O_3 insulating asperity at the contact bump of the switch. This elastic compressible nature of the asperity modulates the effective tunneling area as shown by Hertzian analysis [Figure 4].

Due to the fact that it is the change in area that mostly dominates the change in tunneling current for our case, the *transconductance* of the device is in general low. Nevertheless, this research enables us to study the nature of the micro contacts formed at the tip of the cantilever. The area of the cantilever tip deduced from our data fit closely with the measured surface roughness of our underlying gold layer.

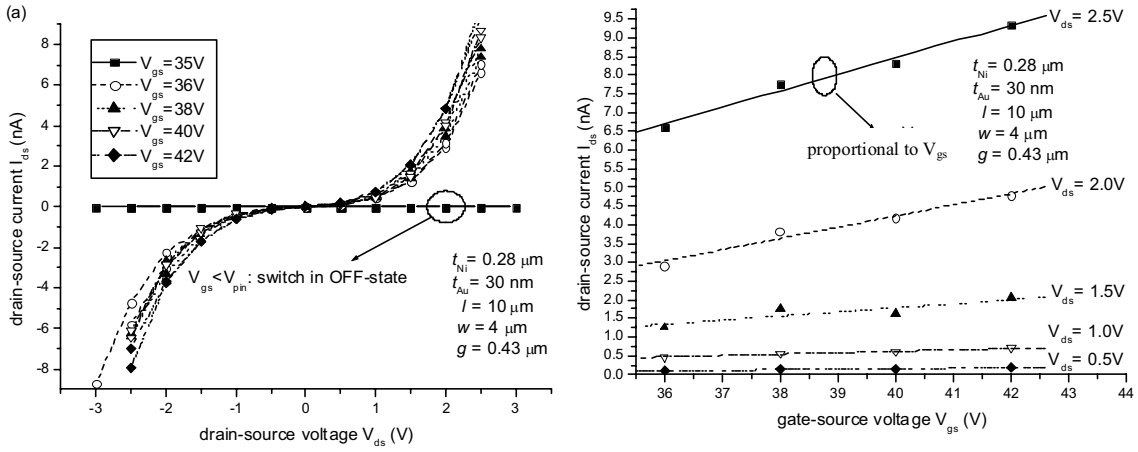

Fig 3. (a) Measured drain current, I_{ds} as a function of drain voltage, V_{ds} for different gate voltage, V_{gs} demonstrating tunneling characteristics, and (b) I_{ds} plotted as a function of V_{gs} for different V_{ds}, demonstrating linearity.

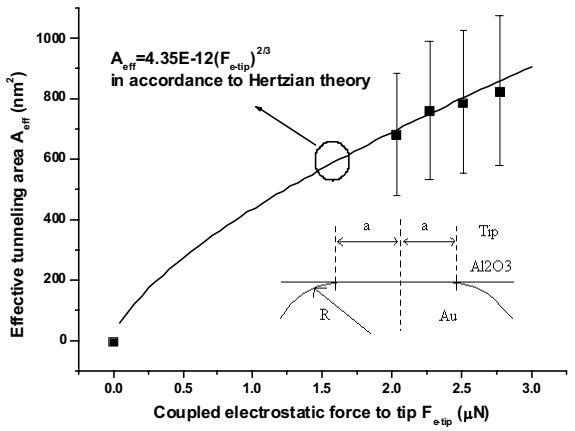

Fig 4. The effective tunneling area A_{eff} as a function of the approximate electrostatic force coupled to the cantilever tip, $F_{e\text{-}tip}$ with the inset showing the Hertzian model for the Al_2O_3 coated tip-Au drain electrode contact.

References

[1] M.A. McCord, A. Dana, and R.F.W. Pease, J. Micromech. Microeng., **8**, 209 (1998).

[2] W.H. Teh and C.G. Smith (submitted).

[3] A.N. Cleland and M.L. Roukes, Appl. Phys. Lett., **69**, 2653 (1996).

[4] P.M. Zavracky, S. Majumder, and N.E. McGruer, J. Microelectromech. Sys., **6**, 3 (1997).

[5] J.G. Simmons, J. Appl. Phys., **34**, 1793 (1963).

Position Measurement Using CCD Based Opto-electronic Gate

J. Vcelak, J. Fischer

Czech Technical University, Department of Measurement, Technicka 2, Praha 6, Czech Republic
email: vcelakj1@feld.cvut.cz, fischer@feld.cvut.cz, http://measure.feld.cvut.cz/groups/videometry

Summary: *This paper presents principles of optical position measurement methods based on opto-electronic gate. The opto-electronic gate increases the resolution by using a CCD line sensor instead of a simple photo detector. The use of the CCD line sensor increases the range and precision of measurement. Two optical measurement methods will be introduced in this article. These methods were implemented and verified on developed opto-electronic gate. Basic principles of these methods, configuration of measuring set-up and main results will be described in this article. We will also introduce innovative and powerful concept of opto-electronic gate hardware construction.*

Keywords: *optical measurement, position measurement, CCD line sensor*
Category: *(10) Application*

1 Introduction

Opto-electronic gates are used for object detection. Simple opto-electronic gates use only one photo detector. The arrangement of measurement of object position is shown in Figure 1a. The detection of spot inherency is shown in Figure 1b. The relation between *x* position and output signal of the photo detector is shown in Figure 1 too. The dimension of used photo detector limits the range of measurement. The power variations of light source cause deviations of the measured value. This problem is in introduced opto-electronic gate solved by using CCD line sensor and intelligent video-signal processing.

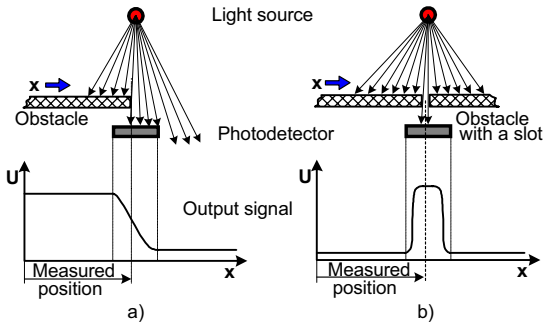

Fig. 1 Position measurement using one photo detector

2. Measuring of object's position

Two methods of measuring object's position will be presented in this paragraph.

2.1 Method A: Determination of slot's position

This method uses a material with a transparent slot, which is illuminated by a diffusive light source. The CCD line sensor scans the profile of illumination. Figure 2 demonstrates the illumination of the CCD line sensor. The function *E(x)* that represents the illumination of the CCD line sensor is symmetric to the point X_t. The point X_t corresponds to the distance, we are interested in.

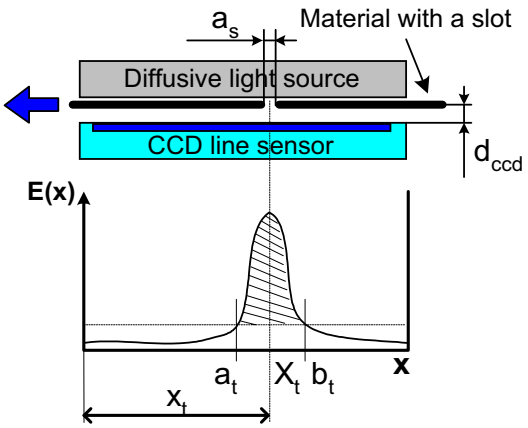

Fig. 2 Measurement of spot position

The relation between illumination *E(x)* and video-signal voltage level *U* is given by the expression (1) (where *K* is sensitivity of CCD and T_{int} is charge integration time).

$$U = K \cdot T_{\text{int}} \cdot E(x) \quad [\text{V}, \text{Vm}^2\text{J}^{-1}, \text{s}, \text{Wm}^{-2}] \qquad (1)$$

The accurate position of the slot is calculated as a centre of gravity of area which is bounded by the function *E(x)* (equation (2)). The centre of gravity of the video-signal's part is during real measurement calculated from a set of *N* video-signal samples (equation (3)) [1].

$$x_T = \frac{\int_{a_t}^{b_t} x \cdot E(x)}{\int_{a_t}^{b_t} E(x)} \qquad (2) \qquad x_T = \frac{\sum_{a_t}^{b_t} n \cdot U_{out}(n)}{\sum_{a_t}^{b_t} U_{out}(n)} \qquad (3)$$

2.2 Method B: Measurement of object's position illuminated by two point light sources

The second method consists in illumination of the object with two point light sources A and B in turns. The measurement arrangement is shown in Figure 3. Firstly source A is switched on and the position of the first optical edge l_1 is recorded. Then source B is switched on and second position of optical edge l_2 is recorded.

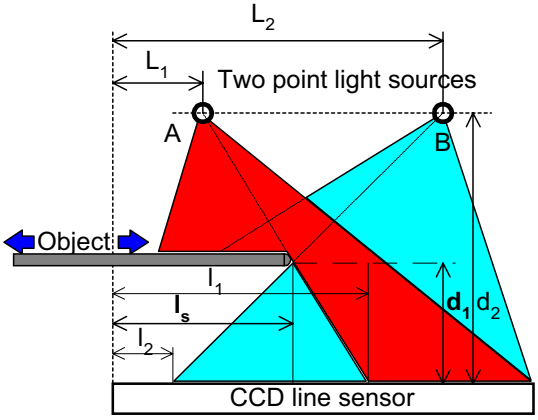

Fig. 3 Measurement of object position usig two poin light sources A and B

Distance d_1 (equation 4) and position of the object l_s (equation 5) are calculated from recorded values l_1, l_2.

$$l_s = \frac{L_2 l_1 - L_1 l_2}{L_2 - l_2 - L_1 + l_1} \qquad (4)$$

$$d_1 = \frac{d_2 \cdot (l_s - l_2)}{L_2 - l_1} \qquad (5)$$

The real form of CCD illumination is shown in figure 4. Positions l_1, l_2 can be determined with comparison of the video-signal with a reference voltage level. Method called photometric interpolation of optical edge is used for more precise determination of object position.

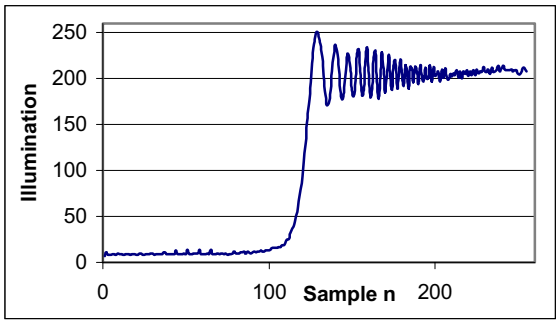

Fig. 4 Detail of CCD illumination in the area of optical edge

LASER diode SLD6505 is used as the point light source. The other details of this method are presented in [2].

3 Hardware construction

Our technical effort has been focused on developing opto-electronic gate that satisfies these requirements:

- As simple electronic construction as possible, compact and small design
- Low cost but fine measurement of object position in industry
- Universal design that allows using the only one device for several measuring methods (including presented methods A and B)

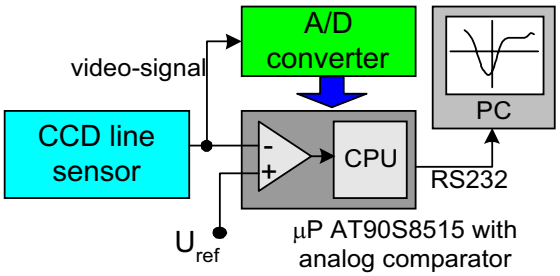

Fig. 5 Block diagram of developed opto-electronic gate

The developed opto-electronic gate consists of three basic parts: microprocessor AVR AT90S8515 that drives the gate, CCD line sensor with 2048 fotoelements and high speed 8-bit A/D converter AD9280 that digitizes video-signal from CCD. The block diagram of developed opto-electronic gate is shown in Figure 5.

4 Conclusion

Both presented methods were implemented into the developed opto-electronic gate. The linearity error of measurement of object's position is in the case of method A 0,2 % FS (FS-full scale, width of the slot was 0.25 mm). The range is limited with the length of CCD line sensor (in our case 28 mm), and the length of diffusion light source (20 mm). The centre of area is calculated directly in AVR microprocessor from stored values of the video-signal. The method B allows more accurate measurement of object position in two normal axes (directions of d_1 and l_s). The repeatability of measurement of one position in direction l_s is 2 µm. The linearity error of the position measurement in the direction l_s is 173 ppm FS and in the direction d_1 is linearity 400 ppm FS (measurement conditions: d_2=65 mm, L_1=8 mm, L_2=20 mm).

5 Acknowledgement

The results of the research project MSM 210000015 were used in this paper.

6 References

[1] F. Heijden : *Image Based Measurement Systems*, John Wiley & Sons, 1994

[2] Fischer, V. Haasz, T. Radil : *Simple Device for Small Dimension Measurement Using CCD Sensor*; 12th IMEKO TC4 International Symposium, Zagreb 2002, p. 433-437.

MISFET Radiation Dose and Diode Temperature Sensor for Environment Monitoring of Electrical and Electronic Equipment at NPP and Space Applications

V. V. Emeliyanov, I.Yu. Kalinkin, O.V. Meshurov, K.I. Tapero and V.V. Ulimov

Research Institute of Scientific Instruments,
8 Building, Turaevo Promzona, Lytkarino, 140080 Moscow region, Russia
email: eldiv@cityline, risi@tsr.ru

Summary: *The work presents the results and development concepts of wide-range MISFET dosimeter and radiation resistant temperature diode sensor manufactured in the form of hybrid integral circuit for Environment Monitoring of Electrical and Electronic Equipment at NPP and Space Applications.*

Keywords: *Environment Monitoring, MISFET dosimeter, diode temperature sensor*
Category: *10 (Applications)*

1 Introduction

In most cases electric and electronic equipment at nuclear power plants and in the spacecraft operate under conditions of extended temperature range and the ionising radiation effect. Monitoring of integral levels of ionising radiation (the deposited dose) and temperature effects is the integral part of the ageing management for equipment of the given class. Cheap and easily adaptive with automatic data collecting systems sensors are needed (employing the same principles in original information data processing is wanted).

From the beginning of the 70th there were developed different types of Metal Insulator Semiconductor Field Effect Transistor (MISFET) dosimeter [1,2]. The advantages of sensors of the given type comprise simple processing of initial information signal – the drop of voltage across the MISFET (ΔV) with fixed current – and possibility of recording the dynamics of collecting and the integral value (dose) of ionising radiation over the total observation term as well. The disadvantage is relatively narrow dynamic range determined as the number of decades between the smallest and the largest detectable dose. For this reason the MISFET dosimeters are usually designed for specific usage mode. The possibility utilisation of silicon diode as radiation resistant sensor has been reported in [3].

In this work the results and development concepts of wide-range MISFET dosimeter and radiation resistant temperature diode sensor manufactured in the form of hybrid integral circuit for Environment Monitoring of Electrical and Electronic Equipment at NPP and Space Applications are presented.

2 MISFET dosimeter

MISFET crystals were manufactured by two different technological procedures. The first employed MOS technology with 400nm thermal gate oxide (SiO_2). In the second case the two layer dielectric was employed – 100nm-thick layer of thermal gate SiO_2 and 100nm-thick chemical vapour deposited Si_3N_4. The electric circuit of the semiconductor MISFET dosimeter is presented in Fig.1.

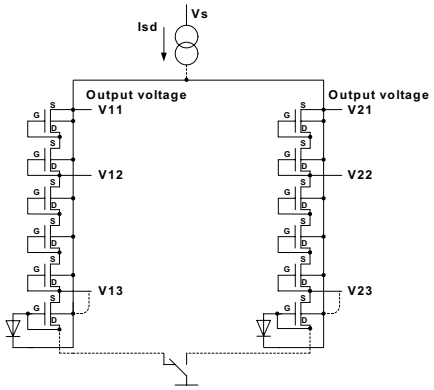

Fig.1. MISFET crystal circuit.

Series connection of five MIS transistors (stack) utilising the principle of substrate voltage control [4] was used to increase the sensor sensitivity (the ratio of signal variation ΔV to dose value). The following values of initial MISFET dosimeter sensitivity were obtained: 3V/krad for MOS-technology (SiO_2) and 1V/krad for MNOS-technology (SiO_2 /Si_3N_4) . The dose dependence ΔV for a single and six MISFETs of different technological origin are presented in Fig.2. Additional terminating connections were made providing possibility of changing sensitivity levels to increase dynamic range of dose recording. The second stack structure based on MISFET crystal

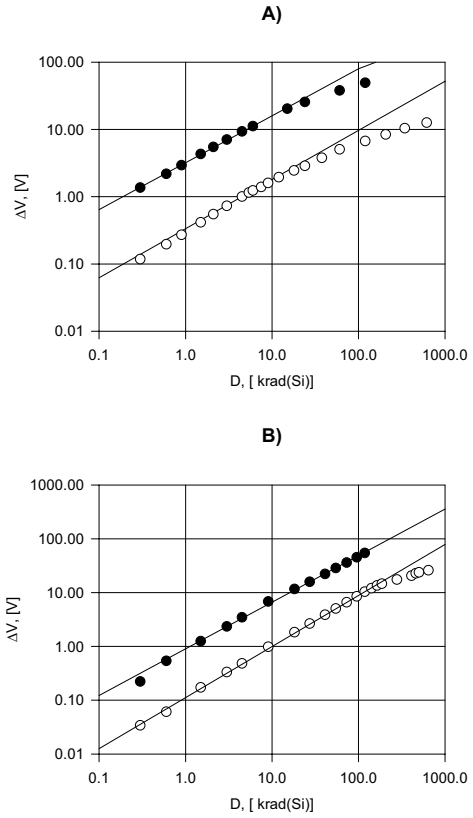

Fig.2. Information parameter shift versus deposited dose: A – SiO_2 gate oxide, B – SiO_2/Si_3N_4 gate oxide; empty symbol - single MISFET, black symbol – six MISFET stack.

was manufactured to implement one-of-a-kind MISFET dosimeters calibration with the aid of X-ray radiation [5].

3 Diode temperature sensor

The p^+-n protecting diode of particular MISFET from the MISFET set of the crystal was employed as the temperature sensor. In contrast with [3] the radiation thermal processing (RTP) has been applied in the present work to fabricate radiation resistant diode temperature sensor. The RTP procedure included high-energy electrons irradiation with the following annealing at a temperature of 350°C-450°C. That made it possible to employ the thermosensor operational point in the optimum zone of current-voltage characteristic (in the low-level injection range) without any additional diode manufacturing technological techniques. It has been proved that after RTP the temperature functions of the direct voltage drop across the diode do not vary up to the dose value no less than 1 Mrad (Si) under effect of γ -radiation of Co^{60} and 1 Mrad (Si) under effect of 100MeV-energy protons.

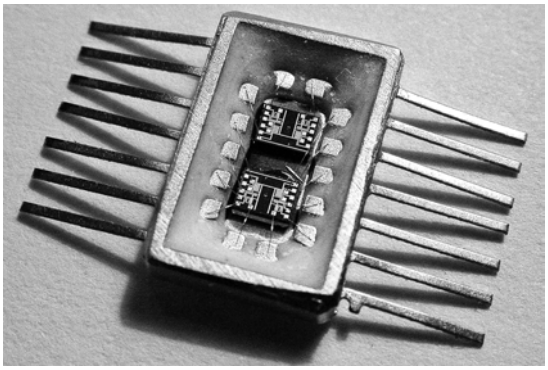

Fig.3. Hybrid microcircuit of MISFET radiation dose and diode temperature sensor.

4 Data collecting systems

For practical implementation the two MISFET crystals are a placed in to the standard chip package of the hybrid IC (see Fig.3). The two systems have been developed to provide operation of the given IC. The first one implies mobile mode of exploitation in the regime of lower power consumption and the operators control while carrying out the monitoring during maintenance works from the built-in key-board. The second is intended for operation in automatic data collecting systems. Both systems are constructed on the base of Atmel Company's AT90S8535 and allow to set up the needed current regimes for sensors, measure the information signal voltage and transfer the data through the RS232 and RS485 interfaces.

References

[1] A. Holmes-Siedle. The Space-Charge Dosimeter: General Principles of a New Method of Radiation Detection. *Nuclear Instruments and Methods* 121 (1974) 169.

[2] J.R. Schwank et al. A Dose Rate Independent pMOS Dosimeter for Space Applications. *IEEE Trans. Nucl. Sci.* 43 (1996) 2671-2678.

[3] Yu. M. Shwarts et al. Temperature sensors with high irradiation resistance for atomic application (technology, design, experiment, theory, application). *Digest of technical papers of the 11th International Conf. on Solid-State Sensors and Actuators. Munich (Germany)* Session 4B2: Flow & Thermal Sensors (2001) 1500-1503.

[4] B. O'Connell et al. Stacked RADFETs for Increased Radiation Sensitivity. *Proc. of the 3th European Conference on Radiation and Its Effects on Components and Systems* (1995) 481-486.

[5] V.V. Emelianov et al. Adjusting of pMOS Dosimeter Characteristics by Electrical Biases under Irradiation. *Proc. of the 12th European Conference on Solid-State Transducers and 9th UK Conference on Sensors and their Applications edited by N.M. White 2* (1998) 1029-1031.

2D velocity and concentration samplers for particle laden flows

F. Larrarte, L-M. Cottineau

Laboratoire Central des Ponts et Chaussées, Route de Bouaye, BP 4129
44341 Bouguenais Cedex, France
email: frederique.larrarte@lcpc.fr

Summary: *Measuring flow-rate and pollutant discharges through sewer networks is required for a number of reasons. In order to achieve such measurement s, a precise knowledge of the hydrodynamic conditions of each candidate measurement location proves critical. The LCPC has thereby become involved in a program on velocity and suspended matter concentration fields. This paper presents the devices developped to obtain2D sampling of the velocities and pollutant concentrations.*

Keywords: *velocity, concentrations, special sampling, sewer*
Category: *10 (Applications)*

1 Introduction

Two phase particle-laden flows have a wide range of applications. Sewage flows may be not the best known but a precise knowledge of pollutant loads is important for designing and operating sewer systems. Sewer systems are often considered as one-dimensional; thus, velocities and concentrations measurement devices typically regard the sewer cross-section as a whole. Previous research results show , that the actual repartition of velocities as well as particles and associated pollutants over a cross-section should be considered[1].

A research program has been conducted to combine numerical and experimental studies in order to assess how real hydraulic conditions can be taken into account to get. how a fairly accurate image of pollutant load conveyed through sewers. The objective of this project is both to decide whether a candidate measurement location is suitable for instrumentation, , and to design a suitable processing for values measured by sensors fitted in this location[2]. The main consequence of these objectives is the requirement of two- and three-dimensional views of the velocity and suspended solid loads. This paperdeals with getting field data about observed concentration values across a sewer section. Other works have been conducted about observed velocities, and extrapolation to 3D configuration by numerical modelling.

2 Review of existing devices

Hughes and al. [3] have proposed an array of acoustic Dopplers to sample the velocities field but it gives only a limited number of measurements in a cross section and the location of those points can not be easily selected. We did not found any other device that can be used in sewer networks.

Wohrle and Brombach [1], Verbank [4] have tried to obtain suspended solids concentrations throughout depth but only in dry weather periods. However, suspended load transport is more important during wet weather periods. At least they have shown that the usual hypothesis about homogeneous distribution of suspended solids is not true. This review shows that no readily available device is convenient for our purposes. Thus we developed new ones.

3 Development of 2D samplers

Among the first conditions to respect, there is security rules that forbid any human presence in the sewer during rain event. Thus, in order to make measurements whatever the meteorological conditions are, the experimental devices have to be operated from the manhole (that is commonly 1 m wide). This implies that the different elements should be easy to handle as some of them have to be carried to the measurement site for each operation.

Some equipement must be left in position in the sewer, and much care has been taken no to impinge the flow of wastewater for too long periods: For instance the sampler is setup in a raised position when not in used.

The atmosphere in the sewer is quite corrosive so the device must be rugged.

Another condition is due to the hydraulic context. Figure 1 shows an example of data continuously monitored on the experimental area since 1997. During the dry weather periods, there is a cyclic

evolution of the water level but each rain generates an increase of the water levels, velocities and rates in proportions that can be tremendous. Hence the samplers need a measurement range wide enough and the sampling locations have to be designed in such a way that sampling can be carried out throughout the whole cross-sectional area. Moreover, in real network, the flow are not stationnary thus the best thing should be to sample, at the same time, all the data.

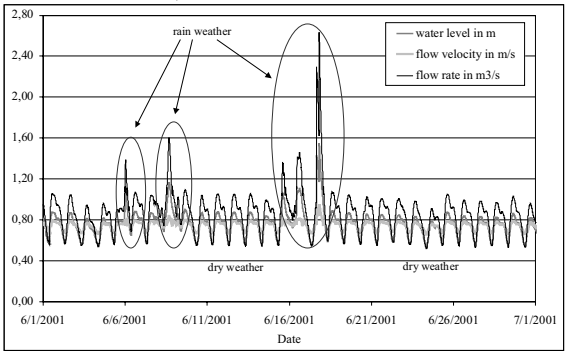

Figure 1: Ranges of water levels, velocities and rates in the experimental area.

All those requirements are difficult to satisfy and the choice has been made to split the problem and to develop a 2D sampler of the velocities field (Cerbère) and another 2D sampler for the concentrations field. It is evident that the more sampling locations are used, the more accurate results can be obtained. However, for the pollutant concentrations, all samples have to be all analysed within the same half day and as soon as possible to avoid any chemical modification. Thus, there should not have to many sampling points. Taking care of all those points, Orphée (Figure 2) has been made. It allows to make vaccuum samplings in up to 24 locations at the same time. Cerbère allows up to three measurements in a vertical with three acoustic Doppler velocimeters. Those sensors can be moved vertically to make profiles and, iterating that process, a 2D sampling of the velocity field can be obtained.

Figure 2: Orphée: the 2D sampler in the raised position

Figure 3: "Cerbère": the 2D remote-controlled device for measuring velocity fields

4 Conclusion

In spite of some reliability problems due to the corrosive atmosphere in the sewer, the 2D samplers Cerbère and Orphée have been set up in a real sewer for more than one year. A set of experimental cases providing either the velocity maps or the suspended solid concentration maps is already available for an egg-shaped sewer. A fairly broad spectrum of flow conditions has been measured, especially as regards the concentrations

References

[1] C. Wohrle and H. Brombach, Wasserwirtschaft, Vol. 81 (1991)
[2] P. Jaumouillié,. Ph. D. thesis Université de Bordeaux I, janvier (2003).
[3] A.W. Hughes, I.M. Longair, R.M. Ashley and K. Kirby., Water Sci. Tech., Vol. 33, No. 1 (1996).
[4] M.A. Verbank., 6th Int. Conf. On Urban Storm Drainage, Niagara Falls, USA, (1993).

Discrimination of contaminant gases with artificial Neural Networks

M. Aleixandre, I. Sayago, M.C. Horrillo, M.J. Fernández, L. Arés, M. García, J.P. Santos and J. Gutiérrez

Laboratorio de Sensores, Instituto de Física Aplicada (IFA), Consejo Superior de Investigaciones Científicas (CSIC), Serrano 144, E-28006 Madrid, Spain
email: manuel@ifa.cetef.csic.es http://www.ifa.csic.es

Summary: *A multisensor based on tin and tin-titanium oxides has been utilised to detect primary pollutants (NO_2, CO, toluene and octane) in dry air. The sensitive layers are deposited by r.f. reactive sputtering. Some tin oxide sensors are doped with Pt. Measurements are carried out with single gases and gas mixtures (two and three gases) in dry air at 250 ºC. The sensor responses are pre-processed with different methods and then analyzed with Principal Component Analysis (PCA) and several Artificial Neural Networks (ANN): Probabilistic Neural Network (PNN) and Multilayer Perceptrons (MLP). A selection of the sensors and of preprocessing techniques was made with a genetic algorithm.*

Keywords: *multisensor, air pollutants, neural networks.*
Category: *10 (Applications)*

1 Introduction

Air pollutants occur both outdoors or indoors, can be natural or man-made. Typical air pollutants from man-made activities include nitrogen oxides, carbon monoxide, sulfur dioxide and hydrocarbons. All these pollutants are called primary pollutants because they are emitted directly into the atmosphere.
The control and monitoring of pollutants for ambient air quality is at the present limited by the techniques currently approved by the existing standards that need the use of costly analytical equipment. Continuous monitoring of pollutant in air is expensive, so that high-density networks of measurements are usually impracticable.
A potentially more cost-effective way of performing such measurements is using metal-oxide gas-sensor arrays. Sensor array systems use the global information formed by the responses of all sensors to discriminate among gases. The signals of the multisensor can be evaluated by techniques of Principal Component Analysis (PCA) and Artificial Neural Networks (ANN) with a selection of the possible features through a genetic algorithm that facilitates the classification task [1].
In this work, gas mixtures have been detected, then a analysis of the feature selection and of neural network had shown that their discrimination is possible.

2 Experimental

The multisensor consisted of 8 sensing elements deposited by r.f. reactive sputtering from SnO_2 and TiO_2 targets. Four tin oxide sensors were doped with different amounts of Pt. The deposition conditions, dopants and thermal treatment were described in previous works [2].

The characteristics of each sensor are listed in Table 1, doping levels are expressed as sputtering times (seconds).

Table 1: Multisensor distribution.

Sensor	Semiconductor material
S1	SnO_2 (300 nm)
S2	SnO_2 (400 nm)
S3	SnO_2 (150 nm) - Pt (8 s) - SnO_2 (150 nm)
S4	SnO_2 (150 nm) - Pt (16 s) - SnO_2 (150 nm)
S5	SnO_2 (200 nm) - Pt (8 s) - SnO_2 (200 nm)
S6	SnO_2 (200 nm) - Pt (16 s) - SnO_2 (200 nm)
S7	SnO_2 (300 nm) – TiO_2 (150 nm)
S8	SnO_2 (400 nm) – TiO_2 (150 nm)

The multisensor device was placed in a stainless steel test chamber and it was characterized by DC electrical measurements.
A flow of 200 ml/s of dry air was used to achieve a line base. Then a automatic system controlled via PC switched the flux of gas with pollutants for 10 minutes. Afterwards dry air was fluxed until achieving a base line stable again. The resistance of the sensors is recorded during all the experiment every 60 seconds.
Measurements were carried out with single gases and gas mixtures (two and three gases) in dry air at 250 ºC. The concentrations go from 50 to 200 ppm for reducing gases and from 0.5 to 2 ppm for NO_2. Every experiment is repeated three times. The number of experiments carried out for binary and ternary mixtures are 72 and 96 respectively.
All the feature extraction and data analysis was made with Matlab.

The gas single PCA in figure 1 shows that only the NO_2 had a very good separation. The other three are slightly overlapped. The separation was worse with the mixtures of gases, so we needed other methods to discriminate among gases.

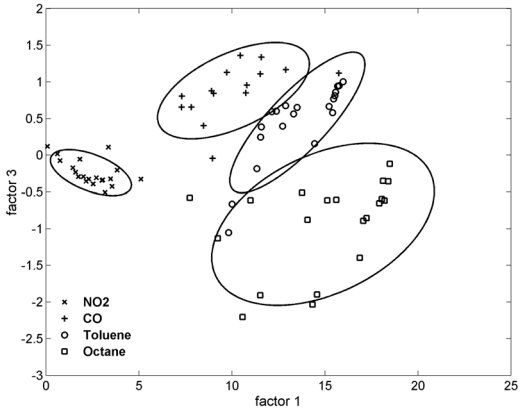

Figure 1: PCA plot.

We had used several neural networks and features subset to correctly classify the mixtures. The best subset of the features include a lot of data, so a genetic algorithm was used to improve the selection of features.

Two kind of neural networks were utilized to classify the different gases, a Multilayer Perceptron and a Probabilistic Neural Network. In both cases each gas was classified by a individual network [3].

A number of different features of the data were used to train the networks: maximum response, response at different times, wavelet expansion of the response curve. All these sets were validated with Leave-one-out cross validation and the results evaluated with the parameters described in table 2. The results of the networks are in tables 3 and 4.

We found that is better to carry out a feature extraction based on the properties of the signal than a general method of pre-processing and feature extraction.

Table 2: Parameter to evaluate the network

		Predicted	
		Gas present	Gas not present
Real	Gas present	A (true-positive)	C (false-negative)
	Gas not present	B (false-positive)	D (true-negative)

Accuracy (Acc.) = A+D/(A+B+C+D)
Sensitivity (Sen.) = A/(A+C)
Specificity (Spe.) = D/(D+B)

A genetic algorithm was used to select the best combination of sensors and features of these sensors. The fitness was the classification errors of a PNN [4]. In a few generations the convergence was reached and a reduction of 50% in the features space was achieved without performance reduction of the networks.

Table 3: Radial basis neural network results

		NO_2	CO	TOL.	OCT.
Responses at 10min	Acc.(%)	79	83	87	85
	Sen. (%)	81	82	82	85
	Spe. (%)	78	84	91	85
Responses at 5, 10 and 15 min.	Acc. (%)	95	89	99	94
	Sen. (%)	95	86	100	93
	Spe. (%)	96	91	98	94
All Points.	Acc. (%)	88	73	92	79
	Sen. (%)	90	74	93	80
	Spe. (%)	86	71	90	78
Wavelet.	Acc. (%)	86	74	90	75
	Sen. (%)	92	75	95	73
	Spe. (%)	80	74	83	76

NO_2: Nitrogen dioxide, CO: Carbon monoxide, TOL: Toluene, OCT: Octane

Table 4: Back propagation neural network results

		NO_2	CO	TOL.	OCT.
Responses at 10min	Acc. (%)	92	87	96	86
	Sen. (%)	93	90	97	87
	Spe. (%)	91	84	95	86
Responses at 5, 10 and 15 min.	Acc. (%)	96	91	97	95
	Sen. (%)	96	91	97	95
	Spe. (%)	96	91	96	94
Wavelet.	Acc. (%)	92	88	96	90
	Sen. (%)	96	91	96	93
	Spe. (%)	95	86	96	88

NO_2: Nitrogen dioxide, CO: Carbon monoxide, TOL: Toluene, OCT: Octane

References

[1] J. W. Gardner and Philip N. Bartlett. Electronic Noses Principles and Applications. Oxford University Press (1999).

[2] M.C. Horrillo, J. Getino, L. Arés, J.I. Robla, I. Sayago and F.J. Gutiérrez. Measurements of VOCs with a Semiconductor Electronic Nose. *J. Electrochem. Soc*., Vol. 145, No. 7, (1998) 2486-2489.

[3] I. Sayago, M.C. Horrillo, S. Baluk, M. Aleixandre, M.J. Fernández, L. Arés, M. García, J.P. Santos and J. Gutiérrez. Detection of Toxic Gases by a Tin Oxide Multisensor. *IEEE Sensors Journal*, Vol. 2, No. 5, (2002) 387-393.

[4] P. Boilot, E.L. Hines, M.A. Gongora, R.S. Folland. Electronic noses inter-comparison, data fusion and sensor selection in discrimination of standard fruit solutions. *Sensors and Actuators B,* 88 (2003) 80–88.

Quantitative Ozone Detection with Ga_2O_3-based Gas Sensors

Ulrich Hoefer[1] and Maximilian Fleischer[2]

[1]Steinel Solutions AG, Allmeindstrasse 10, CH-8840 Einsiedeln, SWITZERLAND
email: ulrich.hoefer@steinel.ch http://www.steinel.ch
[2]Siemens AG Corporate Technology CT MS 2, Otto-Hahn-Ring 6, D-81739 Munich, GERMANY

Summary: *In this paper we present a a micro-processor operated ozone monitor for different applications which is equipped with a Ga_2O_3-based ozone sensor. It is able to detect ozone in the range from 10 ppb to 500 ppb (according to about 20 µg/m^3 to 1000 µg/m^3) with an accuracy of about 10 ppb (or 10%). There is an influence of humidity variations which can be eliminated to a big extent by using the signal of an additional humidity sensor. During long-term stability tests over at least 11000 h continuous operation no systematic drift was observed.*

Keywords: *Ozone sensor, Ga_2O_3, In_2O_3,, O_3,, ozone monitor.*
Category: *10 (Applications)*

1 Introduction

Systems for quantitative ozone measurement often are based on optical systems (chemoluminiscence) which are rather expensive. Commercial low-price semiconductor ozone sensors often are cross sensitive to humidity and their long-term stability of sensitivity is poor. Previous investigations on Ga_2O_3-semiconductor gas sensors showed that this material shows some advantages to other commercial metal oxide gas sensors [1], [2]. Among others Ga_2O_3 sensors show good reproducibility of ground resistance and sensitivity as well as low cross sensitivity to humidity. Additionally the sensitivity and selectivity of Ga_2O_3-based gas sensors can be influenced to a large extent by deposition of additional catalytical or physical filters on the sensor sheet as well as by changing the operation temperature. In this contribution we present a new Ga_2O_3-based ozone sensor which shows a unique long-term stability of ground signal and sensitivity. With the use of this new sensor quantitatively ozone measuring systems have been realised to be used in air quality control systems (public buildings), as ozone monitoring systems in laser printer equipped rooms, systems to monitor the outside ozone concentration (health aspect) or control systems for ozone treating processes of exhaust gas in food manufacturing processes.

2 Sensor preparation

The sensor is based on a Ga_2O_3 semiconductor gas sensor with a thin In_2O_3-layer on its surface [3], [4]. Figure 1 depicts the principal sensor set-up. The sensitivity, response- and recovery time can strongly be influenced by the operation temperature which can be varied between 550°C to 700°C.

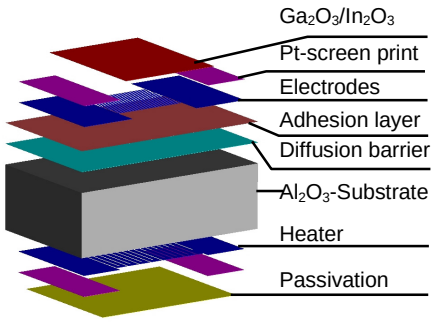

Figure 1: Principal sensor set-up.

The sensitivity is highest at 550°C. Unfortunately the response and recovery times at 550°C are considerable and also the cross sensitivity to humidity is remarkable. These drawbacks can be compensated by increasing the operation temperature. We identified 680°C operation temperature of the sensor chip as suitable for most applications. Figure 2 shows the temperature dependency of sensor response. The response time (t_{90}) is below 60s and the resistance increase is a factor 2 at 200 ppb (400 µg/m^3). The reproducibility of ground resistance and sensitivity is – compared to other metal oxide sensors – extremely good and long-term . Figure 3 shows the typical sensor response during exposure to a stepwise increase of ozone up to 500 ppb. Please note that the slight differences in signal arise due to a real slight increase of ozone during the hole measurement due to saturation of adsorbtion/desorbtion processes in the tubes and chambers. By using these sensors we developed a micro-processor operated ozone monitor for different applications which is able to detect ozone in the range from 10 ppb to 500 ppb (according to about 20 µg/m^3 to 1000 µg/m^3) with a resolution

below 10 ppb. The microprocessor equipped montoring systems are now tested in climatisation control systems where used air (volatile organic compounds) are oxidized by ozone. For security reasons there must be an ozone monitor detecting the limit of 80 ppb. During long-term stability tests over at least 11000h continuous operation no systematic drift was observed. The application and the system performance will be presented at the conference.

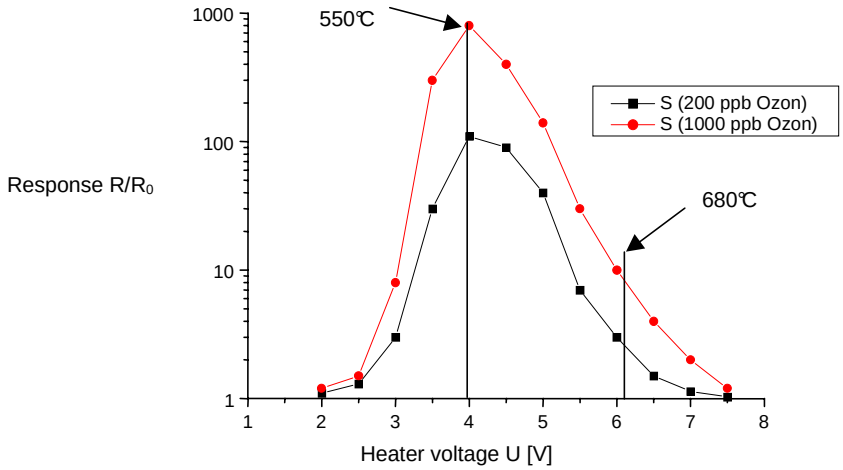

Figure 2: Sensitivity of the sensors to Ozone in wet air in dependence on the operation temperature.

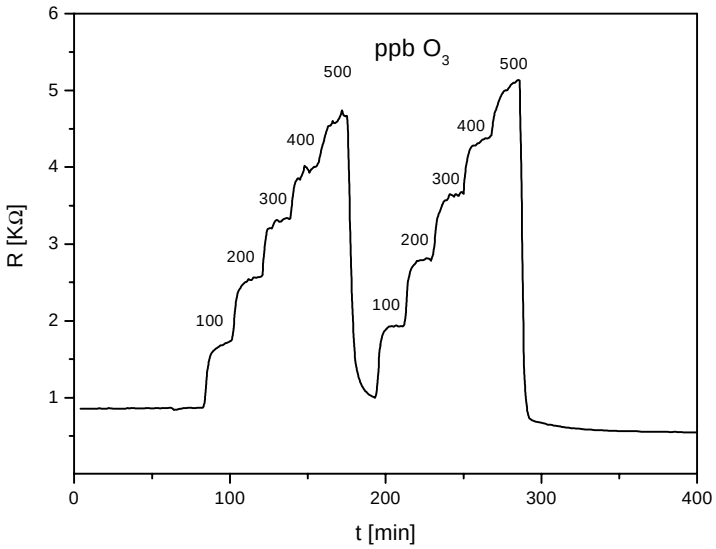

Figure 3: Typical sensor response during ozone exposure from 100 ppb to 500 ppb.

References

[1] M. Fleischer, H. Meixner, *Sensing reducing gases at high temperatures using long-term stable Ga_2O_3 thin films*, Sensors & Actuators, B6-7 (1992) 257-261

[2] U. Hoefer, J. Frank, M. Fleischer: *High Temperature Ga_2O_3-gas sensors and SnO_2-gas sensors: a comparison.* Sensors and Actuators B 78 (2001) 6-11.

[3] U. Hoefer, A.Nauer, J. Frank und M. Fleischer, *Galliumoxid Gassensoren - von der Entwicklung in die Produktion*. Proc. 10. GMA/TG Fachtagung Sensoren und Meßsysteme, 13.-14.3.00 in Ludwigsburg, Germany.

[4] J. Frank, M. Fleischer, M. Zimmer, and H. Meixner, *Ozone sensing using In_2O_3-modified Ga_2O_3 thin films*. IEEE Sensors Journal, 1/4 (2001).

DNA Capacitive Sensor

M. Pighini, M.R. Simone and S. Sunna

[1]Technobiochip scarl., Bio-molecular Labs., via della Marina 39, 57030 Marciana (LI), Italy
email: monica@technobiochip.com http://www.technobiochip.com

Summary: *This paper proposes a new methodological approach that allows the nucleic acids revelation (DNA, RNA, PNA). It is associated to a sensing device comprising a planar array of closely-spaced capacitive sense elements. It correlates a miniaturized capacitive sensor to the biological and medical analysis, in order to develop a new tool, especially for diagnostic purposes.*

Keywords: *DNA-sensor, capacitive array.*
Category: *10 (Applications)*

1 Introduction

In the last years development in microsystems research has reached important goals, as it has important and advanced technological applications. In particular we're going to set up an innovative technology that will have a great impact in the field of the life science.
The "DNA-SENSORS" development is the most innovative branch of the molecular technology because it allows an easy, fast, and reliable way to analyze many *probes* at the same time[1].
The proposed technology, patented by Technobiochip[2], is based on nucleic acid dielectric capacity measurement, in order to reveal its presence or to evaluate its characteristics.
We use a commercial microfabricated array of capacitors (288 x 224 elements), each of them contains independent capacitance-measuring circuitry; therefore each element can be queried separately, and its value is returned on an 8-bit scale.
A single capacitor, or pixel, is shown schematically in Fig. 1, as equivalent circuit.

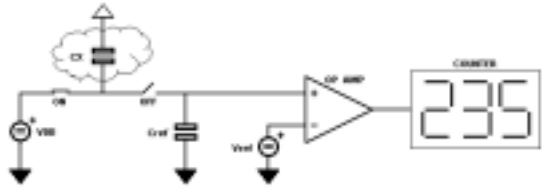

Fig. 1. Scheme of a single capacitive sensor. Cx: unknown capacity to be measured; VDD: internal power supply, used to charge the unknown capacitor *Cx*. Cref : internal reference capacitor; Vref: reference power supply internal to the chip, used to fix a threshold. OP AMP: operational amplifier used as comparator to determinate when the potential across the *Cref* reach the fixed *Vref*. COUNTER: digital circuit.

The chip area is about 11mm x 14mm, and includes more than 64.000 separate sensors, therefore the instrument has the advantage to be compact, multiplexed and reliable. Moreover the great number of obtained results represents a strong internal control

It offers the following advantages:
- The "*real-time*" evaluation of the results, allowing cost and time saving.
- The possibility of recording the DNA concentration, and the determination of very low concentrations.
- The possibility of recognizing the solid phase hybridization.
- The possibility of distinguishing different DNA kind.

Fig. 2. Example of capacitive sensor.

Possible applications, in this way, are:
- Human pathologies diagnostic screening, correlated to know genetic mutations.
- Genetic mutation, deletions or amplifications detection.
- Recombinant antibodies gene expression in transgenic cells.
- Differential genomic study, with applications in several fields: determination of phylogenetic trees, paternity testing, human and animal identity testing for forensic science, proof of descent, pedigree analysis.

2 Results

We have developed a software that converts the measure into an image and analyzes it using all the classical algorithms to classify images. It allows a differential measure between the reference and the sample in few seconds.
The acquired image consists of 288 rows x 224 columns; each image pixel represents the capacity value measured by a single sensor.
The measure range is comprised from 0 and 255 (in fact a capacity measure is sent to the PC as a byte); our software assign to this value a different color according to its magnitude, therefore the final result is a colored image.

We demonstrated the possibility of the sensor to discriminate among different DNA concentrations.
Below the dose-response curve (Fig.3) and the corresponding values (table 1) are reported: the trend shows a light increase for low concentration (within a range between 0 and 5 ng), following an exponential segment within 5 and 15 ng, and at last the plateau around 100 ng.

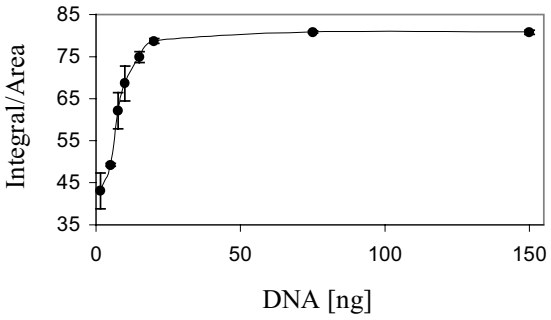

Fig.3. Dose-response curve. The sensor is able to distinguish among different DNA concentrations, as an exponential trend with plateau between 50 and 100 ng can be seen.

Differential elaboration			
ng [DNA]	Differ. Integral	Area	Int. / Area
1,5	7246	189	38,33862
5	73956	1511	48,94507
7.5	68807	1164	59,11254
10	92715	1479	62,68763
15	115441	1560	74,00064
20	114215	1443	79,15107
75	128071	1587	80,70006
150	144555	1778	81,30202

Table 1. Numeric values associated to the dose-response experiment. The y function of the graph is expressed as the ratio between the differential integral of the measurement and the area of the DNA drop.

Our sensor can supply a precise, and absolutely reliable measure in few seconds, without the expensive materials and tools necessity.

This sensor can also recognize the DNA nature: in fact plasmidic DNA (small circular DNA molecule, characteristic of bacterial microorganisms) shows a pick of about 1.1 A.U. (A.U.=Ratio between ε ($\varepsilon_0 \cdot \varepsilon_r$) and ε_o); while genomic DNA shows a pick of 1.9 A.U.

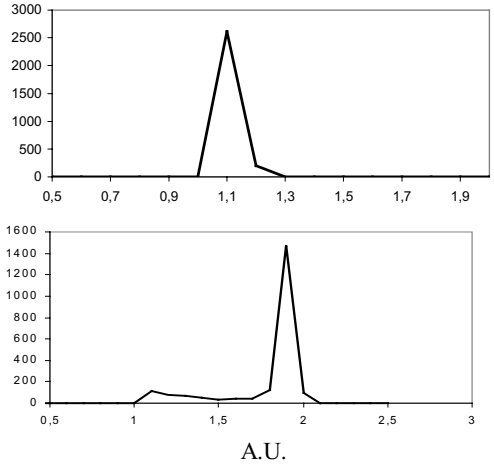

Fig. 4. Graphs showing the ability of the sensor to distinguish between plasmidic and genomic DNA.

Other experiments (not shown) demonstrate that our device is able to distinguish among DNA with different content in (G+C) and among genomic DNA from different species. This allows the possibility to perform taxonomic and phylogenetic studies in a easy and reliable way.

References

[1] M. Cocco, M. Pighini and S. Sinopoli.
Procedure for the revelation of nucleic acids by capacitive sensor to cells matrix. Patent 28 December 2001, N° RM2001A000774. (2001).
[2] J.Wang. From DNA biosensors to gene chip. *Nucleic acid research* 2000 vol. 28, N.16, 3011-3016.

Electrochemical DNA Sensor For Detection Of Genetic Mutations Related To *Neuroblastoma*

S. Sunna, M.R. Simone and M. Pighini

Technobiochip S.c.ar.l, via della Marina 39, 57030 Marciana (LI), Italy
e-mail: s.sunna@technobiochip.com http://www.technobiochip.com

Summary: *The availability of the human genome sequences has enabled identification of numerous mutations related to inherited human diseases, such as tumors. In recent years great progresses have been achieved in development of DNA sensors able to detect the presence of mutated genes in human genome. Our electrochemical DNA sensor is based on the chronopotentiometric monitoring of the hybridization process by a redox active indicator that binds double-stranded DNA more strongly than single stranded DNA. We are currently studying some application of our DNA sensor to reveal genetic mutations related to Neuroblastoma.*

Keywords: *Neuroblastoma, Potentiometric Stripping Analysis (PSA).*
Category: 10 *(Applications)*

1 Introduction

The mutations responsible for numerous inherited human disorders are now known, and this knowledge is steadily increasing as the sequencing of human genome is completed. Therefore the specific detection and analysis of DNA sequences and the study of gene polymorphism play more and more a fundamental role in rapid diagnosis of genetic mutation associated with the presence of disease states. The set up of assay techniques that have the convenience of solid phase hybridization and are rapid, sensitive and readily multiplexed will have a significant impact on genomic and diagnostics. At this purpose, many efforts have been achieved in the development of biosensors able to detect the presence of mutated genes in human genome.

Biosensors are devices that combine a biological recognition agent, which confer selectivity, with a transducer, which provides sensitivity and converts the recognition event into a measurable electronic signal. Hybridization biosensors exploit the immobilization of a single-stranded (ss) DNA probe onto a solid support for the recognition of the complementary sequences. Electrochemical detection of DNA hybridization usually involves monitoring of the increased electrochemical response of a redox-active indicator, that recognizes the DNA duplex (indirect method) and probing hybridization-induced changes in the intrinsic signal of nucleic acid (direct method) [1]. The Technobiochip Electrochemical DNA Sensor enables the monitoring of adsorbed DNA species at carbon electrodes using the Potentiometric Stripping Analysis (PSA) [2]. Ag/AgCl (3 M KCl) and platinum wire were used as reference and auxiliary electrodes respectively. The procedure involves the use of an electroactive indicator, daunomycin hydrocloride, which intercalates the double stranded DNA [3]. The single-stranded DNA is immobilized on the graphite electrode surface using the avidin-biotin high affinity interaction. This procedure involves the formation of avidin layer onto the graphite electrode surface and then the binding of biotinylated DNA (Fig. 1).

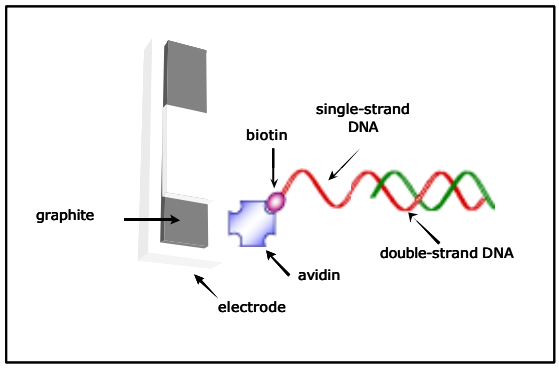

Fig. 1. Schematic diagram of DNA immobilization and hybridization on graphite electrode.

During the stripping process the potential is recorded and processed. The response is recalculated to (dt/dE) vs E and a peak shaped pattern is obtained allowing to reveal the happened hybridization. If the target sequence is present in the sample, a hybrid will be formed on the electrode surface and the increased size of the daunomycin PSA anodic peak compared with a negative peak shows directly the happened hybridization (Fig. 2).

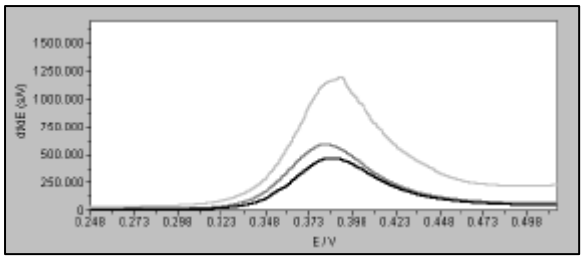

Fig. 2. Sensor response by PSA The black line shows the peak after the probe immobilization. The other lines show the same measurements after: a) interaction with a non-complementary sequence (gray line) and b) hybridization with a complementary sequence (light gray line).

Here we report an example of application of our DNA-sensor application, capable to reveal genetic mutations related to *Neuroblastoma*, the most common solid extracranial tumour in children.

2 Results and Discussions

We used the Technobiochip Electrochemical sensor to reveal genic mutations related to Neuroblastoma. At this purpose we set up a method for screening of the regions 9p21-p23 of chromosome 9, and 1p36 of chromosome 1, whose deletions in *Neuroblastoma* are known, using as marker D9S1810 and D1S244 microsatellites respectively. Data show that our sensor is able to reveal genic deletions related to this cancer (Fig. 3A-3B). These data have been confirmed by classical technique (ECL). Total human genomic DNAs, control (C) and tumoral (T), were labeled with digoxigenin, used for the hybridization step on the same electrodes of Fig. 3A, then they were treated with anti-DIG and exposed to autoradiographic film. Fig. 3C confirms the results obtained with the DNA sensor.

3A)

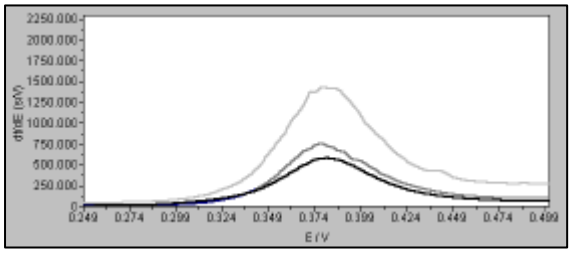

3B)

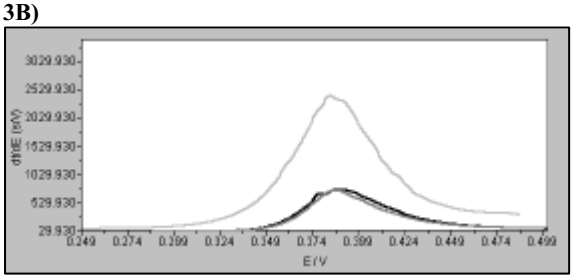

3C)

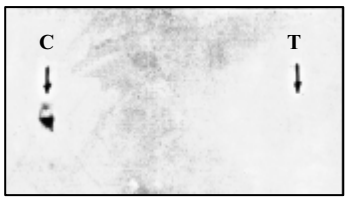

Fig. 3. Use of our device for deletion screening. The black lines show the peaks after the probe immobilization:
A) D9S1810 microsatellite
B) D1S244 microsatellite.
The light gray lines show the hybridization with total human genomic DNA EcoRI cut. The gray lines show the missing hybridization due to the use of total human genomic DNA (EcoRI cut) extracted from tumoral samples.
C) ECL performed on the electrodes shown in Fig. 3B (see text).

Actually we are testing the same system to reveal genic amplifications, in particular *N-MYC* amplification, another frequent genomic alteration in *Neuroblastoma*. In order to evaluate the ability of the sensor to detect different amounts of target DNA, *N-MYC* was hybridized with different concentrations of *N-MYC* itself. The pattern obtained (data not shown) indicates that the sensor is able to discriminate among different quantity of target and then gives the possibility to reveal genic amplifications.
In conclusion, this study has demonstrated the utility of our electrochemical biosensor for detection of genetic mutations associated with human disease, such as tumors. The new biosensor strategy could replace traditional assays for cancer diagnosis, eliminating the radioisotopes use, and needing shorter times.

References

[1] J. Wang, D. Xu, A. N. Kawde and R. Polsky. *Anal. Chem.* 73 (2001), 5576-5581.

[2] P. Mulchandani, W. Chen, A. Mulchandani, J. Wang and L. Chen. *Biosens Bioelectron.* 16 (2001) 433-437.

[3] D. Reha, M. Kabelac, F. Ryjacek, J. Sponer, J. E. Sponer, M. Elnster, S. Suhai, P. Hobza. *J. Am. Chem. Soc*. 124 (2002) 3366-3376.

A Method for Determining the Temperature Dependence of Thermal Drift of Fluxgate Sensors

Elena Despina Diaconu, Constantin Ioan, Mihai Valeriu Macoviciuc*, Cicerone Macovei

National Institute of Research and Development for Technical Physics, 47 Mangeron Bd., 6600 Iasi, Romania,
edia@phys-iasi.ro http://www.phys-iasi.ro
* Miranda Technologies Inc., Saint-Laurent (Quebec), Canada

Summary: *A method based on a Windows application developed in TestPoint that offers a flexible and cheap measurement of some functional parameters of fluxgate sensors is presented. The system allows the automation of the measurement and evaluation of sensor offset, amplitude and phase of the excitation signal, in dependence on temperature variation. A resolution of 0,1 ºC for the temperature measurement and a resolution of 0,488 mV or 4,88 mV, depending on amplification factor, for electric measures are achieved. The results obtained in the evaluation of stability of two types of fluxgate sensors against temperature variation were given.*

Keywords: *magnetic field sensors, temperature variation, virtual instrument*
Category: *10 (Applications)*

Introduction

One of the indispensable requirements for magnetometric sensors is the stability of functional parameters against temperature variations [1,2]. The requirements imposed include a good stability both for the magnetic noise and for the sensor offset in a large temperature interval as well as a good sensitivity of the sensor. An important parameter taken in to account in the study and design of fluxgate magnetometers is the offset and their temperature drift both for sensor and for magnetometric circuitry [3]. The paper reports the investigations made to determine the sensor stability against temperature variation.

Experimental

The studied sensors are Vacquier-Foerster type sensors with open magnetic paths. Classical TFS-3 sensors [4] and direct driven fluxgate sensors [5] were developed. The sensors parameters as sensitivity, offset, temperature drift of the offset and magnetic noise level were measured. The measurements regarding the temperature dependence of sensor parameters were performed in a thermostatic enclosure situated in a multilayer shielding system reducing the ambient field below 1 nT. A virtual instrument [6] offers the display of the measurements results. The used magnetometric circuit, characterized by measurement bandwidth of 0-10 Hz and magnetic noise level lower as 0,3 nT, is a conventional fluxgate magnetometer with synchrony detection and feedback. The useful signal is the second harmonic voltage of the excitation frequency on the pick-up coil of sensors. In order to have a thermal transfer coefficient approximately equal to that of investigated sensor, a sensor similar to them but without magnetic cores was used as temperature sensor. The variation of the voltage obtained from the resistance connected at the two windings in opposite connection gives the temperature variation. The measurements were performed with the magnetic sensor axis oriented on the minimal residual field direction and with the temperature sensor perpendicularly on the first. Electronic circuits for the measurement of amplitude and phase variation of excitation signal were also developed and included in the virtual instrument.

Results and discussions

The calibration of temperature sensor was made by measuring the output voltage for different temperature values between 2,7 and 98 ºC. A resolution of 0,1 ºC for the temperature measurement was obtained.

The transfer characteristic of the electronic circuit for determining the amplitude of excitation signal is linear in the 300 to 1500 mA_{pp} range. The measurements were performed for an excitation frequency of 10 kHz. The phase variation of the excitation signal has as effect a voltage variation at the integrator output in the circuit for phase variation detection. A linearity of this characteristic is observed in the measuring range.

The frequency characteristic of this circuit is linear in the frequency range 5 Hz – 1000 Hz. It results an undistorted signal for the first 100 harmonics of the excitation signal. Because the influence of excitation signal amplitude on the offset value of the magnetometric chain gives a variation with the minim slope corresponding to an excitation voltage of 6 V, all the measurements were performed at this excitation voltage.

Using the proposed device the electric measures were determined with a resolution of 0,488 mV or 4,88 mV, depending on amplification factor.
Figure 1 presents an example of displaying the four measured parameters for a TFS-3 type sensor in the temperature range from 8 to 70 ºC. The bolded curve corresponds to the sensor-offset variation. In order in that they across the right axis of the Graph 3, the other curves correspond to excitation voltage, integrator offset and amplitude of the excitation signal respectively. Graph 1 represents the imposed increase of temperature with the time. The virtual instrument gives also the magnetic noise level of the sensor.
The measured values and the obtained graphs can be stocked as Word or Excel documents.

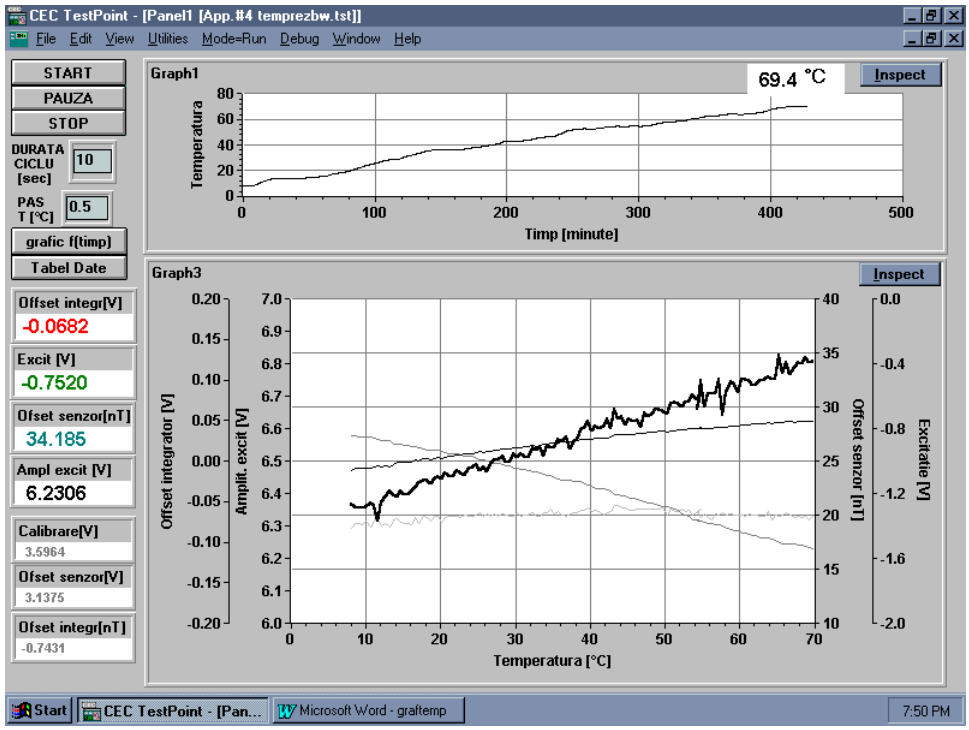

Fig 1: The display of virtual instrument for measurements of functional parameters of a TFS-3 sensor vs. temperature variation

Conclusions

Using a virtual instrument that uses digital instruments and a plug-in acquisition board controlled by a computer, measurements regarding the temperature dependence of some sensor parameters, as sensor and magnetometer offset, amplitude and phase of the excitation signal, were performed. The measurements performed for an excitation frequency of 10 kHz indicate a resolution of 0,1 ºC for the temperature measurement and a resolution of 0,488 mV or 4,88 mV, depending on amplification factor, for electric measures. The method allows the automation of the measurement process and analysis, offering a flexible and cheap measurement system.

References

[1] P. Ripka: Review of fluxgate sensors, *Sensors and Actuators* A 33 (1992), 129-141.

[2] R.S. Popovic, J.A. Flanagan, P.A. Besse: The future of magnetic sensors, *Sensors and Actuators* A 56 (1996), 39-55.

[3] O.V.Nielsen, J.R.Petersen, P.Brauer, B.Hernando, A.Fernandez, J.M.G.Merayo and P.Ripka: Development, constuction and analysis of the Ørsted fluxgate magnetometer, *Meas.Sci.Technol.*, 6 (1995), 1099-1115.

[4] A. Moldovanu, E.D. Diaconu, C. Ioan, E. Moldovanu: Magnetometric sensors with improved functional parameters, *Journ, Magn. Magn. Mater,* 157/158 (1996), 442-443.

[5] E.D.Diaconu C.Ioan A.Moldovanu, E.Moldovanu, H.Chiriac, F.Borza, M. Macoviciuc, C.Macovei: Sensitive direct driven fluxgate sensor with hairpin amorphous wire core, *Proceedings of 14th European Conference on Solid-State Transducers*, Copenhagen, Denmark, (2000), 773-776.

Improvement of a CMOS dual photosensor for laser distance measurement by a floating diode

P. Zivojinovic[1], M. Lescure[1], H. Tap-Béteille[1], X. Belredon[2], J.-P. David[2]

[1]ENSEEIHT-INPT, Laboratoire d'électronique, 2 Rue Camichel, 31071 Toulouse, France
email: zivojino@len7.enseeiht.fr http://www.enseeiht.fr/len7
[2]ONERA-Centre de Toulouse, DESP, 2 avenue E. Belin, 31055 Toulouse, France

Summary: *In this paper, a dual-control photosensor for laser distance measurement technique is presented. Distance is determined from a time-of-flight method. The light transmitted by a high frequency modulated laser diode is reflected on a target and then received by the photosensor. The photosensor is composed of two transparent gates witch are controlled by a coherent signal with the optical power modulation of the laser diode. The photosensor and associated electronic circuit are integrated in CMOS technology. The proposed dual-control photosensor works as a balanced-modulator. In standard CMOS technology, it's shown that a floating diode diffused between the two control electrodes improves charge transfer.*

Keywords: *photosensor, CMOS, laser distance measurement*
Category: *10 (Applications)*

1 Introduction

Distance measurement between range finder and a target can be deduced from the time-of-flight technique. Using a pulsed laser diode is the most common method to measure long distances range (from 10m to 300m) [1]. The reached accuracy is few centimeters approximately. Continuous wave modulation of the transmitted optical power by a laser diode is used in this paper, measuring phase-shift between the modulation signal and the photoelectric current. With a classical method, the high frequency photoelectric current is amplified by a transimpedance amplifier. To improve the signal to noise ratio, a heterodyne technique is used: the low level photoelectric signal is mixed by a balanced modulator, with a local oscillator signal. That permit to measure the phase-shift to an intermediate frequency with a narrow bandwidth.

In this paper, a CMOS dual photosensor is studied. The proposed structure detects the light transmitted by the laser diode. By the control of two gate voltages, the sensor gives two average photoelectric currents. Difference between these currents is proportional to the phase-shift that is proportional in the time-of-flight. The device works like a phase comparator. The operation principle of the sensor is presented in the first section. Then, a CCD compatible structure is proposed in the second one [2- 4]. Finally, the structure is improved to be compatible with CMOS technology.

2 Operation principle of the device.

The device consists of a dual-control photodiode associated with 2 capacitors, C_a and C_b. Depending on the bias voltage applied on the control gates *A* and *B*, the a.c. photoelectric current is averaged successively one of the two capacitors. Electrodes *A* and *B* are respectively controlled in phase and phase opposition towards optical output power modulation of the laser diode. Considering a symmetrical structure $C_a = C_b$, a modulation control with a 1/2 duty cycle and uniform illumination of the photodiode area, the photoelectric current due to day light is considered as a common mode current between output A and output B, and can be separated of the laser power due to reflected light.

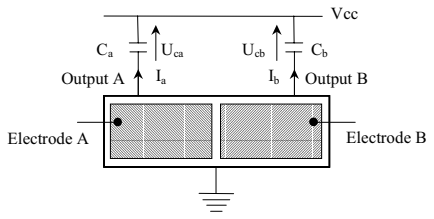

Fig. 1. Principle schema of the dual-control photosensor

This last photogenerated current is delayed of the time-of-flight τ_D:

$$\tau_D = 2.D/c \qquad (1)$$

with *D*, the distance to measure, and *c*, the light velocity. Integrated on one period of the square wave modulation signal, the differential voltage $\Delta U_{ab} = U_{ca} - U_{cb}$, depends on the time-of-flight, that is to say, depends on the distance *D*. By measuring ΔU_{ab}, this distance to measure can be deduced.

3 Double gate photomos

In this section, a first structure is presented in figure 3. In order to be integrated in CMOS technology, CMOS design rules has to be taken in account. Electrodes *A* and *B* are transparent (polysilicon) to laser diode light. To only integrate photoelectric current in capacitors C_a and C_b, electrodes have to be biased respecting equation:

$$V_{th} < V_{electrode} < V_{output} \quad (2)$$

V_{th}: threshold voltage of the MOS transistor.

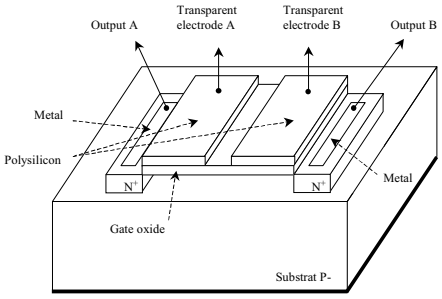

Fig. 2. Dual-control photoMOS sensor.

In this configuration, photoelectric current is transferred to outputs *A* and *B* thanks to the fringing-field at the surface of the semiconductor, as it's used in CCD circuits [5]-[6]. Simulation results of the device, with ISE TCAD software and with classical CMOS technology parameters, show a potential-well is formed between the transparent electrodes *A* and *B*, so this structure isn't compatible with CMOS technology. Actually, a potential-well formed between the electrodes *A* and *B*, would trap photogenerated electrons, so these carriers can't be collected by output diodes.

4 Improvement: dual-control photoMOS with a floating diode

The defect presented in the previous paragraph can be suppressed by inserting a floating diode between the control electrodes *A* and *B*. That is to say, a N^+ diffusion implanted between the two electrodes. Structure presented in figure 3 is compatible with the CMOS technology. The floating diode is not biased by an external circuit, so in darkness condition, this N^+ diffusion potential is the same as the one applied on output diodes *A* and *B*. When the sensor is illuminated, a part of electrons photogenerated are headed for outputs diodes *A* and *B*, the other part for the floating diode are accumulated; the surface electrostatic potential decreases, until the monotony of the variation of the surface potential distribution is reached (figure 3). Contribution of this floating diode makes that the device is independent on the used technology parameters. In homogenous lighting conditions and bias voltages, the output currents ratio between diodes *A* and *B* is 3. Simulations show this ratio and output photoelectric currents are independent on the output diodes bias voltages if relation (2) is verified.

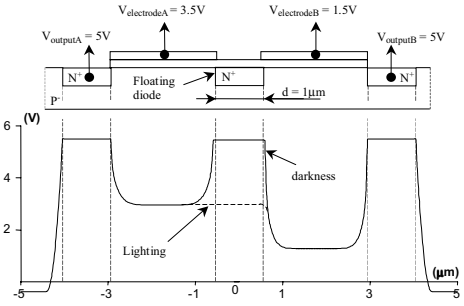

fig. 3. Cross-sectional diagram of the dual-control photoMOS sensor with floating diode inserted between transparent electrodes and surface potential distribution in darkness and lighting conditions. The spacing between electrodes *A* and *B*, $d = 1\mu m$.

5 Conclusions

The operation principle of a dual-control photosensor design for distance measurement with laser beam has been presented. A improvement is presented to make the structure compatible with CMOS technologies. Experimental results must be compared with simulations results to validate the device. For example, non-linearity will appear at high frequency with switching of the bias voltages of the control-electrodes.

References

[1] T. Bosch, M. Lescure. *Laser distance measurements*, SPIE Washington, Mileston series, ISBN 0-8194-2010-7, 1995.

[2] R. Schwarte, Z. Xu, H. Heinol, J. Olk, R. Klein, B. Buxbaum, H. Fischer, J. Schulte. *A new electrooptical mixing and correlating sensor : facilities and apllications of the photonic mixer device (PMD)*, presentation on LASER '97, München, 16-18 June 1997.

[3] P. Gulden, M. Vossiek, P. Heide, R. Schwarte. *Application of the Photoelectronic Mixing Device to optical measurement of presence, distance and velocity*. EUMC 2000.

[4] P. Gulden, M. Vossiek, P. Heide, R. Schwarte. *Novel opportunities for optical level gauging and 3D-imaging with the Photoelectronic Mixing Device*. IEEE instrumentation and measurement, technology conference, Budapest, 21-23 May 2001.

[5] S.M. Sze, *physics of semiconductor devices*, pp 407-422, John Wiley & Son Ltd., Chicchester 1981.

[6] J. E. Carnes, W.F.Kosonocky, E. G. Ramberg, *Drift-aiding fringing field in charge-coupled devices*. IEEE journal of solid-state circuits, vol SC-6, No. 5, pp. 322-326, October 1971.

Semiconductor gas sensors for pyrolysis control in domestic cooking ovens

Sven Rademacher, Karsten Sassenscheid, Harald Böttner and Jürgen Wöllenstein

Fraunhofer Institut für Physikalische Meßtechnik, Heidenhofstr.8, 79110 Freiburg, Germany
email: woellen@ipm.fhg.de http://www.ipm.fhg.de

Summary: *Heating control of the self cleaning (pyrolysis) process for a cooking oven based on metal oxide gas sensors has been examined in the investigation. In order to decrease the power consumption during a pyrolysis process and extend the life time of the oven the idea is to monitor the state of the self cleaning process. Measurements have revealed that a simple control system based on metal oxide gas sensors could result in a significant decrease of the pyrolysis process time. Further, metal oxide gas sensors provide high potential for low cost mass production and, consequently, ovens with a heating control system for the pyrolysis process could easily be commercialised.*

Keywords: *gas sensor, metal oxides, pyrolysis control,*
Category: *10 (Applications)*

1 Introduction

Household appliances are one of the largest markets for electrotechnical and electronic products. The household appliance industry is now slowly starting to introduce more sensors, actuators and electronic control systems into their products. Nowadays, the industry develops ways for integration of microelectronic control to enhance new product features, enabling greater product differentiation and leading to more dynamic and competitive products.

Several work groups have studied the possibility to use electronic noses (complex chemical sensor systems) for detection of odors and gases to monitor the complete cooking process [1]. Two big problems have been identified for these type of systems: difficult to accomplish a system able to monitor the cooking process in a satisfactory way for all type of foods and relatively costly implementation. In this investigation Fraunhofer IPM has studied the possibility to integrate microelectronic control for pyrolytic ovens in order to automatically monitor the self-cleaning process by using semiconductor gas sensors. In contrast to electronic noses, semiconductor gas sensors are well suited for the electronic control of household devices since they provide high potential for low cost mass production.

2 Experimental

We will present the results of a feasibility study for the use of metal oxide gas sensor for the control of heating time/power during pyrolysis in domestic cooking ovens. If the user activate the pyrolytic cleaning system, the temperature of the oven rises to 500°C for several hours with a power consumption of more than 5 kWh burning all the dirt, fat and food residues. During the pyrolysis process the long chained organic molecules in the oven are thermally cracked. The products of the cracking process (decomposition) are gaseous hydrocarbons, water vapour (in the beginning of the process), CO, CO_2, VOCs and ash. CO and VOCs are well detectable with metal oxide gas sensors.

The goal of the experiments was to evaluate the possibility to measure these gaseous products during the self-cleaning process for a future automatical control of the pyrolysis time of cooking ovens in order to save power consumption. Various measurements with the measurement set-up shown in fig 1 where performed, whereas the oven was soiled with different kinds of food residues, e.g. fat or oil. Fig 2 shows a typical measurement result of a pyrolysis measurement. The pyrolysis experiments have shown that metal oxide gas sensors allow the monitoring of the state of the self cleaning process in pyrolytic ovens. A future simple low cost control of heating power during pyrolysis by using a gas sensor will result in mainly two advantages: lower power consumption with an intelligent pyrolysis control and longer lifetime of the oven. Stopping the cleaning process when pyrolysis is finished (i.e. all residues are burned) instead of running the process for a pre set period of time will obviously reduce power consumption, especially in not very dirty ovens.

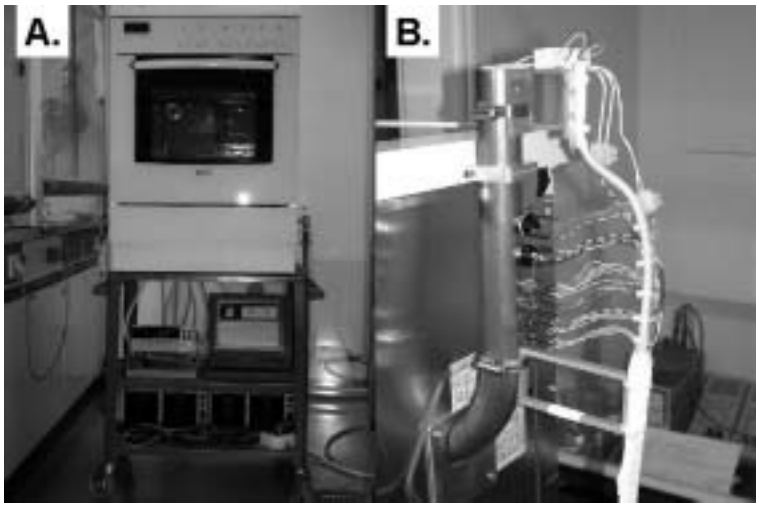

Fig.1: Experimental set-up during the pyrolytic self cleaning experiments (A). The different gas sensors were mounted in the outlet of a commercial oven (B).

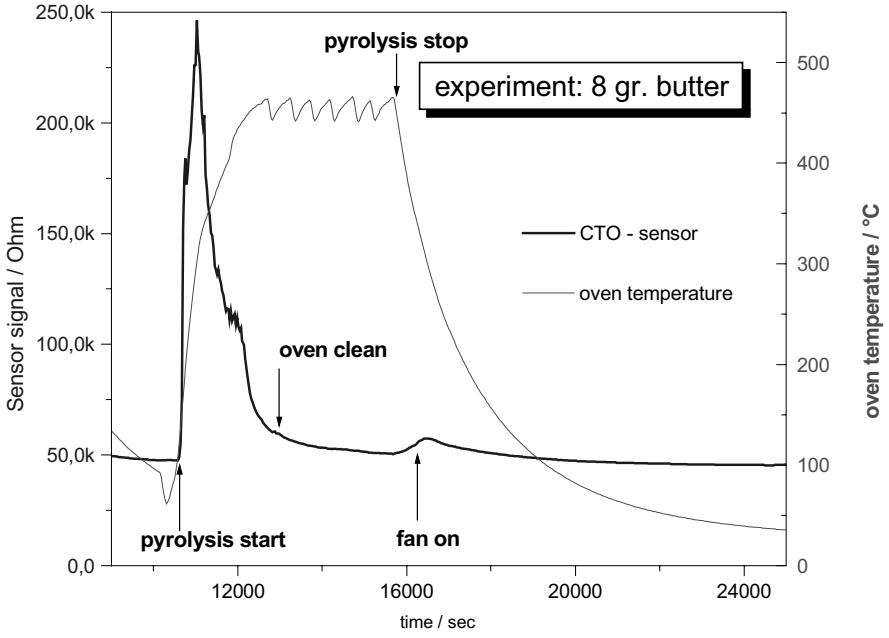

Fig.2: Response of a metal oxide gas sensor and the oven temperature during a pyrolytic self cleaning process. The oven was soiled with 8 gr. butter. The sensor reacts mainly to CO and other gaseous rests of organic components. After 30 min of operation the oven was clean.

Further, the lifetime of a pyrolytic oven is much shorter than that of conventional ovens because the mechanical parts are stressed by the high temperatures during pyrolysis. Consequently, the overall life time can be increased by shortening the cleaning times. Additionally, the experiments revealed that an automatic "switch off" of the oven in case of burning food is possible with a low cost control system based on a metal oxide gas sensor.

Reference

[1] S. Ehrmann, J.Jüngst, J. Goschnick (2000), *Automated cooking and frying control using a gas sensor microarray*, Sensors and Actuators B Chemical - Volume B66, page 43-45,

Silicon Tips as Tool for Electrical Conductivity Characterization in Liquids

F. Javier Ramirez-Fernandez[1], Elisabete Galeazzo[1], Michel O. S. Dantas[1], Henrique E. M. Perez[1], Abdelhamid Errachid[2]

[1]Universidade de São Paulo, Departamento de Engenharia de Sistemas Eletrônicos - Escola Politécnica, Av. Luciano Gualberto, trav. 3, n. 158, 05508-900, São Paulo, Brazil
email: jramirez@lme.usp.br http://sim.lme.usp.br
[2]Laboratory of NanoBioEngineering - Barcelona Science Park, Spain

Summary:

Silicon tips were fabricated by means of sacrificial layers defined with porous silicon and masked by hydrogen ion implantation with adequate thermal annealing. The shape pits are dependent on the mask geometry used by blocking anodization current where PS is not desired. As result, tips present height of 50 microns with a curvature of 2-5 microns or less than 0.1 micron.

Keywords: *silicon tips, porous silicon, hydrogen ion implantation, cellular stimulation, nanoprobe*
Category: *10 (Applications)*

1 Introduction

The realization of three-dimensional microstructures and microelectrodes of different shapes using materials and technologies applied for fabrication of integrated circuits has been a challenging research subject [1]. But several techniques involve a large number of processing steps, which can increase the time of fabrication process resulting in a very expensive and complex way to define microstructures. In this work we describe one alternative for realization of three-dimensional conical and pyramidal tips by using Silicon (Si) microfabrication technology.

These structures were fabricated by means of sacrificial layers defined with porous silicon (PS) and patterned by hydrogen ion implantation (H^+.I.I.) with adequate rapid thermal annealing (RTA) [2]. PS is obtained by electrochemical etching of Si (p-type Si) in hydrofluoric acid (HF) realized by anodic bias into an etching cell [3]. It is a simple and cheap technique as compared with others used in microfabrication of Si. PS layers are easily removed with diluted potassium hydroxide (KOH) at room temperature, as desired.

The use of H^+I.I. as etch-stop technique for anodization process is based on blocking the anodization current flow in selective surface areas. This technique is an option to obtain a stable crystalline superficial layer electrically isolated from the silicon substrate, so it is used as mask to fabricate Si microstructures with PS as sacrificial layer.

Using the potential of this microfabrication technology, in this work Si tips were fabricated with height of 50 microns with a curvature of either 2-5 microns or less than 0.1 micron (Figure 2). The total height of these pits is controlled by anodization time of Si and can be defined with any height ranging to two or three hundred of microns. The shape pits are dependent on the mask geometry used by blocking anodization current where PS is not desired. In this case, the electrical current coming backside of Si during anodization squeezed through the mask opening, leading to a lateral current, responsible for additional anodization under the mask.

2 Experimental details and Results

To form PS on selective areas, a conventional process of anodization is applied. P-type silicon Czochralski wafers, <100> orientation and resistivity about 10 Ωcm were used. The anodization parameters were HF:ethanol solution (1:1), current density (J) of 20 mA/cm^2, and process time of 55 minutes. The experimental parameters of H^+I.I. used are: 50 keV energy and 1.10^{16} H^+/cm^2 dose. Afterwards, RTA is applied to activate the H^+ ion on Si (N_2 environment, T = 450^o C and t = 5 minutes).

As it can be observed in the experimental results showed in this paper, this under etch is nearly isotropic when H^+.I.I. is used as mask.

Figures 1a and 1b show SEM images of silicon "pedestals" obtained with this process, after etching PS layers by diluted KOH (1%). The thickness of the remaining Si (top of the "pedestal") is about 1 micron. By increasing the anodization time, PS will be formed under all mask and the top of the "pedestal" can be removed with PS in KOH etching. Then, a Si probe (or Si tip) is obtained, as showed in Figures 2a and 2c. This type of microstructure can be applied as microelectrode for cellular stimulation [4] or atomic force microscopy scanning probe [5], or as tips to measure the electrical conductivity in liquid at very localized space.

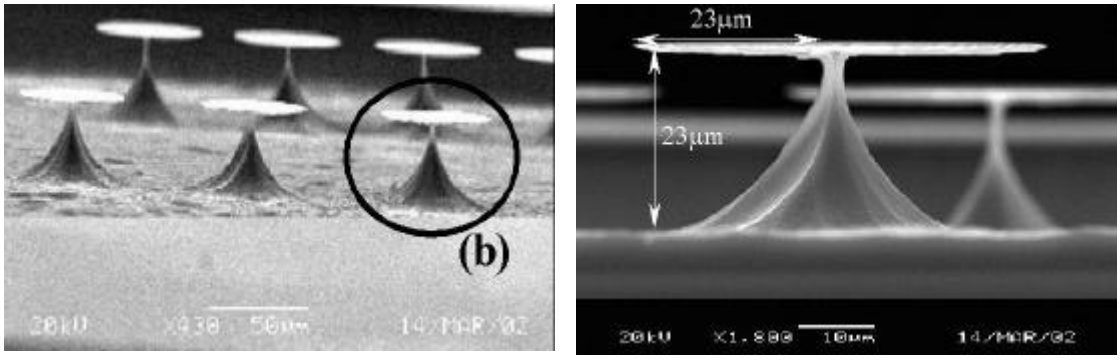

(a) (b)

Fig. 1. SEM photographs showing Si "pedestals" obtained after PS layer etching by KOH: (a) "pedestals". (b) Detail of one "pedestal"; the measurements showed in this image corresponds to the PS layer thickness in depth and laterally (due to isotropic PS formation).

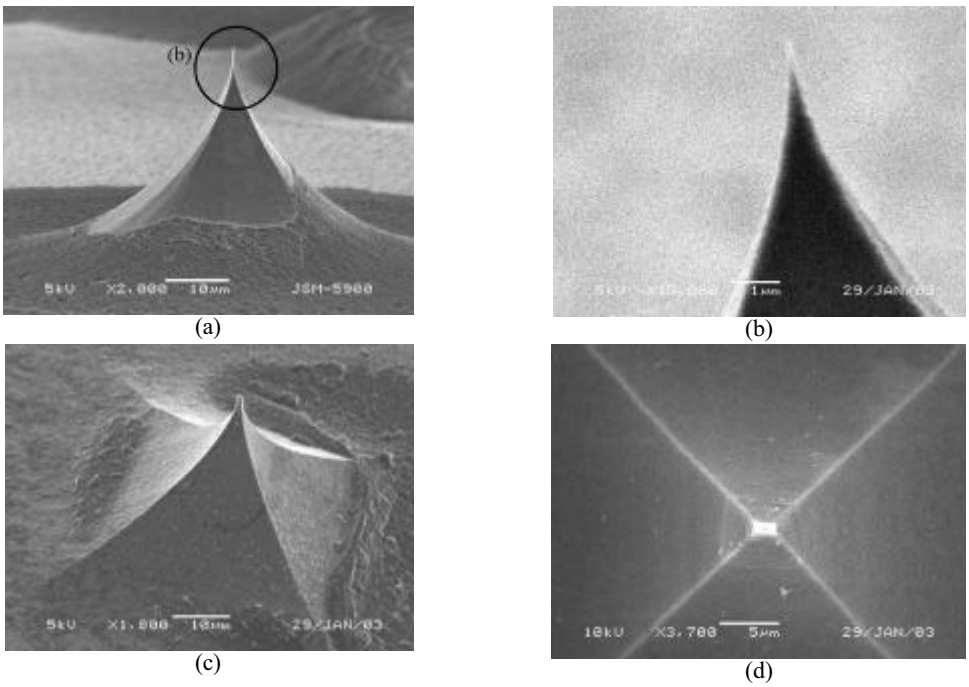

(a) (b)

(c) (d)

Fig. 2. SEM photographs on two types of Si tips. (a) Conical Si tip obtained with circular mask geometry. (b) Detail of this tip. (c) Pyramidal Si tip obtained with quadratic mask geometry. (d) Top view of this tip.

Acknowledgments

The authors would like to thank the Laboratório de Microscopia Eletrônica at LNLS, Campinas, Brazil, for the electron microscopy work.

References

[1] R. J. Grow, S. C. Minne, S. R. Manalis, C. F. Quate, "Silicon Nitride Cantilevers With Oxidation-Sharpened Silicon Tips for Atomic Force Microscopy", *Journal of Microelectromechanical Systems*, 11, n. 4 (2002) 317-321.

[2] E. Galeazzo, W. J. Salcedo, H. E. M. Peres and F. J. Ramirez-Fernandez, "Porous silicon patterned by hydrogen ion implantation", *Sensors and Actuators B*, 76 (2001) 343-346.

[3] E. Galeazzo, "Caracterização e aplicações da fotoluminescência do silício poroso em sensores de gás", *Thesis,* Universidade de São Paulo, São Paulo, 2000.

[4] M. O. Heuschkel, M. Fejtl, M. Raggenbass, D. Bertrand and P. Renaud, "A three-dimensional multi-electrode array for multi-site stimulation and recording in acute brain slices", *Journal of Neuroscience Methods*, 114 (2002) 135-148.

[5] P. A. Rasmussen, J. Thaysen, S. Bouwstra and A. Boisen, "Modular design of AFM probe with sputtered silicon tip", *Sensors and Actuators A,*. 92, (2001) 96-101.

Reliable object classification and people counting system based on an IR diode array

Heinrich Ruser, Boris Ivanov, Michael Horn

Institute of Measurement and Automation,
University of Bundeswehr Munich
D-85577 Neubiberg, Germany
Tel: +49 (0)89 6004-3878; Fax: -2557
heinrich.ruser@unibw-muenchen.de

Summary. *This paper addresses the problem of determining the number of people getting into or out of a room as well as a classification between objects, leading to their identification. For this purpose an IR diode array, working on a reflection light scanner principle, has been designed which combines desired properties like small size and low cost, high reliability and robustness against changing environmental conditions. Essentially two diode arrays of 3...8 emitter-receiver pairs are mounted on both sides of a doorway, enabling the estimation of the size of the object in different dimensions and reducing the requirements with regard to the detection range. The emitters are driven successively in time, hence no signal overlapping and cross-talk occur. From each channel, several echo features like amplitude values, echo width, rise and fall time, sidelobes, local maxima are tracked over time and processed by means of fuzzy logic based echo evaluation. The results show that people can be recognised easily and are well separable from other echoes (motion of hands etc.), making the performance far more reliable than that of ordinary light barriers. Design considerations for applications supporting important home appliances like decentralised, occupation-driven HVAC control are described and extensions for a enlarged detection range and higher resolution are sketched.*

Keywords: IR multi-sensor array, echo feature extraction, object classification, people counting system
Subject category: 10 (applications)

Introduction

Systems for the detection, localisation and identification of persons are very helpful for many tasks in home environments: (1) security issues (e.g. intruder detection), (2) economical and environmental issues (occupancy-driven lighting, heating and ventilation), (3) comfort issues (e.g. user-dependent settings, prediction of user behaviour and presence patterns for automated pre-settings). For simple information about the number of persons in a specific room, its entrance has to be monitored.

For presence detection and counting systems, numerous technical solutions based on a large variety of physical phenomena are available and still refined. Unfortunately, simple systems like widespread mechanical counters, light barriers or passive infrared (PIR) detectors as well as more sophisticated ultrasonic or microwaves motion detectors, vibration shock sensors or vision based systems, are largely dependent on the user's assistance and highly influenced by changes of the environment (air flow, object reflectivity, light, shadows, etc.) [1]. Often it is difficult to distinguish between objects which partly cover.

In order to improve the performance of object detection, distinction and classification, small multi-sensor IR diode arrays mounted on both sides of the doorway are proposed. In Fig. 1, the detection principle is shown.

System description

The optical system consists of N pairs of a highly directional IR emitter diode and a shielded sensitive phototransistor, located close to one another. An pulse NIR emitter diode HSDL-4230 at 875 nm with a 17° beam angle and a photo transistor SFH 309 with a maximum sensitivity at approx. 880 nm have been used. Due to the face-to-face diode mounting, the required maximum range R can be reduced to almost the half of typical door widths ($R \approx 0.6\,m$).

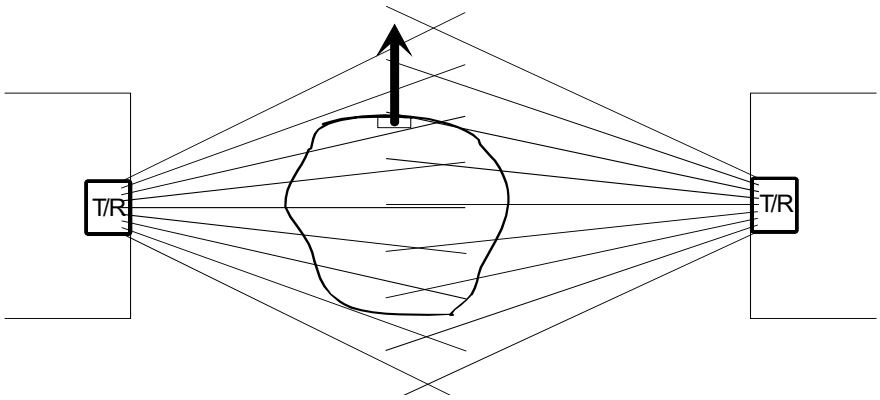

Fig.1. Detection principle: IR diode arrays on both sides of possible objects (top view)

The wide dynamic range of the echo amplitude is contributed mainly to the reflector distance and less to its material-dependent reflectivity, see Fig.2.

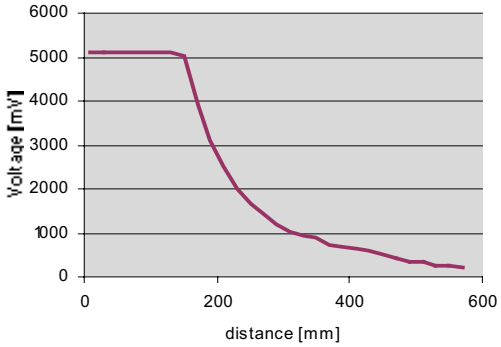

***Fig. 2**. Echo amplitude as a function of reflector distance (averaged)*

The emitters are driven at temporally successive instances, hence overlapping and mutual influence of the echo signals can be excluded. To enlarge the field of inspection, the pairs are inclined outwards, see Fig. 3 for N=3. For a larger number of emitter-receiver pairs, even larger angles can be monitored and the resolution can be improved.

The processing is performed on a low-power 8 bit micro-controller which generates the pulses, handles the timing of emission, determines and stores the received echo features and makes the decision about the object.

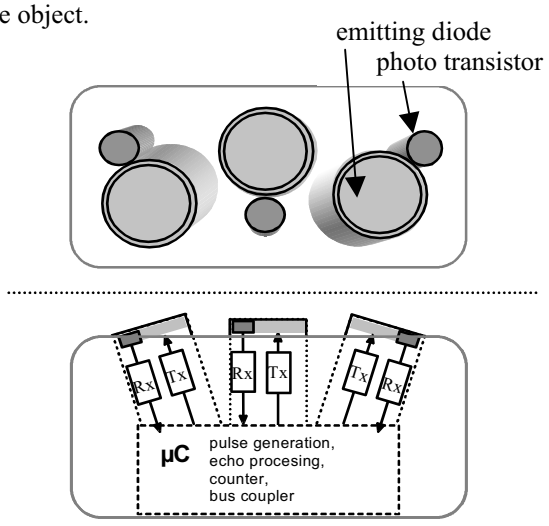

***Fig. 3.** Emitter diodes and receiver photo transistors are paired and slightly inclined: Front and top view as well as a functional model mounted in a doorway.*

Experimental results

For echo identification and array processing, a number of echo features (amplitude values, echo width, rise and fall time, number and shape of local maxima) of echo segments from all separate receivers channels as well as the sum signals are used, separately for both sides of the doorway. With these means, large and long-lasting echoes can be clearly distinguished from short peaks due to motion of hands, accidental stronger reflections etc, see Fig. 4. The detection and classification is further improved if echoes are weighted by fuzzy-logic means and characteristic echo shapes are learned by the system and compared with actual echoes [2].

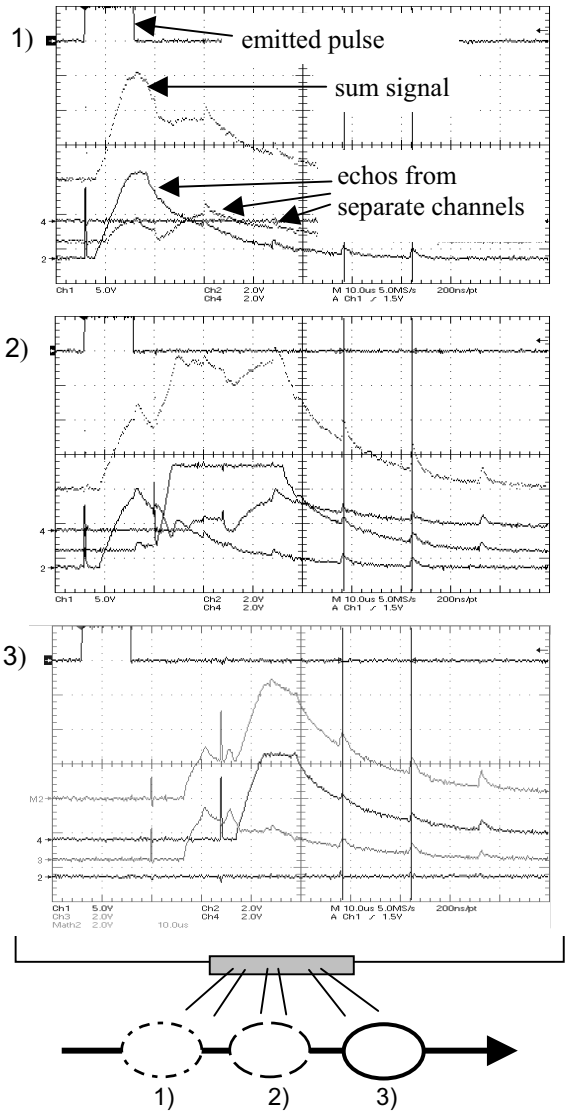

***Fig. 4.** Typical echo signals for a person moving along a 3-pairs array. Small peaks ahead and behind the main echo can be identified as hands in motion.*

References

[1] B. Ivanov, H. Ruser, M. Kellner: Presence detection and person identification in Smart Homes, Int. Conf. Sensors&Systems, St. Petersburg, 2002

[2] A. Albiol, I. Mora, V. Naranjo: Real-time high-density people counter using morphological tools, IEEE Trans. Intell. Transportation, Vol. 2/4, 2001

DC/AC current comparator with fully enclosed magnetic shielding

J. Saneistr, P. Kaspar and P. Ripka

Czech Technical University of Prague, Measurement Dept., Technicka 2, 166 27 Prague, Czech Republic
email: saneisj@fel.cvut.cz http://www.cvut.cz

Summary: *Novel current comparator with amorphous detection cores allows measuring of DC and AC electric current for frequencies up to 1kHz. The instrument integrates the principles of DC comparator and AC instrument current transformer into a single device. The accuracy of 0.03 % was achieved for frequencies from DC up to 300 Hz. Thanks to the magnetic shielding the comparator is more insensitive to close disturbing currents.*

Keywords: *current comparator, current measurement, current sensor*
Category: *10 (Applications)*

1 Introduction

DC/AC contactless current measurement is made by Hall sensors, magnetoresistors, fluxgate sensors and current comparators. Current sensors based on Hall phenomenon and anisotropic magnetoresistance are cheap, small in size; they have low power, but their accuracy is low. Their linearity can be increased by feedback, but large offset errors and sensitivity to magnetic fields and close currents remain problem. Fluxgate-based current sensors are much more precise, but they have low bandwidth and they are power consuming. Current comparators are very expensive, big instruments and they need high power supply, but they are most accurate from all mentioned devices. DC current comparators have usually low bandwidth (typically 1 Hz).

2 Realization of DC/AC comparator

The developed unit is similar to classical DC current comparator such as described in [1]. Conception comes out from DC/AC current comparator, which was described in [2]. The detection core is made of amorphous magnetic material, which allows increasing of excitation frequency up to 12 kHz. This also increases bandwidth of the measured current (standard DC current comparators have usually bandwidth of 1 Hz). At DC and low frequencies the instrument works on the fluxgate principle. At higher frequencies the magnetic cores and mainly the shielding act as a core of the instrument current transformer, which has the secondary winding short-circuited by the low output impedance of the feedback amplifier.

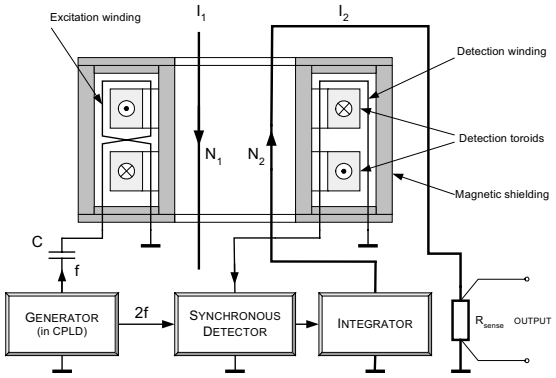

Fig. 1. Block diagram of DC/AC current comparator

The block diagram of the DC/AC current comparator is shown in Fig. 1. Two detection toroids are used to suppress basic harmonic component in the detection winding. These rings are magnetized with 2 x 40 turns in opposite direction. Capacitor C is used for tuning the excitation current into peaks (by forming a non-linear parallel resonance circuit with the inductance of the excitation winding). It allows to deeply magnetize both cores. Detection winding has 20 turns in low capacitance configuration around both detection cores. The cores with windings are placed into fully enclosed magnetic shielding (from annealed permalloy with relative permeability of approx. 25000). This shielding significantly suppresses spatial non-uniformity of detection cores, which causes magnetic error of comparator, suppresses sensitivity to near current and works as a core of the current transformer for higher frequencies of measured current. The winding for compensation current must be wound around the shielding.

Electrical circuit consists of fixed frequency generator (12 and 24 kHz) realized in CPLD – it allows simply set the phase shift between two generated frequencies to adjust synchronous detector in phase with second harmonic of signal

from detection winding. Synchronous detector is realized as switching type – using integrated circuit AD630. Output from AD630 is led into integrator, which works like regulator in the feedback loop. Output current I_2 from this integrator is passing through compensating winding of current comparator and sets zero field in the detection cores. This current is proportional to the measured current I_1 and is sensed on precise resistor shunt.

3 Testing of magnetic shielding effect

Measuring system with flat coil was realized for testing of the effect of magnetic shielding (see Fig. 2.). This measurement shows how much variable is the cross-section of the detection ring, its permeability and turn-density. In ideal case, output voltage of comparator is zero for each rotation angle of flat

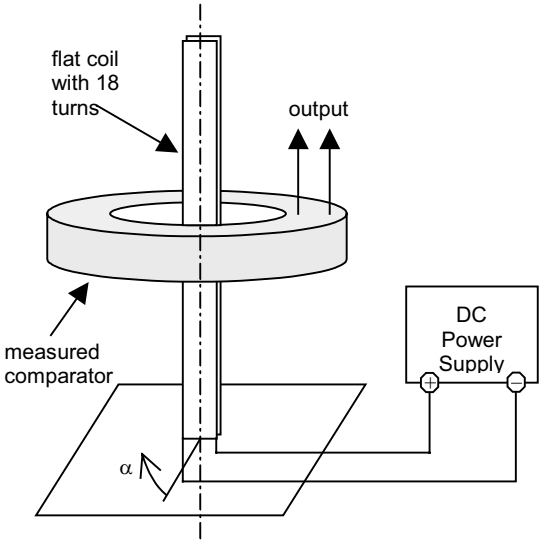

Fig. 2. Measuring system for measuring of magnetic error of the current comparator

coil. Real values measured for two currents (1A and 5A) and for three kinds of magnetic shielding - detection cores without any shielding, half shielding (inner and outer wound toroids) and full shielding (inner, outer wound toroids and upper and lower ring lids) are shown in Fig. 3. The comparator was measured in open loop, the sensitivity was 3 mV/A. Reducing of magnetic error with half and full shielding is clearly visible. For full shielding the magnetic error was below the instrument resolution, which was 2μV, corresponding to 1.3 mA of the measured current.

4 Measuring of comparator precision

The precision of current comparator has been measured only for half shielding (laser machined upper and lower ring lids were not available). Results for measured current 100A (DC/AC) are in Table 2.

Table 2. Measured error of current comparator (differential method)

frequency	amplitude error	angular error
DC	0,032%	-
50 Hz	0,01%	-0,3 min
300 Hz	0,03%	- 2 min
1 kHz	0,21%	2,5 min

5 Conclusion

The developed comparator integrates the principles of DC comparator and AC instrument current transformer into a single device. The accuracy of 0.03 % was achieved for half-shielded cores. Full magnetic shielding fulfills our expectations about elimination of detection core non-uniformity.
Error analysis of fully shielded comparator will be given in final paper.

References

[1] W.J.M. Moore, P.N. Miljanic. The Current Comparator. Peter Peregrinus Ltd., London (1988)

[2] P. Ripka, P. Kejík, P. Kašpar, K. Draxler. Precise DC current Sensors, Proc. IMTC conference, Brussel 1996, 1479-1482

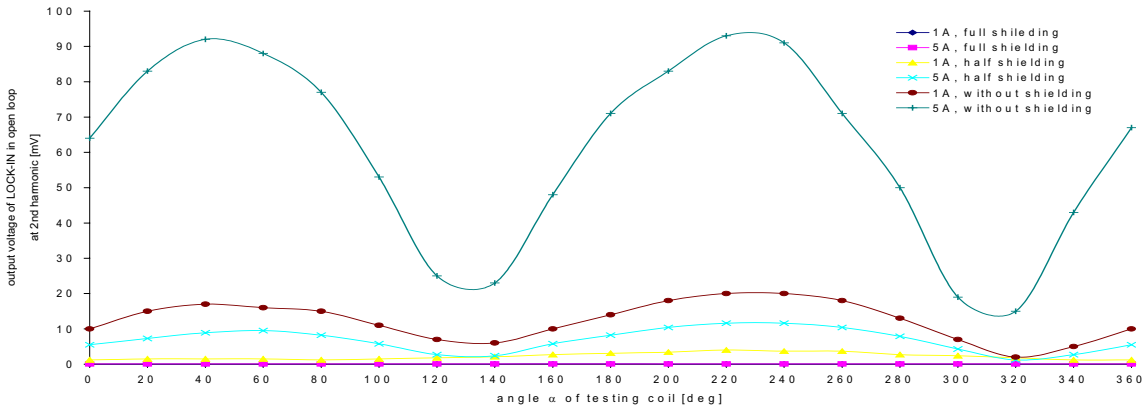

Fig. 3. Magnetic error of current comparator in relation to type of shielding and to testing coil current

Mass Market Demonstrators: a way to smart gas sensors?

P. Mielle [1] and J. L. Ray [2]

[1] INRA, MR Arômes, 17 rue Sully, 21065 dijon, France
email: Patrick.Mielle@dijon.inra.fr http://www.nose-network.org
[2] INRA, UMR SPO, 2 Place Viala, 34060 Montpellier, France

Summary: *There is currently a missing link between sensor designers and application developers. It requires a lot of efforts to end-users to compare different sensors from different sources on their Sensor Array systems. The hardware should be redesigned each time from electrical and mechanical adaptation to the new sensor. Evaluation boards may be a way to an easier interchange of gas sensors from different suppliers, and a first step to "Plug & Play" smart gas sensors.*

Keywords: *gas sensors, screening, characterization, evaluation board*
Category: *10 (Applications)*

1. Introduction

There is currently a high number of available gas sensors, either commercially available, or made by academic laboratories.

However in parallel, two levels of use of the sensors can be distinguished:

- In very large volumes (million of units), as embedded sensors in a dedicated application, i.e. air conditioners, automotive engine control, ovens, explosive gas leak detection, breath analyzers… Sensors are specifically designed for each application.
- In tiny niche applications, typically a laboratory that makes sensors in few tens of units and develops a Gas Sensor Array (E-nose) to address some final applications.

In the latter case, sensors are perfectly characterized, both physically (film thickness, grain size, doping material, annealing, uniformity of hot plate temperature…) and chemically, for most of the common gases.
The main drawback is that these teams have most of the time a weak knowledge of the actual application, but try to find continuously the "killer application" that would lead to an exponential rise of their production. Up to now, we do not have any evidence of the existence of such application!

In parallel, it is notable that some groups are developing applications without designing sensors. One can notice that there is a missing link between sensor designers and final application developers who are obliged to develop special electronics and sensor cells for screening gas sensors from the very large offer.
Each gas sensor, either commercially or academically designed, has its own physical characteristics, on the electrical, mechanical and chemical fields*, i.e.:*

- Heating voltage, temperature probe style and coefficient, polarization current, max. limits…
- Housing style and material, size, pins location and number, gas direction…
- Chemical sensitivity, linearity, concentration range, noise, limit of detection, selectivity…

So, for each type of gas sensor, and even for the same provider, a special electronic board and sensor cell should be designed, which obviously is a waste of time.

2. Evaluation boards

Every group working on sensor application has designed its own electronic board, even if in some cases it is very basic: a regulated voltage, one polarization resistor, an unregulated heating voltage and an acquisition board. This is working, even if in some cases the system response repeatability is a bit weak!
Some sensor manufacturers have tried to help application engineers by proposing some evaluation boards (or demonstrators) for their own sensors.
But in most cases, the board was basic and allowed only the sensor heating and conditioning.
Ten years ago, Coreci (Lyon, France) has proposed an evaluation board for their bulk sensor A5000, that permitted the sensor conditioning, and via analog ports data acquisition, with cyclic programmation of the sensor temperature over time (temperature response time in the 300 ms range).
Microsens (Neuchâtel, Switzerland) [1] proposed an evaluation board that was able in the same time to provide, via a serial link, the sensor conditioning, data acquisition, and in addition a cyclic programmation of the sensor temperature over time (ramping up or down, multiple steps…, temperature response time in the ms range).
After using the Coreci evaluation board, and then developing our own electronic board and acquisition software [2], we evaluated the new

Mass Market Demonstrator (MMD) for AppliedSensor (Reutlingen, Germany) [3].
This tiny board (95 x 44 mm) is able in the same time to provide, via a serial link, the sensor conditioning, data acquisition by Voltage/frequency converter, and a cyclic programmation of the sensor temperature over time (ramping up or down, multiple steps…, temperature response time in the ms range).
The Argus software allows at the same time parameter settings, data acquisition and display, file format conversion, autosampler synchronization and even calibration functions.

3. Experiments

To evaluate the MMD and the delivered sensors, we have used our GC/sensors coupling [4], which allows a fast characterization of the sensor response to multiple chemicals in a single experiment.

3.1. Isothermal mode, standard mixture

The isothermal mode was first evaluated. A standard mixture in solvent was injected.

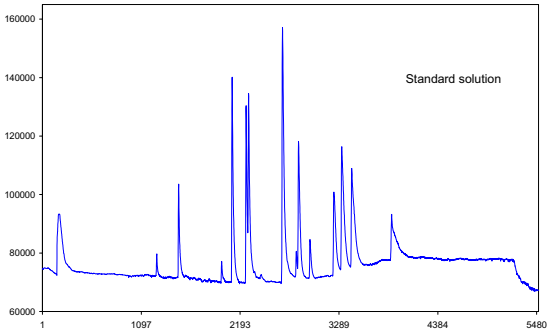

Fig. 1. Sensor response to a standard solution, in the isothermal mode (heating voltage 50 %).
It can be noticed that the sensor response time is fine and that, as expected, the quantitative response is enough high for all the chemicals.

3.2. Isothermal mode, real sample

Then a Solid Phase Micro Extraction (SPME) fiber was exposed to the same chemicals, but released from a real sample in solid phase (wood stave) [5].

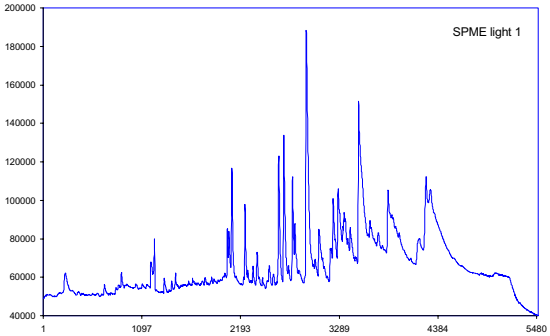

Fig. 2. Sensor response to a SPME fiber desorption, in the isothermal mode (heating voltage 50 %).
The enrichment factor due to the SPME fibre can be seen, with a higher noise level due to the real sample interferents and impurities.

3.3. Temperature modulation, standard mixture

We have also considered the possibility of temperature modulation by using a step-up variation from 30 to 70 % of the heating voltage (by 10 % steps).

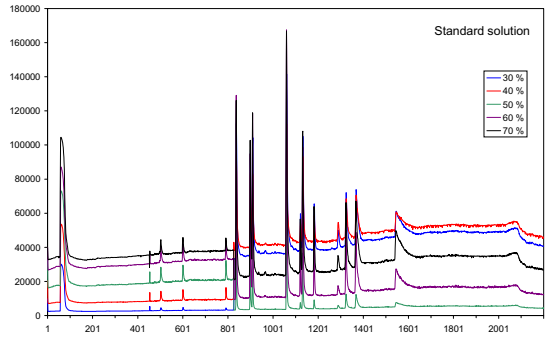

Fig. 3. Sensor response to a standard solution, with a temperature cycling (one curve per temperature).
The selectivity change of the sensor is actual, but the temperature steps were not optimized in that case because the sensor micro-hotplate was not calibrated at this time.

4. Conclusion

The MMD has proven its facility to use and its efficiency. The only weak point up to now is the sampling rate which is limited to 400 ms per point by the serial link, which leads to a 2 second rate for 5 temperature steps. This is a drawback only for rapid applications, such as GC coupling, and could be fixed by the use of a higher rate port, i.e. USB.
This kind of evaluation board may be a good starting point to the development of a "plug & play" smart gas sensor. These smart devices could in the future provide a real interchangeability of sensors in an e-nose system. In the frame of the NOSE EC network, a workgroup is currently working on a proposal for the implementation of a software enabling a normalized data exchange between gas sensors [6].

5. References

[1] www.microsens.ch/products/gas.htm
[2] P. Mielle, F. Marquis, Gas Sensors Arrays (‘Electronic Noses’): A study about the speed / accuracy ratio. *Sensors & Actuators B 68 (2000) 9-16*
[3] www.appliedsensor.com
[4] P. Mielle, F. Marquis, V. Trivier, A novel method for gas sensors characterization. Proceedings of 5 th Italian Conference "Sensors and Microsystems" AISEM, Lecce, Italy., C. Di Natale, A. D'Amico, P. Siciliano eds., Word Scientific publishing, London, UK (2000) 229-233.
[5] J.L. Ray *et al.*, Evaluation of oak wood toasting level by Headspace Comparison with SBSE and SPME. *IEEE Sensors Journal special Issue ISOEN 9, in print.*
[6] www.nose-network.org/members/wg/default.asp.

Development of a new gas sensor for binary mixtures based on the permselectivity of polymeric membranes - Application to carbon dioxide/methane mixture

R. Rego[1] and A. Mendes[2]

[1]Departamento de Química, Universidade de Trás-os-Montes e Alto Douro, Quinta de Prados, Apartado 202, 5001-911 Vila Real Codex, Portugal.
[2]LEPAE, Departamento de Engenharia Química, Faculdade de Engenharia da Universidade do Porto, Rua Roberto Frias, 4200-465 Porto, Portugal;
email: mendes@fe.up.pt Tel.: + 351-22-5081695, Fax: + 351-22-5081449

Summary: *This work describes a new concentration sensor for binary gas mixtures based on the permselectivity of a membrane element. This sensor is especially suited for the very low price and low/medium precision market to determine the carbon dioxide/methane composition in the 0-100% range. The membrane used is poly(dimethylsiloxane) (PDMS) hollow fiber by GKSS, Germany. The calibration curves were obtained at three different temperatures. The reproducibility, response time, reversibility, long-term stability and temperature dependence of the sensor are discussed.*

Keywords: *carbon dioxide/methane mixture, binary gas concentration sensor, permselectivity*
Category: *10 (Applications)*

1 Introduction

There is an increasing need for very cheap sensors for monitoring processes with a great impact in safety and energy savings. Recently it was proposed a new sensor based on the permselectivity effect of membranes [1,2]. When two gases are applied to a permselective membrane, they permeate with different flow rates. Thus when two gases flow along the membrane with constant pressure, the permeate flow depends directly on the feed composition. This flow in turn can be determined by the pressure drop at a calibrated orifice or needle valve, so that the pressure is indirectly correlated to the binary feed gas composition.

The sensor is made of a permselective membrane, a pressure transducer for measuring the permeate pressure and a non-selective barrier (e.g. needle valve). The non-selective barrier is used to control the permeate outlet to the atmosphere. The sketch of the binary gas mixture sensor is shown in figure 1. The gas mixture to be analysed is supplied at a constant pressure that must be higher than the outlet permeate pressure. In our system the feed pressure (P^F) was set to 3 bara (bar absolute), while the permeate pressure after the needle valve (V) was the ambient pressure (P^{amb}). It was assembled a poly(dimethylsiloxane) (PDMS) membrane module with 6 fibers and a useful length of 11.3 cm. The inside diameter of these fibers are 0.71 mm. For this membrane, carbon dioxide is the fastest gas and the methane the slowest. An important application devised for this sensor is for monitoring the carbon dioxide/methane content in the biogas. Other applications are possible.

2 Results and discussion

The calibrations curves were obtained by measuring the permeate pressure at different oxygen feed compositions, keeping constant the feed pressure and temperature. The temperature and feed pressure were kept constant with a thermostatic bath and two pressure regulators in series and were measured with a K type thermocouple connected to a digital thermometer and a pressure transducer. The composition of the feed was measured on-line using an infrared carbon dioxide analyser (Servomex 1440 D). The needle valve was set to 1.838 bara permeate pressure when pure carbon dioxide was fed to the device at 24.9ºC and left unchanged for all experiments. The results are shown in figure 2 and are from two sets of measurements performed in different days and for 10.3, 24.9 and 30.5ºC. For constant feed pressure, a second order polynomial fits quite well the experimental data. The experimental points obtained from two different experiments fall on the same calibration curve. The temperature effect on the response of the sensor was also checked. It can be seen from figure 2 that the PDMS shows a weak dependence towards carbon dioxide permeability of the temperature. The PDMS based sensor enables continuous and rapid carbon dioxide/methane analysis with a reproducible and long-term signal.

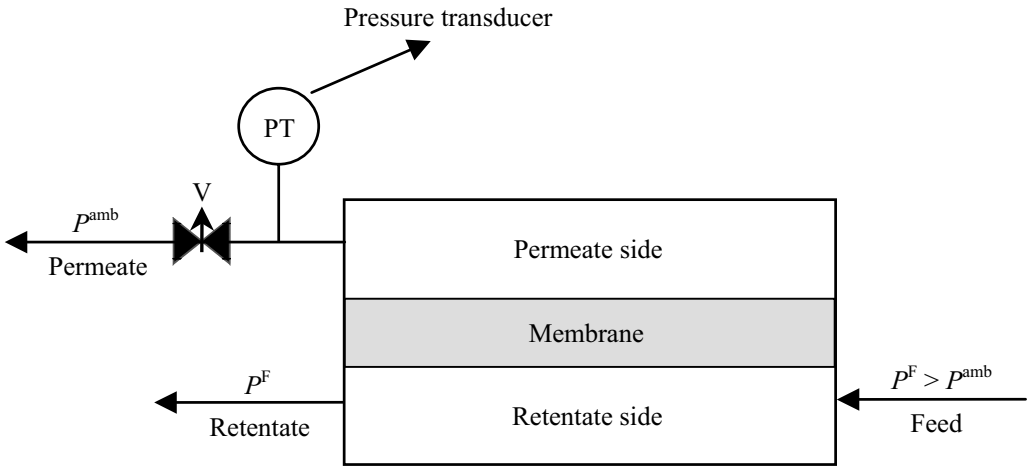

Fig. 1. Sketch of the binary gas mixture sensor.

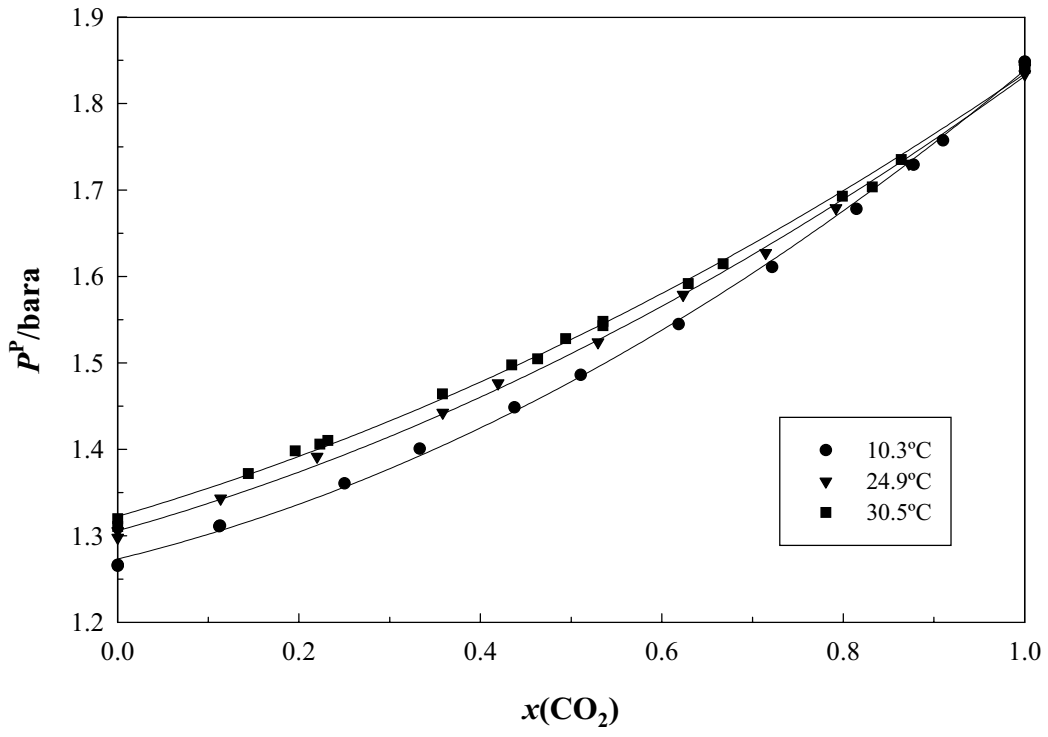

Fig. 2. Permeate pressure (P^P) as a function of carbon dioxide feed molar fraction, $x(CO_2)$, for 3.01 bara feed pressure and for three different temperatures. The maximum permeate pressure was set to 1.838 bara at 24.9ºC. The lines are polynomial fittings.

References

[1] A. Mendes. Gas mixtures concentration sensor and corresponding measuring processes. Patent nº PT102 312 (2000).

[2] R. Rego, N. Caetano and A. Mendes. *Anal. Chem.* Submitted (2003).

Errors of Near-field acoustical holography imaging due to position mismatch of microphone array sensors

P. Grätz[1], Ivona Ihlárová[2]

[1]Brno University of Technology, Dept. of Control and Instrumentation, Bozetechova 2, 61266 Brno, Czech Republic, gratz@feec.vutbr.cz
[2]Institute of Materials and Machine Mechanics, Slovak Academy of Science, Martin, Slovakia

Summary: *This paper deals with the influence of position of sensors in a microphone array on the visualization of sound fields using near-field acoustical holography. Near Field Acoustical Holography (NAH) is one of the most powerful methods for analysing and visualising sound fields. With this method it is possible to reconstruct a 3D field of sound pressure, sound intensity and other quantities from in-plane measured data. A key part for the NAH is the microphone array and influence of its parameters to the precision of the estimation of the acoustical quantities. The goal of this paper is to discuss the effect of the microphone array sensors positions to the three different NAH algorithms.*

Keywords: *microphone array, acoustical holography, visualisation of sound fields*
Category: *10 (Applications)*

1 Near-field acoustical holography

Modern computer graphics makes it possible to visualise sound fields on the basis of measured or calculated data. Visualisation of sound fields has obvious applications in noise source identification, and identifying and ranking noise sources and transmission paths is the first step in practically any noise reduction project.

One of the most powerful methods for experimental determination of the data used for visualisation of sound fields is Nearfield Acoustical Holography (NAH). With this technique it is possible to reconstruct 3D sound pressure fields from sound pressure data measured in a plane close to the source. Since the entire sound field can be reconstructed it is also possible to calculate other quantities than the sound pressure, e.g. the particle velocity, the sound intensity and the radiated sound power.

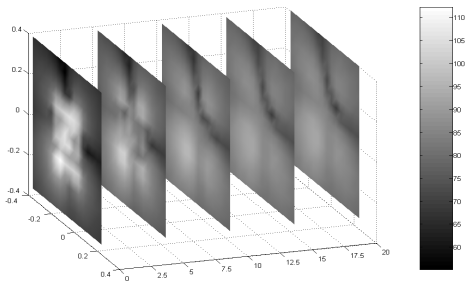

Fig. 1. Sound intensity field above the plate (0, 5, 10, 15, 20 cm) vibrating at 950 Hz, calculated from sound pressure field measured 5 cm above the plate using NAH.

There are several methods for determining the sound field in the measurement plane. In a stationary sound field it is possible to measure the sound pressure with a single microphone using a reference signal. On the other hand, it is necessary to measure the complete sound field in the measurement plane at the same time if the sound field is generated by non-stationary sources, and therefore full two-dimensional microphone arrays are used for this purpose. However, a real microphone array will invariably introduce some errors. The purpose of this paper is to examine how the performance of various NAH algorithms is affected by microphone position error of the microphone array sensors.

2 Position errors of microphone array sensors

To obtain realistic results, a model of simple supported vibrating plate has been developed. All the simulations are then realized with this source. The simulation is based on the comparison of the directly calculated acoustical quantities and the same quantities calculated using NAH and input data from the measurement holography plane. The simulation setup is presented in figure 2.

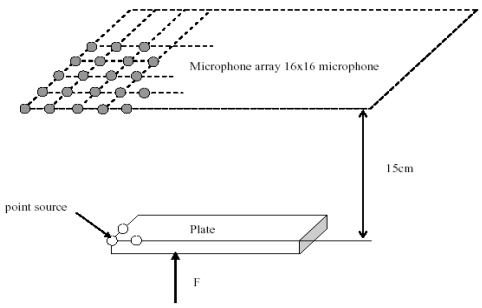

Fig. 2. Simulation setup

Array with 16x16 sensors is used, the distances between the sensors are 5 cm in both *x* and *y* directions and the array is placed 7 cm above the plate. In the previous research the three different NAH algorithms have been tested and optimized:

- NAH with K-space filter (conventional NAH)
- Iterative NAH (Wiener filter)
- SONAH (statisticaly optimal NAH)

Three different sensors position errors have been simulated for the three NAH algorithms:

1. Sensors position mismatch in *xy* plane and in *z* direction.

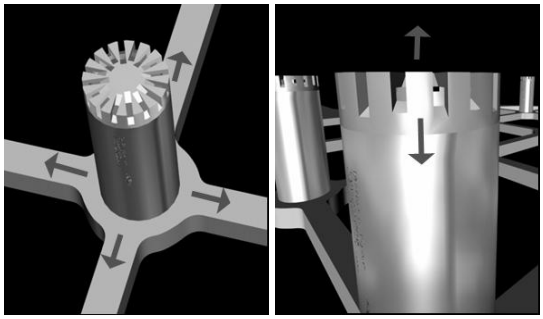

Fig. 3. Sensors position error in *xy* plane and in *z* direction

The results are presented in figure 4.

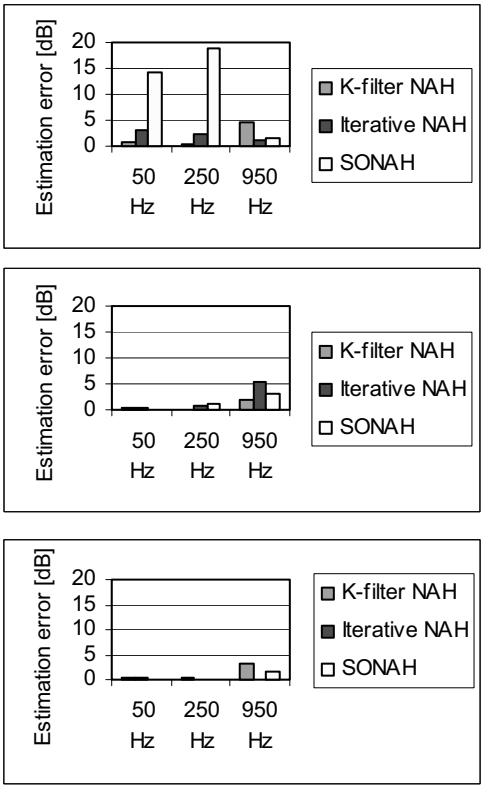

Fig. 4. Estimation error of sound power radiated by vibrating plate for sensors position mismatch 3 mm in *xy* plane (top), in *z* direction (middle) and for ideal sensor placement (bottom), different NAH algorithms and plate driven at 50, 250 and 950 Hz

2. Microphone array area

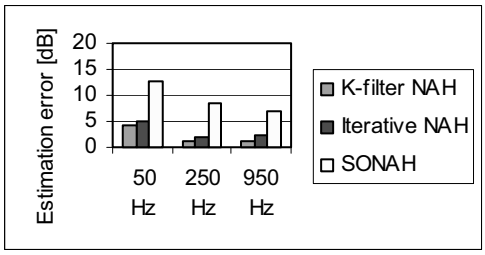

Fig. 5. Estimation error of sound power radiated by plate two times larger than area of microphone array

3. Scattering error from surrounded microphnes

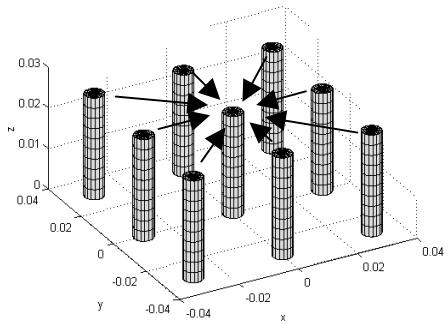

Fig. 6. Scattering error from surrounded sensors

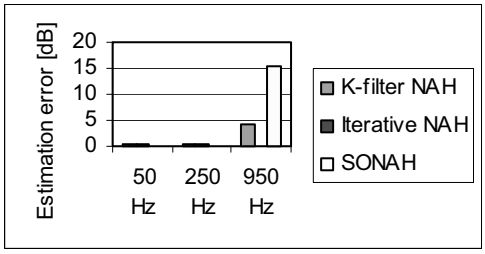

Fig. 7. Estimation error of sound power radiated by vibrating plate for microphone array with scattering error from 8 surrounded microphones

3 Conclusions

From the simulation results it is possible to see that all three algorithms are at low and middle frequencies more sensitive to the sensors position mismatch in the xy plane than in the z direction. The most sensitive is the SONAH and therefore the positions of the sensors must be quite accurate. SONAH then brings very good results. It is also highly recommended to realize the sensor array at least two times larger than the actual size of the sound source. Scattering error is significant only at the high frequencies with SONAH..

References

[1] E. G. Willians. Fourier Acoustics, Academic Press, 2000

[2] J. Hald. Time domain acoustical holography and its applications*, Sound and vibration*, 2001, 16-25

SENSOR ELEMENT FOR A METAL-INSULATOR-SEMICONDUCTOR CAMERA SYSTEM (MISCam)

R. Schwarz[1,2], M. Fernandes[1], J. Martins[1], A. Fantoni[1], M. Vieira[1], P. Sanguino[2], C. Nunes de Carvalho[3], and T. Muschik[4]

[1]Electronics and Computer Department, Instituto Superior de Engenharia de Lisboa (ISEL), Rua Conselheiro Emídio Navarro, P-1949-014 Lisbon, Portugal, E-mail: rschwarz@isel.pt
[2]Physics Department, IST, Lisbon, Portugal
[3]Centro Físico-Molecular, IST, Lisbon, Portugal
[4]Nokia GmbH, Ulm, Germany

Summary: *Light that impinges on the interface between the insulator layer and the semiconductor material of a metal-insulator-semiconductor structure (MIS) will affect the band bending at the interface. This effect is studied in view of using amorphous or microcrystalline silicon based MIS devices for optical image detectors by reading out the local distribution of band bending with a low-intensity scanning laser. In contrast to commercial CCD cameras this detector does not need a lithographical process for defining pixels. In turn, the limited lateral carrier diffusion will define the spatial resolution of the detector. Slow interface states and their charging kinetics will lead to a change in detector response, which could be employed for image storage. Detector degradation is studied with high-intensity laser pulses as a means for fast aging.*

Keywords: *MIS sensor, amorphous silicon, band bending, interface traps*
Category: *10 (Applications)*

1. Introduction

We discuss the operation of a new type of a metal-insulator-semiconductor (MIS) based optical sensor element that relies on light-induced changes in band bending at the semiconductor-insulator interface. Previously, the effect of the change of sign of the spectral response in MIS structures was studied in a-Si:H-based TFT´s with CVD-grown a-SiN:H insulator layers [1], without taking spatial resolution into account.

A MIS-based image sensor system (MIS-camera) would consist of a sensor element as described here together with appropriate optics for guiding the incoming image light and the scanning laser light onto the sensor. Also the electronics part is not discussed here. The MIS sensor takes advantage of the local modulation of the interface potential in low-mobility a-Si:H or µc-Si:H films that reduce lateral re-equilibration of charge The continuous MISCam sensor is read out by the principle of the laser-scanned photodiode (LSP) with a modulated read-out laser [2]. Compared to commercial CCD sensors, no lithographic steps are needed for pixel definition.

Metal-insulator-semiconductor (MIS) structures based on a-Si:H have been used previously to study metastable effects like light-induced defect formation [3] and defect kinetics, since the carrier density can be simply controlled by the gate bias. This is important for the evaluation of the performance of thin-film field-effect transistors (TFT's) which commonly employ a hydrogenated a-SiN insulator layer as gate dielectric.

During a study of the influence of small leakage light on TFT performance Muschik *et al.* have measured a change of sign in the spectral response of a-SiN/a-Si double layers illuminated through a semitransparent gate contact by chopped light [4]. Under zero dc-voltage bias the ac-photocurrent signal was positive in the blue region and negative in the red spectral range as shown in Fig. 1 (a). We also followed the shift of the zero crossing of the phase of the photocurrent at a given wavelength after applying a certain bias voltage under illumination as shown in Fig. 1 (b).

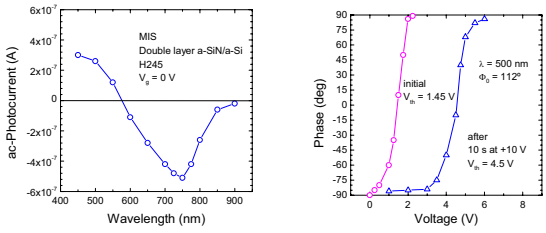

Fig. 1: *(a) Crossover of spectral response in an a-SiN_x:H/a-Si:H MIS structure. (b) Shift of phase flip after voltage stress under illumination during 10 s (After ref. 4).*

2. Single spot characterization

Recently we have again taken up this idea to study the feasibility of an amorphous silicon based MIS image sensor. We first looked for the characteristic of a given single spot. Standard equipment was used for I-V, C-V, and spectral response

measurements. Usually, we used a current-voltage converter followed by an averaging transient digitizer for time-resolved measurements and lock-in technique for the steady-state analysis.
First we show the effect of interface charges in a silicon nitride MIS structure. The analysis of the C-V curve leads to an estimate of the substrate doping level of about 6 x 10^{14} cm^{-3}, with very large interface charge densities of about 5 x 10^{12} cm^{-2} derived from the threshold voltage shift (see Fig. 2). The change in slope is consistent with the existence of fast and slow states at or near the interface. At low frequency of 14 kHz a small dip is seen when the voltage is scanned towards negative values, indicating reemission of trapped charges at a given level of band bending. At 70 kHz the hysteresis is much less pronounced.

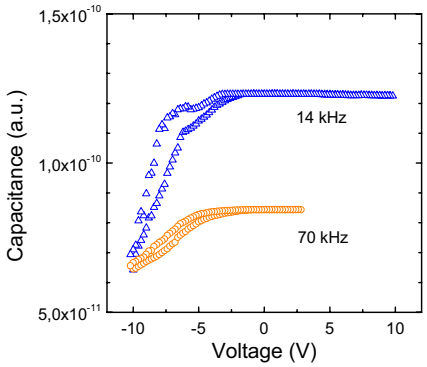

Fig. 2: *C-V curves of SiN MIS structure.*

Fig. 3 shows the I-V characteristics in dark and under illumination with bias light from a HeNe laser. In dark we again obtain a large threshold voltage shift, similar to the C-V results. We tried to fit the I-V curve with a Poole-Frenkel ansatz. The good fit hints to transport via traps in a-SiN:H with an average energy depth of 0.5 eV.

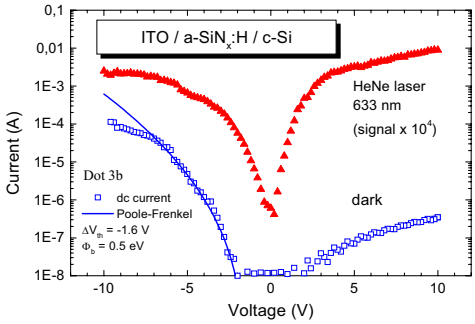

Fig. 3: *Dark and photocurrent as a function of V_g in SiN MIS. The full line is a fit to the Poole-Frenkel ansatz.*

3. Application as image sensor (MIScam)

Following the result shown in Fig. 3, for example at 5 V positive bias, one can conceive the operation of a 2-dimensional readout of a MIS structure where the variation in the ac-photocurrent is monitored as a function of the position. Variable light intensities of an image projected on the sensor, replacing the HeNe laser source in Fig. 3, allows to recover the light intensity distribution.
Two more effects are studied. The presence of slow interface charges allows for image memory by monitoring the threshold voltage shift distribution. Next we looked at sensor degradation by pulsed laser irradiation which not only causes a reversible threshold voltage shift but also a signal degradation.
Colour sensors can be realised by exploiting the effect of control of inverted electric fields in the base and the interface region. Fig. 4 shows the spectral response of the ac-readout of the MIS structure with a broad minimum near 750 nm. This is in contrast to usual response curves in p-i-n diodes. The minimum observed here may stem from the existence of opposite fields that compensate the contribution to the ac-current for a certain generation profile.

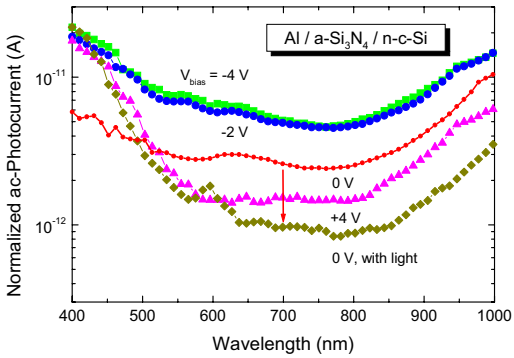

Fig. 4*: Spectral response of the a-SiN on c-Si MIS structure for V_g = -4, -2, 0, and +4 V. The arrow indicates the photosignal quenching effect under illumination .*

Extensive numerical analysis would be necessary to reproduce this behaviour in detail. What is important for the application as a sensor structure is the strong quenching effect seen for additional light bias as shown by the curve with lowest response values in Fig. 4.

References

[1] F. Wang *et al.*, Proc. 2nd Symp. on Thin Film Transistor Techn., Y. Kuo ed., Vol. **94-35** (Electrochem. Soc., Pennington, 1995), p. 233.
[2] M. Vieira, M. Fernandes, J. Martins, P. Louro, A. Maçarico, R. Schwarz, and M. Schubert, IEEE Sensors Journal **1** (2001) 158.
[3] W.B. Jackson, Appl. Surf. Sci. **39** (1989) 273.
[4] T. Muschik, F. Wang, and R. Schwarz, TU Munich, 1993, unpublished.

Electrotherapy of Tumour Cells Using Planar Electrode Arrays

A. Morrissey[1], J.Piggott[1], A. Norman[1], F. Stam[1], D. Soden[2] and C. Dunne[2]

[1]National Microelectronics Research Centre, University College, Lee Maltings, Prospect Row, Cork, Ireland
Email: Anthony.Morrissey@nmrc.ie http://www.nmrc.ie
[2]Cork Cancer Research Centre, Mercy Hospital, Cork, Ireland

Summary: *The objective of this work is the development of planar electrode devices for use in gene and drug therapy microsystems for cancer treatment. Platinum and gold electrodes fabricated on both silicon and flexible polyimide substrates were assessed for efficiency of electroporation. Electroporation involves application of electric fields to target cells, thereby rendering them transiently porous such that uptake of any therapeutic agent present will be greatly enhanced. Uptake and effect is monitored by cell count comparisons, and by luminescence measurements in the case of labelled therapeutics. Electrode arrays were designed subsequent to predictive modelling and simulation of electric fields using FEMLAB.*

Keywords: *electroporation, gene therapy, microelectrodes, cancer treatment*
Category: *10 (Applications)*

1 Introduction

During the next 10 years, cancer will overtake all other diseases as the number one cause of death in developed countries, and will impact significantly on the economics of healthcare delivery. Current cancer treatment uses 3 main modalities alone or in combination, viz. chemotherapy, radiotherapy and surgery. Gene therapy is the treatment or prevention of diseases such as cancer by gene transfer, and is regarded by many as a potential revolution in medicine. DNA delivery is seen as being pivotal in developing gene therapy and DNA vaccination approaches for treating and controlling diseases that are likely to impact clinical medicine and biotechnology over the coming decade.

The objective of this work is the development of planar electrode devices for use in gene and drug therapy microsystems for cancer treatment. The treatment method in question is electroporation [1]. It is hoped that such a treatment method for cancers would give hope to a far greater number of patients, particularly as it is non-surgical and therefore would provide hope to those not suited for such a traumatic procedure. This is particularly the case in elderly patients, and in the case of cancers such as oesophageal for example.

Electroporation is the use of applied electric field pulses to render porosity (and hence permeability) to otherwise non-permeable (to large drug / gene molecules) cell membranes. If a therapeutic agent is now also present locally, then this should yield a localised and highly efficient treatment modality with increased patient comfort during the procedure, as compared with current treatment methodologies. This process has been demonstrated to work for subcutaneous tumours by other authors, for example [2]. Hence, no details of the electroporation theory will be discussed further in this paper.

For the most part, previous work has used large macroscopic needles to deliver the required pulse waveforms to the target sites. This paper will present results achieved from work using microelectrode arrays on both silicon and flexible planar substrates.

2 Experimental

Finite element modeling using FEMLAB was used to predictively simulate electric fields generated from such devices for a range of applied pulse waveforms. The many parameters associated with the latter needed to be varied and optimised (in fact, the work is ongoing). These include voltage applied, pulse shape, pulse duration, frequency, monopolar versus bipolar, etc.. This aided greatly in minimising the number of electrode array design options worthy of investigation.

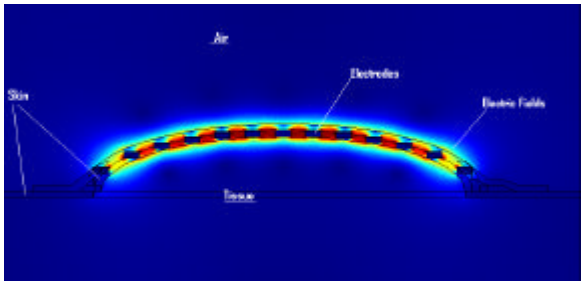

Figure 1: Simulation of electric fields generated at a flexible gold electrode

Platinum and gold electrodes were fabricated by standard lift off technology. Substrates used were both silicon and flexible polyimide of both 25 and 50 microns thickness. Features on the silicon were down to 10 microns, whereas those on polyimide ranged from 100 to 2000 microns. Electrode arrays were packaged in a format suitable to allow *in vitro* studies of the electroporation efficacy using bleomycin as the treatment agent.

Cell transfection efficiency is monitored through measurement of luminescence from labeled therapeutics. Monitoring also includes counts of cell numbers present prior to and post application of the electroporative pulsation in the presence of bleomycin. Procedures used were as in [3].

3. Results and Discussion

Figure 2 shows a typical result obtained from a tumour cell death study using gold electrodes on polyimide. In this case, larger feature (2000 microns) were used. The full paper will include observations on the effect, where any, of electrode metal and array and feature sizes.

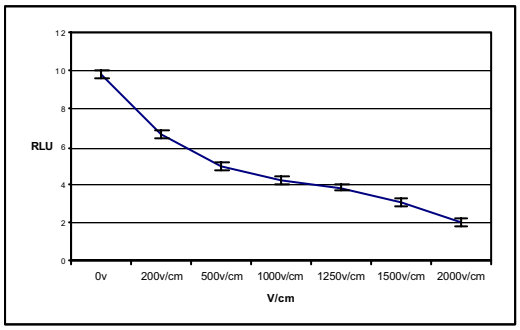

Figure 2: Tumour cell death using 2000?m spaced gold electrodes

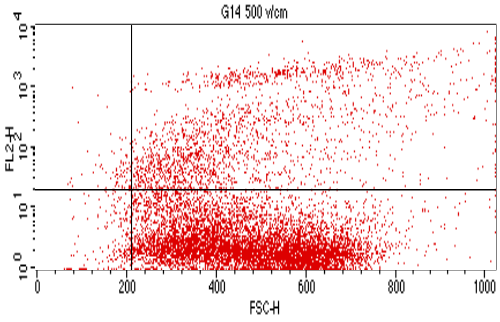

Figure 3: Scatter plot taken after a series of electroporation pulses in presence of bleomycin

Figure 3 shows a scatter plot which is interpreted by basically saying that the upper right corner represents cells which have been successfully electroporated. In the present work, only circa 20% of treated cells were porated but this has more to do with the need for an improved test set up than a measure of success of the process. The main point is that it shows that we have achieved poration with the planar electrodes.

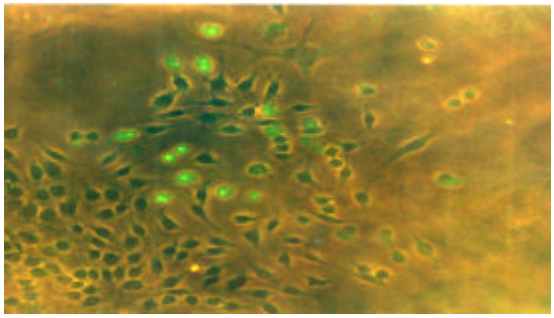

Figure 4: Successful delivery via electroporation of the Green Fluorescent Plasmid to tumourgenic cells *in-vitro*

Figure 4 shows the expression of Green Fluorescent Protein (GFP) in tumour cells. The photo shows the luminescence emitted from labelled agent expressed within the target cells.
Cell impedance was also measured prior to and post application of a range of electric fields. With higher voltages / fields applied, greater decrease in impedance was observed. While this is further evidence of successful electroporation, it is not clear that this can be quantitatively linked to the degree of poration. The indications are that it is probably not. This will be investigated further.

4. Conclusions

Planar electrodes fabricated on rigid silicon and flexible polyimide have both been shown to be capable of achieving electroporation of oesophageal tumour cells. This means they can be used for the development of microsystems for gene and drug therapy. To date, only *in vitro* studies have been carried out in the present work.

5. References

[1] *Fundamentals of electroporative delivery of drugs and genes*, E. Neumann, S. Kakorin and K.Toensing, Bioelectrochemistry, 48, Issue 1 (1999), pp3-16.

[2] R. Heller et al, Cancer, 77, Issue 5 (1996), pp. 964-971.

[3] J. Piggott et al, EMBEC 2002, Vienna, 4th December 2002, pp.724-725.

Photon Counting Reflectometer with Millimeter Resolution

J. Blazej, K. Hamal, I. Prochazka and D. Konarik

Czech Technical University, Dept. of Physical Electronics, Brehova 7, 115 19 Prague 1, Czech Republic
email: blazej@troja.fjfi.cvut.cz http://kfe.fjfi.cvut.cz/~blazej

Summary: *The description and results obtained on experimental sample of photon counting reflectometer are presented. The Single Photon Avalanche Detector based on silicon photodiode is used in experiment. In compare with other systems using time correlated photon counting for this purposes, the unique temporal resolution of used detector and timing system allows achieve millimeter spatial resolution and high dynamical range preserving other parameters as are acquisition time.*

Keywords: *Photon counting, optical time domain reflectometer, picosecond detector*
Category: *10 (Applications)*

1 Introduction

Because high penetration of optical fibers in various branches of industry, where can be used for data transmission, measuring and many other applications, it is useful to have high precise and accurate technique for its diagnostics. The motivation of our work is to apply photon counting detector originally design for laser ranging in new field.

2 Our approach

2.1. Principle

Our realization of optical time-domain reflectometry (OTRD) is based on time correlated photon counting (TCPC) principle. Intensity of reflected light is measured by counting of number of photons detected in short time interval (channel). Absolute temporal position of channel is correlated with begin of fiber. The short laser pulse is injected into fiber and only one or zero reflected photon is detected. This approach allows easy reconstruction of reflected light profile along fiber. It is an optical sampling. Its drawback is a requirement of high number of detection event and consequent dial among repetition rate, acquire time, dynamical range and channel width. Active gating of detector allows data acquiring from selected part of fiber only and rapidly improves experiment yield.

2.2. Experiment

Our experimental setup use as a light source Picosecond Light Pulser (Hamamatsu PLP-02) with wavelength 780 nm and 40 ps FWHM pulse length. As a detector we are using silicon based Single Photon Avalanche Diode (SPAD) detector with 100 μm diode. The SPAD [1, 2] is a diode structure manufactured using a conventional planar technology on silicon. It is controlled by active gating and active quenching circuit. Active gating allows detector activation for selected time interval (in nanosecond scale) and active quenching allows operate detector on high repetition rate (up to 1 MHz).

The single photon detector sensitivity is achieved by biasing the diode above the pn junction break voltage (on Fig. 1 from 1 to 2). In this stage, the first absorbed photon is capable to trigger the avalanche multiplication of carriers - the fast rise time current pulse is generated (on Fig. 1 from 2 to 3). Its amplitude is limited only by external quenching circuit connected to the diode. There is the active quenching circuit, which decreases the voltage applied to the diode bellow the break voltage as soon as an avalanche current buildup is detected (on Fig. 1 back from 3 to 1).

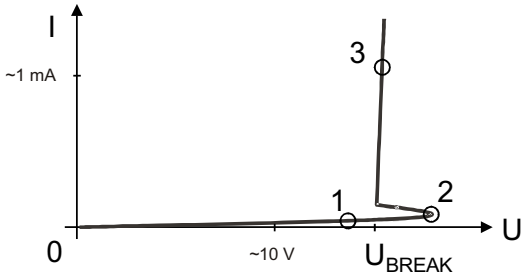

Fig. 1: V-A characteristic of avalanche photodiode in reverse direction, current vs. voltage with significant point described in text as operation in so-called Geiger mode (in analogy with radiation detectors).

The diode voltage is kept bellow the break until next gate signal occurs. Then, the diode is biased above the break, again. The gate signal can be generated in correlation with laser shot or generated from previous one. In the second case very low optical signal intensity is necessary for measured data interpretation.

On Fig. 2 is a block scheme of our experimental setup. The setup is made using bread board optics components. It has table top size. The light from the laser is collimated with spherical lenses and than it is coupled into the fiber through another

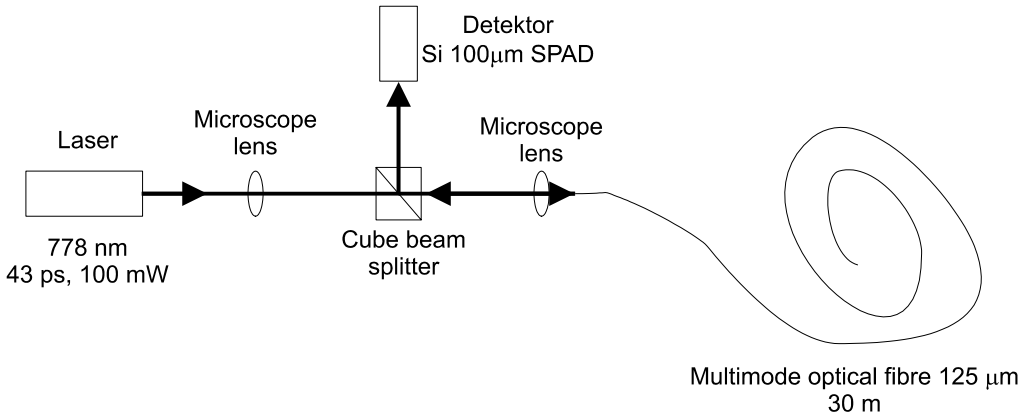

Fig. 2: Photon counting reflectometer experimental setup.

microscope lenses. The light reflected back from the fiber is separated by splitting cube and send into detector and than processed.

Sample of measured data from 30 meters long fiber is on the Fig. 3. The peaks in the graph are reflections on the end of the fiber. Firstly was measured the whole fiber and then was shortened and measured second graph. In graph are these two measured samples together for 7 mm shortened fiber.

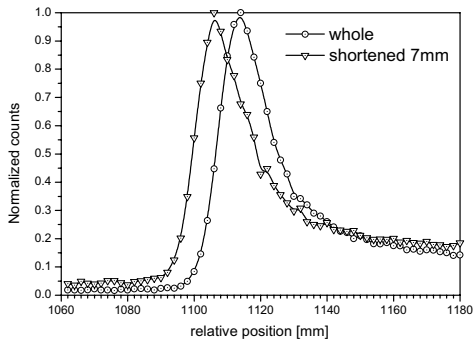

Fig. 3: A sample data demonstrating spatial resolution on strong reflection on the end of the fiber.

3 Conclusion

The experimental sample of reflectometer was constructed. Its temporal resolution is limited by detector and timing electronics parameters and overall time jitter is 64 ps now. It corresponds with 5 mm in spatial domain. Measured dynamical range during daylight operation is more then 1000. Our future work will be focused on improving of dynamical range. Finally, this reflectometer is intended as a base for development of photon counting based distributed fiber sensors.

Acknowledgment

This research was supported by the Grant Agency of Czech Republic, grant No. 102/02/D064.

References

[1] PROCHAZKA, I., HAMAL, K., SOPKO, M., MACHA, I., Novel Contribution in Branch of Ultra-fast Condensated Matter Spectroscopic Photon Counting System. In Solid State Device Research 92, *Proceedings of the 22nd European solid State Device Research Conference - ESSDERC '92*, Leuven, Belgium, September 14-17, 1992, pp. 643-5.

[2] KIRCHNER, G., KOIDL, F., BLAZEJ, J., HAMAL, K., PROCHAZKA, I., *Time Walk Compensated SPAD: Multiple Photon Versus Single Photon Operation*, Proc. SPIE Vol. 3218, p. 106-112, Laser Radar Ranging and Atmospheric Lidar Techniques, Ulrich Schreiber; Christian Werner; Eds., Dec 1997, ISBN 0-8194-2650-4

The study of smart microliter osmotic valve for diabetes therapy

T. Nagakura[1], T. Uchino[2], C. Shibazaki[2], S. Maruo[3], K. Ikuta[3]

[1]Department of Biomedical Engineering Faculty of Engineering Osaka Electro-Communication University,
[2]Department of Medical Electronics Faculty of Medical Engineering Suzuka University of Medical Science,
[3]Department of Micro System Engineering, Graduate School of Engineering, Nagoya University,
[1]1130-70 Kiyotaki, Shijyonawate City, Osaka Prefecture, Zip code 575-0063, Japan Tel : +81-72-876-3317, Fax : +81-72-876-3321
E-mail : nagakura@isc.osakac.ac.jp
[2]1001-1 Kishioka-cho, Suzuka City, Mie Prefecture, Zip code 510-0293, Japan Tel : +81-593-83-8991, Fax : +81-593-83-9666
[3]Furo-cho, Chikusa-ku, Nagoya Prefecture, Zip code 464-8603, Japan Tel : +81 52-789-5213, Fax : +81 52-789-4512

Summary: *The diabetes is a disease by lack of insulin. Insulin is only hormone to reduce the blood sugar concentration. So diabetes increases the blood sugar concentration level. Then insulin supplement therapy is needed for diabetes patient. But, an insulin supplement therapy is depending on experience of a doctor, it is sometimes insufficient quantity of insulin, and it is danger of hypoglycemia attack. But, there are no practical devices for adequate quantity of insulin supplement therapy.*
So we have investigated about the device for the insulin therapy. This device works mechanical actuation by the change of the blood sugar concentration without energy supply and control system. We have applied this device by the micro optical stereo lithography, and have tried to estimate the function.
Keywords: *osmotic pressure, semipermeable membrane, diabetes, glucose concentration, osmotic valve*
Category: *10 (Applications)*

1 Introduction

The diabetes patients are 6% of the population. And the diabetes causes serious complications. The complications are mainly circulatory disease, nephropathy, retinopathy and neuropathy. Retinopathy causes to be blind, nephropathy causes chronic renal failure that is needed for hemodialysis. So it is a noticeably increasing both social and personal burden.

Although the progress of diabetes and complications can be suppressed by strict blood glucose control [1]. The diabetes is a disease by lack of insulin. Insulin is only hormone to reduce the blood glucose concentration. So diabetes increases the blood sugar concentration level. Then insulin supplement therapy is needed for diabetes patient in order not to be high blood glucose concentration level. Because an insulin supplement therapy is depending on experience of a doctor, it is sometimes insufficient quantity of insulin, and it is danger of hypoglycemia attack. So this intensive insulin therapy needs for patient enough knowledge and patience, makes harmful hypoglycemia attack.

So the medical device for blood sugar control has been expected, the various devices have been developed. The artificial pancreas, which senses continuous blood glucose concentration and controls injection quantity of insulin, has not been practical method. We have investigated that the device worked mechanically by the change of the blood glucose concentration. We have applied this concept to valve system fabricated by the micro optical stereo lithography.

2 PRINCIPLE

When the different solutions are separated by a semipermeable membrane, the solvent moves into hyper osmolarity side. The ideal semipermeable membrane allows only solvent to pass through, prevents the substance from passing.

If the a part of solid vessel is closed by a semipermeable membrane, filled with a hypotonic solution, surrounded by a hypertonic solution, the hypertonic solution draws the solvent from the inside hypotonic solution. Then the inside volume in vessel changes. Furthermore, if the other part of a vessel is fixed by a elastic membrane, the change of volume bends the elastic membrane. So the elastic diaphragm is deformed by the difference of concentration of solution between both inside and outside. In other words, the stroke of diaphragm based on the difference of concentration of solution. We called this device an osmotic valve.

The osmotic valve system works as a sensor and an actuator according to the change in blood glucose concentration. And this system does not need control system and power supply system from outside.

When this osmotic valve is used as a insulin injection system, the insulin is injected by the elevation of blood glucose concentration level. Then the blood glucose level reduces by the injected insulin, the valve is closed automatically.

The human serum osmotic pressure is mainly regulated by the Sodium, Potassium, BUN (Blood Urea Nitrogen) and blood glucose (Blood Sugar) concentration. The diabetes is the disease that only control of a blood glucose concentration level failed in these four components. The concentration of Sodium and Potassium are regulated strictly by human homeostasis. The electrolyte and BUN are small size.

Human serum osmotic pressure consists 4 components.
(Osmotic Pressure)=1.8 (Na+K)+BUN/10+BS/18 [mOsm]

	Human normal limits
Osmotic pressure,	290 [mOsm] (in serum)
Na : Sodium concentration,	140 [mmol/l]
K : Potassium concentration,	4 [mmol/l]
BUN : Blood Urea Nitrogen concentration,	10 [mg/dl]
BS : Blood Sugar concentration [mg/dl]	100 [mg/dl]

It is needed for the semipermeable membrane of osmotic valve to prevent from passing through glucose molecule. Because the glucose molecule is the largest among 4 components. It is an important that condition for membrane is a permeability for glucose. On this condition, the osmotic valve can be applied to insulin deliver system in the treatment diabetes.

3 METHOD

FABRICATION

It is necessary for this system to be sealed up strictly, so we made the device by micro stereo lithography. The micro stereo lithography is a method to form micro three dimensions shape, irradiated by ultraviolet laser at photosensitive resin [2]. The micro stereo lithography is one of optical modeling method, which is liquid photosensitive resin is hardened and laminated by high-power ultraviolet laser. Not only microstructure but also 100 mm or larger structure can be processed with an accuracy of 1 μm. The modeling of a 3D structure is designed previously by 3D CAD, and based on this, laser scanning track data are generated for filling contour inside by 3D CAD data. The XY surface is scanned by laser light from upward according to the scanning track data. The resin is hardened in horizontal cross sections.

The osmotic valve consists of semipermeable membrane, elastic membrane for diaphragm and polymer housing. The outer size of osmotic valves that we fabricated are from 2X3X2mm to 10X10X10mm.

MEASUREMENT

We tried to estimate the function of osmotic vale by the displacement of the diaphragm membrane. We measured the displacement of the osmotic valve in the water bath was filled with glucose solution, by the laser displacement meter with 0.1 μm accuracy from outside of water bath. We studied experimentally for the relation between difference of osmotic valve size and change of the glucose concentration.

Furthermore, we did an experiment to confirm whether this osmotic valve could be able to drive in the living body. We tried to insert the osmotic valve under the skin of a rat in anesthesia. We let a rat eat a high concentration glucose solution and raised a blood sugar level. We injected an insulin solution to the body by the osmotic valve. By measured glucose concentration and quantity of the insulin solution, we evaluated valve performance.

4 RESULT

The result of we measured displacement of diaphragm membrane (the valve size: 5X5X3.2mm) was deformed by 120 μm for 10 minutes by a concentration change of the glucose solution of 600 mg/dl. But the valve size 10X10X10mm deformed 10 μm for 10 minutes. It was ascertained that the displacement and the speed of deformation increased as the size of osmotic valve became smaller. The down sizing has various advantages such as the efficiency of osmotic valve, less invasive and cheaper cost. We compared inside volume 17μl with 510μl (about 30 times). As a result, a stroke of a membrane was 12 times. This character of osmotic valve means that the smaller size, the faster and larger quantity insulin can be injected. It is desirable for a clinical device to be small, less invasive, less economic cost and disposable against the infection. It is suggested that this osmotic valve can be suited for insulin therapy.

In order to study whether the osmotic valve could have a possibility to treat diabetes patients, we tried to the preliminary experiment for implantation in subcutis of rat. We confirmed the implanted osmotic valve could deliver insulin and control blood glucose concentration of rat by the change of its blood glucose concentration. So we thought that it has a enough possibility to treat human diabetes patients.

5 DISCUSSION

We made clear the osmotic valve function, for example the displacement velocity and the displacement of diaphragm depend on concentration. And we think that the osmotic valve can be applied to insulin injection system in the treatment diabetes patients by the preliminary experiment of implantation in rat. And blood glucose concentration of diabetes patients fluctuates between about 100mg/dl and 1000mg/dl. This fluctuation is enough osmotic change to actuate our valve system.

The osmotic valve has a character that the greater the variation of blood glucose concentration from normal, the larger quantity and faster injected insulin. In other word, this valve system injects larger quantities and more rapidly in poorly controlled diabetes patients. The diabetes patients usually inject a insulin solution 10-100μl a few times by a day. Well controlled diabetes patients keep their usual blood glucose concentration at not more than 200mg/dl. However, in poorly controlled diabetes patients, even if insulin is injected, blood glucose concentration would ranged from 200mg/dl to 600mg/dl. It is suggested that there is a good possibility of controlling the blood glucose concentration of diabetes patients.

6 CONCLUSIONS

This osmotic valve has a cubic shape with a volume of less than 1ml, and can drive enough quantity of water for insulin therapy. It has been shown that the valve works effectively in the clinical practice and functions well enough.

ACKNOWLEDGMENTS

The present study was partially funded by the 1997 Ministry of Education Scientific Research Grant (0978081), Suzuken Memorial foundation Award 1998, Nakatani Electronic Measuring Technology Association of Japan 1999, Research for the Future Program of Japan Society for the Promotion of Science under the Project "Integrated Fields, Information on Life Systems, Development of Artificial Cellular Device". (1996-2001), I would like to thank Prof. Ikuta and Ikuta Laboratory stuffs, I am also grateful to our stuffs in Suzuka university of Science.

REFERENCES

[1] UK Prospective Diabetes Study (UKPDS) Group, Intensive blood-glucose control with sulphonylureas or insulin compared with conventional treatment and risk of complications in patients with type 2 diabetes (UKPDS 33). LANCET; 352(9131): 837, 1998.

[2] K. Ikuta, S. Maruo, Y. Fukaya and T. Fujisawa, New micro stereo lithography for freely movable 3D structure -Super IH process with submicron resolution-, Proceedings of the IEEE International Workshop on Micro Electro Mechanical Systems (MEMS98), 290-295, 1998.

Design of an Optical Force Sensor for Force Feedback during Minimally Invasive Robotic Surgery

J. Peirs, J. Clijnen, P. Herijgers, D. Reynaerts and H. Van Brussel

Katholieke Universiteit Leuven, Dept. of Mechanical Engineering, Celestijnenlaan 300B, 3001 Leuven, Belgium
email: Dominiek.Reynaerts@mech.kuleuven.ac.be http://www.mech.kuleuven.ac.be

Summary: *A miniature tri-axial force sensor is under development for minimally invasive robotic surgery. To define the required force range and resolution, a needle driver has been equipped with strain gauges, able to measure two force components perpendicular to the instrument shaft. In vivo-tests with different needle types on skin, muscle and liver tissue show that the required force range and resolution are respectively 2.5 N and 0.01 N. The force sensor is based on a flexible structure of which the deformations are measured through reflective measurements with optical fibres.*

Keywords: *force sensor, optical, surgery, force feedback*
Category: *10 (Applications)*

1 Introduction

The introduction of robots in minimally invasive surgery (MIS) of soft tissues can considerably enhance the accuracy of medical interventions. The instruments are mounted on robot manipulators (the slaves) controlled by the surgeon through 'joysticks' (the masters). In this way, the surgeon can perform the operation in a more ergonomic way and his hand movements can be scaled and filtered to remove trembling and to enhance accuracy. Furthermore, additional degrees of freedom can be added at the instrument tip to enhance dexterity [1]. An important problem is that the surgeon lacks tactile feedback. This can be solved by introducing small force sensors in the instruments that enable force reflection in the masters.

2 Force range measurements

2.1 Test set-up

To be able to design the force sensor, the expected force range has to be specified. As few data can be found in literature, a test set-up was built to measure the forces occurring during suturing. Figure 2 shows a needle driver equipped with a 2-component force sensor based on strain gauges. The 4 strain gauges are glued on the instrument shaft with 90° interval. Two opposing strain gauges form a half bridge measuring the X or Y component of the force at the tip. The Z component is assumed to be of the same order of magnitude. The strain gauges are connected to AC bridge amplifiers and sampled at 250 Hz.

The instrument is calibrated by holding it horizontally, with a mass hanging at the tip. The instrument shaft is rotated 360° while measuring the voltages coming from both bridges. From this data it is possible to determine the sensitivity and offset of both bridges, and the orientation of the two strain gauge pairs with respect to each other and with respect to the jaws. The angle between the two strain gauge pairs is required to filter out the cross-sensitivity between both sensing axes.

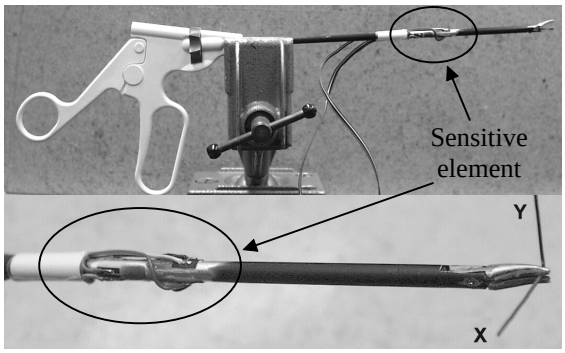

Fig. 1. Needle driver with 2-component force sensor based on strain gauges.

2.2 Measurement results

Suturing tests were performed by a skilled surgeon on an anaesthetized rat. The forces required to push the needle through the tissue depend on the thickness and shape of the needle, and the tissue. Table 1 shows the six tested needle types.

Table 1. Types of needles used in the test.

Size	Cross-section of tip	Shape
6-0 small	Circular	3/8 circle
3-0	Triangular	3/8 circle
3-0	Triangular	Straight
3-0	Circular	1/2 circle
1	Triangular	3/8 circle
1 large	Circular	3/8 circle

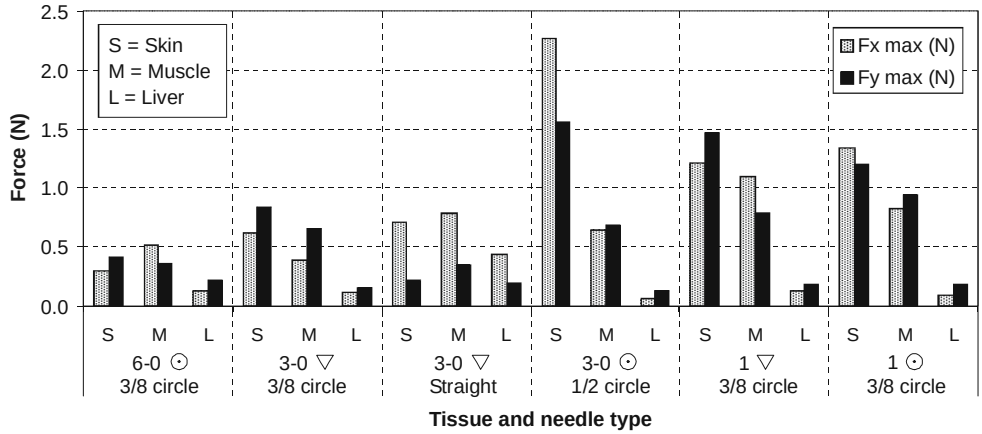

Fig. 2. Peak force occuring during suturing of skin, muscle and liver tissue using different needles.

Figure 2 shows the peak forces for skin, muscle and liver tissue. Skin is clearly the thoughest tissue while liver is the softest. The highest and lowest peak forces are respectively 2.3 N and 0.2 N. These are forces required to puncture the tissue. Other manipulations like oscillatory motions of the needle used to test the strength of the tissue are much lower, sometimes as low as 0.05 N for liver.

3 Sensor design

3.1 Specifications

The sensor will be mounted at the tip of a 5 mm diameter instrument driver with two bending degrees of freedom [1]. This instrument driver has an internal channel of 2 mm diameter through which surgical instruments can be inserted. The sensor should have the same internal and external diameters. As the sensor will be mounted in front of the local degrees of freedom, it should be as short as possible. Three components (F_X, F_Y, F_Z) should be measured with a range of 2.5 N and a resolution of 0.01 N (0.4 % of range). The sensor should be biocompatible, sterilizable and robust.

3.2 Design

A design based on optical fibres was chosen for reasons of safety as no leakage currents or interference signals can originate from it. Figure 3 shows the basic layout of the sensor. It consists of two parts connected by a flexible connection. The upper part is connected to the tool while the lower part is connected to the instrument shaft. Three optical fibres, arranged at 120° intervals in the lower part, measure the distance from the upper part through the intensity of the reflected signal. The fibre can measure the perpendicular distance from the surface or the lateral distance from an edge of this surface, depending on the sensor design (see figure 3). Figure 4 shows the reflected signal for both types of displacement and combinations. A mechanical structure for the sensor's flexibility is currently under development.

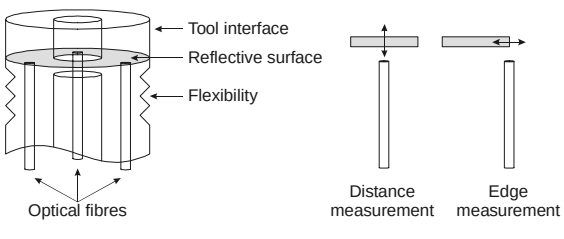

Fig. 3. Position measurement using reflective measurements.

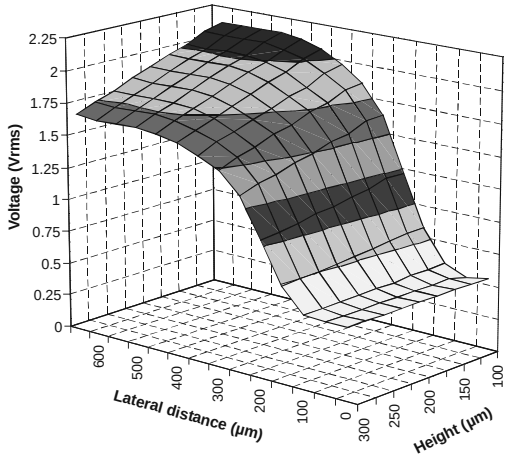

Fig. 4. Reflected signal as a function of perpendicular and lateral distance between fibre and surface edge.

Acknowledgement

This research is sponsored by the Belgian programme on Interuniversity Poles of Attraction (IAP5/06: AMS). The authors assume the scientific responsibility of this paper.

References

[1] J. Peirs, H. Van Brussel, D. Reynaerts and G. De Gersem. A Flexible Distal Tip With Two Degrees of Freedom for Enhanced Dexterity in Endoscopic Robot Surgery. In: *Proc. MME'02, The 13th Micromechanics Europe Workshop*, pp. 271–274, Sinaia, Romania, 6–8 October 2002.

Fibre optic voltage measurement based on the electrostrictive effect using a 3x3 fibre-optic coupler and low coherence interferometric interrogation

M.C.Tomic[1], J.M.Elazar[2] and Z.V.Djinovic[3]

[1]Institut bezbednosti, Kraljice Ane BB, 11040 Belgrade, Serbia
email: mctomic@Eunet.yu
[2]Ben Gurion University, 84105 Beer-Sheva, P.O.B. 653, Israel
[3]Institute for Microelectronic Technology and Single Crystals, Njegoseva 12, 11000 Belgrade, Serbia

Summary: *An interferometric method for remote measurement of voltage by fibre-optic link and sensor head is presented. A PMN:PT electrostrictive transducer is used to convert the electric field strength to displacement. A stable and linear interferometric reading of displacement is obtained by the passive demodulation technique employing 3x3 fibre-optic coupler. Temperature of the sensor head is simultaneously measured by the same fibre-optic configuration. Low coherence interferometric technique is utilized for interrogation of temperature sensor and for distinguishing between signals from two sensors.*

Keywords: *voltage measurement, electric field measurement, electrostrictive, 3x3 fibre-optic coupler, low coherence interferometry, fibre-optic sensor*
Category: *10 (Applications)*

1 Introduction

An optical method for volatage measurement can be based on any of the following effects: Pockels, Kerr, piezoelectric or electrostrictive [1]. Most experimental work and practically realized fibre-optic voltage sensors use the linear Pockels effect. Insertion of electro-optical crystal in a fibre optic configuration is often bulky and vibration sensitive. In the other hand, a sensor using piezo-electric/photoelastic effect [2], where the light path is completely confined in fibre, requires long fibre wound onto piezoelectric crystal, what is also very bulky.

In this paper we propose a different approach, based on the electrostrictive effect in PMN:PT ceramic. The change of dimension of ceramic transduser caused by electric field is detected by the interferometric method previously reported as suitable for remote vibration measurement [3].

The electrostrictive coefficient is very temperature sensitive, so the sensor head temperature have to be known to enable adequate correction of measured values. The temperature sensing is done by the same configuration, where one of fibres serves also as the temperature probe. The temperature is detected via elongation of a short, for instance, aluminium wire, which can be read by classical low coherence interrogation [4].

The proposed configuration offers a simple construction of sensing head, high measurement resolution and possibility of DC voltage measurement. However, because of quadratic nature of electrostrictive effect, the method do not provide information of the sign of the electric field and is not suitable for very low voltage measurement.

2 Theory

A sensor based on the electrostrictive effect measures, in fact, the electric field. The voltage can be measured by detecting the field formed by this voltage between two electrodes. This technique, where the voltage is applied directly to the transducer, can be used only for relatively low voltages. The electrostrictors of resonable size, i.e. below several centimeters, have the breakdown voltage below one kilovolt. Higher voltage can be measured by several electrostrictive transducers posted along the electric field, between the high voltage power line and ground potential. Numerical integration of field strength, measured in, at least, three [5] or four [2] “points”, using the quadrature method of integration, gives the desired voltage difference.

Deformation of electrostrictive transducer is detected by the interferometric technique based on a 3x3 fibre-optic directional coupler, which produces signals with a special phase relationship. Two quadrature signals, which are required for interferometric signal demodulation, can be extracted from these 3x3 coupler signals. In that way, a linear response on transducer strain, along with interferometric sensitivity, is obtained and can be used for voltage measurement.

3 Experiment

The proposed method is verified by the experimental setup shown in Fig.1. The central part of the sensing scheme was a commercially available 3x3 single mode directional coupler. Low coherence light source (LCS) was a superluminescent diode emitting at 1305 nm, with the coherence length of 30μm. Light source was

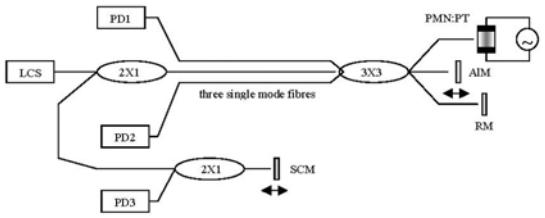

Fig. 1. Experimental set-up

connected to the central input port of the 3x3 coupler, directed via 2x1 fibre optic coupler. Two InGaAs photodiodes, PD1 and PD2, were attached to two other "input" ports of the coupler. The 3x3 coupler's output ports were very short and almost the same length. These were the measuring and the reference arms of the interferometer, directed towards the surface of the electrostrictive transducer (PMN:PT) and the reference mirror (RM), situated in close proximity of transducer. Transducer was a 4 mm thick piece of PMN:PT ceramic, with two electrodes generating electrical field in direction perpendicular to the fibre axis. The third "output" arm of 3x3 coupler was directed towards an Al mirror (AlM), mounted on a calibrated piezoelectric positioner, simulating the elongation of temperature sensing wire. The low coherence read-out interferometer was formed by the another 2x1 coupler, with the scanning mirror (SCM) mounted on the second calibrated positioner. The whole set-up was made without any of bulk beam shaping optical components. The level of line voltage applied to the transducer was settled by an autotransformator, in the range from 0 to 50 V rms.

4 Results

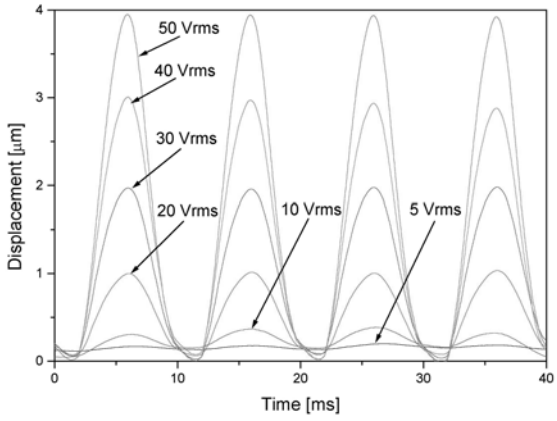

Fig. 2. The measured displacement of the electrostrictive transducer under applied alternating line voltage of 50 Hz.

Waveforms corresponding to six different AC voltage levels, obtained by post-processing of captured data sets, are shown in Fig.2. Signals are phase-unwrapped according to the procedure described in [6]. Note the 100 Hz periodicity and high nonlinearity in proximity of zero voltage, caused by quadratic relation between applied voltage and electrostrictor strain.

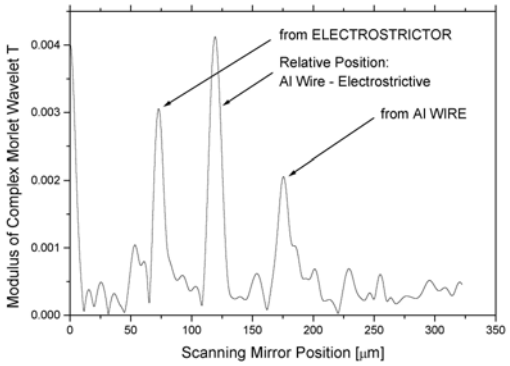

Fig. 3 The low coherence correlogram obtained during the SCM scan

Signal obtained by scanning the read-out interferometer is shown in Fig.3. This is the photodiode PD3 signal processed by the complex Morlet wavelet transform, corresponding to the shape of coherence function of the super-luminescence diode. The position of "Al wire" peak in Fig.3 represents the temperature of sensing head.

References

[1] L. Fabiny, S. T. Vohra and F. Bucholtz, "High-resolution fiber-optic low-frequency voltage sensor based on the electrostrictive effect", *IEEE Photon. Technol. Lett.* 5 (8) 1993 pp. 952-953

[2] K. Bohnert, J. Kostovic and P. Pequignot, "Fiber optic voltage sensor for 420 kV electric power systems" *Opt. Eng.* **39** (11), 2000, pp. 3060-3067.

[3] M.C.Tomic, J.M.Elazar, Z.V.Djinovic, "Low-coherence interferometric method for measurement of displacement based on a 3x3 fibre-optic directional coupler", *J. Opt. A: Pure Appl. Opt*. 4 (2002) pp. S381-S386

[4] Y. J. Rao and D. A. Jackson, "Recent Progress in Fiber Optic Low-Coherence Interferometry", *Meas. Sci.Technol.*, Vol. 7 (1996) pp. 981-999

[5] F.Rahmatian, P. Chavez and N. Jaeger ,"A 230 kV Optical Voltage Transducer Using Multiple Electric Field Sensors", *IEEE Trans. Power Delivery,* **17** (2) 2002 pp. 417-422

[6] M.C.Tomic,Z.V.Djinovic,"Low coherence interferometric method for vibration measurement using 3X3 fiber optic coupler", in A.J.Rogers ed. *Proc. SPIE Vol. 4074*, pp. 419-426, Glasgow, Scotland, May 2000

Mobile Robot Olfactory Sensory System

Lino Marques, Nuno Almeida and A.T. de Almeida

Institute of Systems and Robotics
Department of Electrical and Computer Engineering
University of Coimbra
3030-290 Coimbra, Portugal
{lino,nuno,adealmeida}@isr.uc.pt

Summary. *Olfaction-based mobile robot navigation has captured the interest of many researchers during the last ten years, but till now, most experimental works are done in airflow controlled indoor environments using strong odour concentrations. The main obstacles to research in mobile robot olfaction are the properties of current gas sensors (slow, weakly selective and poorly sensitive) and the difficulty to estimate the physical characteristics of a natural odour plume from sparse measures taken far-away from the odour source. This paper presents an olfactory sensing system that intends to overcome some of those problems. The proposed olfaction sensing system is based on two metal oxide gas sensor arrays and a thermal anemometer. The selectivity of the olfaction system is enhanced by processing the output of each array of different gas sensing elements. The speed of the sensing system is increased by the utilization of gas sensors transient response. The fusion of airflow (amplitude and direction) with previous spatio-temporal concentration measures, gathered along the robot trajectory, allow to obtain usable estimates of local gradients and odour source localization.*

Keywords: Artificial olfaction, mobile robotics, electronic nose.
Category: 10 (Applications)

1 Introduction

Olfactory-based behaviors are among the most common behaviors in the animal world. It is well known that insects and other animals use olfactory sense in a wide variety of behavioural processes, namely to recognize and locate food sources, detect predators, mark areas and trails, and find mates. Recently, there has been an increased interest in integrating olfaction in mobile robots [3, 4, 5, 2]. This "new" robotic sense may improve robot capabilities in natural environments for applications such as: inspection, demining, rescue, prospecting, patrolling, etc. Current works in mobile robot olfaction have been mostly developed under simplified experimental conditions (indoor environments with constant and known airflow and with high gas concentrations). To prosecute the research across real outdoor environments the sensing system should overcome several challenges, namely: the gas sensors should be fast, sensitive and selective enough to detect small odour puffs far away from the source. The transport of odour molecules in natural environments is a phenomenon mainly dominated by turbulent airflow. Following an increasing concentration gradient does not guarantee to find an odour source. First, because far away from the source, the average concentration is too low to measure local gradients and secondly because in all real environments turbulence is a dominant phenomenon, imposing abrupt changes in the measured concentration. Having those aspects in mind, the olfaction system correlates the concentration signals with the wind information to estimate the direction of the source. After sampling the workspace enough to estimate the plume width, the distance from the source can be estimated from the dispersion theory. A successful olfaction system should have the capacity to measure the local airflow velocity and direction.

2 Olfaction sensing system

The proposed olfaction sensing system is composed by two gas sensing nostrils, located on opposite sides, near the top of the robot and a pumping system able to pull air from the robot base to a sensing nostril. A directional anemometer on the top of the robot (see Figure 1). The odour and wind information is processed with the robot's position in order to estimate the odour source localization. Each sensing nostril is composed by four Figaro Inc. metal oxide gas sensors (TGS2600, TGS2602, TGS2610, TGS2620). The pumping system is composed by a pipe and a small controllable DC fan. The fan is only turned on to localize the position of a ground odour source. The proposed thermal anemometer measures airflow intensity and direction using four self-heated thermistors placed around a square wind deflecting pillar (see figure 1). The power dissipated by each sensor depends from the difference between the device temperature and local air temperature and depends from the airflow around the device. The heated

thermistors are operated at constant temperature differential. The compensation for changes in ambient temperature is achieved by a fifth thermistor located inside the square pillar that measures local air temperature.

Fig. 1: Nomad Super Scout mobile robot with olfaction sensing system.

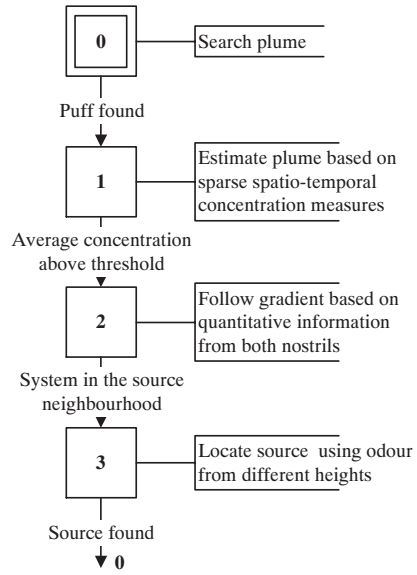

Fig. 2: State flow diagram of robot olfaction system.

Odour searching

The search and localization of an odour source can be represented by Figure 2. The signal processing of each sensing nostril is actively changing in order to be optimized for each detection phase.

In the first phase, far away from the source, the mixture to detect is characterized by sparse puffs with variable, normally low concentrations. In this phase each nostril is used independently for detection of low concentrations (minimum sensor offsets and very high amplification) and fast identification using algorithms that allow the processing of transient data (e.g. feature extraction from wavelet transforms) [1].

After entering in a sustainable area of a plume, the higher concentration levels, allow to employ both arrays in the estimation of local gradients. Here the processing is directed towards the quantification of the main tracked gas substances.

Finally, when the system suspect that it is near or above the source, the system turn-on the air pump and compares the concentrations measured from the ground level with the concentration in the top of the robot. As the distance between the robot and the source decreases, the concentration difference between both levels should increase. As can be seen in Figure 3, moving the robot over a 5 cm diameter ethanol source, and using the concentrations gathered from the robot's base, it is possible to localize with some accuracy (in this case, with an error of 4 cm) the source position.

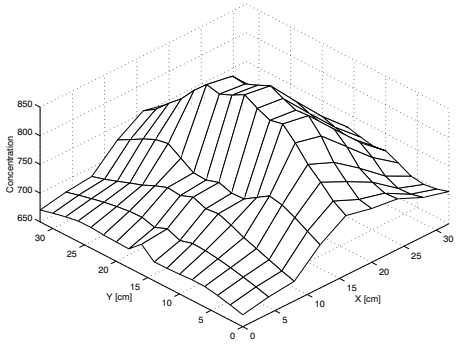

Fig. 3: Odour concentration measured with a scan over a 5 cm diameter ethanol ground source. The source is located in position (16,16). The peak of the measured concentration present a bias of about 4 cm in the X direction.

References

[1] N. Almeida, L. Marques, and A.T. de Almeida. Fast identification of gas mixtures through the processing of transient responses of an electronic nose. In *submitted to EuroSensors*, 2003.

[2] A. T. Hayes, A. Martinoli, and R. M. Goodman. Distributed odor source localization. *IEEE Sensors*, 2(3):260–271, 2002. Special Issue on Artificial Olfaction.

[3] H. Ishida, K. Suetsugu, T. Nakamoto, and T. Moriizumi. Study of autonomous mobile sensing system for localization of odor source using gas sensors and anemometric sensors. *Sensors and Actuators*, A45:153–157, 1994.

[4] Lino Marques, Urbano Nunes, and Aníbal de Almeida. Olfaction-based mobile robot navigation. *Thin Solid Films*, 418(1):51–58, 2002. Selected from 1st Int. School on Gas Sensors.

[5] R.A. Russell. Survey of robotic applications for odor-sensing technology. *Int. Journal of Robotics Research*, 20(2):144–162, 2001.

FLEXIBLE POSITION SENSITIVE DETECTOR BASED ON PIN A-SI:H STRUCTURES PRODUCED BY PAHW-CVD

Isabel Ferreira*, Elvira Fortunato and Rodrigo Martins

CENIMAT, Department of Materials Science, Faculty of Science and Technology of New University of Lisbon, and CEMOP/UNINOVA, Campus da Caparica, 2829-516 Caparica, Portugal

Abstract

The main motivation of the research community in the field of amorphous and microcrystalline silicon films is the deposition of a/μc-Si:H films on polymeric substrates aiming to produce optoelectronic devices on flexible substrates in order to spread out the field of applications. To reach this goal it implies to investigate the possibility of producing a-Si:H films at low temperature (<140ºC) on transparent and flexible substrates such as Mylar. In this work we present data concerning the production of pin a-Si:H devices by hot-wire plasma assisted (HWPA)-CVD technique and used for optical position sensor applications. The objective of this work is to apply such devices to continuous angular velocity measurements of a micro motor. The set of data achieved show the possibility to produce on mylar 80 mm long position sensitive detector with a spatial resolution better than 20 μm and a linearity of ±2%.

Keywords: PA HW-CVD technique, optical position sensors

*T. 351 21 2948564, Fax. 351 21 2957810, e-mail:imf@fct.unl.pt

High Temperature Magnetic Position Sensor Based on a Giant Magnetoresistive Alloy

S. Arana, E. Castaño and F. J. Gracia

Centro de Estudios e Investigaciones Técnicas de Gipuzkoa (CEIT)
Pº de Manuel Lardizábal, 15. P.O. Box: 1555. C.P.: 20.018 SPAIN
Phone: +34 943 212 800 Fax: +34 943 213 076
E-mail: sarana@ceit.es http://www.ceit.es

Summary: *A new circular position sensor based on giant magnetoresistances has been developed. The sensing film is an Ag-Co nanogranular thin film patterned in a circular Wheatstone bridge configuration. This alloy shows a high magnetoresistance of 8% at room temperature within the field generated by a Nd-Fe-B permanent magnet that it provides a sensitivity of 440 μV/V/(º). The operation temperature range of this device is –40ºC~+120ºC although the magnetic film withstands higher temperatures up to 200ºC. These parameters and the contact-less way of sensing make this device suitable for automotive applications. In addition, the sensor is insensitive to contamination, and devoid of friction and electrical contact noise therefore the sensor have a long lifetime.*

Keywords: *magnetoresistance, position sensor, high temperature, magnetic device*
Category: *3 (Magnetic physical devices)*

1 Introduction

The giant magnetoresistive phenomenon was discovered in 1988 [1].The magnetoresistive effect is widely used in various technical areas but in automotive and industrial environments, magnetic sensors are often preferred because of their robustness, insensitivity to dirt and their contact-less way of sensing.
The purpose of this work is to present a magnetic circular position sensor based on a GMR nanogranular Ag_x-Co_{1-x} [2],[3] alloy to build up low-cost and contact-less devices capable to work in harsh environments.

2 Sensor structure and working principle

The working principle of the magnetic position sensor is depicted in Figure 1. A neodymium-iron-boron permanent magnet is attached to an axis whose rotary position determines the output signal. The magnetoresistive sensing film is an Ag_x-Co_{1-x} nanogranular alloy.

Figure 2 displays two of the possible working positions: (a) is the position of maximum output, when two opposite magnetoresistances (R_1 and R_3,or R_2 and R_4) are under the influence of the permanent magnet. In position (b), the bridge output signal is zero, all magnetoresistances are affected equally. The maximum peak to peak voltage can be written as follows:

$$\frac{V_{pp}}{V_i} = \frac{V_{o_{max}} - V_{o_{min}}}{V_i} = \frac{2 \cdot MR(\%)}{200 - MR(\%)}$$

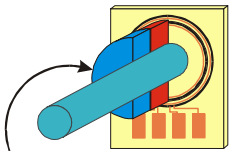

Fig 1. Working principle of the magnetic position sensor

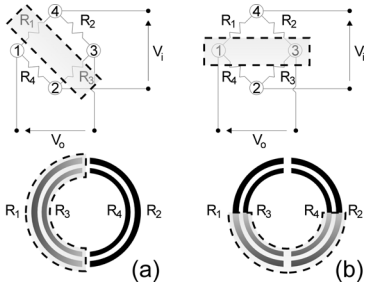

Fig 2. Permanent magnet movement over the Wheatstone Bridge configuration.

2 Fabrication process

The sensor fabrication process may be separated in three major stages. Initially, a 150 nm thick Ag-Co (70%-30% wt.) sensing film is deposited by DC-cosputtering onto Al_2O_3 polished substrates
Next, metallic contacts are defined on sensor surface providing electrical connections. Contacts are deposited by a combination of DC-sputtered Ag layer and RF-sputtered Cr layer. A 300 nm Ag film is thick enough to allow tin or ultrasonic soldering.
Finally, in order to avoid the surface oxidation, a silicon dioxide passivation film is deposited by RF-sputtering over the entire wafer. Contact windows are patterned by chemical etching. When all layers are defined, the sensor is annealed at 300 ºC during 45 minutes.

3 Results and discussion

This GMR material shows a typical magnetoresistance curve for these magnetic alloys. It can withstand very large magnetic fields without changes of its properties, this has been checked up to 1.7 T.

Figure 3 displays the variation in the MR of the nanogranular alloy with magnetic applied field for several thermal treatments. As it can be observed the GMR ratio at room temperature is ~15% under a 1.7 T magnetic field for the 300ºC annealing and ~5% with 0.35 T.

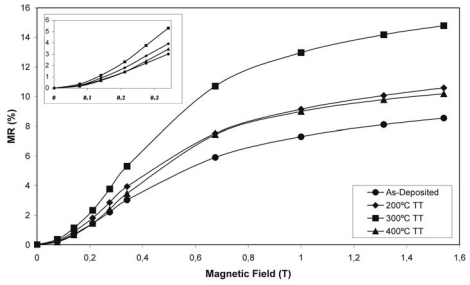

Fig. 3. The magnetic field dependence of the magnetoresistance for several annealing temperatures.

In the final sensor assembly a half-cylinder shape neodymium-iron-boron permanent magnet has been used, and under its influence, the sensor shows a magnetoresistance of 8% at room temperature.

The temperature coefficient of magnetoresistance (TCMR) can be calculated as follows:

$$TCMR = \frac{1}{MR_O}\frac{\Delta MR}{\Delta T} = \frac{\frac{MR_T - MR_O}{MR_O}}{T - T_O} \times 10^6 = 3200\ ppm/^{\circ}C$$

The temperature coefficient of resistance is 850 ppm constant in the operation range. In order to evaluate the thermal stability, long-duration tests have been performed. The sensors have been stored at a temperature of 120 ºC for 100 h. In the Figure 4 two different thermal stability curves can be seen. Firstly, (a) curve shows the thermal behaviour of the sensing film, on the other, (b) curve represents the same test adding a 1.5 µm SiO_2 passivation layer. The passivated curve shows a much lower drift.

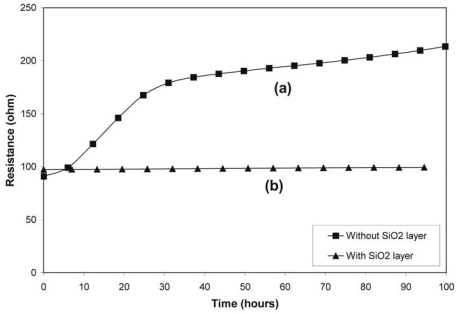

Fig. 4. Two different thermal stability curves adding SiO_2 passivation layer.

The output signal as a function of the magnetic field with a permanent Nd-Fe-B attached to the rotary axis is shown in Figure 5 for an input voltage of 5 V. The period of 360º and a peak to peak voltage of ≈450 mV can be seen clearly. The magnetic bridge sensibility can be written as function of the magnetoresistance value[4]:

$$S_b = \frac{\left|\frac{\Delta V_o(\theta)}{V_i}\right|}{|\Delta\theta|} = \frac{1}{180}\times\left(\frac{V_{o_{max}}(90^o)}{V_i} - \frac{V_{o_{min}}(270^o)}{V_i}\right)$$

$$S_b = \frac{1}{90}\times\frac{MR(\%)}{200 - MR(\%)}\times 10^6 \qquad \left[\frac{\mu V}{V\times(^o)}\right]$$

Introducing MR=8% in this equation, the sensitivity measured is 440 µV/V/(º), at 300ºK.

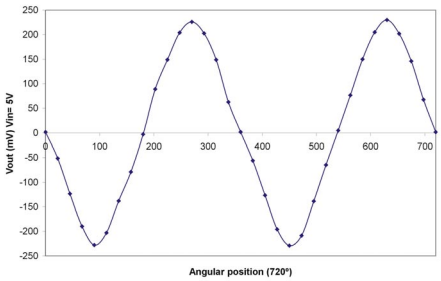

Fig. 5. Output Voltage of a GMR Wheatstone Bridge at room temperature. The input voltage was 5 V.

4 Conclusions

A new GMR sensor has been presented for contactless circular position detection and a simple fabrication process has been developed that it allows low-cost systems designs.

The magnetoresistive sensing element has been a nanogranular Ag-Co alloy which exhibits a negative magnetoresistance change by a magnitude about ~8% under a Nd-Fe-B permanent magnet influence.

The Wheatstone bridge configuration provides a triangular shape signal which peak to peak voltage is more than 400 mV (V_{IN}=5V) at room temperature. The sensitivity displayed by the device is 440 µV/V/(º).

References

[1] M. N. Baibich, J.M. Broto, A. Fert, F. Nguyen Van Dau, F. Petro., P. Etienne, G. Creuzet, A. Friedrich and J. Chazelas, Phys. Rev. Lett. 61, (1988), 2472.

[2] A. Barnard, A. Waknis, M. Tan, E. Haftek, M.R. Parker, and M.L. Watson, "Giant Magnetoresistance Observed in Single Layer Co-Ag Alloy Films," J. Mag. Mag. Mat.114, L230 (1992).

[3] John Q. Xiao, J. Samuel Jiang, and C.L. Chien, "Giant Magnetoresistance in Granular Co-Ag Systems," Phys. Rev. B46, 9266 (1992).

[4] O.J. González, E. Castaño, J. C. Castellano, F. J. Gracia.“ Magnetic Position Sensor Based on Nanocrystalline Colossal Magnetoresistances”. Proc. of Eurosensors XIV. Copenhagen, Denmark.

Capacitive Magnetic Sensor

D. Ciudad[1], C. Aroca[1], M.C. Sánchez[2], E. Lopez[2], P. Sánchez[1]

[1] Inst. Sist. Optoelect. y Microtec.(ISOM), ETSI Telecomunicación UPM, Ciudad Universidad s/n, 28040 Madrid, Spain
[2] Departamento de Física de Materiales, Facultad de Física, UCM, 28040 Madrid, Spain.
email: dciudad@fis.upm.es

Summary: *A new magnetic sensor of a great sensitivity and simplicity is presented. This device is based on a variable capacitor whose plates are formed by a magnetic material in such a disposition that one of them constitues a cantilever. When a repulsive force arises due to induced magnetic poles of the same sign in each two components of the capacitor, the cantilever moves. This sensor is improved by adding a third non magnetic plate permitting the assembly of a Wheatstone bridge.*

Keywords: *magnetic, sensor, cantilever, capacitive*
Category: *3 (Magnetic Physical Devices)*

1 Introduction

As it is well known, magnetic poles are induced in a finite size body when a magnetic field is applied. If two magnetic sheets of the same dimensions are set together, when these poles appear they will produce a repulsive force between them. One of the two plates will be fixed and the other will be placed in such a way that it forms a cantilever whose position could be modified by the magnetic field, as shown in fig1.

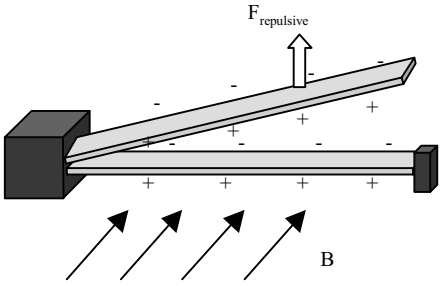

Fig 1. Cantilever and Repulsive Force.

This device constitutes a variable capacitor allowing the measurement of the magnetic field by measuring its capacity. Nevertheless, the accuracy can be duplicated by the use of a Wheatstone's bridge. The second capacitor is obtained by placing a non magnetic plate over the others, leaving space enough to allow the cantilever movement (Fig2-3).

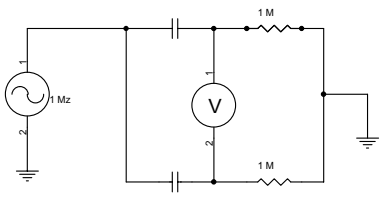

Fig 2. Wheatstone Bridge Circuit.

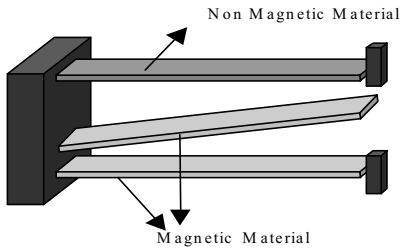

Fig 3. Sensor Description

2 Theoretical Approach

2.1 Output Voltage versus Applied Field

The force between the magnetic poles is:

$$(1) \qquad F = \frac{p^2}{d} \propto \frac{M^2}{d}$$

where p is the dipolar magnetic moment, d is the distance between the two plates and M is the magnetizaton vector.
Assuming that the cantilever is long in comparison to its cross section and that its deformation is small, the maximal deflection z (at its end side) will be:

$$(2) \qquad z \propto \frac{L^3 F}{I}$$

being L the sensor's longitude and I the inertical moment.
In the material surface, if N_d is the demagnetization factor:

(3) $$M = \frac{H}{N_d}$$

The last three formulae leads us to:

(4) $$z \propto H$$

Supposing that our capacitor is equivalent to a parallel plate one of the same dimensions (surface S) and with a plates separation (d) proportional to the deflection (z) of the real capacitor, the following expression is obtained:

(5) $$c = \varepsilon_0 \frac{S}{d} = \frac{Q}{V} \Rightarrow V \propto H$$

2.2 Appropiate Sensor Shape

If the magnetization is bellow its saturation value, and all the variables have been fixed, it is easy to prove that the narrower the capacitor is the less sensitive the sensor is. This is due to the fact that the demagnetization factor increases as the width decreases. Thus, there will be less magnetic poles and the repulsive force between the plates will decrease. However, if the magnetization is that of saturation, the deflection will be reduced as the width increases. The optimal value is obtained when the magnetization is just saturating.

The longitude entails a more difficult issue. At first, the sensitivity grows up with the longitude, but, if the cantilever is too long, it will be difficultly moved because of the gravitational force. In such a case, the device can be modeled by two capacitors in parallel (see Fig.4): the optimal one (Lo) which can be approximated as it has been shown in the previous section and another (L') that only introduces a parasite capacitance. The sensitivity begins to decrease when the longitude increase over a critical value Lo.

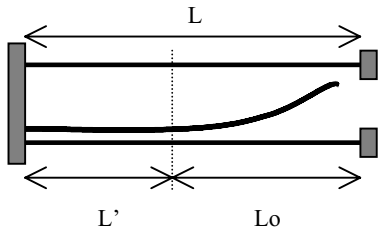

Fig.4 Sensor Section

The gravitational problem can be assumed negligible by setting the surface of the fixed plates parallel to the gravitational aceleration.

3 Experimental Results

To fabricate the sensor, we have used an amorphous material as the magnetic one because it can be easily magnetized. Copper has been used as non magnetic material.

There is a good agreement between the experimental results and the theoretical model (5) and the sensor has a very good linear response. (See Fig.5).

This sensor is highly sensitive to electrostatic fields. To avoid this problem, it must have an appropiate screening.

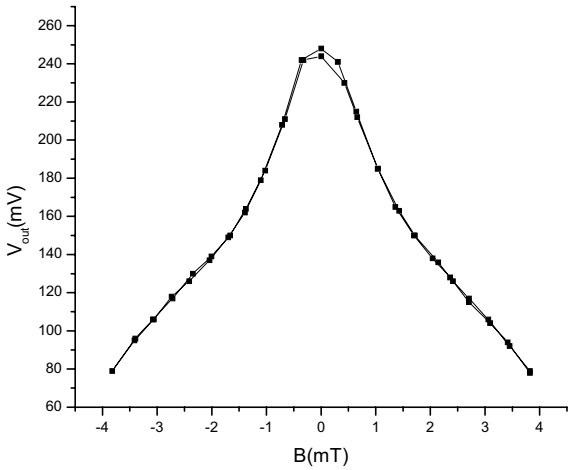

Fig 5. Sensor L = 2.22 cm.

References

[1] Osborn, J.A. Demagnetizing Factors of the General Ellipsoid. *Phys. Rev.* **67** (11-12) (1945) 351-357

[2] Dror Sarid. Scanning Force Microscopy. Oxford University Press, 1941.

MEMS-Based Fluxgate Microsensor for Digital Compass Systems

K. W. Na, H. S. Park, D. S. Shim, J. S. Hwang, and S. O. Choi

MEMS Laboratory, Samsung Advanced Institute of Technology (SAIT), Suwon, 440-600, Korea
email: kyoungwon.na@samsung.com

Summary: *A fluxgate microsensor for digital compass systems was developed. To achieve a high sensitivity, a rectangular-ring shaped soft-magnetic core and an intimate structure of excitation and pick-up coils were designed. These structures effectively prevented magnetic leakage from the core. The fabrication technologies included electroplating for the core and the coils and sputter deposition for seed layer. Photoresists were used for creating micromolds for electroplating both the core and the coils. BCB resist is adapted for the isolation layer between the core and the coils. Completed sensor easily detected a very weak magnetic field such as the earth's magnetic field. The out sensitivity for 2.8 V p–p driving voltage and 3.2MHz driving frequency was 380V/T.*

Keywords: *digital compass, flux gate sensor, MEMS, microsensor.*
Category: *3 (Magnetic physical devices)*

1 Introduction

In recent years, there have been increasing demands for a digital compass to provide the information of portable navigation systems. In the measurements of a weak magnetic field (10^{-10} to 10^{-3}T), the fluxgate sensor has been widely used because of its high sensitivity [1-2]. Fluxgate sensor serves up to 1mT with a resolution of 0.1nT to 10nT. However the conventional fluxgate sensor utilizes bulk or ribbon magnetic core, bobbins for the excitation and the pick-up coils, and electronic circuits for the core excitation and signal processing. These result in the disadvantages of large volume, large weight, and high cost. Moreover the classical approaches have had difficulties in fabricating the sensor with a precise and more complex structures. The fluxgate sensor with flat coils and open core consisting of strips made of etched amorphous tape was described in [3] and [4]. A fluxgate magnetic microsensor using micromachined planar solenoid coils was made by MEMS technique[5]. Fluxgate microsensor with symmetrical core on both sides of the planar rectangular excitation and pick-up coils was described in [6]. However these structures did not allow real miniaturization of the sensor.

In this paper, miniaturization was accomplished by microelectromechanical systems (MEMS) techniques. A new structure was designed to maintain the parameter of the fluxgate microsensor. Micromachining technology also leads to flexibility of fabrication of a microsensor with complex structure.

2 Design

The new sensor described here is based on the concept of a closed rectangular-ring core and micromachined solenoid coils on a silicon wafer. The micromachined sensor structure is shown in Fig. 1. The excitation and pick-up coils were fabricated to be very closely located beside each other. The coils, as shown in Fig. 1, are alternately wound surrounding the rectangular closed core. This intimate structure of the coils effectively reduced the leakage of magnetic flux between the closed core and the coils and enhanced the sensitivity of the fluxgate microsensor.

Each coil has 42 turns made of 6μm-thick copper layer. The coil pitch is 14μm (10μm conductor width / 4μm space). DC resistance of the excitation and the pick-up coils were 47Ω and 45Ω, respectively. Magnetic core was designed into the geometry of a closed rectangular-ring. This effectively decreased the leakage of the magnetic flux of the core due to the generation of the closed-loop magnetic path. As a magnetic material, a 2-μm-thick permalloy (NiFe 81/19) with a DC effective permeability μ_{eff} of about 1100 and a coercive field of 0.1Oe was formed by electroplating. The electroplated permalloy core is 2360μm long and 560μm wide.

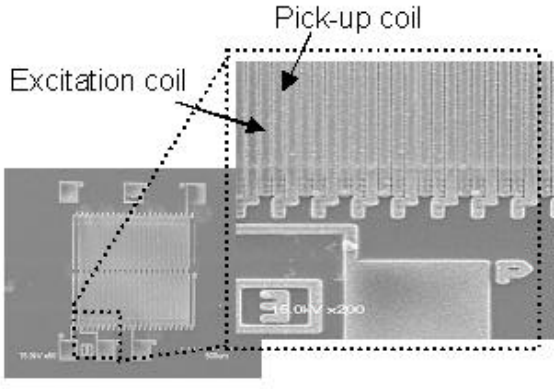

Fig. 1. Structure of macro-machined fluxgate sensor.

3 Sensor Evaluation

For investigating the frequency response of the sensor itself, a weak magnetic field was applied to the sensor as a function of the frequency. The induced second harmonic voltage as a function of frequency is shown in Fig. 2. The maximum sensitivity for square wave excitation is 380V/T for 3.2MHz frequency. The sensor excitation voltage was 2.8V p–p and the external magnetic field was 1Gauss. Figure 3 shows the linear characteristic of the fluxgate microsensor measured for weak fields of – 4Gauss to +4Gauss. The sensor excitation frequency was 1.7MHz at $2.8V_{P-P}$ excitation square wave. We can observe that the output voltage shows a good linear characteristic with the externally induced weak magnetic fields.

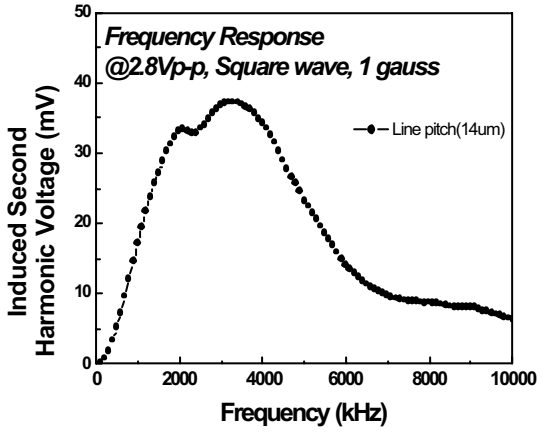

Fig. 2. Frequency response of the fluxgate sensor for 2.8V p–p voltage and 1Gauss external magnetic field.

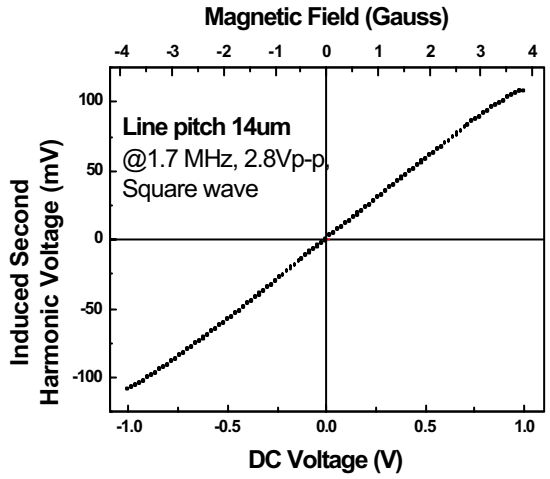

Fig. 3. Sensor linear characteristic for weak magnetic fileds (-4Gauss to +4Gauss).

The output voltages as a function of magnetic field is very linear over the range of –100μT to +100μT. From this excellent linear response, about 280V/T sensitivity was obtained for 1Gauss externally induced magnetic filed. In this sensor structure, the magnetic core with a rectangular-ring shape provides a closed loop flux path with reduced magnetic leakage. The intimate structure of the excitation and pick-up coils causes a deep magnetic coupling with the magnetic core.

4 Conclusions

Using the rectangular-ring shaped magnetic core and the intimate structure of the excitation and pick-up coils improves the properties of the fluxgate microsensor. The new designed fluxgate microsensor has an almost closed magnetic path with respect to the excitation field. The excitation and pick-up coils have a narrow pitch of 14um respectively. This narrow pitch of the coils also provides a deep magnetic coupling between the magnetic core and the coils.

Although the sensor has a miniature size, excellent linear response over the range of -100μT to +100μT was obtained with 280V/T sensitivity at excitation square wave of $2.8V_{P-P}$ and 1.7MHz.

References

[1] F. Primdahl, *J. Phys. E: Sci.* Instrum., 12, 241 (1979).

[2] J. Lenz, Proc. *IEEE* 78(6*), 973,* (1990).

[3] P. Kejik, et al., A new compact 2D planar fluxgate sensor with amorphous metal core, *Sens. Actuators* A 81 (2000) 200–203.

[4] L. Chiesi, P. Kejik, B. Janossy, R.S. Popovic, CMOS planar 2D micro-fluxgate sensor, in: *Sens. Actuators*, 82 (2000) 174–180.

[5] T.M. Liakopoulos and C.H. Ahn, A micro-fluxgate magnetic sensor using micromachined planar solenoid coils. Sens. Actuators A 77 (1999), pp. 66–72.

[6] P. Ripka, S. Kawahito, S. O. Choi, A. Tipeka and M. Ishidad, Micro-fluxgate sensor with closed core, Sensors and Actuators A: Physical Volume 91, Issues 1-2, 5 June 2001, Pages 65-69

A Novel Fabrication Technique using UV-Lithography for Polymer Magnets in Micro Actuators and Generators

M. Feldmann, S. Büttgenbach

Institute for Microtechnology, Technical University of Braunschweig,
Alte Sahlzdahlumerstr. 203, 38124 Braunschweig, Germany
email: m.feldmann@tu-bs.de http://www.tu-bs.de/institut/imt/

Summary: *We report on the fabrication of polymer magnets realized by processing magnetic polymer composites based on the photo resist Epon SU-8 used as a matrix and their integration into a micro actuator or generator. The processing of Epon SU-8 enriched with different hard magnetic powders is shown. Furthermore a fabrication batch process including UV depth lithography employing Epon SU-8 photo resist, electroplating of copper and polishing for the manufacturing of a micro actuator/generator is demonstrated. The result is an electro magnetic device consisting of a permanent magnet as a core in a helical coil in a monolithical build-up.*

Keywords: *magnetic actuation, polymer magnet, SU-8, UV depth lithography, micro coils*
Category: *3 (Magnetic physical device)*

1 Introduction

Magnetic micro actuators have received considerable attention in research with particular interest on fully integrated devices [1-3]. Most actuators developed so far are based on the reluctance principle using soft magnetic materials [4]. In comparison to this hard magnetic materials have the potential for larger forces and deflection. Other developments in the field of magnetic actuators describe devices, which use hybridly assembled permanent magnets [5]. Also commercially available or electroplated permanent magnets are used because of the difficulty in depositing structures with a thickness up to a millimeter [6]. Alternatively polymer magnets, in which small particles of hard magnetic material are suspended in a polymer matrix or binder are developed [7]. This comprises the problem, that in order to obtain a micro fabrication batch process the magnets have to be structured. A possibility to achieve this is screen printing or spin casting [3]. In contrast to this this paper shows the production of permanent magnets using Epon SU-8 photo resist and UV-depth lithography with arbitrary design to their structure. This process is compatible to most standard micro fabrication processes. Furthermore a prototype of a magnetic micro actuator/generator based on this process is presented.

2 Composite fabrication

In terms of a large residual induction B_r and coercive force H_c rare earth alloys such as samarium-cobalt or neodymium-iron-boron have the best magnetic properties. These rare earth magnets usually are sintered at high temperature and pressure to receive these properties.

We use these alloys as powder mixing it with negative tone Epon SU-8 photo resist at different concentration levels. The enriched resist is processed including spin coating, heating, exposure and development. The result is shown in Fig. 1.

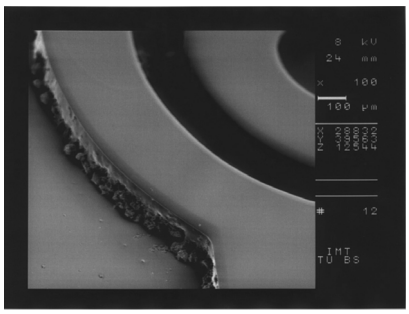

Fig. 1. SEM photograph of the structured Epon SU-8 enriched with samarium-cobalt

Depending on the particle size used the resolution and roughness of the structures are limited. Due to the available sizes of samarium-cobalt (6 µm) and neodymium-iron-boron (9 µm) the smallest structures, which could be developed had a width of 20 µm. Consequently, for better results the particle size has to be reduced. However, the used powders are susceptible to oxidation and corrosion and lose their magnetic properties. Because of this the reduction of the particle size is difficult and other materials might have to be considered.

Decisive for a high residual induction B_r is the height of the fabricated structures and the concentration levels of the resist. These influences are subject of further investigation. Also ceramic ferrites [2] (strontium ferrites with a particle size of 1,5 µm) and some soft magnetic materials such as nickel iron or magnetite will be tested.

3 Magnetic micro actuator/generator

The basic build-up of the micro actuator/generator consists of a movable permanent magnet in a three dimensional helical coil as shown in Fig. 2. The permanent magnet is held by leaf springs at one end, which are used as a suspension.

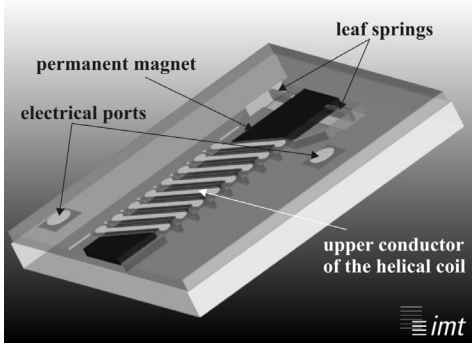

Fig. 2. Schematic of the magnetic micro actuator/generator

Using the device as a generator the leaf springs have also the requirement to allow vibrations of the permanent magnet and serve for the restoring force. The fabrication process of the device includes the electroplating of copper for the lower conductors and via interconnects to the upper conductors (see Fig. 3a) realized by sputter deposition and structuring of a gold-layer. The permanent magnet is wrapped by a sacrificial layer made of copper [8]. The SU-8 is used for producing the high aspect ratio micro molds, the dielectric intermediate layer, the upper conductor bridges, the mechanical structures such as the leaf springs (see Fig. 3b) and for composites containing the magnetic material (see Fig. 3c).

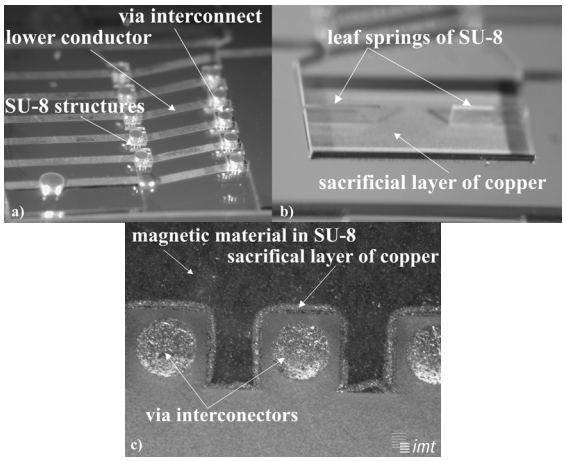

Fig. 3. a) Lower conductors and via interconnects
b) Leaf springs on a sacrificial layer
c) Sacrificial layer, magnetic material and via interconnects after polishing

To achieve satisfactory planarisation after the electroplating of copper and the structuring of the magnetic material a polishing step is needed (see Fig. 3c). After magnetization of the permanent magnet and etching of the sacrificial layer the magnet rod and the leaf springs are movable. The structure height of the micro actuator is 200 µm as shown in Fig. 4.

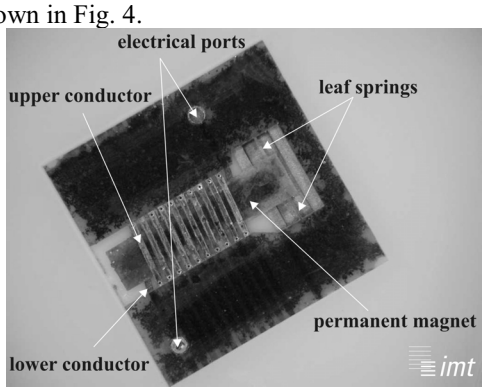

Fig. 4. Micrograph of the actuator/generator

4 Conclusion

We have presented a novel fabrication process for permanent magnets using Epon SU-8 and UV-depth technology as well as its application for producing a micro actuator/generator with a monolithical build-up. The demonstrated technology allows the development of promising magnetic actuators. Magnetic polymer composites are not able to reach the quality of sintered magnets but are a good compromise to combine good magnetic properties with the high aspect ratio and planarisation capabilities of the Epon SU-8 photo resist.

References

[1] W.P. Taylor, O. Brand and M.G. Allen, *IEEE j. Microelectromechanical systems*, vol 7, no 2 (1998), 181-191.

[2] L.K. Lagorce, O. Brand and M.G. Allen, *IEEE j. Microelectromechanical systems*, vol 8, no 1, (1999) 2–9.

[3] L.K. Lagorce, and M.G. Allen, *IEEE j. Microelectromechanical systems Workshop*, San Diego (1996), 85-90.

[4] V. Seidemann, S. Büttgenbach, *Proc. of SPIE - MEMS Design, Fabrication, Characterization, and Packaging*, Vol. 4407, Edinburgh, UK (2001), 304-309.

[5] B. Wagner and W. Benecke, *Proceeding of the 1991 IEEE MEMS conference*, Nara, Japan (1991), 27-32.

[6] H.J. Cho and C.H. Ahn, *Microelectromechanical systems*, vol 11, no 1, (2002) 78–84.

[7] E. Kallenbach, V. Zöppig, H. Kube, F. Beyer, R. Hermann, B. Pawlowski, J. Töpfer, H. Töpfer, *Actuator 2002*, Bremen, Germany, 611-614.

[8] V. Seidemann, M. Feldmann, J. Rabe, S. Büttgenbach, *4th International Workshop on High-Aspect-Ratio Micro-Structure Technology, HARMST '01* (2001), 83f.

Planar Hall Effect Magnetic Sensor for Micro-Particle Detection

L. Ejsing, M. F. Hansen and A. K. Menon

Mikroelektronik Centret (MIC), Technical University of Denmark (DTU), Building 345 East, 2800 Kgs. Lyngby, Denmark
e-mail: loe@mic.dtu.dk http://www.mic.dtu.dk

Summary: *Magnetic sensors based on the anisotropic magnetoresistance (AMR) of Ni have been fabricated and characterized in the planar Hall geometry. The response to an applied magnetic field has been measured without and with a coating of commercially available 2.8 μm magnetic beads for bioseparation (Dynabeads M-280, Dynal, Norway). It is demonstrated that the technique is capable of detecting just a few magnetic beads, i.e., that the technique is feasible for magnetic biosensors.*

Keywords: *anisotropic magnetoresistance, particle detection*
Category: *3 (Magnetic physical devices)*

1 Introduction

Planar Hall effect sensors have been used to detect nanotesla magnetic fields [1,2]. Also, the exchange anisotropy behavior can be characterized using thin films' planar Hall effect [3]. We demonstrate that a planar Hall effect sensor can be used to detect magnetic beads for bioapplications.

The anisotropic magnetoresistance (AMR) effect is present in ferromagnetic materials. It results in a dependency of the resistivity on the orientation of the material's magnetization. The electrical output signal in the planar Hall geometry (Fig. 1) is [4]:

$$V_y = \frac{(\rho_{\parallel} - \rho_{\perp})I_x}{2t}\sin(2\phi)$$

where t is the thickness of the metal layer, I_x is the applied current, and ϕ is the angle between the current and the in-plane magnetization vector. $\rho_{\parallel}$ and $\rho_{\perp}$ are the resistivities when the magnetization is parallel and perpendicular to the current, respectively. For Ni the resistivity variation is approximately 2%.

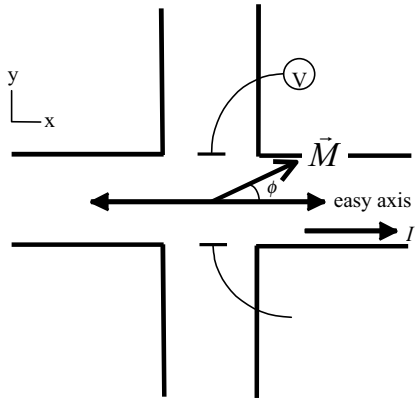

Fig. 1. Planar Hall sensor geometry: The magnetic field to be detected is parallel to the detection plane in the *y*-direction. In this plane, the current is applied in the *x*-direction and a voltage is measured in the *y*-direction.

A schematic drawing of the planar Hall sensor is presented in Fig. 1. Initially the magnetization vector lies along the easy axis and the current direction, in which I_x = 250 μA. A magnetic field applied in the *y*-direction induces a rotation of the magnetization by an angle ϕ. This changes the electrical output signal by the amount V_y.

The planar Hall geometry is ideal for measuring magnetized particles because these have a significant in-plane field component when magnetized parallel to the sensor plane.

1.1 Particle signal

The low-field magnetic volume susceptibility of the M-280 Dynabeads is χ = 0.13 [SI] [5]. From this the low-field magnetic moment of a Dynabead of 2.8 μm in diameter can be estimated as $m = \chi HV$, where H is the applied field intensity, and $V=\pi(2.8\mu m)^3/6$ is the volume of the Dynabead.

The bead is placed on top of the sensor (Fig. 1) with its magnetic moment aligned in the *y*-direction. Assuming dipole behavior, the magnitude of the magnetic flux density is $B_{dip} \approx \mu_0 m/(4\pi r^3)$, where r is the distance from the dipole to the observation point (the sensor surface), and μ_0 is the vacuum permeability. For a bead placed on the sensor surface $r \approx 1.4$ μm.

Calibration of the sensor in homogeneous applied fields up to 0.6 mT yields a linear field response and the sensitivity S = 7.0 μV/mT. At 0.6 mT the dipole field at the sensor from one bead is $B_{dip} \approx$ 0.026 mT and the expected signal change is $V_{dip} \approx$ 0.18 μV. Thus to produce 1 μV change in the signal ~6 Dynabeads are needed. As the dipole field has the opposite direction of the applied external field, the presence of the beads will lead to a reduction of the magnetic field felt by the sensor.

2 Experiments and results

The sensors are fabricated using conventional lithography. Crosses are patterned on a resist coated silicon wafer, and 20 nm of Ni is deposited in an e-beam evaporation system. During deposition a uniform field of 8 mT is applied in order to ensure formation of an easy magnetic axis (Fig. 1). A 2 nm gold layer is deposited on top in order to protect the nickel from corrosion. Finally, the resist is lifted off with the excess of metal to yield the AMR sensors. Bonding pads are made of gold using the same procedure.

Initially, the magnetization is set along one of the easy axes. When the magnetization is rotated away from the easy axis by a field applied in the *y*-direction, the change in magnetization produces an electrical output signal.

The output signal is measured as a function of applied field, $\mu_0 H_{ext}$, between 0 and 0.6 mT, first for the sensor without magnetic beads, then for the sensor with magnetic particles placed on top of the sensor (Fig. 2). The response change is due to the presence of beads.

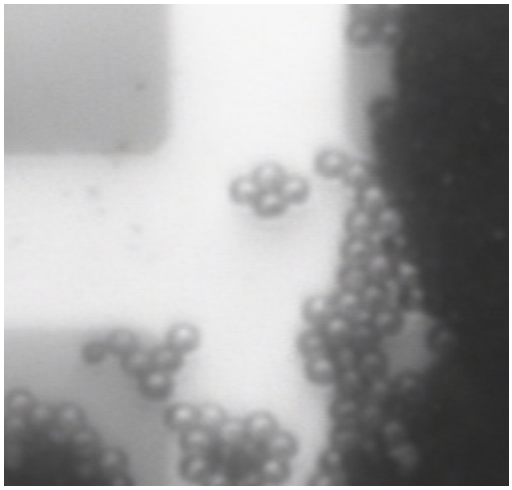

Fig. 2: Sensor area (20μm × 20μm) with 2.8 μm Dynabeads on top. The dark region to the right is a large cluster of beads positioned away from the sensing region.

The sensor area with clusters of beads on top is shown in Fig. 2. The results of the output voltage as a function of applied magnetic field for the sensor with and without particles on top of the sensitive area are shown in Fig. 3. The distinction between the two types of response is clear, which indicates the potential for biosensor applications for this type of sensor.

When the particles are magnetized, the dipole moments align with the applied field. The magnetic field from a dipole has a direction opposite to that of the dipole moment. Hence, the effective magnetic field at the sensor, H_{eff}, and the output signal will be reduced according to:

$$V_y = \mu_0 H_{eff} S \sim \mu_0 H_{ext} S\left(1 - N\chi V / 4\pi r^3\right)$$

where N is the number of beads positioned on the sensor. An estimate of N from the slopes found in Fig. 3 according to this simple analysis leads to N ~ 12. It should be noted that the dipole field at the sensor is most sensitive to beads situated on the sensor, but also that clusters of beads in the vicinity of the sensor can contribute.

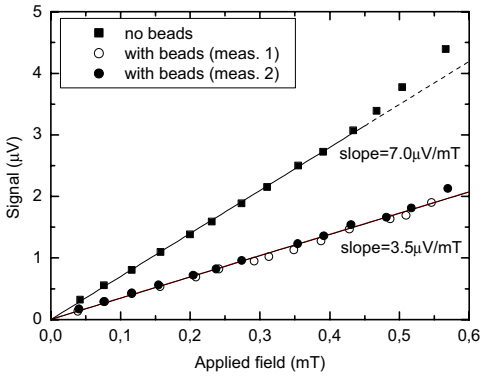

Fig. 3. Offset corrected sensor output signal as a function of applied magnetic field with and without beads. The measurements with beads are conducted twice to ensure repeatability.

Conclusion

It has been demonstrated that the planar Hall effect can be used for detecting commercial micrometer-sized magnetic beads used for bioapplications. Thus, this effect is a potential principle to construct magnetic biosensors, *e.g.*, for DNA detection. An advantage of the planar Hall effect sensor compared to giant magnetoresistive (GMR) sensors is the simple fabrication scheme, which reduces the fabrication cost.

Future work includes optimization and implementation with micro-fluidic systems. The sensor will furthermore be demonstrated as a biosensor where DNA fragments bind the beads to the surface.

References

[1] F. Montaigne, A. Schuhl, F. N. Van Dau, A. Encinas, *Sensors and Actuators* 81 (2000) 324-327.

[2] F. N. Van Dau, A. Schuhl, J. R. Childress, M. Sussiau, *Sensors and Actuators A* 53 (1996) 256-260.

[3] Z. Q. Lu, G. Pan, W. Y. Lai, *J. Appl. Phys.* 90 (2001) 1414-1418.

[4] R. C. O'Handley. Modern Magnetic Materials, *John Wiley & Sons, Inc.* (2000).

[5] http://www.dynal.no

Flow velocity measurement in microchannels using spin valve sensors and superparamagnetic particles

H. A. Ferreira[1,2], D. L. Graham[1], P. Parracho[1,2], V. Soares[1] and P. P. Freitas[1,2]

[1]INESC – Microsystems and Nanotechnologies, Rua Alves Redol 9, Lisbon, Portugal
email: hferreira@inesc-mn.pt http://www.inesc-mn.pt
[2]Instituto Superior Técnico, Physics Department, Avenida Rovisco Pais, Lisbon, Portugal

Summary: *On-chip spin valve sensors were used to measure the flow velocity within fabricated poly(dimethylsiloxane) (PDMS) microchannels. Superparamagnetic particles with dimensions of 250 nm in diameter were introduced into a 100 μm wide microchannel, bonded to the chip surface. The flow velocity was determined by measuring the changes in resistance of a pair of spin-valve sensors, 1.65 mm apart from each other, caused by the passage of ensembles of superparamagnetic particles. Flow velocities ranging from 50 to 300 μm s^{-1} were estimated, depending on the pressure used to drive the flow. The application of this system may provide a means to measure and control flow velocities on microfluidic devices.*

Keywords: *microfluidics, spin valve sensors, superparamagnetic particles, flow velocity*
Category: *3 (Magnetic physical devices)*

1 Introduction

Spin valves sensors are traditionally used in read-heads of hard-disk drives and find several other applications, either in current monitoring devices, in positioning systems and in the automotive industry [1], or more recently in biosensors in combination with the use of superparamagnetic particles [2,3]. Herein is presented the application of these magnetic field sensors to the measurement of flow velocity. The simplest method for flow velocity determination in small fluidics structures is based on collected volumes of fluid per unit time, although providing a rough averaged measurement of the velocity. Other means can provide measurements of flow velocity with micron-scale resolution but rely on complex optical systems [4]. The system presented in this paper offers the possibility of a direct electrical measurement of the flow velocity and in addition, due to the simple electronic setup and integration with a personal computer, allows for an easier implementation of a flow control system.

2 Experimental methods

2.1 Spin valve sensors

The spin valve stack was fabricated by an ion beam deposition system on a 3 in. Si wafer and has the structure Ta 20 Å/ NiFe 30 Å/ CoFe 25 Å/ Cu 26 Å/ CoFe 25 Å/ MnIr 60 Å/ Ta 30 Å/TiW(N) 150 Å. As deposited the spin valve coupon sample has a magnetoresistance ratio (MR) of ~7.5 %. The sensors were defined by standard photolithographic techniques and by ion milling. The spin valve sensors have dimensions of 2 μm × 6 μm (the spin valve stripe is 2 μm × 14 μm and the distance between the leads is 6 μm). Aluminum leads, 1μm thick, were used leading to wire-bond pads. After processing, the average MR of the sensor element is (5.5±0.5 %) due to contact and lead resistance. The average sensor sensitivity was found to be ~0.06%/Oe (~0.4 mV/Oe). Both sensors and leads were passivated with a 2000 Å thick sputtered SiO_2 layer for protection against fluids during experimentation.

2.2 Superparamagnetic particles

The superparamagnetic particles used are 250 nm in diameter composed of iron oxide (magnetite) dispersed in a dextran matrix (Nanomag®-D, Micromod). These particles, being super-paramagnetic, only possess a magnetic moment in the presence of an applied magnetic field. The moment per particle was found to be $\sim 2\times10^{-13}$ emu for a 15 Oe magnetizing field and the magnetic susceptibility per particle for an applied field range of $10<|H|<50$ Oe was $\sim 2.9\times10^{-15}$ emu/Oe [3].

2.3 Microchannels

Microchannels with dimensions of 20 μm height, 100 μm width and 2.6 mm length were fabricated in poly(dimethylsiloxane) (Sylgard®-184, Dow Corning) by a molding technique (similar to the one described in [5]). A metal mask comprised of sputtered 1500 Å of Al and 150 Å of TiW(N) was defined in a quartz substrate by photolithography and ion milling. The mask of the microchannel was used in a UV lamp system to expose a ~20 μm thick photoresist (Clariant AZ4562). After development (AZ351B) only the microchannel structure remained. The PDMS elastomer was prepared using a 10:1 base to curing agent ratio mixture. After degassing the mixture in a primary vacuum for 15 min, the preparation was poured over the photoresist structures and was left for 1h at

65ºC for curing. Finally, the microchannels were released from the mold and were bonded to the spin valve sensor chips, by subjecting both the microchannels and the SiO_2 passivated chips surface to O_2 plasma treatment for 30" [5].

2.4 Experimental setup

After the bonding of the microchannels to the sensor chips, each one of these was mounted in a 40-pin chip carrier. The contacts were made by wire bonding and were protected with a silicon gel (Elastosil E41) (Fig.1).

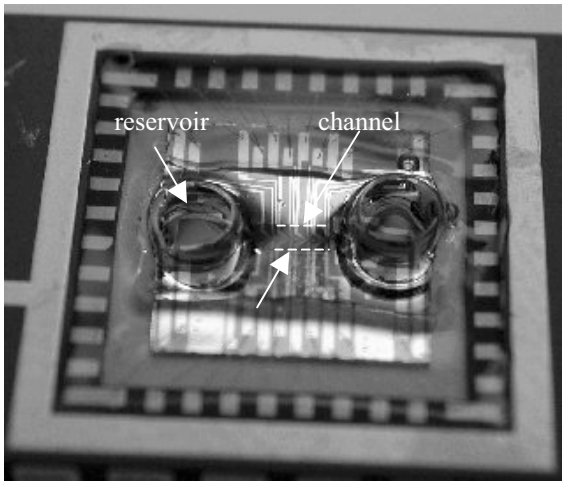

Fig. 1. Spin valve sensor chip with a bonded 1mm wide microchannel mounted in a chip-carrier.

The chip carrier was mounted in a small breadboard housed within an aluminum noise reduction box and co-axial cables were used to make the electrical connections to power sources and general-purpose interface bus (GPIB) controlled multimeters. A small (5 cm diameter) planar electromagnet with a $Ni_{80}Fe_{20}$ circular core was positioned over the chip carrier, in order to apply an in-plane magnetic field (-15 Oe) to induce a moment within the superparamagnetic particles.

The experiments were performed by measuring the voltage drop across two sensors located near the inlet and the outlet of the microchannel (~1.65 mm apart), each sensor with an independent power source (8mA sense currents). The data was acquired by GPIB-controlled multimeters and was fed to a computer. The superparamagnetic particles (in water or pH 7 buffer solution) were introduced through one of the reservoirs (inlet) with a syringe and the fluid movement was achieved by applying pressure with syringes.

3 Results and Discussion

The flow velocity detection was achieved by measuring the time difference between the detection of the passage of ensembles of superparamagnetic particles over each of the magnetic field sensors in use. Control experiments were performed showing that the passage of fluid over the sensors didn't change the sensor response whilst, the passage of the particles over the sensors generated an appreciable signal change due to the magnetic field created by the particles (under a ~15 Oe applied field).

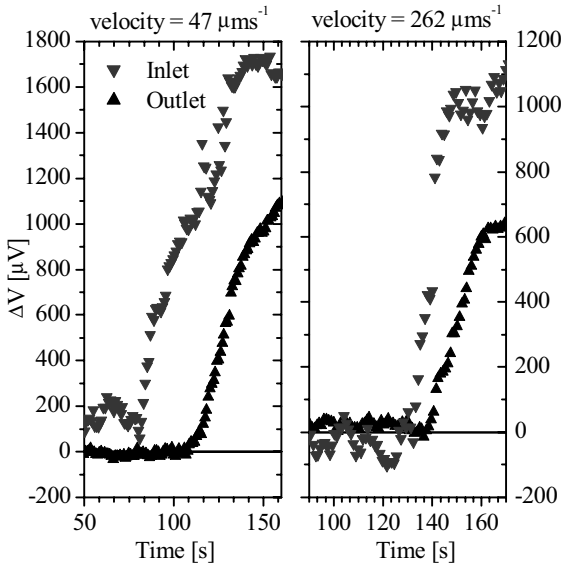

Fig. 2. Flow velocity measurements estimated from the passage of an ensemble of superparamagnetic particles over the spin valve sensors.

Figure 2 shows the detection of the passage of an ensemble of particles over each sensor, one located near the inlet and the other near the outlet of the microchannel. The time difference between the detection signals were taken from the signal rise and velocities of 47 μm s^{-1} and 262 μm s^{-1} were estimated for the flow transporting the particles.

Applications to the study of fluid flow inside microfluic structures as well as the study of fluid properties such as viscosity are envisaged.

References

[1] P.P. Freitas, F. Silva, N.J. Oliveira, L.V. Melo, L. Costa and N. Almeida, Sens. Act. A 81 (2000) 2-8.

[2] D.L. Graham, H.A. Ferreira, P.P. Freitas and J. M.S. Cabral, Biosens. Bioelectron. 18 (2003) 483-488.

[3] H.A. Ferreira, D.L. Graham, P.P. Freitas and J.M.S. Cabral, J. Appl. Phys. (to be published).

[4] C.D. Meinhart, S.T. Wereley and J.G. Santiago, In: Adrian et al., eds. *Laser Techniques Applied to Fluid Mechanics*, pp. 57-70, Springer-Verlag, Berlin (1998).

[5] D.C. Duffy, J.C. Cooper, J.A.O. Scheller and G. M. Whitesides, Anal. Chem. 70 (1998), 4974-4984.

Integrated Metal–Oxide Microsensor Array of Micro-Hotplates with MOS-Transistor Heater

M. Graf, S. Taschini, P. Käser, C. Hagleitner, A. Hierlemann, H. Baltes
ETH Zürich, Physical Electronics Laboratory,
ETH-Hönggerberg HPT-H8, CH-8093 Zürich, Switzerland, mgraf@iqe.phys.ethz.ch

Summary: A monolithic gas sensor system is presented, which, for the first time, includes on a single chip a complete array of metal oxide microhotplates with integrated MOS-transistor heaters (3 in the first realization), as well as advanced analog and digital circuitry for sensor control, signal readout and chip communication. An octogonal-shape microhotplate design with MOS-transistor heaters has been implemented for the three gas sensors. The integrated circuitry consists of a programmable digital temperature regulation, digital sensor readout and a standard serial interface. Distinct SnO_2-based sensing materials with different noble-metal dopings are tested. First chemical measurements with CO and CH_4 have been conducted, the results of which are presented in this paper

Keywords: micro-hotplate array, MOSFET-heater, metal-oxide
Category: Chemical sensors

Introduction

There is a strong interest in microhotplate-based gas sensors due to miniaturization advantages such as low power consumption and the possibility of applying new dynamic sensor operation modes as a consequence of the low thermal mass of such hotplates. Metal oxides are well known to exhibit high sensitivities to environmentally relevant gases such as CO and CH_4. The integration of hotplates, which feature operation temperatures up to 350°C, with CMOS-circuitry is technologically challenging, and first results were presented recently [1]. Most devices are based on resistive heating elements. An alternative approach is the integration of a transistor as heater. Such devices were previously realized in SOI-CMOS [2,3] and also in industrial CMOS technology combined with dedicated post-CMOS-micro-machining [4]. A key advantage of transistor-based heaters is the reduction of the overall power consumption, because no additional transistor is needed on chip for driving the heating current. Moreover, new modes for controlling the temperature are feasible, because the microhotplate temperature is directly adjustable through the gate voltage of the transistor heater, the correlation between temperature and gate voltage being almost linear.

An established drawback of tin dioxide is its lack of selectivity. This situation is usually dealt with by using an array of sensors in combination with multi-component or pattern recognition algorithms. Doping of the tin dioxide also changes the selectivity towards certain gases [5]. Another parameter that can be varied is the operating temperature. An array of microhotplates with individually controlled temperatures, the hotplates of which are covered with different sensitive materials, increases the overall information that can be extracted from metal-oxide-based gas sensing systems. Here, a device is presented, which features three microhotplates monolithically integrated with temperature controllers, readout and interface circuitry. The microhotplates are heated by means of MOS-transistors and are covered with nanocrystalline SnO_2-droplets as sensitive layers. Full advantage is taken of the features offered by applying CMOS-technology. All sensor values can be set and readout via the digital interface, which drastically reduces the packaging efforts since the number of bond wires is the same as for a single microhotplate.

System architecture

The block diagram of Figure 1 depicts the system architecture of the chip, emphasizing its strong modularity. Three digital PID controllers provide independent temperature regulation for each of the hotplates.

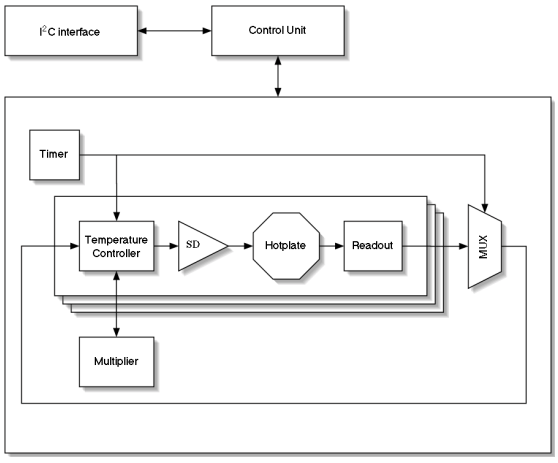

Figure 1*: Block diagram showing the architecture of the sensor chip*

The MOS heating transistor is driven in pulse-density modulation by a first-order ΣΔ-modulator, Analog circuitry is required only for the readout of the metal oxide resistors and the temperature sensors. A single input conversion stage and multiplier are accessed from the three controllers in time-sharing. The PID parameters, the target temperatures, the operation timing can all be programmed by the user via a standard serial interface [6], which also enables digital readout of the sensor values.

Sensor design and fabrication

Figure 2 shows the fabricated chip featuring a tri-sectional floor plan with digital circuitry on the left side, analog circuitry in the center and the three micro-hotplates on the right.

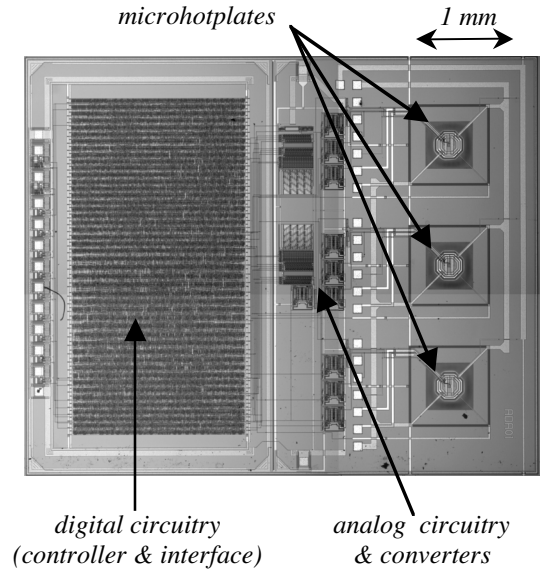

***Figure 2**: Micrograph of the complete chip with microhotplate array and circuitry*

The chip is fabricated in industrial 0.8 µm CMOS technology [7]. In order to establish a good contact to the sensitive layer the electrodes are first covered with Ti/W (diffusion barrier and adhesion layer) and then with a Pt-layer, which is patterned by lift-off. The membranes are released by etching the wafer from the backside with KOH. An electrochemical etch-stop technique is used to preserve the central n-well island, which hosts the heating transistor. The deposition and annealing of the nanocrystalline tin dioxide at 400°C concludes the post-processing sequence, which is fully CMOS-compatible.

Each membrane has a total size of 500 by 500 µm. A ring-transistor configuration is integrated on an octagonal-shape Si-island of the membrane to ensure homogeneous temperature distribution (<2%) over the sensing area and to improve the heating efficiency [4]. A poly-silicon resistor in the membrane center serves a temperature sensor.

Chemical measurements

First chemical measurements have been conducted with the chip. Figure 3 shows the results simultaneously obtained from two microhotplates with different materials at an operation temperature of 300°C in dry air. Membrane A is covered with a Pd-doped SnO_2 layer (0.2wt% Pd), a layer optimized for CO detection, whereas the sensitive layer on membrane C contains 3wt% Pd, which renders this material more selective towards CH_4.

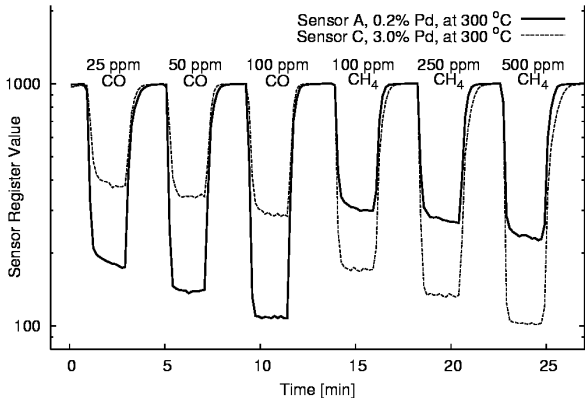

***Figure 3**: Sensor response for two microhotplates with different sensitive layers upon exposure to CO and CH_4.*

References

[1] M. Graf, D. Barrettino, S. Taschini, C. Hagleitner, A. Hierlemann, and H. Baltes, Tech. Digest MEMS 2003, 303

[2] J.A. Covington, F. Udrea, and J.W. Gardner, Proc. IEEE Sensors 2002, Florida, USA, 22.3

[3] C.C. Lu, J.A. Covington, F. Udrea, J.W. Gardner, Proc. EurosensorsXVI, Prague, Czech Republic (2002), 1143

[4] M. Graf, D. Barrettino, S. Taschini, A. Hierlemann, H. Baltes, S. Hahn, N. Bârsan, and U. Weimar, Proc. EurosensorsXVI, Prague, Czech Republic (2002), 456

[5] J. Kappler, N. Bârsan, U. Weimar, A. Dieguez, J.L. Alay, A. Romano-Rodriguez, J.R.Morante and W. Göpel, Fres. J. Anal. Chem. **361** (1998), 110

[6] I^2C by Philips Semiconductors

[7] austriamicrosystems, Unterpremstätten, Austria.

Acknowledgements

The authors would like to thank Advanced Sensing Devices (Germany) namely Dr. Stefan Raible, Dr. Jürgen Kappler and Dr. Nicolae Bârsan for coating the microhotplates. This work is financially supported by the Bundesamt für Bildung und Wissenschaft (contract number 00.0591) and the European Union (IST-2000-28452).

Sensing of hydrocarbons in low oxygen conditions with tin oxide sensors: possible conversion paths

W. Schmid, N. Bârsan and U. Weimar

Universität Tübingen, Institute of Physical Chemistry, Auf der Morgenstelle 8, 72076 Tübingen, Germany
email: wolf.schmid@ipc.uni-tuebingen.de http://www.ipc.uni-tuebingen.de/weimar/

Summary: *The conversion of CO and different hydrocarbons by palladium-doped tin oxide sensors was studied in conditions with low oxygen and low water concentration for temperatures between 200 and 400°C. Although under normal conditions, oxygen plays an important role in the detection of these reducing analytes, relatively large sensor signals could be observed. For most conditions, carbon dioxide and water could be observed as reaction products even in low oxygen content.*

Keywords: *tin oxide, low oxygen conditions, consumption*
Category: *5 (Chemical Sensors)*

1 Introduction

Tin oxide sensors usually work in environmental conditions: with varying amounts of water vapour around, but constant oxygen concentration. Water vapour plays an important role for the detection, as was shown in previous publications [1,2,3]. Usually it is assumed that for reducing gases like carbon monoxide and hydrocarbons (HCs), tin oxide sensors work through oxidation of the analyte with interaction of the doping material [4], but also under conditions with a low concentration of oxygen (below 100 ppm), tin oxide sensors still show a sensitivity against CO and HCs. This work investigates the sort and the amount of products related to sensing during the detection of CO and HCs with tin oxide sensors.

2 Experimental

The measurements were performed at different sensor temperatures (between 200 and 400°C) and different analyte concentrations (cf. Table 1) in dry and humid nitrogen (10 % r.h. at room temperature). An FT-IR gas analyser (Innova Airtech) was used to monitor the gas composition upstream and downstream the sensors and simultaneously, the sensor resistance was recorded. Home-made SnO_2-based thick film sensors [1] doped with Pd were used, consisting of an alumina substrate and screen-printed platinum interdigitated electrodes (front side) and resistive heater (back side). The seven identically prepared sensors were mounted jointly in one chamber, which was alternatively supplied by two separate gas flows, one with nitrogen, the other with varying concentrations of the analytes in nitrogen. The pressure inside the flow system was monitored with a barometer (Vaisala) and used as a correction in the gas analyser. The oxygen partial pressure was measured with a process oxygen analyser (ABB) and recorded together with the resistances of the sensors. To distinguish between the consumption of the sensitive material and the consumption of the transducer, additional measurements are performed with substrates equipped with electrodes and heater only.

Table 1. Analytes and measured concentrations.

analyte	carbon monoxide	propane
measured concentrations [ppm]	10	15
	20	30
	50	50
	100	100

3 Results and Discussion

For conditions with low oxygen concentration and low humidity, propane and CO behave differently: for propane, sensor signal as well as consumption and CO_2 production show a saturation for higher concentrations, with a maximum around 350°C for the sensor signal (see Fig. 1 left). CO on the other hand shows (except for 200°C) an almost linear behaviour , not only for the sensor signal (Fig. 1 right), but also for the amount of CO_2 which is produced in the sensing process.
When 2% (vol.) oxygen are added, the situation changes dramatically: for CO, the sensor signal is reduced around on order of magnitude, and the temperature dependence of the sensor signal is inverted (Fig. 2 right). For propane it is shifted down by a factor of around 2 (Fig. 2 left), but is almost linear to the concentration of propane. For temperatures up to 300°C, adding oxygen results in more consumption and more produced carbon dioxide for CO (Fig. 3), but not for propane (not shown).
For CO, the experimental findings can be explained by assuming the following competitive detection mechanism: in the absence of oxygen, CO can adsorb at the surface of the sensitive layer and act as an electron donor. As shown by the experimental results, the effect in resistance is quite dramatic (>1 order of magnitude change). The maximum coverage is

reached for relative small concentrations for CO (above 100ppm, cf. [5]). In the presence of small amounts of oxygen (intended 0%), two competitive reactions take place: 1) the adsorption of the analyte as electron donor and 2) the reaction of the analyte with adsorbed oxygen species and formation of CO_2, of which the adsorption as electron donor results in the larger electrical effect. The generation of CO_2 is probably due to the residual O_2 still present in the gas and at the surface. At higher oxygen concentrations, the generation of CO_2 is the main reaction, but results in less electrical effect than the direct adsorption, which is confirmed by the decrease in sensor signals and increase in CO_2 generation.

The explanation for propane is still under consideration.

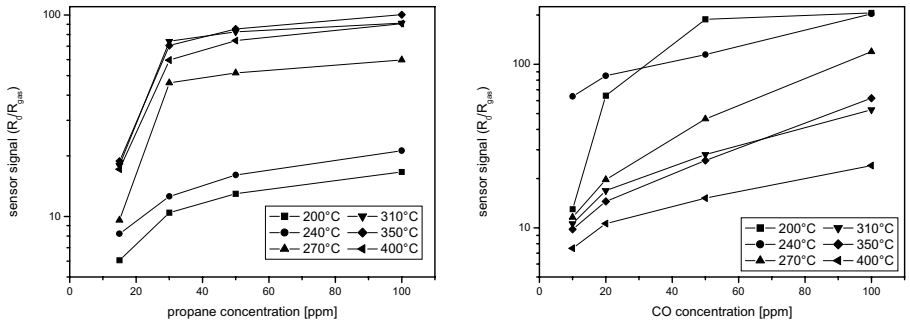

Fig. 1. Sensor signal for propane(left) and CO (right) in dry N_2 without oxygen.

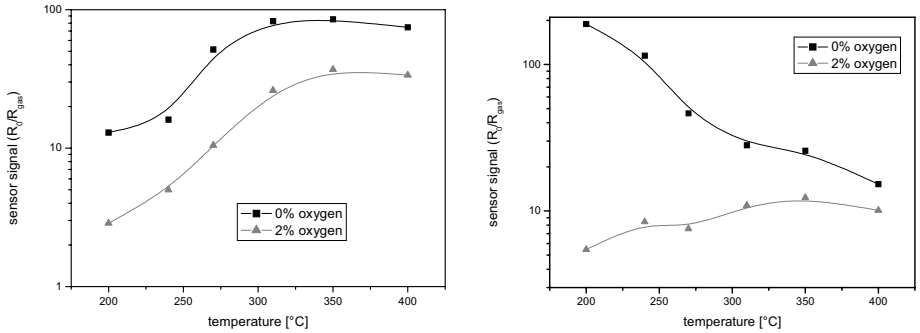

Fig. 2. Sensor signal for 50ppm propane (left) and 50ppm CO (right).

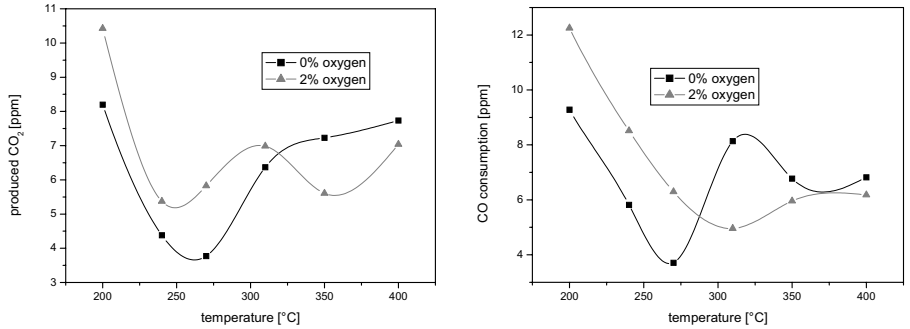

Fig. 3. Produced CO_2(left) and CO consumption for 50ppm CO.

References

[1] J. Kappler, A. Tomescu, N. Barsan and U. Weimar, CO consumption of Pd doped SnO_2 based sensors, Thin Solid Films, 391 (2001), 186-191.

[2] W. Schmid, N. Bârsan and U. Weimar, Sensing of hydrocarbons with tin oxide sensors: possible reaction path as revealed by consumption measurements, Sens. Actuat. B(chem.), 89 (2003) 232-236.

[3] S. Emiroglu, N. Barsan, U. Weimar and V. Hoffmann, In-situ diffuse reflectance infrared spectroscopy study of CO adsorption on SnO_2, Thin Solid Films, 391 (2001) 176-185.

[4] A. Cabot, A. Vilà, J. Morante, Analysis of the catalytic activity and electrical characteristics of different modified SnO_2 layers for gas sensors, Sens. Actuat. B 84 (2002) 12–20.

[5] S. Hahn, N. Barsan, U. Weimar, S. Ejakov, J. Visser, R. Soltis, Oxygen and water interactions at the surface of SnO_2 based sensors, Conf. Proc. EUROSENSORS XVI, Prague (Cz), 2002.

On the use of a catalytic filter to selectively detect benzene with a tungsten oxide sensor

K. Malysz[1], J. Prášek[1], X. Vilanova[2], J. Hubálek[1], P.T. Ivanov[2], E. Llobet[2], J. Brezmes[2], X. Correig[2], Z. Svìrák[3]

[1] Brno University of Technology, Faculty of Electrotechnics and Communication Technologies, Department of Microelectronics, Údolní 53, 602 00 Brno, Czech Republic.
[2]Universitat Rovira i Virgili, Escola Tècnica Superior d´Enginyeria, D.E.E.E.A., Avda Paï sos Catalans, 26, 43007 Tarragona, Spain, xvilanov@etse.urv.es
[3]Brno University of Technology Faculty of Chemistry, Purkynova 118, 612 00 Brno, Czech Republic

Summary: *We present the results on the use of a catalytic filter (Pt-Al_2O_3) printed on a tungsten oxide active layer to selectively detect benzene. It is shown that the effect of the catalytic layer is twofold: First it dramatically increases the sensitivity of the tungsten oxide film to benzene vapours and second, it de-sensitises the film to ethanol. The response of the sensors with catalytic filter to other gases such as CO, CH_4, NH_3 and NO_2 has been studied. The results show that the use of two sensors (one coated with a catalytic filter and one uncoated) allows for the selective detection of benzene in the presence of any of these gases and ethanol.*

Keywords: *gas sensors, catalytic filter, thick film, screen printing, benzene*
Category: *5 (Chemical Sensors)*

1 Introduction

Thick-film semiconductor gas sensors have been intensively studied in the last years. In particular, the screen-printing technique leads to more porous active layers than other deposition techniques such as physical or chemical vapour deposition. A more porous film is preferred since it shows more surface area (higher sensitivity) and is less prone to poisoning than more compact films. In this context, the use of catalytic filters has been reported to remove alcohol interference in CO or CH_4 detection [1,2].

In this work we report on the use of a screen-printed catalytic filter to modify the sensing properties of WO_3 thick-film gas sensors, enhancing their sensitivity to benzene. Benzene, which is carcinogenic, is very relevant to many different applications such as food safety, environmental monitoring, etc. In the next section some details are given on the fabrication of the sensors and the deposition of the catalytic filters. Then the characterisation of the sensors is described. Finally, the results obtained are presented and discussed.

2 Sensor fabrication details

Sensors were fabricated by screen-printing onto alumina substrates. In the first step, a heating element and a temperature sensitive meander were printed on the backside using a commercial platinum paste (Heraeus C3657). After levelling, the substrates were dried (10 minutes at 125ºC) and fired (peak temperature was set to 850ºC). In the second step, interdigitated gold electrodes were deposited on the front side of substrate by using a commercial conductive paste (ESL 8884). After levelling, the substrates were dried (10 minutes at 125ºC) and fired in a belt furnace with a peak temperature of 850ºC. In the third step, the gas sensitive layers were deposited onto the electrodes. Electrode area was 25 mm^2. The sensors were prepared by using a commercial WO_3 powder (Sigma-Aldrich) and mixed with 5% wt Bi_2O_3 to improve adhesion. The active layers were dried at 125°C for 10 min and fired at 850°C.

Half of the samples were then coated with a Pt-Al_2O_3 catalytic filter. An insulating alumina paste was printed to cover the WO_3 layer. After drying a Pt layer (Heraeus C3657) was printed onto the Al_2O_3 layer. The catalytic filter was fired at 850°C.

3 Experimental

The morphology of the sensors was investigated by scanning electron microscopy (SEM). The gas sensing properties of the sensors to ethanol, benzene, nitrogen dioxide, ammonia, carbon monoxide and methane were investigated. The sensors with and without catalytic filter were kept in a temperature and moisture controlled test chamber (40ºC, ±1ºC and 15% R.H.). The sensors were operated at 250ºC, 300ºC and 350ºC (by applying a voltage to the heating resistor) to analyse the effect of temperature on their response. The resistance of the sensors in the presence of either pure air or the different pollutants at different concentrations was monitored and stored in a PC.

4 Results and discussion

SEM analysis: The morphology of the films was investigated by SEM. The tungsten oxide layers were nano-particular with a particle size around 50 nm. Figure 1 shows the SEM image of a section of a sensor with catalytic filter. From the surface toward the substrate (left to right), the different regions labelled correspond to: I Pt-filter, II insulating Al_2O_3, III gold electrode and tungsten oxide layer, IV alumina substrate. SEM results reveal that the catalytic filter is very porous.

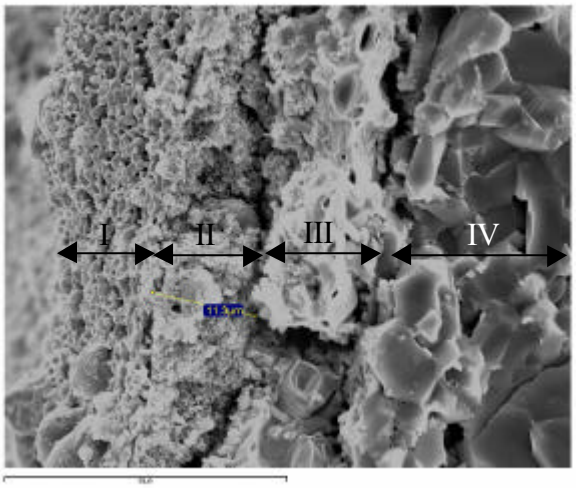

Fig. 1. SEM image of a section of a WO_3 sensor coated with catalytic filter

Gas sensitivity studies: Neither the sensors with catalytic filter nor those without filter were sensitive to CO (tested up to 1,000 ppm) and CH_4 (tested up to 10,000 ppm) at the different operating temperatures studied. Figure 2 shows the effect of the catalytic filter in the detection of benzene and ethanol vapours.

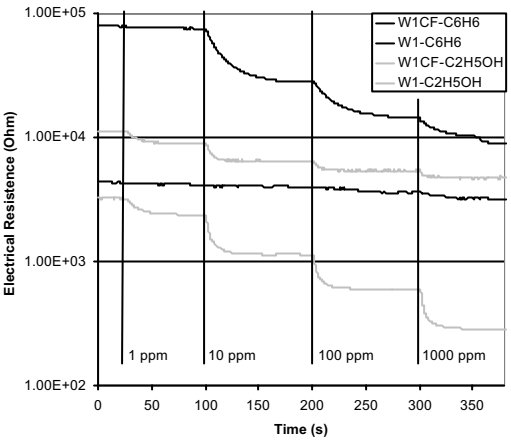

Fig. 2. Responses to ethanol and benzene of WO_3 sensors with (W1CF) and without (W1) catalytic filter, operated at 300°C.

Ethanol or benzene vapours lead to a decrease in the sensors' resistance, which is the normal behaviour of *n*-type metal oxide sensors in the presence of reducing species.

While un-coated sensors (pure tungsten oxide) show high sensitivity to ethanol and negligible sensitivity to benzene, the sensors coated with a catalytic filter show sensitivity to benzene and reduced sensitivity to ethanol. The Pt-based porous catalytic filter is able to burn out most of the ethanol and, sensitivity to these vapours is significantly reduced. On the other hand, it acts as a catalyst enabling the detection of benzene.

The catalytic filter substantially changes the response of the sensor in the presence of NH_3. While the pure WO_3 sensor is almost insensitive to ammonia, the sensors with catalytic filter increase their resistance in the presence of ammonia. NH_3 reacts with oxygen at the filter creating NO_2 and H_2O, then NO_2 (oxidising species) diffuses through the filter and is detected at the surface of the sensor. The catalytic filter does not significantly alter the response of the sensors to NO_2. NO_2 was tested at 0.1, 1 and 10 ppm). All these results are summarised in Table 1. Sensitivity was defined as R_{air}/R_{gas}. Sensitivity figures lower than unity indicate that the sensor resistance in the presence of NO_2 and NH_3 is higher than in air.

Vapour	W1CF	W1
C_2H_5OH (250°C)	2.23	1.74
C_2H_5OH (300°C)	**1.73**	**2.84**
C_2H_5OH (350°C)	1.72	1.73
C_6H_6 (250°C)	1.35	1.09
C_6H_6 (300°C)	**2.29**	**1.07**
C_6H_6 (350°C)	1.20	1.06
NH_3 (250°C)	0.28	1.04
NH_3 (300°C)	0.22	1.01
NH_3 (350°C)	0.24	1.00
NO_2 (250°C)	0.67	0.66
NO_2 (300°C)	0.87	0.87
NO_2 (350°C)	0.97	0.95

Table 1. Sensitivity at different operating temperatures for sensors with (W1CF) and without (W1) catalytic filter. All the gases at 10 ppm exception made of NO_2 at 1ppm.

In conclusion, the inclusion of a Pt catalytic filter on top of a WO_3 gas sensor allows for a selective detection of benzene in the ppm range. The filter works at moderate temperatures (300°C).

References

[1] S. Kitsukawa et al., *Sens. Actuators B* 65 (2000), 120.

[2] G.K. Flingelli et al. *Sens. Actuators B* 48 (1998), 258.

Sputtered and screen-printed metal oxide-based integrated micro-sensor arrays for the quantitative analysis of gas mixtures

M. Stankova[1], P. Ivanov[1], E. Llobet[1], J. Brezmes[1], X. Vilanova[1], I. Gràcia[2], C. Cané[2], J. Hubalek[3], K. Malysz[3], X. Correig[1]

[1]University Rovira i Virgili, Electronic Engineering Dept., Avda Països Catalans 26, 43007 Tarragona, Spain
email: ellobet@etse.urv.es http://www.etse.urv.es
[2]CNM, Department of Microelectronic and Silicon Technology, Campus UAB, Barcelona, Spain
[3]Brno University of Technology, Microelectronic Dept., Brno, Czech Republic

Summary: *Either by screen-printing or sputtering, sensitive layers of nanoparticle tin oxide were deposited on silicon micromachined substrates. The procedures allow the deposition of sensing layers before membranes have been etched, which leads to gas micro-sensors with an excellent fabrication yield. The sensor response to ethanol, acetone and ammonia vapours and their binary mixtures was studied. By using an integrated array of 4 microsensors operated at two different temperatures and a fuzzy ARTMAP neural network, it was possible to identify and quantify the different species (success rate was 100%). These results confirm the viability of the techniques introduced to obtain micromachined sensors suitable for battery-powered gas/vapour monitors.*

Keywords: *metal oxide, r.f. sputtering, screen-printing, micromachined array, quantitative gas analysis*
Category: *5 (Chemical sensors)*

1 Introduction

We report on a method to obtain integrated micromachined gas sensor arrays with a very high fabrication yield. The usefulness of the active-film deposition methods in terms of fabrication yield, sensor performance and compatibility with conventional microelectronic technology is demonstrated.

2 Integrated micro-sensor array

The integrated micro-hotplates with arrays of four microsensors were fabricated on double-side polished p-type <1 0 0> Si substrates 300 μm thick. The structure of the device basically consists of a gas sensing layer, the electrodes, insulating layers and a polysilicon heater. The technological process needed to fabricate the sensors had the following steps [1]: (1) Deposition of the membrane layer. Membranes consisted of a 0.3 μm thick Si_3N_4 layer grown by LPCVD. Each chip had 4 membranes, the size of which was 900 × 900 μm^2 (2) Deposition and patterning of a $POCl_3$-doped polysilicon heating meander of 6 Ω/sq. The temperature coefficient of resistivity (TCR) was 6.79×10^{-4} C^{-1}. The heater is used as a temperature sensor. (3) Deposition of a 0.8 μm thick SiO_2 layer to insulate the heater from the electrodes and the sensing film. (4) Opening of contacts for the heater bonding pads to be accessible. (5) Deposition of either parallel or interdigited 0.2 μm thick Pt electrodes, patterned by lift-off. The electrode area was 400 × 400 μm^2. (6) Patterning of the backside etch mask. (7) Deposition of the sensing layer onto the electrode area. (8) Backside silicon etching with KOH to create the thermally-insulated membranes. (9) Wire bonding and packaging.

The deposition of the active films was either by screen-printing or by r.f. sputtering. The details are as follows:

The screen-printing was made before backside silicon etching and packaging. This procedure avoids damaging the sensor membranes and thus, leads to an excellent yield (>95%). The sensing layer consisted of a 5 μm thick SnO_2 nanopowder. A printable paste was prepared by using an organic vehicle based on therpineol. The paste was printed onto the semi-processed wafers by using a high precision screen-printing machine that allows one-side mask alignment. Wafers were subsequently dried for 15 minutes at 125°C for the organic vehicle to be completely dried, and then fired for 1 hour in a belt furnace at a single level of temperature, equal to 600°C. The sputtering was done on semi-processed wafers using a metallic Sn target at ambient temperature. Pressure was set to 5×10^{-3} mbar, and gas flow was set to O_2=6 sccm, Ar=6 sccm. After deposition, wafers were annealed in air for 2 hours at 400°C.

Sputtered or screen-printed wafers were then ready for backside etching, dicing and packaging.

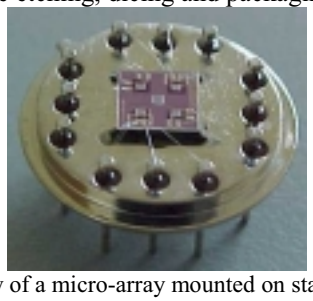

Fig. 1: View of a micro-array mounted on standard TO-8

3 Morfology and gas sensitivity studies

AFM, SEM and EDX were used to study the morfology of the films. For the screen-printed films, grain size was below 40 nm. Grains form agglomerates which create a porous layer. For the sputtered films, grain size was around 80 nm. SEM and AFM showed that the sputtered films were more compact than the screen-printed ones.

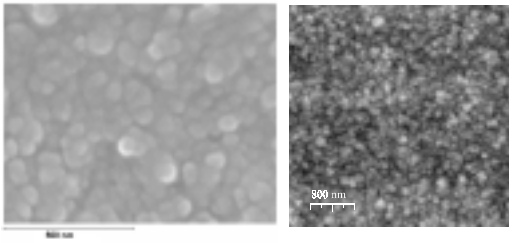

Fig.2: Screen-printed tin oxide Sputtered tin oxide

The sensitivity to different concentrations of ethanol, acetone and ammonia vapours (single gases and binary mixtures) was studied at different operating temperatures. The sensitivity was calculated as the ratio R_a/R_g where R_a is the resistance of the sensor in the presence of clean air (20% R.H., 30°C) and R_g is the sensor resistance in the presence of a diluted volatile.

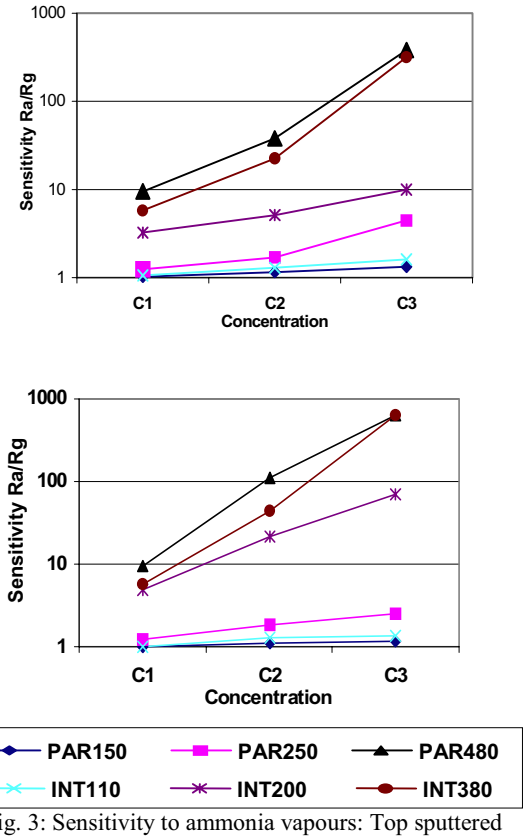

Fig. 3: Sensitivity to ammonia vapours: Top sputtered sensors, Bottom: screen-printed sensors

Operating temperatures were 110, 200 and 380°C for interdigited electrodes and 150, 250 and 480°C for parallel ones. Differences in operating temperatures are due to the fact that membranes with parallel and interdigited electrodes had different values of the heating polysilicon resistors (i.e. 600 Ω and 700 Ω for interdigited and parallel electrodes, respectively) and the same heating current was injected to these resistors. The power consumption of the membranes operated at 480°C was around 80 mW. Devices with interdigited electrodes have higher sensitivities at lower operating temperatures than those with parallel electrodes. These results are in good agreement with the theory of porous active layers with a uniform distribution of active sites, which predicts an increase in sensor response if electrode spacing is reduced and film thickness and electrode length are kept unchanged. The response curves prove that the technological processes employed, lead to very sensitive metal oxide microsensor arrays with a very high yield (more than 95% of the microsensors work after dicing, wire bonding and packaging). The sputtered sensors showed more repeatability than the screen printed sensors: for each vapour or mixture and concentration measured, the ratio between standard deviation of the response and its mean (over 5 replicate measurements) was below 4.6×10^{-2} and 1.1×10^{-1} for the sputtered and screen printed sensors, respectively. The lower this ratio is, the better the repeatability.

4 Quantitative gas analysis

A quantitative analysis of the vapours was performed with a fuzzy ARTMAP neural network. The interdigited electrode sensors were operated at 380°C and the parallel electrode sensors at 480°C. This consisted in a 18- category classification (6 species and binary mixtures × 3 concentrations). Since either the response (conductance change) of the 4 sputtered or the 4 screen-printed sensors were used, the neural networks had 4 input neurones and 18 output neurones. Each measurement was replicated 5 times. Therefore, a total of 90 measurements were available to train and validate the networks. A leave-one-out cross-validation was implemented to estimate the performance of the methods. When the responses of the 4 screen-printed sensors were input to the network an 89% success rate in vapour identification and 82.3% in quantification were reached. On the other hand, when the responses of the 4 r.f. sputtered sensors were input to the network, 100% success rates in vapour recognition and concentration estimation were reached.

5 Conclusions

We have reported a high-yield method to deposit sensing films onto microhotplates before the membranes are etched (this avoids membranes damage during film deposition). The integrated microarrays are suitable for gas mixture identification and quantification.

References

[1] D.G. Rickerby et al., *Sensors Actuators B* 69 (2000) 314-319.

Hybrid CoTPP-SnO_2 chemical sensors

R. Paolesse[1,3], C. Di Natale[2,3], A. Macagnano[3], D. Monti[1], P. Siciliano[4], M. Epifani[4], A. Forleo[4], A. Taurino[4], R. Rella[4] and A. D'Amico[2,3]

[1]University of Rome 'Tor Vergata', Dipartimento di Scienze e Tecnologie Chimiche, via della Ricerca Scientifica 1, 00133 Rome, Italy,
email: roberto.paolesse@uniroma2.it
[2]University of Rome 'Tor Vergata', Dipartimento di Ingegneria Elettronica, via del Politecnico 1, 00133 Rome, Italy
[3]CNR-Istituto per la Microelettronica e i Microsistemi, sezione di Roma, via del Fosso del Cavaliere 100, 00133 Rome, Italy
[3]CNR-Istituto per la Microelettronica e i Microsistemi, sezione di Lecce, via Arnesano, Lecce, Italy

Summary: *Hybrid CoTPP-SnO_2 thin films have been obtained by the sol-gel approach coupled with spin coating technique. These films have been deposited onto interdigital electrodes and their performances as chemical sensors have been measured towards the detection of methanol vapors. These CoTPP-SnO_2 sensors showed fast and reversible responses towards different concentrations of methanol and best results were obtained at 250 °C working temperature, while a sharp decrease was observed at higher temperatures. These results are attributed to the well known catalytic activity of metalloporphyrins, which is not thermally decomposed at 250 °C, as confirmed by optical measurements.*

Keywords: *metalloporphyrins, tin dioxide, chemical sensors, VOC*
Category: *5 (Chemical sensors)*

1 Introduction

A critical step in the development of reliable and high performances chemical sensors is the rational choice of the sensing material, because among others selectivity and sensitivity properties of the sensors critically depend on the sensing material. Both inorganic and organic compounds have been proposed as sensing materials, each of them tuned for the particular application where to be exploited. Recently a novel and promising approach is represented by the development of hybrid materials, where organic and inorganic constituents are combined in the same matrix. The aim is to take advantage of the chemical stability of the inorganic components, exploiting in the same time the reactivity and synthetic flexibility of the organic materials. In this framework the sol-gel technique is one of the most active and promising approach to prepare hybrid materials, because this method allows both an optimal dispersion of the organic compounds in the inorganic matrix and a low temperature preparation of the material [1]. This approach has been widely exploited for the preparation of optical sensors based on silica glasses where several dyes have been entrapped. On the other hand the non-silicate hybrids is a field almost completely unexplored.

Tin dioxide is probably the prototypical example of inorganic oxides exploited as sensing materials and SnO_2-based devices have been widely used for practical applications [2]. The sensing mechanism of SnO_2 involves chemisorbed oxygen at the oxide surface and different metals have been used as dopants to modify the selectivity and sensitivity properties of SnO_2-chemical sensors. On the other hand it is well known that metalloporphyrins (Figure 1) are able to bind and activate molecular oxygen and in particular cobalt porphyrins have been exploited for the electrocatalytic reduction of O_2 [3]. For this reason it is particularly intriguing the exploitation of metalloporphyrins as dopants in SnO_2 based gas sensors.

In recent years our groups have been involved in the development of chemical sensors based on porphyrins or tin dioxide as sensing materials and in this paper the preparation of hybrid Co porphyrin-SnO_2 sensors by sol-gel technique will be reported and some example of their performances for the detection of gaseous analytes will be illustrated and discussed.

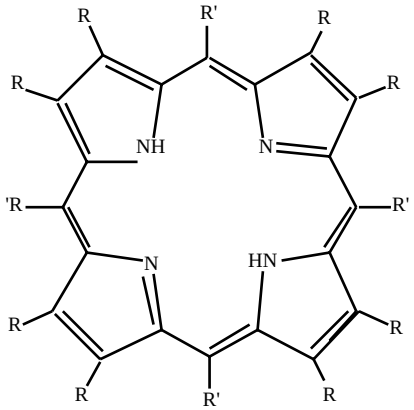

Fig. 1. Molecular structure of porphyrins

2 Experimental

Pure SnO_2 sols were prepared starting from anhydrous $SnCl_4$, water, propanol (C_3H_7OH), isopropanol (2-C_3H_7OH), in the following molar ratios: $SnCl_4$:H_2O: C_3H_7OH:2-C_3H_7OH = 1:9:9:6. For preparing the cobalt porphyrin doped sol, the prescribed amount of the porphyrin dissolved in 5 ml of THF was added to the pure sol, in order to get a Co:Sn atomic ratio of about 1 %.

Thin films were deposited by spin coating technique and then gradually heated at 110 °C to drying. The films used for sensing tests were deposited onto alumina substrates incorporating interdigital electrodes and Pt heater. The devices were then mounted onto a TO-8 socket and placed in a dynamic flow system.

The SEM image of the CoTPP-SnO_2 thin film shows a compact layer. The morphology of the film changes after measurements, as a consequence of thermal treatments, showing however a porous structure.

The sensing performances of the developed CoTPP-SnO_2 sensors were tested towards the detection of methanol vapors. Different concentrations of methanol have been obtained by dilution of saturated vapors of the alcohol with synthetic air. Fast and reversible responses of CoTPP-SnO_2 sensors have been obtained, as reported in Figure 3.

The influence of the temperature on the CoTPP-SnO_2 sensor responses was also studied by exposure to methanol vapors (Figure 4). Best results have been obtained at 250 °C, while higher temperatures showed a dramatic decrease of the sensor responses, probably due the thermal decomposition of the metalloporphyrin.

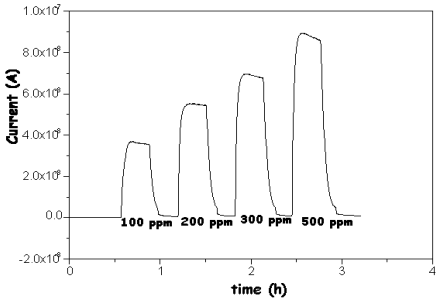

Fig. 3. Dynamical response of CoTPP-SnO_2 sensors to different concentration of methanol at 250 °C

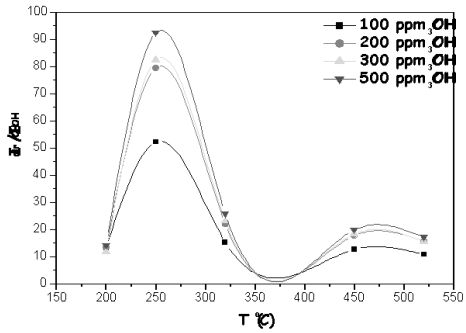

Fig. 4. Response of CoTPP-SnO_2 sensors towards different concentration of methanol as a function of temperature

To investigate the presence of the porphyrin at the different temperatures, the optical reflectance spectra of the CoTPP-SnO2 thin films have been recorded at different temperature. The CoTPP is not thermally decomposed at 250 °C, as showed by the reflectance spectrum reported in Figure 5, where the characteristic bands around 420 and 500 nm are present. At higher temperature (400 °C) these bands disappear, as a consequence of thermal decomposition.

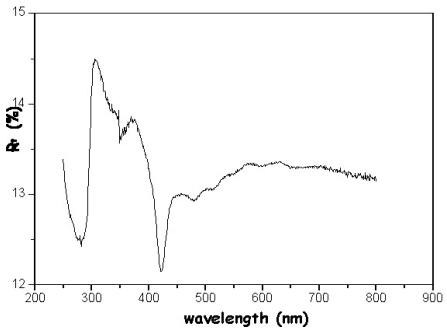

Fig. 5. Reflectance spectrum of CoTPP-SnO_2 thin film after thermal treatment at 250 °C

More detailed characterisation of the sensor responses towards different gases will be presented in the final paper.

References

[1] S. Hofacker, M. Mechtel, M. Mager H. Kraus *Progress in Organic Coatings.* 45 (2002) 159–164.

[2] W. Gopel, K. D. Schierbaum. *Sens. Actuators B* 26-27 (1995) 1–12.

[3] C. A. Pessoa, Y. Gushikem. *J. Porphyrins Phthalocyanines* 5 (2001) 537–544.

Influence of SnO_2 thick film thickness on the detection properties

P. Montmeat, R. Lalauze, J-P. Viricelle, G. Tournier, C. Pijolat

Ecole Nationale Supérieure des Mines, Centre SPIN, LPMG-URA CNRS 2021
158 Cours Fauriel, 42023 Saint-Etienne, France, viricelle@emse.fr

***Summary**: The influence of the thickness of thick film SnO_2 sensors (10 to 80 µm) on their detection performances depends on the studied gases: response to CO presents a maximum while ethanol response continuously decreases with increasing thickness. A simplified geometrical model based on a resistivity distribution within SnO_2 depleted area is presented. This model takes into account the role of gold electrodes which enhance the creation of space charge area thanks to the three boundary points "gas-metal-oxide". Calculations of conductance allow to simulate the influence of the thickness on the gas response.*

Keywords: tin oxide, space charge area, modeling
Category: 5 (Chemical sensors)

1 Introduction

In a previous paper [1], the role of a metal (gold) on the electrical response on tin oxide sensor was investigated thanks to the development of a particular test bench : it allowed to separate the atmosphere surrounding SnO_2 region in contact with gold electrode from the atmosphere in the area between electrodes. The action of oxygen and of reducing gas was under focus and was greatly enhanced in the region containing gold. This result associated with calorimetric tests indicated the creation of specific oxygen species at the metal-oxide interface. A qualitative physico-chemical model based on the electronic effect of these adsorbed species, resulting in the increase of space charge area was proposed (Fig. 1).
The purpose of the present study is to validate the proposed mechanism by a quantitative model, based on geometrical considerations about space charge areas.

2 Experimental

Sensors are constituted of rectangular ($2*4mm^2$) SnO_2 thick film deposited by screen-printing onto α-alumina substrate with a platinum heater on the opposite size. From 1 to 8 deposits were performed, allowing to obtain various layers thickness in the range 10-80µm. The sensing material was then annealed at 700°C during 16 hours. Gold electrodes ($2*1\ mm^2$) were deposited by sputtering. Sensors were tested at 450°C under dry atmospheres : air, carbon monoxide (300ppm) and ethanol (100ppm) in air. The conductance (G) was measured using a dc electrical circuit with a standard resistance and a normalized response was defined by $S= G_{gas}/G_{air}$. For each layer thickness, measurements were conducted with three sensor production batch's.

3 Results

The variations of the conductance and of the normalized response under carbon monoxide S(CO) and under ethanol $S(C_2H_5OH)$ versus the sensor thickness are reported in figures 2 to 4. It can be noticed that the conductance under air increases and that the responses to CO and ethanol present a different behavior: S(CO) has a maximum whereas $S(C_2H_5OH)$ is continuously decreased.

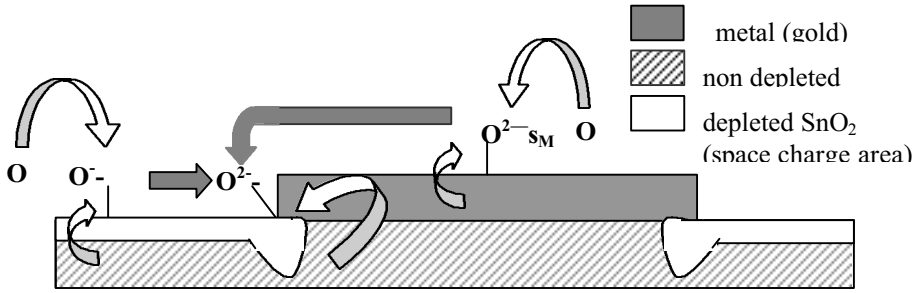

Fig. 1. Proposed mechanism based on space charge area at the three boundary point (gas/metal/oxide) to explain metal effect on tin oxide electrical conduction (from [1]).

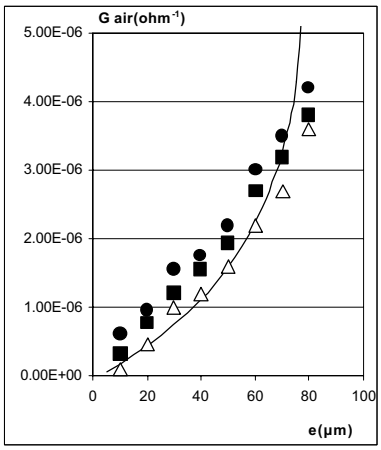

Fig. 2. Conductance variation under air at 450°C versus sensor thickness (points: 3 sensors batch, line: model)

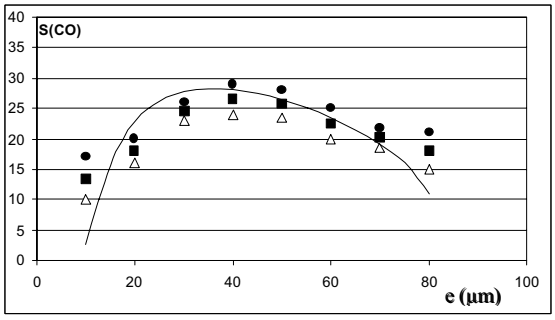

Fig. 3. CO response at 450°C: variation versus sensor thickness (points: 3 sensors batch, line: model)

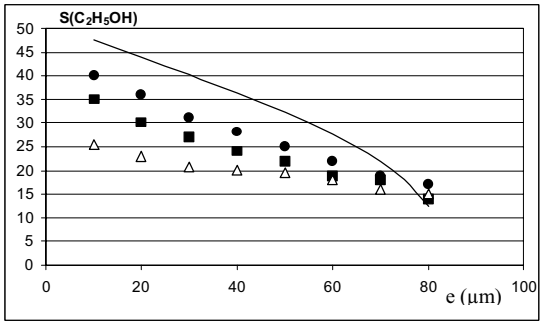

Fig. 4. Ethanol response at 450°C: variation versus sensor thickness (points: 3 sensors batch, line: model)

Taking into account our proposed mechanism (Fig. 1), literature results [2, 4], a geometrical model is proposed. We consider that the sensor is constituted of depleted area located at the sensor surface and under the electrode (three-boundary point), and of non depleted area (Fig. 5). Then, it is supposed that the resistivity ρ_M of the not depleted area is constant and independent on the atmosphere. The resistivity ρ_S of the depleted area is constant within the thin layer thickness "y" but a gradient from ρ_S to ρ_M is considered in the depleted area linked to the electrode. The slope of the gradient depends on the coverage fraction of oxygen species at the three-boundary point (Fig. 1) and thus depends on the atmosphere: it is noted "a" under air and "γa" under gas (Fig. 6). γ is a constant dependant on the nature of the gas, and higher than 1 for a reducing gas as the space charge area is decreased in this case, resulting in a conductance increase.

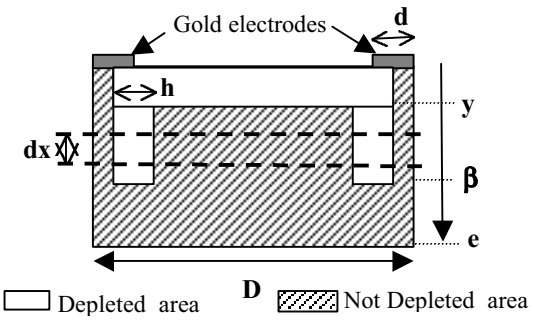

Fig. 5. Schematic representation of space charge area considered for the geometrical modeling

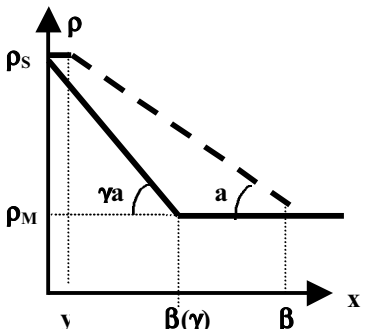

Fig. 6. Resistivity distribution in the depleted area relative to the three boundary point.

On the basis of previous assumptions, it was possible to calculate the conductance and to simulate its variations versus thickness (Fig. 2 to 4). The agreement with experiments is correct if we consider the simplified hypothesis: this model allows to explain the particular shape of the curves. It should be now improved to be more realistic and the parameters (ρ_S, ρ_M, β, y) have to be validated.

References

[1] P. Montmeat, J-C. Marchand, R. Lalauze, JP Viricelle, G. Tournier, C. Pijolat, Influence of metallic electrodes on the electrical properties of tin oxide, Proc. *Eurosensors XVI*,15-18 Sept.2002, Prague, CTU ed, vol. 3, p591.

[2] V.N. Mishra, R.P. Argawal: Effect of electrode material on sensor response, *Sensors and Actuators*, B22 (1994), 121-125.

[3] U. Weimar, W. Göpel : A.C. measurements on tin oxide sensors to improve selectivities and sensitivities , *Sensors and Actuators* B 26-27 (1995), 13-18

[4] O.K. Varghese, L. Malhotra : Electrode sample capacitance effect on ethanol sensitivity of nano-grained SnO_2 thin films , *Sensors and Actuators* B 53 (1998), 19-23.

A Dual Element Multipoint Optical Fibre Water Sensor System Utilising Fourier Transform Signal Processing and Artificial Neural Network Pattern Recognition.

D.King[1], W.B. Lyons[1], C. Flanagan[2] and E. Lewis[2]

[1]ECE Dept, F1 Foundation Bldg., University of Limerick, Castletroy, Limerick, Ireland.
email: Damien.king@ul.ie http://www.ece.ul.ie
[2]Department of Electronic and Computer Engineering, University of Limerick, Limerick, Ireland.

Summary: *A dual element multipoint optical fibre sensor capable of detecting ethanol in water supplies is reported. A U-bend configuration is used for each sensor in order to maximize sensitivity and the sensor system is interrogated using Optical Time Domain Reflectometry (OTDR). The signal processing technique has been designed to optimise the neural network adopted in the existing sensor system. Using Stuggart Neural Network Simulator (SNNS), a feed forward three layer neural network was constructed with the aim of successfully classifying the sensor test conditions based on the frequency domain response of the sensor. In this investigation, the sensors are immersed in distilled water, 25% and 50% ethanol and exposed to air.*

Keywords: *Multipoint Optical Fibre Sensor, U-bend Configuration, Optical Time Domain Reflectometry, Discrete Fourier Transform, Artificial Neural Networks.*
Category: *Applications.*

1 Introduction

Optical fibre sensors possess a number of advantages over conventional electronic sensing techniques, which make them attractive for use in a wide range of application areas. These advantages include safety in chemically hostile environments, immunity to electromagnetic interference, electrically passive operation, sensitivity, weight and versatility. As a result of this, the use of optical fibre sensors for the purpose of environmental monitoring has expanded rapidly over the past decade [1-2].

In this investigation a dual element multipoint sensor was incorporated into a 1Km length of 62.5 μm core polymer-clad silica (PCS) optical fibre. The multipoint sensor utilises evanescent wave absorption sensors as this type of sensor guarantees high sensitivity and a linear dynamic range. In order to maximize sensitivity once the cladding has been removed, a U bend configuration was used for the sensor and the core exposed directly to the measurand. Much experimental work has already been reported for a U-bend sensor detailing resulting sensitivity gains from evanescent wave increases from the curving of the sensing fibre. It has been shown in previous work by *Gupta et al* that the sensitivity of the sensor increases with decreasing bend radius of the probe and also with the increase in refractive index of the fluid under test [3]. The bend radii of the sensors used was measured to be 1mm using a convential optical microscope.

2 Sensor Interrogation

The interrogation of such a sensor uses a technique known as Optical Time Domain Reflectometery, OTDR. OTDR is capable of detecting attenuation as a function of distance along the fibre and therefore is able to locate position and changes in the sensor signals along the fibre [4]. As a result of this, OTDR has found many applications in both single and multipoint sensors where the OTDR instrument is used to monitor the fluctuation in the optical fibre attenuation caused by an external parameter induced by a measurand.

3 Measurement System Configuration

The system configuration for this investigation is shown in figure 1. It comprises of the optical fibre sensors, an EXFO IQ7000 (0.85μm) OTDR and a Pentium MMX 200 MHz PC running LabVIEW [5] Virtual Instrument (VI) programs for data capture and pre-processing.

4 Analysis

The application of a DFT to OTDR output data improves the efficiency of the ANN as it has reduced the computational resources of the network compared with previous work based purely on time domain results [6]. It can be observed from the extracted OTDR peaks shown in figure 2, that it is relatively low frequency information that is of interest in this classification. Due to the low frequency nature of the information, a discrete Fourier transform (DFT) using an FFT algorithm can be directly applied to the OTDR peaks without having to apply any windowing transform. The resulting PSD plots are shown in figure 3. As anticipated, the main PSD area of interest is located in the low frequency region. As a result of the application of the discrete Fourier transform, the OTDR peak information is now more explicit and easier for the user to access in comparison to time-domain based results which require all of the extracted OTDR peak data points.

Using SNNS [7], a feed forward three layer neural network was constructed with the number of input nodes corresponding to the number of points required to represent the sensors frequency domain response, see figure 4. A total of 320 patterns were used to train the ANN, requiring 600 epochs using a *backpropagation* algorithm. 80 patterns were used to test the trained ANN and the results from this test are shown in table 1.

Table 1: ANN Test Results

Test (S1 & S2)	Expected Output	Observed Output Accuracy
Air Air	0 0 0 **1** 0 0 0 **1**	90%
50% Eth 50% Eth	0 0 **1** 0 0 0 **1** 0	91.73%
Water Water	0 **1** 0 0 0 **1** 0 0	92.41%
25% Eth 25% Eth	**1** 0 0 0 **1** 0 0 0	93.02%

References:

[1] Kersey A.D., "A Review of Recent Developments in Fiber Optic Sensor Technology", *Optical Fiber Technology* **Vol2**, pp291-317 1996.

[2] Grattan K.T.V., Sun T., "Fiber Optic Sensor Technology: An Overview", *Sensors and Actuators A* **Vol. 82**, pp40-61, 2000.

[3] Gupta, B.D., et al, "Fibre optic evanescent field absorption sensor based on a U-shaped probe" *Optical and Quantum Electronics,* **28**, pp1629-1639 1996.

[4] Barnoski, M.K., Jensen S.N., "Fiber Waveguides: a Novel Technique for Investigating Attenuation Characteristics", *Applied Optics* **15**, pp2112-2115, 1976.

[5] LabVIEW Function and VI Reference Manual, P/N 321526B-01, Jan 1998.

[6] Lyons W.B., King D, Flanagan C, Lewis E, "A Three Sensor Multipoint Optical Fibre Water Sensor Utilising Artificial Neural Network Pattern Recognition", *Proc OFS2002 – 15th Optical Fiber Sensor Conference Technical Digest*, Portland, Oregon, USA, pp463-466 2002.

[7] Stuggart Neural Network Simulator (SNNS), User Manual, Version 4.1, Report No. 6/95, 1995. http://www-ra.informatik.uni-tuebingen.de/SNNS/

Figure 1: Measurement System Configuration

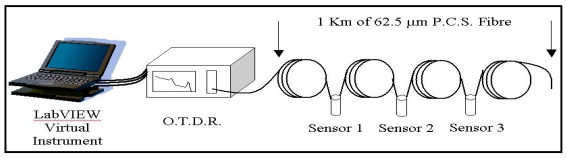

Figure 2: OTDR Sensor Peaks

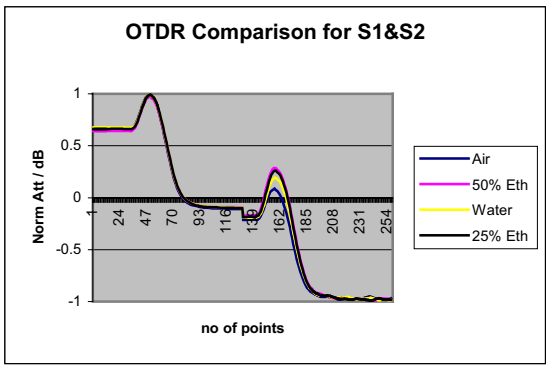

Figure 3: PSD Plots

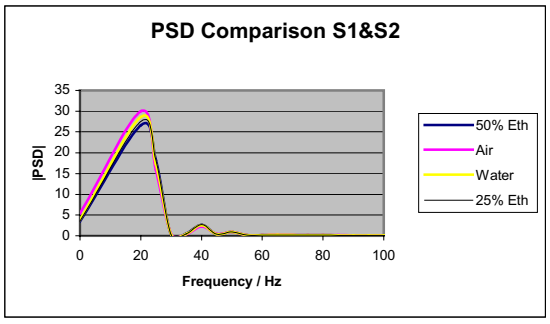

Figure 4: ANN Implemented in SNNS

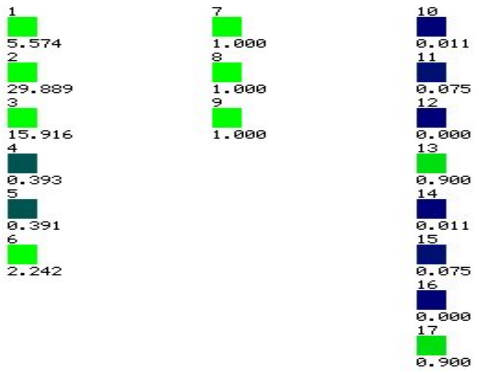

ACTIVE POST-PROCESSING METHOD TO INCREASE THE ELECTRO-MECHANICAL COUPLING IN MICRORESONATORS

M. Koskenvuori[1], P. Rantakari[1], J. Väisäsvaara[1], I. Tittonen[1], T. Mattila[2], A. Oja[2], V. Kaajakari[2], H. Seppä[2], H. Kattelus[2] and J. Kiihamäki[2]

[1]Helsinki University of Technology, Metrology Research Institute, PL 3000, FIN-02015 HUT, Finland
email: mika.koskenvuori@hut.fi http://metrology.hut.fi
[2]VTT Information Technology, PL 1200, FIN-02044 VTT, Finland

Summary: *A post-processing method to reduce the coupling gap between the resonator and electrode in SOI-fabricated microresonator is presented. The method allows a reduction of the coupling gap to a level which is significantly lower that the limits set by the fabrication process. This gap reduction leads to an increased electro-mechanical coupling which results in a reduced impedance level of the resonator which in turn simplifies the noise-matching of the resonator with for example oscillator electronics.*

Keywords: *RF-MEMS, capacitive coupling*
Category: *10 (Applications)*

1. Introduction

We report a post-processing gap adjustment used with a very high-Q (>100 000) 13 MHz bulk acoustic mode microresonator. The gap-adjustment allows the reduction of gap significantly below the minimum linewidth set by the process. This leads to an improvement in electro-mechanical coupling which in turn reduces the impedance level of the resonator, both factors being typically bottlenecks for microresonators.

High coupling constant η between mechanical motion and electrical current is essential for capacitively actuated microelectromechanical resonators. This is even further emphasized in length extensional mode resonators due to the high mechanical spring constant [1].

$$\eta = U_{DC}\frac{\partial C}{\partial x} \approx U_{DC}\frac{\varepsilon_0 A}{d^2} \qquad (1)$$

From Eq (1) it can be seen, that the coupling constant can be increased by increasing the transducer area A or the voltage U_{DC} or by decreasing the gap d. The design with an increased electrode-resonator area presented in [2] is used here to further increase the coupling. However, the area cannot be increased infinitely and the design in [2] is close to the practical limit before the parasitic modes appear. Also the use of very high DC-voltages is not feasible due to the problems with the voltage generation and breakthrough.

2. Operation

The operating idea is based on a moving electrode that is displaced by applying a DC voltage over the comb fingers in Figure 1. The required adjustment voltage is kept low by using the finger structure to increase the area and soft springs to support the structure. In Figure 2, the decrease in the gap can be seen as increased transmission and also as a shift in the resonance frequency caused by increasing capacitive non-linearity. Approximately at U_{adj} = 19 V the voltage causes a displacement that is greater than one third of the initial gap and pull-in occurs. This can be also seen from Figure 2. The idea is similar as presented in [3], but the electrostatic force is increased by using the comb structure with interdigited fingers. Also this is the first time when the post processing gap adjustment is used on length extensional mode resonator.

3. Fabrication and results

The resonator is fabricated on a 10 µm thick SOI-wafer using DRIE and the device layer is released using HF wet-etch.

The gaps in Figure 1 were designed to d = 0.8 µm and D = 0.5 µm, leading to a final electrode-resonator gap of d-D = 0.3 µm. The electrode-resonator gap values, d-D, extracted from the measured data in Figure 2, are 1.1 µm without adjustment voltage and 0.6 µm with an adjustment voltage U_{adj} = 19 V. This would allow the reduction of bias-voltage from 75 V to 22 V while maintaining the coupling constant.

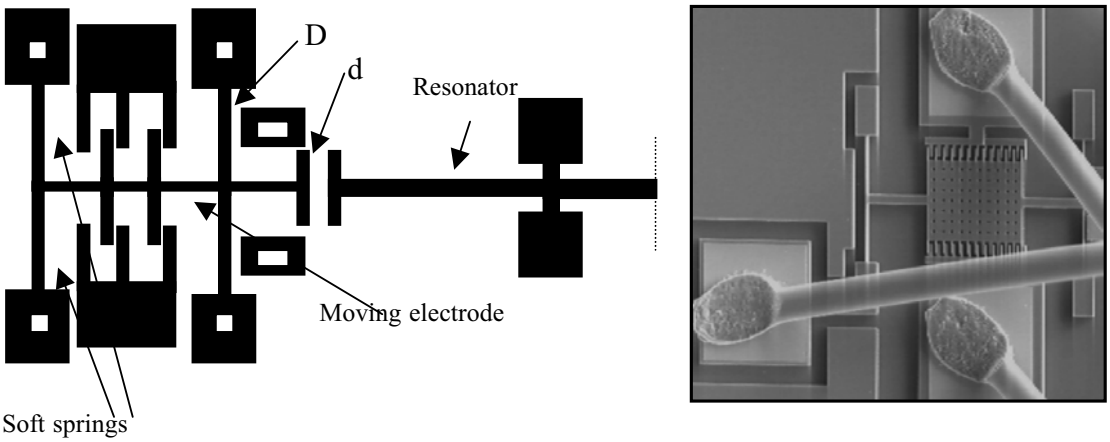

Fig 1. Schematic and SEM views of post-processing gap adjustment structure with interdigited finger comb electrodes. The areas denoted by white rectangles are attached to the substrate and hence immobile.

The widening of the gaps is probably due to the over-etching. The important result, however is, that the electrode-resonator gap can be made 0.5 µm more narrow using an adjustment voltage of no greater than 19 V. The voltage can be even futher reduced by using a double-comb structure which will be presented at the conference. The double-comb structure will also allow a more precise tuning of the gap.

References

[1] T. Mattila *et al.* A 12 MHz Micromechanical bulk acoustic mode oscillator, *Sensors and Actuators A*, **101**, 1 (2002)

[2] M. Koskenvuori *et al.* Enhancing the electromechanical coulping in bulk acoustic mode microresonator, *Proc. Eurosensors XVI*, 383 (2002)

[3] D. Galayko *et al.* High-frequency high-Q micro-mechanical resonators in thick epipoly technology with post-processing gap adjustment , *Proc. Micro Electro Mechanical Systems, The Fifteenth IEEE International Conference on*, 665 (2002)

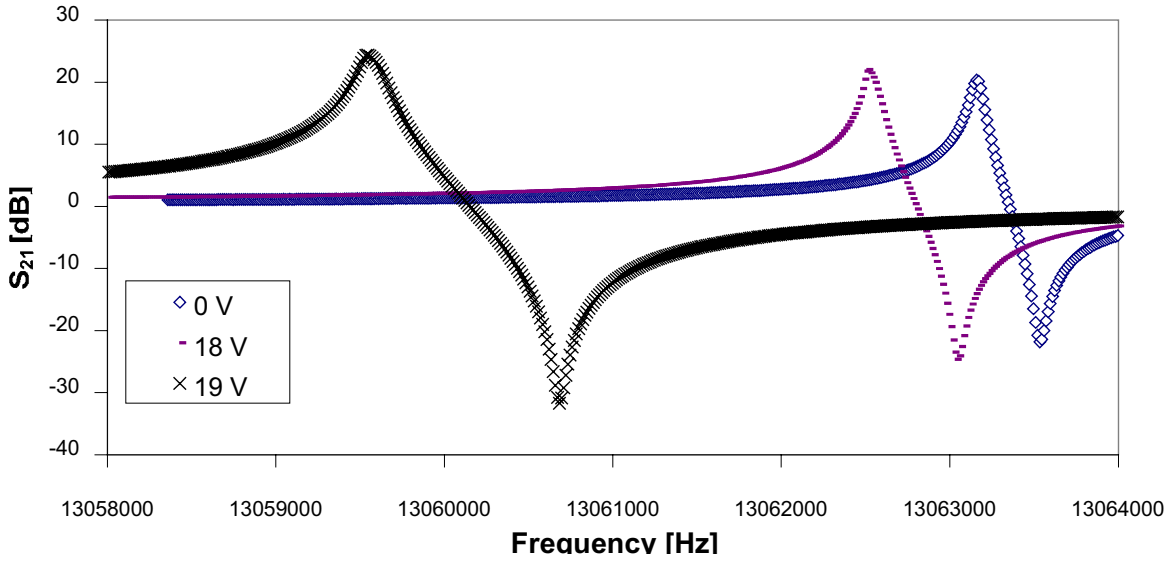

Fig 2. Measured transmission data from a resonator with gap adjustment voltages of *Uadj* = 0 V, 18 V and 19 V. The pull-in behaviour can easily be seen at U_{adj} = 19 V.

Delta-sigma modulation in the sensor feedback loop

A. Cerman, A. Kuna, P. Ripka

Czech Technical University, Dept. of Measurement, Technicka 2, 166 27, Prague 6
email: xcermana@feld.cvut.cz http://measure.feld.cvut.cz/groups/maglab

Summary: *This paper presents a modular fluxgate magnetometer with digitization realized by delta-sigma modulation, which allows us to implement a magnetometer with Δ-Σ modulator inside or outside the sensor feedback loop. Comparison of the results from these two concepts gives us an answer to the question, if phenomenon of Δ-Σ modulator implementation to the sensor feedback loop can bring us some improvement or not.*

Keywords: *delta-sigma modulation, fluxgate magnetometer, digital magnetometer*
Category: *9 (System architecture, electronic interfaces, wireless interfaces)*

1 Introduction

Delta-sigma modulation is a technique used in the high-resolution analog-to-digital and digital-to-analog converters. But in the last several years it has been also applied in the sensor systems, where it is used for direct digitization. Output signal from such systems is a bit-stream, which can be analog or digitally post-processed for obtaining of analog or digital output information.

The main advantage of delta-sigma modulation is possible high-resolution, practically zero non-linearity and relatively simple implementation. The main disadvantage is relatively low frequency response of the system.

Fluxgate sensors are the most-sensitive magnetic sensors working in the room temperature [1]. If they are used in the feedback configuration, their dynamic range usually exceeds 120 dB (it is equivalent to more then 20 bits of resolution) and their non-linearity is less than 10 ppm; they may have frequency range of kHz.

Up to now the application of delta-sigma modulation in the fluxgate sensor feedback loop has been used for micro-sensors with the aim of integration of the whole system (including sensor and interface) to one chip. The results from these projects show, that the limiting factors of these systems are the parameters of used sensors and the potential of interface is not by far reached [1] [2].

If we want to use full potential of the interface, we must use it with standard size precise fluxgate sensors. But question is, if it brings any improvement compare to commonly used digitization of fully analog feedback fluxgate magnetometers output by using of high-resolution A/D converters.

2 Delta-sigma modulation in the fluxgate sensor feedback loop

Basic block diagram of the interface with delta-sigma modulator in the sensor feedback is shown in Fig. 1. System consists of a sensor, output signal analog processing (in case of fluxgate sensor it is amplification and phase sensitive detection), an integrator, a delta-sigma modulator, a 1-bit digital-to-analog converter and a feedback analog low-pass filter. A generator and an excitation drive are also particularity of fluxgate sensor.

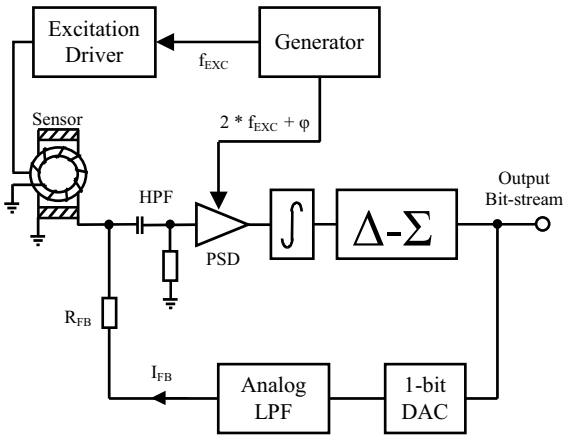

Fig. 1. Sensor interface with Δ-Σ modulator

Compared to the standard analog feedback of the fluxgate magnetometer described for example in [1], the modulator, the 1-bit DAC and the feedback LPF are added into the feedback loop. These additional blocks increase the system order, which brings problems with system stability. But this solution has also one advantage – integrator in the negative feedback loop together with n-order Δ-Σ modulator can bring about (n+1)-order noise

shaping of quantization noise. But this advantage is achieved only if the correct system mode is set (see [3]).

3 Magnetometer with precise fluxgate sensor and delta-sigma modulation

Our magnetometer with standard size precise fluxgate sensor and Δ-Σ modulation directly comes out from the block diagram shown in Fig. 1. This magnetometer is solved as a modular system, which consists of several blocks realized on separate PCBs (see Fig. 2. and Fig. 3.). This solution allows us to build system with modulator outside the feedback loop (standard fully analog fluxgate magnetometer with consequential digitization of its output) and with modulator inside the feedback loop as was described above. Resulting data will be used for comparison of both concepts.

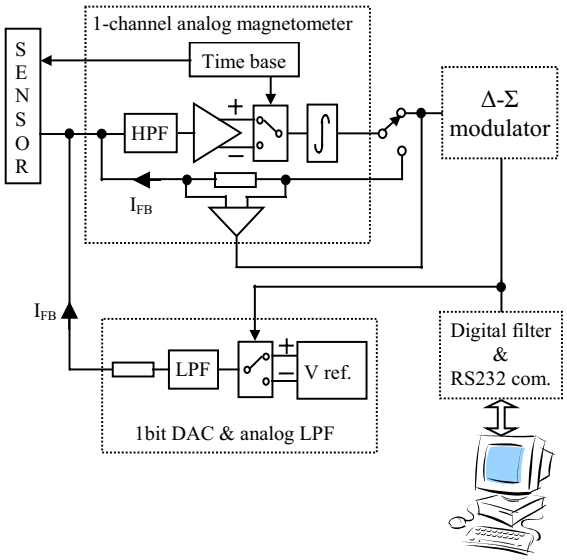

Fig. 2. Modular system with possibility of Δ-Σ modulation inside or outside the feedback loop

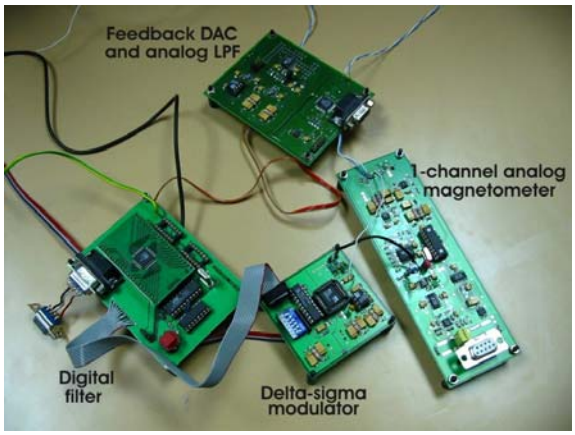

Fig. 3. Modular fluxgate magnetometer with Δ-Σ modulation

As Δ-Σ modulator and digital filter we used ADC system made by Analog Devices, which has nominal resolution of 24 bits. This system consists of two ICs – AD1555 (4th-order Δ-Σ modulator) and AD1556 (digital filter with serial data output). A board with digital filter also includes microprocessor, which controls digital filter modes and handles communication with PC. This two-board A/D converter has effective resolution of 20.3 bits (dynamic range 124 dB) with sampling frequency of 250 sps.

The first tested magnetometer was the magnetometer with Δ-Σ modulator outside the feedback loop. The dynamic range of the whole system (including magnetometer and digitizer) is 110 dB (ie. 18 bits) – measured with the sensor placed in the 6-layer permalloy magnetic shielding. As the effective resolution of the digitizer is 20.3 bits, the limiting factor of the whole system is analog magnetometer, actually its noise. Linearity error is less then 0.01 %. Long time stability is in range ±1.5 nT measured during 6 hours and also with the sensor inside the magnetic shielding. Measuring range of this magnetometer is ±100 μT.

At the present time the configuration with Δ-Σ modulator inside the feedback loop has been measured and tested. After finishing of all tests we will be able to decide if Δ-Σ modulation inside the feedback loop can bring some improvement or not.

4 Conclusion

The principle of application of the Δ-Σ modulation in the sensor feedback loop was described and the modular magnetometer with possibility of configuration with modulator inside or outside of the sensor feedback was designed and has been tested. The results from these two concepts will be compared in the final manuscript. First results show, that adding of the modulator to the feedback loop (and also necessary DAC and LPF) does not bring any improvement of the system parameters, but brings a problem with feedback stability and makes the system more complicated.

References

[1] P. Ripka et al.: Magnetic sensors and magnetometers, *Artech, Boston*, 2001

[2] Kawahito S., Maier Ch., Schneider M., Zimmermann M., Baltes H.: A 2-D CMOS Microfluxgate Sensor System for Digital Detection of Weak Magnetic Fields, *IEEE Journal of Solid-state Circuits,* Vol. 34, No. 12, December 1999

[3] S. Kawahito, A. Cerman, and Y. Tadokoro*:"* A Digital Fluxgate Magnetic Sensor Interface Using Sigma-Delta Modulation for Weak Magnetic Field Measurement", *IMTC 2002, Anchorage, Alaska*, Proc. Vol. A, pp 257-260

Towards a distributed architecture for MEMS integration

B. Lorente[2], J.Oliver[2] and C. Ferrer[1,2]

[1]Centre Nacional de Microelectrònica (CNM-IMB), CSIC
[2]Dept. Informàtica. Universitat Autònoma de Barcelona (UAB)
08193 Bellaterra (Barcelona), Spain
email: carles.ferrer@cnm.es http://www.cnm.es/imb

Summary: *Our main objective in this work has been to develop a distributed architecture for MEMS integration based on a hierarchical communication system. This communication system is based on the use of a dedicated sensor bus composed by only two wires. The reduced number of wires is an extraordinary advantage because produce a minimal interconnection between all the components and as a consequence the size of the microinstrument becomes smaller. The use of distributed architecture permits to develop a flexible and modular solution to integrate sensors and actuators and the data processing.*

Keywords: *distributed architectures, smart sensors, microsystems interface.*
Category: *9 (System architecture, electronic interfaces and wireless interfaces)*

1 Introduction

Silicon technologies make possible to produce sensing microdevices combining extreme sensitivity, accuracy and compactness devices. MEMS: Microelectromechanical systems offer a number of benefits including reducing mass, volume, and power consumption; greater redundancy of system functions and simpler architectures. In view of their remarkable characteristics, it can be expected that such "micro-sensors" will be used extensively wide spread number of applications if an adequate solution is found to reduce the design costs and simplify the electrical interfacing [1],[2],[3].

The problem of interfacing microdevices, as requisite to manufacture and integrate fully functional microsystems, can be separated in the following two levels: the electronic interface and the technological interface, that permits to interconnect different types of microdevices and their associated circuitry.

For the electronic interface, two main interconnection architectures exist: a classical architecture where the sensed data are multiplexed, conditioned and digitized using a dedicated microcontroller, and a distributed architecture where a bus organized system is used. The second approach introduces the advantages of modularity and interchangeability as it permits a flexible interconnection applicable to different sets of microsystems (see Fig. 1).

The main objective of this paper is to show an architectural approach based on the use of a methodological communication system between sensors and actuators that can be applied in the development of micro instrumentation. At this level we apply the concept of smart sensors. An smart sensor is a device which is added a simple interface that allow to connect the sensor to the bus sensor without causing any incompatibility or difficulty to adapt the new element to the bus.

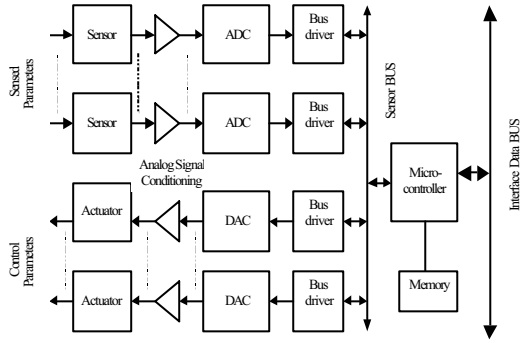

Fig. 1. Distributed architecture.

The global communication system implements a hierarchical protocol communications from the microsystem's devices to the main host. This communication system includes the bus sensor to aid to the development of each micro instrument and an instrumentation bus in other to connect all the microinstruments to the main host.

2 Bus sensor development

The bus sensor has to be a bus that allows transmitting commands, addresses and data. It has to permit the intercommunication between sensors, actuators and a dedicated microcontroller, in such a way that they can communicate to react to the input events received. The terminals of the communication system will be sensors and actuators and the device that makes the join, the microcontroller. In the microcontroller there is to be a control algorithm to give the appropriated commands to sensors/actuators and allow them the response in real time and also it would permit to add local processing with the data obtained by the sensors before to be transmitted to the main host.

So, we will make the design of the communication bus protocol and the appropriated drivers for all the elements we want to interconnect with the bus sensor [4]. These elements are smart sensors (slaves) and the microcontroller (master), to prove the reaction of the final comunication's elements. These drivers will allow giving certain intelligence to the sensor/actuator, making smart sensors/actuators (see Fig. 2).

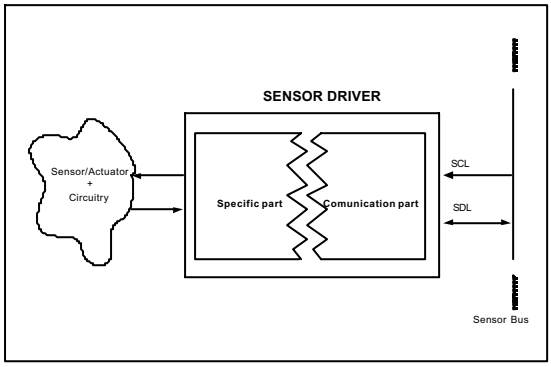

Fig. 2. Smart sensor development.

To make a real time system, the implemented drivers have to give a quick response, so the ideal communications will be at least 1 MHz. This low rate of transmission is due to the low volume of data if we compared the application with another one that requires a high volume of data. With this sensor bus we will integrate discrete sensors that will measure parameters with a low variation rate instead of the array of sensors (p.e. CCDs, etc.) that produce a very high amount of data to be transmitted. So, the chosen data rate is enough to transmit the total amount of data produced by a limited number of sensors

3 Architecture development

To make the communications design system we decided to make a topology bus. In this topology the elements that form the bus are linearly connected. The information frames are propagated trough the bus reaching all nodes (master and slaves). Every node of the bus has to read the frame and identify if the frame is for itself. So they monitor the bus.

In the protocol is not implemented any control through the data transmitted, supposing a very low BER (Bit Error Rate) and in case of error the superiors levels nets will correct the mistakes. This allows to make simpler the protocol and in consequence, with less volume in final implementation, for a better integration.

If we interconnect them in topology bus we can put more sensors, so the microcontroller is not so saturated as in other topology, with signals from different sensors. In that way we can introduce a hierarchical interconnection systems composed by the interconnection sensor level and the system connection level (see Fig.3). With the sensor bus presented previously, the lower parts of the system has been minimized giving more control while we go climbing to the highest parts of the hierarchy.

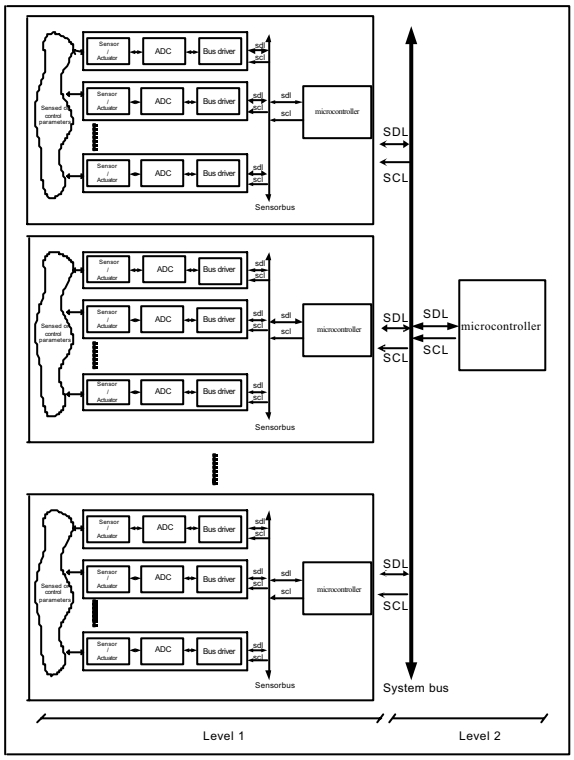

Fig. 3. Sensor level + system connection level.

Acknowledgements

The Spanish CICYT project nº TIC-2002-01048 had financed this work.

References

[1] J. J. Simonne, A Systems Approach to Microsystems Development, chapter 7, in microengineering aerospace systems, editor H. Helvajian, ed. Aerospace Press, CA, USA, 1999.

[2] M. Schlegel, G. Hermann, D. Muller, Multiple Architecture Modeling Design method for Mixed Signal and Multi Domain System Simulation-First Solutions, *Proceedings of the International MEMS Workshop*, Singapore, pp.662-667, 4-6 July 2001.

[3] S.D. Senturia, Microsystem Design, Kluwer Academic Publishers, USA, 2001.

[4] C. Ferrer, B. Lorente, Smart sensors development based on a distributed bus for microsystems applications, *Proceedings of the SPIE's First International Symposium on Microtechnologies for the New Millennium 2003: Smarts Sensors, Actuators and MEMS*. Maspalomas,Gran Canaria, Spain, 19-21 May 2003.

Combined pH-Image Sensor based on Pass-Transistor Operation of ISFET

Arkadiy Morgenshtein[1], Uri Dinnar[1], Claudio G. Jackobson[1] and Yael Nemirovsky[2]

[1] Bio-Medical Engineering Department, Technion, Haifa, Israel
[2] Electrical Engineering Department, Technion, Haifa, Israel
E-mail: arkadiy@tx.technion.ac.il

Summary: *Combined ISFET-APS sensor – a novel technique for simultaneous pH and image monitoring in CMOS ISFET-based Microsystems is presented. The operational concept is based on modulation of V_T drop by pH fluctuations in Pass Transistor ISFET. The operational concept is followed by SPICE simulation results and by applicability discussion. The ability of the combined simultaneous monitoring of images and pH levels expands the variety of clinical applications in which the pH biotelemetry can contribute, and allows implementation of array-type multiple-mode sensing for biomedical applications.*

Keywords: *ISFET, image, microsystem, applications*
Category: 10 *(Applications)*

1 Introduction

The ability of combined ion and image sensing is an important challenge in the development of advanced biotelemetry systems. The design of image sensors in standard CMOS technology is been under extensive research during last decade, basing on Active Pixel Sensor (APS) as the common structure of the CMOS image sensor. In this study a novel concept of integration of the ISFET sensor in the structure of the APS is developed and analyzed. The novel sensor allows a simultaneous chemical and image monitoring by applying the ISFET in Pass Transistor configuration and using the threshold drops in the original APS structure.
First, the APS review is presented followed by the structure of the combined ISFET-APS sensor. The operational concept and simulation results are demonstrated. Finally, the applicability analysis of future biotelemetry microsystems is presented.

2 Combined ISFET-APS

The structure of the APS 0 is shown in Fig. 1. a. The operation is based on the charge integration mode of a photodiode. Before the integration cycle, the diode is been reset to a high voltage by the reset switch M1. The diode and its correlating node are represented by: (a) the sensing capacitance, (b) the current source that is function of photon flux during the illumination and the diode area. After the reset phase stops, the photodiode is discharged according to:

$$C \cdot \frac{dV(t)}{dt} = -i_{photo}$$

The source follower M2 acts as a voltage buffer that drives the output.
Resetting to high V_{DD} voltage by NMOS transistor, as it mostly done in APS, results in losing the range of reset voltage on the photodiode to a value of $V_{DD} - V_{T_{M1}}$, where $V_{T_{M1}}$ is the threshold voltage of the reset transistor operating as Pass Gate. An additional $V_{T_{M2}}$ drop occurs in the output of the sensor because of the source follower.
The threshold drop is considered as an undesired limitation on the dynamic range of the image sensor. However, this drop is an important benefit in ISFET-based sensors [2]. In order to take a full advantage of this effect, the reset MOSFET transistor in the APS structure has to be replaced by ISFET sensor, which will operate in a similar way as reset switch for image sensor, while producing additional data on pH level via the threshold voltage drop.
The structure of the combined ISFET-APS sensor is shown in Fig. 2. The reset transistor M2 is replaced by ISFET sensor. The gate signal of the switch is applied to the reference electrode. The electrode is common for all the ISFETs in the sensors array. This triggers the requirement for additional change in APS operation: the single reference electrode has to be constantly biased, thus the pulsation of reset signal has to be applied to the drain of the reset ISFET, while the gate is constantly kept high (for n-type sensor).

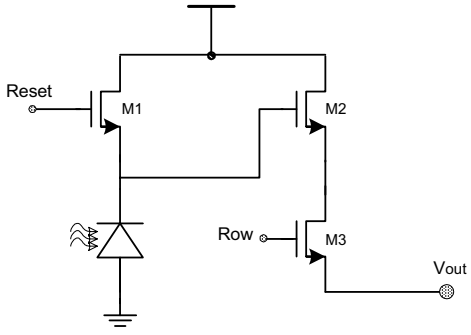

Fig. 1. Structure of the APS sensor.

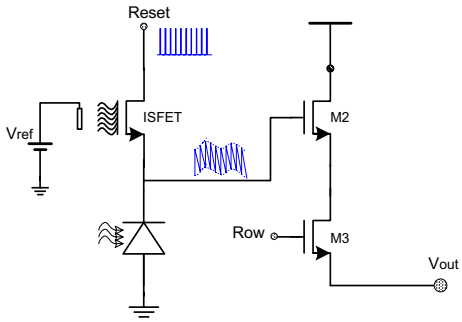

Fig. 2. Structure of the combined ISFET-APS sensor

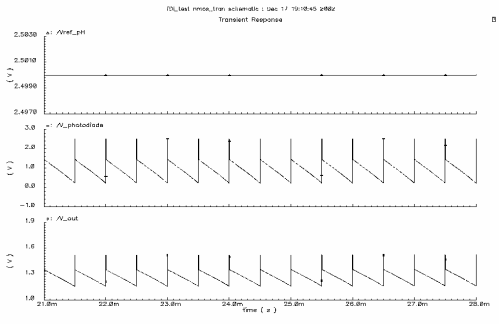

Fig. 3. Transient simulations of image APS sensor

The ISFET sensor is operating as reset transistor, producing a V_T drop in the initial voltage of the diode before the integration. Thus, a modulation of a signal is obtained, while the pH fluctuations influence the upper peak values of the signal in the Reset phase.

After the reset, the Integration phase begins, in which the capacitor is been discharged from the initial value, which was determined by pH value during the Reset phase, to a lower value which is determined by the intensity of the illumination. The operation in the Integration phase is identical to a regular operation of APS in image sensor. Every cycle can be referred as a simultaneous sampling of the values of pH and illumination in a certain location and time.

The APS circuit was implemented in 0.5µm CMOS technology with $3V_{P-P}$ voltage supply. SPICE simulations were performed during the verification of the combined sensor. Fig. 3. presents the transient simulations of regular APS sensor operating in constant illumination. The slope and the overall voltage change during the integration are equal in each cycle for constant illumination. In case of regular APS without pH sensor, the initial and the final values of the integration are equal as well.

The combined ISFET-APS sensor was simulated with AC waveforms imitating the pH-caused fluctuations in V_T of the ISFET. Square wave was applied to the drain to provide the Reset and Integration phases. As a result of pH fluctuations, the upper bound of the output signal is modulated, due to varying V_T drop, and gets the shape and values similar to the changes in V_T of the ISFET. The simulation in Fig. 4. shows the detailed response of the combined sensor to sinus fluctuations in pH, while the illumination is constant. It can be seen, that due to the constant illumination, the slope and the value of the discharge of capacitor are equal in every cycle. The signal is reduced by a certain gain as it passes through the source follower. The responses of both pH and image signals are preserved in the output of the APS.

The ability of the combined simultaneous monitoring of images and pH levels expands the variety of clinical applications in which the pH biotelemetry can efficiently contribute [3]. The measurement of pH levels correlated with image monitoring of the brain surface, allows an efficient locating and identification of trauma injuries in neurosurgery.

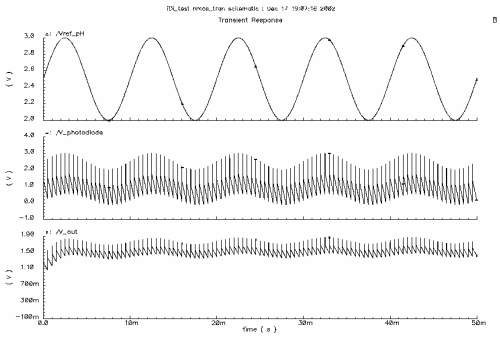

Fig. 4. Response to pH fluctuations of the ISFET-APS sensor with constant illumination.

The combined of pH-image sensor in a biotelemetry pill will allow an efficient and convenient monitoring of gastro-intestinal tract. Combining of the ISFET and APS sensors in arrays with 10-20µm grid will also provide a platform for high-performance recording systems for neuronal monitoring.

3 Conclusions

A concept of novel chemical-image sensor was developed in this study. The combined sensor is based on integration of ISFET sensor as functional part of APS image sensor. The operational concept is based on modulation of V_T drop by pH fluctuations in Pass Transistor ISFET. The verification was performed by SPICE simulations, showing an accurate response of the combined sensor to pH fluctuations. The design allows implementation of array-type multiple-mode sensing for various monitoring applications.

References

[1] Z. Zhou, B. Pain, E. Fossum: A CMOS imager with on-chip variable resolution for light-adaptive imaging, *IEEE International Solid-State Circuits Conference*, pp. 174-175,1998.

[2] A. Morgenshtein, U. Dinnar, Y. Nemirovsky: ISFET Operation in Pass-Transistor Mode without Readout Circuits, submitted to *Eurosensors XVII*, 2003.

[3] P. Bergveld, A. Sibbald: Analytical and Biomedical Applications of Ion-Selective Field Effect Transistors, *Comprehensive Analytical Chemistry*, vol. 12, 1988.

Shape measurement on large surfaces : a new algorithm

S. Pavageau[1], R. Dallier[1], N. Servagent[1] and T. Bosch[2]

[1] Ecole des Mines, Subatech, 4 rue Alfred Kastler, BP 20722, 44307 NANTES cedex 3, France
email: sabrina.pavageau@emn.fr
[2] ENSEEIHT-LEN7, Laboratoire d'Electronique, 2 rue Charles Camichel, BP 7122,
31071 TOULOUSE cedex 7, France

Summary: *We describe a method for profiling large and relatively flat surfaces. For this purpose, the measurement method is based on fringe projection and phase shifting technique. A new algorithm has been also developed to bypass the calibration step.*

Keywords: *fringe projection, profilometry, object reconstruction.*
Category: *10 (Applications)*

1 Introduction

Several optical methods exist which can be employed for the determination of object shapes and profiles [1]. They have the advantages of being non-contact, and rapidly acquiring spatially dense data on large and small surfaces. This article presents a shape measurement method for large and flat surfaces based on the technique of fringe projection. This application forms part of an important stage of a wider research project, dedicated to fundamental research in particle physics, and requires the building of a large detector system whose structural elements are carbon sandwich panels. Controlling the flatness of these large panels (2450*450 mm) is thus essential. The flatness criterion has been determined to be better than 150µm.m^{-1}.

The fringe projection method has been widely exploited for small objects measurements [2]. However, due to some inherent calibration difficulties, relatively few published work have been reported on large area measurements using this method. We report in this abstract a new algorithm which permits the profile of objets to be reconstructed with relative ease. Theoretically, the algorithm may be applied for profiling objects of any arbitrary size. The theory and principles associated with our proposed method are thus discussed.

2 Fringe pattern analysis

Sinusoidal fringes are projected onto the objet from one direction and viewed, with a CCD camera, from another direction (fig 1). These fringes are obtained by direct illumination of an optical grating and projected onto the object whose profile is to be determined. For object surfaces which are deformed, the projected fringes, and hence, their intensities are modulated accordingly.

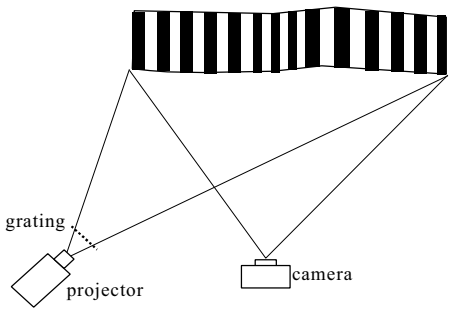

Fig. 1. Scheme of fringe projection.

This resulting intensity distribution is then recorded by the CCD camera and can be given by the following expression

$$I(x,y) = a(x,y) + b(x,y).\cos[\phi(x,y)] \quad (1)$$

where *a(x,y)* and *b(x,y)* are the fringe pattern average and modulation intensities and $\phi(x,y)$ is the phase containing the surface relief deformation.

To extract the phase $\phi(x,y)$ from the intensity distribution, we use a phase shifting method, where the phase is calculated for each pixel.

To determine the phase, several consecutive sets of fringes, each with a constant and pre-determined phase-shift, are projected onto the object. Among the various algorithms available, we have chosen to work with the windowed discrete Fourier transform (WDFT) [3] given by the following expression

$$\phi(x,y) = \arctan\left[\frac{-\sum_{k=1}^{N-1} k.(I_{k-1}(x,y) - I_{2N-k-1}(x,y))\sin\left(\frac{2k\pi}{N}\right)}{N.I_{N-1} + \sum_{k=1}^{N-1} k.(I_{k-1}(x,y) + I_{2N-k-1}(x,y))\cos\left(\frac{2k\pi}{N}\right)}\right] \quad (2)$$

where I_K is the kth fringe intensity recorded and $\delta = \frac{2\pi}{N}$ is the phase-shift. $\phi(x,y)$ lies within the range $[-\pi, \pi]$.

The 2π phase jump, introduced by the "arctan" term, must be removed by the process known as phase unwrapping to recover the surface heights. This process consists of adding or subtracting an adequate multiple of 2π. The result of this process is a phase map, a continuous two-dimensional phase variation of the object surface.

The phase map is then processed to give a set of depth information from which the desired object profile and flatness can be obtained. For small objects, a physical reference plane is used to calibrate the set-up and a simple relation can be found between the object profile and the phase map. However, this method is no longer applicable to objects of large dimensions. Section 3 describe the technique we have employed to profile large object surfaces.

3 Reconstruction algorithm

To obtain the shape of an object from the given phase map, we consider the complete theoretical approach. We also define an exact transformation relating each point on the original grating (known as projector reference) to their respective image points as observed by the camera (receiver reference). This transformation is determined by assuming a virtual plane object surface and leads to a theoretical phase expression (ϕ_{th}). This in turn results in an expression for the height variation (z_{th}) of this object. Each expression depends on the associated geometrical parameters of the experimental set-up (magnifications, grating pitch, distances between the three reference planes : object-projection planes and object-receiver planes, projection and receiving angles), as well as those of the object itself (α, φ, d, corresponding to object angle with respect to the horizontal, the object tilt angle and the distance from the reference origin, respectively).

Assuming that the above parameters are known, we can then calculate the height variation and the profile of the object. The former parameters can be estimated with reasonable ease. Although the geometrical parameters of the object are not easily available from direct measurements, they can, however, be inferred from unwrapped phase. In order to do this, the object surface is divided into many equal elementary planes, P_i, where i represents the i^{th} plane. Since only three points, A_i, B_i, C_i suffice mathematically for the description of a plane, the theoretical phase and height variation expressions for each individual point can therefore be solely determined by the three unknown parameters (α, φ, d as describe earlier). To obtain a good estimate of the above parameters for each plane, we have adopted the following procedure :

1- Define three starting unknowns : α_0, φ_0 and d_0.

2- Then calculate the theoretical phases for the three points A_i, B_i, C_i, given by $\phi_{th_{A_i}}(\alpha_0,\varphi_0,d_0)$, $\phi_{th_{B_i}}(\alpha_0,\varphi_0,d_0)$, $\phi_{th_{C_i}}(\alpha_0,\varphi_0,d_0)$, respectively.

3- Obtain the experimental phases of the three points, given by $\phi_{\exp_{A_i}}, \phi_{\exp_{A_i}}, \phi_{\exp_{A_i}}$, from the phase shifting and unwrapping schemes.

4- The parameters α_i, φ_i and d_i, for a plane P_i, can then be found by fulfilling the below conditions :

$$\begin{cases} \phi_{\exp_{A_i}} = \phi_{th_{A_i}} \\ \phi_{\exp_{B_i}} = \phi_{th_{B_i}} \\ \phi_{\exp_{C_i}} = \phi_{th_{C_i}} \end{cases} \quad (3)$$

5- Concretely, in order to achieve the best possible approximation of the parameters, we exploited a minimising function given by

$$F(\alpha,\varphi,d) = \left|\phi_{th_A}(\alpha,\varphi,d) - \phi_{\exp_A}\right|^2 + \left|\phi_{th_B}(\alpha,\varphi,d) - \phi_{\exp_B}\right|^2 + \left|\phi_{th_C}(\alpha,\varphi,d) - \phi_{\exp_C}\right|^2 \quad (4)$$

where $\phi_{\exp_A}$, $\phi_{\exp_B}$, $\phi_{\exp_C}$ are the measured phases at points A, B and C, respectively, during fringe projection, and ϕ_{th_A}, ϕ_{th_B}, ϕ_{th_C} are the corresponding calculated phases.

The surface height for an individual plane, z_i, can thus be calculated as a function of the geometrical parameters, α_i, φ_i and d_i. Subsequently, the height values for other elementary planes, z_{i+1}, …, z_{i+n}, can be similarly calculated. The entire surface profile of the object can finally be reconstituted from the calculated heights of all elementary planes.

4 Conclusion

This abstract presents a method for full-field shape measurements on large surfaces by exploiting structured light projection. It is non-contact, rapid and can be easily automated. Our algorithm reported here, developed for relatively flat surfaces, does not require any cumbersome calibration procedures and its principal advantage is that it can be applied on both large and small surfaces. Experimental work is currently in progress to validate our algorithm.

References

[1] F. Chen, G.M. Brown, M. Song. Overview of three-dimensional shape measurement using optical methods. *Optical Engineering*. 39 (2000) pp.10-22.

[2] C. Quan, X.Y. He, C.F. Wang, C.J. Tay, H.M. Shang. Shape measurement of small objects using LCD fringe projection with phase shifting. *Optics Communications*. 189 (2001) pp. 21-29.

[3] Y. Surrel. Fringe analysis. In : Photomechanics. Berlin, Springer. 1999, pp.55-102.

A

B

C

D

E

F

G

H

I

J

K

L

M

N

O

P

Q

R

S

T

U

V

W

Y

Z